

REPORT DOCUMENTATION PAGE

Form Approved
OMB No. 0704-0188

Public reporting burden for this collection of information is estimated to average 1 hour per response, including the time for reviewing instructions, searching existing data sources, gathering and maintaining the data needed, and completing and reviewing the collection of information. Send comments regarding this burden estimate or any other aspect of this collection of information, including suggestions for reducing this burden, to Washington Headquarters Services, Directorate for Information Operations and Reports, 1215 Jefferson Davis Highway, Suite 1204, Arlington, VA 22202-4302, and to the Office of Management and Budget, Paperwork Reduction Project (0704-0188), Washington, DC 20503.

1. AGENCY USE ONLY (Leave blank)		2. REPORT DATE 30 Sept 96	3. REPORT TYPE AND DATES COVERED Final; 01 Mar 96 to 31 Jul 96	
4. TITLE AND SUBTITLE 1996 Solid Freeform Fabrication Symposium Proceedings			5. FUNDING NUMBERS G N00014-1-0441	
6. AUTHOR(S) D.L. Bourell, J. Beaman, H.L. Marcus, R. Crawford, J. Barlow				
7. PERFORMING ORGANIZATION NAME(S) AND ADDRESS(ES) University of Texas at Austin Mechanical Engineering MC C2200 Austin TX 78712-1063			8. PERFORMING ORGANIZATION REPORT NUMBER	
9. SPONSORING/MONITORING AGENCY NAME(S) AND ADDRESS(ES) Office of Naval Research Ballston Center Tower One 800 North Quincy Street Arlington VA 22217-5660			10. SPONSORING/MONITORING AGENCY REPORT NUMBER	
11. SUPPLEMENTARY NOTES				
12a. DISTRIBUTION/AVAILABILITY STATEMENT Approved for public release			12b. DISTRIBUTION CODE	
13. ABSTRACT (Maximum 200 words) The Seventh Solid Freeform Fabrication (SFF) Symposium, held at The University of Texas in Austin on August 12-14, 1996, was attended by over 200 national and international researchers. Papers addressed SFF issues in computer software, machine design, materials synthesis and processing, and integrated manufacturing. The continued growth in the research, application and development of SFF approaches was readily apparent from the increased participation over previous years and the diverse domestic and foreign attendees from industrial users, SFF machine manufacturers, universities, and government. The excitement generated at the Symposium reflects the participants' total involvement in SFF and the future technical health of this growing technology. The Symposium was again organized in a manner to allow the multi-disciplinary nature of the SFF research to be presented coherently, with various sessions emphasizing computer issues, machine topics, and the variety of materials aspects of SFF. We believe that documenting the constantly changing state of SFF art as represented by these Proceedings will serve both the people presently involved in this fruitful technical area as well as the large flux of new researchers and users entering the field.				
14. SUBJECT TERMS Solid Freeform Fabrication, SFF, Rapid Prototyping			15. NUMBER OF PAGES 626	
			16. PRICE CODE	
17. SECURITY CLASSIFICATION OF REPORT Unclassified	18. SECURITY CLASSIFICATION OF THIS PAGE Unclassified	19. SECURITY CLASSIFICATION OF ABSTRACT Unclassified	20. LIMITATION OF ABSTRACT UL	

Solid Freeform Fabrication Proceedings

September 1996

Solid Freeform Fabrication is an important and totally integrated approach to design, materials processing and manufacturing. Research results related to it are contained in this proceedings of the SFF Symposium held in Austin, Texas on August 12-14, 1996

SFF Topics covered in the Symposium include:

Applications
Tooling
Processing and Process Development
Materials
Modeling

David L. Bourell, Joseph J. Beaman
Harris L. Marcus, Richard H. Crawford
and Joel W. Barlow, Editors

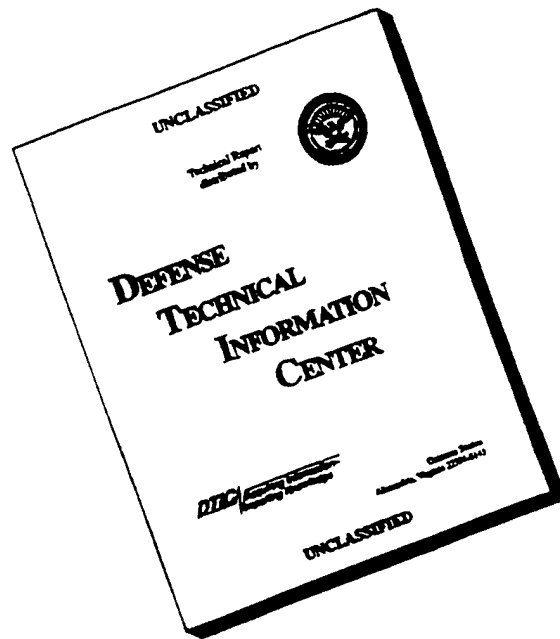
© 1996 The University of Texas at Austin

All rights of reproduction in any form are protected by U.S. Copyright Laws.
Permission to copy, all or portions of the proceedings contents must be obtained
from the authors and The University of Texas at Austin.

Library of Congress ISSN 1053-2153

19961120 033

DISCLAIMER NOTICE



**THIS DOCUMENT IS BEST
QUALITY AVAILABLE. THE
COPY FURNISHED TO DTIC
CONTAINED A SIGNIFICANT
NUMBER OF PAGES WHICH DO
NOT REPRODUCE LEGIBLY.**

Table of Contents

	<u>Page</u>
<i>Preface</i> -----	vi
<i>Applications</i>	
A Time, Cost and Accuracy Comparison of Soft Tooling for Investment Casting Produced using Sterolithography Techniques J. Male, H. Tsang, G. Bennett -----	1
Stereolithography Model in Presurgical Planning of Craniofacial Surgery Ian Jackson, Huinian Xiao, Mansour Ashtiani, Luc Berben -----	9
Biocompatibility of SLS-Formed Calcium Phosphate Implants G. Lee, J.W. Barlow, W.C. Fox, T.B. Aufdermorte -----	15
Using Fabricators to Reduce Space Transportation Costs David S. McKay, Hubert P. Davis, Marshall Burns -----	23
Shape Deposition Manufacturing of Wearable Computers L. Weiss, F. Prinz, G. Neplotnik, P. Padmanabhan, L. Schultz, R. Merz -----	31
Development of Direct SLS Processing for Production of Cermet Composite Turbine Sealing Components - Part I T. Fuesting, L. Brown, S. Das, N. Harlan, G. Lee, J.J. Beaman, D.L. Bourell, J.W. Barlow, K. Sargent -----	39
Development of Direct SLS Processing for Production of Cermet Composite Turbine Sealing Components - Part II T. Fuesting, L. Brown, S. Das, N. Harlan, G. Lee, J.J. Beaman, D.L. Bourell, J.W. Barlow, K. Sargent -----	47
Gaining Competitive Advantage by Using Rapid Prototyping in Aircraft Modification Steven L. Smith, Jerri Paul -----	57
Fabrication of Parts Containing Small Features Using Stereolithography Jouni Partanen -----	63
GelCast Molding with Rapid Prototyped Fugitive Molds Vikram R. Jamalabad, Philip J. Whalen, John Pollinger, Mukesh K. Agarwala, Stephen C. Danforth -----	71
Rapid Prototyping of Mg/SiC Composites By a Combined SLS and Pressureless Infiltration Process M. Wohler, D. Bourell -----	79
Selective Laser Sintering of High Performance High Temperature Metals S. Das, N. Harlan, J.J. Beaman, D.L. Bourell -----	89

Tooling

Selective Laser Sintering of Metal Molds: The RapidTool™ Process	
Uday Hejmadi, Kevin McAlea-----	97
Structural Composites Via Laminated Object Manufacturing (LOM)	
Donald A. Klosterman, Richard Chartoff, Brian Priore, Nora Osborne, George Graves, Allan Lightman, Sung S. Pak, Jerry Weaver-----	105
Laser Deposition of Metals for Shape Deposition Manufacturing	
J. R. Fessler, R. Merz, A. H. Nickel, F.B. Prinz, L.E. Weiss-----	117
Free Form Fabrication of Metallic Components using Laser Engineered Net Shaping (LENS™)	
M. L. Griffith, D. M. Keicher, C. L. Atwood, J. A. Romero, J. E. Smugeresky, L. D. Harwell, D. L. Greene-----	125
Fast Production of Technical Prototypes Using Direct Laser Sintering of Metals and Foundry Sand	
Christian Wilkening-----	133
Direct Manufacturing of Metal Prototypes and Prototype Tools	
Fritz Klocke, H. Wirtz, W. Meiners-----	141
Freeform Powder Molding for Rapid Tooling	
Stephen J. Rock, Charles R. Gilman, Wojciech Z. Misiolek, Daniel F. Walczyk-----	149
Rapid Prototyping of Fine Ceramics -Slurry Casting using Silicon Rubber Mold-	
Takeo Nakagawa, Hiroyuki Noguchi-----	159
Slip Casting as a Rapid Tooling Process	
C. Ainsley and K. K. B. Hon-----	167
Wear & Failure Mechanisms for SL EDM Electrodes	
Alan Arthur, Phill Dickens, Chris Bocking, Richard Cobb-----	175
Rapid Prototyping Using Electrodeposition of Copper	
S.J. Dover, A.E.W. Rennie, G.R. Bennett-----	191
EDM Tooling by Solid Freeform Fabrication & Electroplating Techniques	
R. Ippolito, L. Iuliano, A. Gatto-----	199
Soft Tooling for Low Production Manufacturing of Large Structures	
Cheol H. Lee, Thomas M. Gaffney, Charles L. Thomas-----	207

Processing and Process Development

Recent Developments in Profiled-Edge Lamination Dies for Sheet Metal Forming	
Daniel F. Walczyk, David E. Hardt-----	215
Direct Feedback Control of Gas-Phase Laser-Induced Deposition	
J.L. Maxwell, J. Pegna, D. Messina, D. DeAngelis-----	227

Rapid Laser Forming of Titanium Near Shape Articles: LaserCast™	
M. A. House, E. J. Whitney, D. G. Krantz, F.G. Arcella-----	239
Rapid Prototyping Process Using Metal Directly	
A.F. Ribeiro, John Norrish -----	249
The Liquid-to-Solid Transition in Stereodeposition Techniques	
R. S. Crockett, P. D. Calvert -----	257
Processing of Piezocomposites via Solid Freeform Fabrication (SFF) Techniques	
A. Bandyopadhyay, R. K. Panda, V. F. Janas, S. C. Danforth, A. Safari-----	265
“Curved-Layer” Laminated Object Manufacturing®	
Gary Kalmanovich-----	273
Automating Sheet-Based Fabrication: The Conveyed Adherent Process	
Charles L. Thomas, Kenneth J. Hayworth -----	281
Laser Cutting of Ceramic Composite Layers	
Allan Lightman, Gyoowan Han-----	291
Make-up Fabrication of Big or Complex Parts Using the SLA Process	
W. L. Wang, J. Y. H. Fuh, Y. S. Wong, T. Miyazawa -----	299
Processing of Carbon Fiber Reinforced Composites by Three Dimensional Photolithography	
Chad Greer, Juli McLaurin, Amod A. Ogale -----	307
Design of Stereolithography Trees for Use in the Investment Casting of Stereolithography Patterns	
Christopher S. McDowell, Mark C. Boomer -----	313
Stereolithography System Using Multiple Spot Exposure	
Yoji Marutani, Takayuki Kamitani-----	321
A New SFF Process for Functional Ceramic Components	
S.C. Ventura, S.C. Narang, S. Sharma, J. Stotts, C. Liu, S. Liu, L-H. Ho, D. Annavajjula, S.J. Lombardi, A. Hardy, M. Mangaudis, E. Chen, L. Groseclose -----	327
Fused Deposition of Ceramics (FDC) for Structural Silicon Nitride Components	
M.K. Agarwala, A. Bandyopadhyay, R. vanWeeren, N.A. Langrana, A. Safari, S.C. Danforth, V.R. Jamalabad, P.J. Whalen, R. Donaldson, J. Pollinger -----	335
Solid Freeform Fabrication at the University of Connecticut	
Shay Harrison, James E. Crocker, Tariq Manzur, Harris L. Marcus -----	345
Metal Processing Using Selective Laser Sintering and Hot Isostatic Pressing (SLS/HIP)	
Ronald Knight, Joseph Wright, Joseph Beaman, Douglas Freitag-----	349

Progress in Computer-Aided Manufacturing of Laminated Engineering Materials Utilizing Thick, Tangent-Cut Layers	
Yong Zheng, Sanguen Choi, Brian Mathewson, Wyatt Newman -----	355
SFF Using Diode Lasers	
Tariq Manzur, Chandra Roychoudhuri, Harris Marcus -----	363
Solid State Lasers for Stereolithography	
Jouni Partanen-----	369
<i>Materials</i>	
Metal and Ceramic Components made via CAM-LEM Technology	
Z.E. Liu, P. Wei, B. Kernan, A. H. Heuer, J. D. Cawley-----	377
Fused Deposition of Ceramics and Metals: An Overview	
M.K. Agarwala, R. van Weeren, A. Bandyopadhyay, P.J. Whalen, A. Safari, S. C. Danforth -----	385
Improving the Thermal Stability of Somos™ 6110 Photopolymer Patterns	
Suresh Jayanthi, Bronson Hokuf , John Lawton -----	393
Curing Behavior of Ceramic Resins for StereoLithography	
G. Allen Brady, Tien-Min Chu, John W. Halloran-----	403
Microstructures and Strengths of Metals and Ceramics made by Photopolymer-based Rapid Prototyping	
Walter Zimbeck, Matthew Pope, R. W. Rice -----	411
Mechanical and Dimensional Characteristics of Fused Deposition Modeling Build Styles	
Eric Fodran, Martin Koch, Unny Menon -----	419
Recent Development in Extrusion Freeform Fabrication (EFF) Utilizing Non-Aqueous Gel Casting Formulations	
Greg E. Hilmas, John L. Lombardi, Robert A. Hoffman, Kevin Stuffle -----	443
Filament Feed Materials for Fused Deposition Processing of Ceramics and Metals	
M.K. Agarwala, R. van Weeren, A. Bandyopadhyay, A. Safari, S. C. Danforth, W.R. Priedeman -----	451
Forced Convection in Polymeric Powders	
Jeffrey L. Norrell, Kristen L. Wood, Richard H. Crawford, Theodore L. Bergman -----	459
Low Shrinkage, High Tg Liquid Crystal Resins for Stereolithography	
J. S. Ullett, R. P. Chartoff, J. W. Schultz, J. C. Bhatt, M. Dotrong, R. T. Pogue -----	471
<i>Modeling</i>	
Interfacing Reverse Engineering Data to Rapid Prototyping	
N. K. Vail, W. Wilke, H. Bieder, G. Jünemann -----	481

IVECS, Interactively Correcting .STL Files in a Virtual Environment Stéphane M. Morvan, Georges M. Fadel-----	491
An Adaptive Control Architecture for Freeform Fabrication J. C. Boudreaux-----	499
Thermomechanical Modeling of Successive Material Deposition in Layered Manufacturing R.K. Chin, J. Beuth, C.H. Amon -----	507
Process Insight About LOM Systems Chen Chi -----	515
Finite Element Analysis & Strain Gauging of the Stereolithography/Investment Casting System Richard Hague, Phill Dickens-----	523
Part Quality Prediction Tools for Fused Deposition Processing M. Atif Yardimci, Selcuk I. Gucer, Mukesh Agarwala, Stephen C. Danforth -----	539
Selective Laser Sintering Part Strength as a Function of Andrew Number, Scan Rate and Spot Size John Williams, David Miller, Carl Deckard -----	549
Finite Element Analysis of Curl Development in the Selective Laser Sintering Process K. W. Dalgarno, T. H. C. Childs, I. Rowntree and L. Rothwell -----	559
Modeling Simple Feature Creation in Selective Laser Sintering G. J. Ryder, M. Berzins and T. H. C. Childs -----	567
Extraction of Fault Patterns on SLS Part Surfaces Using the Karhunen-Loève Transform Irem Y. Tumer, Kristin L. Wood, Ilene J. Busch-Vishniac -----	575
Feature Extraction from Tessellated and Sliced Data in Layered Manufacturing Kamesh Tata, Georges Fadel -----	587
Parametric Representation of Part Contours in SLS Process Kenwei Chen, Richard H. Crawford, Joseph J. Beaman-----	597
Techniques for Improved Speed and Accuracy in Layered Manufacturing Andrei Novac, Srinivas Kaza, Zetian Wang, Cheol Lee, Charles Thomas-----	609
The Influence of Natural Convection and Radiation Heat Transfer on Sintering of Polycarbonate Powders J. L. Norrell, M. Kandis, T. L. Bergman-----	619
Keyword Index -----	629
Author/Attendee List -----	633

PREFACE

The Seventh Solid Freeform Fabrication (SFF) Symposium, held at The University of Texas in Austin on August 12-14, 1996, was attended by over 200 national and international researchers. Papers addressed SFF issues in computer software, machine design, materials synthesis and processing, and integrated manufacturing. The continued growth in the research, application and development of SFF approaches was readily apparent from the increased participation over previous years and the diverse domestic and foreign attendees from industrial users, SFF machine manufacturers, universities, and government. The excitement generated at the Symposium reflects the participants' total involvement in SFF and the future technical health of this growing technology. The Symposium organizers look forward to its being a continuing forum for technical exchange among the expanding body of researchers involved in SFF.

The Symposium was again organized in a manner to allow the multi-disciplinary nature of the SFF research to be presented coherently, with various sessions emphasizing computer issues, machine topics, and the variety of materials aspects of SFF. The demand for a forum at the SFF Symposium posed a conflict with the desire to maintain the meeting at three days. The compromise was to move to afternoon parallel sessions for the first time and to extend the meeting to three full days. The poster session was also expanded. We believe that documenting the constantly changing state of SFF art as represented by these Proceedings will serve both the people presently involved in this fruitful technical area as well as the large flux of new researchers and users entering the field.

The Japanese Technology Evaluation Center and its companion World Technology Evaluation Center at Loyola College, under a cooperative agreement with the National Science Foundation, assessed the state of SFF in Europe and Japan. Dr. Fritz Prinz of Stanford University chaired the study and a review of this assessment at the Symposium. The panel participants were Clint L. Atwood (Sandia National Labs), Richard Aubin (United Technologies Research Center), Joe Beaman (University of Texas), Robert L. Brown (The Gillette Company), Paul Fussell (Alcoa Technical Center), Allan Lightman (University of Dayton Research Institute), Emanuel Sachs (Massachusetts Institute of Technology), and Lee Weiss (Carnegie Mellon University). Slides of the original presentation and JTEC report ordering information is available on the worldwide web at <http://itri.loyola.edu/rp/top.htm>.

The editors would like to extend a warm "Thank You" to Gloria Gutchess for her detailed handling of the logistics of the meeting and the Proceedings, as well as her excellent performance as registrar and problem solver during the meeting. We also acknowledge the support efforts of Cindy Pflughoft throughout. We would like to thank the organizing committee, the session chairmen, the attendees for their enthusiastic contributions, and the speakers both for their significant contribution to the meeting and for the relatively prompt delivery of the manuscripts comprising this volume. We look forward to the continued close cooperation of the SFF community in organizing the Symposium. We also want to thank ONR through Grant No. N00014-96-1-0441, ARPA, and The Minerals, Metals and Materials Society and the University of Connecticut at Storrs for co-sponsoring the Symposium with the Mechanical Engineering Department and the Center for Materials Science and Engineering at the University of Texas at Austin.

The editors.

Organizing Committee

Joel Barlow	University of Texas at Austin
Joseph Beaman	University of Texas at Austin
David Bourell	University of Texas at Austin
Richard Crawford	University of Texas at Austin
Harris Marcus	University of Connecticut at Storrs

Advisory Committee

Mr. Dick Aubin	United Technologies Research Center
Dr. Robert Brown	The Gillette Company
Dr. Michael Cima	Massachusetts Institute of Technology
Dr. William Coblenz	Advanced Research Projects Agency
Dr. Sam Drake	University of Utah
Dr. Steven Fishman	Office of Naval Research
Mr. Sean O'Reilly	Ford Motor Company
Dr. Fritz Prinz	Stanford University
Dr. Emanuel Sachs	Massachusetts Institute of Technology
Mr. Greg Sanders	Lost Foam International
Dr. Susan Smyth	General Motors Corporation
Dr. Ralph Wachter	Office of Naval Research
Dr. Michael Wozny	National Institute of Standards and Technology

A Time, Cost and Accuracy Comparison of Soft Tooling for Investment Casting Produced Using Stereolithography Techniques

J. Male, H. Tsang*, G. Bennett

Centre for Rapid Design Manufacture, Buckinghamshire College of Higher Education, UK

*Formation Engineering Services Ltd, Gloucester, UK

Abstract

Investment casting is increasingly widely used in the production of metal prototypes in conjunction with rapid prototyping (RP) technologies. Some types of RP models can be used directly as sacrificial patterns in the casting process, but this can prove costly and time consuming where a number of castings are required.

Soft tooling such as resin tooling and silicon rubber tooling are used to produce a number of wax patterns for subsequent casting, using an RP model as the master. Stereolithography faced tools are starting to be used as in some circumstances they can offer time savings over other soft tooling methods. This paper aims to compare the costs and times taken to produce wax patterns for use in investment casting using the different soft tooling techniques and QuickCastTM build style for use as a casting pattern.

Introduction

Rapid prototyping allows several options for the investment casting process. The QuickCastTM build style that can be used with 3D Systems stereolithography (SL) machines can be used directly as patterns for investment casting. Some problems have been reported due to expansion during the burnout of the model. Patterns may also be produced by Selective Laser Sintering, Fused Deposition Modelling and Laminated Object Manufacture (Dickens *et al*). Producing the investment casting patterns by rapid prototyping can be very successful if only a few parts are needed. However, as the number of prototypes required increases, RP becomes increasingly expensive and time consuming. Soft tooling can then become useful because many wax patterns can be produced relatively quickly and cheaply once the tool is made.

The most common 'soft' methods of tooling are those of resin and silicon rubber. Recently, workers have started to experiment with SL faced tools backed with filled epoxy resin. Additionally, solid SL dies have been fitted to aluminium bolsters, and used as low pressure wax injection moulding tools.

The Direct Shell Production Casting (DSPC) technique can also be used to produce investment casting shells, but this also suffers from high costs when many castings are needed, but may also be used to make moulds directly (Sachs *et al*).

Two metal sintering processes have recently been reported which will enable the direct production of metal tools for wax injection moulding (Klocke *et al*).

Experimental Technique

A test part was chosen from a 'live' project which was suitable for the investment casting process and could not be moulded using a two part tool. It was decided that a four part tool would be required to release the part without the loss of any features. The design, consisting of a core, an 'L' shaped base/back, and two side plates was kept constant throughout the different types of tool made (see figure 4).

Resin Tool

Prior to construction, a sprue bush guide was fitted to the part. The resin tool sections are made by constructing a series of boxes around the SL part sequentially, that will define the split lines and outside edges of the first part of the tool. Location cones and studding to hold the tool together were embedded in the moulding box into each moulding box. Firstly, a metal filled epoxy gelcoat was applied to the surface, which was strengthened by applying six layers of glass fibre, laminated with epoxy resin. This shell was then filled with an epoxy resin/sand mix to create the solid tool section. This process takes 4-10 hours depending on the complexity of the part and moulding box. The resin is left to cure for 12 hours, until it is solid. The moulding box is removed, leaving the first part of the tool, with the SL model partially embedded in it. The next box is then constructed defining the next split lines and edges of the tool. This process then continues until all of the tool sections have been made.

The factors influencing the speed of manufacture of the tool are :

- The number of parts that will make up the tool
- The time taken for the resin to cure - about 12 hours.
- The time taken to construct the moulding box - a complex split line on a detailed part will require more time.
- The time taken to lay down the glass fibre matting - flat and gently curving parts are easily covered, where as bosses require more care, and therefore time.

Silicon Rubber Tool

Silicon rubber tools are widely used to make prototype and short run tools for use with gravity pour or low pressure injection if the mould is supported in a frame (Mueller), especially when polyurethane parts are required.

The tool is created by firstly making a moulding box that will define the outside edges of the tool. The split lines are then defined on the ACES SL part using scotch tape, coloured to make it easier to see in the silicon. The injection point is also defined and attached to the SL part at this point. The part is suspended in the moulding box, and silicon rubber is mixed, degassed, and poured around the part. The rubber is left to set for about 24 hours, which leaves the SL part encased in a solid rubber block. The rubber is cut down to the tape, with jagged lines, so that the tool will fit together well, and separated into its four parts.

The factors that control the speed of production of the tool are as follows:

- The time taken for the rubber to cure
- The complexity of the split line, which will increase the set-up time, and the time taken to cut the tool apart.

SL/Resin Tool

The SL/resin tool is made up from a SL mould face and mould box, which is then backfilled with a sand filled epoxy resin (Tsang *et al*).

The starting point of the SL/resin tool is the creation of the three dimensional solid of the part using a suitable CAD package. Then by using appropriate Boolean operations, the tool faces are generated, and given a wall thickness of >2 mm, and the side walls of the mould faces are drawn to create a cavity for the resin/sand to be poured into. The four parts are then made on the SLA and backfilled with sand filled epoxy resin. Because the location cones and studding for clamping the tool were not included in the SL parts, these four parts had to be backfilled sequentially, which added to the build time considerably.

The factors controlling the speed of manufacture of the tool are as follows:

- CAD time to produce a 3D representation of the tool faces.
- SLA build times
- Resin cure times

Injection of tools and resulting patterns

A moving platen top injection machine was used (a Maymar MV30), which has a closing force of 20 tons applied through the nozzle, and ran at a pressure of 250 psi, with the wax injected at approximately 80 °C. The wax used was a filled Dussek Campbell type 489. The resin tool was successfully injected with 15 waxes. There was no visible wear on the tool. The resin tool needed to be heated up to about 40 °C for the tool to fill, with a cycle time of about 5 minutes. However, after about 5 shots, the tool started to get too hot, and needed 'cooling off' periods.

As the silicon rubber tool would be unable to take the injection pressures, without enclosing it in a box, it was attempted initially to gravity pour the wax into the tool. This did not create sufficient flow to fill the mould, so the wax was poured into a reservoir connected to the tool, and a vacuum of about 0.2bar applied to an outlet on the other side of the tool. Several waxes have been produced using this vacuum casting process.

Unfortunately, the SL/resin tool exploded during the injection process.

QuickCast™ patterns for investment casting

QuickCast™ is a build style that can be used on 3D Systems' stereolithography machines to build models that are used as sacrificial patterns for investment casting. Solid models built using the Ciba Geigy SL5170 and the ACES build style expand during the burnout part of the investment casting process, and can crack the shell of the mould.

Models using the QuickCast™ build style have an exterior skin encasing a honeycomb like internal structure, that should collapse in on itself when the pattern is burnt out (Jacobs).

Investment casting

Shell investment casting involves creating a ceramic shell around a pattern, which is then burned out, leaving a hollow shell. Metal can then be poured into the mould to give the finished part.

Investment casting of waxes is a widely used technique, but only about 85% of parts are successful. This is lower for direct investment casting of SL parts, even using the QuickCast™ build style (Hague *et al*). This reduction in the success rate is due to the stereolithography model not melting during the autoclave process, and expanding, to create stresses in the ceramic shell which may lead to cracking, even when the different build styles are used. Success in casting the SL patterns is also dependent on the experience of the foundry.

Results

The most time consuming tool made was the SL/resin mould. The four part tool took much longer than expected to generate as a 3D CAD file due to the complex split lines and design features incorporated to minimise the SL build time. The SL faces also took a long time to make as the parts took two builds on the SL, and were each close to the size limit of the machine, and so each build itself took a lot of time. Added to this was the time to back the faces with sand filled resin. As the same location and clamping system was used as the epoxy resin tool, the sand/resin backing of each piece also had to be done sequentially, adding more time to the process.

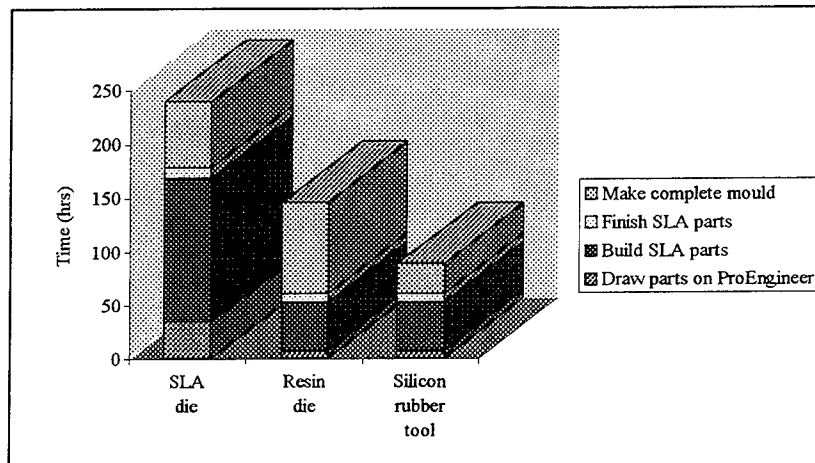


Figure 1. A comparison of the times to produce soft tooling from SL parts using silicon rubber, resin, and SL/resin tooling techniques.

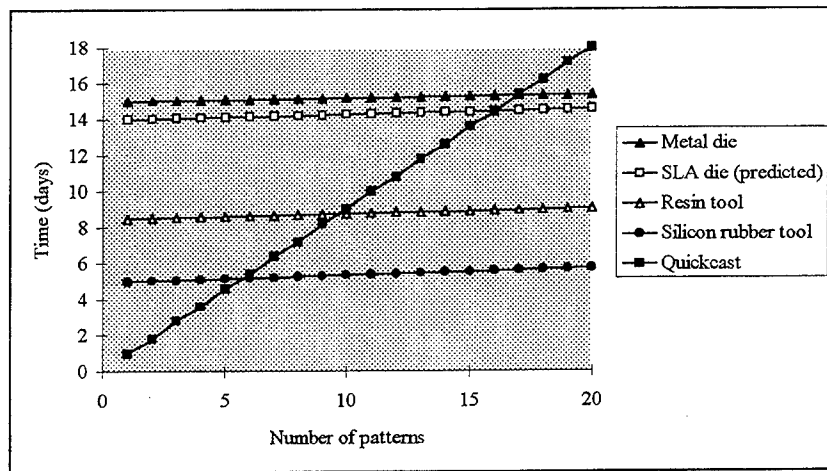


Figure 2. Plot of the time taken to produce casting patterns by the different tooling routes.

During injection of the SL faced tool, the tool failed, meaning that no wax pieces were produced using it. This was due to either the pressure of the moulding machine holding it clamping the tool together, or due to the pressure of the wax injection.

The resin tool took approximately half the time to build than the hybrid tool, but also took almost twice the time of the silicon rubber tool. The reduction in time over the hybrid tool is due to eliminating the lengthy CAD and SL work involved. However, the increase in time needed over the silicon rubber tool is due to the fact that each part of the tool has to be made sequentially. Therefore, the increase in time is primarily due to the part needing a four part tool. The epoxy resin tool was injected successfully and gave a number of wax patterns.

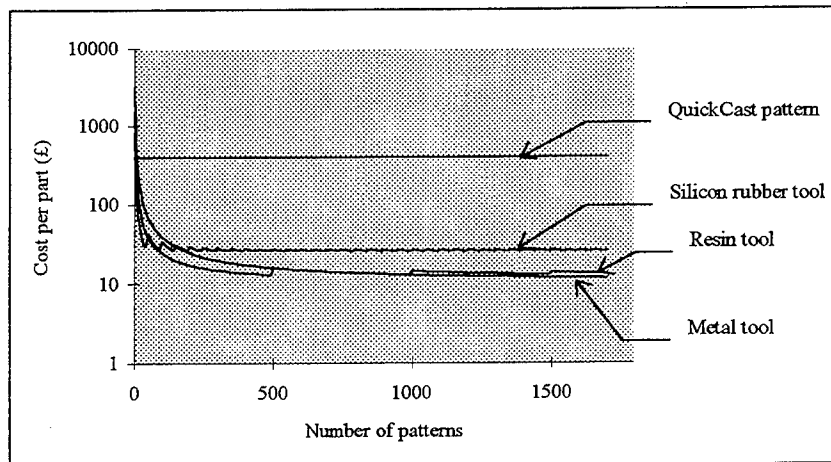


Figure 3. Plot of costs to produce casting patterns by the different tooling routes.

It can be seen that the times involved in producing a casting pattern in the QuickCast build style are significantly faster than producing a mould up to about ten patterns. Above this number, time savings can be made by making a soft tool and injecting or vacuum casting wax into them. The SL build times may be faster than this on larger machines using different recoating techniques, which cut down on the recoating time for each layer.

The soft tools were cost effective when more than about five patterns were required. This is due to the relatively high costs of producing a part by stereolithography.

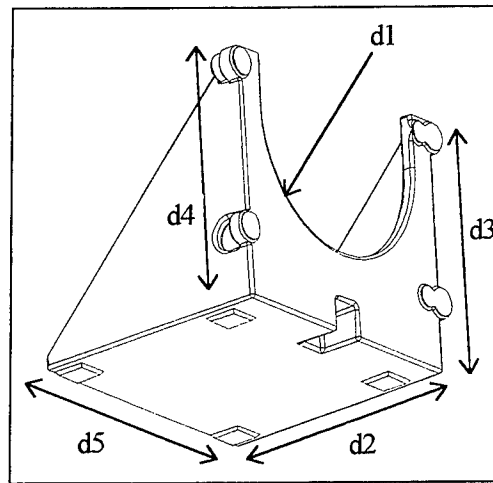


Figure 4. 3D CAD model of part used in this investigation, showing dimensions used over.

The dimensions of the final parts should be as follows:

d1 = rad 55 mm d2 = 120 mm d3 = 120 mm d4 = 120 mm d5 = 140 mm

Model	shrinkage (%)	d1	d2	d3	d4	d3
'Perfect' master	1.6	55.88	121.92	121.92	121.92	142.24
SLA master	1.6	55.79	122.06	122.26	122.24	142.16
Error (actual /percentage)	1.6	-0.09 0.16	+0.14 0.11	+0.34 0.28	+0.32 0.26	-0.08 0.06
'Perfect' casting pattern	1	55.55	121.2	121.2	121.2	141.4
Wax from silicon tool	1	55.73	121.39	121.24	121.14	141.37
Error (actual /percentage)	1	+0.18 0.32	+0.19 0.16	+0.04 0.03	-0.06 0.05	-0.03 0.02
QuickCast pattern	1	55.54	121.91	122.04	122.2	141.47
Error (actual /percentage)	1	-0.01 0.02	+0.71 0.59	+0.84 0.69	+1.00 0.83	+0.07 0.05
'Perfect' finished metal	0	55	120	120	120	140
QuickCast metal	0	55.75	120.4	120.57	120.48	141.57
Error (actual /percentage)	0	+0.75 1.36	+0.4 0.33	+0.57 0.48	+0.48 0.4	+1.57 1.12
Predicted investment casting tolerances		±0.28	±0.45	±0.45	±0.45	±0.53

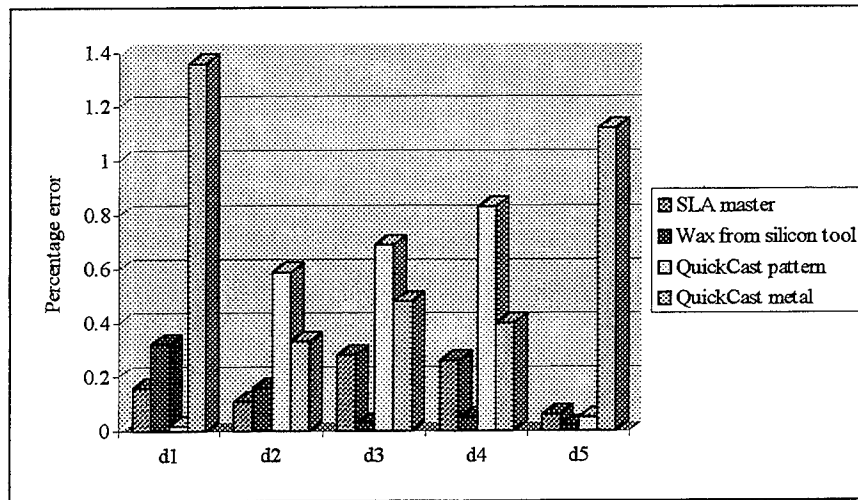


Figure 5. Plot of the percentage dimensional error in the patterns and casting produced.

The casting patterns produced were measured on a co-ordinate measuring machine to give an indication of the accuracy's of the different routes. The wax pattern measured was shown to be very accurate, although flash on the part was more evident than the waxes produced by the resin tool. The wax from the silicon tool also showed markings from where the tape that defined the split lines had been. The metal part produced from the QuickCast pattern showed the largest errors as the measurements also included the variations caused by investment casting. The results from the waxes produced from the resin tools were not available.

The accuracy's obtained have to be considered with relation to the tolerances quoted for the investment casting process, and also the fact that most castings have some kind of machining done on them before use.

Conclusions and Summary

The results show that the hybrid SL/epoxy mould is not effective in reducing times and costs for this test part. This is due to the size of the part, which made building the pieces in SL time consuming. Also, the four part construction with locators and clamps added separately mean that the backing with resin also takes longer than may be possible. The time taken to make the tool could also be minimised in further projects by utilising the flexibility of the combination of 3D CAD and SL.

The resin tool was successful in producing waxes for use in investment casting. The tool was robust enough for the wax injection process with no visible damage to the tool. However, as with the other soft tools, they cannot easily be modified as a metal tool can, and so it is perhaps more important that the design is checked as much as possible before the tool is made.

The silicon rubber mould was the fastest mould to make and the number of parts of the tool does not significantly increase the time required. The disadvantage of the silicon tooling means that the wax cannot easily be injected without mounting the silicon in a box. Also, the

means that the wax cannot easily be injected without mounting the silicon in a box. Also, the life of the tool may be limited to about 50 mouldings.

Method	Total cost of tool (£)	Total time to build tool (days)	Expected total number of patterns	Average error on patterns produced (%)
Resin tooling	1500	8.5	500	N/A
Silicon rubber tooling	800	5	50	0.12
SL/resin tooling	6000	14	0	N/A
QuickCast patterns	400	1	1	0.44
Metal tool	3000	15	5000	N/A

References

Dickens, P.M.; Stangroom, R.; Greul, M.; Holmer, B.; Hon, K.K.B.; Hovtun, R.; Neumann, R.; Noeken, S.; Wimpenny, D.; 'Conversion of RP models to investment castings' Rapid Prototyping Journal, Vol.1, No.4, 1995, pp. 4-11.

Hague, R.; Dickens, P.M. 'Stresses created in ceramic shells using QuickCast models' Proceedings of the First National Conference on Rapid Prototyping and Tooling Research, Great Missenden, England, November 6-7, 1995, pp. 89-100.

Jacobs, P.F. 'QuickCastTM and Rapid Tooling', Proceedings of the Fourth European Conference on Rapid Prototyping and Manufacturing, Belgirate, Italy, June 13-15, 1995, pp. 1-25.

Klocke, F.; Celiker, T.; Song, Y.-A.. 'Rapid metal tooling' Rapid Prototyping Journal, Vol.1, No.3, 1995, pp. 32-42.

Lück, T.; Baumann, F.; Baraldi, U. 'Comparison of Downstream Techniques for functional and technical prototypes - fast tooling with RP', Proceedings of the Fourth European Conference on Rapid Prototyping and Manufacturing, Belgirate, Italy, June 13-15, 1995, pp. 247-260.

Mueller, T. 'Investment casting notes', Rapid prototyping report, Vol. 5, No 8, 1995.

Sachs, E.; Cima M.; Allen, S.; Wylonis, E.; Michaels, S.; Sun, E.; Tang, H.; Guo, H. 'Injection molding tooling by three dimensional printing' Proceedings of the Fourth European Conference on Rapid Prototyping and Manufacturing, Belgirate, Italy, June 13-15, 1995, pp. 285-296.

Tsang, H.; Bennett, G. 'Rapid tooling - direct use of SLA moulds for investment casting', Proceedings of the First National Conference on Rapid Prototyping and Tooling Research, Great Missenden, England, November 6-7, 1995, pp. 237-247.

Acknowledgements

The authors wish to thank Rod Haskell of Finecast (Maidenhead) Ltd for his continual help and support during this project.

Stereolithography Model in Presurgical Planning of Craniofacial Surgery

Ian Jackson,* Huinian Xiao*, Mansour Ashtiani** and Luc Berben***

* Craniofacial Institute, Providence Hospital, Southfield, Michigan

** Stereolithography Laboratory, Troy, Michigan

*** Materialise Inc., Belgium

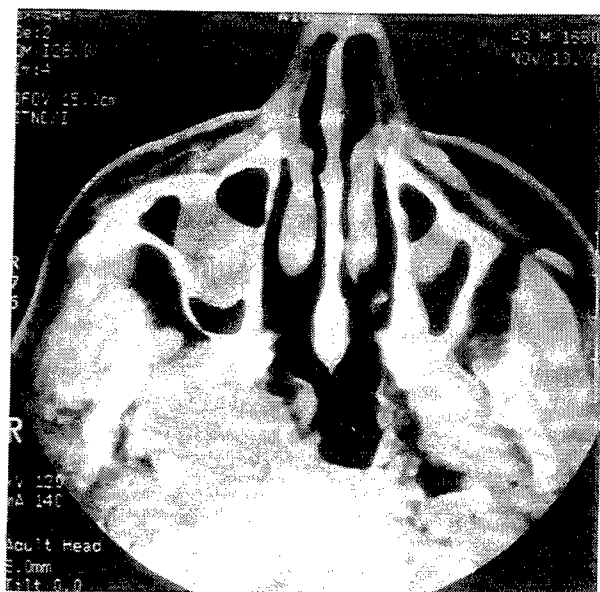
Introduction

A rapid prototyping technique, which was originally used in mechanical engineering, has found applications in medicine. Recently stereolithographic models have been used in complex craniofacial surgeries for visualization, presurgical planning and implant design[1-4]. There are some advantages of model fabrication when preparing for surgery: more accurate evaluation of the patient's condition/deformities, better informed consent for surgery and better-fitting artificial body parts. This paper is a case report in which a sterelithographic skull model was used in the presurgical planning of a complex craniofacial tumor resection.

Case Report

The patient presented with a mass (neurofibroma) in the right infratemporal fossa. MRI scan examination revealed that the mass was wrapped around the internal carotid artery and was high up in the skull base area. Since the mass was in the infratemporal fossa which contains significant vessels and nerves, it was very important to fully study the relationship between the lesion and the surrounding structures in order to decide which surgical approach would be best.

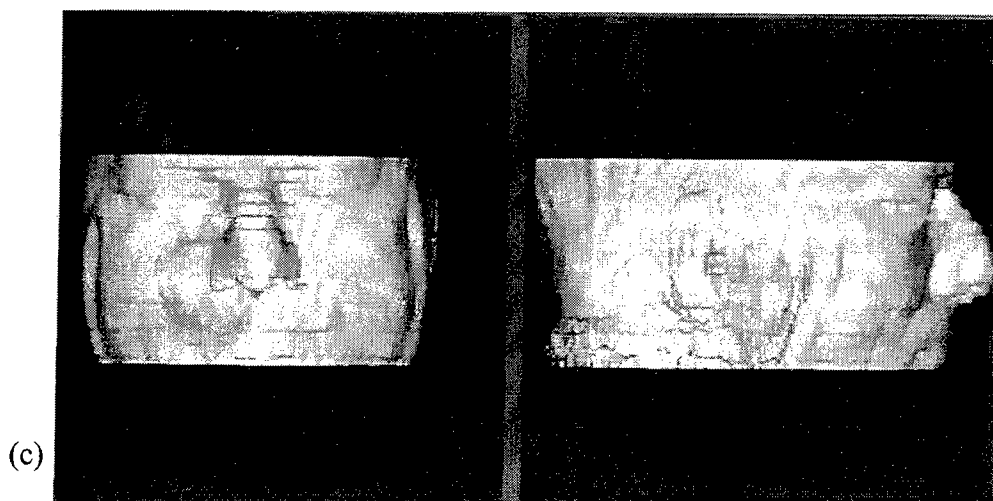
2D and 3D imaging analysis was performed first [Figure 1], following this two solid models were made for further surgical planning, these were based on CT and MRI scans, respectively. The CT data was obtained on a GE HighSpeed Advantage Helical Scanner with 5mm thickness slices. It can be noticed that the lesion was not well shown on



(a)



(b)



(c)

Figure1. 2D and 3D imaging analysis. (a) One cut of CT scan. Notice that the lesion is not shown clearly on CT image. (b) MR angiography of the interested region. (c) 3D profile of the patient's MRI. Lesion was measured as 33cc.

the CT images. The MR scan was done on a GE Signa with contrast and 4mm thickness slices with 2mm spaces between. The skeletal model [Figure 2] was manufactured based on the CT scan by Stereolithography Laboratory in Troy, Michigan. The dual color stereolithography [Figure 3] was fabricated by Materialise Inc., in Belgium, based on the MRI scan, this combined both skin and tumor information. The color stereolithography

was to differentiate different structures in one model. All of work of CT and MRI imaging processing were done by Materialise's medical software. Since both scans were originally for diagnosis purposes, the slices were thicker and the models look a little rough.

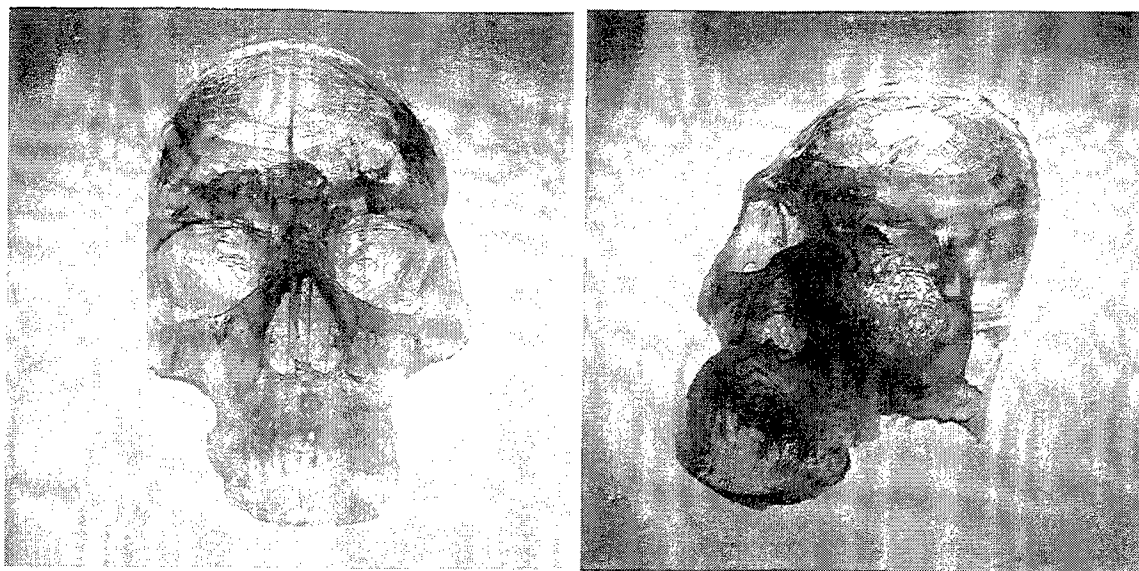


Figure 2. Stereolithography model based on CT scan.

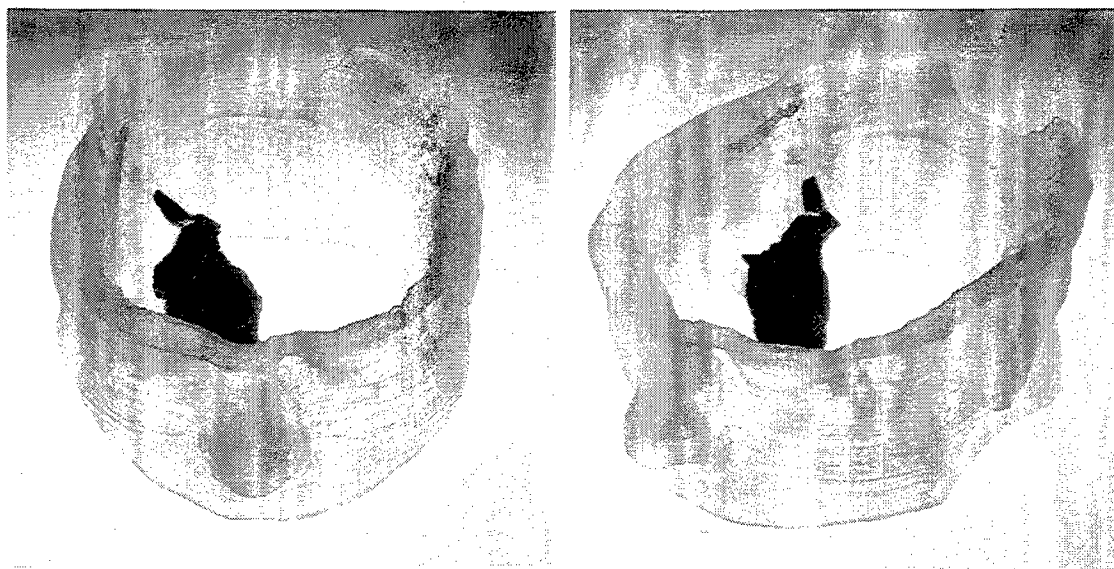


Figure 3. Dual color stereolithography model based on MRI with contrast.

The MRI data were segmented with the MIMICS software with the use of thresholding and 3D region growing. The skin of the patient was selected to serve as reference, the lesion was selected semi-automatically. The stereolithography machine of Materialise was equipped with a special resin (Zeneca, UK). This resin has the ability to color if additional energy is applied to the resin. A first pass of the laser produces curing, with a second pass of the laser, the desired zone is selectively colored. The resolution of this coloration is the same as the building resolution.

This case was the first real case in which selective coloration was used for pre-surgical planning. The total time of making this dual color stereolithography model was 7 hours, which including less one hour for the segmentation and additional editing, one and half hours for calculating complete model and supports, and less than five hours for final fabrication of the model.

The possible approaches to resect the mass were considered. The models helped to show exactly where the lesion lay in relation to the ascending ramus of the mandible. Presurgical planning of the procedure on the stereolithography model enabled us to decide the best approach, this was the mandible swing procedure. In addition, the life-size models of the patient's head, sitting in the operating room during the procedure, gave the surgeon an intuitive view of patient's condition. The mass which measured 5x4.5x2.5cm was resected completely. The patient did very well during the procedure, which lasted two and half hours, and did not require a blood transfusion. He has made an excellent recovery from surgery.

Discussion

Presurgical planning based on 3D CT and MRI has been routinely used in the Institute for Craniofacial and Reconstructive Surgery, Providence Hospital, over the past five years. Advanced graphic technique has allowed the mimic 3D image to be displayed on a two-dimensional surface. As compared to the stereolithographic skull model, it can never be truly three-dimensional. Thus for some complex cases such as the one presented, to

visualize the special relationship of the complicated skeletal areas to soft tissue complexes is difficult. Our preliminary experience with a 3D solid model indicates that a stereolithographic skull model provides the surgeon with additional comfort in planning prior to a complex craniofacial surgery. It is possible to perform real simulation surgery, resulting in significant reduction of operation time and stress on the patient. With the cost continuously decreasing, we hope that this technique can be used more routinely in the clinical setting.

Concerning the quality of the stereolithography model, there are two aspects involved. One is the data acquisition. The reduction of slice thickness and slice distance will result in a fabricated model with greater accuracy. Another is data processing, including properly interpolating imaging data between the single slices and correctly segmenting object of interest (e.g. tumor). In addition, for this particular case, if we can build a model, including the skeletal, tumor and arteries, that combines the information obtained from CT, MRI and Angiography, it will be very helpful. We believe that advances in computer design techniques and enhanced software will solve this problem.

References

- [1]. Lambrecht J. Thomas 'Computed Maxillo-Facial Imaging CAD/CAM of prosthetic implants pre-operation planning anatomic facsimile models computer-aided surgery', CAR 95, 9th International Symposium and Exhibition, Tutorial Notes 73-78, June 1995
- [2]. Bill J.S., Dittmann W., Kubler N., Meier J.L., Pistner H., Wittenberg G., 'Stereolithography in oral and maxillofacial operation planning', Int. J. Oral Maxillofac. Surg. 1995, 24: 98-103
- [3]. Kobayashi M., Fujino T., Kaneko T., Takano J., Chiyokura H., 'Preparation of hydroxyapatite prostheses with laser lithography model', Proceedings of the International Symposium on Computer and Communication Systems for Image Guided Diagnosis and Therapy, 817-820, June 1996
- [4]. Materialise NV (Belgium), Katholieke University (Belgium), Siemens AG (Germany), Zeneca Specialties (UK), 'PHIDIAS laser Photopolymerisation models based on medical imaging, a Development Improving the Accuracy of Surgery', Synthesis Report, Proceeding of North American Stereolithography's 1996 Conference and Annual meeting, March 10-14, 1996 San Diego

Biocompatibility of SLS-Formed Calcium Phosphate Implants

G. Lee*, J.W. Barlow*, W.C. Fox**, and T.B. Aufdermorte***

*Department of Chemical Engineering
The University of Texas at Austin
Austin, Texas 78712

**BioMedical Enterprises, Inc.
14785 Omicron Dr., Suite 205
San Antonio, Texas 78345-3201

***Department of Pathology
The University of Texas Health Science Center at San Antonio
San Antonio, Texas 78284

Abstract

A method for fabricating artificial calcium phosphate bone implants by the Selective Laser Sintering (SLS) process has been developed that can fabricate complex and delicate calcium phosphate bone facsimiles from a variety of data inputs including Computed Tomography(CT) files (1). This paper discusses two *in vivo* biocompatibility studies of SLS-formed calcium phosphate implants in both rabbits and dogs. Histologic analysis shows a high degree of biocompatibility and bone ingrowth in both studies.

Introduction

Much attention has been given to develop materials that can assist in the regeneration of bone defects and injuries (2). Although efforts has been great in developing a biocompatible material, little research has been done toward the rapid and automated shaping of replacement bones using these materials. A human body is composed of 206 different bones and every bone is different in size from person to person. Specially, bones in craniofacial or maxillofacial area are prone to be very complex in shape as well as vary in size. For example, reconstruction of the oral cavity could benefit from an implant that matched the shape of the patient's original anatomy, fit the defect and guided the regeneration of the soft tissue.

As described earlier, we developed a process that uses SLS to form complex geometries from calcium phosphate powders (1). This process, coupled with the well established medical imaging technology of Magnetic Resonance Imaging (MRI) and CT, can precisely reproduce accurate facsimiles of any skeletal bone. The present study examines the biocompatibility of implants made by this process in rabbit and dog animal models.

Materials and Methods

Powder preparation Monocalcium phosphate, monohydrate (MCP, Food grade) and Dicalcium Phosphate Anhydrous (DCP/A, USP/FCC grade) were obtained from Rhone-Poulenc Basic Chemical Co. as raw materials. Specimens with Ca/P ratio of 0.5 to 0.9 were formed in a two step process. The first step involved the mechanical mixing of MCP and DCP/A in such a way that the resulting powder contained a Ca/P ratio of 0.9. For example, 0.8 mole of DCP/A and 0.2 mole of MCP were mechanically mixed and fired at a controlled temperature about 950 °C to obtain a solid solution of β -calcium pyrophosphate (3), β -2CaO•P₂O₅. The resultant sintered cake was then either ball milled or ground by mechanical blender, and selectively sieved to obtain powders with particle size less than 75 μ m.

Following previously established procedures (4), a poly(methymethacrylate-co-n-butyl methacrylate) latex polymer was synthesized as a binder. The melt flow index of polymer was tailored about 7.7 g/10 min. at 200 °C and 75 psi, as measured by a Kayness Galaxy I capillary rheometer. This flow range had been previously discovered to allow the binder to flow and rapidly wet the inorganic material under SLS process conditions.

Calcium phosphate powder was coated with polymer by spray drying a slurry of particulate and emulsion binder. The spray drier used in this study is a pilot -plant scale Anhydro Laboratory Spray Drier # 1 with co-current rotary atomizer. This spray drying process produces a free flowing powder that has the desired agglomerated morphology. Spray drying condition were as follows. Solids content of slurry was 45 wt. %, inlet temperature, 175°C, outlet temperature, 110°C, and atomizer speed was above 30,000 rpm. Polymer content in coated powder was 22 wt. % as determined by Thermal Gravimetric Analysis (TGA).

SLS processing Spray dried material were processed using a beta test workstation SLS™ Model 125 equipped with modulated 25 W CO₂ laser. Laser output power, beam scan speed, scan spacing and powder bed temperature were controlled to optimize the green strength according to the shape of the implants. Optimal settings for *Energy Density* (5) were found to be in the range of 1 to 1.5 cal/cm².

Post Processing SLS-formed green objects were infiltrated with calcium phosphate solution, fired to remove the polymeric binder, then fired at higher temperature to sinter the calcium phosphate particles. The parts were subsequently infiltrated with DCP/A solutions in diluted phosphoric acid by submersing them in the solutions. The capillary action of the pores drew the infiltration solution into the part. After the pores were filled with infiltrant, the parts were allowed to dry prior to firing. The firing temperatures were controlled to be lower than the initial sintering temperature to avoid further shrinkage, but high enough to provide atomic diffusion and chemical reactions to occur between Ca and P in the infiltrant and that of the green part. When the green part was first infiltrated, the Ca/P ratio and solids content of the infiltrant were chosen to facilitate a clean burn out of polymer. After debinding, the extent of infiltration and the concentration of the infiltrant

were varied to achieve desired density, pore structure, mechanical strength and a final Ca/P ratio. This approach allowed the density of the final product and its chemistry to be precisely controlled in the final firing step.

Material characterization The effect of post processing on calcium phosphate chemistry was studied by X-ray diffraction. The microstructure of the prepared specimen was evaluated by mercury porosimetry and scanning electron microscopy (SEM). The SEM was primarily used to visualize surface morphology and the internal structure of samples.

The pore structure of the *in vivo* oral implant, described below, was measured by mercury porosimetry (Poresizer 9320, Micromeritics). Prior to porosimetry measurements, the oral implant was heated to expel the absorbed moisture and then stored in a desiccator until analyzed. The sample in the Poresizer was initially evacuated to 25 $\mu\text{m Hg}$. Mercury was then admitted and pressure was increased up to 30,000 psi. Assuming a contact angle of 130° (6), pore diameters ranging from 200 to 0.006 μm were measured. Figure 1 shows a typical pore size distribution. From mercury intrusion analysis, the total pore area 1.82 m^2/g and median pore diameter 33 μm were measured. The measured porosity was about 30 %, which is smaller than the observed value, about 50 %, from geometrically-based density measurements. This could indicate that some closed pores are present in the part.

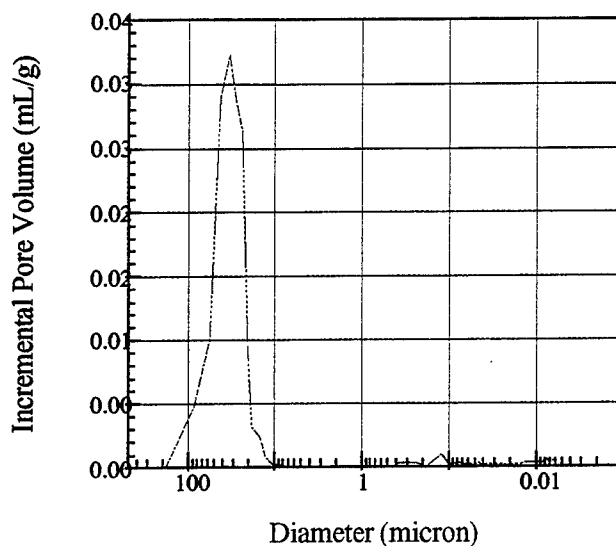


Figure 1. Pore size distribution of oral implant

Two test methods, compression and 4-point bending, were used to quantify the strength of the specimens by a MTS Sintech 1/S material test frame. Typical strengths are in the range 2,000 psi in compression and 2,200 psi in 4-point bending.

Implant preparation and animal studies. Preliminary *in vivo* biocompatibility studies were carried out with rabbits. Tiny rectangles, 0.12" x 0.16" x 0.05", were prepared by a process that simulated SLS process conditions. Calcium metaphosphate was mixed with

the same polymeric binder used previously (1) and poured into the cavity of the mold without compaction. The mold was heated to form polymer-bound "green" parts. The green parts were then fired at about 920°C to remove the binder and to sinter the calcium phosphate. One of the prepared calcium phosphate specimens was implanted over the frontal lobe of the skull in each of four New Zealand White Rabbits. The cortex of each skull was decorticated to cause minor hemorrhage and create a small defect in which the implant could rest. At twelve weeks the animals were sacrificed. Implants and bone were retrieved and embedded in plastic, sectioned and analyzed.

More elaborate *in vivo* biocompatibility studies were carried out in dogs. Anatomical measurements of the original geometry of the dog alveolar ridges were taken to determine their anatomy. AutoCad engineering computer-aided design software was then used to design the oral implants. These implants were rectangular shaped and tapered so as to decrease their buccal-lingual width apically, see Figure 2. The sides and bottom of these implants had large hexagonal macropores of about 2.4mm that penetrated entirely through the device. These macropores were aligned so they intersected within the implants. Tooth extraction of the first mandibular molar bilaterally was performed in six dogs and bone was cut from the extraction site to prepare a defect in the alveolar ridge. The first molar was extracted bilaterally from the mandible. Primary closure was achieved and the dogs were allowed to heal for eight days. After the 8-day healing period, the extraction defect in the alveolar ridge was surgically exposed. Implants were placed in the ridge and primary closure was achieved. Dogs were put on soft food for the duration of the study. Radiography was performed to obtain data giving an indication of the implants osteoconductive properties and its biocompatibility. Radiographs were taken immediately post-operatively and at four weeks into the study.

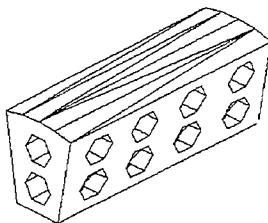


Figure 2. Designed oral implant

Results and Discussion

A histologic section of the calcium phosphate implant after twelve weeks implantation in rabbit's frontal skull is shown in Figure 3. The implant shows a high degree of biocompatibility and bone ingrowth. No evidence of foreign body giant cell or macrophage response was found in or adjacent to the specimen. There was no acute or chronic inflammation, and a high degree of bone apposition and infiltration is observed. Mineralized new bone is present throughout a significant portion of the implant closest to the underlying calvaria. Osteoid, or a collagen matrix with bone forming potential, fills the majority of the rest of the implant. It is suggested from this histology that, in time,

the specimen could be completely filled with dense mineralized bone. A higher magnification of the histologic section is shown in Figure 4. Direct bone apposition and ingrowth are visible across the interface and throughout the implant. Host bone is directly connected to bone within the implant providing good mechanical stability.

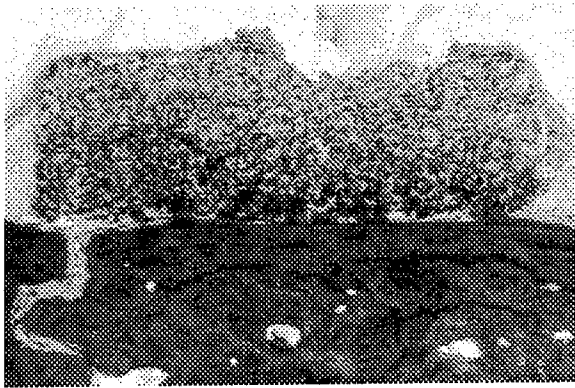


Figure 3. Histologic section of implants taken overlying the rabbit calvaria. (40x original magnification)

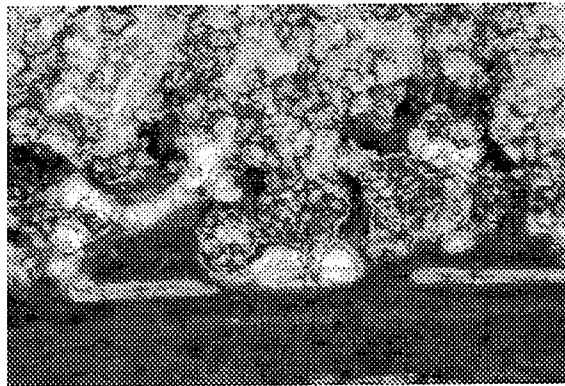


Figure 4. Histologic section of implant taken overlying the rabbit calvaria (100x original magnification)

A scanning electron micrograph of surface of the SLS formed oral implant is shown in Figure 5. This surface is imaged at 150 times of the original magnification and 100 μm measure is visible in the lower right of the image. In Figure 6, the polished surface is shown at the same magnification. It is clear from these pictures and mercury intrusion analysis, that some of the pores are larger than 100 μm and that the pores are open and well interconnected. These issues are critically important to the successful development of a osteoconductive bone implant material. It is known that mineralized bone growth into porous implants required a minimum interconnected pore size of 100 μm , and the pore size showing the potential for the ingrowth of osteoid tissue, was found to lie between 40 and 100 μm (7).

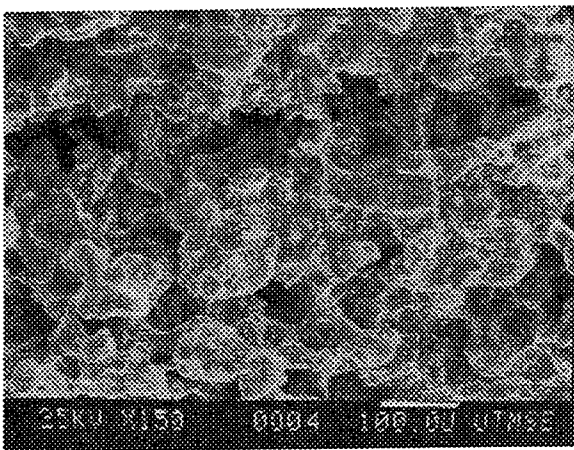


Figure 5. Scanning electron micrograph of the surface of SLS-formed implant.

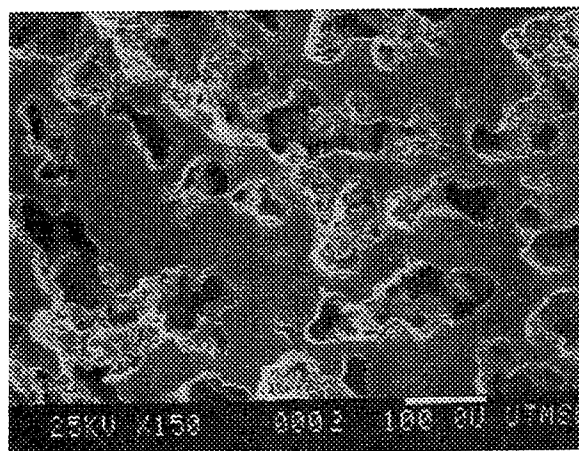


Figure 6. Scanning electron micrograph of a polished surface of SLS-formed implant.

Figure 7 shows the periapical radiograph of a SLS-formed alveolar implant. This image was taken immediately post-operative. The rectangular form of the implant and hexagonal form of the macropores are visible in this radiograph. In Figure 8, a radiograph image taken four weeks following placement of the implant is shown. Crestal resorption and bone infiltration into the apical macropores and apical portion of the crestal macropore are evident from the film.



Figure 7. A radiograph of a SLS-formed alveolar implant with micro- and macropores.

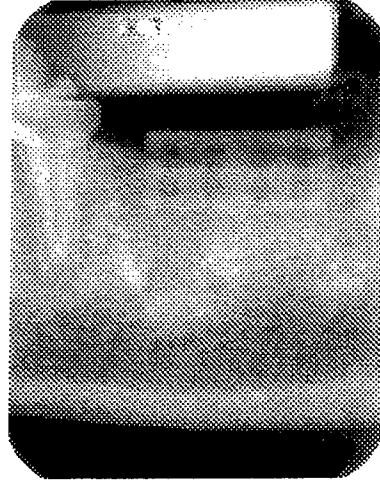


Figure 8. A radiograph of a SLS-formed alveolar implant with micro- and macropores.

As a demonstration of this bone fabrication technique, a human anatomical facsimile was formed from CT images using SLS. This inferior view of the maxilla shows some dentition and anterior nerve and vascular foremen with great resolution.



Figure 9: Ca/P human maxilla formed from CAT images using SLS.

Conclusion

Based on the excellent biocompatibility of material and the great extent of bony tissue ingrowth shown in the rabbit *in vivo* study, the calcium phosphate powder system for the SLS process has been established. As a starting material Ca/P ratio 0.9 was synthesized and formed by SLS. Oral implants in alveolar ridges of dogs show excellent integration with host bone after only four weeks of implantation. This study shows that a porous, resorbable calcium phosphate synthetic bone material can be precisely fabricated with complex geometry and successfully used *in vivo* for filling and replacing defective bone.

Acknowledgments

The authors gratefully acknowledge partial support for this work by the State of Texas Advanced Technology Program, No. 265, BioMedical Enterprises, Inc., and the United States Air Force Armstrong Laboratory through contract F41624-95-C-2008.

References

1. G. Lee and J.W. Barlow, "Selective Laser Sintering of Calcium Phosphate Powders," *Solid Freeform Fabrication Symposium Proceedings*, **1993**, The University of Texas at Austin, Texas, pp.191-197.
2. S.F. Hulbert, L.L. Hench, D.Forbes, and L.S. Bowman, "History of Bioceramics," *Ceramics in Surgery* edited by P. Vincenzini, **1982**, Elsevier, Amsterdam, pp 3-29.
3. W.L.Hill, G.T.Faust and D.S. Reynolds, "The Binary System P_2O_5 - $2CaO$ • P_2O_5 .", *Am. Jour. Sci.*, **1944**, 242 (9), 457-477.
4. N.K.Vail, *et al.*, "Development of a Poly(methyl methacrylate-co-n-butyl methacrylate) Copolmer Binder System", *J. Appl. Polym. Sci.*, **1994**, 52, 789-812.
5. J. C. Nelson, *et al.*, "Selective Laser Sintering of Polymer-Coated Silicon Carbide Powders," *Ind. Eng. Chem. Res.*, **1995**, 34, 1641-1651.
6. E.W. Washburn, "Note on a Method of Determining the Distribution of Pore Sizes in a Porous Material," *Proc. Natl. Acad. Sci.*, **1921**, 7, pp115-116.
7. J.J. Klawitter and S.F. Hulbert, " Application of Porous Ceramics for the Attachment of Load Bearing Internal Orthopedic Applications," *J. Biomed. Mater. Res. Symposium*, No.2, **1970**, pp161-229.

Using Fabricators to Reduce Space Transportation Costs

Dr. David S. McKay, Assistant Chief for Exploration and Technology
Lyndon B. Johnson Space Center, Houston, Texas

Hubert P. Davis, President
Davis Aerospace Company, Canyon Lake, Texas

Dr. Marshall Burns, President
Ennex Fabrication Technologies, Los Angeles

Copyright © 1996, Ennex Corp.

Abstract

Ever since the Apollo landings, one of the primary barriers to more ambitious space projects has been the exorbitant cost of lifting equipment and construction components off of the Earth. Fabricators offer an intriguing solution by allowing for the use of native materials on the Moon, Mars, or other destinations in the production of tool and building parts. This paper discusses

- The kinds of objects that can be practically made in this fashion,
- Fabricator processes suitable for extraterrestrial environments,
- Raw materials available, and
- The impact of this use of technology on the cost of space projects.

Introduction

When the European settlers came to America, they brought their hammers, axes, saws, and barrels of nails. With these tools and materials they built cabins, barns, and forts. They did not, however, bring wood, the most important construction material they would need, because they knew they would find plenty of timber at their new home site. In fact, in many cases they had to get to work cutting down trees not only to provide lumber for construction but also to provide clear land to plant crops.

When we go to the Moon, Mars, and the Asteroids, we know we will not find any trees or wood. But we will find plenty of other construction and industrial materials, such as iron, aluminum, and magnesium, from which we can build shelters, factories, and machinery. The presence of these materials could save us the expense of launching steel beams and aluminum habitat shells, except for one major problem. What will stand as the modern analog of the settlers' hammers, axes, and saws? What tools can we take with us to turn celestial rocks and dust into walls and girders?

Until recently, this was a "Catch-22" situation. We need refineries and foundries to process raw ore into building materials. But refineries and foundries are large, heavy facilities that consume voluminous materials in their own construction. So how can a lunar or other celestial settlement be bootstrapped out of the indigenous soil?

The answer may lie in additive fabricators. A fabricator¹ (or *fabber*) is an ultra-modern machine that *makes things automatically*. Fabricators use raw materials and computer data to generate three-dimensional, solid objects you can hold in your hands, submit to testing, or assemble into working mechanisms. They are being used by manufacturers around the world for low-volume production, prototyping, and mold mastering. They are also used by scientists and

¹ For more background on fabricators, see *Automated Fabrication—Improving Productivity in Manufacturing* by Marshall Burns, Prentice Hall, 1993, ISBN 0-13-119462-3.

surgeons for solid imaging, and by a few modern artists for innovative computerized sculpture. Manufacturers report enormous productivity gains from using fabricators.

As the quality and speed of fabricator output steadily improves, we are gradually moving toward a time when these machines will be able to participate in the construction of large structures and make parts to be incorporated into working machinery. The ability of several processes to work with metals may allow the launch of one or a small number of fabricators to spawn the construction of an entire colony.

This paper investigates several of the issues important to evaluating the opportunity to reduce transportation costs by using fabricators for on-site generation of machine parts and construction components. The important issues are:

- **Items to be made.** What can we expect to practically make in space using the kinds of fabricators discussed here?
- **Suitable fab processes.** What fabrication processes are suitable for operation in a space environment?
- **Raw materials.** What materials are readily available in space for fabricator feedstock, and what is their suitability for the candidate processes?
- **Benefits.** How will the ability to make these items on-site affect the cost of future space projects?

The investigation of these issues cannot be done uniformly for all off-Earth locations. Each celestial body has differences in the composition of its surface materials, and in environmental factors, such as gravity, temperature, radiation, etc. Furthermore, space-based fabricators are not limited to operation on the surface of a celestial body, but could also include orbiting facilities. The cost of lifting raw materials off of small bodies like the Moon is very much smaller than for Earth. Thus, in cases where there are advantages for operating a fabrication process in the micro-gravity available in orbit, this also becomes a candidate location.

What Shall We Make?

There are some definite rules about when a project is appropriate for a fabricator. These rules do not apply in the same way off the face of the Earth. One of the rules is that you don't use a fabricator when the job can be done more economically by another process, such as casting or extrusion. However, this rule is stated in a context that assumes that there are foundries, extrusion presses, and other typical manufacturing equipment within shipping distance. None of this equipment currently exists in space, and transporting it would be very expensive. Therefore we may find it practical to use fabricators, at least in the initial stages, to make blocks, bars, beams, rails, and other simple shapes that one would not consider running in an Earthbound fabricator.

With a fabricator, the opportunity arises to make changes to designs that would otherwise not be practical. For example, if a construction project calls for an arrangement of posts and beams, one would normally, on Earth, order them in standard shapes and lengths and then cut them on-site to the required lengths and weld them into the needed configuration. The individual sections of all the posts and beams are all identical because it is more economical to order them that way. But if each section is being created individually in a fabricator, this allows the engineers to apply special characteristics to individual components. For example, one might want to design flanges or other connection hardware directly into specific sections of individual posts and beams. With well designed connection hardware fabricated as integral to the construction elements, one may be able to design buildings as "erector sets" ready for assembly, without the need for the crew to perform any specialized tasks, such as welding or drilling of bolt holes.

Another novel design might apply in making bricks. Two problems with making bricks in a fabricator on Earth would be the time it takes to solidify their large bulk and the cost of the fabricator raw material. But again, those problems may be eliminated by the differences of the extraterrestrial situation. First, the raw materials for the fabrication processes anticipated may be essentially free and abundant, like timber was to the American settlers. Second, it may not be necessary to solidify the entire bulk of the bricks. Subject to the engineering requirements of the construction project, it may be sufficient to solidify only an exterior shell of the brick, which would then contain the remaining mass of unconsolidated raw material inside. Such a brick would provide just as much radiation shielding as a fully solid brick, yet take much less time to fabricate.

A fabricator provides the opportunity to transform a mundane brick into a functional construction element. On Earth, bricks are simple rectangular blocks because that makes them easy to cast. But, like the posts and beams discussed above, bricks in a fabricator could be made with connection hardware that could reduce or eliminate the need for mortar. Moreover, bricks could be designed with internal channels or external mounting brackets for ductwork, wiring, lighting elements, hazard detectors, and other functional subsystems.

For vehicles, it is not likely that we would use fabricators right away to make highly complex systems, such as engines and brakes. However, many other vehicle parts could be practically made on-site, such as frame members, body panels, axles, and wheels. Also, when problems occur with engine and brake systems, a fabricator could be used to make replacement parts.

In an unfamiliar space environment, unanticipated situations will arise constantly to challenge the crew. When constructing an outpost from Earth-supplied components, the crew would have to meet those challenges by “making do” with whatever is at hand. But with a fabricator, the crew can respond to challenges by inventing and fabricating new tools and new kinds of construction elements at will. The inventive designs may come from the space crew itself, or the designs may be conceived by the support crew on Earth and transmitted to the outpost for local fabrication there.

Given these considerations, one might expect the items made in a space-based fabricator to include

- Construction elements, such as posts, beams, and bricks, individually designed for mating to neighbors and provision of appropriate functionality.
- Conduits for plumbing, air management, and space radiators.
- Fixtures and fittings, such as brackets, joints, etc.
- Large vehicle elements, such as frame members and wheels, as well as replacement parts for complex vehicle systems, such as engines and brakes.
- Hand tools, such as mallets and wrenches, as well as parts and fittings for power tools, including bases for heavy machinery.
- Structural and functional elements of technology projects, such as solar power collectors, telescopes, transmitters, etc.

An immediate concern that arises in considering the use of fabricators to make such items is the quality of fabrication. Today’s fabricators do not yet match the physical properties available from more mature manufacturing processes, such as investment casting and bulk sintering. And even if Earthbound fabricators do become developed to the point of competing adequately on the basis of material properties, space-based fabricators will still be experimental devices that cannot promise matching properties because they will be working with foreign materials and subject to a different environment in terms of gravity, atmosphere, radiation, etc. However, in considering this issue, one must be careful not to apply the extraordinary quality standards normally used in space projects today. One must recall that the primary reason for these lofty standards is that there is generally no opportunity to replace components that malfunction in space. This fundamental assumption is negated by the introduction of fabricators to the supply system. Thus, while one does not want to take any chances with the safety of building construction or hand-held tools, in general it will be acceptable to apply ordinary, Earth-like quality standards to items made in space-based fabricators.

Suitability of Processes for Space-Based Fabrication

Fabricators today are categorized as either subtractive or additive, depending on whether they work by carving away material from a solid block (CNC machining) or by building up the desired object from an amorphous material. Since subtractive fabricators require billets or other bulk stock as raw material, they are not considered here, and we focus on strictly additive processes.

There are three basic categories of additive fabrication technologies: aimed deposition, selective sintering, and selective curing. These are briefly described in the following subsections, along with comments on their use in space.

Selective sintering

In selective sintering, a powder is caused to melt in specific locations, and the melted powder then fuses into a contiguous solid, which builds up the shape of the desired object. Although most fully developed for use with thermoplastics, there has been successful study of its application to metal and ceramic powders. There are three approaches to achieving sintering of a metallic or ceramic feedstock:

- Using a very high-energy beam to achieve sufficient heating to directly melt a standard, high-melting-point metal or ceramic.²
- Using a beam of moderate energy with a low-melting-point alloy or a mixture that includes a low-melting-point component.³
- Using a metal or ceramic powder either with a polymer coating or with a polymer component mixed into the powder. The selective sintering process then actually operates on the polymer coating or component in order to form a "green body" which is later subjected to bulk heating to burn out the polymer and cause direct fusing of the metal.⁴

On Earth, the energy beam is generally supplied by a laser, although electron beams have also been proposed. In space, an excellent source of thermal energy is likely to be concentrated sunlight.

Selective sintering is a promising technique for near-term testing of space applications. This is because some success has been demonstrated in applications to metals already, and because raw metal and ceramic powders are available on the Moon (see *Raw Material* below). Any of the three approaches listed above may be used. For polymer-coated powders, the polymer would need to be supplied from Earth, but the mass of polymer consumed would be small compared to the mass of metal fabricated, so the goal of reduced transportation costs would be accomplished.

Aimed deposition

In aimed deposition, a stream of material is aimed at specific locations on the growing object to build it up. The material may be deposited in the form of droplets or in a continuous bead. A number of projects have studied application of this technique to metals.⁵ It may be suitable for use in space, using feedstocks melted in a solar-heated crucible. This is a promising technique, which could emerge as the method of choice for fabricating in metals. However, the application of the technology to metals is quite immature. Many issues need to be resolved in Earthbound development before it is practical to test this technique for space applications.

Another idea which would fall into this category is Pegna's technique for fabricating in concrete.⁶ Pegna selectively deposits Portland cement on successive layers of sand and initiates a bonding reaction in each layer by wetting with steam. A more efficient use of water would have to be developed for this to be practical for use in space.

² An example of the use of a high-energy beam, although not with a powder feedstock, is in *Electron beam solid freeform fabrication of metal parts* by V. R. Davé, J. E. Matz, and T. W. Eagar in *Solid Freeform Fabrication Proceedings*, University of Texas, September 1995, page 64..71.

³ *Accuracy and mechanical behavior of metal parts produced by lasersintering* by T. Pintat, M. Greul, M. Greulich, and C. Wilkening in *Solid Freeform Fabrication Proceedings*, University of Texas, September 1995, page 72..9.

⁴ *Selective Laser Sintering and Fused Deposition Modeling processes for functional ceramic parts* by E. Alair Griffin and Scott McMillin in *Solid Freeform Fabrication Proceedings*, University of Texas, September 1995, page 25..30.

Effect of processing parameters in SLS of metal-polymer powders by B. Badrinarayan and J. W. Barlow in *Solid Freeform Fabrication Proceedings*, University of Texas, September 1995, page 55..63.

Free form fabrication of high strength metal components and dies by C. C. Bampton and R. Burkett in *Solid Freeform Fabrication Proceedings*, University of Texas, September 1995, page 342..5.

Effect of particle size on SLS and post-processing of alumina with polymer binders by P. Kamatchi Subramanian, J. W. Barlow, and H. L. Marcus in *Solid Freeform Fabrication Proceedings*, University of Texas, September 1995, page 346..52.

⁵ *Thermal design parameters critical to the development of solid freeform fabrication of structural materials with controlled nano-liter droplets* by Melissa Orme and Changzheng Huang in *Solid Freeform Fabrication Proceedings*, September 1995, p 88..95.

"Incremental fabrication" builds directly in metal by Marshall Burns in *Rapid Prototyping Report*, January 1992.

⁶ *Application of cementitious bulk materials to site processed solid freeform construction* by Joseph Pegna in *Solid Freeform Fabrication Proceedings*, University of Texas, September 1995, page 39..45.

Formulations and applications of lunar concrete have been extensively studied by William Agosto and colleagues at NASA.⁷

Selective curing

In selective curing, a liquid resin is caused to cure (harden) in specific locations to grow the desired object. The Earth-based version of this, using organic photopolymers, is not practical for space applications because of the absence of organic base materials. However, the abundance of silicon on the Moon may offer the basis of a whole new industry in silicon-based polymers. Today's *silicones* are polymers with an alternating silicon-oxygen backbone. They can be made into photopolymers, but currently this is done by hanging organic functional groups on the inorganic backbone. It is possible that we will see fully inorganic photopolymers in the future, or polymer resins that are subject to another form of selective curing, such as thermal or voltaic. If such materials do become available, it will be interesting to consider their use in fabricators on the Moon or other silicon-rich environments.

Process Schematics

Fig. 1 illustrates a selection of possible schemes for space-based fabricators. The techniques illustrated fall into the categories of sintering (a and d) and droplet deposition (b and c). All of these particular techniques use heating as part of the process, which in the illustrations is supplied by an integrated solar collector. The advantages of this source of heating, as well as an alternative, are discussed below.

The system in Fig. 1(a) is essentially equivalent to the sintering fabricators made by DTM (Austin, Texas) and EOS (Munich, Germany), except that the process heat is supplied by focused sunlight instead of by a laser beam. Such a device works as follows. A platform is provided on which to build the desired object. Successive layers of raw powder are deposited from a hopper on top of each other, with the entire cake of powder layers resting on the platform. The platform is mechanized for vertical motion, and is lowered by the thickness of one layer each time a new layer of powder is deposited. In this way, the top surface of the powder cake is maintained at a constant level. The platform and powder cake are enclosed in a chamber which is maintained at an elevated temperature at which the powder is not hot enough to fuse, but does not need a great deal of additional heat to bring it up to a temperature at which it will fuse. Each time a new layer of powder is deposited, a beam of concentrated sunlight from a solar collector is scanned across it to raise selected regions of the layer to the fusing temperature. Where the solar beam strikes, the grains of powder melt momentarily and fuse to each other and to the underlying layer. The beam is controlled by data from a CAD design of the object to be built; the regions of powder which are scanned in each layer of powder make up one cross section of the desired object. After each cross section is formed in this way, the platform is lowered, another layer of raw powder is deposited, and the process is repeated until the complete object is formed.

Fig. 1(b) and (c) show two methods of aimed deposition. The technique in Fig. 1(c) deposits molten droplets of material, very much like the fabricators made by BPM, Sanders, and 3D Systems today. Fig. 1(b) shows an alternative technique which is being studied with lasers at national research laboratories in both Germany and the United States.⁸ Here, instead of melting the material in a crucible, a stream of powder is aimed at the correct locations and the falling powder is melted in mid-stream. This process may offer significant advantages in the fabricated material properties at the cost of the increased mechanical complexity needed to synchronize the scanning of the light beam and the powder deposition stream.

Fig. 1(d) shows a variation on the sintering process suggested to us by Kenneth J. Hayworth of Ennex Fabrication Technologies. In today's commercial fabricators, the fabrication chamber is bound by walls that limit the size of

⁷ *Lunar cements/concretes for orbital structures* by William N. Agosto, John H. Wickman, and Eric James in *Engineering, Construction, and Operations in Space IV* (Proceedings of Space '94, Albuquerque, February 26 .. March 3, 1994), American Society of Civil Engineers, New York, 1994, page 157..68.

⁸ *Approaches to prototyping of metallic parts* by W. König, T. Celiker, and H.-J. Herfurth in *Proceedings of the 2nd European Conference on Rapid Prototyping and Manufacturing*, University of Nottingham, July 1993, page 303..16.

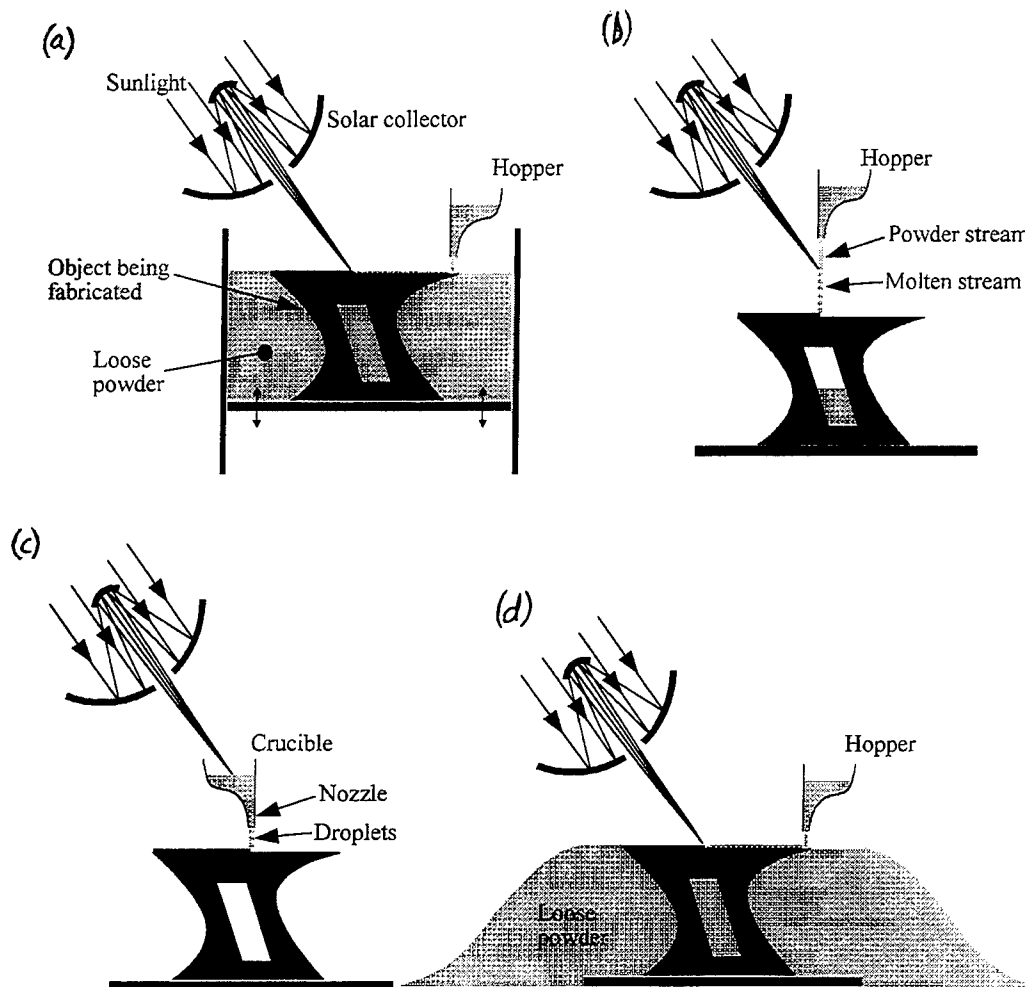


Fig. 1. Schematics of four heat-based fabricator systems using focused sunlight as the source of process heat. Those shown are adapted from processes currently used on Earth, (a) selective sintering of powder deposited on a descending bed, (b) melting in place of an aimed powder stream, (c) deposition of molten droplets, and (d) selective sintering with an uncontained powder bed. See the text for a more detailed description of each system.

Note a conspicuous difference among the techniques is in the residual material in unprocessed regions. Sintering leaves loose powder in cavities not scanned by the heating beam, as seen in (a) and (d). Droplet deposition, as in (c), is able to leave hollow cavities, although the formation of horizontal ceilings as in this illustration may be problematic. Melting of a deposited powder stream, as in (b), is the most flexible, able to fill void regions with loose material from the hopper or leave them partially or completely empty.

objects that can be built. The purpose of the chamber is not only to contain the loose powder, but also to provide an inert, unperturbed environment. On the Moon, where there is essentially no atmosphere, an inert, unperturbed environment is available without an enclosed chamber. With containment of the loose powder by a built-up embankment, it may not be necessary to work in a chamber at all. This would simplify and reduce the mass of the equipment needed for a lunar sinterer by eliminating the walls of the chamber as well as the elevator device needed to move the build platform within these walls.

Solar heating

All of the processes illustrated in Fig. 1 use heating as part of the fabrication process, and show this heat provided by a solar collector integrated into the fabricator. The use of a solar collector has several advantages over a laser.

First, a solar collector has a much longer life than a laser, and does not need to be recharged or replaced on a regular basis as a laser does. Second, although a modest amount of electricity would be needed to power the controls of the solar collector, thermal power is provided freely by sunlight, whereas a laser requires electricity for thermal power as well as for controls.

Taking up these advantages, NASA has already been studying the provision of a solar-collector utility for use by various materials processing experiments on the Moon.⁹ This communal solar collector would use optical waveguides to provide concentrated sunlight to the equipment needing it. Thus, the first lunar sinterer might not need to include its own solar collector, but may be able to plug into a waveguide from the communal system instead.

One important advantage of providing the concentrated sunlight through an optical waveguide is that it allows the main part of the fabricator to be physically separated from the solar collector. Even if the fabricator uses its own, dedicated solar collector, this would allow the collector to be located in a place of constant sunlight while the main part of the fabricator is located in constant shade, where thermal regulation would be easier to provide by space radiation. An example of a pair of such locations would be in the vicinity of the crater near the lunar South Pole studied recently by the Clementine probe. There are highlands at the rim of this crater which are constantly bathed in sunlight throughout the month-long lunar "day," while other regions inside the crater are continuously shadowed. An optical waveguide a few kilometers long could connect a solar collector at the rim with a fabricator below for potentially non-stop operation.

Raw Material

The raw material available for local supply to a fabricator depends on the particular celestial body on which it is located, as well as the specific region of that body at which it is placed. For simplicity, we will limit most of the following discussion here to the body which is the most studied, our Moon. Mars appears to be largely similar to the Moon in composition, but with some important differences. The asteroids, on the other hand, offer a variety of compositions, including some with carbon-based compounds. The availability of carbon will be very important when more is known about it and the means are available to travel to it.

The lunar surface¹⁰ is composed largely of minerals and glasses, mostly oxides of silicon, aluminum, iron, calcium, magnesium, and titanium. Eons of meteorite impact have pulverized a great deal of this material into a fine powder with grains mostly in the range of ten to 100 microns. Three of the schemes suggested in Fig. 1 require powdered feedstock (a, b, and d), and these processes will naturally benefit from this abundant, naturally available powder.

One of the important challenges in working with this lunar soil is separation of the constituent materials into usable fabricator feedstock. There is some debate over the use of magnetic separation of iron particles from the soil. While some experts contend this should be feasible, others point out that such a process will result in a greater concentration of ferrous agglutinates (shock-melted, fused soil particles).

Another intriguing potential source of metallic iron is the reduction of mineral oxides.¹¹ This process has been extensively studied as a method of generating free oxygen, a commodity of obviously great value. NASA's prime candidate for oxygen extraction is pyroclastic glass (volcanic ash from early lunar eruptions). Tests of this lunar material have yielded the greatest free oxygen with byproducts of silicates and iron metal. Unfortunately the solid

⁹ *Optical waveguide solar energy system for lunar material processing* by Takashi Nakamura, Constance L. Senior, James M. Shoji, and Robert D. Waldron in *Engineering, Construction, and Operations in Space IV* (Proceedings of Space '94, Albuquerque, February 26 .. March 3, 1994), American Society of Civil Engineers, New York, 1994, page 1266..77.

¹⁰ *Mineralogical and chemical properties of the lunar regolith* by David S. McKay and Douglas W. Ming in *Lunar base agriculture: Soils for plant growth*, ASA-CSSA-SSSA, Madison, WI, 1989, page 45..68.

¹¹ *Lunar oxygen production—A maturing technology* by Carlton C. Allen, Gary G. Bond, and David S. McKay in *Engineering, Construction, and Operations in Space IV* (Proceedings of Space '94, Albuquerque, February 26 .. March 3, 1994), American Society of Civil Engineers, New York, 1994, page 1157..66.

byproducts are intimately mixed and it is a subject of debate whether the iron component may be economically separated in a useful form.

If obtaining reasonably pure metallic feedstock remains difficult, useful properties may still be obtained from fabrication processes performed directly on pyroclastic glass or other raw mineral stock. A glassy material may offer a reasonable softening temperature to allow for sintering, and with enough bulk to overcome brittleness may be a suitable material for containers and low-impact tools and construction elements.

Benefits

It is difficult to estimate the cost of transporting goods from Earth to another celestial body when there is no working transportation system available for the job. Estimates for the Moon range from \$7,000 to \$30,000 per kilogram and even possibly much higher, depending on whose scenario one has faith in. At these costs, the ability of fabricators to eliminate the transportation of a great deal of necessary equipment and construction elements will be a tremendous boon to any extensive space mission.

Perhaps more important than a quantitative dollar savings is the fact that one or more on-site fabricators would allow crew members to respond to emergencies and devise situational inventions which could make the difference between failed and successful missions. Also, if the fabricators were placed in advance and operated remotely for a period of time, the crew could arrive at a site which is already supplied with the tools and components needed to get to work on the objectives of the mission.

Next Steps

The way to begin evaluating whether space fabricators are workable is to test the concept with physical experiments. These experiments should be performed by robotic operation on the lunar surface after first confirming their feasibility in Earthbound tests. NASA has identified several terrestrial materials that simulate the properties of various lunar soils. One good simulant, called JSC-1, is available in large quantities, has the grain size distribution of actual lunar soils, and yields metallic iron as a byproduct of oxygen extraction.¹² We recommend that NASA engage in a program to design a lunar-surface apparatus, which would be built and first operated on Earth using JSC-1 or another lunar simulant. This would provide a low-risk way to prove out the concept and advance it in stages to actual implementation in future space missions. Coordinating these experiments with others on oxygen production and optical waveguides (as well as possibly solar wind gas extraction) may providing opportunities for sharing resources and lowering cost and launch mass.

Conclusion

As a commercial technology, additive fabricators are less than a decade old on Earth. The various methods are undergoing very rapid refinement and improvement. These methods present new possibilities for building up objects from celestially available materials. This new capability will allow explorers to venture forth with fabricators to build their homesteads and their industrial facilities. It has long been recognized that machines with such capability would be necessary to really make space settlement feasible, just as the European settlers needed their saws and hammers to begin building a home in America from native timber. It may be that fabricators will be the breakthrough that finally cracks the barrier to space habitation.

¹² JSC-1: A new lunar soil simulant by David S. McKay, James, L. Carter, Walter W. Boles, Carlton C. Allen, and Judith H. Allton in *Engineering, Construction, and Operations in Space IV* (Proceedings of Space '94, Albuquerque, February 26 .. March 3, 1994), American Society of Civil Engineers, New York, 1994, page 857..66.

Shape Deposition Manufacturing of Wearable Computers

Weiss, L.*, Prinz, F.***, Neplotnik, G.*, Padmanabhan, K.*, Schultz, L.* and Merz, R.**

(*) Carnegie Mellon University

(**) Stanford University

Abstract

Shape Deposition Manufacturing (SDM) is a solid freeform fabrication methodology which can fabricate heterogeneous structures, i.e., multi-material structures with embedded components. One application is to build-up electromechanical devices such as conformally shaped computer packages with embedded electronics. The goal is to be able to quickly design and manufacture, in small lots, personalized, rugged units for specialized applications. One example, which is described in this paper, is the manufacture of an underwater computer, the 'Frogman', which is built-up in layers of polyurethane.

Background

Current solid freeform fabrication (SFF) methodologies create 3D shapes by building up layers of material using material additive processes. One advantage of SFF is the capability to rapidly fabricate arbitrarily complex shapes. SFF processes which use selective material deposition techniques have additional advantages. They can be used to build up heterogeneous structures, i.e., multi-material shapes with embedded structures[1,2,3]. The capability to fabricate heterogeneous structures is important because this capability enables novel designs which would not be practical to build with conventional manufacturing processes[4]. One class of heterogeneous structures is embedded electronic devices which are fabricated by building up nonconductive housing packages and simultaneously embedding and interconnecting electronic components within the housing. With this approach it is feasible to rapidly and economically fabricate compact, rugged, customized computer modules in small lot sizes. The military is particularly interested in the capability to manufacture mission-specific, conformal shaped 'smart' devices such as wearable computers tailored for an individual soldier or a small military unit. These computers might store maps, equipment descriptions, help to log data, or provide communication links. This paper describes the use of Shape Deposition Manufacturing (SDM), an SFF process which can build heterogeneous structures to fabricate a water-proof, wearable embedded computer called the 'Frogman.' SDM is reviewed in the next section.

Shape Deposition Manufacturing (SDM)

SDM integrates material addition processes with material removal processes (Figure 1). Individual layer segments are deposited as near-net shapes, then accurately machined to net-shape, with a CNC mill, before additional material is deposited[5]. Each layer is composed of primary material(s) and complementary shaped sacrificial supporting material which is removed when the part is completed. At selected layers, prefabricated components can be placed on the current upper surface before subsequent deposition takes place, thus permanently embedding the component.

Several alternative material deposition processes are available for SDM. Embedded electronic devices are built up with polyurethane, to form the housings, and sacrificial wax which is removed by melting. Polyurethanes are deposited as 2-part resin/activator mixtures, while the wax is deposited with a hot-glue gun. In the Carnegie Mellon and Stanford SDM testbeds, the parts are built on pallets which are transferred from station-to-station using robotic automation.

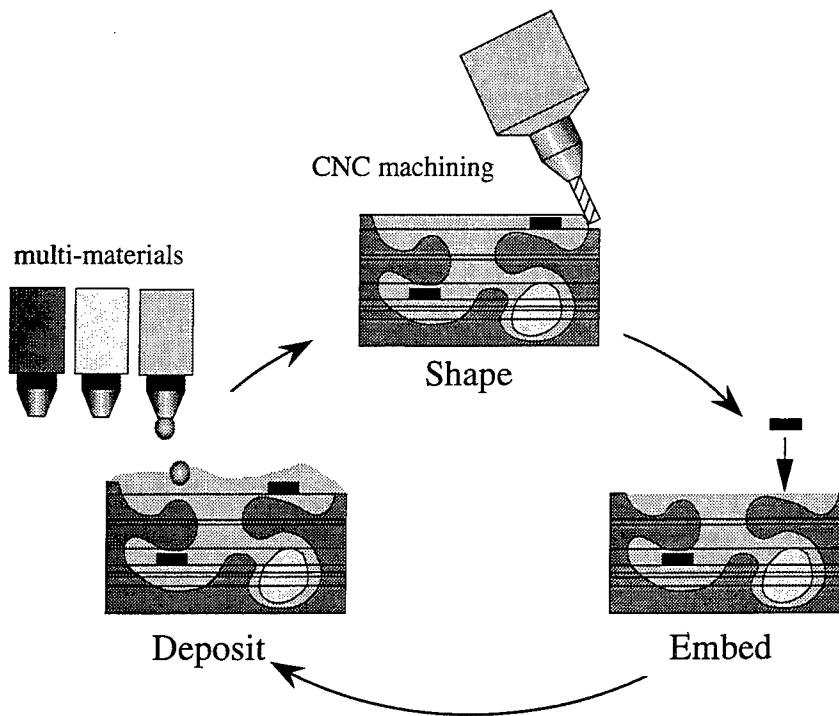


Figure 1. Shape Deposition Manufacturing

The basic SDM strategy is to slice the CAD model of the part into layers while maintaining the corresponding 3D geometry of the outer surfaces. The layer thicknesses vary depending on the local part geometry. Each layer is further decomposed into layer segments, or ‘compacts’, such that: undercut features need not be machined, but formed by previously shaped compacts, and each compact is composed of a single material. For example, Figure 2 shows the sequence for depositing and shaping the compacts and for embedding a component in a layer of a heterogeneous structure.

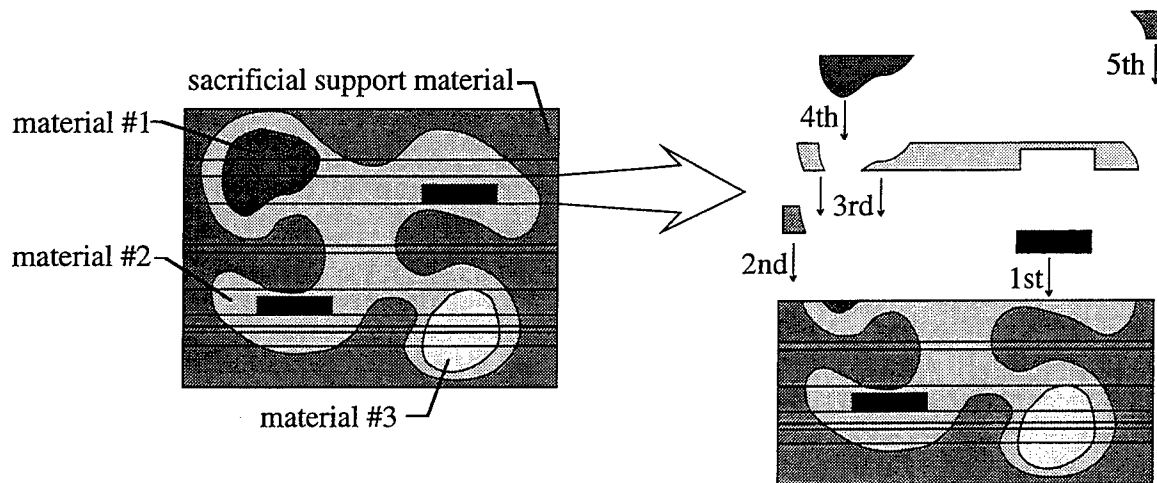
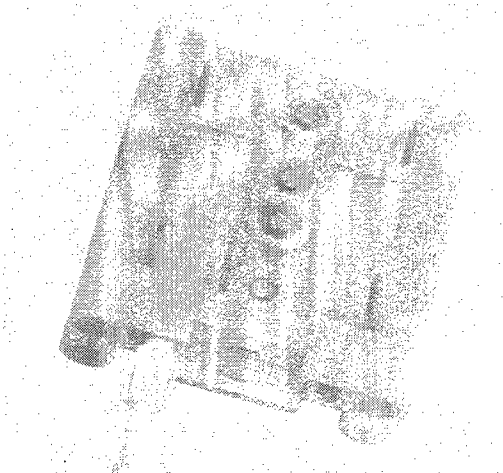


Figure 2. Deposition and shaping sequence.

Wearable Computers Built With SDM

Several generations of wearable computers, such as the 'VuMan' series[6], have been designed and built at Carnegie Mellon using conventional packaging methods. Recently, the use of SDM been investigated as an alternative method to manufacture these devices. For example, the shape deposited VuMan shown in Figure 3a is a computer which can store maps for navigational aids, or detailed assembly drawings for service and maintenance applications. The graphical information is displayed on a commercially available heads-up display (Reflection Technology, Inc., 'Private Eye') as shown in Figure 3b. The graphical information is stored on PCMCIA cards.

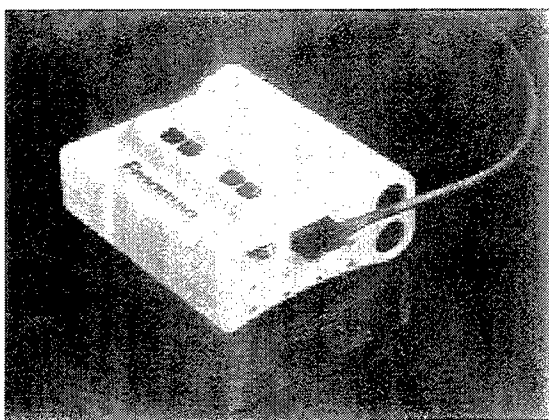
After completion of the VuMan-SDM, there was a request to repackage it, using the same set of PCBs, so that it would be waterproof to a depth of at least 100 feet. Several modifications had to be made, including using a different polyurethane formulation, incorporating waterproof switches, connectors and access covers, as well as using fewer batteries. A conformal shaped rear surface was also required so that the unit could be comfortably strapped to a diver's leg. A commercially available waterproof heads-up display would be interfaced to the unit. This waterproof Vuman, called the 'Frogman', is shown in Figure 3c. The important points are that retooling was not required to manufacture the Frogman and that embedding facilitates waterproofing. The construction of Frogman is described in the next section.



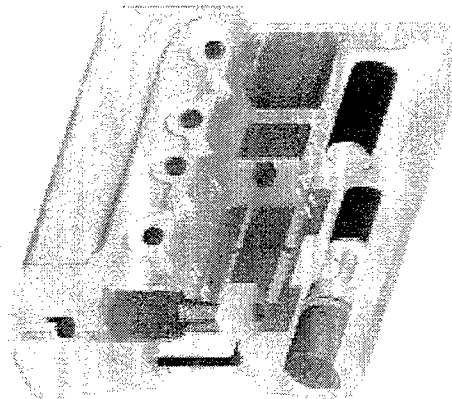
a. VuMan-SDM



b. Heads-up display.



c. Frogman



d. CAD rendering of Frogman

Figure 3. Wearable computers built with SDM.

Construction of Frogman

A cut-away, CAD rendering of Frogman is shown in Figure 3d. The unit is a four layer polyurethane structure. The polyurethane (Adtech Plastic Systems Corp., LUC-4180) is a two-part mixture which was deposited manually for this experiment. Each layer takes approximately 12 hours to gel before it is hard enough to be machined. The cured material has a tensile strength of 8 Kpsi with 15% elongation. A sacrificial wax support material (Kindt-Collins Company, MASTER Protowax) is deposited with a hot-glue gun. The Frogman contains two layers of printed circuit boards (PCBs); the first PCB is located on top of the first polyurethane layer, and the second PCB is located on top of the second PU layer. The two PCBs are electrically interconnected with vias made using pin receptacles (Mill-Max Mfg. Corp., pin receptacle #0136) which are more commonly used to make conventional IC sockets. The steps for making an embedded interconnect are depicted in Figure 4. While the Frogman has only two layers of PCBs, the interconnect system is designed so that each via can be extended upward to an arbitrary number of layers.

In addition to embedding PCBs and vias, several other waterproof devices must be formed within the growing shape, including indicating lights, switches, accessible battery and PCMCIA card compartments, and an external connector. To form an indicating light (e.g., power off/on indicator), a translucent lucite pipe is first glued to the lens of a surface mounted LED (Figure 5a). The LED and pipe are then embedded in the next layer of polyurethane. Then both the plastic pipe and the polyurethane are machined to form a sealed, blended surface (Figure 5b). Switches are formed using magnetic reed switches (Figure 6a). After a reed switch is embedded in a layer of polyurethane, a receptacle is cut-out over it and a prefabricated, spring-loaded magnetic button is glued into the receptacle (figure 6b). In operation, the force required to activate the switch assembly is independent of the water depth since water will flow around the spring.

In order to connect to a heads-up display, a commercially available, vulcanized underwater female connector (Underwater Systems, Inc., Micro_Mini Square #MM8S) is used. Since polyurethane will not bond to rubber, a polyurethane clamp with an internal O-ring is first bonded around the cable connection from the connector to the PCB (Figure 7a). Tape is also placed on the connector face to protect it from subsequent deposition. The connector is then placed on a polyurethane layer and embedded in the next layer (Figure 7b). In operation, water, which penetrates between the rubber/polyurethane interface, is stopped at the embedded clamp.

The PCMCIA card is housed in a compartment which is sealed with a removable, gasketed cover. The compartment is formed by first cutting out a section into a layer of polyurethane for the PCMCIA receptacle as depicted in Figure 8a. Then, a prefabricated teflon cover, with attached metal anchors for the cover screws, is placed in guides cut into the compartment opening. The PCMCIA receptacle (which is affixed to the bottom of a PCB) is then placed into the compartment as depicted in Figure 8b. The next layer of polyurethane is deposited over that to form the entire compartment (Figure 8c). The teflon cover can be removed to access the PCMCIA receptacle, since the polyurethane does not stick to teflon (Figure 8d).

The battery compartment is formed with the aid of a teflon coated, aluminum mandrel which is removed when the entire computer is completed. First, a locating channel for the mandrel is cut into a layer of polyurethane, and the mandrel is placed in that channel adjacent to a PCB segment (Figure 9a). The mandrel contains a copper contact ring which will remain embedded in polyurethane once the mandrel is removed (Figure 9b). This ring, which is soldered to the PCB, will form a battery contact and also act as an anchor for attaching the battery compartment cap (Figure 9c). The rear of the mandrel locates a second battery contact which is soldered to the PCB. After the mandrel is placed, the next layer of polyurethane is deposited over it. When the mandrel is removed, batteries are placed within the formed polyurethane tube, then a copper insert is locked into the retainer ring, a brass screw is screwed into the insert to contact the battery, a gasket is placed over the screw, and the prefabricated battery cap is screwed in place.

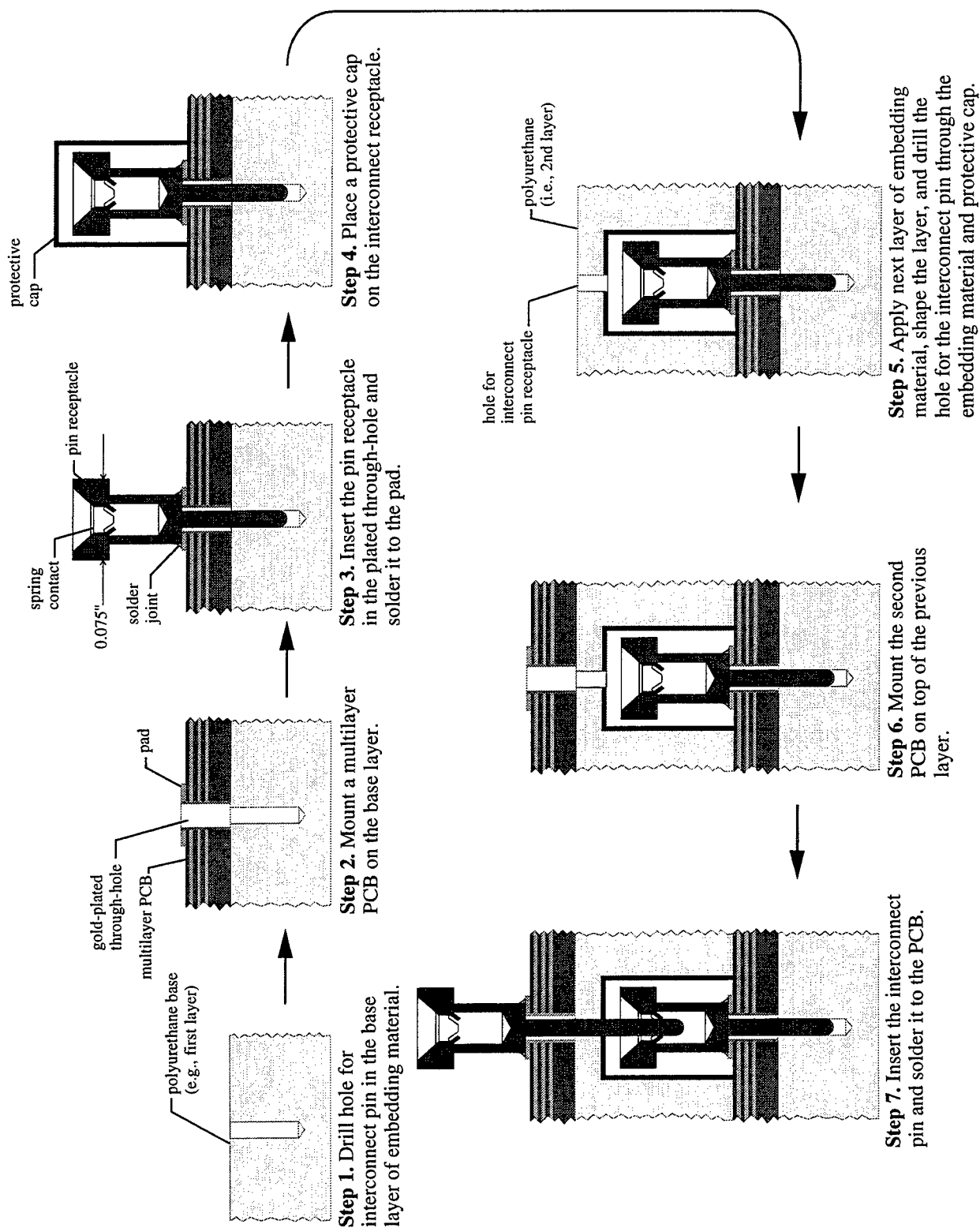


Figure 4. Sequence for installing vias.

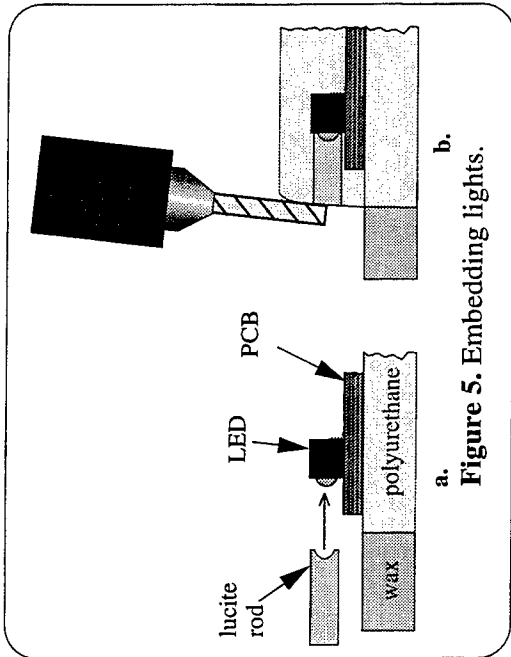


Figure 5. Embedding lights.

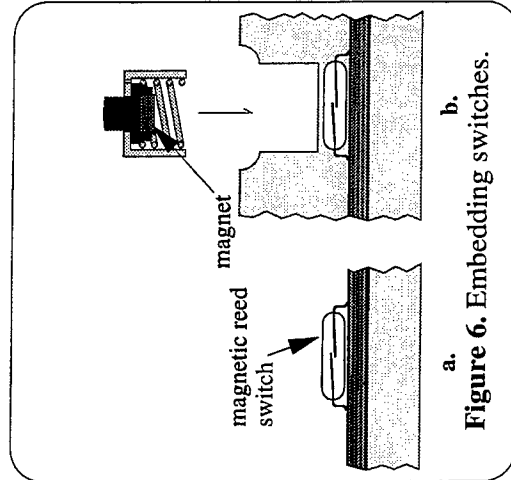


Figure 6. Embedding switches.

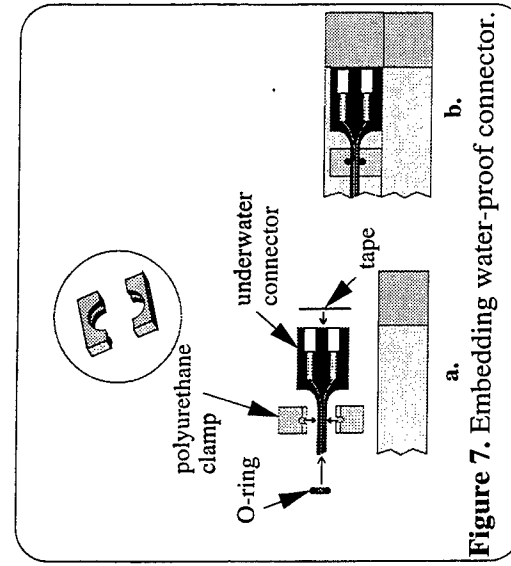


Figure 7. Embedding water-proof connector.

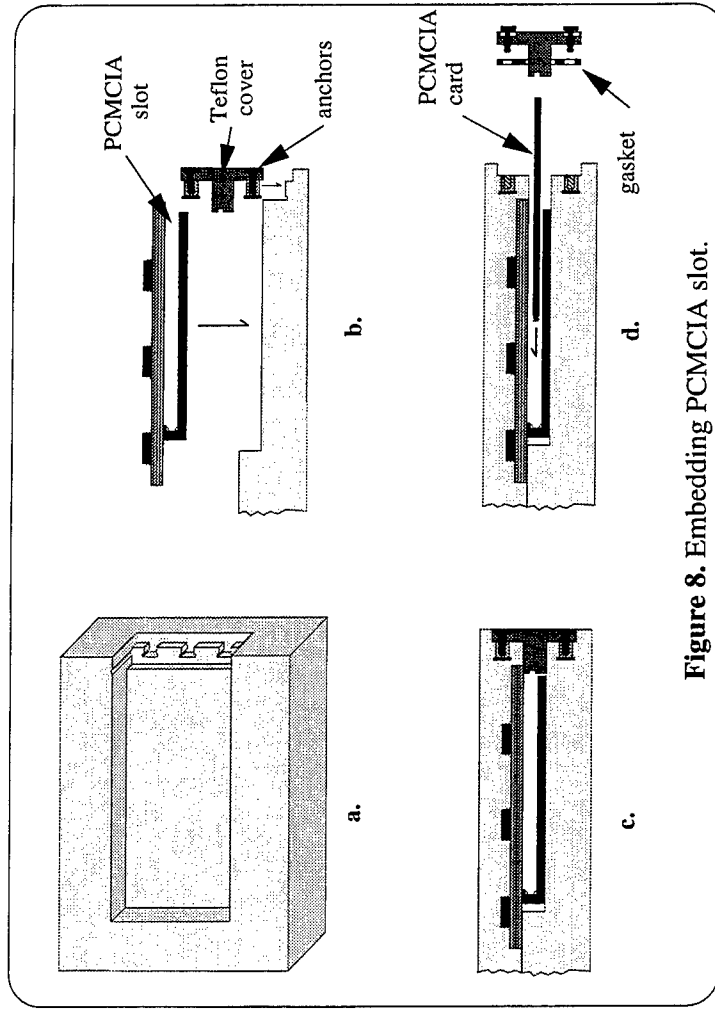


Figure 8. Embedding PCMCIA slot.

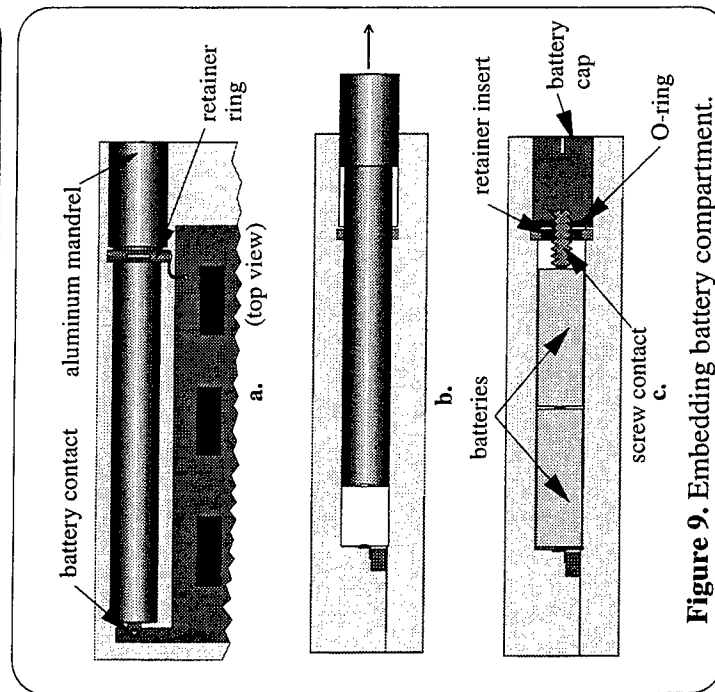


Figure 9. Embedding battery compartment.

Discussion

There are several issues which must still be addressed in order for freeform fabrication of embedded electronic structures to be a practical manufacturing approach. One key issue is that embedded devices are not easily repairable. While we have made repairs by drilling into completed units to expose and replace failed components, this takes considerable expertise. To minimize product failure, we test each layer of electronics as the units are built up. Assuming that embedded devices can be built up reliably, and that they fail predominantly in infant modes, then these products would be analogous to high-end processors, such as Pentiums, for which consumers are willing to pay a premium price even though they cannot be repaired.

It currently takes several days to build an embedded electronic structure with SDM due, in part, to the relatively long time required for each layer of polyurethane to gel. With the current formulation, each layer of polyurethane takes approximately 12 hours to cure before it can be machined. While the Frogman was built in about 10 working days, which included the time it took to debug some new embedding strategies, it is estimated that one could be manufactured in ~60 hours by using more efficient machining plans and with full automation. To increase the net through-put, one option would be to build multiple devices, in parallel, using a palletizing system to both store and register the work pieces. Products would be queued so that as some layers are curing, others are being machined. The goal is to be able to manufacture 10 to 20 units per week (*i.e.*, a product with the complexity of the Frogman) using a single CNC machining center. Larger batch sizes could be built using additional machining centers.

An important quality measure of wearable computers is weight. The mechanical structure amounts to a significant portion (50% or more) of the total system weight. High bending stiffness and strength can be maintained by placing stiff and strong materials as close to the surface as possible. The rest of the inside structure can be filled with less dense material capable of preventing the transmission of vibratory and shock loads to the electronic components. The combination of high-strength, dense materials in the vicinity of outside surfaces, with lower density materials inside, allows minimizing weight while keeping bending and buckling strength at an acceptable level. While the Frogman was manufactured with a single material, SDM multi-material processing will enable designers to choose proper material combinations and create unique material distributions to build innovative and light computer devices which could not be fabricated with conventional methods such as injection molding.

Thermal and mechanical design specifications of wearable computers are highly interlinked and dependent upon each other. Three dimensional distribution of circuit components is controlled by device shape which, in turn, is determined by external specifications, as well as the arrangement of user-interface components (*e.g.*, switches, connectors, displays). The current design methods used for Frogman required extensive and time consuming human interaction to link electronic and mechanical designs. For rapid production, automated links between electronic and mechanical design through proper CAD software are necessary.

References

- [1] Beck, J.E., Prinz, F.B., Siewiorek, D.P. and Weiss, L.E., "Manufacturing Mechatronics Using Thermal Spray Shape Deposition," Solid Freeform Fabrication Symposium, The University of Texas at Austin, August, 1992.
- [2] Weiss, L.E., Prinz, F.B., Adams, D.A. and Siewiorek, D.P., "Thermal Spray Shape Deposition", Journal of Thermal Spray Technology, Vol. 1, 1992, pp. 231-237.
- [3] Prinz, F.B., Weiss, L.E. and Siewiorek, D.P., "Electronic Packages and Smart Structures Formed by Thermal Spray Deposition", 1994, U.S. Patent No. 5,278,442.

- [4] Weiss, L.E., "Solid Freeform Fabrication Processes," Proceedings of the NSF Workshop on Design Methodologies for Solid Freeform Fabrication, Carnegie Mellon University, June 6, 1995
- [5] Merz, R., Prinz, F.B., Ramaswami, K., Terk, M. and Weiss, L.E., "Shape Deposition Manufacturing", Proc, 1994 Solid Freeform Fabrication Symp., Austin, 1994, eds. H.L. Marcus et al., pp. 1-8.
- [6] Smailagic, A. and Siewiorek, D.P., "The Vuman 2 Wearable Computer", IEEE Design & Test of Computers, Sept., 1993, pp. 56-67.

Acknowledgements

This work was supported by the Defense Advanced Research Projects Agency. The authors also wish to thank Dan Siewiorek, Dick Martin, Asim Smailagic, Randy Casiola, Drew Anderson, Tom Martin, Cigdem Yasar, John Stivorik and Krishnan Ramaswami for their contributions to this research.

Development of Direct SLS Processing for Production of Cermet Composite Turbine Sealing Components - Part I

T. Fuesting[†], L. Brown[†], S. Das[‡], N. Harlan[‡], G. Lee[‡], J. J. Beaman[‡], D. L. Bourell[§], J. W. Barlow[‡], K. Sargent[§]

Abstract

This paper presents the development to date of SLS (selective laser sintering) technologies for production of cermet composite turbine sealing components, the particular application being an abrasive blade tip. The component chosen for the application is an integral part of the low pressure turbine in a IHPTET (Integrated High Performance Turbine Engine Technology) demonstrator engine. Both indirect and direct SLS techniques are being developed. Initial trials and process development involved the use of fugitive polymeric binders. Sequential refinements were performed to develop a binderless direct SLS process. Results from mechanical testing indicate that acceptable microstructure and properties are attainable by SLS with substantial cost savings as compared to the currently employed production method. This is the first instance of direct SFF methods applied to a functional component.

INTRODUCTION

Since its inception in the 1930's, the gas turbine engine has grown to be the workhorse power plant of modern aircraft. Advanced technology propulsion systems are very important from an overall system affordability viewpoint since higher engine performance can result in a smaller airframe. In 1988, the United States Department of Defense and the National Aeronautics and Space Administration combined forces with industry to focus gas turbine engine research and development efforts toward the goal of doubling current levels of propulsion capability by the turn-of-the-century. Known as the IHPTET (Integrated High Performance Turbine Engine Technology) program, this aggressive technology development plan's specific goals are to increase thrust-to-weight, reduce fuel burn, and reduce the cost of high performance gas turbine engines.

Increased affordability can be accomplished by either increasing engine performance without cost penalty or by decreasing engine cost without sacrificing performance. The two principal aspects that IHPTET is targeting to reduce engine life cycle cost are engine unit acquisition cost and, operating and support costs. The technological developments required to lower the cost of future engines are advanced materials, innovative structural designs, improved aerothermodynamics, advanced computational methods, and advanced manufacturing techniques. The integration of these advanced technologies will not only provide the benefit of improved performance, but will also help to make engine systems more robust and more affordable. IHPTET cost reduction studies¹ have found that a key to engine cost reduction is cost effective fabrication and manufacturing. These studies have also shown that several principal factors can contribute to lower manufacturing costs for the advanced technology engine, including its smaller size, reduced parts count and cost effective manufacturing methods.

An example of advanced manufacturing methods that can impact cost reduction of engine components is SFF. This technology is striving towards decoupling cost from volume² by making it possible to produce the first unit at a recurring cost equal to the hundredth unit³. The IHPTET program has chosen an application to demonstrate this technology. It is a cermet composite component that is an integral part of the low pressure turbine in an IHPTET demonstrator engine.

[†] Allison Engine Company, Indianapolis, Indiana

[‡] Laboratory for Freeform Fabrication, University of Texas at Austin

[§] Wright Laboratory, Wright-Patterson AFB, Ohio

This paper begins with a brief background on gas turbine sealing technology. The objectives for pursuing the research described herein are discussed next. The potential for significant cost savings by pursuing SLS as a manufacturing technique is demonstrated. The Allison Engine Co. "standard cermet" production technique is described, followed by a description of materials and methods used in this research. The results section compares properties of cermet material processed by SLS with those of cermet produced by the standard production technique. Problems encountered with materials interaction in the cermet composite and their solutions are discussed. Conclusions and plans for future work are presented.

BACKGROUND

Gas turbine efficiency is highly dependent upon minimizing leakage of the gas away from and around the working gas path. Therefore, clearance between rotating and static parts is critical. This clearance changes with component expansion and contraction due to the thermal cycling experienced in gas turbines. One of the primary methods developed for accounting for this expansion and contraction is an abradable seal system^{4,5}. This seal system works by attaching a cermet composite abrasive blade tip (ABT) to the sealing surface of the rotating component. The circular stationary component is coated with an appropriately engineered semi-porous abradable ceramic which is abraded by the rotating cermet to form a shroud type gas path seal around the rotating component.

The semi-porous ceramic component is relatively inexpensive and simple to manufacture. However, the abrasive cermet (0.035-0.060 inches thickness) is difficult to manufacture on a production scale and contains expensive components. The cost of the raw materials makes scrap highly undesirable. Manufacturing of this layer typically involves rolling and pressing a mixture of the ceramic and metal alloy powders with an organic binder to the correct thickness. The rolled mat is then vacuum sintered. It is evaluated for proper microstructure, machine ground to proper thickness, laser cut and metallurgically bonded to the rotating hardware. This complete process is labor intensive and can result in a significant amount of scrap if stringent manufacturing processes are not adhered to.

Due to the difficulties encountered with standard abrasive cermet production, an alternate approach for producing this material is desired. Since the standard production material is capable of being laser cut to final shape, laser sintering of the constituent powders was the primary alternate approach chosen. SLS (Selective Laser Sintering) is a rapid manufacturing technique that builds parts from a powder base. SLS creates freeform 3-dimensional solid objects without the use of any tooling or human intervention. Details on this process are described elsewhere^{6,7,8}.

SLS has been commercially developed by DTM Corporation and is in use for prototyping models from polymeric powders and for creating investment casting wax patterns. More recently, DTM has introduced RapidTool, a technology for creating prototype metal tooling from polymer coated metal powders⁹. This process uses indirect SLS techniques¹⁰ which involve the use of fugitive polymer binders to produce a "green" shape that is subsequently post-processed by binder burn-out, sintering and infiltration to produce high density metal and ceramic parts and tooling^{11,12,13,14,15}. A functional metal part, porous or fully dense, has not been made previously by direct SLS. The terminology "direct SLS" implies a binderless SLS process in which the material constituents are directly laser sintered to produce a high density part requiring little or no post-processing.

The expensive and difficult to manufacture abrasive cermet composite can potentially be

directly laser sintered, therefore making it an ideal part for processing by direct SLS. An SLS process for producing abrasive cermet composite can potentially provide a uniform, repeatable manufacturing process that would eliminate much of the manual labor as well as reduce scrap and make all unsintered fall off materials reusable.

OBJECTIVES

The primary goal of research described herein is to develop an SLS process capable of producing the cermet. The cermet produced by SLS must have properties equivalent to the current production material used by Allison Engine Company. The process developed should allow for possible reuse of all unsintered fall off material. Another goal is to eliminate a low melting point braze constituent which will extend oxidation life and possibly allow higher operating temperatures.

Reducing production costs and achieving a repeatable production process are the primary motivation for pursuing SLS as a manufacturing technique in this application. The typical manufacturing method of tape casting and rolling requires a fixed amount of material input per lot, independent of the actual parts needed per lot size, up to lot sizes producing 1000 parts. For prototype lot sizes to produce 100 parts or less, this method becomes expensive considering the cost of the materials involved. Moreover, sintered material left over after the laser cutting step, "fall-off", is scrap. Since direct SLS does not utilize a binder, it eliminates nearly all scrap material by enabling recycling of all fall-off materials from a lot. This significantly reduces the cost and results in the primary portion of the cost savings. The remainder of the cost savings are realized by elimination of labor intensive tape casting and rolling in the currently employed production process. A cost break-down, shown in Figure 1, was performed to illustrate the potential benefits of developing an SLS process. The details and assumptions used to formulate this break down are provided in Table 1. Obtaining a repeatable production process also results in very large cost savings which are not directly measurable. The current production process has variable yield, resulting in a significant amount of scrap due to unacceptable porosity.

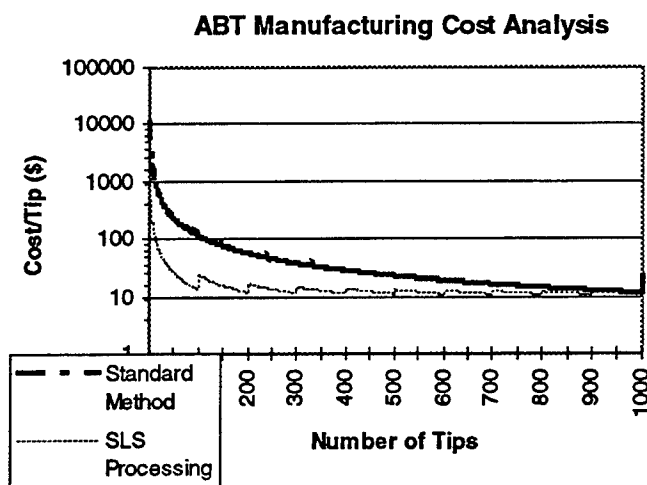


Figure 1. Standard method Vs SLS processing cost comparison

Assumptions

SLS - Lot size of 100, 90% efficiency, material costs \$900
Standard method - Lot size of 1000, 80% efficiency, material costs \$10,000

	Material	Mixing and Casting	Cutting and Programming	Grinding	Sintering
SLS	\$900	2 hours	4 hours	$0.5 + (0.02 \times N)$	0
Additional Lots	\$900	2 hours			
Standard	\$10000	8 hours	$4 + (0.03 \times N)$	$0.5 + (0.02 \times N)$	8 hours
Additional Lots	\$10000	8 hours			8 hours

N= number of cermet preforms

Table 1. Cost breakdown

MATERIALS AND METHODS

Standard Cermet Production

The standard abrasive cermet composite is composed of two different types of titanium coated ceramic abrasive grit, a nickel alloy matrix, and a lower melting point cobalt based braze material. The compositions of the metal alloy components are provided in Table 2. The titanium coating on the ceramic grit functions as a bonding interlayer to promote a metallurgical bond as opposed to a mechanical interlocking bond which would result from using uncoated grit. A metallurgical bond is more effective in preventing grit pull out which occurs during rubbing or abrading of the cermet composite. Physically or mechanically interlocked grit has a high tendency to be pulled out of the matrix by the shear forces encountered during rubbing. Removal of grit particles results in reduced abrasive for cutting a clear path which has two consequences: (1) the metallic matrix will be rubbing the ceramic abrasable seal material, increasing friction forces and reducing efficiency, and (2) occurring but less likely, the pullout introduces a gap for compressed gas to leak around the working path. Additional details are described elsewhere^{16,17}.

Material	Ni	Co	Cr	Al	Ti	W	Si	B	Mo	Ta	Hf
Mar-M-247	Bal	10.0	8.4	5.5	1.0	10.0		0.01	0.7	3.1	1.4
*CMSX-3	Bal	4.6	7.8	5.6	1.0	8.0			0.5	6.0	0.1
Ø Amdry 788	21.0	Bal	22.0			14.0	2.0	2.0			
* CMSX-3 is a registered trademark of Cannon-Muskegon Corp.											
Ø Amdry 788 is braze alloy from Sulzer Plasma Technik, Inc.											

Table 2. Nominal compositions of matrix materials used in the cermets

To produce a "lot" of this material via tape casting and rolling, a fixed amount of material input is required regardless of the lot size. These materials are mixed by low energy ball milling followed by the addition of an organic binder. The mixture is then tape cast and subsequently rolled to eliminate porosity and obtain the desired thickness. After rolling, the material is fired in a vacuum furnace to burn off the binder and consolidate the mixture by melting and diffusing the braze constituent. After densification the material is metallographically analyzed to determine whether it meets homogeneity and porosity requirements. To meet homogeneity requirements,

the sintered material must exhibit no discrete layering or agglomeration of abrasive particles which would result in grit pullout causing a decrease in efficiency. Porosity requirements allow for no more than 20% linear porosity as determined from a metallographic montage using a line intercept method. If the material meets these specifications, coupons are removed and brazed into the gage section of a test bar conforming to ASTM E139 and subjected to an application specific stress-rupture test. The details of this test are provided in the results section of this paper.

The strength and oxidation resistance of the cobalt braze component are factors currently limiting the application temperatures. There are alternate methods of making brazeless cermet, such as HIP (hot isostatic pressing), ROC (rapid omni-directional compaction) and Electro-deposition. However, they are more labor intensive. Therefore, development of a direct SLS process for production of brazeless cermet will not only provide significant cost savings but also performance enhancement over that of the braze containing composition.

Cermet Production by SLS

Apparatus

The apparatus used for this research included SLS workstations equipped with Nd:YAG and CO₂ lasers. The indirect SLS work was done at ambient atmosphere using a 25 Watt CO₂ laser. The direct SLS work was conducted on SLS workstations equipped with 100 Watt and 250 Watt Nd:YAG lasers, powder bed heating capability and controlled atmosphere.

Processing Methods

Two SLS processing methods were investigated concurrently. The most desired method is direct SLS which involves directly melting and consolidating selected regions of a powder bed to form a desired shape having high or full density. Direct metal laser sintering involves melting the component matrix and obtaining the appropriate amount of flow from the molten material. The appropriate amount of flow is critical and can be described as the flow that eliminates porosity, produces a highly dense part maintaining dimensional tolerances and minimizes other defects such as hot tearing. The appropriate amount of flow is controlled by several factors such as atmosphere, powder bed heat and three characteristic variables affecting laser energy density: laser power, scan spacing and scan speed.

These SLS processing parameters can be refined within a working window depending upon the mechanical properties desired. In addition, a post-process heat treatment may be applied to modify the microstructure. The parameter used for microstructure refinement was the energy density¹⁸ defined as

$$A_N = \frac{P}{v \cdot \delta} \text{ (J/cm}^2\text{)}$$

where

P is the incident laser power (Watts)

v is the laser scan speed (cm/s)

δ is the scan spacing (cm)

An alternative method investigated is indirect SLS. The term "indirect" implies that the metal powder is not melted directly by the laser. Instead, a low glass transition temperature polymer binder either mixed into the powder or present as a coating on the powder particles softens and flows during selective laser sintering. This polymer acts as the binding phase, giving

strength to the “green” part. The “green” part is post processed to burn off the polymer and sinter the metal powder. The goal of this processing method was to develop the procedure into a process that incorporates laser volatilization of the binder immediately before or during direct SLS.

Indirect SLS material preparation

The constituent components were combined according to the compositions shown in Table 3 below and ball milled in a tungsten carbide container. The composition of the cobalt braze was varied to determine its effect on the final properties of the sintered composite, providing an optimized composition with respect to braze content. The amount of cermet grit remained constant in all mixtures. All grit except the grit used in Mixture 5 was coated with titanium.

Material	Composition 1	Composition 2	Composition 3	Composition 4	Composition 5	Composition 6
Alloy	Bal	Bal	Bal	Bal	Bal	Bal
Braze	24.3 wt. %	21 wt. %	18 wt. %	15 wt. %	24.3 wt. %	24.3 wt. %
Grit	Ti Coated	Ti Coated	Ti Coated	Ti Coated	Uncoated	Ti Coated
Binder	2.0 wt. %	2.0 wt. %	2.0 wt. %	2.0 wt. %	2.0 wt. %	2.0 wt. %

Table 3. Indirect SLS compositions

Initial trials indicated that there was a sporadic problem with grit segregation. To eliminate this problem, a slurry was created by adding acetone. The slurry was mixed in a motor driven stirrer. During mixing, the acetone evaporated leaving a highly viscous slurry paste which was pressed to form a thin cake and dried to volatilize the remaining solvent. The cake was crushed using a mortar and pestle to form a coarse powder composed of roughly 500 μm particle agglomerates. SEM micrographs are provided in Figure 2.

The agglomerate powder was placed in the stainless steel mold of a compression molding press. The platens of the molding machine were preheated above the binder softening temperature. Pressure was maintained during heat up and cool down. The fractional density of the bound and pressed preform was measured, using the linear intercept method, at 60%.

Indirect SLS processing

SLS processing included cutting the desired shape from the pressed preform using a 25 Watt CO_2 laser. Several passes were necessary at this laser power to completely penetrate the 0.060” preform thickness. Use of higher laser power of the order of 100 Watts would facilitate cutting the shape in a single pass. Other process trials addressed the volatilization of the binder utilizing low power scanning to facilitate direct SLS processing.

Direct SLS material preparation

Material preparation for the direct SLS method was simpler. The metal alloy and ceramic constituents were combined according to mixture 3 shown in Table 3 above and blended for 4-6 hours prior to loading in the SLS chamber.

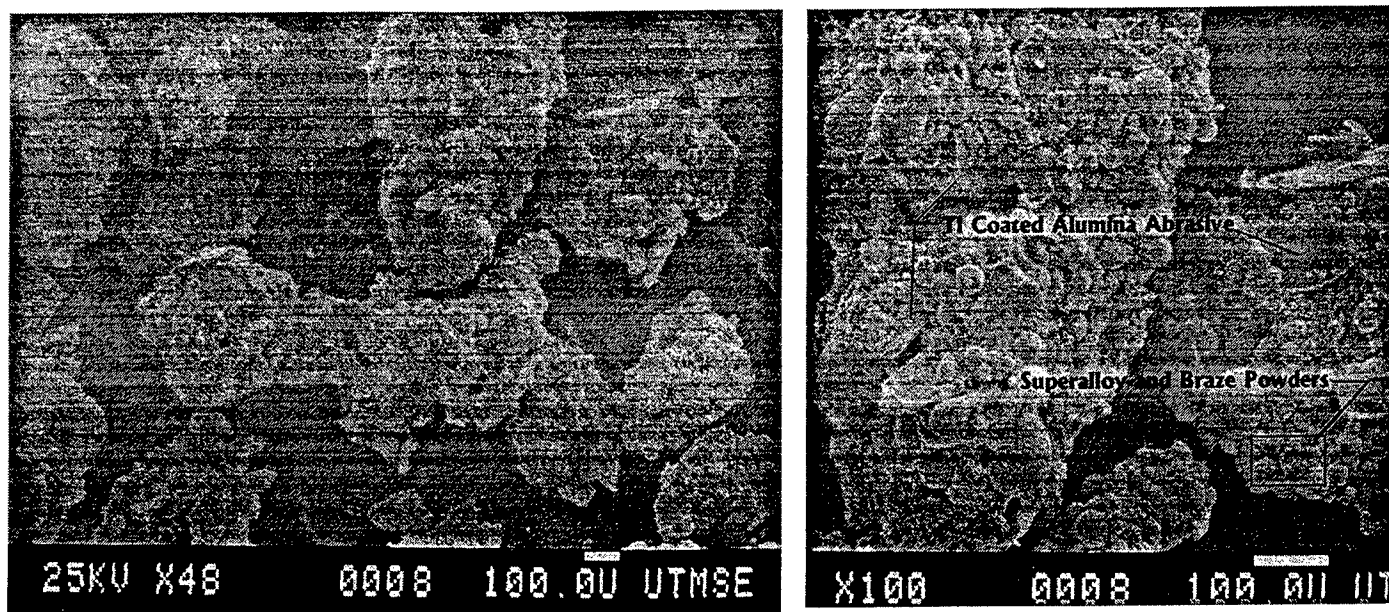


Figure 2. SEM micrographs of Agglomerates

Direct SLS processing

To characterize the behavior of the metallic constituents of this material system with respect to laser irradiation, the superalloy and the cobalt braze were individually processed by SLS. These initial screening trials indicated that structurally sound monolithic single layers could be produced. Typical microstructures from these trials are shown in Figures 3 through 5. However when the metal alloys were blended together the material exhibited severe balling. The balling of the alloy mixture is demonstrated by the photomicrograph of the sample in Figure 5. The uniform dendritic microstructure is indicative of thorough melting and mixing.

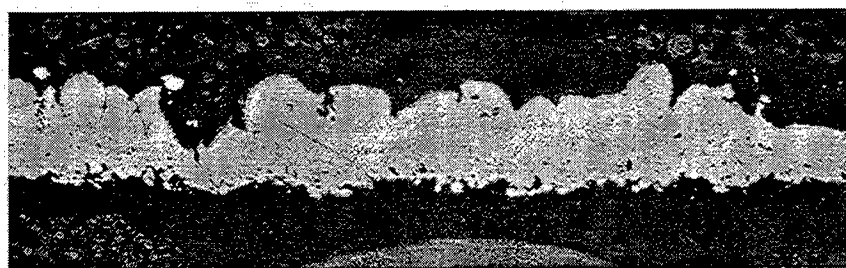


Figure 3. Direct SLS Mar-M-247, no etch, magnification 50X

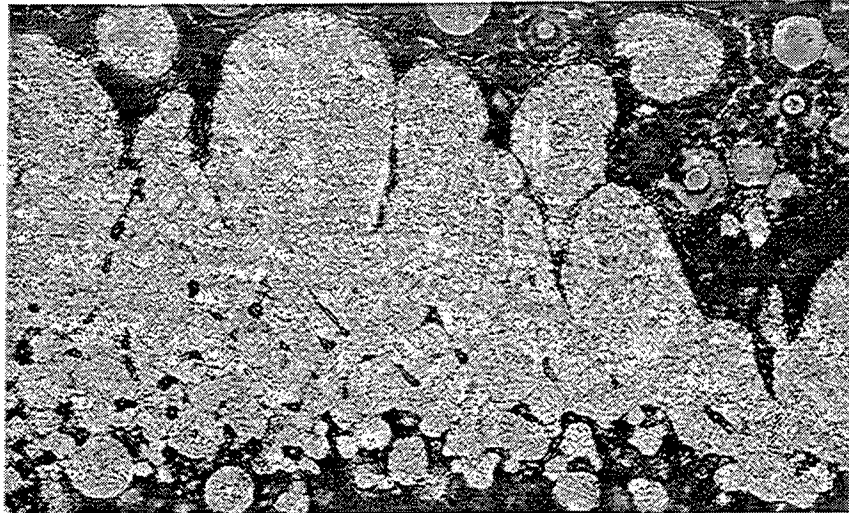


Figure 4. Direct SLS cobalt braze, no etch, magnification 200 X

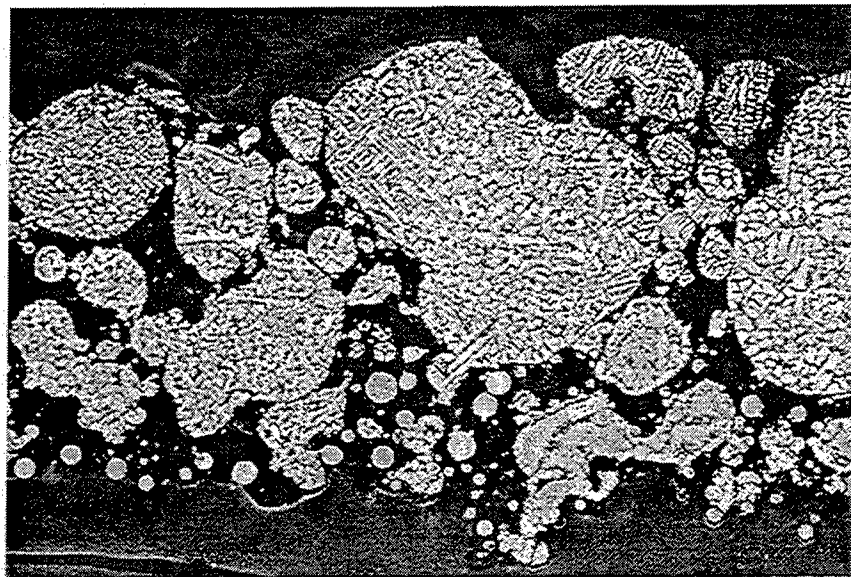


Figure 5. Direct SLS Mar-M-247 & braze alloy, magnification 200 X

As stated earlier, one of the goals of this research was to investigate the elimination of the cobalt braze alloy from the material system. Due to the severe balling exhibited by the standard mixture recipe, direct SLS of a brazeless cermet composition was pursued. This composition was formulated by replacing the weight fraction of the cobalt braze by the nickel base superalloy. This composition was utilized in all direct SLS experiments conducted for the remainder of the program.

Development of Direct SLS Processing for Production of Cermet Composite Turbine Sealing Components - Part II

T. Fuesting[†], L. Brown[†], S. Das[‡], N. Harlan[‡], G. Lee[‡], J. J. Beaman[‡], D. L. Bourell[§], J. W. Barlow[‡], K. Sargent[§]

RESULTS AND DISCUSSION

Indirect SLS

Coupons from each of the compositions shown in Table 3 were fired in vacuum to burn off the binder and fully consolidate the coupons. Shrinkage measurements taken from these coupons placed the shrinkage at 4%-6%. Metallographic evaluations revealed that all samples possessed relatively uniform grit distribution. A typical microstructure is provided in Figure 6.

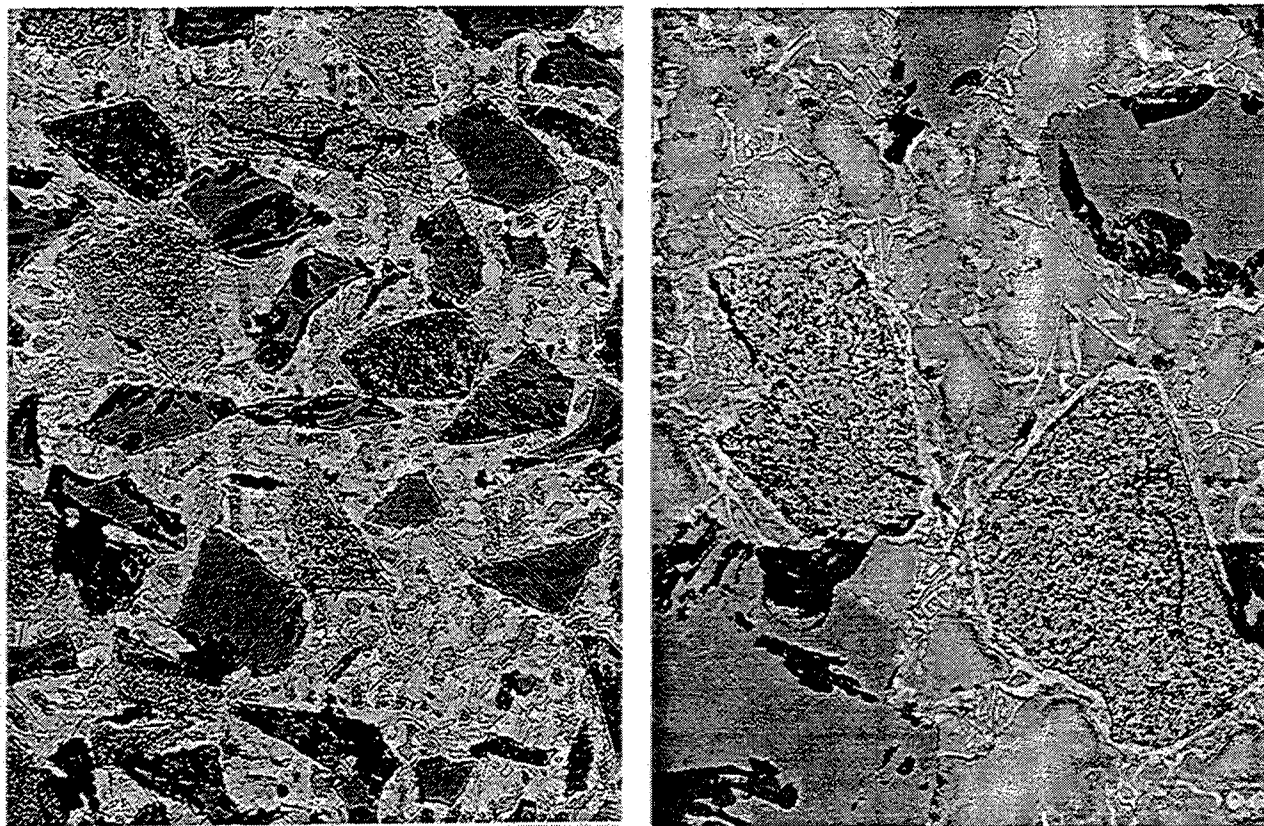


Figure 6. Typical microstructure of indirect processed material, magnifications 100X & 250X. However Compositions # 4 and #5 illustrated substantial pullout of grit particles during polishing.

The microstructures of Composition #4 is provided in Figure 7. In Composition #4 the grit pull out was associated with the reduced braze content and in Composition #5 this was associated with the alumina used which did not have a titanium coating. This experiment effectively illustrated that the titanium coating on the alumina is necessary. The minimum braze content for an indirect process was established at approximately 18% by weight.

Samples of Compositions #2 and #3 were manufactured according to the process detailed

[†] Allison Engine Company, Indianapolis, Indiana

[‡] Laboratory for Freeform Fabrication, University of Texas at Austin

[§] Wright Laboratory, Wright-Patterson AFB, Ohio

above. The samples of Composition #3 had circular patches removed which were surface ground and brazed using a braze alloy into the gage section of a single crystal stress rupture bar. The acceptance criteria requires that the sample survive a minimum of 2100°F/35 hours. The results of the four specimens are provided in Table 4. Only one sample did not meet the qualification criteria, this sample failed at the braze joint, indicating a bond defect.

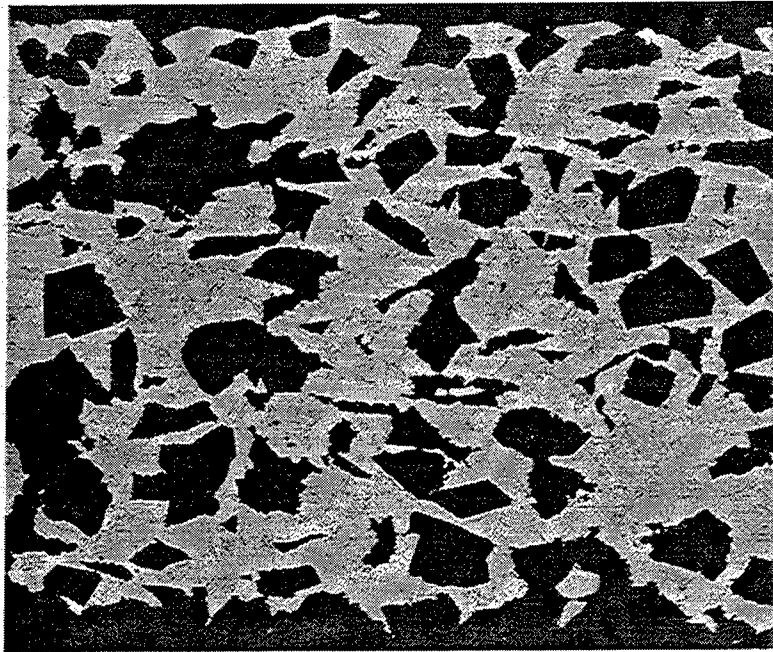


Figure 7. Microstructure of Indirect Processed Composition # 4 illustrating grit pull-out, magnification 100 X

Sample	Stress (psi)	Time (hrs)	Temperature (°F)
3-AM	500	50	2100 48 hrs.
3-BM	500	50	2100 No failure
3-CM	500	50	2100/8.2 hrs. Braze Failure
3-DM	500	50	2100 No failure

Table 4 Stress rupture test results of indirect SLS processed cermet

Rub coupons were also manufactured from the samples and rub tested at room temperature. The results are provided in Table 5. A schematic of a rub test is provided in Figure 8.

Processing	Composition	Volumetric Rub Ratio	Linear Rub Ratio
Indirect	3	170	13
Indirect	2	511	14
Allison conventional	3 Equivalent	140	144

Table 5 Rub testing of indirect processed material against seal material (Quantabrad 2)

Evaluation of room temperature rub testing results on Compositions #2 and #3 provided interesting results. The evaluation involved linear rub ratios which is the ratio of ceramic rub scar depth to abrasive cermet height loss which is not an extremely precise measurement due to the fact that tip height loss, if not significant, is not easily and accurately measured. In general, linear rub ratios in excess of 10 are good and meet abrasive blade tip goals. The indirect SLS materials evaluated met this goal.

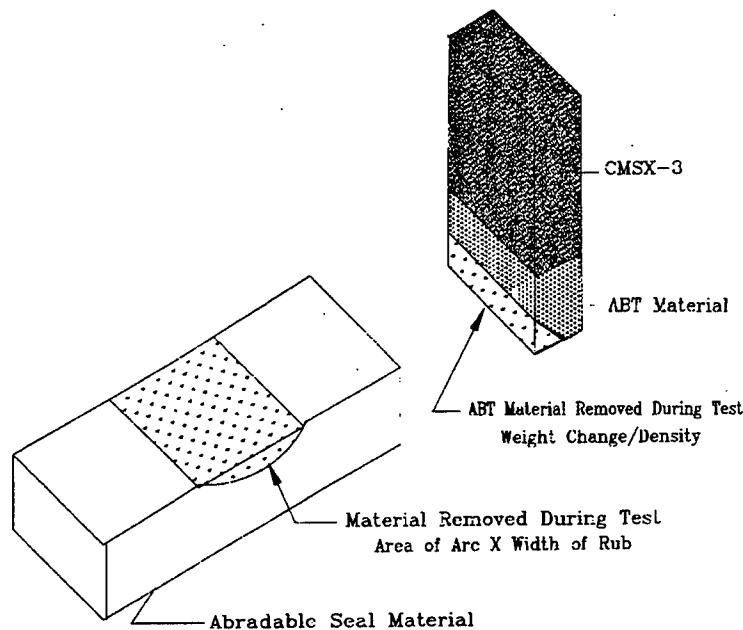


Figure 8. Illustration of Rub Testing

A more accurate measure is a volumetric comparison which is the ratio of rub scar arc depth multiplied by the rub scar width to the tip weight loss divided by the abrasive density. Simply stated this is the ratio of the abradable seal material rub scar volume to the volume lost on the abrasive tip.

As the data indicates, the volumetric comparison provides different results than the linear rub ratio comparison. A volumetric rub ratio in excess of 30 is considered good. The volumetric comparisons indicate the results of the SLS processed material are very good. It is to be noted that all of the above materials would be considered equivalent based on the limited number of tests run. To distinguish one as being better than another, a statistically significant number of tests from different lots of materials would need to be conducted and then reviewed with

accompanying stress rupture data.

The testing of indirect SLS processed cermet indicated that it was comparable in microstructure and mechanical properties to the material processed by the standard technique. Therefore a final process demonstration was completed to illustrate that production of blade tips via the indirect process is feasible.

A small lot of material was manufactured to produce 4 pieces of hardware. The parts were laser scanned to final shape accounting for 4% shrinkage. The parts were subsequently fired in vacuum. Two of the four pieces of hardware produced are illustrated in Figure 9. The microstructure of the parts, presented in Figure 10, was very uniform and passed all requirements.

As discussed earlier, follow-on development was aimed at volatilizing the binder using low power scans of the laser. These experiments were canceled due to the coating of laser optics and chamber apparatus by the volatilization of the binder.

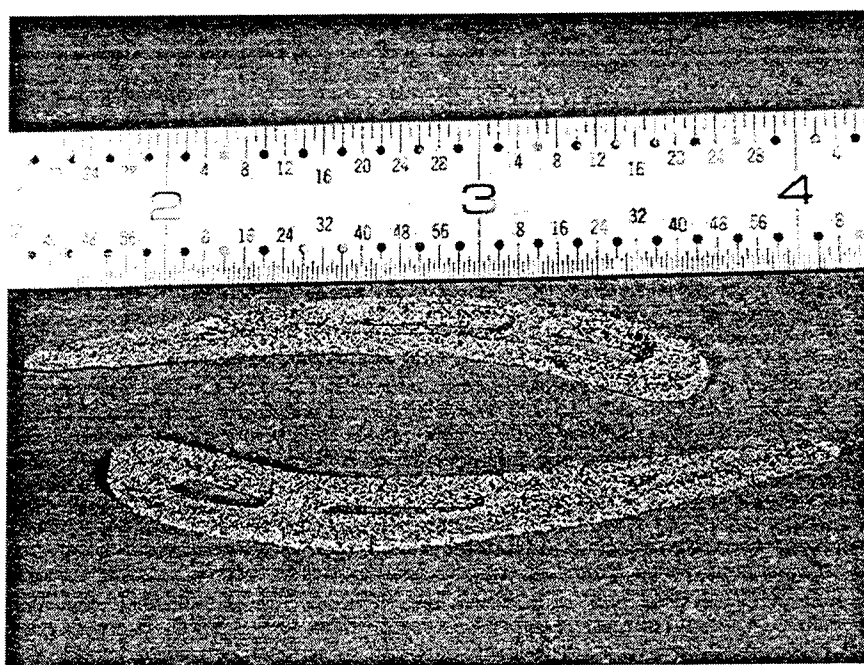


Figure 9. Blade Tips Produced via Indirect SLS Process

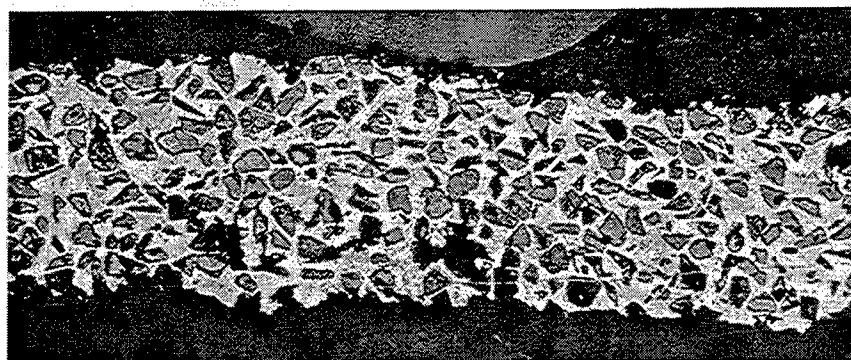


Figure 10. Typical microstructure of Indirect Processed blade Tip, Minimal Porosity and Agglomerates, magnification 25X.

Direct SLS

Direct SLS trials indicated that full through thickness melting was achieved with energy densities of approximately 1400 J/cm^2 . However, these samples illustrated porosity entrapped around grit particles. The porosity began to be eliminated when energy density levels were in the 3000 J/cm^2 range. This transition also corresponds with the point at which the microstructure changes from very fine equiaxed to dendritic. Examples of the changes in microstructure are provided in Figures 11 through 13. It is interesting to note that the very fine grained microstructure, ASTM grain size 10-12, noted on samples produced at less than 2500 J/cm^2 would be very useful in monolithic metallic materials due to the fact that it would behave superplastically¹⁹. This would allow SLS of parts allowing for a variety of uses or additional manufacturing techniques to be incorporated. This type of microstructure coupled with a post-process heat treatment would potentially enable production of equiaxed grain parts as opposed to the dendritic microstructure achieved from castings, thus providing more uniform and improved mechanical properties^{19,20,21}.

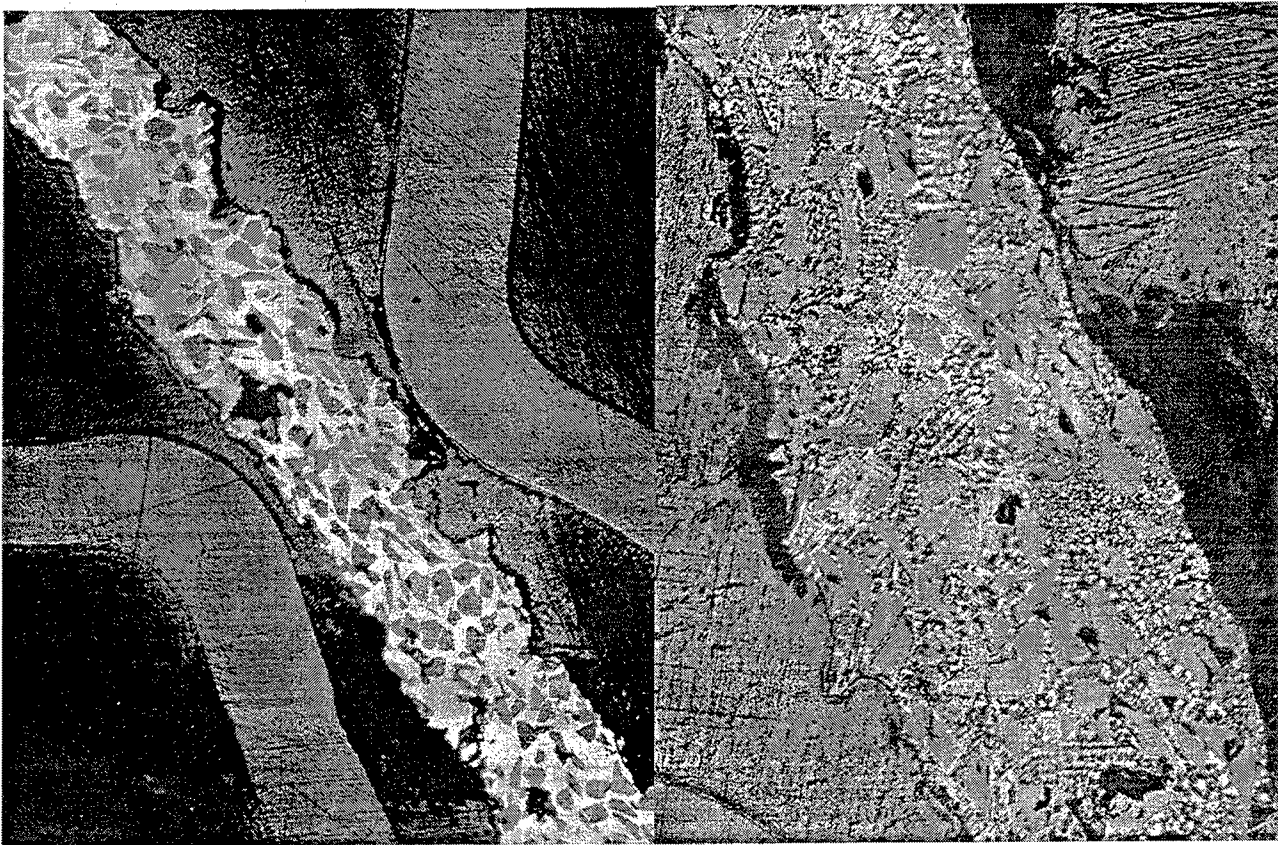


Figure 11. A sample produced at 2088 J/cm^2 energy density illustrating good microstructure, magnification 20 X and 50X. The 50 X photomicrograph of the etched sample illustrates a primarily dendritic microstructure with minimal entrapped porosity. The majority of the entrapped porosity is located at the boundary of a small equiaxed fine grain area.

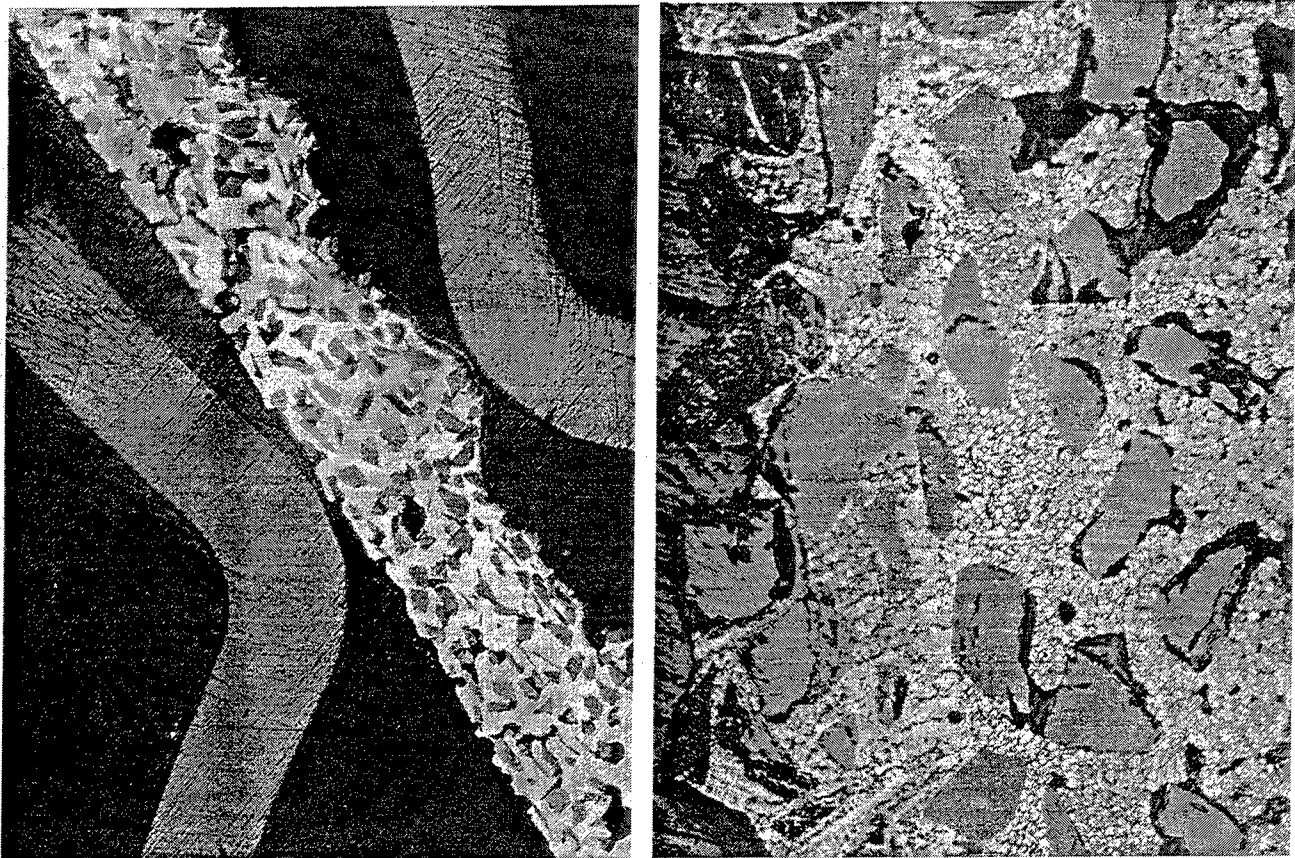


Figure 12. A sample produced at 1485 J/cm^2 energy density illustrating entrapped porosity around the grit particles, magnification 20 X and 100X. The 100 X photomicrographs illustrate the entrapped porosity and the fine equiaxed grain microstructure that result from the low energy density.

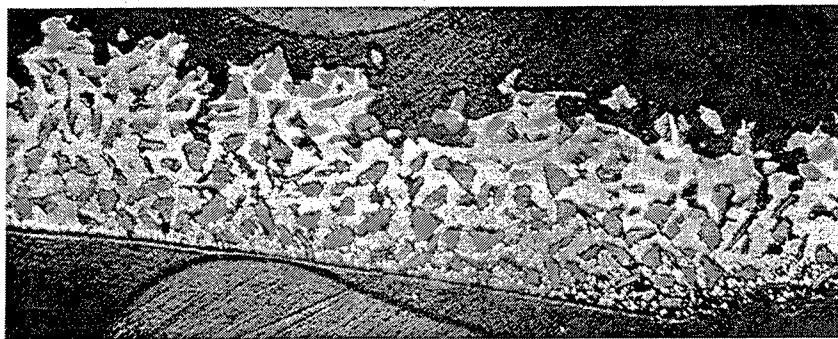


Figure 13. A sample produced at 1277 J/cm^2 energy density illustrating incomplete through thickness melting and entrapped porosity around the grit particles, magnification 20 X.

Process Parameters for Characterization

From the experiments described above a window of parameters that produced acceptable microstructures was available for mechanical property characterization. The energy density chosen for mechanical property characterization was 3202 J/cm^2 .

Coupons were manufactured for rub testing and stress rupture testing. The mechanical testing specimens were fabricated and tested according to procedures described previously in the Indirect SLS section. The results are shown in Table 6.

Sample	Stress (psi)	Time (hrs)	Temperature (°F)
K442	500	50	2100 No Failure
L240	500	50	2100/15 hrs Braze failure
C274	500	50	2100 No Failure
N444	500	50	2100 No Failure

Table 6. Stress rupture test results of direct SLS processed cermet

Rub coupons were also manufactured from the samples and rub tested at room temperature. The results are provided in Table 7.

Processing	Composition	Volumetric Rub Ratio	Linear Rub Ratio
7/4 - A	SLS Brazeless	161	31
7/4 -B	SLS Brazeless	168	23
Allison Conventional	Brazeless	187	37

Table 7. Rub testing of direct processed cermet against seal material (Quantabrad 2)

These results indicate that the brazeless cermet material composition processed by direct SLS is equivalent to the standard cermet. For sample L240, the failure occurred at the braze joint, indicating a bond defect. Additional testing is required to establish improvement in performance attained by elimination of the braze constituent.

CONCLUSIONS

Direct SLS of cermet abrasive composites and monolithic metallic materials have been developed under this program. The processing parameters developed can be modified such that SLS of a variety of fully dense monolithic metallic materials can be conducted. The parameters for SLS of monolithic materials are adjustable such that the resulting microstructure can be tailored to a specific need. Energy densities of approximately 2000 to 4000 J/cm² are required to eliminate porosity retained around grit particles in the superalloy cermet composite. For this particular composite material the energy density should be such that the microstructure produced is just barely transformed to fully dendritic. Energy densities in the range 2500-3500 J/cm² will produce a fully dendritic microstructure. Energy densities of 1900 to 2200 J/cm² will produce a very fine grained equiaxed fully dense superalloy microstructure which may exhibit superplastic properties at elevated temperatures.

The mechanical testing results indicate that direct SLS can produce microstructure and properties equivalent to or better than the conventional labor intensive process.

The production of a small lot of abrasive cermet components and the recycling of all fall off material have proven that the process is production ready and dramatically reduces production costs as outlined in the cost analysis.

Compared to the conventional processing method, direct SLS offers the following benefits:

1. Reduced labor and variability by eliminating tape casting and rolling.
2. Repeatable production process.
3. Binderless process.
4. Elimination of lower melting point braze constituent from the composition.
5. Recyclable fall off material, minimal scrap from any lot size.

Indirect SLS offers the following benefits:

1. Reduced labor and variability by eliminating tape casting and rolling.
2. Repeatable production process.
3. Reduced labor in obtaining the correct thickness and porosity.
4. Ability to manufacture much smaller lot size as compared to conventional manufacturing method.

The indirect SLS process has some disadvantages as compared to the direct SLS process. These are:

1. Fall off material may possibly not be recyclable.
2. Requires handling the parts in the delicate green state which may produce additional scrap.

The next stage of research under this program will focus on developing a high yield, repeatable production process.

ACKNOWLEDGEMENTS

Partial funding for this work was provided by the United States Air Force, Contract No. F33615-94-C-2424. The remainder of the resources were provided by Allison Engine Company and the University of Texas at Austin.

REFERENCES

- ¹ Skira, Charles A., *Cost Reduction of Advanced Turbine Engines*, 31st AIAA/ASME/SAE/ASEE Joint Propulsion Conference and Exhibit, July 1995.
- ² Proceedings of the First Air Force, Wright Laboratory S&T Affordability Exit Criteria Workshop.
- ³ Dix, D.M. and Riddell, F.R., *Projecting Cost-Performance Trade-offs for Military Vehicles*, Attachment to Anita Jones letter to JAST program office on IHPTET AFFORDABILITY, dated 31 August 1994, Aeronautics & Astronautics, September 1976.
- ⁴ Yeaple, F., *Gas Turbine Rotor Grinds Own Tip Seals*, Design News, 1-5-87, pp. 106-107.
- ⁵ Helms, Harold E., Heitman, Peter W., Lindgren, Leonard E. and Thrasher, Samuel R., *Ceramic Applications in Turbine Engines*, Noyes Publications, Park Ridge, New Jersey, 1986, pp. 131-137.
- ⁶ Beaman, Joseph J. and Deckard, Carl R., *Solid Freeform Fabrication and Selective Powder Sintering*, 15th NAMRC, North American Manufacturing Research Conference Proceedings, 1987, pp. 636-640.
- ⁷ Deckard C. R., M. S. Thesis, Department of Mechanical Engineering, The University of Texas at Austin, 1986.

- ⁸ Deckard, C. R., Ph.D. Dissertation, Department of Mechanical Engineering, The University of Texas at Austin, 1988.
- ⁹ *Rapid Prototyping and the Selective Laser Sintering Process: Tooling*, product literature, DTM Corporation, Austin, TX.
- ¹⁰ Vail, N.K., *Preparation and Characterization of Microencapsulated, Finely Divided Ceramic Materials for Selective Laser Sintering*, Ph.D. dissertation, Department of Chemical Engineering, The University of Texas at Austin, 1994.
- ¹¹ Vail, N. K., Barlow, J.W. and Marcus H.L., *Silicon Carbide Preforms for Metal Infiltration by Selective Laser Sintering of Polymer Encapsulated Powders*, Solid Freeform Fabrication Symposium Proceedings 1993, The University of Texas at Austin, pp. 204-214.
- ¹² Deckard, Lucy and Claar, Dennis T., *Fabrication of Ceramic and Metal Matrix Composites from Selective Laser Sintered Preforms*, Solid Freeform Symposium Proceedings 1993, The University of Texas at Austin, pp. 215-222.
- ¹³ Stucker, Brent E., Bradley, Walter L., Norasetthekul, Somchin (Jiab) and Eubank, Phillip T., *The Production of Electrical Discharge Machining Electrodes Using SLS: Preliminary Results*, Solid Freeform Fabrication Symposium Proceedings 1995, The University of Texas at Austin, pp. 278-286.
- ¹⁴ Bampton, C.C. and Burkett, R., *Free Form Fabrication of Metal Components and Dies*, Solid Freeform Fabrication Symposium Proceedings 1995, The University of Texas at Austin, pp. 342-345.
- ¹⁵ Wohlert, M. and Bourell, D., *Rapid Prototyping of Mg/SiC Composites by a Combined SLS and Pressureless Infiltration Process*, Solid Freeform Fabrication Symposium Proceedings 1996, The University of Texas at Austin.
- ¹⁶ Brown, Lawrence E. et. al., US Patent 5,264,011, 11/23/93.
- ¹⁷ Brown, Lawrence E. et. al., US Patent 5,359,770, 11/1/94.
- ¹⁸ Nelson, James C., *Selective Laser Sintering: A definition of the process and empirical sintering model*, Ph.D. dissertation, Department of Chemical Engineering, The University of Texas at Austin, 1993, pp. 153.
- ¹⁹ Sims, Chester T., Stoloff, Norman S. and Hagel, William C., eds., *Superalloys II*, Wiley Interscience, New York, 1987.
- ²⁰ Woulds, M. and Benson, H., *Development of a Conventional Fine Grain Casting Process*, Proceedings of the Fifth International Symposium on Superalloys - Superalloys 1984 sponsored by TMS.
- ²¹ Brinegar, J.R., Norris, L.F. and Rozenberg L., *Microcast-X Fine Grain Casting - A Progress Report*, Proceedings of the Fifth International Symposium on Superalloys - Superalloys 1984 sponsored by TMS.

GAINING COMPETITIVE ADVANTAGE BY USING RAPID PROTOTYPING IN AIRCRAFT MODIFICATION

Authors:

Mr. Steven L. Smith

Manufacturing/Producibility Engineer, Raytheon-Waco

Ms. Jerri Paul

Process and Management Consultant, Raytheon-Waco

Masters Candidate, University of Texas at Austin

1.0 INTRODUCTION

Raytheon-Waco (formerly Chrysler Technologies Airborne Systems) is an aircraft modification facility in Waco, TX, specializing in military, executive, and head-of-state aircraft modifications. Raytheon-Waco has over 25 years of aircraft modification experience, and is a leading contractor for major US and foreign government programs that require system design, airframe modification, installation, flight testing, and post-delivery technical and logistical support. Current programs at Raytheon-Waco include foreign government Head-of-State wide-body aircraft modifications consisting of luxury interiors, secure communications, and airframe modifications, and US and foreign military aircraft modifications involving electronics, communications, avionics, and airframe modifications.

The aircraft modification industry is highly competitive, with a variety of very competent companies constantly trying to increase market share and move into new markets. Raytheon-Waco has focused primarily on military communications and transport aircraft, and Head-of-State wide-body aircraft. Due to increasing competition and customer cost-consciousness, Raytheon-Waco is working to reduce cost and cycle time while maintaining its reputation for delivering on time and within budget. There is also movement into other markets, such as lower-cost wide-body executive aircraft.

Raytheon-Waco is currently transitioning to a paperless design process, with the ultimate goal of performing all design, analysis, manufacturing, and aircraft installation from CAD models without requiring paper drawings. Increased use of electronic models will also allow more parallel processes to be performed, eliminating many of the sequential design steps currently required. Among the steps that will be performed in parallel will be detailed design, manufacturing and installation planning, technical publications, and design analysis. Without improved initial designs, parallel work will only lead to increased rework and wasted effort. Rapid prototyping is a key factor in reducing risks associated with concurrent processes, and its benefits are critical to efforts to reduce the cost and schedule of future aircraft modifications.

2.0 RAPID PROTOTYPING AT RAYTHEON-WACO

2.1 RAPID PROTOTYPING NEED

Traditional high-volume production is seldom required at Raytheon-Waco. Most of the commercial wide-body and military modifications are unique designs that are similar to traditional prototypes in that the designs are constantly evolving, typically only small pieces and

sub-assemblies of previous designs can be re-used, and lessons learned in previous aircraft modifications **only** have limited application. Reducing cost and cycle time for many aircraft components by quickly and cheaply producing prototypes of new designs for customer approval and design verification on the aircraft prior to part fabrication was a real need, and was the driving factor **behind** the acquisition of rapid prototyping (RP) equipment. Potential manufacturing and tooling uses of RP technologies also contributed to the decision to invest in RP, but were **not** the driving factors.

2.2 RAPID PROTOTYPING EQUIPMENT

In 1995, Raytheon-Waco began investigating rapid prototyping equipment to be used primarily by design engineers to ensure form, fit, and function of parts and assemblies. This led to the purchase of a 3D Systems SLA-500 Stereolithography Apparatus (SLA) in early 1996. In the SLA process a solid physical part model is made directly from 3-D CAD model data within a relatively short period of time, usually less than one day. The model is built by successively laser curing layers of photopolymer resin until the part is completed. After the model has been built, it is removed from the SLA processing chamber and placed in a Post Curing Apparatus (PCA), where the model is flooded with intense ultraviolet light to complete the polymerization process. It is then finished using a variety of sanding and painting techniques. The total processing time is typically one to three days.

2.3 SLA IMPLEMENTATION

Raytheon-Waco has a laboratory dedicated to rapid prototyping, with the SLA-500, an accompanying centrifuge and PCA, as well as a model finishing facility. The SLA technician is responsible for finishing each model, including post-curing, removing excess resin, sanding, painting, and when necessary bonding models into assemblies. The SLA technician works directly with engineers considering SLA models to determine if they have a good application, modify CAD models to improve the SLA model quality, and ensure that the part model can be built in the SLA-500. He will also input the appropriate shrink factors into the build process for models used as tooling.

SLA modeling is part of a move to paperless design, fabrication, and installation in order to reduce costs and compress schedules. The process of ordering an SLA model is completely electronic, and requires 3-Dimensional (3D) surface or solid models. New design work at Raytheon-Waco is done in Pro/Engineer¹ 3D solid modeling, which has a standard .STL file output that can be input into the 3D Systems software. There is also an approved ISO 9001 procedure and work instruction for electronically ordering SLA models.

3.0 SLA IN DESIGN

In the six months since obtaining RP capability, Raytheon-Waco has realized significant benefits from using SLA, with potential for even larger benefits in the future. Specific advantages have been seen in the design process and in an increase in customer input and satisfaction. Allowing the designers, engineers, management, purchasing, and customers to review physical models of designs before releasing a drawing is expected to reduce the number of engineering change orders issued during the design and production phase. In addition, check fitting full scale SLA models of various parts and assemblies in the aircraft is expected to reduce

last minute changes resulting from airframe variations. These applications will in turn reduce the amount of lost production time, retooling, rework, and scrap waste incurred during manufacture and installation. Following are some specific examples of uses of SLA in the design process.

3.1 INCREASING CUSTOMER INVOLVEMENT IN DESIGN

3.1.1 Aesthetic Review

One of the first uses of SLA was in producing models of artistic complex-curved surfaces used in luxury interiors prior to producing part drawings or beginning design work on many interfacing components. These models were reviewed with the customer, who determined that the initial design needed to be changed. Without rapid prototyping, these design changes would not have been made until much later, and possibly not until the parts had been fabricated and significant design had been done on interfacing parts, resulting in additional design changes. SLA models have become common elements of customer reviews, beginning with the earliest stages of the design process.

3.1.2 Functional Reviews

SLA models were made of electronic control panels to demonstrate proposed Air Force C-141 transport cockpit upgrades. The panels were approximately 5" x 3" and showed the expected configurations of meters and switches. The SLA panels were assembled into an on-site cockpit simulator, allowing Air Force customers, including pilots, to provide specific input on changes to increase ergonomics and functionality of the new cockpit elements. Previously, only 2-D drawings were available at this stage in the design process, and cockpit mock-ups were only available much later.

SLA models of several critical parts of a system being integrated into a military aircraft were made for design review meetings with the primary contractor and Air Force representatives. Scale models were reviewed in a series of meetings and several design changes were made. Program officials estimated that without the SLA models, the changes would not have been made until much later at a cost of about \$10,000 in time and materials. The same program also produced full-scale SLA models of lofted contoured panels that were taken to the aircraft to confirm existing data and determine fastener locations. The SLA models used in this program have saved many times their expense in time and materials by avoiding design changes later in the project.

3.2 AIDING THE DESIGN PROCESS

3.2.1 Aiding Design Engineering

Engineers at Raytheon-Waco have been encouraged to use SLA models to better visualize complicated designs and confirm that the design will meet their requirements. Some engineers have had models made of small parts they are designing so that they could take them to the aircraft to confirm form and fit of the part before proceeding with additional design work. These same parts are then available to other engineers considering similar designs, or designing parts that must interface with the modeled parts.

An SLA model was made of an exit duct and a machined fitting for a galley being redesigned for a foreign Head of State aircraft. The fitting was a Y-shape with complex contoured flanges.

The model was used by the design engineers and the customer to identify interface requirements and recommend design changes to increase manufacturability and serviceability. The exit duct SLA model was used for a producibility review, and will become a washable sand mold to make a fiberglass part. The SLA model will increase the manufacturability of the part and allow the manufacturer to decrease the lead-time and costs associated with a prototype part.

3.2.2 Verifying Designs with SLA Models

In order to verify fit with existing plumbing interfaces and avoid interference with other structures, SLA models of a custom plumbing system were created for a commercial VIP lavatory refurbishment. The SLA models were installed in the aircraft and revealed interference problems that would not have been detected until much more costly metal parts were fabricated later in the program. New models of design changes were also produced to verify all changes prior to creating drawings. These models will also be available for other engineers to use to ensure that other systems properly interface or avoid interference with the lavatory plumbing fixtures. It is expected that the total savings from using plumbing models will involve reduced engineering changes late in the project, fewer rejected parts, easier installation into the aircraft, and less engineering time required throughout the project.

A military program produced SLA models of a duct manifold and air delivery plenum interfaces. The manifold model was used to ensure conformity to primary aircraft structure before fabrication of the high cost, long lead-time item. The SLA plenum interfaces were made to be assembled into a full-functioning mock up in the systems integration laboratory. The production plenum interfaces were critical items for a mock-up that was needed to meet contract schedules, but delivery was delayed by the supplier by several months. The SLA plenum interfaces were made in under a week and have been successfully installed into the mock-up that will be powered up and shown to customers at a subsequent design review.

4.0 SLA IN FABRICATION

Raytheon-Waco has used rapid prototyping in fabrication in a variety of ways, and has plans to expand current capabilities. The most common direct use of SLA in fabrication is in tooling, although there are some indirect uses of SLA that will aid manufacturers in visualizing and understanding parts to be produced.

4.1 CASTING

SLA models have been used as tooling for investment casting. ACES² (solid) models have been used as a master pattern for creating epoxy tooling, which was then used to make expendable wax patterns for forming the investment shell. Quickcast³ (hollow) models have also been used directly as expendable patterns in creating investment shells for casting. Both methods have proven to be accurate, reliable, and lower-cost alternatives to machined tooling for low-quantity investment casting. Most of the casting applications at Raytheon-Waco involve quantities too low to justify machined tooling expense, so the ability to reduce tooling cost through SLA is a significant advantage. It is also estimated that cycle times are reduced by at least 25% compared to the more traditional investment casting process.

ACES models have also been used as tooling for precision sand casting. Accurate, scaled models of parts have been used in place of machined tooling for forming precision sand molds, reducing cost and time for tooling by an order of magnitude. The final castings were high quality, with no noticeable differences due to RP tooling. Two castings for use in wind tunnel testing were produced in under one week from beginning the SLA model to casting delivery, and the pattern is available for making more parts in the future if necessary.

4.2 RAPID TOOLING FOR INJECTION MOLDING

Raytheon-Waco has begun working with a plastics vendor to produce rapid tooling for low-volume injection molding. The injection molding vendor's tooling engineers will work with Pro/E part models to design the mold and then Raytheon-Waco will build the mold with the SLA-500. Raytheon-Waco has also interacted with tooling vendors to produce rapid tooling with SLS⁴ technology for higher durability molds. Rapid tooling will allow Raytheon-Waco to afford to purchase very low-quantity injection molded parts that will save weight and be cost-competitive with machined aluminum parts. It is also expected that rapid tooling will reduce the time to receive injection molded parts by at least three weeks per order.

4.3 METAL DEPOSITION MASTER TOOLING

The first significant use of SLA in fabrication was in producing a complex-shaped lavatory sink with unique cross-sections. This sink was too deep and irregular for traditional processes such as stamping or deep-drawing to be reliable. The process that was used involved making a plaster tool from a SLA master pattern, and then depositing a nickel alloy on the plaster tool. It is estimated that this process saved Raytheon-Waco over \$140,000 for a single aircraft, in addition to the likelihood that the parts would not have been delivered within the required schedule if traditional processes had been used. This process was so successful that it has been used on other aircraft for similar circumstances, and is planned for other such instances in the future.

4.4 COMPOSITE PANEL TOOLING AT RAYTHEON-WACO MANUFACTURING FACILITY

The SLA lab is working with the Raytheon-Waco composite panel fabrication personnel to develop a system for producing tooling. The SLA model will serve as tooling, with the composite panel built directly on the SLA model, or for parts that require autoclaving or heating the SLA model can be a master pattern for producing plaster tooling. Traditionally, this type of tooling is machined metal, so the potential for saving time and cost is great.

4.5 TEMPLATES FOR CABINETS AND TRIM

SLA templates can also be used to aid fabrication of VIP aircraft components. The templates will be used by cabinet makers or composite panel producers in forming complicated shapes, and also by machine shops or other vendors that will be fabricating parts to mate with the complicated surfaces. It is expected that templates will reduce the amount of rework required to achieve quality interfaces for complex surfaces that require manual operations to produce.

5.0 MODELS USED IN TESTING

The most significant use of SLA models in testing has been for specialized pressure taps to measure duct manifold static pressure while experimenting with various air handling system

configurations. These pressure taps are small tube-like protrusions with a round base that had previously been made out of aluminum at a cost of approximately \$85 each. The SLA pressure taps were produced at a cost of \$45 for 100, allowing higher levels of stocking to reduce the likelihood of a program having to wait two weeks or more for machined parts to be made. The SLA pressure taps were designed to be used in testing of air-conditioning and other low-temperature applications due to the sensitivity of the SLA resin to heat and humidity. The total program savings from using SLA are \$8455 per run.

SLA models are also being used in wind-tunnel testing. Scaled models of designs for new under-wing pods for Navy aircraft were produced, and were matched to existing scale aircraft models to test the impacts on flight dynamics from the addition of the pods to the aircraft. The SLA models were produced in far less time and significantly cheaper than metal castings of the same design, and were able to withstand the stresses of wind tunnel operation. The use of SLA models in the wind tunnel is expected to dramatically increase the flexibility and reduce the cost of wind tunnel testing new designs for aircraft modifications.

6.0 SUMMARY OF RAPID PROTOTYPING BENEFITS

Raytheon-Waco has made significant use of the SLA-500 in the five months it has been on-site. There have been over 300 parts made, with over 150 different designs for at least twelve different aircraft programs. Much of the cost and time savings associated with using SLA models is very hard to reliably quantify, but conservative estimates are that over \$350,000 has been saved through finding changes and problems early, reducing fabrication costs, and the reduced cost of in-house SLA modeling versus service bureau costs. There have also been substantial intangible benefits, such as increased customer involvement early in the design process and improved engineering designs due to the opportunity to visualize designs and create models that can be fitted into assemblies. The largest unquantified benefit from on-site SLA modeling has been increasing the ability of Raytheon-Waco to meet contract schedules through time savings in design, analysis, and manufacturing.

7.0 CONCLUSION

Raytheon-Waco has had in-house SLA capability since February, 1996, and has already realized significant benefits from rapid prototyping. These have taken the form of increased customer input early in the design process, improved engineering designs through the ability to better visualize CAD models, and decreased fabrication costs for a variety of parts and manufacturing methods. These benefits have far exceeded the original expectations in both quantity and variety, and have more than justified the acquisition of in-house rapid prototyping technology. It is expected that rapid prototyping will play an ever-increasing role in Raytheon-Waco's efforts to reduce operating costs, compress delivery schedules, and enter the next century as one of the world's premier aircraft modification centers.

FOOTNOTES:

1. Pro/Engineer is a registered trademark of Parametric Technologies, Corp. (PTC)
2. ACES is a trademark of 3D Systems
3. Quickcast is a trademark of 3D Systems
4. SLS is Selective Laser Sintering, a registered trademark of DTM Corp.

Fabrication of Parts Containing Small Features using Stereolithography

Jouni P. Partanen

3D Systems, 26081 Avenue Hall, Valencia, California 91355

ABSTRACT

The StereoLithography (SL) process has benefited from many advances in the last four to five years. These include new resins with reduced shrinkage and curl distortion, enhanced software, and improved scanning techniques. One can produce highly accurate parts for most dimensions within a few mils of the design value as shown in numerous accuracy and benchmarking studies. SLA systems use a laser beam focused to a spot size of 200 -250 μm . This limits the range of applications where SL can provide accurate models to parts which do *not* contain very small features *i.e.* wall thickness values less than about 300 μm . Industries that manufacture products involving components with small features include electronics and medical.

In this presentation we describe an extension of the SL technology to applications involving small features. This capability is achieved by reducing the laser focal spot size in an SLA-250 to 75 μm . The technological principle behind the spot size reduction is described in the presentation, together with process issues and applications of the technology.

1. INTRODUCTION

Common applications of Rapid Prototyping and Manufacturing (RP&M) are in the automotive and consumer electronics industries. Typical models build by RP&M techniques are from a few centimeters to half a meter in all three dimensions[1,2]. Even if these applications often require parts to be accurate within 0.1 mm or better of its design dimensions, they do not usually have features with dimensions in the tenth of a millimeter scale. Thus most of the RP&M techniques have not been developed to be capable of 100 micron or better resolution. However, there are many applications of RP&M in the electronics and medical industries which would require less than two hundred micron resolution. One example is electronic circuit board connectors that can have pin densities as high as 2 pins per millimeters.

This paper describes an extension of a commercial StereoLithography Apparatus (SLA) to applications requiring about 100 micron resolution. A specialized unit for ultra high resolution (about 10 micron) is described in Ref. [3]. In section 2 we discuss what is required from an RP&M system to achieve a certain resolution. Section 3 describes how the resolution of laser based RP&M is controlled by diffraction. Some properties of 3D Systems Stereolithography Apparatus, SLA-250, are presented in the following section together with a solution for increased resolution. The performance of the high resolution SLA is characterized

using a generic connector test part as described in Section 5. Some real world applications are shown in the following section.

2. RP&M EQUIPMENT RESOLUTION

All the various RP&M systems build 3 dimensional parts in layers. The resolution in the direction normal to the layers (defined here as the z direction) is limited by the layer thickness. The resolution in the plane of the layers (x - y plane) depends on the method used to define the borders of each layer. In RP&M systems which use lasers to shape individual layers, the laser spot size at the working medium is one of the main factors defining resolution. Figure 1 shows schematically the effect of the spot size on the smallest feature that can be built by two different approaches. In the case where a laser is used to solidify the either liquid or powder into the desired shape the minimum positive feature is controlled by the laser spot size (Fig. 1(a)). If the laser is used to remove material around the part the spot size controls the minimum negative feature (Fig. 1(b)). Because useful parts contain both positive and negative features we can say that the resolution is essentially limited by the spot size. In those RP&M methods which do not use lasers the circle in Fig. 1 can be thought to represent the droplet size, the width of extruded material, or the width of the cutting tool.

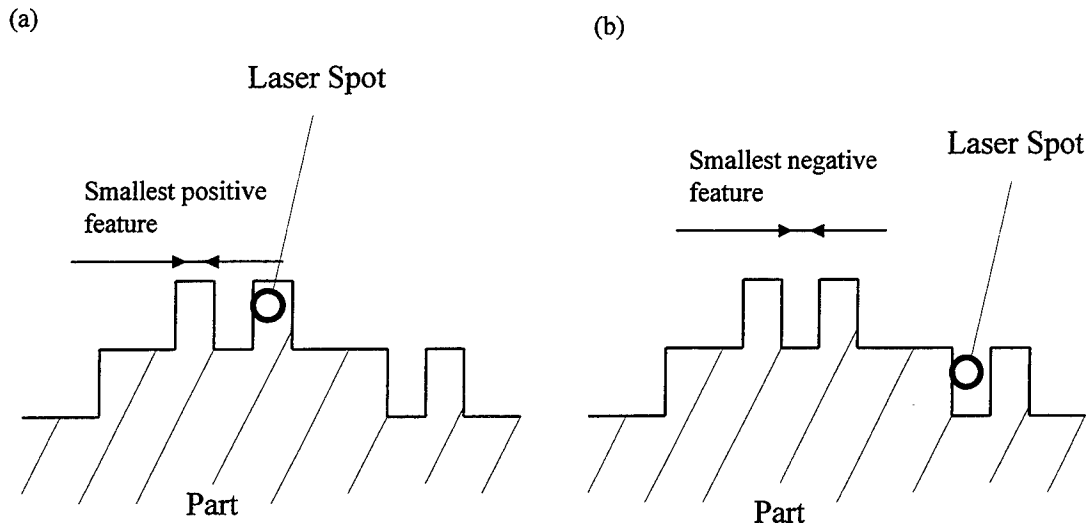


Fig. 1. Relation between the smallest features that can be build and the laser spot size for laser based RP&M technologies in the two cases where laser is used either to solidify (a) or remove (b) material.

Even if the spot size in Fig. 1 is the limiting factor for system resolution it is not the only factor affecting the x - y resolution. There are number of other effects which have to be taken into account: 1) The solidification process can extend beyond the photoinitiation point. 2) The effect of heating can extend beyond the spot size in both sintering and cutting. 3) The particle size and the size of nonuniformities in the raw material affect the resolution. 4) The small features have to be sufficiently strong to survive the process as well as their own weight. The aim of this paper is to demonstrate that the laser spot size is the main factor defining the resolution of SL, and features as small as 100 μm can be built using SL, when the spot size is reduced to 75 μm .

3. LASER SPOT SIZE

The physical principle which controls the spot size at the working surface of an RP&M system is diffraction. It relates the spot radius W_0 at the working surface, (measured at $1/e^2$ of the peak intensity), to the laser wavelength λ , the distance f from the working surface to the last optical element, the diameter D of the beam at that element, and the laser beam quality characterized by the mode purity parameter M^2 . The relation can be written as:

$$W_0 = C \frac{\lambda f}{2D} M^2 \quad (1)$$

where the numerical value of the coefficient C depends on the exact definition of the quantities given above, as well as the precise mode shape[4,5]. However, for the present purpose it is sufficient to know that C is close to 1.5.

The equation (1) clearly demonstrates the benefits of short wavelength lasers for high resolution RP&M technology. The ultraviolet lasers used in stereolithography have a wavelength λ from 0.32 - 0.36 μm , about 1/30 of the wavelength λ , 10.6 μm , of the carbon dioxide laser commonly used in other RP&M techniques.

4. HIGH RESOLUTION SLA-250

The spot diameter $2W_0$ of a commercially available SLA-250 is typically 200 - 250 μm . The three parameters in Eq. (2) which we can use to reduce the laser spot diameter in an SLA-250 are: the distance f from resin surface to the scanning mirror (last optical element), the mirror diameter D , and the mode purity parameter M^2 . Changing either the size of the scanning mirrors to allow a larger beam diameter D , or the distance f from the scanning mirrors to the resin surface, would involve a significant hardware development program. The mode purity parameter M^2 of an HeCd laser used in SLA-250 is typically about 5. It can be reduced to about 1.5 (laser beam clean-up) with a rather simple optical arrangement, allowing a spot diameter $2W_0$ of about 75 μm at the resin surface.

In addition to the reduction of the spot size, the laser power will also diminish in the laser beam clean-up process. The reduction of laser power, far from being a negative, is actually

useful in order to preserve drawing accuracy with the smaller spot size. This can be seen from the expression for the laser scanning speed V_s

$$V_s = \sqrt{\frac{2}{\pi}} \frac{P_L}{W_0 E_c} \exp(-C_d/D_p) \quad (2)$$

where E_c and D_p are resin parameters (critical exposure and penetration depth, respectively). For constant cure depth C_d , the laser scanning speed V_s is proportional to the ratio of the laser power P_L and the spot radius W_0 . Thus, in order to avoid excessively high scanning speeds, the laser power should be reduced in proportion with the spot size. In some cases, even further reduction in power is needed for accuracy. Fig. 2 shows experimentally determined laser power values P_L available at different spot diameters $2W_0$ in an SLA-250 with a 30 mW HeCd laser. For the studies reported here we chose a 75 μm spot diameter with 3 mW of laser power.

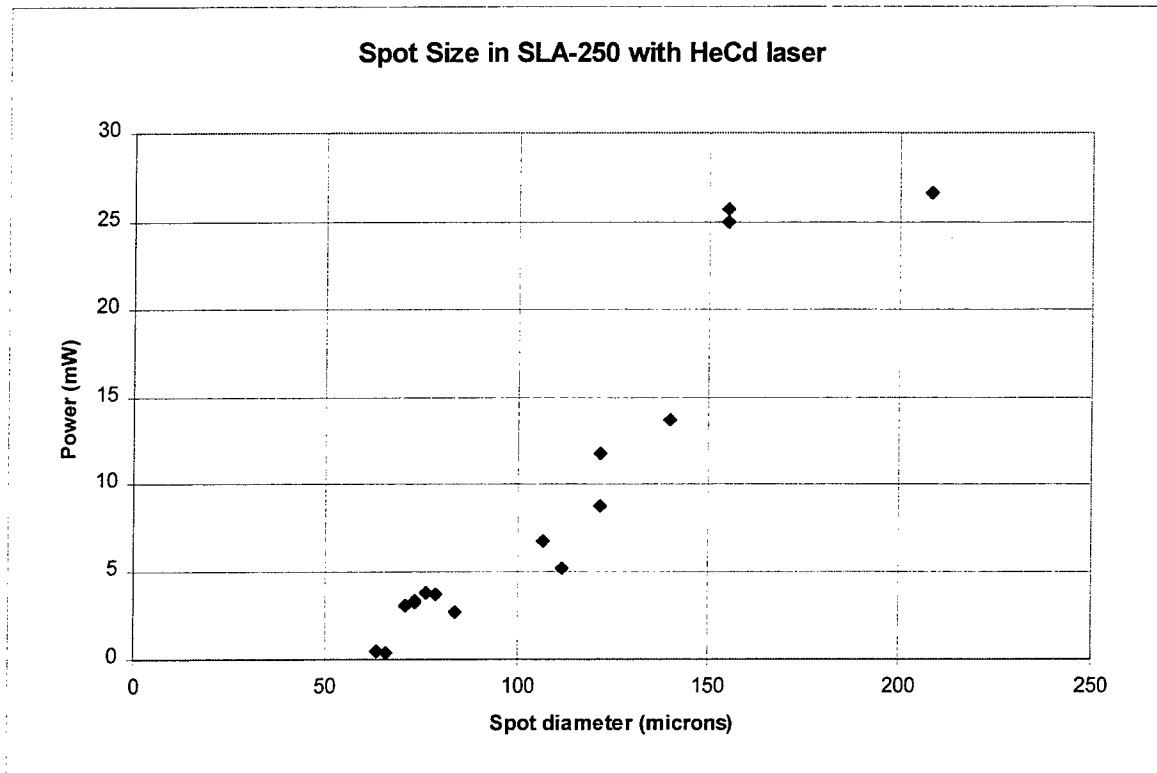


Fig. 2. The power available after beam clean-up as a function of spot size from a typical HeCd laser.

5. CONNECTOR TEST PART

We have designed a simple connector test part (T-PART) for the resolution studies. The test part has three sets of pins with pin densities of 1 pin/mm, 2 pins/mm, and 3.3 pins/mm. To our knowledge, the 1 pin/mm density is typical for high density connector, the 2 pins/mm density is in the range of the highest densities commercially available at present, and the 3.3 pins/mm density is close to the highest densities expected in the near future.

We have built many of the test parts using the modified high resolution SLA-250 (Small Spot SLA). Fig. 3 shows a microscope photographs of all 3 sets of pins of one T-PART built using the Small Spot SLA. Using the T-PART, we also did studies of the width the solidified line L_w as a function of the specified cure depth C_d . Fig. 4 shows the results as compared to a simple theory of cured linewidth (Eq. 4-40 in Ref. [1])

$$L_w = 2W_0 \sqrt{2C_d/D_p} \quad (3)$$

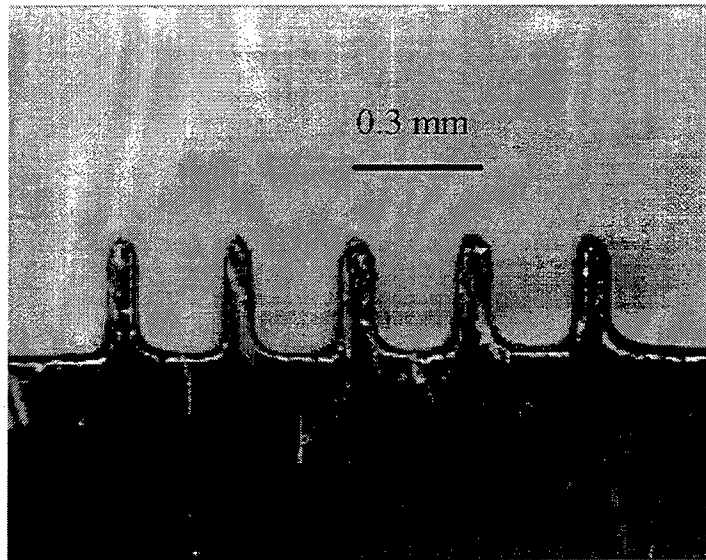


Fig. 3(a). The 3.3 pins/mm pattern in the T-PART build with Small Spot SLA

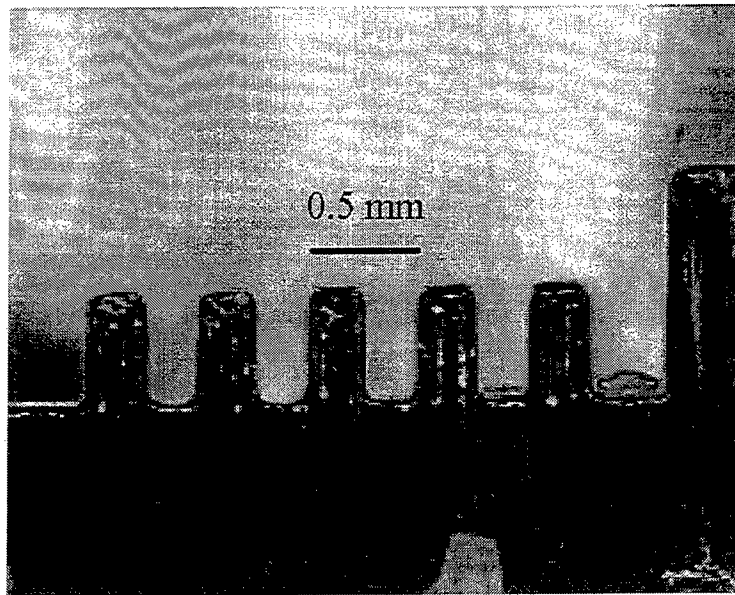


Fig. 3(B). The 2 pins/mm pattern in the T-PART build with Small Spot SLA

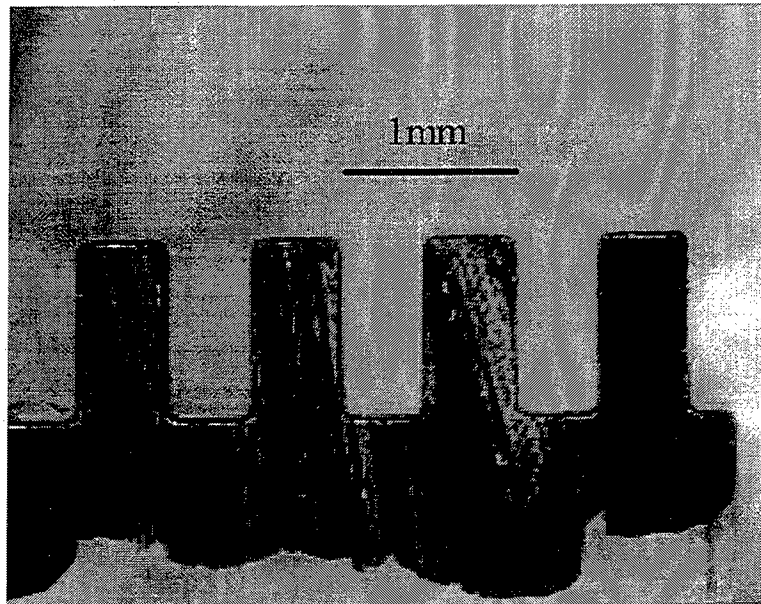


Fig. 3(C). The 1 pin/mm pattern in the T-PART build with Small Spot SLA

6. APPLICATIONS

The experiments described above have been performed at 3D Systems. In addition, 3D Systems has started a co-operative research program with some of its customers relative to practical applications of the Small Spot SLA. The small spot capability offered for these companies matches closely the one described in Section 4.

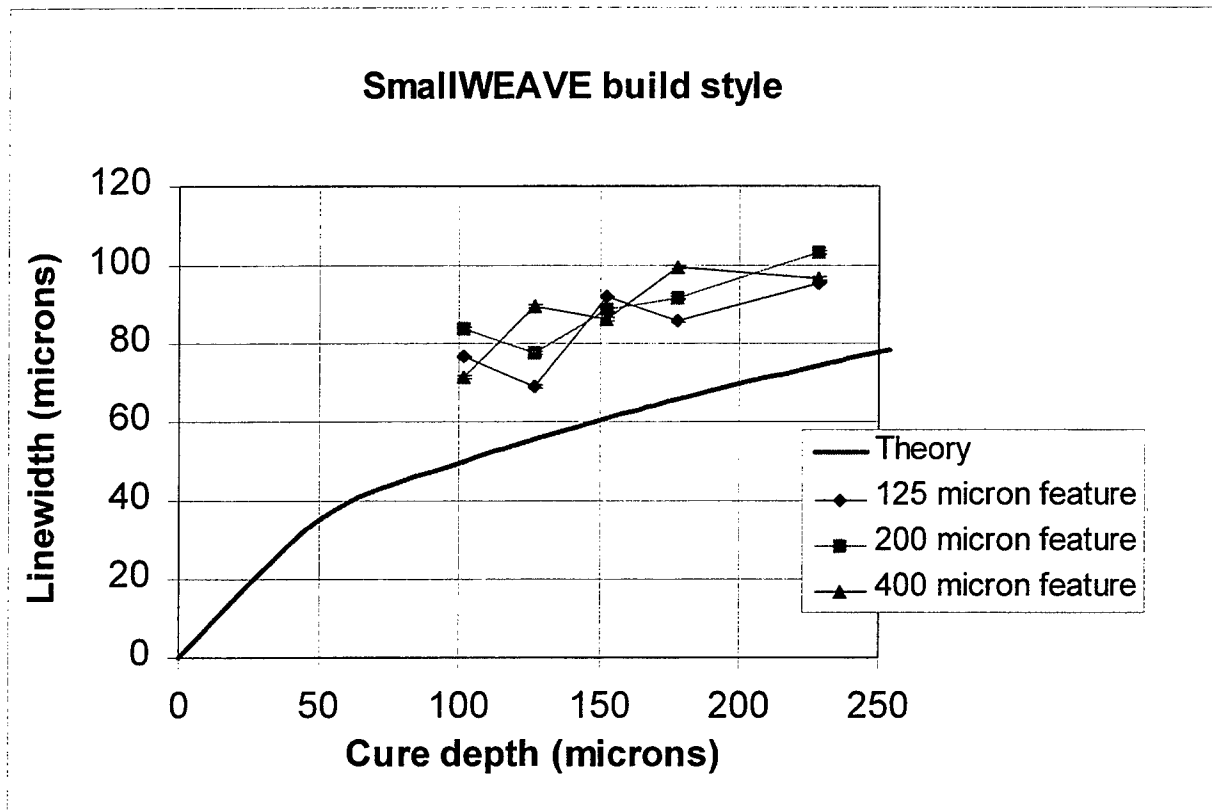


Fig. 4. Experimentally determined line width L_w as a function of the border cure depth C_d in Small Spot SLA.

Small Spot SLA is being used presently by five companies: One of these is applying the technology to the medical field in developing smaller tools for less invasive surgery. Another company is using their Small Spot SLA in the electrical connector industry as described above. The other organizations are applying the high resolution capability in many different fields as a internal job shop for a multi-industry company, and independent service bureaus. There are also companies using other approaches to reduce the spot size in stereolithography to a diameter between 100 μm and 200 μm .

7. CONCLUSION

We demonstrate in this paper that stereolithography can be easily extended to higher resolution by simply reducing the spot size of the laser on the working surface of an SLA system. We have successfully built connector test parts that have 300 μm pitch (3.3 pins per mm).

REFERENCES

- [1] P. F. Jacobs, Ed., "Rapid Prototyping & Manufacturing: Fundamentals of Stereolithography," Society of Manufacturing Engineers, Dearborn, Michigan, 1992.
- [2] P. F. Jacobs, Ed., "Stereolithography and other RP&M Techniques," Society of Manufacturing Engineers, Dearborn, Michigan, 1996.
- [3] K. Ikuta, K. Hirowatari, and T. Ogata, "Ultra High Resolution Stereolithography for Three Dimensional Microfabrication," Proceedings of the Fifth International Conference on Rapid Prototyping - 1994, University of Dayton, Dayton, Ohio, 1994.
- [4] A. E. Siegman, *Lasers*, University Science Books, Mill Valley, CA, 1986.
- [5] W. F. Hug, "Lasers for Rapid Prototyping & Manufacturing," *Rapid Prototyping & Manufacturing: Fundamentals of Stereolithography*, Ed: P. F. Jacobs. pp. 59 - 78, Society of Manufacturing Engineers, Dearborn, MI, 1992.

GELCAST MOLDING WITH RAPID PROTOTYPED FUGITIVE MOLDS

Vikram R. Jamalabad, Philip J. Whalen
AlliedSignal Research and Technology, Morristown, NJ 07962.

John Pollinger
AlliedSignal Ceramic Components, Torrance, CA 90509.

Mukesh K. Agarwala, Stephen C. Danforth
Rutgers University - Center for Ceramic Research, New Brunswick, NJ 08854.

ABSTRACT

A technique for the rapid manufacture of ceramic components has been developed using rapid prototyping to generate molds for the required components. The process entails the fabrication of fugitive tooling using rapid prototyping techniques from which ceramic articles are formed using gelcasting. In the gelcasting process, the mold cavities are filled with a fluid suspension of ceramic powder which sets to a solid form through the polymerization of gelling additives and application of heat. The mold is carefully removed by dissolution or heat treatment leaving the intact gelcast part. The "green" gelcast part is subsequently dried and sintered to full density. Computer aided manufacturing of the tooling using solid freeform fabrication techniques allows for complex shapes to be manufactured with minimal tooling cost. The technique is ideal for the manufacture of ceramic parts in small batch conditions or for prototyping of functional parts in design cycles. Cost and time reduction of a magnitude can be achieved.

KEYWORDS: Solid Freeform Fabrication, Molds, Gelcasting, Ceramic Processing, Structural and Functional Ceramics.

INTRODUCTION

Solid Freeform Fabrication (Rapid Prototyping / Manufacturing) is fast maturing into a means for the manufacture of structurally sound functional components. Until recently, only plastic and polymeric parts have been manufactured by SFF techniques. 3D Systems' Stereolithography¹, the earliest of the techniques, is used for manufacturing plastic parts. Apart from design purposes, these parts are used as investment casting positives. Structural use of SLA parts is limited. Griffith *et al*² have used ceramic suspensions in the SLA resin bath and have shown some progress in generating ceramic parts.

Extensive work has been reported in the use of Selective Laser Sintering (SLS) by Bunnell *et al*³ for the freeform fabrication of metal parts. Cima *et al*⁴ have demonstrated

the 3 Dimensional Printing (3DP) process for both, metal and ceramic parts. Fused Deposition of Ceramics (FDC), based on Fused Deposition Modeling (FDM™) has been shown to be feasible (Agarwala *et al*⁵). In addition, some novel technologies that are in early stages of development (SALD, by Zong⁶ and Marcus) could lead to the manufacture of structural components.

Indirect methods of manufacturing structural components using solid freeform fabrication have been used since the inception of these techniques. Part positives for investment casting can be made by almost all SFF processes. Investment casting wax parts (Stratasys Inc's FDM™ machines), paper parts (Helisys Inc's LOM™ machines), polymeric parts (Sanders-Prototype Inc's MM-6PRO Model Maker™, MIT's 3DP machines) and photopolymeric parts (3D Systems Inc's SLA™ series machines) have been utilized. Ceramic slurry (usually a refractory like silica) is set around the part positives before the parts are melted away to leave a cavity for casting.

The development of complex shaped ceramic structural components and devices is severely hampered by the high cost of ceramic prototype manufacturing and the overheads of short production runs. Machining of sintered, fully dense ceramic articles is extremely hard, time consuming and expensive. This has led to the development of many net shape fabrication techniques. Injection molding and slip casting are two of these techniques. Both require some form of precision tooling, effectively driving up cost.

The overall cost of a component will, in most cases, be driven by the cost of the tool fabrication. Time consuming and expensive machining operations are required for tool preparation. The necessity of this tooling also precludes the use of iterative approaches in design, since changes in component design require significantly high levels of re-investment in time and capital. For injection molding, high quality water-cooled dies are required. At the same time, these need to be rapidly dis-assembled to eject the part. Very large cross-section parts also cannot be manufactured due to binder burnout problems. Complex porous tooling is required for slip casting. Variations in particle distribution lead to warpage and an inability to hold tolerances.

RAPID PROTOTYPED MOLDING FOR GELCASTING

Ceramic gelcasting is a process whereby a ceramic slurry containing appropriate monomers is poured into a tool and then "gelled" through a catalyzed reaction. This gelation polymerizes the monomer resulting in a relatively rigid solid. Metal and ceramic particles in the suspension can be gelled in this manner. Low cost multi-part metal (aluminum) tooling is used for ceramic gelcasting. While this works for relatively simply shaped parts, for complex parts, fugitive tools or molds which are removed by dissolution can be used. Gelcast tooling must have several key features. The tool must be stable at the temperatures required for gelling (40 to 60 C). In addition, the tool must be structurally sound to support the ceramic suspension during the gelling process.

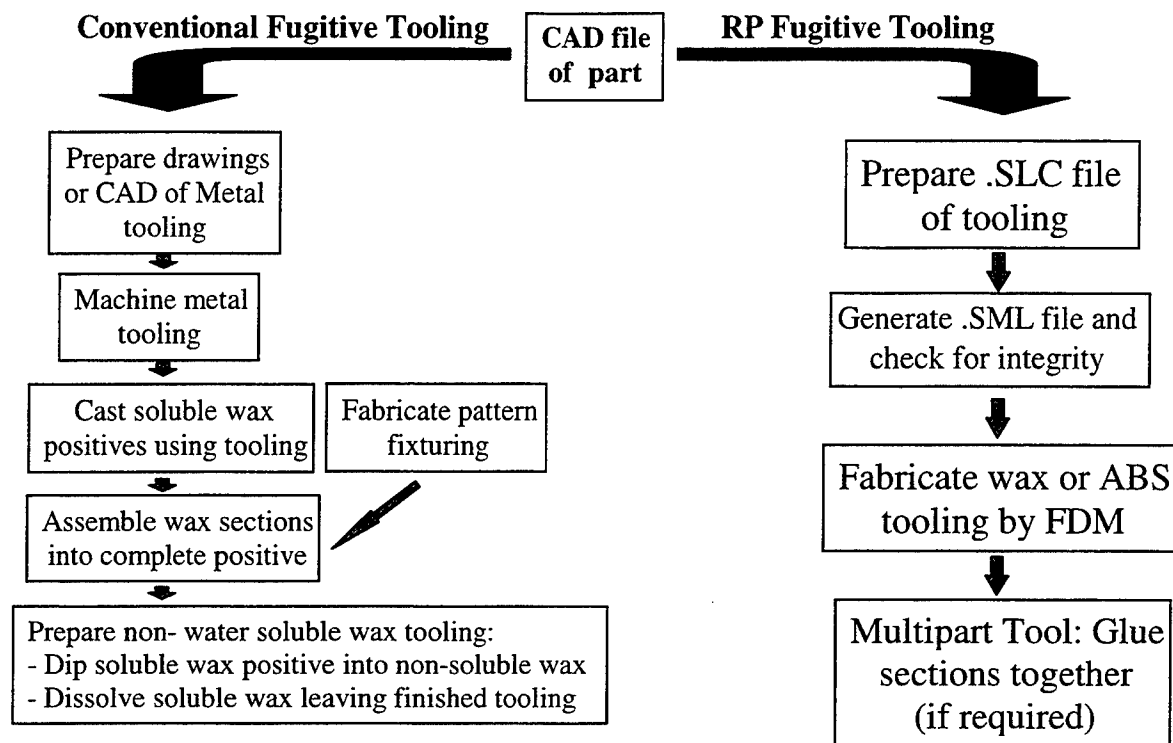


Figure 1. Process for fabrication of Fugitive Tooling

The fabrication of conventional fugitive tooling is a very labor intensive process with long lead times. Figure 1 shows how the fabrication of fugitive tooling can be significantly simplified through the use of solid freeform fabrication techniques. Using a large ceramic turbine nozzle doublet component (Figure 3) as an example, the cost savings of using rapid prototyped fugitive tooling was examined (Tables 1 & 2). The results show that significant time and cost savings can be realized for both the production of the initial part and subsequent components.

Mold design is a relatively mature area of work. Rapid prototyping procedures provide an efficient means of manufacturing molds directly from the envisioned CAD models. Minimal tooling investment is required, apart from the prototyping machinery itself. Complex shapes with non-extractable surfaces and blind holes can be designed with ease. The direct fabrication of fugitive tooling from a CAD file significantly reduces the time and cost of fabricating complex net shape ceramic components by eliminating excessive machining. The additional benefit is that changes in the component design can be easily accommodated without additional capital equipment investments. The details of fabricating gelcast tooling using rapid manufacturing techniques and using that tooling for ceramic gelcasting, shown schematically in Figure 2, is described below.

1. The CAD model of the component is scaled up to allow for shrinkage.
2. A mold is designed for the component with the following features -
 - Part orientation for minimal mold overhangs and elimination of air pockets.

- A solid lining for the mold cavity, created by conformally offsetting the component surface and building a part “perimeter.”
 - A honeycombed mold support structure behind the mold cavity. The honeycomb structure increases the ratio of surface area to volume of the mold material and results in more efficient dissolution.
 - Add appropriate reservoirs, gatings and risers for easy filling of the slurry.
3. If a mold design has large overhangs or sections in which support structures are hard to remove, multi-part molds are built and assembled using appropriate adhesives. Locating holes are built into the mold to enable accurate alignment of the parts.
 4. Support structures are added as required. These are preferably of materials dissimilar to the part material.
 5. The molds are built on the appropriate RP platform of acetonitrile butadiene styrene (ABS) or investment casting waxes.
 6. Molds are tested for integrity by filling with water and holding for a period of time.
 7. The ceramic gelcasting slurry is poured into the cavity of the mold so that all air pockets are removed.
 8. Gelation is then achieved by elevating the temperature.
 9. The entire assembly is immersed in a bath of solvent (acetone, alcohol, toluene) and the mold is dissolved. In the case of wax, elevated temperatures can be used to melt away the mold.
 10. The formed ceramic component that is left behind is dried and sintered.

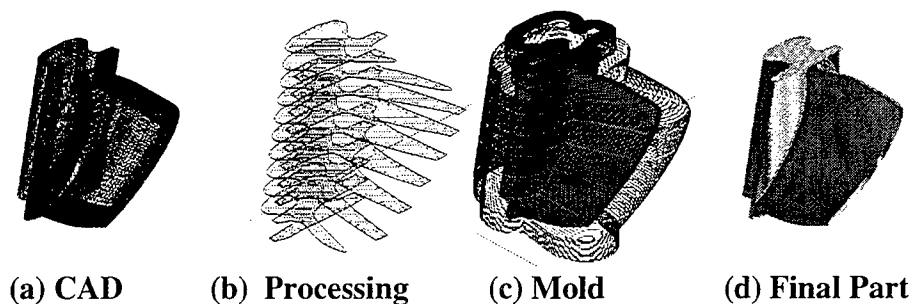


Figure 2: Schematic of the Gelcasting Process for a Ceramic Turbine Blade.

The cost advantages of this technique are manifest in the following: (a) Minimal machining is required in the fabrication of a complex ceramic component. (b) Rapid generation of molds with varying component parameters enables quick turnaround in iterative part design. (c) Defects and part rejection caused by problems with mold disassembly are minimized. (d) Doing away with physical means of removal ensures that thin sections and delicate protrusions can be manufactured.

EXAMPLE

To demonstrate the feasibility of using rapid prototyped fugitive tooling to fabricate complex ceramic components the entire process was exercised on a ceramic turbine

nozzle doublet based on a metal nozzle design used on the Pegasus[®] engine. A CAD file was developed by reverse engineering a full size metal component using CAT scanning techniques. This file was used to prepare a fugitive tool using the procedure described above. Several tools were produced and parts were gelcast using AS800 silicon nitride. The parts were dried and sintered to high density. Figure 3, shows a turbine nozzle doublet tool fabricated using a Stratasys FDM1600TM and silicon nitride gelcast part that was cast in an RP tool.

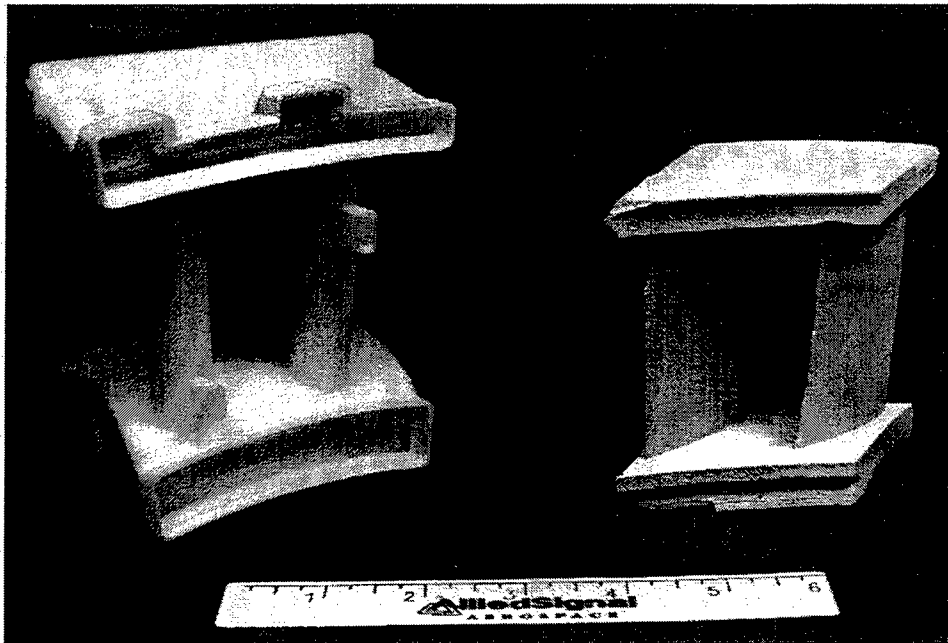


Figure 3: Fugitive Tooling and a Ceramic Gelcast of a Doublet

FUTURE DIRECTIONS IN THE DEVELOPMENT OF RP FUGITIVE TOOLING. While the feasibility of using RP tooling for gelcasting ceramic articles has been demonstrated the true cost savings of using this approach will not be realized until significant experience in handling this process is obtained. In particular, the ability to obtain a crack free part on the first iteration is highly dependent on mold design. Issues with eliminating designs which trap air and excessive mold material on certain parts of the tool need to be addressed. Work on the development of more suitable fugitive tool materials will also help move this technology forward. Surface finish issues which are relevant to most layered manufacturing techniques will also need to be resolved.

CONCLUSIONS

By combining the processes of rapid prototyping to fabricate tooling and ceramic gelcasting to fabricate parts, a means of manufacturing ceramic components in a rapid and inexpensive manner has been developed. Complex shaped parts that are hard to machine, slip cast or injection mold can be manufactured by this method. The cost

^a Rolls Royce engine component, supplied by the Office of Naval Research.

benefits are realized by time savings by eliminating costly tool machining procedures. The technique enables the use of iterative design and the fabrication of parts with unique structures (complex protrusions, thin sections).

ACKNOWLEDGMENTS

This work was sponsored by the Defense Advanced Research Projects Agency and the Office of Naval Research under contract # N00014-94-0115. Thanks are due to Barry Draskovich and the gelcasting team at AlliedSignal Ceramic Components, the engineering group at Stratasys Inc., Ed Pankowski at FabTek Inc. and Rolf Hubert at Sanders-Prototype Inc.

REFERENCES

- [1] Jacobs, P. F., *Rapid Prototyping & Manufacturing: Fundamentals of Stereolithography*, Society of Manufacturing Engineers, Dearborn, MI, 1992.
- [2] Griffith, M. L., T.-M. Chu, W. C. Wagner and J. W. Halloran, "Ceramic Stereolithography for Investment Casting and Biomedical Applications", [7], 1995.
- [3] Bunnell, D. E., S. Das, D. L. Bourell, J. B. Beaman and H. L. Marcus, "Fundamentals of Liquid Phase Sintering During Selective Laser Sintering", [7], 1995.
- [4] Cima, M. J., J. Yoo, S. Khanuja, M. Rynerson, D. Nammour, J. Giritlioglu, J. Grau, E. M. Sachs, "Structural Ceramic Components by 3D Printing", [7], 1995.
- [5] Agarwala, M. K., R. van Weeren, K. R. Vaidyanathan, A. Bandyopadhyaya, G. Carrasquillo, V. R. Jamalabad, N. A. Langrana, A. Safari, S. H. Garofalini, S. C. Danforth, J. Burlew, R. J. Donaldson, P. J. Whalen, C. Ballard, "Structural Ceramics by Fused Deposition of Ceramics", [7], 1995.
- [6] Zong, G., *Solid Freeform Fabrication using Gas Phase Selective Area Deposition*, Ph.D. Dissertation, University of Texas, Austin, TX, 1991.
- [7] Marcus, H. L., J. J. Beaman, D. L. Bourell, J. W. Barlow and R. H. Crawford, *Proceedings of the Solid Freeform Fabrication Symposium*, The University of Texas at Austin, Austin, TX, 1994, 1995.

Process	One Time Cost per mold design	Time (hours)	Outsourcing or Material Costs (\$)	Labor (hrs) Professional Technician
Obtain CAD file of part and convert to .STL				
Determine best orientation for mold build: create .SLC files and iterate to minimize support	XX	4	-	4
Design and create mold file (.SLC)	XX	4 to 16	-	4 - 16
Generate .SML file and check integrity: fix aberrations	XX	4	-	4
Build mold on Stratasys FDM 1600		44	\$70 (ABS)	1
Multipart Mold: Glue sections together		4	< \$1	4
Clean up mold and check mold for leakage		4	--	1
TOTALS		60 - 76	\$ 70	12 - 24
			@ \$78/hr	@ \$ 55/hr
TOTAL \$			\$ 70	\$ 936 - \$ 1872
				\$ 330

First iteration would take 60 to 76 hours and cost from \$ 1116 to \$ 2272. Subsequent iterations of the same mold would take 48 - 52 hours at a cost of \$ 180 - \$ 400/mold.

Table 1. Cost Analysis for ABS FDM tooling for Gelcasting the Ceramic Turbine Nozzle Doublet

Process	One Time Cost per mold design	Time (hours)	Outsourcing or Material Costs (\$)	Labor (hrs) Professional Technician
Obtain CAD file of part and convert to .STL				
Prepare drawings or CAD of metal tooling	XX	4 weeks		120
Machine Metal tooling	XX	6 weeks	\$20,000	
Cast water soluble wax positives using metal tooling		5-10 hrs	~ \$ 1	5 - 10
Fabricate pattern fixturing	XX	3 weeks*	\$2,000	
Assemble wax sections into a complete positive		6 hrs		6
Prepare non-water soluble wax tooling				
-Dip soluble wax positive into non-soluble wax		24 hrs	~ \$ 1	3
-Dissolve soluble wax leaving finished wax mold		36 hrs		4
TOTALS		11 weeks	\$22,002	120
TOTAL \$				@ \$78/hr
				@ \$ 55/hr

* Concurrent with metal tooling fabrication

First iteration would take ~ 11 weeks and cost from \$ 32352 to \$ 32627. Subsequent iterations of the same mold would take 71 to 76 hours at a cost of \$ 990 to \$ 1265/mold.

Table 2. Cost Analysis for the Fabrication of Standard Wax Tooling for Gelcasting the Ceramic Turbine Nozzle Doublet

Rapid Prototyping of Mg/SiC Composites by a Combined SLS and Pressureless Infiltration Process

Martin Wohlerl and David Bourell
Center for Materials Science and Engineering
The University of Texas at Austin
Austin, TX 78712

Introduction

The expanding market for metal matrix composites (MMCs) presents a unique niche application for rapid prototyping / manufacturing. MMCs are well suited to RP for two reasons. First, these relatively new high performance materials are largely used in high cost, low production applications which are easily accommodated by RP techniques. Second, the hard and brittle ceramic reinforcement phases used in MMCs add cost and complexity to traditional production methods. Special tools or processes are required to machine these materials, and the cost and design limitations imposed by the production of a mold limit the competitiveness of casting [1,2]. In comparison, the additive nature of Selective Laser Sintering (SLS) avoids the problems associated with machining of the ceramic phase, and the wide range of geometries which can be produced ensures the versatility of the process.

Process Description

The new RP process consists of three steps: the production of a porous ceramic preform by SLS of polymer coated powder, a polymer debinding / firing cycle, and the infiltration of the metal matrix into the preform. A schematic of these steps is shown in Figure 1.

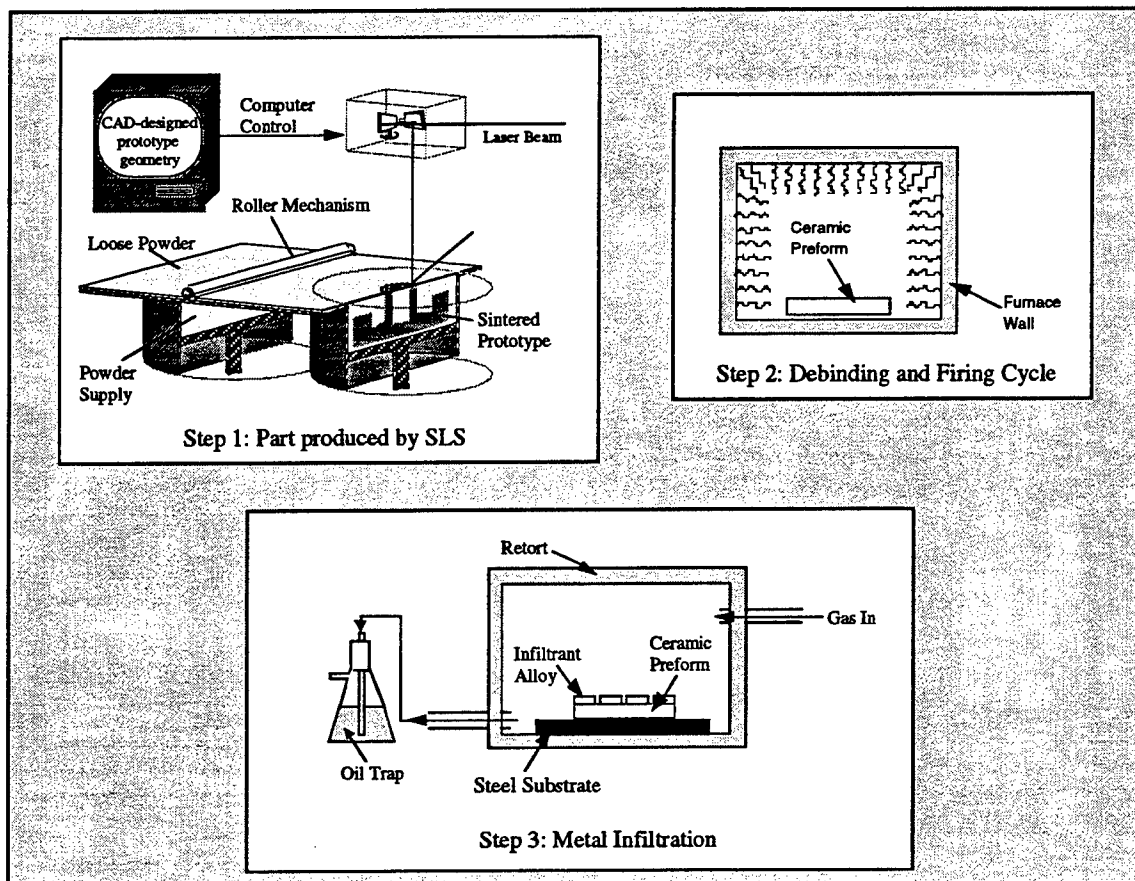


Figure 1. Schematic showing the three steps of the new production process.

SLS of Ceramic Preforms

The production of a porous ceramic preform by SLS is central to the new process. The part geometry is established at this stage and will remain unchanged throughout the remaining processing steps. The production of the preforms did not pose any substantial problems; however, the use of a new proprietary polymer binder formulation did prompt a series of short investigations to establish the optimal coating thickness and scanning parameters to provide maximum density and strength. It was established that a 4.5 wt% polymer coating and fluence of approximately 4 cal/cm² provided optimal properties [3]. The density of the preforms was typically 40 vol%. The production of higher density preforms was prevented by the poor packing behavior exhibited by the angular SiC particles. Use of a bimodal particle size distribution or the availability of more spherical particles should substantially increase this value. A micrograph of the fracture surface of a scanned preform is shown in Figure 2. The average particle size is 50 μ m (280 mesh).

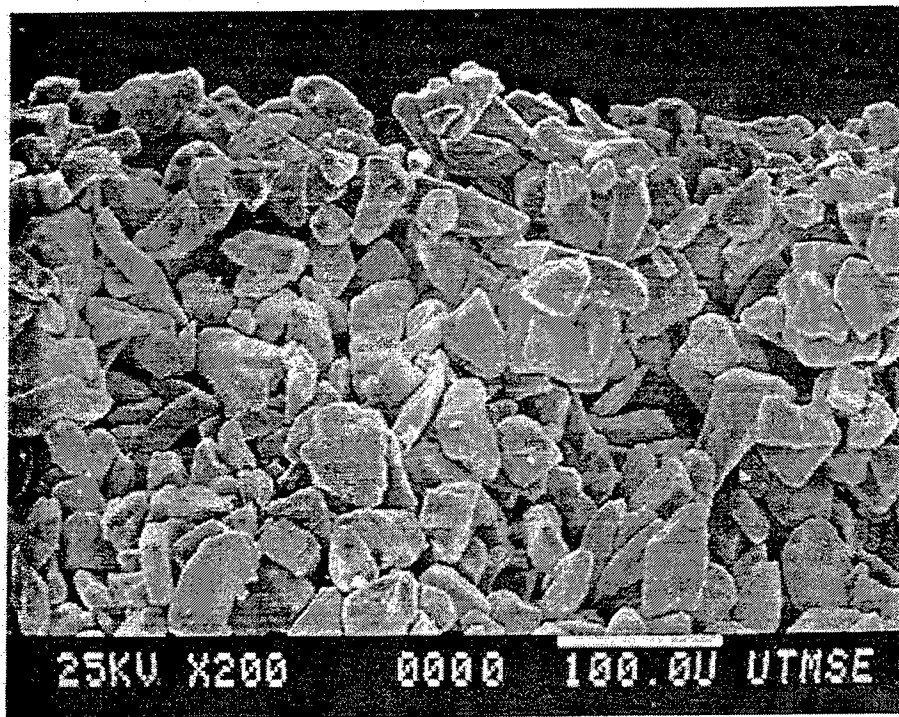


Figure 2. Scanning electron micrograph of a preform fracture surface transverse to the build direction.

The selection of SiC as the ceramic reinforcement phase was based on its wide availability and its high thermal conductivity, which makes it useful in electronics packaging applications (discussed later). In theory, any ceramic reinforcement phase can be selected which is available in powdered form, compatible with the polymer binder, and stable under the laser beam. Previous work done with alumina suggests that it would be a suitable alternative.

Debinding and Firing

Before the metal matrix can be infiltrated into a preform, the polymer binder remaining on the surface of the SiC must be removed. This is accomplished by heating the preform to 400 °C in air. At this temperature, the polymer is volatilized and leaves the surface as a vapor. The preforms are now quite fragile, and further handling or attempts at infiltration typically result in damage to the preform. The addition of a firing step greatly improves the strength and handleability of the

preforms. By holding the preforms at 1100 °C for 2 hours, a thin layer of the SiC is converted to SiO₂. The formation of the silica layer allows light bonding between the individual particles; however, no real sintering or densification of the preform occurs at this stage. Sintering of the SiC directly was not attempted because of the high temperature and inert atmosphere which are required. Even with the addition of boron and free carbon as sintering aids, processing temperatures of 2150 °C are typically used during commercial processing of SiC powders [4]. Such processing conditions would have added substantially to the cost of the production process. Future work may be directed toward the elimination of the polymer debinding and perform oxidation step by directly sintering the SiC under the laser beam. Preliminary experiments have indicated that such processing is possible.

Pressureless Infiltration

Infiltration of the porous preforms with the metallic matrix is the final step in the production process. This process is not as readily achieved with a metal-ceramic material system as it is with the more common metal-metal systems such as the iron-copper and copper-solder systems used in other RP processes. The obstacles associated with this process are due to the relative surface energies required to drive the infiltration process. In a spontaneous or pressureless infiltration process, the surface tension of the liquid infiltrant must be lower than the surface energy of the solid matrix. Because the surface energies of ceramic materials tend to be quite low, this situation rarely occurs. As the table below shows, the surface energies of typical ceramics are lower than the surface tensions of common metals and alloys.

Surface Energies of Common Alloys and Ceramic Materials [5-8].

Material	Temperature (°C)	Surface Energy (mN/m)
Pt _(l)	1770	1865
Fe _(l)	1120	1835
Cu _(l)	1120	1270
Al _(l)	660	914
Mg-8Al _(l)	600	571
SiC _(s)	RT	3800
TiC _(s)	1100	1190
Al ₂ O _{3(s)}	1850	905
ZrO _{2(s)}	RT	770
SiO _{2(s)}	1300	310

For the magnesium-SiC material system which we are considering, the values shown in the table suggest that infiltration should not be difficult because of the relatively high surface energy of SiC. This high value is misleading. The surface energy for SiC listed in the table was established for a perfectly clean surface of SiC at room temperature. The exposed surfaces of most SiC, including the particles in the preform, are no longer SiC, instead they have formed a surface layer of SiO₂. As can be seen, the surface energy of silica is among the lowest of the common ceramic materials. It is the surface layer of silica which effectively prevents the infiltration of most alloys.

Because of the unfavorable surface energies of these materials, processes such as squeeze casting have been developed which use an externally applied pressure to overcome the surface energy considerations and force the liquid into the matrix. Such a process is not suitable for this

application because it requires the production of a mold. An alternative approach to pressure infiltration is the incorporation of a reactive species such as magnesium, lithium, or titanium into the infiltrant alloy [9-11]. It has been shown that the presence of these elements promotes wetting. Sessile drop experiments with SiC and aluminum have recorded a change in contact angle from 112° to 83° with the addition of 5 wt% Mg to the aluminum [9]. It has been proposed that the change in wetting behavior is due to reactions between the magnesium and the oxide layer present on the surface of the SiC [12]. The Al-Mg-O and Mg-Si-O ternary phase diagrams are shown in Figure 3. As can be seen, the system is fairly complex with many possible stable phases. Fosterite (Mg_2SiO_4), Spinel (MgAl_2O_4), and Mullite ($3\text{Al}_2\text{O}_3 \cdot \text{SiO}_2$) were suggested as the most likely reaction products. The exact nature of the reaction at the interface has not been definitively established, but the experimental evidence for superior wetting behavior provided by magnesium suggested that a magnesium based alloy would make a suitable infiltrant. For the infiltration experiments, a common die casting alloy AZ91D was selected. Aside from its ability to wet the SiC, this alloy provides low weight and high thermal conductivity.

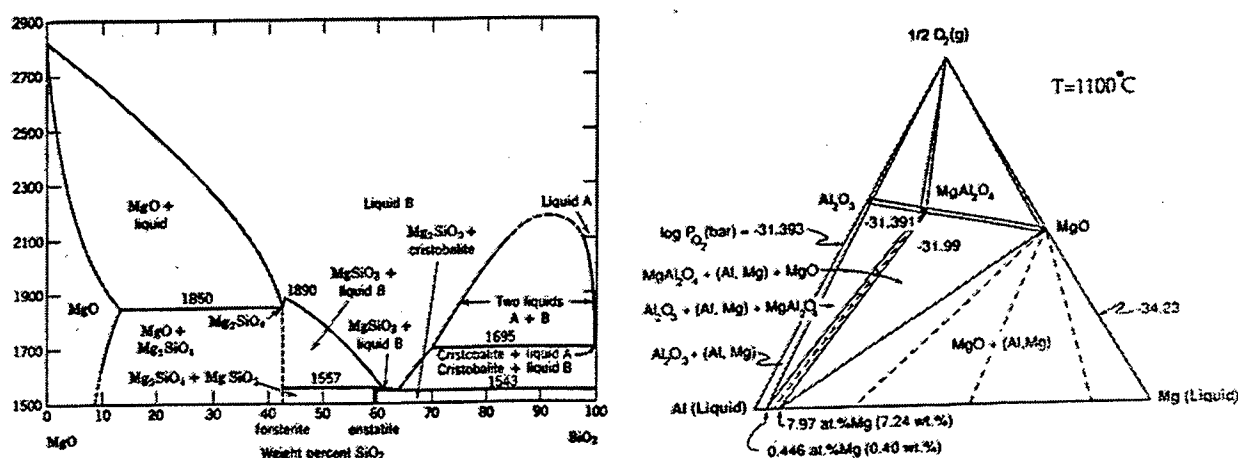


Figure 3. Phase diagrams for the Mg-Si-O and Al-Mg-O systems [13,14].

Infiltration Experiments

To prevent oxidation of the preform and infiltrant alloy, the infiltration process must be performed in a controlled atmosphere. A sealed retort capable of being evacuated and backfilled with inert gas was required for successful infiltration. A purge cycle consisting of evacuation to approximately 100 mTorr followed by a backfill with inert gas to atmospheric pressure was repeated twice before the heating cycle was begun. The purge gas was allowed to flow through the retort during the entire experiment. The gas was vented through an oil trap which provided a slight positive pressure in the retort. Strips of the infiltrant alloy approximately 3 mm thick were placed directly on top of the SiC preforms. This arrangement ensured the shortest infiltration distance for the part geometry used in these experiments. A steel substrate was used to support the preform and prevent reactions between the magnesium alloy and the retort. A schematic of the experimental set up is labeled as Step 3 in Figure 1. Following the purging of the retort atmosphere, the process cycle consisted of a one hour ramp to the infiltration temperature, a one hour hold, and a slow cool to room temperature.

Previous research conducted by Aghajanian et al, indicated that a nitrogen based atmosphere is required for spontaneous infiltration [15,16]. The preforms manufactured by SLS behaved similarly, with no infiltration occurring in helium or argon atmospheres. When a nitrogen atmosphere was used, the infiltration proceeded readily, if somewhat slower than is observed with other materials systems. A processing temperature of 670 °C was sufficient to infiltrate a 1 cm thick preform in one hour. Typical microstructures are shown in Figure 4. As can be seen, the

SiC is well distributed throughout the sample, with no clustering or layering evident. The level of porosity is also quite low. It was observed that two factors must be controlled to limit porosity. First, the infiltration time must be sufficient to allow complete infiltration; short infiltration times (30 minutes) frequently resulted in incomplete infiltration. Second, no large pores may be present in the preform prior to infiltration. Pre-existing pores will be retained after infiltration, presumably due to the lack of capillary action to draw the liquid into the pores.

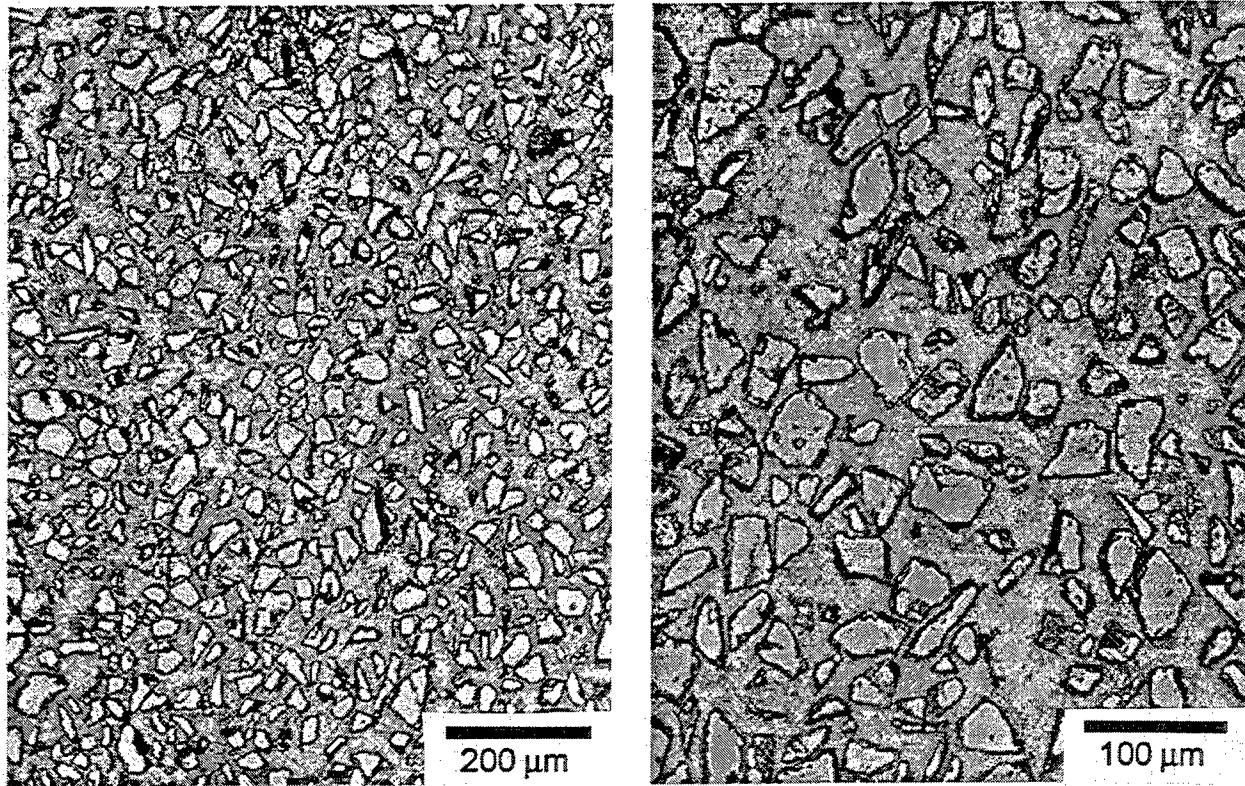


Figure 4. Micrographs of the infiltrated preforms. a)100X b)200X

Thermal Properties

The use of MMCs for electronic packaging materials has been suggested because of their high thermal conductivity and low thermal expansion. To prevent thermal stresses from arising at the interface between the chip and the packaging, the coefficients of thermal expansion (CTEs) must be matched. For this application a CTE equivalent to that of silicon 6.7 ppm/°C is required. Because the magnesium alloy has a relatively high CTE (27.2 ppm/°C) [17] a large volume fraction of SiC is required to achieve the desired value. Theoretical models indicate that as much as 80 vol% SiC may be required. In practice, concentrations of SiC somewhat less than this value appear to be adequate [18]. For the approximately 40 vol% SiC present in the samples produced by SLS, average CTE values of 11.9 ppm/°C were obtained with TMA testing. It was noted that the CTE values were similar in directions parallel and transverse to the SLS build direction, which was expected based on the uniform microstructure.

Clearly, a higher volume fraction of SiC is required to obtain the desired CTE value. Due to time constraints, the production of preforms with a bimodal powder size distribution was not possible; however, a similar structure was produced by infiltrating existing preforms with additional SiC. A slurry consisting of 79.7 wt% water, 20 wt% 1200 mesh SiC, and 0.3 wt% sodium dedocyl sulfate (a surfactant) was infiltrated into the preforms. The preforms were then processed with a debinding, firing, and metal infiltration process identical to that used with the previous samples.

The addition of the 1200 mesh powder increased the volume fraction of SiC to approximately 48%. The increased SiC content resulted in a decrease in CTE to 7.1 ppm/°C. A value which closely approaches the desired 6.7 ppm/°C. The presence of the additional SiC provided the added benefit of improving the strength and handleability of the preforms after the firing cycle. The one problem associated with this process is the nonuniform distribution of the SiC. As can be seen in the micrographs in Figure 5, the smaller SiC tends to form clusters around the larger particles. This fact, coupled with a decreasing concentration gradient away from the surface of the sample, led to occasional warping of the preforms during the firing stage. This problem should be alleviated by producing the preforms directly from a bimodal particle mixture.

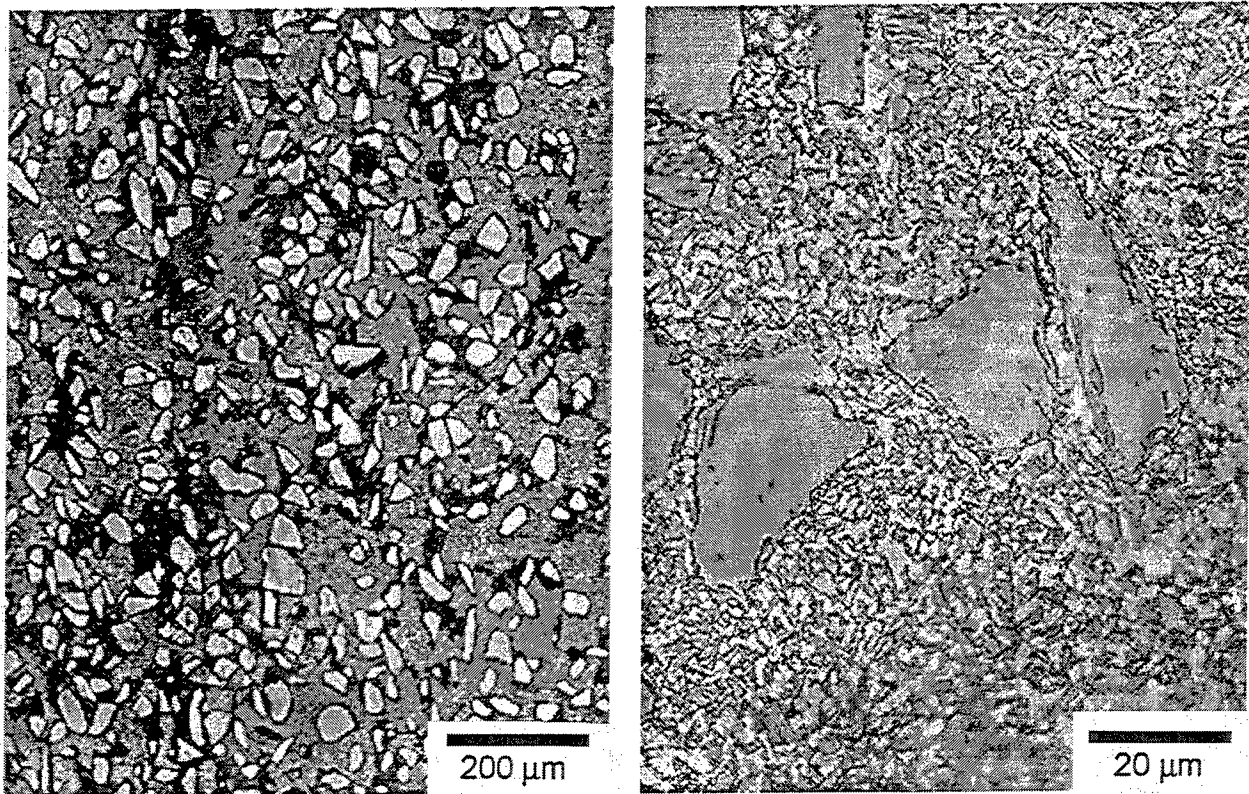


Figure 5. Micrographs showing clusters of 1200 mesh SiC particles. a)100X b)1000x

Geometry

After the processing procedure had been demonstrated with simple rectangular test coupons, several more complex geometries were infiltrated to determine if accurate dimensions could be retained. Two of the test geometries are shown in Figure 6. Three different parameters were considered. First, the thin walls and small features of the test pieces are far more delicate than the simple rectangular bars. These areas are prone to damage or collapse during handling of the preform or during the infiltration process itself. Optimization of the binder coating thickness to improve green part strength, and a firing cycle of sufficient length and temperature ensured that these features were accurately retained.

Second, holes of varying dimensions were present in the test geometry to determine if over-infiltration would occur. It was determined that the surface tension effects which drive the infiltration process are quite weak and close particle spacing is required for infiltration. Holes as small as 2 mm in diameter were still too large to provide a sufficient capillary force with which to draw in the infiltrant and remained uninfiltrated. A related concern is the small amount of excess infiltrant which must be provided in any infiltration process to ensure that the part will be

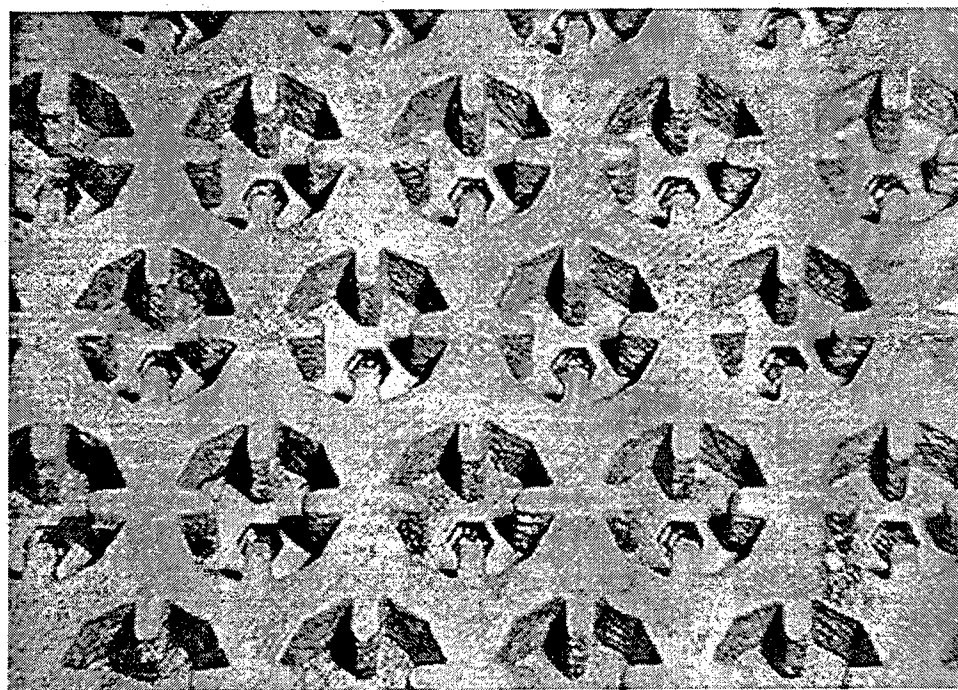
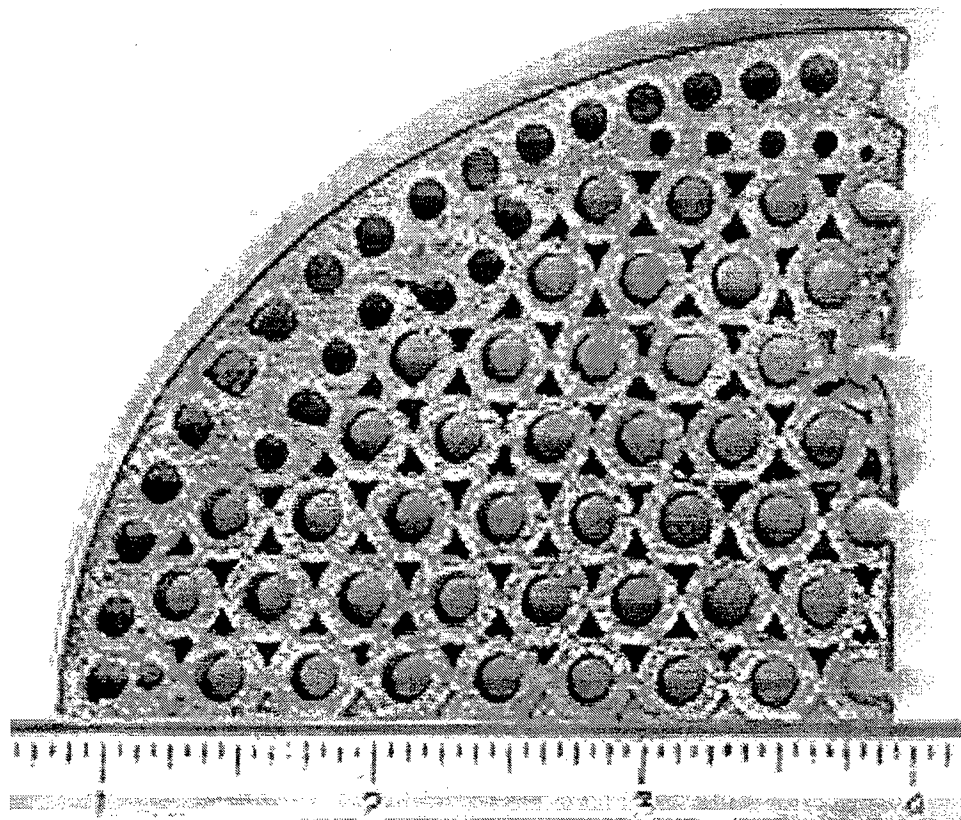


Figure 6. Fully infiltrated test parts. Parts were finished by bead blasting following the infiltration step. (Top scale in inches)

completely infiltrated. This excess material collects at the bottom of the preform along the surface of the substrate such that it would occasionally block through holes in the parts. The presence of Second, holes of varying dimensions were present in the test geometry to determine if over-infiltration would occur. It was determined that the surface tension effects which drive the infiltration process are quite weak and close particle spacing is required for infiltration. Holes as small as 2 mm in diameter were still too large to provide a sufficient capillary force with which to draw in the infiltrant and remained uninfiltrated. A related concern is the small amount of excess infiltrant which must be provided in any infiltration process to ensure that the part will be completely infiltrated. This excess material collects at the bottom of the preform along the surface of the substrate such that it would occasionally block through holes in the parts. The presence of the excess magnesium does not cause substantial difficulties in the processing of the parts because it is very easily removed. The great difference in hardness between the excess magnesium alloy and the composite part allows abrasive bead blasting or tumbling processes to quickly remove the excess material. The high hardness of the ceramic phase effectively limits any additional material removal once the surface of the composite is reached.

The third concern is warping or large scale distortion of the preform. Warpage was observed in some of the test pieces. It appears that the infiltration process disrupts the light bonding which exists between the SiC particles. The weakened structure of the preform tends to conform to the shape of the substrate. This distortion suggests that parts with overhanging features may present problems during infiltration. Two possible methods to alleviate this problem include packing the preform in a supporting powder bed which is not infiltrated by the magnesium, or using a ceramic binding agent such as a preceramic polymer [19] which can be decomposed to provide a SiC "glue" to hold the individual particles together.

Conclusions

A process has been established for the rapid manufacturing of MMCs based on Selective Laser Sintering. Parts with complex geometries, containing between 40 and 50 vol% SiC were successfully produced. The low thermal expansion and high thermal conductivities provided by these materials may make them suitable for applications such as electronic packaging. Future work on this process will focus on direct SLS processing of the SiC which would allow the removal of the polymer binder along with the current debinding / firing stage. Additionally, the incorporation of a ceramic precursor to the preform may provide higher SiC content and improved preform strength and stability during the infiltration process.

References

1. N. Tomac, K. Tønnessen, "Machinability of Particulate Aluminum Matrix Composites," Annals of the CIRP, 41 (1) (1992), 55-58.
2. T. S. Srivatsan and D. M. Bowden, ed., Machining of Composite Materials Proceedings of the Machining of Composite Materials Symposium ASM/TMS 1-5 November, 1992.
3. M. Wohlert and D. Bourell, "Production of Full Density Metal-Matrix Composites by a Combined Selective Laser Sintering / Metal Infiltration Process" To be published TMS Proceedings October 6-10, 1996 Fall Meeting Cincinnati, OH.
4. D. Richerson, Modern Ceramic Engineering Properties, Processing, and Use in Design, 2nd ed. (New York, NY: Marcel Dekker, Inc., 1992), 540.
5. R. Pampuch, Constitution and Properties of Ceramic Materials (Elsevier, 1991), 68.

6. L. E. Murr, Interfacial Phenomena in Metals and Alloys (Addison-Wesley, 1975), 101-107.
7. C. T. Lynch, ed., Practical Handbook of Materials Science (Boca Raton, Florida: CRC Press, Inc. 1989).
8. W. D. Lynch, H. K. Bowen, and D. R. Uhlmann, Introduction to Ceramics 2nd Edition (Wiley & Sons, 1976), 183.
9. D. Han, H. Jones, and H. V. Atkinson, "The wettability of silicon carbide by liquid aluminium: the effect of free silicon in the carbide and of magnesium, silicon and copper alloy additions to the aluminum," Journal of Materials Science, 28 (1993), 2654-2658.
10. M. Gupta et al. "Wetting and interfacial reactions in Al-Li-SiCp metal matrix composites processed by spray atomization and deposition," Journal of Materials Science, 26 (1991), 6673-6684.
11. M. Kobashi, T. Choh, "The wettability and the reaction for SiC particle/Al alloy system," 684-690.
12. S.Y. OH, J. A. Cornie and K. C. Russell, Ceramic Engineering and Science Proceedings, 8 (1987), 912.
13. A. M. Alper, ed., Phase Diagrams in Advanced Ceramics (San Diego, Ca: Academic Press, Inc., 1995), 96.
14. W. D. Lynch et al., p.288.
15. M. K. Aghajanian et al., "The fabrication of metal matrix composites by a pressureless infiltration technique," Journal of Materials Science, 26 (1991), 447-454.
16. M. K. Aghajanian et al., "A New Infiltration Process for the Fabrication of Metal Matrix Composites," SAMPE Quarterly 7 (1989), 43-46.
17. Robert S. Busk, Magnesium Products Design, (New York, NY: Marcel Dekker, Inc., 1987), 167.
18. K. Schmidt, C. Zweben, and R. Arsenault, "Mechanical and Thermal Properties of Silicon-Carbide Particle-Reinforced Aluminum," Thermal and Mechanical Behavior of Metal Matrix and Ceramic Matrix Composites, ASTM STP 1080, (1990), 155-164.
19. J. M. Schwark and Mark J. Sullivan, "Isocyanate-Modified Polysilazanes: Conversion to Ceramic Materials," Mat. Res. Soc. Symp. Proc. 271 (1992), 807-812.

Selective Laser Sintering of High Performance High Temperature Materials

S. Das, N. Harlan, J. J. Beaman, D. L. Bourell

Laboratory for Freeform Fabrication

University of Texas at Austin

Abstract

Hot Isostatic Pressing (HIP) of high performance metal parts is currently done using either a shaped metal container or a pre-fabricated ceramic mold depending on the part material and geometry. An alternative method of HIP encapsulation that allows complex part geometry, short cycle time and minimal potential for container-powder bed interaction is desired. Integral, fully dense metal skins with complex geometry can potentially be constructed by direct selective laser sintering (SLS). The advantages of in-situ HIP encapsulation by direct SLS include the elimination of a secondary container material and any associated container-powder bed interaction, reduced pre-processing time and a short HIP cycle. Single and multi-layer specimens of Inconel 625, Ti-6Al-4V and 17-4 PH stainless steel were produced by direct SLS. Closed porosity in Inconel 625 and 17-4 PH stainless steel samples ranged from 0 to 12% and area porosity from 0.5 to 20%, depending on the laser energy density. Direct SLS samples of Inconel 625 were subjected to helium leak testing and found to be impervious, with a leak rate less than 1×10^{-10} atm cc/s. These samples met the criteria for containerless hot isostatic pressing.

OBJECTIVE

An in-situ canning technique using direct selective laser sintering (SLS) is being developed for hot isostatic pressing (HIP) of high performance components. The process developed should be an integral canning technique with near net shape capability for complex parts and require minimal processing steps. The integral can must be leak free and cannot interact adversely with the powder bed. The process should not be limited by the can properties. The objective of this research is to produce highly dense skins of high performance metals acceptable for containerless HIP. Containerless HIP requires an outer shell with a helium leak rate¹ of less than 10^{-9} std cc/sec.

CONVENTIONAL HIP TECHNIQUES

Shaped Metal Can

Shaped metal cans are commonly used to encapsulate metal powder for HIP. They are largely made of low carbon steels, stainless steels, titanium and titanium alloys based on the powder to be processed and processing conditions. The container material is chosen such that minimal interaction occurs between the container and the powder at the processing temperature. Encapsulation containers are processed from sheet metal using standard metal working processes². Welded joints demand special attention, as they are a common point of failure during the HIP cycle. Container fabrication becomes expensive for part geometry more complex than a simple cylinder, thus sheet metal encapsulation is limited to generally simple designs. After HIP, the container must be removed by either machining or chemical methods. The process limits

imposed by the properties of the canning material, such as its melting temperature, are a drawback to the shaped metal encapsulation method.

Ceramic Mold Process

More complex shapes are typically produced using the ceramic mold process³. This process is similar to investment casting, except dry powder is poured into a ceramic mold instead of molten metal. The production of a near net shape is advantageous because it minimizes scrap losses and machining steps. However, outgassing and heating cycles are long during this process because the ceramic mold is surrounded by a large volume of pressure transmitting medium⁴. The long cycle time and pre-processing steps necessary in the ceramic mold method make it a time consuming and expensive process. Non-metallic contamination is also a possibility.

SLS/HIP

In the proposed direct SLS/HIP process, an impermeable high density skin is formed around the shape of a complex part by selective laser sintering. The interior of the part is laser sintered to intermediate density. The encapsulated partially sintered part is evacuated, sealed and processed by HIP to full density. This process can be followed by final machining, if necessary. Figure 1 shows a schematic of the process.

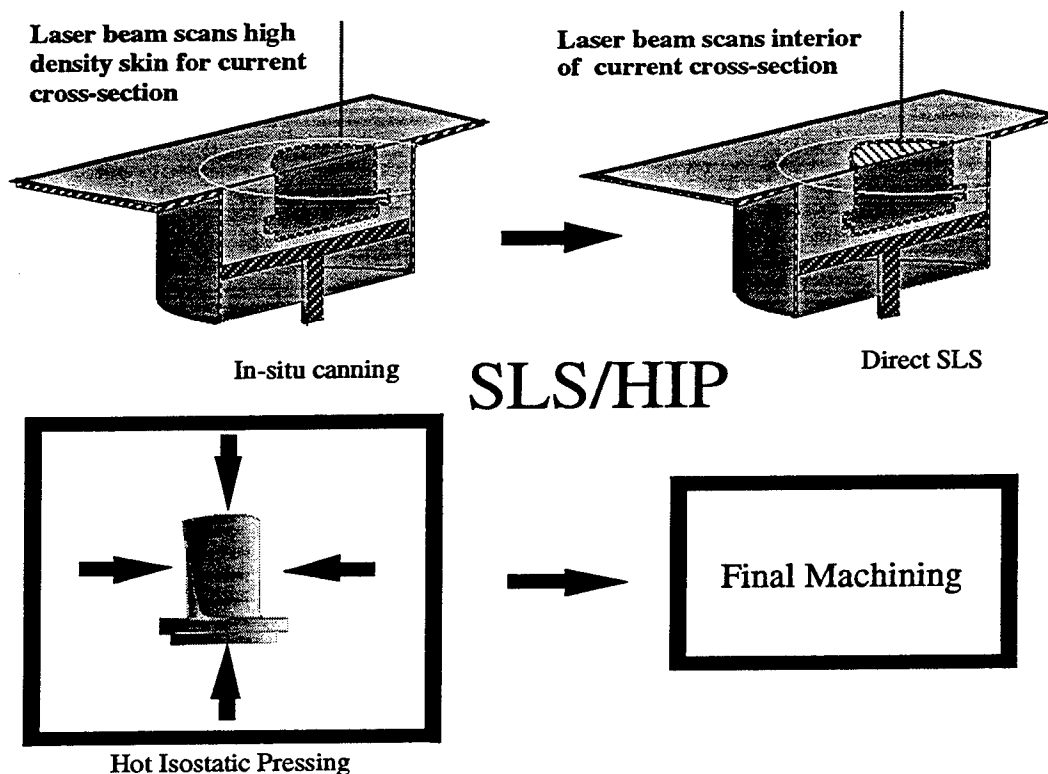


Figure 1. SLS/HIP Process

The direct SLS/HIP method has several advantages over conventional HIP methods. Since an integral skin is produced, the subsequent HIP process is considered containerless. There are no secondary canning steps, no adverse container-powder reactions and no container removal steps. A long out-gassing/heating cycle is not necessary. SLS/HIP allows production of complex shapes that cannot be achieved through standard sheet metal processing for a reasonable cost. As in the ceramic mold method, a near net shape is produced, minimizing scrap and machining steps. SLS/HIP has clear advantages over both the shaped metal can and ceramic mold HIP techniques.

EXPERIMENTAL

A computer controlled, high power Nd:YAG laser was used to process metal powders by selective laser sintering. Materials used in screening trials included spheroidized Inconel 625 (Anval Corp.), a flaked elemental blend of Ti-6Al-4V (Micron Metals, Inc.) and a spheroidized 17-4 PH stainless steel powder (Ametek Corp.), each with a -325 mesh particle size.

Laser energy density⁵ was varied between 1000 J/cm² and 2500 J/cm² as defined by the Andrew number equation,

$$A_N = \frac{P}{v \cdot \delta} (\text{J/cm}^2)$$

where

P is the incident laser power (Watts)

v is the laser scan speed (cm/s)

δ is the scan spacing (cm)

Samples prepared by direct SLS were cross-sectioned and prepared for optical microscopy. Closed porosity measurements were made using an AccuPyc 1330 gas pycnometer by comparing measured density to theoretical density. Area porosity was calculated from the optical micrographs.

To successfully HIP an object to full density, a barrier must be provided to prevent pressurized gas from entering the porous body. Due to high pressures involved in HIP (typically of the order of 15 ksi), openings as small as 0.1 μm can produce unacceptable leak rates. Leak testing is commonly performed on samples prior to HIP to ensure successful compaction. The impermeability test screening and procedure for integral can SLS parts is based on the Metals Handbook article on containerless HIP⁶. As a general guideline, the maximum helium leak rate through the barrier must not exceed 10⁻⁹ cc/s at atmospheric pressure. Such a low leak rate is required because at typical HIP pressures, the leak rate will be 1000 times greater than that at

ambient pressures. Shown below is a schematic of the leak test apparatus used to test laser sintered Inconel 625 samples.

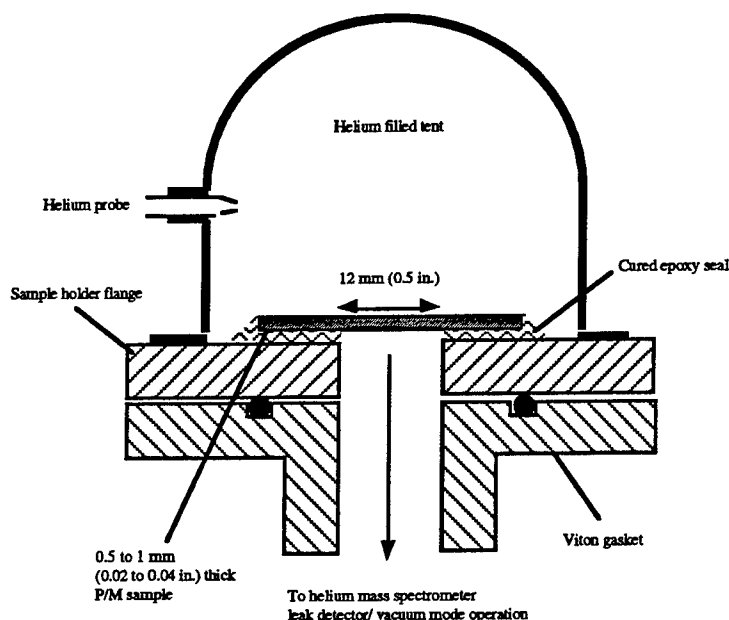


Figure 2. Leak Testing Apparatus

RESULTS AND DISCUSSION

Inconel 625

Closed porosity on the Inconel 625 coupons ranged from 0% to 10%. Area porosity measurements ranged from 4% to 20%. A small amount of closed porosity is acceptable in the integral skin because it does not contribute to leakage through the skin. Micrographs of the samples sintered under a highly inert environment are shown in Figures 3 and 4. The energy density used to sinter the sample is listed in the caption.

Leak testing showed that the Inconel 625 specimens are impervious to helium, with a leak rate of less than 1×10^{-10} atm cc/s. This leak rate is an order of magnitude lower than that acceptable for containerless hot isostatic pressing.

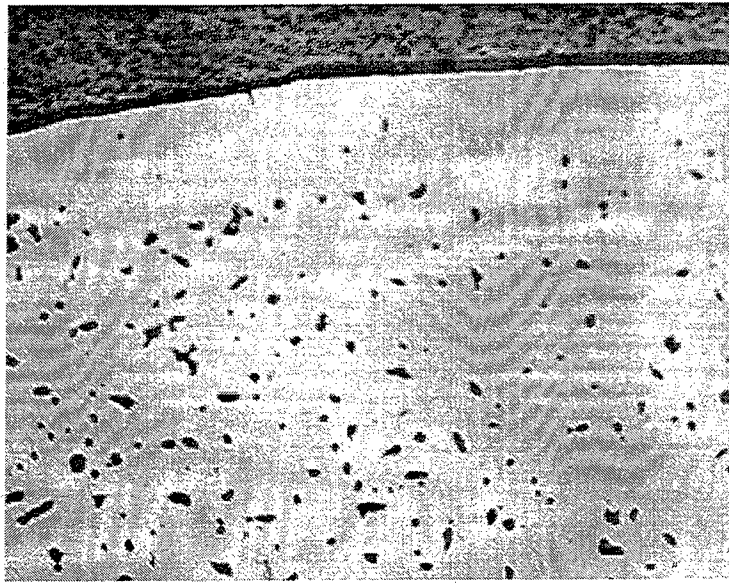


Figure 3. Inconel 625, Energy Density = 2230 J/cm^2 , 1.8 mm viewfield, 100X

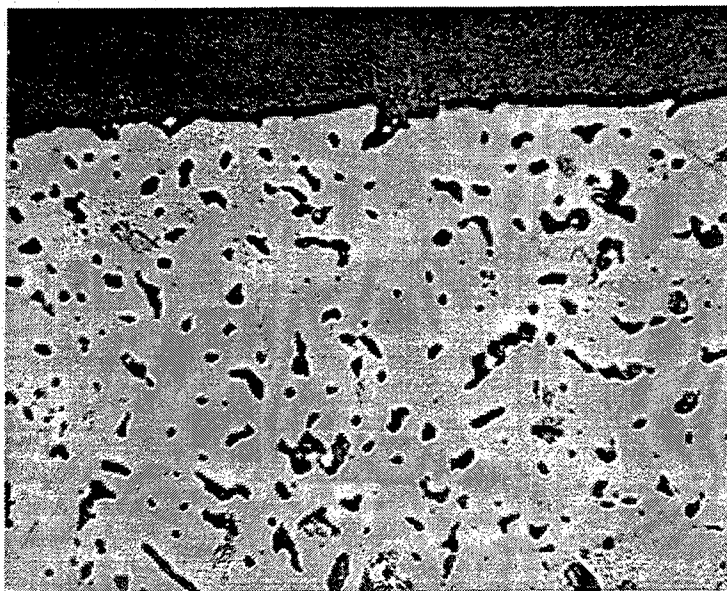


Figure 4. Surface of Inconel 625, Energy Density = 2134 J/cm^2 , 1.8 mm viewfield, 100X

Ti-6Al-4V

The titanium alloy tended to ball during SLS processing. Rather than melting into a smooth layer, the material tended to form clumps of dense regions. A micrograph of a dense region is shown in Figure 5.

Closed porosity was measured as 1% to 3% for the entire sample. Area porosity was measured as 2.5% in a dense region.

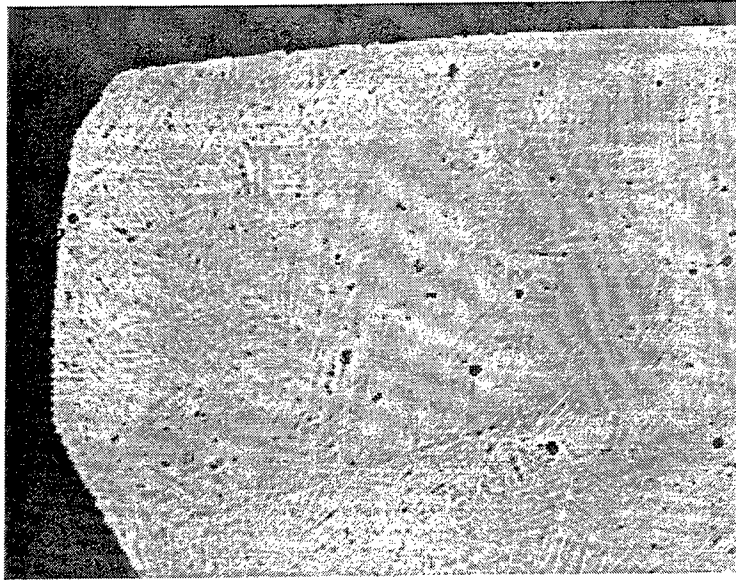


Figure 5. Ti-6Al-4V, Energy Density = 1061 J/cm², 1.8 mm viewfield 100X

17-4 PH Stainless Steel

Closed porosity measurements on 17-4 PH SS coupons prepared by direct SLS ranged from 3.2% to 12.2%. Area porosity was measured as 0.9% and 3.6% for a band across the sample. The porosity level in the 17-4 PH samples is acceptable for the production of an integral skin because it is mostly closed porosity. A typical micrograph of one of the samples is shown in Figure 6.

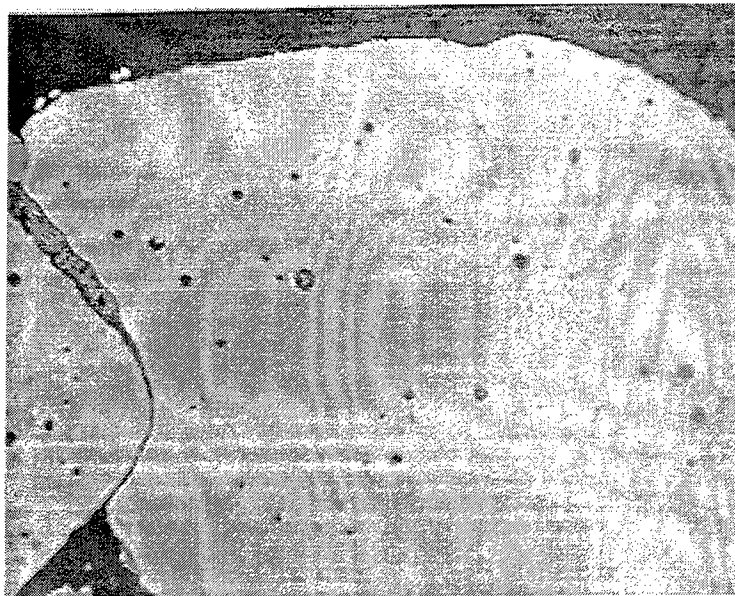


Figure 6. 17-4 PH SS, Energy Density = 1045 J/cm², 1.8 mm viewfield, 100X

The micrograph shows that several scan line widths of material flowed together to form larger bands. These bands are almost fully dense, exhibiting only 0.6% area porosity.

CONCLUSIONS

Preliminary materials screening studies to date on Inconel 625, Ti-6Al-4V and 17-4 PH stainless steel indicate the feasibility of constructing integral HIP containers by direct SLS. Samples of Inconel 625 produced by direct SLS meet the leak rate requirements for containerless hot isostatic pressing. Optical micrographs from the screening trials for Inconel 625 and 17-4 PH stainless steel show mostly closed porosity.

ACKNOWLEDGMENTS

This research was supported by the Office of Naval Research, contract N00014-95-C-0139, "Low Cost Metal Processing Using SLS/HIP".

REFERENCES

- ¹ *Hot Isostatic Pressing of Metal Powders*, Metals Handbook, Vol. 7, 9th Edition, p. 436.
- ² *Hot Isostatic Pressing of Metal Powders*, Metals Handbook, Vol. 7, 9th Edition, p. 429.
- ³ Koizumi, M. and Nishihara, M., ed., Isostatic Pressing Technology and Applications, (Elsevier Science Publishers: London, 1991), pp. 147-149.
- ⁴ Atkinson, H. V., and Rickinson, B. A., Hot Isostatic Pressing, (Adam Hilger: Bristol, England, 1991), pp. 64-65.
- ⁵ Nelson, J. C., *Selective Laser Sintering: A Definition Of The Process And Empirical Sintering Model*, Ph.D. dissertation, Department of Chemical Engineering, The University of Texas at Austin, 1993, p. 153.
- ⁶ *Hot Isostatic Pressing of Metal Powders*, Metals Handbook, Vol. 7, 9th Edition, p. 436.

SELECTIVE LASER SINTERING OF METAL MOLDS: THE RAPIDTOOL™ PROCESS

Uday Hejmadi
Kevin McAlea

Materials and Process Development Group
DTM Corp., Austin TX 78759

ABSTRACT

Complex three dimensional parts can be manufactured directly from CAD data using rapid prototyping processes. SLS® Selective Laser Sintering is a rapid prototyping process developed at the University of Texas at Austin and commercialized by DTM Corporation. SLS parts are constructed layer by layer from powdered materials using laser energy to melt CAD specified cross sections. Polymer, metal, and ceramic powders are all potential candidate materials for this process. In this paper, a commercial SLS process - the RapidTool Process - which allows metal molds to be rapidly manufactured is described. With this process, a polymer coated carbon steel powder is used to fabricate a "green part" in the SLS machine. The green part is then placed in a furnace with blocks of copper and, in a single furnace cycle, the polymer coating is removed and the steel skeleton is infiltrated with the copper. The resulting steel/copper composite material has durability and thermal conductivity similar to aluminum and can be hand finished using standard techniques. A finished mold core and cavity set which can be used to mold at least 50,000 parts with most plastics can be prepared in approximately ten days. The cost to produce most mold geometries with the RapidTool Process is also competitive with traditional mold-making methods .

INTRODUCTION

Since 1989, when the first stereolithography [1] machine was commercialized, Rapid Prototyping (RP) has been used primarily to produce plastic parts. Improvements to the materials and the processes have led to extensive use of rapid prototyping in a number of applications such as concept modeling, functional testing and patterns for investment casting and soft tooling. However, one of the drawbacks of RP parts especially for concept modeling and functional testing application is that they do not reflect all the characteristics of the final production parts. First, the range of materials currently available is limited to nylon, nylon / glass composites [2], Trueform™ PM [3], polycarbonate, ABS [4], wax and photopolymers based on acrylate and epoxy chemistries. Therefore, the user is limited to these materials even though the production parts may be of a different material. Second, even if the RP material is acceptable, RP processes may not reflect all the properties of production processes. For instance, injection molding, a common plastic shaping process, introduces anisotropy in properties due to material flow which cannot be reproduced in any RP process. Therefore, there is a need to rapidly manufacture prototypes or small scale production parts with materials and properties similar to that of production parts.

The RapidTool process is a method to fabricate near net shape injection molding inserts using a combination of SLS and traditional powder metallurgy techniques. With the RapidTool process, the user can produce prototype plastic parts in the material of choice with the characteristics of injection molded parts.

OVERVIEW OF RAPIDTOOL PROCESS

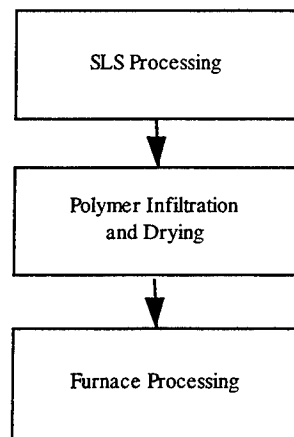


Figure 1: Process flow diagram for RapidTool process

The various steps in the RapidTool process are shown in Figure 1. First, polymer coated steel powder is processed in a SLS machine (Sinterstation™ 2000). The porous parts (commonly referred to as “green” parts) produced in the SLS equipment are then infiltrated with an aqueous emulsion of a polymer and a hardener and dried. The parts are then processed in a furnace to remove the organic binder and impregnate the voids with copper.

SLS PROCESS

The strength of the green parts, an indication of the handling durability in the green stage, is an important characteristic when choosing the material system and the SLS process conditions. The green strength of the parts depends on the extent of polymer to polymer bonding as reflected in the size of the polymer bonds between the iron particles (Figure 2). Green strength increases with an increase in either the total laser energy delivered to the powder (defined in equation 1) or the binder level in the feed material [5]. However, there are practical limitations to both variables. Excessive laser energy causes a reduction in strength due to thermal degradation of the binder. In addition, as the binder level in the feed material increases, shrinkage during furnace processing increases. Therefore, it is preferable to minimize binder content in the feed material.

$$\text{Laser energy (J/sq. cm)} = \frac{\text{Laser power (W)}}{\text{Scan speed (cm/s)} * \text{scan spacing (cm)}} \quad \text{----- (1)}$$

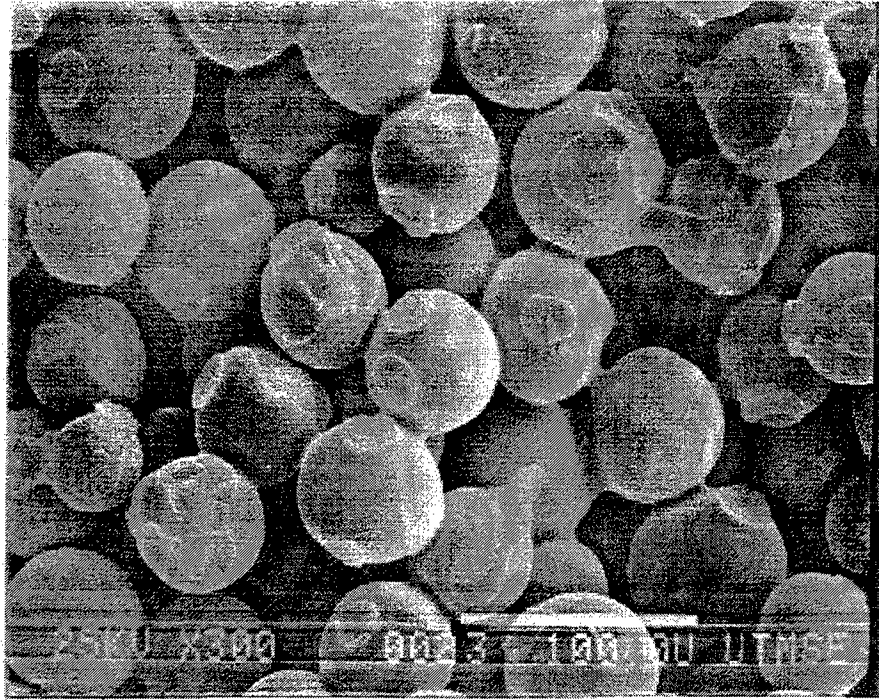


Figure 2: Fracture surface of green part showing the polymer necks between the iron particles.

The second important attribute of a green part is its density. A high green density is desirable since shrinkage and distortion during the furnace cycle increase with decreasing part density. Although it is possible to compensate for the shrinkage in the SLS process, it is still desirable to minimize distortion by maximizing density. The green density of the parts depends on the packing efficiency of the material in the powder bed. Since there is no pressure or vibration applied during the SLS process, the packing density of the powder in the bed is typically between its apparent density and the tap density values. Packing efficiency depends on a number of factors including particle size, particle size distribution and particle shape [6]. Interparticle friction and agglomeration cause finer particles to pack less efficiently than coarser particles. Similarly, irregular particles do not pack as efficiently as spherical particles. Hence, large spherical particles are preferable to fine irregular particles for efficient packing. However, the particle size sets a lower limit on the layer thickness during the SLS process.

The feed material for the selective laser sintering process is spherical steel powder (0.8% carbon) coated with an organic binder. The binder content is 0.8% by weight. The mean particle size is 55 micron. As indicated in Table 1, the feed material has a narrow particle size distribution. The apparent and tap densities of the feed material are also shown in Table 1.

Typical SLS processing conditions are indicated in Table 2. These SLS parameters yield green parts with the highest strength while maintaining the accuracy of the green parts. The strength of the green parts (3 point bend strength standard MPIF B312) under the optimum conditions shown in Table 2 is 400 psi (2 MPa). The density of the parts in the green stage is 4.3 gms/cc.

Table 1 Particle size distribution and packing densities of polymer coated steel powder.

Particle size	d10	43 microns
	d50	55 microns
	d90	65 microns
Particle shape		Spherical
Apparent packing density		4.1 gms/cc
Tap density		4.3 gms/cc

Table 2: Optimum SLS processing conditions

Processing Condition	Value
Laser power	30 W
Scan speed	155 cm/s
Distance between scans	50 - 100 microns (0.002' - 0.004")
Layer thickness	125 - 250 microns (0.005" - 0.010")
Part bed temperature	Room temperature
Feed bed temperature	Room temperature

After SLS processing, excess powder next to the parts is brushed away using fine brushes and compressed air. Since, there is no significant change in the properties of the excess powder in the build volume, it can be reused for subsequent builds.

The green parts are infiltrated with an aqueous emulsion of a polymer and a hardener. Infiltration occurs by capillary action when the parts are placed in the emulsion. After infiltration, the parts are dried in a convection oven at 50°C. After drying, the polymer and hardener react to form a crosslinked material.

If the parts from the SLS machine are processed in a furnace, without the polymer infiltration step, they would exhibit shrinkage in the direction of gravity due to a "creep-like" phenomenon. Above the glass transition point of the binder, the polymer coating on the metal powder softens allowing the metal particles to slide past each other. The amount of settling in the direction of gravity depends on the height of the features. As Figure 3 indicates, the uninfiltrated parts exhibit linear shrinkage varying from about 1.5% to 4.5% as the feature height varies from 0.5" (1.25 cm) to 2.0" (5.0 cm). Variable shrinkages cannot be easily compensated by scaling the dimensions of the computer model used in the SLS process. In contrast, the crosslinked material in the polymer infiltrated parts does not soften during the furnace cycle. Hence, they exhibit a uniform linear shrinkage of 2.5% and computer model can be scaled to compensate for it.

FURNACE PROCESSING

After the polymer infiltration and drying stage, the parts are subjected to a thermal cycle in a retort type furnace. The various stages of the furnace cycle are shown in a time - temperature plot (Figure 4). Between 350°C and 450°C, the organic binder is removed from the parts by thermal decomposition. The porous nature of the parts helps in the easy removal of the binder without any defects such as blisters or cracks. At temperatures above 750°C, the steel particles sinter to develop a porous skeleton. The steel skeleton has to be strong enough to withstand capillary

forces during the copper infiltration stage. Therefore, sintering is done at 1000°C for 8 hours. After sintering, the furnace temperature is increased to 1120°C. At this temperature, the copper melts and infiltrates the part. Since liquid copper has excellent wetting characteristics with respect to iron surfaces (contact angle = 0°) [7], infiltration occurs by capillary forces and no external pressures are required. A reducing atmosphere (70% nitrogen - 30% hydrogen) is maintained inside the furnace to ensure reduction of iron oxides on the powder prior to copper infiltration.

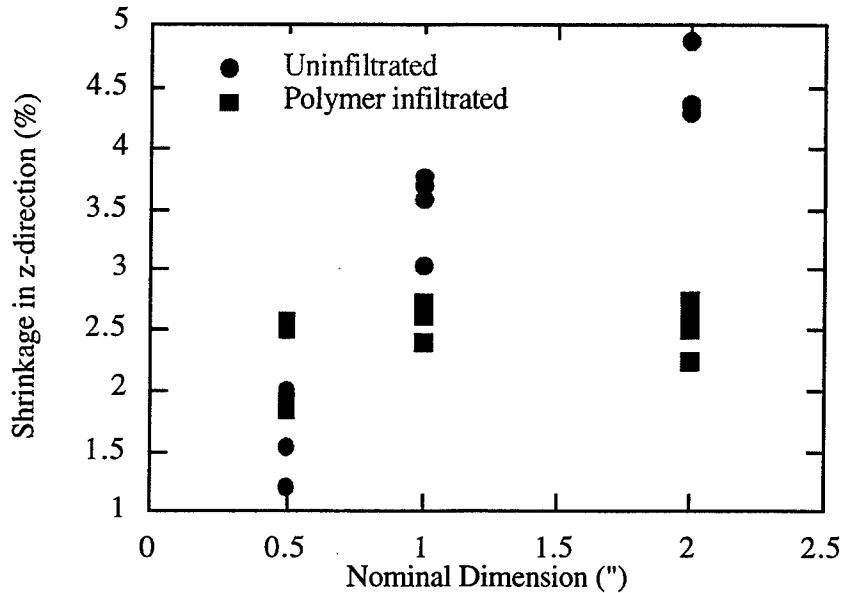


Figure 3: Vertical shrinkage of features with varying masses

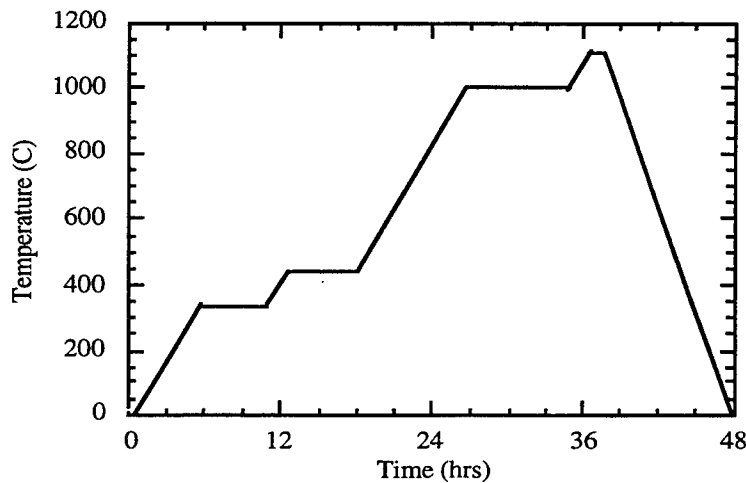


Figure 4: Time - temperature plot for the furnace treatment of green metal parts.

Parts are arranged in a graphite crucible as shown in Figure 5 and then placed inside the furnace. Inside the crucible, the parts are laid on an flat alumina plate. The alumina plate acts as a barrier for the diffusion of carbon from the crucible into the parts. In addition, the ceramic plate minimizes distortion in the parts by supporting them during the furnace cycle.

Infiltrant grade copper pressed into pellets is used for infiltration. The copper infiltrant contains about 2 percent by weight iron which prevents part erosion due to dissolution of the iron matrix in liquid copper. The copper pellets are placed on a graphite incline about 0.25" (6.4 mm) in front of the parts. When the copper melts, it flows towards the parts due to gravity and ensures part-to-part consistency in infiltration. It has been determined that consistent infiltration efficiency improves the dimensional accuracy of the final parts.

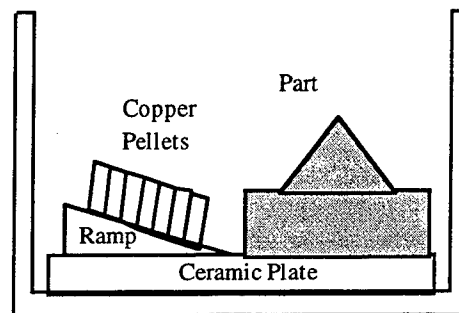


Figure 5: Arrangement of part in a graphite crucible prior to the furnace cycle.

Table 3: Mechanical and Thermal Properties of steel-copper composite material.

Property	Test Standard	RapidTool Material	Al 7075 T6	P20 steel
Yield Stress (0.2%elongation)	ASTM E8	255	505	750
Tensile Strength (MPa)	ASTM E8	475	570	950
Elongation (%)	ASTM E8	15	11	20
Elastic Modulus (GPa)	ASTM E8	210	72	207
Hardness (HRB)	ASTM E18	75	81	180 - 210
Thermal Expn. Coeff (mm/m°C)	ASTM E831	14.4	23.6	1.7
Thermal Cond. (w/mK)	ASTM E831	91	130	29

The parts exhibit a shrinkage of 2.5% in the horizontal direction and 4.0% in the vertical direction. The shrinkage of the parts during the furnace cycle is anisotropic due to settling of the material after debinding.

The mechanical and thermal properties of the steel-copper composite system made by SLS is compared against that of other common prototype mold materials such as Al 7075-T6 and P20 steel (Table 3).

RAPIDTOOL APPLICATION PERFORMANCE

The surface finish (Ra) of RapidTool inserts after the furnace process is 10 microns. While this surface finish is adequate under certain circumstances, in most cases a better surface finish is desired. Conventional mold finishing techniques such as grinding, polishing and electrical discharge machining (EDM) can improve the surface roughness to 0.6 micron Ra.

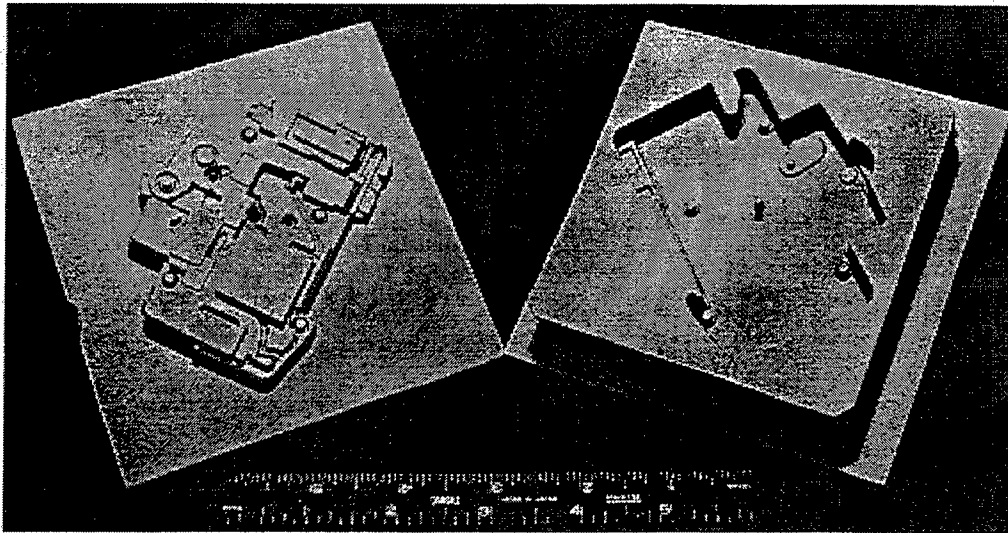


Figure 6: Steel-copper core and cavity inserts produced by the RapidTool process.

Table 4: Cost comparison for core and cavity inserts shown in Figure 6 produced by RapidTool process and by conventional processes

Item	RapidTool Process	Conventional Process
Material Cost (\$)	419	80
Processing Cost (\$)	1,331	
Finishing Cost (\$)	5,175	28,125
Total Cost (\$)	6,925	28,205
Total Time (hrs)	202	625

Total processing time for a core and cavity insert set, each measuring 6"x6"x1.5", is about 100 hours. The time estimate includes SLS processing and furnace processing but does not include any mold finishing time. Mold finishing time depends on the complexity of the mold and the skill of the mold maker. An economic analysis comparing the processing costs for the parts shown Figure 6 is shown in Table 4. The finishing costs for the RapidTool inserts and the costs for fabricating a set by conventional processes was quoted by a external vendor. It can be seen that

although the raw material for the RapidTool process costs more than that of conventional processes, the total costs for the RapidTool process is lower compared to conventional processes.

RAPIDTOOL MATERIAL AND PROCESS ENHANCEMENTS

Several enhancements to the RapidTool process are being investigated. As described in the previous sections, the polymer infiltration and drying steps are designed to minimize gravity induced creep during the furnace cycle. Changes to the steel powder morphology and binder chemistries are being examined to eliminate the polymer infiltration step completely resulting in a reduction in processing time and an improvement in part accuracy.

An alternate method to fabricate molds for plastic injection molding is being investigated. In this method, porous core and cavity inserts would be fabricated by SLS using a polymer / metal feed material. However, the green parts will not be infiltrated with copper as in the RapidTool process. Instead, the green parts will be infiltrated with a crosslinkable liquid epoxy and cured. It is expected that these steel/epoxy mold inserts can be processed faster compared to the RapidTool process since no furnace processing is required. However, these inserts will be less durable than the steel / copper molds produced by the RapidTool process.

SUMMARY

The RapidTool process is a method to make near net shape parts using a combination of SLS and conventional powder metallurgy techniques. The primary application for the steel copper composite material produced by this process is in the fabrication of prototype molds for plastic injection molding. Mechanical and thermal properties of the steel-copper composite is similar to that of aluminum 7075 used in conventional mold making process. Total SLS and furnace processing time for a core and cavity insert set is about 100 hours. Fabricating molds via the RapidTool process can result in significant time and cost saving when compared to traditional mold making methods.

REFERENCES

1. P.F.Jacobs, *Rapid Prototyping and Manufacturing: Fundamentals of Stereolithography*, Society of Manufacturing Engineers, Dearborn, MI 1992.
2. P.Forderhase and R.Corden, "SLS Prototypes from Nylon", *Solid Freeform Fabrication Symposium Proceedings*, University of Texas, TX, 1994, p 102-109.
3. K.McAlea, "SLS Technology Advances", *Proceedings of the Rapid Prototyping and Manufacturing Conference*, Dearborn MI, 1996
4. J.W.Combs, W.R.Priedman, P.W.Turley, "FDM® Technology Process Improvements", *Solid Freeform Fabrication Symposium Proceedings*, University of Texas, TX, 1994, p 42-49.
5. U.Lakshminarayan and K.McAlea, "Advances in Manufacturing Metal Objects by Selective Laser Sintering (SLS™)", *Proceedings of the 1996 World Powder Metallurgy Conference*, Washington D.C., 1996.
6. R.M.German, *Particle Packing Characteristics*, Metal Powder Industries Federation, Princeton NJ 1989.
7. R.M.German, *Liquid Phase Sintering*, Plenum Press, New York, 1985.

STRUCTURAL COMPOSITES VIA LAMINATED OBJECT MANUFACTURING (LOM)

Donald A. Klosterman, Richard P. Chartoff, Brian Priore,
Nora Osborne, George Graves, Allan Lightman

Rapid Prototype Development Laboratory and
Center for Basic and Applied Polymer Research
University of Dayton
Dayton, OH 45469-0130

Sung S. Pak
Helisys, Inc.
Torrance, CA 90505

Jerry Weaver
The Jerico Company
Templeton, MA 01468

ABSTRACT

An innovative, rapid prototyping (RP) technology is being adapted for the automated manufacture of composite tools and molds. The technology is a direct extension of the Laminated Object Manufacturing (LOM) process. LOM is an established technique that is used to create solid prototypes by sequentially cutting and laminating layers of adhesive paper. With this process a full scale, geometrically complex prototype can be created directly from a CAD image in less than a day. This report provides a description of how LOM is being applied for the production of functional composite laminates, such as composite tools and molds. Several material systems have been examined, including monolithic ceramics (SiC), ceramic matrix composites (SiC/SiC), and polymer matrix composites (glass/epoxy). Realistic tools and molds are being created from these materials using the LOM process with little modification. However, post processing (ceramic densification, polymer post cure) is necessary to obtain articles with good mechanical properties. Technical solutions are being developed for maintaining geometrical accuracy during the post processing cycles. The mechanical properties and performance of the LOM-produced parts are reported herein. Overall, this technology holds great promise for lowering the cost of tooling due to the ability to create geometrically complex objects rapidly using a highly automated processing sequence.

I. INTRODUCTION

The rapid prototyping and manufacturing of monolithic ceramics, ceramic matrix composites, and polymer matrix composites is being studied by an industry/university collaborative team lead by

University of Dayton and Helisys, Inc. This technology, based on Laminated Object Manufacturing (LOM), will provide a capability for producing high performance, near-net-shape ceramic and polymer matrix composites (CMCs and PMCs, respectively). The technical objectives of the program are: 1) to produce CMC parts with structural integrity similar to CMC parts made by current techniques, 2) to develop a commercially viable machine capable of automated fabrication of these parts, and 3) to demonstrate the generic nature of the technology by making PMCs suitable for structural applications. In this report, a description will be given of the technical progress achieved to date.

II. EXPERIMENTAL DEVELOPMENT AND DISCUSSION

LOM Process

The standard LOM process is illustrated in **Figure 1**. In this study, a LOM 2030 machine in its current commercial configuration was used for all work. As described herein, certain modifications to the process were employed, such as manual feed of sheet preform materials. However, some composite parts were able to be fabricated with the normal, fully automatic process.

Production of Ceramic Articles

The rapid prototyping and manufacturing of monolithic and composite ceramics is being addressed by an industry/university collaborative team funded by the Defense Advanced Research Projects Agency and the Office of Naval Research. This technology, based on LOM, will provide a capability for producing high density, near-net-shape ceramic matrix composites. As a necessary first step in the overall program, the production of monolithic ceramic objects is being developed. To date, monolithic silicon carbide (SiC) and aluminum nitride (AlN) parts have been produced. Among several others, tooling for polymer composites is a promising application for these ceramic systems. The favorable thermal conductivity of AlN or SiC would provide a durable tool with the inherent heat transfer advantage that a metal tool has to offer, but with less thermal expansion, and at a lower cost.

Appropriate ceramic preforms were developed using a standard tape casting process. These "tapes" contain a ceramic powder at approximately 60 vol% and a polymeric binder system. Ceramic tapes were made with thicknesses of 150-175 μm and 300-325 μm , widths of 20 cm, and lengths of 1 m. A significant effort was required to obtain the proper binder formulation for effective tape lamination. Three ceramic systems have been investigated: a coarse, infiltratable SiC composition with average diameter of 30 μm ; a bimodal SiC composition with coarse and fine ($\approx 2 \mu\text{m}$) particles; and a sinterable AlN composition with average particle size near 2 μm .

Ceramic tapes were laminated to form three dimensional objects using a LOM 2030 machine at the University of Dayton. The placement of tapes was performed manually because the tapes were not long enough to form continuous rolls nor strong enough to survive the feed mechanism. Otherwise,

the building of ceramic parts was conducted with the same degree of automation as with paper parts.

"Green" is a term that refers to the state of a ceramic article prior to densification. Green objects tend to be fragile and are prone to damage. Most LOM-produced green objects are soft and easily deformed due to the flexibility of the ceramic tapes. Therefore, a partial binder burnout cycle was used to stiffen the parts in order to facilitate green state handling. This cycle involved careful heating of a part to slowly volatilize the plasticizer while leaving the polymer intact. Prior to densification, the polymer binder was removed with a higher temperature burnout cycle developed using thermogravimetric analysis data.

SiC parts were densified by two separate processes, either by using silicon infiltration or reaction bonding (reactive metal infiltration). These methods of densification result in net shape parts with little or no dimensional change. In the reaction bonding process, free silicon reacts with *in situ* carbon that has been formulated with the ceramic tape. This reaction ($\text{Si}^0 + \text{C} \rightarrow \text{SiC}$) happens immediately upon infiltration and increases the SiC content of the part without significant shrinkage. The sintering of AlN parts has not yet been addressed. However, sintering shrinkage and warpage are expected to be primary issues.

Examples of parts made on the LOM system are given in **Figure 2** and in previous reports [1, 2]. The flexural strength of the infiltrated and reaction bonded SiC parts is approximately 160 MPa at room temperature (4-point bend test). This value is expected to increase significantly with current research aimed at improving the lamination efficiency.

Helisys, the manufacturer of the LOM 2030, has developed several hardware and software changes for improved ceramic handling. These modifications will be implemented on an updated LOM machine that will be made commercially available. To facilitate more efficient laser cutting of refractive materials, a pulsed CO_2 laser with a 700 W peak power will be used. To prevent oxidation of carbides and nitrides during laser cutting, a blower that supplies a thin layer of inert gas over the cutting surface has been implemented. Since ceramic prepregs are costly, the material feed mechanism has been redesigned to minimize waste while providing full automation.

Ceramic Matrix Composites

Work is also progressing toward the ultimate goal of producing ceramic matrix composites with the LOM system. Al_2O_3 and SiC ceramic tapes containing SiC whiskers or SiC continuous fibers are being considered. The initial challenge here is tape casting. Incorporating reasonable percentages of fibers uniformly distributed in tapes presents obvious challenges. Novel approaches to this are being developed as well as alternate approaches.

One alternate, novel approach to the fabrication of SiC/SiC composites involves the layup of separate, alternating layers of monolithic ceramic tape and fiber/resin prepregs. This concept was tested by using the same SiC ceramic tapes used to make monolithic, reaction bonded SiC parts (see previous section). A separate fiber preform was developed by making prepregs of continuous SiC fibers (NicalonTM, Dow Corning) and a furfural thermosetting resin (Furcarb UP-440, QO Chemicals). The advantages of this technique are the relative ease of preparation of the preforms,

avoidance of fiber abrasion from the ceramic particles, and potential for high fiber volume fraction in the final CMC. Furfural resin was chosen because it produces a high char yield when heated to high temperatures. Therefore, the furfural serves a dual role: as a binder during the part fabrication, and as a carbon source during the reaction bonding process.

Several nine-layer CMC plates were fabricated by sequentially laminating ceramic tapes and fiber preforms by hand pressing with a warm iron (80-100 °C) for 5 seconds per layer. A copper vapor laser, subsequently described, was used to cut the preforms immediately after the lamination step. The furfural resin adhered well to the ceramic tapes. Subsequent post curing of the resin, performed by placing the final CMC plate in a heated press (175 °C, 5 psi), produced robust “green” CMCs. Traditional binder burnout was carried out in an oven, followed by pyrolysis of the furfural. Finally, reaction bonding was performed by infiltration with silicon.

CMC squares made by this technique are pictured in **Figure 3**. The initial experiments involved the determination of appropriate carbon levels in the ceramic tape and total furfural level in the fiber prepreg. After several formulation iterations, the ability to produce flat, visually attractive CMC panels with no delaminations was achieved as illustrated in **Figure 3**. This accomplishment demonstrated the basic feasibility of this CMC fabrication approach. However, the mechanical properties of these panels were low (flexural strength = 50 MPa, 25 °C, 4-point bend) due to significant porosity. Future work will increase the integrity of LOM CMCs by all of the following strategies: 1) minimize porosity with the use of a more appropriate cure cycle for the furfural resin (in this study not enough time was allowed for debulking of water and solvents from the prepreg, which accounts for most the porosity observed in the samples), 2) incorporate a necessary fiber interface through fiber coatings, and 3) minimize fiber degradation with lower infiltration temperature and/or SiC fibers with lower free oxygen content (e.g. “high Nicalon” or “stoichiometric” silicon carbide).

A second challenge in LOM processing of advanced fiber prepregs is cutting the fibers. CO₂ lasers cannot cut continuous fibers effectively due to severe burn damage near the cut region. The laser cutting of fiber prepregs is being investigated with a 20W, pulsed copper vapor laser that delivers 2.7 mJ per pulse at a repetition rate of 8000 Hz. The laser can be focused to a spot size of around 80 μm and is quite effective in “cleanly” cutting SiC fibers, as illustrated in **Figure 4**. The cutting mechanism involves photoablative erosion rather than pyrolysis.

Production of Polymer Composites

The feasibility of adapting the LOM process for the rapid prototyping and fabrication of polymer composite parts has been demonstrated. It was found that arbitrary, complex shaped parts can be made from a range of composite prepregs with an ease and versatility similar to the original LOM paper material. However, due to the transient temperature and pressure application associated with the LOM process, a secondary, post processing step is required for final part consolidation and cure advancement. Without the post cure, the functionality of LOM composite parts is severely reduced and the parts are not suitable for the targeted tooling applications. Currently, technical solutions are being developed for maintaining geometrical accuracy during the post processing cycles.

The performance of two composite prepreg systems has been evaluated in the LOM process. Both are epoxy/glass fiber systems. The first material was specifically designed for the LOM process to duplicate the handling characteristics of paper; it required no modifications to the current LOM machine or build sequence. The prepreg was comprised of a non-woven glass fiber mat coated on the bottom side with a layer of highly B-staged epoxy resin. This prepreg was supplied on nine inch wide rolls. Because the prepreg was primarily designed to process as similar to the LOM paper as possible, the measured properties of composites made from this material were not good. Due to the one-sided distribution of highly B-staged resin, LOM processing resulted in a layered structure with alternating resin rich areas and layers of unimpregnated fibers (see **Figure 5**). Since the resin did not flow significantly during processing, consolidation was poor. Additionally, fully cured parts were dimensionally stable only at temperatures up to 110⁰C, as indicated by laboratory mechanical analysis results in **Figure 6**, because the fully cured matrix resin had a particularly low glass transition temperature.

Despite these findings there have been several preliminary field reports noting the adequacy of this prepreg for producing prototype injection molds. For example, a user at one beta test site was able to inject a total of 40 shots using polypropylene, acetal, glass filled acetal, neoprene, and nylon. The prototype mold, however, had to be treated differently than traditional tool steel because of its lower thermal conductivity and use temperature. For example, the runner length had to be extended to prevent hot, molten plastic from contacting the mold prematurely. Additionally, a cycle time as long as 5 minutes was required due to long cooling times. In an attempt to increase the wear resistance and thermal transport of LOM molds, Helisys has developed a metal coating process involving hydroforming of thin copper sheets.

The second material system, a commercially available aerospace-grade prepreg, was much more promising for creating high performance, functional polymer composite parts using LOM. This prepreg consisted of unidirectional "E" glass fibers in an epoxy matrix and was supplied on twelve inch wide rolls. Some modifications to the LOM build sequence were required to process this type of material. Most notably, fully automated processing was not possible with the current LOM machine. The prepreg was a "high flow" system since the resin was minimally B-staged and evenly distributed through the prepreg thickness. Thus a release ply was required on top of the layup to prevent the prepreg from sticking to the heated roller during the lamination step. Immediately after lamination, the cycle was again interrupted to manually remove the release ply (the prepreg carrier film was used in this case). However, the improved performance of the material compensated for the additional processing steps. The reduced B-staging of the resin, compared to that of the first prepreg, resulted in a better bond between layers (see **Figure 7**) which minimized delamination. Fully cured parts exhibited a use temperature of up to 200⁰C and mechanical properties comparable to more traditionally made epoxy/glass composites (see **Figure 6** and **Table 1**, respectively). However, this material system has not yet been tested in field applications such as injection molding and autoclave tooling.

The use of an aerospace-grade composite material in the LOM process combines the best aspects of traditional polymer composite fabrication and rapid prototyping. The enhanced mechanical properties associated with polymer composites are not sacrificed to achieve the complex, freeform shapes common to rapid prototyping. But in order to further develop this promising new fabrication

method, additional improvements are needed in both the LOM process and prepreg formulation. These developments include methods for automating the layup procedure and fine-tuning the prepreg's degree of B-staging and fiber volume to facilitate processing without forfeiting material performance. Issues involving mechanical automation are being addressed currently by Helisys, Inc.

III. FUTURE COMPOSITE DEVELOPMENTS

The process development component of the program is focused on machine modifications. These include a flat tape feed mechanism, a rotating building stage for changing fiber orientation layer-by-layer, an in-situ curing/heat treating device, and a curved layer layup capability. The latter is a highly innovative, key concept for composite fabrication by the LOM process. In conventional composites, the laminate plies conform to the surface of a tool. To facilitate such lamination on the LOM, in place of the current planar layup geometry, a "curved surface" algorithm is being developed. This algorithm also will improve surface finish and allow the fiber reinforcement to remain continuous in the plane of curvature. The curved layer building concept is illustrated in **Figure 8**. Also under development are various processing methods for improving the ease of part removal from the crosshatched support material.

IV. REFERENCES

1. Klosterman, D.A., R.P. Chartoff, and S.S. Pak, "Affordable, Rapid Composite Tooling via Laminated Object Manufacturing," Proceedings of the 41st International SAMPE Symposium and Exhibition, Anaheim, CA, March 24-28, 1996, pp. 220-229.
2. Klosterman, D.A., R.P. Chartoff, N.R. Osborne, G. Graves, and A. Lightman, "Structural Ceramic Components via Laminated Object Manufacturing," Proceedings of the International Conference on Rapid Product Development, Messe Stuttgart, Germany, June 10-11, 1996, pp. 247-256.

V. ACKNOWLEDGMENTS

The work reported here was performed under a grant by DARPA/ONR, N00014-95-1-0059, with Dr. William Coblenz and Dr. Steven Fishman acting as program officers. A portion of the glass fiber/epoxy work was performed under U.S. Army Aviation and Troop Command Contract DAAJ02-95-C-0020, "Rapid Fabrication of Fully Functional Models by LOM," with Clay Ames acting as program officer.

VI. ILLUSTRATIONS

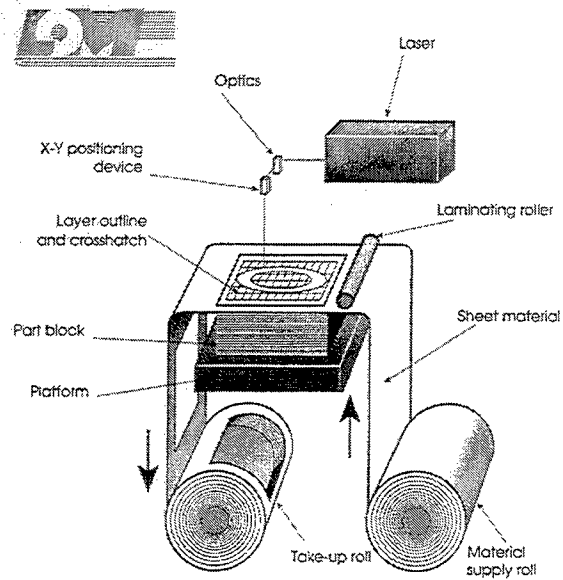


Figure 1 : Schematic of the LOM process for making paper prototypes.

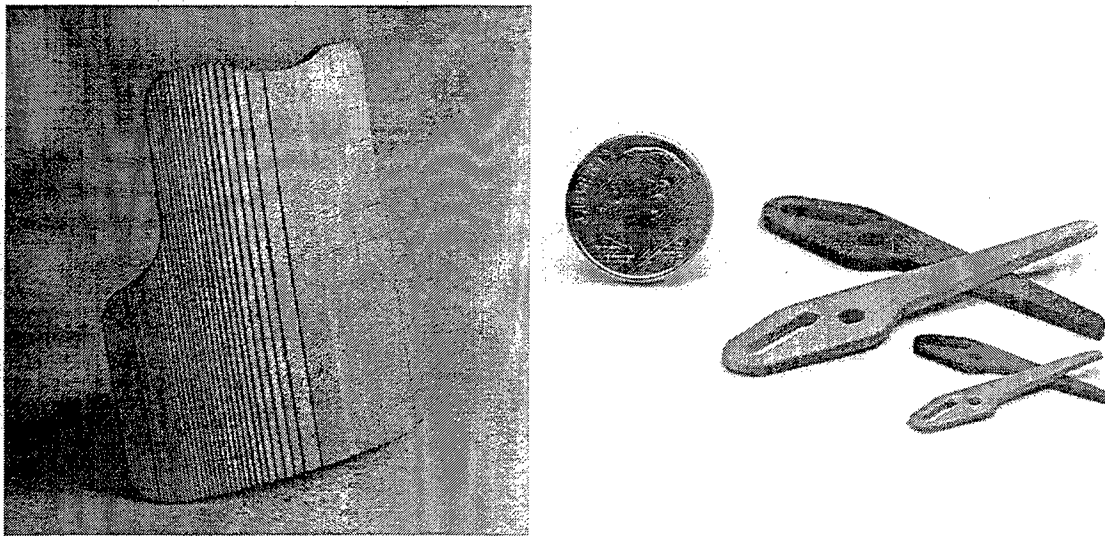


Figure 2 : (left) SiC, miniaturized body armor (7.5 cm x 7 cm x 1.6 cm) and (right) AlN and SiC laparoscopic cutters made with LOM.

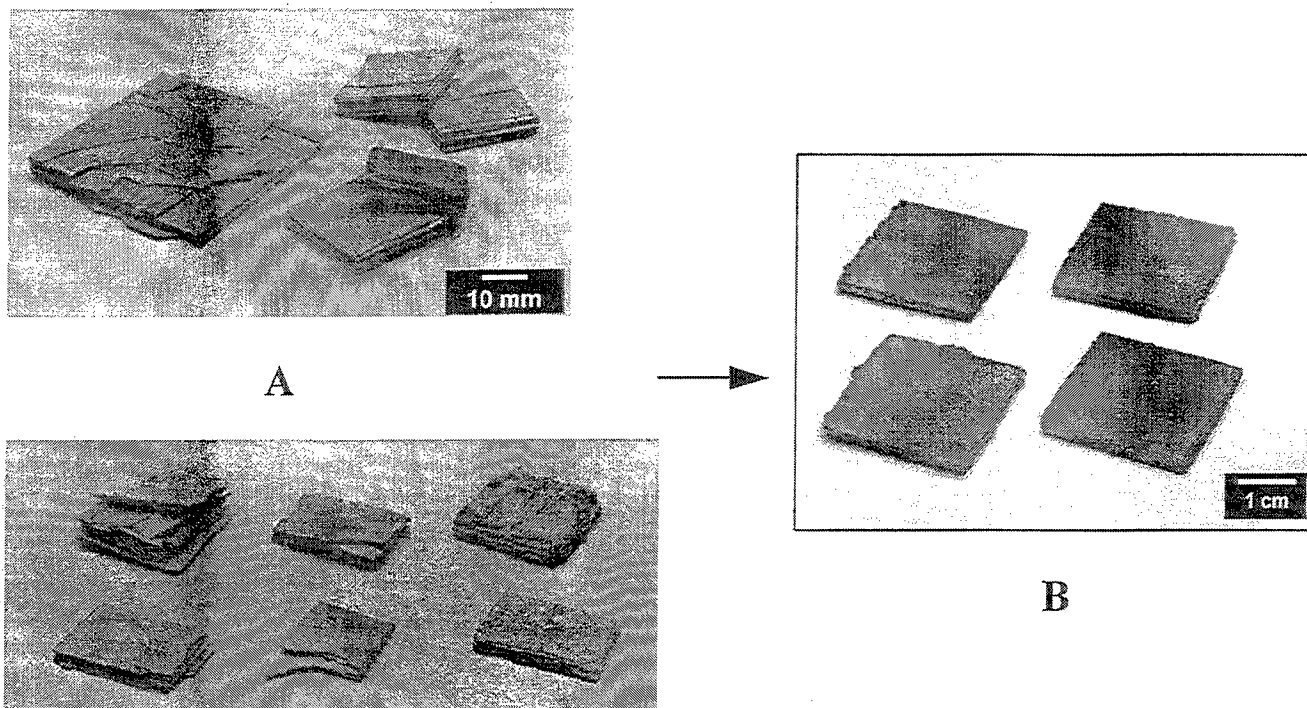


Figure 3 : CMC development has evolved from a) initial formulation screening for both ceramic tape and fiber prepreg, to b) the ability to form flat CMC plates without delamination. All samples were densified through the reaction bonding process.

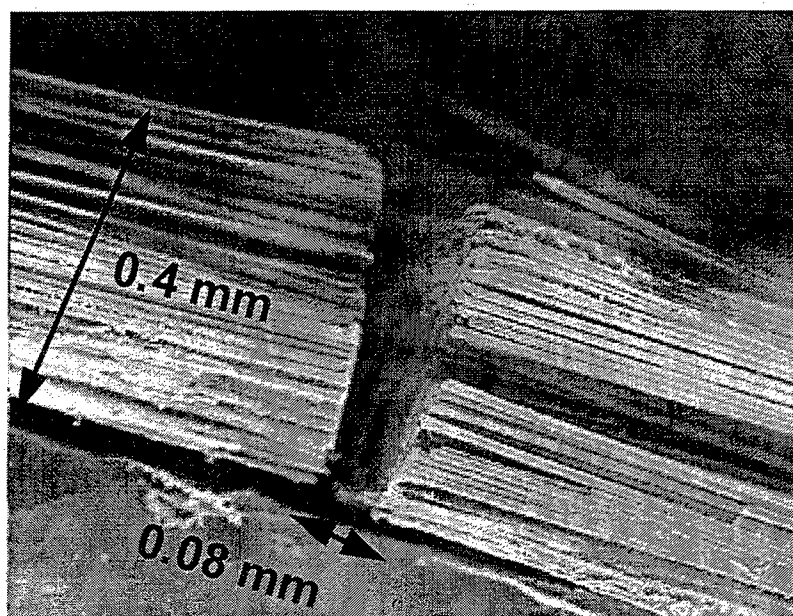


Figure 4 : Thick, SiC fiber prepreg cut with a copper vapor laser operating at 8000 pulses/sec and 2.7 mJ per pulse. Such high quality fiber cutting will be required to enable the LOM of polymer and ceramic matrix composites.

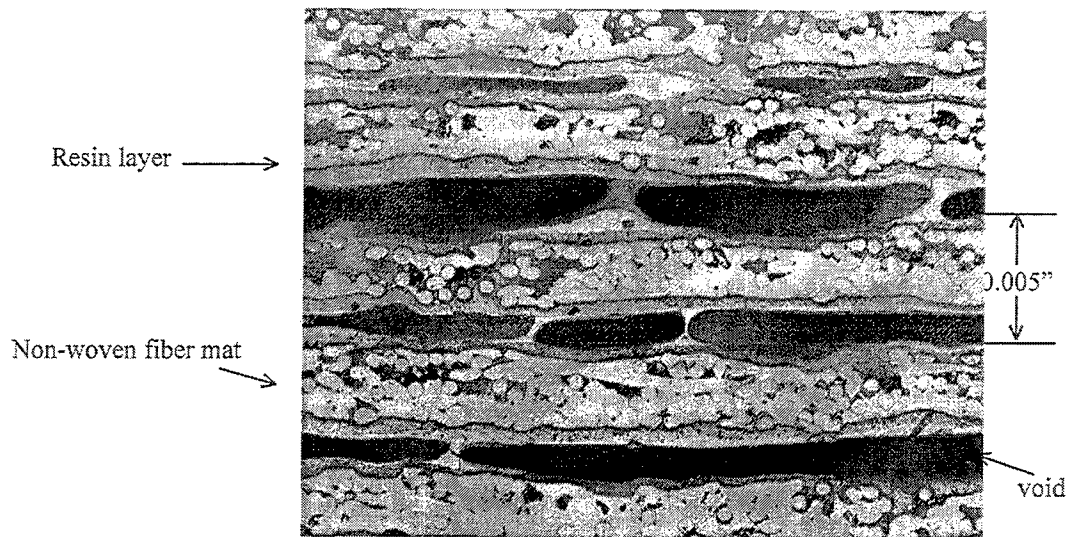


Figure 5 : Photomicrograph of a composite panel made with the LOM-designed prepreg. Note the resin's inability to penetrate into the fiber mat and the large scale voids entrapped in the resin rich layers.

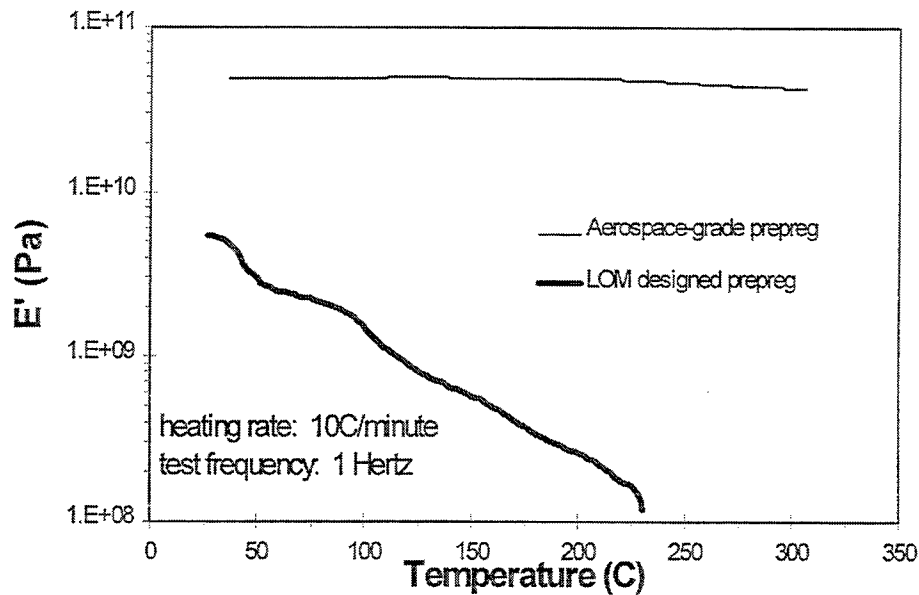


Figure 6 : Dynamic Mechanical Analysis, three point bend test method, of post cured LOM composites indicating useable temperatures for both materials.

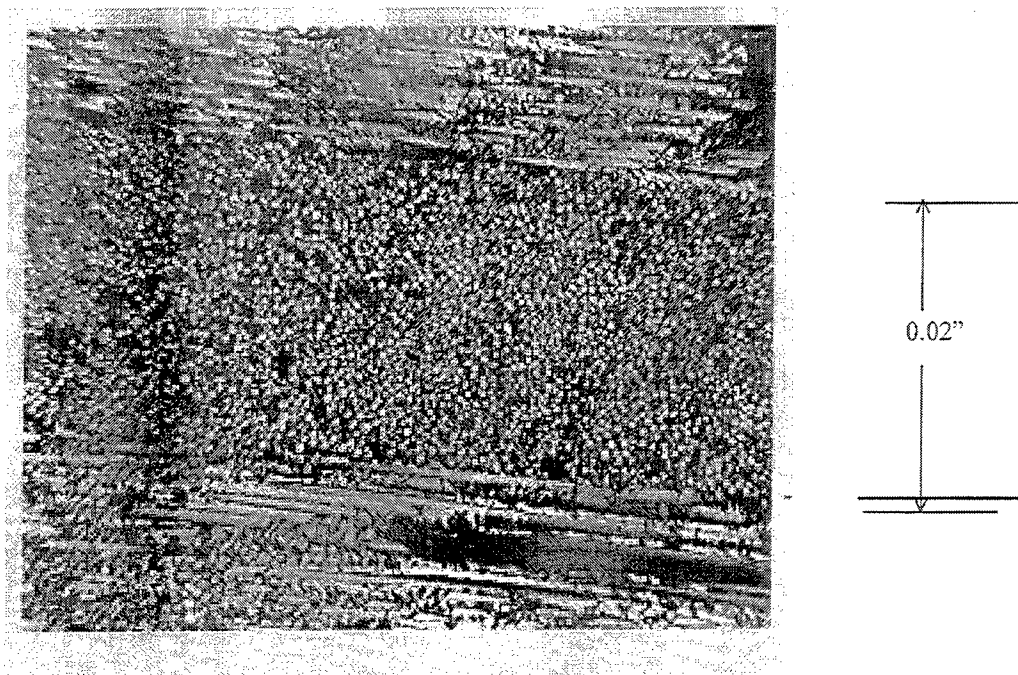
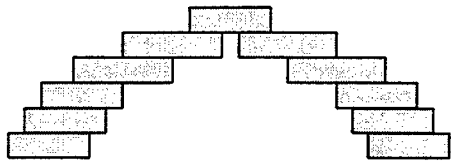


Figure 7 : Photomicrograph of a cross section of a LOM processed, aerospace-grade composite part. Shown in the field of view are four layers: $90^{\circ}/0^{\circ}/0^{\circ}/90^{\circ}$ (from top to bottom).

Table 1: Room Temperature Mechanical Properties of LOM Processed and Post Cured Aerospace-grade Composites

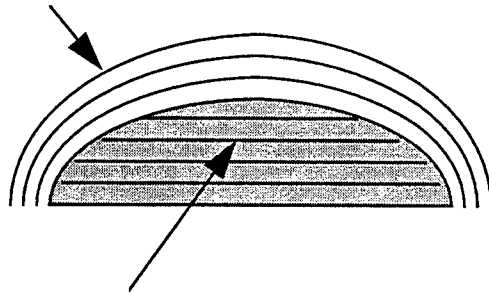
Test Method	LOM Processed Ultimate Strength (MPa)	Supplier Data Ultimate Strength (MPa)
Tension (0° orientation) ASTM-D-3039	712.9 ± 37.2	1000
Compression (0° orientation) ASTM-D-695	895.6 ± 57.9 357.1 ± 80.0 (no post cure)	792
Flexure (0° orientation) ASTM-D-790	1189.3 ± 51.0	1310
Interlaminar Shear ($0^{\circ}/90^{\circ}$ orientation) ASTM D-2344	42.6 ± 3.9	55

Original Process (flat layers only)



Curved Layer LOM

2. drape continuous sheets
of material followed by
thermoforming



1. create tool using current process

Figure 8 : Curved Layer LOM concept. Curved layer parts will be built by draping the composite preforms over a tool that has been custom prefabricated with the existing flat layer process. The draped sheets will be rolled or thermoformed into place.

Laser Deposition of Metals for Shape Deposition Manufacturing

J.R. Fessler, R. Merz, A.H Nickel and F.B. Prinz
Stanford University

L.E. Weiss
Carnegie Mellon University

Abstract

A laser/powder deposition process has been added to the Shape Deposition Manufacturing system at Stanford University. This process is more robust than previous SDM metal deposition processes, consistently producing fully dense, near-net shape deposits with excellent material properties. Material is deposited by scanning the laser across a surface while injecting metallic powders into the melt-pool at the laser focus. A number of parts have been produced with the system, including an injection molding tool, multimaterial structures and simple mechanisms. Currently research is being performed to improve the finish quality of the parts. One of the main areas of research involves controlling thermal stresses which can lead to warpage and delamination. Selective deposition techniques and the use of low coefficient of thermal expansion materials such as INVAR™ show promise for reducing deformations caused by internal stresses.

1. Shape Deposition Manufacturing

Shape Deposition Manufacturing (SDM) is a layered manufacturing technique which uses sequential steps of material deposition and removal to form three dimensional structures. (See Merz *et al.*, 1994 for a detailed description of the process.) In SDM, an off-line process planner first automatically decomposes the CAD solid model of the part into layers and three dimensional sections and generates deposition and cutting paths. Unlike most other Solid Freeform Fabrication (SFF) techniques, SDM retains a three dimensional representation of the part and creates variable layer thicknesses which are dictated by the geometry of the part. Layer boundaries are strategically inserted at heights where there are transitions between undercut and non-undercut surfaces or changes in material. As a result, layer thicknesses will range anywhere from a few thousandths of an inch to the practical limits of the deposition and shaping equipment. This adaptive layer splitting reduces build time by reducing the number of layers to the theoretical minimum, and five-axis shaping eliminates the stair-step effect found in other layered manufacturing techniques.

The individual layers are built by depositing material into a near-net shape and subsequently machining it to the final dimensions using a five-axis CNC mill. These operations are alternately performed on part material and additional sacrificial support material. The support material encases each layer, provides a platform for deposition of the next layer, and supports overhanging part geometry. This process is repeated, layer by layer, until the part is complete. After the final layer has been deposited, the support structure is removed to reveal the part in its final, fully-functional state.

Since SDM is a layered manufacturing technique, it exhibits many of the advantages of other SFF processes including the inherent simplicity of building a complex three dimensional shape using a number of simpler individual layers, and access to the interior of the part during the build process. The use of a sacrificial support structure provides other advantages including securely fixturing the part during the build and the ability to produce complex features, such as overhangs and internal cavities. The addition of CNC milling to the process results in part tolerances and surface finishes which are superior to those which would be obtained through a

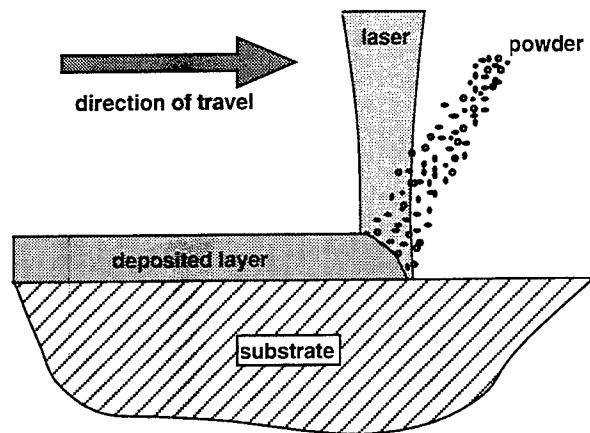


Figure 1: Schematic of laser deposition.

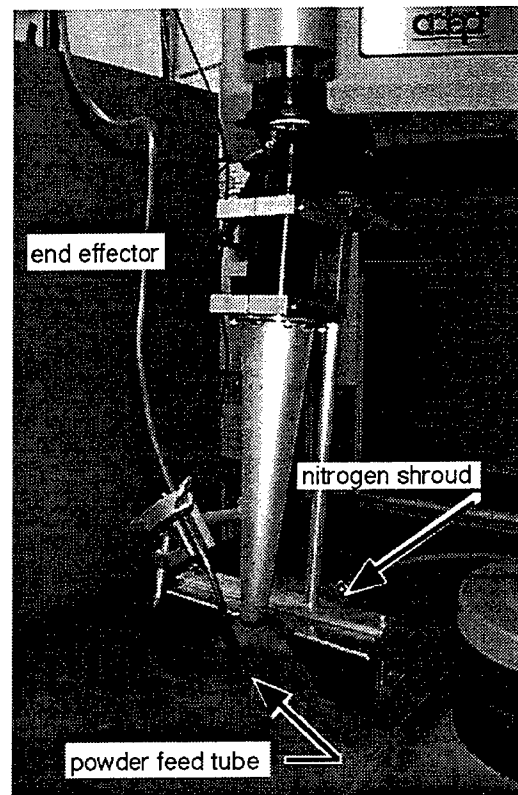


Figure 2: Laser deposition apparatus.

purely additive process. Finally, the wide range of materials available to the SDM process means that fully functional parts can be made in a single, fully automated production step. The technique is sufficiently robust that parts can be made from virtually any machinable material which can be deposited incrementally and for which a suitable support material can be found. Currently the range of materials includes a variety of metals and polymers as well as ceramics in the green state.

2. Laser Deposition System

2.1 System Description

The laser system is one of several metal deposition processes which have been incorporated into SDM. It has a number of advantages over previous SDM deposition techniques including more robust deposition, more accurate placement of the deposited material and the ability to produce functional gradient materials by simply mixing powders during deposition. The process is very similar to laser cladding or laser welding in which the laser forms a melt pool on the substrate into which metal powder is injected. The injected powder fuses onto the substrate as the laser scans over the part, leaving a bead of deposited material in its wake. (Figure 1) Because material is deposited only where the laser strikes the surface and the laser can be positioned accurately, it is easy to selectively deposit material only where necessary and reduce machining time in subsequent processing operations.

The laser is a 2.4 kW CW Nd:YAG laser which is delivered to the focusing optics through a 25 m long, 600 μm diameter fiber. The end of the fiber is equipped with an end effector which can vary the focal length from 130 to 450 mm, with corresponding changes in the focal spot diameter of 1.2 to 4.8 mm. Most artifacts presented in this paper were produced with the substrate approximately 10 mm beyond the focal point and a 2.5 mm spot size. The powders are fed into the melt pool through a simple gravity-driven, off-axis feed nozzle, and the powder feed rates are

controlled with an auger-style dry material feeder. Both the laser end effector and the powder feed nozzle are mounted to the end of a four degree of freedom robotic manipulator arm. Since the powder is added directly to the melt pool, the deposition head can move in any direction on the surface. However, the thickness of the deposit does change with direction, with the thickest deposits occurring when the robot travel is in the plane of the laser and powder delivery. The milling operations used in SDM, however, remove any excess material which may be deposited, and control the final thickness of the deposits. During deposition, the area around the laser spot is flooded with inert gas to shield the deposits from air and reduce oxidation. Typically, large flow rates of nitrogen (approx. 150 liters per minute) are used, but smaller flow rates (approx. 15 liters per minute) of Argon or Argon-Helium have also been used successfully. The choice of shield gas largely depends on the material being deposited; for example, the use of nitrogen as a shield gas during titanium deposition could result in formation of unwanted titanium nitride. Figure 2 shows a picture of the deposition apparatus mounted on the robot arm.

2.2 Material Properties

The laser system successfully deposits a range of materials including stainless steel, titanium, INVARTM, aluminum, bronze and a variety of corrosion resistant, hardfacing materials. The majority of the artifacts produced with the system, however, have been made from a material very similar in composition to a 316L series stainless steel. This material has moderate strength and hardness and excellent corrosion resistance. Corrosion resistance is important during the acid etching process which removes the copper support structure. The system reliably deposits approximately 30 g/min of fully dense material into a near net shape. The material properties of the resulting material are very similar to those for a cold worked 316L series stainless steel, as shown in Table 1. Tensile test measurements were taken in two orthogonal directions, parallel to the direction of a single line of deposition and perpendicular to the deposition lines. Visually, the tensile specimens show evidence of some anisotropy in the crystal structure upon fracture, but the material strength is essentially the same for the two directions.

	316L stainless ¹		Deposited stainless	
	annealed	cold finished	parallel	perpendicular
Hardness (Rockwell B)	76	95 max.	90	90
0.2% Yield Strength (MPa)	170	310	490	470
Tensile Strength (MPa)	450	620	630	620

Table 1: Comparison of material properties for deposited stainless steel and standard 316L stainless steel.

3. Artifacts Produced with Laser System

This section will present a few of the parts produced with the laser system including an injection molding tool, multimaterial structures and simple mechanisms. In general these were produced using the laser to deposit the part material and a "microcaster" to deposit the support structure. The microcaster is another SDM metal deposition technique which forms molten droplets above the surface of the part. These droplets then fall and bond to the part (Merz *et al.*, 1994). As a result, less energy is transmitted to the part, and less geometric distortion is observed. The laser system has been used to deposit bronze for support structures, but the laser tends to excessively remelt the substrate and distort the part geometry.

¹ Material properties for 316L stainless steel from Metals Handbook, Tenth Edition, Vol.1, ASM International, Materials Park, OH, 1990.

Figure 3 shows a photograph of an injection molding tool produced with the laser system. Each half of the tool has dimensions of approximately 152 mm by 102 mm by 32 mm and is made primarily from 316L stainless steel. One half of the tool, shown schematically in Figure 4, has four copper deposits for temperature equilibration. Both halves of the tool have a "U"-shaped channel for water cooling during the molding process. All surfaces of the mold cavity have a 1° taper to facilitate removal of the plastic part. The halves were made in three and five layers respectively, and each required approximately eight hours of automated material deposition and milling. An additional eight hours were required to etch the copper from the cooling channels using nitric acid. Portions of the cavities contained small features which could not be cut with endmills and these were finished with EDM.

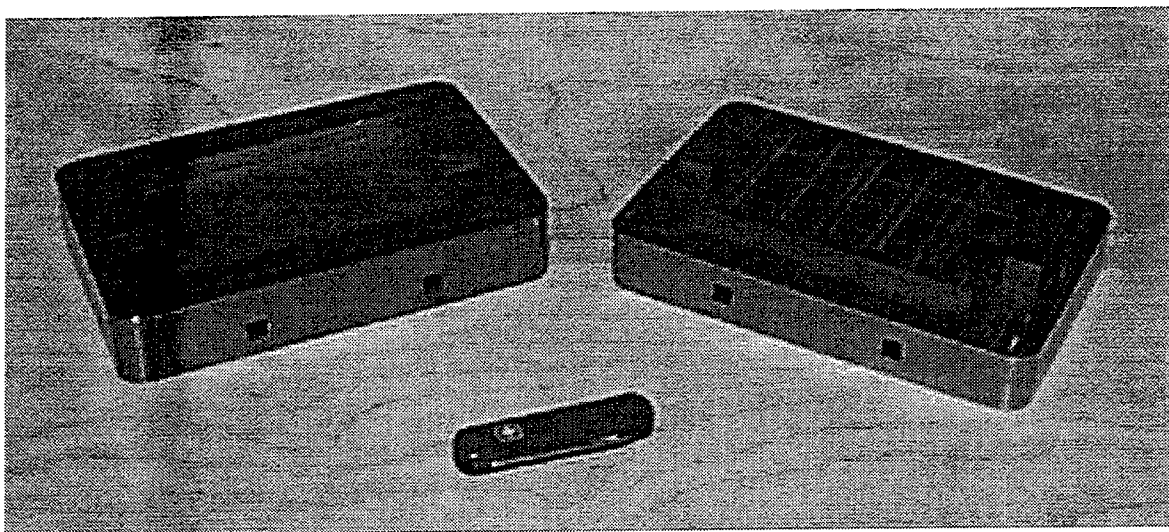


Figure 3: Photograph of injection molding tool made with laser system.

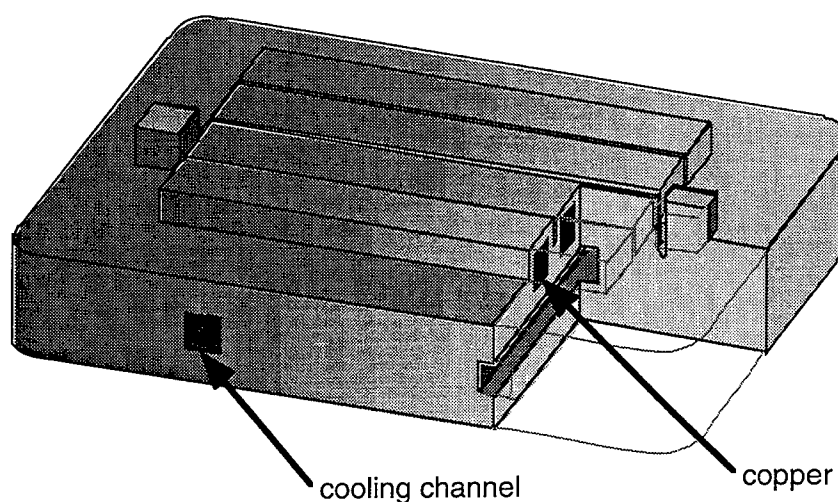


Figure 4: Schematic of half of injection molding tool with copper deposits.

As demonstrated by the copper deposits in the tool described above, SDM can create multimaterial structures. For instance, the laser system has also been used to deposit INVAR™, a low coefficient of thermal expansion (CTE) nickel alloy, onto copper which was previously deposited onto steel. Such multimaterial structures will have significant advantages in a wide variety of applications. In composite forming, for example, the steel substrate would provide a solid base for the die, the copper would serve to equilibrate temperatures and eliminate hot spots in the tool, and the low CTE metal would resist geometry changes due to thermal expansion. The laser system is particularly suitable for producing multimaterial parts because different materials can be continuously alloyed during the build process by simply mixing the powders which are fed to the melt pool.

The laser system has also been used to produce simple assemblies and mechanisms. The use of a sacrificial support structure enables the system to produce a single structure which will become multiple entities once the support structure is removed. For instance, a hollow cube has been made with a sphere trapped inside. A hole much smaller than the diameter of the sphere was drilled into the cube to allow nitric acid to etch away the copper support material and free the sphere. Other assemblies have been made, such as a wheel which spins on a hub and a disk which slides freely in a rectangular frame but cannot be removed. Finally, the system was used to create the simple mechanism shown in Figure 5. In this mechanism, a piston is connected to a crank shaft with a connecting rod. Turning the crank causes the piston to move back and forth in its chamber. This mechanism was made in 12 layers and required approximately 24 hours to fully deposit and shape. An additional 4 hours were required to etch away the support structure.

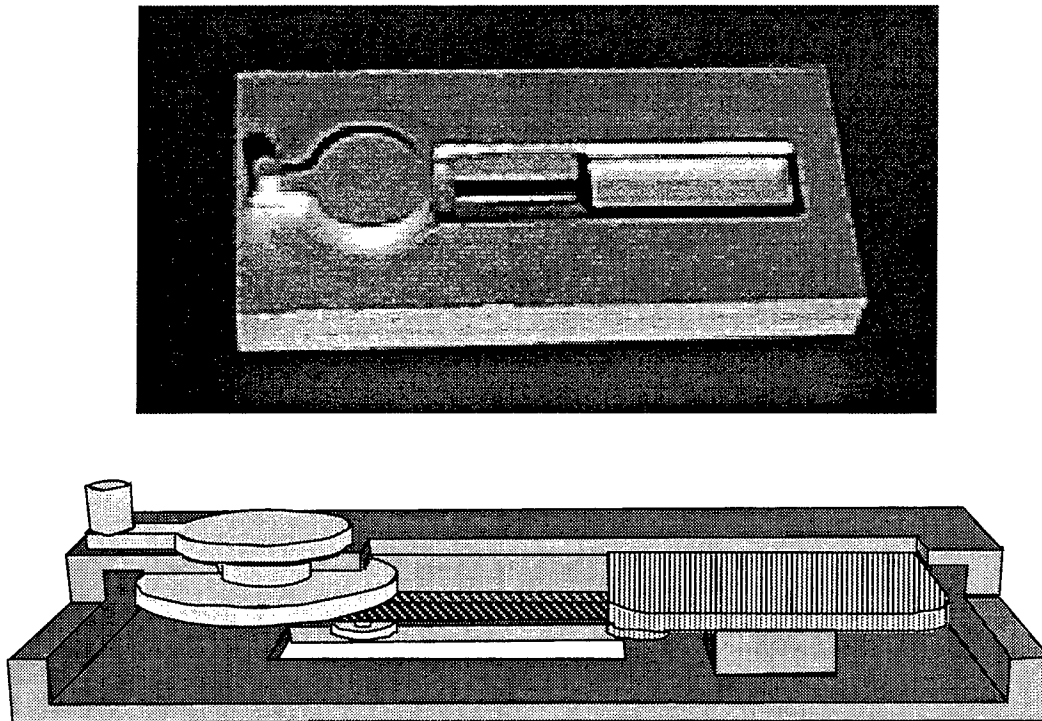


Figure 5: Crank and piston mechanism.

4. Research Issues

4.1 Thermal Stresses

Although a number of artifacts have been successfully produced with the laser system, there are a number of issues, primarily concerned with part quality, which need to be addressed. One of the most important issues which limits the quality of parts produced with SDM is the accumulation of residual thermal stresses. These stresses, which result from fusing and constraining materials of differing temperatures (see Chin *et al.* 1995), can cause warpage, delamination and surface finish defects in the final part. Two primary approaches are being investigated to minimize deformation due to thermal stresses: selective deposition and multimaterial deposition. Selective deposition can reduce deformation of the final part by allowing much of the deformation produced during cooling to occur before the deposit is fully constrained. In this approach the surface area of the deposits is significantly increased by depositing a series of small patches which are later joined together to form large patches of material. These "towers" are only constrained on the bottom and their large surface area to volume ratio allows them to relax significantly as they cool. The individual patches are then "stitched" together to form the solid block. In the second approach, a material such as INVAR™, which has a very low coefficient of thermal expansion (CTE), is used to fill much of the solid center of a part while the outside surface of the part is tailored to the application of interest. For instance, the primarily INVAR™ part may be coated with a thin layer of either wear resistant or corrosion resistant material. The SDM process is suitably robust that multimaterial and selective deposition techniques such as these can be implemented. It should be noted that at high temperatures INVAR™ shows similar thermal expansion characteristics to stainless steel, but at high temperatures the yield strength of both materials is very low. Thus, much of the shrinkage at high temperatures will result in plastic deformation and minimal build-up of internal stresses. At lower temperatures, however, the yield strengths of the materials rise and they build-up internal stresses in accordance with their shrinkage. In this regime, where the stresses accumulate, INVAR™ has a near zero CTE, which results in much lower residual stress levels.

To test the feasibility of these techniques, a series of rectangular beams were produced to measure the relative deflections produced by deposition. In each of the tests, a single layer of material was deposited onto constrained steel substrates. The substrates were 150 mm long, 25 mm wide and 9.5 mm thick low carbon steel flat ground stock. The deposits were milled to a uniform size of 15 mm by 100 mm by 3 mm, and the deflections of the bottom surface were measured. Two deposition techniques, standard and tower, and two materials, stainless steel and INVAR™, were used for this test. The standard deposition technique is a simple continuous scan of the laser across the surface. For the tower technique, individual towers 15 mm long, 4 mm wide and 3 mm tall are built spaced 7.5 mm apart. After the towers cool, material is deposited in the spaces between them to create a solid beam, see Figure 6.

Figure 7 shows the measured deflections of the bottom surface of the steel substrate for several cases. The results show that the deformation of simple beams due to internal stresses can be significantly reduced through both selective deposition and the use of a low CTE material such as INVAR™. The use of INVAR™ reduced the deflections by a factor of 2 as compared to stainless steel. Using the tower deposition technique reduced the deflections by a factor of three. A combination of both INVAR™ and the tower technique reduced the deflections by a factor of 10 over the standard technique with stainless steel. These experiments need to be extended to larger two-dimensional patches and other geometry to see if similar results are obtained.

4.2 Other Research Issues

Aside from thermal stresses, other issues need to be resolved to assure the fabrication of very high quality parts with the laser system. One of the primary issues involves the interactions

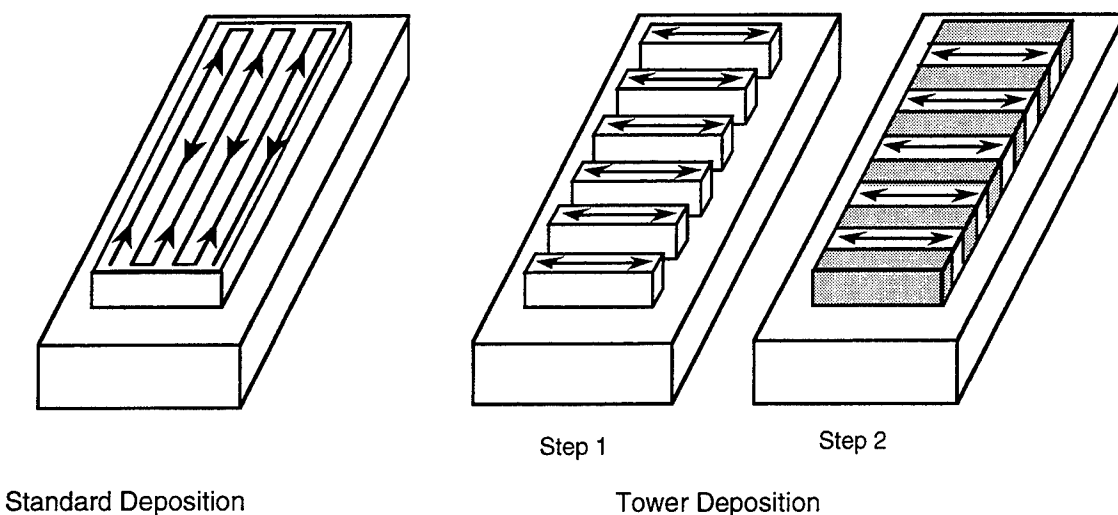


Figure 6: Schematic of two deposition techniques.

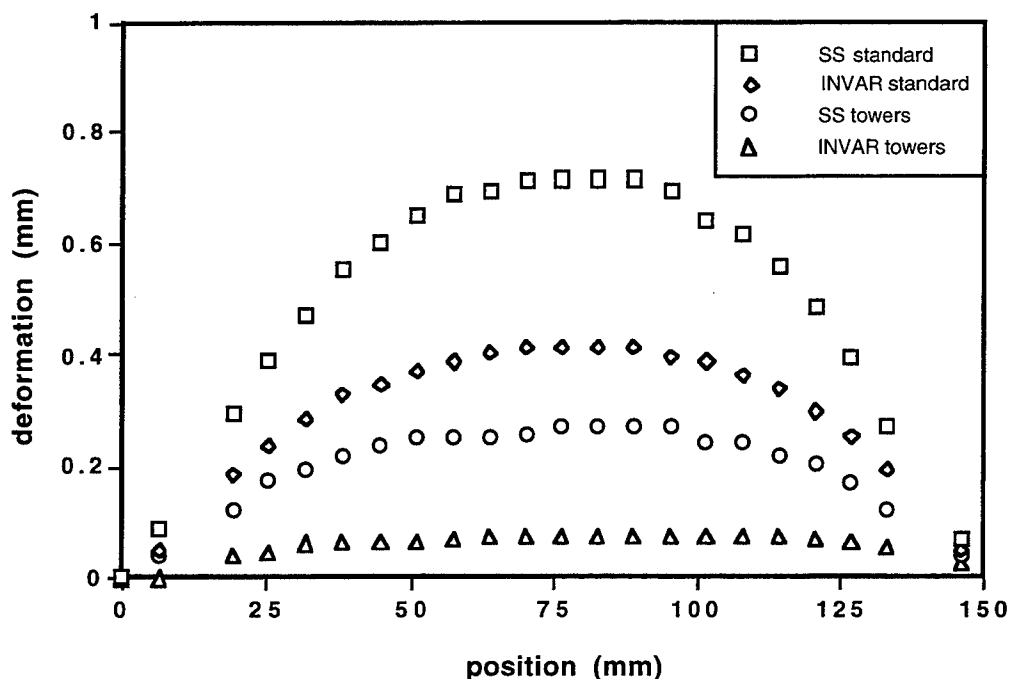


Figure 7: Comparison of standard and selective deposition techniques using stainless steel (SS) and low CTE metal (INVAR)

between the part material and the support material. In SDM one must be able to deposit part and support materials onto one another without destroying the geometry of the underlying material. With the laser system this is not always an easy task because the process requires remelting of the substrate to ensure bonding. Unfortunately this means that if the laser beam hits a sharp corner it will melt the material, and the corner will be rounded as a result. Currently, techniques are under investigation which will coat the support material with a buffer layer which could be melted by the laser without destroying the geometry of the part underneath. Such a buffer layer will be deposited with an alternate technique such as microcasting or thermal spraying which does not substantially remelt the substrate. Such a technique would significantly improve the surface finish of part material which has been deposited directly onto support material.

Another area which has yet to be explored is the possibility of creating functional gradient materials through powder mixing during deposition. A single deposited layer could easily have continuously varying material properties such as hardness or corrosion resistance. This would lead to parts with tough cores and hard surfaces without distinct interfaces between the two materials. Coefficients of thermal expansion could also be selectively chosen to reduce stresses during deposition or control expansion during use.

5. Conclusions

A laser/powder metal deposition process has been incorporated into the SDM system. In principle this technique is a laser cladding process with the goal to build three dimensional structures rather than coat a surface. A variety of metals including stainless steel, bronze, titanium, aluminum and INVAR™ can be deposited in near net shape and then shaped using a five-axis CNC mill. In the process, a melt pool is created on the surface of a part by a 2.4 kW Nd:YAG laser which is delivered fiber optically to the work piece. Powder is added to the pool through a gravity-driven off-axis powder feed system. With the current deposition parameters the system can deposit approximately 30 g of fully dense metal per minute. Testing of the most commonly deposited metal, a 316L stainless steel, shows that the material properties of the deposited metal are similar to those for the bulk material in a cold-formed state. Some anisotropy in the crystal structure has been observed corresponding to the direction of deposition, but this anisotropy does not appear to affect the material strength.

A number of artifacts have been produced using the laser to deposit the part material. These parts illustrate the capability of the system to produce injection molding tools, multimaterial structures and even simple mechanisms. There are still several issues regarding part quality which must be addressed. The first is thermal stresses which accumulate as the part cools and can lead to warpage or delamination. To address this issue, a study is being performed to evaluate the effectiveness of selective deposition patterns and low CTE metals for controlling internal stresses. Preliminary results from beam studies indicate that significant reductions in warpage can be achieved through allowing the material to cool before it is completely constrained and using a low CTE metal such as INVAR™. A combination of the two techniques showed warpage reduction of 90% over the standard case but did increase deposition complexity. The second issue regards the interactions between part material and support material. Good bonding of the deposited layer can only be achieved if the substrate is remelted. This remelting, however, can result in rough surfaces once the support material has been removed. Techniques for nondestructively coating the support material with a buffer layer of the part material are being investigated. Substrate remelting by the laser would be confined to this buffer layer, and the geometry of the support material underneath would be preserved. Continued research in these two areas should lead to substantially improved part quality.

Acknowledgements

The authors gratefully acknowledge the Defense Advance Research Projects Agency (#F33615-94-C-4450 and #F33615-95-C-5560) and the Office of Naval Research (#N00014-96-1-0354) for their support of this research.

References

- Chin, R.K., Beuth, J.L. and Amon, C.H. (1995) "Control of Residual Stresses in Shape Deposition Manufacturing," Proceedings Solid Freeform Fabrication Symposium, The University of Texas at Austin, pp. 221-228.
- Merz, R., Prinz, F.B., Ramaswami, K., Terk, M., and Weiss, L.E. (1994) "Shape Deposition Manufacturing," Proceedings Solid Freeform Fabrication Symposium, The University of Texas at Austin, pp. 1-8.

FREE FORM FABRICATION OF METALLIC COMPONENTS USING LASER ENGINEERED NET SHAPING (LENSTM)

M. L. Griffith, D. M. Keicher, C. L. Atwood,
J. A. Romero, J. E. Smugeresky*, L. D. Harwell, D. L. Greene

Sandia National Laboratories
Albuquerque, NM 87185, *Livermore, CA 94551

INTRODUCTION

Solid free form fabrication is one of the fastest growing automated manufacturing technologies that has significantly impacted the length of time between initial concept and actual part fabrication^{1 2}. Starting with CAD renditions of new components, several techniques such as stereolithography³ and selective laser sintering⁴ are being used to fabricate highly accurate complex three-dimensional concept models using polymeric materials. Coupled with investment casting techniques, sacrificial polymeric objects are used to minimize costs and time to fabricate tooling used to make complex metal castings⁵.

This paper will describe recent developments in a new technology, known as LENSTM (Laser Engineered Net Shaping)^{6 7 8 9}, to fabricate metal components *directly* from CAD solid models and thus further reduce the lead times for metal part fabrication. In a manner analogous to stereolithography or selective sintering, the LENSTM process builds metal parts line by line and layer by layer. Metal particles are injected into a laser beam, where they are melted and deposited onto a substrate as a miniature weld pool. The trace of the laser beam on the substrate is driven by the definition of CAD models until the desired net-shaped densified metal component is produced.

EXPERIMENTAL

The system consists of a Nd:YAG laser, a controlled atmosphere glovebox, a 3-axis computer controlled positioning system, and a powder feed unit. The positioning stages are mounted inside a controlled atmosphere glove box, backfilled with argon, operating at a nominal oxygen level of 2-3 parts per million. The beam is brought into the glovebox through a window mounted on the top of the glovebox and directed to the deposition region using a six inch focal length plano-convex lens. The powder delivery nozzle is designed to inject the powder stream directly into the focused laser beam and the lens and powder nozzle move as an integral unit.

A CAD solid model is sliced into a sequence of layers, and translated into a series of tool path patterns to build each layer. Each layer is fabricated by first generating an outline of the key component features and then filling the cross-section using a rastering technique. This file is used to drive the laser system to produce the desired component one layer at a time, starting from the bottom of the part. A schematical representation of the LENSTM fabrication process is shown in Figure 1. A solid substrate is used as a base for building the LENSTM object. The laser beam is focused onto the substrate to create a weld pool in which powder particles are simultaneously injected to build up each layer. The substrate is moved beneath the laser beam to deposit a thin cross section, thereby creating the desired geometry for each layer. After deposition of each layer, the powder delivery nozzle and focusing lens assembly is incremented in the positive Z-direction, building a three dimensional component layer additively. To insure that a uniform deposition was achieved for each layer independent of direction, a specialized powder delivery nozzle and powder feeder have been developed⁹.

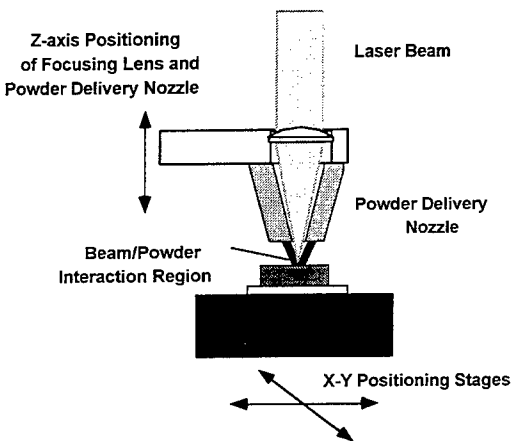


Figure 1: Schematic of the LENS process.

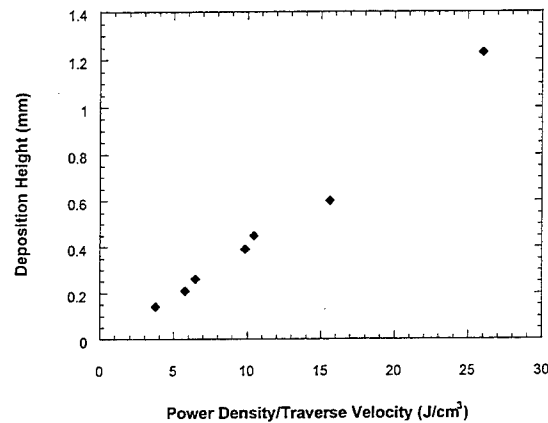


Figure 2: Build height as a function of the volumetric exposure.

RESULTS

A. Laser/Powder Interactions

(i) Process Parameters

Our initial research was to demonstrate the role of the processing parameters for thin walled geometries. Statistically designed experiments were done using Inconel 625 to identify significant process variables and to begin to understand the deposition process⁶. The process variables considered were: component velocity, laser irradiance, Z-axis increment, and powder volumetric flow rate. The response variables used in evaluating the experimental results were: the material build-up height, the melt depth into the previous layer, and the ratio of these two variables. The tests were performed by depositing ten layers of metal in a single wall for each of the experimental conditions, where the material was deposited in only one direction of travel. Metallographic analysis was used to measure the response variables and to evaluate the experiment results. Analysis of this data for the Ni-based super alloy 625 has shown that there is a linear relationship between the layer build-up height and total volumetric exposure. The

volumetric exposure is the ratio of the laser irradiance to the component travel speed. A graph of these experimental results is shown in Figure 2.

Complete melting of the powder occurred for all tests. In addition, textured growth of the deposited material occurred across the deposition layer boundary in nearly all cases for thin-walled parts. The build up height was measured from the original surface to the top of the deposited structure. Similarly, the melt depth was taken to be the depth of the dissolution region. Previous work^{6,8} shows there was little intergranular melting in the substrate region. The intergranular melting which has occurred was only a fraction of the substrate grain size. This suggests that for the conditions used in this testing the heat affected zone is relatively small.

For each new material processed by the LENS technique, test matrices are set up to determine the correct parameters to build near net parts. This has been done for a variety of materials: stainless steels, nickel-based alloys, H13 tool steel, and some tungsten. After thin-walled parts are built, solid block test matrices are performed to understand the inter- and intra-layer parameters needed to build fully dense parts.

(ii) Diagnostics

Several diagnostic techniques are used to monitor and to understand the LENS process. These include: laser Doppler velocimetry for powder flow and relative density of the powder entering the laser beam¹⁰, time resolved infrared imaging for thermal characteristics¹¹, high magnification, high speed digital imaging for process understanding⁶, and standard video imaging.

High speed, high magnification imaging allowed the LENSTM process to be effectively slowed down to visualize the molten metal/powder interaction region. It appears that particles do not become molten until they are, in fact, actually injected into the melted metal puddle in the deposition region. Two powder sizes were used to study the process and weld pool behavior. For the smaller particle size (-325 mesh), the melt puddle appear to be stable and well behaved. For the larger particle size distribution (-80 to +325 mesh), the molten puddle was very energetic and unstable. For the larger powder size distribution, the particle size was a significant fraction of the deposition region width. Directing the larger particles into the molten deposition region causes a larger displacement of the liquid metal thus adding more energy to the oscillations of the melt pool. Further studies are required to draw more quantitative conclusions for the effects of particle size on the powder deposition process.

B. Three-dimensional components

After determining the basic LENSTM parameters for a material, a hollow geometry is typically fabricated. Figure 3 is a picture of an H13 tool steel part. The tallest geometry we can build in the LENSTM platform is 6 inches. For this geometry and material, the dimensional variance along Z is only 0.002 inches for the wingspan section of the thunderbird. The surface finish on extruded shapes is typically 250 μ inch.

From our understanding of the LENSTM parameters, solid geometries are fabricated. With a solid geometry, understanding the hatch spacing (line by line spacing) is critical for building

100% dense components. Figure 4 shows a housing built out of 316 stainless steel (SS316). This part is very accurate in X and Y dimensions but the build height needs better control. The error in X and Y is less than $\pm 0.005''$; however, Z can vary by as much as $\pm 0.015''$ where the substrate extracts the thermal energy from the first few layers. By understanding the thermal behavior along with the LENS™ parameters, we should be able to control the Z height.

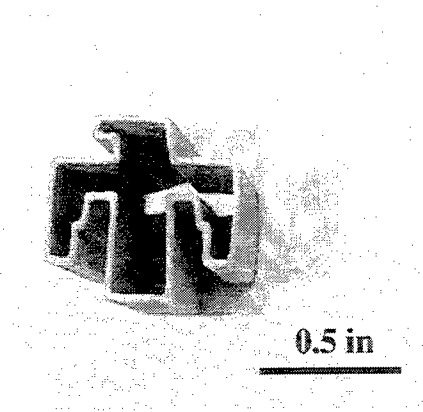


Figure 3: Thin-walled geometry fabricated from H13 tool steel.

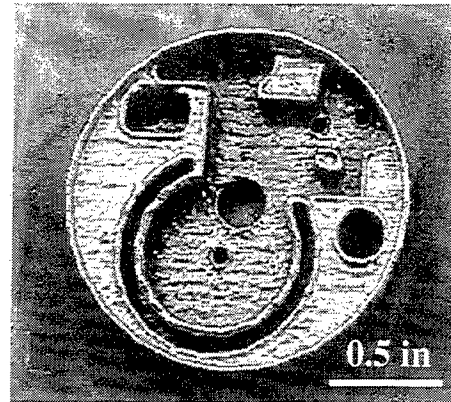


Figure 4: Solid geometry fabricated from 316 stainless steel.

Currently this process is being developed as a free-form fabrication process in which no support structures have been needed. Preliminary results from angle build studies suggest that the maximum angle which can be achieved in a single width deposition is approximately 30° and about 15° for solid parts. A horizontal rotation axis has been added to the LENS system and will expand the geometries which can be built.

Although visual analysis of sample cross-sections exhibited no obvious signs of porosity, helium pycnometry, Archimedes' method, and ultrasonic imaging were used to quantify the density for LENS processed materials. Both the pycnometry and Archimedes method showed the LENS processed materials to be fully dense. Ultrasonic imaging showed that the SS316 processed material had a few microvoids on the order of $1\text{-}5\text{ }\mu\text{m}$ in the interior of the solid. Electron microprobe analysis indicated that there was no apparent difference in composition between the deposited material and the original substrate (which is same material).

C. Accuracy

Photographs of tolerance test parts used to measure the dimensional accuracy of the LENS™ process are shown in Figures 5 and 6. In building these components, it was determined that the dimensions in the X-Y plane could be maintained to less than ± 0.002 inches (0.02 mm). The dimension in the Z or growth direction could only be maintained within ± 0.015 inches (0.4 mm). The angle in the pyramid of Figure 6 is maintain within ± 0.015 inches (0.4 mm). These results are extremely promising and further work will allow improvements in the dimensional accuracy to be achieved. The surface finish appears to be a strong function of the powder particle size with the smaller powder particles giving a better surface finish. Although the surface finish of the “as

built" component is somewhat rough, a small amount of finishing will produce an accurate, high polished surface.

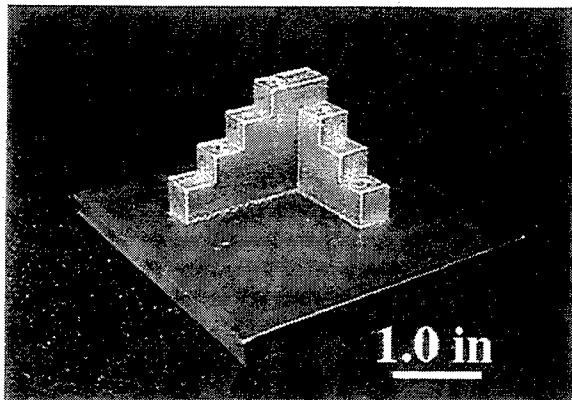


Figure 5: Accuracy test part with step geometry and cylindrical holes.

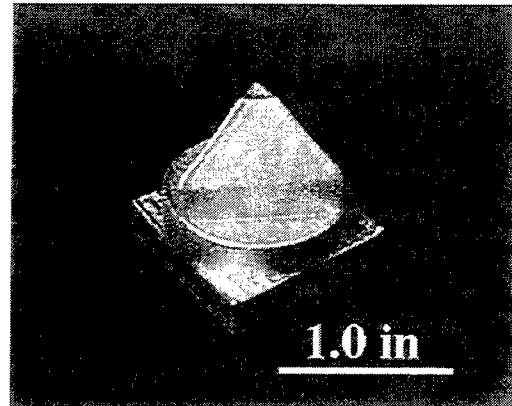


Figure 6: Square-circle-pyramid accuracy test part.

D. Mechanical Testing

Results from preliminary tensile testing of the deposited 316 stainless steel are given in Table 1. Eight bars have been tested to date, six with the layers perpendicular to the tensile pull direction, and two samples with the layers parallel to the tensile pull direction. A third set of data is given for conventionally processed, annealed 316 stainless steel¹². In all cases, the strength properties of the fabricated 316 stainless steel bars significantly exceeds that for the reported value of the annealed material. The elongation for the LENS fabricated have similar ductility where an elongation of 50% (in 1 inch) is achieved. Particle size did not effect the strength properties; but some of the early tensile samples were fabricated with a glove box oxygen content around 20-50 ppm, which lead to premature reduction in ductility. With low oxygen content (< 2 ppm), the ductility values were always greater than 50%.

Table 1: Mechanical tensile test results for LENS fabricated SS316 bars. Plane orientation represents the layer build style with respect to the tensile pull direction.

Plane Orientation (w.rt. tensile direction)	Yield Strength (ksi)	Ultimate Tensile Strength (ksi)	Elongation% (in 2.54 cm)
perpendicular (-325 mesh)	65	115	36-66
perpendicular (+100/-325 mesh)	65	115	51
parallel (-325 mesh)	86	117	33
annealed bar ¹²	35	85	50

Metallographic cross-sections of volumetric LENS fabricated parts exhibit no textured grain growth across the deposition layers. Moreover, Poisson's ratio is isotropic, and the tensile results do not show any preferred properties for specimens made with the layers perpendicular or parallel to the pull direction.

Preliminary work with H13 tool steel shows that it is readily possible to make components with a hardness value of 59.3 (Rockwell C).

SENSORS

Although this process has proven to be very robust, a significant amount of work remains to develop the LENS™ process for operation in a manufacturing environment. The current system operates as an open-loop system, where it depends solely on the reliability of the laser and other system components to reproduce a given result. Preliminary results from current experimentation suggests that improvements can be made in process reliability by implementation of sensors for monitoring the process and providing a response signal for closed-loop process control.

Research in the area of sensors to monitor the LENS process and for closed loop control is ongoing. Sensors being developed include: powder mass flow for accurate flow conditions¹⁰, thermal monitoring of the weld pool and the workpiece to obtain uniformity in fabrication and resulting material's properties¹¹, pyrometry to monitor characteristics of the weld pool for feedback control¹¹, and in-situ, z-height determination of the workpiece in relation to the nozzle to obtain accurate parts.

CONCLUSIONS

The feasibility of fabricating fully dense, solid metallic components directly from a CAD solid model has been demonstrated. The material properties obtained using alloys such as the Inconel 625 and 316 stainless steel are comparable to a conventionally processed wrought material, in some cases the material properties obtained in the LENS™ fabricated structure far exceed those for annealed materials. Dimensional studies have shown that very precise tolerances can be achieved in the horizontal build plane and the data generated from these studies has suggested ways to control and improve dimensional accuracy in the vertical fabrication direction. Further work is underway to continue to improve the material surface finish and modified fabrication techniques are being explored to overcome angular limitations imposed by the current fabrication approach.

ACKNOWLEDGMENT

Work supported by the U. S. Department of Energy under contract DE-AC04-94AL85000.

REFERENCES

1. M. Burns, Automated Fabrication: Improving Productivity in Manufacturing, Prentice Hall, Englewood, NJ, (1993).
2. T. Wohlers, "State of the Industry", Proceedings of the Rapid Prototyping & Manufacturing '96 Conference, published by the Society of Manufacturing Engineers, Dearborn, MI, (1996).

-
3. P. Jacobs, Rapid Prototyping and Manufacturing: Fundamentals of Stereolithography, published by the Society of Manufacturing Engineers, Dearborn, MI, (1992).
 4. K. McAlea, R. Booth, P. Forderhause, U. Lakshminarayan, "Materials for Selective Laser Sintering Processing", 27th International SAMPE Technical conference, Vol. 27, Diversity into the Next Century, proceedings of SAMPE '95, Albuquerque, NM , October 12-14, 1995, p. 949.
 5. M. D. Baldwin, C. L. Atwood, and M. C. Maguire, "Integration of Rapid Prototyping into Investment Casting", Proceedings of the Rapid Prototyping & Manufacturing '95 Conference, published by the Society of Manufacturing Engineers, Dearborn, MI, (1995).
 6. D. M. Keicher, J. L. Jellison, L. P. Schanwald, J. A. Romero and D. H. Abbott, "Towards a Reliable Laser Powder Deposition System Through Process Characterization," 27th International SAMPE Technical conference, Vol. 27, Diversity into the Next Century, proceedings of SAMPE '95, Albuquerque, NM , October 12-14, 1995, p. 1029
 7. D. M. Keicher, J. A. Romero, C. L. Atwood, J. E. Smugeresky, M. L. Griffith, F. P. Jeantette, L. Harwell and D. Greene, "Laser Engineered Net Shaping (LENS™) for Additive Component Processing", proceeding of Rapid Prototyping and Manufacturing '96, Dearborn, MI, published by the Society of Manufacturing Engineers, Dearborn, MI, April, 1996.
 8. D. M. Keicher, J. A. Romero, C. L. Atwood, J. E. Smugeresky, M. L. Griffith, F. P. Jeantette, L. D. Harwell and D. L. Greene, "Free Form Fabrication using the Laser Engineered Net Shaping (LENS™) Process", proceedings of the 1996 World Congress on Powder Metallurgy and Particulate Materials, Advances in Powder Metallurgy, published by the Metal Powder Industries Foundation, Princeton, NJ.
 9. D. M. Keicher, J. A. Romero, F. P. Jeantette, and L. P. Schanwald, "A Method and System for Producing Complex Net-Shape Objects", patent pending.
 10. L. P. Schanwald, "Two Powder Stream Diagnostics for Laser Processes", ICALEO '95 The 14th International Congress on Applications of Lasers & Electro-Optics, San Diego, CA (11/13-95-11/16/95).
 11. L. P. Schanwald, "Two Thermal Monitors for High Power Laser Processing", proceedings of the 1996 World Congress on Powder Metallurgy and Particulate Materials, Advances in Powder Metallurgy, published by the Metal Powder Industries Foundation, Princeton, NJ.
 12. Alloy Digest Typical Value (gauge length of 5.8 cm), ASM International p. ss-114.

Fast Production of Technical Prototypes Using Direct Laser Sintering of Metals and Foundry Sand

Christian Wilkening
EOS GmbH

1. Introduction

Currently most RP-Parts are used for visualisation, assembly checks and some functional testing. The next stage between these functional prototypes and the pre-series is technical prototypes, which are used for final functional testing and optimisation of the production process. These must not only have the same material as the series parts, but must also be manufactured with the same production process. Due to the second of these requirements layer manufacturing processes cannot be used to build these prototypes directly, but they can be used to make the negative moulds or tools.

Two new RP-processes based on laser sintering now have the capability to produce the moulds and tools via very short and fast process chains. Both have already been in commercial use in Europe for about one year.

The first process manufactures tools for injection moulding of plastic parts by Direct Metal Laser Sintering (DMLS). The second process, called the Direct Croning Process (DCP), is used to build sand moulds and cores for sand casting of metal parts directly from Croning-Sand without any tools. These technologies have been developed by EOS GmbH, Munich, and are marketed under the names EOSINT M and EOSINT S respectively.

2. Direct Metal Laser Sintering (DMLS)

The most important application for laser sintering of metals is the production of tooling and moulds for injection moulded parts. Two fundamental approaches are possible:

- Indirect laser sintering with organic binder followed by solid state sintering in a furnace /1/
- Direct liquid phase sintering (DMLS).

EOS has concentrated on DMLS, because the indirect process chain makes it very difficult to achieve the narrow tolerances required in toolmaking without repeated iterations. With DMLS it is possible to get very close to the final geometrical and material properties already in the direct sintering process, thereby avoiding the loss of time and accuracy associated with secondary sintering processes.

2.1. Material and process

The basic composition of the DMLS material was developed and patented in the late 1980s by Electrolux Rapid Development, Finland for tooling production by pressureless furnace sintering. EOS now owns the exclusive worldwide licence to these patents. The composition of the bronze-nickel based powder was described at the last two SFF symposia in Austin /2/, /3/. By using the right parameters the typical shrinkage due to the liquid phase sintering can be completely compensated by an expansion of the material caused by diffusion of the

components so that this material has no net volume change during the laser sintering process. This eliminates the need for a high temperature environment, which is otherwise required to reduce the internal stresses induced during laser sintering of other metal powders. The DMLS-process works at ambient temperature.

Due to the small laser focus of 350 μm and the comparatively high scanning speed of 300-800 mm/s the duration of heating is short enough to avoid oxidation even without inert gas atmosphere. The phosphor content of the third material component inhibits oxidation of the powder mixture and also improves the wetting of the solid particles in the molten phase.

This short reaction time of few milliseconds was the reason for the relatively poor mechanical properties of the first laser sintered samples of the initial powder mixture, which had been optimised for furnace sintering. The wetting and the diffusion reaction were not completely finished because the available time was simply too short.

During the last nine months the mechanical properties and the reliability of the process have been significantly improved by adapting the material composition to the specific requirements of the laser sintering process. The most important variations are an increased content of the liquid phase, an enlarged surface area for the diffusion and an optimisation of the laser and scanning parameters.

The tensile strength of the green part has been improved from 81 N/mm² last year to currently 150 N/mm² and the bending strength from 150 to 300 N/mm².

The resulting porosity of these parts when sintered without shrinkage to obtain the highest accuracy is approximately 25%.

The green parts can be machined just like an aluminium part by milling, grinding, drilling etc. and the strength is already sufficient for special applications like blow-moulding or vulcanisation moulds.

These figures can be improved by an infiltration process that fills the pores. The preferred infiltration fluid is a high temperature epoxy resin, because this secondary process has no influence on the accuracy due to the relatively low heat impact to the metal. The result of the infiltration is an improvement of the bending strength to approx. 400 N/mm² and a smoothing of the surface. The hardness after the infiltration is 108 HB.

The infiltration is driven by the capillary forces, only the rear side of the mould must be dipped into the resin. This procedure needs about half an hour, the post curing in a simple oven at 160°C needs about two hours. Preheating of mould and resin to 60°C accelerates this process and reduces the residual porosity.

Silver-based infiltrants are currently in the evaluation phase. Although the mechanical properties can be improved, the cost of the necessary equipment and the loss of accuracy due to a shrinkage of more than 2% are a major disadvantage [3].

The negligible shrinkage of the DMLS process enables an accuracy of epoxy infiltrated parts of 0.05 to 0.1% in the first trial, which is even comparable to stereolithography. The limit for the accuracy is the mean particle size of 35-40 μm . Typical layer thicknesses of 80-100 μm are used to obtain a comparable resolution in the z-direction.

The roughness of the infiltrated part is about $R_a = 3..5 \mu\text{m}$, which is comparable to a rough EDM surface. With standard manual polishing, a roughness of $R_a < 1 \mu\text{m}$ is possible.

The heat conductivity of the sintered tools of 110 W/mK is slightly lower than the value of aluminium.

2.2. System

All EOS laser sintering machines are designed according to the specific requirements of the used material and optimized for the intended application.

The main difference between the sintering systems for metal and for polymers is the design of the optics and the laser, because the much higher sintering temperature of approximately 900 °C requires a higher power density. Therefore the focus diameter was reduced to 350 µm and the laser power was increased to 250 Watts. The power density thereby was increased from 25 W/mm² for plastic powders to 700 W/mm² for metal. More powerful lasers are still in the test phase.

Since no preheating of the powder is needed, the design of the process chamber is less complicated.

The working area of the EOSINT M 250 machine is 250 mm square, the maximum part height is 150 mm. With a density of the sintered material of 6,1 g/cm³ the maximum weight of the part is more than 50 kg.

2.3. Applications

The most important application of DMLS is the production of prototype tooling for injection moulding. The process is especially useful for complex moulds.

If the geometry of the tool is simple enough to be manufactured just by milling, the rapid tooling processes generally cannot compete against high speed milling machines.

However if EDM is required for some details in the tools, the DMLS process is usually faster and often less expensive than the conventional methods.

Sintering and infiltration of the mould inserts needs only 1-2 days, depending on the size. The time needed for CAD design of the tool and for finishing and mould assembly is the same as in the conventional process for aluminium tools. The building accuracy of the split planes is sufficient that only manual finishing is needed, thereby eliminating the need for the expensive and time consuming design of an offset on these planes and an additional machining step.

Using DMLS several service bureaux have made many projects in a total processing time of only one week, including tool concept, CAD design of the tool, DMLS, infiltration, finishing, mould assembly and injection moulding.

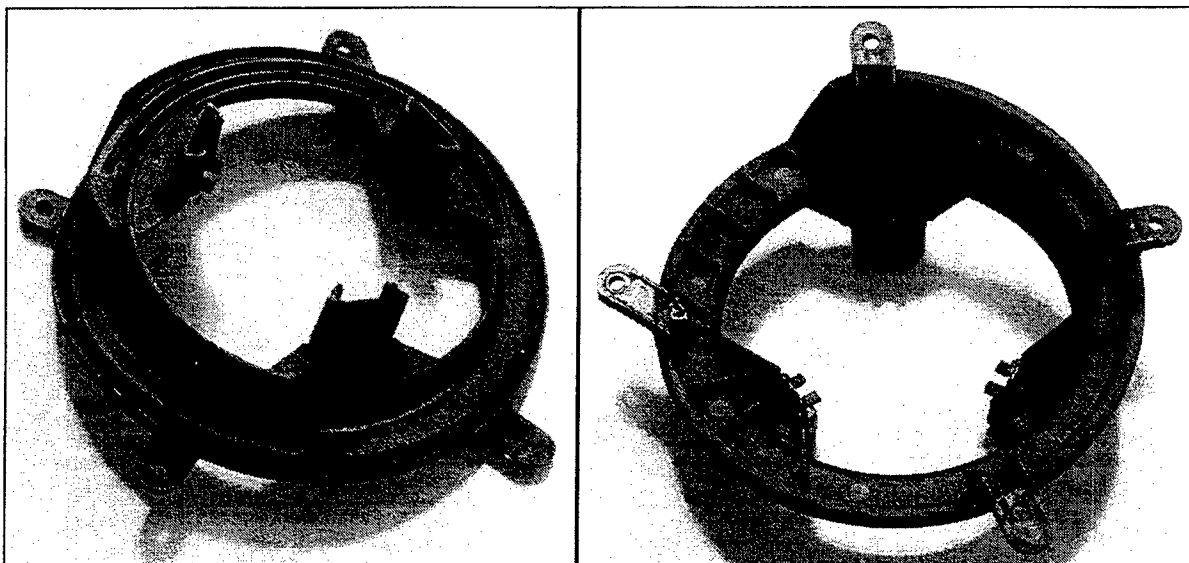


Fig 1: Top and bottom view of a motor holder, PA66/35%GF, dia 230mm

ambient temperature this coating is dry and hard. The total resin content of the mixture is about 5 %, which is comparable to standard foundry sands. The use of this material for building moulds and cores by laser-sintering has been patented by EOS.

At a temperature of 150 - 200 °C the polymerisation reaction starts and leads to an irreversible thermoset bonding between the sand particles. In the conventional foundry process the Croning sand is poured over hot steel tools having the positive part geometry, in the Direct Croning Process the energy input is completely provided by a CO₂ laser. No additional preheating of the process chamber or the sand is necessary. The process also does not require an inert gas atmosphere.

The sand costs are about 1% of typical stereolithography resins and unsintered sand can be reused several times.

Due to the low binder content the shrinkage of the material is negligible (< 0.1%). The accuracy of the sintered moulds is therefore only limited by the positioning accuracy of the scanners and the particle size (for fine details).

The surface quality of the cast parts is comparable to the typical figures for conventional sand casting. If a smoother surface is required, these specific regions can be coated with the commonly used ceramic blackwash.

DCP without blackwash	50 - 80 µm
DCP with blackwash	25 - 30 µm
Green sand	50 - 70 µm
Croning shell	20 - 40 µm

Table 1: Roughness R_a of aluminium castings depending on the mold material

Generally every alloy that can be used for sand casting can also be used with DCP moulds. So far various alloys of aluminium, magnesium, iron and steel have been cast successfully.

3.2. System

The EOSINT S700 sand laser-sintering machine is the first RP system to use a twin-laser setup. Each laser has its own scanner and they operate simultaneously and in parallel to effectively double the building speed. Each of these scanner heads has a working area of 380mm square, which allowing for a small overlap in the middle gives a total building area of 720 mm by 380 mm. The maximum part height is also 380 mm.

The sintered parts are removed from the machine in a container and separated from the loose sand in an external recycling station. The machine can immediately start the next job. The high maximum part weight of more than 200 kg requires a special handling system for the part containers, which is supplied with the machine.

A pneumatic handling system is also included in the machine for automatically refilling with sand without interrupting the building process.

The twin head design and the high scanning speed of 2000 mm/s enable a very high process productivity. Depending on the complexity of the geometry the typical rate is 0,8 - 1.5 kg part weight per hour.

3.3. Applications

Like laser sintering of thermoplastic materials, DCP has very few limitations on the part complexity. Almost every geometry which can be cast can also be built with this process. The limits of sand casting (e.g. a minimum wall thickness of 1.5-2 mm) can be achieved without problem.

DCP often allows the design of the mould to be significantly simplified, for example no draft angles are needed, undercuts are easily possible and the number of the necessary core-pieces can often be reduced. (see Fig 3)

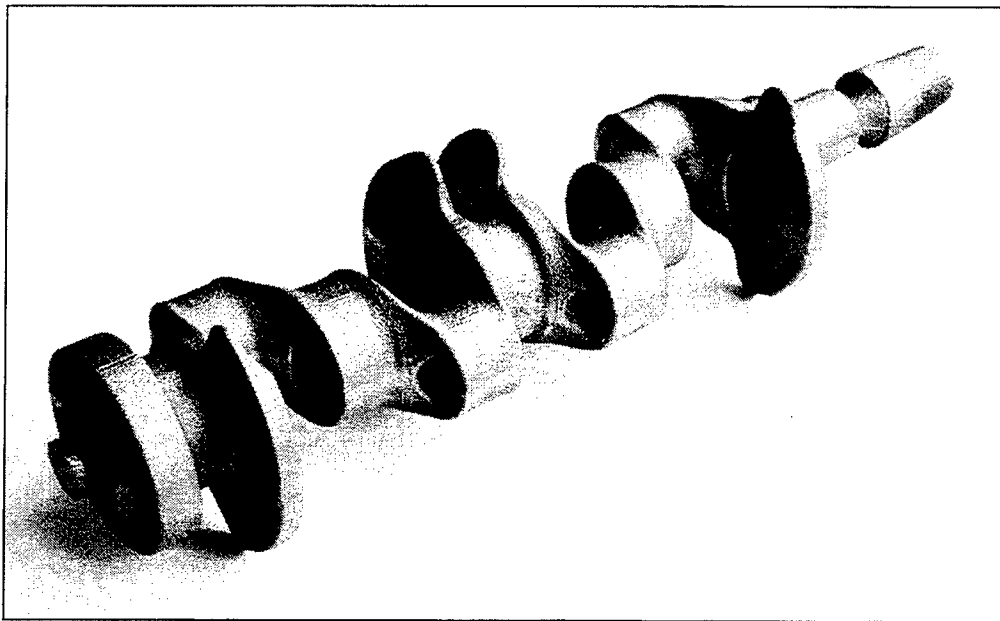


Fig 3: Crankshaft with 9 hollow bearingseats, casted in a two-part mould

Although DCP has many applications including hydraulic parts, pump components etc., the most important one is the production of prototype parts for engine development.

The potential of this process is impressively demonstrated by the example of cylinder head development. Due to the extremely complex geometry of this component with internal water cooling channels, valves and many inlet/outlet channels, prototype tooling is very complicated and difficult to manufacture. The time required between CAD design and the first casting using conventional methods is 15-20 weeks. Because the design of the cylinder head has a very significant influence on the engine performance, many iterations and optimisations are necessary for this component. Therefore this part is usually the most time-critical component which determines the duration of the engine development.

The build time for a 1-cylinder head using DCP is only 2 days, for a 4 cylinder head about one week. Together with the additional design of the mould and the runner/gating system which is needed anyway, the total processing time of a new head can be reduced to 2 - 3 weeks, which means a time saving of 80%! The DCP-produced cylinder heads are virtually identical to series parts and can run in test engines.

These figures are based on the experiences of the beta customer BMW, who was involved in the development of the system and the process from the start. With the two units that were installed in their foundry 6 and 12 months ago they have already cast almost 100 different engine designs. The other partners of the beta test programme are Mercedes Benz and several service bureaux that work for the automotive industry.

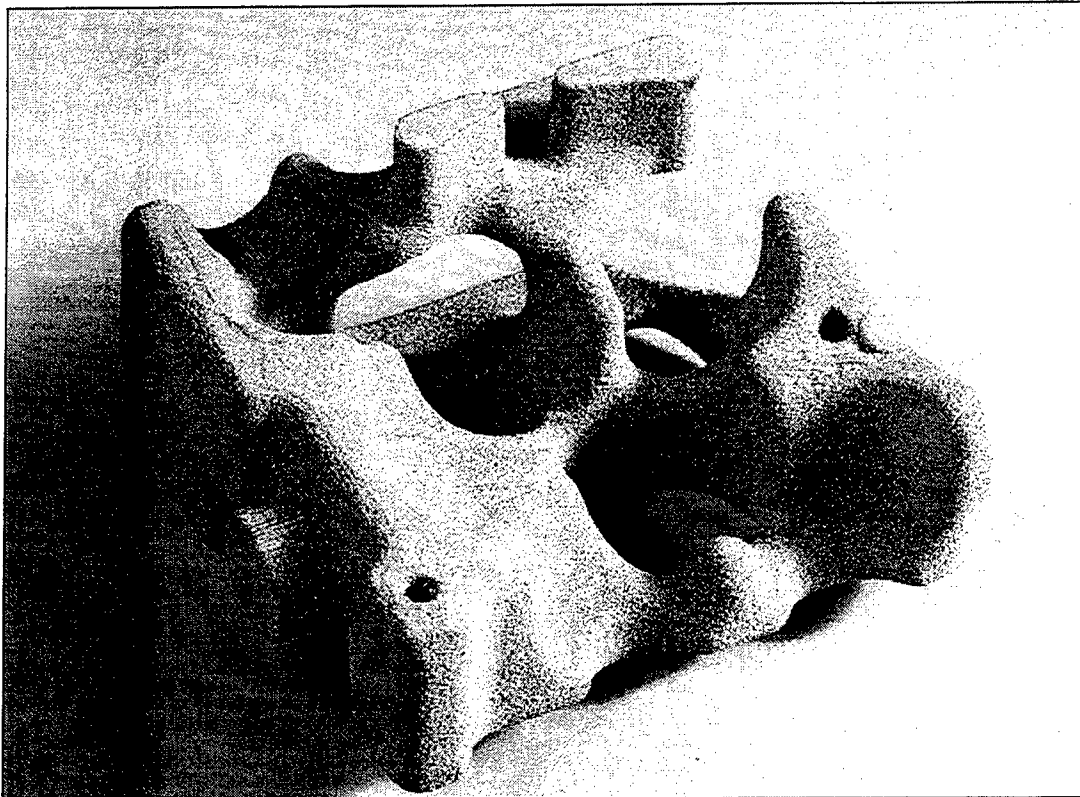


Fig 4: Core for the water cooling jacket of a 1-cylinder test engine

The high build speed makes it possible to produce not only single prototypes but also small series. The biggest order so far for one of the service bureaux was the production of 1000 complicated cores (120 x 120 x 80 mm) for a water jet system.

4. Conclusions

The production of technical prototypes (i.e. in series materials and with series production techniques) by Rapid Prototyping was until recently only possible via Rapid Tooling process chains involving at least one conversion process, due to the limitations of the available RP materials. The recent introduction of Direct Metal Laser Sintering (DMLS) and the Direct Croning Process (DCP) has for the first time enabled the direct production of tooling and moulds for injection moulding and sand casting respectively, and thereby the fast and efficient production of technical prototypes in both plastics and metals. This marks a very significant advance in Rapid Prototyping and Tooling technology. The ability of DCP to directly manufacture one-off and small-series parts with identical quality to conventional sand-cast series parts has also for the first time made the breakthrough into true Rapid Manufacturing.

Since neither the sharpness of the edges nor the levels of form and dimensional accuracy achieved meet the requirements of a pre-series tool, the contour of the part is milled. The upper surfaces also undergo a milling operation to keep the distance between the upper edge of the last deposited layer and the lower edge of the powder nozzle constant, Figure 2. Similar to the other Rapid Prototyping techniques, the workpiece is created layer by layer.

process steps

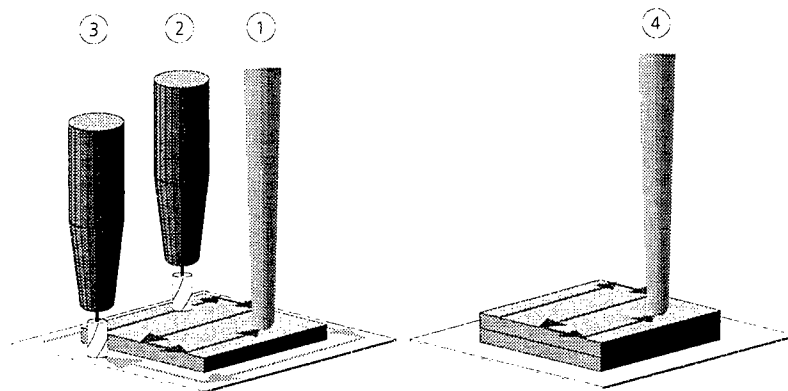


Figure 2: Process steps of CMB

CMB allows processing of numerous metallic materials ranging from bronze through steel to hard alloys which are frequently used to protect against wear. Since CMB is, in contrast to conventional cutting operations, a generative process, narrow, deep grooves may easily be produced using a constant, low engagement depth of the milling tool. The suitability of this method for automation in comparison to e.g. conventional 5-axis milling is a powerful advantage. By virtue of the layer-by-layer nature of this technique, the CAD data may be processed quickly and with considerably less effort.

The test facility at the Fraunhofer IPT is essentially a high speed milling machine supplied by the Albrecht Rödgers company on which a laser generating head has been mounted, Figure 3. To date, simple geometries have been built using different materials in order to investigate the principle underlying the CMB process (Figure 3).

Selective Laser Sintering

Current approaches to sinter metallic powders are concentrated on the direct or indirect sintering of the chosen material. Indirect sintering, deploying a binder phase (e.g. a polymer), has the advantage that only the binder material needs to be melted, most of the time at a low temperature allowing manufacturing of metallic parts using conventional plastic sintering machines. However, the workpiece must be debinded and infiltrated, causing loss of accuracy and prolonging the time needed for manufacture. Direct sintering is aimed at melting the chosen material during the SLS process directly, eliminating the need for debinding. However, since processes currently industrially available leave the parts with a porosity of about 70%, infiltration is still necessary to achieve full density. Another problem related to direct sintering of metallic

These technologies have also introduced new technical innovations which are pushing RP technology forwards. EOSINT M 250 is the first commercial system to build parts directly in metal, while EOSINT S 700 is the first RP system worldwide to use two laser-scanner systems in parallel for increased productivity.

Due to the considerable time-saving benefits of these new technologies they have established themselves very rapidly in Europe. EOSINT M and EOSINT S systems have been in use at service bureaux and industrial end-users since the summer of 1995, including such reference names as BMW, Mercedes and Electrolux. These companies are already experiencing the technical and commercial advantages of true Rapid Tooling, and the growing user-experience being generated by the rapidly expanding customer base is indicating a number of exciting new applications which will be reported in future.

References

- /1/ Badrinarayan B. and Barlow, J. W., "Metal Parts from Selective Laser Sintering of Metal-Polymer Powders", Solid Freeform Fabrication Symposium, Austin 1992, 141-146
- /2/ M. Sindel, T. Pintat, M. Greul, O. Nyrhilä, C. Wilkening, "Direct Laser Sintering of Metals and Metal Melt Infiltration for Near Net Shape Fabrication of Components", Solid Freeform Fabrication Symposium, Austin 1994, 94-101
- /3/ T. Pintat, M. Greul, M. Greulich, C. Wilkening, "Accuracy and Mechanical Behavior of Metal Parts Produced by Laser Sintering", Solid Freeform Fabrication Symposium, Austin 1995, 72-78

Direct Manufacturing of Metal Prototypes and Prototype Tools

Prof. Dr.-Ing. Fritz Klocke, Dipl.-Ing. H. Wirtz, Fraunhofer Institute of Production Technology,
Aachen, FRG

Dipl.-Phys. W. Meiners, Fraunhofer Institute of Laser Technology, Aachen, FRG

Abstract

Due to the limited mechanical characteristics of the materials which can currently be processed using industrially available Rapid Prototyping machines, a lot of research is focused on the development of techniques which allow a direct manufacturing of metallic parts. These include Selective Laser Sintering and Controlled Metal Build Up. Both methods produce the workpiece not by removal of material but by a layerwise deposition and local melting or sintering of a powder material without part-specific tooling.

Controlled Metal Build Up is a new Rapid Prototyping technique similar to Fused Deposition Modeling combining laser generating/welding with conventional 2½ dimensional milling. Due to the excellent surface quality and high dimensional and form accuracy achievable with Controlled Metal Build Up, this technology offers an interesting alternative to the conventional time consuming processes for the manufacture of prototype tools required for limited production runs.

With respect to Selective Laser Sintering, a test facility was developed for experimental investigations into the direct sintering of low and high melting metallic powders without the use of a polymer binder as well as ceramic powders. Great potential is expected from Selective Laser Sintering concerning the prototyping of molds and dies.

This paper will discuss current developments for these two techniques as well as point out possible applications and future developments.

Introduction

Recent developments in Rapid Prototyping have to a large extent been focused on the manufacture of prototypes with characteristics closely corresponding to the characteristics of the serial part being developed, allowing functional testing [1, 2, 3, 4]. The production of a prototype suitable for functional testing requires the prototype to be identical to the serial part in shape, material and production process. While the first requirement is being thoroughly addressed through e.g. constant improvement of machine accuracy, the second requirement has only sufficiently been met for a small number of plastics [1, 3, 4]. During 1995, two commercial Rapid Prototyping systems for the manufacture of metal parts (DTM RapidTool, EOS EOSINT M) were released [5, 6]. The fast generation of metallic tools e.g. for injection molding enables

the production of prototypes in large quantities that exactly match the characteristics of the serial part.

However, these two new Rapid Prototyping systems have some drawbacks. The RapidTool process brought into the market by DTM, utilizing a polymer-coated steel powder for Selective Laser Sintering, is characterized by several time consuming infiltrations and part shrinkage during burn-out of the binder [5]. EOS selectively sinters a bronze-nickel powder and parts also need to be infiltrated to achieve full density [6]. Both processes require extensive part finishing [5, 6].

To overcome the problems associated with part density and accuracy, the IPT has developed a new process called Controlled Metal Build Up (CMB) in close cooperation with Albrecht Röders GmbH & Co. KG, Soltau, Germany, which combines laser generating with high speed milling.

Research being conducted in the field of Selective Laser Sintering is focused on the machinability of conventional tool steel to high densities as well as light metals and ceramics.

Controlled Metal Build Up

Controlled Metal Build Up is based on laser generating, a technique pioneered at the Fraunhofer Institute of Production Technology IPT [7, 8, 9, 10]. A metal powder is blown into a focused laser beam and completely melted inside a nozzle, Figure 1. A fine bead of material is deposited beyond the nozzle onto the surface of the workpiece while the equipment is moved to scan the inner regions and the outline of the part.

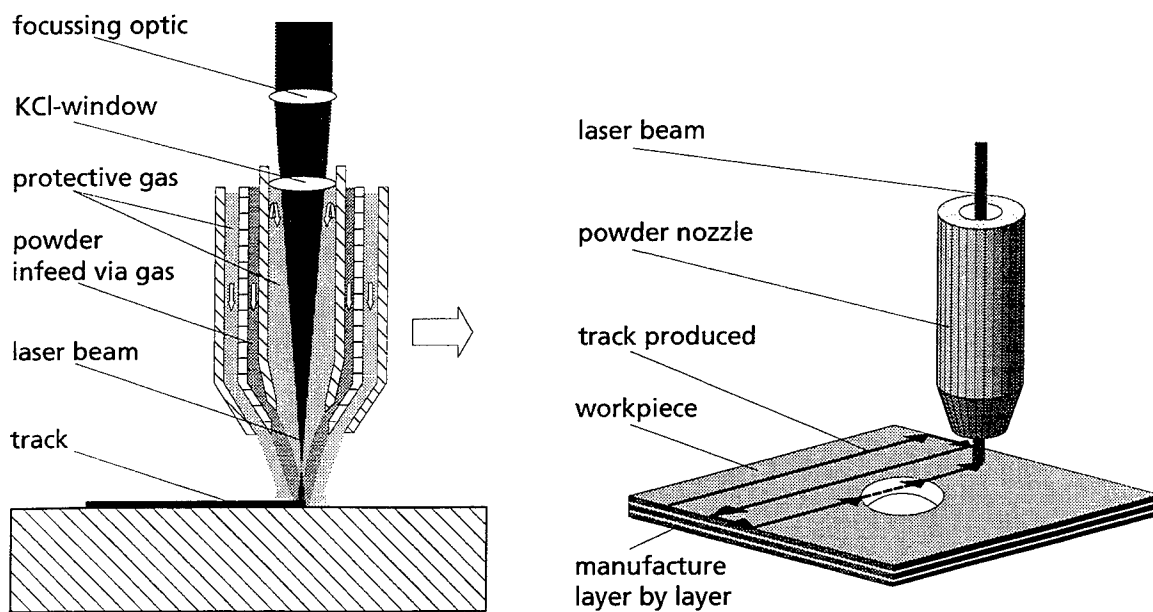


Figure 1: Powder nozzle used for CMB and principle of operation

Since neither the sharpness of the edges nor the levels of form and dimensional accuracy achieved meet the requirements of a pre-series tool, the contour of the part is milled. The upper surfaces also undergo a milling operation to keep the distance between the upper edge of the last deposited layer and the lower edge of the powder nozzle constant, Figure 2. Similar to the other Rapid Prototyping techniques, the workpiece is created layer by layer.

process steps

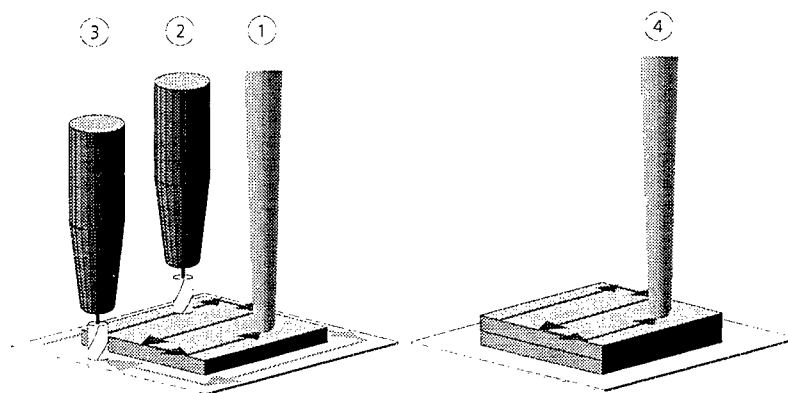


Figure 2: Process steps of CMB

CMB allows processing of numerous metallic materials ranging from bronze through steel to hard alloys which are frequently used to protect against wear. Since CMB is, in contrast to conventional cutting operations, a generative process, narrow, deep grooves may easily be produced using a constant, low engagement depth of the milling tool. The suitability of this method for automation in comparison to e.g. conventional 5-axis milling is a powerful advantage. By virtue of the layer-by-layer nature of this technique, the CAD data may be processed quickly and with considerably less effort.

The test facility at the Fraunhofer IPT is essentially a high speed milling machine supplied by the Albrecht Rödgers company on which a laser generating head has been mounted, Figure 3. To date, simple geometries have been built using different materials in order to investigate the principle underlying the CMB process (Figure 3).

Selective Laser Sintering

Current approaches to sinter metallic powders are concentrated on the direct or indirect sintering of the chosen material. Indirect sintering, deploying a binder phase (e.g. a polymer), has the advantage that only the binder material needs to be melted, most of the time at a low temperature allowing manufacturing of metallic parts using conventional plastic sintering machines. However, the workpiece must be debinded and infiltrated, causing loss of accuracy and prolonging the time needed for manufacture. Direct sintering is aimed at melting the chosen material during the SLS process directly, eliminating the need for debinding. However, since processes currently industrially available leave the parts with a porosity of about 70%, infiltration is still necessary to achieve full density. Another problem related to direct sintering of metallic

powders is shrinkage and the induction of thermal stresses resulting in distorted and curled parts. The development of materials with virtually no shrinkage (EOS) has to some extent eliminated this problem, however neglecting the desire to be able to produce parts out of the material used in series production.

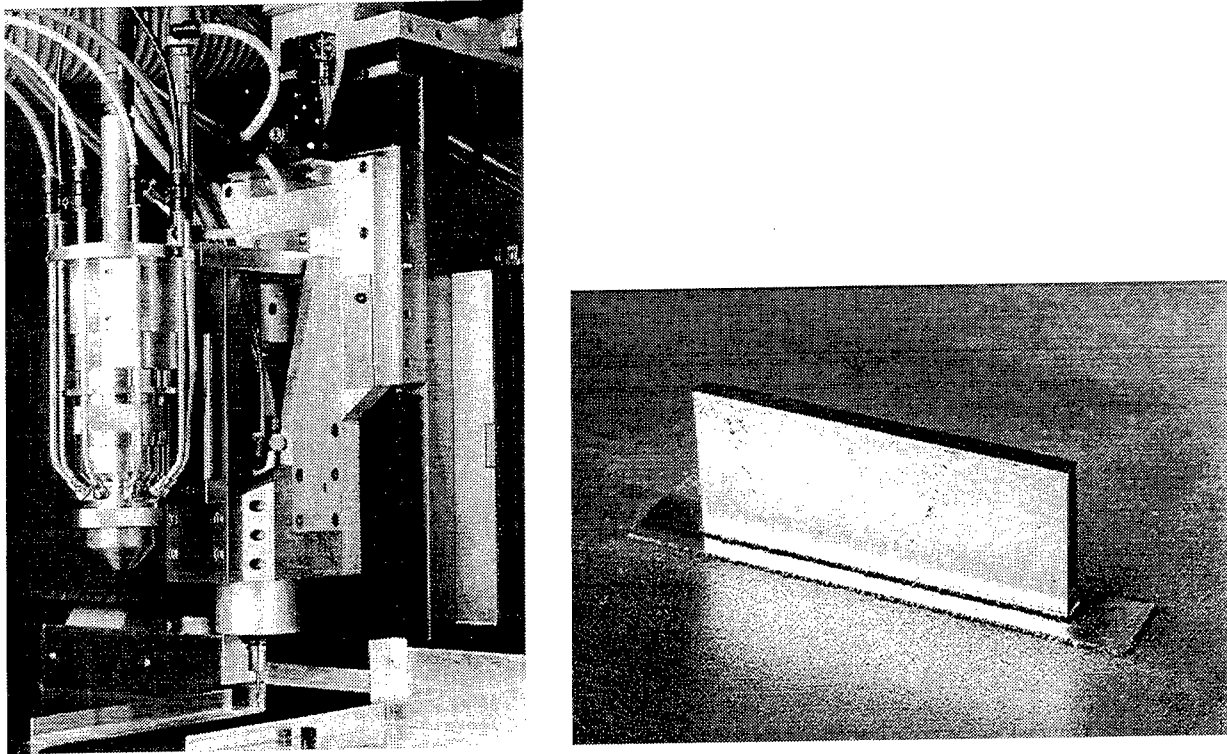


Figure 3: CMB test facility at the IPT and simple generated geometry

A test facility was developed at the IPT for direct sintering of powder materials. The process chamber of the test facility may be flooded with inert gas to avoid oxidization during sintering. The powder is supplied by a powder cylinder and spread across the part cylinder with an aluminum wiper. The test facility is equipped with a Nd:YAG-Laser with a maximum output power of 300 W.

Research conducted at the Fraunhofer Institute of Production Technology is focused on the direct sintering of metallic parts. Emphasis is put on achieving high densities during the SLS process by a careful adjustment of the process parameters, while maintaining a good surface quality. This way it is hoped that infiltration can be dispensed with without increasing the effort necessary for finishing.

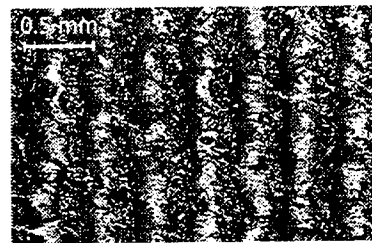
Figure 4 demonstrates the influence of laser power P_L , scan velocity v_s and hatch spacing h_s on typical workpiece quality parameters. Here, a single layer of bronze was sintered using 3 different energy densities by varying the above mentioned parameters according to

$$E = \frac{P_L}{h_s \cdot v_s}$$

and measuring the resulting sintering depth, density and surface roughness.

material: CuSn 89/11
particle size: $< 45 \mu\text{m}$

▨ variation of hatch spacing
▤ variation of scan speed
■ variation of laser power



$P_L=61 \text{ W}$, $v_s=84 \text{ mm/s}$, $h_s=0,4 \text{ mm}$

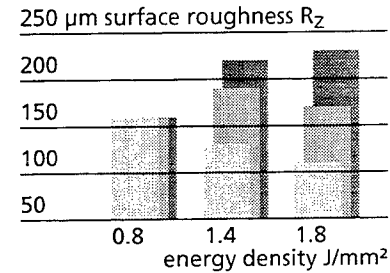
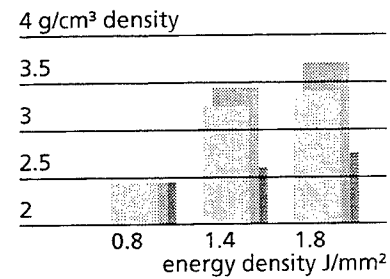
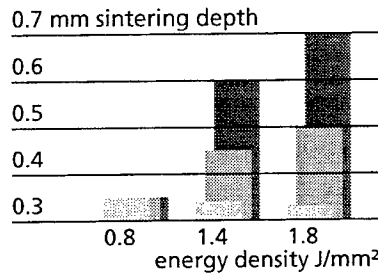


Figure 4: Influence of energy density on layer sintering

Increasing the energy density by increasing laser power or decreasing scan velocity leads to higher sintering depths, while decreasing hatch spacing has almost no influence on the thickness of a layer. A possible explanation is that for small hatch spacings, most of the light of the laser beam is reflected or absorbed from the previously drawn, solid line which has a coefficient of absorption significantly less than the one of the powder. The amount of energy absorbed by the line melts the material again without adding further to the sintering depth. The amount of energy absorbed by the powder itself is small for small hatch spacings, thus not increasing the sintering depth any further.

The density of the single layer increases with increasing energy density. A variation of hatch spacing or scan velocity has a greater effect on density than a variation of laser power, since the melted agglomerates of material are positioned closer together for slower scan speeds and smaller hatch spacings. Thus, an increase in scan velocity may not be compensated by an increase in laser power.

The surface roughness increases with increasing laser power. Higher laser powers lead to the formation of large, segregated agglomerates, being the reason for a poor surface quality. Decreasing the scan velocity also causes an aggregation of solidified material, increasing surface roughness until the velocity is so low that it allows formation of continuous solid lines. Once continuous solid lines may form, the surface quality is enhanced. Decreasing hatch spacing improves surface quality due to a continuous melting of small amounts of powder that attach to the previously solidified material.

The Fraunhofer Institute of Production Technology is working in collaboration with the Fraunhofer Institute of Laser Technology on the development of SLS of steels, light alloys and ceramics. By a careful adjustment of process parameters, especially scan vector length, the

Fraunhofer Institute of Laser Technology was able to produce SLS test parts made of stainless steel with a density greater than 95% and an acceptable surface quality. Figure 5 shows the test parts (the surface was milled to visualize the full density of the workpieces) and a cross-sectional view, displaying the low porosity. A tool was sintered for verification of the suitability of this process for injection molding, Figure 6.

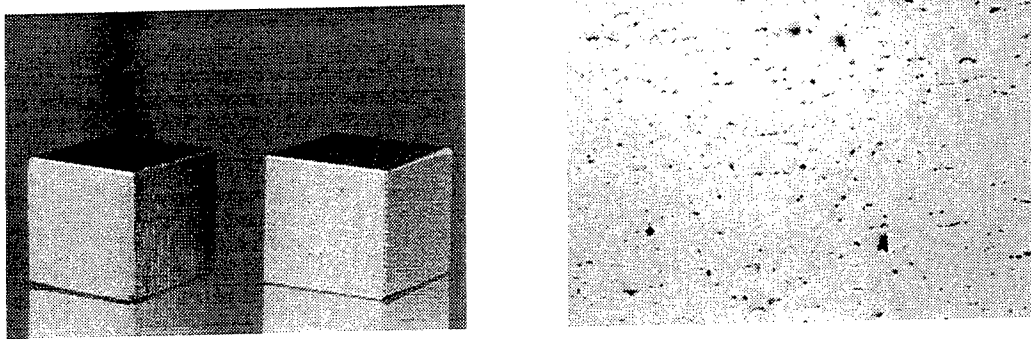


Figure 5: Stainless steel test parts ($10 \times 10 \times 10 \text{ mm}^3$) and cross-sectional view

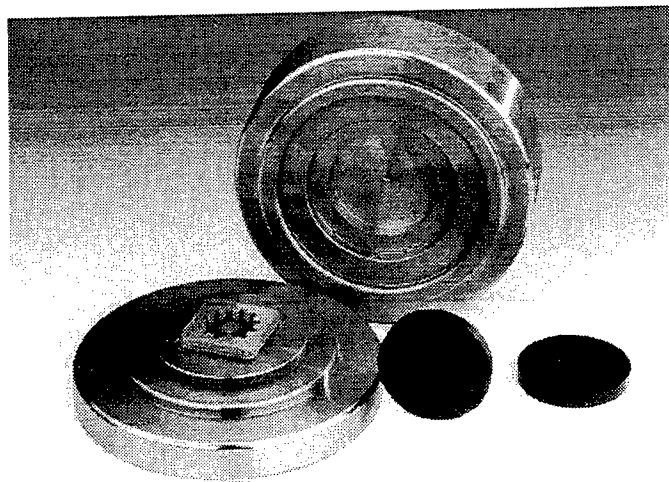


Figure 6: Stainless steel tool for injection molding of rubber parts

The ILT and IPT were also able to sinter silicon carbide (SiC) directly without utilizing a binder material, Figure 7. The resulting green part may be infiltrated with silicium and reaction sintered to a fully dense ceramic part.

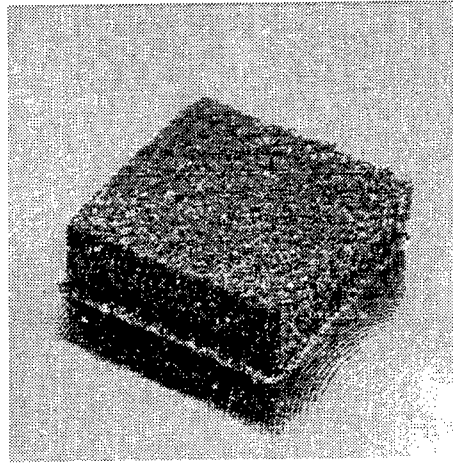


Figure 7: Test part ($10 \times 10 \times 3 \text{ mm}^3$) sintered from SiC ceramic

Conclusion

Controlled Metal Build Up and Selective Laser Sintering are both promising methods for generating parts and tools out of powder materials. While two commercial SLS processes for the sintering of metal materials are commercially available, there are still many issues that need to be dealt with to make SLS of metals and ceramics applicable for widespread industrial use. Research at the Fraunhofer Institute of Production Technology is focused on the production of fully dense, accurate parts with a good surface quality through both of the above mentioned processes. The manufacture of various test parts have shown the feasibility of these methods for the rapid prototyping of parts and tools. Current developments in collaboration with the Fraunhofer Institute of Laser Technology are aimed at gaining a deeper understanding of the principles of SLS of metals, especially steel, and extending the machinable range of materials to ceramics.

References

- [1] Venus, A. D.
Opportunities for Selective Laser Sintering (SLS) in Integrated Rapid Product Development
Proceedings of the 4th European Conference on Rapid Prototyping and Manufacturing, 13.-15.06.1995, Belgirate, Italy, pp. 55-67
- [2] Haferkamp, H., Bach, F.-W., Gerken, J., Marquering, M.
Rapid Manufacturing - Direct Production of Metal Parts with Laser Radiation
Proceedings of the 4th European Conference on Rapid Prototyping and Manufacturing, 13.-15.06.1995, Belgirate, Italy, pp. 123-135

- [3] Forderhase, P., Ganninger, M., McAlea, K.
Nylon and Nylon Composite SLS Prototypes
Proceedings of the 4th European Conference on Rapid Prototyping and Manufacturing,
13.-15.06.1995, Belgirate, Italy, pp. 185-195
- [4] Gebhardt, A.
Rapid Prototyping - Werkzeug für die schnelle Produktentwicklung
Hanser-Verlag, München, Wien, 1996
- [5] Process Enhancements - DTM's RapidTool
Rapid Prototyping Report, vol. 5, nr. 9, 1995, pp. 5-6
- [6] New Equipment - EOS Introduces Sintering Machine for Metal Parts
Rapid Prototyping Report, vol. 5, nr. 12, 1995, p. 5
- [7] Klocke, F., Clemens, U.
Rapid Tooling Combining Laser Generating and High Speed Milling
Proceedings of the 5th European Conference on Rapid Prototyping and Manufacturing,
04.-06.06.1996, Helsinki, Finland, pp. 211-221
- [8] Klocke, F., Celiker, T., Song, Y.-A.
Rapid Metal Tooling
Proceedings of the 4th European Conference on Rapid Prototyping and Manufacturing,
13.-15.06.1995, Belgirate, Italy, pp. 225-246
- [9] König, W., Celiker, T., Song, Y.-A.
Rapid Prototyping of Metallic Parts
Proceedings of the 3rd European Conference on Rapid Prototyping and Manufacturing,
06.-07.07.1994, Nottingham, UK, pp. 245-256
- [10] König, W., Celiker, T., Herfurth, H.-J.
Approaches to Prototyping of Metallic Parts
Proceedings of the 2nd European Conference on Rapid Prototyping and Manufacturing,
15.-16.07.1993, Nottingham, UK, pp. 303-316

FREEFORM POWDER MOLDING FOR RAPID TOOLING

Stephen J. Rock^{†‡}, Charles R. Gilman^{†‡}, Wojciech Z. Misiolek[†], and Daniel F. Walczyk[†]

[†]Rensselaer Polytechnic Institute
New York State Center for Advanced Technology
in Automation, Robotics and Manufacturing
Troy, New York 12180
-and-

[‡]Manufacturing Solutions, Inc.
Troy, New York 12180

ABSTRACT

Tooling development can be quite time consuming and costly. Several iterations may be required, and later product or process modifications may necessitate tooling redesign. Rapid prototyping techniques capable of meeting the structural requirements of short-run and end-use tooling will have a significant impact on the product development cycle. This paper presents a technique for producing tooling using the Freeform Powder Molding process. Resulting tooling can be made from a wide variety of readily available metal powders, and mechanical properties can be tailored for customized tool design and fabrication. The example presented in this paper focuses on the rapid production of tooling for sheet metal forming.

1. INTRODUCTION

Since the emergence of the first commercial Solid Freeform Fabrication (SFF) processes, SFF system production rates have been unable to match the rates of conventional high-volume manufacturing operations such as injection molding, die casting, and stamping. While substantial progress has been made toward producing SFF components from engineering materials, throughput limitations continue to remain a formidable obstacle to the deployment of SFF systems in production. If these systems can be used to produce tooling for high-volume manufacturing processes, then throughput limitations can be surmounted while realizing many of the benefits associated with SFF, and more generally with Rapid Prototyping (RP). This use of RP to make tooling offers one means for realizing Rapid Tooling (RT). Rapid tooling allows early implementation of production manufacturing techniques and materials to evaluate product designs earlier in the development cycle than is possible where conventional techniques are used to fabricate tooling.

This paper introduces a technique for quickly producing tooling based on the two-material Freeform Powder Molding (FPM) concept [1], and the notion of freeze molding [2]. While much work has been published on the use of RP parts as patterns [3-5], particularly for casting applications [6-8], this work describes the *direct* use of an RP part as a mold for shaping metal powder. The resulting molded metal object then serves as tooling for sheet metal forming. Before discussing details of tooling production, a brief introduction to FPM and freeze molding are provided.

1.1 Freeform Powder Molding

The FPM process relies on material behavior differences to selectively define component shape [1]. By arranging powders with different diffusion kinetics within some confining volume, it is possible to process the entire volume and cause only one of the materials to consolidate while the other remains a loose powder. This is illustrated in Figure 1, where material that consolidates is termed *part powder* and material which does not consolidate is termed *tool powder*. In this example, the part powder represents a part which will become the tooling used for metal forming.

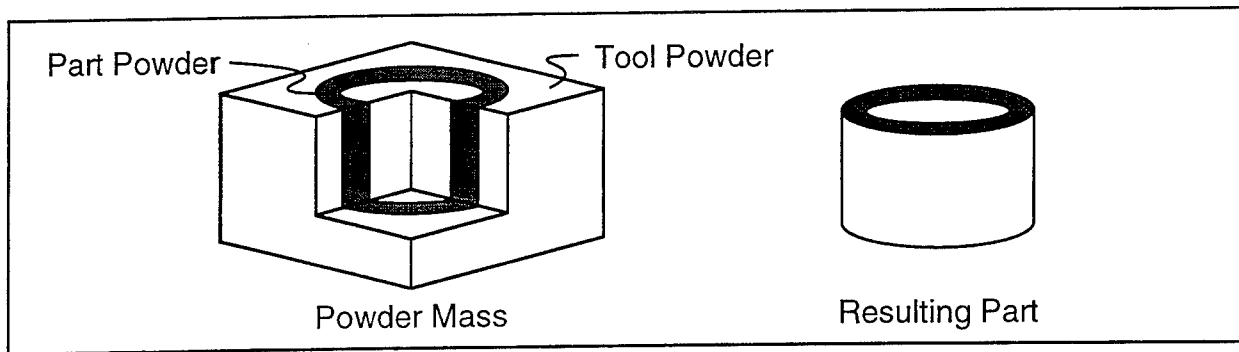


Figure 1 - Freeform Powder Molding Two Material Concept [1]

The tool powder essentially forms soft tooling which both supports, and in conjunction with the part powder, defines the shape of the resulting component.

Although originally envisioned as a layer-wise SFF process, the underlying process concept can be applied when alternative shape defining techniques such as freeze molding are employed. Powder can be shaped by molding, and then surrounded with tool powder to preserve its shape during carrier melting and subsequent removal.

1.2 Freeze Molding

Freeze molding, also referred to as freeze casting, presents a low-cost alternative to powder processing techniques requiring costly tool sets. Freeze molding was originally explored to bring concurrency to FPM process development and distortion compensation research [9]; however, the results of this work suggest it has merit as a secondary material conversion alternative for RP. A slurry of powder and carrier is introduced into a mold at low (or no) pressure and the mixture is frozen [2]. Molds can be fabricated from a variety of inexpensive materials which can be easily machined or they can be produced by a variety of commercial RP processes. Since the powder slurry is not injected into the molds under high pressure, the geometric complexity of the molds may be limited.

Aqueous carriers are used because they can be easily frozen. Carriers may contain additional constituents which support the development of green strength after shaping of the powder compact and sublimation of the principal carrier component. The presence of some organic binder is particularly important if the compact is dried rapidly, as this can cause cracks within the compact [10]. Unfortunately, carrier sublimation takes a long time and this disadvantage is similar to the debinding operation necessary with powder injection molding [2].

While typical freeze molding requires carrier sublimation and compact green strength development, these are not required when coupling freeze molding with FPM.

2. RAPID TOOLING PRODUCTION PROCEDURE

The following procedure is used to produce tooling. A mold is created by RP and used to shape a powder mass. This powder is subsequently sintered to realize a solid component which has the physical properties required of tooling. The resulting tooling is used to make the final desired component, which in this application is formed sheet metal. Figure 2 depicts the sequence of operations used for rapid tooling production. While oversimplified by this depiction, this procedure was quite straight-forward and efficient to implement. The complete rapid tooling sequence from die design to sheet metal forming could be completed in only four days given this simple forming geometry.

2.1 Powder Selection & Preparation

Rapid tooling was fabricated using both Anval 316 stainless steel powder with a particle size of -325 mesh/ $+16\ \mu\text{m}$ and Novamet 4SP elemental nickel powder with a particle size of $-20\ \mu\text{m}/+10\ \mu\text{m}$. Both powders are chemically compatible with the carrier used during freeze

molding. Both powders also have relatively small particles to promote rapid sintering to maximum density given loose powder preforms. The small particles help to develop a fine grained microstructure in the resulting sinter-body which leads to improved mechanical properties. Both powders have particles of spherical morphology so they pack to a high initial density, relative to irregularly shaped powder, in the absence of external compaction pressure.

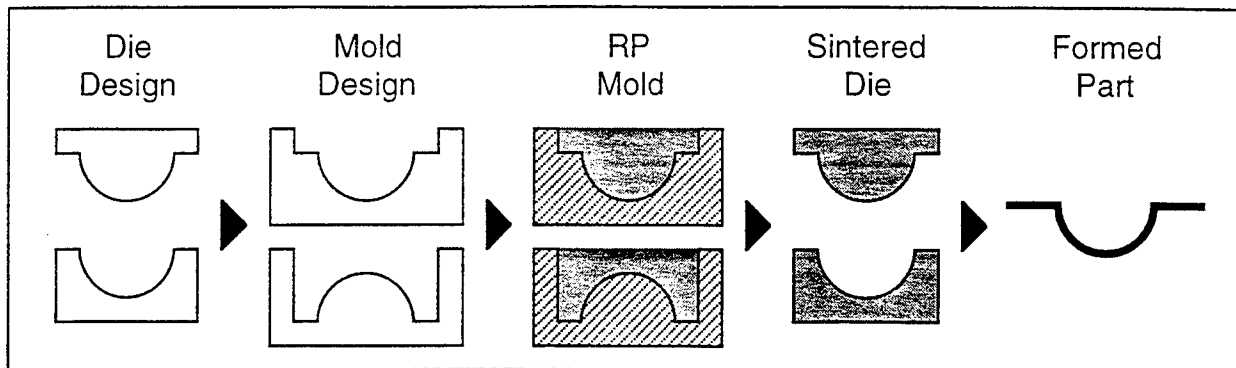


Figure 2 - FPM Rapid Tooling Procedure

An aqueous carrier comprised of water with 10% by volume ethyl alcohol to facilitate particle wetting was used in this work. This carrier was selected because it was easily frozen and later removed from the powder. No additional organic binding constituents were necessary since the modified freeze molding procedure does not require that the compact develop green strength or that it withstand sublimation which may lead to crack formation. Each powder was manually stirred into the carrier, and sufficient carrier was used to ensure the powder remained completely saturated.

The powder used to support the rapid tooling in the frozen state and during sintering, known as *tool powder* given the FPM process definition, was Norton #204 yttria zirconia. Also spherical in shape, this powder has a broad powder size distribution below 180 μm . It is important that this powder have sufficiently different diffusion kinetics such that it will not sinter at the given processing conditions.

2.2 Mold Fabrication & Filling

Molds suitable for shaping the powder slurry described previously can be made in a variety of ways provided the mold material can withstand the temperatures required to freeze the powder slurry and is compatible with slurry chemistry. To realize the many benefits of rapid prototyping which contribute to this rapid tooling process, the molds should be produced using manufacturing automation guided by CAD model information. A major goal of this effort was to show that RP parts can be used directly to cast the powder slurry. Molds were produced both by the Stereolithography process and by NC machining. These are shown in Figures 3 and 4, respectively. Relatively simple die shapes were selected for the sheet metal forming example in this paper to simplify mold design and fabrication.

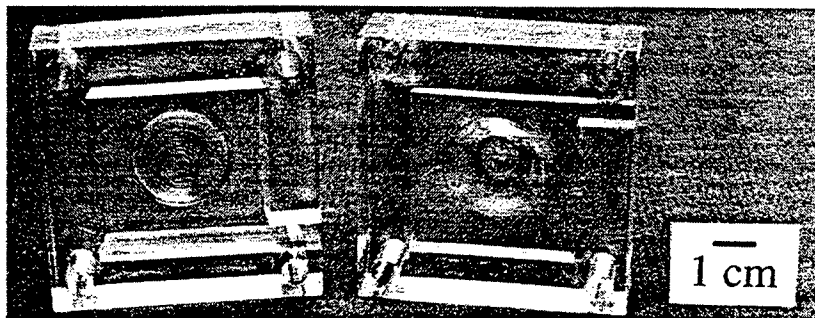


Figure 3 - SOMOS 6110™ SLA Mold Set

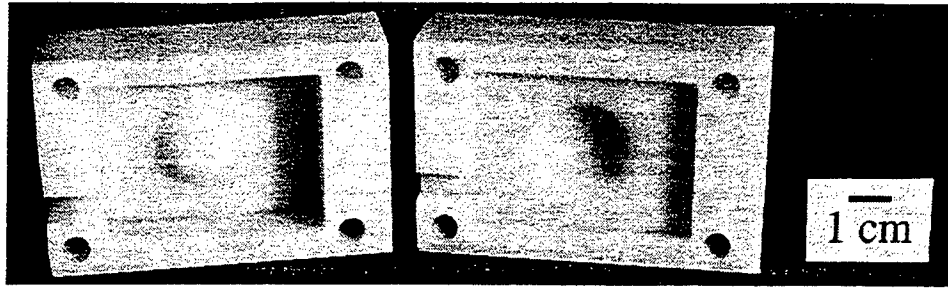


Figure 4 - Acetal Resin NC Machined Mold Set

This tooling geometry is similar to the ball punch deformation test specified by ASTM E643 [11]. Sintering furnace size also restricted the tooling size.

The molds were designed to produce dies with a suitable clearance to accommodate the 0.033" sheet metal thickness. A draft angle of 3° was designed into the vertical walls of the mold to facilitate part ejection. Each mold is designed to attach to a backing plate (not shown) which provides a flat surface on the back of each metal forming tool necessary for attachment to press equipment. Molds are filled from one side via a rectangular gate. Mold filling is performed manually under the influence of gravity. The molds are lightly tapped as the powder slurry is added to facilitate the powder fill.

2.2.1 Stereolithography Molds

One set of molds was fabricated directly by Stereolithography (SLA) using a 3D Systems SLA-250/40. The molds were fabricated from the recently introduced DuPont SOMOS™ 6110 epoxy photopolymer resin using 0.006" thick build layers.

Geometry for these molds was designed using Pro/Engineer and exported as an STL facet file with a chordal deviation set to 0.0004" to minimize tessellated surface artifacts. Such artifacts were nearly impossible to observe in the manufactured parts; however, the well-documented spatial aliasing (stair-stepping) caused by layer-wise fabrication was evident. The molds were used in as-manufactured condition without manual post-processing (e.g. sanding, polishing, etc.), with exception of the manual filling of a small hole added for trapped-volume pressure equalization during resin recoating [12]. Prior to slurry filling a silicone-based molding release agent was applied to the SOMOS 6110 material.

2.2.2 NC Machined Molds

Another set of molds was fabricated by NC machining using an acetal resin (DuPont Delrin™). This material machines easily and yields a high quality surface finish without subsequent hand finishing. It has been used extensively in other freeze molding shaping applications [9].

Molds were fabricated by NC machining to illustrate the potential role that more conventional manufacturing processes hold for rapid tooling. The benefits of solid modeling and ease with which information is handled by SFF processes became painfully clear during the 2D mold design and CAM path planning steps leading to cutting the molds. These activities accounted for much greater delay than actually cutting the plastic mold material. However, for a fair comparison to be made between SFF and NC machining RP approaches, both processes should be driven from a 3D solid model.

2.3 Modified Freeze Molding

A variant of the freeze molding procedure described in section 1.2 was used to shape the powder which ultimately becomes the rapid tooling of interest. Molds filled with the powder/carrier slurry were frozen using dry ice, with both the SOMOS 6110 and acetal molds first cooled to in a refrigerator freezer to reduce the potential for mold damage due to thermal shock [12].

After 30 minutes in the dry ice, the molds were returned to room temperature ($\sim 20^\circ\text{C}$) and allowed to warm for approximately 4 minutes. The molds are inverted and tapped gently until the

still-frozen powder mass is released from the mold. The frozen powder mass is placed in a furnace boat on a layer of FPM tool powder and then subsequently surrounded with more tool powder before slurry melting begins.

The frozen powder slurry is allowed to melt, as the furnace boat remains at room temperature throughout storage and transport to the sintering furnace. The FPM tool powder is sufficient to retain tool powder shape during carrier melting. The presence of the tool powder may also facilitate carrier removal through capillary action by wicking the carrier away from the part powder as has been demonstrated for debinding powder injection molded components [2]. Since sublimation is not required for carrier removal and since the part does not need to develop green strength to be self-supporting, no organic binder constituents are used in the carrier mixture.

2.4 Carrier Removal & Sintering

The carrier used for freeze molding must be evaporated and the powder used for rapid tooling must be sintered. This is accomplished using a sintering furnace under protective atmosphere. Tooling was produced in both 316 stainless steel and nickel. For both powders, the sintering process was begun by heating the furnace to 85° C. This temperature was held for 1.5 hours. Then, the furnace temperature was increased to 115° C. This temperature was held for 1.5 hours to remove the carrier. Lengthy debinding times required for freeze drying sublimation are cited as a potential disadvantage of freeze molding [2]; however, it is unclear if the three hours used here is comparable to these times. Furnace temperature was then increased at 10° C/min. to a maximum sintering temperature of 1200° C for both 316 stainless steel and nickel powders. The powder was held at these temperatures for 45 minutes. The furnace cool-down commences at a rate no faster than 5° C/min. Sintering time is selected to minimize grain growth and is consistent with that recommended in the literature [13]. The nickel powder is sintered in an inert atmosphere of argon. The 316 stainless steel powder is sintered in a reducing atmosphere of dry hydrogen. The sintering cycles and atmospheres have not been optimized for the specific powders used.

3. EXPERIMENTAL RESULTS & DISCUSSION

The procedure described above was used to sinter dies for the example application of sheet metal forming. Fully dense material was not required for this demonstration; however, infiltration may be used in applications where improved mechanical properties or non-permeable tooling is required. This procedure should be suitable for producing prototype and short-run production tooling for a variety of other manufacturing processes such as injection molding, composite lay-up, sink-type EDM, extrusion, and thermoforming. The results presented below illustrate the potential utility of the FPM rapid tooling technique described here.

3.1 Part Ejection

Part ejection from the NC machined molds was relatively straight-forward. After allowing a short period for mold warming following freeze molding, gentle tapping is used to eject the resulting part. The part surface appeared quite smooth and even fine features on the molds, such as the marks from cutter rotation along tool paths, were visible on the molded part.

Part ejection from the SLA molds was slightly more difficult. Despite the use of mold release, a significantly longer duration was required to allow the molds to warm before parts could be ejected. While this may be due to different thermal conductivity of the mold materials or different geometries of the molds, inspection of the mold suggests that many of the 0.006" layers comprising the SLA part create undercuts which hinder part ejection. Figure 5 shows a magnified view of the near vertical mold walls. Despite the presence of a 3° draft angle on these walls, it is thought that significant thermal expansion of the frozen mold must occur before the part can be ejected.

Upon ejection, many small fragments of the molded powder slurry (still frozen) are found resting loose on the top surface of the mold. This suggests that even thermal expansion of the mold does not fully release the frozen mass in all locations. These fragments can be removed by suction

before they melt, and their breakage from the molded part does not appear to significantly impact tooling performance for the example application.

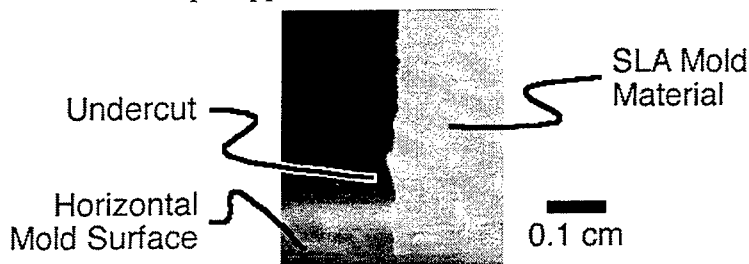


Figure 5 - SLA Mold Wall Undercuts

Similar artifacts likely exist with other layer-based SFF processes, and this illustration is not intended to suggest that the SLA process is unsuitable for this application. In fact, the SOMOS 6110 epoxy resin molds withstood both the thermal cycle of molding and impact required for part ejection without damage. In contrast to past experience with fragile parts made from early SLA resins, the SOMOS™ 6110 parts appeared to be quite tough. Constructing parts from finer resin layers or employing some additional finishing operation(s) may improve part ejection.

3.2 Sintered Dies

After sintering as described in section 2.4, the dies must be removed from the FPM tool powder in which they were embedded. This is accomplished simply by brushing the loose tool powder from the dies. Figure 6 shows the resulting nickel die set (left) produced by the SLA molds and the 316 stainless steel die set (right) produced by the NC machined molds.

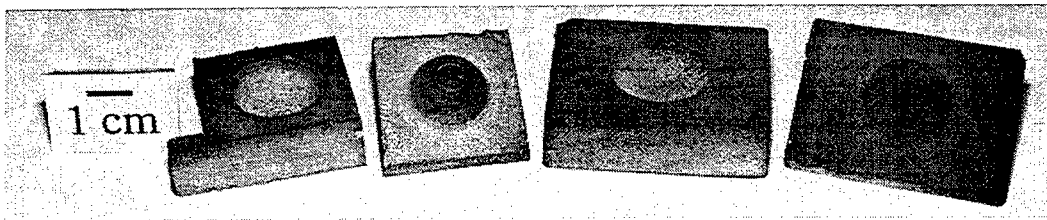


Figure 6 - Sintered Nickel Die Set from SLA Molds (left), and Sintered SS316 Die Set From NC Machined Molds (right)

The layer-wise stair-stepping of the SLA molds transfers to the die-set, with some evidence of sharp corners of the stair-steps being damaged during mold ejection. Although not clearly visible in Figure 6, the NC machined dies pick-up fine detail from the mold surface showing the concentric paths of the ball mill used to fabricate the mold protrusion.

3.2.1 Dimensional Change

Material shrinkage resulting during consolidation caused dimensional reduction of both die sets. On average, the nickel shrunk 15.4% when measured linearly. The 316 stainless steel shrunk 3.4% when measured linearly. When material shrinkage is uniform it is possible to account for it simply by model scaling. Shrinkage experienced at prescribed processing conditions would typically be determined prior to mold design, and this shrinkage taken into account to over-size the mold geometries by an appropriate dimension. In this experiment, the additional steps of shrinkage compensation were not performed and a smaller-than-designed mold geometry was accepted for demonstration purposes.

Some non-uniform shrinkage was observed along the die axis held vertical during mold filling. This is believed to be caused by the development of density gradients in the compact as a result of mold filling. Deviations of 0.3% and 0.4% were observed on the female 316SS and nickel dies; however, the male dies exhibited deviations of 1.2% and 3% for the respective die material. This increased error is thought to result from poor mold filling due to the small mold gate

in the male die molds, as shown in Figures 3 and 4 above. Alternate gate geometries or improved mold filling techniques will likely eliminate this non-uniformity.

3.2.2 Microstructure

Analysis of the microstructure confirms the expected — tooling sintered from loose powder is rather porous. Figure 7 shows the microstructures of the sintered nickel and 316 stainless steel die materials.

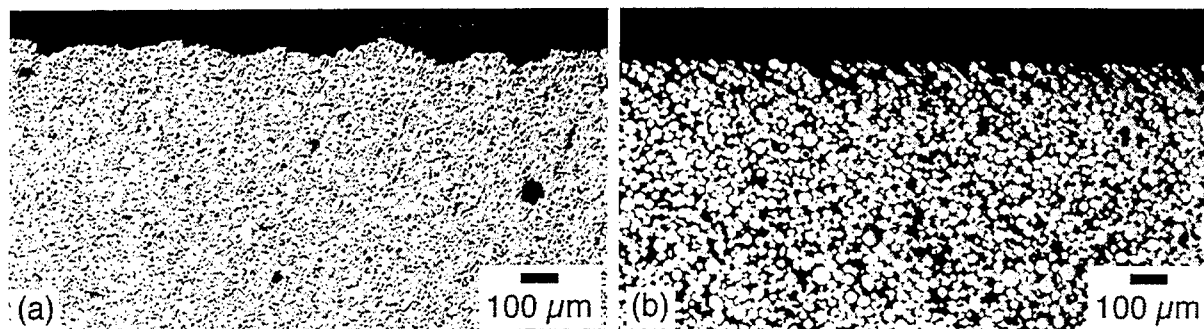


Figure 7 - Microstructure and Edge of (a) Nickel and (b) 316 Stainless Steel FPM Rapid Tooling

Optical density measurements using image processing techniques indicate densities of 80% of theoretical for the nickel dies and 60% of theoretical for the 316 stainless steel dies. However, density improvement should be possible with an optimized sintering schedule.

These micrographs also illustrate the surface quality obtained on the near vertical edges (shown horizontally in this figure) of the tooling made by the SLA molds (a) and by the NC machined molds (b). The rougher surface finish of the SLA molds transfers to the tooling. However, surface roughness as related to particle size must also be considered. The internal microstructure of the parts reflects the spherical morphology of the powders used to produce them. Note that both parts are porous and appear to be only stage one sintered. This enables application of infiltration or impregnation to realize fully-dense tooling, and either of these operations would serve to somewhat smooth the surface finish of the tooling. Pores resulting from gas entrapment during molding have been observed in some sintered material, and measures must be taken to eliminate these in practical situations.

3.3 Metal Forming

The sintered dies were installed on a press and forming was attempted on 0.033" low-carbon mild sheet steel. This steel fractured during pressing on the unlubricated dies. Examination of the metal flow of the sheet after forming suggests that high die friction near the fillet between the female die parting plane and the hemispherical depression is probably responsible for this forming failure. Instead of attempting to improve die surface finish manually, as is common even with production tooling, a 0.005" teflon film was used as an interpolator between both dies and the sheet metal during a second forming trial as suggested by [14]. This time the material did not fracture and forming was successful. Figure 8 illustrates both the failed (a) and successful (b) forming trials using the SLA molded die set and the successful (c) forming trial using the NC machined molded die set.

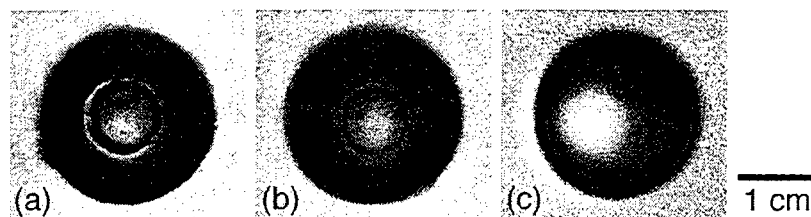


Figure 8 - Metal Forming Results on 0.033" Sheet using (a) Unlubricated Dies from SLA Molds, (b) Dies from SLA Molds with Teflon Interpolator, and (c) SS316 Dies from NC Machined Molds

Although applying an interpolator sheet to the die surface instead of manual finishing may not be an economically viable alternative for high-volume part production, it is suitable for prototyping and low-volume work where minimizing die fabrication time is advantageous. Analyzing the affect of additional forming variables, such as pressing rate or binder tension were beyond the scope of this research effort.

4. CONCLUSION

The preceding results indicate that FPM/freeze molding is a useful secondary material conversion option for RP. This conversion route uses RP parts directly as tooling for powder shaping. This method can be used to quickly fabricate tooling from conventional materials as well as a number of high performance materials that can only be processed using powder metallurgy. This paper focused on sheet metal forming, however, a variety of other tooling such as injection molding cores and cavities, composite lay-up forms, EDM electrodes, extrusion dies, and thermoforming tooling may also be produced using this approach.

Turn-around-time for the tooling featured in this report was relatively short. In an ideal case, in-process time breaks down as follows:

- Day 1: Design formed part geometry and die geometry, fabricate RP molds that evening;
- Day 2: RP molds in transit;
- Day 3: Prepare powder slurry, fill & freeze molds, eject parts and embed in FPM tool powder, remove carrier and sinter over-night;
- Day 4: Remove solid tooling from embedding powder; use dies to press and form sample.

Since mold filling and ejection are manual operations, and the resulting powder compact is fragile, more than one molding attempt may be required to realize a preform of suitable quality. If full density tools are required, additional time must be allocated for infiltrating, impregnating, or hot isostatic pressing.

Additional investigation is certainly required to determine how the FPM/freeze molding approach described in this paper compares with alternative secondary material conversion options for RP and alternative rapid tooling methods. It must also be contrast with direct methods for tooling production. The FPM rapid tooling procedure eliminates the need for the production of molds from RP patterns by directly creating the mold. This removes one shape conversion operation which reduces delay and may increase tooling precision. If layer-based SFF parts are used as molds, this technique still suffers the delay associated with layer-wise additive material build-up; however, this delay must only be incurred once during mold production. The resulting molds can be used to shape powder multiple times. Consequently, the "cost" of layer-wise fabrication may be amortized across multiple parts — whether these parts represent rapid tooling or end-use components. Alternatively, when relatively simple geometries are involved, NC machining can be performed quite efficiently on plastic mold material. Driven by appropriate CAM software, this is an RP/RT path which should not be overlooked.

ACKNOWLEDGEMENTS

This research has been conducted at the New York State Center for Advanced Technology (CAT) in Automation, Robotics and Manufacturing at Rensselaer Polytechnic Institute and supported in part by Manufacturing Solutions, Inc. The CAT is partially funded by a block grant from the New York State Science and Technology Foundation.

The authors wish to thank Gerd Beckmann, of Beckmann Engineering, for the initial suggestion of the use of freeze molding and Bill Carter, of General Electric's Corporate Research and Development Laboratory, for help with early freeze molding demonstrations. Many of the results featured in this paper would have been impossible without the generous contribution of SOMOS™ 6110 epoxy SLA parts by Bronson Hokuf of DuPont's Somos Solid Imaging Materials Group. His generosity and helpful suggestions are greatly appreciated. Powders used in this work were kindly donated by Anval, Norton Industrial Ceramics Corp., and Novamet Specialty

Products. The authors are grateful for the assistance of Norm Gendron in preparing the metallography results featured in this paper.

LITERATURE CITED

- [1] Rock, S. J. and C. R. Gilman, "A New SFF Process for Functional Part Rapid Prototyping and Manufacturing: Freeform Powder Molding," In: Solid Freeform Fabrication Symposium Proceedings, H. L. Marcus, et. al. (eds.), pp. 80-87, The University of Texas at Austin, Austin, TX, 1995.
- [2] German, R. M., Powder Injection Molding, Metal Powder Industries Federation, Princeton, New Jersey, 1990.
- [3] Fussell, P. S. and L. E. Weiss, "Steel-Based Sprayed Metal Tooling," In: Solid Freeform Fabrication Symposium Proceedings, J. J. Beaman, et. al. (eds.), pp. 107-113, Austin, TX, 1990.
- [4] Muller, T., "Using Stereolithography to Prototype Die Cast Parts," In: The Third International Conference on Rapid Prototyping Proceedings, R. P. Chartoff and A. J. Lightman (eds.), pp. 309-312, The University of Dayton, Dayton, OH, 1992.
- [5] Schaer, L., "Spin-Casting Fully Functional Metal and Plastic Parts from Stereolithography Models," In: The Sixth International Conference on Rapid Prototyping Proceedings, R. P. Chartoff and A. J. Lightman (eds.), pp. 217-236, The University of Dayton, Dayton, OH, 1995.
- [6] Greenbaum, P. Y. and S. Khan, "Direct Investment Casting of RP Parts: Practical Commercial Experience," In: Second European Conference on Rapid Prototyping and Manufacturing Proceedings, P. M. Dickens (ed.), pp. 77-93, The University of Nottingham, England, 1993.
- [7] Sarkis, B. E., "Rapid Prototype Casting (RPC): The Fundamentals of Producing Functional Metal Parts from Rapid Prototype Models using Investment Casting," In: The Fifth International Conference on Rapid Prototyping Proceedings, R. P. Chartoff, et. al. (eds.), pp. 291-300, The University of Dayton, Dayton, OH, 1994.
- [8] Denton, K. R. and P. F. Jacobs, "Quickcast™ & Rapid Tooling: A Case History at Ford Motor Company," In: The Fifth International Conference on Rapid Prototyping Proceedings, R. P. Chartoff, et. al. (eds.), pp. 301-319, The University of Dayton, Dayton, OH, 1994.
- [9] Rock, S. J. and W. Z. Misiolek, "Distortion Control for P/M-Based Rapid Prototyping of Advanced Material Components," presented at 1996 World Congress on Powder Metallurgy and Particulate Materials Proceedings, APMI/MPIF, Washington, D.C., 1996.
- [10] German, R. M., Powder Metallurgy Science, 2nd ed., Metal Powder Industries Federation, Princeton, NJ, 1994.
- [11] "ASTM Standard E643: Standard Test Method for Ball Punch Deformation of Metallic Sheet Material," In: Metals - Mechanical Testing; Elevated and Low-Temperature Tests; Metallography, Vol. 03.01, American Society for Testing and Materials (ASTM), Philadelphia, PA, 1995, pp. 567-569.
- [12] Hokuf, B. R., Jul. 22, 1996, DuPont Somos Solid Imaging Materials Group, private communication.
- [13] Chiaverini, V. and G. Jeszensky, "Sintered Stainless Steel," In: Advances In Powder Metallurgy, J. M. Campus and R. M. German (eds.), vol. 5, Metal Powder Industries Federation, Princeton, New Jersey, 1992, pp. 359-372.
- [14] Walczyk, D. F., "Rapid Fabrication Methods for Sheet Metal Forming Dies," 1996, Ph.D., Massachusetts Institute of Technology.

Rapid Prototyping of Fine Ceramics

-Slurry Casting Using Silicon Rubber Mold-

by

Takeo Nakagawa, Hiroyuki Noguchi

1. Introduction

Layered manufacturing is a rapid prototyping method which is drawing attention for being able to produce real models directly from three-dimensional CAD data. The most commonly used rapid prototyping is the laser stereolithography method using photopolymer resins. Recently, models made by the method can be converted to metal by the lost investment casting. For ceramics parts, layered manufacturing using powder as the material was considered as an ideal method¹⁾, but due to the low density of the R/P model, at the moment, slurry casting is the only method which can be applied to manufacture these parts from the practical view point.

In this study, the method of producing green powder parts by copying models using highly practical slurry casting shown in Fig.1 was investigated. Generally, plastic molds are used as the molds for copying in slurry casting, but in terms of separability from the mold, disassembly

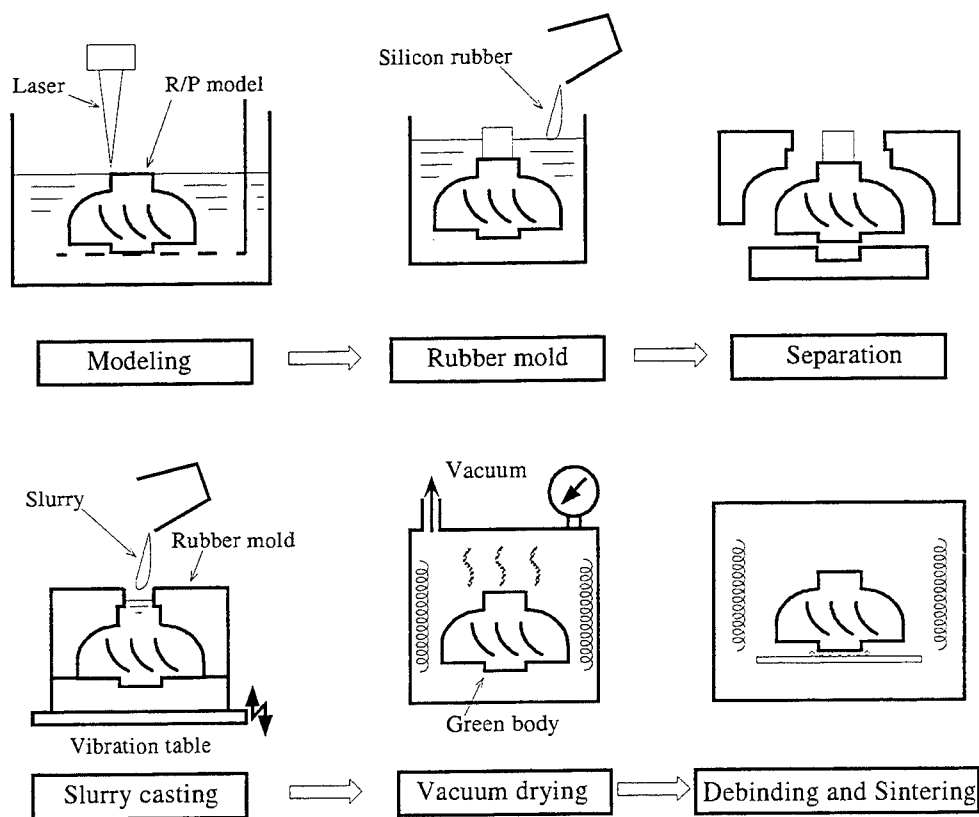


Fig.1 Forming process for slurry casting of fine ceramics using silicon rubber mold

of the mold, and wear of mold, the use of silicon rubber molds should prove to be more advantageous. Similar method has been reported to have been successful in the production of Si_3N_4 turbochargers by using metal molds and a special binder and heating. Nothing is known about of this method yet. Experiments to find a binder for slurry casting in room temperatures using rubber molds without water absorbability showed that there is an extremely promising binder²⁾ made of water soluble phenol developed as a sand mold for casting. As a result of using this binder, a rapid prototyping method for ceramics with a high level of practical use was developed.

2. Forming Method

Fig. 2 shows the forming process applied in this experiment. First, the laser stereolithography model is copied onto silicon rubber to make the rubber mold, ceramics slurry containing water and binder is poured into this rubber mold, and the forming process is carried out. Because the rubber mold has good copiability but is not water-permeable, excessive binder content will cause the green part to collapse after debinding even if the slurry had solidified. For this reason, it is necessary to keep the binder content as low as possible in the process. In this experiment, two types of green parts were made-a simple venus status (using type A slurry) and a complicated turbo fan (using type B slurry).

First, the percentage of alumina powder making up the green part was set at 48% for type A and 47% for type B. Investigations were also carried out on the percentage of mixing the binder, hardener, dispersion agent, defoaming agent, and water in slurries containing 52% and 53% binder to make slurry with good liquidity. This slurry was poured into the rubber mold to produce the green parts. After the slurry hardened, the green parts were removed from the rubber mold, after which vacuum drying, debinding, and sintering were performed.

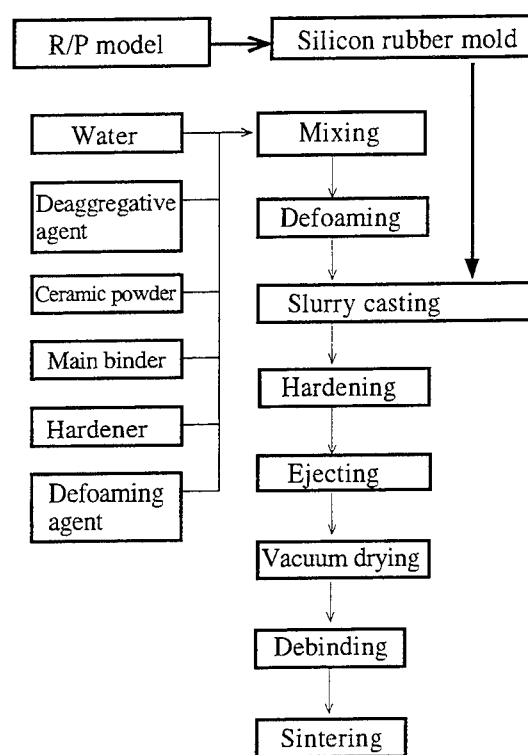


Fig.2 Forming process of ceramics

3. Experiment results

(1) Making the slurry

Taking into consideration the sintering characteristics of alumina ceramics, the binder content making up the slurry was set at 52 vol% for type A and 53 vol% for type B. The problem with these binder contents was how to make a slurry that can be poured in easily, has low viscosity, and will produce green parts with appropriate strength. The results of preliminary experiments showed that the slurry viscosity is affected by the content of the binder considerably. Therefore for type A, the binder content was decreased to the level the green part did not collapse when separated from the rubber mold. Table 1 shows the mixing ratios of the type A and type B slurries used in this experiment.

It was also found that the order of mixing the materials is important for making low viscosity slurry. To make the slurry, first appropriate amounts of water and dispersion agent are mixed (too much dispersion agent will on the other hand cause the slurry viscosity to increase). Alumina powder is mixed with this mixture little by little at a high speed using a mixer to disperse the alumina powder agglomerate into primary particles. Next, the binder is added, followed by the hardener, and defoaming agent. This process was found to produce a low viscosity slurry.

(2) Slurry viscosity

Fig. 3 shows the relation between time and slurry viscosity when the hardener is added to the type A and B slurries used in the experiment. The horizontal axis indicates the time from the mixing of hardener into the slurry. The hardener was mixed for 15 seconds. Measurement results showed that the more the binder, the higher the slurry viscosity, and the quicker the hardening speed. In this experiment, the amount of

Table 1 Mixing ratio of materials

Material	Mixing ratio (vol%)	
	Type A	Type B
Alumina powder, Average size: $0.5 \mu\text{m}$	48.0	47.0
Main binder (water soluble phenol)	8.5	19.3
Hardener	1.9	3.0
Dispersion agent	0.6	0.6
Water	41.0	30.1
Defoaming agent	≤ 0.0001	≤ 0.0001

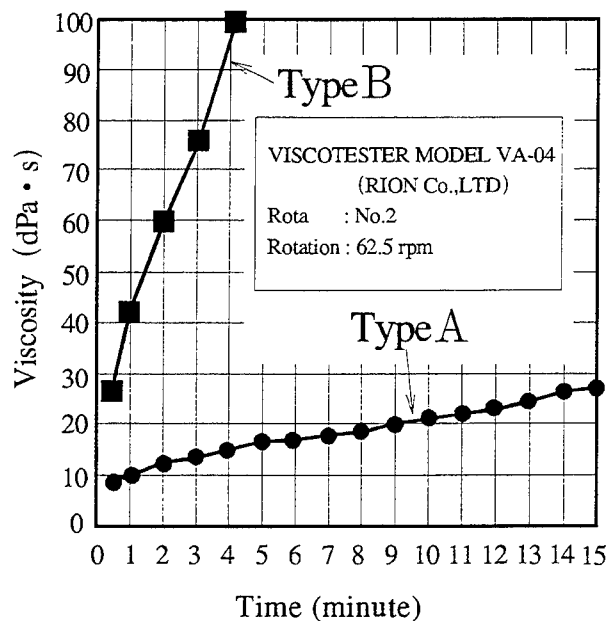


Fig.3 Relation between time and viscosity

hardener added was 20 wt% of the binder. The speed at which the slurry hardens can be investigated using the amount of hardener mixed and the type of hardener used. When the amount of hardener added is reduced, the hardening speed slows down but the demerit is it takes a long time for the green part to reach the strength at which it can be removed from the rubber mold. On the other hand, when the hardener amount is increased, it reduces the time taken for the green part to reach the strength at which it can be removed from the rubber mold, but the demerit is the slurry viscosity increases rapidly, and this decreases the time the pourable low viscosity slurry state is retained. The higher the viscosity of the slurry, the more the bubbles produced during pouring will not escape.

When the content of the hardener was increased for the type B slurry during one process performed, it was found that the pouring time was short (90 seconds), but the turbine-shaped green part could be removed in one hour. In this case, however, it was difficult to perform vacuum defoaming of the slurry after the hardener was added.

The slurries used in this experiment were also found to undergo thixotropy when the binder was added. For this reason, the viscosity increases according to the amount of binder added. For slurries not added with the hardener, it was possible to maintain low viscosity at a uniform level by adding vibrations. Even when the hardener was added, the vibrations added helped to slow down the speed at which the viscosity increased.

The slurry is poured while placing the rubber mold on vibration table and vibrating it. Because this pouring process is performed in air, a slight amount of bubbles were found in some of the complex shaped green parts. But it should be possible to produce bubbles-free green parts by carrying out the pouring process in vacuum.

To compare the viscosity of the slurry containing binder and that not containing a slurry containing alumina powder, water, and deflocculant and having a powder density of 48 vol% was made and its viscosity was measured. The results showed that slurry that does not contain binder has a very low viscosity of 0.6 dPa-sec, indicating that the binder amount affects the viscosity of the slurry to a great extent.

(3)Strength of green part

The green part must have sufficient strength to be removed from the rubber mold after the slurry solidifies. The strength is determined by the amount of binder contained and the amount of binder hardened. In this experiment, two types of rubber molds with different shapes were used. The statue (Venus) -shaped green part was easy to remove from its rubber mold due to its simple shape. The green part strength is sufficient if it does not collapse when held by the hand. The strength of the turbo fan-shaped green part on the other hand has to be increased because the contact area between the rubber mold and green part is large and the wing part is thin. The compressive strength before and after drying was studied for the type A and type B slurries used in this experiment.

Table 2 shows the results. The compressive strength of the green part when removed from the mold was 5 kgf/cm² for type A and 76 kgf/cm² for type B. After vacuum drying these green parts for one hour at 100°C, the compressive strengths increased for both types, to 85 kgf/cm² for type A and 300 kgf/cm² for type B. The reasons for the increase are; the green part shrinks when dried and causes the strength to increase, and the heating of the green part causes the unhardened parts of the phenol resin (the binder) to harden and this increases the strength.

Table 2 Compressive strength of green parts

	Compressive strength (kgf/cm ²)	
	Before drying	After drying
Type A	5	85
Type B	76	300

One method of increasing the green part strength quickly is to heat the rubber mold after pouring in the slurry. But in this case, it is essential to seal the mouth of the rubber mold for pouring in the slurry to prevent the moisture in the slurry from evaporating. If evaporation takes place, the green part may shrink and crack. As the green part will not shrink as long as there is no evaporation, cracking will not occur even if the green part is removed after a long time.

(4)Drying, debinding, and sintering of green part

Due to the good liquidity of the slurry used, vacuum defoaming was also carried out satisfactorily. The green part was found to contain a high amount of water after hardening and this was removed by vacuum drying quickly. After drying, air channels made up of holes from the water escaped out were formed in the green part. The presence of these air channels enabled the high speed debinding. Because the phenol resins used as the binder is a thermosetting resin, the green part did not deform easily even when heated during debinding. The normal sintering was performed after debinding. Fig. 4 shows the effects of the sintering temperature and retention time on the

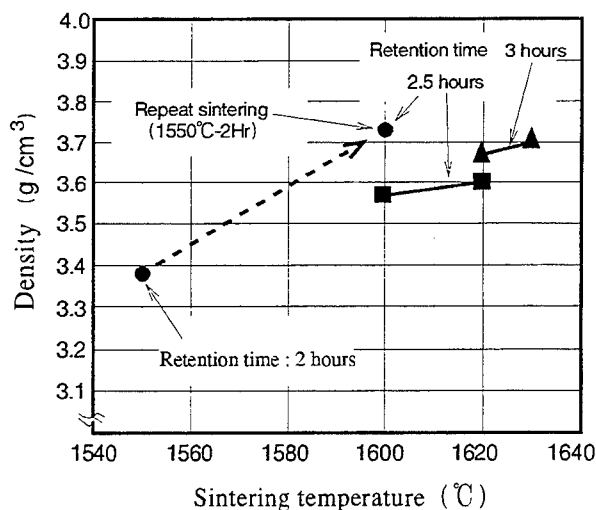
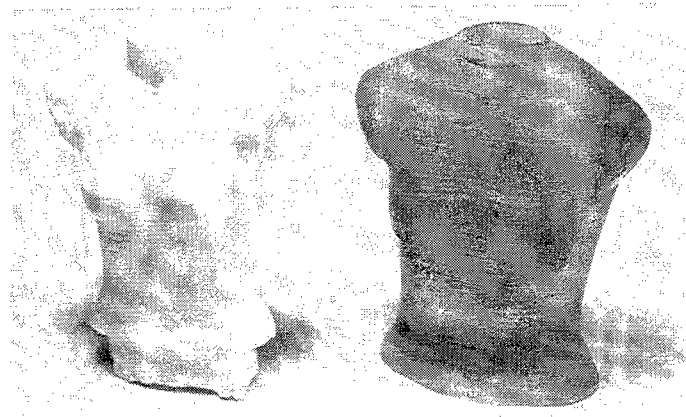


Fig.4 Effects of sintering temperature and retention time on density

density, and Fig. 5 shows the laser stereolithography model ,the rubber mold and the sintered product.

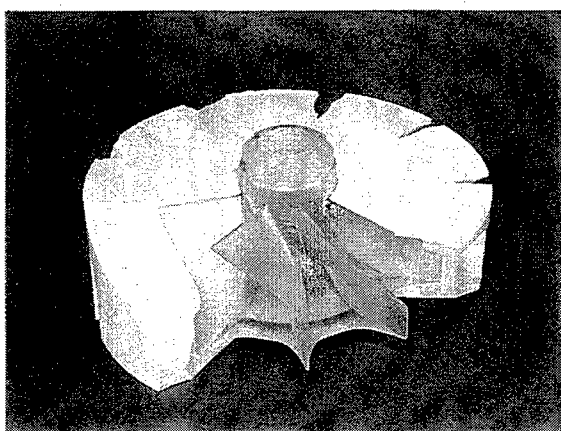


Enlarged surface of sintered product

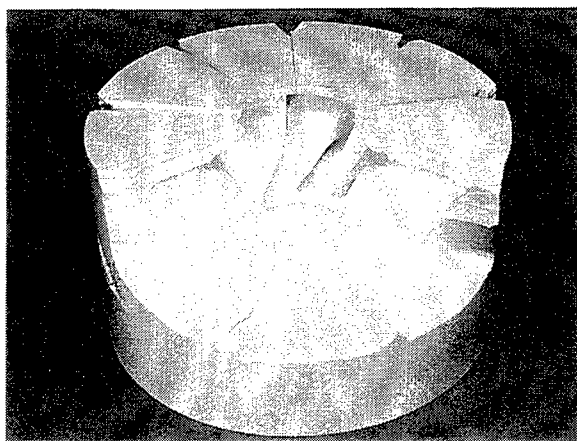


Sintered product

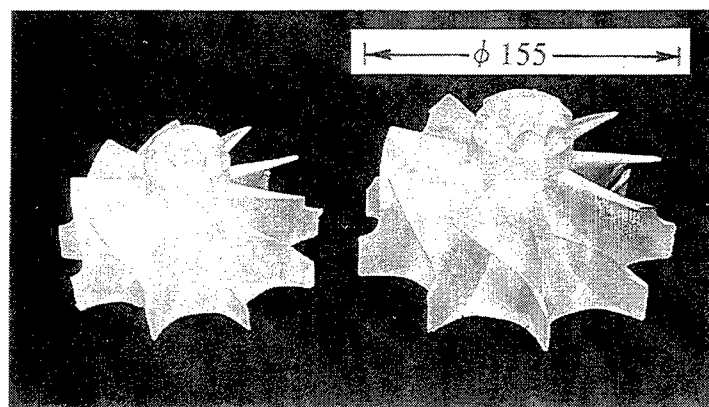
Model



Rubber mold



Separated rubber mold



Sintered product

Green part

Fig.5 Laser streolithography model,rubber mold and sintered product

4. Conclusion

In this study, a rapid method of producing ceramic parts was developed. In the method, slurry is poured into a rubber mold copied from a laser stereolithography model made by layered manufacturing to obtain the green part. For the type A slurry, the weight of the sintered part was 100g and the porosity was 6%. For type B, because the weight of the sintered part was heavy (700g), and the sintering temperature and time were insufficient, the porosity was 12%, but this could be improved.

When the slurry had a certain level of viscosity and thixotropy, the binder and powder did not separate after pouring and forming, and the density of the green part was even. In addition, because this method produces air channels in the green part, debinding is good, which makes the method applicable to large ceramic green parts. Moreover, as the silicon rubber mold can be used repeatedly, the method can be applied not only to trial productions but small-lot production as well. The good copiability of the slurry also enables ceramic green parts copied with detailed patterns to be produced.

These above results indicates that this method may become one of the main methods of manufacturing ceramic parts using layer manufacturing. At present, studies are being carried out on a slurry casting method using metal powder as an attempt to apply this method to molds.

Acknowledgement

Authors would like to say their thanks TOYOTA MOTOR for giving us 3D CAD data of turbo charger roter, CMET for supplying the its R/P model, Mitutoyo and MIYAGAWA KASEI INDUSTRY for sintering test of green part.

Reference

- 1) Stereolisography of ceramics: T.Himmer, T.Nakagawa, H.Noguchi; Proc. of the 10th the Japan R/P Symposium
- 2) Japanese Patent Application 1989-215750

SLIP CASTING AS A RAPID TOOLING PROCESS

C. Ainsley and K.K.B. Hon
Rapid prototyping centre
Department of industrial studies
University of Liverpool, UK

ABSTRACT

The paper discusses the slip casting of stainless steel as a method of forming injection moulding tooling. Main steps involved in the precision slip casting of stainless steel and the effects of major parameters such as casting rate have on accuracy are fully discussed. The slip casting process has numerous technical advantages over conventional and rapid tooling processes especially there is strong potential for producing mass production tooling.

INTRODUCTION

The slip casting process has been used for hundreds of years in the ceramic industry for the production of products such as tea pots and toilets. The basic process of slip casting involves the suspension of a powder material in a solution. The powder and solution mixture (slip) is then cast into a porous mould which removes the solution from the powder by capillary action. This then leaves the powder in the form of the mould. This powder part (green part) can then be removed from the mould and then fired in an oven in order to give it strength. The objective of this investigation is to study the possibility of forming injection moulding tools via this method. So raising the concerns of dimensional accuracy, surface finish, and the mechanical / thermal properties of the resulting tool, these are the main factors investigated

The principal reason for undertaking this investigation, was due to the growing industrial demand for low cost tooling, which can be produced in a greatly reduced lead time, to that of conventional tooling methods. The current market for moulds and dies in the USA is about 20 billion dollars¹. The lead time for the delivery of a injection mould, in the USA ranges from 1200 to 3800 hours², depending on the complexity and the size of the mould. For these two reasons there is great interest in the variety of rapid tooling methods that are evolving. This is also the rational for investigating the slip casting method as a potential route to the production of tooling.

The perceived reasons why slip casting has some competitive advantages over conventional and Free Form Fabrication (FFF) tooling methods are:

- The method of production is both suited to that of one-off production and mass production, thus allowing flexibility.
- The process costs are extremely low with very little material wastage and little manual intervention.
- The process is a relatively low skilled in most aspects of the process cycle, this is very different to that of conventional tool making.
- The forming of the porous moulds can be done in a number of ways, such as casting from a FFF model, machining of the mould from a solid block and additionally the material can be carved / sculpted.

- The process has the potential to cross over into other tooling areas such as EDM electrode formation, die casting tools, press tools and possibly, punch tools.
- The process will possibly allow the production of complex composite tools i.e. A tool can be formed with a very hard surface material and a softer backing material, which could be used for either cost or thermal considerations.
- The process has the ability, to allow the production of designer cooling systems³. This is where cooling channels for the injection moulding tool, can be designed for that specific cavity and core. The main advantage being that the cooling system will be optimised because of freedom from geometrical constraints imposed by conventional methods.
- The advantages of this process over that of direct tool production on one of the current FFF systems, is that the users are restricted to those systems and their system accuracy. Also, if the tool is produced directly on the FFF machine then, the stair case effect has to be removed from the tool, in what could be a very hard material.
- The process offers greatly reduced lead times to that of the conventional tooling methods, which can be up to 6 months⁴. It is estimated, that tools produced via this routes should take under two weeks to produce, for a given pattern.
- It is also possible that the process will be useful for the production of other products apart from tooling e.g. filters, gears, injection moulding machines reciprocating screws and in general low volume wear resistant parts.

As is apparent from the above points, there are a lot of possible applications of this process, giving advantages over both conventional and FFF injection moulding tool forming methods. The main reasons for the investigation into this process is the speed, cost and the range of unconventional tooling materials that the process will possibly allow to be formed via this route.

THE PROCESS

The work carried out into the process of casting Stainless steel was an extension of the work started by Lidaman⁵ and then later by Hausner⁶. The basic process route of slip casting is illustrated in figure 1. The steps involved in the production of a slip cast part are as follows:

1. Casting of the porous mould on the FFF model. It is important that the FFF model is treated in order to ensure that the model is released from the mould and that bubbles do not form on the surface of the mould.
2. Mixing of the powder and the solution. It is important the two parts are completely mixed and the powder is distributed evenly throughout the solution.
3. Once the two parts are mixed properly, the solution can then be poured into the porous plaster mould. It is important to ensure that bubbles are removed from the mixture.
4. Once cast, the part is left to dry in the mould until all the solution is removed from the powder.
5. The part can then be extracted from the mould and any casting features can be removed at this stage. It is important that the part is not removed from the mould unless it is completely dry, as there is some indication that the part can be distorted by the handling of a powder part, if not in the dry state.

6. The part is then place in a oven and fired until the desired density is achieved.
 7. Once fired the part is then infiltrated with a lower melting point material, in order to give the part a full density.
- After infiltration, the part can be polished for the mounting onto the mould base.

ACHIEVING ACCURATE HIGH QUALITY SLIP CASTINGS

There is an obvious need to produce castings that are accurate, but it is also desirable to have the castings with as high quality possible. The quality is measured in terms of the following criteria:

- Surface reproduction.
- Density. This should be as close to theoretical as possible, i.e. 74 % of solid density for mono sized particles and 79% for bimodal particles sizes ⁷.
- Particle size distribution. This should be uniform through out the sample.
- Gas entrapment. This should be minimised within the sample.
- The slip should completely fill the mould, which allows complete shape and feature reproduction.
- The part should have a green strength that will allow part processing.

Hausner ⁶ identified that the basic variables of the process which affected the quality of the parts were:

- | | |
|---|-----------------------------------|
| 1.\ Casting rate (Rate of drying in the mould). | 2.\ Mould material |
| 3.\ Particle size and shape. | 4.\ Solid to liquid ratio. |
| 5.\ Moisture content of the mould | 6.\ Air entrapment. |
| 7.\ Type and amount of deflocculant. | 8.\ Density of the liquid. |
| 9.\ Reaction of the powder with the liquid. | 10.\ Mould porosity |
| 11.\ ph of the solution. | 12.\ Temperature of the solution. |
| 13.\ Rate of drying after elimination from the mould. | 14.\ Slip viscosity |

All these variables were stated to have an effect on the quality of the slip cast parts produced. It has also been shown that some of them affect the accuracy of the parts produced. Of those variables put forward by Hausner ⁶ there is apparent interplay of the variables with factors such as viscosity being affected by the particle size, particle shape, ph of the solution, liquid to solid ratio, reaction of powder with liquid, type an amount of deflocculant and density of liquid used. Viscosity is also a very important parameter in terms of achieving a good casting. If the viscosity of the mixture is too high it will aggravate air entrapment, give poor detail pick up and possibly will prevent the mould from filling correctly. Therefore it can be seen that achieving a mixture with a low viscosity is important. Of the factors affecting the viscosity, one of the most important is that of the ph of the mixture, as this allows alteration of the viscosity without any detrimental effects on the other variables.

The ph of the mixture can effect the viscosity because the ph is a measurement of the ion content in aqueous solution. Stainless steel with the addition of the correct chemicals, can get the particles to react in such a way by forming a double electric layer around each of the powder particles as illustrated in figure 2. This helps to suspend the particles in the solution, by the forces of repulsion that are generated by these electrically charged layers.

Previous research by Hausner⁶ into the optimum pH value of the stainless steel slips, derived a value around 9.8. It is assumed that Hausner⁶ made the assumption that the slip acted in a Newtonian manner as there is no information to the contrary. By repeating same experiments using different deflocculant and powder material to that used by Hausner⁶, it is considered inappropriate to assume the slip to be Newtonian, as slips using other powders do not act in this manner. The experiments were carried out using a constant stress rheometer and a Philips PW9421 pH meter with a Unicam CE1 glass electrode. The results of the viscosity measurements, of mixtures of the same composition but with different pH values, can be seen in figure 3.

As can be seen from the figure 3 which shows the viscosity's against shear stress for mixtures of the same powder/liquid ratios but at different pH values, the slip acts in a non-Newtonian manner. If we consider the viscosity's at shear rates equivalent to that of pouring, which is in the range of 0.1 to 1 γ/s ⁸ the slip seems to act in a Newtonian manner. This can be seen in figure 4, which is a plot of viscosity at pour shear rates over the range of pH values, calculated using cross curve fit algorithm.

It is apparent from figure 4, the viscosity is lowest for the slip when the pH value of the solution is about 9.7 which corresponds to the values derived by Hausner⁶. The viscosity plays an important role in achieving of a good casting and the control of the pH of the solution allows the solid to liquid ratio to be higher than if pH was not controlled. The reason why this is important is that it allows the process greater control on the casting rate of the slip in the porous mould, which has been shown to affect the accuracy of the casting. This is of extreme importance in this application of this process.

The effect of the casting rate can be seen in figures 5 & 6. These show data derived from an experiment where two solid to liquid ratios were selected. The two selections being the extremes of the workable range. The high solid to liquid ratio gives a very high viscosity solution which is usable on simple shapes for casting. It is important to note that if the ratio was any higher, the slip enters into the region of unusable. At the other end of the range, with a low solid to liquid ratio the slip has a very low viscosity, which makes the production of good castings relatively easy. Further decrease of the solid/liquid ratio does not seem to give large gains in reduction of viscosity.

The mixtures were then cast into plaster moulds which had been soaked in an aqueous solution of release agent for different amounts of time. The purpose of this was to control the moisture content of the porous plaster moulds. Once dry, the resultant casting was then measured using a CNC co-ordinate measuring machine. Figures 5 & 6 show the % shrinkage of the diameter of a cylindrical cast sample. As shown by the data, the faster the casting rate the better in terms of the reduction of shrinkage and increase in repeatability, which is desired in order to achieve an accurate tool. The problem with the casting rate being very high is that it can cause difficulties in terms of the quality of the part after firing. This is assumed to be due to the migration of the smaller particles to the surface of the porous mould, caused by

the high casting rate. This causes the surface of the cast part to be hard and on firing the part will either crack, or will develop a crazy paving effect on its surface. For this reason, it is important that the casting rate is carefully controlled in order to give the desired effects of accuracy and cast parts which will sinter correctly.

SINTERING OF THE GREEN SLIP CAST PARTS

The firing of the samples has been performed in a tube furnace from temperatures ranging from 1000 to 1300 degrees C. The samples are placed in an alumina boat and then sealed into a Quartz tube into which a gas comprising of 10 % hydrogen and 90 % Argon is pumped in. It is important to note that the gas has to have an extremely low dew point. This is especially important at the low sintering temperatures. The sample was placed on the alumina boat in order to reduce distortion due to friction generated during the sintering process⁹. The quartz tube was used to cope with the massive thermal shock of the process e.g. room temp to 1200 degree C in 20 minutes. It was found that neither alumina or porcelain tubes could tolerate this thermal cycling and would usually crack causing oxidation of the part.

The Sintering of the slip cast samples has many parallels to that of sintering of metal injection moulded (MIM) parts, in terms of the starting green density's and the fact that the particles are spherical. The main variation of the slip cast green parts is that there is a lot less binder in the slip cast parts, with only less than 0.34% (by mass) or 5% vol in comparison to that of MIM which is in the region of 20 - 40 % vol¹⁰. In terms of sintering, the slip cast parts do not really need to have a debinding stage in the firing process and therefore can be put into the furnace at temperature. In terms of the samples used, it usually reached the temperature of the furnace in under 20 minutes.

The disadvantages of the green slip casting parts in the firing process, is the release agent that sticks to the green parts after extraction from the mould. This generates problems, in terms of pulling particles from the surface of the green part as it burns during the firing process. The problem being that the particles can then stick to the part in the sintering process, causing a rough surface on the sintered part. The effect of this can be reduced by firstly sintering the part at a relatively low temperature. At this stage the particles can be brushed off by hand and then the part can be resintered at a greater temperature to achieve the desired density. However, it should be noted that this problem usually occurs only when using relatively large powder particles (average particles size of 20 microns). These will usually have a greater casting rate than small particle sizes, so the soak time of the porous moulds needs to be longer thus giving rise to more release agent on the green sample.

The sample once at the maximum density which allows the keeping of the accuracy with low distortions, can then be infiltrated with a lower temperature metal. One of the most common metals for infiltration into the steel parts is copper alloys. Copper alloy also works on stainless steel, but another infiltration alloy under investigation at this point is aluminium. This is not as simple as infiltration of copper alloys but could possibly offer some advantages to the final injection moulding tool.

SUMMARY / CONCLUSIONS

The factor that is important in terms of the accurate slip casting of stainless steel powder is the casting rate, which can effect the shrinkage of the cast part and the shrinkage variation. To achieve accurate parts, the faster the casting rate the better, within the range of casting rates studied in this investigation. However, obtaining the fastest casting rate possible is not always the best solution, as the faster the casting rate, the greater seems to be the migration of the smaller particles towards the surface of the mould, which can cause problems in the sintering process.

The method used in the investigation is not the only method available for the control of the casting rate. Methods such as changing the porosity of the plaster mould (by altering the water to plaster ratio), control of temperature of the slip, changing of the particle size and different casting methods are also believed to have an effect, such as (vacuum casting or centrifugal casting processes). Also under consideration was quality of the casting. It was stated that many variables that can affect the quality of the cast part. One of the most important with regards to the casting process is the viscosity of the slip. The important factor in control of viscosity was the ph of the slip. This can have a large effect on the viscosity and therefore on the quality of the slip cast part.

The sintering stage of the process is not dissimilar to that of the sintering parts produced via the MIM process. The major advantage is that very little binder is used in the process. It is also important to note that the sintering in this application, is only to the stage where accuracy is maintained with very little distortion and that the porosity in the sinter parts are still interconnected. This is to allow the infiltration material to flow into the sintered part and thus give the part full density.

The results obtained so far has given great encouragement that slip casing will be suitable in terms of accuracy. It is also expected that the number of shots that the injection moulding tool produced via this method is estimated to last, to be at least 20,000 shots. Considering that the Keltool process which is similar to, the slip casting, can produce injection moulding tools which can last over 1 million shots¹¹. Another comparison which can be taken into consideration is that epoxy resin tools have lasted over 100,000 shots¹². This is only the start, with super hard composite tools, there is no reason why slip casting method, cannot be used to manufacture injection moulding tools which can be used for mass production.

REFERENCES

1. *Destfani, J.D.*, "Mold and die making in transition", Tooling and Production, April 93, pp 69-71.
2. *Shanahan, J.E.*, "CNC EDM in Die and Mold Production", Presented at the SME manufacturing, 1992.
3. *Sachs, E.M, Cima, S, Allen, E.*, "Injection molding by three dimensional printing", Proceedings of the 4th European conference on Rapid prototyping and manufacturing, 1995, pp 285-297.
4. *Altan, T, et al.*, "Advanced techniques for die and mold manufacture", Annals of the CIRP, vol 42, no 21, 1993, pp 707 -717.

5. *Lidman, W.G, Rubio, R. V*, "An Investigation of the slip casting mechanism as applied to stainless steel powder", Atomic energy division Tech paper (Sylvania electrical products), 1956.
6. *Hausner, H.H*, "Slip casting of metal powders", *Perspective in powder metallurgy*, 1967, pp 221-238.
7. *White, H.E, et al*, "Particle packing and particle shape", *Journal of American ceramic society*, vol 20, no 20, 1937, pp 155-166.
8. *Barns, H.A, Hutton, J.F, Waltera .K*, "An Introduction to rheology", Elsevier, 1989.
9. *Amaya, H.E*, "Size and distortion control in MIM processing", *Advances in powder metallurgy*, vol 2, 1991, pp 285-296.
10. *Ruder, A, Buckremer, H.P, Hecker, R, Stover, D*, "Wet powder pouring an accelerated PM process", *Proceedings of the int conf on powder metallurgy aero 91 Lousanne*, 1991, pp 8-1,8-8.
11. *Anon*, "Rapid Tools in sintered metal", Marketing material by 3D systems and Keltool, 1995.
12. *Jenkins, B.A*, "Cast plastic tooling the new hope in tooling", *Automotive Plastics RETEC* 1987, pp 164 - 167.

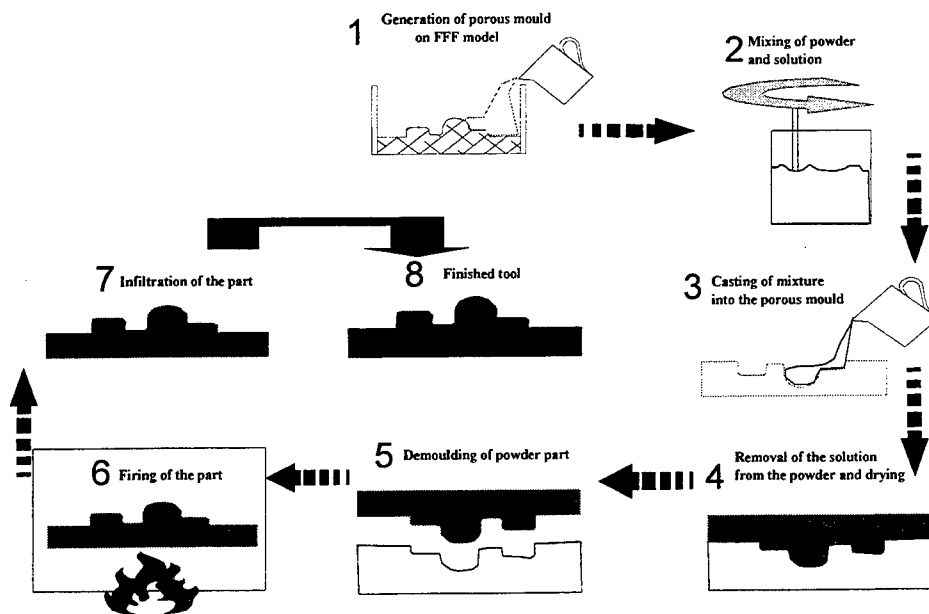


Figure 1 The slip casting process

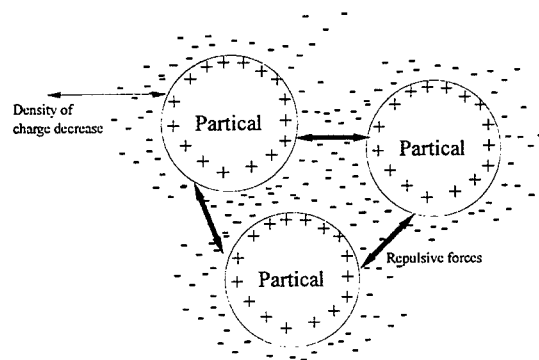


Figure 2 The double electric layer

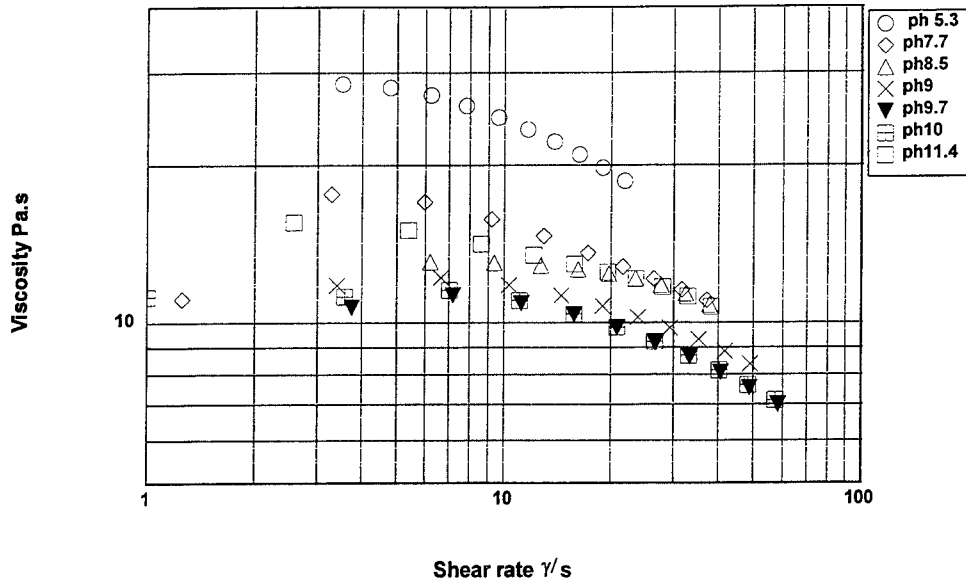


Figure 3 Viscosity against shear rate over a range of ph values

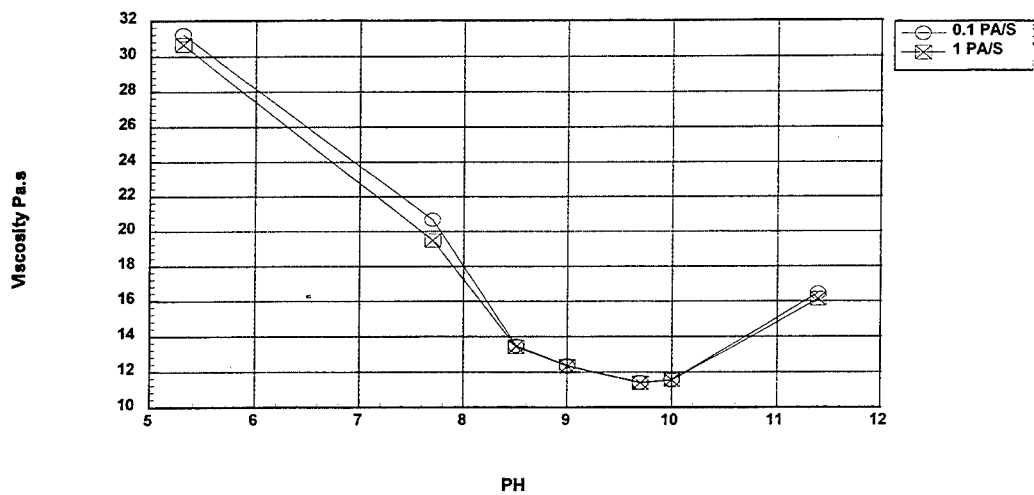


Figure 4 Viscosity against ph for shear rates equivalent to gravity pouring

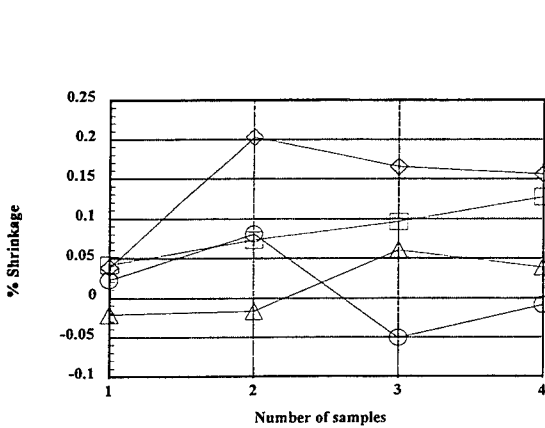


Figure 5 Shrinkage variation with casting rate with high solid to liquid ratio

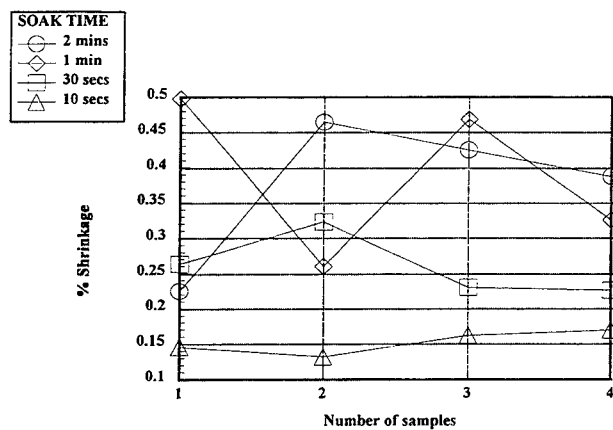


Figure 6 Shrinkage variation with casting rate with low solid to liquid ratio

WEAR & FAILURE MECHANISMS FOR SL EDM ELECTRODES

Alan Arthur*, Phill Dickens*, Chris Bocking, Richard Cobb***

***Department of Manufacturing Engineering & Operations Management,
The University of Nottingham, UK**

****GEC-Marconi Materials Technology, Hirst Division, UK**

ABSTRACT

The principle of Electro-Discharge Machining (EDM) electrode manufacture using rapid prototyped StereoLithography (SL) models has been proposed and discussed in previous published material by the authors [1,2,3,4]. Applying a thin electrodeposited coating of copper to SL models has provided a direct route from model to tool cavity. A number of current factors present limitations to the application of these electrodes. This paper outlines and addresses the factors affecting electrode quality and performance. Premature failure of SL electrodes is attributed to a number of wear and failure mechanisms which are being investigated at The University of Nottingham. An overview of experimental and theoretical work is presented.

1. INTRODUCTION & BACKGROUND

The recent emergence of Rapid Prototyping (RP) techniques has provided a route to faster product modelling. A number of commercial process routes from models through to tooling are currently being developed. The integration of RP with established downstream tooling techniques is essential to the continued expansion of the RP application base. This paper focuses on the manufacture of production tooling for injection moulding using RP models. The use of thin coated models as EDM electrodes is discussed. It is intended that the methodology of process optimization being undertaken with SL models can be applied to EDM electrodes manufactured by alternative RP technologies. The potential for application of RP to EDM electrode production has been discussed in previous published material by the authors [1,2,3,4], and it is sufficient to provide only a broad outline here.

The increase in demand for small tools for plastics and rubber component production over the past ten years is likely to continue. This has applied pressure on tooling manufacturers to reduce lead times and costs. EDM is a process widely used in the manufacture of the mould cavities for plastics and rubber. The EDM work typically accounts for 25%-40% of overall production time. A large proportion of the EDM time is consumed by the manufacture of electrodes [5]. The application of RP to electrode manufacture could provide an opportunity to move from product verification to tooling with significant reductions in time and cost. A number of possible routes to RP electrodes have been proposed [3], and classified as 'direct' or 'indirect'. Direct production is the use of RP models as electrodes, whilst indirect routes use RP cavities (or masters) as an

intermediate step to electrode manufacture.

To date the various techniques applied to the transformation of RP models to electrodes have not provided a realistic alternative to conventionally machined electrodes. At the University of Nottingham thin electroplated copper coatings have been applied to metallized StereoLithography (SL) models and these have been used as finishing electrodes. The functions of roughing and finishing electrodes for EDM die sinking are fundamentally different. The roughing electrode is an approximation of the geometry required in the cavity, with respect to size and detail. The primary function of this electrode is the bulk removal of material from the workpiece. However, the closer this electrode is to the profile of the required cavity the less work is needed to be done by the finishing electrode. The function of the finishing electrode is to provide a cleaning cut which generates the final profile and detail of the tool cavity. To satisfy their specific functions the roughing and finishing electrodes are manufactured to different specifications.

The finishing electrode is not used to remove substantial volumes of workpiece material but must maintain its geometry through low tool wear. The surface finish of the electrode must be as smooth as possible to reduce the necessity for post processing of the tool surface. It is clear from experimental trials that the SL electrodes are currently unsuitable for mass material removal; where high amperage applied during EDM generates high surface temperatures at the electrode which cannot be dissipated effectively through the SL substrate. This results in premature failure of the electrode. An appropriate thickness for the copper coating has been determined, which will sustain EDM finishing cuts using an optimized machine set-up [4]. Simple electrode profiles have been used to erode cavity depths up to 16mm (Figure 1) far in excess of that usually required of a finishing cut, i.e. up to 1mm. The low Material Removal Rate (MRR) makes the use of the coated electrodes for depths of several millimetres uneconomic with respect to machining efficiency.

The methodology for producing SL coated finishing electrodes is detailed in earlier work [2,3,4] and it is appropriate to provide only a summary of the processing steps here:-

- i) Production of SL model in SL5170 epoxy resin, using ACES™ build @ 0.15mm layers
- ii) Application of high conductivity silver paint (10µm thickness)
- iii) Electrodeposition of copper from acid copper sulphate bath solution (175µm thickness)

2. COPPER COATING SL MODELS

2.1 Sizing of SL models - surface offsetting

Deposition of copper onto SL models causes oversizing, which can compromise geometric accuracy. It is necessary to determine the proposed thickness of deposition and undersize the SL model accordingly. Electrodeposition generates a non-uniform coating, favouring particular features. This variability can be controlled to a degree but it is impossible to completely eradicate the problem.

The requirement for a mean copper deposit of 175µm has been determined through experimental work, to achieve EDM performance. The external surfaces of the CAD and SL model must have a negative offset applied to accept this deposit.

2.2 Controlling copper deposition

The performance of plated EDM SL electrodes is dependant on the accuracy and quality of the applied plating. The uniformity of an electrodeposit over the surface of a plated model will depend in part on the way in which the current density varies from point to point over the surface (primary current distribution). Also the type of solution and operating variables contribute to variability (secondary current distribution or Macro Throwing Power - MTP). Control of plating determines the accuracy of the electrode and its EDM performance. The factors affecting current distribution and MTP are; Geometry, Electrical/Electrochemical, Chance factors.

Geometric considerations relate to the size as well as the shape of the model. Electrical/Electrochemical control concerns the state of the electrolyte and the model. Chance factors are somewhat more difficult to control relating to the condition of the surface of the model, the necessity for pretreatment, and variability during the plating process.

2.3 Achieving coating quality

Simple model geometries used to date have presented few problems of material distribution, however, work is now progressing to more complex surface profiles requiring measures to be taken with respect to copper deposition. A number of techniques are currently commercially used to improve metal distribution on the model during plating :-

- Screens - Screens are physical shielding elements which are used to selectively blind areas of the model thus reducing copper deposition in those areas.
- Robbers - These are additional conductive elements, suitably placed adjacent to regions of the electrode attracting a greater thickness, that "rob" a greater proportion of the current and minimise thickness variations.
- Conforming anodes - Instead of using a simple geometry anode (source) a unit conforming to the profile of the model can be produced. Unfortunately this can be expensive and is unlikely to be practical for one-off prototype plating.
- Anode focusing - This technique employs screening positioned close to the model, focusing the fields through onto the model where required.
- Bi-polar electrodes - These are conducting elements that do not comprise part of the electrical circuit but nevertheless, when suitably placed in recesses or cavities where deposit thicknesses will be low, generate additional plating fields in these regions, again improving the metal distribution.

These techniques are further enhanced by considering size and position of the model relative to the anode and the size and shape of the plating bath, which all affect the polarisation field. Periodic reverse and pulsing are methods of varying the deposition rate to prevent preferential build up. Periodic reverse allows for the removal of excess deposits, whilst pulsing can generate a better quality of deposit through on-off current switching. Further information on current and metal distribution can be found in the literature but a good introduction will be found in reference [6].

To overcome problems associated with material deposition the above techniques are being considered for plating complex SL models. In addition other bath plating solutions are being tested with respect to coating properties and deposition.

3. OBSERVATIONS ON SL ELECTRODE WEAR & FAILURE

3.1 Electrode wear characteristics in EDM

Wear measurement of EDM electrodes is commonly described as Tool Wear Ratio (TWR) which is a volumetric calculation of material removed from the electrode relative to material removed from the workpiece. This TWR is an important comparator but does not identify the variability of electrode wear with respect to geometry. An understanding of the elements or features on an electrode which are subjected to a greater intensity of wear is of fundamental importance to their accuracy and performance. Using SL electrodes, it is important to provide a controlled deposit of copper allowing for sacrificial wear.

The volumetric wear of SL electrodes was measured for a number of tests with different thicknesses of copper coating. The thickness of coating had no apparent influence on the volumetric wear of the electrodes (Figure 2). For erosion of a 4mm cavity the average TWR was calculated as 0.6%. The performance of solid copper under identical EDM conditions was 0.5%. Electrodeposited copper is likely to contain some inclusions or contamination, and plating solutions are often modified with levelling and brightening agents. It is likely that these impurities effect the properties and efficiency of the copper. The difference in wear between deposited and stock copper appear to reflect this.

3.2 Classification of electrode failure

Electrode failure can be expressed as wear or catastrophic. Wear failure describes the loss of geometry of the electrode due to sacrificial material removal. This wear compromises the geometric definition of the electrode outside of its specified tolerance. Catastrophic failure occurs as damage to the electrode which renders it dysfunctional through rupture or distortion.

3.3 Electrode wear failure

As discussed in section 3.1 the general wear characteristics of a SL electrode are similar to a machined solid copper electrode. Currently SL electrodes are being tested for use in finishing cuts which generally will require a cut depth of less than 0.5mm. A shallow cut such as this does not introduce substantial wear at the electrode and therefore wear is not likely to cause failure, unless the copper layer is very thin at the outset. With improved plating techniques and EDM process optimization it may be possible to improve machining efficiency to use them as semi-roughing or roughing electrodes, and therefore apply these SL electrodes to deeper cuts. At that point wear is likely to be a more important factor.

3.4 Catastrophic failure

Catastrophic failure of SL electrodes manifests itself in a number of ways. All damaged electrodes appear to have failed due to overheating. Failure can be classified by the apparent damage. The following definitions are proposed:-

- Edge failure - Here the external edge or corner of an electrode receives a high concentration of spark discharges during EDM causing overheating and results in the copper layer splitting (Figure 3).
- Peppering - This effect is believed to be caused by inclusions or contamination of the copper deposit, which is are highlighted by the EDM process. The defect appears as multiple penetrations of the copper layer (Figure 4). More recent work has highlighted a possible problem with porosity introduced during the plating process, which the acid copper sulphate solution has a tendency to close up (Figure 5). This porosity may form the nucleus for peppering failure.
- Delamination - Delamination is seen as the rippling of the copper layer where it has delaminated from the SL substrate. Adhesion between them two is dependant on the physical bond with the metallizing interface. Differential thermal expansion of SL and copper, and the lack of bonding between materials is the most likely cause of this failure. Where an area of copper is bounded by edges which constrain free movement/expansion, the heat concentration results in a blistering of the copper (Figure 6).
- Rupture - Perhaps the most common damage to be found to date is the rupture of the copper layer (Figure 7). This failure was seen with all early tests using SL electrodes. Having performed a detailed optimization programme of tests with EDM this mode of failure has been virtually eradicated. The use of high amperage in EDM is the primary factor influencing this rupture, causing a spark discharge of an intensity too great for the copper layer to sustain. The excessive heat generated at the discharge explodes the coating where the thermal energy cannot be dissipated efficiently. The inability of the thin copper coating to transmit the spark energy is and will probably remain the single biggest obstacle to high material removal with these electrodes.
- Distortion - The build up of thermal energy in the electrode during EDM is in part due to the insulating properties of the SL substrate. SL resin reaches its glass transition temperature (T_g) around 60°C , above which the material softens. Where the SL model is coated with a relatively thin copper veneer this can result in distortion of the SL electrode. Once this begins to occur there is little support afforded to the copper veneer, and over a short time the composite electrode distorts (Figure 8).

The effects described above may combine to cause ultimate failure of the electrode. A more detailed understanding of their causes is required, to extend the life of the electrodes and their machining efficiency.

4. HEAT TRANSFER IN SL ELECTRODES

The influence of electrode coating thickness on the machining performance has been examined. Using electrodes of thicknesses in the range $100\mu\text{m}$ to $300\mu\text{m}$ the MRR performance was measured, applying an optimized machine set-up (refer to section 5.2).

Tests show electrodes with copper coating thickness of $150\mu\text{m}$ susceptible to failure. The behaviour and control of the EDM removal mechanism is not finite and there is inevitably some variability in electrode performance at any given coating thickness. Some electrodes with $150\mu\text{m}$ copper thickness were successfully used to erode the 4mm cavity depth without sustaining

damage. However, the likelihood of test failure can be avoided by using coatings of thickness exceeding $175\mu\text{m}$. Performance with respect to MRR for electrodes with copper between $175\mu\text{m}$ and $250\mu\text{m}$ does not appear to vary significantly. MRR for these thicknesses is typically $3.85\text{mm}^3/\text{min}$ (Figure 9). The performance of solid copper tablet electrodes under the same conditions as the above tests generate a MRR of $4.40\text{mm}^3/\text{min}$. It is reasonable to expect the performance of the coated SL electrodes to approach that of the solid copper as layers of progressively greater thickness are tested. This relationship is being investigated with coatings of greater than $300\mu\text{m}$ thickness.

The effect of coating thickness on MRR and failure is believed to be a function of the efficiency of heat or energy dissipation from the electrode front face, at the spark gap.

4.1 Differential linear expansion at the electrode

The work of Hague [7] established the thermal expansion characteristics of SL5170 resin. Plotting the data for SL5170 against copper an accelerating deviation is seen between the two materials with increase in temperature (Figure 10). Using copper coated SL electrodes inefficient heat dissipation induces stresses at the material interface, where the mechanical bond is subject to shear forces as the copper restricts the free expansion of the SL substrate. This results in delamination, thinning or tearing of the copper.

4.2 Heat dissipation

At the electrode

The ability of an SL electrode to absorb or dissipate energy during EDM is directly related to thickness of the conductive coating. Figure 11 shows the calculation of 'theoretical thermal conductivity' of test tablets. Composite coatings of $10\mu\text{m}$ Silver with $100\mu\text{m}$, $150\mu\text{m}$, and $200\mu\text{m}$ copper are plotted for energy absorption against temperature in the range 20°C to 140°C . The rate of theoretical energy absorption (Watts) increases with greater copper thickness. The actual thermal conditions at the electrode coating during EDM are being investigated. Using thermal labels it has been established that electrode temperatures during EDM do not exceed 100°C , applying an optimized machining set-up described below. This measurement has been taken at the interface of SL substrate and metallizing layer, by countersinking thermal labels into the SL model viewable through the back of the model face.

In the dielectric

The dielectric used in EDM is multi-functional its primary tasks being the clearing of the spark gap, and suppressing/containing the spark by forming an enclosed channel between electrode and workpiece which collapses as the spark is absorbed. The secondary function of the dielectric is the dissipation of thermal energy from the machined surface. The dielectric acts as a heat sink for both the electrode and workpiece, transferring high heat intensity from the spark gap to the circulating dielectric. This function is of less importance during EDM with solid machined electrodes but is a crucial factor when using SL models as excess heat is seen as the main cause

of failure at the electrode. The dielectric flow is used to best effect by incorporating direct flushing at the spark gap during electrode 'off' times. This is referred to as pulse flushing from a point source. In this way the debris can be ejected and heat removed in the most efficient manner.

At the tool/workpiece

The heat generated at the tool surface is dissipated both into its body and into the dielectric. the workpiece is generally metallic and solid, fixed to the EDM machining table. This system ensures efficient thermal conduction, provided sufficient dielectric flow and low ambient tank temperature are maintained. Using electroplated SL electrodes the MRR is low and therefore the heat emissions do cause excessive temperature gradients. Temperatures measured during EDM at the workpiece do not differ substantially from the dielectric.

5. ENHANCING SL ELECTRODE PERFORMANCE

The key to exploiting the full potential of SL electrodes is a double edged sword, requiring optimization and balance of electrode and process. The quality and physical properties of the electrode must be matched effectively with the applied machining conditions. Application of the electrodes demands a detailed understanding of the EDM factors which influence its performance.

5.1 Controlling copper quality & distribution

Deposit quality

It is clear from the work carried out to date that one of the routes to catastrophic failure of the electrode results from defects within the copper coating. Electrodeposits have a different microstructure to bulk metals due to the nature of the deposition process. In the case of the acid copper electrolyte, in order to produce smooth deposits, certain organic additives are introduced to the electrolyte that modify the grain structure. The grains produced in the presence of these additives tend to be columnar, with grain boundaries normal to the substrate surface. If the deposition process is not adequately controlled in terms of electrolyte composition, contamination and deposition conditions, then the structure of the deposit will become variable. The grain boundaries then become regions of weakness which allow rapid localised degradation of the deposit during the machining process. Even with the best process control conditions, it is unlikely that columnar microstructures would be ideal coatings for EDM electrodes. This is because such a structure tends to promote the continuity of any porosity initiated at the metallised surface. Sites of such intrinsic porosity then become zones where the discharge spark rapidly weakens the coating leading to its failure.

It is therefore very important that a very tight control of the plating electrolyte and its conditions of use is exercised. Organic additives are decomposed during the plating process and can form compounds that interfere with the growth of the deposit, leading to the development of high internal stress or other forms of deposit degradation e.g. nodule formation and powdery deposits. Organic contaminants may be removed using activated carbon but this also necessitates

the analytical control of the original additives to ensure that these are not removed also.

It is important to ensure that particulates do not contaminate the electrolyte as these could become incorporated into the deposit. Particulate inclusions can easily act as preferential erosion sites during discharge machining leading again to early and random failure. Continuous filtration can minimise this but ultimately, the best form of cure is prevention of the contamination by employing very clean environments.

Finally, to ensure a consistent deposit, chemical analysis of the electrolyte components carried out on a regular basis, combined with appropriate deposit testing is essential.

Deposit distribution.

The distribution of metal over a complex geometry is dependent on many factors as has previously been mentioned. Whilst it is possible to formulate an acid copper electrolyte to exhibit an improved distribution, other formulations of copper electrolytes are available that offer a significant improvement over even the best acid copper system. These electrolytes are based on copper compounds in the form of chemical complexes. Unfortunately, these are required to operate at temperatures close to the Tg of the SL model (55 - 60 C). Work is being carried out to evaluate the properties of these electrolytes under conditions more suited to the SL models. Besides improved distribution, these electrolytes produce finer grained equiaxed deposits and should reduce the tendency to pore continuity. By using these electrolytes in conjunction with the physical methods of improving metal distribution, the difficulty of obtaining a uniform deposit can be minimised. As with the acid copper electrolyte, these electrolytes require tight analytical control and the exclusion of contaminants to offer optimum performance.

5.2 Controlling the EDM process

Efficiency of EDM with the SL electrodes was sought through optimization of MRR using a series of Fractional Factorial Experiments (FFE's). The L18 test array prescribed by Taguchi [8] provided a suitable structure for examination of seven adjustable EDM parameters at three levels. The performance data for these tests is described by Figure 12. Details of these tests have been presented in earlier published material [3,4]. Fixing parameters where their performance was seen to be optimized a specification for machine set up was derived. This set-up has formed the basis for testing of more complex model electrode profiles and the continuing evaluation of electrode performance. The relationships between the various adjustable EDM parameters are complex, however the use of FFE's as outlined above has determined a start point from which improvement in coating techniques should offer potential for improvements in both machining efficiency (MRR) and electrode wear.

Improving the quality and distribution of the copper deposit is likely to yield greater resilience against electrode failure, providing an opportunity for enhanced EDM performance. A cycle of continual improvement has been established.

6. CONCLUSIONS & FURTHER WORK

The potential for application of copper coated SL models is currently limited by a number of factors. Work at The University of Nottingham is seeking to identify and address the limitations. The efficiency of the SL electrodes depends on the quality of the electrodeposited copper coating and the EDM machine set-up. Optimization of both areas is being sought through an on-going research programme.

The inefficient heat/energy dissipation from the front face of the electrode during EDM causes catastrophic failure. Classification of failure modes associated with this heat 'burn out' have been proposed. The factors contributing to failure are being investigated. A thermal model is to be developed, providing a means of predicting electrode behaviour.

The principle of manufacturing electrodes for EDM using SL has been demonstrated. Further work should provide an opportunity for greater machining efficiency.

7. ACKNOWLEDGEMENTS

The authors would like to thank the following for their support and assistance in this research work; UK Engineering and Physical Science Research Council (EPSRC), Rolls Royce (Aerospace) plc, GEC-Marconi Materials Technology - Hirst division, Nuns Street Platers (Derby), and fellow workers at the University of Nottingham

8. REFERENCES

- [1] A.Arthur & P.M.Dickens, "*Rapid Prototyping of EDM electrodes by StereoLithography*" Presented at the International Symposium for ElectroMachining (ISEM) XI, Lausanne, Switzerland, April 17-20 1995
- [2] A.Arthur & P.M.Dickens, "*The potential for Rapid prototyped EDM electrodes using StereoLithography models*" Presented at the 1st National Conference on Rapid Prototyping and Tooling Research, Buckinghamshire College (Brunel University), UK, November 6-7 1995 pp 221-235
- [3] Alan Arthur, Phillip Michael Dickens, & Richard Charles Cobb, "*Using rapid prototyping to produce electro discharge machining electrodes*" Rapid Prototyping Journal, Vol 2, No.1, February 1996, pp 4-12. ISSN 1355-2546
- [4] A.Arthur & P.M.Dickens, "*Material removal & tool wear rates in EDM with StereoLithography electrodes*", Presented at the 5th European Conference on Rapid Prototyping and Manufacturing, Espoo, Helsinki, Finland, June 4-6 1996 pp 157-169 ISBN 0-9519759-5-1
- [5] Semon, G. A practical guide to Electro-Discharge Machining (2nd ed.), 1975 (Publ. Ateliers des Charmilles, Geneva), Chapter 9 pp 63-76
- [6] Vagramyan, A.T. , Solov'eva, Z.A. Technology of Electrodeposition, 1961, (Robert Draper, UK) pp 308-384
- [7] Hague, R. Dickens, P.M. Stresses created in ceramic shells using Quickcast™ models, Proceedings First National Conference on Rapid Prototyping and Tooling research, Buckinghamshire College UK, 6th-7th November 1995. ISBN 0852989822 pp 89-100.
- [8] Ross, P.J. Taguchi techniques for Quality Engineering, 1988, (McGraw-Hill, UK) pp 228 ISBN 6100897425

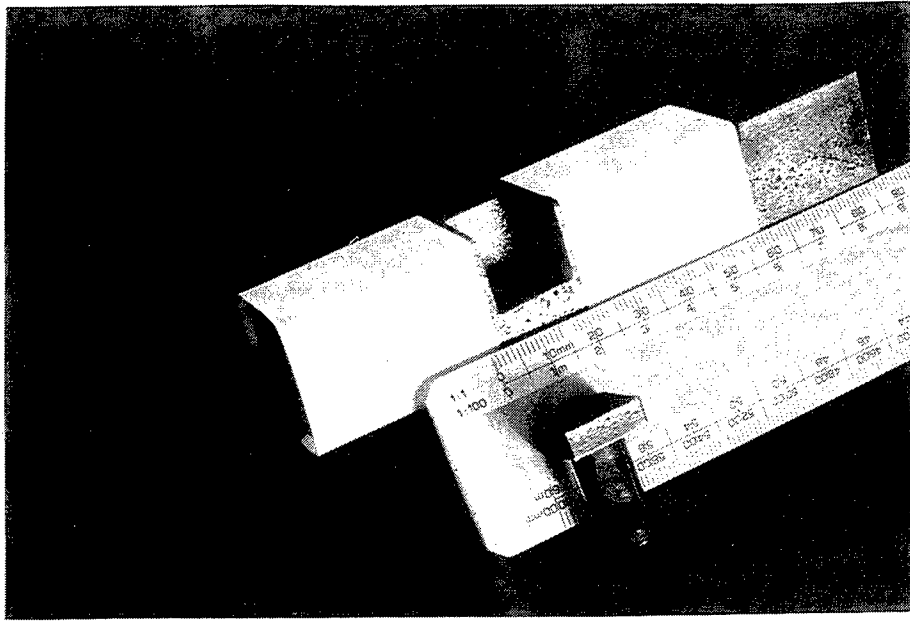


Figure 1 SL 'tablet' electrode and 16mm deep EDM cavity in tool steel

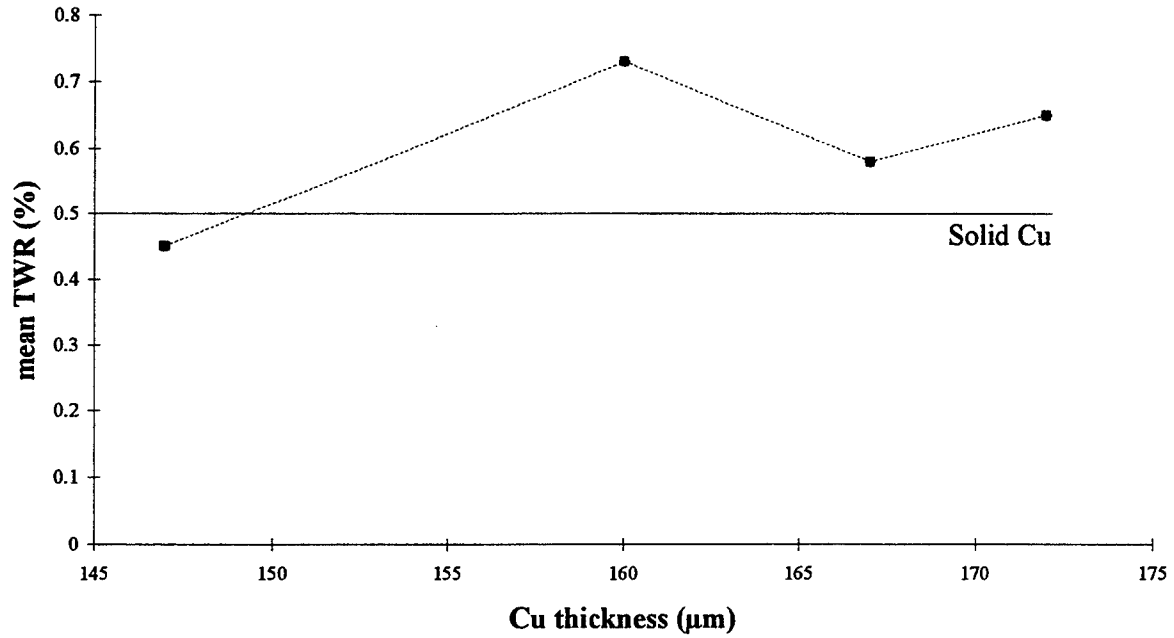


Figure 2 SL EDM electrode TWR versus copper thickness

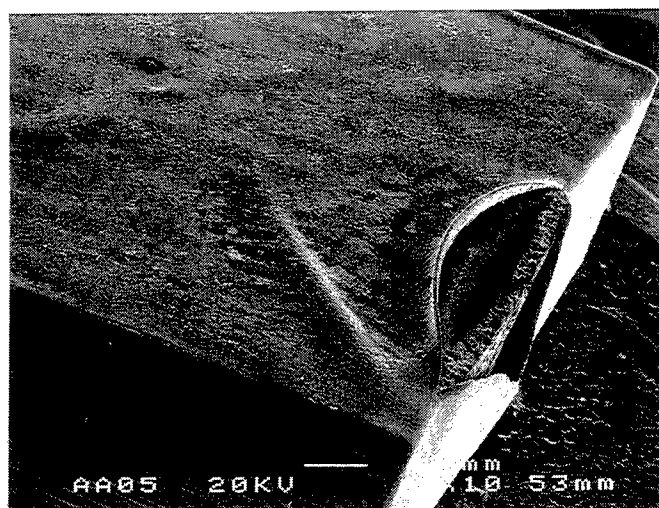


Figure 3 Electrode failure - Edge failure (15mm x 15mm SL 'tablet' electrode)



Figure 4 Electrode failure - Peening (15mm x 15mm SL 'tablet' electrode)

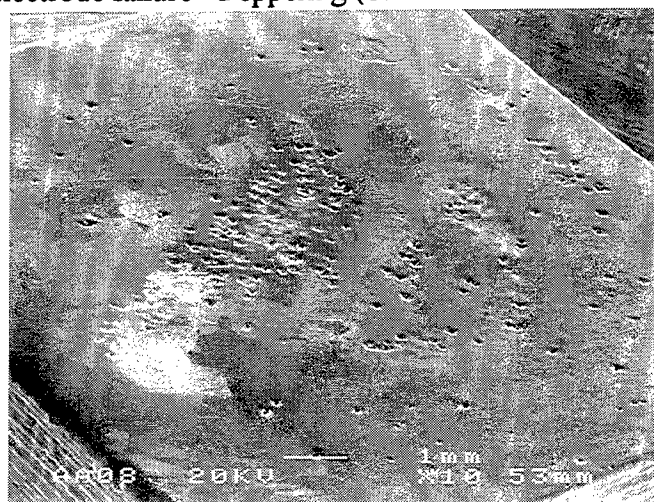


Figure 5 Porosity in electrodeposited copper, highlighted by pyrophosphate plating (15mm x 15mm SL 'tablet' electrode)

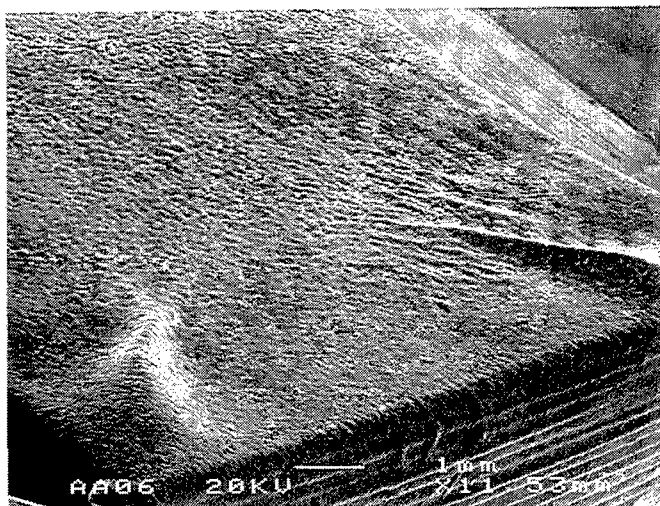


Figure 6 Electrode failure - Delamination (15mm x 15mm SL 'tablet' electrode)

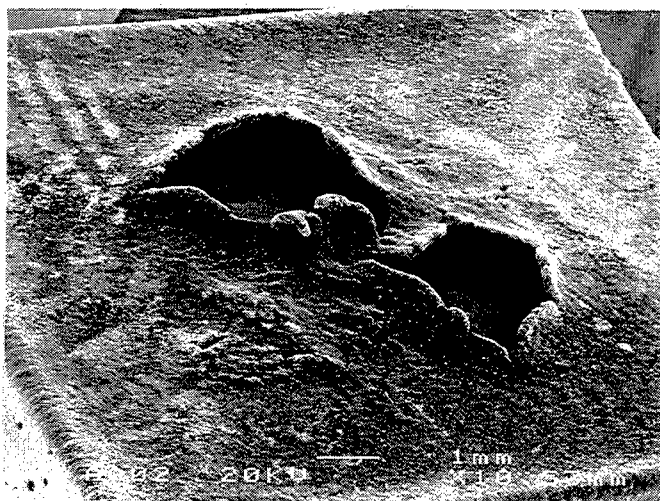


Figure 7 Electrode failure - Rupture (15mm x 15mm SL 'tablet' electrode)

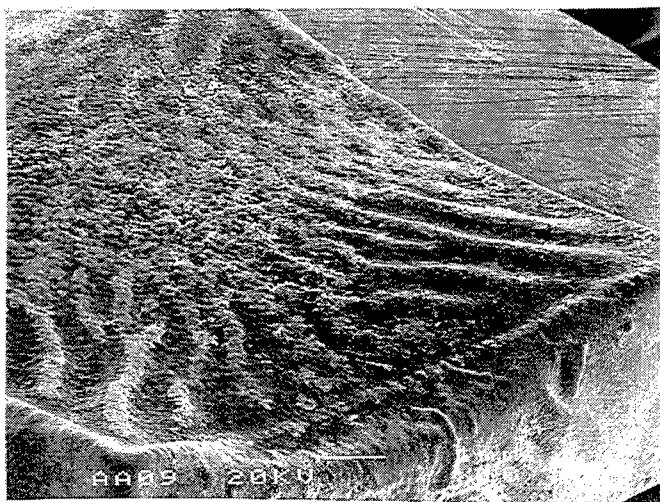


Figure 8 Electrode failure - Distortion (15mm x 15mm SL 'tablet' electrode)

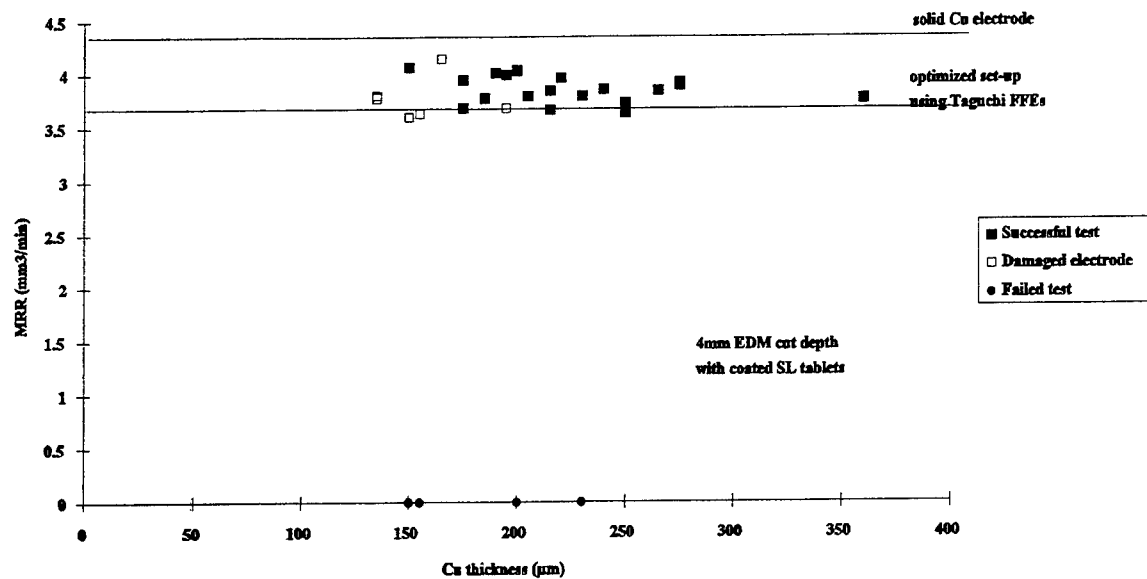


Figure 9 SL EDM electrode MRR versus copper thickness

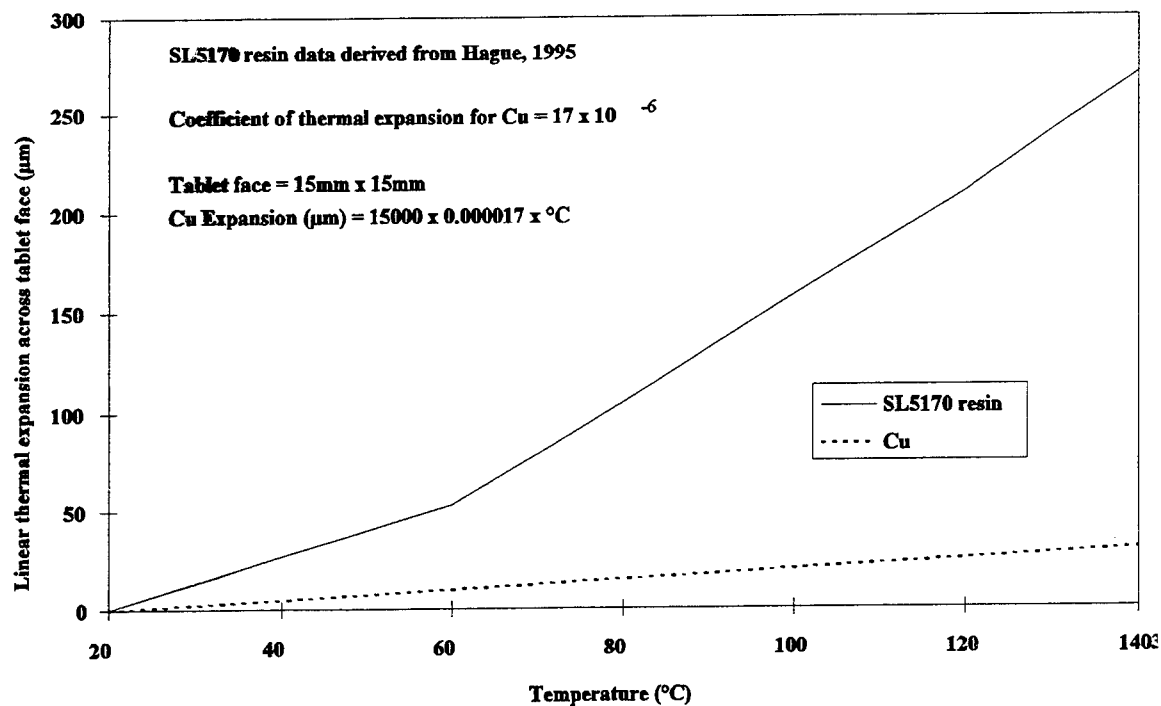


Figure 10 The differential linear thermal expansion of SL tablets and applied copper coatings at elevated temperature

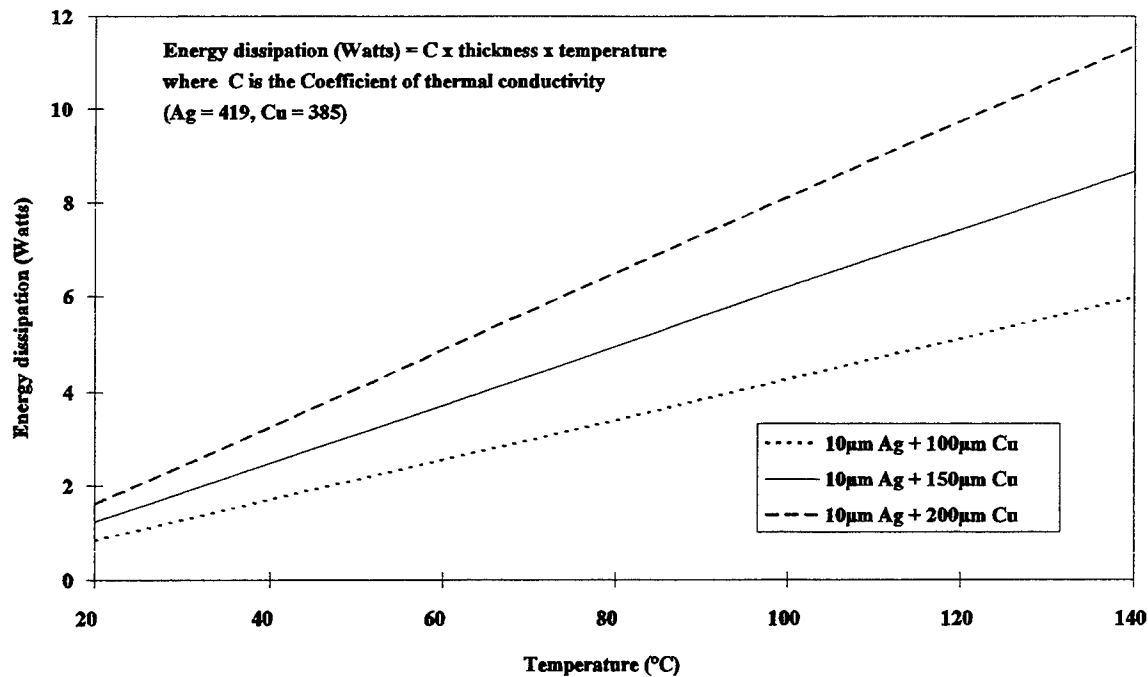


Figure 11 SL EDM electrode capacity for energy dissipation versus coating thickness

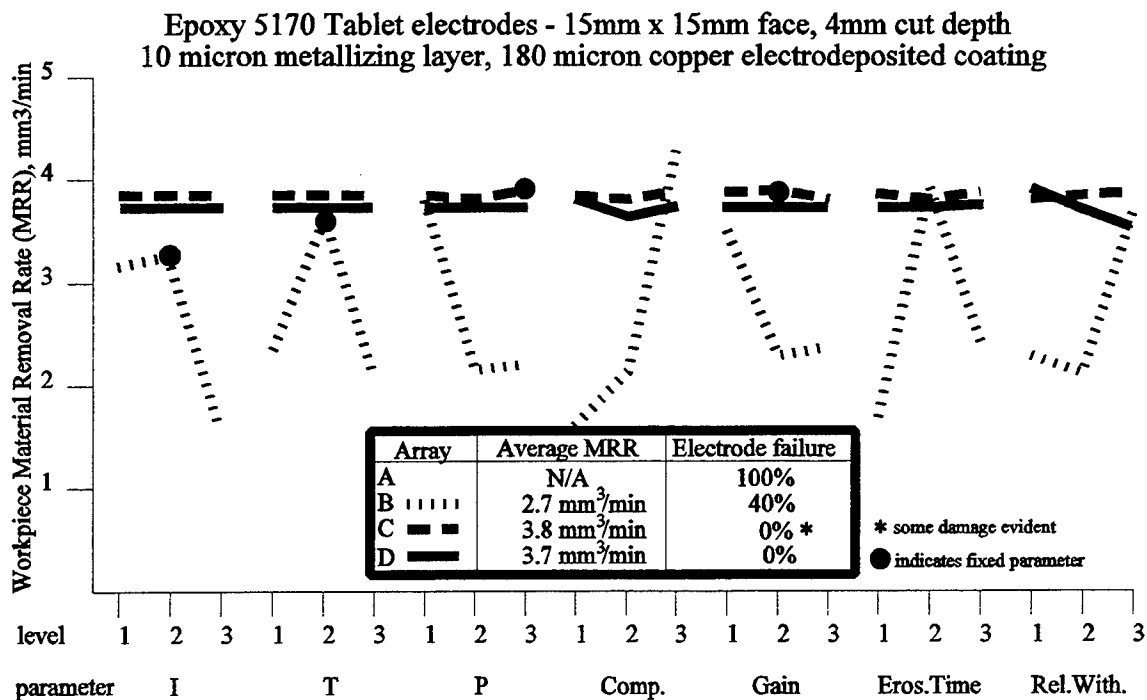


Figure 12 SL EDM electrode Material Removal Rate (MRR) optimization

Rapid Prototyping using Electrodeposition of Copper

S J Dover, A E W Rennie and G R Bennett

Centre for Rapid Design & Manufacture, Buckinghamshire College of Higher Education, UK

Abstract

Injection mould cavities and EDM electrodes were produced from High Speed Selective Jet Electrodeposition (HSSJE). The performance of the electrodes in the EDM process and the surface finish of the tools produced were studied. Studies were made into optimising the HSSJE build process.

Introduction

More and more emphasis is now being placed on Rapid Tooling as a means of creating parts. The current emphasis is on downstream processes from established RP techniques. In contrast, this paper looks at the usage of High Speed Selective Jet Electrodeposition (HSSJE), using copper as a deposition element and its application to create SFF parts directly for injection moulding tools and EDM electrodes.

Conventional Electrodeposition

Electroplating is a process whereby a potential is applied between two conducting electrodes placed in a solution containing metal ions (electrolyte). As a result of an excess of electrons, metal ions are reduced at the surface of the negative electrode (cathode) and form a deposit of metal atoms on the surface. This grows at a rate proportional to the current passed. Metal ions from the positive electrode (anode) dissolve into the electrolyte. However, this process causes a depletion of copper ions in the electrolyte in the vicinity of the cathode as the rate of deposition tends to be significantly faster than their rate of replacement by migration due to the electric field. As a consequence, a concentration gradient develops which results in a diffusion flux. This electrolyte layer adjacent to the electrode is referred to as the Diffusion Layer. Fick's First Law of Diffusion states that the mass transport of ions by diffusion is proportional to the concentration gradient. A limiting current exists beyond which the rate of deposition would be such that diffusion and migration cannot re-supply the metal ions fast enough to maintain an excess concentration of ions. At the limiting current (i_L) as soon as metal ions reach the surface they are reduced and the metal ion concentration at the surface approaches zero. The thickness of the diffusion layer δ is governed by both the hydrodynamic conditions of the electrolyte and the bulk metal ion concentration (c_b). Higher rates of bulk electrolyte movement result in a thinner diffusion layer. The maximum concentration gradient (c_b/δ) is thus governed by the hydrodynamic conditions and the bulk concentration and this determines the limiting current density which can be expressed by equation [1].

$$i_L = \frac{n F D c_b}{\delta (1 - t)} \quad [1]$$

where n is the number of electronic charges carried by each metal ion, F is Faraday's Constant, D is the diffusion coefficient and the term $(1 - t)$ accounts for the migration of the ions under the electric field, where t is the transport number of the metal ion concerned.

In general, within electrolytes, metal ions are usually surrounded by charged or polarised molecules. In an aqueous solution these are usually water molecules. Other species such as CN^- ions can be made to form complex molecules around the metal ions, often resulting in a net negative charge (in this case the complexes are still reduced at the cathode despite their electrostatic repulsion to it). Usually the complexes adsorb onto the cathode (via weak Van der Waals type bonds) allowing surface diffusion, where the complexes move to more energetically favourable sites such as steps or holes. Finally, electrons are donated by the cathode and the metal ions are reduced to atoms which are then held by metallic bonds to the cathode.

High Speed Selective Jet Electrodeposition

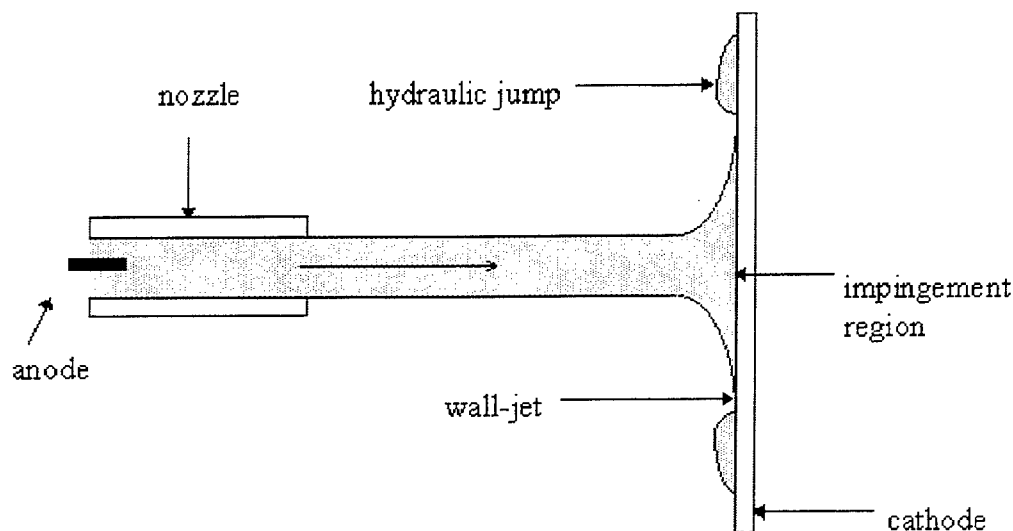


Figure 1. Schematic of the high speed selective jet electrodeposition process.

High Speed Selective Jet Electrodeposition (HSSJE), patented by NASA in 1974, uses a free standing jet of electrolyte impinging onto the cathode substrate as shown in Figure 1. A current is passed from an anode which is placed upstream from the nozzle. Away from the impingement region an extremely thin radial wall jet layer of electrolyte forms. The electrical resistance of this wall jet is high in comparison to the impingement region so no deposition can occur there. As a result, deposition occurs mainly in the impingement region and the immediately surrounding area. Furthermore, due to the continual supply of fresh electrolyte and the hydrodynamic conditions created the thickness of the diffusion layer δ is smaller and hence the mass transport of metal ions to the surface of the cathode can be made substantially higher than in the case of traditional electroplating. Consequently, higher current densities and thus higher deposition rates can be achieved than is conventionally possible. A more detailed discussion of the process is given by Bocking(1) and Chen(2). By moving the nozzle in relation to the substrate whilst deposition is occurring, it is possible to selectively "write" tracks and patterns at relatively fast rates without the need for masking the substrate.

However, at the very high current densities found with HSSJE, the time allowed for surface diffusion is much lower and deposits can be rough, porous, hard and contain higher internal stresses. Also, since the diffusion layer is much thinner any small elevation in the cathode surface will protrude into a region of higher metal ion concentration. This produces a locally enhanced current density and the protrusion is magnified. By this effect, the maximum current density that produces a good deposit is set well below the maximum current density as described earlier. In order to facilitate higher speeds of deposition, higher concentrations of metal ions are often used. In addition, higher temperatures increase the diffusion rate of metal ions and jet deposition benefits from electrolytes operating at elevated temperatures. Also many electrolytes contain constituents that are corrosive to the metal that is deposited. Consequently, deposits produced by HSSJE may be re-dissolved by the flowing electrolyte during "writing" operations.

As organic additives used in conventional techniques (brighteners, levellers etc.) are usually adsorbed onto the cathode (a time dependant phenomenon), their fraction of incorporation is largely dependent on the current density. High current densities and thus high rates of deposition will result in less incorporation into the deposit. Hence at high current densities these additives are less effective. Conventional electrolytes are very different from good HSSJE electrolytes, to the extent that HSSJE electrolytes often will not work in conventional plating baths.

Due to the low currents (despite the high current densities) associated with HSSJE, build rates are measured in grams per hour. Hence it would take an extremely long time to build a large metal tool using a single nozzle. Either improvements must be made in the deposition rates or multiple nozzles must be used, possibly with varying apertures for combined dimensional accuracy and speed. Feedback/levelling systems are required to build large deposits due to the factors that amplify surface imperfections. However, provided the parts are reasonably shallow, this could be omitted. Also, overhangs and support structures may prove difficult to produce and indeed deposits will have profiles fitting Gaussian functions(4) which slope asymptotically towards the substrate surface. Hence it is likely that the edges of layers and parts will not have straight vertical sides. Overhangs could be produced from a nozzle to substrate angle of less than 90°. The mass transfer characteristics of an oblique jet have been previously documented by Chin & Agarwal(3). This method may not be amenable to the usual CAD \Rightarrow STL \Rightarrow SLI \Rightarrow vector file process found with other RP systems. Hence this process is suited to small complex tools and EDM electrodes rather than prototypes as these will require overhangs and support structures.

Experimental

The electrolyte composition used was 0.5M sulphuric acid and 0.8M copper sulphate. No organic additives were used. The gantry system used was based upon a Roland Plotter DXY 885, controlled via a QBASIC program running on a PC through a RS232C interface with the pen up/down function modified to switch on and off the current to the nozzle. The temperature was controlled via a thermocouple and 200W collar heater through which the electrolyte was pumped en route to the nozzle and the flow rate monitored using the same PC. The QBASIC program was written to draw the particular geometry of the shape to be produced, although more recently a program has been written to slice ASCII .STL files and use the data to create a 'vector file' to control the motion of the plotter.

Unfortunately, the minimum scan speed allowed by the plotter was 10mm s^{-1} . This is above the optimum scan speed due to the finite nucleation time for copper deposition. If the speed is too fast then only the trailing side of the substrate under the jet will have had enough time for full nucleation to occur. This results in a lower effective surface area of deposit and, therefore, a higher current density and a lower quality of deposit(4).

For all experiments, a nozzle of internal orifice diameter $820 \pm 20\mu\text{m}$ was used with a nozzle to substrate distance of between 1 and 3mm. A polished copper block was used as a substrate for the deposition of EDM test electrodes and untreated copper clad PC board as a substrate for all other experiments. An electrolyte flow rate of $180 \pm 40\text{ ml min}^{-1}$ was used and the temperature was kept at 22.7°C with a standard deviation of 0.8. The current was controlled by a current source circuit with a FET at its heart.

The production of the shape shown in Figure 2 was undertaken using HSSJE except the central pins radii were decreased and the outer square perimeter shrunk by 0.4 mm to allow for the approximate width of the deposit. The circle was left unaltered due to difficulties with the software although with the .STL file slice routine, this has since been rectified. All nozzle scanning was carried out horizontally as shown in Figure 2. Electrodeposited copper tracks were laid with a lateral spacing of 0.025mm. It was intended to create an injection moulding tool cavity from this and to test its performance in the EDM process.

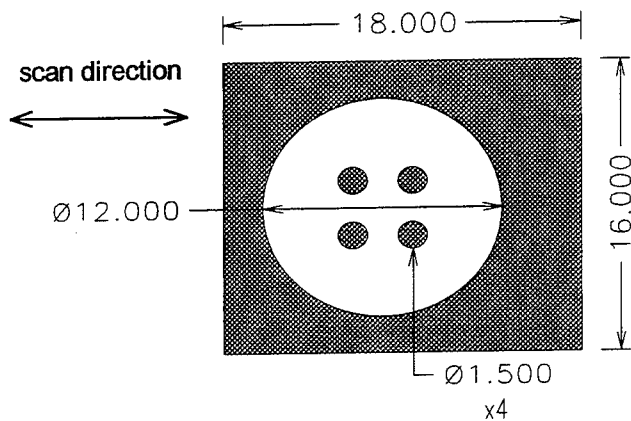
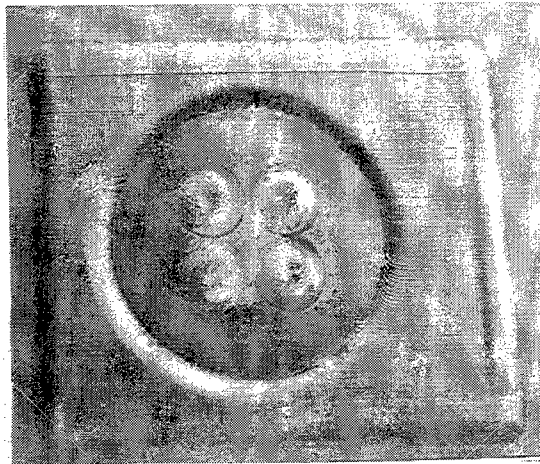


Figure 2. The first test piece.



The piece shown in Figure 3 was built at 30 mA (56.8 mAmm^{-2}) with 40 layers. The build height was approximately 0.15mm. It was noticed that the central pins were beginning to roughen in the centre and tiny spots were beginning to build disproportionately high. Three theories were considered for this phenomenon.

Figure 3. A sample built at 30mA (56.8 mAmm^{-2}) for 40 layers.

Firstly, too high a current will produce a rough surface as described above and eventually vertical columnar growth will occur. Secondly, once a track is deposited the substrate surface is no longer

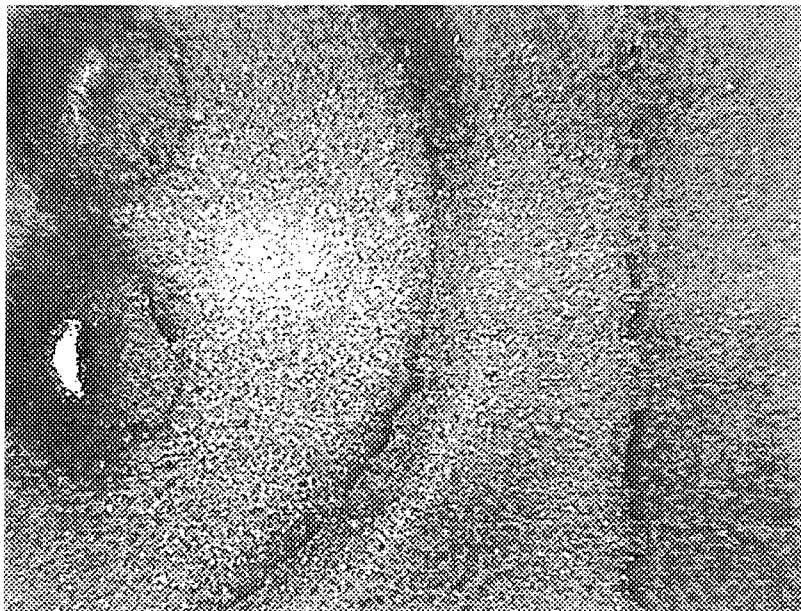
flat. A second track next to the first track will not produce an identical profile as the first track (being slightly raised from the surface) will tend to attract the current from the second, slightly raising it above the second track. Edge effects occur in a similar fashion. Even if the deposited surface is perfectly flat, the edges will be slightly rounded, eventually asymptotically approaching the initial substrate surface. As a result of this rounding, the edge of the deposit will attract more current from the interior of the deposit. This produces edges which are higher than the interior of the deposit with corners being higher still. The nature of the pins are that they have a large edge to deposit area ratio and hence this unevenness of the surface is exaggerated.

Finally edge effects occur due to the finite acceleration/deceleration time of the gantry system. As the nozzle moves to the end of the piece, the current is switched off but since the nozzle does not stop immediately, a higher charge per unit area is delivered to the substrate. This can easily be solved by lowering the current proportionally as the velocity decreases, however, it was intended to see if the process could work with a minimum of complexity. In addition to these three effects, once any surface protrusion occurs it begins to attract more current due to the nature of the electric field, further increasing the deformity of the surface.

To determine which of these effects is responsible for the degradation of the surface of the pins, or if a mixture to what extent each are responsible, it was decided to build the same height at the lower current (and lower current density) of 20mA (37.9mAmm^{-2}) for 60 layers. It was noticed that this system still showed the same uneven growth. Therefore, the effect cannot be due to an excessive current density.

Surface Roughness

The surface roughness of the samples were measured in a region away from any edges.



Two samples, one with 140 layers at 7mA (13.26mAmm^{-2}), one with 10 layers at 20mA (37.9mAmm^{-2}) were found to have Ra values of 0.32 and 0.27 μm respectively. The surface appeared shiny with an almost mirror finish.

EDM Performance

The test geometry was deposited onto a solid copper block at 20mA (37.9mAmm^{-2}) for 40 layers and used as an electrode to spark erode into a block of mild steel. A pulse

Figure 4. The surface of a HSSJE deposit after its use as an EDM electrode.

current of 5A was used and the electrode was plunged into the steel by approximately 0.3mm. The results were good and the electrode after sparking is shown in Figure 4. The electrode showed some wear especially around the outer edge of the deposit. This may be due to poor adhesion or internal stress in the deposit.

Edge effects

A second test piece was created to investigate the edge effects. The piece was as shown in Figure 5 with the dimension x being variable. All experiments on this piece were performed using the same experimental conditions except the track spacing was 0.1mm. Current (densities) of 7 mA (13.26 mAmm^{-2}) and 14 mA (26.52 mAmm^{-2}) were used with between 500 and 3000 layers. All scanning was performed left and right as shown in Figure 5. With each sample produced, the heights at each of the points displayed 1 to 11 in Figure 5 were measured from the bottom of the substrate (epoxy/glass fibre PC board) using a micrometer with a conical probe with a flat circular tip of 0.5 mm diameter. It was generally found that the two corners (points 11 and 12) were the highest (merely an addition of two edge effects), the ridge at the end (point 10) was next, followed by the sides (points 8 and 9), followed by the top of the flat (points 5, 6 and 7). This indicated that both edge effects are significant. The three values of interest for each deposit were the difference between the average height of the middle of the flat top of the deposit (points 5, 6 and 7) and the average height of the top of the substrate (points 1, 2, 3 and 4), the standard deviation of the average height of the middle of the flat top of the deposit (points 5, 6 and 7) and the standard deviation of all the flat top (points 5, 6, 7, 8, 9, 10, 11 and 12). These three values were named the useful height, the S.D. of useful height and the total S.D. of the deposit respectively.

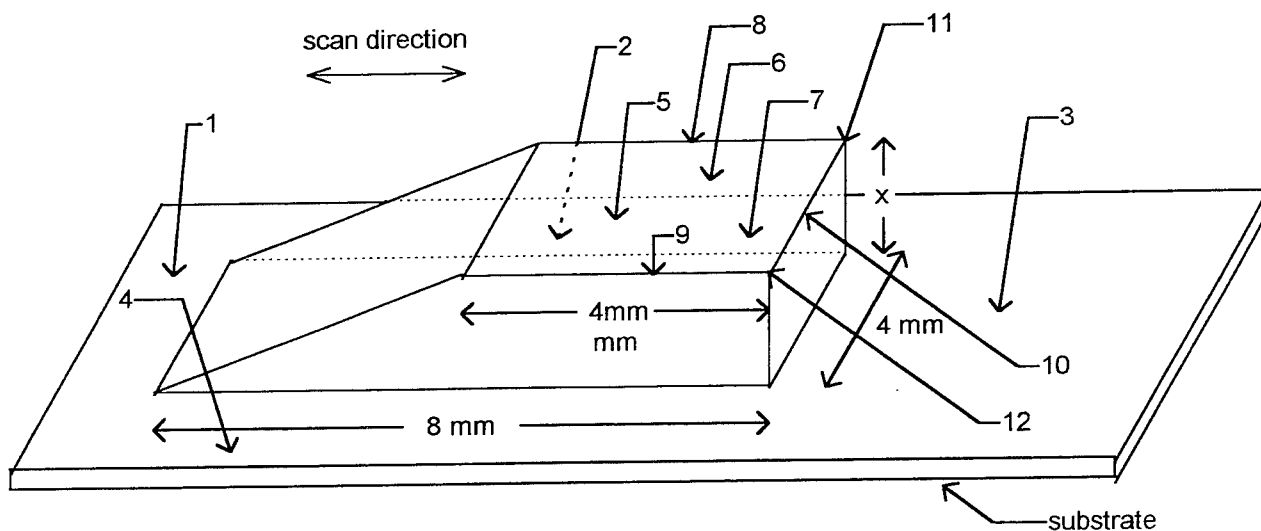


Figure 5. The second test piece.

Figure 6 shows the variation of the useful height with number of layers. The graph shows that for the range of samples shown, the useful height remains linear with a build of $0.2 \mu\text{m}$ per layer (at 7mA) indicating that if the surface were to be levelled (e.g. by milling) then any build height in the region studied could be used between each milling operation.

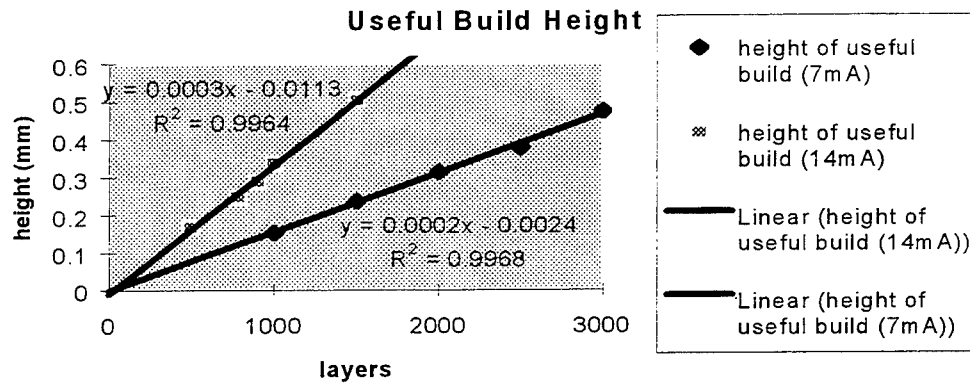


Figure 6. The variation of the useful build height versus number of layers at 7 and 14mA (current density at the nozzle exit is 13.26 and 26.52 mAmm⁻² respectively).

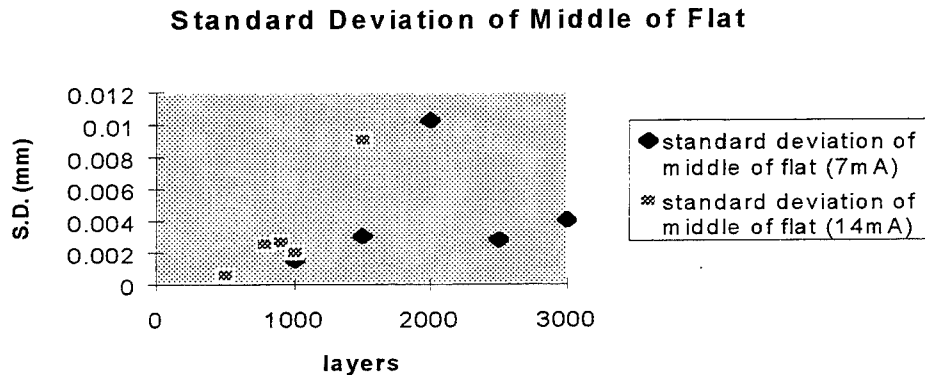


Figure 7. The variation of the standard deviation of the height of the flat section versus number of layers at 7 and 14mA (current density at the nozzle exit is 13.26 and 26.52 mAmm⁻² respectively).

Figure 7 shows the variation of the standard deviation of the useful height with the number of layers. It suggests that the unevenness of the flat top of the deposit increases with the number of layers although the data shows no clear trends. This is probably because three measurements is not enough to calculate each standard deviation point accurately.

Figure 8 shows the variation of total standard deviation (points 5, 6, 7, 8, 9, 10, 11 and 12) of all available samples against the useful build height. The useful build height was used instead of the number of layers as it allows for the different build rates associated with different currents used. It also allows for any minor deviation in current from that stated and for deviations in the build time (i.e. the plotter moving too fast/slow causing less/more deposit per layer). It shows that the data is fairly consistent for both currents used although more data is needed at the high end of the graph. It also suggests that the deposit becomes more deformed with increasing

thickness in an exponential manner confirming that any surface imperfections attract more current and are thus further magnified.

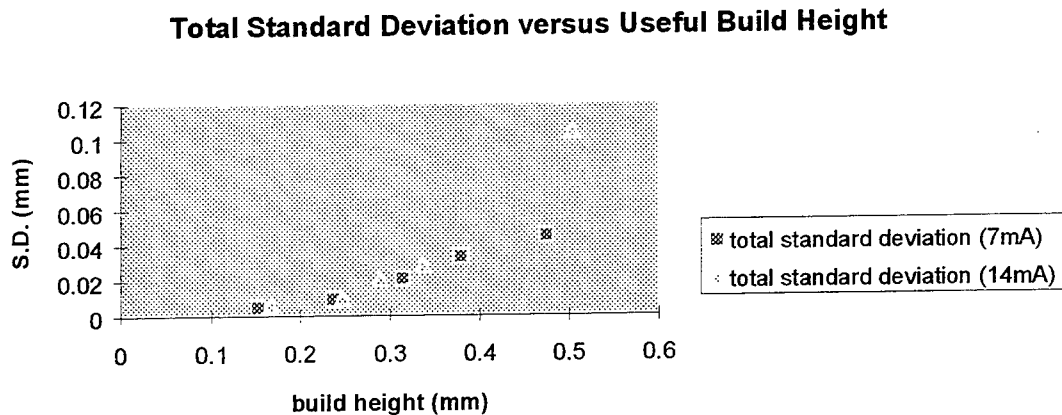


Figure 8. Graph showing the useful build height against the total standard deviation of all measurements of the deposit.

The results indicate that for a particular height of build, the size of the deformities in the deposits are independent of the current used (for the currents used) up to approximately 0.4 mm, beyond which further results are required.

Discussion

The results also indicate that parts higher than 0.5mm cannot be built without a levelling system or active current control. Parts that are less than 0.5mm will have a horizontal inaccuracy proportional to nozzle diameter. Build speed is ultimately inversely proportional to nozzle area. Hence, a compromise is necessary unless multiple nozzles are to be used. In addition, some geometries are more problematic than others, e.g. small pins. Other inaccuracies exist, including the shallow sloping sides. However, the possibility exists to make SFF parts with micron layer thickness. The process produces adequate EDM electrodes directly although care must be taken. For parts larger than 0.5mm high active current control or a levelling system is necessary.

References

- (1) BOCKING, C.E., High Speed Selective Jet Electrodeposition of Gold and Gold Alloys using Single Circular Jets, Doctoral Thesis, Institute of Polymer and Materials Engineering, Loughborough University of Technology, 1994.
- (2) CHEN, T-J., Selective Jet Plating, Doctoral Thesis, University of Illinois, 1981.
- (3) CHIN, D-T., AGARWAL, M., Mass Transfer from an Oblique Impinging Slot Jet, J. Electrochem. Soc., September 1991, **138** No. 9, pp.2643-2650.
- (4) BOCKING, C.E., DOVER, S.J., BENNETT, G., 'An investigation into the suitability of high speed selective jet electrodeposition for rapid tooling,' First National Conference on Rapid Prototyping and Tooling Research, Nov.1995, pp.157-173, MEP.

Acknowledgements

C.Bocking of GEC & the technicians of Dept. Eng. Tech., Buckinghamshire College.

EDM TOOLING BY SOLID FREEFORM FABRICATION & ELECTROPLATING TECHNIQUES

R. Ippolito, L. Iuliano, Politecnico di Torino (ITALY)
A. Gatto, Università di Ancona (ITALY)

Abstract

The term "Rapid Tooling" refers to the rapid creation of tools in much the same way as Solid Freeform Fabrication (SFF) means the rapid creation of models. This revolutionary approach offers both designers and manufacturers attractive advantages in the form of time compression and cost reduction. Timesaving is of vital significance in the production of EDM electrodes for the fabrication of moulds and dies. The employment of SFF and electroplating for this purpose is described. The performances of these new type of electrodes were compared with those obtained conventionally in terms of dimensional tolerances, surface roughness and working time. The surfaces of both electrodes and workpieces were also examined by SEM microscope.

1. Introduction

Constant improvements in the performance of Solid Freeform Fabrication (SFF), also well known as Rapid Prototyping (RP) technologies [1,2,3] and both terms will be used in the paper, have greatly extended their market. This is particularly true with regard to Rapid Tooling (RT), the name given to the fabrication of tools used to make small runs of parts for construction of the prototypes of mass-produced objects. Both the technical and the commercial literature, in fact, show that other undeniably interesting applications are overshadowed by rapid tooling.

A sector of major importance that has so far received little attention is the fabrication of electrodischarge machining (EDM) electrodes, especially those employed in the manufacture of small and medium-sized dies and moulds. The application of RP techniques in the direct mould manufacture by metallisation [4] has some limits:

- it is fairly easy to use only for the production of simple plastic injection moulds and probably for sheet metal drawing dies;
- it can be employed to make simple dies without the moving parts needed to make the undercuts.

The fabrication of an EDM electrode by SFF, on the other hand, would be followed by unrestricted conventional manufacture of the die or mould. The economic aspects of this combination have still to be determined.

2. Production of EDM electrodes by Solid Freeform Fabrication

The RP model [5] itself could, in principle, be used as the electrode, or employed as a master for the creation of the final electrodes through further processes. The first alternative is unfeasible, since SFF techniques cannot be easily used for the direct production of metal objects, and even if the present limitations were overcome the metal structure would be unsuitable for an electrode. The second requires further operations, but results in good precision and an excellent finish.

Three methods can be used to obtain an electrode from a RP negative master:

- copper spraying: this has proved feasible in a number of tests. Its drawback is that electrode wear is considerable during machining due to the porosity of the copper;

- investment casting: this method has proved satisfactory in other applications. Electrodes made in this way, however, are unsuitable for EDM, since their structure results in marked granular corrosion and rapid deterioration;
- electroplating: the RP model is coated with a conductive lacquer and clad with a layer of copper in a galvanic bath. This method is inexpensive, since the forming operation is unmanned. In addition, the copper is very pure and dense. The long processing time required and some geometrical limits, however, are the drawbacks.

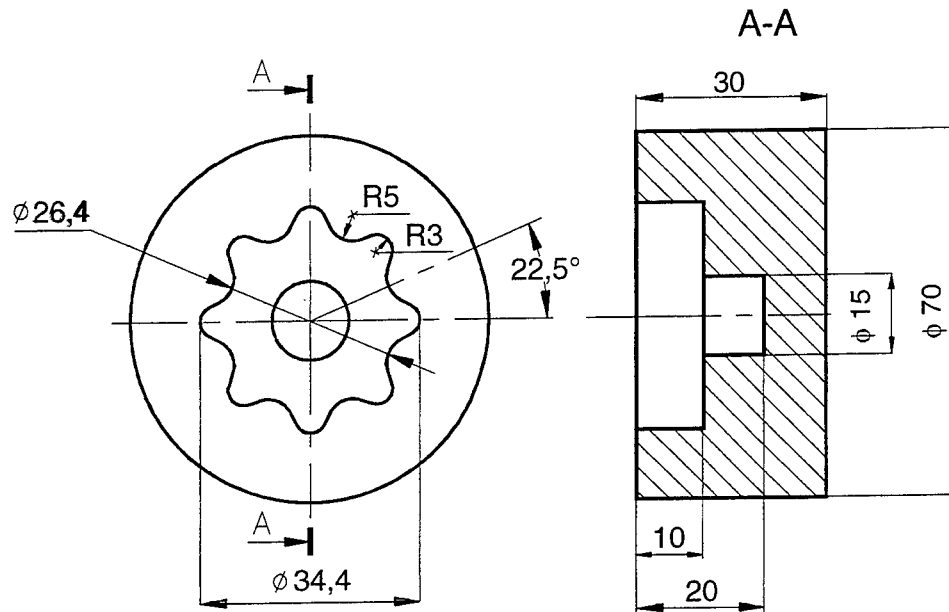


Figure 1: Negative master of the EDM electrode.

Electroplating offers the best trade-off between advantages and disadvantages. In the light of the current capacities of RP techniques [6,7] in terms of dimensional tolerance and surface finish, it may be supposed that the electrodes produced in this way will only be suitable for roughing operations.

2- Experimental work

The feasibility of constructing an electroplated EDM electrode was initially investigated with a part whose geometry was relatively complex (fig. 1), yet readily measurable with a co-ordinate measuring machine (CMM). Electroplating was carried out in an experimental cell (fig. 2) designed and built for the purpose at the University of Ancona. It has an acid bath and a soluble copper anode, and is equipped with:

- a temperature control system to keep the bath at 23°C, (range of recommended temp.: [20÷30]°C);
- a fumes exhaust system;
- a controlled voltage D.C. supply unit connected to a continuity set, since if copper were deposited chemically during a power failure it could prevent the build-up of the plating layer when the current comes on again.

The process parameter values have been chosen to maximise the growth rate of the layer once it is a few millimetres thick.

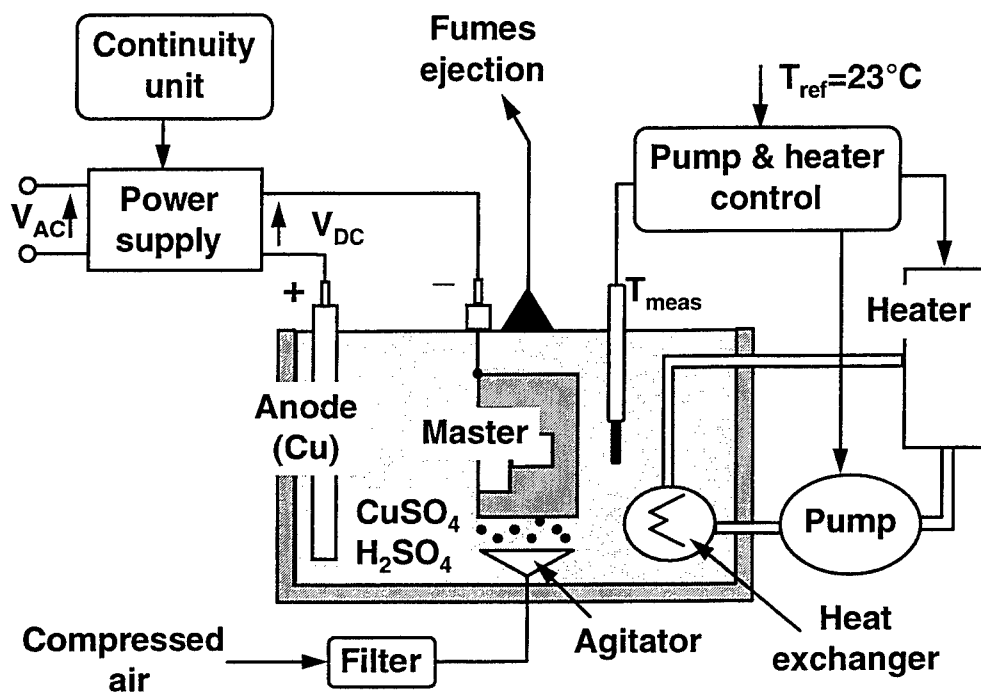


Figure 2: Sketch of the Cu electrodeposition cell.

The type of conductive paint applied on the surface of the negative master is one of the factors that determine the quality of the result, since it has a great influence on the rate of growth and the dimensional precision. Preliminary tests were run with copper and silver charged paints and with gold sputtering. A silver paint was chosen on the basis of four parameters: ease of application, covering power, growth rate and geometrical resolution. The master was built by stereolithography (SLA), as this widely used technique ensures good resolution and a good surface finish [7].

The first question to be settled was the dimensional stability of the master in the galvanic bath, since one of the main problems with polymers is their hygroscopic behaviour. The master was formed on a 3D System machine with the new CIBATOOL SL5170 epoxy resins. A wax master was also made with a Desktop NC manufacturing system.

Both masters were covered with an approx. 3 mm layer of copper. Insertion of a metal stem and filling of the shell with resin to stiffen the structure obtained by electroplating and lock the stem inside it completed construction of the electrode. The dimensional tolerance, the shape errors (flatness, roundness and cylindricity) and both horizontal (\rightarrow) and vertical (\uparrow) surface roughness of the two masters and electrodes were measured and the results are illustrated in Table I.

The precision of the two masters is much the same and the electrodes obtained from them are of practically the same quality. In view of this demonstration of the stability of the SLA and the fact that it showed no signs of alteration and could therefore be used again after removal of the copper shell, it was decided to make two more electrodes:

- one from the SLA master as before;
- the other by conventional milling with an NC machine tool.

Both electrodes were then used to make a cavity in a block of AISI 1040 carbon steel. The SLA master, copper electrode and workpiece are shown in fig.3.

Table I: Master and electrode dimension, shape and roughness measurements.

Element	Max n 90% [*]	Shape error (μm)			Ra (μm)	
		Flatness	Roundness	Cylindricity	→	↑
Wax master	299	9	15	29	4	5
Electrode	590	34	14	198	4	5
RP master	240	3	17	41	5.4	6.2
Electrode	204	16	14	26	5.4	6.2

[*] n: number of tolerance unit (5).

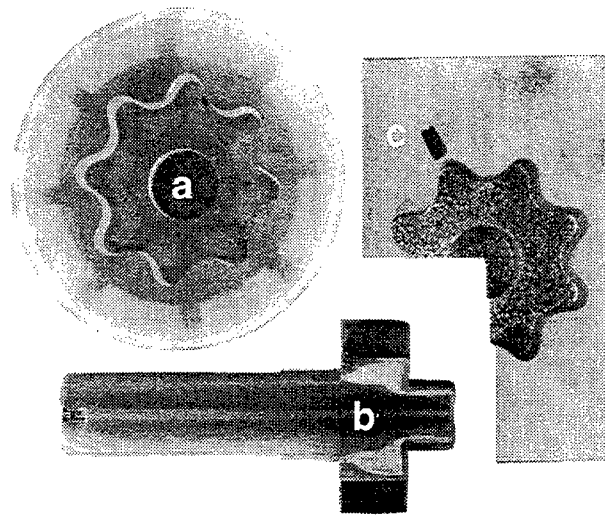


Figure 3: a) SLA master, b) Cu electrode, c) workpiece; both electrode and workpiece were sectioned to make SEM observations. On section of electrode is visible the deposited layer of copper.

The EDM parameter values were set for each test for evaluation of electrode performance. Dimension, shape and surface roughness measurements were taken from the masters, electrodes and workpieces. Both electrodes and the machined workpieces were also examined at SEM.

As can be seen in Table III, the dimension and shape tolerances of the two electrodes are of the same order of magnitude (see also fig. 4). There are two reasons for this: the conventional milled electrode was made to wide machining tolerances for roughing operations; the intrinsic difficulty of obtaining tighter tolerances when working on a malleable material such as electrolytic copper.

4. Results and discussion

4.1 Machining performance

EDM is very slow when compared with conventional material removal processes. As much material as possible is usually removed by conventional drilling and milling to save time and minimise electrode wear. This was not done in our study since the aim was to assess tool performance under the hardest conditions

A commercial EDM machine was used, with hydrocarbon as the dielectric. The test parameters were: voltage (V), the discharge time (t), and the efficiency ratio (t), defined as the ratio between t and the duration of the test sequence (discharge plus idle time). The test consisted of two stages: machining of the cylindrical part of the electrode only; machining of the whole electrode, including the part with the more complicated shape. The parameter values are set out in Table II. The electrode obtained from the SLA master used more current at the same voltage. Its removal rate (Vas), however, was faster than that of the conventional electrode.

Table II: EDM test parameter values.

	Conventional	SFF (SLA)
<u>First stage</u>		
t [ms]	300	300
V [V]	$\cong 45$	$\cong 45$
I [A]	7	14
t [t/p]	0.9	0.9
Vas [mm ³ /min]	13	18
t [h]	2.2	1.6
<u>Second stage</u>		
t [ms]	750	750
V [V]	$\cong 45$	$\cong 45$
I [A]	18	20
t [t/p]	0.9	0.9
Vas [mm ³ /min]	255	302
t[h]	3.9	3.3

4.2 Geometrical and roughness measurements

The geometrical and shape tolerances of the masters, electrodes and workpieces were determined with a CMM, which measures parts at all points with the same nominal dimensions. The surface roughness of the parts was evaluated with a Hommel T 1000 Stylus instrument using a sampling length of 4.8mm. As regard the dimensional error our evaluation model [7] introduces the number of tolerance unit (**n**) for 90% of the observations as the quality index. It is included in the third column of Table III and is also illustrated in fig.4. The shape errors (flatness, roughness and cylindricity) are listed in the forth, fifth, and sixth columns, and the roughness measurements in the seventh and eighth columns.

As can be seen, there are no significant differences in the maximum tolerance grade and the roughness measurements of the workpieces. The worse flatness and cylindricity of the part machined with the electrode derived from the SLA master can probably be attributed to the difficulty in its assembly.

It can therefore be asserted that the technology of galvanic deposition of copper in thickness on models constructed by SLA can be used with success for the production of EDM electrodes to be employed in roughing operations.

4.3 SEM observations

After machining the surfaces of both electrode, derived by SLA master and the workpiece were sectioned, cleaned ultrasonically and observed at SEM microscope.

Table III: Comparison of the results of the EDM electrode manufacturing methods.

Method	Element	Max n 90%	Shape error (mm)			Ra (μm)	
			Flatness	Roundness	Cylindricity	→	↑
Conventional	Electrode before machining	422	5	7	24	3.5	3.8
	Electrode after machining	456	8	7	16	4.1	4.4
	Workpiece	480	20	11	24	16	13
SFF (SLA)	RP model	240	3	17	41	5.4	6.2
	Electrode before machining	204	16	14	26	5.4	6.2
	Electrode after machining	220	6	16	25	6.6	7.1
	Workpiece	518	84	20	68	14	13

The shallow craters, roundish remolten parts and cracks (fig.5) reported for EDM of various types of steel [8] were observed on the workpiece.

In the horizontal zone of the hole, the globular parts are present in greater quantity with respect to the vertical surface (fig.6); this fact is imputable to the different efficiency of washing on the inside of the hole during the machining. A similar difference was noted on the electrode in the form of a greater iron contamination (see the arrows in fig.7) from the workpiece on the horizontal as opposed to the vertical part. Reciprocal tool-workpiece contamination has also been reported for EDM operations with conventional tools [8]. The outer white layer and the altered layer immediately below it are similar to those observed by other authors [9].

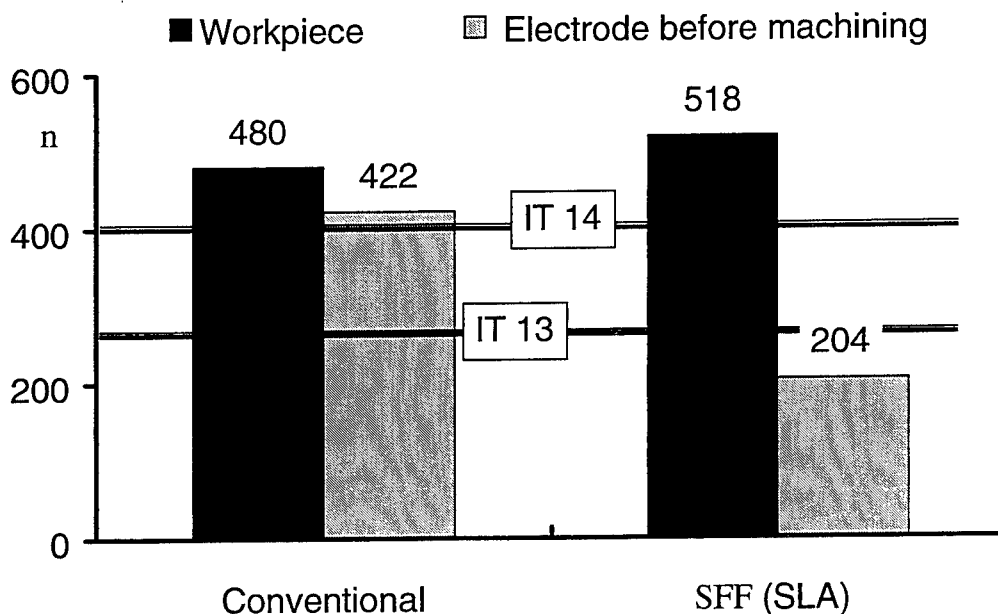


Figure 4: Comparison of both electrodes and workpieces in terms on number of tolerance unit for the 90% of observations.

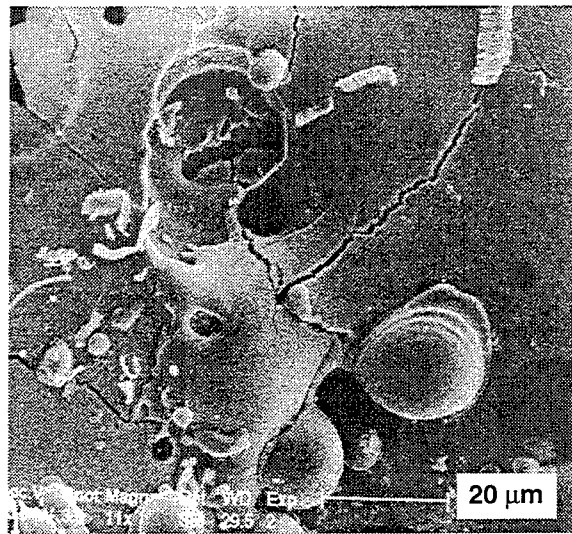


Figure 5: SEM image of the vertical surface of the hole

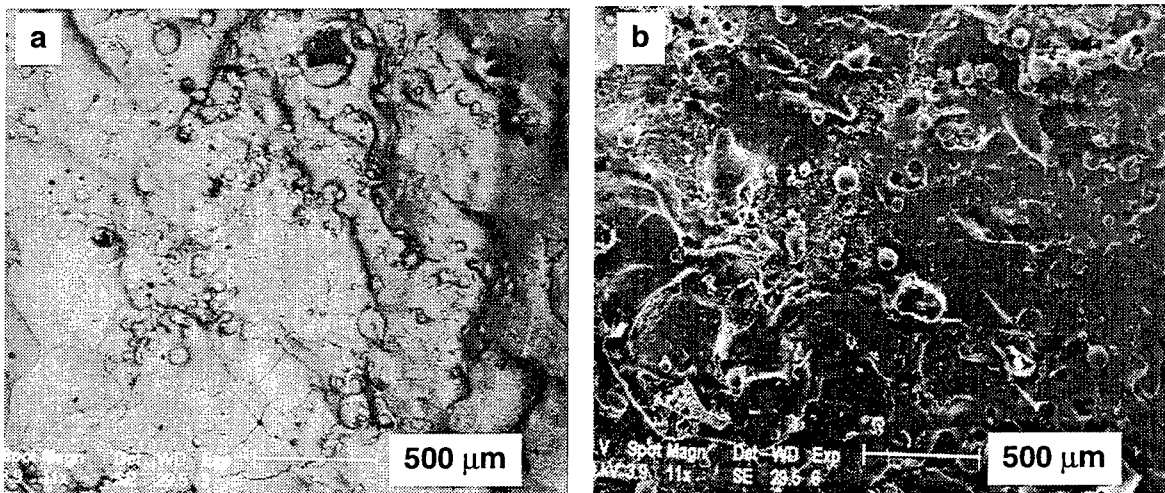


Figure 6: SEM image of the vertical (a) and horizontal (b) surface of the workpiece.

5. Conclusions

Four conclusions can be drawn from this study:

1. the method proposed gives electrolytic copper electrodes from SLA masters. Other SFF techniques can not be used, because they do not allow an acceptable surface finish to be obtained;
2. the dimensional precision of these electrodes is on a par with that of those produced conventionally for the same type of operations;
3. the deep thickness obtainable suggests that a 0.5 - 1 mm machining allowance can be provided for conventional finishing, which would mean that the method could equally be used to produce EDM electrodes for surface finishing operations;
4. the performance of these electrodes is decidedly superior to that of a tool obtained by mechanical machining from a bar nominally of the same material.

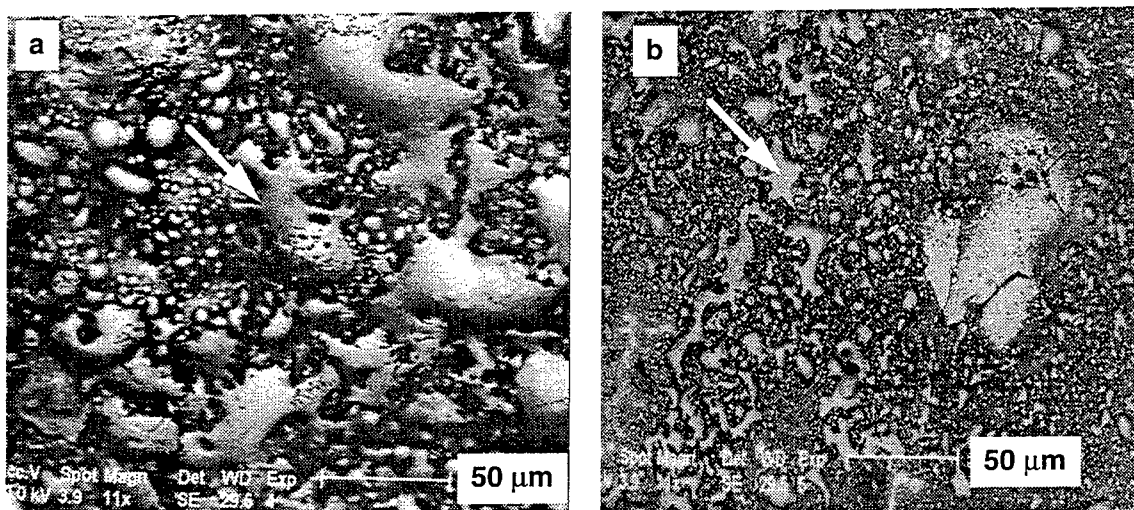


Figure 7: SEM image of the horizontal (a) and vertical (b) surfaces of the electrode.

No assessment can yet be made of the economic aspects of this method, since its feasibility requires further study.

Endurance tests are now in progress to determine the behaviour of the new electrodes over time, together with trials of the method in the fabrication of an injection mould. Their completion will allow initial conclusions to be drawn concerning the time and cost required for the production of an electrode of average complexity.

6. References

- [1] Bourrell D.L., Beaman J.J., Marcus H.L., Barlow W.J., 1990, Solid Freeform Fabrication an Advanced Manufacturing Approach, Solid Freeform Fabrication Symposium, pp.1-7.
- [2] O'Really Sean, 1993, FFF at Ford Motor Company, Solid Freeform Fabrication an Advanced Manufacturing Approach, Solid Freeform Fabrication Symposium, pp.168-177.
- [3] Biorke O., 1992, Layer Manufacturing a Challenge of the Future, Tapir, Trondheim Norway.
- [4] Iuliano L., Gatto A., De Filippi A., 1995, Metallisation and rapid tooling, 4th Eur. Conf. on Rapid Prototyping and Manufacturing, pp. 261-276.
- [5] Jensen K. L., 1992, Making electrodes for EDM with rapid prototyping, 2nd Eur. Conf. on Rapid Prototyping and Manufacturing, vol. 1: pp. 157-165.
- [6] Childs T.H.C., N.P. Juster, 1994, Linear and geometric accuracies from layer manufacturing, Annals of the CIRP, vol. 43/1: pp. 163-166.
- [7] Ippolito R., Iuliano L., Gatto A., 1995, Benchmarking of rapid prototyping techniques in terms of dimensional accuracy and surface finish, Annals of the CIRP, vol. 44/1: pp.157-159.
- [8] Lee L.C., Lim L.C., Narayanan V., Ven Katesh V.C., 1988, Quantification of surface damage of tool steels after EDM, Int. J. Mach. Tools Manufact., vol.28, N°4: pp. 359-372.
- [9] Dauw D.F., Albert L., 1992, About the evaluation of wire tool performance in wire EDM, Annals of the CIRP, vol. 41/1: pp. 221-225.

7. Acknowledgements

The authors express their thanks to Prof. L. Felloni for help and encouragement.

SOFT TOOLING FOR LOW PRODUCTION MANUFACTURING OF LARGE STRUCTURES

Cheol H. Lee, Thomas M. Gaffney, Charles L. Thomas
Department of Mechanical Engineering, University of Utah

ABSTRACT

A new technique for building large prototypes from layered substrate relies on a higher order construction algorithm to produce accurate prototypes from thick layers. The process is capable of producing a 4' by 8' by 20' object in less than two days. Using this technique to produce molds instead of parts allows construction of large castings and composite structures. Example parts include composite airfoils, a 19 foot canoe, and a custom fairing for a racing car.

INTRODUCTION

The common construction technique used by rapid prototyping (RP) devices commercially available in the current market such as Stereolithography (SLA) [9], Laminated Object Manufacturing (LOM) and Fused Deposition Modeling (FDM) [10], produce prototypes from 2D layers producing a stepped shape. Current devices move and work only vertically which is referred to here as the stepped cut algorithm (SCA). This stepped algorithm results in poor accuracy unless the layers are thin and thus is not efficient for building large prototypes.

There is a growing demand for prototypes of large objects, that can not be met by current techniques because of their size limitations. New prototyping techniques, using higher order construction algorithms (HOCA) developed at The Manufacturing Processes Laboratory at The University of Utah (MPL) address this problem. In this paper, two advanced algorithms are discussed as demonstrations of HOCA; ruled cut algorithm (RCA) and curved cut algorithm (CCA). The MPL has recently developed Shape Maker II (SM2) to implement RCA, and has been developing Shape Maker III (SM3) for CCA. These two new RP devices allow production of large prototypes up to 4' by 8' by unlimited length using HOCA. The devices cut 1/2" to 1.5" thick sheets of polystyrene foam using an electrically heated wire as a cutter.[1]

The polystyrene foam parts produced from these machines have little direct application other than as form models due to the poor mechanical properties of the foam. However, using techniques described below, the models can be converted to full strength engineering structures. The foam models can be used as expendable patterns for construction of large polymer composite structures. If the surface strength of the model is improved with a coat of fiberglass, the model can be used as a reusable pattern for low production quantities. Using a latex layer vacuum formed to the model surface, a rapidly changeable reusable mold can be produced. The text below introduces the HOCA algorithms and describes the various manufacturing applications.

CONSTRUCTION ALGORITHMS: Stepped Cut Algorithm (SCA)

SCA is the simplest algorithm used by most of existing RP devices. Since it uses a 2D profile instead of 3D for each layer, only vertical motions of a cut device are allowed. It assumes the geometry of a top cross section is same as bottom cross section of a layer. In other words, it

ignores changes in shape along with building direction. Thus, SCA is inaccurate with thick layers, and acceptable in the case of very thin layers or layers not changing shape in the cut direction. These algorithms are explained pictorially in Fig. 1.

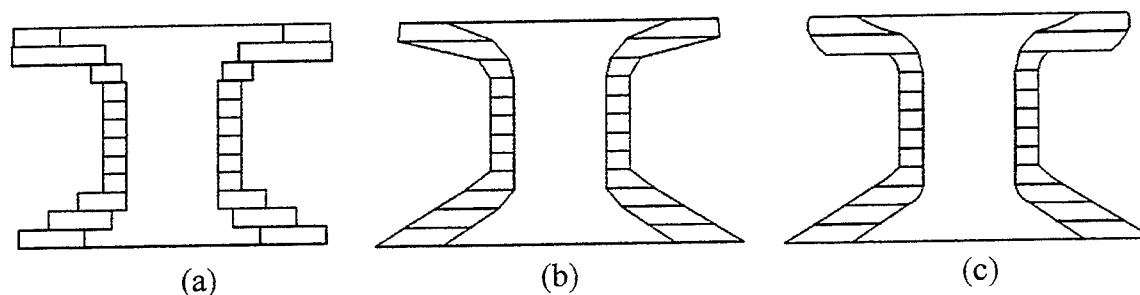


Figure 1: Cross section of a model with three construction algorithms: a) Stepped cut algorithm (b) Ruled cut algorithm (c) Curved cut algorithm

CONSTRUCTION ALGORITHMS: Ruled Cut Algorithm (RCA)

RCA produces layers of finite thickness that have general ruled surface edges. After getting geometry information of top and bottom cross sections of a layer, a control program must find the desired cutter path by matching the two cross section geometry's. With RCA, the cutter path is considered as a series of first order polynomial functions as follows;

$$\frac{x - x_1}{x_2 - x_1} = \frac{y - y_1}{y_2 - y_1} = \frac{z - z_1}{z_2 - z_1}$$

where $A(x_1, y_1, z_1)$ and $B(x_2, y_2, z_2)$ are points on the bottom and top cross sections of a layer.

Using RCA the cutter follows the exact geometry of the top and bottom cross section of each layer and approximates the geometry in between with a ruled surface. In comparison with SCA, RCA reduces error dramatically for parts with sloped or curved edges, and allows increased layer thickness with small errors. Increasing the layer thickness with small error means reducing manufacturing time and making large objects with an acceptable level of error. RCA has been successfully implemented as Shape Maker II (SM2), a RP device developed at the MPL.

CONSTRUCTION ALGORITHMS: Curved Cut Algorithm (CCA)

Though RCA is an advanced algorithm in comparison with SCA, performance can be further improved with CCA. CCA accommodates the all capabilities of RCA and adds more functionality for a more accurate approximation of actual object geometry. Among algorithms discussed here, CCA is the best for complex 3D shapes. To define a function representing a curved shape, the knowledge of coordinates of at least three points are required and an arc is completely specified by these three points. Two points, top and bottom points of a layer, are known since geometry information of cross sections can be obtained by slicing STL object, and it is reasonable to get a third point from an additional cross section spaced between the upper and lower surfaces of the intended slice. Three methods of manipulating these three points to get a function of a curve are discussed below.

Arc method : An arc can be defined by a center point, radius, and start and end points. Start and end points become top and bottom points of a layer to be matched. Center and radius can be found by calculating crossing point of two lines, which divide lines in half passing two of three points and are perpendicular to the lines.[1] If the three known points are $A(x_1, y_1, z_1)$, $B(x_2, y_2, z_2)$ and $C(x_3, y_3, z_3)$, the center and radius of an arc can be calculated as follows;

Step 1: shift and rotate : Shift points by $(-x_1, -y_1, -z_1)$ then rotate points about z axes in order to lie points on x-z plane. New points will be;

$$\begin{bmatrix} A^1, B^1, C^1 \end{bmatrix} = \begin{bmatrix} x_4 & x_5 & x_6 \\ y_4 & y_5 & y_6 \\ z_4 & z_5 & z_6 \end{bmatrix} = \begin{bmatrix} \cos \theta & \sin \theta & 0 \\ -\sin \theta & \cos \theta & 0 \\ 0 & 0 & 1 \end{bmatrix} \begin{bmatrix} x_1 - x_1 & x_2 - x_1 & x_3 - x_1 \\ y_1 - y_1 & y_2 - y_1 & y_3 - y_1 \\ z_1 - z_1 & z_2 - z_1 & z_3 - z_1 \end{bmatrix}$$

where $\theta = \arctan \frac{y_2 - y_1}{x_2 - x_1}$ and $y_4 = y_5 = y_6 = 0$

Step 2: center and radius : Find center (x_c, y_c, z_c) and radius r of an arc with A^1, B^1 and C^1 on x-z plane. As described above, a center is a cross point of two lines;

$$z = -\frac{x_5 - x_4}{z_5 - z_4} \left(x - \frac{x_5 - x_4}{2} \right) + \frac{z_5 - z_4}{2}$$

$$z = -\frac{x_6 - x_5}{z_6 - z_5} \left(x - \frac{x_6 - x_5}{2} \right) + \frac{z_6 - z_5}{2}$$

Thus,

$$x_c = \frac{\left[\frac{(x_5 - x_4)^2}{2(z_5 - z_4)} - \frac{(x_6 - x_5)^2}{2(z_6 - z_5)} + \frac{z_5 - z_4}{2} - \frac{z_6 - z_5}{2} \right]}{\left[\frac{x_5 - x_4}{z_5 - z_4} - \frac{x_6 - x_5}{z_6 - z_5} \right]}$$

$$y_c = 0$$

$$z_c = \frac{\left[\frac{(z_6 - z_5)^2}{2(x_6 - x_5)} + \frac{(z_5 - z_4)^2}{2(x_5 - x_4)} + \frac{x_6 - x_5}{2} - \frac{x_5 - x_4}{2} \right]}{\left[\frac{z_6 - z_5}{x_6 - x_5} - \frac{z_5 - z_4}{x_5 - x_4} \right]}$$

$$r = \sqrt{(x_c - x_4)^2 + (z_c - z_4)^2}$$

and cutter path on x-z plane can be defined as;

$$(x^1 - x_c)^2 + (z^1 - z_c)^2 = r^2, \quad y^1 = 0$$

Step 3. Rotate about z axes (x_1, y_1, z_1) to original coordinates resulting (x, y, z) as follows;

$$\begin{bmatrix} x \\ y \\ z \end{bmatrix} = \begin{bmatrix} \cos \theta & -\sin \theta & 0 \\ \sin \theta & \cos \theta & 0 \\ 0 & 0 & 1 \end{bmatrix} \begin{bmatrix} x^1 \\ y^1 \\ z^1 \end{bmatrix} + \begin{bmatrix} x_1 \\ y_1 \\ z_1 \end{bmatrix}$$

Smooth surface method : For smooth surface of prototypes, the slopes at the top and bottom points of a layer should be equal to the slope of the same points of adjacent layers. The cutter path is defined by slopes at top and bottom points, and length of a path. Like the above method, all parameters are calculated in the x-z plane, then transform the coordinates to original system.

$$\left. \frac{dz}{dx} \right|_{layer i}^{top} = \left. \frac{dz}{dx} \right|_{layer i+1}^{bottom}, \quad \left. \frac{dz}{dx} \right|_{layer i}^{bottom} = \left. \frac{dz}{dx} \right|_{layer i-1}^{top}$$

$$length = \int L = \sum_{i=1}^n L_i$$

Second order method : Three points can define a second order polynomial. Three parameters in a second order function can be also found in x-z plane with known three points; top, bottom and middle points.

$$z = ax^2 + bx + c$$

NEW PROTOTYPING DEVICES: Shape Maker II (SM2)

SM2 is designed as 4 axis device as shown in Fig. 2 [1]. Two ends of a cutter, an electrically heated wire, are supported by carriers and each carrier moves in two independent directions (x,y). Thus, SM2 is able to cut ruled surface edges up to 45 degree (current machine design limit) implementing RCA. Each cutter carrier has a ball with a hole in the middle so that a cutter freely slides inside ball and adjusts its length when it tips. The current cutter design allows cutting thermoplastic foam less than 1.5 in thick. All axes are driven by stepper motors and a custom control software developed at MPL. Construction speed varies with geometry, and is roughly 6 in/hr for large objects when layer thickness is 1 in.

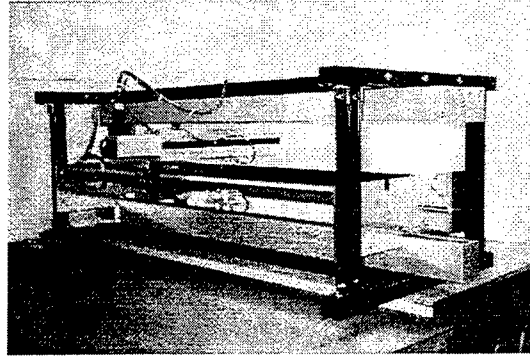


Figure 2: Shape Maker II [1]

NEW PROTOTYPING DEVICES: Shape Maker III (SM3)

SM3 is an 8 axis device which is an advanced version of SM2. It can produce curved surface parts using CCA. Four axes are used to position the top and bottom cutter carriers in x and y axes. In addition, there are tipping mechanisms to give angles to the cutter in three directions : one angle in common for the top and bottom of the cutter, and one independent angle at each end of the cutter. The last axes controls the length of the hot wire cutting surface. The control software will calculate 8 parameters $(x_1, y_1, x_2, y_2, \theta_1, \theta_2, \theta_3, \ell)$ and drive 8 motors. SM3 is currently under development.

APPLICATION TO COMPOSITE TOOLING

Mold tooling using fiber and resin is considered "soft" by comparison to steel mold tooling. Metal mold tooling is usually used for large production, while composite mold tooling is used for low production and critical applications where thermal expansion is a concern.[7] With traditional mold tooling methods, making a mold has required many steps of processing and handwork taking a couple of months in many cases. This traditional paradigm can be improved by applying RP technology to mold tooling. Furthermore, composite tooling can also take advantage of patterns/molds tooling made by a RP device. In this paper, the applications of foam patterns/molds made by Shape Maker to composite tooling of large structures are introduced.

The proposed techniques have many advantages. First, foam patterns/molds for full scale large composite parts can be made economically, accurately within few days using Shape Maker (SM). Second, this technique eliminates several steps, and handwork normally needed in traditional mold tooling techniques which reduces manufacturing costs and time from months to few days.[7] Third, the computerized prototyping process is a semi-automated process, thus, increases accuracy. Finally, dealing with a 3D CAD drawing object is also a lot easier than working with the disposable 2D mylar drawings from traditional processes.

However, as thermoplastic foam is used, some limitations of foam mold tooling have been found. Since the maximum working temperature of polystyrene foam is around 140F, only low temperature cure epoxy resins are acceptable. Moreover, compressive yield strength is in the range of 23 to 44 psi. Thus, high pressure autoclave processing is not appropriate. Finally, the choice of resin is limited to phenolics or epoxies to avoid dissolving the foam.[5]

When applying foam patterns/molds made by SM to composite laminates, two methods are applicable. First, lay-up a final composite structure directly on the foam pattern or mold made by SM, and vacuum bag and cure at room temperature. Second, lay-up an intermediate composite mold tool on the foam pattern, so that the foam pattern becomes reusable, and lay-up final composite structure on the intermediate mold tool and cure at high temperature in an autoclave.[5] Examples of both cases are demonstrated and described below.

DEMONSTRATION: Foam Patterns

Tail Stabilizer Wing: This is the demonstration of a composite structure made by lay-up directly on a foam pattern. In this case, the foam pattern becomes a permanent part of the composite and, thus, can make only one final composite structure. A tail stabilizer wing for a military jet was created using a solid modeling CAD software. The chord length and chord height of the base cross section are 19.5 in. and 2.5 in. respectively, and those of top cross section are 10 in. and 1.25 in. The wing tapers along the length of 58 in. 58 layers of 1 in thick extruded polystyrene foam were cut using SM2, and assembled on a registration board as shown in Fig. 3. The accuracy of the foam pattern was improved by applying a thin plaster coat on the foam pattern and sanding. This process required 13 hours with a material cost of \$45. The final composite part was made by applying three layers of plain weave 7 oz. E-glass fiber with a room temperature cure epoxy resin on the foam pattern. The finished composite wing was allowed to cure for 5 days. The initial foam pattern and final composite wing are shown in Fig. 4.[5]

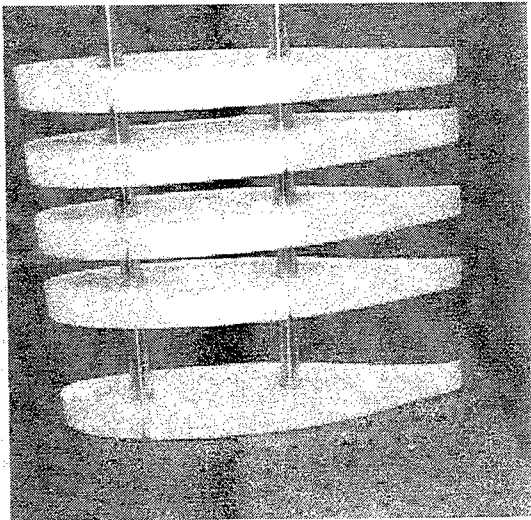


Figure 3 : Registration process of layers Figure 4 : Foam and composite pattern of tail stabilizer wing.[5]

Custom Fairing for a Racing Car: When desirable, the foam pattern can be used to create low production tooling instead of making only one part. For producing multiple composite parts, two step processes are involved. First, the foam pattern of a Formula I race car fairing was fabricated using SM2 requiring about 6 hours and \$18 for materials. The foam model was transformed into a more rugged intermediate positive pattern by applying a resin and fiber glass weave on the foam pattern. Surface imperfections were minimized by a coating of epoxy putty and sanding. The final composite car fairing was produced by coating the intermediate pattern with a room temperature cure epoxy and fiber glass weave.[5] The intermediate pattern is reusable as many times as its surface lasts. An intermediate and finished composite car fairing are shown in Fig. 5.



Figure 5: Intermediate Mold Tool and Finished Composite Fairing.[5]

DEMONSTRATION: Foam Molds

Fiber Reinforced Concrete Canoe: A foam prototype is used here as a large negative mold tooling. A disposable foam mold of a full scale 19 ft fiber reinforced concrete canoe was fabricated requiring \$350 for materials, 25 hours labor, and consuming 54 sheets of 4' by 8' by 1" expanded polystyrene foam to cut 240 layers as shown in Fig. 6. The mold was coated with a thin layer of plaster, and the composite canoe was laid up by applying alternating layers of Type III Portland Cement and a mat of fiberglass Stucco Mesh until reaching the designed wall

thickness of 0.375 in. The concrete was allowed to cure for about one week before removing from the foam mold. The final concrete canoe is shown in Fig. 6.[5]

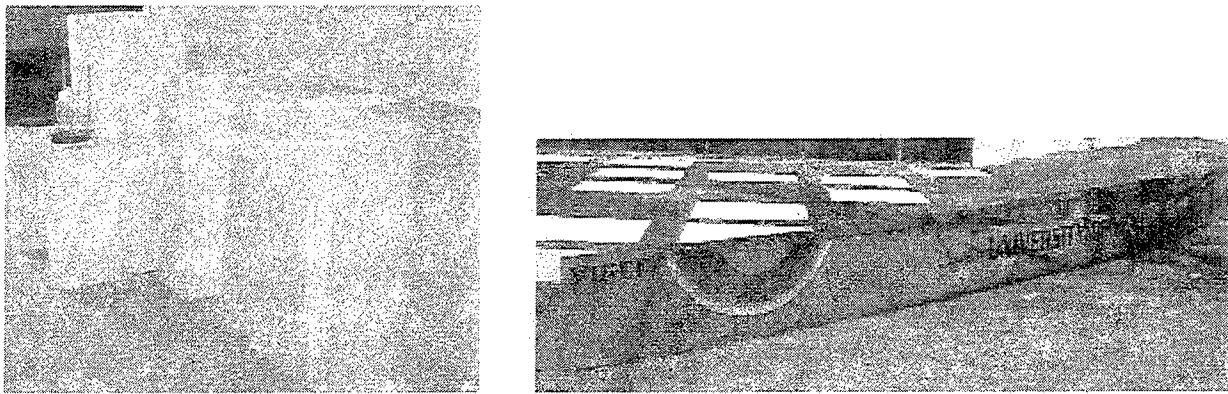


Figure 6: Canoe Foam Mold and finished canoe.

Wind Turbine Blade Airfoil: When curing fiber/resin systems, a certain amount of pressure is required. Without pressure, fiber/resin ratio varies throughout the structure and obvious flaws exist within the laminates. Since the compressive yield strength of polystyrene foam is in the range between 23 to 44 psi, vacuum bagging, which can provide pressure less than 22 psi, is the primary source for consolidating the lamina and drawing out excess resin to achieve the best fiber to resin volume ratio.

An example of this process is shown for multiple composite parts using a vacuum bagged negative foam mold of a 1/5 scale of NASA LS(1)-417MOD wind turbine blade. The blade was made by SM2 assembling 36, 1 in thick layers requiring 3 hours and \$40 for materials. The foam mold was coated with plaster and sanded for a smooth surface. Then, a 0.01 in thick layer of latex rubber was vacuum formed onto the foam mold as shown in Fig. 7 (a) which provides a release ply and minimizes small surface defects on the foam mold. The application of 5 layers of

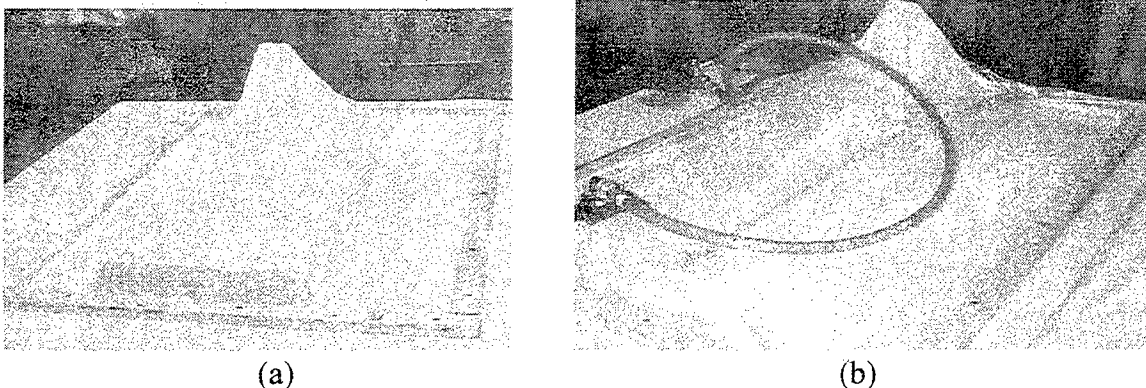


Figure 7: Vacuum Bagging Process for Wind Turbine Airfoil: (a) Latex Rubber Vacuum Formed on the Foam Mold (b) Vacuum Bagged Wind Turbine Skin Panel.[5]

7 oz. plain weave E-glass fiber and room temperature epoxy resin was used to form the composite mold tooling. Next, the entire assembly was vacuum bagged as shown in figure 7 (b). The composite was allowed to cure to a self-supporting state for three hours, and cure 5 days at room temperature. The final composite structure is shown in Fig. 8.[5]

CONCLUSION

This paper presents various new techniques for full scale composite tooling of large structures using foam patterns/molds made by Shape Maker. Foam patterns/molds can be made rapidly, economically, and accurately by SM2, producing final composite parts through the proposed methods which reduce manufacturing time and cost. Though limitations on temperature, pressure and choice of resin are found, the experiments show that most composite mold tools can be fabricated in a short time at lower cost than traditional processes. In all, the application of foam parts made by SM to composite tooling techniques is successful in manufacturing large composite structures.

REFERENCES

- [1] Lee, C. H., Gaffney, T. M., Thomas, C. L., *Proc. of the 6th ICRP*, SME, 131, (1995).
- [2] Thomas, C. L., *An Introduction to Rapid Prototyping*, Schroff Development Corp., Mission, Kansas, (1995).
- [3] Sollner, G., Molitor, M., *Composite Application: The Future is Now*, Ed. Thomas Drozda, SME, Dearborn, Michigan, pp. 194-201, (1989).
- [4] Sauer, G. L., *Composite Application: The Future is Now*, Ed. Thomas Drozda, SME, Dearborn, Michigan, pp. 165-174, (1989).
- [5] Gaffney, T.M., *Rapid Prototyping Composite Mold Tooling and Patterns*, Thesis, U. of Utah, under prep.
- [6] Kruth, J. P., *Annals of the CIRP*, **40** (2),603, (1991).
- [7] Thomas, C. L., Gaffney, T. M., Kaza, S., Lee, C. H., *Proc. of the 1996 IEEE Aerospace Appl. Conf.*, IEEE, **4**, 219, (1996).
- [8] Suh, K. W., *Handbook of Polymeric Foams and Foam Technology*, Ed. Daniel Klemper and Kurt Frisch, Oxford University Press, New York, 151, (1991).
- [9] Jacobs, P. F., *Rapid Prototyping & Manufacturing: Fundamentals of StereoLithography*, 5th ed., SME, Dearborn, MI, (1992).
- [10] Crump, S. S., *Proc. of the 2nd ICRP*, SME, 351, (1991).
- [11] Kochan, D., *Solid Freeform Manufacturing*, Elsevier Science, New York, (1993).
- [12] Wohlers, T. T., *Manufacturing Engineering*, **107**, 77, (1991).



Figure 8: Finished mold tool for turbine skin panel.[5]

Recent Developments in Profiled-Edge Lamination Dies for Sheet Metal Forming

Daniel F. Walczyk¹, David E. Hardt²

Introduction:

The Profiled-Edge Lamination (PEL) method was developed by the Walczyk and Hardt [1] as an improvement over the current method of stacking and bonding contoured laminations in terms of the lead-time and cost of tooling development for sheet metal forming dies. It is also a viable alternative to conventional CNC-machining of such dies. In pursuit of successful commercial realization of the PEL method in industry, this paper discusses several important issues including:

- the origin of this method and advantages over other tooling techniques
- the general procedure for creating PEL machining instructions
- determining the geometric error introduced by the straight bevel approximation
- the propensity for PEL die delamination from high forming loads
- methods for cutting bevels into die laminations and
- the machinery needed for PEL die fabrication.

Future research and developmental work on the PEL die method will also be outlined.

I. Background on the PEL Die Method:

Using a laminated construction for sheet metal forming dies is a relatively new idea. Kunieda and Nakagawa successfully created a sheet metal forming die made of horizontally-oriented laminations by slicing up a CAD model of the 3-D forming surface and using the resulting data to CNC laser-cut the required contours out of sheet material [2]. The contoured laminations were secured to one another by a combination of cementing with adhesives, clamping with bolts, and laser-welding the edges. Nakagawa et al. formed a solid tool out of stacked laminations by diffusion-bonding the laser-cut laminations together [3]. Since the lamination edges were cut normal to the surface and not beveled, the forming surface of the resulting dies had a stepped profile and thus needed to be CNC-machined with finishing cuts, ground, and polished in order to achieve the necessary smoothness. Some industries completely avoid this secondary smoothing operation used to remove the stepped profile by filling in the steps with epoxy or some other tough material [4].

Weaver was granted a patent for a laminated tooling with the contours machined into each lamination using beveled edges and not just normal cuts [5]. This change in the art obviates a smoothing operation and only requires a grinding and polishing operation as shown in Figure 1a. The smoothing operation also becomes unnecessary as the laminations get very thin and the resulting steps between laminations are negligible. For instance, LOM can create a forming die for low force forming that has nearly smooth surfaces since laminations are as thin as 0.05 mm. The biggest limitation with current LOM paper/adhesive models is that they have low compressive strength (26 MPa). This is one-fifth the compressive strength of the cast epoxy (140 MPa) that is used in forming dies. Other materials (e.g. ceramic & metal tape) for LOM models are currently being developed that may take higher compressive loads.

As previously mentioned, Walczyk and Hardt recently introduced the PEL method of constructing sheet metal forming dies [1]. As seen in Figure 1b, a PEL die generally comprises a

¹ Assistant Professor, Department of Mechanical Engineering, Aeronautical Engineering & Mechanics, Rensselaer Polytechnic Institute, Troy, NY.

² Professor, Department of Mechanical Engineering, Massachusetts Institute of Technology, Cambridge, MA.

plurality of die lamination members, each die lamination member being substantially planar and each being disposed in a vertical plane and stacked together side-by-side in an array. The top edge of each die lamination is simultaneously profiled and beveled in such a way as to approximate a segment of the intended die surface. Specifically, this top edge is continuous in the y-direction and approximated in the x-direction. The die lamination members may be held together in a stacked array by any suitable means, but preferably with a clamping frame as shown in Figure 1b. A common registration corner and the bottom edge of each lamination allows for easy and uniform registration in the clamping frame. One or more holes uniformly positioned in the sides of each lamination allows the whole array to be clamped so that no adhesive or other means of holding the array of die lamination members together is required. If the shape of the forming surface has to be change during the die development, the die laminations can easily be separated for re-machining to update the die shape. The PEL die can be made into a solid die apart from this process by suitable means (e.g. diffusion bonding) if needed or desired. Generally at least a portion of the die lamination members have a continuously changing beveled top edge. When placed together in a vertical stacked array, the top edges of the die lamination members, in the aggregate, form the top surface of the die. The advantages that a PEL array construction has over the contoured lamination stack shown in Figure 1a is summarized in table 1.

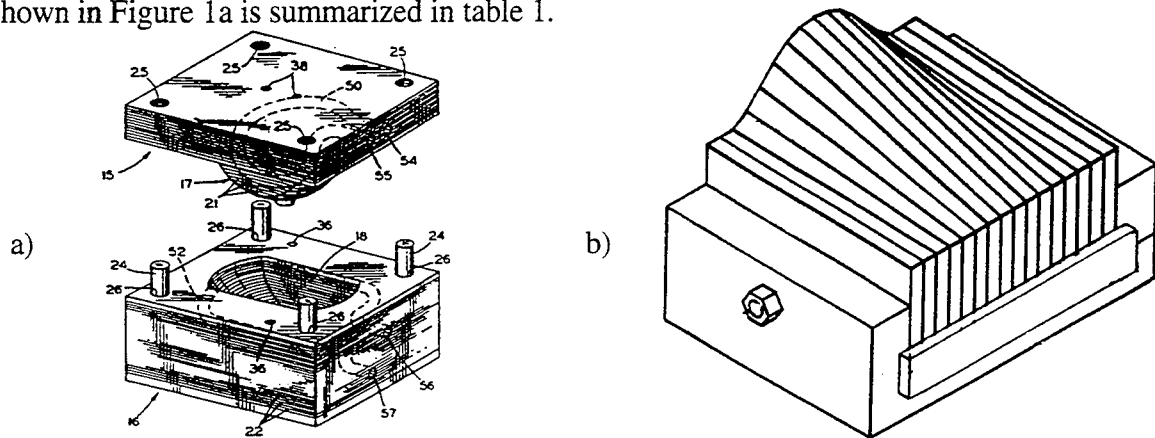


**Figure 1 - a) Stack of contoured, beveled laminations (Weaver Die) and
b) an array of Profiled-Edge Laminations.**

Table 1 - Comparison of laminated die constructions

Stack of Contoured Laminations	Array of Profiled-Edge Laminations
Difficult to automate the handling of laminations during cutting.	Laminations can slide past the profiled-edge cutting means since only top edge is cut.
Difficult to register laminations during die assembly.	Laminations are easily registered with a base plate and an edge guide.
Difficult to secure lamination stack into a rigid tool.	Lamination only needs to be clamped from the side.
Typically, laminations need to be permanently secured. Reshaping of die surface requires CNC-machining.	Unclamped laminations can be individually recut to new die shape.

II. Creating PEL Machining Instructions from a CAD Model:

The first step in the process of creating a PEL die consists of creating a 3-dimensional model of the die's forming surface. The surface model may be created by a die designer using CAD software; or by a locus of surface coordinates defined by an iteration of a closed-loop control algorithm, an FEA model of the die, or a reverse engineering scan from a coordinate measuring machine. The details of extracting the PEL machining instructions from a surface model of a die are beyond the scope of this paper. However, to illustrate the data manipulation process required, the general procedure of using a CAD surface model for this purpose will be discussed.

The intersection of a 3-dimensional CAD surface model and a Y-Z cutting plane situated on the X-axis at a certain point is a 2-dimensional curve. Furthermore, if the Y-Z plane is

repositioned along the X-axis by constant increments such as 1 mm, the collection of curves produced by each of the same plane/surface intersections will approximate the shape of the original 3-D surface. The algorithms developed by Phillips et al. and Bobrow for determining the intersection of two arbitrary surfaces (analytic or parametric) can be used [6,7]. The true 3-D surface between two adjacent curves can be approximated by connecting them with a bevel. This connecting bevel constitutes the profiled-edge of each PEL die lamination. The reader will note that the approximation of the 3-D surface gets better as the curves get closer together, i.e. as the x-increment decreases. This collection of curves serves as the machining database for creating a PEL die with the desired forming surface.

Any one of several cutting methods (e.g. laser cutting, machining with an endmill, abrasive waterjet cutting, plasma-arc cutting) can be used to create the bevels into the top edges of the die laminations. These methods will be discussed in more detail in a later section. With whatever method is used, the data needed for cutting the compound bevels is the position point P_1 on the nearside of the lamination with coordinates (x_1, y_1, z_1) and a unit directional vector $\vec{V} = V_1 \cdot i + V_2 \cdot j + V_3 \cdot k$ or just written as (V_1, V_2, V_3) . As shown in Figure 2a, the vector components of \vec{V} defined by P_1 and P_2 (coordinates x_2, y_2, z_2) are

$$V_1 = \frac{x_2 - x_1}{|\vec{V}|} = \frac{t_L}{|\vec{V}|}, \quad V_2 = \frac{y_2 - y_1}{|\vec{V}|}, \quad \text{and} \quad V_3 = \frac{z_2 - z_1}{|\vec{V}|}. \quad (1)$$

where:

$$|\vec{V}| = \left[t_L^2 + (y_2 - y_1)^2 + (z_2 - z_1)^2 \right]^{\frac{1}{2}}$$

Point P_1 is easy to determine because x_1 and y_1 will be prescribed and z_1 is explicitly defined by the nearside intersection curve (see Figure 2a). Point P_2 is harder to define since there is no particular one associated with the defined point P_1 . To determine P_2 , an iterative procedure which minimizes the geometric error introduced by the straight bevel approximation is required. When P_2 is determined then the bevel cutting head will only require translation along the Y and Z-axes, i.e. x_p is kept constant, and rotation about the two orthogonal axes.

There are many forming dies used in industry for such processes as stretch forming and rubber forming that only have mild curvatures and low draws. For these types of die shapes, reasonable die shape fidelity, i.e. small deviations of the machined shape from the desired CAD shape, can be achieved even if the bevel cutting head is only allowed to rotate about the Y-axis. This will allow for simple planar beveling but not compound 3-D beveling like that shown in Figure 2. The position point P_1 and orientation vector \vec{V} of the bevel cutting head are defined by (x_1, y_1, z_1) are coordinates $(0, V_2, V_3)$, respectively.

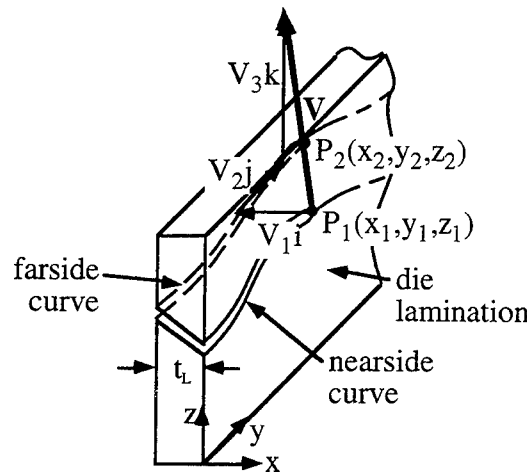


Figure 2 - Die lamination profiled edge made by 3-D beveling.

III. Geometric Error Introduced by Straight Bevel Approximation:

By observing the X-Z plane cross section of a die lamination in Figure 3, it is evident that the straight bevel of the profiled edge will deviate from the desired die surface. During the grinding and polishing operations on the die surface, this deviation or shape error is increased for convex cross-sectional profiles, as shown in figure 3a, because of material removal. For the same reason, i.e. material removal, the shape error is decreased for concave cross-sectional profiles as shown in Figure 3b. Therefore, the extent of material removal during the smoothing operation directly affects the shape integrity of the forming die. The standard method for determining the die shape error is to directly measure the surface with a coordinate measuring machine and then compare that data with the reference CAD shape.

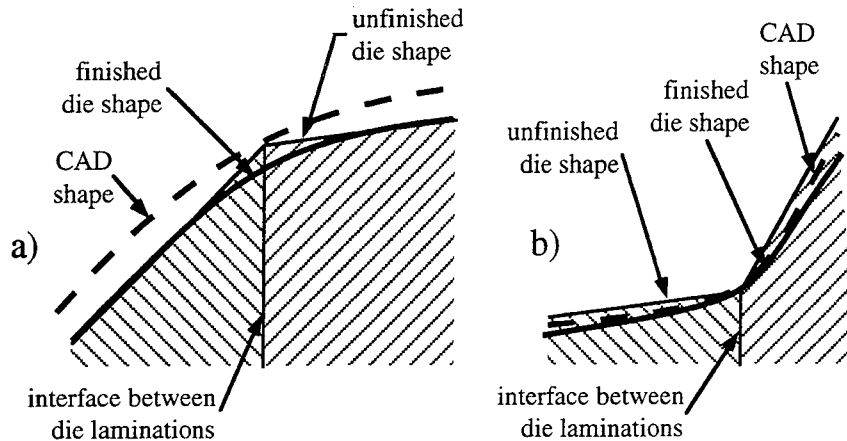


Figure 3 - Shape error due to smoothing of a) convex and b) concave die geometries

Instead of direct measurement, the maximum error introduced by the straight bevel cutting of the die lamination profiles can be estimated by considering the cross-sectional geometry from the CAD database as shown in Figure 4. The actual cross-sectional curve of the die surface model can be determined using currently-available CAD software for comparison with the straight bevel. The task of extracting this curve is very cumbersome. A simpler way to determine the maximum shape error is to estimate the die's cross-sectional curve between points (x_1, y_1) and (x_2, y_2) with a parabola. A parabola is used because it easily curve-fits 2 coordinate points with known slopes. This parabola is defined by bevel end coordinates (x_1, z_1) and (x_2, z_2) , and the corresponding instantaneous x-z slopes $\frac{\partial z_1}{\partial x_1}$, $\frac{\partial z_2}{\partial x_2}$. The coordinates and slopes are easily obtainable with many

CAD programs (e.g. ProEngineer™). The general equation of a parabola in the X-Z plane is

$$(x - h)^2 = 4 \cdot p \cdot (z - k) \quad (2) \quad \text{if it opens upwards, i.e. } \frac{\partial z_1}{\partial x_1} < \frac{\partial z_2}{\partial x_2}, \text{ and}$$

$$(x - h)^2 = -4 \cdot p \cdot (z - k) \quad (3) \quad \text{if it opens downwards, i.e. } \frac{\partial z_1}{\partial x_1} > \frac{\partial z_2}{\partial x_2}$$

where:

p = parabola's focal length and
 (h, k) = the vertex coordinates.

Fitting a parabola to the die lamination cross-section shown in Figure 4 yields the following substitutions into equ. 2;

$$h = x_1 - 2 \cdot p \cdot \frac{\partial z_1}{\partial x_1}; \quad k = z_1 - \frac{(x_1 - h)^2}{4 \cdot p}; \quad p = \frac{x_2 - x_1}{2 \cdot \left(\frac{\partial z_2}{\partial x_2} - \frac{\partial z_1}{\partial x_1} \right)} \quad (4)$$

and the following substitutions into equ. 3;

$$h = x_1 + 2 \cdot p \cdot \frac{\partial z_1}{\partial x_1}; \quad k = z_1 + \frac{(x_1 - h)^2}{4 \cdot p}; \quad p = \frac{x_2 - x_1}{2 \cdot \left(\frac{\partial z_1}{\partial x_1} - \frac{\partial z_2}{\partial x_2} \right)}. \quad (5)$$

The slope m of the line which passes through points (x_1, y_1) and (x_2, y_2) is found by the relation

$$m = \frac{z_2 - z_1}{x_2 - x_1}. \quad (6)$$

The point (x_p, y_p) on the parabola with the same slope is found by setting the first derivative $\frac{\partial z}{\partial x}$ of equ. 2 and equ. 3 equal to m . If the parabola opens upward, then

$$x_p = h - 2 \cdot p \cdot m \quad \text{and} \quad z_p = k - p \cdot m^2. \quad (7)$$

If the parabola opens downward, then

$$x_p = h + 2 \cdot p \cdot m \quad \text{and} \quad z_p = k + p \cdot m^2. \quad (8)$$

To find the distance e between the line passing through (x_1, y_1) and (x_2, y_2) and the parallel line passing through (x_p, y_p) , a line is constructed through (x_p, y_p) which is perpendicular to the other two lines, i.e. slope = $-\frac{1}{m}$. This perpendicular line intersects the (x_1, y_1) and (x_2, y_2) line at point (x_g, y_g) . The values of this new intersection point are found from the equations

$$x_g = \frac{m \cdot x_1 + \frac{x_p}{m} - z_1 + z_p}{m + \frac{1}{m}} \quad \text{and} \quad z_g = z_1 + m \cdot (x_g - x_1). \quad (9)$$

The maximum distance e between the parabola and the straight line representing the bevel represents is the largest error. It is calculated with the equation

$$e = \sqrt{(x_p - x_g)^2 + (z_p - z_g)^2} \quad (10)$$

If desired, the error estimated with equ. 10 can be expressed as a function of lamination thickness t_L so that an optimization procedure for choosing the thicknesses, interface placement, and orientation of the laminations can be implemented. The goal of this procedure would be to minimize the overall bevel approximation error.

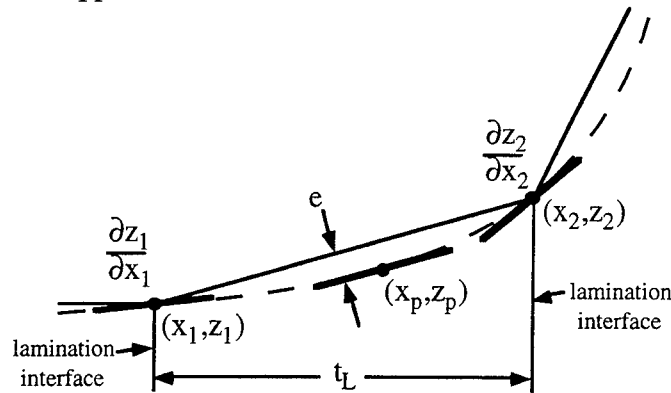


Figure 4 - Shape error estimation of a beveled die lamination

IV. Bevel Cutting Methods For Die Laminations

Once the intersection curves that define the top profiled-edge bevels of each lamination are extracted from the CAD model, the corresponding die laminations can then be fabricated. This machining database can then be used to either cut new die lamination blanks or to recut existing die laminations into a new shape. Machining bevels into the die lamination edge can be accomplished

by several methods. As seen in Figure 5a, the flute-edge of a standard endmill mounted in the spindle of a 4 or 5-axis (X, Y, and Z-translation, Y and Z-rotation) CNC milling center can be used to cut bevels into a suitably-fixed die lamination. This machining method relies on the application of high machining forces to make a wide cut in the workpiece. To minimize the amount of material removed while cutting the bevel, a very narrow kerf can be cut into the die lamination using unconventional machining methods like traveling-wire EDM, abrasive water-jet cutting, plasma-arc cutting, or laser cutting (both CO₂ and Nd:YAG) as seen in Figure 5b. Each of these methods require CNC-controlled axes that move in X, Y, Z translation, and Y, Z rotation.

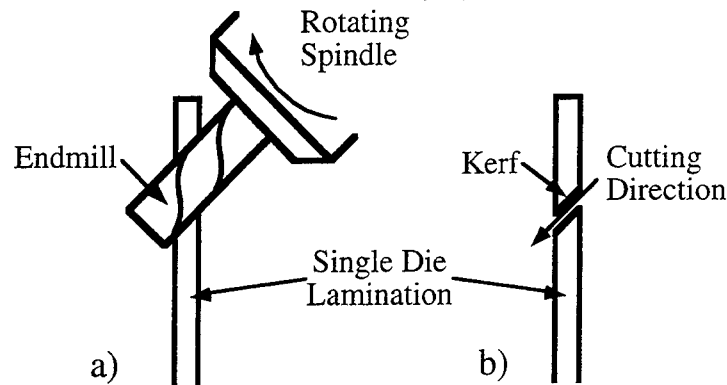


Figure 5 - Cutting bevels into die laminations by a) flute-edge endmilling and b) by unconventional machining methods.

The important characteristics of any bevel cutting method are maximum achievable bevel angle, maximum cutting feedrate (speed), cut surface quality, cutting accuracy, amount of material removed, tool wear, extent of metal burring, and machine cost and the effect of material hardness on cutting speed. Quantifying the performance specifications of each of the aforementioned bevel-cutting methods is necessary so that the most suitable one(s) for machining PEL die laminations are identified.

Suitable methods for cutting bevels include machining with the flute-edge of an endmill, abrasive water jet cutting, plasma-arc cutting, and laser cutting. Although wire-cut EDM produces kerfs of excellent quality and accuracy, an extremely slow cutting feedrate makes it impractical for bevel cutting. The other cutting methods were investigated in detail through a series of bevel cutting experiments to determine how rapidly and accurately each one will machine steel PEL laminations. The lamination material used for all cutting experiment was 1.47 mm thick SAE 1010 cold drawn steel sheet. Steel was used for the cutting experiments since it is arguably the most common material for sheet metal forming dies [8]. The basis of evaluation for each beveling method will be the quality characteristics of the bevel cut that it makes. The quality characteristics are defined in figure 6.

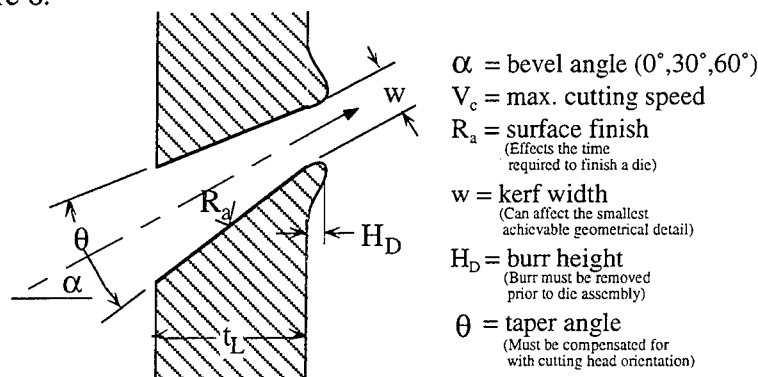


Figure 6 - Quality characteristics of a bevel cut.

The following equipment was used for the bevel cutting experiments:

- a Cincinnati-Milacron 3-axis machining center with a 6.4 mm diameter 4-fluted carbide endmill.
- An OMAX JetMachining System with a 0.76 mm cutting nozzle diameter and 80 grit garnet abrasive, i.e. 0.267 mm average particle size.
- a Hypertherm HD-1070 HyDefinition Plasma-Arc unit with O₂ plasma & shield gas, 130 volt DC output voltage and 30 amp output current.
- a Laserdyne 5-axis, model 780, CNC laser cutting system with a Lumonics JK704 Nd:YAG laser (maximum 400 watts of average output power).

Further details on all of these cutting experiments can be found in reference [9].

Summary of Bevel Cutting Methods:

For the purpose of comparing the candidate bevel cutting methods, the beveling performance measures (cutting force, maximum f_m , maximum α , taper angle, kerf width, machining burr height, and kerf surface finish) of each method, with process parameters set to their optimal levels, are listed in table 2. Plasma-arc cutting is noticeably absent from this table since it became apparent that this method was not suitable for bevel cuts. Bevels at angles up to 45° yielded very large tapers (>10°) in the kerf, excessive dross ($H_p=0.9$ mm) which was welded to the metal, and a large Heat Affected Zone (HAZ). The large HAZ caused the cut edge of the lamination to warp slightly. The maximum bevel angle achieved was 60° but the kerf edge closest to the cutting nozzle was consistently obliterated from an over-zealous oxidation (self-burning) of the metal during cutting. Consequently, the following comparisons are only made between flute-edge endmilling, AWJ cutting and laser cutting:

- Flute-edge endmilling involves the application of a high cutting force with a cutting tool to remove the unwanted lamination material. The higher cutting forces significantly deflect the cantilevered portion of a lamination being beveled. AWJ cutting and laser cutting, i.e. non-contact cutting methods, cause negligible deflection to the lamination.
- All three cutting methods are capable of high cutting speeds but the maximum speed is highly dependent upon the material composition and hardness with flute-edge endmilling and AWJ cutting. The maximum laser cutting f_m is only dependent on laser power, i.e. proportional to q_{laser} , which means that higher cutting rates than that listed in table 2 are achievable.
- The maximum bevel angle for all three methods is around $\pm 80^\circ$.
- The kerf from AWJ cutting has a very large, consistent taper of around 10° for all bevel angles that must be compensated for during bevel cutting. Laser cutting creates only a slight kerf taper. Flute-edge endmilling leaves no appreciable kerf taper unless there is significant deflection of the lamination and cutting tool during beveling.
- The width of the kerf affects the smallest radius of curvature achievable for a PEL's profiled edge. Of the three beveling methods, laser cutting creates the narrowest kerf. The kerf from AWJ cutting is also narrow but not as much as that cut with a laser. The kerf width from endmilling is much larger, i.e. the diameter of the cutting tool.

- Flute-edge endmilling leaves a very large machining burr, especially at larger bevel angles. AWJ cutting and laser cutting, on the other hand, yield much smaller machining burrs. Laser cutting with a pure oxygen assist gas yields a porous, brittle edge burr (i.e. iron oxide) which is easily removed from the cut lamination without having to grind it off.
- Flute-edge endmilling yields the smoothest surface finish of all the methods although the finish deteriorates at higher bevel angles from more machining chatter. AWJ cutting offers the most consistent surface finish for all bevel angles.

Table 2 - Comparison Table of Bevel Cutting Methods using Optimal Parameter Settings

Cutting Method		Flute-Edge Endmilling	Abrasive Water Jet Cutting	Nd:YAG Laser Cutting with Hard Optic Beam Delivery
Cutting Force		Significant (lamination bends 1-2 mm at high bevel angles)	Small (momentum transfer from abrasive)	Negligible
Maximum f_m for 0° bevel cut (meters/min)		0.46 (affected by material hardness and composition)	0.31 (affected by material composition)	0.44 for $q_{laser}=0.3$ kW (max. $f_m \propto q_{laser}$)
Maximum α		$\tan^{-1}\left(\frac{L_f}{t_L}\right) = 85^\circ$	at least 75°	80°
Kerf Taper Angle θ		None	$+10^\circ$	-1° to -2°
Nominal 30° Bevel	w (mm)	6.4 (tool \varnothing)	0.7	0.1
	H_D (mm)	2.8	0.1	0.04 (porous edge burr)
	R_a (μm)	0.7	3.4	4.4

Based on the preceding analysis and discussion, the authors rank the suitability, i.e. best to worst, of these three bevel cutting methods for cutting steel laminations as follows:

- 1) Nd:YAG laser cutting because feedrate is only dependent on laser power, tool wear is non-existent, cutting force is negligible and the kerf is the narrowest of all,
- 2) Abrasive water jet cutting since feedrate is dependent on material hardness and the kerf taper is the largest among the three methods, and
- 3) Flute-edge endmilling since the cutting force, kerf width, edge burr, and feedrate's dependency on material hardness is the greatest overall.

V. Machinery for Fabricating PEL Dies:

As with CNC-machining of a sheet metal forming die, the two most important specifications of equipment used to fabricate PEL dies are to 1) get as close to near net shape as possible thereby minimizing the need for a post-grinding or finishing operation and 2) accomplish this task as fast as possible. The key to meeting these specifications are the correct choice of a bevel cutting method, as discussed in the previous section, and the efficient handling of die laminations during the cutting. There are two options for efficiently cutting PEL die laminations: retrofitting a commercially-available cutting machine or developing a dedicated, stand-alone machine.

For compound beveling of PEL die laminations, a 5-axis machining center (e.g. 3 translational & 2 rotational axes) is required to correctly position the cutting nozzle during the profiling process. Currently, there are numerous 5-axis conventional machining centers, and a few laser and AWJ machining centers that can be used to machine compound bevels. Using any of

these 5-axis machining centers, a die lamination blank must first be vertically secured to the machine's workbed and then the profiled-edge is machined. The die lamination can be handled manually or the machining center can be retrofitted with an automatic handling mechanism.

Five-axis laser machining centers are much more expensive than comparable AWJ or CNC machines. For example, a Laserdyne Model 780 BeamDirector™ 5-Axis laser machining center with a Lumonics JK704 laser currently sells for around \$625K. Other laser machining centers vary in price from \$500K to \$700K. In contrast, a Cincinnati-Milacron Sabre-1000 CNC 3-axis vertical machining center retrofitted with a Tsudakoma TTNC-201 tilting rotary table that has a similar work volume as the Laserdyne system sells for around \$120K. For \$180K, a company can purchase a Jet Edge® model 55-30 AWJ cutting system that's mounted to a 5-axis, robot-controlled gantry table and has a similar work volume as the laser system. With any of these systems, the estimated cost of a custom-built lamination handling mechanism has not been added to their overall cost.

Dedicated PEL Die Fabrication Machine:

Both conventional CNC and laser machining centers are designed for general industrial use and not optimized for cutting die laminations in terms of speed, cost, and factory floor space required. Taking into account the high cost of commercially available equipment and the added cost of a custom-built lamination handling mechanism, a dedicated stand-alone machine for fabricating PEL dies is proposed by the authors as a cost-effective alternative to retrofitting currently-available 4 and 5-axis cutting machines. This specialized apparatus will be called a Die Lamination Profiling (DLP) machine. For industry to embrace the PEL die method, these machines will be required to fabricate dies in a rapid and efficient manner. Several machine DLP machine concepts have already been developed.

VI. Propensity for PEL Die Delamination:

If the PEL die laminations are bonded together then the composite structure becomes a continuous die. To keep the PEL die easily re-machinable, the die laminations are simply clamped together with a rigid frame as shown in Figure 1b. In a clamped configuration, individual laminations have a propensity to delaminate, i.e. separate from adjacent laminations, by elastically deforming or buckling under the high forming loads encountered. As seen in Figure 7a, the die shape changes when a lamination(s) bends elastically resulting in dimensional changes to the parts formed. For this reason, it is important to investigate the elastic bending and buckling behavior of a clamped lamination subjected to typical forming loads.

Excessive deformation of any of the clamped die laminations beyond a certain maximum value, i.e. $\delta > \delta_{\max}$, will be considered a die failure. Ideally a PEL die should emulate a continuous die whose surface deformation is essentially negligible (e.g. 0.01 mm for a steel die). However, a more practical design requirement for PEL dies is to make sure that the dimensions of the formed part are within the specified tolerances. The maximum deformation value (δ_{\max}) of a die lamination is explicitly determined from this requirement.

Referring to Figures 7a and 7b, a group of deflected laminations (due to high forming loads) can be roughly modeled as cantilevered Euler beams in a parallel configuration. This assumes that the frictional shear forces at the interfaces between adjacent laminations are negligible. The deflection δ of a single rectangular lamination (see Figure 8a) can be estimated using the relation

$$\delta = \frac{4 \cdot F_{\text{bending}}}{E \cdot b} \left(\frac{a}{t} \right)^3 \quad (11)$$

where: a = lamination height
 b = lamination width
 t = lamination thickness

E = tensile elastic modulus of the lamination material

F_{bending} = horizontal component of the lamination's total forming load.

By rearranging equation 11, the spring rate k_L of the lamination is then

$$k_L = \frac{F_{\text{bending}}}{\delta} = \frac{b \cdot E}{4} \left(\frac{t}{a} \right)^3 \quad (12)$$

The mode of mechanical failure of a lamination from the vertical component of the forming load F_{buckling} will be some form of buckling behavior. As stated by Timoshenko et al., "in the calculation of critical values of forces applied to the middle plane of a plate at which the flat form of equilibrium becomes unstable and the plate begins to buckle, the same methods as in the case of compressed bars can be used" [10]. Therefore, the critical buckling load $F_{\text{b,critical}}$ for the lamination shown in Figure 8a can be estimated using the Euler column buckling formula

$$F_{\text{b,critical}} = \frac{k \cdot E \cdot b \cdot t^3}{12 \cdot a^2} \quad (13)$$

where: k = factor that depends on the end support conditions of lamination.

If the lamination can be modeled as a simple cantilever beam then k is 2.47. If the movement of it's upper edge is restricted horizontally then k is 20.2.

The forming forces on a lamination consist of an effective normal load F_n and a perpendicular frictional load $\mu \cdot F_n$ at the lamination (die) and sheet metal interface where μ is the frictional coefficient. These loads are shown in Figure 7. The total forming load F_T has a magnitude of $F_n \cdot (1 + \mu^2)^{\frac{1}{2}}$. As shown in Figure 8b (vector diagram), F_T typically points inward to the die. This is a desirable situation since convex portions of the laminated die will tend to be pushed together during forming. In terms of F_T , the bending and buckling loads are $F_T \cdot \sin(\alpha - \tan^{-1} \mu)$ and $F_T \cdot \cos(\alpha - \tan^{-1} \mu)$, respectively.

As an example, let us investigate the bending and buckling propensity of one particular lamination in the male PEL die described in reference [1]. The lamination chosen is located 2.8 centimeters in from the edge along the X-axis. It's profiled edge forms half of the upper bend radius for one of the benchmark part side walls. A maximum forming load of 50 kN is predicted by the FEA simulation of the forming process. Since the upper bend radii on the male die takes most of the total forming load, the estimated maximum normal force that this particular lamination experiences is approximately 6.0 kN. Additional data on the lamination is $a=1.9$ cm, $b=6.4$ cm, $t_L=1.47$ mm, $E=200$ GPa, $\mu=0.2$ (for greased steel on steel) and $\alpha=\text{bevel angle}=30^\circ$. As a result the bending and buckling components of the total forming load are 2.0 and 5.8 kN, respectively. Furthermore, the prescribed dimensional tolerance of the benchmark part is ± 0.1 mm. Since this lamination is backed by 35 adjacent laminations of similar size in the direction of the bending load, the estimated bending deflection is only 0.04 mm according to equation 11. This deflection is well below the die's dimensional tolerance. This simple deflection analysis doesn't even take into account the symmetrical loading on the male die which will tend to counteract the high forming load applied to this sample lamination. Finally, if we assume a worst case buckling scenario where the lamination is unsupported on it's top edge, the critical buckling load is 23 kN according to equation 13. This value is well above the maximum assumed buckling load of 5.8 kN so that buckling will not be a problem.

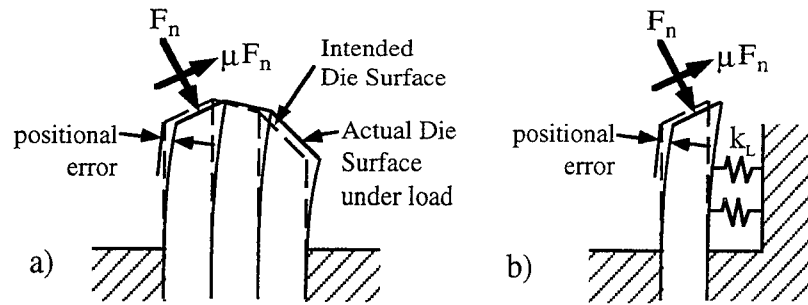


Figure 7 - a) Group of die laminations subjected to forming loads and **b)** modeled as cantilevered Euler beams in a parallel configuration

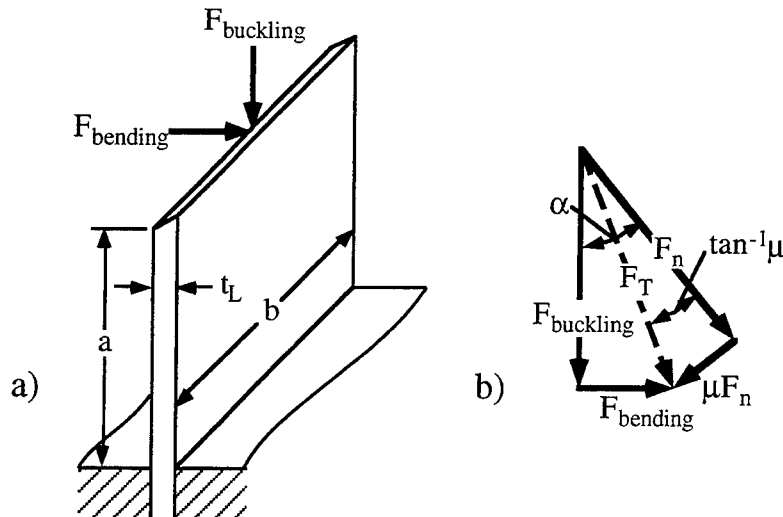


Figure 8 - a) A single rectangular die lamination subjected to bending & buckling loads and **b)** vector diagram of the said loads.

Conclusions and Planned Future Work

In terms of handling laminations during processing, registering and clamping the laminations into a rigid die, and reshaping the die during the tooling development process, the PEL method for fabricating sheet metal forming dies improves upon the current method of stacking and bonding contoured laminations. In this paper, the general procedure for extracting the machining instructions for each die lamination is outlined for die shapes that require either 3-D or simple planar beveling. A method for easily estimating the geometrical error caused by the straight bevel approximation of each machined lamination is also introduced. Three cutting methods - machining with the flute-edge of an endmill, abrasive water jet cutting, and especially Nd:YAG laser cutting - are shown to be viable techniques for machining bevels into die laminations. Finally, in a completely assembled PEL die, the propensity for die delamination is shown to be more sensitive to bending failure than buckling failure.

Future developmental work to help establish PEL dies as a viable alternative to conventional CNC-machining of sheet metal forming tools includes:

- developing a algorithm that will determine the best orientation of the PEL laminations, with respect to the die shape, to minimize the overall error from the straight bevel approximation.

- bevel cutting experiments with other die materials like tool steel, Invar, aluminum, epoxies, and certain other plastics suitable for sheet metal forming
- developing a Die Lamination Profiling machine.
- an investigation of all available methods for permanently bonding PEL laminations together into a solid tool (e.g. diffusion-bonding).

Acknowledgments:

This work was supported solely by the National Science Foundation Grant No. DDM-9202362.

References:

- [1] Walczyk, D.F., and Hardt, D.E., "A New Rapid Tooling Method for Sheet Metal Forming Dies," *Proceedings of the Fifth International Conference on Rapid Prototyping*, Dayton, Ohio, June 12-15, 1994.
- [2] Kunieda, M. and Nakagawa, T., "Manufacturing of Laminated Deep Drawing Dies by Laser Beam Cutting," *Proceedings of the 1st International Conference on Technology of Plasticity*, Vol. 1, Tokyo, Japan, 1984, pp. 520-525.
- [3] Nakagawa, T., Kunieda, M. and Liu, S.D., "Laser Cut Sheet Laminated Forming Dies by Diffusion Bonding," *Proceedings of the 25th International Machine Tool Design and Research Conference*, U. of Birmingham, England, April 22-24, 1985, pp. 505-510.
- [4] Discussion with **Dastidar, P.**, Senior Engineer, Advanced Manufacturing, Carrier Corporation, Syracuse, N.Y., May 16, 1995.
- [5] Weaver, W.R., "Process for the Manufacture of Laminated Tooling," *U.S. Patent #5031483*, Issued July 16, 1991.
- [6] Phillips, M.B., and Odell, G.M., "An Algorithm for Locating and Displaying the Intersection of Two Arbitrary Surfaces," *IEEE Computer Graphics and Applications*, Vol. 4, No. 9, Sept. 1984.
- [7] Bobrow, J.E., "NC Machine Tool Path Generation from CSG Part Representations," *Computer-Aided Design*, Vol. 17, No. 2, March 1985, pp. 69-76.
- [8] Semiatin, S.L. et al., *Metals Handbook: Volume 14, Forming and Forging*, Ninth Edition, ASM International, Metals Park, Ohio, 1988.
- [9] Walczyk, D.F., "Rapid Fabrication Methods for Sheet Metal Forming Dies," *Ph.D. Thesis*, Dept. of Mechanical Engineering, Massachusetts Institute of Technology, Cambridge, MA, 1996.
- [10] Timoshenko, S.P., and Gere, J.M., *Theory of Elastic Stability*, McGraw-Hill Book Co., New York, 1961.

Direct Feedback Control of Gas-Phase Laser-Induced Deposition

J. L. Maxwell¹, J. Pegna, D. Messina, D. DeAngelis

Center for Integrated Electronics and Integrated Manufacturing, Rensselaer Polytechnic Institute, Troy, New York 12180-3590

Tel: (518) 276-6030, Fax: (518) 276-2623, email: pegnaj@rpi.edu.

Abstract: Three-dimensional laser Chemical vapor deposition (3D-LCVD) or SALD, was used to prototype metallic and ceramic microstructures. Iron, nickel, and steel metal forms were grown from organic and halogen based precursors. Through the simultaneous use of multiple precursors, specific nickel-iron based alloys were produced. By observing the emission spectra during growth, a measure of the volumetric growth rate, was obtained. Direct, PID control of the process was then possible using the growth rate measurement as real-time feedback. Calibrated infrared photographs of evolving microstructures were taken at various wavelengths, giving a measure of the temperature gradient over the growth zone. While radiation contributes to heat losses at high temperatures, enhanced convection is the dominant heat transfer mechanism due to the small dimensions of the heated area. Enhanced growth rates, induced by convective flow, were also observed. The heat and mass transfer coefficients were determined for various processing conditions, and compare well with experimental data. Axi-symmetric rods may also be grown in both the kinetic and transport-limited regimes, and a systematic study of the precursor pressure and deposit temperature during growth yielded distinct growth regimes, influenced by the interplay of heat losses and diffusive transport.

Keywords: Solid Area Laser Deposition, Chemical Vapor Deposition, Graphite, Iron, Nickel, Nickel-Iron Alloys, PID Process Control.

1. Current Affiliation: Institute for Micromanufacturing, Louisiana Tech University, Ruston, La 71270

1 INTRODUCTION

Laser-induced chemical vapor deposition (LCVD) has been explored extensively as a thin-film metallization tool. In contrast, three-dimensional laser chemical vapor deposition, 3D-LCVD (or SALD), is a mode of pyrolytic deposition where more elevated structures can be generated, as exemplified in figures 1, 2, and 3. Our interest in 3D-LCVD is in its use as a free-form rapid-prototyping tool for micro to milli-scale mechanical objects.

Past attempts at control of the 3D LCVD process have been for the most part open-loop, growth rates and required process conditions being estimated from empirical data. The purpose of this work was to determine a method for measuring and controlling the volumetric deposition rate during 3D-LCVD.

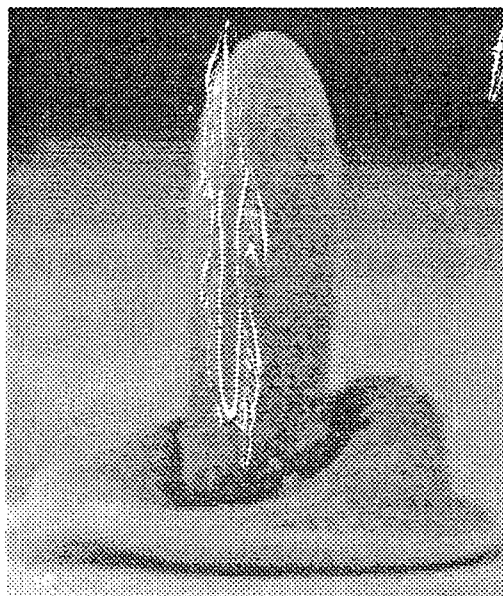


FIGURE 1. Sample Nickel Structure.

In this work, the volumetric growth rate was measured directly from the emission spectra associated with the pyrolytic reaction. This rate measurement was used to control the input power and instantaneous growth rates. Applications include control of laser direct writing over varying substrate topography, control of undesirable features in layered growth, and implementation of continuous 3-dimensional deposition.

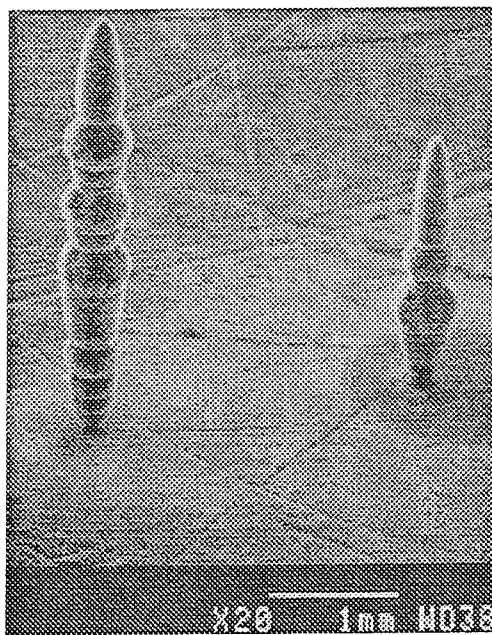


FIGURE 2. Sample Nickel-Iron alloyed structure.

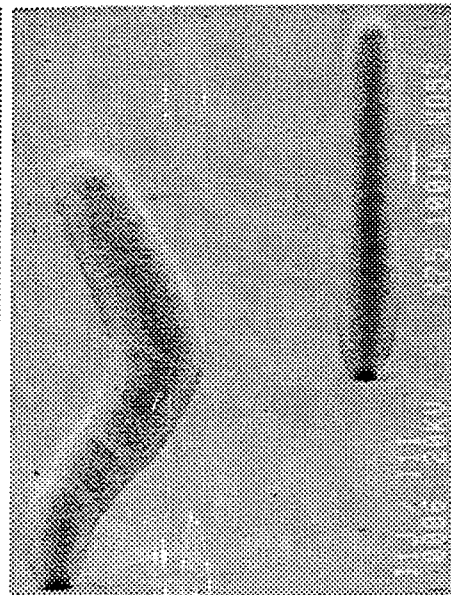


FIGURE 3. Sample 3-D graphitic structures.

Besides demonstrating the potential of 3D-LCVD for the prototyping of alloys, the purpose of the experiments was also to determine variations in final deposit compositions—so that the temperature changes during rod growth can be determined—as well as the difference in activation energies (E_a) of the iron and nickel carbonyl precursors. This result, however, will not be discussed within the scope of this paper. For more information on this subject, the reader is referred to [Maxwell et al., 1996].

2 EXPERIMENTAL

The 3D-LCVD reactor at Rensselaer consists of a custom quartz tube with a port for viewing and laser input. The chamber is connected to a pumping station via a gate valve. The vacuum chamber and gas-delivery system are enclosed within a ventilated hood for safety purposes.

Iron pentacarbonyl was delivered to the reaction chamber via an evaporator. In this experiment, the room-temperature vapor pressure of $\text{Fe}(\text{CO})_5$ was used to fill the chamber. In most cases, the partial pressure of the precursor reached 20 mbar.

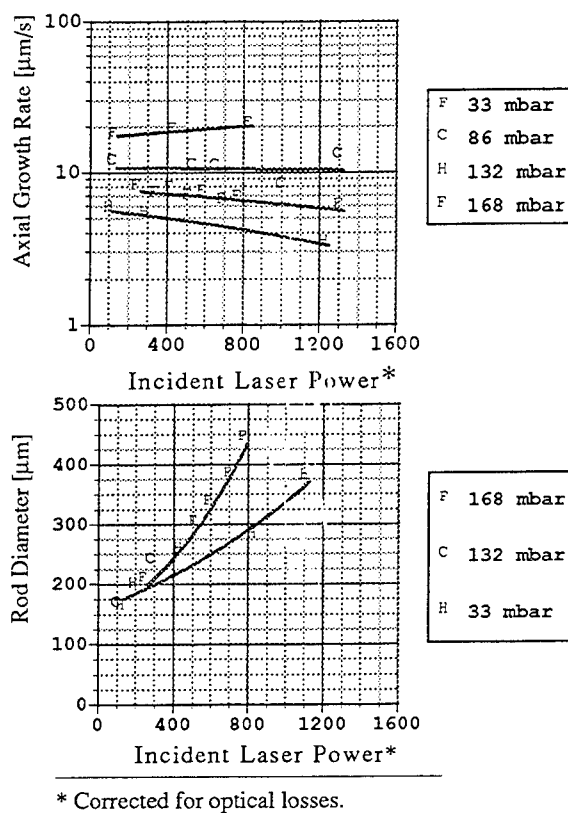


FIGURE 4. Nickel average axial growth rates and diameter vs. input power.

Both ethylene and nickel tetracarbonyl were metered into the reactor from commercial cylinders. For the growth of pyrolytic graphite, ethylene pressures of up to 930 mbar were employed. Ni(CO)_4 partial pressures of up to 250 mbar were possible. Iron pentacarbonyl was delivered to the reaction chamber via an evaporator. In these experiments, the room-temperature vapor pressure of Fe(CO)_5 was used to fill the chamber, i.e. 20 mbar.

The beam source was a Spectra Physics argon-ion laser, with a maximum output of 8 watts (multi-mode) at the 488/514 nm primary lines. At these wavelengths, iron and nickel have normal spectral reflectances of 65% and 52% respectively [Touloukian, 1970]. Gaussian spot radii of 25 μm ($1/e^2$) or greater were used throughout the experiments, and it was found that while the commencement of growth on the substrate

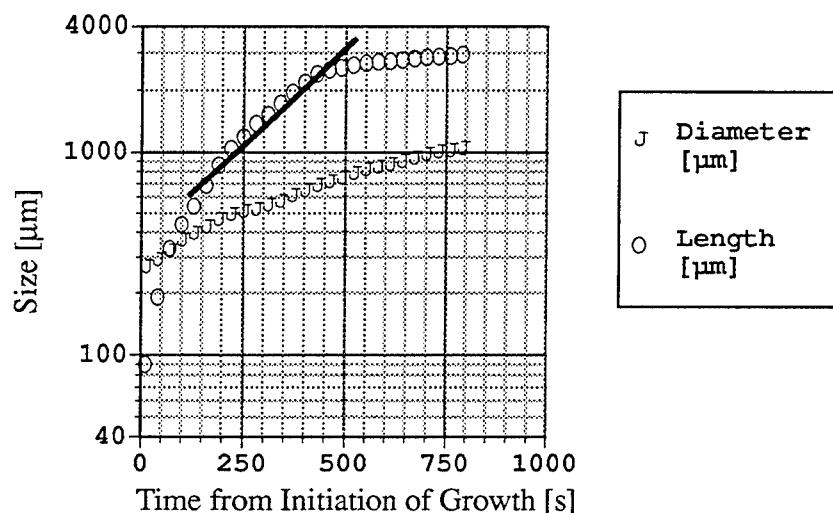


FIGURE 5. Nickel rod length and mid-length diameter vs. time

depended greatly on the power density—requiring small spot sizes for the laser powers available—the 3-D, steady-state growth of rods was nearly unaffected by the beam waist over a distance several times the Rayleigh range (250 μm). The optical system consisted of a Newport 10x beam expander and 200 mm focal length CVI achromat. A long pass filter was used to block the UV laser lines below 420 nm.

A silicon photodetector, covered with narrowband filters, was mounted to one of the chamber windows, at a distance roughly 200 mm from the sample. Using a two-decade pre-amplifier, the sensor could measure emissions as small as 0.25 mW at the substrate (at 656 nm). In this arrangement, the sensor had a time response on the order of milliseconds; however, the amplifier was heavily filtered with a time-constant of approximately 1/30 s. The amplified signal was recorded by an Omega Nubus data acquisition system, with a typical sample period of 0.05-0.10 seconds, and was later time averaged as needed for real-time control. Proportional-Integral-Derivative (PID) Control of the laser power was implemented using Omega Workbench™ software with output to the LCD retarder mentioned previously.

For analysis of the sample composition, both Auger electron spectroscopy (PHI 545C Scanning Auger Microprobe) and an electron microprobe (Geol Superprobe 733) were employed. Prior to the microprobe analysis, the samples were sectioned, polished, and lightly etched in a Kalling's solution, a mixture of isopropyl alcohol, HCL, and CuCl_2 .

3 RESULTS AND DISCUSSION

3.1 NI GROWTH

Ni(CO)₄ vapor pressures ranged from 25 to 200 mbar throughout the experiment, and rods could be initiated at pressures of less than 25 mbar. At similar partial pressures, the axial growth rate was higher than that of the ethylene-grown structures, exceeding 18 mm/s at the highest powers. Surprisingly, preliminary results for the axial growth rate show that the highest normal growth rates values were obtained at the lowest pressures, as indicated in Figure 4 (top.)

As for steady state diameter, experimental results recorded in Figure 4 (bottom) indicate that increasing pressure broadens the rod, just as for ethylene at partial pressures below 200 mbar. Interestingly, for all Ni(CO)₄ pressures, the diameters approach a non-zero asymptotic diameter, approximately 60 mm wide. One possible implication is that, for these pressures, it may not be possible to grow narrow Ni structures thinner than 100 mm, thereby limiting the resolution of the process. Further experiments at very low laser powers (<100 mW) and small beam waist diameter are needed to confirm this phenomenon.

Figure 5 displays measurements of length over time for a typical rod, as well as the diameter of the rod during the same time period (820 s). One can see that the axial rate rises rapidly to the steady-state growth rate (indicated by the slope of the solid line), and then the axial rate slows to a new terminal rate, Rt. At the same time, the rod diameter at mid-length grows steadily, beginning at 250 mm, ultimately reaching over 1000 mm in diameter. Perhaps the most significant result from this figure is that, while the steady-state axial rate greatly exceeds the radial rate (hence the rod), the terminal rate, Rt, and the radial rate are nearly the same.

Consequently, for metals under a de-focused beam, the entire rod grows at a uniform rate, and the temperature gradient along the rod is small.

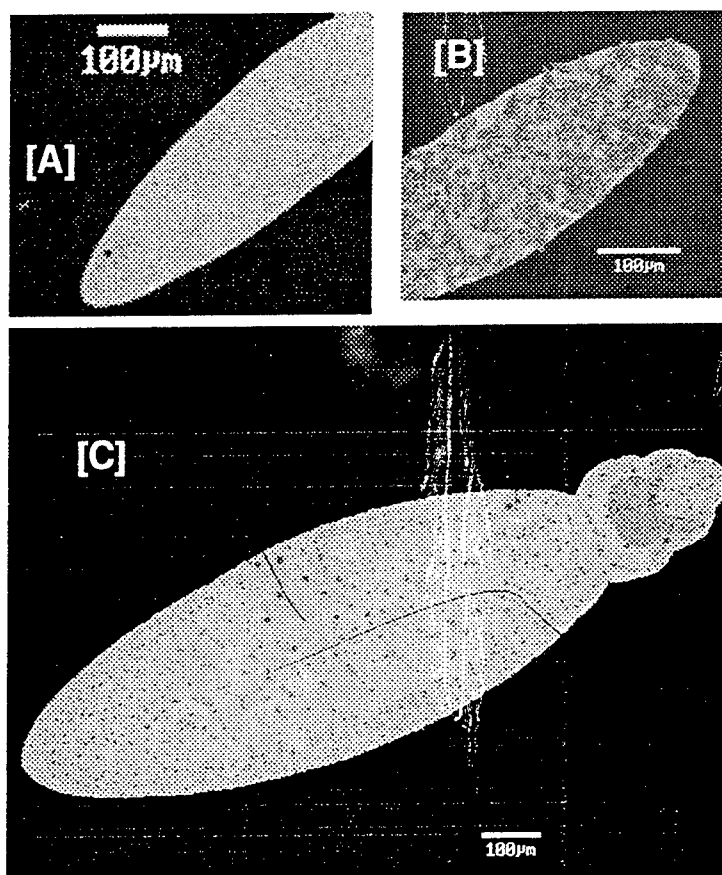


FIGURE 6. Ni-Fe rods cross-sections showing the sample's microstructure. All rods were grown at 20mbar partial pressure of Fe(CO)₅ and at laser power of 190mWatts. The respective precursor and deposit concentrations are reported below.

Sample	Gas Mixture		Deposit Composition	
	Fe(CO) ₅ Conc. (%)	Ni(CO) ₄ Conc. (%)	Fe Conc. (%)	Ni Conc. (%)
A	50.0	50.0	52.0	48.0
B	42.0	58.0	29.0	71.0
C	55.6	44.4	48.0	52.0

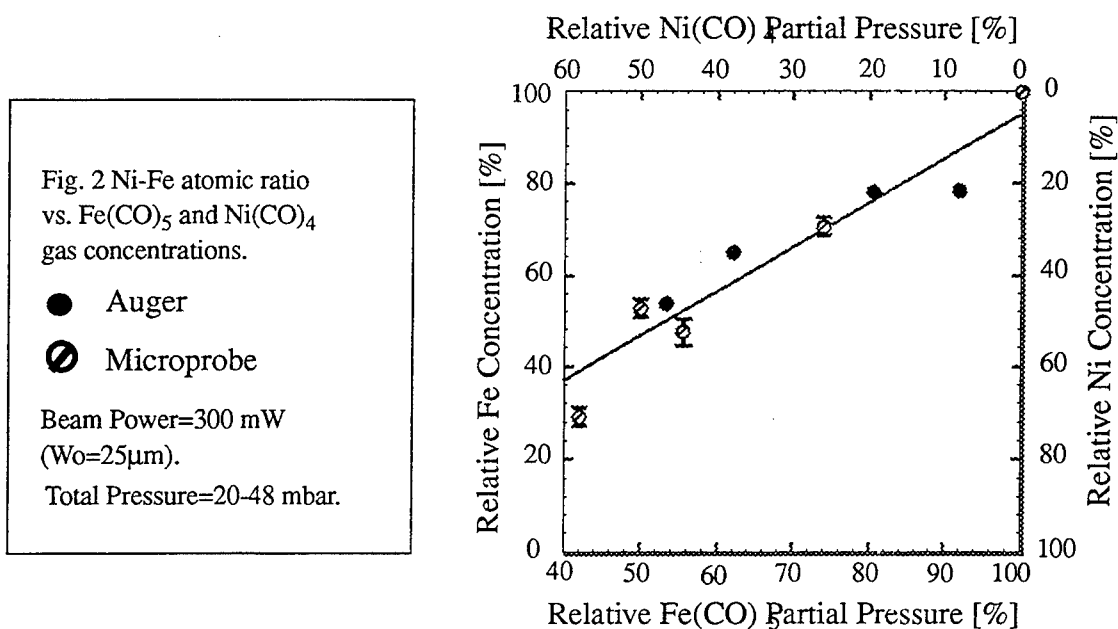


FIGURE 7. Rod composition vs. gas mixture composition for Auger and Microprobe measurements.

3.2 NI-FE GROWTH

Sample structures were grown from various precursor mixtures of Nickel and Iron carbonyls. The sample composition was shown to vary with the precursor partial pressures and demonstrated the capability for alloying as well as fabricating functionally graded materials.

Alloy Composition: Figure 6 shows the cross-section and microstructure of several rods grown at the same incident power, but differing precursor concentrations. The $\text{Fe}(\text{CO})_5$ precursor partial pressure in Figure 6.B is the lowest of the three cases (42%); the $\text{Fe}(\text{CO})_5$ pressure increases in the case of Figure 6.B to 50%, and reaches its maximum value at 55.6% in Figure 6.C.

Throughout each sample, the ratio of Ni-Fe (in at.%) remained nearly constant due to the large capacity of the reactor chamber. The samples exhibited regions that were heavily oxidized regions, and, in the case of Figure 6.B, inclusion of graphitic flakes. Yet the relative composition of the deposit remains constant to within ± 2 percent. Figure 7 summarizes the final composition of the Ni-Fe rods versus the gas mixture in which they were grown. The partial pressures of $\text{Ni}(\text{CO})_4$ and $\text{Fe}(\text{CO})_5$ were varied as a percentage of the total chamber pressure, giving rods of similar atomic Ni-Fe ratios. In all cases, the chamber was filled with $\text{Fe}(\text{CO})_5$ to 20 mbar, and $\text{Ni}(\text{CO})_4$ was added to give a specific relative gas concentration. It is apparent that any Ni-Fe alloy may be produced in this manner, including high-temperature super-alloys with Ni concentrations greater than 25%.

3.3 VOLUMETRIC GROWTH RATE MEASUREMENT

Growth Rate Measure: Using a stationary beam with focus at the substrate, straight-sided needles of graphite, nickel, iron, and nickel-iron alloys up to 7 mm in length could be deposited without moving the laser focus. Note that this is many times the diffraction-limited Rayleigh Range of the beam focus ($260\mu\text{m}$).

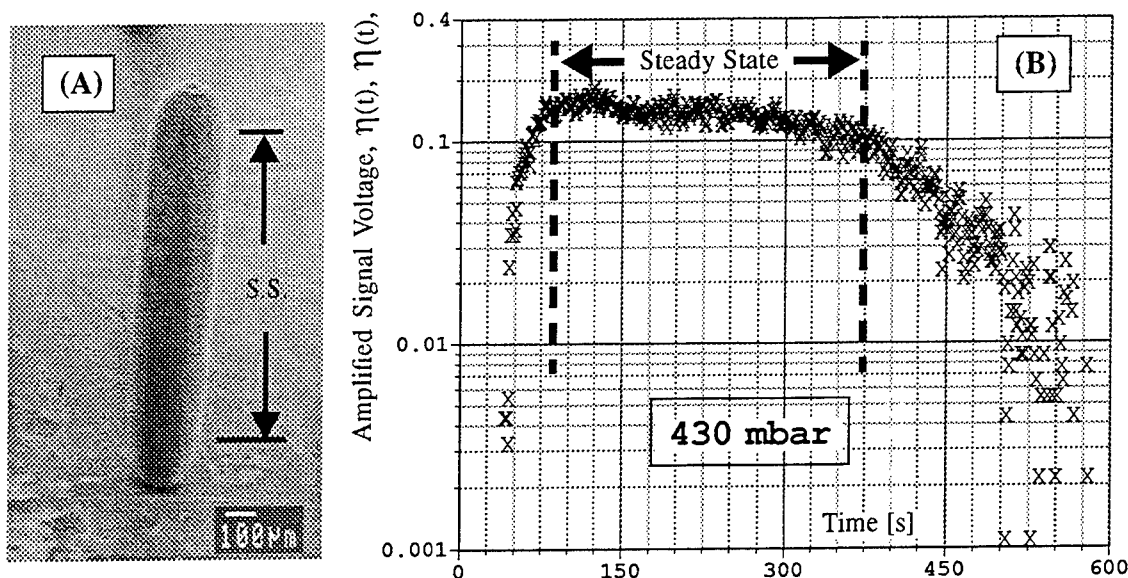


FIGURE 8. Typical emission signature at 656 nm for graphite rod growth.

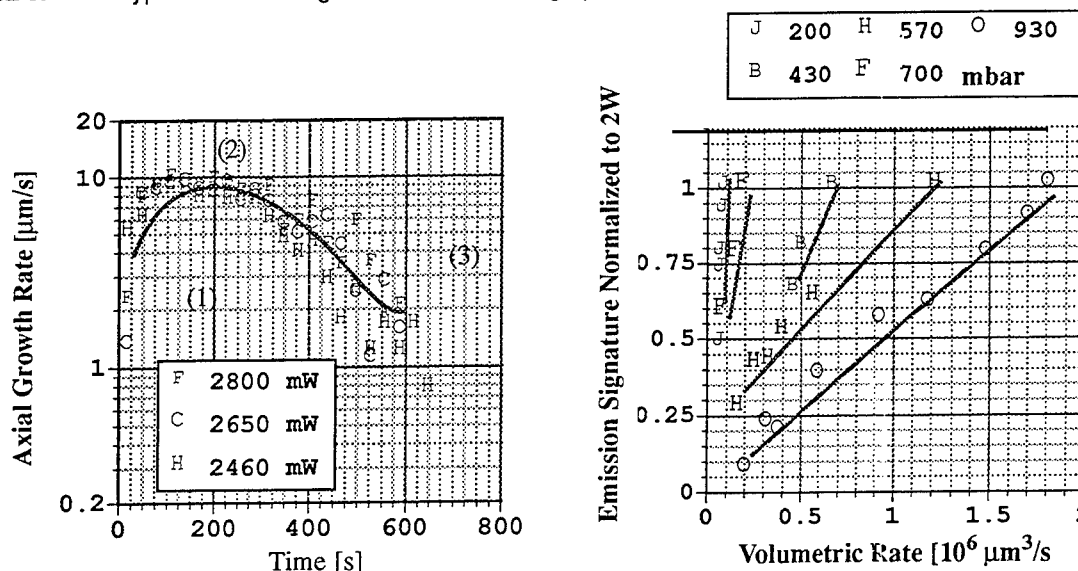


FIGURE 9. Correlation of emission signature to volumetric growth rate for graphite rod growth.

The normal deposition rate, R_n , of rods deposited in this manner is defined as the local rate at any surface point where growth occurs. The axial deposition rate, R_o , is the normal growth rate at the center of the rod, along the beam axis. The final radius of a rod, R_s , can be estimated at any axial point by integrating the component of the normal deposition rate perpendicular to the beam axis over time. The volumetric deposition rate, R_v , of a *cylindrical rod* depends on both the axial rate and diameter deposited over time. The normal rate, R_n , varies exponentially with laser power in the kinetic regime, while at high incident powers, it may become transport limited.

Growth Regimes. Figure 8 shows the emission signature vs. time for a typical graphite rod. Figure 9 correlates the emission signature to the volumetric growth rate. After a brief delay, representative of thin film nucleation and coalescence at the substrate, rapid axial growth commences, eventually rising to a peak rate. This interval is denoted the transient regime,

labeled (1) in Figure 9. Once the peak rate is attained, the rod grows at a constant axial rate, and it is over this steady-state regime —labeled (2) in Figure 9— that the bulk of the rod is grown. Eventually, (at approximately 300 seconds, labeled (3) in Figure 9) the axial rate slows, dropping linearly as the beam broadens and the surface temperature decreases; this is known as the tail regime.

Volumetric Rate Measure. Emission spectra produced during the pyrolytic decomposition of ethylene were monitored using the photodetector and filters described previously. The hydrogen-Alpha line at 656 nm was found to be several orders of magnitude brighter than the background thermal emissions. This spectral line represents the $n=3 \rightarrow n=2$ transition in the Balmer Series of atomic hydrogen, as occurs following disassociation of hydrogen from C_2H_4 as well as from the thermal ionization of H_2 . Since ethylene dissociates at a lower temperature than the ionization potential of hydrogen, the measured emission spectra were primarily due to the liberation of atomic hydrogen during pyrolysis of C_2H_4 .

Since the signal strength is proportional to the total number of disassociated hydrogen ions returning to the ground state, it was hypothesized that the emission signature is representative of the volumetric deposition rate. This was confirmed by Figure 9, where the steady-state signal amplitude is plotted vs. measured volumetric rate along lines of constant pressure. Each curve is normalized to the amplitude of the emission at incident powers of 2000 mW. Observe that in each case, the signal strength is linearly proportional to the volumetric rate. When sufficiently well calibrated for the precursor partial pressure and viewing position, the signal amplitude can be used as an absolute measure of volumetric rate.

3.4 AXI-SYMMETRIC CONTROL OF 3D-LCVD

The one-to-one correspondence of volumetric rate and radius (at any given pressure) makes it possible to create a very stable controller for 3D-LCVD. If the spectral emission signature is fed back to the laser power controller, and compensation is made in the laser power to obtain a desired volumetric growth rate, one obtains direct control over the axi-symmetric 3D-LCVD process. Proportional-derivative-integral (PID) control was used to set the laser power in real-time with feedback from the emission signature.

To demonstrate, a series of samples were grown in this manner, such as the structures shown in Figure 10. All samples were grown at 200 mbar, so that the axial rate would be transport limited and to allow sufficient time for the controller to respond to the growth. (At 930 mbar, rods grow so rapidly that the steady-state regime passes in just a few seconds.) The laser power was set at maximum power to initiate growth on the graphite substrate through the transient regime. The feedback controller was then engaged after the rods had reached their steady-state radius (labelled 1 in Figure 10.A. The sample in Figure 10.A was grown using a linearly decreasing setpoint over the length labelled (2), while the sample in (B) was grown with an exponentially decaying total laser power in place of the PID control.

The most promising feature of this control technique is that the output shape is similar to the input waveform; the linear setpoint decay in (A) resulted in a straight cone, while the sinusoidal growth input in (C) resulted in periodic bulbs. The opposite is true for open-loop laser power control, where an exponential decay in the power is required to produce a linearly tapered rod.

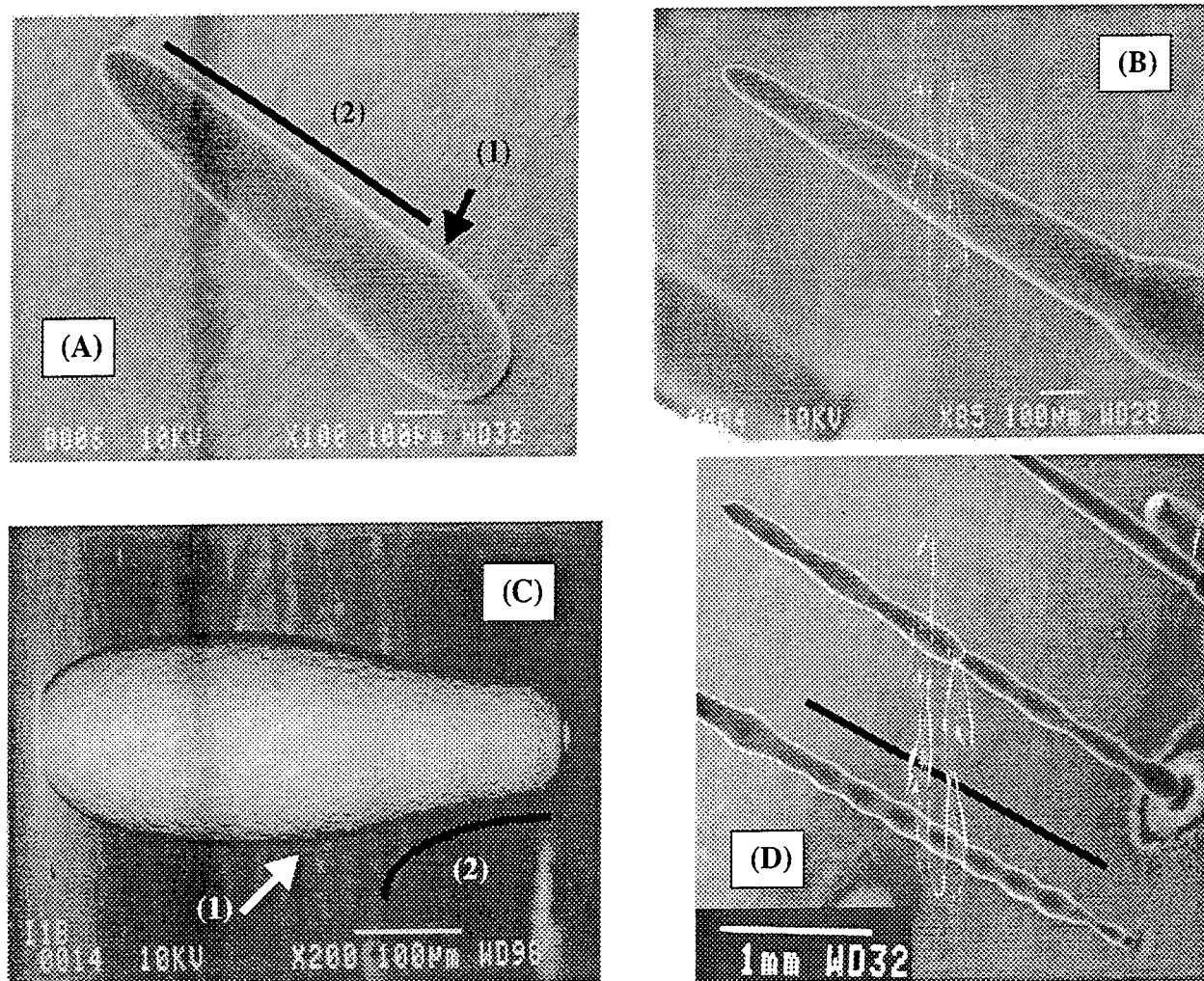


FIGURE 10. Sample graphite rod structures grown using the emission signature as a feedback to the PID controller.

3.5 GRAPHITE TEMPERATURE MEASUREMENTS

Temperature Gradient Measurements: In this section, the temperature gradient over several graphite rods will be measured from the blackbody radiation emitted during their growth. Kodak High Speed infrared emulsion no. 2681 was employed throughout the experiments. A standard 250 mm telephoto lens was used in combination with a 250 mm achromat, achieving a 1.2x magnification of the object on the film. Exposures were made at various wavelengths using narrow-band filters.

Temperature Measurements: Figure 11 displays several successive photographs of the same rod taken at various wavelengths; the frames were taken during the steady-state growth regime in rapid succession. The rods were viewed at a $45 \pm 1^\circ$ angle from the laser axis. The resolution of the photographs is approximately $7 \mu\text{m}$, and the direction of the incident beam is shown by the dashed, blue arrows. The brightest regions are the surface of the rod; these are color-coded red, orange, and yellow, in descending intensity according to the color bar. The gas surrounding the rods also emits weakly, and this appears primarily as green, blue, and purple surrounding the brighter regions.

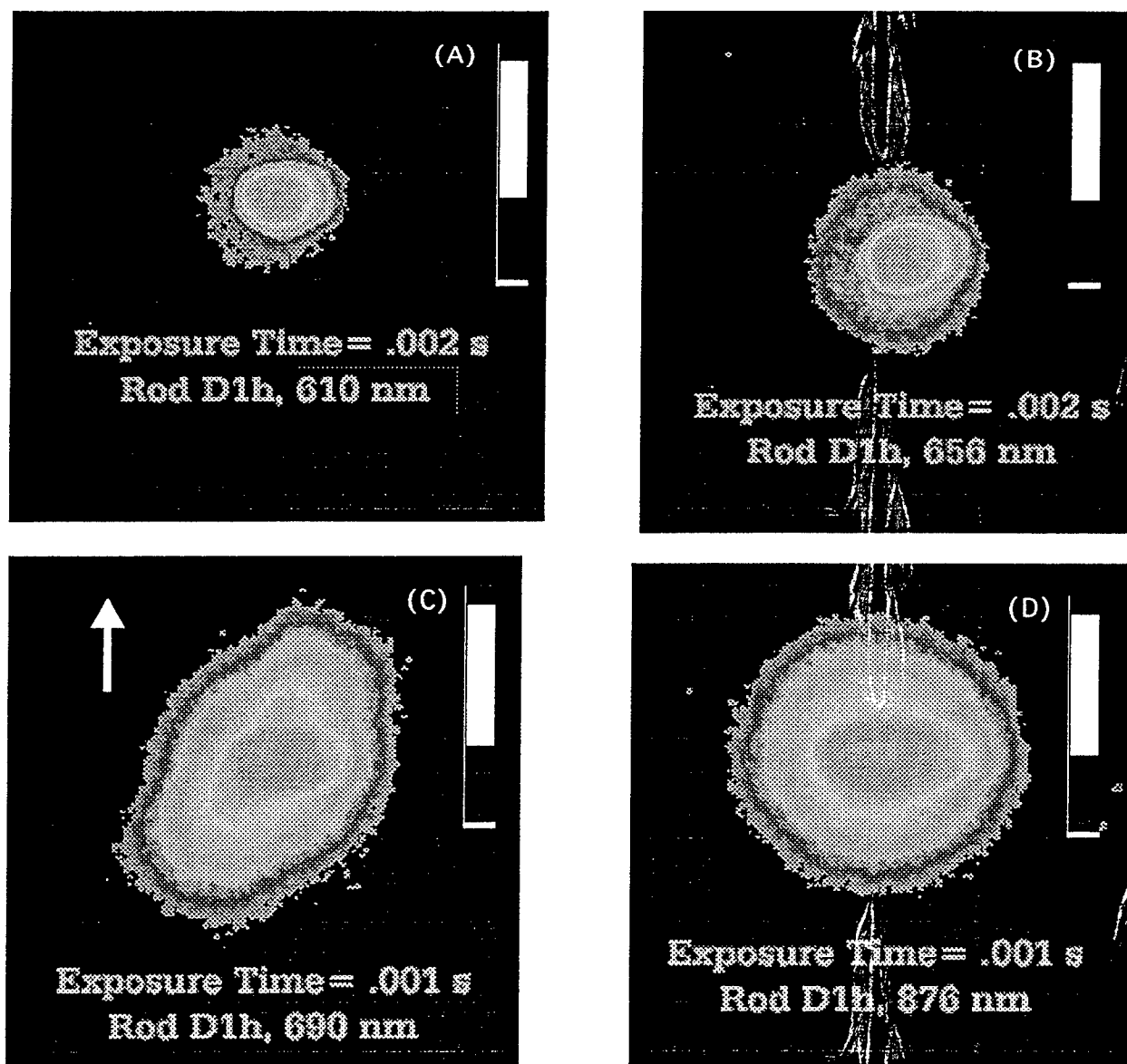


FIGURE 11. Temperature measurement at various wavelengths during rod growth.

Finally for the rod grown at 2930 mW, the power is sufficient at the tip to reach graphite's sublimation temperature of 3925 K; in fact, SEM photos of this rod exhibit slight dimpling, such as found more prominently on rods grown at higher laser powers—and previously attributed to mass transport limitation. A slight warpage near the rod tip is also visible, possibly due to softening of the graphite at excessive temperature. It remains to be seen if the dimple effect is entirely caused by diffusion limitation, sublimation, or a combination of both phenomena.

4 CONCLUSIONS

Controlled 3-dimensional laser-induced vapor deposition of Ni-Fe alloys is feasible from nickel and iron carbonyls, producing alloys with less than ± 2 at.% compositional variance. Sustainable steady-state growth rates of up to $30 \mu\text{m/s}$ are possible. Further studies will determine the detailed microstructure and hardness of the Ni-Fe deposits, as well as the activation energy of $\text{Fe}(\text{CO})_5$.

In addition to controlling the laser power, the emission signature could also be used for focal positioning, comparing the actual emission amplitudes with the expected steady-state rates, compensating to maintain the steady-state focal position.

Direct feedback control of the growth rate will also be essential for layered growth, as previous attempts to build-up shapes by repetitive scanning have proven to be unstable. As one layer is grown over another using open-loop control, perturbations in the thickness of the underlying deposit induce exponential perturbations in the next layer (kinetic regime), yielding irregular deposits. With growth rate control, compensation can be made for such perturbations, and rate-controlled 3D-LCVD can be used for both layered and continuous growth.

Similarly, the growth control method could be used to obtain consistent direct writing results over varying topographies and substrate materials.

5 ACKNOWLEDGEMENTS

The authors wish to thank the National Science Foundation (Grants: NSF ECS-9314071 and NSF DDM-9057059) for their generous support. Grateful acknowledgments also go to Ray Dove of the Rensselaer MRC microscopy laboratory for the SEM photos, Dr. Hudson of the Rensselaer Materials Engineering Department, for use of the Auger Microprobe, Norm Gendron, of Rensselaer, for advice in sectioning the samples, and David Wark of the Rensselaer Geology Dept. for contributing to the x-ray microprobe analysis. Thanks finally to the CIEEM staff for helping to dispose of the iron and nickel carbonyls.

6 REFERENCES

- [Bäuerle, 1984] D. Bäuerle, Laser Processing and Diagnostics, Springer Ser. in Chem. Phys., 39, 166-182.
- [Zong, 1992] G.-S. Zong, Ph.D. Thesis, University of Texas at Austin, Department of Materials Science.
- [Westberg et al., 1993] Westberg, H., Boman, M., Johansson, S., Schweitz, J.-A., J. Appl. Phys., 73, 7864-7871.
- [Maxwell et al., 1993] J.L. Maxwell, J. Pegna, and A. Ostrogorski, Proc. Solid Freeform Fabrication Symposium, Austin, TX, 253-271.
- [Lehmann et al., 1991] Lehmann, O., Stuke, M., Applied Physics A, 53, 343-345.
- [Wallenberger et al., 1993] F.T. Wallenberger, P.C. Nordine, Science, 260, 66-68.
- [Wallenberger et al., 1992] Wallenberger, F. T., Nordine, P. C., Materials Letters, 14, 198-202.
- [Rytz-Froidevaux et al., 1981] Rytz-Froidevaux, Y., Salathé, R. P., Gilgen, H. H., Physics Letters, 84A, 216-218 (1981)
- [Arnone et al., 1986] Arnone, C., Rothschild, M., Black, J. G., Ehrlich, D. J., Appl. Phys. Lett., 48, 1018-1020.
- [Maxwell et al., 1995] J.L. Maxwell, J. Pegna and E. Hill, Proc. Solid Freeform Fabrication Symposium, Austin, TX, 143-150.
- [Bäuerle, 1986] D. Bäuerle, Chemical Processing with Lasers, Springer-Verlag, NY, 93 (1986).
- [Maxwell et al., 1996] J.L. Maxwell, J. Pegna and D. Messia, Real Time Growth Rate Measurements and Feedback Control of Three-Dimensional Laser Chemical Vapor Deposition, Submitted to Applied Physics A.

- [Touloukian, 1970] Y.S. Touloukian, Thermophysical Properties of Matter, 1, IFI/Plenum, NY.
- [Armstrong et al., 1990] Armstrong, J. V., Enrech, M., Decrouez, C., Lunney, J. G., Coey, J. M. D., IEEE Transactions on Magnetics, 26, 1629-1631.
- [Garrett et al., 1934] A.P. Garrett, H.W. Thompson, J. Chem. Soc., 1817 (1934).

Rapid Laser Forming of Titanium Near Shape Articles: LaserCast™

M. A. House¹, E. J. Whitney², D. G. Krantz³, and F. G. Arcella¹

¹ The Johns Hopkins University Applied Physics Laboratory, Laurel, MD 20723

² Pennsylvania State University Applied Research Laboratory, State College, PA 16802

³ MTS Systems Corporation, Eden Prairie, MN 55344

ABSTRACT

An ongoing collaborative program sponsored by the DoD Advanced Research Projects Agency (DARPA) and the Office of Naval Research (ONR) continues to show promising results in the development of a new laser based manufacturing process. The program's goals are to develop and demonstrate a laser based, rapid manufacturing system (LaserCast™) for titanium and its alloys. Economical precursor powders are being laser formed into integral, 100% dense, near-shape articles by sequentially fusing multiple metal-powder layers in a controlled environment. A CO₂ continuous wave (CW) high energy laser has been used to form commercially pure (CP) titanium, Ti-6Al-4V, and Ti-5Al-2.5Sn in varied geometries from 1-inch square bars to a 4-inch diameter (1-inch wall) cylinder. Materials characterization tests, revealing excellent chemistry control and mechanical properties, are presented. Large near-shape structures may be formed directly from metal powders, without using molds or dies, by direct download and post-processing from a Computer Aided Design (CAD) database. Economic projections indicate significant reductions in manufacturing costs and "time to market" production cycles when the LaserCast process is used instead of conventional casting and forging processes.

INTRODUCTION

Previous work in the laser based rapid prototyping of titanium metals and alloys has been reported[1,2,3,4]. The conventional routes to titanium which include the double, and triple, vacuum consumable arc remelt of consolidated Kroll sponge to drive off magnesium, chlorine, hydrogen and other more volatile processing constituents, and the subsequent forging, casting, or deep machining processes necessary to obtain titanium (alloy) structurals for aerospace and marine applications, may be by-passed by the laser based rapid prototyping process being developed in this program. As an example, present practice to deliver a 330-pound forged titanium bulkhead for a hypersonic aircraft requires starting with a 6,000-pound ingot and working the metal through a series of forging blocker dies, heat treatments, and a final machining[5]. This poor fly-to-buy ratio is also impacted by sometimes lengthy delays in forging or casting schedules. An economic analysis shows that substituting the present manufacturing process with the LaserCast™ flexible manufacturing process could decrease the cost of the bulkhead by 60% and decrease manufacturing time by 50% or more. A second example is the manufacture of pump components for cryogenic fluids. These components have been made from Ti-5Al-2.5Sn extra-low interstitial (ELI) alloy. This alloy is no longer commercially available at reasonable prices or schedules; the demand for

The views and conclusions contained in this document are those of the authors and should not be interpreted as necessarily representing the official policies, either expressed or implied, of the Defense Advanced Research Projects Agency of the U.S. Government.

this specialized alloy has diminished to only a few low volume customers. As a result, these customers may have difficulty meeting delivery schedules. A new process to rapid prototype in titanium and its alloys is also of interest because it would facilitate the interests of the DoD in agile manufacturing, the virtual factory, and the ability to fabricate metallic parts and structures directly from electronic drawings without molds or dies[6]. Thus, electronic drawings may be forwarded to a laser based rapid prototyping site, and the drawings may be processed by slicing codes, and post-processed into computer numerical control (CNC) instructions to direct the laser in constructing the required part by controlled layer-by-layer fusion of the metal powder into the desired geometry. The term LaserCast™ will be used below to describe the product of this laser forming process.

DEVELOPMENT EFFORTS

Program efforts, thus far, have been primarily directed at development of process parameters specific to laser fusion of titanium powders, qualification of inexpensive precursor titanium and alloying powders, and qualification of the resulting LaserCast material. Qualification of the powders and LaserCast material has been governed by industry standard test and analysis specifications. The specification and design of a production system is pacing the continuing development efforts. A functional requirements specification (FRS) coupled with a preliminary conceptual design has been completed. Additionally, detailed design efforts targeting specific equipment and control objectives are in progress.

Laser and Environmental Control Apparatus - Development System

A Convergent Energy (formerly United Technologies Industrial Lasers) 14 kW CO₂ CW (Model SM14 Mod 1) laser operating at 10.6-μm is used for all experiments. The laser beam mode is best characterized as a mechanically generated multi-mode 01* configuration. The beam is delivered to the work piece via a series of mirrors. The laser beam is focused by a parabolic mirror with an f-number of 16. The laser beam can be oscillated in one direction (i.e., linear dither) using a Spawr Industries Type 252 scanner. Alternatively, an omni-directional laser dithering mechanism has been fabricated and integrated into the development LaserCast system. Beam motion is accomplished through a 3-axis gantry controlled by an Aerotech Unidex CNC controller. Other laser functions controlled by the CNC are laser shutter and relays for support equipment and gas.

The metal target and powder are contained in a specially designed atmosphere control apparatus that consists of two boxes fabricated from stainless steel. Each box has a porous floor covering a plenum. The plenums are pressurized using high purity argon gas creating a uniform up-sweep of argon. The outer box provides atmosphere control and supports a lid. The plenum in the inner (target) box supports the metal target and powder. Zero grade argon (guaranteed minimum purity 99.998%) is used for all laser operations. Oxygen levels are continuously monitored in the target chamber (at the powder fusion point) and in the powder feeder using a Delta F Model FA35550A oxygen probe.

A vision system consisting of a closed circuit television camera (CCTV) with strobe illumination is installed on the lid. Signal output is displayed real time on a TV screen and

captured on SVHS tape for subsequent evaluation. This visual feedback is used by the developers to access *in situ* process integrity and make adjustments to process parameters for subsequent laser runs. This information will also provide valuable information for the development of real-time process control sensors for next generation LaserCast systems. A schematic of the current research system is shown in Figure 1.

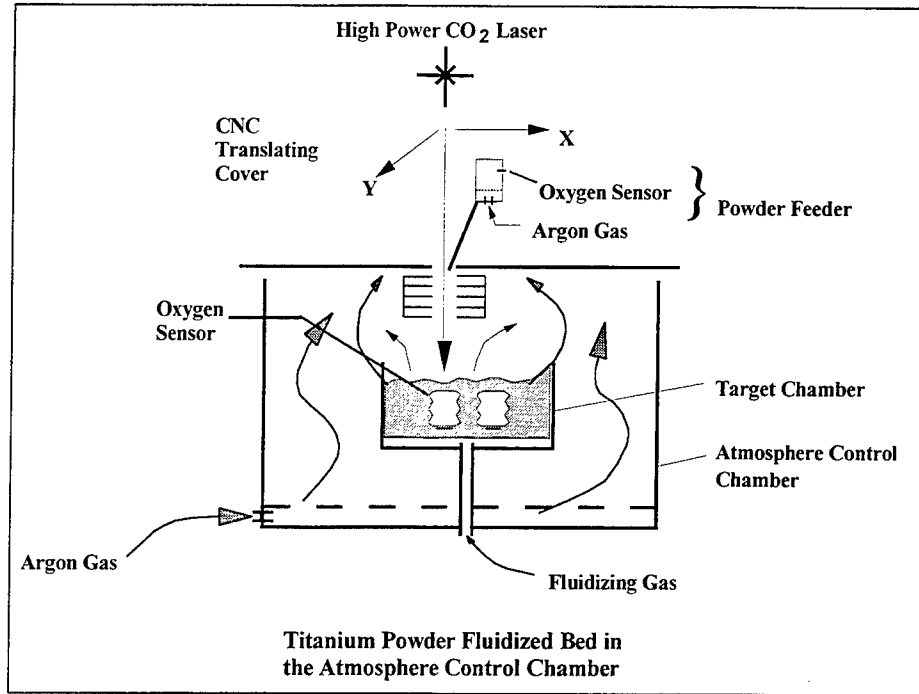


Figure 1. Schematic of LaserCast Development System[1]

Control of the processing parameters and conditions are established to minimize the possibility of unacceptable levels of contamination. All processing parameters are controlled, monitored, and documented. The major processing steps for producing a titanium near-shape are given in Table 1.

The authors have adopted the term 'ingot' to describe the resulting product. To date, two ingot shapes have been produced under this program as shown in Figure 2. These are:

- Linear ingots approximately 6-inches long by 1-inch wide by 2-inches high.
- Cylindrical ingots approximately 4-inches O.D. by 2-inches I.D. by 2-inches high.

Target Material

Two basic types of targets have been used. The first is a simple plate target which was found to bow extensively during processing. A box beam starter target was subsequently used. The box beam target provides additional rigidity which significantly reduces target bowing. All starter targets are CP certified to ASTM B-265-93 Grade 2.

Table 1. Major Processing Steps to LaserCast a Shape: Development System

Step Number	Description
1	Load target into target chamber and purge with argon to 50-ppm oxygen or less and maintain
2	Load powder de-gas chamber, heat and purge with argon to 50-ppm oxygen or less and maintain
3	Align laser to target
4	Monitor oxygen level, initiate laser run
5	Charge target chamber with powder from de-gas chamber
6	Fluidize powder using target chamber gas (deposits powder on target)
7	Level powder on target
8	Run laser over the target in a pre-defined path
9	Repeat steps 6-9 until the desired shape is completed
10	Cool under argon and remove from box

Mechanical Testing and Chemical Analyses

Mechanical testing and chemical analyses have been performed on LaserCast CP titanium and Ti-6Al-4V alloy materials. All mechanical testing is performed in accordance with applicable ASTM specifications [7]. Chemical analyses of precursor powders and LaserCast products was performed by more than one laboratory, using industry standardized LECO and inductively coupled plasma/mass spectrometry (ICP/MS) techniques, to obtain multiple independent analyses. The results of the testing and analyses were compared to the applicable sections of ASTM B 367-93[8]. Test results on the LaserCast Ti-5Al-2.5Sn ingots will soon be available.

RESULTS

Results of dimensional stability, chemical analyses, and mechanical testing are presented in this section. The results of each test are shown in comparison to a commercial specification where applicable.

Dimensional Stability

Distortion of a flat, unsupported starter target during laser processing can be significant. Initial ingots were formed on simple 0.25-inch thick plates. These plates bowed extensively due to the thermal cycling and the resulting residual stresses caused by laser processing. As the ingot is built the amount of restraint created by adding material increases and distortion effectively stops after approximately 0.50-inch of build-up.

Hollow box beam starter targets have been implemented to alleviate the extensive bowing. These targets are welded from 0.25-inch thick plate and have exterior cross section

dimensions of 1.25-inch x 1.25-inch. The additional rigidity of the box beam targets significantly reduces bowing.

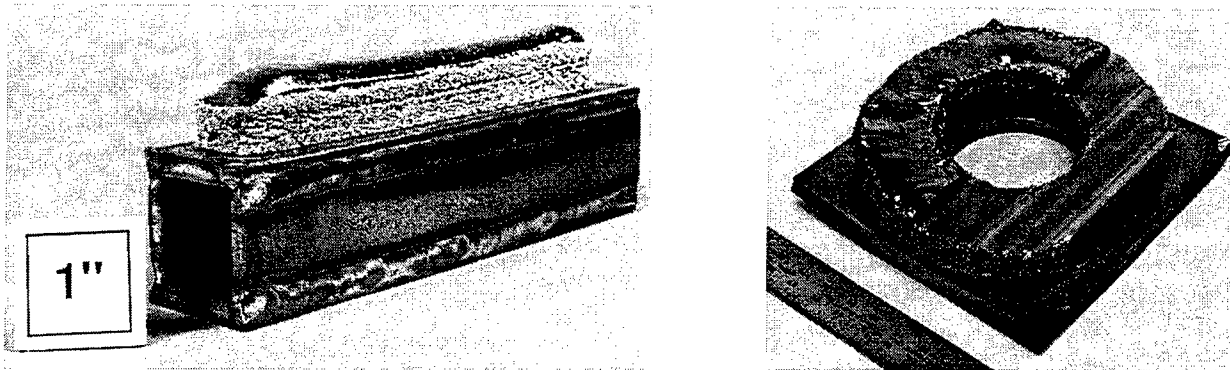


Figure 2. Typical LaserCast Ingot Research Shapes

Chemical Analyses of Ingots

Table 2 shows the results of chemical analyses performed on ingots of CP titanium and Ti-6Al-4V. Results are in the post mill-annealed condition as previously described. The results are compared to ASTM B367 grade C2 and grade C5 respectively.

Table 2. Chemical Analysis of LaserCast Ingots: CP titanium(C2) and Ti-6Al-4V (C5)

Elements	ASTM B367 C2 (wt.%)	LaserCast Ingot C2 (wt.%)	ASTM B367 C5 (wt.%)	LaserCast Ingot C5 (wt.%)
Oxygen	0.40 max	0.25	0.25 max	0.25
Nitrogen	0.05 max	0.13	0.05 max	0.04
Aluminum	N/A	-	5.5-6.75	5.79-5.95
Vanadium	N/A	-	3.5-4.5	3.75-3.85

Oxygen pick-up in the ingot material is a primary indicator of process integrity. Oxygen pick-up during ingot formation is held to less than 200-ppm [4]. Similarly, nitrogen pick-up was also held to less than 100-ppm. This is a result of maintaining a good working argon environment, free of atmospheric gases.

Mechanical Testing

Mechanical qualification of LaserCast ingots has consisted of multiple room temperature tensile tests and hardness testing of the respective tensile specimens. Results are in the post mill-annealed condition as previously described. Table 3 lists the results.

Table 3. Mechanical Property Results of LaserCast Ingots

Test	ASTM B367, C2	LaserCast Ingot C2 (wt.%)	ASTM B367, C5	LaserCast Ingot C5 (wt.%)
Hardness (max)	96 HRB (17 HRC)	30 HRC	39 HRC	37
UTS - ksi (min)	50	116	130	143
YS - ksi (min)	40	130	120	126
% Elongation 1-inch gage length (min)	15	<<15	6	6.2
No. of Tensile Specimens	N/A	2	N/A	6

Hardness values are listed as maximums. UTS, YS, and % Elongation values are listed as minimums.

The C5, Ti-6Al-4V, ingot's yield strengths exceeded ASTM requirements while maintaining acceptable levels of hardness and ductility. It is noted that, while the oxygen levels are near the upper limits of the specification, the nitrogen levels are well below specified maximums. These mechanical properties are supported by post test examination of the fractured surfaces which display a uniformly dimpled ductile failure [4].

The excessively high hardness and strength of the C2, CP titanium, ingots and the corresponding low ductility are a result of the high concentrations of oxygen and nitrogen in the titanium precursor powder [9]. This hardening effect is also present in C5, Ti-6Al-4V, ingots produced using this titanium precursor powder [4]. The material properties listed in Table 3 for C5, Ti-6Al-4V, material were obtained by using precursor powders with acceptable levels of interstitial oxygen and nitrogen. The LaserCast process yields grain structure that is significantly more refined than conventionally cast thick sections.

PRODUCTION SYSTEM DEVELOPMENT

Figure 3 contains an overall functional block diagram of the LaserCast system design which shows its major components; the LaserCast Workcell and Controller. Supporting components include a 14 kW Laser Generator and a workstation (used for CAD to CNC database translation).

The LaserCast workcell, shown in Figure 4, contains a number of integrated mechanical subsystems consisting of a process chamber, chamber lid and laser positioner, laser beam delivery and oscillation, powder delivery, gas delivery, and water cooling. Some notable characteristics of the workcell are:

- The size of the chamber can vary depending on customer requirements. Present scale-up designs are for a maximum 10-foot x 16-foot (plan-area) LaserCast structure.
- The modular design facilitates streamlined subsystem improvements (e.g., change in chamber size, laser technology).
- The design provides flexibility to use higher power lasers for increased build rates. Smaller fiberoptic lasers can also be incorporated without major re-design.

- The environment is maintained via a simple sliding lid seal and a turbulator orifice for the laser beam. The turbulator is designed to break up the backflow of atmospheric gases into the chamber as hot chamber gases are exhausted.
- Present scale-up designs are for build rates in excess of 12-in³/hour for titanium.

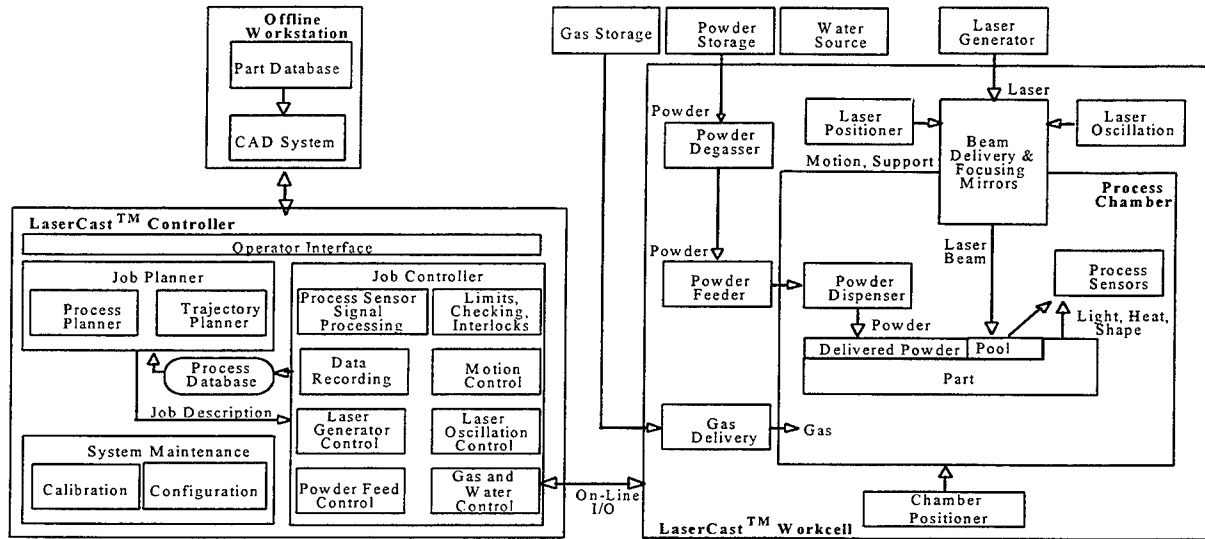


Figure 3. Functional Block Diagram of a Production LaserCast System

The LaserCast controller has a user interface that allows the operator to plan and program the specific processing parameters and paths for the LaserCast workcell. In addition, workcell sensor feedback will assist the operator in calibration and maintenance planning and execution. The LaserCast controller is being designed to accept input from Rapid Prototyping (RP) industry standardized file formats such as STL. This allows the LaserCast system to be used with the numerous 3D CAD and other third party CAD translation programs that can output solid model geometry in STL format.

The decision to use the STL file format enables the use of commercial STL post-processing software such as slicing software and automatic support structure generation. This has benefits in operator familiarity and in economics-of-scale issues such as bug fixes and acquisition costs.

The controller will use sophisticated process sensing and feedback strategies to maintain process quality. Process variables include gas rates and composition, powder feed rates, laser power, laser/target relative motion, dithering rates and fill patterns, and melt-puddle shape and size. Monitoring these variables and adjusting the process to maintain desired characteristics is a complex but necessary task. For example, the build-up rate of the ingot is dependent on precursor powder geometry and feed rates (which affects pre-fusing density). Therefore, the CAD description of the part will need to be sliced in real time based on the current ingot height in the LaserCast cell.

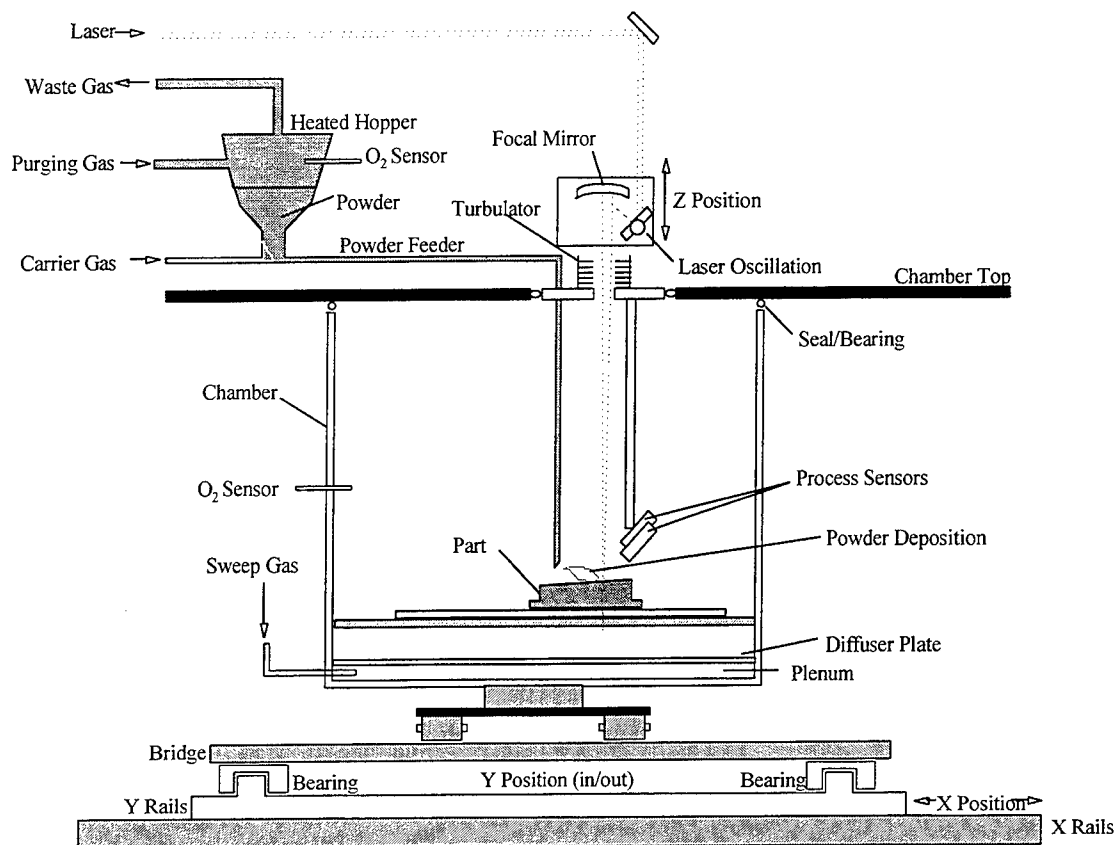


Figure 4. Conceptual Drawing of Production LaserCast Workcell

CONCLUSIONS

Results of experiments to date are very encouraging. Production of structurally useful, 100% dense, titanium alloy material has been demonstrated using this unique LaserCast process. The CP titanium and Ti-6Al-4V material produced under this program exceeds commercial ASTM B367 casting specification in ultimate strength, yield strength, elongation, and chemical constituency requirements. Oxygen pick-up in the ingot material is consistently held below 200-ppm, and nitrogen pick-up is below 100-ppm. It is anticipated that when ELI titanium powder is used (0.040 wt % O₂, 0.006 wt % N₂), the LaserCast process will be able to produce alloys such as Ti-5Al-2.5Sn ELI for cryogenic applications. This process is capable of rapid prototyping large titanium structures with a variety of alloying elements and in CNC directed flexible geometries. Direct use in replacement of castings, or as quick delivery forging pre-forms, is projected.

Selection of quality precursor titanium and alloying powders is critical to the success of the process. Titanium powder from different suppliers and manufactured using different techniques has been investigated and the results published [4]. The wide variation in powder chemistries requires the user to be especially selective when procuring powders for the LaserCast process.

The processed near-shape titanium articles fabricated by this process require additional manufacturing to obtain net shape and surface quality requirements. For some applications machining may suffice. The near-shape LaserCast articles should provide a quality forging and hot isostatic press (HIP) pre-form for larger articles and where application requirements require additional metallurgical refinement. This process is especially favorable to producing large forging pre-forms where tooling costs are often prohibitive. A near-shape forging pre-form can be produced by this process in a few weeks that will eliminate the need for many of the initial forging blocker die and heat treatment operations. This will offer a significant savings in cost as well as time to market.

A preliminary evaluation of the economics of titanium parts production from a dedicated LaserCast manufacturing cell cost center was explored. Results indicate that titanium parts can be delivered at 50% or less of the present cost of similar forged, HIP'd, or conventionally cast structures. Time to market can also be significantly reduced by 50% or more.

FUTURE WORK

Further work is planned to perform additional material qualification tests on Ti-6Al-4V and ELI Ti-5Al-2.5Sn ELI alloy ingots. Additionally, plans include the fabrication of two prototype structures with guidance from two aerospace-defense contractor companies and delivery of these structures for their evaluation. Refined economic projections for metallic parts produced by a commercial system, and the detailed design of that system, are also planned.

Process refinement is continuing with several key system hardware improvements planned. An enhanced processing chamber is being developed that will facilitate production of larger articles measuring 30-inches x 30-inches in plan view cross section and up to 12-inches thick with a maximum weight of 500-pounds. A unique circular dithering laser beam (to supersede the current linear dither) has recently been added to the system to provide flexibility in forming complex geometries. Continuous laser processing will be supported by the addition of a unique powder feeder, to provide continuous deposition of powder, and active cooling on critical heat affected components.

The production system development is in progress. Detailed design efforts for the production system have been initiated based on a completed FRS and a preliminary conceptual design. Key components of the production system have been identified and their design accelerated to allow for prototyping. These key components include a unique powder feeding system (including the capability to change powder constituents on-the-fly to make graded-composition alloys) and process feedback sensing subsystems. A potential customer for the first production system has also been identified.

ACKNOWLEDGMENTS

This program is sponsored by the DoD Defense Advanced Research Projects Agency (DARPA) under the direction of Dr. C. Robert Crowe and Dr. L.N. Durvasula. Dr. George Yoder at the Office of Naval Research (ONR) is the technical agent for the contract under ONR Contract

Number N00014-95-C-0029. The authors also extend their appreciation to colleagues on the development teams at The Johns Hopkins University Applied Physics Laboratory (P. Pandolfini, P. Cohen, and Z. Smith); at The Pennsylvania State University Applied Research Laboratory (J. Tressler, W. Rhoades, C. Sills, M. Brought, D. Hardy, and R. Knee); at MTS Systems (B. Cleveland, D. Harvey, and T. Hessburg), and Dr. H. B. Bomberger (consultant).

Independent laboratory chemical analysis was provided, under contract, by Howmet Corporation, Quality and Technical Services, Whitehall, MI, and Spectrochemical Laboratories, Inc., Pittsburgh, PA.

REFERENCES

1. F.G. Arcella, E.J. Whitney, and D. Krantz, "Laser Forming Near Shapes in Titanium", *International Congress on Applications of Lasers and Electro-Optics (ICALEO)*, Laser Materials Processing, Vol. 80, Edited by J. Mazumder, A. Matsunawa, C. Magnusson, Laser Institute of America, 1995, pp.178-183.
2. F.G. Arcella, "Laser Forming of Near Shapes", *Titanium '92, Science and Technology*, Vol. II, Edited by F.H. Froes and I.L. Caplan, a TMS Publication, 1993, pp.1395-1402.
3. F.G. Arcella, "Rapid Prototyping in Titanium with Intelligent Systems", *Proceedings 41st Sagamore Conference*, Edited by W.N. Roy and S.M. Walsh, U.S. Army Research Laboratory, Materials Directorate, 1995, pp.145-156.
4. F.G. Arcella, E.J. Whitney, M.A. House, P.H. Cohen, H.B. Bomberger, "Materials Characterization of LaserCast™ Titanium", *Proceedings 1996 World Congress on Powder Metallurgy & Particulate Materials*, P/M Laser Manufacturing, Washington DC, June 16-21, 1996.
5. S.W. Kandebo, "F-22 Team Characterizes New Materials, Processes", *Aviation Week and Space Technology*, 1995, p.46.
6. M.A. House, E.J. Whitney, and T. Hessburg, "Rapid Manufacturing of Titanium", *Proceedings, 1995 Defense Manufacturing Conference*, Dallas, 1995.
7. "Standard Test Methods for Tension Testing of Metallic Materials", ASTM E8-94c, *American Society for Testing and Materials*, 1994.
8. "Standard Specification for Titanium and Titanium Alloy Castings", ASTM B 367-93, *American Society for Testing and Materials*, 1993.
9. "Heat Treatment, Structure and Properties of Nonferrous Alloys", C.R. Brooks, *ASM International*, 1982.

RAPID PROTOTYPING PROCESS USING METAL DIRECTLY

Dr. A. F. Ribeiro, Lic.Informática, MSc, PhD.

Departamento de Electrónica Industrial, Univ. do Minho, 4800 Guimarães, Portugal.

e-mail: fernando@dei.uminho.pt

Prof. John Norrish, MSc.

Faculty of Engineering, University of Wollongong, Wollongong, Australia.

e-mail: John_Norrish@uow.edu.au

Abstract

Rapid Prototyping emerged in the USA in the late 80's and it made the whole industry rethink their way of making prototypes. Several new different process have emerged since then and these vary in materials, times, prices, finishing quality, etc. However, not many have achieved acceptable results with using 100% pure metal. Some heavy industry want prototypes made with metal in order to assess not only the shape of the prototype but also its hardness conditions and functionality of the component in real situations. This technique is still under development at several different places and although some research have been done recently the results are not yet as desired.

In the last couple of years a Rapid Prototyping process involving direct deposition of metal had been under development (as a PhD research) at Cranfield University. The process entails the use of a Gas Metal Arc fusion welding robot which deposits successive layers of metal in such way that it forms a 3D solid component.

A solid model is first drawn using a CAD system, then data indicating the kind of layers and dimension is incorporated and the solid is automatically sliced. This slicing routine also generates reports on the welding time and conditions for the production of the component and automatically generates the robot program.

Depending on the complexity of the component, the time from drawing the component to being ready to press the robot start button to make the component can take less than a couple of hours.

Several test components were produced with good characteristics and perfectly acceptable surface finishing. This paper describes the process and shows some samples.

1. Introduction

The current process was first briefly described by Ribeiro in ¹ and as the work is now finished it is here described in more detail.

Rapid Prototyping is a technique to produce prototypes in a short period of time to make companies more competitive. The advantages are tremendous and some of them are: reducing the

prototyping time production; the techniques are 'automatic' which means there is less need to have a skilled operative; these processes are less wasteful since they normally operate as an additive process instead of subtractive process; using a CAD program, it is very easy to implement changes in the component and being only necessary to "re-print" it; in most of these processes it is possible to make more than one prototype in one operation; it is possible to leave the automated machining centre machine working with little supervision around the clock.

But traditional RP processes also has some disadvantages like: the size of the prototype is limited by the size of the machine; the machines normally used are very costly; it is not always possible to make the prototype in the required material for final component (most of these techniques use wax, photopolymers, thermoplastics and ceramics or even paper for the initial model). Sometimes, it is very important not only to observe the prototype but also to test it and sometimes to use it. Since typical rapid prototyping samples have limited mechanical, thermal and chemical properties of the materials that can be manufactured these cannot be tested or even used. Techniques which prototype components in 100% metal are not common although some attempts have been made.

To overcome this problem a technique for rapid prototyping components using Robotic Arc Welding has been investigated in the present work.

In this process the component is formed by melting and depositing the metal using the GMA welding process. A CAD drawing system is used to create the initial solid shape and a welding robot is used to manipulate the welding torch.

2. Background

There have been a few attempts at rapid prototyping using welding techniques, but most of these used Numerically Controlled (NC) machines or special purpose automatic machines instead of robots. Where robots have been used these have been programmed manually.

In these the robot was programmed to do only one shape and it was not possible to modify the shape without re-programming again the robot (manually). The robot program was not linked to any CAD package unlike all the other rapid prototyping methods. In none of these cases was the component designed in a CAD package which means that no changes, previews or analysis of the components were possible.

In fact most of the tries that have been made were with very simple geometric shapes such as cylindrical shapes. In some cases they simply involved depositing metal on turn tables with the welding gun stationary. In these attempts the metal deposition rates were very high and the component's final quality was not very recommendable.

3. Working Principle of this Process

The component is first drawn in a CAD system as a 3 dimensions solid model. Then, this has to be sliced like any other RP process although this slicing is slightly different. Instead of

calculating the borders of the intersection between a plane and the solid, the centre line is what's required. The centre line represents the path that the robot has to follow in order to deposit the weld bead at the right places to build up the component. The welding parameters are automatically generated by the program (according to the metal to be used) in order to achieve the required bead geometry and stable operating parameters. These parameters were derived from welding studies carried out by Norrish ² and parametric equations generated by Ogunbiyi and Norrish ³. Besides the welding parameters, the slicing software automatically generates reports containing time taken for making the component, quantity of material needed, final approximate weight, etc. After the 3D model has been sliced with the routines developed by the author, a program reads the resulting lines/polylines and automatically generates the robot program for making the component and this can be simulated with the use of a robot simulation program to check for collisions or other problems such as access. The robot program may be modified if necessary.

The last step to be carried out is to compile the robot program and to upload it to the robot. The robot is now ready to start welding or in other words to start building up the component as far as the welding system is operational.

4. Apparatus

A graphical description of the rapid prototyping hardware used is shown in Figure 1. The dotted arrows represent ideal situations and not the real work cell.

A computer is connected to the robot controller via a serial cable RS-232-C and also to a printer. The power source and welding consumables are connected to the welding torch which is mounted on the robot arm. The robot builds the component on a table. This table should ideally be controlled by the robot (dotted arrow).

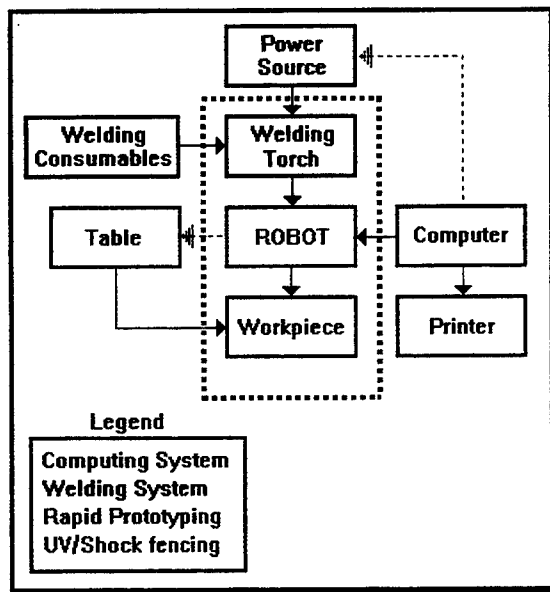


Figure 1 - Rapid Prototyping work cell Hardware

The individual components of the system used here were:

- An ASEA IRb 2000 robot from ABB. This is not a specifically welding robot but a 6 degrees of freedom robot with an S3 controller.
- The Table used for the second case study was a stand alone turn table but for the rest of the samples no turn table was used.
- For most of the components built, the Power Source used was a Migatronic BDH 320 although some tests were later on carried out with a Migatronic BDH 550. The Welding Torch was a BINZEL PUSH/PULL torch.
- The computer used for the CAD, off-line programming and downloading, was a PC with an Intel 80486 microprocessor running at 66 MHz with 16 Mbytes of RAM memory. The hard-disk capacity was 250 Mbytes.
- The whole work cell had a fence all around it with glasses containing an Ultra Violet (UV) filter to protect the eyes of the operators in the environment. The robot and table alone had another fence with another UV filter. This second fence was also to protect the physical movements of the robot (shock) and also to protect the eyes from the rays. Should the fence be opened, a circuit would go off and the robot/power source would stop working immediately.
- The consumables were all the necessary ones to a Gas Metal Arc Welding process like the wire, gas and contact tips.

The software used was AutoCAD release 12 for DOS as the CAD system, the Slicing Routine was created by the author of this paper and the Off-Line program to compile and download the robot program was SPORT 1.0.

The use of this particular Hardware/Software is not mandatory. Any suitable Personal Computer could be used. A possible limitation is the **Slicing** program which was developed to work with AutoCAD release 12, but this could be translated to any other language and CAD system. The robot used is not a limitation. In fact this robot was not even fitted with the normal welding robot options. Any other robot could be used if the robot program was generated in the desired language.

5. Test Samples

Three components were chosen to be shown and described in this section although several other were built up.

5.1 Chimney

The first one consists of a 'chimney' shape. The idea was to continue the cylinder in its top part but due to lack of material (and due to its price) it had to be interrupted.

It took about half an hour to draw it in a CAD system and about another half an hour to slice, generate the reports and generate the robot program. This was done in three separate robot programs although it could be done all in one.

It is about 250 mm height and weighs 4,240 Kg (without the base plate) and it lost around about 3 millimeters in height. The width was planned to be 5.6 mm and in the end it was measured and it varied ± 0.3 mm. At the location where the robot moves up (from layer to layer) was slightly higher (about 1 mm) than the rest of the component. After observing this problem, the other components were made using a spiral technique to avoid abrupt movements upwards. The welding parameters are of extremely importance for the final dimensions, final surface finishing and final quality and these can make the whole difference between a good component and a bad component. The component here described can be seen in Figure 2.

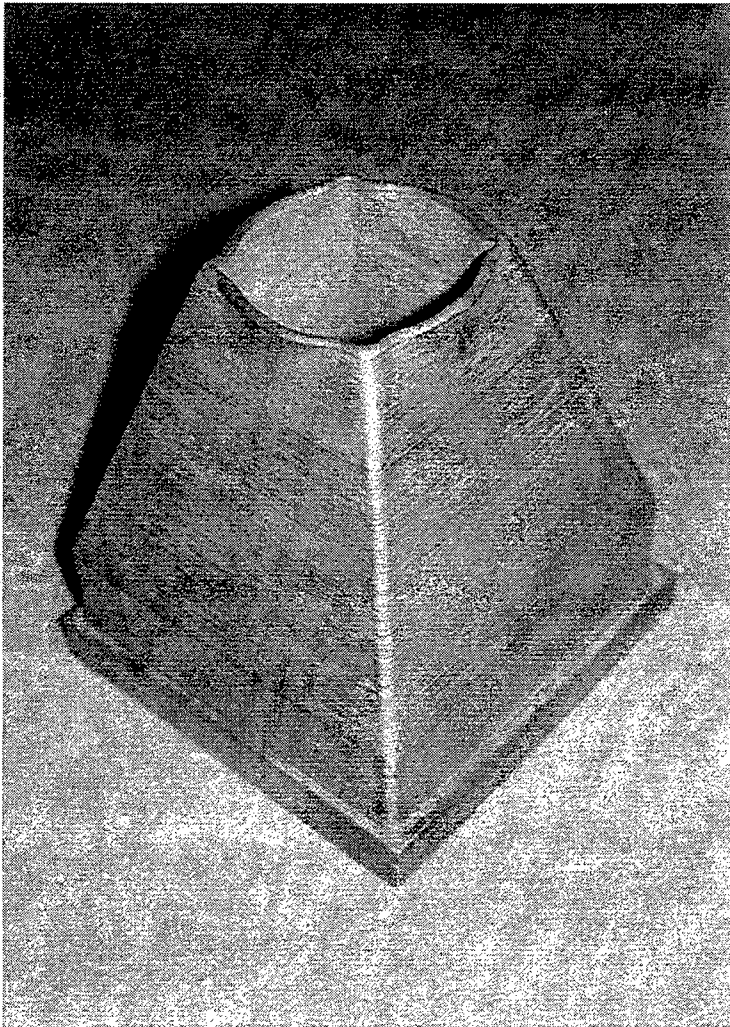


Figure 2 - 'Chimney' shape

5.2 'Bow Tie'

This component consists of a 'bow tie' shape and was intended to study increase of radius and consequent loss of height.

It took about half an hour to draw it in a CAD system and about another half an hour to slice, generate the reports and generate the robot program.

It is about 200 mm height and weighs around about 3 Kg (without the base plate). The width was planned to be 5 mm and in the end it was measured and it varied ± 0.2 mm. This component was done with four 'up movements' by the robot which means that instead of moving the whole bead height all in one go it did it in four separate places reducing though the height in that location. Like in the previous component the welding parameters are of extremely importance for the final dimensions, final surface finishing and final quality and these can make the whole difference between a good component and a bad component. This component achieved a good surface finishing, very near geometrical expectations (less than 1 mm in height lost).

The component here described can be seen in Figure 3.



Figure 3 - 'Bow Tie' shape

5.3 Pint Glass

This component consists of a 'pint glass'. It took just under half an hour to draw it in a CAD system and about fifteen minutes to slice, generate the reports and generate the robot program.

It is about 180 mm height and weighs around about 3 Kg (without the base plate). The width was planned to be 6 mm and in the end it was measured and it varied ± 0.2 mm. This component was done with a spiral technique which means that instead of moving the whole bead height all in one go it was moving up as it goes along the circle reducing though the height in a particular location. Like for every component the welding parameters are of extremely importance for the final dimensions, final surface finishing and final quality. This component achieved a good surface finishing, very near geometrical expectations (less than 0.5 mm in height lost).

The component here described can be seen in Figure 4.



Figure 4 - 'Pint' glass

6. Conclusions

The reason for making a prototype, should not only be to visualise but also useable to test and assess it in its final function. Therefore, it is important to make the prototype with the same material used in the real and final component. This process allows components to be made with metal successfully.

This technique can be used to make not only the prototype but also the final component with the desired metal for 'one-off' production. Therefore, this represents also a new production technique more suitable for low volume production.

Another advantage with this new technique is that different metals can be used during the build up of the component to achieve different structural characteristics in different parts of the same component. This would not be possible with casting. The welding can be stopped at any time, the filler material changed, and the welding started again as far as the metals are compatible. The time to change the wire and the welding parameters is not very long.

In this process the slices are automatically created, the ARLA robot program generated completely automatically and it was not essential to use a robot simulation package to test it, although simulation can be used to save on line time. This means that this process is very automatic with almost none intervention from the user (except for drawing the component in a CAD system).

Several components were made with perfectly acceptable quality in surface finishing, mechanical characteristics and dimensions. The welding parameters are of extremely importance in this process. They represent the difference between a good component and a bad component.

7. Acknowledgements

Mr. Ribeiro would like to thank John Norrish for his support in this project and his expertise in the welding field and also Dr. McMaster for his academic help in the work. My very special thanks go to John Savill for his strong support in welding all of the components and for solving in an efficient way the practical problems which arose as well as encouraging me to new ideas. A special thank you for my wife is also deserved for her understanding during the difficult periods of this project. My new employer (Universidade do Minho) and my Portuguese sponsor (JNICT) also deserve a big thank you.

¹ RIBEIRO, A. F. M., NORRISH, J. AND MCMASTER R., "Practical case of Rapid Prototyping using Gas Metal Arc Welding", 5th International Conference on Computer Technology in Welding, Paris, France, 15-16 June 1994.

² Norrish, J., "Advanced Welding Processes", Institute of Physics Publishing, 1992.

³ NORRISH, J., Ogunbiyi B., "An Adaptive Quality Control concept for robotic GMA Welding", 5th International Conference on Computer Technology in Welding, Paris, France, 15-16 June 1994.

THE LIQUID-TO-SOLID TRANSITION IN STEREODEPOSITION TECHNIQUES

R.S. Crockett, P.D. Calvert
University of Arizona, Tucson, AZ

Introduction

Stereodeposition is a broad category of Solid Freeform Fabrication techniques that accomplish the layerwise buildup of an object through the direct placement of bulk material. All stereodeposition techniques involve writing a path of liquid material, which rapidly undergoes a transformation to a solid. This transformation can occur by cooling, removal of solvent, or a catalyzed chemical reaction; the only requirement is that initial solidification provide sufficient change to support the next cross-sectional layer. Post-processing can later be performed on the object as a whole to achieve final properties, such as completion of polymerization or burnout of binder and sintering of ceramic particles.

This family of layerwise processing techniques lends themselves to the production of a wide range of materials, including functional ceramics¹, engineering polymers, and composites². Beyond this, stereodeposition has the potential to produce complex, functionally gradient materials³ and ultimately enable the chemical processing of exotic material systems which mimic biological processes⁴. The key to this flexibility is stereodeposition's ability to operate under a wide range of liquid-solid transformation rates. The first generation of stereodeposition processes have selected material systems with object precision and ease of operation as the driving goal. This leads to the extrusion of thermoplastic materials with a high viscosity (1000-10000 cps)^{1,2} or to systems with a reaction rate $< 1 \text{ s}^{-1}$ ⁵. The more interesting end of the spectrum for expanding the range of materials, however, is systems with low viscosity and low reaction rates combined with significantly higher shrinkages. In extending the use of stereodeposition from thermoplastics and other high-solidification rate materials, it is necessary to understand how the characteristics of a material system of interest impact the freeforming process. This paper presents current efforts at the University of Arizona to model the deposition and transformation in stereodeposition techniques, followed by a brief discussion on the impact of material characteristics on the operation of stereodeposition systems.

Stereodeposition Techniques and Solidification Strategies

The original and simplest method of rapidly transforming a bead from liquid to solid is through removal of heat. In the Stratasys Fused Deposition Modeling (FDM) process, a wax or low viscosity polymer in the form of a filament is melted and deposited, solidifying upon cooling. By using the polymer as a binder for ceramic particles, this process has been extended to produce ceramic greenbodies in the Fused Deposition of Ceramics (FDC) process². Advanced Ceramics Research (ACR) employs a similar technique, using a high pressure (0.5 to 4.5 kpsi) extrusion apparatus to produce high molecular weight polymer objects and ceramic greenbodies from feed rods. In all of these processes, the liquid-solid transformation occurs quite rapidly. This transformation is determined by heat flow for glass-forming materials or by much slower crystallization kinetics in waxes and Nylon. Even in these cases, however, the time scale is probable less than 1 minute.

The Reactive Stereodeposition process⁶, originally developed to produce ceramic objects, involves significantly slower transformation rates. In Reactive Stereodeposition, a highly-loaded ceramic slurry is dispensed through a syringe in an appropriate 2-D pattern; a sufficient binder polymerization rate is achievable by a catalyzed reaction, combined with rheology changes, to

rigidize the slurry sufficiently to support the weight of successive layers. Catalysis can be triggered by the activation of a component already present in the slurry. Depending on the type of polymer binder, the activation can be in the form of heat, light, or a change in pH. It is also possible to introduce a catalyst in a mixing chamber immediately before the slurry is deposited. This technique has been used by ACR to produce alumina and silicon nitride parts from slurries containing ceramic powders or inorganic fibers dispersed in liquid acrylic monomers⁷, which are polymerized by dispensing on a heated surface.

A stereodeposition system developed at the University of Arizona⁶ employs ethyl silicate, a metal alkoxide compound, as a binder. Rigidization is achieved initially by the rapid evaporation of ethanol and recovery from shear thinning during the deposition process. Gelation of the binder is then triggered by the addition of a base catalyst (NH₄OH) through a spray of ammonia water applied to the surface. Full curing takes hours, and is allowed to continue in the object as a whole by suspending the greenbody in a sealed container above a mixture of ethanol and ammonium hydroxide. This provides a wet, basic environment for the continuation of curing without drying. After curing is complete (approximately 24 hours), the environment is modified to allow for drying at a slow rate. This system has been used to produce silica, mullite, and fiber-reinforced borosilicate glass greenbodies.

In extending the Reactive Stereodeposition system to the slowest liquid-solid transformation rates, initial solidification must result primarily from rheology changes of the slurry, which are often sufficient to support the shape of a deposited bead for an extended period of time. In this case, polymerization of the binder can occur as a separate, later step. Thus the slurry's rheological properties, and especially the impact of shear thinning and solvent removal, become driving criteria for slurry development.

Modeling the Liquid-to-Solid Transition

Deposition and Bead Stability

Stereodeposition shares with other freeforming techniques a relationship between write speed and cross-sectional path area, with operational boundaries defined by the characteristics of the material. The flow of a viscous material through a deposition orifice (figure 1a) is controlled by Hagen-Poiseuille flow⁸, in which flow rate (Q) is reduced for high fluid viscosity (η) and small orifice sizes (R) or long tip length (L) at a given deposition pressure (P_{GAGE}):

$$Q = \frac{\pi R^4 P_{gag}}{8\eta L} \quad (1)$$

Once the material leaves the dispensing tip, conditions for bead stability during writing impose a limit to the head speed. For a given volume flow rate, bead cross sectional area is inversely proportional to head speed (figure 1b). As speed is increased, bead area is reduced; above a certain speed (equivalent to a minimum cross sectional bead area), the bead will tear, producing gaps in the final part. The minimum achievable area at the maximum head speed is a similar geometry to the problem of an axisymmetric liquid bridge⁹, which is stable up to a height limit on the order of the square of the tip height above the surface divided by π :

$$A_{min} = 2lR' = \frac{l^2}{\pi} \quad (2)$$

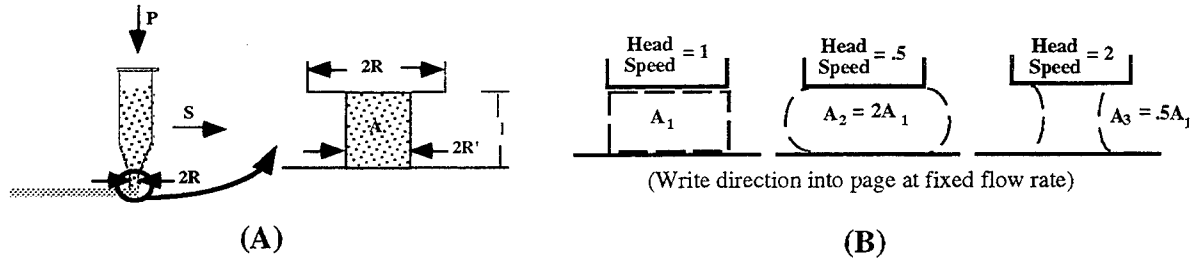


Figure 1. Deposition geometry.

Combining equations (1) and (2), we have the imposed condition for depositing a continuous bead with a minimum cross sectional area:

$$\frac{\pi R^4 P_{gage}}{8\eta LS} > \frac{l^2}{\pi} \quad (3)$$

While liquid properties are not directly involved in the stability limit presented in equation (2), the impact of exceeding the stability limit and the ability of a material to “neck down” from R to R' varies based on the Weber number and the Reynolds number of the liquid¹⁰. The Weber number contains the magnitude of the surface tension, with low surface tension liquids less susceptible to forming individual droplets. Because it is also associated with splashing, the Weber number is an important parameter in the resolution of individual write paths in the 3-D Printing process¹¹.

Bead Spreading

If the deposited bead conforms to a Bingham-type rheology with an increasing yield strength caused by polymerization and solvent removal, it is possible to derive a differential equation for the rate of increase of bead width (S_{SL}).¹²:

$$\frac{dS_{SL}}{dt} = \frac{1}{\eta} \frac{A}{S_{SL}^2} \frac{(F(\theta) - F_Y(t, \theta))}{l} \quad (4)$$

Here η is the liquid viscosity and A is the bead cross sectional area. The driving force for spreading per unit of bead length (F/l) and restraining force per unit of bead length (F_Y/l) are found by a force balance performed at the edge of the spreading bead (figure 2a). Substituting appropriate equations for forces and for the bead width in (4) produces an equation for the change in bead contact angle over time:

$$\frac{d(\phi)}{dt} = \frac{A}{R^2 \phi \eta R} \left[\frac{(1 - \cos \theta)}{\phi} - \frac{\tau_Y(t) R}{\gamma_{LV}} \right] \quad (5)$$

In this equation, γ_{LV} is the surface tension of the deposited liquid, τ_Y is the liquid yield strength, and R is the radius of curvature of the surface onto which the bead is dispensed (an individual bead in the previously deposited layer). Geometrical constraints (figure 2b) produce a relationship between ϕ and θ :

$$\left(\frac{\sin \theta}{\tan \phi} + \cos \theta \right)^2 \left(\frac{2A}{R^2} + \phi - \sin \phi \cos \phi \right) = \theta + \phi - \sin(\theta + \phi) \cos(\theta + \phi) \quad (6)$$

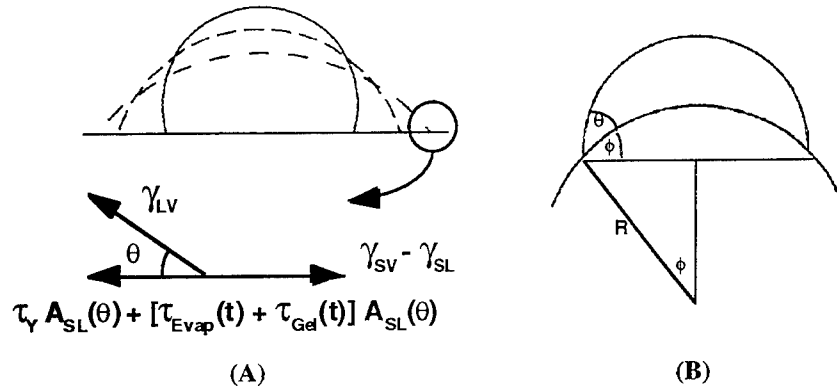


Figure 2. Force balance and bead geometry.

Solidification Cases

For the purpose of further simplifying the model, the spectrum of solidification rates associated with existing stereodeposition systems can be classified into 0, moderate, and fast, corresponding to no property changes, surface property changes, and bulk property changes of the liquid during bead spreading. The simplest case of equation (5) occurs when the yield strength of the liquid is constant and no property changes occur during the spreading process. This is the situation that occurs in the slowest Reactive Stereodeposition systems. The bead will continue to spread at a rate controlled by surface tension, viscosity, and bead geometry. It will stop at a final contact angle occurring when $d\phi/dt = 0$:

$$\frac{(1 - \cos \theta)}{\phi} = \frac{\tau_Y R}{\gamma_{LV}} \quad (7)$$

Under conditions of moderate diffusion rates, the yield strength of the liquid is increased in a surface shell, without changing the bulk properties of the liquid. This occurs in chemically reacting systems or when there is a loss of solvent from the surface during dispensing. In this case, the bulk viscosity remains constant, but the yield strength increases with time due to the formation of a "shell" which increases in thickness. The final contact angle now depends on time, based on the permeability of the solidifying shell (P) and the driving force for mass transfer (ΔC):

$$\frac{1 - \cos \theta}{\phi} = \frac{\tau_Y R}{\gamma_{SL}} \left[1 + \frac{(2P\Delta C t)^{\frac{1}{2}}}{R\phi} \left(\frac{\tau_{Y,solid}}{\tau_Y} - 1 \right) \right] \quad (8)$$

Permeability is usually associated with a gas passing through a film and is expressed, for example, as cm^3 gas at standard temperature and pressure passing per second through 1 cm^2 of a membrane 1 cm thick when the pressure difference across the membrane is 1 cm of mercury. If a linear relationship exists between external vapor pressure and a corresponding equilibrium concentration within the membrane, permeability can be expressed in terms of the more fundamental diffusion coefficient, which has units $\text{cm}^2 \text{s}^{-1}$. The driving force for mass transfer is either a concentration gradient or capillary pressure gradient, depending on the characteristics of the solidifying material.

If the diffusion is fast enough, the bulk properties of the liquid change appreciably during spreading. This is the case with solidification due to thermal diffusion, such as occurs in the cooling of a thermoplastic from a melt (FDM). A typical way to mathematically treat this case is to define a "gel time" at which the viscosity and/or yield increases dramatically. In this situation, the liquid properties would be treated as a step function.

Material Parameter Groups and "System Contact Angle"

There are a number of key parameter groups which can be identified from the spreading model presented above. In the absence of property changes, the final contact angle of a deposited bead is controlled by:

$$\alpha = \frac{\tau_Y R}{\gamma_{LV}} \quad (9)$$

Because of its use in rheology discussions, it is useful to introduce the "index of plasticity":

$$\beta = \frac{\tau_Y}{\eta} \quad (10)$$

With this definition, the rate of bead spreading is controlled by:

$$\frac{\alpha}{\beta} = \frac{\tau_Y R}{\gamma_{LV}} \times \frac{\eta}{\tau_Y} = \frac{\eta R}{\gamma_{LV}} \quad (11)$$

This parameter grouping is the same as that which controls the rate in amorphous material sintering processes¹³ and capillary penetration of liquids¹⁴.

Finally, the time-dependent solidification or "strength diffusion" term becomes:

$$\delta = \frac{(2P\Delta C)^{\frac{1}{2}}}{R} \left(\frac{\tau_{Y,solid}}{\tau_Y} - 1 \right) \quad (12)$$

Using these groupings, the full solution to bead spreading is:

$$\frac{d(\phi)}{dt} = \frac{A}{R^2 \phi} \frac{\alpha}{\beta} \left[\frac{(1 - \cos \theta)}{\phi} - \alpha \left[1 + \frac{\delta^{\frac{1}{2}}}{\phi} \right] \right] \quad (13)$$

After the first few deposited layers, the system will achieve a "system contact angle", where the newly deposited bead spreads until it's final radius equals the radius of the bead onto which it was deposited. Under these equilibrium conditions, R is a function of the square root of A , eliminating one system variable. The full bead spreading solution thus involves a 3-dimensional material "parameter space" of α , β , and δ . Current work at the University of Arizona is on verifying this model, and results will be presented at next year's symposium.

The Effect of Material Parameters on Process Results

Generalizing about the parameter groupings derived above, α represents a liquid's resistance to motion. It is in effect a ratio of the restraining force to the driving force, thus a large α represents a system similar to extrusion, where flow is limited. β determines the system's response time, with a small β (high viscosity) indicating a "sluggish" system. One example of how these parameters interact to effect process results is the phenomenon of casteling, wherein irregularities in deposited lines grow into large peaks and troughs in the course of forming multiple

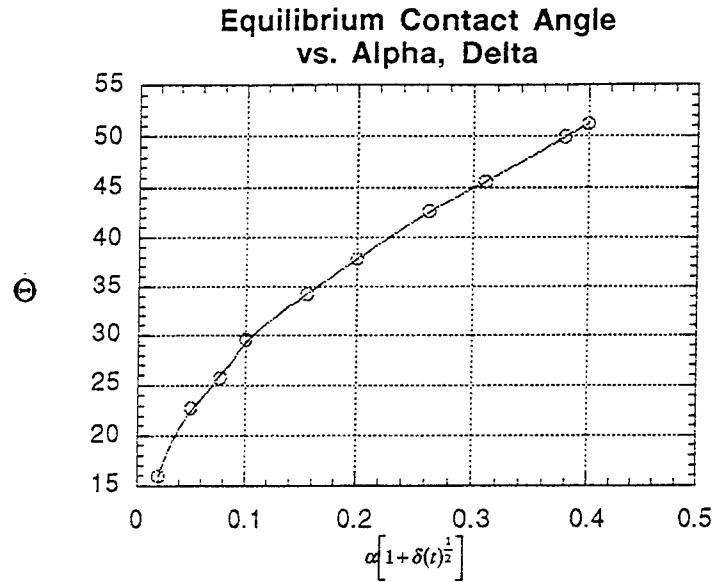


Figure 3. Dependence of system contact angle on material parameters.

layers. This occurs under either low alpha (bead tears easily), or high beta (bead cannot respond to disturbances rapidly enough).

An important relationship is the effect of beta on spreading time, which in turn determines the impact of delta on total liquid property changes during bead spreading. Figure 3 presents a plot of system contact angle vs. alpha, delta, and spreading time (and thus beta) as determined by the model. It can be seen from this figure that the larger any of these three parameters, the larger the resulting system contact angle. The system contact angle determines the ultimate precision of the part in a direct tradeoff between path width and layerwise resolution (figure 4b). A bead with a cross-sectional area of 1 mm² which achieves a contact angle of 5° will result in a path width of 3.9 mm and layerwise resolution (layer thickness h in figure 4a) of 510 μm. Increasing the contact angle to 40° by increasing alpha, delta or beta reduces the path width to 2.4 mm at the expense of an increased layer thickness of 820 μm. Also associated with contact angle is the *surface roughness*, the difference between the maximum and minimum radii of the deposited beads (figure 4a). The cases presented above have an inherent roughness of 17 and 70 μm, respectively. It is important to note, however, that in producing a solid, the outer surface (the circumference of a layer), may be written with more care than the interior of the layer. Line width is thus not necessarily the limiting factor to build time.

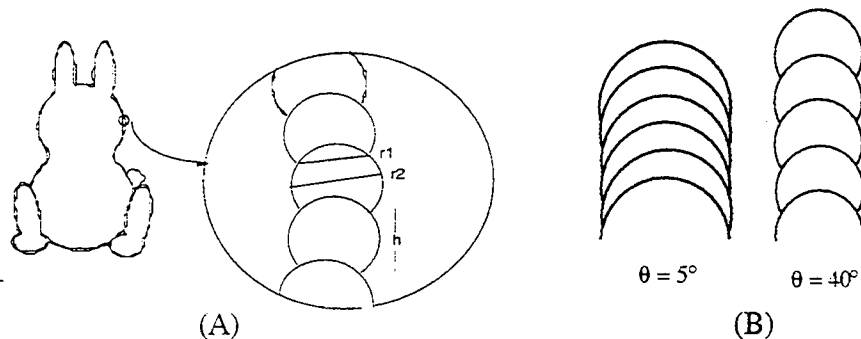


Figure 4. (A) Resolution (h) and surface roughness (r2-r1).
(B) Dependence on contact angle.

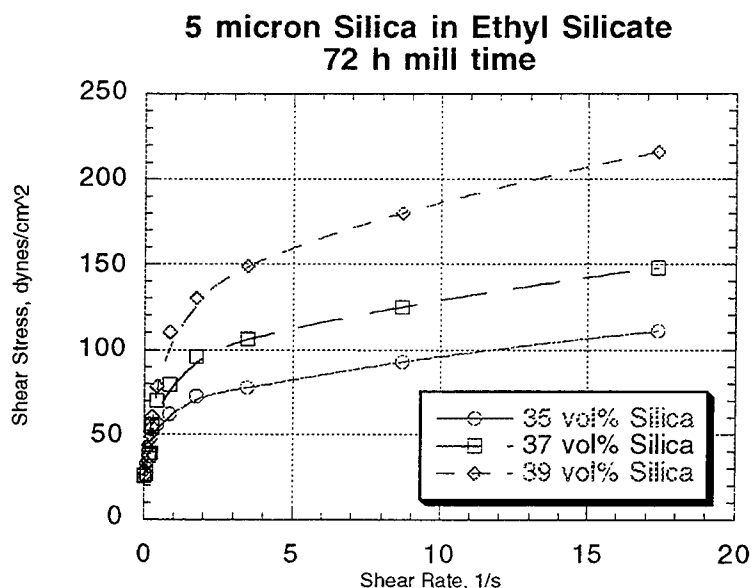


Figure 5 - Rheology of typical ceramic slurry used for reactive stereodeposition.

A low beta relative to alpha is useful in controlling the contact angle and providing time flexibility. The downside to this, however, is the lack of flow which can create diamond-shaped flaws between individual paths. A strategy we use extensively in our reactive stereodeposition process to achieve a desirable amount of flow and a reasonable contact angle is to adjust the rheology to produce a shear-thinning, Bingham plastic liquid with a yield point.

For our systems, at least, this is achieved by the addition of a solvent to thin the liquid plus 1-2 vol% fumed silica to develop a shear-dependent rheology (figure 5); the yield strength of these liquids is established at 5%-10% of the ratio of liquid surface tension to bead cross-sectional area. Viscosities on the order of 100 cps during deposition under shear rates of 100 s^{-1} allow for dispensing at 10 psi. The fluid viscosity then rapidly increases to greater than 10^4 cps during the spreading, as the shear rates drops below 10^{-1} s^{-1} . This allows a reduced spreading rate and sufficient yield to control the final contact angle. The extreme extension of this strategy is where a stable contact angle is reached after a period of flow by recovery from shear thinning without any solidification occurring; curing is then performed as a separate step on the surface of an entire layer.

Clearly, solidification during bead spreading modifies the impact of the liquid properties and thus the final contact angle of a bead. Solidification rate also controls the time required between placement of adjacent beads and layers to prevent further shape changes, as well as the inter-layer adhesion and shape limitations of the final object. An obvious objection to a freeforming approach is the long processing time needed to react a sequence of layers. Our rule of thumb has been that reaction should be complete to the point of solidification within one minute for a layer. This gives reasonable process times for layers which are 0.1-1mm thick. A typical diffusion coefficient in liquid is 10^{-5} - $10^{-6} \text{ cm}^2\text{sec}^{-1}$, which corresponds to a diffusion length of 0.1-0.5 mm in a minute. This suggests a maximum layer thickness in this range for chemical reactions involving diffusion out of products or loss of solvent. If diffusion, rather than reaction rate, is limiting it should be possible to write thinner layers faster to obtain faster overall processing. Thermal diffusion is generally much faster than mass diffusion and is unlikely to limit the forming rate in materials that solidify by cooling.

Rapid reaction will result in adiabatic heating of the layer, especially in monomer-rich systems with poor thermal conductivity. We have observed waves of reaction, which we attribute to such thermal autoacceleration, moving through partly-formed parts. Thus self-heating can limit the overall rate at which material is deposited. With our system, at least, too rapid reaction, in relation to the time to write a layer, also results in poor interlayer bonding and later delamination.

This paper has focused on the importance of understanding the impact of material properties on the stereodeposition process, specifically in the critical liquid-solid transition. While we have touched on some of the key issues, there is still much to be understood. The ultimate motivation, however, is that a solid understanding will increase the range of material systems compatible with stereodeposition techniques, allowing this method to produce increasingly novel materials.

ACKNOWLEDGMENTS

The authors would like to thank the Space Engineering Research Center for its financial support.

REFERENCES

- ¹ K. Stuffle, A. Mulligan, P. Calvert, J. Lombardi, "Solid Freebody Forming of Ceramics from Polymerizable Slurry", *Proceedings of the Solid Freeform Fabrication Symposium*, University of Texas at Austin, September, 1993. pp.60-63.
- ² M.K. Agarwala, *et. al.*, "Structural Ceramics by Fused Deposition of Ceramics", *Proceedings of the Solid Freeform Fabrication Symposium*, University of Texas at Austin, August, 1995. pp.1-8.
- ³ G.E. Hilmes, "Recent Developments in Extrusion Freeform Fabrication (EFF) Utilizing Non-Aqueous Gel Casting Formulation", to be published in the *Proceedings of the Solid Freeform Fabrication Symposium*, University of Texas at Austin, August, 1996.
- ⁴ P.D. Calvert and R.S. Crockett, submitted to *Chemistry of Materials*.
- ⁵ See, for example, rate discussions for Selective Laser Sintering (p 55), Stereolithography (p. 134), and Shape Deposition Modeling (p.118), *Proceedings of the Solid Freeform Fabrication Symposium*, University of Texas at Austin, August, 1995.
- ⁶ R.S. Crockett, *et. al.*, "Predicting and Controlling Resolution and Surface Finish of Ceramic Objects Produced by Stereodeposition Processes", *Proceedings of the Solid Freeform Fabrication Symposium*, University of Texas at Austin, August, 1995. pp. 17-24.
- ⁷ P. Calvert, R. Crockett, J. Lombardi, J. O'Kelly, K. Stuffle, "Extrusion Methods for Solid Freeform Fabrication". *Proceedings of the Solid Freeform Fabrication Symposium*, University of Texas, Austin, August 1994. pp. 50-55. 1994.
- ⁸ White, Frank M., Fluid Mechanics, McGraw-Hill Book Company, New York, 1986, p305.
- ⁹ Middleman, Stanley, Modeling Axisymmetric Flows, Academic Press, San Diego, 1995. p. 173.
- ¹⁰ *ibid*, p. 112.
- ¹¹ M.J. Cima, *et. al.*, "Ceramic Components from 3-D Printing", Presented at the 98th Annual American Ceramic Society Meeting, Indianapolis, April 14-17, 1996.
- ¹² R.S. Crockett, "The Liquid-to-Solid Transition in Stereodeposition Techniques", University of Arizona dissertation, in preparation.
- ¹³ Sherer, G.W., "Viscous Sintering of Inorganic Gels", pp. 265-300 in Surface and Colloid Science, vol. 14, ed. E. Matigevic. Plenum Press, New York, 1987.
- ¹⁴ Reed, James, Introduction to the Principles of Ceramic Processing, John Wiley & Sons, New York, 1988. p. 24.

Processing of Piezocomposites via Solid Freeform Fabrication (SFF) Techniques

A. Bandyopadhyay, R. K. Panda, V. F. Janas, S. C. Danforth and A. Safari

Department of Ceramic Science and Engineering and

Center for Ceramic Research

Rutgers University, Piscataway, NJ 08855-0909

Abstract

Fused Deposition and Sanders prototyping were used to manufacture PZT-polymer composites with various architecture for transducer applications. Two separate processing routes, direct and indirect, were utilized to make these composites. In the direct processing route, Fused Deposition of ceramics (FDC) was used to form green ceramic structures. For the indirect processing route, molds of the negative of the structures were made using FDMTM and Sanders prototyping techniques. Molds were infiltrated with a PZT slurry and dried. These structures were subjected to a binder burn out cycle to remove the mold polymer and binder. Structures were sintered and infiltrated with an acoustic epoxy, cut, polished and poled for electro-mechanical characterization. Among the various composites produced via the direct and indirect processes were: 3D honeycomb, 3-3 ladder, 2-2 annular and 1-3 rods. Composites with features as fine as 50 μm were manufactured and characterized. Properties of piezoelectric composites produced by SFF techniques compared to conventionally processed composites.

I. Introduction

Piezoelectric materials have the ability to convert electrical energy into mechanical energy and vice versa. These materials are used as ultrasonic transducers in two different modes, active and passive. In the active mode, the piezoelectric material only receives signals while in the passive mode, it will both send and receive signals. The various applications for these transducers include: medical imaging, hydrophones, microphones, phonographic pick-ups, speakers, strain gages, ignitors, nondestructive evaluation, and medical applications such as osteosynthesis, lithotripsy, and transdermal drug administration. The total US market for ultrasonic technology was \$3.3 billion in 1995, and was projected to grow to ~\$5.0 billion by year 2000[1].

Several ceramic and polymer materials exhibit piezoelectric behavior. Among the ceramic materials lead zirconate titanate (PZT) is being the most extensively used material in piezoelectric transducers. Piezoelectric ceramics have a relatively large value of d_{33} , the longitudinal piezoelectric charge coefficient, but their hydrostatic charge coefficient (d_h) and voltage coefficient (g) are low. Moreover, there is a poor acoustic match between the ceramic and the media through which it is transmitting or receiving a signal[2]. Piezoelectric polymers have low density and higher g_h values with good acoustic matching, but they have low electromechanical coupling coefficients (k_p and k_t), with relatively high cost of fabrication and poling[3]. Piezocomposites consisting of a piezoelectric ceramic in an inactive polymer combine the desired piezoelectric sensitivity and dielectric constants of piezoceramics and low density and greater flexibility of polymers. These composites have shown better

electromechanical properties than monolithic materials. Various composite structures with innovative architectures have been explored over the last two decades. The connectivity or the microstructural arrangements of the ceramic and the polymer phase/s in the piezocomposites is a critical parameter for the electromechanical performance of the composites[4]. Numerous processing routes have been explored to fabricate composites with various connectivities including, 0-3, 1-3, 2-2 and 3-3. Here, the first digit refers to the number of dimensions in which the piezoelectric ceramic phase is connected and the second digit refers the same for the polymer. One of the applications for these composites is in ultrasonic imaging for medical applications where the imaging resolution can be increased by operating these transducers at higher frequencies. An increased operating frequency usually increases the noise to signal ratio which can be minimized by using fine scale piezoelectric transducers[5]. Some of the processing techniques developed for processing piezoelectric ceramic/polymer composites with numerous connectivities are listed in Table 1.

In this work, solid freeform fabrication (SFF) methods were used to make piezoelectric composites with novel architectures. Over the last decade, several SFF methods have been developed as techniques to fabricate polymer, metal or ceramic structures on a fixtureless platform directly from a CAD file[6]. During design verification or product development stage, SFF techniques offer great flexibility to manufacture prototypes with various shapes, sizes and functionality. For example, 1-3 piezocomposites are widely used for transducer applications and they are fabricated using various techniques including, injection molding, dice and fill, tape lamination and lost mold[5]. In conventional processing, a change in design for 1-3 piezocomposites is not only cost intensive, but also very time consuming. SFF techniques offer the possibility of processing these 1-3 piezocomposites with different rod spacing, rod size, rod geometry or a volume fraction gradient in ceramic materials from surface to inside with superior properties at a similar cost of production with no extra time for processing. The Fused Deposition process, commercialized by StratasysTM Inc. (Eden Prairie, MN), and the ink jet printing process, commercialized by SPI (Wilton, NH), were used for this work. Indirect and direct processing routes were used for processing these piezoelectric ceramic/polymer composites. In the indirect processing route, a polymer mold or the negative of the structure was fabricated using SFF techniques. The mold was infiltrated with ceramic slurry, dried and then heat treated to remove the mold polymer and the binder. In the direct processing route, a green ceramic structure was directly formed using Fused Deposition of Ceramics (FDC) and then heat treated to remove the binder[7]. The structures were then sintered and back filled with an epoxy to form the composite.

This paper focuses on fabrication of PZT/polymer composites with 1-3 (using MM6-Pro, Sanders Prototype), 2-2 and 3-3 connectivities (using Fused Deposition technique). Physical and electromechanical characterization of these composites are presented, and advantages of the SFF approach are highlighted.

II. Processing

The Fused Deposition and Sander Prototype processes were used to form piezoelectric ceramic/polymer composites. These composites were processed via two different routes: (a) direct and (b) indirect. Both methods are schematically shown in Fig. 1. In the direct

processing route, FDC was used with a PZT powder loaded polymer filament as the feed material for a direct layered manufacturing of the 3D green ceramic structure. Commercially available polymer/wax was used to create the molds for the indirect process. Piezoelectric ceramic/polymer composite structures were processed via lost mold technique[8]. In both the indirect and the direct routes, the final composite was formed by embedding the ceramic structure in an acoustic epoxy, and then electroding and poling them. Physical and electromechanical properties were then evaluated.

II.a Direct Fused Deposition of Piezoelectric Ceramic/Polymer Composites

The 3-3 ladder structures with various orientations were built using the direct manufacturing technique with filaments of thermoplastic binder filled with PZT powder. A commercially available spray dried PZT-5H powder (Morgan Matroc Inc., Cleveland, OH) was used. Filaments were fabricated with 52 volume percent solids loading in a six-component thermoplastic binder system. Compounding or mixing of the powders with binders was done at 100°C using a Haake Rheocord System 40 (Passaic, NJ) at 100 rpm for one hour at a stabilized torque. The compounded mix was granulated before filament fabrication. Filaments of 1750 (+/- 50) μm in diameter were fabricated using an Instron capillary rheometer at a temperature of 65-75°C using a constant cross head speed of 1 mm/minute. A 3D Modeler™ by Stratasys™, Inc. (Eden Prairie, MN) was used for Fused Deposition of Ceramics (FDC) process. The liquifier temperature was maintained between 140-200°C while the temperature of the surrounding environment was in the range of 30-40°C. After processing, the green part was removed from the foam bed for further processing.

II.b Indirect Processing of Piezoelectric Ceramic/Polymer Composites

In this process, polymer molds having the negative of the desired structures were formed via Sanders Prototype and FDM™. Molds were built using Stratasys™ commercial investment casting wax or ICW-04 and SPI's commercial wax. A ceramic slurry containing a high solids loading (45 volume %) of lead zirconate titanate (PZT) developed for the lost mold technique used to infiltrate the polymer molds[9]. The high solids slurry minimized cracking in the samples during solvent drying and binder burnout. Excess ceramic slurry on the top acted as a base for the structure after the burnout of the mold.

II.c. Firing

A three-stage binder burnout cycle in air was developed for the polymers in the structure. The specimens were heated from room temperature to 350°C at a rate of 1°C/min. and held for 1 hour to allow most of the polymer mold to evaporate. The temperature was then increased to 550°C at a rate of 1.5°C/min. and held for 2 hours to burnout the binder. A third soak at 800°C for 1 hour, with a heating rate of 3.5°C/min., was necessary to impart sufficient bisque strength to the ceramic structures for mechanical handlability. The specimens were cooled to room temperature, and sealed in a crucible containing an excess lead source. The specimens were then heated at a rate of 3.5°C/min to 1285°C, and held for 1 hour to sinter the PZT ceramic.

II.c Characterization

The sintered samples were embedded in Spurr epoxy (Ernest F. Fullam Inc., Latham, NY) and cured in an oven at 70 °C for 12 hours in air. After removing the base and polishing both of the sides parallel to each other, the volume percent of PZT (V_{PZT}) in the composite was calculated. The polished surfaces were then coated with silver paint and the composite specimens were poled in a corona poling apparatus at 70°C, 25 kV for 20 min., with a needle to specimen separation of 4.5 cm. 3-3 composites were poled perpendicular to the ceramic roads/mold X-Y plane and 1-3 composites were poled parallel to the rod length. The electromechanical properties were measured after aging the specimens for a minimum of 24 hours. The capacitance (C_p) and the dielectric loss factor ($\tan \delta$) were measured, before and after poling, at 1kHz using a RLC digibridge (Model 1689M, Gen. Rad. Inc., Boston, MA). The d_{33} coefficient of each composite was measured at 100 Hz using a piezo d_{33} meter (Model CPDT-3300, Channel Products Inc., Cleveland, OH). The composite impedance behavior versus frequency at resonance was used to measure the series and parallel resonant frequencies. Using these values, the electromechanical coupling coefficients were calculated[9]. Scanning electron microscope (Model 1400 SEM, Amray Corporation) pictures of the ceramic structures were taken after sputter coating them with gold.

III. Results and Discussion

Various composites architectures were fabricated using both direct and indirect processing routes and three of them, 1-3, 3-D honeycomb and 3-3 ladder structures were characterized.

III a. Piezocomposites Processed via Indirect Processing Route

1-3 PZT ceramic/polymer composites were fabricated via the indirect processing route. Molds of 1" X 1" X 0.1" were created using Sanders Prototype. A .stl file for cross-hatch pattern was used to create these molds with a road width of 100 μm and an inter road gap of 150 to 350 μm . Fig. 2a shows an SEM micrograph of the mold for 1-3 structure fabricated by Sanders Prototype. The figure shows a mold wall thickness of 100 μm and an inter road gap of 350 μm . Sanders prototype uses two different nozzles to deposit build and support materials and a milling operation to adjust the layer thickness. During fabrication of these molds, due to milling operation, some of the support materials went inside the holes. These small chips of the support materials can also be observed from Fig. 2a. Fig. 2b shows the 1-3 PZT ceramic structure processed from one of these molds via lost mold technique. The rod surfaces are not smooth because of the entrapment of the support materials inside the holes. The figure shows square rods of 300 μm width separated by gaps of 70-90 μm . Volume fraction of PZT ceramic (V_{PZT}) was 48% for this 1-3 composite. Similar structures with different rod widths, spacings and volume fractions of ceramic were also fabricated using these molds. Table II shows the properties of these composites processed via SFF techniques.

Composites with various novel architectures were processed via Fused Deposition. A "3-D honeycomb" piezoelectric ceramic/polymer composite structure (3-3 connectivity) was one of them. Molds for 3-D honeycomb structures were fabricated using Stratasys™ 3-D Modeler™.

Fig. 3a shows the optical micrograph of the top view of a typical mold for 3-D honeycomb structure and Fig. 3b shows an SEM micrograph of the sintered ceramic structure prior to epoxy infiltration. The PZT ceramic structure is a honeycomb structure where uniformly spaced holes are connected in all three directions. The holes were created when the sacrificial polymer was evaporated during heat treatment. The volume fraction of the ceramic phase in these structures can be varied by changing the diameter of the holes, the spacing between the holes, or both the hole diameter and spacing. Several 3-D honeycomb composites were fabricated with 10 to 60 volume percent PZT (V_{PZT}). It has been observed that as the volume fraction ceramic increases, both the relative dielectric constant K and the piezoelectric charge coefficient d_{33} increase[10]. Fabrication of 3-3 composites has been reported earlier via the replamine and BURPS processes[11-12]. Measurements of electromechanical properties of 3-D honeycomb structures processed via SFF technique show superior results over conventionally processed composites due to the controlled phase periodicity inherent in these composites.

III b. Piezocomposites Processed via Direct Processing Route

Piezoelectric ceramic/polymer composites with 3-3 ladder structures were processed via direct SFF processing by FDC and their electromechanical properties were characterized. Composites with other shapes and connectivities, such as, c-ring and 2-2 annular structures, were also fabricated via direct FDC. Miyashita et al.[13] first reported the 3-3 ladder connectivity composites made by stacking fired PZT rods. In 3-3 ladder structure, ceramic rods are placed parallel to each other in each layer and perpendicular to each other in every consecutive layers. Fig 4 shows an SEM micrograph of a typical heat treated ceramic ladder structure prepared by the direct FDC method prior to epoxy infiltration. The ladder structures were built by using a raster fill strategy with a fixed inter-road spacing. The consecutive layers were built 90° to one another. Ladder structures with various orientations other than 90° between consecutive layers were also built using this technique. It can be observed that ceramic rods with $\sim 300\ \mu\text{m}$ diameter are uniformly spaced $\sim 250\ \mu\text{m}$ apart. These composites show a significantly improved electromechanical properties compared to the conventionally processed composites. A group of various composites processed via direct and indirect SFF techniques are shown in Fig. 5. At present, piezoelectric actuators, such as, moonie, rainbow structures, are being processed via direct processing routes using PZT powder loaded thermoplastic filaments.

Conclusions

In this work, the solid freeform fabrication (SFF) techniques such as, Fused Deposition (FD) and Sanders Prototype, were used to form a variety of piezoelectric ceramic/polymer composites. The indirect and direct methods were used to process these composites. For the indirect method, molds were made by both SFF techniques and then infiltrated with a PZT ceramic slurry. The structures were dried and heat treated to burn the mold polymer and binder out and sintered in a crucible with excess lead. For the direct FDC method, filaments of PZT powder loaded in a thermoplastic binder were used for direct fabrication of ceramic structures. Structures were heat treated to burn the binder out and sintered. Sintered structures were back

filled with desired acoustic epoxy, cut, polished and poled. Electromechanical properties were evaluated and compared with conventionally processed composites. Composites processed via SFF techniques showed excellent electromechanical properties for transducer applications.

Acknowledgments

The authors would like to thank the Office of Naval Research (ONR) and Defense Advanced Research Project Agency (DARPA) for the financial support under contract numbers N00014-93-1-1059 and N00014-94-C-0115, which made this work possible. The authors would like to thank Dr. Mukesh Agarwala for helpful discussion at various stages and Farhad Mohammadi, Tom McNulty, Pat Teung, Marc Rubin and Kevin Allen, for their technical assistance during processing. The authors would also like to thank Rolf Hubert of Sanders Prototype Inc. for providing us some of the wax molds that was used for 1-3 structures.

References

1. "Ultrasonic Technology Provides Benefits," *Amer. Ceram. Soc. Bull.*, **74**[7], 25 (1995).
2. T. R. Gururaja, *Amer. Ceram. Soc. Bull.*, **73**[5], 50-55 (1994).
3. L. F. Brown, pp. 539-550 in Proc. 1992 IEEE Ultrasonics Symposium. IEEE, Piscataway, NJ, 1992.
4. Newnham, R. E., D. P. Skinner and L. E. Cross, *Mater. Res. Bull.*, **13**, 525, (1978).
5. V. F. Janas and A. Safari, *J. Amer. Cer. Soc.*, **78**[11], 2945 (1995).
6. D. L. Bourell, J. J. Beamen, H. L. Marcus, and J. W. Barlow, "Solid Freeform Fabrication, An Advanced Manufacturing Approach"; pp. 1-7 in Solid Freeform Fabrication Proceedings (Austin, TX, August 1990). Edited by J. J. Beamen, H. L. Marcus, D. L. Bourell, and J. W. Barlow. University of Texas at Austin, 1990.
7. M. K. Agarwala, R. van Weeren, R. Vaidyanathan, A. Bandyopadhyay, G. Carrasquillo, V. Jamalabad, N. Langrana, A. Safari, S. H. Garofalini, S. C. Danforth, J. Burlew, R. Donaldson, P. Whalen, and C. Ballard, in Solid Freeform Fabrication Proceedings (Austin, TX, August 1995). Edited by H. L. Marcus, J. J. Beamen, D. L. Bourell, J. W. Barlow, and R. H. Crawford. University of Texas at Austin, 1995.
8. K. Lubitz, A. Wolff, and G. Preu, *Ferroelectrics*, **133**, 21-26 (1992).
9. R.K. Panda, V.F. Janas, and A. Safari, Submitted to *J. Amer. Ceram. Soc.*, (1996).
10. A. Bandyopadhyay, R. K. Panda, V. F. Janas, M. K. Agarwala, S. C. Danforth and A. Safari, submitted to the *J. Amer. Cer. Soc.*, June 1996.
11. D. P. Skinner, R. E. Newnham, and L. E. Cross, *Mat. Res. Bull.* **13**, 599-607 (1978).
12. T. Shrout, T., W. A. Schulze, and J. V. Biggers, *Mat. Res. Bull.* **14**, 1553-1559 (1979).
13. M. Miyashita, K. Takano, and T. Toda, *Ferroelectrics* **28**, 397-400 (1980).

Table I : Methods for making piezoelectric ceramic/polymer composites. [5]

Processing Technique	Connectivity	Scale (μm)	Key Limitations
Pick and Place	1-3	>100	Slow, Breakage
Dice and Fill	2-2, 1-3	>50	Single Phase, Area
Injection Molding	2-2, 1-3, 3-1	>40	Mold Cost
Tape Lamination	2-2, 1-3	>20	Flatness
Fiber Processing	1-3, 2-3, 3-3	>20	Fiber Strength
Lost Mold	2-2, 1-3, 3-1	>50	Mold Cost
Moonie	3-0	--	Mass Production
Solid Freeform Fabrication	1-3, 2-2, 3-3	>50	Mass Production

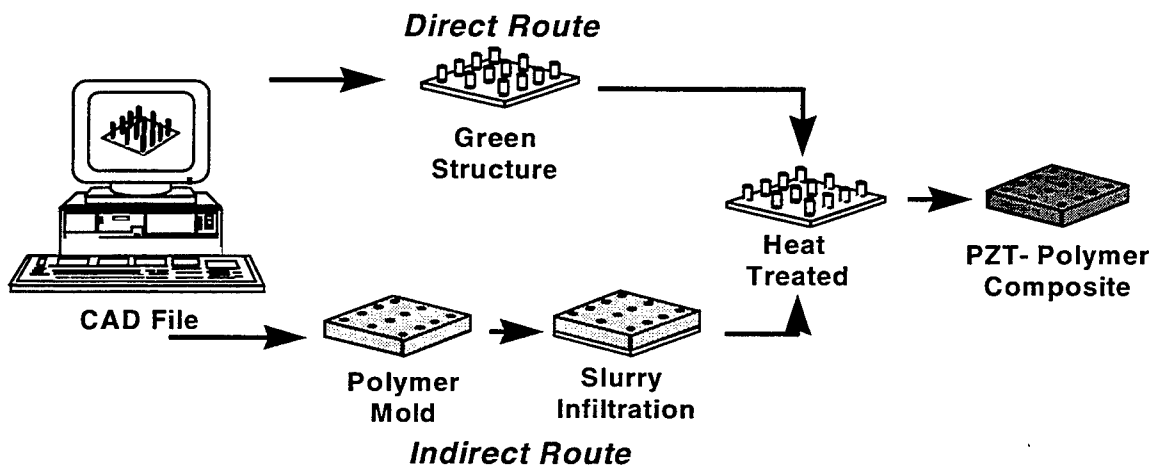


Fig. 1: Schematic of PZT/polymer composite fabrication steps using direct and indirect SFF techniques.

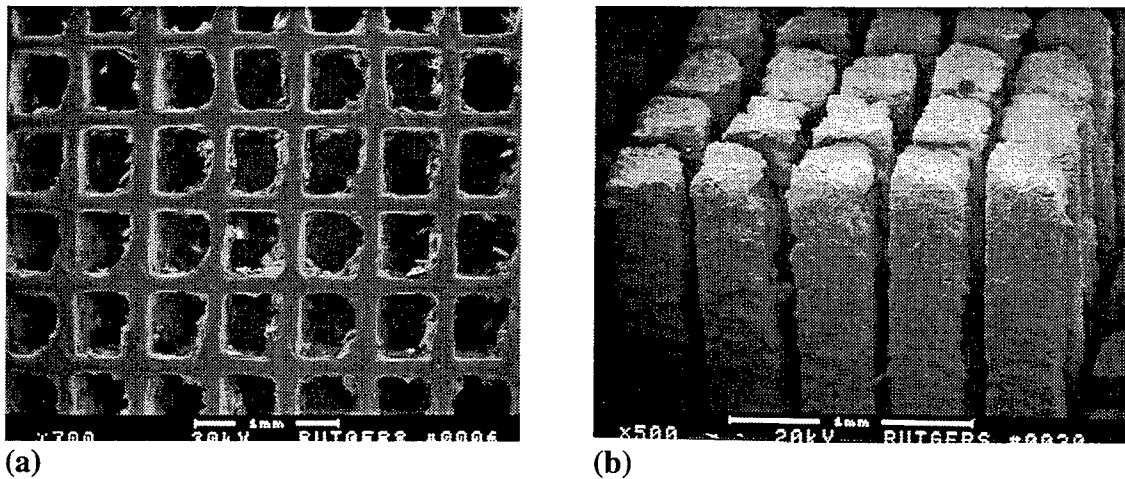
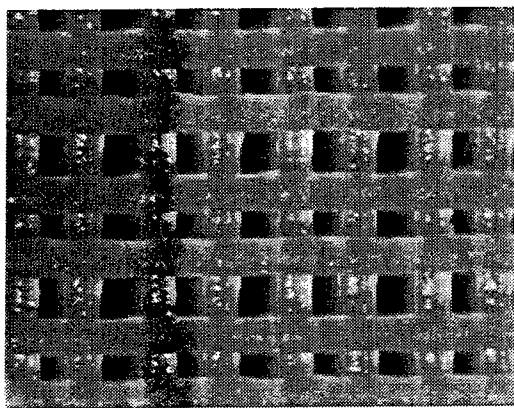


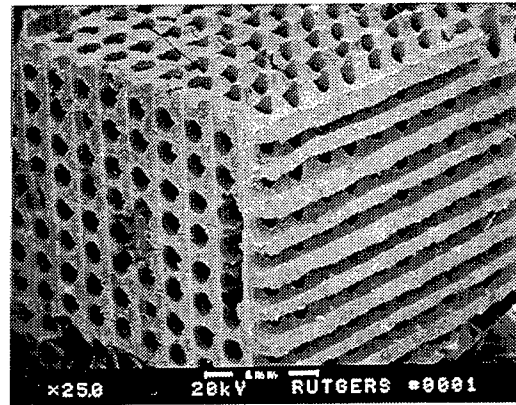
Fig 2 : (a) SEM micrograph showing a top view of a polymer mold fabricated by the Sanders Prototype.
(b) A 1-3 sintered ceramic structure obtained from these molds.

Table II : Electromechanical properties of piezoelectric composites processed via SFF and conventional techniques.

Composite Type	V_{PZT} (%)	Ceramic Width(μm)	Polymer Width(μm)	K	d_{33} (pC/N)	k_t (%)	k_p (%)
3-D Honeycomb	28	120	320	320	290	45	25
Ladder	70	300	200	1300	290	50	30
Ladder Angular (15°)	60	250	200	1540	370	60	23
Sanders 1-3	48	300	80	970	280	66	28



(a) 500 μm



(b)

Fig 3 : (a) Optical photograph showing a top view of polymer mold made by FDMTM.
(b) SEM micrograph of a sintered 3-D honeycomb structure obtained from these molds.

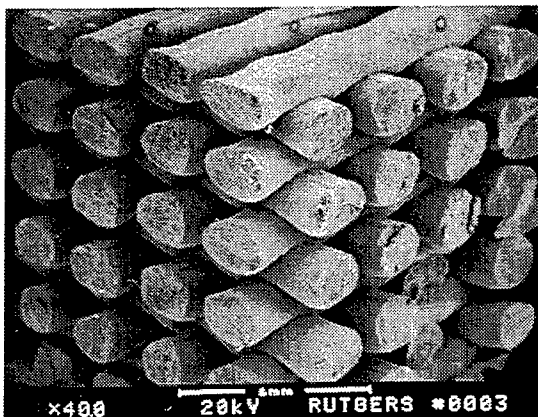


Fig 4 : SEM micrograph of a 3-3 ladder structure of sintered PZT ceramic.

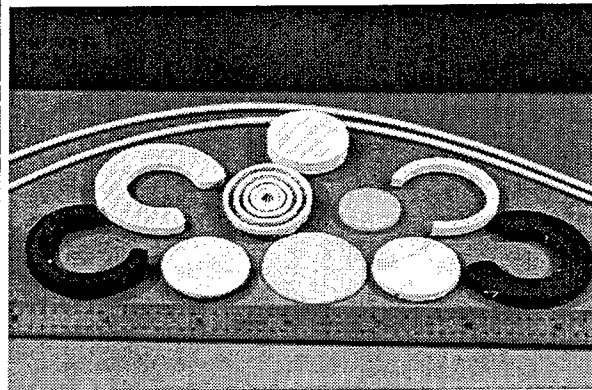


Fig. 5 : Photograph of polymer molds and PZT ceramic parts made by SFF technique.

“Curved-Layer” Laminated Object Manufacturing[®]

Gary Kalmanovich
Helisys[™] Inc.

Abstract

A process where a freeform solid object is built by bonding cut layers of material together is called a Laminated Object Manufacturing process. Until today, all of the LOM processes utilized straight forward planar cross-sections of the intended object for manufacturing. The “Curved-Layer” project’s objective is to perform the LOM manufacturing process on a non-planar cross-section. Thus, the layers are going to be bonded together as non-planar surfaces providing additional strength to the built part as well as expedition of the built time for many objects. This project entails both software and hardware development for the implementation of the manufacturing process.

1. Introduction

Laminated Object Manufacturing (LOM[™]) is a process where a solid freeform object is manufactured with lamination of cut layers of sheet material. Until today all of the (LOM) processes have been implemented using straight forward lamination of material cut flatly based on planar cross-sections. The “Curved-Layer” project’s objective is to perform the LOM manufacturing process on a “curved,” non-planar, cross-section. This is especially useful for thin, non-flat parts. This project entails numerous approaches and techniques that are not currently available commercially. Consequently, an innovative effort is required to perform a build of an LOM part on a non-planar surface. A substantial modification of the conventional (planar) LOM process is necessary in both software and hardware.

2. Planar LOM Process

The planar process for laminated object manufacturing has been utilized by Helisys Inc. for rapid prototyping for some time. The most basic description of the process can be provided using a cutting and bonding cycle, see Figure 1. It is important to outline the main stages of the current process in order to better understand what needs to be done for the “Curved-Layer” project.

a) In the implementation of the current machine, the cutting is performed using a plotter system that transports a mirror and a focusing lens over the x-y envelope of a flat cross-section of the part corresponding to the [$z = \text{current height}$] plane. Everything, including the focusing lens, is fixed on the x-y plotting mechanism because the flat-layer is always parallel to the plotter’s operational plane.

b) Once a layer is cut, a new, virgin layer is bonded on top by a heater-roller. Note, the material has heat sensitive adhesive on the bottom side. The heater roller is flat in the y direction and is designed to apply equal pressure and temperature to the part as it rolls over it.

[®] Laminated object manufacturing is a registered trademark of Helisys Inc. Torrance, CA

^{*} This work was sponsored in part by a grant from DARPA.

[™] LOM and Helisys are trademarks used by Helisys Inc. Torrance, CA

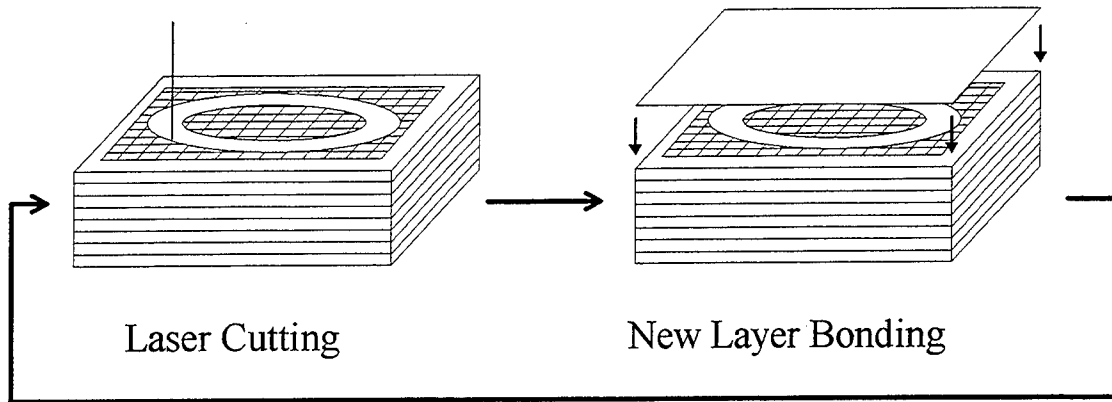


Figure 1 Planar LOM process

c) After bonding, the height of the part is measured and a new cross-section is computed by intersecting the part (.STL) file and the [$z = \text{current height}$] plane. After all the segments defined by the intersection of part facets with the height plane are identified, processing such as ordering, cross-hatching, beam-offset, among others are performed.

d) When the necessary calculations are completed, the new material is cut, thus returning to the beginning of the cycle, i.e., return to a).

The current planar LOM process is composed of components that in their design are inherently planar. The laser cutting, due to variable distance; the new layer bonding mechanism; the dependence on the part height measurement, because of reliance on part flatness; the planar cross-section, among all of the other 2D software components; and all the other LOM elements need to be rethought.

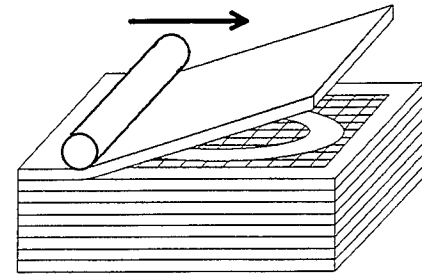


Figure 2 Roller bonding

3. "Curved-Layer" LOM Process

The "Curved-Layer," non-planar LOM process in its concept is almost identical to the regular, planar LOM process, i.e., compare Figure 3 to Figure 1. However, the two processes have to be

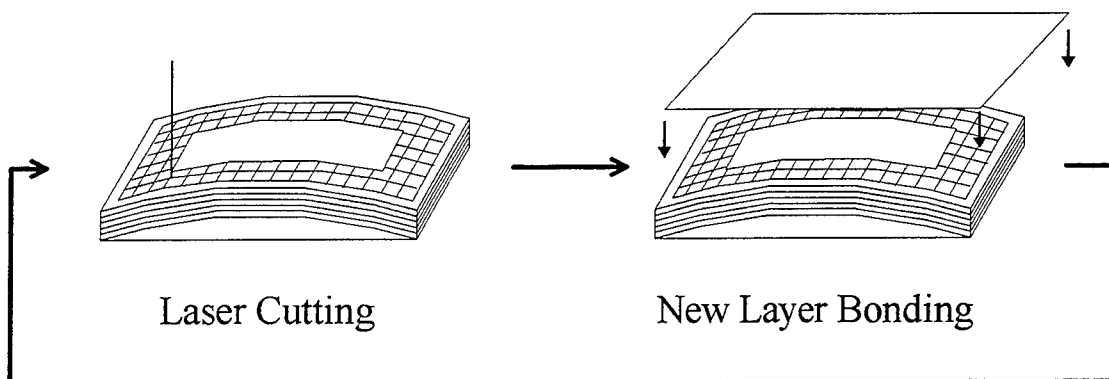


Figure 3 "Curved-Layer" LOM process

very different in their implementations. In this section, the relevant differences and their implications for both hardware and software are discussed.

3.1 Non-Planar Base

The planar LOM process uses a base constructed by adding flat layers of material to the metal platform. Afterwards, the part build cycle is begun on top of the base. The first major difference that the non-planar LOM process requires is the capability to form a base for the "Curved-Layer" build, see Figure 4. This is actually an intricate problem in itself. Many circumstances such as

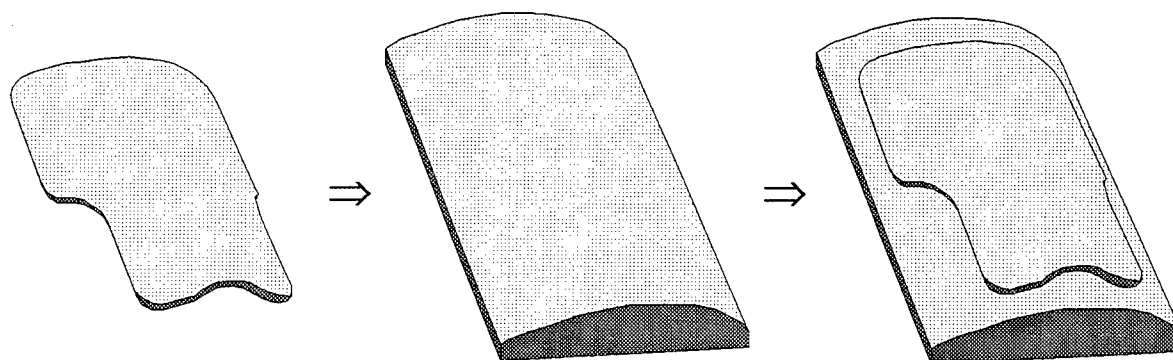


Figure 4 "Curved-Layer" base

holes in the original object, high slopes, and etc. may prevent the implementation of a non-planar part build because their presence in the base might interfere with the possibility of adding new layers of material. Therefore, such circumstances need to be eliminated in base creation itself. Thus, the software for such base generation needs to have intelligence to identify and address such features. Currently, the software developed uses some coarse heuristic approaches to remove the undesired extrusions, etc. However, this method is not foolproof, though we have been able to create satisfactory bases for most object files we tried.

Another new issue that exhibits itself is the base alignment issue. Right now, we create the base by having the software construct a .STL file for this base and consequently building the base from the .STL file using the conventional, planar, LOM process. Because the base is created separately, prior to the non-planar build of the part, the base needs to be placed in perfect alignment with where the computer's representation for the base perceives it to be. At this point, we do not think it to be practical to add new and very involved complexities of designing a closed loop system for automatic alignment. However, a manual procedure needs to be worked out for performing this task.

3.2 Non-Planar Cross-Section

In order to identify the path required to cut on the recently bonded layer of material, we need to intersect the "Curved-Layer" with the object, i.e., identify the segments that constitute the intersection of the two, see Figure 5.

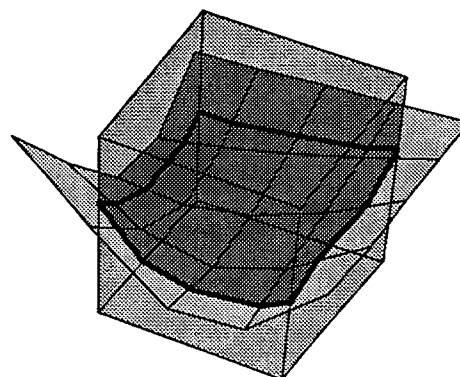


Figure 5 A "Curved-Layer" intersecting an object (cube)

The mathematical “Curved-Layer” representation, in turn, needs to be a very accurate depiction of the actual top layer freeform. For planar layers the height measurement is taken after every new layer is laminated. Unfortunately, for non-planar layers there is a different height at every point. Thus, either a closed loop system is needed to measure a layer’s profile at every layer, where we will gauge the height at every point on the layer, or this can be accomplished with a very accurate open loop system, where the height at every point will be approximated with a mathematical model as the part grows. Just as the case with alignment, because a measurement system would bring in considerable extra complexity and become a major detraction from the actual problem at hand and because if needed this feature it can be added later, we decided to proceed with an open loop approach at this time.

3.2.1 Height grid representation

We looked at a number of candidates for the model to represent the non-planar layer. After appreciable consideration we decided to use a height grid system. In this system, we divide the xy-plane into an evenly spaced grid and store the height (z) values as elements of this grid, see Figure 6. This approach has the advantage of being much more elementary than most of the other models. Also, by using this model, the update and initial values for the non-planar layer are more fundamental and can be obtained using more tangible methods.

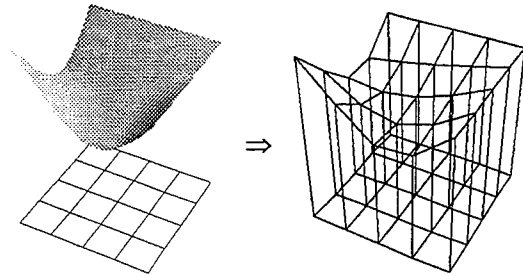


Figure 6 Height grid representation

3.2.2 Initial values

The initial values for the heights are first obtained by intersecting the triangles at the bottom of the object’s .STL file with the vertical lines originating at the bottom of the grid, see Figure 6. Then, “foreign” values for the heights are filtered out using the same heuristic approaches that are used for the generation of the non-planar base generation. Note, this filter and the filter used for base generation are to have the same parameters in order to obtain an exact correspondence between the top layer of the base and the representation for the first layer.

3.2.3 Update

After a new successive layer has been added above the previous one, a new “Curved-Layer” representation needs to be obtained. This new layer is not a perfect replica of the old layer. Though, it should be a “smoothened” version of the previous layer, see Figure

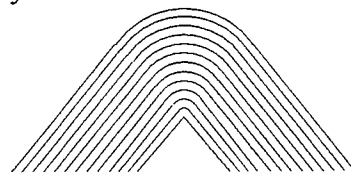


Figure 7 Part growth

7. Because we have no way to measure these new heights, an open loop method was developed to approximate the new, updated grid heights for this new layer. The approach chosen for this case consists of taking a point from the previous grid along with four of the original surrounding points on that grid; constructing four triangles originating from our desired point; lifting each of the triangles by the material thickness in the direction of their respective normal vectors; fitting a curved surface tangent in desired places to the four offset triangles (a third degree polynomial is used); and finally taking the z-height value on that polynomial at the desired location in the xy-plane, see Figure 8.

This approach for updating the layer representation due to an addition of an extra layer has advantages over other methods we considered because, this method can model the smoothing that results after successive addition of layers. It also is superior to a 3D triangle based format of modeling curved layers, because this method does not grow in complexity. For this method, with each successive layer, the fineness of the grid remains exactly the same and thus the computational complexity is not increased, unlike most of the other methods we considered for which the complexity tends to grow by a factor with every layer. Moreover, in simple tests this method seems to perform very well in modeling the build growth even after a few hundred layers.

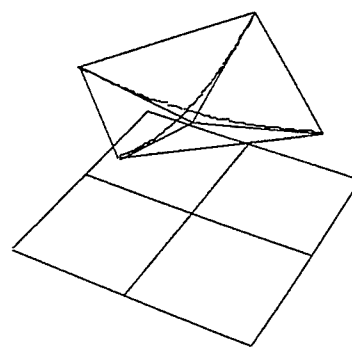


Figure 8 New layer model

3.2.4 A non-planar cross-sectional cut

An intersection between a non-planar layer and the object representation constitutes a non-planar cross-section, i.e., an object's periphery along which we would need to cut, see Figure 5. This intersection consists of segments that correspond to facet intersections, see Figure 9.

At times, the facet intersections lead to hard to handle, degenerate cases of triangle intersections, see Figure 9(c,d). These occurrences are numerically very unstable and lead to problems with extra and missing segments. Though for planar cross-sections, these cases are extremely rare and they can be avoided in a vast majority of occurrences, unfortunately for non-planar case, this is much more likely to occur and not as easy to avoid. This has a potential to be a major problem for certain parts.

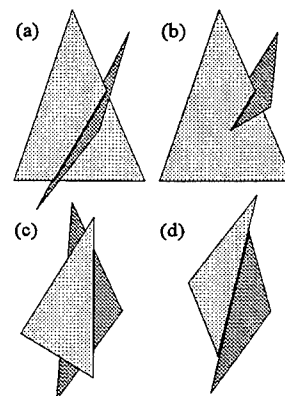


Figure 9 Facet intersections

3.2.5 Generalization of segment handling to 3D

The current LOM software for the planar process contains many routines for handling and utilizing the collections of segments in two dimensions, i.e., sorting, rearranging, beam offset, cross-hatching, etc. Most of these routines are just as much an absolute necessity for curved slicing as they are for planar slicing, e.g., arrangement of segments into continuous loops. Others, such as crosshatching are also very important. And finally, features such as the beam offset (to account for the thickness of the beam) are desirable and come with very little cost, assuming the other components are incorporated.

We have extended the segment handling capability of the planar LOM software to 3D almost entirely, see Figure 10.

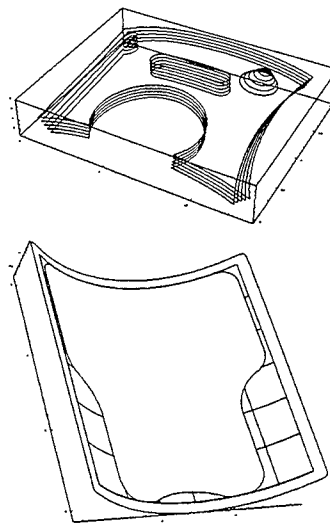


Figure 10 Segment handling

3.3 Non-Planar Cutting (Focusing)

As mentioned earlier, the distance from the focusing lens to the cutting surface varies for “curved layer” cutting. Because the plotter transporting the focusing lens is a 2D device and the surface is no longer flat, the cutting surface will be out of focus if the cutting is done in the conventional, planar manner. This is another major difference between the two processes that need to be addressed.

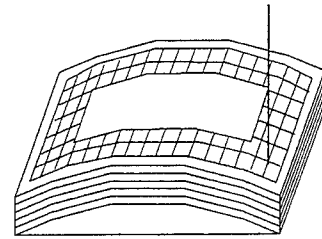


Figure 11 Non-planar cutting

3.3.1 Platform compensation

One approach to keep the laser constantly in focus is to move the platform supporting the part to compensate for the variability in height. This approach, in concept, does not require any hardware changes. Unfortunately, in practicality, this is not true because the currently used motion control boards, as well as most motion control boards on the market, do not support circular arc motion in 3D. However, it is possible to implement the current motion using the current hardware if we stop the cutting motion every once in a while in order to adjust the height, see Figure 12. Nonetheless, this method is not the most practical because the motions of the platform are slow and are not always smooth. Moreover, the jitters resulting from platform motion can interfere with cutting. Redesign of the platform system is costly, time consuming, and does not guarantee a satisfactory result.

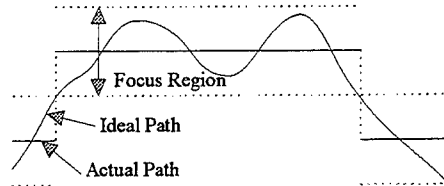


Figure 12 Platform compensation

3.3.2 Large focal distance lens

Another method, to compensate for the variable part height, we are considering is to increase the focal distance of the lens, i.e., the focus region is extended by using a lens that focuses the beam further from itself, see Figure 13. The drawback of this approach is that the width of the beam at the focus spot is not as tight as it is with the original lens. As a result, it is not certain that we will be able to cut the material with this new lens. At this time, we are making the necessary hardware changes (to the lens housing, etc.) in order to try to cut with it at real time speeds.

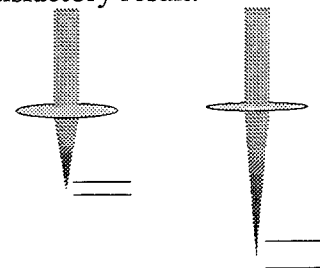


Figure 13 Large focal distance lens

3.3.3 Controlled focal distance

Finally, the last method we are exploiting for this problem is the possibility of moving the focusing lens up and down so that the laser is kept in focus on the cutting surface. If the other methods are found not satisfactory then this method will be developed fully. The only drawback of this method is that the added weight of the focusing system will effect the balance of the plotter. Thus, the plotter might have to be modified.

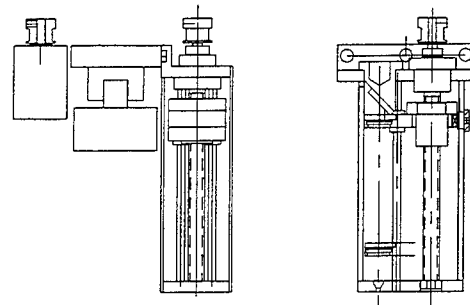


Figure 14 Controlled focal distance

Of the three, this method is the most general with the fewest drawbacks, though it is the hardest to implement because it requires a mechanical, an electronic, and a software redesign effort.

3.4 Non-Planar Bonding

The bonding issue is of most concern to us and is the issue that seems to be the least open to workable solutions. It is not completely apparent how one is to deliver both heat and pressure uniformly to a loose sheet of material on a surface of a non-flat object so as to achieve smooth bonding with no ripples. Many approaches have been considered and rejected due to one drawback or another. We are still considering a few approaches, but are in the design stages for only one, though it too has many drawbacks.

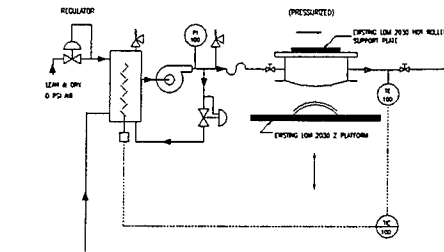


Figure 15 Bladder bonding

We are building a hot rubber bladder bonding mechanism. The bladder is to be filled and pressurized with circulating hot air. The rubber surface (siliconized rubber, so it can withstand high temperatures) comes in contact with the part by raising the part on the platform into the bladder. A previous non-pressurized prototype has produced some favorable results.

3.5 Sheet Feeding

Because often it is much more accommodating to produce many materials in sheets as opposed to rolls, especially the materials we are considering for "Curved-Layer" building, the idea of a sheet feeder for the material is being considered. (Thus far the LOM process has only been implemented with rolls of LOM material.) However, the mechanical design of such a mechanism would require an almost exact knowledge of many characteristics of the material in question. Thus far, the materials to be utilized are only being developed. Such characteristics as stiffness, texture, lamination to the stack, and etc. are still not known. Moreover, if the material is too brittle, not stiff enough, or sticks to the stack too much, it might not be possible to implement a sheet feeding mechanism at all.

4. Summary

The "Curved-Layer" project to modify the LOM process from planar to non-planar build necessitates a substantial design effort. Many issues such as mechanical, electrical and software need to be addressed. In this paper we discussed our progress on many of these issues and what our concerns at this point in time are. Major components of the software effort have either been implemented or are in the implementation stages. Though, some new software components will be necessary when certain hardware designs are finalized. Also, the hardware components still necessitate a substantial effort in their design and implementation. We are going into uninvestigated territory and experimentation is needed before a final satisfactory product can be formed.

Automating Sheet-Based Fabrication: The Conveyed-Adherent™ Process

Prof. Charles L. Thomas, Department of Mechanical Engineering, The University of Utah
3209 Merrill Engineering Building, Salt Lake City, Utah 84112
(801) 585-6939, fax: (801) 581-8692, e-mail: CThomas@ME.Mech.Utah.edu

Kenneth J. Hayworth, Engineer, Ennex Fabrication Technologies
10911 Weyburn Avenue, Suite 332, Los Angeles, California 90024
(310) 824-8700, fax: (310) 824-5185, e-mail: KenH@Ennex.com

Copyright © 1996, Ennex Corp.

Abstract

A new automated fabrication technology is described which breaks the fabrication process into spatially separate layer-formation and layer-bonding stages. The technique uses sheet material on a substrate as feedstock and cuts cross-section contours into the material before conveying the material on the substrate to a stacking station. Advantages include (a) speed, (b) versatility in fabrication materials, and (c) ability to fabricate hollows, embed or cast secondary materials, and selectively enhance or degrade material properties on a regional basis.

A prototype fabricator has been built which automates all aspects of this process except weeding. Applications demonstrated using this machine include traditional rapid prototyping and visualization-model creation as well as functional machines taking advantage of embedding and cast-in-place techniques.

I. Introduction

The current commercial paradigm for automated fabrication (autofab) encompasses layered fabrication of plastic, paper, metal, or ceramic objects. The paradigm consists of decomposition of a 3-D object into 2-D cross sections and sequential construction of each cross section in a "form in place" strategy. In a form-in-place technique, successive layers are bonded to the previous layer as they are formed. Each of the devices available for doing this has unique advantages and disadvantages which allow several commercial systems to compete successfully with no single system dominating all applications.

This specialization is clearly demonstrated by comparing the Sanders thermoplastic droplet deposition process to the laser cut paper layering process of Helisys. The Sanders machine can produce layers as thin as 0.0004 inches which allows objects to be constructed with surfaces where the 3-D aliasing (or stair step effect) is greatly reduced. This process is excellent for producing small models of jewelry or similar items. The Helisys machine would have a difficult time producing these objects, and would require hand finishing to achieve a smooth surface finish. However, the Helisys machine is capable of producing models up to 32" by 22" by 20" in a single build. The Helisys device is capable of building a model significantly faster than the Sanders machine[1]. Since the Helisys device only needs to laser-cut the edges of each cross section to create each layer, the process is very efficient for large heavy-bodied objects, but not as useful for thin-walled structures.

To date, the prototyped objects are primarily considered models since their material properties and construction accuracy do not generally meet the capabilities of the intended production system[2,3]. In addition, while the construction speed varies from device to device, the current commercial systems typically cannot build at a rate much higher than 20 cubic inches per hour. The machine manufacturers recognize these limitations and are

introducing solutions to the problems. Many of the commercial systems are introducing techniques for producing patterns for investment casting or direct production of tooling for injection molding. Achievable tolerances remain in the range of 5 to 10 thousandths, however, which limits the use of these models in fine tolerance applications. 3D Systems has recently introduced a thermoplastic droplet deposition device that is an attempt to address the build speed issue. Their Actua™ device is reported to be less accurate than their stereolithography machine, but faster.

In order to further address these problems, researchers are attempting to provide a larger variety of construction materials. They are attempting to work with metals and other traditional engineering materials[4,5,6]; they are attempting to work with multiple materials simultaneously[4,6]; and they are developing much faster processes aimed at production of large objects[7].

II. Form-then-Bond Fabrication

The work discussed in this paper is an attempt to improve the speed and flexibility of autofab processes by stepping outside the form-in-place paradigm to a “form-then-bond” technique. In this approach, layers of an object are first formed, and then registered and bonded together as separate operations. This change in paradigm produces devices that behave differently than the existing systems, with these differences resulting in both advantages and disadvantages. Physical realization of this process has been shown to be quite inexpensive.

An inexpensive manual system based on the form-then-bond approach has given an indication of its potential. JP System 5 Desk Top Rapid Prototyping offered by Schroff Development Corp. of Mission, Kansas, employs an off-the-shelf cutting plotter along with custom modeling and slice generation software to create cross sections from sheet materials with a pressure-sensitive adhesive backing. The sheets are manually weeded of excess material and stacked after cutting. Although weeding and stacking each sheet can be tedious, construction of many objects can often proceed quite rapidly. A similar system was briefly offered several years ago by the Swedish company, Sparx AB. Case Western University and CAM-LEM Inc. have proposed an automated form-then-bond process with sheet handling performed by a robotic system.

Automating a form-then-bond process produces added potential for improved build speed. The form-in-place paradigm requires that each layer be bonded and formed sequentially, in close succession. In a form-then-bond technique this is not required. It is not even necessary to perform both operations on the same machine. One of the anticipated implementations of this device includes one or more cutters that produce sheets ready for stacking, and one or more stacking devices that are fed a collated stack of construction sheets and produce the registered and bonded object. Using this arrangement, the two processes don't have to wait on each other. If the stacker is faster than the cutter, one stacker could service several cutters, etc.

This potential for build speed increase can be investigated by expressing the build time for a fabrication process in a general equation:

$$T_{build} = T_{pre} + \sum_{i=1}^n T_{layer(i)} + T_{post}$$

where T_{pre} is preprocessing time, $T_{layer(i)}$ is the creation time for the i th layer, and T_{post} is the post-processing time. While the details of what goes on during the pre- and post-processing times vary from process to process, we will focus here on the variation in T_{layer} . The form this term of the equation takes depends on the specific technique used to create the layers of the object. We discuss here two overlapping classification schemes: 1) location of formation (form-in-place and form-then-bond) and 2) formation technique (volume building, periphery cutting, and 2-D mask). Only periphery cutting is today represented both in form-in-place devices, in which case it is called a “stack-first” process, or as a form-then-bond, “cut-first,” process. For example stereolithography is a form-in-place volume-building technique that creates a cross section by sequential curing voxel by voxel; Laminated Object Manufacturing is a form-in-place periphery-cutting (stack-first) process; Cubital's Solid Ground Curing is a form-in-place 2-D mask

process; and the JP5 (as well as the Conveyed-Adherent device discussed later in this paper) use a form-then-bond periphery-cutting (cut-first) process. Each layer creation scheme has a unique equation for calculating $T_{layer(i)}$, as shown in Table 1.

Location of Formation	Formation Technique	Examples	Layer-creation time
Form in place	Volume building	SLA, SLS, FDM	$T_{layer(i)} = T_r + \frac{A_i}{dv}$
	Stack first	LOM	$T_{layer(i)} = T_r + \frac{C_i}{v}$
	2D mask	Solider (Cubital)	$T_{layer} = T_r + T_c$
Form then bond	Cut first	JP5, Conveyed-Adherent	$T_{layer(i)} = \max\left\{\frac{C_i}{v}, T_r\right\}$

Table 1 Layer-creation time in various fabrication processes. In the equations, T_r represents the delay time between active geometry creation for each layer (e.g., recoating time for stereolithography or layer bonding time for LOM), A_i is the area of the i th cross section, C_i is the i th cut length, v is the cutting or laser-scanning velocity, d is the width of the line created by a volume-building process, and T_c is the cure time in a 2-D mask process. The second term on the right-hand side of each equation represents the time required for active geometry creation. Note that for a form-then-bond process the active geometry creation and the delay time (in this case layer registration and bonding) occur in parallel.

Using the equations in Table 1 with constants selected for convenience (not exactly corresponding to any real process), the qualitative behavior of the different process classes can be investigated. The build speed as a function of geometric complexity (e.g., thin walled vs. thick walled) is investigated in Fig. 1 using a simple cube that is hollowed into a rectangular tube. The geometry is varied by changing the wall thickness of the tube, and the complexity is varied by adding multiple copies to the build volume. For this geometry the area of each layer is $A = l_o^2 - l_i^2$, and the periphery length to be cut is $C = 4l_o + 4l_i$. Note that the build time increases for a volume-building process as the wall thickness increases, while the build time decreases for a periphery-cutting process (since the total

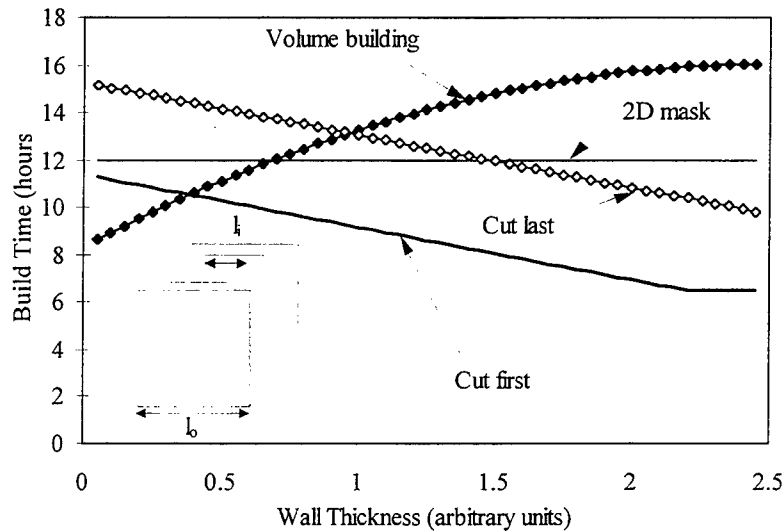


Fig. 1 An example of how build time for the several types of fabrication processes can vary with respect to the geometry being formed.

cut length decreases with increasing wall thickness in this example). The 2-D mask process is independent of the wall thickness. The build time for the cut-first (form-then-bond periphery cutting) process is shifted downward since the cutting and stacking processes run in parallel. Note that the build time becomes independent of wall thickness when the periphery cutting time drops below the register and stack time.

III. Automating Form-then-Bond Fabrication

Ennex Fabrication Technologies has automated form-then-bond fabrication with the development of the Conveyed-Adherent™ process. This jump to full automation solves the difficulties of sheet handling and stacking and potentially provides significantly improved speed and convenience. Automation is achieved by the use of a substrate to carry each formed layer in succession to be stacked and bonded to the previous layers. This technique has the potential to address many concerns in the fabricator market and to open up new markets previously not in reach because of price. A schematic of the process is shown in Fig. 2.

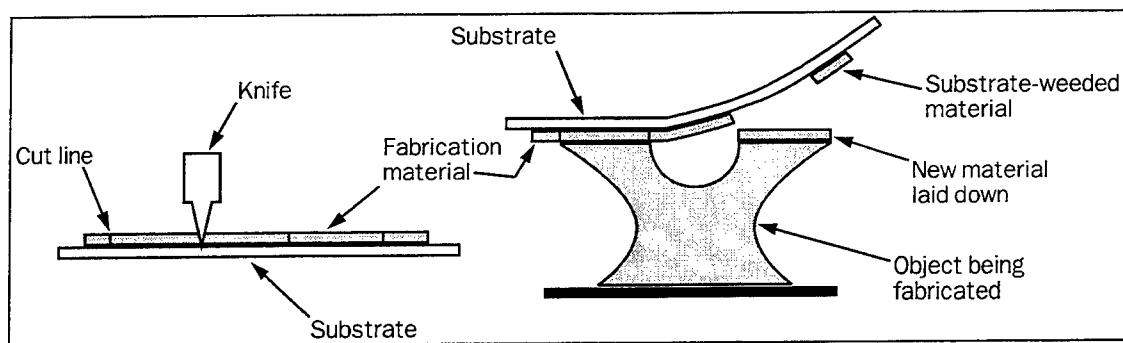


Fig. 2 The two stages of the Conveyed-Adherent™ process, layer formation on the left and layer bonding on the right.

Process Overview

The basic construction material required by the Conveyed-Adherent process is any sheet material which can be cut and bonded to itself, along with a release liner or backing paper referred to here as the substrate. A 2-D plotting device is used to cut the outlines of cross sections of the desired object into the sheet material without cutting through the substrate. In addition to the outline contours, the plotter can also cut parting lines and outlines for support structures. When required, the sheet is then “weeded” to remove some or all of the negative material. Finally the material is inverted so that the substrate is facing up and the material is brought into contact with the top of the growing object, and bonded to it. The substrate is then peeled off to reveal the new layer just added and a fresh surface ready to bond to the next layer. The process is started by applying an initial layer of adhesive on a stacking platform.

The Prototype Genie™ Fabricator

The Conveyed-Adherent process has been implemented in the laboratory of Ennex Fabrication Technologies in a working prototype called the Genie fabricator, named for the mythical creature in Arab literature which could grant its owner any object desired. A picture of the machine, with a model of an automobile it has built placed in its build area, is shown in Fig. 3.

The prototype Genie fabricator operates automatically, except for weeding, with processing monitored by a variety of sensors. Material jams and other machine faults are detected by sensors for limits of travel and arrival of material at each station.

The prototype Genie fabricator has built several objects, including various geometrical and automotive models in several colors. The models are attractive, although they suffer from problems due to registration errors and curl caused by internal stresses arising in the process. Research is underway to eliminate these problems and improve the quality of output of the fabricator. An example object made is shown in Fig. 4.

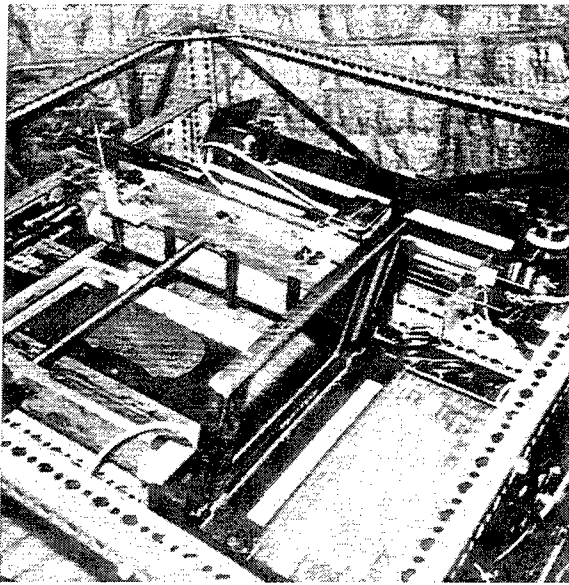


Fig. 3. The prototype Genie™ fabricator in the laboratory of Ennex Fabrication Technologies.

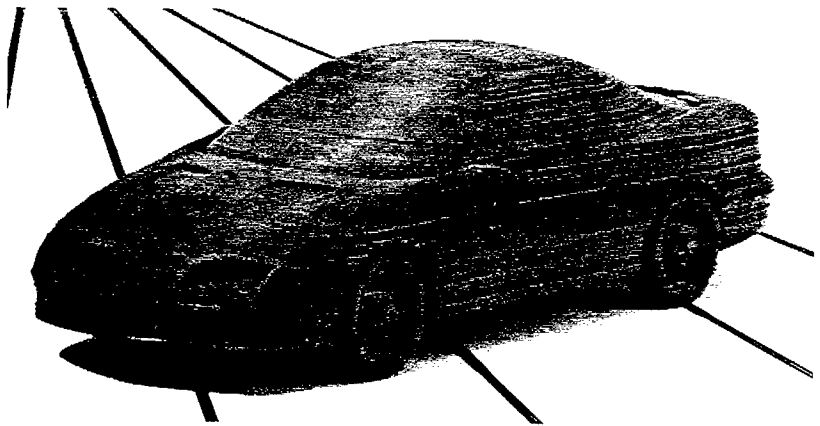


Fig. 4. Automobile model built on the prototype Genie fabricator at Ennex Fabrication Technologies. The car measures $9\frac{1}{2}$ by $3\frac{3}{4}$ inches by 3 inches high. (Model data courtesy Viewpoint Datalabs International)

Materials

Many materials have been tested in the process, including label paper, adhesive-backed foam material, and sign maker's vinyl. Objects made from vinyl or paper are somewhat flexible due to the flowability of their pressure-sensitive adhesive. The paper material can be made more rigid by coating with epoxy or glue. The foam material is used to build patterns for investment casting, resulting in metal objects. Ceramic and metal tapes for the process are under development by Lone Peak Engineering. Potentially any material can be used that can be produced as a sheet, cut by a knife, and undergo some form of bonding from layer to layer.

Plotting

Layer cross sections are cut using a cutting plotter designed for the sign making industry. These plotters are capable of high dimensional accuracy with knife speeds up to 30 inches per second. Cutting plotters accept sheets of various widths up to over a meter wide and the vertical plotters, as opposed to bed plotters, have no limitation to length of sheet since the material is pulled back and forth through the machine. These machines can cut a wide variety of materials including the ceramic and metal tapes mentioned above, as well as very thin (less than a

thousandth on an inch) and thick (up to .035 inch and more) materials. The knives for these plotters include high precision blades as well as cryogenically treated metal blades to increase knife lifetime. A plotter is available which has a knife along with a color ink-jet printer. This would allow color to be incorporated into the material by a process proposed by Kinsie [8]. In the prototype Genie fabricator, plotting is performed by a CAMM I cutting plotter made by Roland Digital Group.

Weeding

Weeding is the term used in the sign making industry for the process of removing the unwanted material around the letters and graphics coming from a sign plotter. To our knowledge there are no mechanical weeders available that can handle weeding of general complex shapes. These complex weeding operations are currently performed manually using tweezers and a good eye.

A mechanical weeder allows one to overcome some of the limitations of stack-first technology. The stack-first process, in its current realizations, has no means of removing negative material during a build and hence produces output of a solid block of material. This requires that the negative material complementary to the object be "diced" by a cross-hatched pattern of parting lines, which add considerably to the process time. After fabrication, the negative material is chiseled away to reveal the finished object. Thus, in the stack-first process, enclosed voids cannot be made, as well as embedded macro-composite structures and colored objects.

The engineering of a weeder, like the engineering of so many successful artificial intelligence programs, must use tricks and overt constraints to solve a less general problem. Some of the constraints are obvious, such as that the sheet is held down so as to remain a 2-D problem, and extra cuts can be provided to reduce difficult-to-weed shapes into smaller, simpler shapes. Some "tricks" that can be used to reduce the amount of mechanical weeding necessary are discussed below.

One trick to reduce the load on the weeder is to realize that most of the negative material can be dealt with using a few well-placed parting lines, so that the object can be easily broken out of its block-like enclosure by a simple turn of the wrist. The use of flexible materials makes this post-processing step particularly simple when compared to processes producing rigid final objects. A weeder is needed only in small regions of the object like enclosed voids or close approximations thereof. Therefore the weeder may be operating on only a fraction of the layers of an object and may be weeding only a small fraction of the negative space even on those layers.

Another trick, called substrate weeding, has the potential to drastically reduce the work load of the weeder. Each successive layer of material containing the cross section of the desired object as well as its negative material is pressed on top of the growing object. If there is a void space below a section of the negative space (i.e. the last layer was successfully weeded) this section will have nothing to adhere to. It will remain on the substrate and be tossed out with it. Thus, in principle, all that is needed to prevent growth of one of the problem negative regions is to weed its first layer. All subsequent sections will find no section below them to adhere to.

The actual practice of this powerful technique is not as simple as the above description may imply. There are several factors that limit the ease with which substrate weeding can be used. One factor is overlap of negative material onto positive material. If a negative region grows larger with the height of the object, the section of negative material on any given layer will find at least a small ledge below it on which to adhere. The degree to which this causes a problem depends on how large the ledge is and on the relative strength of adhesion to the fabrication material and to the substrate. Another factor is cross-boundary linking. Unlike a laser, a knife does not remove material when it makes a cut and the cut material has a tendency to self-heal. The linkage between already-cut sections within a layer is relatively weak, but can overpower lay-down adhesion for a small region whose cut periphery is large compared to its area.

The prototype Genie fabricator does not have a mechanical weeder. Layers that require weeding are handled by a special diverter that routes material to a station where it can be weeded manually. Due to substrate weeding, the number of layers on which this must be performed is small.

Lay-Down, and Peel-Off

The cut and weeded sheet is fed to a lay-down platen. The platen aligns the new sheet with the growing object and applies the pressure needed to bond the layers. Several designs are possible, including the simple roller used in the Genie fabricator, as well as arc-sections of rollers with much gentler slopes. A roller platen may approach the stack from the side or it may "land" on the stack from above. One problem that can occur is the formation of bubbles, trapped pockets of air, between the layers. Research at Ennex Fabrication has investigated the effect of various platen configurations on bubble formation and other relevant issues.

After the material is laid down, the substrate must then be peeled off. For substrate weeding to occur there are two competing forces which must be balanced against each other. As described in the weeding section, one force is the adherence of the material to the last layer, and the other force is the adherence of the material to the substrate. The process must ensure that no positive material is carried away by accident and that no negative material needing weeding is accidentally laid down. For instance, a small radius-of-curvature peel-off device will tend to favor leaving negative material.

The prototype Genie fabricator uses a simplified design in which a single roller performs lay-down and peel-off simultaneously. The roller lays down the material on its leading edge and peels off the substrate at its trailing edge. The substrate, along with any substrate-weeded sections of the layer, are automatically dropped at the far end of the roller's travel. The roller "lands" on the stack by the raising of the stack under the control of a vertical sensor. Proper registration has been one of the difficulties to be overcome in the design of the fabricator. Table 2 documents the improvement in layer registration that has been realized through several design iterations. Registration values reported are estimated values for registration error alone. They do not include error due to distortion, etc. The values in the first column are an estimate of typical registration error, ignoring the extreme values. Values in the second column represent the extreme values caused by machine jams, etc.

Design iteration	avg. error (in)	max. error (in)	frequency
1st iteration	0.015	0.035	50%
2nd iteration	0.005	0.035	<10%
3rd iteration	0.002	0.020	<1%

Table 2 Registration improvement in the prototype Genie fabricator. The average registration error of the prototype Genie fabricator, as well as magnitude and frequency of maximum registration error, has been reduced with each iteration of the design.

Data Formats

The Genie fabricator accepts a special layer-specification data format which includes the graphical instructions for each cross section and will include layer headers containing information about weeding, changing of feedstock material (such as color), and process pausing for manual embedding of components by the operator.

A special feature of the Genie fabricator is the ability to change the length of the build envelope for any layer in a build. This length is also specified in the data format.

IV. Demonstrated Applications

Several distinct advantages are realized in the form-then-bond paradigm. When using a cut-sheet process, it is possible to weed the negative areas of each construction layer before stacking, allowing the construction of hollow structures. These hollow structures can be filled during production producing cast in place internal structures. Objects may be inserted into these hollow spaces during construction producing a hybrid of fabricated and off-the-shelf components. Construction sheets of different materials can be used resulting in objects built of several different materials in a single build. By combining the ability to embed components in voids and cast plastic into voids along with cut patterns designed to *weaken* the material selectively, the material properties within an object can be selectively specified. One part of the object can be of rigid polyurethane, another bordering it can be of greater flexibility than even the original feed stock material. These techniques are demonstrated in the fabricated objects described below.

Embedded and Cast-in-Place Car Axles

The axles of two car models built in the Genie fabricator (e.g., see Fig. 4) serve as simple examples of cast-in-place and embedding techniques. If built in the same vinyl used for the bodies of the cars, the axles would have sagged under the weight of the cars. Instead, voids were designed into the car bodies, wheels, and support material to allow casting plastic in a shape which would look like an axle in the visible portions and function like anchors inside the vinyl wheels and body. For one car, the axles were formed of polyurethane resin cast into the voids at the last layer before the void closed during the build. For the other, steel axles were embedded in place with plastic extruded by a hot glue gun cast around them in the cavities. Both car models were in their complete form when the last layer was put down on the machine.

Robotic Manipulators

Fig. 5 shows a dual-link robotic manipulator (or robot finger) built in the Genie fabricator with cast-in-place rigid plastic stiffeners, use of two materials to provide a rigid manipulator frame with flexible joints, and control cables inserted during fabrication. The manipulator is designed to be functional at completion of fabrication.

The dual-link, four-degree-of-freedom manipulator demonstrates embedding of wire and tubing as well as casting-in-place of plastic. More importantly, the finger's design necessitated a new way of thinking about how a fabricator is used. Some of the shapes specified in the CAD file correspond to actual pieces of the build object made in the fabrication (vinyl sheet) material, while others correspond to voids and walls of molds to hold the casting resin, and still others must specify supports for embedded objects before the casting resin locks them in place. This is

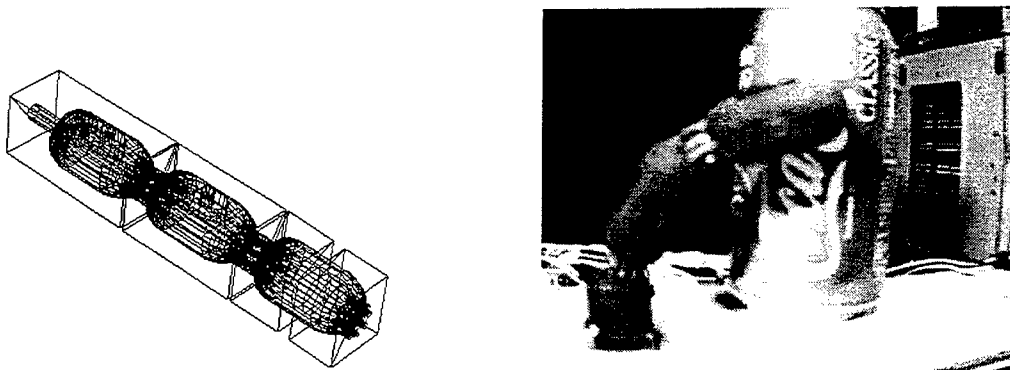


Fig. 5 Dual-link robotic manipulator made on the prototype Genie fabricator at Ennex Fabrication Technologies.
Left: CAD design; right: photograph of fabricated manipulator.

very different from designing a monolithic prototype model for a fabricator to build where only support structures need be specified. This has some of the flavor of designing a skyscraper where initial framing and access ways for build materials and construction equipment are just as important as the final product specifications. This will become even more acute when more and more of the embedding and casting operation, here done by hand, are automated into the actual fabricator itself. Then the fabricator's ability to make arbitrarily complex monolithic shapes will provide problem constraints in the form of voids, supports, and fasteners to the very difficult problem of automated assembly itself.

A CAD design, shown on the left side of Fig. 5, was created in TriSpectives, which specified the vinyl outer body of the three manipulator segments. A hollow cavity was specified inside each segment for the cast plastic "bones". A cylinder of 6 mm diameter was specified to run down the long axis of the manipulator to hold a flexible plastic tube. This tube and two springs fitting tightly around it hold the segments together, provide flexible joints, and in the final product provide a tube for electrical wiring, etc. Eight smaller-diameter cylinders were placed radially around this central tube to hold metal pull cables and their housings. Holes were left in the tops of the segment cavities to allow pouring of the casting resin. The resin seeps into the voids left in each segment and forms the bones while at the same time locking the vinyl, tube, pull wires, and joint springs in place. The pull-wire housing provides a low friction surface for the wire to run in even while the housing itself is embedded in the solidified resin. The eight pull wire ends are terminated in the solidified resin locking them in place such that when one pulls the free end of the wire exiting the last segment of the finger the corresponding joint bends.

The right side of Fig. 5 shows the finished finger mounted on a platform and connected to four servo motors allowing computer control of its four degrees of freedom. Future directions include embedding the servo motors, along with rechargeable batteries, micro controller, pressure and strain sensors, and associated wiring in a quadruped robot with legs resembling the above manipulator. From our experience with the above manipulator we expect this robot to be very durable. It will be completely protected from the elements since its sensitive components are encased in a homogenous mass of solidified resin and its movable joints have no bearing surfaces. When you include the fabricator's ability to provide arbitrary complexity to the shape of the outer body skin we see that this is a different sort of robot from the ones built in most research labs today.

A single-link manipulator was built on the JP5 fabricator in a similar fashion. The frame for this manipulator was produced from multiple layers of paper; the hinge was constructed from four layers of vinyl. The dual-material build was realized by weeding an interior void from four interior layers of the paper and producing four vinyl construction sheets that contained only the hinge material. To construct a multiple-material layer, first a paper layer was applied, then the vinyl layer was laid down in the voids of the paper layer.

Motor-Driven Model Car

A model car was fabricated with interior voids for embedded devices. In this example the solid STL file was modified by adding interior voids before construction. An electric motor, cables, battery pack, and switch were installed as the layers were assembled. After the last layer was in place, the switch was activated and the model car drove across the room.

V. Conclusions

The Conveyed-Adherent process is an automated "form-then-bond" fabrication technique that has been demonstrated in the production of engineering prototypes and functioning machines. The new process shows potential to be many times faster than existing devices. It has demonstrated fabrication in multiple materials side-by-side. It also has demonstrated the potential to produce functioning machines through the use of embedded components and cast-in-place internal structures.

Notes and Acknowledgments

The authors would like to acknowledge the assistance of Marshall Burns, Paul Ashman, and Mark Walther of Ennex Fabrication and Don Brock of the Manufacturing Processes Laboratory at the University of Utah. The Conveyed-Adherent process was developed by Ennex Fabrication Technologies and is covered by U.S. Patent Number 5,514,232 and other pending patents. The manual form-then-bond process commercialized by Schroff Development Corp. as JP System 5 Desk Top Rapid Prototyping was developed at the Manufacturing Processes Laboratory at the University of Utah and is protected by a pending patent. "Conveyed-Adherent" and "Genie" are trademarks of Ennex Fabrication Technologies of Los Angeles.

References

1. *Next-day delivery: A comparison of rapid prototyping systems* in *Rapid Prototyping Report*, pp. 4-6, July 1996.
2. Burns, Marshall, *Automated Fabrication—Improving Productivity in Manufacturing*, PTR Prentice Hall, Englewood Cliffs, NJ, 1993.
3. Thomas, Charles, *An Introduction to Rapid Prototyping*, Schroff Development Corp., Mission, KS, 1995.
4. Merz, R., Prinz, F. B., Ramaswami, K., Turk, M., and Weiss, L. E., *Shape deposition manufacturing*, Proceedings: SFF Symposium, pp. 1-8, 1994.
5. Geiger, M., Steger, W., and Matthias, S., *Multiphase jet solidification—A new process towards metal prototypes and a new data interface*, Proceedings: SFF Symposium, pp. 9-16, 1994.
6. Thomas, Charles L., Wang, Zetian, Kaza, Srinivas, and Bailey, Andrew, *Shapemaker I: An Inexpensive Introduction to Rapid Prototyping*, Proceedings of the Sixth International Conference on Rapid Prototyping, 1995.
7. Thomas, Charles L., Gaffney, Thomas M., Kaza, Srinivas, Lee, and Cheol L., *Rapid Prototyping of Large Scale Aerospace Structures*, Proceedings of the 1996 IEEE Aerospace Applications Conference.
8. Kinzie, Norman F., *Three-dimensional Printing: A tool for solid modeling*, Proceedings of NCGA Conference, pp. 812-822, 1991.

LASER CUTTING OF CERAMIC COMPOSITE LAYERS*

Allan Lightman[†] and Gyoowan Han
University of Dayton Research Institute
Dayton, Ohio 45469-0150

ABSTRACT

The Laminated Object Manufacturing (LOM) process lends itself to use of a variety of materials that can be delivered in sheet format. Studies are underway to investigate the use of monolithic and fiber reinforced (composite) ceramic tapes. The laser cutting process presents a challenge due to the refractory properties of the fibers and, in some cases, their high thermal conductivity. The cw CO₂ laser's thermal degradation process currently used is not suitable for these materials. The evaluation of potential alternative lasers has focused on pulsed systems that use either photoablation together with thermal processes or thermal shock with thermal degradation. We will describe preliminary results achieved in our study of the photoablation process using a copper-vapor laser.

INTRODUCTION

As the technologies for solid freeform fabrication (SFF) mature, the new development emphasis is shifting from hardware to materials and applications. A major goal is the development of engineering materials which can be processed by SFF systems to develop mechanical properties equivalent to those derived from standard mass-production methods. This goal is being achieved on a limited scope and new materials are being developed. Another goal is the development of technologies that permit freeform fabrication using materials which traditionally require molds. This would eliminate the long delays and large expense associated with the production and testing of new parts made from these materials.

Objects fabricated from ceramics are desirable for many reasons, including their thermal properties and abrasion resistance. Production of ceramic parts traditionally requires the use of molds for casting the green part. Typically, the density of ceramic in the green part is on the order of 50% so the densification stage is accompanied by significant shrinkage and associated dimensional distortion. The result is that several iterations are usually required in order to approach the desired net shape after firing. Production of the initial molds and their subsequent modification during iterative development is time consuming and prohibitively expensive for consumer applications. Consequently, the use of ceramic parts has been limited to high value applications, such as military and aerospace, and to consumer applications having simple geometry and without stringent dimensional requirement, since few, if any, iterations would be required.

* This program is sponsored by DARPA under Contract No. N000114-95-1-0059, administered by ONR.

[†] Author to whom correspondence should be addressed.

Realizing that development cost and time were limiting factors to the use of ceramic materials, DARPA initiated programs to develop new concepts for SFF production of ceramic materials. Particular interest focused on high-performance ceramics (non-oxide) and fiber-reinforced ceramic matrix composites (CMC). Laminated Object Manufacturing (LOM)¹ is particularly suited to the implementation of fiber-reinforced CMCs. The material is delivered to the build chamber in tape or sheet format, which permits fabrication of parts with traditional unidirectional or multidirectional fiber placements. The LOM process was developed using a cw CO₂ laser to cut the material layers (initially paper based). While this laser is suitable for cutting materials which can be thermally degraded (selectively burned), it proved to be unsuitable for use on the high-performance CMCs. Either the melt temperature of the fibers was too high to be reached under reasonable laser illumination (laser power and exposure time), or the heat conductivity of the fibers was so high that the thermal energy was quickly transported away from the interaction zone and degraded the surrounding material (or both).

One aspect of the current development program is the investigation of alternative laser sources for use in cutting the layers of CMC. This paper will focus on the results obtained using a copper-vapor laser - a high pulsed repetition frequency (PRF), medium-power, metal-vapor laser that can be tuned to operate in the green (511nm). The paper will show that the PRF can be the limiting factor for cutting speed, so this laser presents a good test bed to evaluate the LOM process. Pulsed Nd lasers converted to the visible or UV (frequency doubled [532nm], tripled [355nm], or quadrupled [266nm]) present intriguing alternatives, and their application is being studied. Preliminary results will be shown for comparison.

EXPERIMENTAL SIMULATOR

A table-top LOM (TTLOM) system was constructed to simulate fabrication with the commercial hardware and provide ready access to all components of both hardware and software. The system, Figure 1, is stabilized by tying all components to an optical table and a rigid build platform. Material is fed by hand into the build stage, permitting the use of limited supplies of the materials under development. The LOM process² cuts out the periphery of the part layer by

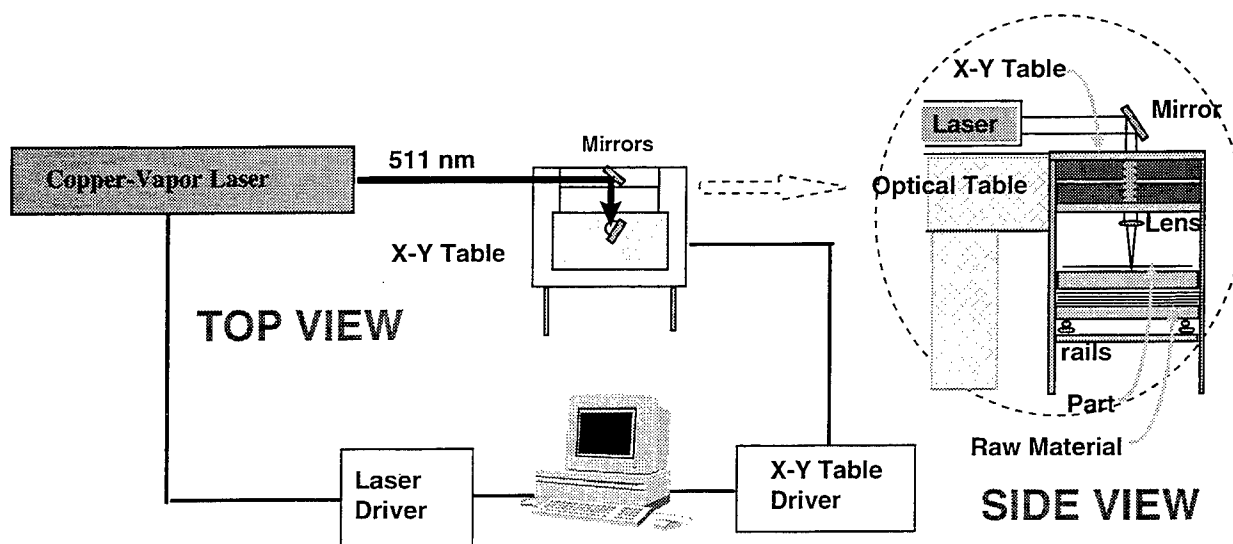


Figure 1. Schematic diagram of the TTLOM system.

layer, by moving the focused laser spot across the material layer via an X-Y table under computer control. In the TTLDM, the X-Y table provides a working space of 20"x20" and a positioning accuracy better than 0.001". The material is introduced into the build chamber by rolling out the build stage (roller bearing and precision rail support), removing a sheet of material from beneath the build platform and attaching it to the top of the construction material on top of the build platform (thus maintaining the top layer at the same height), and then sliding the platform back until it contacts the fixed stops which accurately registers it under the X-Y table.

The copper-vapor laser was custom designed for this study³ using an unstable resonator to provide higher energy per pulse and better beam quality than would be achieved using standard stable resonator configurations. Prior studies of laser-material interactions indicated that deposition fluence would be a critical parameter. Thus, it was important to develop a high beam quality so that the beam could be tightly focused. The output beam has a flat intensity profile, 18mm nominal diameter, and a divergence of 0.3mrad[‡]. The beam is focused with a 100mm lens and the focused spot is characterized, using a scanning knife-edge, in X and Y (Figure 2). Note the hot-spot 85μm from the center in the X profile. This hot-spot does not emerge from within the beam until near the focus, so it is difficult to remove by spatial filtering. It is thought to result from the geometry of the unstable cavity.

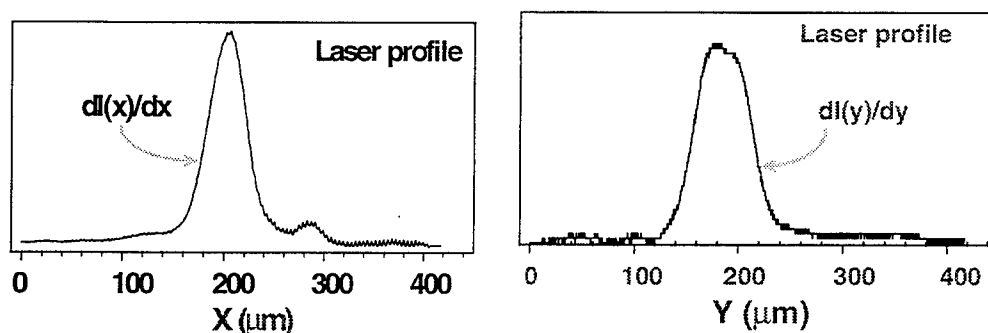


Figure 2. Copper-vapor laser profiles at the focal spot.

The laser's maximum power is 20W at 8 kpps (20ns pulse), delivering 2.5mJ per pulse to the material. The laser focus spot is an oval with axes of 80μm x 100μm, yielding a peak deposited fluence of $4 \times 10^9 \text{ W/cm}^2$. Two types of experiments are initially performed when testing a material. The material removal rate is determined as a function of the energy per pulse and the residual material, in the vicinity of the cut, is studied as a function of the energy deposited per pass. The first study establishes the threshold for material removal⁴ which determines the optimal cutting rate. The second study determines the depth of material removal per pass that is possible without damaging the material. Successive passes are required to cut through the full layer.

The copper-vapor laser is a discharge heated system, best operated at full rated power. In order to characterize the dependence of material removal vs. fluence, a set of custom neutral density (ND) filters is needed (standard ND filters are destroyed under exposure to this laser).

[‡] Note: This is a metal vapor laser so it is subject to beam degradation as the metal is redeposited within the laser cavity [the same as the HeCd laser used in stereolithography].

The filters, inserted in the optical path at the laser head, are made from screen mesh and they scatter the beam. As a result, the laser spot broadens, requiring that the focus be remeasured under each operating condition.

The material removal rate per scan is varied by controlling the scanning speed of the X-Y table, since the speed determines the overlap of the laser spots. Overlap reduction is achieved by increasing the scanning rate. Retracing does not impact the ultimate through-cut rate which is only a function of the laser-material interaction, as long as there is no overhead time associated with retracing. Studies were made at different scanning speeds and the slowest speed, with no material damage, was selected. Studies of the cut depth as a function of the number of scans were made to investigate potential beam guiding effects and material damage from cumulative buildup.

Two materials were investigated. The first is a tape composed of SiC particles and chopped Nicalon fibers. The material is held together with a polymer binder. The solids loading is 65% - 70% by volume. This material was formulated to provide high ceramic volume density so that the part dimensions will remain stable when the binder is burned out. The second material was developed from a Nicalon tow, with the continuous fibers distributed into a quasi-uniform sheet. The material was held together with a sparse application of polymer binder. This material was developed using a novel concept for implementing fiber reinforcement and is the most challenging material for the laser cutting applications.

MATERIAL REMOVAL

Single Pass (vary Fluence)

Material removal processes have been studied in a variety of operating conditions. Srinivasan^{4,5} has performed considerable analyses of laser-material interactions in the UV using excimer laser sources. These studies provided the initial motivation for the studies reported here. While the excimer laser has the desirable property of operating in the deep UV (less than 200nm, depending on gas used), it can only be used as a flood source, since it requires an exposure pattern mask to define the illumination pattern. It is not suitable for use as a focused spot to be scanned in an arbitrary profile that changes from layer to layer. The copper vapor laser can be focused and it has a high PRF, but it operates in the visible (511nm, 578nm). Srinivasan's⁴ results using XeCl (308nm) showed material effects similar to his deep UV studies (173nm and 193nm), indicating that it might be possible to extend this mode of interaction into the visible. The results indicate that the laser is absorbed according to a traditional Beers' law profile. This model should apply as long as the laser pulse is shorter than the time needed for the effluent plume to be developed. Otherwise, the laser would get absorbed away from the surface, heating the plume and potentially damaging the bulk material. Results of our study on the Nicalon tape are shown in Figure 3.

In fixed energy per pulse systems like the copper-vapor laser, the existence of a threshold fluence (F_{TH}) for material removal establishes an optimum fluence for the cutting process. In operation, this optimal exposure is achieved by selecting the focusing lens to provide the calculated focal spot diameter. The maximum cutting rate can be shown to occur when

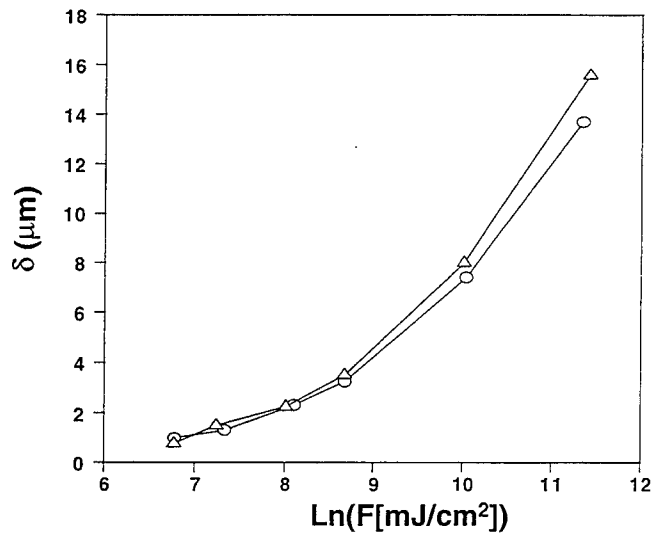


Figure 3. Material removal depth as a function of the laser fluence. (The line serves only as a guide.)

Eq. (1). For the Nicalon tape used in this study the threshold fluence is about $1 \text{ J}/\text{cm}^2$. Eq. (1) determines that optimum cutting will occur when the laser pulse delivers 2.3 mJ into the $200 \mu\text{m}$ focus. For most lasers, it is not possible to vary the PRF and change the energy per pulse while maintaining the average power. Currently, Nd lasers are limited to PRFs on the order of 100 pps by system considerations (heating) and the energy per pulse can exceed the optimum described above. The excess energy will then couple into the material, degrading the cut quality. (Figure 4) Energy per pulse reduction is only achieved at the expense of laser performance. Further laser development is required to provide a range of operating parameters allowing selection of the best laser for the application. The energy per pulse of the copper-vapor laser is about the desired level and its high PRF results in faster cutting for the materials used in this program.

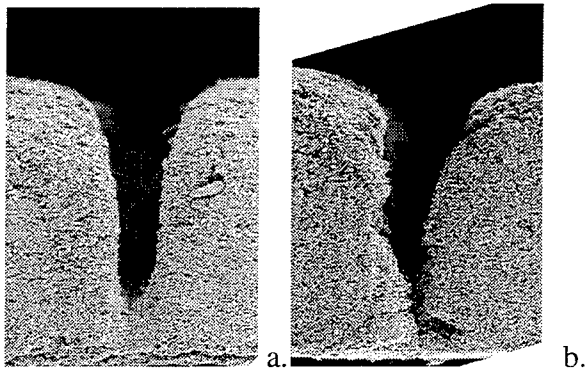


Figure 4. Laser cut profiles for different laser operating conditions. (a) Copper-vapor laser - 1.8 mJ per pulse at 511 nm (14 W , 8 kpps , 20 ns , 5 overlap, 7 pass). (b) Nd:YAG tripled - 25 mJ per pulse at 355 nm (0.5 W , 20 pps , 3 ns , 2 overlap, 3 pass).

$$F = 7.4 (F_{\text{TH}}). \quad (1)$$

Satisfying (1) impacts the choice of laser operating conditions. In typical SFF applications, such as LOM, it is desired to maintain a kerf on the order of $200 \mu\text{m}$. This fixes the illumination area. If the system is to be operated at optimum fluence, the energy per pulse is then also determined. If the laser's operational envelope is only limited by average power, then the optimum operating condition will occur when the PRF is adjusted so that the energy per pulse is that determined using

Multiple Pass (vary Overlap)

Preliminary studies were made with the Nicalon tapes. The cut surface was examined for a recast layer or other indications of damage to the material. It is important that the cut surface present open porosity after binder burnout so the part can be infiltrated. The edge surface, Figure 5, shows a clean cut with ceramic powder, binder, and fibers clearly evident, indicating no thermal damage to the edge.

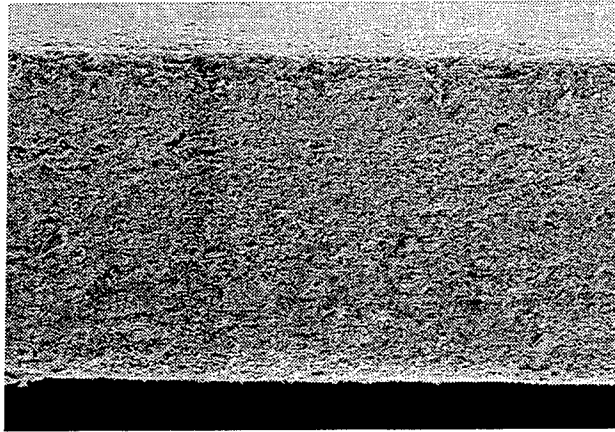


Figure 5. Cut edge of Nicalon tape by copper-vapor laser, 1.75mJ per pulse, 5 pulse overlap, 11 passes. Tape is about 350 μ m thick.

The copper-vapor laser was used to cut the Nicalon tape and the fibers derived from the tow (16 spot overlap). Scanning electron microscope (SEM) pictures of the cut profile (Figures 6a, b, c) were used to study the linearity of the material removal under multiple rescanning. Figure 7 shows initial linearity but as the depth increases there is evidence that another phenomena is occurring which blocks the laser's direct access to the material. This occurs at depths approaching 400 μ m when the laser kerf is about 80 μ m, indicating that there may be a maximum aspect ratio of about 5:1 for clean cuts. Another series of studies was made on Nicalon fibers spread into a tape from a tow. Preliminary results show successful laser cutting (Figure 8). Experiments using a

Nd:YAG laser were performed and the data is under study. Preliminary results show that deposition of too much energy per pulse damages the material, just as seen in Figure 4 with the tape.

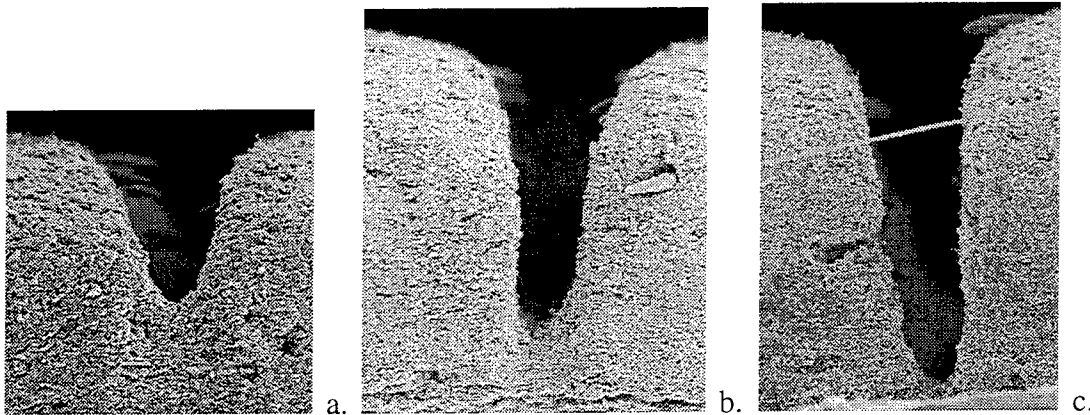


Figure 6. Multiple pass material removal, copper-vapor laser and Nicalon tape. (a) 4 passes. (b) 7 passes. (c) 10 passes. Laser kerf is about 80 μ m.

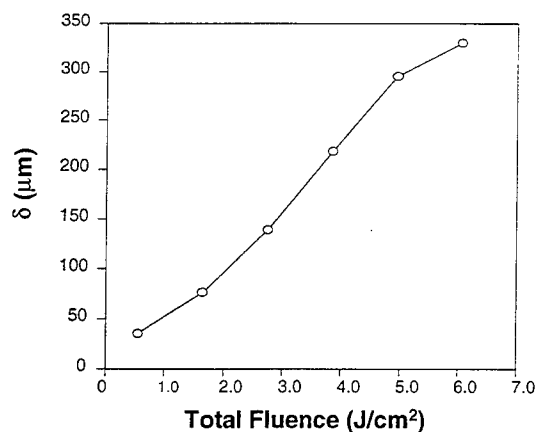


Figure 7. Material removal rate (Nicalon fiber) as a function of total fluence deposited for the copper vapor laser. (The line is only a visual guide.)

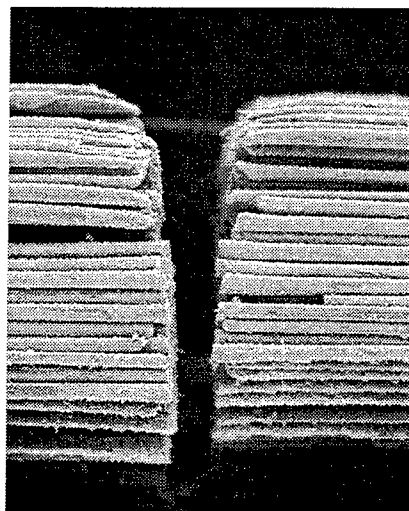


Figure 8. Copper-vapor laser penetration of Nicalon fibers. Median kerf is 80μm and fiber diameter is about 10μm. (511nm, 14W, 8kp/s, 20ns, 5 overlap, 13 pass)

Preliminary results using the frequency multiplied Nd:YAG indicate there is a difference in the interaction of the Nd laser and the copper-vapor laser (Figure 9). The principal difference in the operating conditions is that pulse length of the Nd is 3ns versus the 20ns of the copper-vapor.

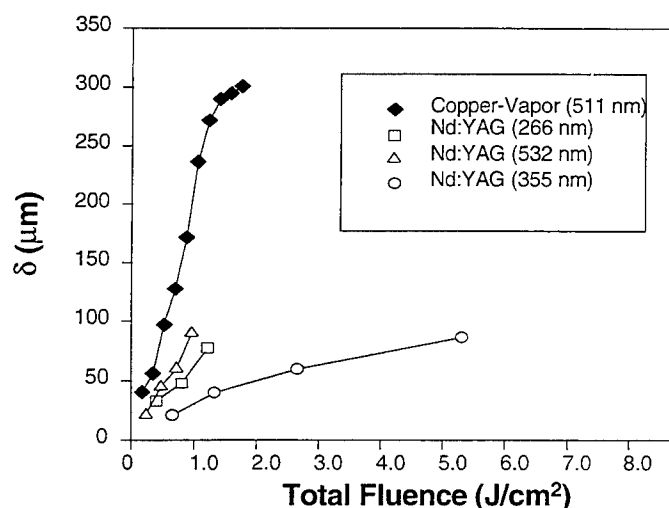


Figure 9. Observed depth of material removal as a function of laser fluence. Graph compares measurements of copper-vapor and frequency-converted Nd.

The Nd laser focal spot has not yet been fully characterized so the observed differences in the rate of ablation cannot be attributed at this time. The computed fluences were based on the optical system parameters, assuming a diffraction limited focus. The measured kerf was in agreement with the assumptions.

CONCLUSIONS

A copper-vapor laser successfully cut through fiber reinforced ceramic tapes and tapes composed entirely of ceramic fibers. The operating performance of the copper-vapor laser is closely matched to the desired parameters

for optimal performance with the materials used. Comparative studies of material removal rate using a frequency converted Nd laser indicate that the material interaction is dependent on both wavelength and pulse length. The laser-material interaction has not been conclusively determined and further studies are needed.

ACKNOWLEDGMENTS

The authors appreciate the technical assistance of John Murphy and Sergio Torres with the apparatus, and J. Douglas Wolf with the images and analysis of the kerf. The authors thank Don Klosterman and Richard Chartoff for their guidance with the materials under study. We also thank Dr. Ulf Westblom and the Coherent Laser Group for their assistance with the Nd:YAG study.

REFERENCES

- ¹ Helisys Corporation, Torrance, CA 90503.
- ² Jacobs, P., **Rapid Prototyping & Manufacturing**, SME 1992.
- ³ CJ Laser, Inc., Dayton, OH 45439.
- ⁴ Srinivasan, R., in Lambda Highlights 1986-1993, published by Lambda Physik GmbH.
- ⁵ Srinivasan, R. and B. Braren, *Ultraviolet Laser Ablation of Organic Polymers*, Chem. Rev. 89, 1303, 1989

Make-up Fabrication of Big or Complex Parts Using the SLA Process

W. L. Wang, J. Y. H. Fuh, Y. S. Wong and T. Miyazawa

Department of Mechanical & Production Engineering
National University of Singapore
10 Kent Ridge Crescent
Singapore 119260

ABSTRACT

Rapid prototyping is a highly flexible manufacturing technology which can produce big or complex parts without any special fixtures and tools. But it is often a costly and time consuming process to produce big and complex parts. To solve this problem, this paper proposes the make-up fabrication process. The process cuts the CAD models of big or complex parts into several small components, optimizes the building orientation and the layout of the multiple objects and then uses the SLA process to build. The paper discusses the basic process, the discretion rules of the CAD models and the optimization of the layout of multiple objects in the simultaneous building.

Introduction

Rapid prototyping has brought new thoughts into the manufacturing engineering. It is a highly flexible manufacturing technology which can produce complex parts without any special fixtures and tools. By using discretion-accumulation shaping principle[1], rapid prototyping technology is totally different from traditional forcing (e.g. moulding or forming) and removing (e.g. milling or turning) manufacturing processes. The process has the following characteristics:

- Manufacturability is independent of the complexity of the parts;
- Manufacturing cost is independent of the batch of the parts.

This means that when changing the shapes, batches, and processing requirements of the parts, there is no need to re-design and re-manufacture the special tools. By modifying the CAD models and adjusting the process parameters, the new parts can be built quickly.

Although the history of rapid prototyping is short, the development of this technology is very fast. According to the present status of the rapid prototyping techniques, there are still many aspects to be improved. For example, most RP machines cannot build big parts, the processing accuracy cannot meet the industrial requirements, the processing time is very long, and the

processing cost is still very high. To solve these problems, this paper proposes the make-up fabrication process. Make-up fabrication process [2] means that cut the CAD models of the big or complex parts into several simpler or smaller components according to their geometrical features before building the part, optimize the building orientation, generate support structures, optimize the space layout, and then build the physical models by the traditional RP processes.

The Basic Steps and Advantages of the Make-up Fabrication

From the application point of view, it is feasible to build big or complex parts using the make-up method with this technique. The basic steps are shown in Figure 1. The following briefly describes this process.

Construction of the CAD model

The construction of the CAD model can be achieved using a CAD software or by reverse engineering using digitizing methods. This procedure is not different from the routine design; it provides a data model for further processing.

Discretion of the big or complex parts

Discretion means to cut the complex or big parts into several simpler and smaller pieces for convenient building in the fabrication process. For the maximum use of the SLA technique, the cutting principles of the CAD models are to simplify the complex or big parts into simpler and smaller ones that can be easily handled. This can be done according to the geometric feature and characteristics. The discretized parts should utilize planar surfaces as much as possible. The number of cutting surfaces can be one, two, three or even more.

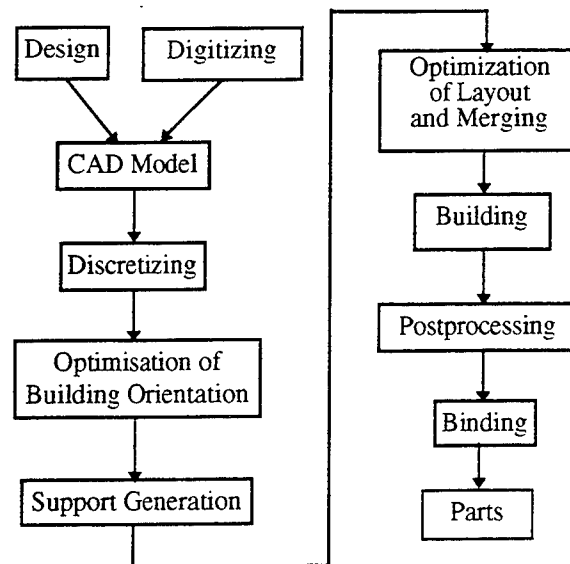


Fig 1 The make-up fabrication process

Optimization of the building orientation

Building orientation can greatly affect the final processing accuracy of the parts. It is very

important to choose an optimal orientation for part building. Factors must be considered in this step including accuracy, building time, and support generation, etc. After these factors are examined, the final orientation is determined for the building process.

Support generation

After the optimal orientation has been chosen, the support will be generated for the subsequent operations. Because of the simplification of discrete, the support structure can be more easily constructed. This step can be achieved by the existing RP software.

Layout optimization and merging

After all the necessary supports have been generated, the components of the parts must be merged to form a single model file. In such case, the effective use of the building space is very important. The layout of the components should consider 2D and 3D cases to achieve a good use of the building space.

Slicing and building

In this stage, 3D models will be sliced into 2D cross-sectional contours for building. For most SLA processes, the slicing thickness is constant. In the make-up fabrication process, the constant thickness is applicable. The time-saving of using variable slicing is not obvious to this process. The building process can be the same as the existing SLA process.

Post-process

Post-process includes the removal of the support structures, surface finishing, position and gluing, and the post cure processes. Because of the simplicity of the supports, the post-process (cut the supports off, then position and glue all the components into a complete one) is simpler. Besides the position and gluing, the post-process is quite similar to the traditional SLA process.

Advantages

The make-up process has more advantages than that of the traditional rapid prototyping processes. Generally speaking, it has three main advantages:

- Improve the processing accuracy. Because all components of big or complex part are built by their own optimization orientation, every part can achieve its highest accuracy.
- Simplify the generation and removing of the support structures. Because there are no hang-up and other slope surfaces, all the support structures can be based on the bottom planes. These will simplify the generation and removing of the support structures.
- Reduce the building time. Because the height of fabrication is reduced, the total building time will be greatly reduced.

Geometrical Discretion of the CAD Models

The geometrical discretion is the key procedure in the make-up fabrication process. The results of the discretion will directly affect the processing time and accuracy. The general principle of the

discretion of the CAD models is to cut the models based on geometrical features. It is known that most CAD softwares are feature-based modeling systems. In the make-up fabrication process, the discretion is also based on features, but the process is reversed. The make-up fabrication is also called feature-based manufacturing process [3]. The following discusses the basic rules to discretize the CAD models:

1. Cutting the cantilever structures. In the SLA process, cantilever structures directly affect the processing accuracy, building time and stability. But the cantilever structures are very common in the actual parts. Cutting the cantilever structures from the CAD models will greatly improve the processing accuracy (the cantilever structures are composed of horizontal cylindrical surfaces or other lower-slope surfaces), shorten the building time (for long or big parts, discrete components will greatly reduce the building height), and increase the stability in processing (when one part is cut into several pieces, the center of gravity will be lowered).

The cutting pattern will be dependent on the geometrical features, processing requirements, possible building orientation and user's experience. The cantilever structures can be cut by a plane or a regular surface.

2. For the rotational parts, the cutting strategy is to cut the part in several segments equally. This discretion will improve the building efficiency without affecting the surface accuracy. For example, the tibia bone, often used in medical applications, is a thin and long bone. If the bone is built in a horizontal direction, the generation of the support is difficult and the surface finish is poor. When it is built in a vertical direction, the building time will be much longer. When using geometrical discretion methods, the long and thin bone can be cut into several pieces. Building the components in a vertical direction, the generation of the support structures will be simpler, the building time is shorter and the processing accuracy also becomes better.

3. For free form and cylindrical surfaces, if the result of orientation optimization is not satisfactory, the geometrical discretion could be used to cut the solid with the free form or cylindrical surfaces. For example, when the angle between the normal vector of the surface or the axis of the cylinder with the building direction is greater than 30° , the surface or cylinder should be cut off to form a new building unit. The cutting boundary should adopt the original boundary as much as possible. The cutting plane should be a plane so as not to generate new surfaces.

4. For the parts with a down-slope surface, the parts should be discretized. Generally speaking, the down-slope surface needs complex support structure. This means that the generation and removing of the support structure will be more difficult. Besides, this building case also leads to a bad surface finish. Hence, this kind of features should be discretized and then built separately.

5. For the slope plane, it should be discretized. The result should make it possible to realize the slope plane either parallel or perpendicular to the building direction.

The Optimization of the Building Orientation

The optimization of the building orientation is a very important procedure to obtain high processing quality and efficiency. It will greatly affect the processing accuracy, time and stability and support generation. There are many literatures [4~6] devoted to this topic. For example, Cheng [4], et al., developed the building orientation algorithm based on the multi-objective optimization in which the processing accuracy is used as the primary objective and the building time as the secondary objective. Seth and Dutta [5] investigated this problem using the generation of the support structures. Frank and Fadel [6] tried to solve this problem using the expert-system-based selection for the preferred build direction. Because of the complexity of the orientation, it is hard to optimize the building orientation considering all factors. In this paper, a new method which considers the processing accuracy and building time simultaneously will be used (by using discretion method, the support structures will become quite simple, and the stability can also be greatly enhanced).

Suppose the objective function of the orientation optimization to attain the best possible accuracy is defined as [4]:

$$Q = \vec{N}_i \vec{\xi} \quad (i = 1, 2, \dots, m) \quad (1)$$

or

$$Q_i = \sum_{j=1}^n N_{ij} \xi_j \quad (-1 \leq \xi_j \leq 1) \quad (2)$$

where:

Q_i = the objective value of the i th orientation of the built part;

$\xi = (\xi_1, \xi_2, \dots, \xi_n)$ the weighting vector consisting of the weights assigned to each surface type;

$N_{ij} = (N_{i1}, N_{i2}, \dots, N_{in})$ the input vector consisting of the numbers associated with the surface types for the respective orientation;

i = the i th orientation of the part;

j = the j th type of the surface of the part in an orientation;

n = the possible number of surface types in an orientation; and

m = the possible number of orientations for building the part.

By using the above functions, the objective values of all possible building orientations can be calculated.

For the objective function of the building time, it can be calculated by the following equation:

$$R_i = n_i t_w + \sum_{j=1}^{n_i} \frac{A_{ij}}{u} \quad (3)$$

where:

R_i = the objective value of the i th orientation of the building time;

n_i = the slicing number of the i th orientation;
 t_w = the waiting time between the layer building;
 u = the scanning area of the laser beam in the unit time; and
 A_{ij} = the area to be scanned on the j th cross-section under the i th building orientation.

Hence, when considering the above two factors simultaneously, the final objective function of the optimization of the building orientation is given by:

$$P_i = \frac{Q_i}{R_i} \quad (4)$$

In this equation, Q_i is the objective value of the processing accuracy in the i th orientation. R_i is the objective value of the processing time in the i th orientation. P_i is the objective value, the ratio of the processing accuracy to the processing time and it is similar to the ratio of the performance to price. The bigger the P_i is, the better the processing quality will be. Thus the maximum objective value of the optimal building orientation should be:

$$P_{max} = \max \{ P_i \} \quad (i = 1, 2, \dots, m) \quad (5)$$

where m is the number of the candidate orientations.

The Optimization of the Layout of Multiple Parts in Simultaneous Building

For the make-up fabrication process, after the parts are discretized into several components, it is natural to consider the layout of the multiple parts in the simultaneous building. If the parts are randomly placed on the building platform, the processing efficiency, cost and time will not be optimized. For the best use of the building space, reducing the building time and improving the building efficiency, optimizing the layout is necessary. For the simple and few discrete components, the layout can be easily determined by experienced users. But for complex and big components, the optimal layout will be difficult to determine intuitively.

For the layout optimization, it is assumed that the user has oriented the part for the desired build, using the multi-objective progressive optimization method [4], or an expert system [6]. Then the layout can be divided into two categories: one is the 2D layout, the other is the 3D layout[7]. The main objectives in the 2D layout are the better usage of the building platform and the close packing of the parts. The objectives of the 3D layout focus on maximizing the number of parts and the volume of the vat that is utilized. The detailed algorithms about multiple part placement can be referred to literature [7].

Case Study

Figure 2 gives the CAD model of an example brake part. With the optimization algorithm of the building orientation, the result is given in Figure 3. From the figure, it is easy to find that although the overall processing accuracy can reach the best result, there are still two cylindrical

surfaces and one slope plane which are not placed in the optimal direction. So the good accuracy cannot achieve. In such case it must be discretized into several pieces so that the building accuracy can be improved. Besides, because of the horizontal placement of the cylinder, one small area contacts with the building platform, the support generation and the stability are also not good. After the building, it is also difficult to remove the support structures from the part.

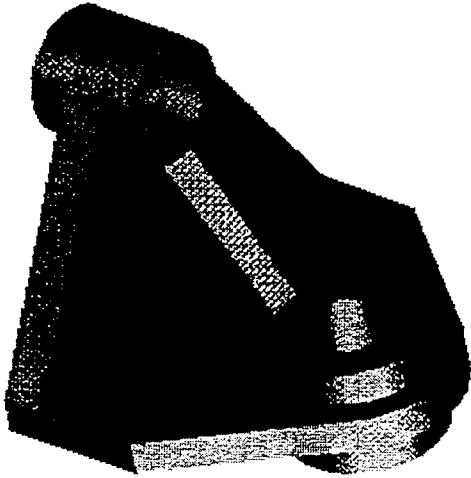


Fig. 2 The CAD model of the brake

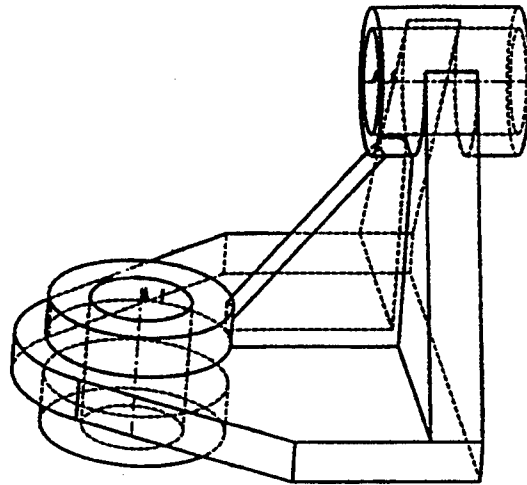


Fig. 3 The optimal building orientation

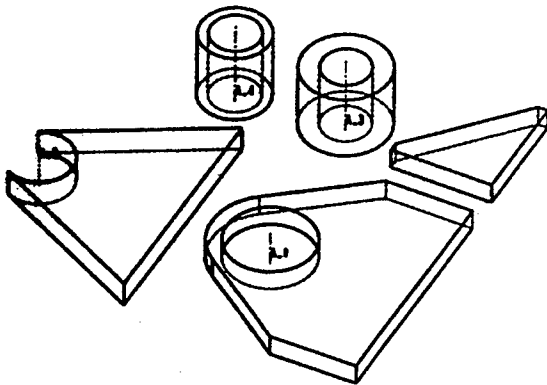


Fig. 4 The discretization result of the CAD model

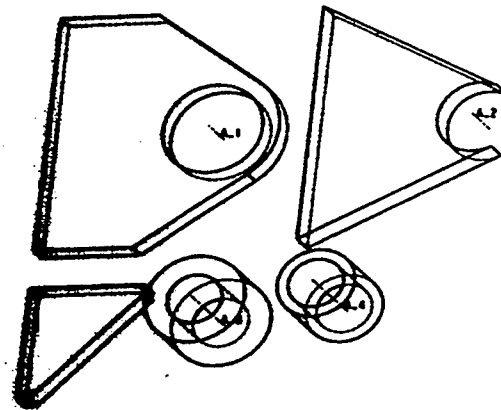


Fig. 5 The optimization of the layout

By using the make-up fabrication process, the problems can be solved. According to its geometrical features, the CAD model can be discretized into five components, as shown in Figure 4. All these components are very simple in geometry and very easy to optimize the building orientation and generate or remove the support structures. Besides, because of the building height is lowered, the building time can also be reduced. Figure 5 gives the final layout of the five components when they are built.

Conclusion

In this paper, the make-up fabrication process has been proposed and discussed. The process discretizes the big or complex parts into small or simple components so as to achieve the better processing accuracy, reduce the building time, simplify the generation of the support structures and enhance the processing stability of the SLA process. The paper presents the cutting rules to an existing CAD model and gives the discussions on the optimizations of the building orientation and the layout when multiple parts are built simultaneously.

References

1. Yan, Y. N., Zhang, W., Lu, Q. P., Diao, Q. J., Shi, X. M., "The principle and development of RP&M based on discretion - accumulation concepts", Chinese Mechanical Engineering, Vol. 5, No. 2 (1994), pp64-66
2. Wang, W. L., Yan, Y. N., Zhang, X. P., "The software systems of the laser rapid prototyping technique", Chinese Mechanical Engineering, Vol. 5, No. 1 (1994), pp18-20
3. Wang, W. L., Studies on slicing solid manufacturing (SSM) technique, Ph.D. dissertation, Department of Mechanical Engineering, Tsinghua University, P. R. China, 1995
4. Cheng, W., Fuh, J. Y. H., et al, "Multi-objective optimization of part-building orientation in stereolithography", Rapid Prototyping Journal, Vol.1, No. 4(1995), pp12-23
5. Seth, A. and Dutta, D., "On the computation of the part orientation using support structures in layered manufacture", Technical Report, UM-MEA-94-14, The University of Michigan, Ann Arbor, MI, July 1994
6. Frank, D., Fadel, G., "Expert-system-based selection of the preferred build direction for rapid prototyping process", Journal of Intelligent Manufacturing, (1995) No. 6, pp339-345
7. Wodziak, J. R., Fadel, G. M., Kirschman, C., "A genetic algorithm for optimizing multiple part placement to reduce build time", The Second International Conference on Rapid Prototyping, Dayton, OH, 1991.

Processing of Carbon Fiber Reinforced Composites by Three Dimensional Photolithography

Chad Greer, Juli McLaurin, and Amod A. Ogale*
Department of Chemical Engineering
Clemson University
Clemson, SC 29634-0909

ABSTRACT

The reinforcement of photoresins with continuous carbon fibers is discussed in this paper. The processing was conducted in an automated desktop photolithography unit (ADPU) developed and built in-house. Continuous fibers were added *in situ* to the photoresin to obtain composite samples containing over 20 vol% of the fibers. The tensile strength of these composites improved by at least a factor of 2 as compared to that of the pure photoresins. It is also noted that the photoresin could be partially cured to develop sufficient green strength in the composite samples even though the fibers are opaque to ultraviolet radiation. These results indicate the potential of this technique to produce functional composite components in conjunction with a 3-D photolithography apparatus.

INTRODUCTION

Conventional photolithography is limited to coating applications because the depth of cure of photoresins is limited to a maximum of a few millimeters. However, this limitation has been overcome in, Stereolithography, a free form fabrication technique (1-3). Unfortunately, at the present time, only pure photopolymers can be used in the commercial stereolithography units. The resulting parts do not possess the properties that are needed for functional applications.

In view of the shortcomings encountered in pure resins, improvement of polymer properties was attempted by adding a reinforcing phase. Preliminary research at Clemson University has demonstrated the feasibility of processing of composite materials by 3-dimensional photolithography (4, 5). Our study showed that composite samples prepared manually with 20 vol% glass and quartz fibers had mechanical properties typically an order of magnitude better than those of pure resins. In a recent study (6), the properties of resins reinforced with continuous glass fibers in an automated desktop photolithography unit (ADPU) are discussed.

The objective of this study was to investigate if carbon fibers could be used as the reinforcing phase in conjunction with the automated 3-D photolithography technique. Description and evaluation of the test samples prepared by the above technique are presented, and the mechanical properties of these parts are compared with those of the pure resin.

* To whom correspondence should be addressed

EXPERIMENTAL

The photoresin used in this research was Du Pont Somos 3100 (designated "S31"). The resin has a viscosity of less than 1000 cP. The carbon fibers were Thornel T300 (Amoco Performance Products). A 3K tow was split into half and used for preparing samples.

The automated desktop photolithography unit (ADPU) was designed and built in-house to allow *in situ* addition of fibers (7). The part is built on a metal platform that is positioned manually to control the thickness of the resin. The various components of the ADPU are: a fiber dispensing device (FDD), a UV-light source, a silica fiber optic cable, and a focusing probe. The light source and the FDD are mounted on a circular plate which can traverse in the X-Y direction and rotate about the Z- axis; all of the motions are computer controlled.

Pure resin as well as continuous fiber composite samples were prepared in the ADPU. The thickness of the liquid resin layer was about 0.7 mm. The fiber tows were primarily dispensed at a spacing of 1mm, although other tow-spacing intervals can also be realized in the ADPU. The pure resin samples were cured at a speed of 15 cm/min, whereas composites were processed at a velocity of 36 cm/min. The tensile samples were nominally 10 cm long, 1 cm wide, and 0.1 cm thick.

The tensile properties of the samples were evaluated in an ATS Universal Tester 900 at a crosshead speed of 0.1 in/min. Two sets of samples were prepared and tested; each set consisted of 5 samples. Set A was postcured in a postcuring apparatus (PCA) for one hour on each side, whereas Set B was postcured for 2 hours on each side. The width and thickness of specimens were measured to the nearest 0.025 mm at three to five points along their length. However, the surface of most of the composite samples was irregular. Therefore, the determination of the composite strength is subject to an uncertainty of about $\pm 20\%$.

RESULTS AND DISCUSSION

A photograph of the entire set of samples is displayed in Figure 1, whereas a close-up of two samples is displayed in Figure 2. The edges of the samples display irregularity and the effect is more pronounced at the end of the sample. A part of this problem could be attributed to the somewhat irregular 1.5K carbon fiber tow which was obtained manually by splitting a 3 K tow. The interior of the sample appears to be free of gross defects. Uneven surface, however, is evident in all of the samples. Such roughness was a consequence of the rather high volume fraction (≈ 20 vol%) of carbon fibers that were dispensed.

The tensile strength of carbon fiber reinforced S31 resin composites are reported in Table I for both of the sets. Initially it was assumed that because carbon fibers are opaque to UV radiation, they would inhibit the curing of the photoresin. Therefore, samples cured for a longer time would display a higher strength. However, the experimental results were rather surprising in that the samples postcured for a total of 2 hours (Set A) had a higher strength (83.5 MPa) than those cured for 4 hours (42.4 ± 13.1 MPa). It is surmised that the additional postcuring rendered the samples very brittle and led to an increase in microcracks and defects within the postcured samples. Further, visual inspection of the tested samples revealed that most of the matrix resin had "solidified" in both sets, although its extent of cure remains undetermined. The reasons for these anomalous results are being probed further.

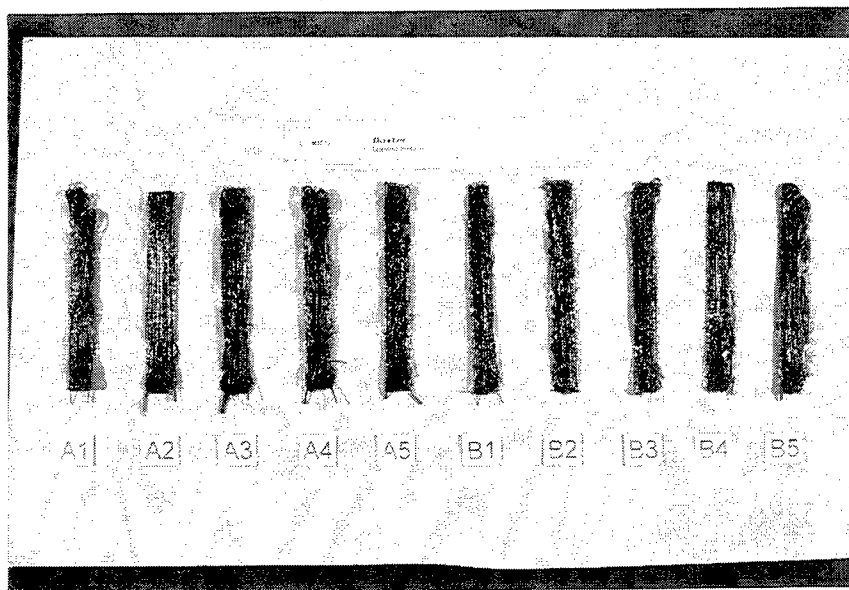


Figure 1. A photograph of the carbon fiber reinforced S31 photoresin samples produced in the ADPU.

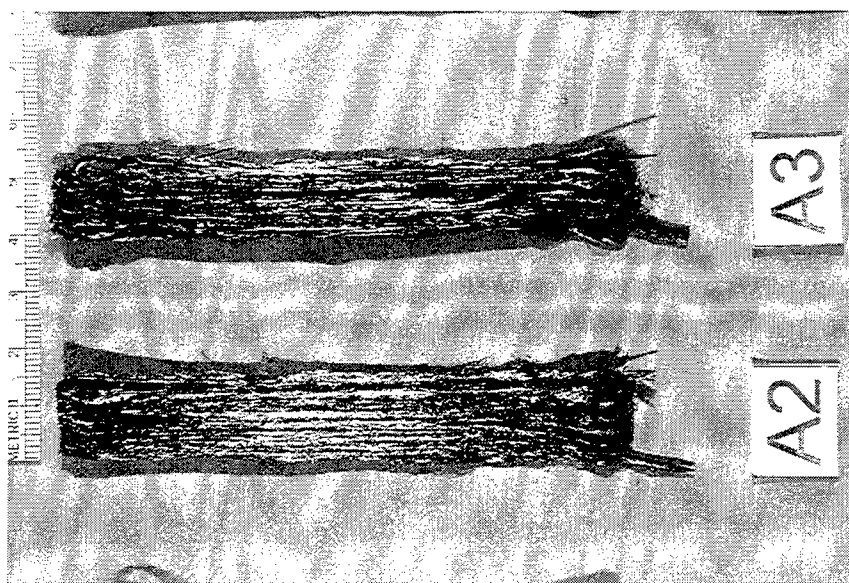


Figure 2. A close-up view of two samples, A2 and A3, from the set that was postcured for a total of 2 hours.

Table I. Tensile strength of pure resin and composite samples prepared in the automated desktop photolithography unit (ADPU). Set A was postcured for a total of 2 hours, whereas Set B was postcured for a total of 4 hours.

Material	Fiber Volume %	Tensile Strength (MPa)
Pure S31	0	34.0
Carbon fibers/A1	30.5	52.5
A2	25.9	122.6
A3	25.7	86.5
A4	26.6	92.3
A5	25.8	63.4
B1	26.4	34.4
B2	24.8	27.4
B3	24.9	41.5
B4	26.3	61.7
B5	23.9	47.0

The tensile strength of unidirectional composites has been predicted with the simple rule-of-mixtures (8,9),

$$\sigma_c^* = \sigma_f^* v_f + \sigma_m' (1 - v_f) \quad (1)$$

where σ_c^* is the strength of the composite lamina, σ_f^* is the strength of the fibers, σ_m' is the stress in the matrix at the fiber failure strain, and v_f is the fiber volume fraction. For a value of 3.0 GPa for the tensile strength of the carbon fiber tows, the strength of the fiber reinforced resins was predicted to be 835 MPa, as described in Table II. It is evident that the strength of the carbon fiber reinforced composites falls very short of the predicted value, and indicates the potential for improvement of the existing process for handling carbon fibers. Additional work is in progress to investigate the behavior of such carbon fiber composites.

Table II. A summary of the tensile strength of pure resin and composite samples prepared in the automated desktop photolithography unit (ADPU).

	v_f (%)	Tensile Strength (MPa)	Predicted Strength (MPa)
Pure S31	0	34.0 ± 2.1	--
S31/carbon (Set A)	26.9 ± 2.0	83.5 ± 24.4	835

CONCLUDING REMARKS

This paper summarized the development of a three dimensional composite photolithography process to produce carbon fiber reinforced resins. An experimental apparatus, automated desktop photolithography unit (ADPU), was used to produce fiber reinforced samples in near net-shape without the use of molds. For a carbon fiber content ranging up to 30 vol%, the strength of composites displayed a 2-3 fold increase over that of the pure resins. Thus, 3-D composite photolithography combines the advantages of rapid prototyping techniques with the improved mechanical properties of fiber reinforced composites.

ACKNOWLEDGMENT

Financial support through Grant No. DMI-9400213 from the Division of Design, Manufacturing, and Integration, National Science Foundation is gratefully acknowledged.

REFERENCES

1. Jacobs, P. F., *Rapid Prototyping & Manufacturing: Fundamentals of Stereolithography*, McGraw-Hill: New York, New York, 1992.
2. Deitz, D., "Stereolithography Automates Prototyping," *Mechanical Engineering* **Feb. 1990**, 34-9 (1990)
3. Muraski, S., "Make it in a Minute," *Machine Design* **Feb. 1990**, 127-32 (1990).
4. Renault, T., A. A. Ogale, R. L. Dooley, A. Bagchi, and C. C. Jara-Almonte, "Photolithography for Composites Manufacturing: Continuous Glass Fiber/Polyacrylate Composites," *SAMPE Quarterly* **22(2)**, 19-25 (1991).
5. Ogale, A. A., T. Renault, R. L. Dooley, A. Bagchi and C. C. Jara-Almonte, "Photolithography for Composites Development: Discontinuous Reinforcements," *SAMPE Quarterly*, **23 (1)**, 28-38, 1991.
6. T. Renault, A. A. Ogale, R. Charan, and A. Bagchi, "Selective Reinforcement of Photoresins with Continuous Fibers Using 3-D Composite Photolithography," accepted for publication in *J. Advanced Materials*.
7. Renault, T., "Processing of Fiber Reinforced Photoresins by 3-D Photolithography," PhD Dissertation, Clemson University, Clemson, South Carolina, 1994.
8. Nielsen, L. E., *Mechanical Properties of Polymers and Composites*, Marcel Dekker, Inc.: New York, New York (1974).
9. Hull, D., *An Introduction to Composite Materials*, Cambridge University Press: Cambridge, England (1981).

Design of Stereolithography Trees for Use in the Investment Casting of Stereolithography Patterns

Christopher S. McDowell*, Mark C. Boomer

Johnson & Johnson Professional, Inc., 325 Paramount Dr., Raynham, MA 02767

Investment Casting Stereolithography Patterns

Stereolithography (SL) has become a useful tool in rapid prototyping of metal parts due to advances in resins and buildstyles for producing investment casting patterns. The production of the patterns, however, has been only one obstacle to the successful application of SL to investment casting. Difficulties in pattern removal from investment casting shells has been a major concern for foundries handling SL patterns, limiting even the most experienced foundries to 90% yields. In addition to shell cracking, improper and inadequate gating of SL patterns can lead to casting defects or failure to produce a satisfactory part. The costs of SL pattern generation, shell production, and raw metal stock, and the tight time requirements of rapid prototyping demand that higher foundry yields be achieved.

The investment casting process begins with the generation of a pattern. The pattern reflects the desired part geometry with an allowance for metal shrinkage. One or more patterns are attached to a structure which will provide a pathway for the molten metal to reach the patterns. This structure is known as a tree and consists of feed tubes that carry molten metal to one or more gates. Gates connect the feed tubes to the patterns. Once the SL patterns are affixed to the tree, a ceramic shell is created around the tree and patterns. The shell is formed by repeatedly dipping the tree/pattern assembly into a slurry of ceramic and allowing each coat to dry before repeating the process. Sand is frequently poured over the ceramic before it dries to add strength to the shell. Once the shell is complete, the pattern and tree are removed from the shell by melting or burning. The shell may then be filled with molten metal, which solidifies in the cavities left behind by the patterns. Finally, the shell is broken away and the metal parts are cut from the tree.

3D-Systems' (Valencia, CA) development of the QuickCast™ (QC) buildstyle has made the rapid generation of accurate investment casting patterns possible. The use of traditional wax trees in investment casting SL patterns, however, has limited the scope of SL in investment casting to pattern generation. This paper focuses on the use of SL to create trees for investment casting, and explores the possibility of using SL trees instead of wax trees. Casting SL patterns and trees may be effective in improving foundry yields, reducing the amount of metal required to create a casting, and even improving the quality of the resulting castings.

Applications of SL trees

Pattern geometry has a significant impact on the degree of difficulty in investment casting SL patterns. Thin and narrow features on SL patterns act as stress risers during pattern removal and may lead to shell failure. Thick sections and large geometries, while presenting less of a problem in terms of pattern removal, are difficult to adequately feed and may require strategic placement of feed tubes and gates. Development of SL trees for investment casting may address both of these aspects of investment casting SL patterns by making tree geometries flexible and by eliminating the use of autoclaving as part of the pattern removal process. Parametric Technology's Pro/Engineer® (Waltham, MA) solid modeling software was used in conjunction with 3D-Systems' SLA 250/40™ and Maestro™ software to create the trees used in this work.

Preventing Shell Cracking During Pattern Removal

Pattern removal represents the most significant problem arising from the use of QC patterns. Autoclaving is the traditional investment casting wax removal process. However, QC patterns exhibit extreme swelling upon exposure to steam during autoclaving, due primarily to the absorption of water. Part geometries such as thin walls, small holes, and sharp corners cannot readily collapse inward as this swelling occurs, resulting in shell cracking around the patterns. To avoid this problem, most foundries bypass the autoclaving step and subject shells containing SL patterns to direct burnout of the patterns in a flash-fire oven, typically the mold-preheat furnace.

While work continues on resins that are less sensitive to moisture, flash-firing remains the most promising route towards removal of patterns with difficult geometries. The use of the flash-fire technique, however, merely relocates the potential for shell failure when wax trees are used. Although the QC patterns generally have a greater coefficient of thermal expansion than the wax¹, their relatively open internal structure allows the pattern to fail and collapse inward during burnout, before sufficient stress is generated to crack the shell. The expansion of the solid wax tree, however, can build up tremendous pressure along the tree and lead to shell failure. It is important to note that some SL pattern geometries necessitate the use of a thick shell, in which case the use of a wax tree may not be precluded.

Changing shell composition to improve shell strength² may allow the processing of SL patterns without a substantial increase in shell thickness. However, for foundries whose processing of SL parts is only a small fraction of overall part production, or as in regulated industries where changes to shell composition require lengthy validation procedures, changing shell compositions to handle SL patterns is unrealistic. Increasing shell strength by increasing shell thickness is possible, but at significant cost due to several factors. First, an increase in shell thickness typically requires patterns to be spaced farther apart, decreasing the number of patterns that can be applied to the tree. Second, the additional process time required to augment the shell thickness adds to the total time required to produce the shell. As time is an essential element in RP processing, such an increase may be unacceptable. Finally, the increased usage of shell materials adds cost to the tree, as does the additional labor required for processing.

When pattern geometry requires avoiding autoclaving, it is possible to create an SL tree to which SL patterns may be attached prior to burnout and which provides better survivability of the shell. A properly designed SL tree can also improve the circulation of combustion gasses, a critical factor in the successful burnout of SL patterns³.

Key to the successful use of the SL tree for reducing shell cracking is the incorporation of features designed to facilitate the collapse of the tree during the initial moments of burnout. The primary principle of SL tree design is the use of the ACESTM, or solid, buildstyle, and the generation of a thin-walled, hollow geometry. This geometry can reproduce the desired shell volume while using less SL resin than an identical part made in the QC buildstyle. Additionally, the thin-walled part collapses at a lower stress during burnout and requires less oxygen to completely combust, freeing up oxygen for the combustion of the patterns. Since a good surface finish on the tree is not critical, the tree can be built 0.006" thick layers. QC patterns are typically built using 0.004" thick layers to improve surface finish. As a result of the larger layer thickness, the time to build an ACES tree is substantially less than the time it would take to build the same tree as a QC pattern.

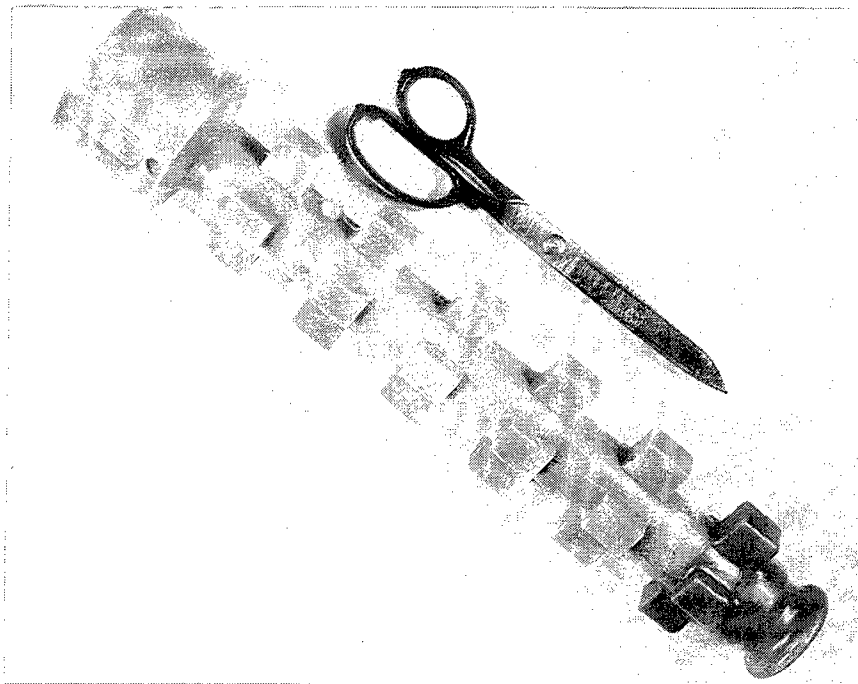


Figure 1 - Wax tree used for investment casting of production and prototype parts. Scissors are for scale.

Figure 1 shows a wax tree currently used to cast orthopedic implants in production. The tree is injection molded with a threaded insert in the mold that allows a threaded rod to be screwed into the tree for manipulation during dipping. This tree was used in conjunction with QC patterns to cast prototype parts in ASTM F-75, a Cobalt-Chromium-Molybdenum alloy. The components had thin sections and sharp edges, and it was difficult to drain excess resin from the patterns during processing. Autoclaving the mold to remove the SL patterns and wax tree proved disastrous; the ceramic mold was completely destroyed by the expansion of the SL patterns. Extensive shell cracking was also observed after flash-firing the mold to remove the patterns and wax.

Shell failure caused by flash-firing was observed along the length of the tree, and was attributed to stresses generated by the thermal expansion of the wax during the early stages of burnout. An attempt to remove the wax by slow heating (with the intent of subsequently burning out the SL patterns) in a convection oven also led to shell failure. To alleviate the cracking problem, an SL tree was created that mimicked the external geometry of the wax tree.

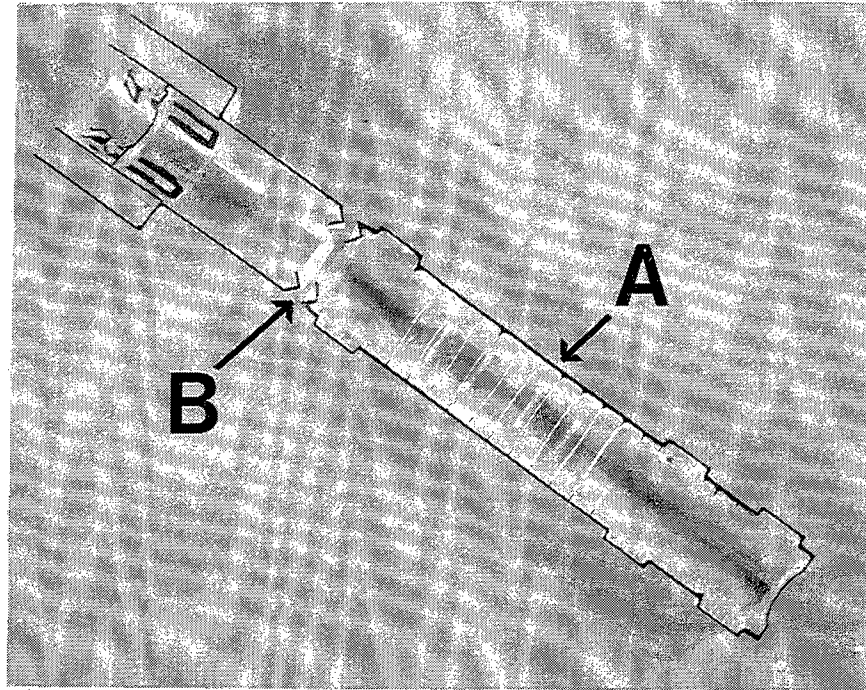


Figure 2 - Section through an SL tree. The SL tree reproduces the external geometry of the wax tree shown in Figure 1.

A cross section of the SL tree is shown in Figure 2, where several

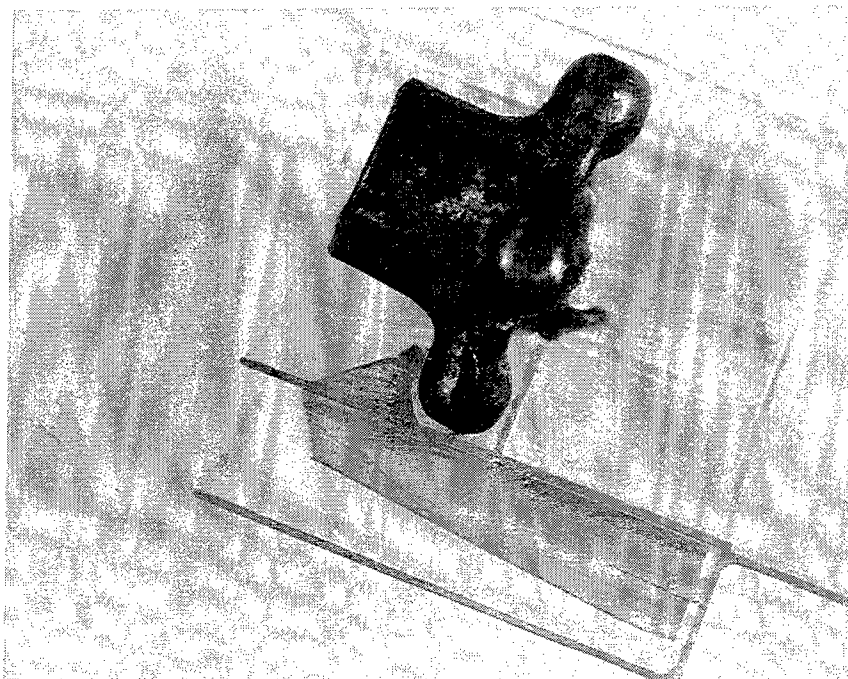


Figure 3 - Section of SLA tree showing support structure for threaded insert.

important features of the tree are revealed. Perhaps the most notable feature of the tree is its thin walls (A). At 0.025" thick, the walls of the tree were strong enough to hold QC patterns and survive general handling during shelling, but thin and weak enough to break readily as stresses developed during firing. All corners and edges were filleted and rounded to reduce stress concentrations in the ceramic shell.

Another notable feature of the tree is the joint (B) connecting the two portions of the tree. The tree was too large to

be built in a single piece on the SLA 250, so it was split in Pro/Engineer prior to building. The joint needed to be strong enough to hold the weight of the patterns on the lower half of the tree. The joint, a “bird’s beak” type of connection, was sufficiently strong to hold the two parts together. The benefit of this type of joint is that it collapses into a narrowing “v” shape as circumferential stresses arise in the tree during firing. A simple flange-type of joint would be more structurally resistant to failure during burnout, transmitting stress to the shell and potentially leading to shell failure. Figure 3 shows a close-up of the top portion of the SL tree of Figure 2. A reinforcing structure was added to the tree to accommodate the threaded insert (shown in place) which was present in the original wax tree. The insert was placed into the tree and rotated 45 degrees to lock it into position under the reinforcement. The structure was made independent of the wall of the tree, and was strong enough to support the weight of the shelled tree. The strength of the insert reinforcement was not transmitted to the outer wall of the SL tree, preventing the transfer of additional stress to the ceramic shell during firing.

Figure 4 shows cross sections through two flash-fired ceramic molds made from the tree geometry shown in Figure 1. To create a ceramic shell strong enough to withstand flash firing of a wax tree required 11 slurry/sand layers. A section through the fired shell is shown in Figure 4a. The shell in Figure 4b was created over the SL tree shown in Figure 2. The shell over the SL tree survived firing even though only 6 slurry/sand layers were applied. Producing the ceramic mold by using an SL tree saved 2 days in the shell production area and reduced the weight of materials (slurry & sand) by 66%.

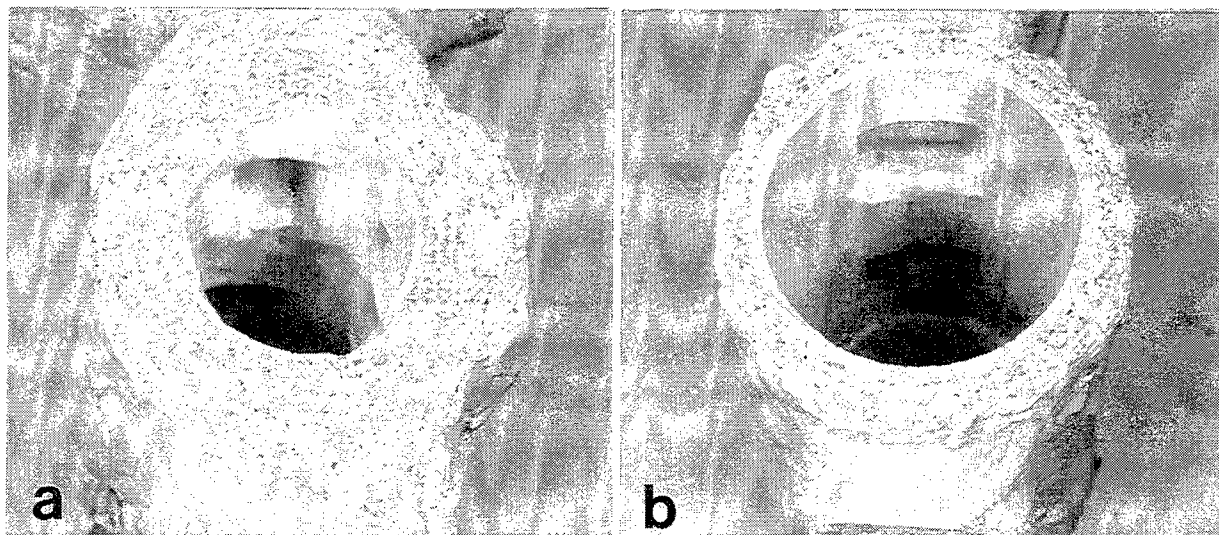


Figure 4 - a) Fired and sectioned investment casting shell showing thickness of ceramic mold created over a wax tree. b) Fired and sectioned shell showing thickness of ceramic mold created over a SL tree. The I.D. of the shells was the same.

Optimizing the Investment Casting of SL Patterns

Due to the large variety of pattern geometries encountered in prototype development, the gating and feeding of SL patterns remains, largely, an art. Foundries rely on experience for ensuring adequate fill of the mold as well as control over the actual filling and solidification of the

metal. The usual strategy for feeding these parts is to apply excess gating, accepting less than optimal metal flow and extra finishing work on the castings. As an alternative, development of an investment casting tree might be performed in conjunction with the original solid model for the part. This would promote visualization of the entire casting process early on, perhaps eliciting design changes that improve the castability of the part.

When prototype parts need to be cast from expensive alloys, the elimination of metal waste becomes an important criterion for designing the tree. Using feed tubes and gates with circular cross sections minimizes heat loss in the shell while the metal is being poured, allowing the use of smaller diameter feed tubes and gates.

Since part complexity is not generally an issue in SL fabrication, complex features may be added to improve the metal flow characteristics of the mold. For instance, the outer surface of the tree might be grooved slightly to promote the laminarity of metal flow through the ceramic mold upon casting. Reducing turbulent metal flow through molds can reduce the chance that small ceramic fragments in the mold become trapped in the casting. Smooth gate-part transitions and bends in the tree can also help to promote laminarity.

When part geometries contain thick cross sections, metal shrinkage can cause voids to appear in the castings. To avoid shrinkage cavities, a reservoir of molten metal called a riser is created by forming a volume in the shell that solidifies after the part, allowing additional molten metal from the riser to fill the part cavity as solidification takes place. To keep the metal in risers molten, they must often be very large. Maximum heat retention is accomplished when the surface area of the mold is small in relation to the mass of metal in the riser. By using SL, hollow cylindrical or semi-spherical risers (geometries with low surface area/volume ratios) could be created and added to the tree to prevent shrinkage cavities.

Provisions must generally be made for handling the tree during the shelling process. In the example above, a special feature was made for allowing a threaded insert to be placed into the SL tree. This insert must be removed prior to burning out the shell. As an alternative to a separate, threaded insert, screw threads could be modeled directly into the SL tree.

Determining the Cost of SL Trees

As the production of SL parts can be expensive, minimizing the use of SL resources, including resin, build time, and post processing requirements is critical in making the use of SL trees feasible. Since surface finish and dimensional accuracy of SL trees is relatively unimportant, trees should generally be positioned to minimize build height. In the example described earlier, the lower, long portion of the SL tree was built lying on its side. Supports were generated inside the part, however, they did not contribute significantly to the strength of the part and were left in place (reducing the amount of post processing required). The total part height was reduced to about 2 inches, and though the tree was slightly out-of-round (the effect of cure depth and overcure characteristic of the SL process) there were no adverse effects on the performance of the

tree. The tree consumed only 60g of resin (about \$4 worth of resin).*

The small cross-sectional areas of these SL trees require minimal scan time. SL trees do not require any special build parameters, and can be placed into a build when there is extra room in the SL apparatus, to be built along with other ACES style parts. About 3 hours were required to model the SL tree from the above example in Pro/Engineer.

SL trees may also be used for proofing out tree geometries prior to producing production tooling for injecting wax trees. Optimization of tree geometry in the production of large numbers of castings can have tremendous impact on production costs. The flexibility offered by solid modelling and SL technology allows timely experimentation with a number of parameters of tree geometry that ultimately affect the raw metal requirements and quality of the castings.

SL trees clearly provide benefits over wax trees in reducing shell cracking when SL patterns with difficult geometries are to be cast. SL trees may also be employed to reduce shell material and process time, improve foundry yields, reduce raw metal stock requirements, and improve the quality of the casting, providing ample economic return on the investment of producing the SL tree.

Conclusions

The demanding pace of rapid prototyping and the high cost of SL patterns require higher foundry yields than are currently achieved. The use of SL trees in the investment casting of SL patterns has the potential to improve foundry yields significantly, through improved gating of parts and a reduction in shell failures during pattern removal. The SL ACES buildstyle in conjunction with solid modeling software packages can be used to create thin-walled tree geometries possessing an array of features that can significantly reduce shell stresses developed during flash-fire burnout and improve the flow of metal into the mold. The time savings associated with improved foundry yields and elimination of the autoclaving step can be one of the most significant advantages of the use of SL trees. While the initial cost of designing and producing an SL tree may be higher than that to produce a wax tree, the potential to ensure shell survival during pattern removal, conserve expensive alloys, and produce high quality castings may justify the added expense.

References

1. K. Losse, "Investigation of Optimum Process Parameters for Burnout of SLA Parts for Manufacturing of Metallic Parts Through Investment Casting," Proceedings, Prototype Research and Manufacturing '96, SME, Dearborn, MI April 23-25, 1996.
2. M. Guerra, W.D. Roberts, and A.T. Bozzo, "Factors Affecting Shell Strength and the Effect of Dry Time on Shell Strength," 22nd EICF Conference, Paris, 22-25 April, 1992.
3. C. Atwood et al, "Producing Castings from Rapid Prototyping Patterns," presented at Prototype Research and Manufacturing '96, SME, Dearborn, MI April 22, 1996.

* Due to the wide variation in pricing of SL parts between service bureaus and in-house facilities, no attempt will be made here to estimate an overall cost for producing the tree.

Stereolithography System Using Multiple Spot Exposure

Yoji MARUTANI, Takayuki KAMITANI

Faculty of Engineering
OSAKA SANGYO UNIVERSITY
3-1-1 Nakagaito, Daito City
OSAKA, 574 JAPAN

ABSTRACT

A new method of making 3-D objects is proposed. A discharge lamp is used as a UV light source, and to make the fabrication time shorter, multiple spots exposure using optical fibers is employed. The light is distributed to some optical fibers. The output side of each fiber is arrayed linearly and the emitted lights are focused on the surface of the photosensitive resin. As the fiber array is raster-scanned, the light transmission of each fiber is controlled by the optical shutter independently according to the pixel data at the corresponding position to be irradiated. Small-sized stereo-lithography systems can be realized economically by this method.

1. INTRODUCTION

The rapid prototyping is a method to make 3-D models by mutual bonding of raw material on the basis of digital data. Stereolithography is one of the methods using a UV laser and photopolymer resin, and is now applied to the fabrication of industrial models, medical models from CT or MR images[3], etc.. However the cost and size of present stereolithography systems have issues because of the UV laser. Presently commercially available systems are very expensive. As rapid prototyping(R/P) become popular, small and inexpensive systems are requested.

When stereolithography was first proposed, a discharge lamp was used as a UV light source[1]. However it did not put to practical use because of its low accuracy and energy efficiency. Commercial high-precision systems were realized using UV lasers[2]. But they have been very expensive and bulky.

Although some R/P systems, such as FDM and LOM are relatively inexpensive. They can not give more stable reaction process and transparent, complicated models than stereolithography.

Here, we propose the new method to realize smaller and more inexpensive stereolithography systems[4]. In the system, a discharge lamp is used as a UV light source, and to make the fabrication time shorter, multiple exposure spots are employed. Using this method, the small-sized stereo-lithography system can be realized economically. In this paper, the principle of the method, hardware and software of the experimental system and some results of experiences are mentioned.

2. PRINCIPLE OF OPERATION

Fig.1 shows the configuration of the system. The UV light from the discharge lamp is introduced to the quartz optical fibers. The fibers are arranged at the optical head and consists the emitting unit. Images of their output ends are formed on the surface of the resin. The light emission of each fiber is controlled by the electromagnetic shutter independently. The shutter is consisted of the electric solenoid and the thin metal blade. The optical head is moved by the signal from the computer. As it moves, the data of sectional pattern are applied to each shutter of the fiber.

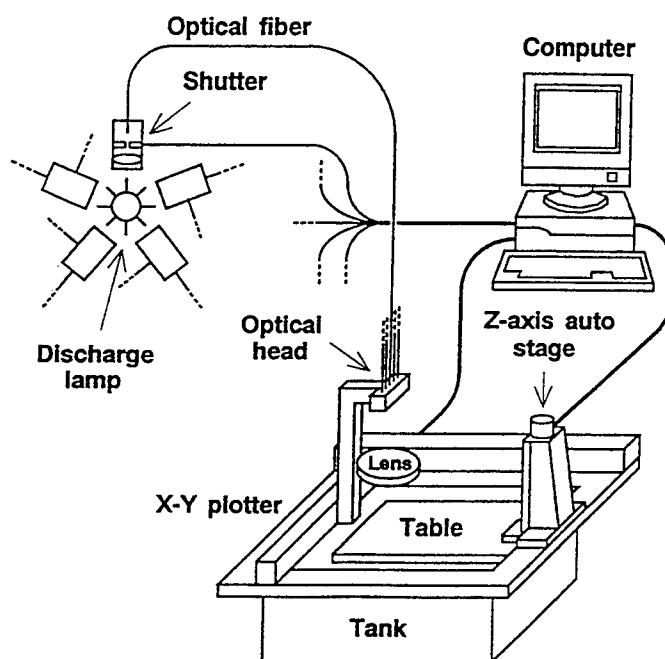


Fig.1 Schematic diagram of the system.

In general, two methods to make 2-D pattern exist : masking method and spot-scanning method. Masking method needs active optical mask. But no such masks are available on the market. So we adopted spot-scanning using optical fibers as flexible optical paths. To make use of light effectively, the multiple fiber system is employed.

In the computer, 3-D CAD data are sliced mathematically and sectional patterns, then these patterns are converted to the pixel image by painting process and stored in the buffer memory one by one. As the optical head moves, the light pattern at the head is controlled by the shutters according to the sectional image in the memory. The pixel data of corresponding position of each optical fiber are read out from the memory and given to the optical shutters.

After exposing whole the surface, the table goes down by the thickness of one layer. The new liquid resin layer covers the solidified layer, and next exposure is done using next sectional image. The thickness is same as that of slicing of the CAD data and is less than the depth of solidification. So the solidified layers unite each other firmly.

One of the difficulties of the system is the existence of gaps between fibers. The gaps cause the non-solidified part and prevent making models perfectly. Filling up of them is done by the software and/or hardware technology. The gaps between each fiber at the optical head are considerably broad because of the clad and the guard sheath of the optical fiber. So the trace of the optical head also has very broad gaps. In this system, to fill the broad gap between the traces, two methods are adopted. In one method, as shown in Fig.2(a), after scanning in X axis, the head moves by one pixel in the Y axis. Next scan runs between the last traces. If the gap is more than one pixel, this scanning are repeated until the gap are buried. In another method, as shown in Fig.2(b), the fiber array is set oblique to the scanning direction. On scanning, close exposure between each trace is established. By adjusting the angle of the head, the pitch of the traces can be changed freely.

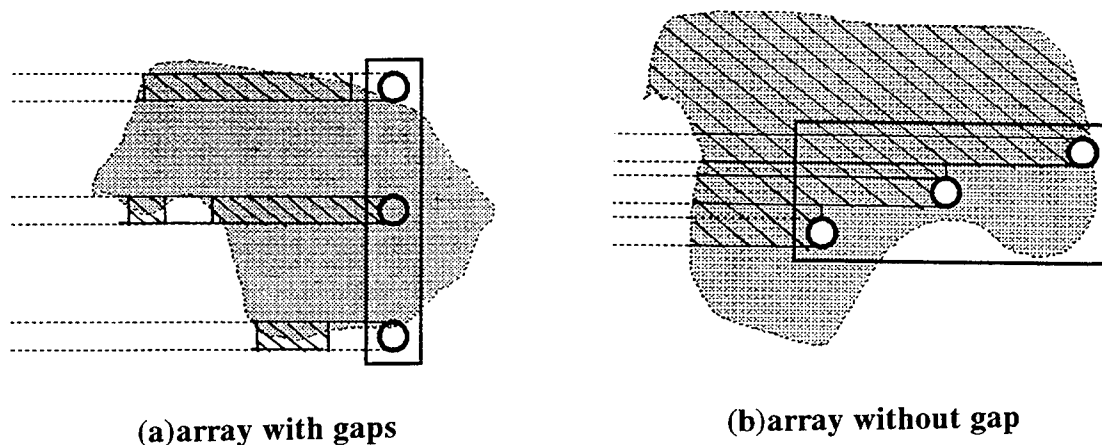


Fig.2 Scanning path.

The finest width or diameter of solidified part is determined by the diameter of the light spot imaged on their surface. To make fine structure, the image of the fiber end should be as small as possible.

3. EFFICIENCY OF LIGHT COLLECTION

The light from a discharge lamp is dispersive, so it is impossible to concentrate it at a spot. Fig.3 shows the optics of the system. A lens is used to collect and concentrate the dispersing light. Let the focal length of the lens be f , the diameter of it be D , radiance of the light source be B , and magnification of the image be m . Then the irradiance E of the image is generally expressed as follows,

$$E = \pi B(D/f)^2/4(1+m)^2 \quad (1)$$

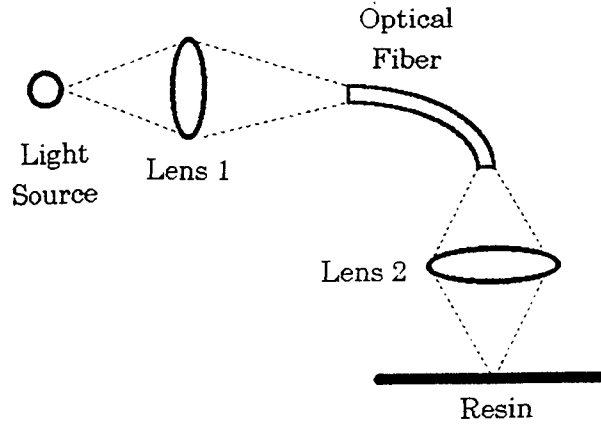


Fig.3 Optics of the light source.

At the input end of the optical fiber, the dispersive light from the lamp is collected to the core of the optical fiber. The optical fiber can accept only limited light which has restricted angle of incidence. Let the maximum incident angle be θ_m . To transfer all the light passing through the lens aperture to the optical fiber, the distance b between the lens 1 and the fiber end should be

$$b = (D/2)/\tan \theta_m \quad (2)$$

As the magnification m is $m=b/a=(b/f)-1$, using eq.(1),

$$E = \pi B \tan^2 \theta_m \quad (3)$$

The radiant energy Φ transmitted by the optical fiber is the product of E and the area of the core S .

$$\Phi = \pi S B \tan^2 \theta_m \quad (4)$$

To improve Φ , it is necessary to select the optical fiber having large θ_m and S . The distance between the lamp and the lens 1 is calculated so as to make the image of the light source on the fiber end. The length of the optical system is $a+b$. To minimize this, condition $b=2f$ is necessary, because $a+b=bf/(b-f)+b$.

At the output of the optical fiber, according to eq.(1), f/D and m should be small to maximize the light quantity on the resin. f/D can be made smaller by selecting the lens, and m can be small by adjusting the optical system.

4. EXPERIMENTS

In the experimental system, a X-Y plotter was used and the optical head was attached instead of its pen. A 150W Hg-Xe discharge lamp (HAMAMATSU Co. L2482) as the UV light source and five quartz optical fibers with core diameter 0.4mm were used. The resin was ADEKA HS-673. The system was controlled by a personal computer through serial and parallel interface.

To measure the resolution and the solidification rate, the resin was exposed by single fiber. As illustrated in Fig.4, thin glass plate is set afloat on the surface of the resin. The transmission rate of the plate is about 92% with UV and visible light. Fig.5 shows the relation between the irradiation time versus the diameter and depth of solidified part. With visible light, the exposure time is improved.

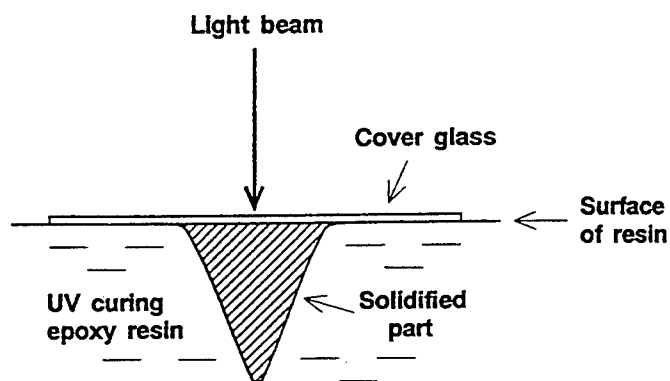


Fig.4 Illustration of the shape of solidified resin.

In a example of commercial system using a 100 mW UV laser, a layer 0.08 mm in diameter and 0.2 mm in thickness is solidified at scanning speed of 770 mm/sec. the volume production rate is 9.7 mm³/sec. From Fig.5, our system produces 0.58 mm³ in 2 sec. So about 34 fibers are equivalent to the ability of 100 mW UV laser.

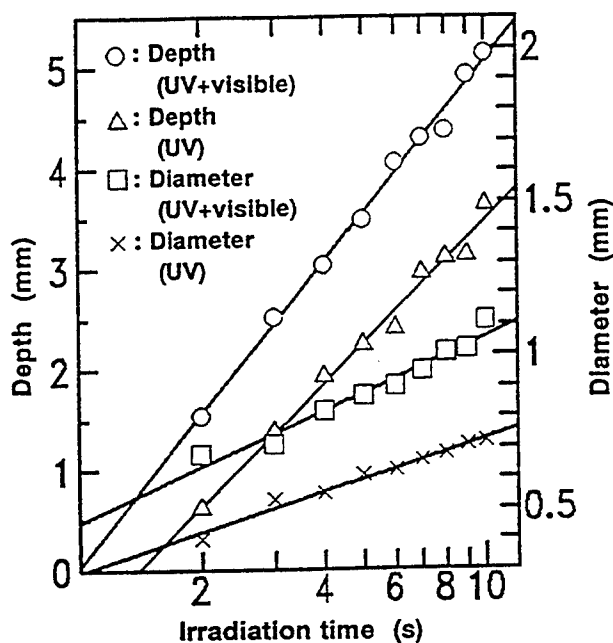


Fig.5 Relationship between the size of the solidified resin and irradiation time.

Fig.6 shows examples of 3-D objects made by the system. Five spots with 0.5 mm diameter were used, and gaps between spots were 4 mm. The exposure time in each spot was 2 sec.

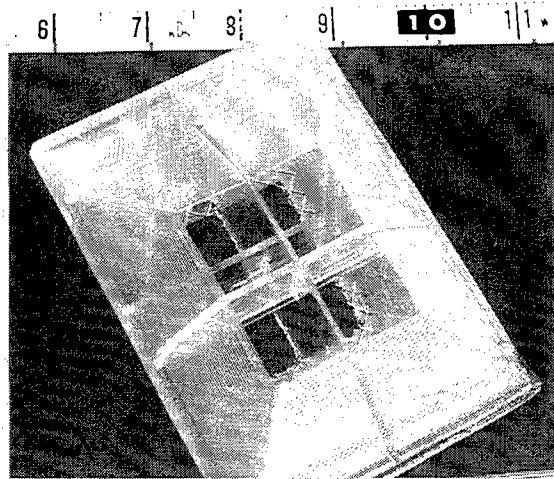


Fig.6 An example of 3-D object.

5. CONCLUSION

By using a discharge UV lamp economical and small-sized stereolithography system can be realized, and the multiple spot exposure method leads to high fabrication speed. The resolution of this system is determined by the spot size of optical fiber. Generally the incoherent light can not be concentrated without energy loss. The finer the spot size, the less the total optical power. So the proposed method may be suited to the rough models.

REFERENCES

- [1] Kodama,H:"Automatic Method for Fabricating a three-dimensional Plastic Model with Photo-hardening polymer",Rev. Sci. Instrum., Vol.52, No.11, pp1770-1773('81)
- [2] Nakai,T.,Marutani,Y.:“Shaping 3-D Objects Using a UV Laser and Photopolymer”, Conf. on Laser and Electro-Optics '86, ME-2('86 San Francisco)
- [3] Nakai,T.,Marutani,Y.:“Applications of UV Laser Fabrication to Organ Models Interpolated from Computed Tomography and Magnetic Resonance Images”, Applied Optics, Vol.31, No.25, pp5375-5379('92)
- [4] Kamitani,T.,Numata,Y.,Marutani,Y.:“Rapid Prototyping System Using an Optical Fiber Array” ,Record of the 1995 Kansai-Section Joint Convention of Institutes of Electrical Engineering, Japan, G12-49.

A NEW SFF PROCESS FOR FUNCTIONAL CERAMIC COMPONENTS

Susanna C. Ventura, Subhash C. Narang, Sunity Sharma, John Stotts,
Chunling Liu, Susan Liu, Lung-Hua Ho, and Durga Annavajjula
SRI International, Menlo Park, CA

Steven J. Lombardo, Anne Hardy, Mike Mangaudis, and Eric Chen
Saint-Gobain/Norton Industrial Ceramics Corporation, Northboro, MA

Lance Groseclose
Allison Engine Company, Indianapolis, IN

ABSTRACT

SRI International in collaboration with Saint-Gobain/Norton Industrial Ceramics Corporation and Allison Engine Company is developing a new SFF process, Direct Photo Shaping, for the fabrication of functional ceramic components. The process is based on the layer-by-layer photocuring of ceramic slurries containing monomers curable by visible light. Each layer is photoimaged by a liquid crystal display (LCD) or a digital light processing (DLP) projection system. After binder removal and sintering, the properties of silicon nitride tiles prepared according to the Direct Photo Shaping process were found to be comparable to properties of tiles formed by conventional methods.

INTRODUCTION

Rapid prototyping is presently being applied to the fabrication of nonstructural materials by means of computer-aided design/computer-aided manufacturing (CAD/CAM) technology, wherein computer files descriptive of the object are used to create parts made from materials such as UV-curable polymers. The components fabricated in this fashion are considered nonfunctional, and their main application is for iterative design evaluation in molding making. There is an increasing demand to extend rapid prototyping technology to the fabrication of functional components with engineering properties and dimensional tolerances comparable to those of conventionally produced components.

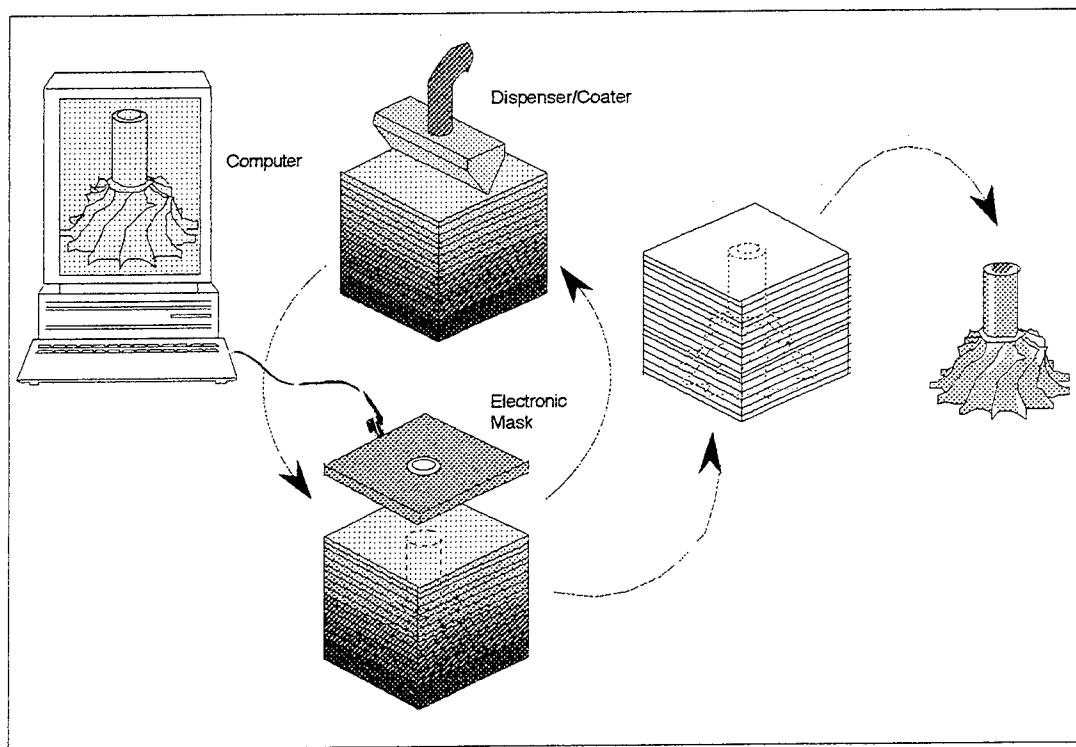
The development of solid freeform fabrication (SFF) manufacturing technology is expected to allow the fabrication of functional prototypes from advanced ceramic, metallic, and multiphase materials for structural and electronic applications. The SFF approach to net shape forming holds great promise for rapid prototyping of ceramic components through simplification of the processing cycle (e.g., elimination of the time consuming steps of pattern making and mold fabrication).

In this paper we describe a new SFF process, Direct Photo Shaping, and its use for the fabrication of silicon nitride components.

DIRECT PHOTO SHAPING PROCESS

The Direct Photo Shaping process is described in Figure 1. A liquid crystal display (LCD) or a digital light processing (DPL) projection system are used as an electronic mask to build lithographic images onto a photopolymerizable slurry containing ceramic powder. A visible light source is coupled with the projection system. The image to be projected is changed according to the CAD model information. The photopolymerizable slurry contains the ceramic powder, a dispersant, photocurable monomers, and a visible light initiator. The slurry is dispensed onto the build platform and leveled with a doctor blade. Each film is photoexposed by visible light projection. After each exposure, a new film of photopolymerizable dispersion is applied on the build platform. When the fabrication is complete, the green ceramic body is removed from the platform and rinsed with a suitable solvent to dislodge any uncured material.

The ceramic forming process is based on photo-gelcasting, since the green body is formed by photocuring of a slurry of the ceramic powder in a solution of photopolymerizable monomers. Gelcasting [1] has been shown to produce complex-shaped, near-net-shape parts. Gelcast green bodies are generally strong and machinable, and after sintering, highly dense ceramic parts are obtained.



CM-320581-331

Figure 1. Schematic illustration of the Direct Photo Shaping process.

EXPERIMENTAL

Powder Production

Silicon nitride powder (Ube Industries, Yamaguchi, Japan) and 4 wt% Y_2O_3 sintering aid were coprocessed by aqueous milling to reduce the particle size and to homogeneously distribute the sintering aid. Milled slurries were passed through a magnetic separator to remove iron contamination and were then filtered and concentrated. The concentrated slurries were dried by freeze drying. Details of the powder processing have been previously described [2].

Ceramic slurry

Ceramic slurries were prepared by ball-milling the silicon nitride powder in the photocurable monomers, after addition of a suitable dispersant, a solvent/plasticizer and the photoinitiator. The viscosity of the ceramic slurries was determined with a Brookfield DV-II+ viscometer.

Component Fabrication

Tiles (3"x3"x0.5") were formed according to three different methods to compare their mechanical properties. Tiles were prepared by multilayer deposition and photoexposure to a quartz tungsten-halogen lamp. The photocurable slurry comprised of 68 wt% silicon nitride, a suitable dispersant, photocurable monomers, plasticizer, and a visible light photoinitiator. Each layer applied was 2 mil thick. Additionally, tiles were formed by either uniaxially pressing the dry powder followed by isostatic pressing (30 ksi) or by thermally curing (120°C) monolithic tiles formed from a slurry of the same composition as used for the SFF process.

Other complex shape samples were prepared by direct photoexposure using a 1000 watt xenon arc lamp from Oriol Corporation, Stratford, CT with a filter that allows only the transmission of radiation from 420 nm to 630 nm, and reduces thermal effects.

Binder solvent was removed from the photocured samples by heating in air to 450°C over 48 hours and then heating to 650°C. Samples were presintered to improve their handling strength after the binder removal and were then densified by HIPing using glass encapsulation.

Sample Characterization

Samples for microstructural evaluation were prepared by polishing fracture surfaces and then plasma etching using a 95% CF_4 /5% O_2 carrier gas [3]. This etching technique removes the Si_3N_4 and leaves the intergranular phases. Sintered densities were measured in deionized water using the Archimedes method.

Specimens for flexure testing were machined either to 1.5 mm x 2 mm x 25 mm or 3 mm x 4 mm x 50 mm size. Specimens were cut both parallel and perpendicular to the deposition direction. In both cases the lamination direction was parallel to the long dimension. Flexure strength was measured by four-point bending in accordance with ASTM method C1161. Hardness was measured with a Vickers diamond indenter at a load of 0.5 kg. Fracture toughness was measured by both the indentation method and the controlled flaw method.

RESULTS

By pretreating the silicon nitride powder with a suitable dispersant, we were able to prepare slurries containing silicon nitride up to 55 vol%. These slurries were photocured as thin strong films. The typical working thickness of each layer used in our multilayer deposition process was about 2 to 4 mil. The slurry composition was optimized to improve interlayer adhesion and eliminate any possible delamination during debinderization. This was achieved by reducing the layer stiffness and using additives to produce a tacky top layer. This optimization allowed us to prepare freeformed tiles, that after debinderization and densification, were found to have mechanical properties comparable with that of silicon nitride pressed samples.

After binder removal, the samples showed no blistering or discoloration and tiles prepared with the optimized slurry composition showed minimal delamination. Carbon analysis showed no residual carbon. After HIPing the samples were >98% dense, as shown in Table 1, and no evidence of the original layers was observed by SEM examination of cross-sectional surfaces of the SFF tile. Figure 2 shows representative etched surfaces for a sample prepared by the SFF method and for a tile formed by dry pressing. Both samples show a pronounced bimodal distribution of grain sizes and as is typical of *in situ* reinforced Si_3N_4 show a pronounced acicular microstructure.

Figure 3 shows two representative silicon nitride green parts, SRI and DARPA logos, that were initially selected to demonstrate the feasibility of Direct Photo Shaping to build multilayers with variable cross-section and contours.

Mechanical Properties

Table 1 summarizes the mechanical property data for tiles formed by dry pressing, thermal gel casting a monolithic tile and layered tiles formed by the solid free form method. The three forming techniques were used to assess the effect of the forming technique on the mechanical properties and to verify that the solvent and polymers could be removed without deleteriously affecting the densification and the mechanical properties. In many cases, the gelled monolithic tiles could be processed to near full density and the mechanical properties were comparable to those measured for tiles formed by dry pressing. This indicated that the organic solvents/polymers could be removed without affecting the mechanical properties of the Si_3N_4 . In some cases the monolithic samples showed lower densities and strengths than the dry pressed and layered samples; this was attributed to slight differences in the HIPing cycles which were used for these samples. The sample formed by the solid free form technique showed similar properties to the dry pressed samples with MOR values slightly in excess of 1 GPa. The flexure strengths for the layered tiles were not dependent on the orientation relative to the casting direction. Fracture toughness measured by Vickers indentation was $4.0 \text{ MPa m}^{1/2}$ for the dry pressed samples and $4.5 \text{ MPa m}^{1/2}$ for the solid freeform sample. Fracture toughness as measured by controlled indentation was slightly higher, as is typically observed, and was comparable to values previously reported on optimized slip cast material of the same composition [1].

Table 1

SUMMARY OF MECHANICAL PROPERTY DATA FOR TILES FORMED BY
UNIAXIAL PRESSING, THERMAL GELATION AND LAYER-BY-LAYER
FABRICATION METHOD

Sample	Forming	Density	Hardness	K _{IC} (MPa √m)		MOR (MPa)		Weibull parameters	
		(g/cc)	(GPa)	Indent	Indent Fracture	3x4x50 mm	1.5x2x25 mm	beta	n
C012	Press	3.22	17.0	4.0	5.9	844	937	23	30
L08	Press	3.22	15.5	4.0	6.1	832	976	24	30
L02	Gelled	3.22	NA	NA	5.2	839	NA	NA	NA
L08	Gelled	3.10	15.8	3.8	4.1	580	779	13	13
#202a	SFF	3.21	16.5	4.5	NA	NA	1018	16	15
#202b	SFF	NA	NA	NA	NA	NA	1052	25	15

Note: Specimens for 202a were cut so that the casting planes were parallel to specimen faces; specimens for 202b were cut so that the casting planes were perpendicular to the specimen faces. In both cases the lamination direction was parallel to the long dimension of the specimen.

CONCLUSIONS

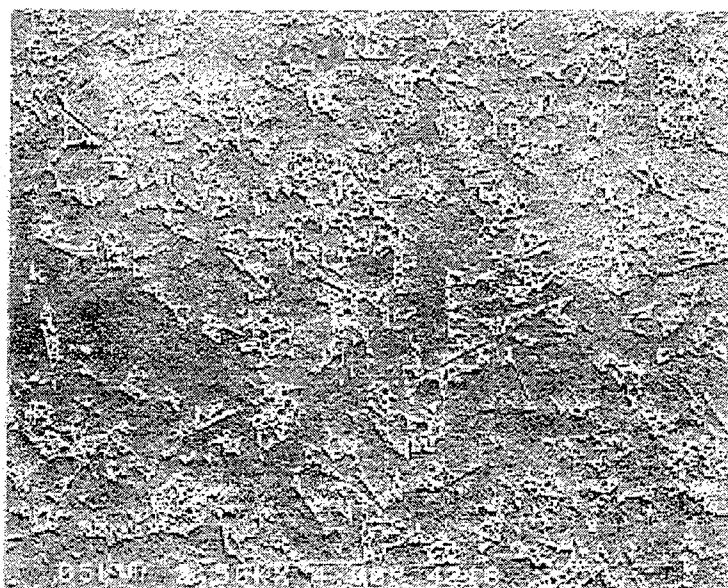
We have described a new SFF process, Direct Photo Shaping, based on the additive fabrication of layers photoimaged by a liquid crystal display (LCD) or a digital light processing (DLP) projection system. By optimizing the slurry composition we fabricated layers that adhered to each other and showed minimal delamination after removing the binder. Mechanical properties of silicon nitride tiles prepared according to the Direct Photo Shaping process were comparable to properties of tiles formed by dry pressing and were slightly in excess of 1 GPa.

ACKNOWLEDGMENTS

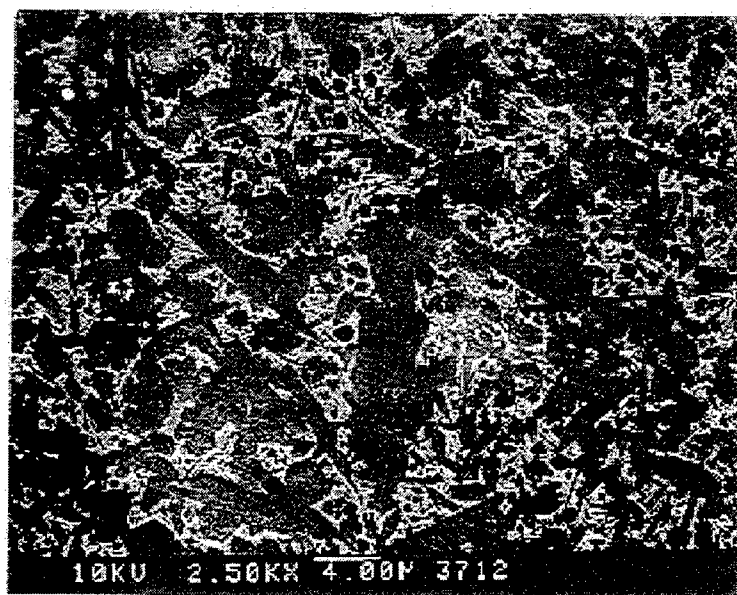
This work has been done under the support of DARPA/ONR contract No. N0001495C0019. The authors would like to thank Dr. William Coblenz of DARPA and Dr. Steven Fishman of ONR for their continuous support and valuable suggestions.

REFERENCES

1. O.O. Omatete, M.A. Janney, and R.A. Strehlow, "Gel Casting- A New Ceramic Forming Process", *Ceram. Bull.* 70(10), 1991.
2. V.K. Pujari, D.M. Tracey, M.R. Foley, N.I. Paille, P.J. Pelletier, L.C. Sales, C.A. Wilkens and R.L. Yeckley, "Reliable Ceramics for Advanced Heat Engines," *Am. Ceram. Soc. Bull.*, 74 (4), 86-90, 1995.
3. K.N. Seibein and W.M. Lovington, "Plasma Etching of Si_3N_4 "; pp 319-329 in *Microstructural Science*, vol. 16. Edited by H.J. Cialoni, M.E. Blum, G.W.E. Johnson, and G.F. VanderVoort, ASM International, Metals Park, OH, 1985.



(a)



(b)

Figure 2. Representative microstructures of (a) a sample prepared according to Direct Photo Shaping process and (b) a sample prepared by uniaxially pressing.

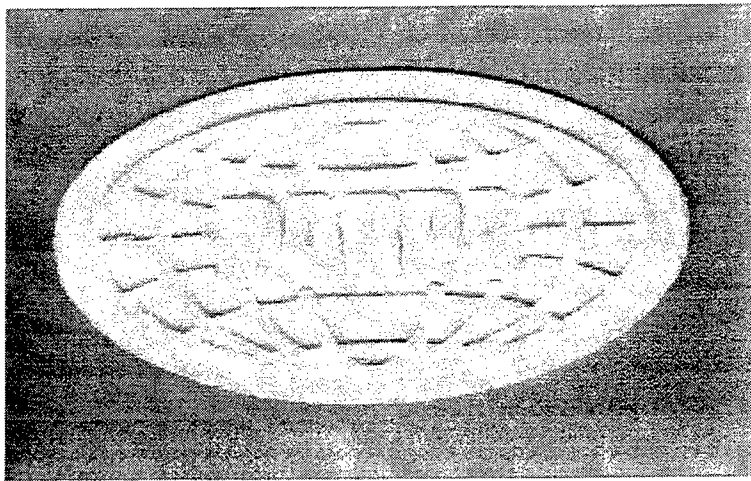
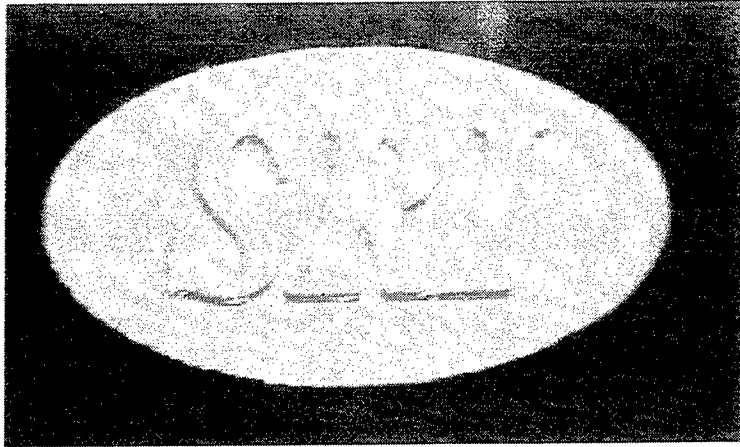


Figure 3. Representative green silicon nitride parts built by Direct Photo Shaping.

Fused Deposition of Ceramics (FDC) for Structural Silicon Nitride Components

M.K. Agarwala, A. Bandyopadhyay, R. van Weeren,

N.A. Langrana*, A. Safari, and S.C. Danforth

**Center for Ceramic Research and *Dept. of Mechanical Engineering
Rutgers - The State University, Piscataway, NJ.**

V. R. Jamalabad, P. J. Whalen, R. Donaldson, and J. Pollinger

AlliedSignal Inc., Morristown, NJ.

Fused Deposition of Ceramics is an SFF technique based on commercial FDM™ technology, for fabrication of structural and functional ceramic components. This study describes, in detail, process improvements made in pre-FDC, FDC, and post-FDC fabrication steps to achieve functional properties in commercial GS-44 silicon nitride components. Microstructural characterization of sintered FDC parts reveals microstructures similar to conventionally processed silicon nitride material. Mechanical properties of FDC processed silicon nitride bend bars and toughness samples were evaluated. These property evaluation studies demonstrate that mechanical properties similar to commercial GS-44 silicon nitride materials can be achieved using FDC. The study also describes results achieved on fabrication of complex components from silicon nitride using FDC.

I. Introduction

Most of the SFF techniques have been commercialized for fabrication of polymer and plastic parts for design verification and form and fit. Recently, some of these techniques are being explored for fabrication of structural metal and ceramic components [1]. Direct fabrication of parts and molds from metals and ceramics using the SFF techniques has created an opportunity to reduce lead times and costs in the development of new products. Such an opportunity for manufacture of new ceramic parts in a matter of days offers several advantages over conventional ceramic processing which can take weeks or months to produce the parts or complex tooling for the parts. The ability to do cost effective, iterative design using SFF techniques enables designers to create components using ceramic design guidelines from the start rather than components designed for metals. Some of these SFF techniques have been developed for ceramic part manufacture and are commercially used in production of parts [1]. One such technique called Fused Deposition of Ceramics (FDC) has been developed and demonstrated for structural ceramics [2-6]. FDC is based on an existing Fused Deposition Modeling (FDM™) technology, commercialized by Stratasys Inc., for processing of polymers and waxes [1,7,8].

Fused Deposition of Ceramics (FDC)

Fused Deposition of Ceramics (FDC) has been developed to create functional ceramic components using ceramic-polymer feedstocks [2-4]. These feedstocks are extruded into filaments of 0.070" nominal diameter, which are then used as the feed material for fabrication of three-dimensional green ceramic objects using a commercial FDM™ system, 3D Modeler™. During FDC processing, the polymer/wax acts as a carrier and binder for the ceramic particles as the material flows out of the heated extruder head. The green ceramic object thus created is then subjected to conventional binder removal and sintering processes, to produce fully dense structural ceramic components. As in the case of any manufacturing process, there are several inter-related process variables which determine the success and quality of parts fabricated by FDM™ and FDC processes. Poor control and optimization of these variables results in the presence of flaws/voids in the parts which are detrimental to the structural properties of the part.

The FDM™ process was originally designed for wax and polymer materials to serve the purposes of form and fit and positives for investment casting. Consequently, of chief importance to the end users is the external dimensional accuracy and to some extent, surface finish of the final parts. The presence of internal defects in parts built by FDM™ has not been a priority in the development of the FDM™ process. The prevention or elimination of these defects, such that ceramic components with functional engineering properties could be made by FDC, is the focus of current FDC research [5,6]. As will be shown here, structural properties have been obtained in a commercial grade silicon nitride through process control at every stage of the FDC process. Further, it is shown that it is possible to rapidly fabricate complex shaped ceramic components.

II. Development of Green Filaments for FDC

Successful FDC processing starts with fabricating filaments of $0.070'' \pm 0.001''$ diameter to be used as feed material in the FD hardware. However, for a filament material to be suitable for FD processing, it must possess certain thermal and mechanical properties [4,8]. The key variables that require careful attention and simultaneous optimization in developing the filaments for FDC processing are: viscosity and adhesion behavior of the material, and the flexural modulus and strength of the filaments. By tailoring the ceramic particle characteristics and/or binder chemistry the properties can be optimized in ways similar to that used by the ceramic injection molding industry. Based on the constraints imposed by these variables for FDC processing, a series of thermoplastic binders have been developed to enable FDC processing. These binders, called the RU series of binders, are four component systems in which the amount of each component was tailored to achieve appropriate viscosity, adhesion behavior, flexibility and stiffness in the final ceramic filament. Table I shows the four components of the RU series of binder, the role each component plays in the mixed system, and weight percent range of each component. Appropriate tailoring of these components along with the selection of a suitable surfactant for the specific particle system being used have enabled FDC processing of several ceramic systems [3].

The work reported here is based on FDC using an *in-situ* reinforced silicon nitride, referred to as GS-44*. The GS-44 powder is pre-treated with 3 weight % oleyl alcohol which serves as an appropriate dispersant for GS-44 [4]. RU9 and RU11 binder formulations were used in this study for GS-44. RU9 formulation contains 20.25% wax, 18.75% polymer, 34.5% tackifier, and 26.5% elastomer while the RU11 formulation contains 27% wax, 30% polymer, 21% tackifier, and 22% elastomer by weight. Mixing of the required amount of GS-44 powder, pre-treated with dispersant, with the binders was done using a torque rheometer mixer. GS-44/binder feedstocks containing 55 volume % GS-44 were used for FDC processing. The compounded feedstock was granulated and sieved for filament extrusion. Continuous lengths of $0.070'' \pm 0.001''$ diameter flexible filaments were fabricated using a single screw extruder and wound onto a spool [4].

III. FDC Processing

FDC processing, using commercial FDM™ systems, employs the same build strategies used in FDM™ processing of polymers. First, material is deposited as a perimeter defining the boundaries of a given layer of the part followed by raster motion of the liquefier head depositing material inside these boundaries as a series of adjacent roads. This two step strategy is repeated layer-by-layer, creating a three-dimensional green ceramic part. Therefore, any debonding between adjacent roads and adjacent layers, or incomplete filling of any regions of the part will result in property limiting defects in the final sintered ceramic parts. Strength or property limiting defects in FD processed parts have three primary causes.

* AlliedSignal Ceramic Components, Torrance, California

- Surface defects such as, surface finish, stair step formation, etc. due to limitations in the current state of all SFF technologies.
- Internal defects due to poor optimization of feed filament material, i.e. non-uniform flow rate.
- Internal defects due to current FDM™ hardware and software limitations.

Surface defects arising in FDC parts due to poor surface finish inherent to SFF processing have been eliminated via post-FDC surface finishing operations, as is a common practice in most SFF processing applications. As shown in Figure 1, the green FDC GS-44 Si₃N₄ parts fabricated using RU binders do not exhibit any delamination or any debonding between adjacent roads. Microstructurally, individual roads and layers are indistinguishable in the green state. Several internal defects were, however, observed in the early FDC processed parts. Defects arising due to poor control of filament diameter and poor FDC process optimization have been eliminated by better control of filament diameter (to ± 0.001 ") during fabrication by single screw extrusion and by optimization of FDC processing conditions. However, two key defects remained, namely, sub-perimeter voids and inter-road defects. These were largely due to limitations in the current FDM™ build strategy and FDM™ system hardware and software. Defects arising due to these limitations have also been observed in commercial FDM™ wax and polymer materials [5].

Sub-Perimeter Voids: During raster filling of a layer, voids are left due to incomplete filling at points where the raster segment turns around at the perimeter. The FDM™ system generates tool paths with sharp turns in the build file for complete filling at these locations. However, due to the constant velocity of the liquefier, the actual liquefier tool path during deposition is curved. The result of such an action is incomplete material fill at these intersections. The size and occurrence of the sub-perimeter void depends on the build conditions (road width and thickness, and liquefier head speed) and the angle between the raster line and the perimeter curve [6]. Figure 2 shows schematically how these voids are created and strategies that have been implemented to eliminate them, discussed below.

Since sub-perimeter voids are predictable and the cause of their existence is known exactly, several solutions are feasible for eliminating them. A simple way of eliminating these defects is to give a negative offset to the perimeter. This results in the liquefier head "plowing" into the perimeter during raster motion, as shown in Figure 2b, ensuring void-free parts. However, the negative offset to the perimeter needs to be optimized for each build condition such that the "plowing" action does not result in excessive flow of material at these locations. An alternative solution is to alter the tool path such that the actual tool path does not leave any unfilled regions. This approach includes extending the corners of raster segment turns, at the perimeter, closer to the perimeter [6], Figure 2c. Such a change in the tool path in the build file results in an actual tool path motion which is a closer approximation of the sharp turn rather than the curved turn. This solution of altering the path of raster segment at the intersection with the perimeter has recently been developed and implemented successfully for FDC.

Inter-Road Defects: Defects between adjacent roads (inter-road defects) can occur in one of two following forms : 1) if there is no physical contact between adjacent roads, defects will be present as voids between adjacent roads, which can be easily observed in the green state, or 2) if there is physical contact between adjacent roads but the bonding between them is not strong, then the defect between adjacent roads may be present as a weak interface. Such a weak interface is not easily observed in the green state but can cause serious damage to the structural integrity of the part during binder removal and/or sintering. These inter-road defects result from various sources.

Poor bonding between adjacent roads can arise from inconsistent material flow due to variation in filament diameter or filament slippage between rollers. This has been overcome by fabrication of filaments with controlled diameter and by optimization of the roller drive system,

respectively. Inter-road defects also arise due to excessive cooling of previously deposited adjacent roads when the road vector length is large. This is analogous to poor sintering between adjacent scan lines in SLS or print lines in 3D Printing when the vector lengths are large [1]. As done in SLS and 3D Printing, bonding between long vector length raster segments in FDC parts has been improved by providing a negative gap between roads such that the roads partially overlap. Further improvements in inter-road bonding have been made by optimizing the build environment temperature and optimization of the amount of tackifier in the binder chemistry to provide for optimum adhesion and hence bonding characteristic.

Defect Free FDC Processing: A series of square cross-section (1/2" X 1/2") bars were fabricated using a slice thickness of 0.01", road width of 0.02", negative gap between roads of 0.002" and a negative offset was provided to the perimeters to account for the sub-perimeter voids. FDC of GS-44/RU binder systems was done at 150°C-155°C at a liquefier head speed of 0.5"/second. These bars were then used for mechanical property evaluations after binder removal and sintering. Fabrication of complex components by FDC was demonstrated by fabrication of a top section of a tactical missile radome. The radome .stl file was scaled up by 20% in all three directions to accommodate the shrinkage during sintering and surface finishing operations. The file was then sliced using a slice thickness of 0.01" and then truncated in the Z-direction to obtain only the top 4.8" of the scaled-up version of the radome. The scaled-up radome had a base diameter of 3.1", wall thickness of 0.075" and an angle of inclination of approximately 72°. The green radome was fabricated in 12 hours without the need for any support structure using the same FDC conditions used for 1/2" square bars mentioned above. However, no negative gap was provided between roads as the vector lengths of raster segments were short enough to allow complete inter-road bonding. In addition to bars and radome, several other simple and complex shaped parts were fabricated, Figure 3.

IV. Binder Removal and Sintering of FDC Parts

As mentioned earlier, the RU family of binders being used for FDC are multi-component with different thermal degradation temperature ranges, Table I. For these binder systems, binder removal was done in two stages. In the first stage (room temperature to 450°C), 90 to 95 weight % of the binder was removed in a flowing nitrogen environment. During this stage, different heating rates were used in different temperature intervals to prevent surface as well as internal cracking of the samples. At low temperatures (< 200 °C), liquid binder component(s) were removed via capillary action to the surrounding setter bed material of activated charcoal, in a process called wicking. Such a loss of binder by capillary action creates surface connected internal pore channels that make further removal of binder much easier and prevents sample cracking during the process. At a higher temperature (200°C to 450°C), the remaining binder was removed by evaporation and decomposition. The residual binder (5 to 10 weight %) after the first stage, mostly present in the form of carbon, was removed in the second stage of the binder removal process by placing the sample in an alumina crucible without any setter bed and heating in air to 500 °C. The heating rate and the soaking time at different stages are dependent on the size and shape of the part. The maximum cross-section FDC samples which have been successfully processed for binder removal without any defects are currently limited to 1/2"X1/2".

The GS-44 raw material powder contains primarily α -Si₃N₄ and a small volume (<10%) of oxide sintering aids. During high temperature gas pressure sintering, these oxide additives melt and provide a liquid phase for densification of the porous compact. As densification proceeds, the α -Si₃N₄ transforms to β -Si₃N₄ through a solution-reprecipitation process. When densification is complete, the sintering aids remain in the grain boundaries as amorphous phases. Sintering of the radome section was done in a machined graphite fixture to prevent any deformation of the part.

V. Physical and Mechanical Properties

Density: The properties of green, brown, and sintered FDC square cross-section bars were compared with similar bars fabricated by extrusion of GS-44 bars with the same binder chemistry used for FDC. Binder removal and sintering procedures for extruded bars were the same as those for FDC parts. Iso-pressed GS-44 samples were used as control samples for property comparison with FDC and extruded samples, since iso-pressing of GS-44 is a conventional manufacturing approach for GS-44 silicon nitride components. Bulk densities of green FDC parts initially were 85%-90% due to internal build defects arising from FDM™ build strategy, discussed earlier. After implementation of novel strategies to eliminate the FDM™ related build defects, the bulk densities of green FDC parts were consistently greater than 96%. As shown in Table II, the sintered densities of FDC samples, after implementation of strategies to eliminate build defects, were comparable to those of extruded and iso-pressed samples.

Shrinkage: Shrinkage measurements in FDC samples were made to detect anisotropy between the build plane (X-Y plane) and the build direction (Z axis). Significant anisotropic shrinkage behavior is commonly observed in parts fabricated by SFF techniques where the shrinkage is greater in the build direction than in the build plane [1]. In the FDC samples in this study, a similar anisotropic shrinkage behavior was observed between the build direction and the build plane. Before elimination of FDM™ related build defects, the linear sintering shrinkage in the build plane was 12-15% while that in the build direction was 17-20%. However, after implementation of the defect eliminating strategies, this anisotropy in shrinkage has been reduced with average build plane shrinkage of $16.6 \pm 1.3\%$ and the build direction shrinkage of $19.3 \pm 1.6\%$. It has been observed that the degree of anisotropy in shrinkage is directly related to the total defect population in the parts. Parts with low defect population exhibit a smaller degree of anisotropy in shrinkage compared to parts with higher defect population, since most of the defects typically exist between layers. Therefore, as the defect population decreases, the parts' greater isotropy in the green state translates to more isotropic shrinkage upon sintering. Sintered samples with densities greater than 98% theoretical density show a difference of 2-3% in shrinkage between the build direction and build plane, which is far less than reported by other SFF techniques, suggesting a more uniform microstructure in FDC processed green parts.

Mechanical Property: ASTM MilSpec B 4-point bend tests were conducted on samples machined from extruded, FDC and iso-pressed GS-44 bars. As shown in Table II, average bend strengths of 824 ± 110 MPa measured for FDC samples are comparable to those for extruded and iso-pressed samples. Three point bend test were also carried out with indented samples where an indentation was created by applying a 20 Kg load using a Vickers indenter on the tensile surface of the sample. This test gives a qualitative idea of the fracture toughness of the samples where a higher failure strength indicates a higher fracture toughness. As shown in Table II, average indented failure strengths indicate similar fracture toughness behavior for FDC, extruded and iso-pressed samples.

Microstructure: Sintered FDC parts were observed under optical and scanning electron microscopes (SEM) to evaluate the microstructures for the following : (a) FDC build related defects, (b) delamination during binder removal and sintering, (c) evidence of road and layerwise build strategies, and (d) GS-44 Si₃N₄ microstructure. Figure 4 shows SEM fractographs of FDC and iso-pressed samples tested under indented three point bend loading. Although some FD defects can be observed on the fracture surfaces of FDC samples, they didn't have a significant effect on the failure strength. Other than a few FD related defects, the fracture surfaces of conventionally and FDC processed samples appear similar. The microstructures in the directions perpendicular and parallel to build direction were similar. Individual roads and layers were indistinguishable. There were no discernible signs of layerwise fabrication.

As shown in Figure 5, the sintered FDC radome section maintained its overall conical shape and straight sides with a sintered angle of inclination of 71°. The sintered wall thickness was 0.065" accounting for 13.3% linear shrinkage in X-Y build plane. The sintered base diameter was 2.6" leading to measured shrinkage in the diameter at base of 16.1%. The shrinkage in build direction (Z) of 20.8% was slightly greater than expected shrinkage of 20%, with the final vertical height of 3.8". Although, the density of the radome was measured to be greater than 98% of theoretical density of GS-44, several defects were observed on the surface and internally, detected using X-ray radiography. Most of these defects were primarily due to the FD build approach used.

VI. Conclusions

GS-44 silicon nitride parts have been formed using a new method, Fused Deposition of Ceramics, FDC. Simple and complex shapes have been produced with high green density after most of the FDC build defects were eliminated. The process has been developed to produce green parts with largely defect-free internal microstructures. It has been demonstrated that FDC green parts can have the binder removed and be sintered to densities and strengths comparable to those produced by conventional ceramic processing approaches. Development of such a process as FDC will enable ceramic design engineers to rapidly fabricate complex shapes and verify the design for not only form and fit but also for performance.

Acknowledgments

This work has been done under the support of DARPA/ONR contract No. N00014-94-0115. The authors would like to thank Dr. Clifford P. Ballard of AlliedSignal Research and Technology; Mr. William R. Priedeman and Jim Comb of Stratasys Inc., and Mr. Ron Knight and Joe Wright of Lockheed Martin Inc., for their support and help in this work.

References

1. Proceedings of the Solid Freeform Fabrication Symposium, Vol. 1990, 1991, 1992, 1993, 1994, 1995, Edited by H.L. Marcus, J.J. Beaman, J.W. Barlow, D.L. Bourell, and R.H. Crawford, The University of Texas at Austin, Austin, Texas.
2. M.K. Agarwala, et. al., "Structural Ceramics by Fused Deposition of Ceramics," *ibid.*, Reference #1, Vol. 6, 1995, pp.1-8.
3. M.K. Agarwala, et. al., "Fused Deposition of Ceramics and Metals: An Overview," *ibid.*, Reference #1, Vol. 7, 1996.
4. M.K. Agarwala, et. al., "Filament Feed Material for Fused Deposition Processing of Ceramics and Metals," *ibid.*, Reference #1, Vol. 7, 1996.
5. R. van Weeren, et. al., "Quality of Parts Processed by Fused Deposition," *ibid.*, Reference #1, Vol. 6, 1995, pp. 314-321.
6. V. Jamalabad, M.K. Agarwala, N. Langrana, and S.C. Danforth, "Process Improvements in the Fused Deposition of Ceramics (FDC) : Progress Towards Structurally Sound Components," Proc. of the ASME Design for Manufacturing Conf., Aug. 1996, Irvine, CA.
7. U.S. Patent # 5,121,329, June , 1992.
8. J.W. Comb and W.R. Priedeman, "Control Parameters and Material Selection Criteria for Rapid Prototyping Systems," *ibid.*, Reference #1, Vol. 1993, pp. 86-91.

TABLE I
Binder Components in the RU Series of Binders

Binder Component	Weight % Range	Component Role	Thermal Degradation Temperature Range
Polymer	10 - 45	Acts as a backbone	100 - 510 °C
Elastomer	30 - 65	Imparts flexibility	275 - 500 °C
Wax	15 - 50	Viscosity modulator	200 - 500 °C
Tackifier	10 - 40	Promotes adhesion	190 - 475 °C

TABLE II
Physical and Mechanical Properties of GS-44 Parts Processed via Isopressing, Extrusion and FDC

Properties	Isopressed	Extruded	FDC
Green Density*	57%	> 98%	> 96%
Sintered Density (% Theoretical)	> 99%	> 99%	> 98%
Linear Shrinkage	16% in all directions	18% in all directions	X-Y: $16.6 \pm 1.3\%$ Z: $19.3 \pm 1.6\%$
4-Point Bend Strength (MPa)	867 ± 50	820 ± 150	824 ± 110
Vickers Indented 3-Point Bend Strength (MPa)	365 ± 5	345 ± 10	354 ± 10

* Iso-pressed green density refers to bulk density of iso-pressed GS-44 without binder. Green densities of extruded and FDC samples correspond to bulk density of samples from 45 volume % RU binder and 55 volume % GS-44 mix. Therefore, GS-44 bulk densities in extruded and FDC samples are >54% and >53%, respectively.

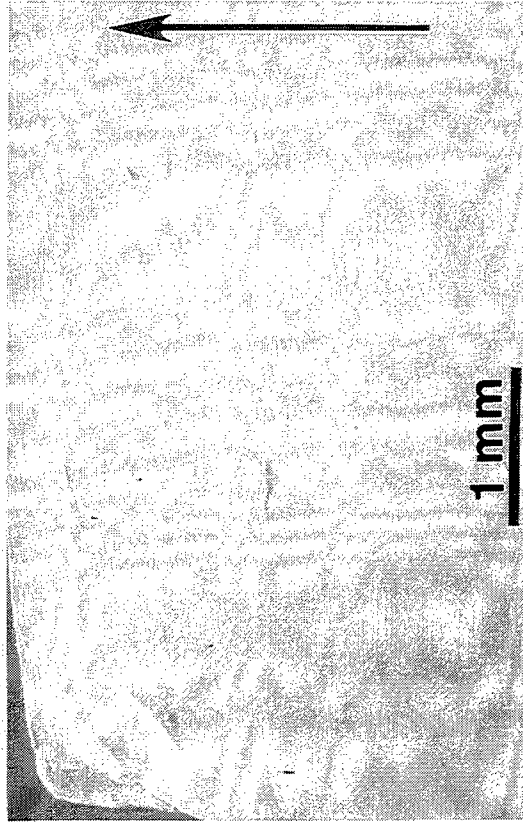


Figure 1: SEM micrograph of a cross section of a green FDC GS-44 part showing no delamination or debonding between adjacent roads and layers (arrow indicates the build direction).

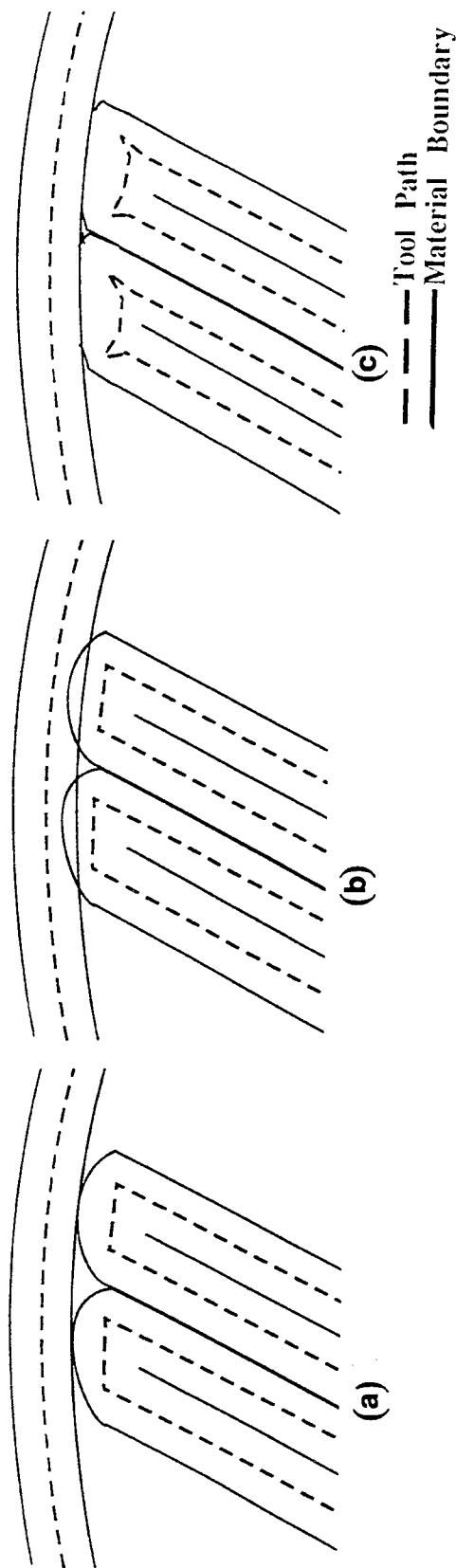


Figure 2: Schematics of raster fill patterns (a) as used in the FDM™ systems showing sub-perimeter voids at the perimeter and raster fill line intersection, (b) with a negative offset for the perimeter showing "plowing" of the raster segment into the perimeter and minimization of the sub-perimeter void, and (c) with altered tool path at the turns near the perimeter showing minimization of the sub-perimeter void.



Figure 3: Simple and complex green GS-44 parts, including two tactical missile radome sections, fabricated by FDC processing without the need for build support structures.

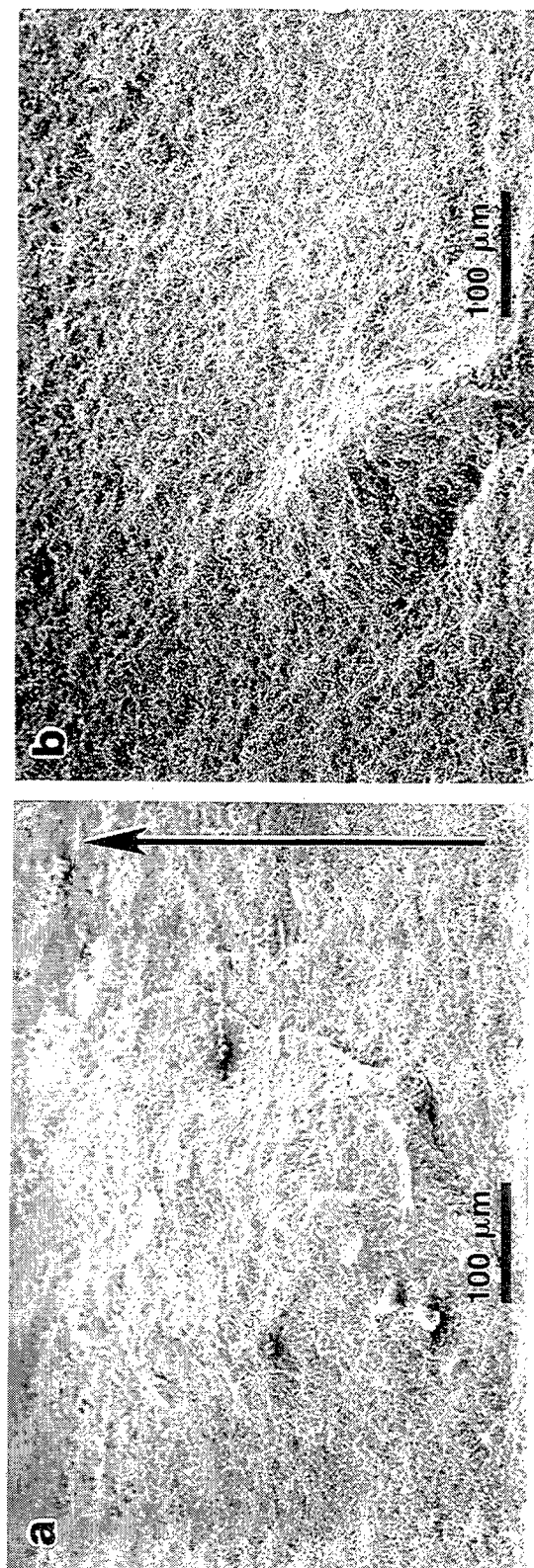


Figure 4: SEM fractographs of indented 3-point bend samples fabricated by (a) FDC (arrow indicates the build direction) and (b) iso-pressing.

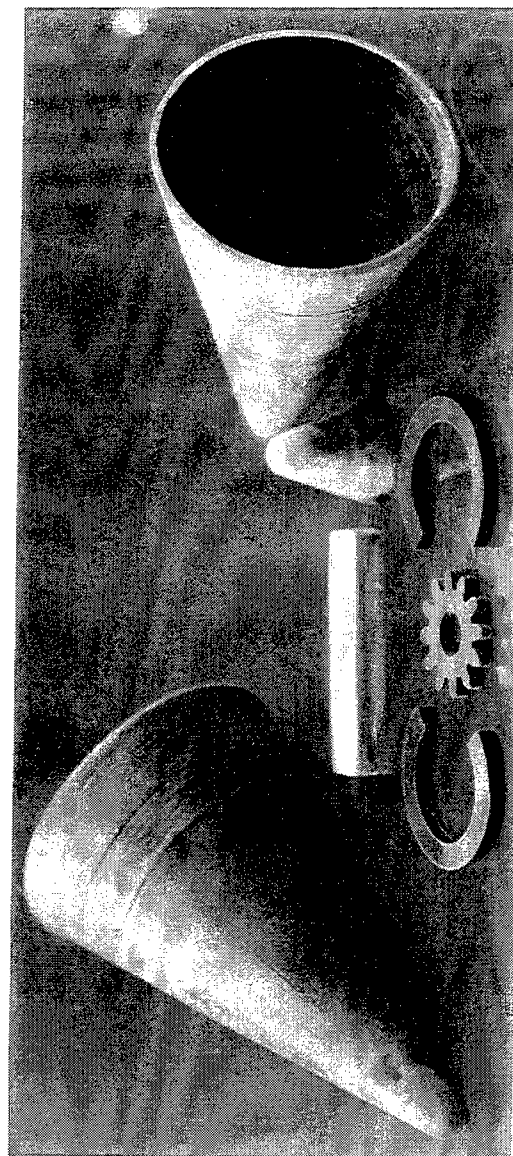


Figure 5: Sintered FDC GS-44 samples, including two tactical missile radome sections.

Solid Freeform Fabrication at The University of Connecticut

by Shay Harrison, James E. Crocker, Tariq Manzur, and Harris L. Marcus

Institute of Materials Science
University of Connecticut
Storrs, CT 06269-3136

Abstract

Gas phase solid freeform fabrication research at The University of Connecticut focuses on two main procedures, Selective Area Laser Deposition (SALD) and Selective Area Laser Deposition Vapor Infiltration (SALDVI). A SFF research laboratory is under construction at UCONN, with two new operation systems. These systems possess temperature control, data acquisition capabilities, *in-situ* video monitoring, and the ability to fabricate SALDVI parts up to four inches wide by four inches long. The procurement of a harmonic generating Nd:YAG six watt laser, capable of producing output at 532, 355, and 266 nanometer wavelengths, as well as a coupled effort with the Photonics Center at the University providing laser diodes at a variety of wavelengths, presents the opportunity to explore interactions involved in gas reactions driven by lasers. Investigations of material systems will include ceramic carbides, nitrides, and their composites, as well as metals.

Selective Area Laser Deposition (SALD)

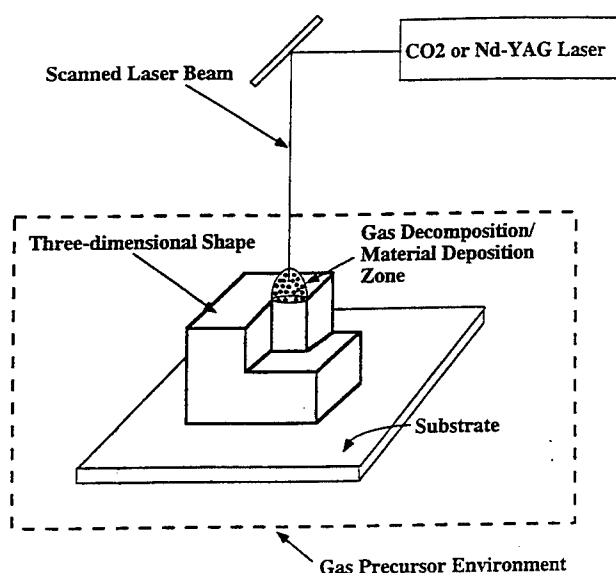
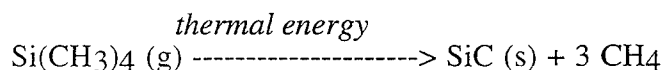


Figure 1--Schematic of SALD

Introduction

SALD¹⁻⁴ and SALDVI⁵ are two gas phase SFF techniques that utilize local chemical vapor deposition (CVD) to create shapes and structures in an additive manner. Both form solid deposition products from the decomposition of gas precursors by a laser beam in an environmentally controlled vacuum chamber. Because the decomposition is localized around the beam spot area, the size and shape of the solid reaction product can be manipulated by computer-operated scanning of the laser beam. The differences between the two procedures involve the interplay between the solid product and the substrate upon which deposition takes place. SALD merely uses the substrate as a base for beginning deposition on, and shapes are created from consecutively scanned layers. In SALDVI, the solid product infiltrates a thin layer of powder at the substrate, filling the porous spaces between powder particles. Once a powder layer has been scanned and infiltrated, a fresh powder layer is spread out over the previous one and the infiltration process begins again. Figures 1 and 2 represent the SALD and SALDVI processes, respectively. An example where SALD and SALDVI has been performed is with tetramethylsilane as the gas precursor for silicon carbide deposition, according to the following equation:



(g)

where carbon is also unintentionally deposited by decomposition of the methane by-product.

SFF Laboratory

At present, the SFF laboratory entails two systems, a larger 15 inch tall by 28 inch diameter water-jacketed, stainless steel vacuum chamber and a smaller 8 inch tall by 8 inch diameter stainless steel vacuum chamber. The larger 15 inch tall system encloses a powder delivery system (PDS) for performing SALDVI experiments. The smaller chamber is used for SALD experiments. The main components of the PDS are a supply piston, a target piston, a roller, and three motors with encoders. The roller spreads a controlled amount of powder from the supply piston to the target piston when cued by the computer. Shapes up to 4 inches by 4 inches in size can be fabricated in this system. Each system has a custom built laser stand capable of supporting any one of the lab's three lasers: a 50W CO₂ (10.64 μm wavelength), a 150W Nd:YAG (1.06 μm wavelength), and a harmonic generating Nd:YAG with a 6W output at the primary 1.06 μm wavelength, as well as various diode lasers. Two computer controlled -xy stages provide the motion to generate the 2-D scan in each layer. In the larger system, the chamber and the laser are stationary, and the stage moves the laser beam by translating the optics. The smaller chamber rests on the -xy stage and moves under a stationary laser beam. An optical pyrometer based on a two head design with a range from 200 to 1500°C monitors the deposition temperature and also provides feedback for closed loop temperature control by adjusting the laser power. A video camera provides *in-situ* visual monitoring and recording of the deposition process. A gas delivery manifold delivers multiple gas precursors to the reaction chambers, operating presently in a static gas mode. A photograph of the large system and hood is found in Figure 3.

SALDVI of Silicon Carbide/Silicon Carbide Composite Shapes

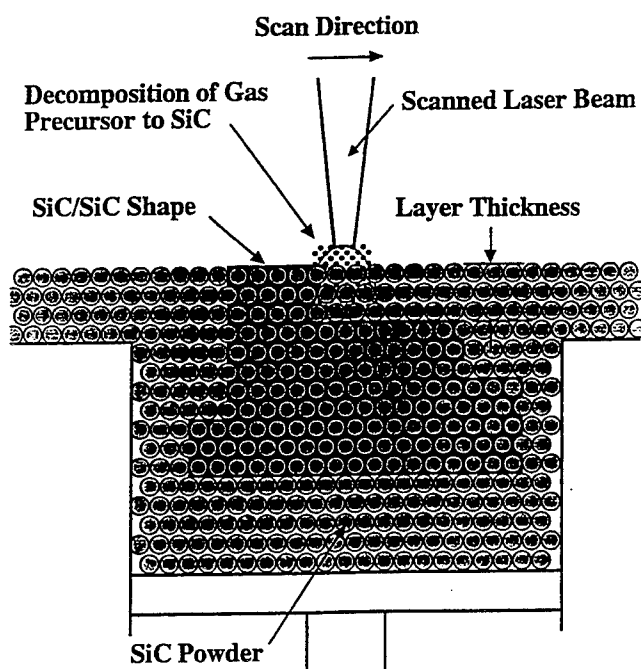


Figure 2--Schematic of SALD

Experiments

To demonstrate the laser scanning capability of the larger system, two shapes were deposited using the SALD process. Two different scanning programs produced silicon carbide deposits in the shapes of a disc and a rectangle. The operating conditions for deposition included 12.5 watts of power from a CO₂ laser, a 2 millimeter diameter beam spot, 75 torr of tetramethylsilane gas precursor, and an approximate scan speed of 1 millimeter per second. Each scanning program was repeated ten times to yield multilayer deposits. Figure 4 presents a 500 X magnification SEM micrograph of the 10 layer rectangular scan sample. Based on an estimated laser spot dwell time of 6 seconds at points in the layer, a growth rate of 50 microns per minute was calculated. This growth rate calculation assumes an adequate deposition temperature (*hot spot*) across the entire 2 millimeter diameter laser beam, with a roughly circular beam shape.

A third SALD deposit was produced using the novel approach of a diode laser for the energy source. This diode laser is a McDonnell Douglas #ISO-550, operating at 808 nanometers and producing 50 watts continuous wave(cw) and 600 watts pulsed maximum output. The diode laser experiment, run under a static motion condition, produced a circular deposit with some infiltration into the powder substrate. The growth parameters included 15 watts cw laser power for 5 minutes, 75 torr of tetramethylsilane gas precursor, and an approximate 5 millimeter beam spot diameter with a gaussian distribution.

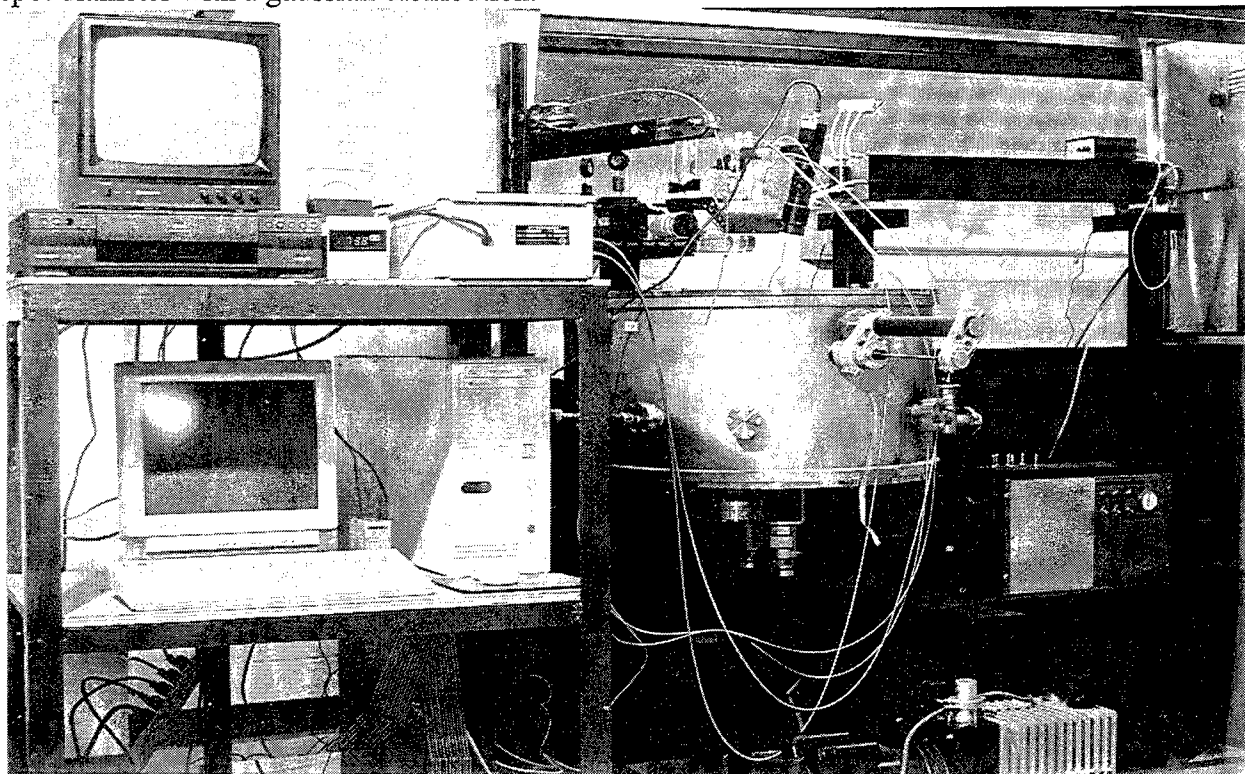


Figure 3--Workstation in SFF Lab at UCONN

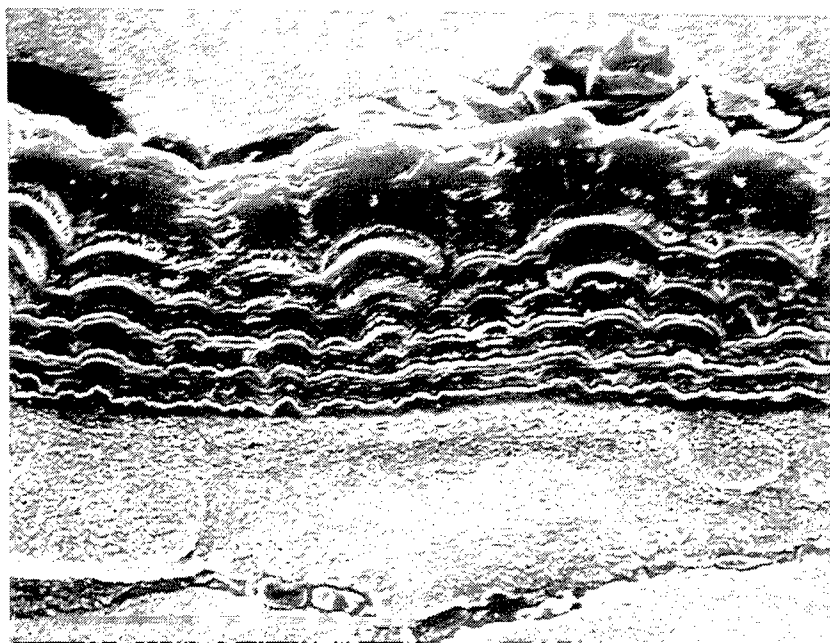


Figure 4--SEM micrograph of 10 layer SiC SALD deposit

Future Work

A variety of experimental areas in the SALD and SALDVI arena will be addressed. The control of the composition of material deposition will be a major factor in the silicon carbide foundry concept. The goal of the foundry is to deposit silicon carbide with *in-situ* electromechanical devices. Other investigations will focus on the role of laser wavelength in the gas precursor decomposition. Attempts will be made to couple certain laser wavelengths to specific material system excitations in order to produce partial photolytic, partial thermal decomposition mechanisms. Finally, efforts to work with different material systems will involve boron nitride, using boron tribromide and boron trichloride precursors, and metals such as titanium and cobalt, along with various ceramic/ceramic and ceramic/metal composites.

Conclusions

The Solid Freeform Fabrication laboratory at The University of Connecticut has been under assembly and construction for much of the past year. Experimental work in gas-phase SFF recently began, and emphasis will be placed on the SALD and SALDVI processes. Process parameters, process interactions, and a variety of material systems will be under investigation under a closed loop, feedback controlled system. The SFF program at UCONN maintains a World Wide Web site at: <http://www.ims.uconn.edu/~hmarcus>.

Acknowledgments

The authors would like to gratefully acknowledge the support of the Office of Naval Research, grant #N00014-95-1-0978, and the Institute of Materials Science and the Photonics Research Center at The University of Connecticut.

References

1. G. -S. Zong, R. Carnes, H. G. Wheat, and H. L. Marcus, "Solid Freeform Fabrication by Selective Area Laser Deposition", Proceedings of the Solid Freeform Fabrication Symposium, edited by Joseph J. Beaman, Harris L. Marcus, David L. Bourell, and Joel W. Barlow, The University of Texas at Austin, Austin, Texas, August 6-8, 1990, pp. 83-90.
2. J. L. Maxwell, J. Pegna, and A. G. Ostrogorsky, "Thermal Analysis and Modeling of Steady-State Rod Growth During Gas-Phase Solid Freeform Fabrication", Proceedings of the Solid Freeform Fabrication Symposium, edited by Harris L. Marcus, Joseph J. Beaman, Joel W. Barlow, David L. Bourell, and Richard H. Crawford, The University of Texas at Austin, Austin, Texas, August 9-11, 1993, pp. 253-270.
3. F. T. Wallenberger and P. C. Nordine, "Strong, Pure, and Uniform Carbon Fibers Obtained Directly from the Vapor Phase", *Science*, vol. 260, pp. 66-68, 2 Apr. 1993.
4. O. Lehmann and M. Stuke, "Laser-driven Measurement of Three-dimensional Microstructures Generated by Laser Rapid Prototyping", *Science*, vol. 270, pp. 1644-1646, 8 Dec. 1995.
5. B. R. Birmingham and H. L. Marcus, "Silicon Carbide Shapes by Selective Area Laser Deposition Vapor Infiltration", Proceedings of the Solid Freeform Fabrication Symposium, edited by Harris L. Marcus, Joseph J. Beaman, Joel W. Barlow, David L. Bourell, and Richard H. Crawford, The University of Texas at Austin, Austin, Texas, August 8-10, 1994, pp. 348-355.

Metal Processing Using Selective Laser Sintering and Hot Isostatic Pressing (SLS/HIP)

**Ronald Knight and Joseph Wright
Lockheed Martin Vought Systems**

**Joseph Beaman
The University of Texas at Austin**

**Douglas Freitag
Bayside Materials Technology**

ABSTRACT

In July of 1995 the Office of Naval Research (ONR) awarded a contract to Loral Vought Systems entitled Low Cost Metal Processing Using SLS/HIP. The two-phase, four-year program is co-sponsored by ONR and the Defense Advanced Research Projects Agency, DARPA. The program addresses the DoD and Navy need to improve the reprocurment, remanufacture and repair methodology for high value metal parts. The specific program objective is to develop and demonstrate Selective Laser Sintering (SLS) as a lower cost, flexible and faster method of fabricating spare and replacement, small/medium sized powder metal parts for DoD weapon systems. Current activity is focused on development of a high temperature SLS workstation and on selective laser sintering trials on candidate metal powders including Inconel, molybdenum and titanium.

SLS Background

Selective Laser Sintering (SLS) was conceived in the mid-1980's by staff of the University of Texas as a method for rapidly prototyping solid, functional parts without part specific tooling. SLS converts heat-fusible powders into solid objects by using a laser beam to melt and fuse the powder particles together. The laser is rastered across the powder bed using scanning mirrors which are servo-driven from 3-D CAD data which describes the part to be fabricated. SLS is an additive layer process in which the part is built up in layers approximately 0.005 inches thick. The powder bed provides the support for the part build so that no tooling is needed. SLS is one of the most versatile rapid prototyping methods in that it is applicable to plastics, ceramics, and metal powders. The SLS process has been commercialized for making plastic parts and metal tools by the DTM Corporation of Austin, Texas.

Our Concept

The Department of Defense has a large number of high value metal parts in service which are produced by hot isostatic pressing. HIP metal parts typically require powder encapsulation in a can or skin, which must be removed after HIPing. This canning and can removal operations are

a large contributor to the cost of HIP parts while limiting their complexity. Our technical concept is to use the SLS process to form the integral metal skin which is required for encapsulation of powder metal parts prior to hot isostatic pressing (HIP). Typically the encapsulation skin is a sacrificial layer of a different material which must be removed after the HIP cycle. Our concept is to SLS form the skin integral with the HIP part using the same powder material, as illustrated in Figure 1. In this way the skin becomes the outer surface of the HIP part and does not have to

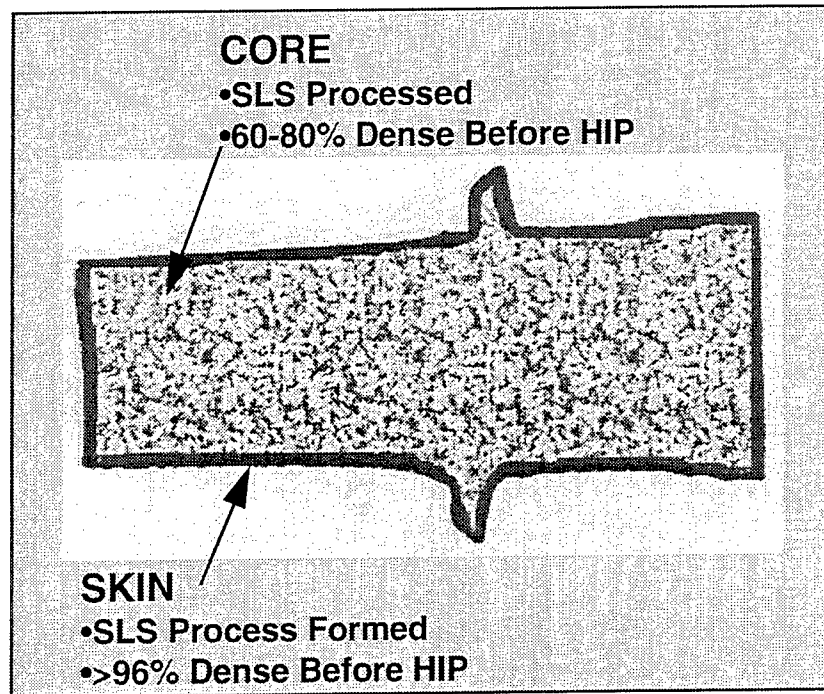


Figure 1 Selective Laser Sintering Concept for Powder Metal HIP Parts

be removed. SLS will be used to liquid phase sinter the powder metal, forming a fully dense skin integral with the core part which has been SLS processed to approximately 70% dense.

To execute the program the following team members have joined forces:

- Lockheed Martin Vought Systems: Prime contractor and responsible for HIP technology development and test and evaluation
- The University of Texas at Austin: SLS equipment development, process development and process modeling.
- Bayside Materials Technology: Economic analyses and component selection trade studies
- MATSYS: HIP process modeling
- DTM Corporation: SLS beta machine development

Program Phases

As shown in Figure 2 the program is structured into 2 phases: Phase 1, SLS/HIP Materials & Process Development, and Phase 2, SLS Beta Machine Development. Phase 1 objective is to develop the materials and processing science to produce functional metal parts

using SLS with integrated canning and HIP post processing. Key technical issues being addressed in Phase 1 include: impermeability of the SLS skin; wetting of the metal powders and the resulting density; part properties equivalent to baseline; dimensional tolerances and surface finish. The Phase 2 objective is to validate the performance and commercial viability of the high temperature SLS process through demonstration of an high temperature SLS beta test machine.

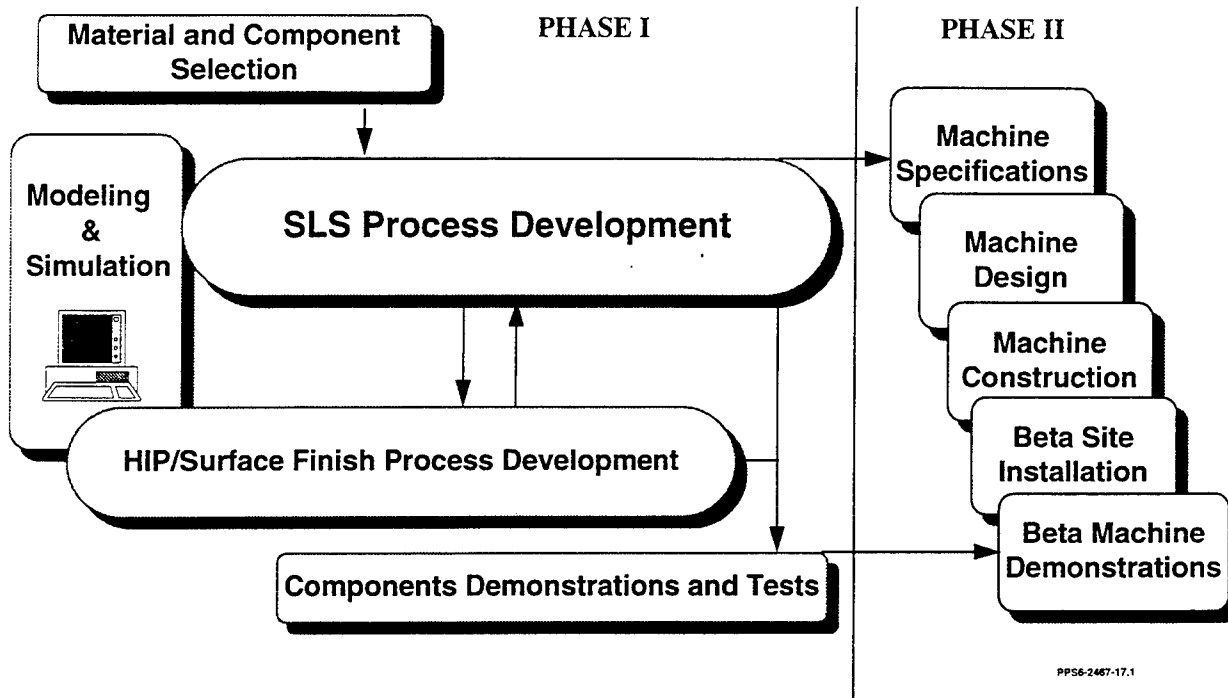


Figure 2 SLS/HIP Program Task Flow Diagram

Current Status:

The initial program task is to select two materials and components on which to demonstrate the SLS technology. To this end a comprehensive survey of Navy installations and Lockheed Martin Vought Systems products is being conducted. From the initial survey candidate materials are being identified for SLS screening trials to aid in downselecting the materials and components to demonstrate. The survey criteria is: sinterable powder metal parts with complex geometry, that can be SLS processed in our current 7 inch by 7 inch processing chamber. We are nearing completion of our survey of Naval installations (depots, centers, shipyards, etc.) to identify demonstration components and materials. We have completed the survey of Lockheed Martin Vought Systems programs to identify candidate demonstration components. To date, based on our survey, the four leading materials/component candidates are:

- Inconel 625 super alloy for an aircraft engine vane
- Molybdenum rotary valve for the MK-46 torpedo
- Titanium guidance section housing for the AIM-9 air-launched tactical missile.
- Stainless steel detent link assembly for an ATACMS ground based missile launcher.

These component are shown in Figure 3.

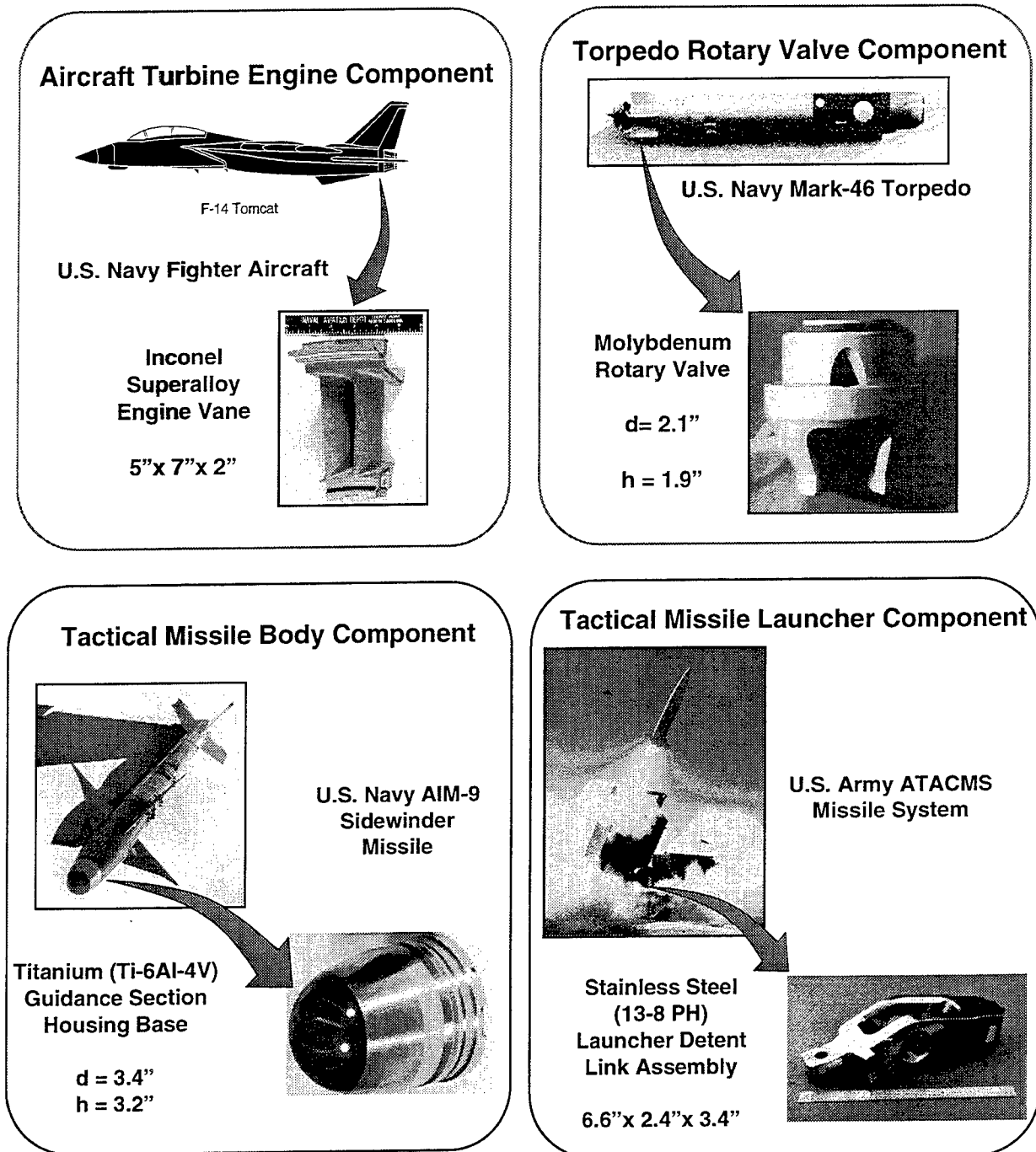
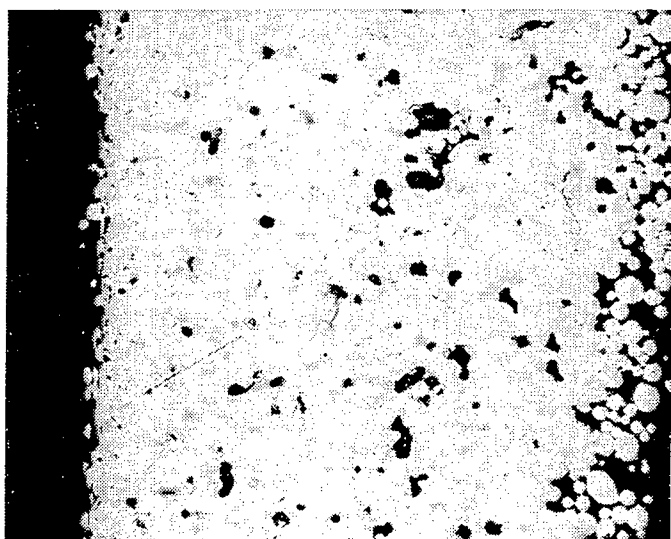


Figure 3 Candidate Demonstration Components and Materials

In preparation for the powder metal SLS screening trials The University of Texas has modified their high temperature SLS workstation with atmosphere controls and laser systems for processing the high temperature powder metals.. The laser scanning control software has been written and validated. Powder metal SLS processing trials are currently underway. Materials processed in the on-going SLS trials include Inconel 625 superalloy, Stainless Steel 17-4PH,

Titanium Ti-6Al-4V, and Molybdenum. Fully dense single layer coupons of Inconel 625 were produced by SLS. The single layers of Inconel 625 were leak tested and shown to have a leak rate of less than 10^{-10} atmospheric cc/s, thereby meeting the criterion for HIP post-processing. Multi-layer coupons of Inconel 625 processed by SLS showed closed porosity at the interface layer, meeting the requirement for HIP processing. Initial SLS trials on single layer coupons of 17-4PH stainless steel indicate a nearly fully dense microstructure with closed porosity. Preliminary trials on titanium and molybdenum have demonstrated that these materials can be melted by SLS processing. Research is underway to produce an integrally canned volume of Inconel 625 by direct SLS for HIP post processing.



Inconel 625 Single Layer

Nd:YAG laser power: 31 Watts

Scan speed: 0.7 in/sec

Figure 4 Photomicrograph of SLS Processed Inconel Skin

ACKNOWLEDGEMENTS

This research is being conducted under sponsorship of the Office of Naval Research and the Defense Advanced Research Projects Agency via contract N00014-95-C-0139.

Progress in Computer-Aided Manufacturing of Laminated Engineering Materials Utilizing Thick, Tangent-Cut Layers

Yong Zheng¹, Sangeun Choi², Brian Mathewson³, and Wyatt Newman⁴

Abstract

This paper presents recent progress in extending the CAM-LEM process to 5-axis laser cutting for fabrication of laminated engineering components directly from sheet materials. The present extensions enable construction of layered objects from thicker layers by cutting all layers with shaped edges. Use of thicker material layers offers the opportunity for faster build rates and/or improved surface finish. We describe our system and present initial experimental results in utilizing tangent-cut layers for object fabrication. Utilizing surface-tangent information introduces new computational complexities in converting CAD descriptions into machine process control commands. We present an algorithm for achieving this conversion, and we illustrate its successful performance.

1 Introduction

CAM-LEM is a Solid Freeform Fabrication process under development through a joint project between Case Western Reserve University and CAM-LEM, Inc. [1,2]. In this process, as is common to all SFF technologies, each part originates from a computer description, which is analyzed and decomposed into boundary contours of thin slices. In CAM-LEM, these individual slices are laser cut from green sheet stock per the computed contours. The resulting part-slice regions are extracted from the sheet stock and stacked to assemble a physical 3-D realization of the original CAD description. The assembly operation includes a lamination procedure that fixes the position of each sheet relative to the preexisting stack and achieves intimate interlayer contact, promoting high-integrity bonding in the subsequent sintering operation. The laminated green object that has been rendered monolithic is then fired to densify the object and control microstructural evolution. The result is a 3-D part which exhibits not only correct geometric form, but functional behavior as well.

One of the problems inherent in all layered manufacturing processes is the stair-cased surface finish resulting from discretization of layers in the build direction. This stair-cased surface finish can be reduced by minimizing the thickness of each layer, but at the expense of fabrication speed. Until now, little effort has been made to interpolate the surface in the build direction.

In [3] we introduced the kinematic theory for a tangential cutting version of the CAM-LEM system; this paper presents recent progress in developing the system described. We have constructed a 5-axis cutting table platform that allows us to laser cut boundary edges tangential to

¹ Department of Electrical Engineering and Applied Physics, Case Western Reserve University.

² Department of Mechanical Engineering, Case Western Reserve University.

³ CAM-LEM, Inc., Cleveland, Ohio, 44108.

⁴ Associate Professor, Department of Electrical Engineering and Applied Physics, Case Western Reserve University, Cleveland, Ohio, 44106.

the physical model surface. Tangential cutting enables us to approximate the edge surface with first-order interpolation in the vertical direction, thus eliminating the stair-cased characteristic found in parts made using other RP/SFF technologies.

Several aspects of this approach are discussed here: a description of the hardware used in the system; some initial experimental results in object building with tangent-cut thick layers, and an improved algorithm for generating machine-control commands for tangent cutting from a model's CAD description.

2 Five-axis Tangential Cutting System

The CAM-LEM tangential cutting system, shown in Figure 2.1, is designed to cut successive layers of a part derived from a CAD model description out of sheet material. The system is comprised of three major components: a laser for cutting; a 5-axis cutting table platform for translating and orienting the sheet material relative to the laser; and a material handling robot. The laser is mounted vertically above the 5-axis cutting table. A 4-axis rectilinear robot (to left, not shown) is positioned in front of a platform for loading/unloading sheet material and for selectively gripping and stacking cut contours.

Our 5-axis system consists of 3 translational axes (x,y,z) and two rotational axes (roll and pitch) that position and orient a 6"x 6" cutting table beneath the laser. Sheet material is clamped to the cutting table with vacuum pressure exerted through aluminum honeycomb cells. The cutting table is mounted with an offset 77.5 mm above the intersection of the two rotary axes to maximize clearance with the laser. To achieve the required positions and orientations for cutting the desired tangents about the boundary of a part slice, motion of the x and y axes must be coordinated with the roll and pitch angles of the cutting table. Vertical (z-axis) motion is incorporated in order to keep the material at the laser focal point, at which air ejected from a nozzle helps remove debris and assist cutting.

The maximum orientation angle of the cutting table surface is constrained by the clearance of the laser nozzle such that the pitch and roll axes are limited to ± 73 degrees of motion from vertical during cutting.

Experimental evaluation of the tangential-cutting capability of our system is shown in figures 2.2 and 2.3. Figure 2.2 shows a cross



Fig. 2.1: Five-axis tangential cutting system

section of angled cuts made with our system in a sheet of 6mm polystyrene foam. The material was initially oriented such that the laser beam was normal to the material surface. A series of 9 straight 30-mm lines was cut in the material, with the horizontal position increased 7.5mm and the angle increased 9 degrees each step. The final cutting angle tested was 72 degrees. At this final angle, the material thickness cut was 3.2 times deeper than that at normal. As shown, laser cuts in this material were uniform, straight and clean. We are currently investigating angled laser cutting effectiveness in alternative materials, including tape-cast ceramics.

Figure 2.3 shows an additional test in which the potential value of laser cutting is illustrated. This figure shows two 100-mm diameter spheres constructed from layers of 6mm Styrofoam.

On the left, the sphere is approximated with 14 layers of circular cross section and vertical edges. Poor surface approximation is obvious (particularly in regions where the object's tangent plane is nearly horizontal) due to the exaggerated step size of vertical discretization corresponding to thick layers. The sphere on the right in Fig. 2.3 is comprised of 14 tangent-cut layers, each a frustum of a cone. The first and last layers shown required a tangent angle of 55 degrees from vertical. (The top and bottom layers of the sphere are missing, as the required tangent angle of 75 degrees exceeded our system's limit of 73 degrees imposed by kinematic interference.) It is apparent that the tangent-cut thick slices produce a dramatically better surface approximation than normal-cut slices.

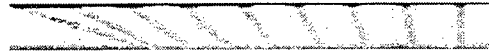


Fig. 2.2: Tangent-cut tests in 6mm polystyrene foam

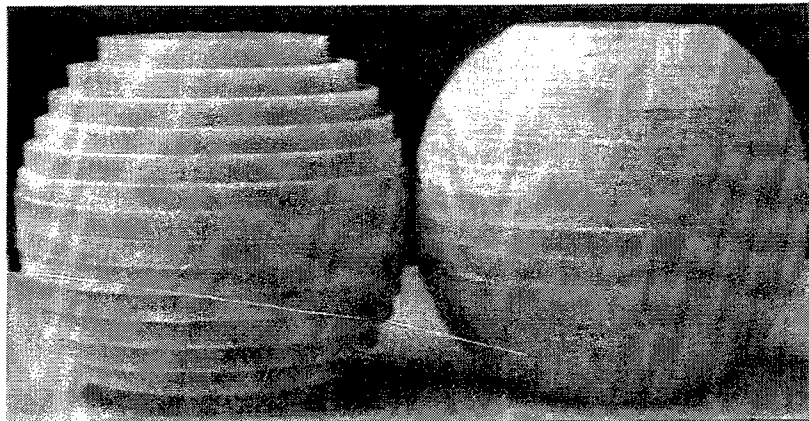


Fig. 2.3: Styrofoam spheres without and with tangential cutting

For the simple example of Fig 2.3, laser-cutting trajectories were computed analytically. To handle an arbitrarily complex part, however, it is necessary to derive kinematically and dynamically feasible laser-cutting trajectories directly from the part's CAD description. This topic constitutes the remainder of this presentation.

3 Trajectory Generation for Tangential Cutting

To exploit the prospective advantages of tangent cutting, it is necessary to deduce machine trajectories from CAD files. Most CAD packages have the ability to compute and report the surface normal or tangent plane at a given point on the surface. Also, files exported in the

ubiquitous STL representation include surface-normal information for every triangular facet. However, this information is not entirely adequate for laser cutting of thick layers. Rather, the relevant constraints for tangent-cutting thick layers are: 1) the contour at the top surface of the thick layer should match the cross section of the CAD model at the corresponding z-height; 2) the contour at the bottom surface of the thick layer should match the corresponding cross section of the CAD model; and 3) both contours must be realizable in terms of a sequence of straight-line segments (“spans”) joining points on the top contour to points on the bottom contour.

Our approach is to reduce the edge surface of a layer into a *ruled surface* formed by moving a line (*rule*) connecting the points on two curves (rails). In considering cutting a layer physically, the contours around the top and bottom surfaces are the rails, and the laser beam is moved as a rule along the contours. Given such a ruled surface, one can deduce the unique inverse kinematics for control of each joint of the cutting platform such that the laser line is directed collinear with the moving rule. An additional important consideration is that the corresponding trajectory should satisfy the constraints of maximum velocity and acceleration of each joint of the laser-cutting system, as well as maximum material removal rate of the laser and maximum laser dwell time (or minimum cutting speed) to avoid excessive burning or melting of the target material.

In this section, we present our method for computing feasible cutting trajectories for realizing good approximations of surface reconstruction in the generation of thick layers.

3.1 Surface Reconstruction from Contours

The problem of surface reconstruction from successive contours is not new. Keppel [4] used triangular facets to stitch successive contours into 3-D layers. He recognized that this problem could be transformed into an equivalent graph-search problem. Fuchs, et. al. [5], analyzed this problem in detail and proposed an optimized search algorithm. Here, we adopt a similar graph-search approach, and modify the result to accommodate the dynamic constraints of the cutting process and of the 5-axis motion. While our approach is extensible to arbitrary contours, we present it for the case of polyline contours, as would result from slicing an STL file.

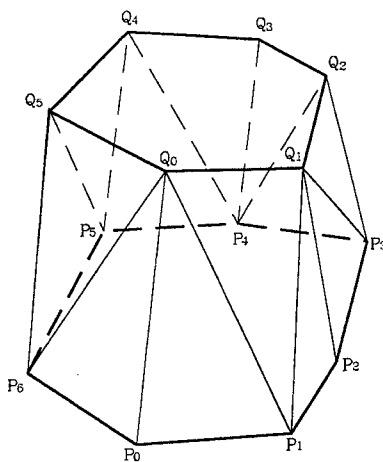


Fig. 3.1 (a): Stitching contours with triangular facets

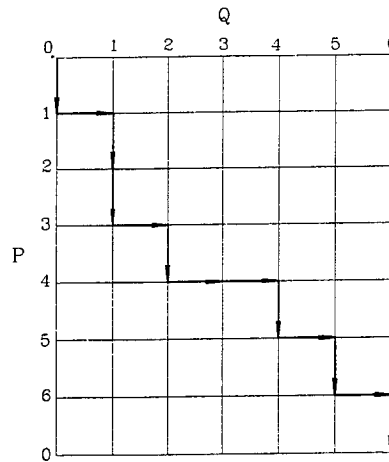


Fig. 3.1 (b): Graph corresponding to the stitching of fig. 3.1 (a)

We presume that successive contours lie in parallel planes, and that each contour is comprised of a sequence of line segments, described by a sequence of points within the respective plane. Figure 3.1 (a) shows an example, in which (P_0, P_1, \dots, P_6) represents the bottom contour and (Q_0, Q_1, \dots, Q_5) represents the top contour. In Figure 3.1 (a), each segment, such as (P_0, P_1) in the bottom contour or (Q_0, Q_1) in the top contour, is a *contour edge*. Each line that connects the top and bottom contours is a *span*, such as (P_0, Q_0) , (P_1, Q_0) , (P_1, Q_1) Figure 3.1 (b) is the expansion of a directed toroidal graph. Folding the upper edge over to connect with the lower edge forms a cylinder, then joining the left and right edges forms a toroid. In Figure 3.1, each span in (a) is mapped onto (b) as a *graph node*, and each contour edge in (a) is mapped onto (b) as a *graph edge*. In this way, a triangular stitching can be mapped onto the directed graph as a cyclic path that starts and ends at the same node. The path illustrated in Figure 3.1 (b) represents the stitching in Figure 3.1 (a).

Given a pair of contours, there exist $\frac{(m+n)!}{m!n!}$ possible different stitchings where m is the number of points in the bottom contour and n is the number of points in the top contour. Given a criterion to associate a cost with each span (a node in the graph), the surface reconstruction problem can be formulated as a shortest-path search problem in graph theory. Several criteria have been proposed. We have found the "minimum square span length" to be a good cost function. The result is a surface reconstruction between successive layers which is a good approximation to the original surface, and which can, in principle, be created by laser cutting.

3.2 Problems in Faceted Tangential Cutting

While the reconstructed surface illustrated in Figure 3.1 (a) may be a good approximation to the original surface, the use of triangular facets is problematic for trajectory generation. Indeed, it is possible to compute a realizable inverse kinematic trajectory for each of the triangular facets. For example, the facet defined by vertices at (P_0, Q_0, P_1) can be generated by a laser-beam trajectory which is initially collinear with span (P_0, Q_0) , then pivots about point Q_0 , while tracing out edge (P_0, P_1) of the bottom contour, ending up collinear with span (P_1, Q_0) . While this solution is geometrically consistent, it defines a trajectory with excessive dwell time at point Q_0 , which is likely unacceptable for laser cutting. In addition, applying the same technique to the next facet, (Q_0, P_1, Q_1) , would prescribe pivoting the laser beam about the point P_1 on the bottom contour. The abrupt change from pivoting about a point on the top contour to pivoting about a point on the bottom contour corresponds to a discontinuous velocity reversal of one or both of the orientation axes. Discontinuous velocity changes are physically unachievable; instantaneous velocity reversals, as required to cut typical successive triangular facets, implies an extreme case of a dynamically unsuitable trajectory.

3.3 Trajectory Smoothing in Parameter Space

We can improve upon the trajectory generation implied by the surface reconstruction of Figure 3.1 by further interpreting the graph of Figure 3.1(b). This graph represents an abstraction of the surface reconstruction problem, and a graph search applied to this representation resulted in the path shown in Figure 3.1(b), defining the surface reconstruction of Figure 3.1(a). We next re-associate the abstract graph of Figure 3.1(b) with physical dimensions by interpreting the Q axis as the path length along the top contour, and the P axis as the path length along the bottom contour. We introduce the new variables u_t and u_b to be path-length variables, ranging from 0 to

1, defining the fractional completion of the traversal of the top and bottom contours, respectively. The dimensionless graph of Q vs. P of Figure 3.1(b) is translated to a graph in u_t vs. u_b , rescaled such that each graph edge of Figure 3.1(b) is assigned a length proportional to the length of the corresponding contour segment. The resulting plot is the path-length distance along the top contour vs. path-length distance along the bottom contour. This plot defines the motion of endpoints of a span sweeping out the ruled surface joining the top contour to the bottom contour.

From this viewpoint, the dynamics problem of velocity reversals at facet boundaries is apparent. A horizontal path segment in u_t vs. u_b indicates zero velocity of u_b , corresponding to the laser line pivoting about a point in the bottom contour. Similarly, vertical path segments in u_t vs. u_b indicate pivoting about a point on the top contour. Path segments sequencing from vertical to horizontal (or vice versa) indicate velocity reversals in orientation. In the parameter space u_t vs. u_b we can see that the ideal path, with respect to a smooth dynamic trajectory and constant laser cutting speed, would be a 45-degree line from $(u_b, u_t) = (0,0)$ to $(u_b, u_t) = (1,1)$. In contrast, the ideal path with respect to optimized surface reconstruction, without regard to cutting or motion dynamics, consists entirely of vertical and horizontal segments. To achieve good surface reconstruction with consideration of dynamic constraints, we spatially low-pass filter the computed path in u_t vs. u_b to produce a smoothed path. This smoothed path constitutes an approximation to the computed, faceted surface reconstruction, but it eliminates the rapid velocity changes corresponding to the transitions between the computed facets.

In practice, we low-pass filter u_t vs. u_b by defining separate functions of time, $u_t(t)$ and $u_b(t)$. These functions are initially derived from the computed graph of u_t vs. u_b , then low-pass filtered to produce smoothed path-length vs. time functions. The resulting smoothed functions define endpoints of a moving span between the top and bottom contours. At each instant in time, the coordinates of these endpoints can be computed, and the corresponding inverse kinematics for the laser cutter yields an unambiguous solution for control of the 5-axis system.

Our smoothing approach redefines the surface between the top and bottom contours, smoothing over discrete changes in surface normal. However, discrete changes in surface normal are sometimes deliberate (e.g., in defining the faces of a cube) rather than artifacts of reconstruction. When it is desired to preserve a particular span (e.g., the edge of a cube) identically, we can do so by defining the corresponding values of u_t and u_b to be constant vs. time in the definitions of $u_t(t)$ and $u_b(t)$ for a duration exceeding the time constant of our low-pass filter. The result will produce a graph of u_t vs. u_b that includes the desired span.

3.4 Illustration of Trajectory Smoothing in Parameter Space

Here we illustrate the surface reconstruction and trajectory smoothing technique with a realistically complex example. Figure 3.2 (a) is the wire frame display of a layer edge surface reconstructed with the triangular stitching algorithm described in section 3.1. Contour data comes from two sections of an STL model of a human head. The top contour has 344 segments and the bottom contour has 345 segments.

Figure 3.2 (b) shows the span trajectory smoothed with our spatial filter. First, we defined discretized functions $u_t(t)$ and $u_b(t)$ using 1200 samples of u_t and u_b . A moving central-

average filter of window width 19 was applied to both series $\{u_t\}$ and $\{u_b\}$. Comparing Figures 3.2 (b) to (a) shows the effect of our smoothing algorithm. An attempt to cut the layer defined by Figure 3.2(a) would result in slow execution, poor tracking, and excessive laser-induced ablation at pivot points. The layer defined by Figure 3.2(b) yields a well-behaved trajectory specification, as well as a smoother surface reconstruction. Note, though, that the top and bottom contours, respectively, of the two models (3.2(a) and 3.2(b)) are identical. The smoothing algorithm does not distort the part boundaries at the slice planes. Thus, layers constructed with smoothed surfaces can be expected to mate identically with the layers immediately above and below within a stacked assembly comprising a 3-D part (e.g., as in Fig 2.3).

At the time of this writing, our trajectory smoothing algorithm has not yet been incorporated into the control of our new 5-axis platform. Surface reconstruction and smoothing is currently performed off line. To reduce the size of datafiles required to drive the laser cutter, surface reconstruction and smoothing is being converted to an on-line process, computed during cutting.

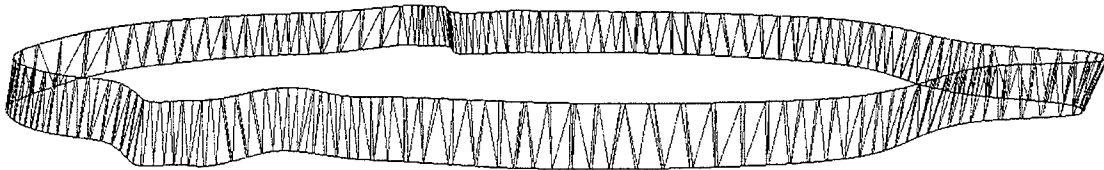


Fig. 3.2 (a): Span trajectory from surface reconstruction

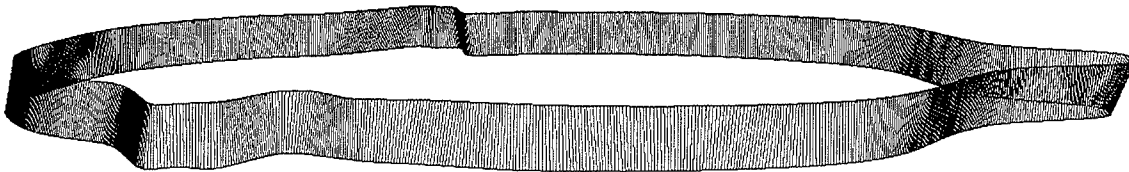


Fig. 3.2 (b): Smoothed span trajectory

4 Discussion and Conclusion

The work in progress presented in this paper has demonstrated the feasibility of extending the CAM-LEM technique to the fabrication of components using tangent cutting to optimize surface finish and build time. The current capabilities and limitations of our experimental 5-axis laser-cutting system were illustrated, and the potential for improving build rate and/or surface quality was demonstrated with a simple physical example fabricated with our system.

A significant challenge encountered in our research has been the derivation of a suitable laser-cutting trajectory from CAD information. While CAD models typically incorporate sufficient information to specify the surface tangent planes at arbitrary surface points, such information is not adequate for generating cutting-trajectory profiles. Instead, an optimal surface approximation must be computed, based on a sequence of line-segment spans connecting top and

bottom boundaries of a layer. In addition to achieving a good approximation to the original surface, the surface reconstruction algorithm must also result in a kinematically and dynamically desirable laser-cutting trajectory. We have presented an algorithm which accomplishes this for contours consisting of polylines, as is the case for slices of models stored in the STL format.

In continuing work, we are extending our surface-reconstruction and smooth trajectory-generation algorithm to work with non-polygonal contours, including arcs and NURBS. Further, this algorithm is being converted to a real-time process to be executed during laser cutting. On-line translation of CAD models to cutting trajectories will permit use of more compact data files while offering improved resolution.

Initial tests of angular laser cutting of materials has been encouraging. However, we have seen that the maximum practical cutting angle can be restrictive for some materials. Laser-cutting parameters, including cutting speed, laser power, air-jet effects, and laser optics, will have to be explored for optimizing cutting quality for materials of interest for CAM-LEM processing.

References

- [1] B. B. Mathewson, W. S. Newman, A. H. Heuer, and J. D. Cawley, "Automated Fabrication of Ceramic Components from Tape-Cast Ceramic," in *Solid Freeform Symposium Proceedings*, University of Texas at Austin Publishers, Austin, TX, August, 1995.
- [2] J. D. Cawley, Z. Liu, W. S. Newman, B. B. Mathewson, A. H. Heuer, "Al₂O₃ Ceramics Made by CAM-LEM Technology," *Solid Freeform Symposium Proceedings*, University of Texas at Austin Publishers, Austin, TX, August, 1995.
- [3] W. Newman, Y. Zheng, and C. C. Fong, "Trajectory Generation from CAD Models for Computer-Aided Manufacturing of Laminated Engineering Materials," in *Proceeding of the 26th International Symposium on Industrial Robots*, pp. 153-158, Singapore, October 4-6, 1995.
- [4] E. Keppel, "Approximating Complex Surfaces by Triangulation of Contour Lines," *IBM J. Res. Dev.*, 19:2-11, January 1975.
- [5] H. Fuchs, A. M. Kedem, and S. P. Uelson, "Optimal Surface Reconstruction from Planar Contours," *Commun. ACM*, 20:693-702, October 1977.

Acknowledgements

The authors wish to thank Ting-Chu Ko, Department of Materials Science and Engineering, CWRU, for experimental assistance in the performance of this work. The authors also thank Professors J. D. Cawley and A. H. Heuer, also of CWRU's MSE Department, for numerous technical discussions contributing to this research. This work was supported by National Science Foundation grant DMI94-20373, by NSF Young Investigator Award number IRI92-57269, and by ONR grant N00014-95-10107. This support is gratefully acknowledged.

SFF Using Diode Lasers

Tariq Manzur*
Chandra Roychoudhuri*
Harris Marcus⁺

*Photonics Research Center (PRC)

⁺Institute of Materials Science (IMS)

University of Connecticut, Storrs, CT 06269

ABSTRACT

Rapid prototypings using direct selective laser sintering (SLS) of metal/ceramic powders have a great potential for design and fabrication of near net shape of metal/ceramic parts. At presents CO₂, Nd:YAG and Excimer are the only possible solutions for the heavy duty manufacturing applications. At the University of Connecticut, researchers advanced the concept of rapid prototyping and other desk top manufacturing tasks such as welding, sintering, drilling, marking, soldering of electronic components, face hardening of metal and other materials applications by the use of high power diode lasers.

Utilizing SLS techniques and approaches designed to harness the full potential of diode lasers, computer controlled sintering system was developed. The system is capable of producing complex three dimensional shapes of metal/ceramic parts from CAD/CAM solid model data files. In the paper direct sintered Fe-Bronze parts using high power laser diodes has been demonstrated. The system comprises of high power laser diodes (25 W cw, $\lambda=980$ nm and 60 W pulse or cw, $\lambda=810$ nm), beam scanning systems, atmospheric controlled chamber, and CAD/CAM software.

INTRODUCTION

Recent advance of diode laser technology makes possible of desk-top manufacturing of metal/ceramic parts directly from a computer model without part-specific tooling or intervention. These technologies have been termed Solid Freeform Fabrication⁽¹⁾ and differ dramatically from normal fabrication techniques due to their additive nature. Normal machining operations fabricate a part by removing a material until the remaining desired component specific material is left. Additive processes, however, build up the desired part by selectively sintering of powders' layer by layer. The benefit of this technology is greatly reduced fabrication time and cost and capability to achieve, in one operation, shapes that would otherwise require multiple operations or in some cases, be impossible to manufacture with current standard techniques.

For the last two years, we have been working on Solid Freeform Fabrication (SFF) desk-top manufacturing techniques. This technique is adopted from the Selective Laser Sintering (SLS) process. At the University of Connecticut desk-top manufacturing SLS test bed uses diode laser to selectively sinter metal/ceramic powders without any polymeric binder.

Many of the industrial desktop manufacturing applications require directed laser beam energy that has high total power and brightness. In many situations, it is also important to deliver an extremely small spot of concentrated laser energy to a tiny area. Figure 1 shows a variety of laser-processing tasks that can be performed with intensities in the range of 10^3 to 10^8 W/cm². Focused diode lasers, despite relatively low output power per stripe (~1W), emit 10^6 to 10^7 W/cm², a range suitable for many laser manufacturing jobs. The engineering difficulty is to collect 100 to 1000 watts from numerous diodes and deliver the power within a small spot with high brightness. Photonics Research center (PRC) at the University of Connecticut is in the process of acquiring high brightness laser diode systems that can deliver CW power exceeding 1 kW with power density reaching 100 kW/cm² in a spot not exceeding 600 micrometers⁽³⁾.

Noted for their small size, greater than 40 percent electrical-to-optical plug in efficiency, ease of modulation and low power requirements (about 300 watts), diode lasers are an ideal source of direct thermal energy for a multitude of industrial tasks. Moreover, they are much less expensive than competing lasers and interface easily with computers and robotic arms. Since diode lasers have tremendous mass production capabilities their price per watt is expected to drop steadily as high-volume applications continue to open up. At moderate volumes, the current market price for non-fiber-coupled diodes has dropped to about \$30 per delivered watt of raw diode energy as compared to \$150 per watts CO₂ or Nd:YAG lasers.

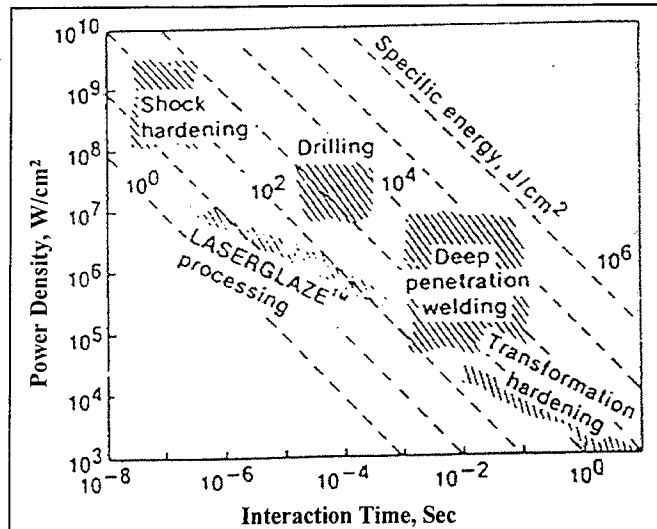


Fig. 1 Beam-material interaction spectrum². A large number of commercial processes of surface material processing can be carried out at cw intensity levels from 1 kW/cm² to 1 MW/cm².

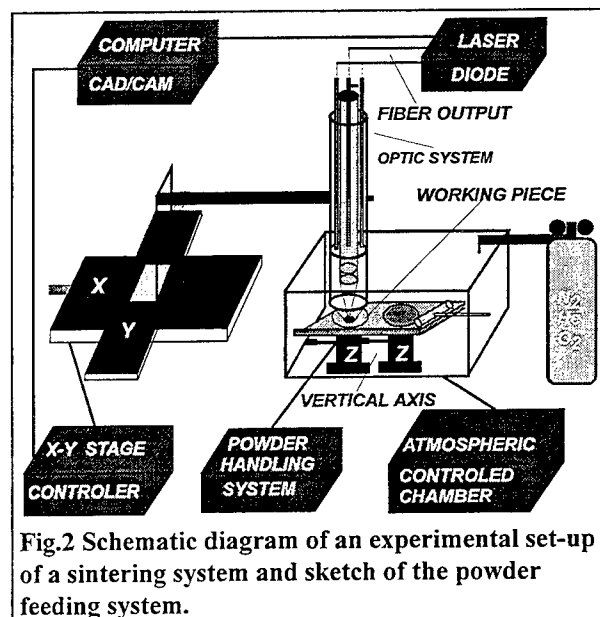


Fig.2 Schematic diagram of an experimental set-up of a sintering system and sketch of the powder feeding system.

EXPERIMENTAL SETUP

To demonstrate the use of diode lasers for sintering-based SFF, an experimental apparatus was constructed (Fig. 2). The system consists of a fiber-coupled diode laser array, optical delivery system, powder feeding system, oxidation prevention system and laser scan control system⁽⁴⁾. In this setup, the SFF device generates three-dimensional parts from CAD/CAM data files by selectively bonding multiple layers of powder using high-power diode lasers. PRC has three high power CW laser diode systems in use from three different companies: 1) 60 W @ 810 nm, 2) 25W @ 980 nm and 3) 50 W @ 808 nm. These systems can deliver intensity up to $10\text{kW}/\text{cm}^2$.

MATERIALS

For sintering, the materials used in the present study were Fe-Bronze (Cu-Sn) premixed powder, grade 661($\text{Fe}_{34-36}\text{Cu}_{58-60}\text{Sn}_{6-7}$). Particle size was 100 to 200 μm . The alloy was supplied by Pyron Metal Powders Inc., from Maryville, Tennessee.

RESULTS

Some examples of elementary (SSF) sintered parts with multiple sintered layers made from Fe-Bronze premix powders are shown in Fig. 3. Other sintering examples include a sintered strain gauge also made from Fe-Bronze premix powder (Fig. 3d). To suit the requirements of researchers for these particular sintering experiments, the delivery end of the diode laser's

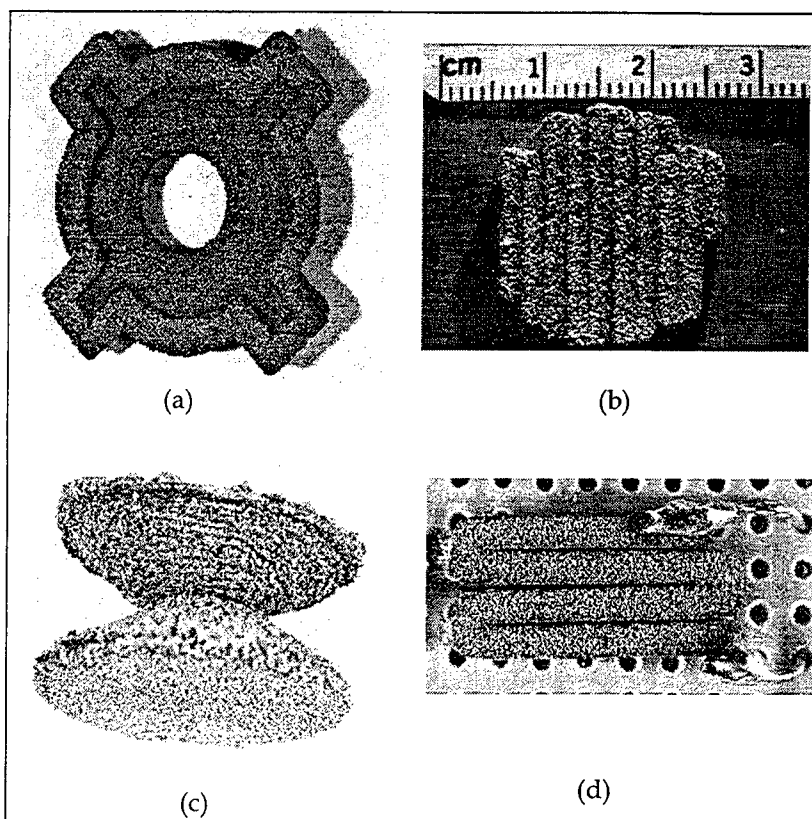


Fig. 3 (a-c) The sintered samples made from iron-bronze premix powder in an argon atmosphere.

Fig. 3 (a, b) The sintering laser spot size was 0.8 mm carrying, 15 W cw power at a 2mm/sec & 1 mm/sec scanning speed. The layered fan shape disk has 8 layers, each layer being 0.5 mm thick., (c) 14 W cw power at 1 mm/sec scanning speed. The layered conical shape has 36 layers, each layer being 0.5 mm thick.

Fig. 3 (d) Our first attempt to fabricate a strain-gauge by SFF techniques from iron-bronze premix powder. The sintering laser spot size was 0.8 mm carrying a power of 14 W cw, scanning at a speed of 0.8 mm/sec. The sintering was done in a flowing Ar-gas. The sample has 6 layers, each layer being 0.5 mm thick. Length and width of the sintered folded sample is 16 mm and 8.3 mm respectively. The groove size is around 100 μm .

optical fiber was attached to an OPC re-imaging unit from "Opto Power Inc.". This unit can produce a spot size of 0.8 mm (<0.37 N. A.) on the sintering bed from 2.16 mm (0.11 N. A.) fiber bundle. Using the re-imaging unit, researchers were able to achieve transmission efficiency in excess of 90 percent.

LASER PROCESSING PARAMETERS (Table 1):

Sample	Power	Scan-Speed	# of Layers	Energy density
Fig. 3.a	15 W	2 mm/sec	8	14.92 kJ/cm ³
Fig. 3. b	15 W	1 mm/sec	10	29.84 kJ/cm ³
Fig. 3 c	14 W	1 mm/sec	36	27.85 kJ/cm ³
Fig. 3. d	14 W	0.8 mm/sec	6	34.82 kJ/cm ³
Fig 4 c	12 W	2 mm/sec	4	11.94 kJ/cm ³
Fig. 4 d	14 W	1 mm/sec	4	27.85 kJ/cm ³
Fig 5, #1	12 W	2 mm/sec	4	11.94 kJ/cm ³
Fig 5, #2	16 W	2 mm/sec	4	15.92 kJ/cm ³
Fig.5, # 3	10 W	1 mm/sec	4	19.89 kJ/cm ³
Fig. 5, #4	12 W	1 mm/sec	4	23.87 kJ/cm ³
Fig. 5, #5	14 W	1 mm/sec	4	27.85 kJ/cm ³
Fig. 5, #6	16 W	1 mm/sec	4	31.83 kJ/cm ³

- Energy density = Power/(Spot size x Scan speed) = P_D /Scan speed
- P_D = Power density
- Laser wavelength: 980 nm
- Laser spot diameter: 0.8 mm
- Layer thickness: 0.5 mm
- Powder bed temperature varies between 80^o ~ 100^oC

DENSITY of a SLS Parts:

The sintered SLS parts density is around 50% of the theoretical density with about 50% open porosity. Cu₇₅-Pb₂₅ samples prepared by SLS techniques have higher density (70% of theoretical) compared to Fe-Bronze sample.

CURLING of a SLS Parts:

In this research we have also observed the curling and bending of the sintered parts. In our research we have observed that fast scanning speed and high power reduces the curling. To investigate it further we fabricate different samples on different substrates (Brass screen, Cu strip, iron strip and on powder). Our finding is that using powder bed substantially reduces the curling. Powder beds trapped the laser radiation and increase the temperature of the bed, which is essentially reducing curling.

Microstructure and Microhardness:

Mechanical properties of SLS process sintered parts depend mostly on the amount of energy that goes into the surface during SFF processing. The amount of energy density during laser sintering for the powder depends on the absolute power at the spot and the scan speed of the laser beam. To study the effects of energy density of the sintered parts, different samples were prepared from Fe-bronze powder at varying power and scan speeds. Table 1 shows the lists of samples prepared at different processing parameters. Figure 5 shows that as the energy density increases the microhardness of the sample decreases. Increase of energy density on the powder bed increases temperature and decreases the cooling rate. This causes grain growth. Figure 4 (c, d) show the evidence of grain growth due to an increase of energy density. Due to the grain growth of the sintered Fe-Bronze samples the microhardness decreases (Fig. 5).

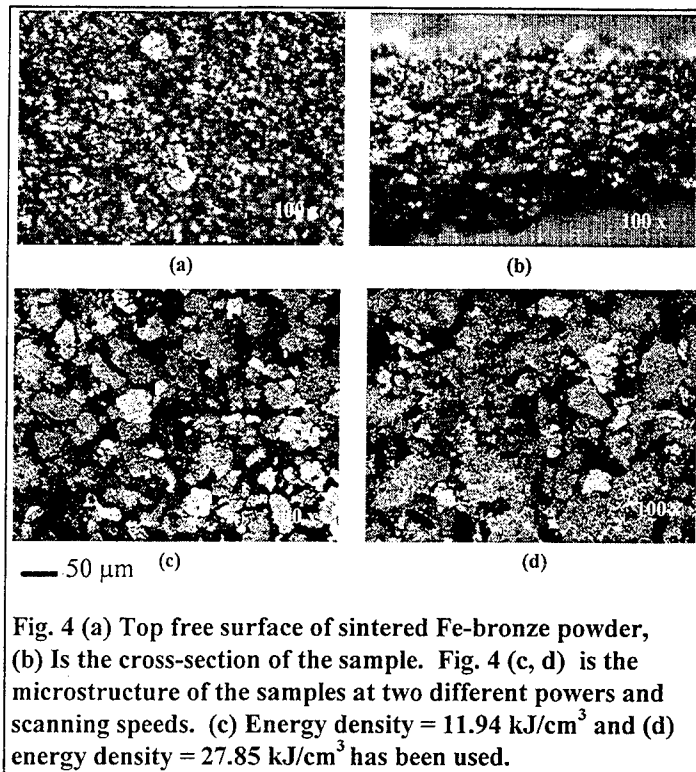


Fig. 4 (a) Top free surface of sintered Fe-bronze powder, (b) is the cross-section of the sample. Fig. 4 (c, d) is the microstructure of the samples at two different powers and scanning speeds. (c) Energy density = 11.94 kJ/cm³ and (d) energy density = 27.85 kJ/cm³ has been used.

MARKING

Presently, ink-jet or bubble technologies are the leading methods for marking consumer products. However, due to the high consumable cost of the inks and solvents used in these processes along with the associated environmental concerns, laser techniques are making rapid inroads as viable alternatives. Semiconductor diode laser arrays operating in

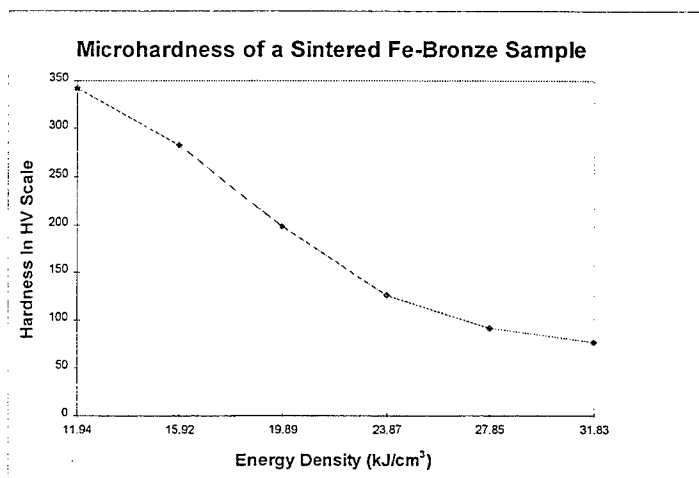


Fig. 5 As energy density increases the microhardness of the sintered Fe-Bronze sample decreases, making the sample softer.

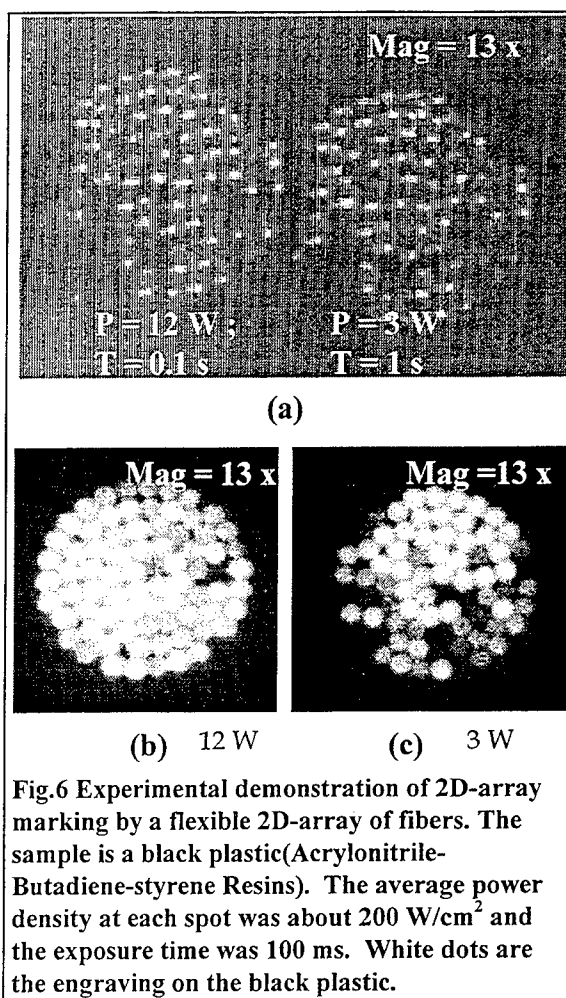
the 10 to 200 watt output range have tremendous promise in this market. Utilizing Opto Power's OPC-B060-812-FC, laser diode, the University of Connecticut research team has shown that it can mark black plastic with a 2D-array of fiber bundles coupled to high power diodes (Fig. 6). This is now being pursued for the SFF diode laser proximity

CONCLUSION

The sintering results are just a part of a continuing effort to determine the performance parameters of high-power semiconductor diode lasers and their effectiveness in desktop manufacturing of small objects. In addition to sintering, the scope of this work includes marking, engraving, cutting, drilling, soldering and wire stripping. Of these applications, individually addressable 2D of array sintering has been given the most attention to date. Specifically the UConn research team is exploring the feasibility of this new idea with initial implementation in the area of marking or engraving.

REFERENCE

1. "Solid Freeform Fabrication Symposium Proceedings 1990-95" Austin, Texas; Harris Marcus, David Bourell, Richard Crawford, Joel Barlow.
2. Beam-material interaction spectrum, "Macro-materials processing". Proc. IEEE 70(6), 555-565(1982); C.M Banas and R. Webb.
3. Design Approaches for Laser-Diode Material-Processing Systems Using Fiber and Micro Optics; "Optical Engineering/Nov 1994/ Vol. 33, No. 11; W. Chen, Chandra Roychoudhuri.
4. Potential Role of High power Laser Diode in Manufacturing "SPIE Photonics West Conference", San Jose, California, Jan 27, 1996, pp 490/SPIE Vol. 2703; Tariq Manzur, Tony DeMaria, Weiquin Chen, Chandra Roychoudhuri.



Solid State Lasers for Stereolithography

**Jouni P. Partanen
3D Systems, Inc.
26081 Avenue Hall, California, 91355**

ABSTRACT

Stereolithography is a Rapid Prototyping & Manufacturing (RP&M) technique which is used to produce 3 dimensional plastic parts directly out computer files generated by CAD. Stereolithography systems use ultraviolet lasers to solidify liquid resin into the desired form as defined by the CAD file. In recent years, solid state laser technology has reached the point where it can be applied to stereolithography (SL). Frequency tripling of the powerful lines of diode pumped Nd/YAG, Nd/YVO₄, and Nd/YLF lasers results in wavelengths of 355 nm (YAG, YVO₄), 351 nm (YLF), and 349 nm (YLF). All these lines are applicable for SL. Commercial diode pumped lasers with tens or even hundreds milliwatts in the ultraviolet are already available. Efficient frequency tripling of the Nd/YAG, Nd/YVO₄, or Nd/YLF lasers requires pulsed operation. The pulse repetition rates at maximum average power are typically between 1 and 30 kHz. This talk describes the issues relating to the applications of pulsed all solid state lasers in SL.

1. INTRODUCTION

Stereolithography (SL) is a Rapid Prototyping & Manufacturing (RP&M) technique which is used to produce 3 dimensional plastic parts directly out of files generated by Computer Aided Design (CAD) programs. RP&M systems build the 3-dimensional objects by first converting the CAD file data into a form of successive 2-dimensional slices. These slices (thin layers) are then formed and joined to 3-dimensional parts using many different methods. In stereolithography, these slices are formed by solidifying a thin layer on the surface of photocurable resin vat using an ultraviolet (uv) laser. The uv laser beam is focused from above to the surface of the vat and the area to be solidified is scanned by two fast moving mirrors - one for each horizontal direction. A new layer of resin is solidified directly above the previously solidified layer attaching immediately to all of the layers below it. Thus the part grows inside the liquid photopolymer vat.

Lasers are today about 35 year old technology. Since the beginning there has been applications of lasers in many different fields. During the last 10 years, the laser technology has reached the large consumer market through lasers in CD players and in fiberoptic communications. These high volume applications use diode lasers which are made using semiconductor technology. These lasers are inexpensive, efficient and reliable. Many other technologies that apply lasers are also considering the use of diode lasers for the same three reasons. Unfortunately, diode lasers are not available at the ultraviolet wavelengths used in

stereolithography. However, diode lasers can be used to pump other solid state lasers in order to achieve all solid state laser system for the ultraviolet wavelengths. Although these laser systems are rather complicated and thus not that inexpensive, they can both be more reliable and efficient than the gas laser technology presently used in SL. In addition, diode laser pumped solid state lasers for ultraviolet can be made much smaller than the gas lasers at the same power level.

2. OPTIMAL WAVELENGTH

Commercially available photopolymer initiators have their optimal absorption at certain specific wavelengths. Laser beams at wavelengths shorter than 300 nm are not usually suitable for SL because photons at that energy are absorbed by all molecules of the resin. The photons absorbed by other molecules than the photoinitiators do not cause polymerization. In the wavelength range 310 - 355 nm the pool of efficient initiator molecules is largest[1]. Thus almost all commercial SL systems use HeCd lasers at 325 nm or Argon Ion lasers at 351 nm. The photoinitiator molecule absorption cross sections σ are usually very different at the wavelengths of 325 nm and 351 nm. Therefore the photopolymer resins are different for SLA systems with either HeCd or Ar Ion lasers. Because the absorption cross sections σ are usually larger at 325 nm than at 351 nm less photoinitiator is needed, and the wavelength around 325 nm is preferred for stereolithography. HeCd lasers generally provide up to 40 mW of power at 325 nm for the SLA-250 (250 mm \times 250 mm build area) and Argon Ion lasers can run up to 600 mW of power at 351 nm for the SLA-500 (500 mm \times 500 mm build area). The average lifetimes of both HeCd lasers and ultraviolet Argon Ion lasers have been extended beyond 4000 hours in the last couple of years.

3. POSSIBLE SOLID STATE LASERS

There are at least 3 different possible approaches for all solid state ultraviolet lasers for stereolithography: 1) direct diode laser, 2) frequency doubled diode laser, and 3) frequency converted diode pumped solid state laser.

As mentioned in the introduction direct ultraviolet diode lasers are not yet available. Red diode lasers at 630 nm are the shortest wavelength lasers that are commercially available. In the last couple of years, the lifetimes of blue lasers have improved beyond 100 hours and more research has been directed towards ultraviolet diode laser technology. However, commercial uv diode lasers are probably 5 or even 10 years away from today.

Red (630 - 690 nm) diode laser technology has developed significantly in the last two years. Frequency doubling of 670 nm laser leads to wavelength of 335 nm, close to optimal for SL. Reasonable high power (> 0.5 W) single mode diodes lasers are already commercially available and frequency doubled versions could be developed in few years.

Frequency converted ultraviolet diode pumped solid state lasers are commercially available in many different form. Frequency tripling of the powerful lines of Nd/YAG, Nd/YVO₄, and Nd/YLF lasers results in wavelengths of 355 nm (YAG and YVO₄), 351 nm

(YLF), and 349 nm (YLF). A frequency doubled Nd/YVO₄ as applied to SL will be describe in the following sections.

4. FREQUENCY TRIPLED Nd/YVO₄ LASER

Nd/YVO₄ laser has its strongest lasing line at the wavelength of 1064 nm. Frequency tripling of that line results to the wavelength of 354.7 nm. Frequency tripling of a laser beam is a two step process which uses nonlinear optical crystals. It is shown schematically in Fig. 1. The first step is frequency doubling that combines two infrared photons (1064 nm) into a single photon of visible green light (532 nm). In a doubling process the frequency is doubled and consequently the wavelength is divided by two. The second step of tripling process is frequency mixing as shown in Fig. 1. In this step one green photon (from the doubling process) is mixed with one of the original infrared photons inside another nonlinear crystals. In this process frequencies of the doubled and the original are added up leading to three times the original frequency and to one third of the original wavelength. Fig. 2 shows a practical implementation of the frequency tripling. Original infrared photons (not visible in the photo) arrive from right of the doubling crystal housing. The green photons (visible in the photo) exiting this housing are steered by two mirrors to the mixing crystal housing. All three wavelength (infrared, green, and ultraviolet) photons exit mixing crystal to left (only the green ones are visible in the photo). The infrared and green photons are removed from the beam later by dichroic mirrors.

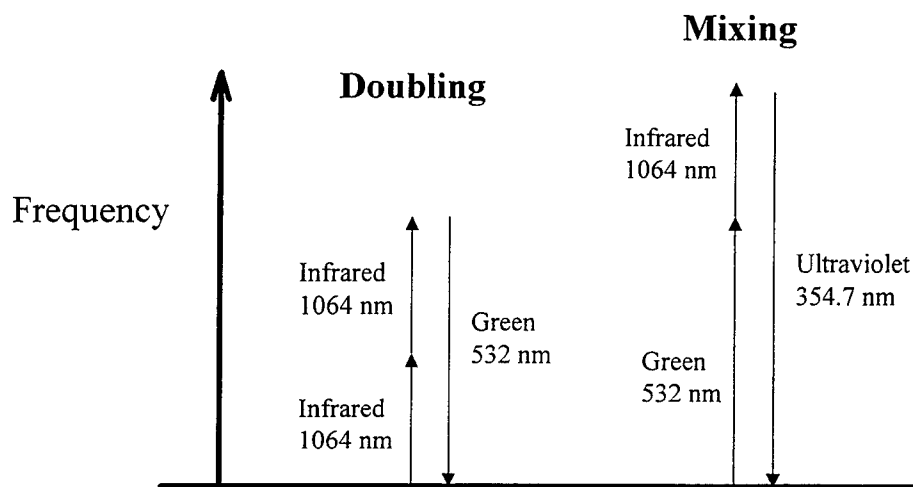


Fig. 1. Schematic diagram of the frequency tripling process.

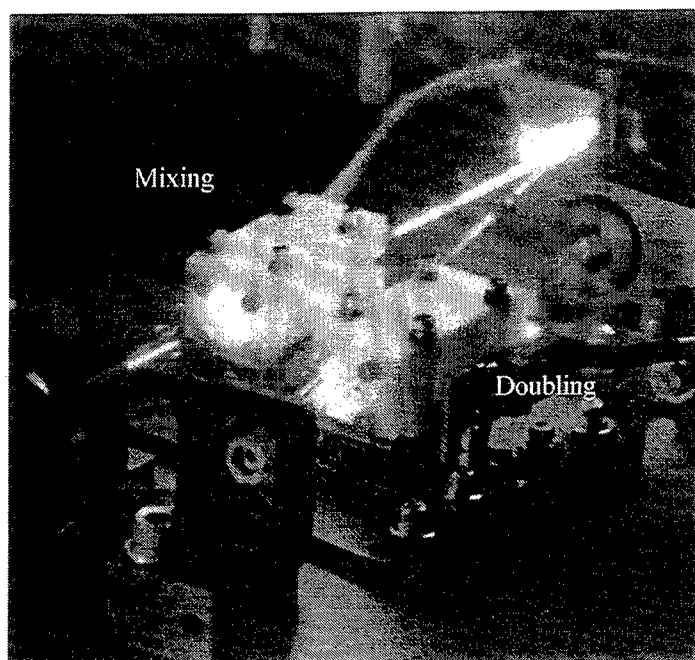


Fig. 2 Photograph of a frequency tripling apparatus.

The nonlinear crystals used in the frequency tripling process require the laser power to be in the range of kilowatts. In order to generate efficiently tens or hundreds of milliwatts of frequency tripled power, the infrared Nd/YVO₄ laser is made with a Q-switched cavity. A schematic diagram of the power output from a Q-switched laser cavity is shown in Fig. 3. The light comes out from the cavity in typically 10 ns pulses. The period between successive pulses is typically 30 μ s. Thus the power during the short laser pulse can be many thousands times higher than the average power with a Q-switched cavity and therefore the frequency tripling process can be efficient at the infrared laser power level of a few watts.

5. STEREOLITHOGRAPHY WITH PULSED LASERS

There are new factors that have to be considered when a pulsed laser is applied to SL, since all previous experience is based on cw (continuous wave) gas lasers. First, the instantaneous power during the 10 ns pulse of frequency Nd/YVO₄ laser is more than 3 orders of magnitude higher than the average power or the power of a typical gas laser applied in SL. However, we do not expect any significant optical damage problems at these power levels yet. Also it is questionable if the polymerization process is similar if the same amount of exposure is applied either in 10 ns or in 30 μ s. Because there are no important chemistry related characteristic time constants in the range from 10 ns to 30 μ s, we expect that the polymerization process for the repetitive pulsed laser should proceed as if the exposure were applied with a cw laser. To address this problem we have used a pulsed frequency tripled Nd/YLF laser at 349 nm in an SLA with SL5180 resin that has designed for Argon Ion laser at 351 nm. The

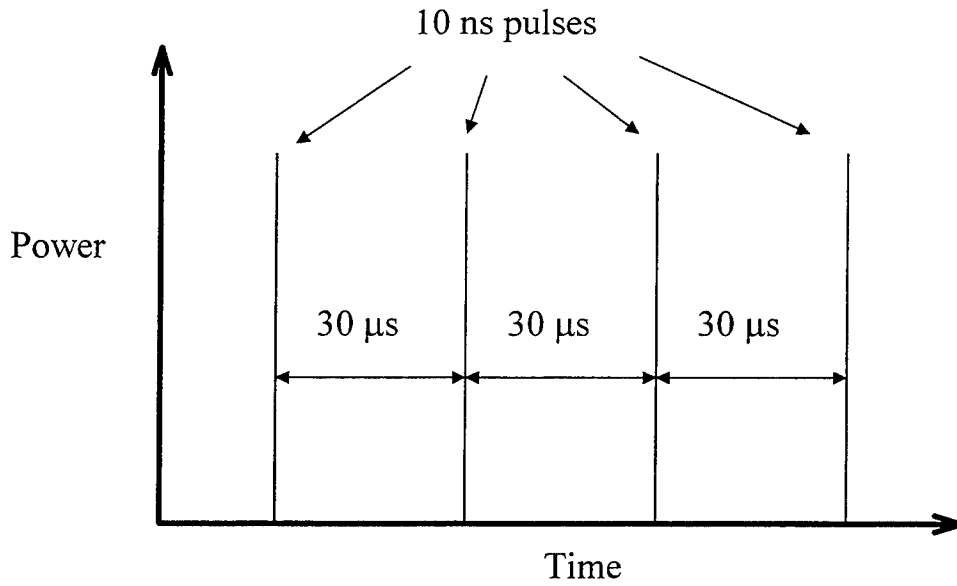


Fig. 3. Schematic diagram of output from a Q-switched Nd/YVO₄ laser cavity.

Windowpanes test [2] results are shown in the Working Curve of Fig. 4. A least mean square fit leads to resin parameters, critical intensity $E_c = 15.0 \text{ mJ/cm}^2$ and penetration depth $D_p = 5.0 \text{ mils}$. These are within experimental error of the default values, critical intensity $E_c = 16.2 \text{ mJ/cm}^2$ and penetration depth $D_p = 5.2 \text{ mils}$, for a cw Argon Ion Laser. On the basis of these Windowpanes and other subsequent experiments, we conclude that we do not observe any significant difference in polymerization if the same exposure is applied either cw lasers or high repetition rate ($> 1 \text{ KHz}$) Q-switched pulse laser.

Another factor to be considered is related to scanning speed. In order for the cured line to be continuous and without large modulation, we require the time between the laser pulses to be shorter than the time required to travel laser spot half width W_0 using the scanning speed V_s . Based on the analysis presented in Ref. [3] it is straightforward to derive a criteria for the minimum pulse repetition frequency F_{\min}

$$F_{\min} = \frac{V_s}{W_0} = \sqrt{\frac{2}{\pi}} \frac{P_L}{E_c W_0^2} \exp\left(-C_d/D_p\right) \quad (3)$$

Here P_L is the average laser power and C_d is the expected depth of cured line. In Fig. 5 we plot the minimum repetition frequency F_{\min} as a function of the laser power. We assume the properties of the SL5180 photopolymer resin ($E_c = 16.2 \text{ mJ/cm}^2$ and $D_p = 5.0 \text{ mils}$), the cure depth $C_d = D_p$, and a spot diameter $2W_0 = 250 \text{ μm}$.

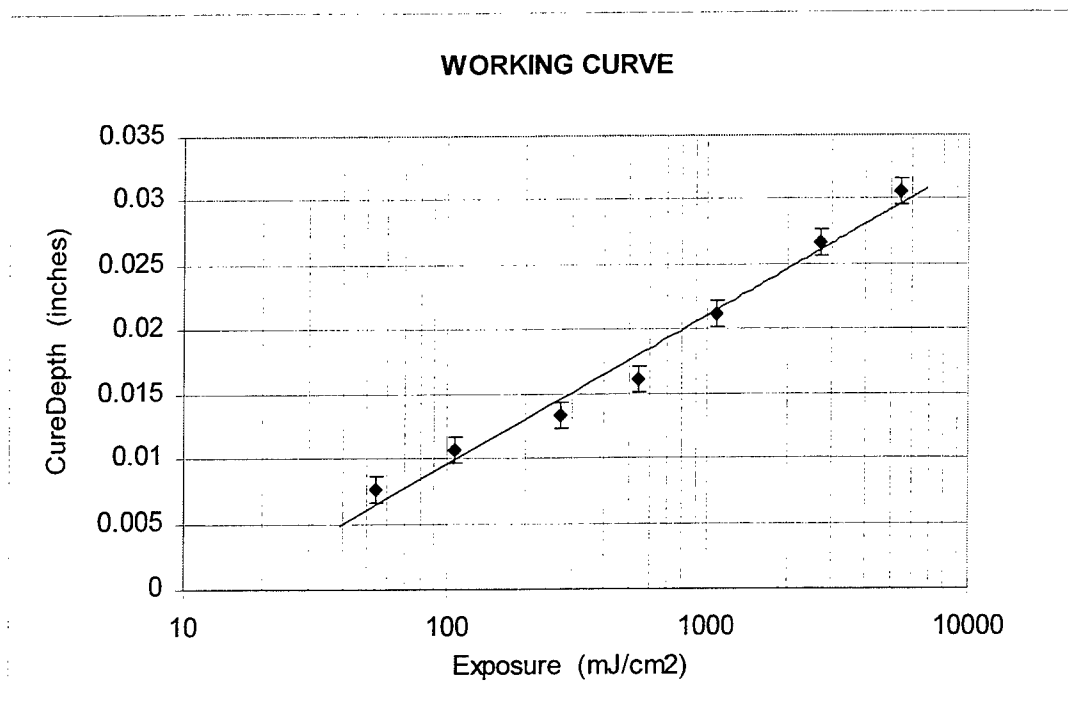


Fig. 4 Working curve for SL5180 resin determined for pulsed frequency tripled Nd/YLF laser at the wavelength of 349 nm.

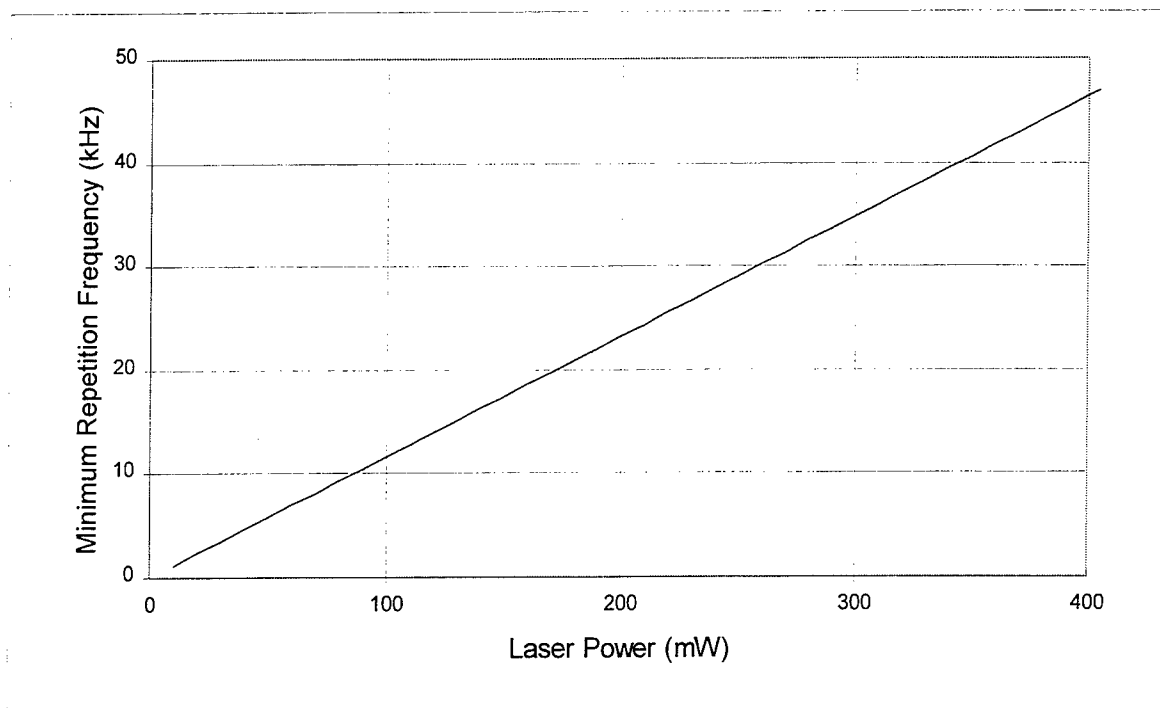


Fig. 5. Minimum Repetition Frequency for a pulsed laser as a function of average power.

6. OPTOLASERTM

It was mentioned in the introduction that diode pumped solid state lasers can be made much smaller than the gas lasers presently used in SL. 3D Systems has taken advantage of this in the development of the frequency tripled diode pumped Nd/YVO₄ laser (OptoLaserTM) for the SLA 350. Because the laser cavity itself can be made compact all the beam conditioning optics needed for SL are included in the OptoLaserTM head. A schematic diagram of the OptoLaserTM head is shown in Fig. 6. The laser for SLA-350 is manufactured by Spectra-Physics Lasers, Inc. As a result of internal beam conditioning optics, all elements can be factory prealigned with custom tooling.

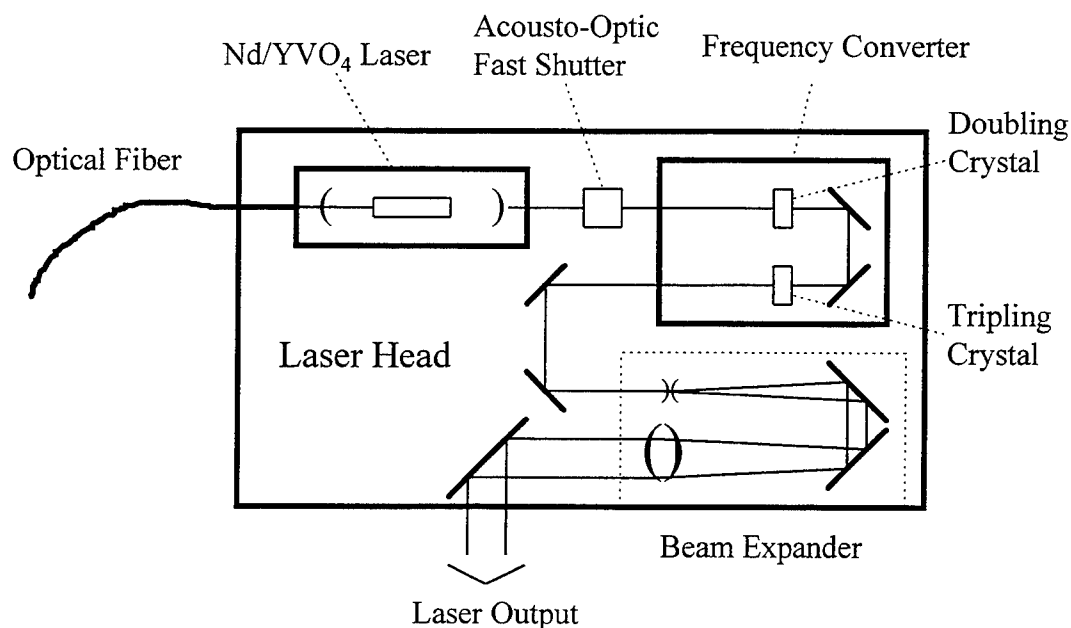


Fig. 6. Schematic diagram of the OptoLaserTM head used in SLA350.

7. CONCLUSION

Ultraviolet solid state lasers have reached maturity level where they can be applied to stereolithography. Their main advantages are: compactness, efficiency, and life expectancy. This paper discusses issues that relevant in application of all solid state lasers for stereolithography.

REFERENCES

- [1] M. Hunziker and R. Leyden, "Basic Polymer Chemistry," *Rapid Prototyping & Manufacturing: Fundamentals of Stereolithography*, Ed: P. F. Jacobs. pp. 25 - 58, Society of Manufacturing Engineers, Dearborn, MI, 1992.
- [2] H. Nguyen, J. Richter, and P. F. Jacobs, "Diagnostic Testing," *Rapid Prototyping & Manufacturing: Fundamentals of Stereolithography*, Ed: P. F. Jacobs. pp. 249 - 285, Society of Manufacturing Engineers, Dearborn, MI, 1992.
- [3] P. F. Jacobs, "Fundamental Processes," *Rapid Prototyping & Manufacturing: Fundamentals of Stereolithography*, Ed: P. F. Jacobs. pp. 79 - 110, Society of Manufacturing Engineers, Dearborn, MI, 1992.

Metal and Ceramic Components made via CAM-LEM Technology

Z. E. Liu, P. Wei, B. Kernan, A. H. Heuer, and J. D. Cawley

Department of Materials Science and Engineering

Case Western Reserve University, Cleveland OH

Abstract - CAM-LEM (Computer-Aided Manufacturing of Laminated Engineering Materials) is an SFF technology suitable for many engineering materials for which feedstock is available in sheet form; lamination and post-processing procedures are materials specific. Two methods for producing sheetstock, tapecasting and compression molding, are discussed and contrasted. Ceramic and metallic components that have been produced via CAM-LEM are described.

1. Overview of Process - Computer-aided manufacture of laminated engineering materials (CAM-LEM) is a sheet-feedstock-based process for rapid prototyping capable of producing functional components directly using engineering materials (advanced ceramics, metals, or engineering polymers). An outline of the process is given in a companion paper [1] and prior publications [2-4]. A significant unique feature to CAM-LEM is that it is a "cut-then-stack" approach in which the production of pseudo-2D contours via laser cutting and stacking are carried out as separate operations. This approach required the development of an automated process for precise manipulation of cut sheet stock [2], but offers three basic advantages. First, because each sheet is manipulated independently, it is possible to incline the feedstock during laser cutting so that the "tangent cutting" can be used to improve surface finish or increase build rate [1]. Secondly, as solid sheets are used, CAM-LEM offers a great deal of flexibility in the choice of materials that can be employed. Many materials are commercially available as sheets and essentially all powders can be pre-processed (in most cases, using a binder system) to produce sheet stock of a microstructure optimized for post-assembly thermal processing. Of particular interest for the production of ceramic and metal components, the use of a separate pre-processing step to produce sheet feedstock allows the use of very fine powders when desired without the typical flowability issues arising. Thirdly, because cut outlines are added sequentially, it is possible to build using a variety of feedstocks and to produce green assemblies that have spatially varying composition both from layer-to-layer and within a given layer.

The issue of tangent cutting is discussed elsewhere [1]. The following will address: the characteristics of feedstock suitable for CAM-LEM processing; the processes used for fabricating sheetstock; lamination; resultant microstructures within fired components; and typical components.

2. Sheet Feedstocks - The focus of this discussion is powder-based sheetstock, of which there are two classes that exhibit different characteristic behavior. The first is produced by tape casting [5]. Green tape produced by this method has roughly 55 vol. % inorganic powder, 15% organic binder, and the balance porosity. The porosity is typically finely divided, but continuous. The binder is typically linear, glassy and soluble in relatively benign solvents. Two types of alumina tapes have been used in CAM-LEM experiments; one cast from a nonaqueous suspension in a solution of polyvinyl butryal and the other cast from a suspension in a water-based acrylic emulsion. Such tapes are characterized by a high compressibility, low stiffness, and (depending on the glass transition temperature of the binder) a susceptibility to viscous flow

under low loads. Both commercial tapes (Coors Electronic Materials, Chattanooga TN) and CWRU-produced tapes were used. For components built from these tapes, binder removal was effected through pyrolysis. The polymer was thermally decomposed volumetrically through controlled heating. The presence of continuous porosity allows gaseous decomposition products to be vented, minimizing the build-up of internal pressures.

The other class of tape is produced by compression molding or extrusion. In all the experiments described, sheet stock was fabricated by compression molding of a commercial granulated injection-molding feedstock (BASF, Wyandotte MI) [6]. In contrast to the tape-cast material, such feedstock contains virtually no porosity. Depending on the shape, size and size distribution of the inorganic powder, the feedstock has a solids loading of between 45 and 65 vol. %. The binder system has two components, the major phase being polyoxymethylene (POM) which is highly crystalline, nonpolar, and insoluble in most solvents. The sheetstock is strong, stiff, and of low compressibility. Due to its nonporous nature, binder removal is accomplished using a catalytic process. In the presence of gaseous nitric acid, POM depolymerizes at a temperature substantially below its melting point. Thus, the system is phenomenologically a "shrinking core" process; the polymer decomposes at the receding surface and the resultant gases are vented through the porous shell. Within the core, the polymer remains a crystalline solid.

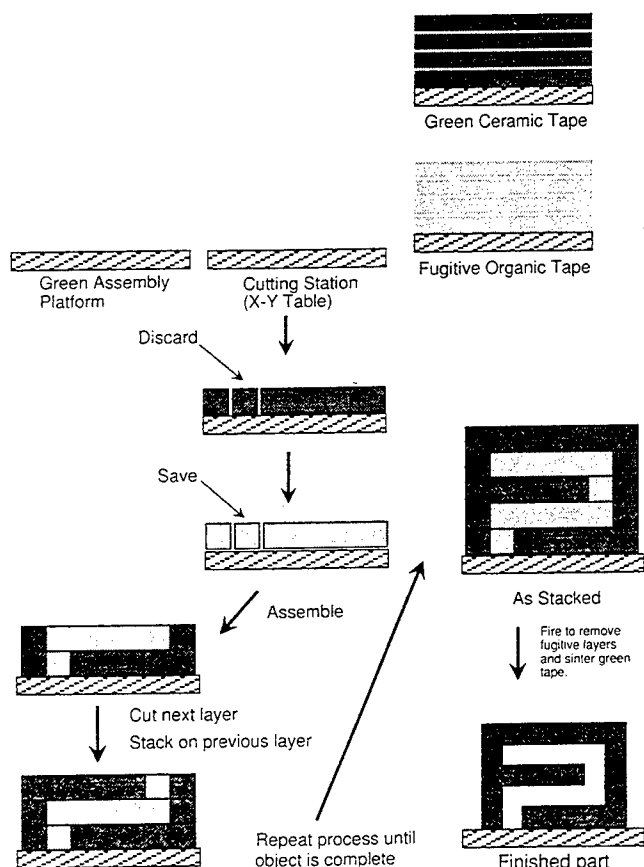


Figure 1. Schematic representation of the use of two feedstocks in CAM-LEM.

As illustrated in Fig. 1, by using a cut-then-stack approach CAM-LEM offers the opportunity to build individual layers of two different types of materials, one of which can serve as a "fugitive," i.e., it can provide for temporary support during build, but is removed after lamination is complete, but prior to final densification. Beyond their use as temporary supports, such fugitives can serve as a pressure-transmitting medium during lamination, allowing a component of complex geometry to present a simple external shape after assembly. Two types of materials have been used as fugitives, one for each class of sheetstock.

For tape-cast sheetstock, the fugitive was also tape cast. The binders, solvents and procedure were essentially unchanged, but the filler was different. Rather than using a finely divided ($\approx 0.5 \mu\text{m}$) sinterable alumina, a coarse alumina ($\approx 10\text{-}15 \mu\text{m}$) mixed with low-ash corn starch was used. Upon heating to inter -

mediate temperature, the base material (fine alumina) developed modest strength prior to densification, whereas the fugitive tape was converted to a loose flowable powder that was easily removed.

The fugitive for the compression molded sheetstock was a commercial POM polymer sheet. During catalytic debinding, the polymer sheet decomposed, the small residue left behind during debinding being removed by pyrolysis during the initial stage of the sintering heat treatment.

3. Laser Cutting Behavior - Laser cutting is a complex function of laser beam intensity, table velocity, thermal properties of the green tape, tape porosity, and binder chemistry. As currently implemented, the laser cutting system employs a gas jet that is coaxial to the laser beam and which impinges directly on the sheetstock. Good laser cutting is associated with high absorption of laser light, low thermal conductivity of the tape, and temperature-independent high stiffness. Most materials give good cutting behavior. The only materials that have proven difficult to cut with a low power CO₂ laser are those that are of low absorption and which exhibit a broad softening range, e.g., nylon and polyethylene.

The characteristics of the laser-cut edge differ depending on the nature of the sheetstock. Some degree of taper is associated with all laser cutting. For tape-cast sheetstock, taper angles were on the order of 7-8°, whereas for the compression molded sheetstock, taper was roughly one-half, ≈4°. There was evidence of a heat-affected zone in the tape-cast alumina sheetstock; an approximately 50 μm thick dense skin at the laser-cut edge. In contrast, for the dense POM powdered metal tape, there was no observable change in microstructure right up to the laser cut edge. There are at least two plausible origins of the dense skin associated with laser cutting tape-cast sheetstock, localized melting and resolidification or viscous flow of the porous polymeric binder in the heat-affected zone. The second appears more likely, as stringer formation and beading were both found when laser cutting polymeric sheet that had a tendency to melt. The consequence of the densified layer on final microstructure after sintering remains an area of research activity.

4. Lamination Methodology and Firing Schedules - Very different techniques were used to laminate the tape-cast PVB sheetstock and the compression-molded POM sheetstock.

4.1 Solvent-Based Method of Tacking and Lamination of Tape-Cast PVB Alumina Tape -

The use of solvents to soften the surface of the interface of mating tapes and aid in lamination is not a new idea, but conventional practice, for example, in the fabrication of multilayer ceramic substrates typically involves large strains (>10%) and are not suitable for lamination of green stacks when it is necessary to preserve precise external dimensions. The advantage of solvent lamination over thermocompression is that only the near-surface region of the tapes is softened, so that deformation is localized.

4.1.1 Adhesive Formulation - In these studies, an ethanol/toluene mixture was applied between sheets during stacking. The resultant tacky surfaces ensured that successive sheets were immobilized as they were added to the stack. The volatile nature of pure ethanol and toluene, coupled with capillary suction into the porous green tape, it caused difficulty in depositing and

maintaining a uniform film of solvent. Evaporation was suppressed and the viscosity increased through the addition of polypropylene glycol (1000 m.w.) to form an adhesive solution that rendered surfaces persistently tacky. In most experiments, a triaxial formulation consisting of 40 wt.% ethanol, 20 wt % toluene and 40 wt.% polypropylene glycol was used. Both solvents were removed by vapor phase transport through the porous tape during drying. Polypropylene glycol is a plasticizer for PVB and is presumed to migrate away from the interface during the initial stage of firing, either by capillary action into the pore space and/or by dissolution into the binder.

4.1.2 The Lamination Process - Figure 2 schematically outlines the steps of the adhesive lamination process which was developed for CAM-LEM technology. Using this process, 30 layer samples consisting of 25.4 mm square sheets were stacked and laminated. [In these experiments manual, rather than robotic, stacking was used for experimental convenience.] In the first step, a layer of tape was placed on a smooth, glass plate and brushed to remove cutting debris. Once the surface was clean, adhesive was uniformly applied to the entire surface with an atomizer (approximately 3×10^{-4} gm/mm²). The next layer of tape was added to the stack and rolled with a 0.45 kg, finely polished, aluminum roller (50.8 mm diameter). Rolling was initiated at the center of each layer, followed by 5 complete strokes traversing the entire surface of the slice. This process was repeated for each additional layer. On completion of the stack, samples were vacuum-degassed, by placing the rolled stack in a latex bag and evacuating (using shop vacuum) with a micro-pipette and holding for 30 minutes. After evacuation, the sample was sealed within the bag, uniaxially pressed at room temperature to 1 MPa and held for 10 seconds.

The sample was removed from the bag, dried, and fired. Samples were debinded by heating at 0.2 °C/min. to 800°C, and then more rapidly heating at 3 °C/min to 1560°C for sintering. Dimensional changes were measured after each stage with a micrometer, and all samples were sectioned after sintering. Die penetrant was used to aid in delamination and crack detection.

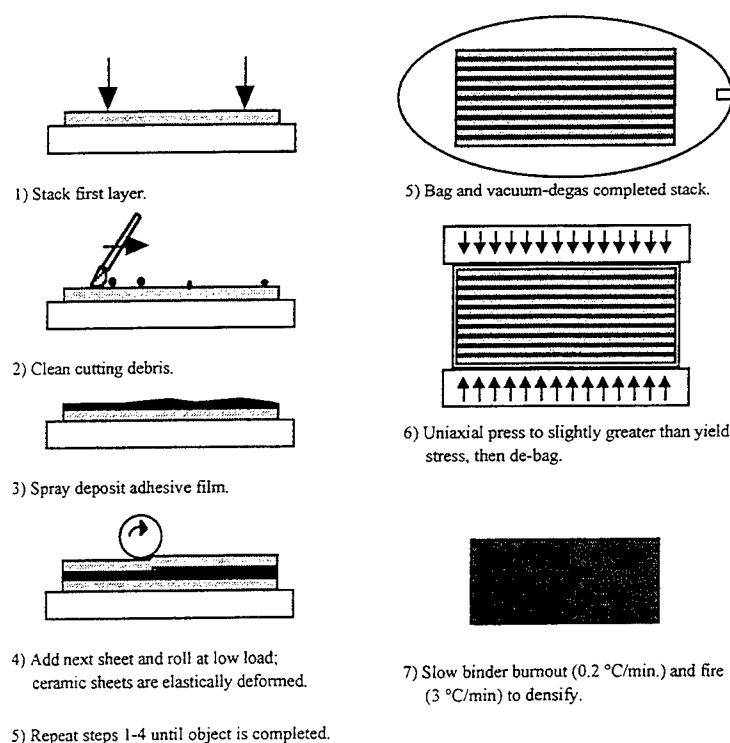


Figure 2. Schematic of the adhesive lamination process.

Thirty-layer samples were used to test the adhesive lamination process. In all samples made to date, the 30 layers completely fused together and no lamina-

tion seams were detected; in marked contrast to the high density of lamination defects observed using other techniques, such as warm isostatic pressing. The rolling load was very small (< 0.45 kg.) and the applied stress was only one-half of the yield stress for the tape. No dimensional changes could be detected in the green state after rolling. The function of the roller is to ensure conformation of each tape to the underlying stack, and to express both bubbles and excess fluid, so that a thin uniform layer of the adhesive solution is left at each interface. The vacuum degassing step was included to assist in the removal of bubbles and excess fluid, but it was subsequently determined to be unnecessary. It is during the uniaxial pressing step that yielding occurred, but, even during this step, dimensional changes were small, $\leq 0.5\%$ linear change. All samples demonstrated linear shrinkages of $\approx 15\%$ during sintering, which is typical for these tapes.

4.1.3 Fugitive Tapes - The adhesive lamination process requires that the applied load, during uniaxial pressing, be effectively transmitted throughout the entire stack, so that all interfaces are approximately equally loaded. Thus, it is highly desirable to prepare a fugitive that has a mechanical response similar to that of the baseline tape, particularly at small strains. The need to match mechanical properties proved to be the key criterion for a successful fugitive. This is demonstrated in Figs. 3-5.

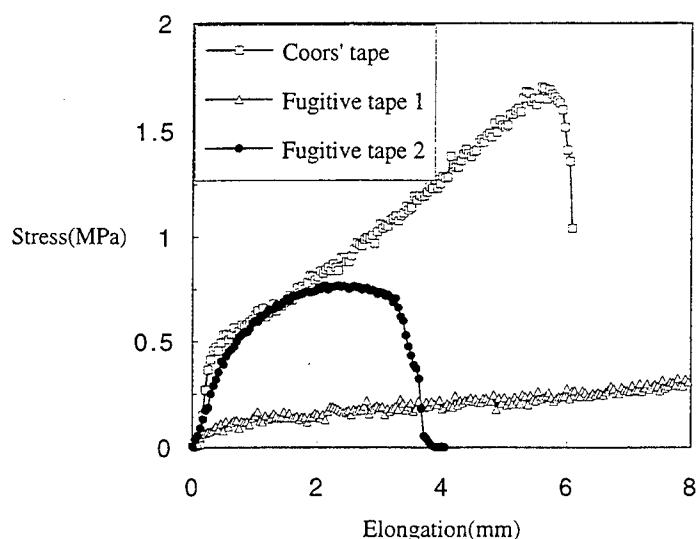


Figure 3. Mechanical behavior of two fugitives compared to the baseline alumina tape.

Figure 3 shows stress-strain curves from tensile tests of two fugitive tapes (prepared with small filler, but different binders) compared to that for the baseline PVB alumina sheetstock. Fugitive-1 is of lower stiffness and yields at a significantly lower stress than the baseline material. Although Fugitive-2 also deviated from the baseline at large strains, its behavior reasonably approximates that of the baseline material at small strain. The consequence of this on lamination behavior is readily seen in the simple, but asymmetric, specimens shown in Fig. 4 and 5.

Specimens were prepared using each of the fugitives, laminated, fired, sectioned, and examined with the aid of a die penetrant. As evident in Fig. 4, the softer fugitive was ineffective as a pressure transmitting medium so that lamination defects were present in the final piece. The fugitive designed to match the base line material was completely successful and the microstructure of the finished piece is devoid of lamination defects, Fig. 5.

4.2 Thermocompressive Lamination of POM Powdered-Metal Tape - Because the compression molded POM tapes are nonporous and the polymer is insoluble, adhesive lamination cannot be used with this type of sheetstock and thermocompression was needed. Initial experiments attempted uniaxial forging at modestly elevated temperatures. However,

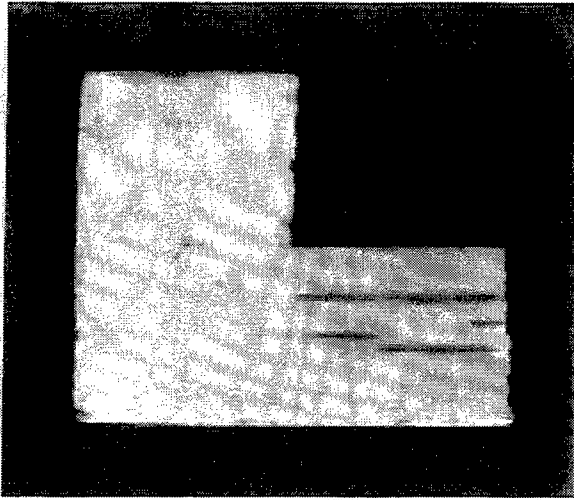


Figure 4. Cross section of a sample laminated with fugitive-1. Note the delamination revealed by die penetrant.

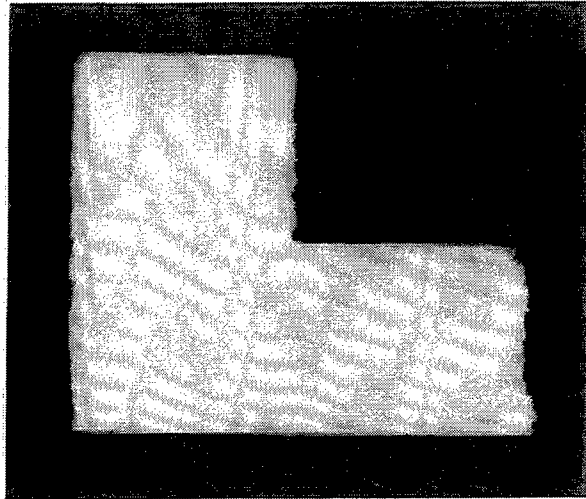


Figure 5. Optical micrograph of a sample laminated with fugitive-2, in which there was no delamination.

control proved difficult, as the polymer remained stiff and unyielding over a wide range in temperature, but then suddenly became fluid and susceptible to gross deformation. A system was needed that would provide both a confining pressure and accommodate a variety of shapes.

The procedure adopted, “quasi-isostatic pressing,” involves burying the piece in a low friction powder (120 μm spherical graphite granules) within the cavity of a large diameter (relative to the piece dimension) uniaxial press. The temperature is raised and a load applied to the rams. With the powder as a pressure transmitting medium, the applied load on the piece is anisotropic; the load parallel to the pressing direction is roughly twice that perpendicular to the pressing direction [7].

This method is very effective at achieving 100% lamination efficiency. Backing plates were sometimes necessary to preserve flatness and, in some instances, surface texture developed during pressing. The primary issue for such lamination is the absence of an adhesive to tack sheets together during stacking. In these experiments, registration of the individual cut sheets was achieved through the use of fugitive pins machined from a block of commercial POM. In addition, the selective application of a water-soluble glue (polyethylene oxide) to the exterior surface during building was used.

5. Catalog of CAM-LEM Parts - Although a wide variety of sheetstocks are compatible with CAM-LEM technology[2], including a wide variety of green ceramic tapes (e.g., silicon nitride, PLZT, and zirconia), the primary material that has been used to date is a commercial high-alumina material. Figure 6 is a catalog of photographs of some of the alumina pieces that have been produced. Each of these pieces was chosen to test a particular feature of the CAM-LEM process. The ceramic head (CAD file downloaded from the internet) demonstrates the ability to manufacture relatively large blocky components which require large areas of lamination and have a large characteristic distance for binder burnout. The amphitheater flange (CAD file created in AutoCAD™) demonstrates the ability to preserve flatness across wide spans and to process

Alumina Parts made by CAM-LEM

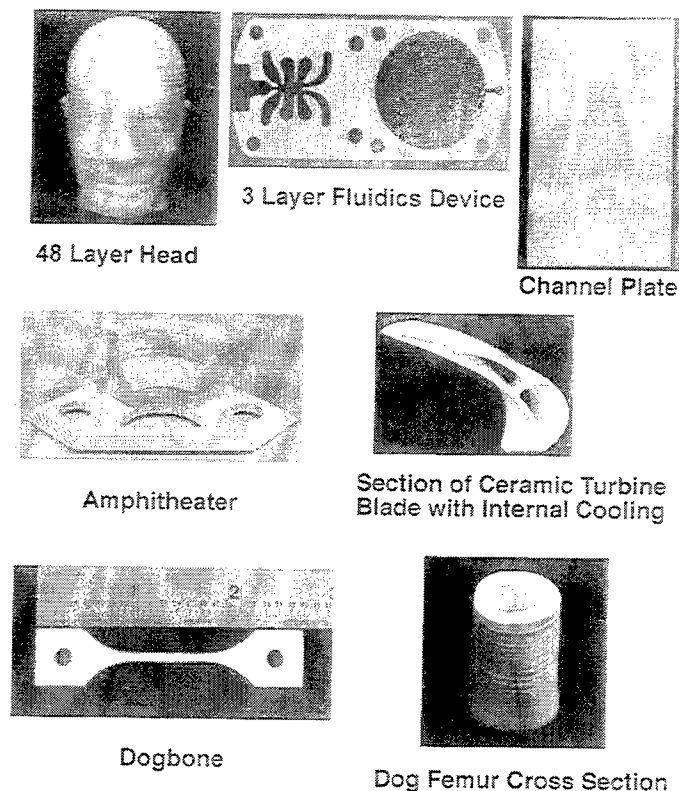


Figure 6. Catalog of ceramic CAM-LEM parts.

The channel plate is actually a three-layer structure, the serpentine structure is a ≈ 2 m. long capillary channel and it is sandwiched between dense plates that have small holes (0.5 mm dia.) that serve as an inlet and outlet. The fluidics device (CAD files modified in AutoCAD™) is a ceramic prototype of a production component that was manufactured to tolerance and performance tested by the manufacturer of the metallic equivalent.

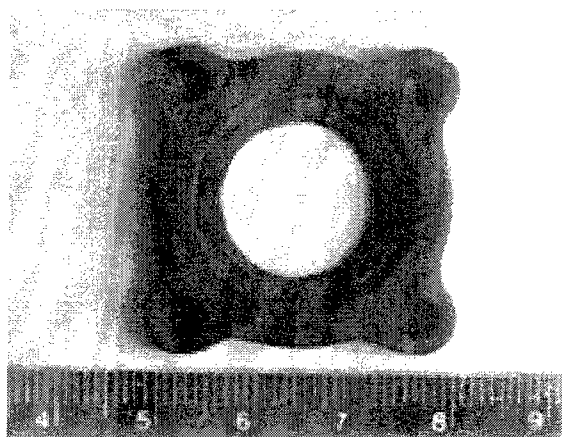


Figure 7. Stainless steel made by CAM-LEM.

components with both thick and thin walled sections. The dogbone test specimen (CAD file created in AutoCAD™) illustrated the ability to produce both test specimens and actual components using the same process, so that material property data can be collected on material of equivalent microstructure to that which will be put in service. The section of a dog femur, the ceramic turbine blade and the channel plate all illustrate the ability to produce hollow shapes that are difficult to produce using hard tooling. The dog femur (CAD file derived from computed tomography scan of an actual bone) has an irregular interior cavity from which it would be difficult to extract an insert after forming. The section of a ceramic turbine blade (CAD file modified in Pro/Engineer™) shows a regular shape that is equally difficult to produce, in this case because of the twist of the interior voids.

Figure 7 show a metallic thrust plate that was fabricated from 316L stainless steel. The CAD file was generated in Pro/Engineer™ using a blueprint that was supplied. The sheetstock was compression-molded tape made from commercial feedstock. This piece demonstrates that components can readily be made using a sheetstock that is nonporous and stiff. Also of significance is the demonstration that conventional POM polymer sheet can be used as a fugitive phase; they are of adequate stiffness and can be readily removed during catalytic debinding.

6. Summary - Two classes of sheetstock have been produced that are compatible with CAM-LEM technology for the production of engineering. Each type of sheetstock can be used to produce both engineered ceramic and metallic components. Different lamination methodologies have been developed for each class of feedstock. An array of components have been produced in alumina, and a limited set has been produced in stainless steel.

Acknowledgments - The authors would like to acknowledge technical discussions with Prof. W. S. Newman, and Messrs. S. Choi, and Y. Zheng of the Electrical Engineering and Applied Physics Department at CWRU, and Mr. B. Mathewson of CAM-LEM, Inc. The experimental help of Messrs. D. Noernberg, and T. C. Ko; and the financial support of the Office of Naval Research (grant # N00014-95-10107) and the National Science Foundation (grant # DMI 94-20373) also are acknowledged.

References

- [1] Y. Zheng, S. Choi, B. Mathewson, and W. Newman, "Progress in Computer-Aided Manufacturing of Laminated Engineering Materials Utilizing Thick, Tangent-Cut Layers," these proceedings.
- [2] B. B. Mathewson, W. S. Newman, A. H. Heuer, and J. D. Cawley, "Automated Fabrication of Ceramic Components from Tape-Cast Ceramic," p. 253 in *Solid Freeform Symposium Proceedings*, University of Texas at Austin Publishers, Austin TX, 1995.
- [3] J. D. Cawley, Z. Liu, W. S. Newman, B. B. Mathewson, and A. H. Heuer, "Al₂O₃ Ceramics Made by CAM-LEM Technology," p. 9 in *Solid Freeform Symposium Proceedings*, University of Texas at Austin Publishers, Austin TX, 1995.
- [4] J. D. Cawley, A. H. Heuer, W. S. Newman, and B. B. Mathewson, "Computer-Aided Manufacturing of Laminated Engineering Materials," *Am. Ceram. Soc. Bull.*, 75 [5] 75 (1996).
- [5] R. E. Mistler, "Tape Casting: The Basic Process for Meeting the Needs of the Electronics Industry," *Am. Ceram. Soc. Bull.*, 69 [6] 1022 (1990).
- [6] J. Ebenhöch, "Injection Molding of Hardmetals Using a Polyacetal Based Binder System," p. 261 in *Advances in Particulate Materials, vol. 4: Metal and Ceramic Injection Molding* Metal Powder Industries Federation, Princeton NJ, 1994.
- [7] W. M. Goldberger, "Electroconsolidation Rapidly Densifies Powder Preforms," *Adv. Mater. Proc.* 141 [6] 43 (1992).

Fused Deposition of Ceramics and Metals : An Overview

M.K. Agarwala¹, R. van Weeren¹, A. Bandyopadhyay¹,
P.J. Whalen², A. Safari¹, and S.C. Danforth¹,

¹Center for Ceramic Research, Rutgers University.

²AlliedSignal Research and Technology

Fused Deposition of Ceramics (FDC) and Metals (FDMet) are SFF techniques, based on commercial FDM™ technology, for rapid fabrication of functional ceramic and metal parts from powder/binder materials. This work demonstrates the possibility of applying FDC and FDMet to a variety of ceramic and metal particulate systems for fabrication of components/parts/devices for wide ranging applications such as tooling, investment casting cores and shells, structural and functional components, etc. Several particulate ceramic and metal systems have been explored for FDC and FDMet. The particulate systems explored vary in particle size from nano-crystalline (WC-Co) to coarse (>100 µm SiO₂) particles. The material systems explored for FDC and FDMet vary from conventional ceramic and metal systems such as SiO₂ and stainless steel to advanced materials such as Si₃N₄ and PZT. FDC and FDMet of such a variety of material systems using a commercial FDM™ system has been made feasible by development of a unique series of binders, as well as optimized FD processing, binder removal techniques and sintering conditions.

I. Introduction

SFF techniques have been commercialized for fabrication of polymer and wax parts for design verification and form and fit [1]. Wax and polymer parts made by SFF have also been used to produce metal and ceramic parts using a two-step process. Once a wax or polymer part is built by SFF, it serves as the positive for investment casting of metallic alloys [1]. Also the wax and polymer materials are being used to make molds for ceramic slurry and gel casting [2,3]. The direct production of metallic or ceramic prototypes for functional applications and testing is currently a major focus in the field of SFF [1, 4-7].

Most of the SFF techniques used for fabrication of metal and ceramic parts employ polymeric binder systems to bond the ceramic or metal particles together to form a green part [1,3-7]. Once a green part is formed by the SFF technique, further processing follows the approach of conventional green forming techniques, such as powder injection molding. The fabricated green part is processed to remove the binder from the part and then sintered or infiltrated with a lower melting second phase. However, fabrication of green metal or ceramic parts by various SFF techniques have been far from trivial. In the SFF techniques, effort is required in developing the proper binder chemistry and often tailoring the *as-received* commercial ceramic or metal powders to allow SFF processing. Once the binder and particulate systems have been developed, the SFF processing conditions are optimized to fabricate high quality green bodies.

This article discusses the results of a new SFF technique, called Fused Deposition of Ceramics (FDC) and Metals (FDMet), which has been applied to a wide range of ceramic and metal systems [3,6,7]. FDC and FDMet are based on an existing Fused Deposition Modeling (FDM™) technology, commercialized by Stratasys Inc. for polymers and waxes [8,9].

II. Fused Deposition of Ceramics (FDC) and Metals (FDMet)

Fused Deposition of Ceramics (FDC) and Metals (FDMet) is being developed to create functional ceramic and metal components using ceramic or metal powders mixed with organic binder systems. The mixed powder-binder feedstock is extruded into filaments of 0.070" nominal diameter, which are then used as the feed material for fabrication of green ceramic or metal parts

using a commercial FDM™ system. The FDC/FDMet green part is then subjected to conventional binder removal and sintering processes to produce fully dense structural ceramic/metal components. As in the case of any manufacturing process, there are several inter-related process variables which determine the success and quality of parts fabricated by FDC or FDMet.

Successful FDC/FDMet processing starts with fabrication of filaments of uniform diameter ($0.070'' \pm 0.001''$) to be used as feed material in the FD hardware. However, for a filament material to be suitable for FD processing, it must possess certain thermal and mechanical properties [9,10]. The key variables that require careful attention and simultaneous optimization in developing the filaments for FDC/FDMet processing are: viscosity and adhesion behavior of the material, and the flexural modulus and strength of the filaments. Based on the constraints imposed by these variables, a series of thermoplastic binders have been developed to enable FDC/FDMet processing. These binders, called the RU binder series, are four component systems - an elastomer, tackifier, wax, and a polymer. The amount of each component was tailored to achieve appropriate viscosity, adhesion behavior, flexibility and stiffness in the green filaments [10]. Appropriate tailoring of these components and selection of a suitable surfactant for a specific particle system have enabled FDC/FDMet processing of several ceramic and metal systems.

FDC/FDMet using the RU series of binder has been demonstrated for Si_3N_4 , fused SiO_2 , Al_2O_3 , lead zirconium titanate (PZT), stainless steel and WC-Co. In each of these particle systems, initial trials for FD were done using a basic composition of the RU binder series, called RU1, which has 30% wax, 35% polymer, 20% elastomer, and 15% tackifier by weight. Further optimization of the binder from the RU1 composition was done, if needed, to achieve the needed flexibility in the filaments to allow automated FD processing or to lower the viscosity to enable FDC/FDMet processing. As reported elsewhere [10], the binder chemistry has been nearly optimized for Si_3N_4 to yield flexible and continuous filaments. FDC/FDMet of other materials has been demonstrated without much variation in the binder composition from the RU1 chemistry. Mixing of the ceramic or metal powder with the binders was done in a torque rheometer mixer to achieve 50 to 65 volume % particle loading. The particle loading achieved in a specific particulate system depends on the particle size and particle size distribution and whether or not a suitable surfactant is used. These factors determine the viscosity of the mixed feedstock which should not exceed a certain limit which will prevent FD processing. Filaments were fabricated from the mixed feedstock using a capillary rheometer or a single screw extruder [10].

Once suitable filaments were fabricated, FDC/FDMet processing was done using a commercial FDM™ system, 3D Modeler™, hardware and software. Build strategies used in the FDC/FDMet were largely the same as those for FDM™ processing of wax and polymers. However, some novel build strategies were developed and implemented to prevent and eliminate property limiting internal defects which arise in conventionally processed FD parts [11]. The choice of slice thickness and road widths for FDC/FDMet were determined by the nozzle diameter, which in turn is determined by the maximum particle size in the specific ceramic or metal system. The FDC/FDMet green parts were further processed to remove the RU binder completely. The binder removal process is done in two stages such that the RU binder is completely removed without any cracking or damage to the part [6,7]. The sintering of the FDC/FDMet part is done by conventional sintering operations for the specific particle system used under consideration.

FDC of Silicon Nitride

Although several ceramic and metal systems have been investigated for the FDC/FDMet processes, the most extensive work to date has been done using an *in-situ* reinforced Si_3N_4 from AlliedSignal Ceramic Components of Torrance, California. *As-received* Si_3N_4 powder coated with appropriate surfactant was used in this study with 55 volume % Si_3N_4 in the mixed powder/binder feedstock. The RU series of binder used for FDC of Si_3N_4 has been optimized to

result in flexible and continuous $0.070'' \pm 0.001''$ diameter filaments fabricated by single screw extrusion [10]. FDC of Si_3N_4 has been done successfully using novel build strategies employed with a commercial FDM™ system to result in sintered parts with physical and mechanical properties comparable to those obtained by conventional processing of Si_3N_4 [7]. FDC of Si_3N_4 has also been demonstrated by fabrication of complex engineering components. Details of the FDC process for Si_3N_4 and their results can be found elsewhere [7].

FDC of Fused Silica

Fused silica, alumina, and zircon are commonly used for fabrication of investment casting tooling. Traditionally, investment casting ceramic shells and cores are manufactured using machined positive patterns of the parts or by injection molding of the actual cores and shells. SFF techniques have been used directly or indirectly for fabrication of investment casting cores and shells. Indirect fabrication involves SFF fabrication of the positive pattern from wax and polymers for the mold. The wax or polymer positive is then used to form a ceramic shell by sequential dipping of the pattern in a ceramic slurry [1]. The wax or polymer is then melted out of the shell followed by firing the shell. Direct fabrication of such ceramic shells and cores for investment casting has been commercialized using the 3D Printing process [5]. The study reported here demonstrates the feasibility of using the FDC process for fabrication of silica parts for investment casting with properties comparable to parts fabricated by conventional core making techniques.

A commercial grade silica powder used for injection molding of investment casting cores by Certech Inc. of Woodridge, New Jersey, was used for FDC in this study. The particle size of the *as-received* silica powder was in the range of $0.01\mu\text{m}$ - $150\mu\text{m}$, with an average particle size of $70\mu\text{m}$. Conventionally, injection molding of cores done by Certech uses 68 volume % silica such that linear shrinkage during firing is limited to $\sim 1\%$, with a final density of $\sim 70\%$ of theoretical density. In order to have comparable shrinkage and final density in the FDC parts, the RU1 binder was mixed with 65 volume % silica powder. Filaments fabricated by capillary and single screw extrusion were straight and stiff with insufficient flexibility for continuous winding onto a spool. A series of $0.25'' \times 0.25'' \times 2.5''$ bars for modulus of rupture (MOR) tests and simple core shape were fabricated by FDC, Figure 1. After binder removal, the bars were fired at Certech Inc. at 1225°C for 6 hours, Figure 2. MOR testing was done to evaluate the mechanical properties. The bars were also used for physical property evaluations, which are critical in determining whether or not the parts can be used for investment casting applications. These physical and mechanical properties were compared with those of injection molded samples of the same grade of silica.

As shown in Figures 3, the microstructure of fired FDC silica samples is comparable with that of fired injection molded samples with no evidence of delamination or inter-road debonding. Similarly, the physical and mechanical properties of the FDC processed samples compare very favorably with the reported properties of injection molded parts, Table I, and were within the commercial upper and lower acceptable limits reported by Certech's specification data sheet. For example, although the average cristobalite level in FDC samples is lower than those in injection molded samples, the levels are well within the acceptable limits of 20% and 7%, respectively. The starting volume fraction of silica in FDC samples is lower (65%) than that in injection molded parts (68%), while the final bulk density of both FDC and injection molded parts are similar. Therefore, the linear shrinkage observed in FDC samples was slightly higher. Since the number of FDC samples tested was few (10) in comparison to injection molded samples used for reporting data in product data sheet, the standard deviation for the properties in FDC samples (shown in parenthesis in Table I) indicate a wider spread in the FDC values compared to the injection molded samples. However, this study demonstrates that FDC is a viable SFF technique for direct fabrication of investment casting ceramic cores and shells using commercial grade powders with resulting properties comparable to those of conventionally processed parts.

FDC of Piezoelectric ceramics

Piezoelectric materials have the ability to convert electrical energy into mechanical energy or conversely convert mechanical energy into electrical energy. The applications for devices from these materials include transducers, microphones, phonographic pick-ups, speakers, accelerometers, strain gages, ignitors, and various medical diagnostic systems. Several ceramics exhibit piezoelectric behavior, with lead zirconium titanate (PZT) being the most extensively used. Piezoelectric ceramic/polymer composites, consisting of a piezoelectric ceramic, such as PZT, in an inactive polymer, have shown superior properties when compared to monolithic single phase materials. The piezoelectric properties have been vastly improved over the last two decades through fabrication of numerous innovative structures [12]. However, most of the processing techniques lack the flexibility of fabricating novel structures.

SFF techniques, specifically FDC in this study, provide an opportunity to control the fabrication of these complex structures as material is deposited one volume element at a time only in desired locations and is directly controlled by the computer through the component CAD file [1]. Such flexibility, of SFF in general and FDC in particular, allows deposition of material at a very fine scale only in desirable locations and leaving the other areas unfilled [3]. Once the desirable green ceramic structure of PZT is fabricated, the remaining unfilled regions are filled by the inactive polymer phase, following binder removal and sintering. Such an approach results in complex geometries of piezocomposites to be fabricated with relative ease. In this study, *as-received* spray-dried PZT powder from Morgan Matroc Inc. of Cleveland, Ohio, was used. Green PZT filaments containing 50 volume % PZT powder and 50 volume % RU1 binder with a surfactant and plasticizer was used, Figure 4. Several simple shapes with intricate internal structures, such as ladder structures, were formed using FDC, Figures 4 and 5. After binder removal and sintering of the green FDC PZT parts, the parts were infiltrated with an inactive polymer to form the final desired piezocomposites. The piezoelectric properties of the piezocomposites by FDC were measured and found to be significantly better than those reported for conventionally processed PZT composites. Further details and results on FDC of piezoceramics can be found in these proceedings [3].

FDMet of Stainless Steel

As mentioned earlier, one of the major applications of SFF technologies has been to fabricate polymer or wax positive patterns for investment casting of metallic alloys. Such an approach has been successfully adopted by automotive and aerospace industries in investment casting of critical components from metals [1]. To further maximize the benefits of SFF technologies, direct fabrication of such metal components by SFF techniques are being developed. This study demonstrates the feasibility of using FDMet for fabrication of green parts from powder stainless steel which can then be further processed by binder removal and sintering to result in a fully dense steel part.

Precipitation hardened stainless steels are commonly used in various industrial and military applications where resistance to corrosion and high mechanical performance at temperatures to 400°C are necessary. Typically these steels are available in wrought form and the parts are fabricated by conventional thermomechanical processes. The precipitation hardened steel used in this study was a 17-4PH grade (also referred as Type 630) stainless steel powder of -325 mesh particle size. Powder with 60% by volume was mixed with RU1 binder composition and extruded into stiff, straight filaments of 0.070" nominal diameter using a capillary extrusion process. Simple green stainless steel shapes were created at 110°C using the commercial FDM™ system, Figure 6. Following binder removal, the parts were sintered at 1350°C for 1 hour in a mild reducing atmosphere (H_2+N_2), Figure 7. Although sintered parts exhibit high density (92%-95% of theoretical), close examination of sintered parts reveal internal delamination and cracking in the

parts. Further experiments with capillary extruded green rods (3/8" diameter) of the same composition revealed cracking and bloating occurring during the binder removal process. It is expected that once the binder removal is optimized to prevent defects, stainless steel FDMet parts with properties and microstructures comparable to that of wrought formed parts can be achieved.

FDC of WC-Co

Tungsten carbide (WC)-based composites have a good combination of properties including high hardness, toughness, and wear and abrasion resistance. These properties make them suitable for a variety of tooling applications such as metal cutting, mining, rock drilling, dies, and wear parts. The basic tungsten carbide-cobalt (WC-Co) material has been modified over the years to produce a variety of cemented carbides for these applications. Conventional powder metallurgical techniques are used for processing and fabrication for these materials. Today, new techniques are being developed to reduce costs and improve performance. One of these new technologies include synthesis and use of nanocrystalline WC-Co powders. As SFF techniques are being explored for metals and ceramics and the SFF technologies have also led to significant growth and demand in Rapid Tooling applications, it is only natural to explore SFF techniques for WC-Co.

In this study, FDC was explored as an SFF technique for fabrication of WC-Co shapes. Two different grades of commercial WC-Co powders were used in this study, nanocrystalline WC-15Co from Nanodyne, Inc. and WC-15Co from Valenite, Inc. Due to the extremely fine particle size and high density ($\sim 14 \text{ g/cm}^3$) of these materials, the viscosity of the RU1 binder mixed with only 50 volume% of these WC-Co was too high to allow successful FDC processing using commercial FDMTM systems. To allow successful FDC processing, the RU series binder was tailored and a suitable dispersant was developed to lower the viscosity of 50-55 volume % WC-Co loaded binder system. Initial FDC trials with the RU binder formulation and use of dispersant, indicate that it is possible to achieve high solids loading (50-55 volume%) of nanocrystalline WC-Co and attain a viscosity level low enough for FDC processing at 200°C [10]. Further development of binder and dispersant are expected to result in optimized FDC processing of WC-Co with sintered properties comparable to those of conventionally processed WC-Co.

FDC of Alumina

Alumina is a commonly used ceramic in many structural applications. FDC of alumina has been demonstrated by Lone Peak Engineering of Draper, Utah, with very much the same approach as reported here [4]. In the study by Lone Peak Engineering, FDC was done using commercial grade A-16SG alumina powders and thermoplastic binders with suitable plasticizers and dispersants. As discussed elsewhere [4], FDC processed alumina parts in the study exhibited greater than 97% theoretical density after sintering.

Conclusions

This article demonstrates that FDC and FDMet are SFF techniques which are practical for rapid fabrication of structural and functional parts/components from powder/binder mixtures. A unique series of binders developed for FDC/FDMet have been uniformly applied to a wide range of ceramic and metal systems for FD processing. The materials studied here demonstrate that *as-received* commercial powders can be readily used for FDC/FDMet with sintered parts exhibiting properties comparable to those of conventionally processed parts from the same material. By tailoring the RU series of binder and proper selection of dispersants and optimization of the FD process and binder removal procedures, different material systems can be readily developed for FDC/FDMet processing.

Acknowledgments

The work on various material systems has been done through support from DARPA, ONR (Contract No. 00014-94-0115), and the New Jersey Commission on Science and Technology (NJCST). The authors would also like to thank Drs. C. Ballard and S. Das of AlliedSignal Research and Technology, Drs. E. Krug and G. Carrasquillo of Certech Inc., Mr. W. Priedeman of Stratasys Inc., Drs. R. Sadangi and L. McCandlish of Nanodyne Inc., and Dr. S. Raghunathan of Valenite Inc. for their help and support in developing FDC/FDMet of these materials.

References

1. Proceedings of the Solid Freeform Fabrication Symposium, Vols. 1-7, 1990 - 1996, Edited by H.L. Marcus, J.J. Beaman, J.W. Barlow, D.L. Bourell, and R.H. Crawford, The University of Texas at Austin, Austin, Texas.
2. V.R. Jamalabad, et. al., "Gel Cast Molding with Fugitive Molds," *ibid.*, Reference #1, Vol.7, 1996.
3. A. Bandyopadhyay, et. al., "Processing of Piezocomposites via SFF Techniques," *ibid.*, Reference #1, Vol. 7, 1996.
4. E.A. Griffin and S. McMillin, "SLS and FDM Processes for Functional Ceramic Parts," *ibid.*, Reference #1, Vol.6, 1995, pp. 25-30.
5. M.J. Cima and E.M. Sachs, "Three Dimensional Printing: Form, Materials, and Performance," *ibid.*, Reference #1, Vol. 2, 1991, pp. 187-194.
6. M.K. Agarwala, et. al., "Structural Ceramics by Fused Deposition of Ceramics," *ibid.*, Reference #1, Vol. 6, 1995, pp.1-8.
7. M.K. Agarwala, et. al., "Fused Deposition of Ceramics for Structural Silicon Nitride Components," *ibid.*, Reference #1, Vol. 7, 1996.
8. U.S. Patent # 5,121,329, June , 1992.
9. J.W. Comb and W.R. Priedeman, "Control Parameters and Material Selection Criteria for Rapid Prototyping Systems," *ibid.*, Reference #1, Vol. 4, 1993, pp. 86-91.
10. M.K. Agarwala, et. al., "Filament Feed Materials for Fused Deposition Processing of Ceramics and Metals," *ibid.*, Reference #1, Vol. 7, 1996.
11. V. Jamalabad, et. al., "Process Improvements in the Fused Deposition of Ceramics (FDC) : Progress Towards Structurally Sound Components," Proc. of the ASME Design for Manufacturing Conf., Aug. 1996, Irvine, CA.
12. V.F. Janas and A. Safari, "Overview of Fine-Scale Piezoelectric Ceramic/Polymer Composite Processing," J. Amer. Ceram. Soc., 78[11], 1995, pp. 2945-2955.

Table I
Physical and Mechanical Properties of Fused Silica
Processed by FDC and Injection Molding

Processing Technique	Bulk Density (g/cm ³)	Apparent Density (g/cm ³)	Porosity (%)	Absorption (%)	Modulus of Rupture (psi)	Linear Shrinkage (%)	Cristobalite Level (%)
FDC	1.58 (0.01)	2.26 (0.00)	30.0 (0.52)	19.0 (0.5)	1825 (243)	1% - 4%	11.5
Injection Molding	1.58 (0.00)	2.29 (0.01)	31.2 (0.4)	19.7 (0.3)	1788 (96)	1.53 (0.3)	16.9

Numbers in parantheses are standard deviation of the data reported.



Figure 1: Green fused silica parts, a MOR bar and a section of a core for investment casting, processed by FDC.

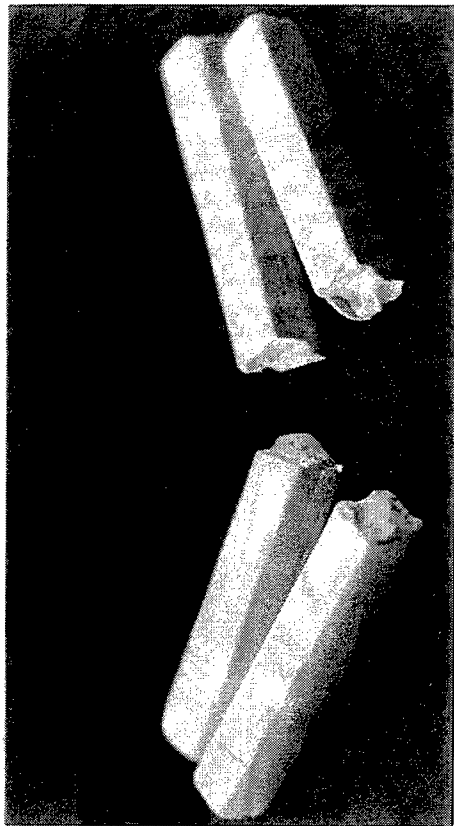


Figure 2 : Fractured fired fused silica MOR bars made by FDC.

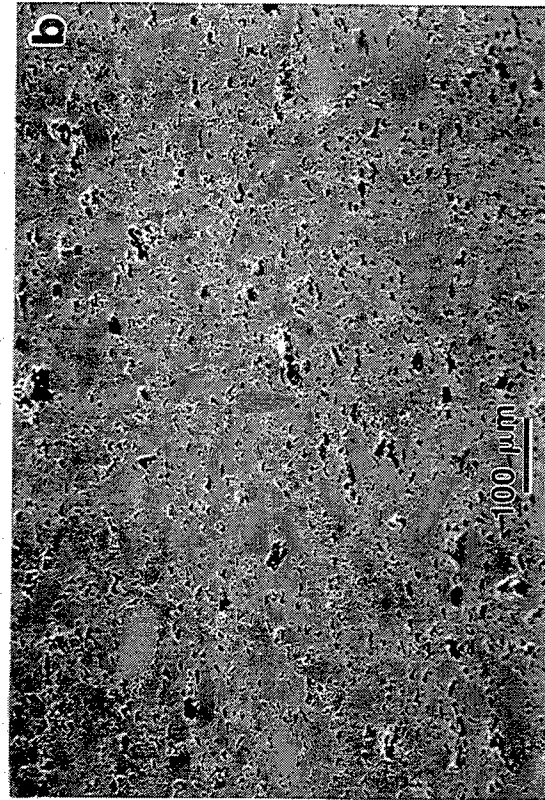
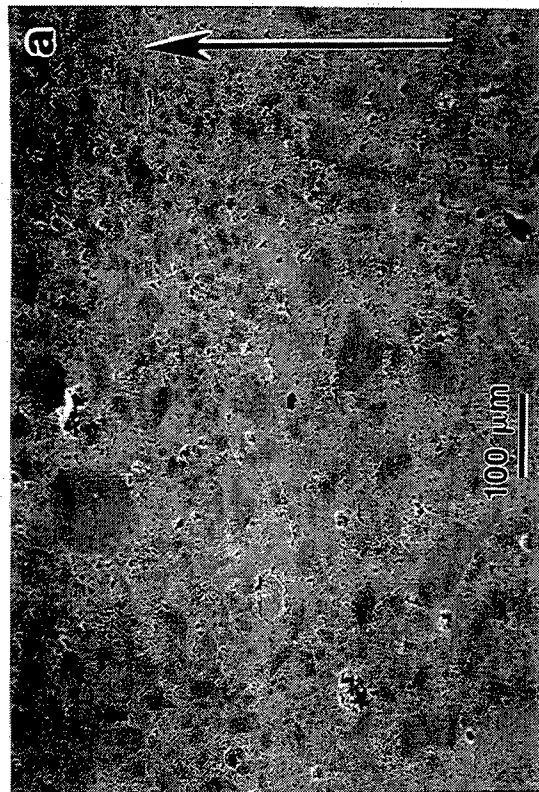


Figure 3: SEM micrograph of a polished cross section of fired fused silica samples processed by (a) FDC (arrow indicates the build direction) and (b) Injection Molding.

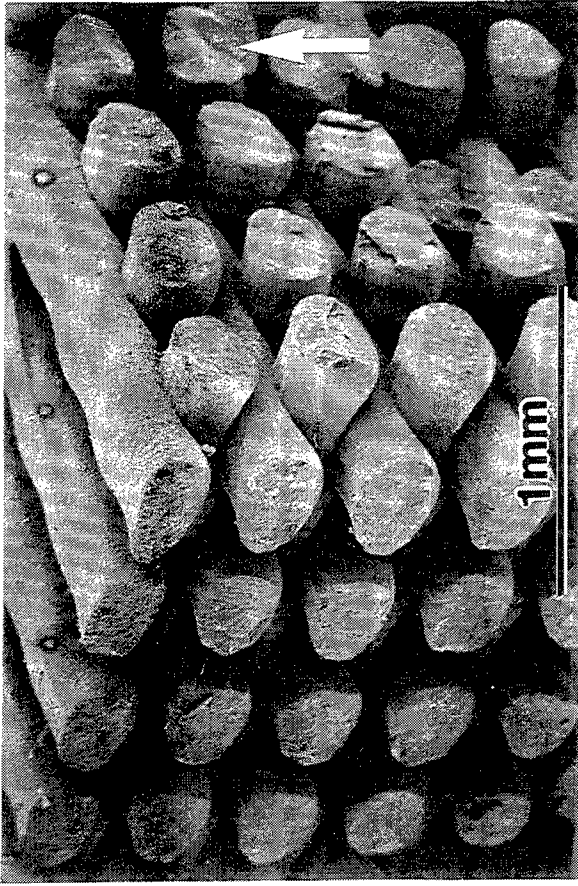


Figure 5: SEM micrograph of a sintered PZT three-dimensional ladder structure fabricated by FDC processing (arrow indicates the build direction).

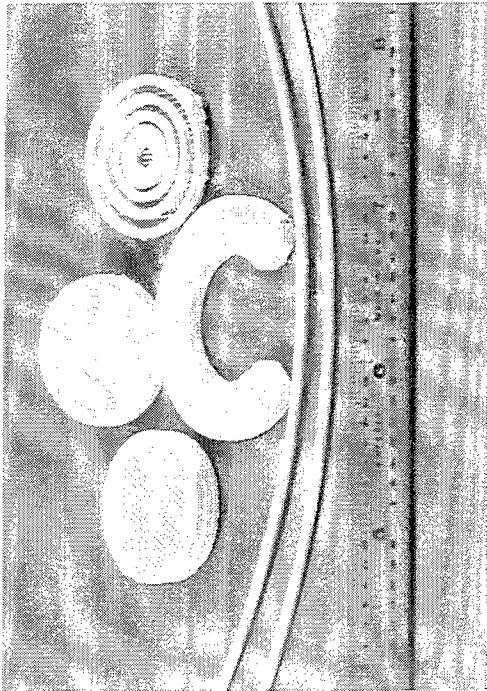


Figure 4: Green PZT filament used for FDC processing and structures and shapes for piezoelectric applications fabricated by FDC processing.

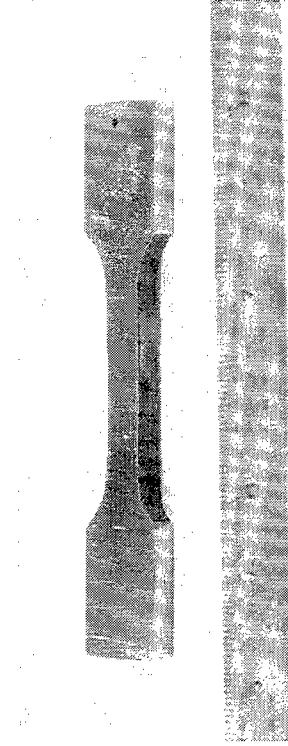


Figure 7: Sintered stainless steel (17-4PH) tensile coupon fabricated by FDMet processing.

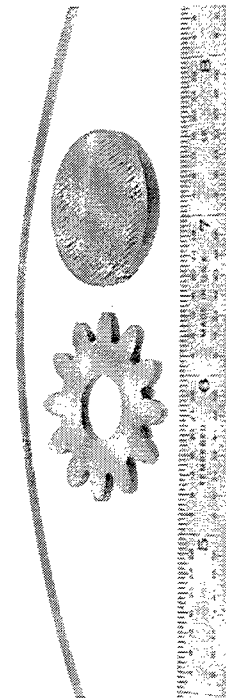


Figure 6: Green stainless steel (17-4PH) filament used for FDMet and parts fabricated by FDMet processing.

Improving the Thermal Stability of Somos™ 6110 Photopolymer Patterns

*Suresh Jayanthi, Bronson Hokuf and John Lawton
DuPont Somos™ Materials Group
Two Penn's Way, Suite 401
New Castle, DE 19720
Tel:302-328-5435 ; Fax:302-328-5693*

Abstract:

With the increased emphasis on functional testing and tooling applications using stereolithographic rapid prototyping (RP) techniques, the need for RP materials with improved thermal stability is becoming more pronounced. Glass transition temperature and Heat deflection temperature are two commonly used measures to determine the thermal stability of a polymeric material.

This paper shows the effect of different postcuring techniques on the heat deflection temperature (HDT) of DuPont Somos™ 6110 photopolymer. In addition, the benefits of using heat transfer mediums which provide neutral buoyancy and thus minimize thermal distortions are discussed.

Introduction:

The epoxy based stereolithographic photopolymers possess good dimensional and mechanical properties. The good dimensional properties are mainly attributed to the inherently low shrinkage during photocuring compared to the earlier acrylate based photopolymers. However, a major limiting factor of the first generation of epoxy photopolymers was their lower photo sensitivity. The recently introduced second generation epoxy resin **DuPont - Somos™ 6110** provides significant improvements in photo sensitivity, allowing increased throughput from the stereolithography (SL) systems. Somos™ 6110 is used in the Helium-Cadmium laser systems like SLA-250™ from 3D Systems Inc., USA and STEREOS DESKTOP™ from EOS Inc., Germany.

With the improvements in speed and physical properties possible from epoxy materials, the focus has now turned towards functional applications of the SL patterns. The SL patterns are now being widely used in a range of applications such as silicone rubber molding, injection molding as well as investment casting. With the ever increasing use in these tooling applications, the need for greater thermal stability of these patterns has become crucial.

This study focuses on methods aimed at improving the thermal stability of Somos™ 6110. The two main parameters that were looked into are the glass transition temperature (T_g) and the heat deflection temperature (HDT). These two parameters are related to the internal changes in the material.

Using the standard measuring techniques these two parameters were determined for the Somos™ 6110 epoxy photopolymer under various thermal postcure conditions. The relationships between these two parameters were studied with the objective of enhancing the HDT. Although no extensive quantitative data on the dimensional variations with thermal cure are available at this stage, a few preliminary results are presented.

Thermal Stability:

Two different temperature-dependent mechanisms exist in polymeric materials. The first mechanism is a reversible process representing the softening of a material with increasing temperature and is used to characterize the thermal stability. The second mechanism is the irreversible decomposition of the material due to heat. In this study we are primarily concerned about the first mechanism.

The thermal stability of polymeric materials can be expressed either by a temperature or time limit (at some specified temperature) up to which the material remains useful. A material is stable if no noticeable change occurs over any length of time or if any changes that occur are reversible. Typically, the point of thermal instability is observed by noting the onset of phase transitions that take place within the material. Two types of transitions are commonly observed on heating or cooling a plastic - a first order and a second order transition[1].

A first order phase transition is observed when the material properties change abruptly. A second order phase transition is much more gradual and can usually be related to the amorphous segments of the polymer. The most prominent of the several second order phase transitions is the glass transition. It is an intrinsic material property characterizing a reversible softening behavior. According to ASTM E1142, glass transition is defined as, "the reversible change in an amorphous material or in amorphous regions of partially crystalline material, from (or to) a viscous or rubber condition to (or from) a hard and relatively brittle condition". The glass transition temperature (T_g) is usually taken as the approximate midpoint of the temperature range over which the second order transition takes place.

Besides the occurrence of transitions, certain properties of the plastic are continuously changing with temperature. The vibration of the chain segments increases with temperature and this motion weakens the cohesive forces between the molecules. Decreased cohesion results in softening of the material (compromising its structural stability) and correspondingly affects the physical properties. On the basis of practical experience, criteria have been established which

determine the limit of structural stability under load and heat. One such criterion is the HDT. A brief review of Tg as well as HDT will be provided below which will help us better understand the experimental results.

Glass Transition Temperature:

Glass transition is an important parameter in deciding the applications of many crystalline and non-crystalline polymers. It represents the temperature ranges at which the polymer matrix transitions from the glassy state to the flexible state. Below the Tg, however, the unreacted groups may not be able to crosslink due to lack of matrix mobility. The polymer chain segments cannot move around -- they are frozen in place and the behavior of the material changes from ductile to brittle. Above the glass transition temperature there is enough mobility within the object matrix to allow segmental chain motion, and the chains can move more or less freely around. As the temperature increases this freedom continues to increase until the matrix approaches the "liquid" state (if the polymer is not crosslinked). Even lightly crosslinked (or thermoset) polymers will have a glass transition that involves the motion of the linear chain segments between the crosslinks. If the crosslink density becomes high enough the glass phase transition will disappear.

Some of the main molecular parameters influencing the Tg are [2]:

- Chain stiffness
- Internal plasticization and
- Intra molecular forces

The mobility of the polymer chains is primarily affected by the barrier to their rotation around the backbone carbon-carbon bonds within the polymer matrix. This in turn is determined by the size of the substituent groups on the carbon atoms. The larger the substituent or the more hindered the rotation because of multiple anchoring (Van der Waals' forces between the side groups on the chain), the higher the Tg.

Inclusion of low molecular weight materials (as side chains on the carbon-carbon bonds) which generally have lower Tg, plasticizes the polymer. Therefore, the higher the concentration of low molecular weight side chains the lower the Tg of the material. The internal plasticization can either be due to inter-chain or intra-chain plasticization. Inter-chain plasticization is caused by small molecules that solvate and allow the polymer chains to move and become flexible. Water, for instance, can act as a plasticizer lowering the Tg. Intra-chain plasticization occurs when the primary chain of the polymer has long side chains (which act as plasticizers or chain softeners).

Crosslinking has the opposite effect of a decrease in molecular weight. Increasing crosslink density increases Tg correspondingly. Most of the highly crosslinked thermoset polymers are amorphous.

Several methods exist to experimentally determine the T_g . One of the most commonly used methods is differential scanning calorimetry (DSC). It is based on the power compensated null balance principle, in which the energy absorbed or liberated by the specimen is exactly compensated by adding or subtracting an equivalent energy to a heater located in the sample holder [3]. As the sample material passes through the glass transition upon heating, its (apparent) specific heat abruptly changes due to an increased motion in the material. In practice, specimens of thin flat disks of the material, usually less than 0.6 mm thick, are encapsulated inside an aluminum pan (0.08 mm thick) with a lid crimped in place to ensure uniform heat transfer. Platinum resistance heaters and thermometers are used in the DSC to carry out temperature and energy measurements. Another commonly used method for determining T_g is differential mechanical analysis (DMA). Values obtained using DMA are typically higher than those obtained using DSC [4]. In this study DSC was used.

Heat Deflection Temperature:

As mentioned before, the T_g is an intrinsic material property characterizing the reversible softening behavior of the material. Many techniques have been developed to determine, in a well-defined way, the maximum usable temperature of a material due to softening. Heat deflection temperature (HDT) measurement is one such practical technique.

The HDT is the temperature of the material at which a certain deformation is induced under flexural load of the test specimen. The test provides a measure of the thermo-mechanical stability of the material. A rectangular specimen 5" x 1/2" x 1/8" is placed on two supports 4" apart, immersed in a heat transfer medium (oil bath) with a load applied at its center to give a maximum fiber stress of 66 psi. Higher loads were not used because there is no advantage to using higher loads when measuring deflection temperature of the present-day plastics with present-day instruments¹. With the bar immersed and the load applied, the temperature is raised at a rate of 2 °C/min. The temperature at which a deflection of 0.010 inches occurs is noted as the HDT under flexural load of the material. The experimental testing reported in this study was done according to the ASTM D 648 standard.

Experimental Discussion:

The eventual physical properties are greatly influenced by the postcuring conditions used. The most common postcure techniques employed in curing green patterns are ultraviolet (UV) and thermal cure. The UV cure is intended to polymerize any uncured liquid trapped within the solid by irradiating the patterns

¹ASTM D 648 - 82 (Reapproved 1988) - Standard Test Method for Deflection Temperature of Plastics Under Flexural Load. Annual Book of ASTM Standards 1993. Section 8.

with broad-band UV light. Thermal cure, however, induces additional polymerization by increasing the mobility of the polymer chains allowing additional chemical reactions to occur. In this study several thermal postcuring techniques to improve the thermal properties were investigated.

With thermal postcuring techniques, concerns regarding dimensional distortions become important. At elevated temperatures due to the softening behavior of the material, distortions are likely to occur in unsupported regions under the influence of gravity. One way of reducing these thermally induced gravity distortions is to heat treat the specimens in a dense heat transfer medium like silicone oil. The silicone oil also acts as a uniform heat transfer medium. The silicone oil used in this study is a commercially available DOW CORNING® 550 fluid which has a specific gravity of 1.1.

Besides the gravity induced distortions mentioned above, thermal treatment can induce distortions due to swelling. Though this behavior has not been extensively investigated, a few preliminary experiments have been performed and the results are discussed later.

Another factor which can influence the dimensional stability as well as the glass transitions is the humidity. The Somos™ 6110 is designed to produce good dimensional characteristics at higher humidities. Studies are underway to study the effects of humidity on the glass transition and will be reported at a later date.

The experimental plan is essentially divided into three components. First, the T_g is determined using the DSC approach. Second, the HDT is determined using the ASTM D648 standard by thermally postcuring the specimens in air at various temperatures. Third, the HDT is determined by thermally postcuring the specimens in a silicone oil medium at various temperatures.

For the T_g determination, sample specimens 0.2 mm thick and 25 mm cross-section, were imaged in Somos™ 6110 using a SLA-250™. The imaged specimens were cleaned with tripropylene glycol monomethyl ether (TPM) and isopropyl alcohol to remove the residual uncured liquid polymer. Thermal postcuring was done in a programmable convection oven. The green parts are considered to be postcured at 25 °C (ambient temperature) while the UV parts are considered to be postcured at 40 °C (the UV chamber temperature). For the HDT determination, the specimens were made with dimensions as specified in the ASTM D 648 standard. The green HDT specimens were cleaned as mentioned above. Four HDT specimens were used at each postcure condition. The green T_g and HDT specimens were later postcured under conditions described in Table 1.

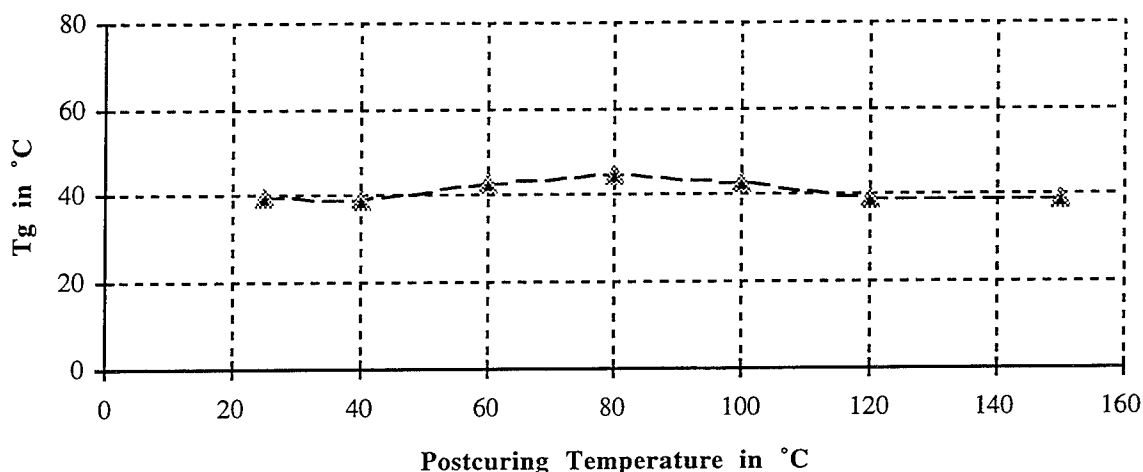
The T_g specimens were later measured for the glass transition using a DSC apparatus. The specimens were initially chilled below 0 °C before heating. A standard 10 °C/min. rate of temperature increase was used for all measurements with a maximum temperature of 100 °C. The results from the DSC measurements

are as shown in Figure 1. The Tg is measured as the inflection point in the glass transition phase curve on a temperature versus specific heat graph. The Tg of the material ranges from 39 °C and 44 °C. This seems to indicate that no significant changes in the phase transitions are taking place as a result of thermal postcuring. The variation of Tg with thermal postcuring in silicone oil has not been investigated. However, no significant differences may be observed.

Table 1: Postcuring Conditions for Tg Determination

#	Postcure Temp.	Description
1	25°C	Green patterns (ambient curing)
2	40°C	UV cured patterns (UV chamber temp.)
3	60°C	0.5hr ramp up; 1hr at 60°C; 0.5hr ramp down.
4	80°C	0.5hr ramp up; 1hr at 80°C; 0.5hr ramp down.
5	100°C	0.5hr ramp up; 1hr at 100°C; 0.5hr ramp down.
6	120°C	0.5hr ramp up; 1hr at 120°C; 0.5hr ramp down.
7	150°C	0.5hr ramp up; 1hr at 150°C; 0.5hr ramp down.

Figure 1: Influence of Postcure Conditions on Tg for Somos™ 6110



The heat deflection temperatures of the specimens postcured in air are shown in Figure 2. The HDT appears to improve with the postcure operations. Table 2 describes the postcure conditions of the specimens immersed in a silicone oil medium whose density was selected to provide neutral buoyancy for the part and thus reduce distortions during postcure. Four specimens were used at each postcure condition. The heat deflection temperature of the specimens postcured in silicone oil are shown in Figure 3. As shown in Figures 2 and 3, the HDT appears to improve

with the thermal postcuring. The HDT of the specimens postcured in silicone oil appears to be higher than the air postcured specimens. This may be because the specimens postcured in oil had a longer cure cycle and therefore were held at an elevated temperature for a longer duration. Longer and more gradual rate of increase in temperature appears to improve the HDT. However, the HDT appears to reach a peak at a postcuring temperature of 100 °C in silicone oil, while the trend in air postcured specimens appears to be more linear. This result needs to be further investigated.

Figure 2: Influence of Postcure Conditions on HDT for Somos™ 6110

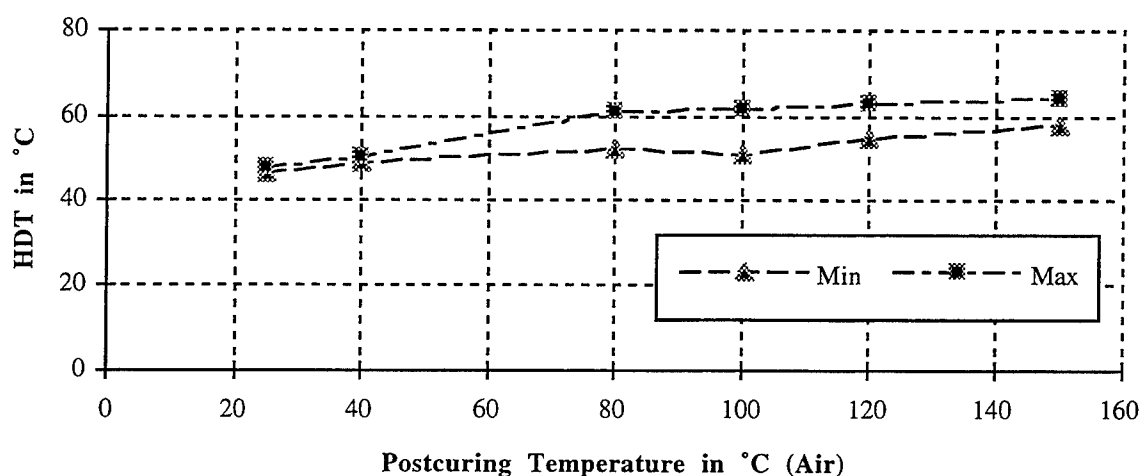


Table 2: Postcuring Conditions for HDT Determination in Silicone Oil

#	Postcure Temp.	Description
1	25°C	Green patterns (ambient curing)
2	40°C	UV cured patterns (UV chamber temp.)
3	60°C	2hr ramp up; 1hr at 60°C; 2hr ramp down.
4	80°C	2hr ramp up; 1hr at 80°C; 2hr ramp down.
5	100°C	2hr ramp up; 1hr at 100°C; 2hr ramp down.
6	120°C	2hr ramp up; 1hr at 120°C; 2hr ramp down.
7	150°C	2hr ramp up; 1hr at 150°C; 2hr ramp down.

In the thermal Postcuring of the SL patterns dimensional stability concerns are critical. Efforts are underway to fully characterize the nature of dimensional distortions induced during thermal postcuring. A few preliminary studies have been done to determine the changes in the dimensions of the specimens. Our results show that both UV as well as thermal postcuring increases the dimensions

by 0.1% to 0.13%. Though the thermal postcuring in silicone oil does seem to improve the dimensional increase, the specimens showed lesser gravity distortions. However, specimens which were conditioned in a desiccant chamber at 0% relative humidity for two days and thermally postcured showed a drop in the dimensional increase. Figure 4 illustrates the this phenomena. This result seems to indicate that thermal postcuring in the absence of moisture helps maintain the dimensional stability.

Figure 3: Influence of Postcure Conditions on HDT for Somos™ 6110

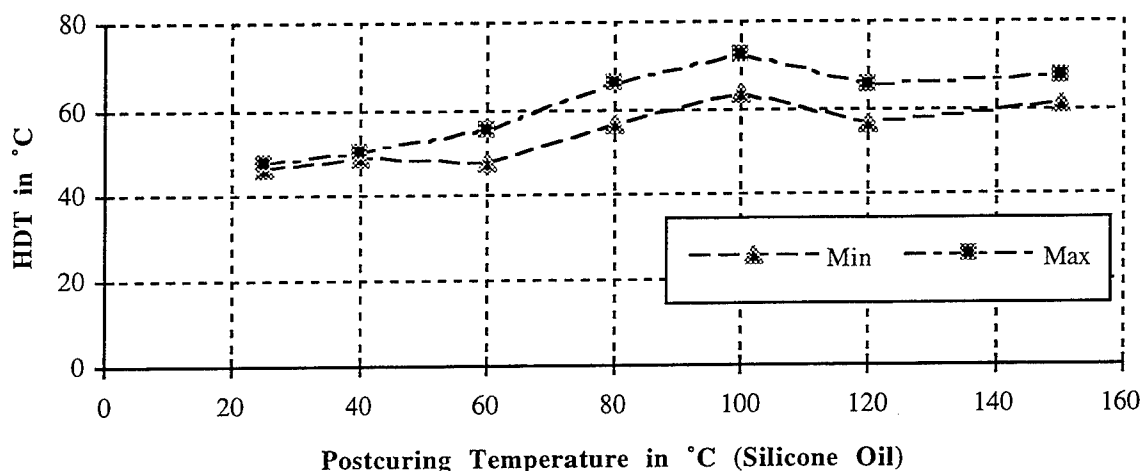
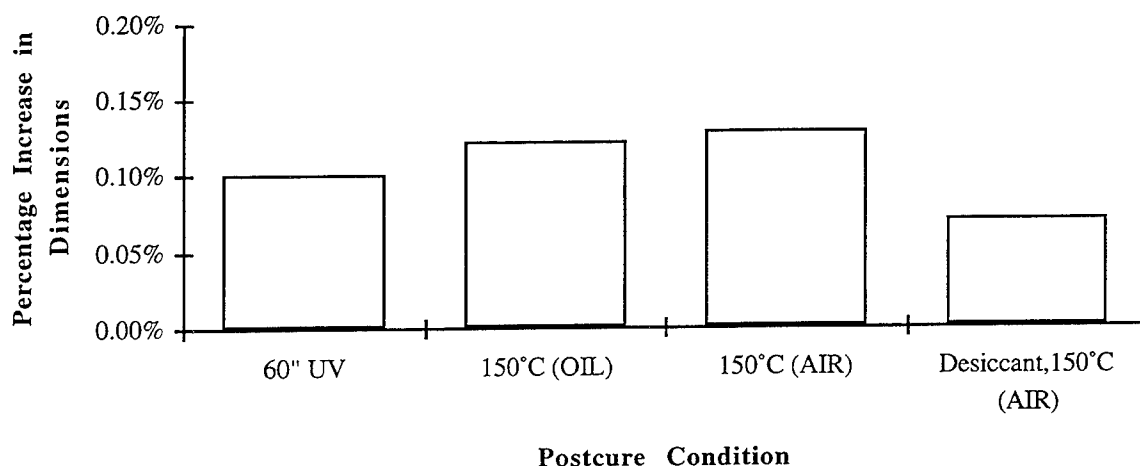


Figure 4: Increase in Length of HDT Specimens due to Postcuring of Somos™ 6110



Conclusions:

- The Tg does not vary significantly with thermal postcuring.
- The HDT, however, shows a increase of 15 to 25 °C under the same postcure conditions.
- The Tg is lower than the HDT of the material.
- Thermal postcuring in silicone oil improves the HDT over postcuring in air - perhaps due to extended time at temperature.
- Better dimensional stability can be achieved by conditioning the parts at 0% RH before thermal postcuring.

References:

- [1] Gerhard F.L. Ehlers, "**Thermal Stability of Plastic Materials**", *Engineering Design for Plastics*, Reinhold Publishing Corporation, New York 1964.
- [2] James E. Mark, Adi Eisenberg, William W. Graesky, Leo Mandelkern, Jack L. Koenig, "**The Glassy State: and the Glass Transition**", *Physical Properties of Polymers*, American Chemical Society, Washington D.C, 1984.
- [3] Harvey E. Bair, "**Glass Transition Measurements by DSC**," *Assignment of the Glass Transition*, ASTM STP 1249, R.J. Seyler, Ed., American Society of Testing and Materials, Philadelphia, 1994, pp.50-74.
- [4] Chartoff , R. P., Weissman, P. T., and Sircar, A., "**The Application of Dynamic Mechanical Methods to Tg Determination in Polymers: An Overview**," *Assignment of the Glass Transition*, ASTM STP 1249, R.J. Seyler, Ed., American Society of Testing and Materials, Philadelphia, 1994, pp.88-107.

Acknowledgements:

This presentation is a result of the efforts of many people in the Somos™ Materials Group. We would like to acknowledge the valuable assistance rendered to us by Mimi Keating and Al Colombo in the evaluation of the test specimens. We would like to thank Dr. Daniel Mickish and Dr. Glen Thommes for their continuous support and advice.

Inquiries:

Inquiries regarding this study may be directed to Suresh Jayanthi at the address listed or by e-mail to jayantss@esvax.dnet.dupont.com.

Curing Behavior of Ceramic Resin for Stereolithography

G. Allen Brady, Tien-Min Chu and John W. Halloran
Materials Science and Engineering Department, College of Engineering
The University of Michigan, Ann Arbor, MI. 48109

ABSTRACT

Ceramic green bodies have been created with stereolithography methods by using ultraviolet curable suspension of ceramic powders, a "ceramic resin", on a Stereolithography Apparatus (SLA). A minivat system with mini-recoater blade was designed to run small batch experiments on an SLA-250/40 machine. With the ceramic resins developed from hydroxyapatite for biomedical application and from alumina and silica for making metal casting molds, ceramic green bodies were built. Diagnostic parts of these ceramic resins were made with the Accumax diagnostic kit (3D Systems) and the curing parameters determined. The effect of shrinkage stress and scattering will be discussed.

Introduction

Since the early 1990's, the Stereolithography (SL) technique has been the predominant fabrication method for rapid prototyping[1]. The SL technique involves solidification of a liquid resin by a UV-laser source. The laser cures one layer by "drawing" it on the surface of a vat of resin. The 3-dimensional part is built layer by layer. The research at the University of Michigan is focused on developing new materials, particularly ceramic materials, for use in a Stereolithography Apparatus (SLA)^a. These ceramic resins are used in the same manner as the traditional epoxy or acrylate resins. However, instead of producing a 100% polymer part, these ceramic resins yield a ceramic green body consisting of approximately 50% ceramic and 50% uv-polymerized binder. Current materials include alumina, silica and hydroxyapatite (HA). Potential applications for the alumina and silica resins include cores and shell molds for investment casting as well as functional ceramic prototypes. HA ceramics have significant biomedical applications[2,3].

These ceramic resins are fluid suspensions of ceramic particles in a uv-curable medium. For ceramic processing purposes, the resins must be highly loaded (at least 50 volume%) to produce reliable, dense finished ceramic parts. For SL processing purposes, the resins must have a low viscosity (< 5000 cps) to undergo the recoating process^b, and self-leveling.

The cure depth is defined in the "Working Curve" equation,

$$C_d = D_p \ln \frac{E}{E_c} \quad (1)$$

where E is the average exposure dose supplied by the laser (controlled by scanning speed, v_s), C_d is the user definable cure depth and D_p and E_c are resin parameters respectively known as depth

a. Model SLA250/40, 3D Systems, Valencia, CA.

b. Recoating here refers to the doctor-blade type of recoating found on SLA 250

of penetration and critical exposure. A schematic of resin curing under a laser is shown in Figure 1. While intensity attenuation for traditional resins used for SL is limited by absorption, the intensity decrease of the uv-radiation in these turbid suspensions is controlled by scattering. The following relation has been used to describe the effect of scattering on cure depth[3,5],

$$C_d = \left(\frac{2}{3} \cdot \frac{d}{\phi \beta \Delta n^2} \right) \ln \frac{E}{E_c} \quad (2)$$

where ϕ is the volume fraction solids, d is the particle size and Δn is the difference in index of refraction between the suspended particles (ceramic) and medium (photocurable monomer resin). The β term involves interparticle spacing and wavelength of radiation.

Materials and Methods

Three resins systems are examined in this work, alumina-aqueous, silica-acrylate and hydroxyapatite-acrylate. Details of resin fabrication are given elsewhere[3]. The alumina-aqueous resin is 52vol% solids with a monomer solution consisting^c of 27% N-hydroxymethacrylamide, 3% methylene bis-acrylamide, 35% water and 35% ethylene glycol. The silica-acrylate resin has 43vol% solids, and the monomer solution is 30% 2-ethoxyethoxy ethyl acrylate and 70% hexane diol diacrylate. The HA-acrylate resin has 40vol% solids and the monomer solution is 66% octyl-decyl acrylate, 22% hexane diol diacrylate and 12% trimethylolpropane triacrylate.

All parts were produced on an SLA 250/40 with a He/Cd laser source. Typically, the laser power at the surface of the resin was about 30 mW. The machine was equipped with an exchangeable minivat (1L to 2L) with a recoating arm (shown in Figure 2) for small sample experiments. Some single layer parts were produced in a glass petri dish on an adjustable stand rather than the minivat. The Windowpane technique[1] was used to measure the cure depth as a function of exposure from which the resin parameters, D_p and E_c were determined for each resin. After curing in the SLA-250, parts were postcured 30 minutes in a uv chamber and allowed to dry at ambient temperature. To remove the photopolymers from the postcured parts, a burnout was performed in air. The parts were heated slowly (1°C/min) to 500°C, held 1 hour, then cooled. To sinter the alumina parts, they were heated in air to 1550°C (10°C/min), held 1 hour then cooled.

Results

The cure depth as a function of energy dose is plotted in Figure 3 for the ceramic resins and the standard epoxy resin. In each case, the cure depth is linear with $\ln(E)$, although the slopes(D_p) do differ widely. The resin parameters were determined from these data and are listed in Table 1. In each case, the linear relation between the cure depth and $\ln(\text{energy dose})$ is apparent. The effect of these resin parameters are shown qualitatively in the cured line profiles shown in Figure 4 for silica and alumina. As the D_p decreases, the cured profile becomes wider and more shallow. A "Block M" shape was made in alumina and HA and also in SL 5170 for comparison. An epoxy M, an alumina M after post-curing and an alumina M after sintering are shown in Figure 5 (from right to left respectively). From this photo, curing and drying shrinkage of the alumina-aqueous resin is not much larger than that of the SL 5170. The significant portion of shrinkage occurred in the sin-

c. all percentages are given in weight percent unless otherwise noted.

tering step, approximately 12% (linear). No cracking or significant warping occurred during either curing, drying, or sintering. A fracture surface of one section of the alumina M is shown in Figure 6. The image to the left shows a scalloped edge resulting from the wide, shallow shape of the cured line profile. At higher magnification in the right image, the interface between two layers appears to have sintered very well with no remnants of the layered processing evident.

Table 1. Resin Parameters

Resin	$D_p, \mu\text{m}$	$E_c, \text{mJ/cm}^2$
Cibatool® SL-5170	119	10.2
Al_2O_3 -Aqueous	69	19.4
SiO_2 -Acrylate	260	13.4
HA-Acrylate	56	10.8

A portion of a the Block M shape built from HA-acrylate is shown in Figure 7. The side surface also has a scalloped appearance, but the layers appeared to be knit together well. However, shrinkage cracking occurs during curing and is shown in Figure 8 to occur between the borders on the layers.

Discussion

All resins used in this work follow a predictable relation between cure depth and energy dose. Work is continuing to increase the stiffness and solids loading of these ceramic resins. Layer cure depths of 200 μm to 600 μm are achievable with the silica resin, 180 μm to 300 μm for the alumina resin and 200 μm to 300 μm for the HA resin. Parts have been built with adequate layering. The microstructure of a part fabricated in the alumina resin reveals no remnants of layered processing.

Side scattering produces the scalloped edges found on some initial parts built at Michigan. A side view of several cured lines drawn one upon another are shown in Figure 9 which illustrates the scalloping effect. The phenomenon also occurs in alumina-aqueous resins. The refractive index difference (Δn^2) in the alumina-aqueous is approximately 0.076. Reducing Δn^2 by using an acrylate-based solution ($n=1.447$ vs. 1.425 for aqueous solution) would reduce Δn^2 to 0.064, subsequently decreasing the level side-scattering while increasing the cure depth.

Shrinkage cracking occurred in the acrylate resin systems (with both silica and HA). This cracking did not occur in the alumina-acrylate system which only experienced minor shrinkage (<3% linear). There are two simple ways to alleviate these shrinkage stresses. One is to employ an unreactive diluent in the acrylate solution. This decreases the concentration of the acrylate bonds in the resin and thus the curing shrinkage. For example, in the alumina-aqueous system, water and ethylene glycol are unreactive diluents which dry after curing. The second method is to make use of new build styles. Build style refers to the algorithms used to generate the path of the laser when drawing each layer. The power of optimizing the build style to control shrinkage is seen

in the use of SL5170 epoxy resin with the ACES™ build style. The theoretical shrinkage is 6.2%, but use of this build style manages the shrinkage to an effective 0.05% in the x and y directions! Experimentation on build styles for the specific ceramic resins is currently underway.

Scattering contributes to lower depths of penetration by the uv-radiation as well as to larger line widths. The overall shapes of the line profiles are more shallow than in the unfilled resin also due to scattering. As a result, more radiation is delivered in a sideways direction which increases the line width. In order to build accurate parts, this increased line width must be dealt with in the build style. Work is underway to characterize and model the shape of the cured line profile for these resins. Despite the progress made to date on elementary fabrication, shrinkage issues and the effect of scattering emphasizes the need to fully exploit the capabilities of the SLA-250 by creating new build styles to both accommodate the modified line profile and alleviate shrinkage and distortion.

Acknowledgment

The research on the refractory ceramics is supported by the Office of Naval Research under contracts N00014-95-1-0527 through Dr. S. Fishman and R. Wachter and the research on bioceramics is supported through the University of Michigan by a Rackham Grant to T-M. Chu.

References

1. P. F. Jacobs, Rapid Prototyping & Manufacturing-Fundamentals of Stereolithography, 1st ed., Society of Manufacturing Engineers, Dearborn, MI (1992).
2. G. de Lange, "The Bone-Hydroxyapatite Interface", pp. 61-75 in *Handbook of Bioactive Ceramics*, Vol. 4, (eds.) T. Yamamuro, L. L. Hench and J. Wilson, CRC Press, Inc., Boca Raton, FL, 1990.
3. C. A. van Blitterswijk, J. J. Grote, W. Kuijpers, W. T. Daems and K. de Groot, "Macropore Tissue Ingrowth: A Quantitative and Qualitative Study on Hydroxyapatite Ceramic", *Biomaterials*, **7** 137-143 (1986).
4. M. L. Griffith, "Stereolithography of Ceramics", Ph.D. Thesis, University of Michigan, March, 1995.
5. M. L. Griffith and J. W. Halloran, "Free Form Fabrication of Ceramics by Stereolithography", submitted to *Journal of the American Ceramic Society*.

FIGURES

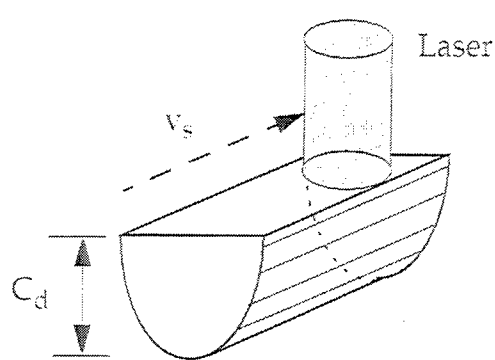


Figure 1 Schematic of a cured line profile generated by laser scanning on the resin surface.

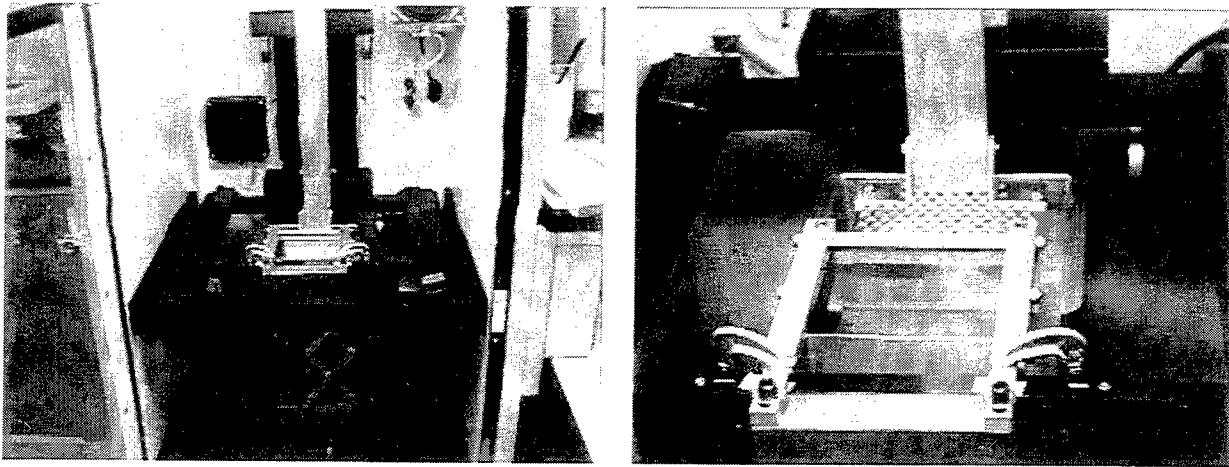


Figure 2 Photos of exchangeable minivat system. Elevator platform and recoating blade are shown at the right.

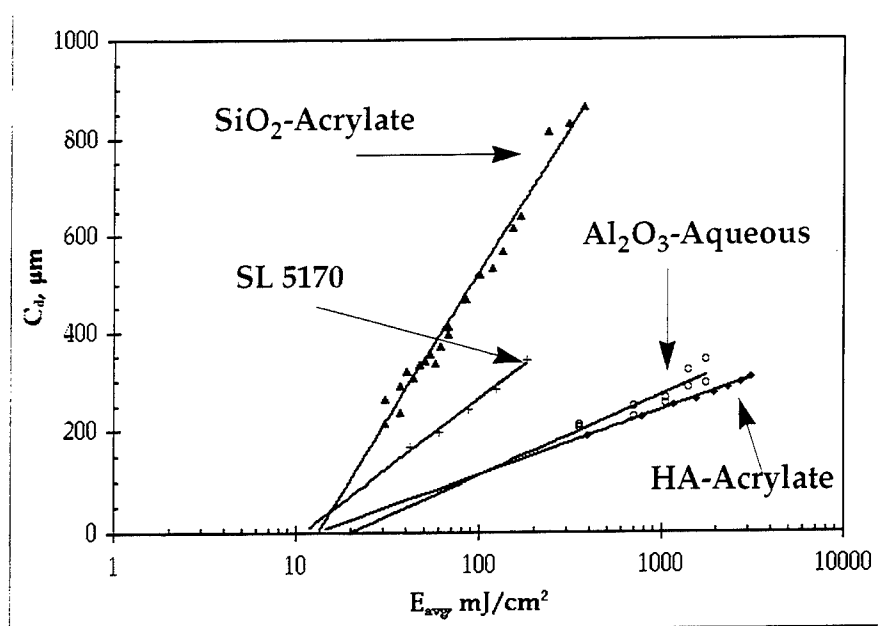


Figure 3 Working curves for silica-acrylate, alumina-aqueous, HA-acrylate resins.

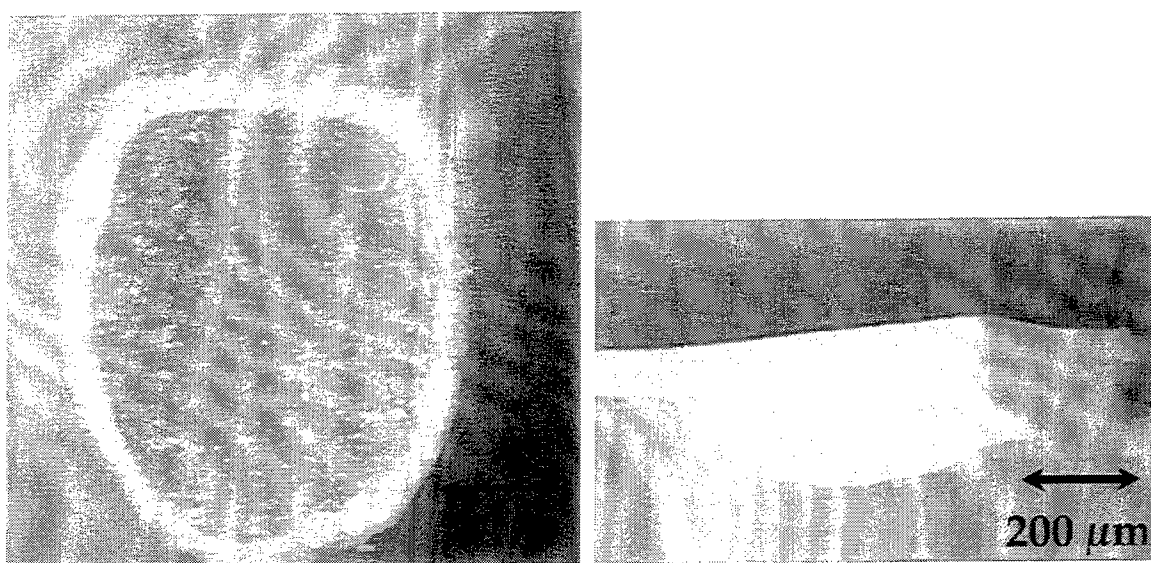


Figure 4 Cured line profile for silica-acrylate resin (left) and alumina-aqueous (right).



Figure 5 Block M's: epoxy on the right, alumina-as cured in the center and alumina-after sintering at 1550°C for 1 hour.

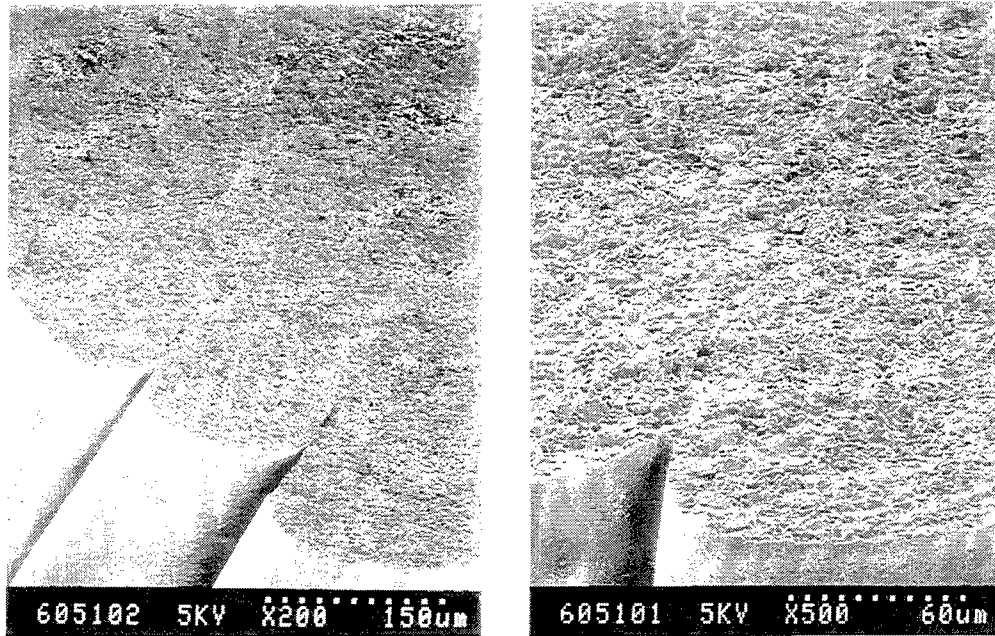


Figure 6 Fracture surface of sintered alumina “Block M” made from alumina-aqueous resin. Note scalloped edges on left. Close-up picture on the right shows no evidence of layering.

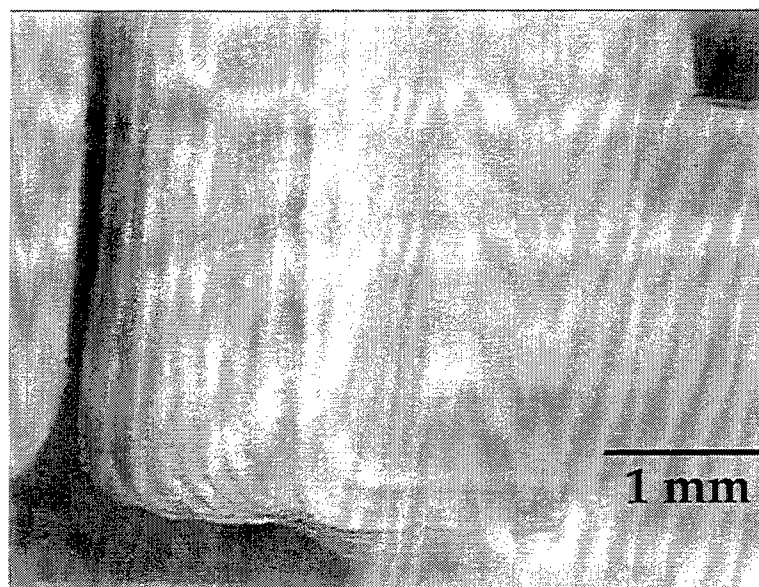


Figure 7 Tilted view of HA-acrylate “M” showing scalloped edges. Note contrast between border and fill regions.

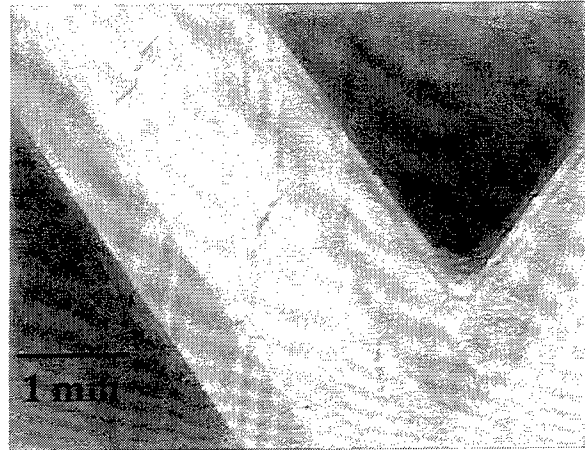


Figure 8 Shrinkage cracks in HA-acrylate between borders.

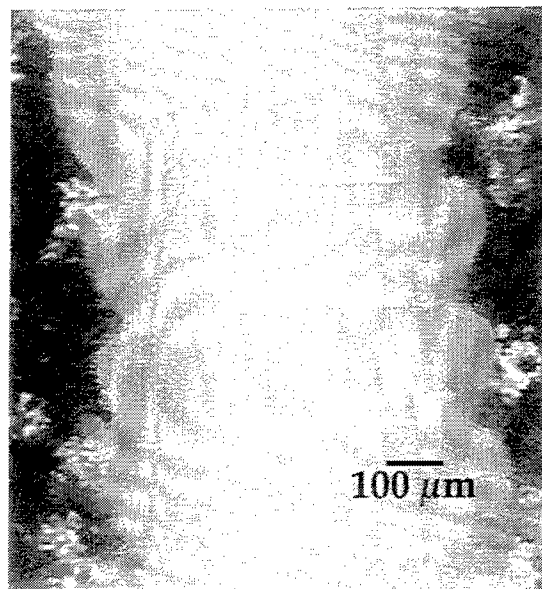


Figure 9 Stacking of cured profiles in HA-acrylate resin.

Microstructures and Strengths of Metals and Ceramics made by Photopolymer-based Rapid Prototyping

Walter Zimbeck, Matthew Pope, Ceramic Composites, Inc., Annapolis, MD 21401 410-224-3710;
and R.W. Rice, Consultant, Alexandria, VA 22301 703-971-4379

ABSTRACT

Metal and ceramic flexure specimens were fabricated using a photopolymer-based rapid prototyping technique. Photosensitive resins (inks) were produced by dispersing 50 - 55 vol% metal or ceramic powders in a photopolymer resin. Laminates 0.2" thick were built up by repeated application of layers 3 - 10 mils thick followed by curing under a UV flood lamp with photomasks. The layered samples were thermally processed to remove the photopolymer binder and sintered to high density. Densities, microstructural characterization and flexure strengths are reported for silicon nitride, alumina, zirconia, stainless steel, and tungsten.

I. INTRODUCTION

Freeform fabrication of metal and ceramic components offers a number of advantages including cost and time efficient functional prototyping and small lot production, the ability to fabricate complex shaped designs using materials which have historically been difficult to shape form, and the possibility of fabricating new material architectures with unique properties tailored for specific applications. In demonstrating the feasibility of freeform fabrication processes, several issues must be addressed:

1. Demonstration that desired physical properties are achievable;
2. Determination of dimensional accuracy and uniformity; and
3. Demonstration of shape intricacy capability.

This paper reports on progress made by Ceramic Composites, Inc. (CCI) on demonstrating the physical properties achievable by photopolymer-based fabrication of a variety of metals and ceramics. Photopolymer-based freeform fabrication of metals and ceramics has several unique and significant advantages relative to other SFF processes such as LOM of ceramic and metal tapes, Fused Deposition of Ceramics, Selective Laser Sintering and 3D Printing. These advantages are based in the large existing infrastructures of core related technologies. For example, 1) the photopolymer industry is large and growing with a wide variety of existing resins and a strong R&D infrastructure for new resin development; 2) the photolithography infrastructure supporting the electronics industry is substantial and provides the hardware base for large area, high speed and high accuracy photocuring; and 3) photopolymer-based fabricators, led by 3D Systems' SLAs are by far the most prevalent fabricators in use and come with a considerable body of R&D from which new innovations and process improvements will emerge.

W.R. Grace and Co. initiated development of ceramic/photopolymer resins in 1992, however due to major corporate restructuring, Grace abandoned development and the technology was transferred to CCI in 1994. CCI seeks to commercialize this technology through the sale of metal and ceramic resins compatible with current photopolymer-based fabricators and/or by offering service bureau capability for metal and ceramic components.

Photopolymer-based fabrication of metal and ceramic objects entails formulating a colloidal suspension of fine inorganic particles in a photosensitive resin. This metal or ceramic resin can be used as the feedstock material in photopolymer-based fabricators such as 3D Systems' SLA machines and Cubital's Solider systems to build "green state" metal or ceramic objects. Subsequent thermal processing of the part burns-off the photopolymer binder and sinters the inorganic particles to high density.

Photopolymer-based fabrication of metals and ceramics poses a number of challenges which are not encountered with conventional StereoLithography and Solid Ground Curing of polymer parts. The initial challenges are:

- Achieving high solids loading in the resins while maintaining low viscosity and stable particle suspension;
- Formulating the resin to provide good interlayer adhesion, minimal shrinkage during cure, and nondisruptive binder burnout;
- Determining the binder burnout and densification conditions to give high density and desirable properties;

The remainder of the paper describes how these issues were addressed and presents results for the various materials under development.

II. EXPERIMENTAL

II.1 Resin Formulation

A number of tradeoffs must be made in formulating metal or ceramic resins. For high density and high strength parts it is desirable to maximize the solids volume fraction of fine sinterable particles in the resin. For materials with high specific gravity, such as tungsten (19.3 g/cc), smaller particle size powders are additionally appealing because of their lower sedimentation rates (Stoke's Law), thereby enabling stable suspensions. However, smaller particles and higher solids loading result in higher viscosity and commensurately longer layer application times. To achieve as-sintered material with high density (>95%), 45 vol% solids loading in the resin is typically a minimum requirement, with >50 vol% desired. In order to achieve high solids loadings with fine particles, resin formulations must typically include dispersants and/or coupling agents for steric and electrostatic stabilization to prevent particle agglomeration. Smaller particles and higher solids loadings also result in lower cure depth, which require the use of thinner layers.

Typically a blend of at least two photomonomers is used in order to achieve the desired resin properties. Key resin properties are:

- low viscosity
- stable particle suspension
- cured surface tack for interlayer adhesion
- low cure shrinkage
- sufficient cured strength, rigidity and toughness

In addition to dispersants and/or coupling agents, other additives are commonly used such as plasticizers, thickeners, solvents, and anti-foaming agents to improve these and other resin properties. The procedure used to mix the ceramic or metal resins entails mixing the liquid ingredients together followed by addition of the ceramic or metal powders. Typically, the powders are added in increments to maintain flowability of the resin.

The final addition to the mixture are the photoinitiators or sensitizers. The photoinitiators act as absorption sites for the incident photons producing free radicals which initiate crosslinking of the monomers. Photoinitiators are typically added in concentrations of 0.1 - 4 % based on the weight of the crosslinkable monomers. The type and concentration of photoinitiators used has a significant effect on cure depth, speed of cure and the working curve of the resin.¹

II.2 Layer Application and Curing

For the purposes of building flat samples, a manual laminate building apparatus is used (Figure 1). The piston height is set to a depth below the top surface equal to the desired layer thickness. Ceramic or metal resin is poured onto the piston and a blade caster resting on the top surface is used to spread a uniformly thick layer of resin. The layer is cured using an ultraviolet lamp (Fusion UV Curing Systems) and a photomask, which is placed just above the surface of the resin. By repeating the process, multilayer laminates are built.

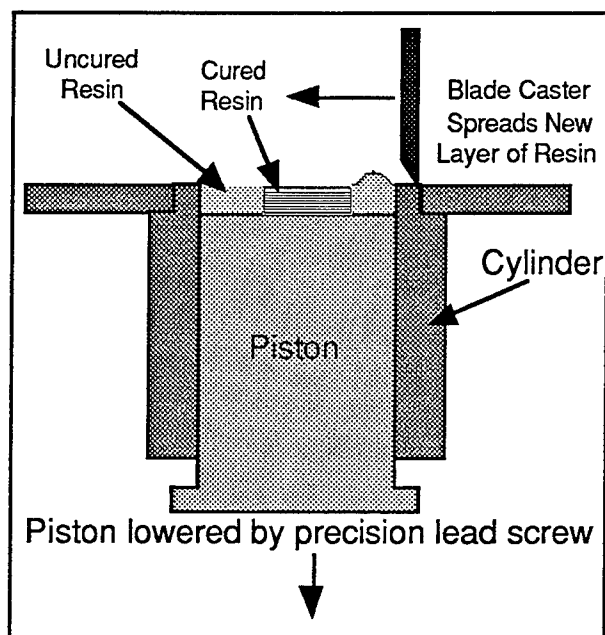


Figure 1. Laminate building apparatus

II.3 Binder Removal and Sintering

Once the green state part is built, it is thermally processed to remove the organic (mostly photopolymer) binders and subsequently sintered to high density. The binder burnout stage is critical and requires carefully controlled temperature ramp-up, particularly when the organic constituents begin to decompose and gaseous by-products are generated. Gases formed during rapid decomposition can build up internal pressure and cause delamination, blistering and bloating of the part, especially in thick sections. Differential scanning calorimetry (DSC) and thermogravimetric analysis (TGA) can be used to determine the temperatures at which decomposition occurs. A burnout schedule can be derived from these data which results in non-disruptive rate of weight loss during the heating cycle. Above 500°C, most of the organic phases have been removed and heating can be continued up to the respective sintering temperatures. Sintering schedules commonly used in powder metallurgy or powder processing of ceramics can be used to sinter components to high density providing sufficient green densities had been achieved.

III. RESULTS

III.1 Alumina

Alumina resins were made using A16 SG powder ($\sim 0.4 \mu\text{m}$ average particle size, APS) from Alcoa. The photopolymer formulation consisted of three commercially available acrylate based monomers. At 45 vol% solids loading the resin viscosity is ~ 1200 cPs. At 50 vol% solids the viscosity increases to $\sim 3,000$ cPs, still well within the practical viscosity range for layer

building using the blade casting technique shown in Figure 1. Crystalline alumina shows high spectral transmittance (~ 0.8) from 300 nm out to about 4 μm wavelengths,² and the alumina resins show good depth of penetration at the principal output wavelengths of the lamp (400 - 425 nm). At a five second exposure, which roughly correlates to an exposure dose of 100 mJ/cm², the cure depth is 0.033". At two and one second exposures the cure depths are 0.015" and 0.003", respectively.

Using a 50 vol% alumina resin, samples 0.1" and 0.2" thick were built with 0.005" thick layers. Some delamination problems were encountered when layers 10 and 15 mils thick were used, possibly due to stresses resulting from shrinkage of the resin during curing. Differential scanning calorimetry (DSC) and thermogravimetric analysis (TGA) tests were performed on small pieces of cured alumina resin. TGA tests showed weight loss beginning at $\sim 150^\circ\text{C}$ and ending at $\sim 480^\circ\text{C}$. DSC tests showed two exothermic peaks in this range, one centered at $\sim 275^\circ\text{C}$ and one centered at $\sim 400^\circ\text{C}$. Based on this data an 18 hour binder burnout cycle was derived. Sample weight loss during binder removal is in the range 15 - 18%. After binder removal, the samples were sintered in air at 1600°C for 2 hours.

Sintered densities ranged from 90% to greater than 98% theoretical. Samples with densities below 98% exhibited voids caused by air bubbles in the resin and delamination defects particularly near the edges. Samples with densities exceeding 98% showed no voids or delaminations and were the result of improved resin preparation and layer building techniques. Figure 2 shows opposing fracture surfaces of an alumina sample with a large void at the corner and two delaminations. Figure 3 shows a dense alumina sample with no laminar artifacts visible which was produced further into the development. The sintered grain size of these samples was typically in the range 30 to 50 microns, indicating extensive grain growth due to over sintering.

Strength data was obtained by three point flexure tests. Small flexure samples were diced from the larger specimens and tested as-is without surface grinding or chamfering. Samples with density $>98\%$ (see Figure 3) exhibited strengths of ~ 350 MPa (53,700 psi) which is typical of cold pressed and sintered A16 alumina. Samples with delaminations and voids (see Figure 2) exhibited strengths in the range 200 - 300 MPa.

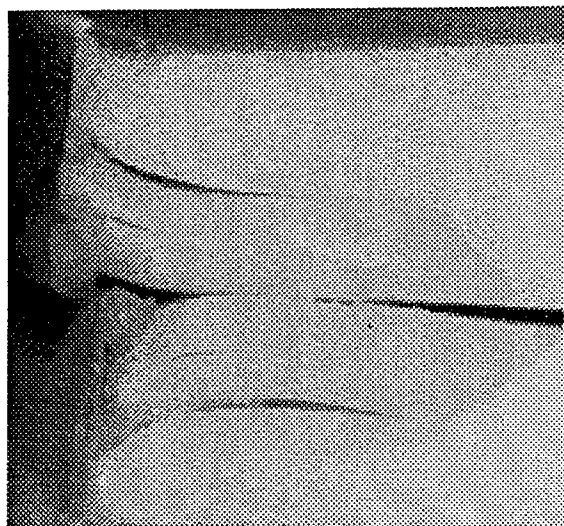


Figure 2. Alumina sample fracture surface showing delamination and void.

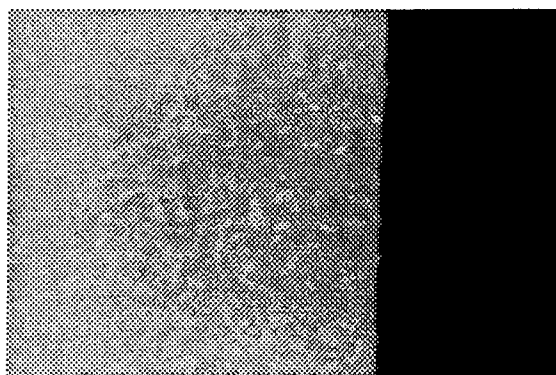


Figure 3. Alumina sample fracture surface showing no lamination artifacts or visible defects.

III.2 Silicon Nitride

Silicon nitride resins were made with a 70:30 mixture of SN E3 (0.7 μm APS) and SN E10 (0.3 μm APS) powder from Ube. Alumina and yttria sintering aids were used at 5 wt% of the silicon nitride powder. The photopolymer mixture that was used for alumina resins was also used for the silicon nitride resins. At 45 vol% solids the silicon nitride resin has a viscosity of $\sim 3,500$ cPs and at 50 vol% the viscosity increases to $\sim 5,000$ cPs. Relative to the alumina resins, the silicon nitride resins exhibit very limited cure depth. The maximum cure depth observed was 0.004". Griffith and Halloran³ have derived a relationship between cure depth and resin properties which shows that the penetration depth is inversely proportional to the square of the difference in refractive index (RI) between the ceramic and the UV curable solution ($1/\Delta n^2$). The RI of the photopolymer mixture is roughly 1.45. The RI of alumina is 1.7 and the RI of silicon nitride is 2.1. Thus, the $1/\Delta n^2$ factor is roughly 7 times higher for alumina resins compared to silicon nitride resins, accounting for much of the observed difference in cure depth.

Using a 50 vol% silicon nitride resin, samples 0.1" thick were built using a layer thickness of 0.002". A few samples were made with 0.005" thick layers, resulting in uncured resin between each cured layer. The uncured resin layers act as slip planes which accommodate shrinkage during cure so that no curling of these samples was observed. However, binder burnout and sintering of these samples resulted in severe delaminations. A binder burnout schedule identical to the one used for alumina resins was used for the silicon nitride samples.

Several different sintering schedules were carried out under 1 atm. nitrogen, but difficulties in temperature control resulted in samples that were at best 90% dense with some degree of delamination. The maximum three point flexure strength of these samples was 412 MPa and the laminar nature was evident in the fracture surfaces. One silicon nitride sample was hot pressed at 1800°C. This sample was fully dense with no laminar defects visible and flexure strengths ranging from 505 to 757 MPa with an average from three specimens of 636 MPa. Figure 4 is an SEM photograph of the microstructure of the hot pressed silicon nitride sample showing a high concentration of the acicular β grains.

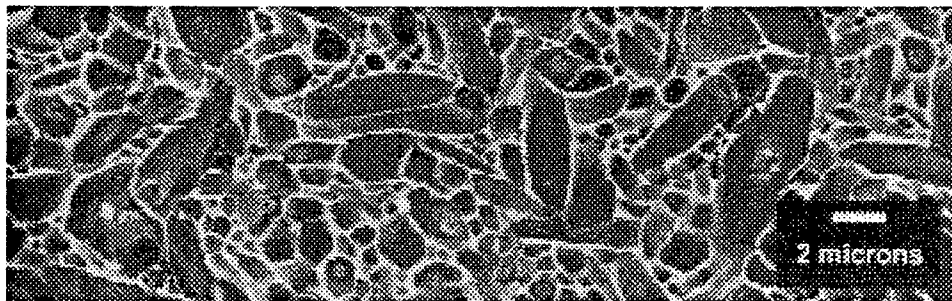


Figure 4. 5000x electron micrograph of the hot pressed silicon nitride sample.

III.3 Stainless Steel

Stainless steel resins were made using 316L stainless steel powder with particle size $<16\mu\text{m}$ (Anval, Inc.). The resin formulation had to be adjusted to include higher viscosity monomers which prevented rapid settling of the relatively large and dense ($\rho = 7.9\text{ g/cc}$) stainless steel particles. Resins with 55 vol% solids content exhibited relatively low viscosity. The viscosity of these resins was not measured, although they have lower viscosity than the 45 vol% alumina resins, which were measured at 1,200 cPs. Stainless steel is opaque at the wavelengths of interest; thus, light penetration is dependent on spacing between particles and reflectivity of the particles. At 400 nm, roughened stainless steel plate has a reflectivity of $\sim 0.9^4$. The reflectivity would likely be lower for $16\mu\text{m}$ stainless steel particles. The maximum cure depth achievable with the 316L resins was 0.003" - 0.004" with exposure doses comparable to those used for the silicon nitride resins.

Using a 55 vol% 316L resin, samples 0.1" and 0.2" thick were built with 0.002" thick layers. Binder removal and sintering of the stainless steel samples was conducted in a reforming gas environment (4% H_2 in argon) to prevent oxidation of the stainless steel. In this atmosphere, the onset of thermal degradation begins at $\sim 280^\circ\text{C}$ and continues up to $\sim 480^\circ\text{C}$. In this temperature range, the ramp rate was held to $0.3^\circ\text{C}/\text{minute}$. Three sintering temperatures were evaluated, 1000°C , 1100°C and 1125°C , which resulted in sample densities of 81%, 92% and 95%, respectively. The samples sintered at 1100°C were placed on graphite setter material during sintering. These samples exhibited brittle fracture behavior and strengths between 314 and 355 MPa. The samples sintered at 1125°C were placed on alumina setter material during sintering and showed considerable ductility in fracture and strengths between 397 and 455 MPa. The brittle behavior of the samples sintered on graphite setter material was probably a result of carbide formation on the surface in contact with the graphite. The ductile nature of the other stainless steel samples indicates that if any carbon residue is left during binder burnout, it is not significant enough to cause carbide embrittlement of the stainless steel. Figure 5 is a photograph of one of the 95% dense 316L samples after flexure testing showing the ductility of the material. Figure 6 shows a fracture surface of another 95% dense 316L sample. The 0.002" thick layers are barely visible in this photograph, although the laminar artifacts did not appear to weaken the material and may tend to strengthen the material by redirecting crack growth along the interface between layers.

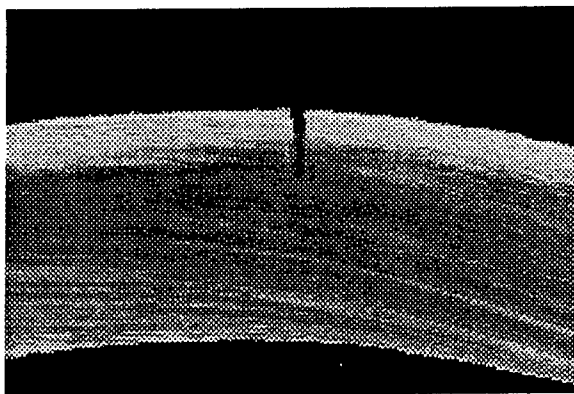


Figure 4. 316L stainless steel sample after flexure test, showing considerable ductility.

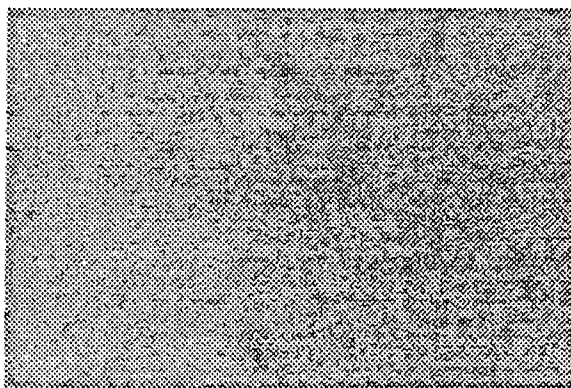


Figure 5. Fracture surface of a 316L stainless steel sample showing 0.002" thick layers.

III.4 Tungsten

Tungsten's high density (19.3 g/cc) requires that special consideration be given to resin formulation in order to minimize particle settling rates. High settling rates will result in non uniform intra- and inter-layer solids volume fraction and non uniform shrinkage during sintering. High viscosity monomers and additives are being used to reduce particle settling in the resins. Stokes' Law shows that particle size also has a large effect on settling rates. While smaller particles result in lower settling rates, other effects must also be considered and tradeoffs made. For example, smaller particles are desirable for better sinterability, fine sintered grain size and generally higher strength as well as lower settling rates in the resin. However, smaller particles result in higher resin viscosity at the same solids volume fraction or lower solids volume fraction at the same resin viscosity. As shown by Griffith and Halloran (see reference 3), smaller particle size also results in shallower cure depth. Thus, resins were formulated with particle size powders ranging from 0.8 μm up to 10 μm APS and settling rates, viscosity and cured depth tests were conducted. Although testing is not complete, results indicate that particles sizes between 2 and 5 μm are a good compromise, providing satisfactory cure depth (0.002" - 0.003"), workable settling rates, and solids loadings of 50 vol% while maintaining practical viscosity.

The 0.002" - 0.003" cure depths achievable with these tungsten resins require an exposure dose of roughly 3,000 mJ/cm², which is 2 - 3 times higher than used on the stainless steel resins. One factor which may at least partially explain the higher required dose, is tungsten's relatively high absorptivity at the wavelengths of interest.⁵ The much higher absorptance of tungsten at 400 nm (~0.52) compared to stainless steel (~0.12) indicates that the tungsten particles act as absorption sites and are competing with the photoinitiators for incident radiation. Thus, higher exposure doses are required to achieve curing of the tungsten resins.

IV. SUMMARY AND CONCLUSIONS

The objective of this work was to demonstrate that physical properties, particularly strength, similar to conventionally processed materials could be achieved by photopolymer-based freeform fabrication. A variety of metal and ceramic resins were formulated and samples were built using a manual laminate building apparatus and a UV flood lamp/photomask system. Density and flexure strength data showed that high densities and strengths could be achieved using this process. Resin properties and as-sintered densities and strengths of all the materials are summarized in Table 1.

Potential limitations to using these resins with commercial photopolymer-based fabricators were also identified. Based on the resin properties observed, it appears that alumina resins have high compatibility with commercial photopolymer-based fabrication systems. Work is underway

with alumina resins to demonstrate this compatibility and complex shape building capability. Similar compatibility is expected for other oxide ceramics such as silica, zirconia, mullite, etc. The compatibility of silicon nitride and stainless steel resins with commercial systems is lower primarily due to the limited cure depth (0.003" - 0.004" maximum) of these resins. This is at the typical lower limit of layer thicknesses currently recommended with commercial systems, although alternative layer application methods which can apply thinner layers uniformly could potentially be developed for these commercial systems. Tungsten resins have limited cure depth (0.002" - 0.003" maximum) but also involve challenges not encountered with the other materials. Keeping the tungsten particles suspended in the resin is difficult and may require a layer application system which includes an agitated resin storage tank to maintain suspension. Tungsten resins also appear to have much higher E_{crit} , the minimum exposure dose required to achieve gelation, which could significantly extend build times. Further research will more clearly define the limitations and equipment requirements for tungsten resins.

Table 1. Summary of resin properties and as-sintered densities and strengths.

Material	Solids vol% in Resin	Resin Viscosity	Cure Depth (max)	Density	Flexure Strength (max)
Alumina	50	~3000 cPs	>0.033"	>99%	360 MPa
Zirconia*	40	---	~0.006"	>97%	530 MPa
Si ₃ N ₄	50	~5000 cPs	0.004"	90% & >99%#	412 & 757# MPa
Stainless Steel	55	<1200 cPs	0.003"	95%	455 MPa
Tungsten	50	----	0.0025"	----	-----

*Zirconia resin developed and tested at W.R. Grace prior to CCI involvement.

#This silicon nitride sample hot pressed to full density.

V. ACKNOWLEDGMENTS

Ceramic Composites, Inc. would like to thank the NASA and Air Force SBIR programs for supporting this work.

VI. REFERENCES

- ¹Jacobs, P.F., "Rapid Prototyping and Manufacturing, Fundamentals of StereoLithography," Society of Manufacturing Engineers, Dearborn, MI, 1992, pp. 87 - 91.
- ²Thermal Radiative Properties of Non Metallic Solids, Vol 8, Y.S. Touloukian and B.P. DeWitt, Thermophysical Properties Research Center, Purdue University, ISI/Plenum, 1970, pp. 168 - 169.
- ³M.L. Griffith, and J.W. Halloran, *Proceedings of the SFF Symposium*, University of Texas at Austin, Austin Texas, 1994, pp. 396 - 403.
- ⁴Thermal Radiative Properties of Metallic Elements and Alloys, Vol 7, Y.S. Touloukian, and B.P. DeWitt, Thermophysical Properties Research Center, Purdue University, ISI/Plenum, 1970, pp. 1293 - 1294.
- ⁵Thermal Radiative Properties of Metallic Elements and Alloys, Vol 7, Y.S. Touloukian, and B.P. DeWitt, Thermophysical Properties Research Center, Purdue University, ISI/Plenum, 1970, pp. 825 - 826 and 1293 - 1294.

**MECHANICAL AND DIMENSIONAL CHARACTERISTICS OF FUSED
DEPOSITION MODELING BUILD STYLES**

Eric Fodran[⊕], Martin Koch⁺, and Unny Menon⁺

**⊕ MATERIALS ENGINEERING DEPARTMENT
+ INDUSTRIAL & MANUFACTURING ENGINEERING DEPARTMENT**

**CALIFORNIA POLYTECHNIC STATE UNIVERSITY
SAN LUIS OBISPO, CA 93407, USA**

1. Abstract

As rapid prototyping becomes more prominent, industry relies more on the mechanical properties of the builds. Fused Deposition Modeling (FDM) tensile samples were constructed and tested in order to characterize the mechanical properties of Acrylonitrile Butadiene Styrene (ABS) FDM builds. Parameters such as fill gap, line width, and slice thickness were varied in the production of the FDM samples. This was performed independently to isolate the effect of each parameter on mechanical properties. Results include the ultimate tensile strength, yield strength, elongation, energy to fracture, modulus of elasticity, and dimensional analysis. High magnification fracture surface analysis was also performed to aid in the characterization of sample failures.

2. Introduction

The mechanical properties of polymers are characterized in the same manner as metals using stress strain curves and the parameters derived from those curves. Polymer materials display the brittle and ductile behavior observed in metals as well as behaving in a highly elastic manner (Berns 1991).

All forms of mechanical stress have components of tensile loading. In bending, the layer of material on the outside of the bend radius is in tension. In shear, the material at 90° to the direction of shear is in tension. In torsion, the material on the entire circumference is in tension. Even in compression, there is a component of tensile loading through the center of the sample due to the elastic properties of plastics (Gere and Timoshenko 1990), (Berns 1991). Due to this wide influence of tensile strength, it is the most common property referred to when considering general strength of materials (Berns 1991).

There can be one or two phases during the failure of a polymer under tension. The material may first yield, which results in a reduction of its load carrying capacity, but continue to elongate. The second phase is "brittle and rapid failure" (Gere and Timoshenko 1990). Yielding occurs when the load to overcome the intermolecular secondary forces is less than that required to break primary molecular bonds. Within the yielding phenomena, the long chain-like molecules begin to uncoil and slip past each other. If the load persists, the material will continue to elongate with continued molecular orientation. Further loading results in considerable molecular orientation in which the molecules are almost completely aligned in an anisotropic fashion in the direction of loading. At this point the load begins to be resisted by primary molecular bonds. The load carrying capacity may then increase until the primary bond strength within the molecular chains is exceeded and the material undergoes rapid brittle failure (Berns 1991).

Accurate experimental results will depend on the load being distributed uniformly throughout the gage section. If the load distribution is non-uniform, the true length in which deformation occurs will not be known. In such cases, using the gage length in the calculations will produce erroneous values. Surface

defects and contamination are other common causes of erroneous tensile data. Nicks, scratches, bubbles, or other defects on the surface of test samples serve as an initiation site for fractures. As the test starts, stress builds uniformly throughout the gage section of the sample as the molecules distribute the stress evenly among themselves. The molecules bordering a surface defect cannot distribute the stress to the molecules on the other side of the defect (Courtney 1990).

If the defect arises from solid contamination, the adhesive attraction of the molecules to the defect is low. The stress is channeled from the molecules bordering the defect to the molecules located where the defect stops. Concentration of the stress occurs where the two sides of the defect meet at 90° to the direction of loading. The stress will increase rapidly at the concentration point and primary molecular bonds will break. A crack will develop which will then serve as a defect itself and will propagate through the material by the same action that initiated at the original defect.

Rate of deformation is another important factor in determining measurements obtained from testing. Stress in a sample is actually the polymer's response to deformation. A tensile testing machine pulls on a sample causing deformation. The resistance to the deformation is the value which is measured and used to calculate tensile properties. A high rate of deformation allows less time for molecules to mobilize and uncoil to locally relieve the stress. This results in less deformation before primary bonds are broken and potentially a lower stress value at failure. Significant reductions can also be seen in yield and ultimate elongation. To prevent such phenomena, sufficient cross head speeds are selected per tensile test.

After the proper testing parameters are obtained, tensile tests will be conducted in accordance to ASTM standard D 638 (Figure 1). All data which is obtained from testing will then be tabulated for interpretation.

3. Fused Deposition Modeling

The polymer to be tested will be FDM constructed ABS. Fabrication of a FDM piece is a multi-step procedure. Using a computer, a three dimensional image is first sliced into cross-sectional planes. These planes are used by the Stratasys 1600 rapid prototyping machine to build the part, layer-by-layer (Figure 2). The first layer of the part is bonded by the FDM machine to a support platform via an extruded path defined by the shape of the first computer-sliced area. The FDM platform is lowered a preset distance after the first layer has been laid down. Material is then extruded over the surface of the first layer and bonded to form the second layer. The process repeats until the complete three dimensional structure is constructed.

Van Weeren et al (Weeren 1995) here examined the quality of FDM constructed pieces with respect to the defects in ceramic materials. Our investigations focus on ABS, the most widely used material for FDM manufacturing at this time. This study on the strength of ABS-FDM builds will

form the basis of future research on enhancing ABS-FDM RP parts by post processing with epoxies or other composite supplements to enhance strength for lower density ABS builds for FDM machines.

When a molten polymer is joined to a solid polymer, incomplete bonding can result. This can cause lower tensile strength along this bonding interface. Once the melt comes in contact with the solid, the bond loses its structural integrity along the surface of separation. This occurs because polymer molecules can only reestablish a high degree of interlinking across the surface by a slow diffusion process that is driven by thermal (Brownian) motion (Courtney 1990).

4. Visual and Dimensional Analysis

In order to verify the builds produced by the FDM machine, Scanning Electron Microscopy was performed. At high magnification, parameters such as fill gap, line width, and slice thickness can be confirmed prior to actual testing of the samples (Figure 3). After testing of the samples is completed, SEM analysis can again be employed to characterize the failure of the specimens (Figure 4). Dimensional analysis was performed throughout experimentation (Figure 5). This analysis can thus verify the dimensional integrity of the FDM constructed builds.

5. Experimental Results and Discussion

Initial experimentation was performed on samples which were constructed in accordance to three different build style parameters. The parameters for these build styles have been summarized in the following table:

Build Style Sample #	Layer Width	Raster Angle	Gap	Road Fill
1	0.010"	45°, 45°	0	0.020"
2	0.010"	45°, 45°	0	0.015"
3	0.010"	Contour	0	0.020"

Experimentation has yielded the following results:

Build Style/ Sample#	Peak Stress (MPa)	Fracture Stress (MPa)	Elongation at Fracture (mm)	Modulus (GPa)	Energy to Fracture (J)
1	17.33	15.51	0.851	0.961	0.125
2	19.42	16.81	1.21	1.02	0.21
3	21.15	17.23	1.04	1.08	0.18

This preliminary empirical data demonstrates the contour constructed specimens exhibit the strongest properties under such tensile forces. In the case of the contour constructed samples, the ABS lines in the necked gage section of the sample are all aligned in an anisotropic orientation in the axis of loading. Such orientation would then lead to quantify the resistance of the lines themselves, not the bond forces between them, as in the case of samples 1 and 2.

Further research was performed on enhancing ABS-FDM parts by post processing with several different epoxies and adhesives. The tensile specimens were constructed from the same design, altering only the gap between $+45^{\circ}/-45^{\circ}$ rasters. The gaps selected for this experiment were 0.02", 0.03", and 0.05". Build parameters are summarized in the following table.

Build Style/Sample#	Layer Width	Raster Angle	Gap	Road Fill
1	0.010"	$45^{\circ}, 45^{\circ}$	0	0.020"
2	0.010"	$45^{\circ}, 45^{\circ}$	0	0.015"
3	0.010"	Contour	0	0.020"

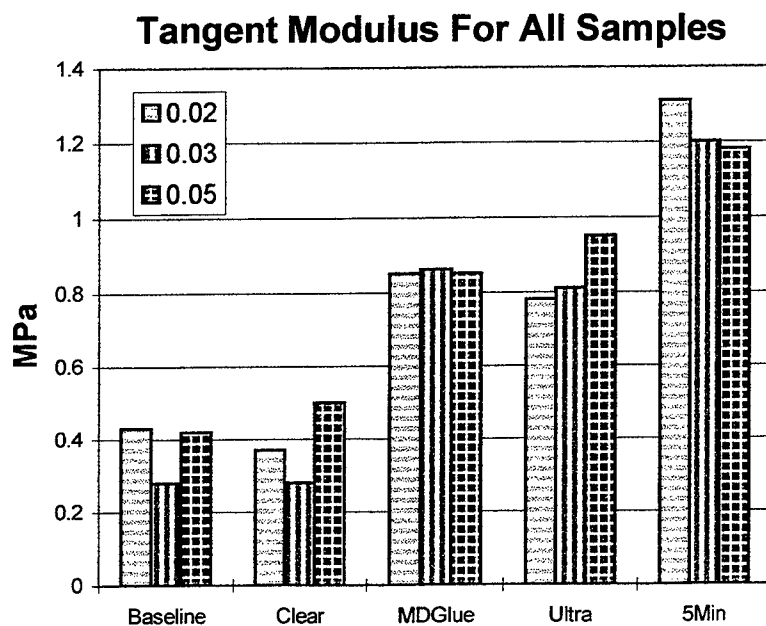
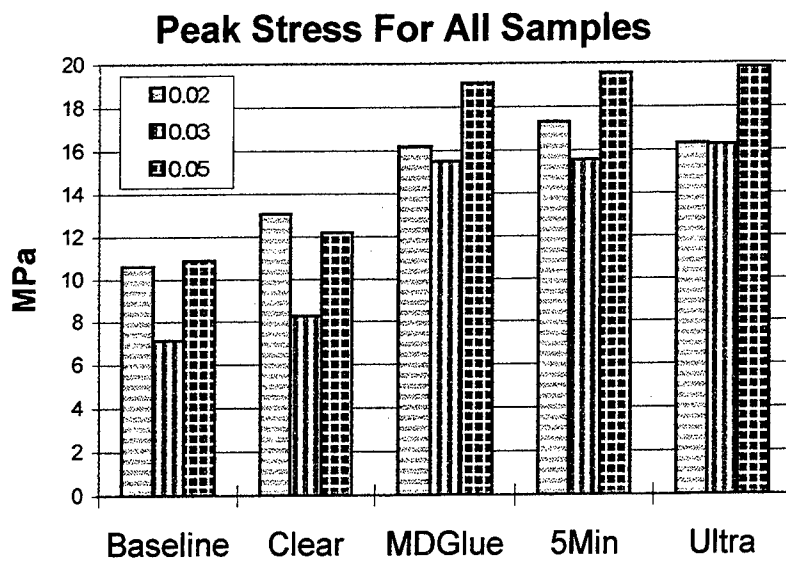
Four bonding agents which were ABS compatible were selected and impregnated into tensile specimens by hand lay-up techniques. After proper cure time the specimens were tested in accordance to ASTM D 638. The following tables and charts summarize the results from the performed tensile tests:

Peak Tensile Stress (MPa) for Post-Processed Specimens

		Gap		
		0.02"	0.03"	0.05"
Adhesive	Baseline	10.58	7.12	10.87
	5Min	17.30	15.53	19.54
	MDGlue	16.18	15.49	19.08
	Clear	13.05	8.25	12.16
	Ultra	16.29	16.25	19.82

Tangent Modulus (MPa) for Post-Processed Specimens

		Gap		
		0.02	0.03	0.05
Adhesive	Baseline	0.43	0.28	0.42
	5Min	1.31	1.20	1.18
	MDGlue	0.85	0.86	0.85
	Clear	0.37	0.28	0.50
	Ultra	0.78	0.81	0.95



The data and graphical illustrations clearly illustrate an increase in the tensile strength of the specimens as a result of applying any of the bonding agents. The tangent modulus was also increased with the addition of the bonding agents in all but one of the four cases.

Photomicrographs obtained through scanning electron microscopy illustrate the surface topography of the fracture surface of the tensile specimens tested. Failure of the samples impregnated with the bonding agents have been characterized and placed into one of several categories. With the bonding agents acting as a matrix and the ABS polymer as a reinforcing/filler material, the fracture surfaces were categorized as exhibiting one of the following appearances: brittle matrix failure and ductile polymer failure, mutually ductile failure, and mutually brittle failure (Figures 6 -).

The fracture surface of the "MDGlue" adhesive demonstrated the highest degree of mutually ductile failure modes of all the samples analyzed in all build styles (Figures 6 - 12). Figure 12 at 580X clearly illustrates the similar ductile fracture surface of the matrix and fiber. Note also the mixed modes of adhesive and cohesive failure at the fiber matrix interface (Figure 7).

The fracture surface of the samples impregnated with the "Clear" adhesive also demonstrated a considerable degree of mutually ductile failure (Figures 13-16). In contrast to the samples impregnated with the "MDGlue" adhesive, the "Clear" samples exhibited all adhesive failure at the matrix/fiber interface without indication of any cohesive failure (Figures 13, 14).

Both the "5Min" and "Ultra" adhesives resulted in fracture surfaces which exhibited brittle failure of the matrix and ductile failure of the fibers (Figures 17 - 24 and Figures 25 - 32 respectively). In all of the figures for the two adhesives a definite lack in deformation prior to fracture is evident.

It has been determined that the mechanical properties of FDM modeled samples can be manipulated by the standard in which they are built. The properties can easily be altered by the modification of one of the criterion of FDM construction. In addition the mechanical properties can again be improved by the impregnation of common bonding agents. Not only can adhesive be selected to increase the mechanical properties, but also can also to control the mode of failure between the bonding agent and polymer fiber.

6. Acknowledgments

Use of the rapid prototyping research equipment employed in this project has been made possible by the U.S. Department of Defense under ARPA/DURIP GRANT NUMBER: DAAH04-95-1-0064 for "Research Instrumentation to Enable Functionality Improvement of Rapid Prototype Components and Rapid Deployment of Advanced Materials". This paper has been made possible by the team efforts of Larry Gowens, Robert Niel, and Edna Rodriguez, led by Eric Fodran.

7. References

Michael L. Berns (1991) Plastics Engineering Handbook of the Plastics Industry, 5th Edition, New York, Van Norstrand Reinhold.

Thomas H. Courtney (1990) Mechanical Behavior of Materials, New York, McGraw-Hill.

James M. Gere and Stephen P. Timoshenko (1990) Mechanics of Materials, 3rd Edition, New York, PWSKENT Publishing Co.

Weeren R. , Agarwala M. , Jamalabad V. R. , Bandyopadadyay A. , Vaidyanathan R. , Langrana N. , Safari A. , Whalen P. , Danforth S. C. , Ballard C. (1995) Quality of Parts Processed by Fused Deposition. **Solid Freeform Fabrication Conference Proceedings**, University of Texas, Austin, September 1995, pp 314-321.



Figure 1: Tensile load frame with FDM constructed sample, approximate sample size ~80mm.

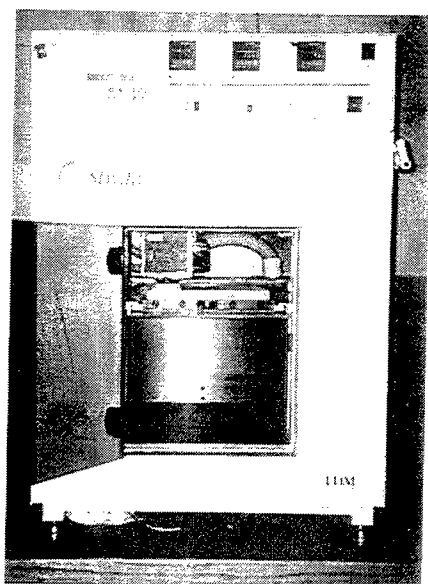


Figure 2: Stratasys 1600 FDM apparatus in process.

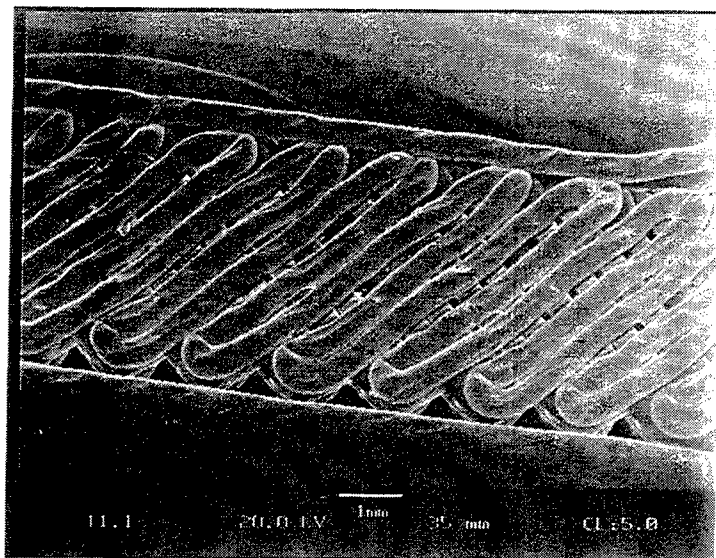


Figure 3: Surface roads and side view if slices.

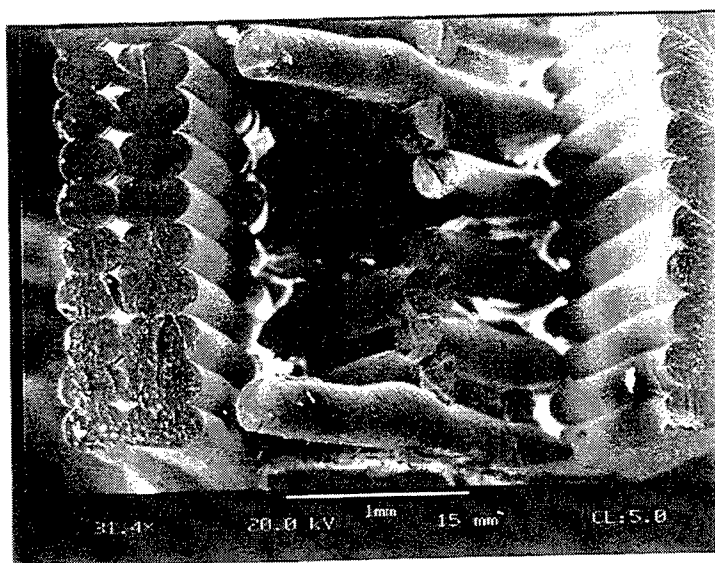


Figure 4: Fracture surface of FDM constructed ABS tensile sample.

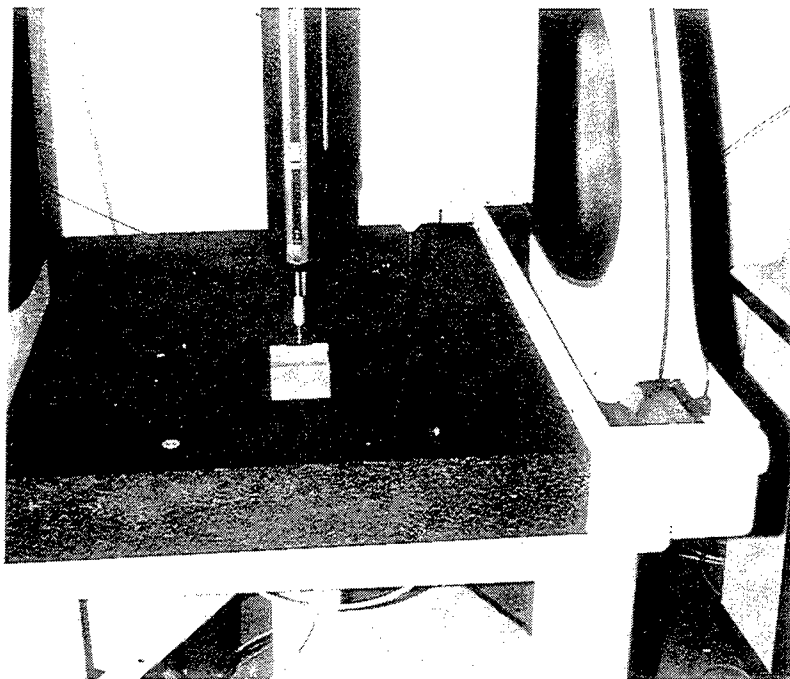


Figure 5: Dimensional analysis apparatus.

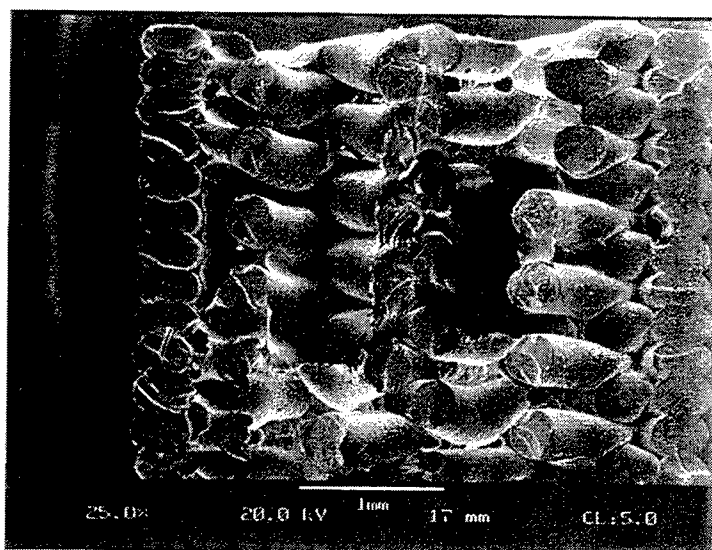


Figure 6: Fracture surface of MDGlue impregnated sample at 0.02" gap and 25X.

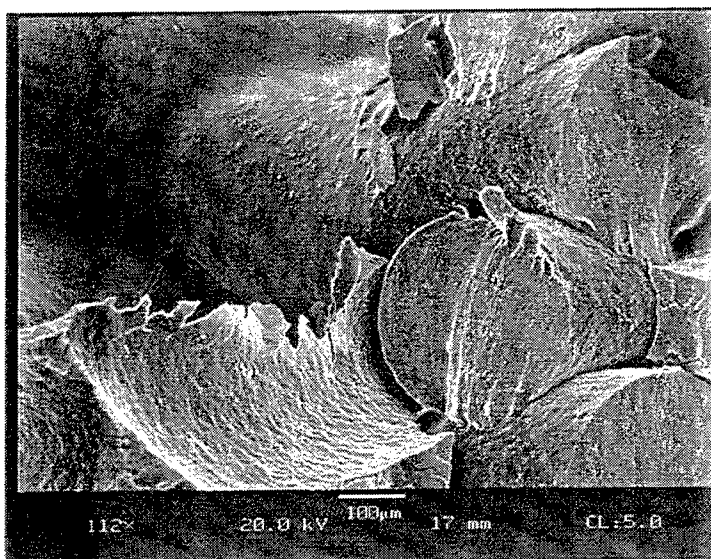


Figure 7: Fracture surface of MDGlue impregnated sample at 0.02" gap and 112X.
Note the mixed cohesive and adhesive failure at the fiber/matrix interface.

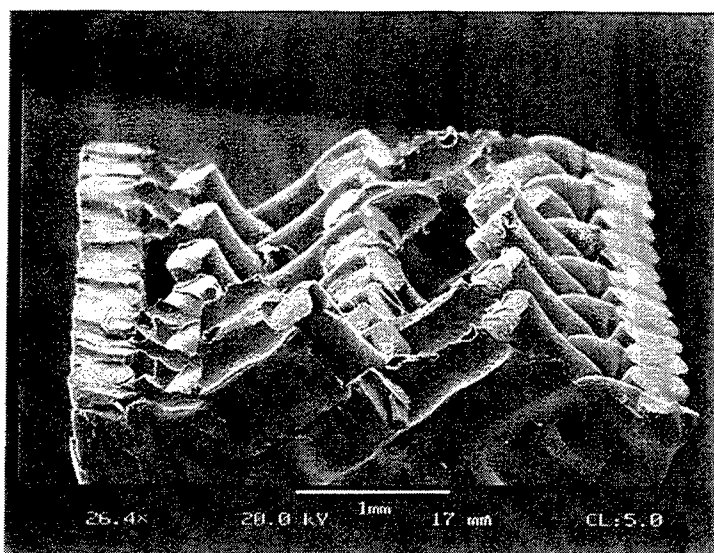


Figure 8: Fracture surface of MDGlue impregnated sample at 0.02" gap and 26.4X.

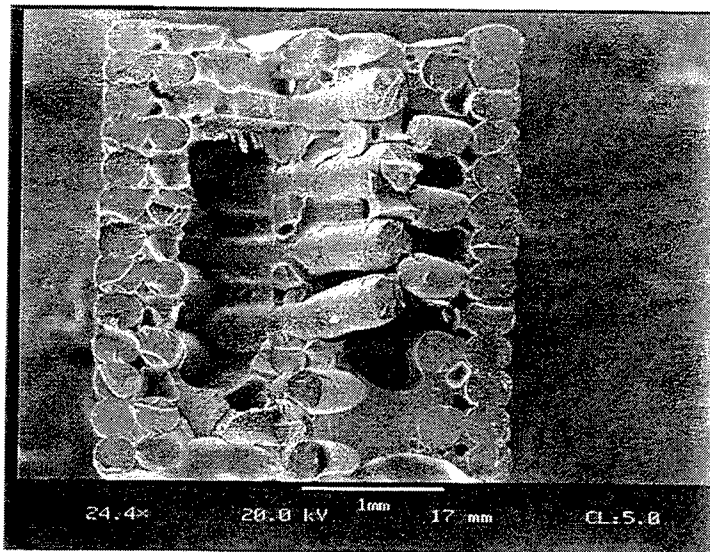


Figure 9: Fracture surface of MDGlue impregnated sample at 0.03" gap and 24.4X.

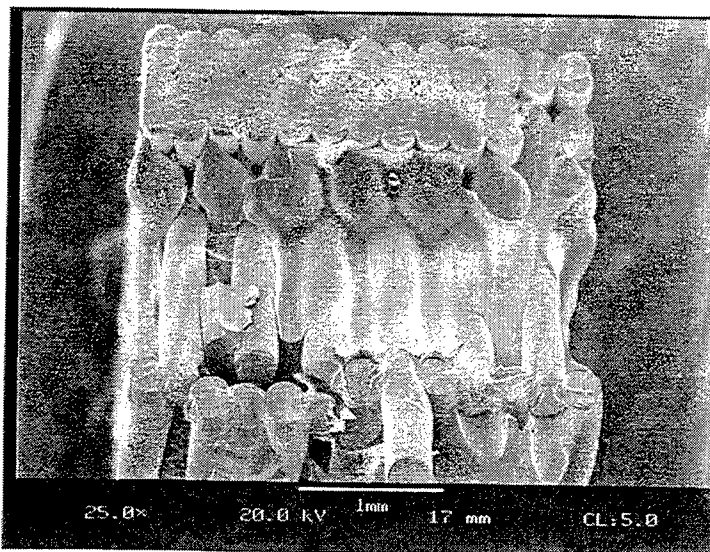


Figure 10: Fracture surface of MDGlue impregnated sample at 0.05" gap and 25.8X.

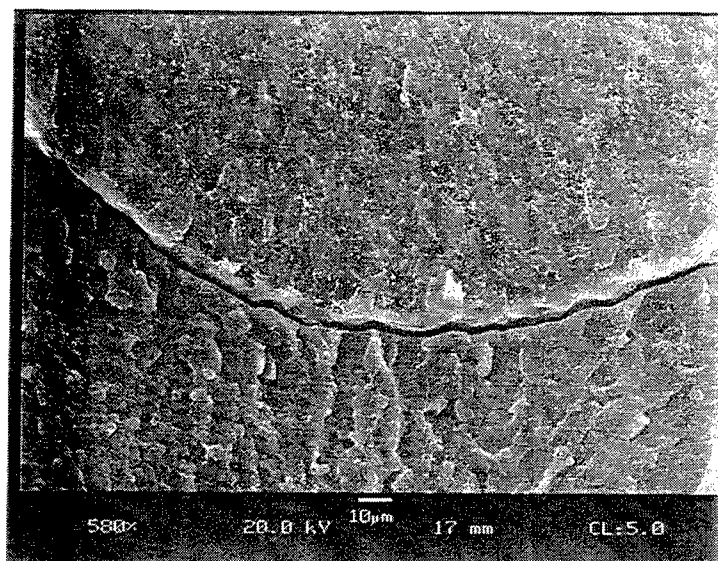


Figure 11: Fracture surface of MDGlue impregnated sample at 0.05" gap and 580X.
Note the similarity of the ductile appearance between the polymer fiber in the upper portion of the photomicrograph and the adhesive matrix in the lower.

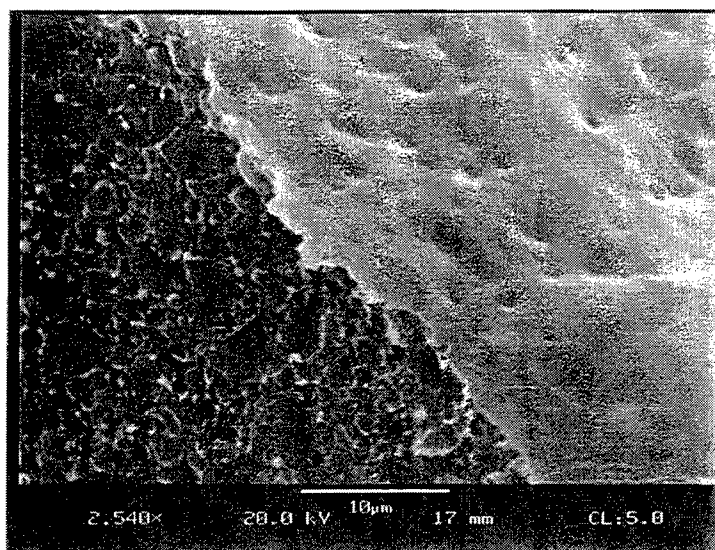


Figure 12: Fracture surface of MDGlue impregnated sample at 0.05" gap and 2540X.
The lower left portion of the photomicrographs illustrates the fracture surface of the adhesive at high magnification, while the upper right displays the adhesive fracture at the interface.

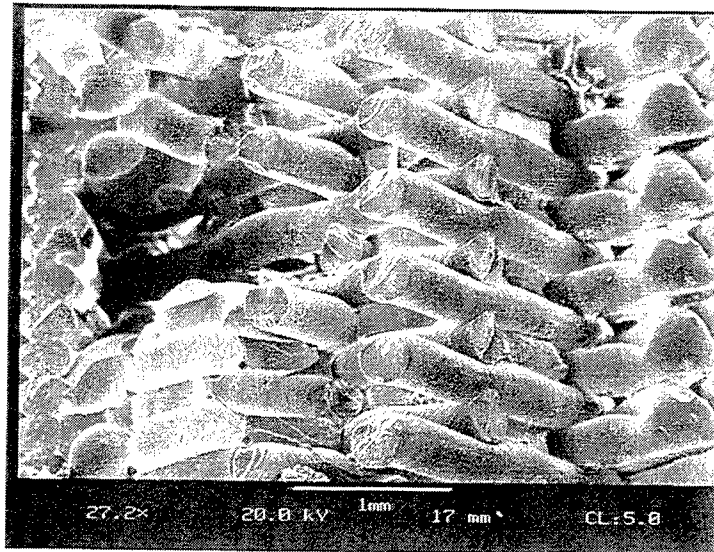


Figure 13: Fracture surface of Clear impregnated sample at 0.02" gap and 27.2X.

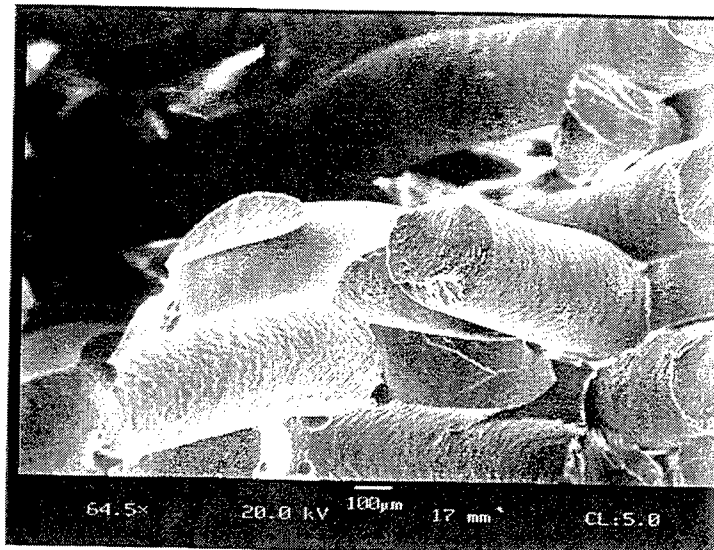


Figure 14: Fracture surface of Clear impregnated sample at 0.02" gap and 64.5X.
Note the pure adhesive failure of the highly ductile matrix.

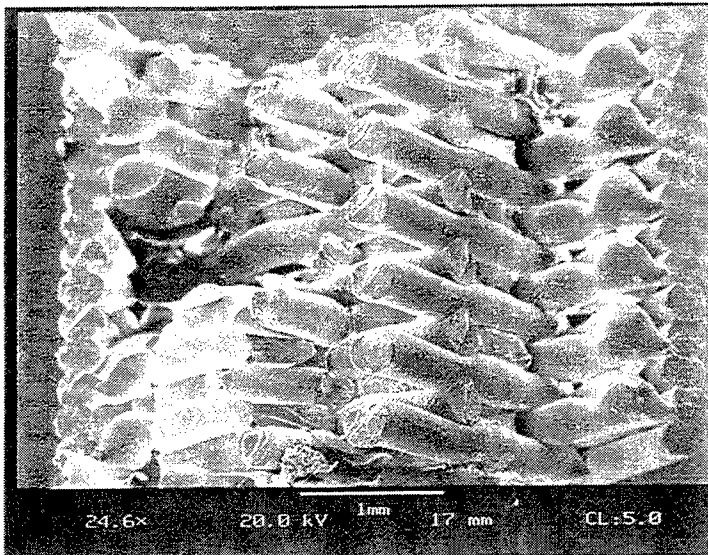


Figure 15: Fracture surface of Clear impregnated sample at 0.03" gap and 24.6X.

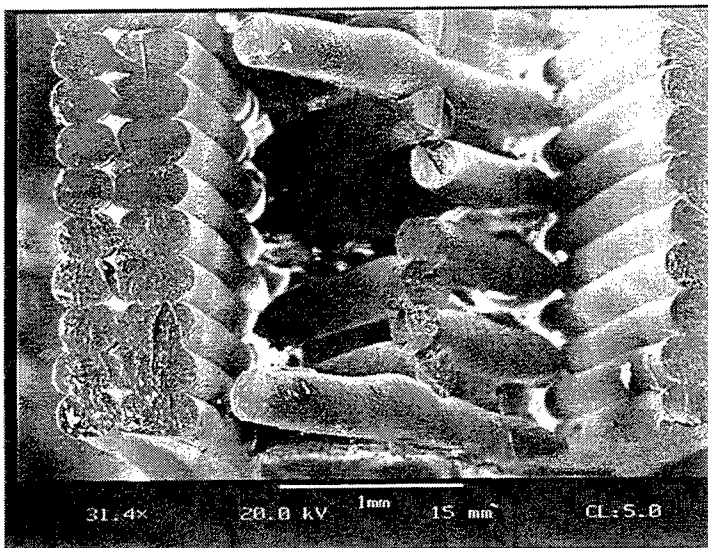


Figure 16: Fracture surface of Clear impregnated sample at 0.05" gap and 31.4X.

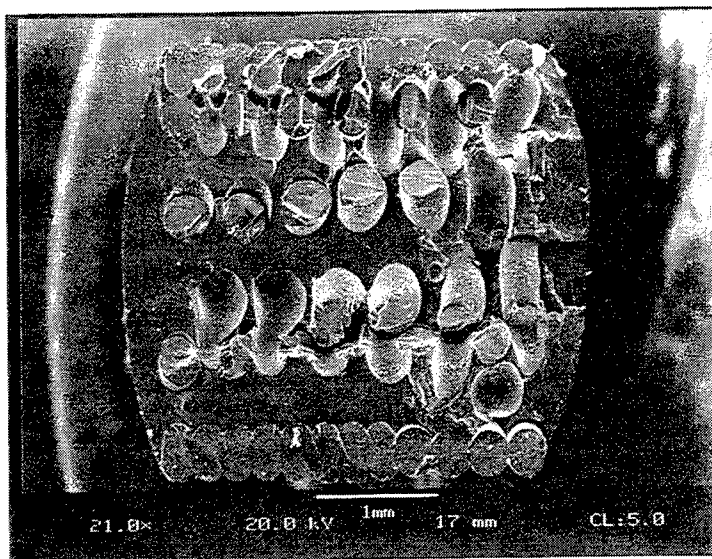


Figure 17: Fracture surface of 5Min impregnated sample at 0.02" gap and 21.0X.

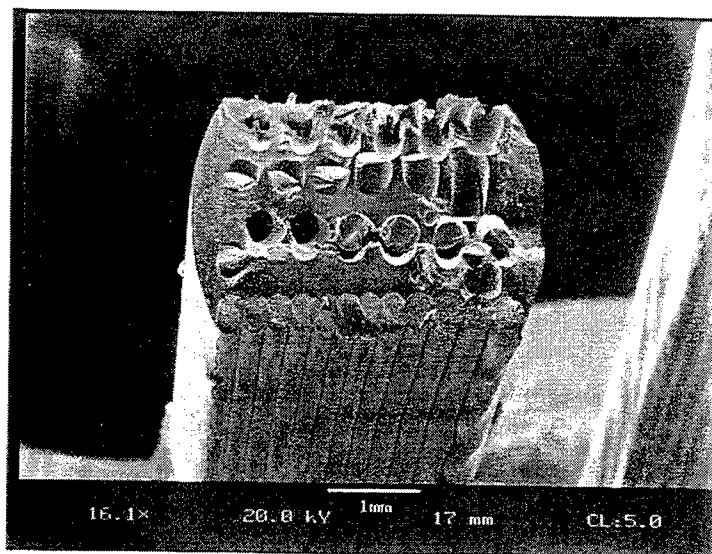


Figure 18: Fracture surface of 5Min impregnated sample at 0.02" gap and 16.1X.
Note the lack of deformation in the adhesive.

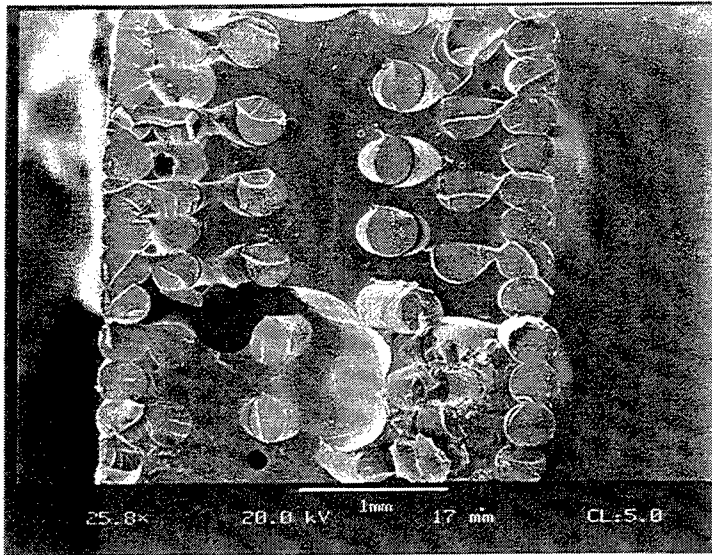


Figure 19: Fracture surface of 5Min impregnated sample at 0.03" gap and 25.8X.

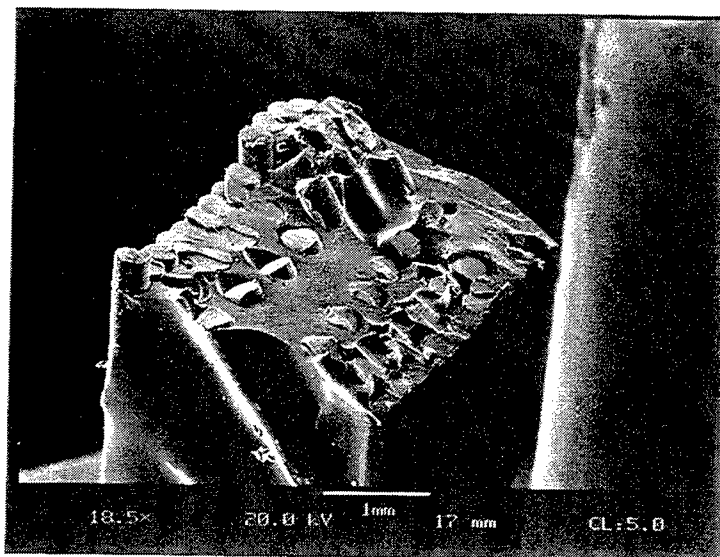


Figure 20: Fracture surface of 5Min impregnated sample at 0.03" gap and 18.5X.

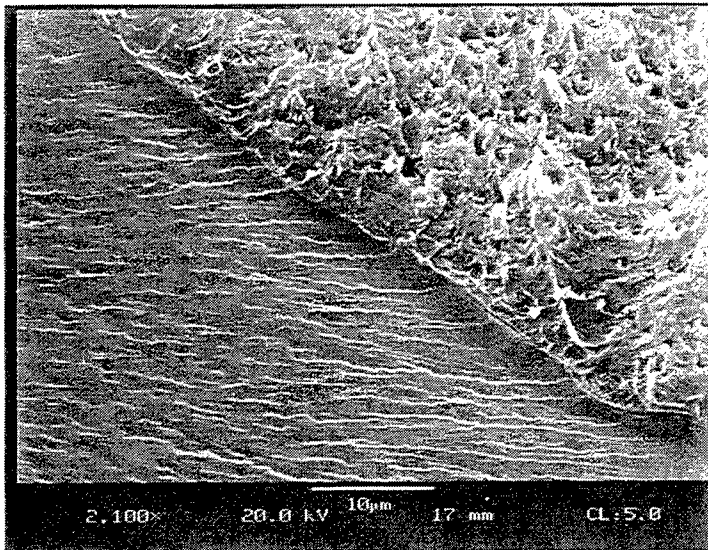


Figure 21: Fracture surface of 5Min impregnated sample at 0.03" gap and 2100X.
Note the difference in appearance between the ductile failure of the polymer fiber in the upper right as compared to the brittle failure of the matrix in the lower left.

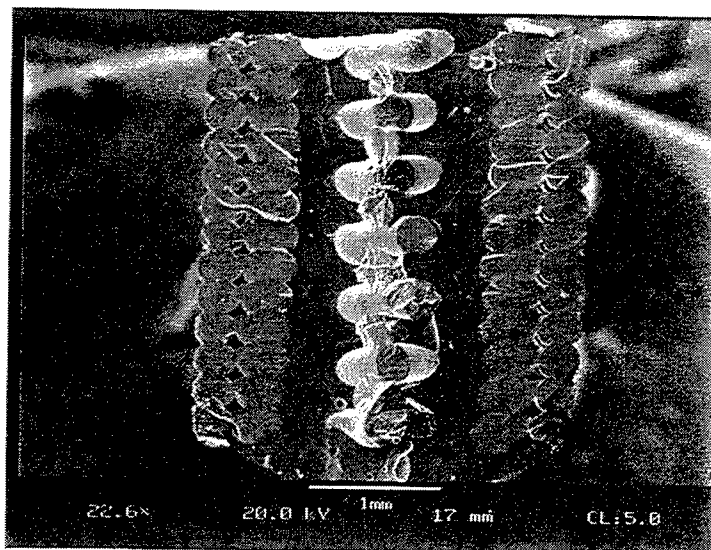


Figure 22: Fracture surface of 5Min impregnated sample at 0.05" gap and 22.6X.

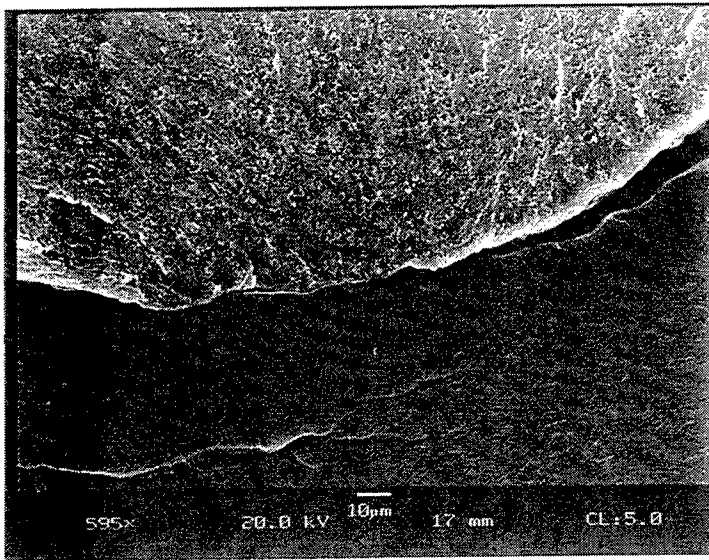


Figure 23: Fracture surface of 5Min impregnated sample at 0.05" gap and 595X.
Note the difference in appearance between the ductile failure of the polymer fiber in the upper half as compared to the brittle failure of the matrix in the lower.

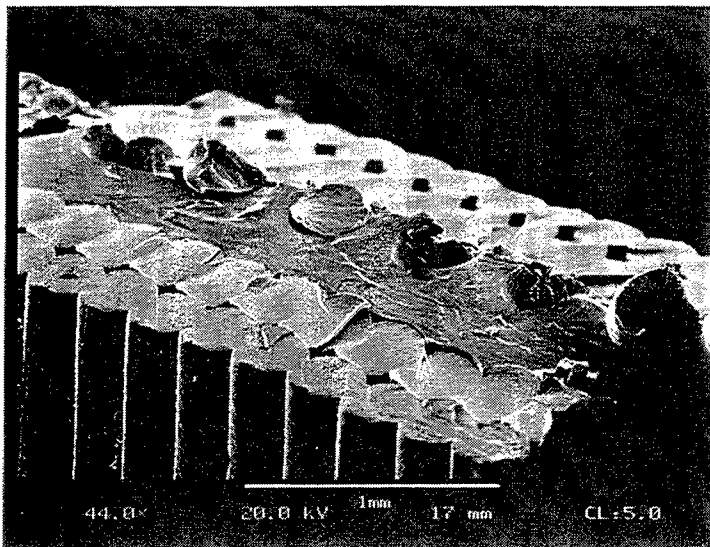


Figure 24: Fracture surface of 5Min impregnated sample at 0.05" gap and 44X.

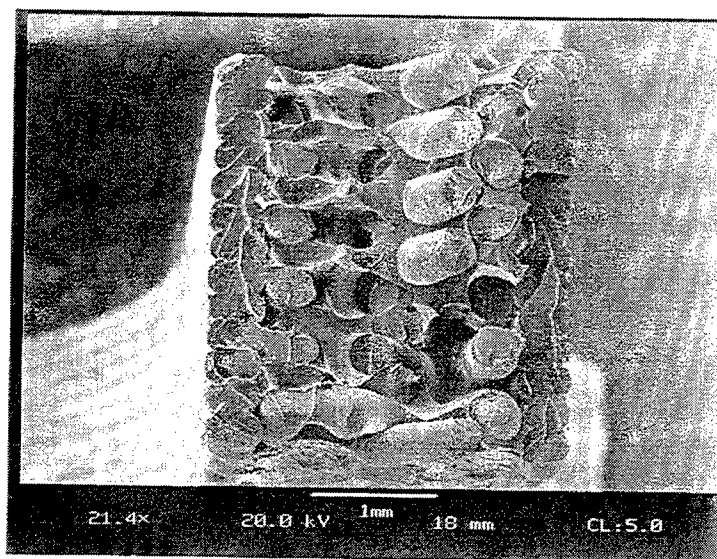


Figure 25: Fracture surface of Ultra impregnated sample at 0.02" gap and 21.4X.

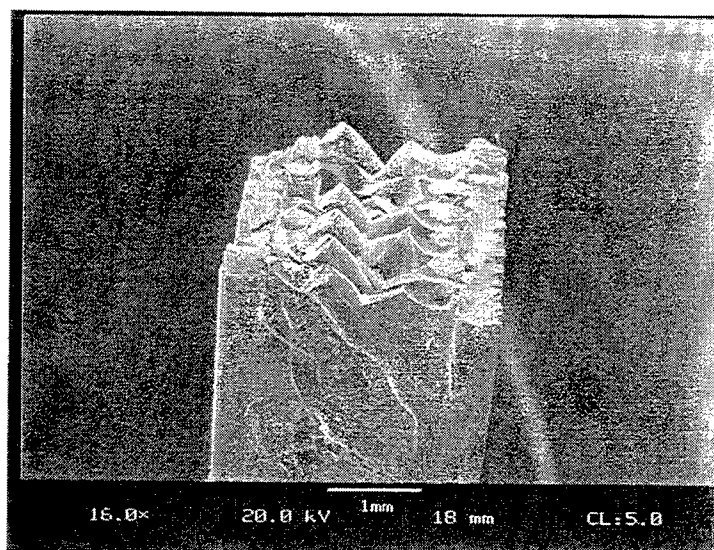


Figure 26: Fracture surface of Ultra impregnated sample at 0.02" gap and 16X.

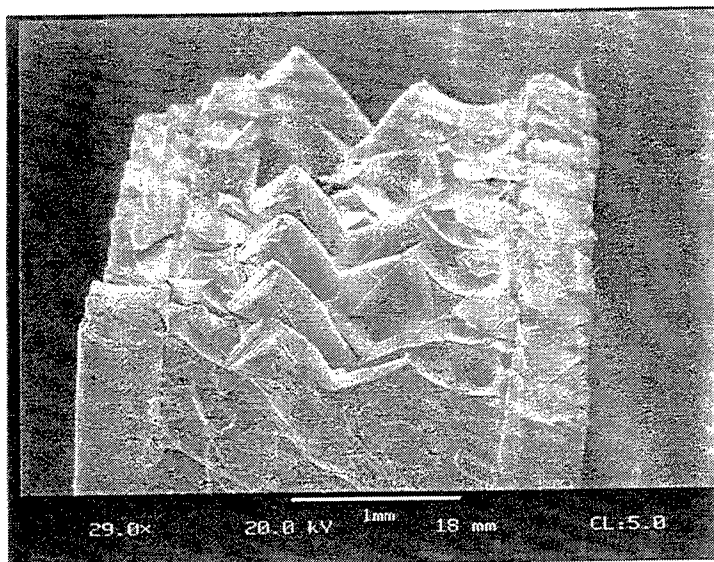


Figure 27: Fracture surface of Ultra impregnated sample at 0.02" gap and 29X.

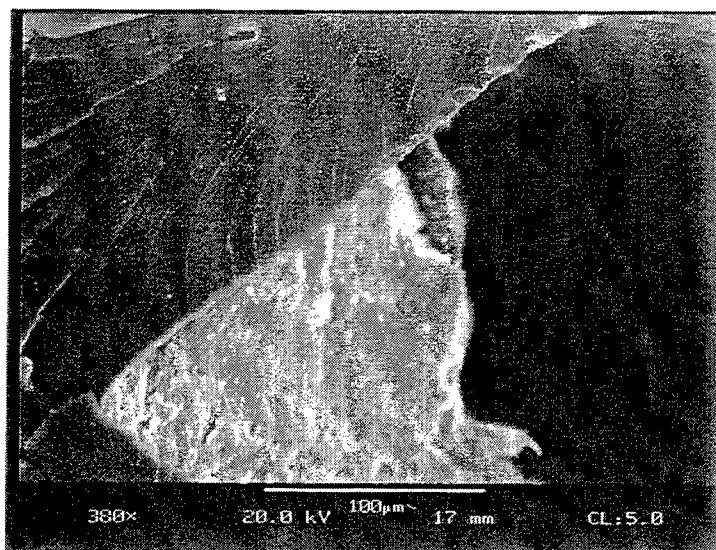


Figure 28: Fracture surface of Ultra impregnated sample at 0.02" gap and 388X.
 Note the difference in appearance between the ductile failure of the polymer fiber in the center of the photomicrograph as compared to the brittle failure of the matrix at the perimeter.

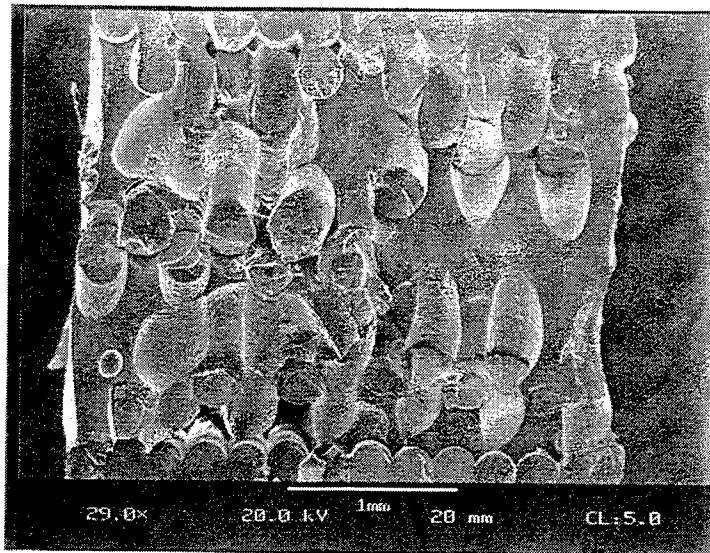


Figure 29: Fracture surface of Ultra impregnated sample at 0.03" gap and 29X.

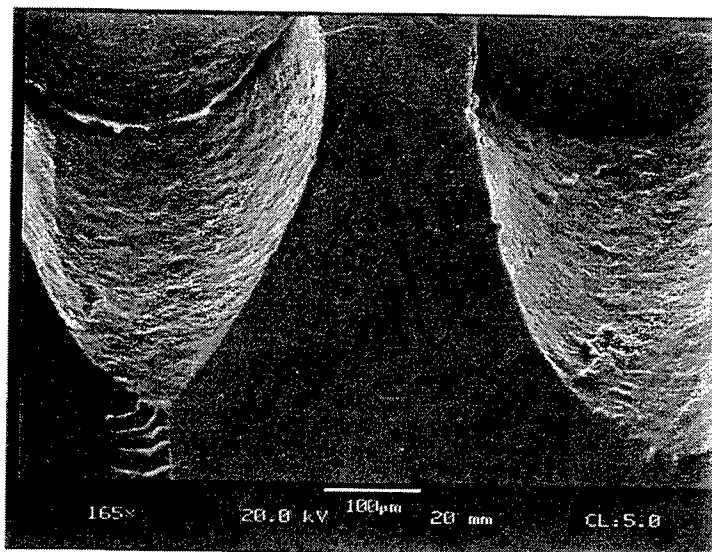


Figure 30: Fracture surface of Ultra impregnated sample at 0.03" gap and 165X.
Note the difference in appearance between the ductile Adhesive failure at the fiber/matrix as compared to the brittle failure of the matrix.

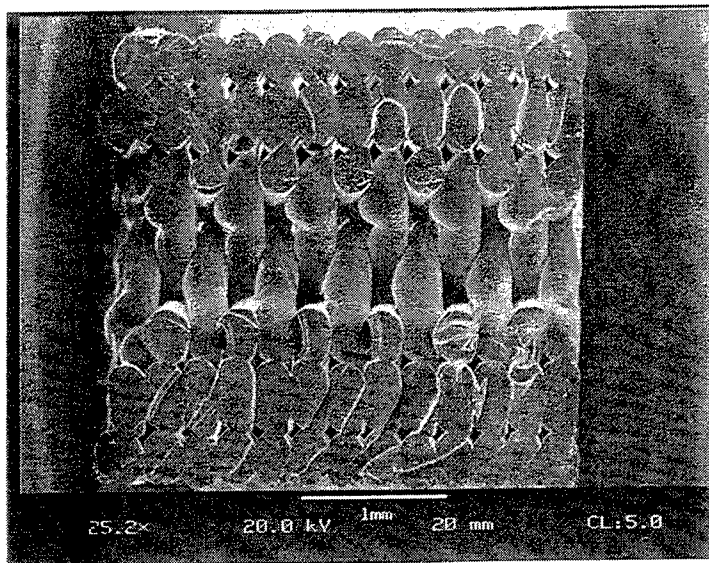


Figure 31: Fracture surface of Ultra impregnated sample at 0.05" gap and 25.2X.
Note the lack of deformation in the adhesive.

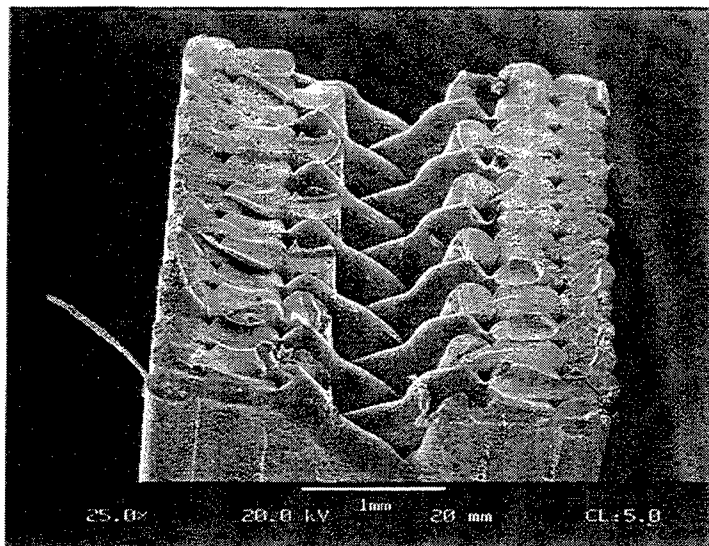


Figure 32: Fracture surface of Ultra impregnated sample at 0.05" gap and 25X.
Note the lack of deformation in the adhesive.

RECENT DEVELOPMENTS IN EXTRUSION FREEFORM FABRICATION (EFF) UTILIZING NON-AQUEOUS GEL CASTING FORMULATIONS

Greg E. Hilmas, John L. Lombardi, Robert A. Hoffman, and Kevin Stuffle
Advanced Ceramics Research, Inc.
Tucson, Arizona

ABSTRACT

Extrusion Freeform Fabrication (EFF) was shown to be an extremely versatile method for fabricating Functionally Graded Materials (FGMs). The approach is inexpensive and potentially feasible for grading between any thermodynamically compatible ceramic-metal, ceramic-ceramic, or metal-metal material combination. Several material systems were investigated in this study including alumina-304 stainless steel, zirconia-304 stainless steel, alumina-Inconel 625, zirconia-Inconel 625, alumina-nickel aluminide, zirconia-nickel aluminide, titanium carbide-Inconel 625, titanium diboride-nickel aluminide, and tungsten carbide-nickel aluminide. A controlled gradient was demonstrated between the end members for all of the above compositions. The FGMs were hot pressed to achieve near theoretical densities, providing flexural strengths as high as 1000 MPa for the zirconia-304 stainless steel FGM.

The FGM systems developed in this program have a wide variety of potential commercial and government applications including cutting tools and other components requiring wear resistant surfaces, aircraft engine and automotive engine components, light and heavy armor systems, and electrical insulators and heat-sinks for the electronics industry, to name a few.

INTRODUCTION

The main objective of this study was to utilize current novel manufacturing techniques for the fabrication of functionally graded materials (FGMs). FGMs have a graded transition in composition and are attractive as a method for taking advantage of the properties of two vastly different materials within the same body. FGMs differ from coated materials or conventional composites in that they are microstructurally inhomogeneous. The graded composition eliminates many of the problems associated with the presence of discrete interfaces in conventional composites such as poor mechanical integrity and transport losses due to low interfacial adhesion. It also can eliminate problems associated with thermal expansion mismatch which is not trivial for most high temperature applications. The use of slurry formulations combined with state-of-the-art freeform fabrication technologies would allow potential FGM compositions to be rapidly prototyped.

Solid freeform fabrication (SFF - also known as 'Rapid Prototyping') is a rapidly developing technology that has significant commercial potential [1-4]. It is a computer controlled, layer by layer, additive process where the desired part is first reduced to geometric sections through the use of Computer Aided Design (CAD) software. The method for transferring the CAD design to the fabrication of an actual component is quite complex and dependent on the SFF technology being utilized. However, the fabrication of solid, three-dimensional objects without tooling has rapidly progressed from producing simple models to producing complex functional prototypes. Parts can now be produced in a number of materials including wax, thermoplastics, thermosets, photopolymers, paper, metals, ceramics and glass fiber reinforced composites.

ACR is actively involved in developing its own Extrusion Freeform Fabrication (EFF) technology as a rapid and flexible prototyping and manufacturing process [5,6]. Two in-house systems have been developed which successfully freeform CAD designed complex parts using

polymer and ceramic engineering materials including Al_2O_3 , ZrO_2 , Si_3N_4 and SiC , as well as PEEK and polycarbonate thermoplastics. The technologies are also amenable to processing composite materials, e.g., short C fiber filled PEEK. The next technological breakthrough lies in gaining the ability to rapidly fabricate FGMs to be used as a screening process for evaluating potential FGM components. When a successful FGM composition is found, direct application of the technologies can be utilized to prototype functional three-dimensional parts. The goal of this study was to develop a rapid, flexible, and precise fabrication method for producing and evaluating potential FGMs. Nine different ceramic-to-metal graded compositions were successfully prepared during this study, resulting in a method which appears promising as a low-cost high pay-off approach for fabricating and screening potential FGMs.

EXPERIMENTAL

Development of Polymerizable Slurries

The following eight ceramic- or metal-based polymerizable slurries were produced during this study: Al_2O_3 , ZrO_2 , 304 S.S., NiAl, Inconel 625, TiB_2 , TiC and WC. The slurries were prepared by ball milling the respective raw powder(s) into two different acrylate monomer vehicles. The compositions of the two liquid vehicles utilized in the study are outlined in Table 1. Liquid vehicle #1 is based upon 'gel casting' formulations similar to those developed by Oak Ridge National Laboratory for injection molding [7,8]. Liquid vehicle #2, developed at ACR, was found to be the preferred vehicle for all of the starting powders, achieving the highest solids loadings with the shortest milling time. Typical solids loadings achieved for the metal and ceramic slurries were in the range of 44 to 58 vol.%. The rheological properties of the slurries were also characterized using a Brookfield Model VIII viscometer.

TABLE 1. Polymerizable Liquid Vehicles

Liquid Vehicle No.	Additive	Liquid Volume %
1	DBE (Dibasic Esters)	18.5
	Triton X-100	20.5
	HDODA	55
	TMPTA	6
2 [†]	Propylene Carbonate	61 - 63
	N,N' - dimethylacrylamide	32.5
	Dispersant	4.5 - 6.5
	(various - see Table 2)	

[†] All slurries formulated with liquid vehicle #2 also contained 3 wt.% N,N'-methylenebisacrylamide with respect to N,N'-dimethylacrylamide weight. This is added as a cross-linking agent.

The curing or gelation process required to solidify the liquid slurries utilized initiators to start the free radical polymerization of the monomers contained in the slurries. Most of our work in the past has relied on peroxide-based initiators such as benzoyl peroxide (BPO) which is a common free radical initiator. BPO proved to be unstable in the presence of the transition metal powders used in this study and was believed to catalytically decompose and prematurely gel the metal filled slurries [9]. This precluded the use of BPO in any of the slurries since the ceramic slurries would come in contact with the metal slurries during extrusion. Consequently, other more chemically stable initiators had to be used. It was found through extensive testing that peroxyketal and peroxyarbonates had greater stability than BPO in the presence of the metal powders. In particular, Lupersol TBEC (Elf Atochem, Philadelphia, PA) was found to be the best in all cases and was almost completely miscible in the liquid vehicle. The initiator was added to the slurries (1.5 grams per 100 ml of slurry) just prior to extrusion.

Fabrication of FGM Billets

The next step involved the formation of 'green' billets having a graded composition between various ceramics and metals. Nine functionally graded billets were prepared including: Al_2O_3 to NiAl, ZrO_2 to NiAl, Al_2O_3 to 304 S.S., ZrO_2 to 304 S.S. FGM's, Al_2O_3 to Inconel 625, ZrO_2 to Inconel 625, WC to NiAl, TiB_2 to NiAl, and TiC to Inconel 625. In order to produce FGMs, the EFF machine was configured with dual extrusion cylinders having separate slurry reservoirs for the individual ceramic and metal slurries. The flow of the individual slurries was passed through a Y-block, into a small mixing head containing an in-line static mixer, and out through a deposition needle. The extrusion head then swept out the designed path while depositing the liquid slurries to build up the 3-dimensional FGM body. The desired composition at each point was controlled in the CAD package by proportioning the rate of flow from the two extruders utilizing computer control. All of the FGM billets were ~1 cm thick in the green state and contained 4 - 6 graded layers plus two layers of each end member.

The 'green' FGM billets were subsequently thermally gelled and loaded into a graphite die lined with boron nitride. The graphite die was then placed into a binder burn-out furnace and heated at $\sim 1^\circ\text{C}/\text{min.}$ to 500°C and held for 2 hours in a flowing nitrogen atmosphere in order to pyrolyze the organic binder in the billets. The billets were subsequently induction hot pressed according to the following heating schedule and the hot pressing conditions outlined in Table 2:

- 1.) Heat at $20^\circ\text{C}/\text{min.}$ from room temperature to 1100°C
- 2.) Heat at $10^\circ\text{C}/\text{min.}$ to the final hot pressing temperature
- 3.) Apply load (25 MPa) at 1000°C
- 4.) Remove load after 60 min. at final hot pressing temperature
- 5.) Cut furnace power for cool down ($\sim 15^\circ\text{C}/\text{min.}$).

Table 2. Hot Pressing Condition for the FGM Billets

FGM Billet	Hot Pressing Temperature ($^\circ\text{C}$)	Hold Time at Temp. (min.)	Atmosphere
Al_2O_3 -304 S.S.	1250	60	800 torr Ar
ZrO_2 -304 S.S.	1250	60	800 torr Ar
Al_2O_3 -NiAl	1350	60	800 torr Ar
ZrO_2 -NiAl	1350	60	800 torr Ar
Al_2O_3 -Inconel 625	1175	60	800 torr Ar
ZrO_2 -Inconel 625	1175	60	800 torr Ar
TiC (Ni,Mo)-Inconel 625	1175	60	800 torr Ar
TiB_2 (Ni)-NiAl	1350	60	800 torr Ar
WC (Co)-NiAl	1350	60	800 torr Ar

The final hot pressing temperatures were restricted by the melting points of the individual metals in order to avoid flow of the metals out of the graphite die as well as to prevent reactions with the graphite. In general, hot pressing was accomplished at temperatures 200 degrees below the melting temperature of the metals. Unfortunately, this had the potential to limit the densification of the ceramic phases. ZrO_2 is known to hot press to near theoretical density at low temperatures (e.g., 1250°C) making it an attractive ceramic constituent for these particular FGM compositions.. However, Al_2O_3 does not densify as readily at these low temperatures (typically requiring $>1450^\circ\text{C}$ hot pressing temperatures) and was therefore a less attractive ceramic constituent for the FGM compositions being studied. The TiC, TiB_2 , and WC ceramics required some liquid phase sintering aids in order to achieve near theoretical densities at these low hot pressing temperatures. Since these ceramic materials have been extensively studied as potential and even current production cutting tool materials, a survey of the literature revealed a variety of metallic additions which would act as suitable liquid phase sintering additives allowing these ceramics to be densified in the range of 1200 to 1400°C [10-16]. It was decided to utilize 8 wt.%

Ni + 2 wt.% Mo additions for the TiC, a 10 wt.% Ni addition for the TiB₂, and a 6 wt.% Co addition for the WC.

Materials Evaluation

The experimental densities for the FGM billets were determined utilizing the Archimedes' density method, taking the average of three samples. Scanning electron microscopy (SEM) and energy dispersive spectroscopy (EDS) were performed at the University of Arizona using a Hitachi 2460N electron microscope equipped with a Noran EDS system equipped with a light element window and a silicon/lithium detector. Cross-sections of the billets were cut into ~5 mm x 5 mm squares, mounted in epoxy, and polished to a 1 μ m diamond finish followed by a brief polish with a 0.05 μ m SiO₂ slurry. The samples were then coated with a conductive gold-palladium coating and observed in the SEM at 25 kV. Preliminary mechanical property evaluations were performed in the form of four-point flexural strength measurements. Flexure bars (~4 mm wide x 4 - 5 mm long x 45 mm long) were cut and ground from each of the FGM billets.

RESULTS

Development of Polymerizable Slurries

The only powder which presented some difficulties in working with and producing a workable slurry was the Inconel 625. Using liquid vehicles #1 and #2, slurry formulations were attempted with the Inconel powder but were not successful in the first several trials. The Inconel had a tendency to settle rapidly and not remain well dispersed. It also exhibited a strong shear thinning behavior which led us to believe that the surface chemistry of this particular powder was quite complex compared to the other powders. We eventually solved both the surface chemistry and settling problems by utilizing two dispersants simultaneously and a 360,000 molecular weight polyvinylpyrrolidone additive as a thickening agent, respectively.

All of the ceramic and metal slurries were found to exhibit a thixotropic rheology whereby the apparent slurry viscosity rapidly decreased with increasing shear rate. Thixotropic rheology is a beneficial characteristic of the EFF slurries since it enables low pressure extrusion and accurate deposition of the freeformed material with minimal layer spreading once the slurry is deposited.

As an example, figure 1 below depicts the typical rheological behavior for the Al₂O₃ EFF slurry developed in this study. From the plot it can be seen that the slurry is highly thixotropic such that a fourfold difference in apparent slurry viscosity is observed at high versus low shear rates. The viscosity plot was fit to the Cross rheological model [17] and an expression relating this curve fit is given below:

$$\eta = 7750\dot{\gamma}^{-0.715}$$

where η is the apparent viscosity and $\dot{\gamma}$ is the shear rate. The -0.715 exponent in the expression signifies that the fluid is strongly shear thinning and is similar to values observed for other highly thixotropic fluids (i.e. gel toothpaste)[18]. This suggests that EFF compatible slurries should typically have Cross rheological model exponents of similar value.

Fabrication of FGM Billets

The FGM billets typically came out of the hot press with a slight bow to them, concave on the metal side and convex on the ceramic side. Despite the gradient from ceramic-to-metal through the thickness of the billet, the pure metal side of the billets had a thermal expansion coefficient 2 to 3 times that of the pure ceramic side. In effect, the metal side contracted more than the ceramic side upon cooling instead of remaining flat and placing the ceramic into compression, therefore the billets would warp slightly. This placed the ceramic side of the billets in tension. For the NiAl

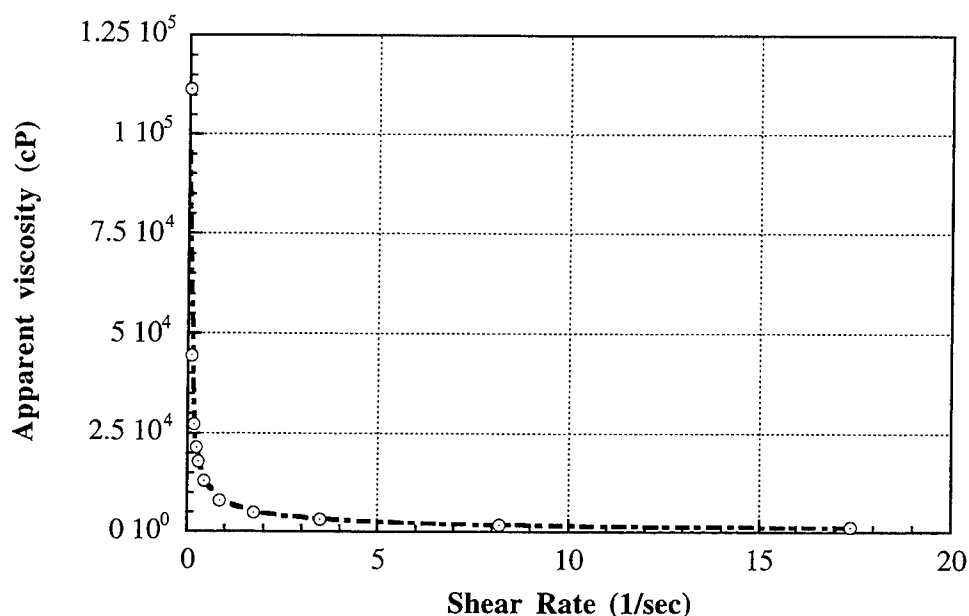


Figure 1. Apparent viscosity vs. shear stress for the Al_2O_3 slurry.

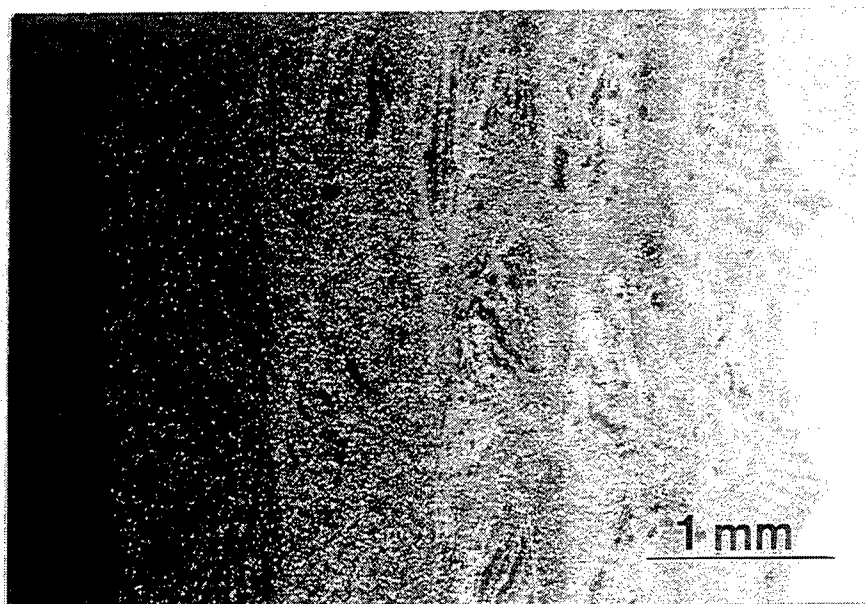
containing FGM billets, the cooling stresses led to cracks on the ceramic side of the billets. However, these were through-thickness cracks and not delamination cracks. For the ZrO_2 -NiAl and Al_2O_3 -NiAl billets the pure ceramic side was able to be ground away without propagating the surface cracks and flexural bars could be produced for mechanical testing. For the $\text{WC}(\text{Co})$ -NiAl and the $\text{TiB}_2(\text{Ni})$ -NiAl billets the cracks had already propagated through the billets after hot pressing, leaving pieces too small for the fabrication flexure bars but large enough for SEM analysis.

Materials Evaluation

The SEM results for two representative FGM billets are shown in Figures 2 and 3. The majority of the FGM billets did not show any intermixing between the graded layers during hot pressing. The only exception was the $\text{TiC}(\text{Ni, Mo})$ -Inconel 625 billet which was completely intermixed after hot pressing to the point where individual graded layers were impossible to determine. The result still demonstrated a uniform transition between ceramic and metal, but there remained a definite segregation of the end members. The ZrO_2 -304 S.S., Al_2O_3 -NiAl, and ZrO_2 -Inconel 625 FGM billets contained cracks running perpendicular to the graded layers in their ceramic end member. We believe these cracks to be the result of tensile residual stresses generated during the cooling cycle after hot pressing.

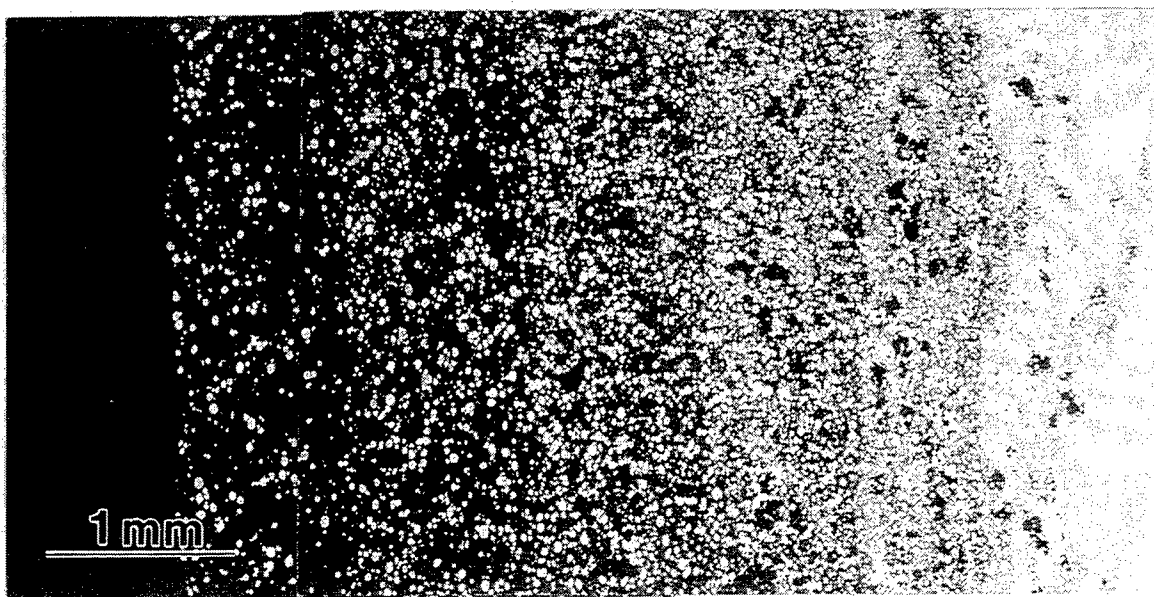
The majority of the FGM billets achieved in the range of 94-97% of their theoretical density with the Al_2O_3 -304 S.S. billet being the lowest at 87% of theoretical. The theoretical densities were based on 50 vol.% each of the two end members which is what the EFF software program was designed to produce during extrusion. The experimental density data for the FGM's fits well with what was observed in the SEM and the hot pressing temperature limits imposed on the ceramic phases. For the most part, the pure metal end members are near 100% of their theoretical density, while the pure ceramic end members were still reasonably dense (84-94%) despite the low hot pressing temperatures.

For most of the FGMs, the low ceramic densities coupled with a tensile residual stress state on the ceramic side, developed during cooling from the hot pressing temperature, led to low strengths (typically 100-160 MPa) when the four-point bend tests were performed with the ceramic side as the tensile surface. However, when the metal side was tested as the tensile surface, the strength values always increased. In fact, for the ZrO_2 -304 S.S. and Al_2O_3 -304 S.S. FGM billets the strengths, ~1000 and 780 MPa, respectively, were higher than the theoretical strengths of most of



Al_2O_3 —————> 304 SS

Figure 2. SEM micrograph of a cross-section of the Al_2O_3 -304 Stainless Steel FGM billet, a plot demonstrating its composition profile (experimentally vs. theoretically determined), and EDS spectra from the end members of the FGM.



Al_2O_3 —————> Inconel 625

Figure 3. SEM micrograph of a cross-section of the Al_2O_3 -Inconel 625 FGM billet, a plot demonstrating its composition profile (experimentally vs. theoretically determined), and EDS spectra from the end members of the FGM.

the end members. Figure 4 shows a load-deflection curve for the ZrO_2 -304 S.S. FGM system with the 304 S.S. in tension. The ceramic actually spalled off the compressive side of the bars prior to failure during many of the flexure tests. When the flexure bars were tested with the

ceramic side in tension, the crack would pop in on the tensile side of the bar at a low load but would then be deflected several times by the ceramic-metal graded layers. This resulted in tests that showed materials with low strengths but having an extremely high work-of-fracture. In the end, the bars were visibly bent and cracked but remained intact.

The remaining FGM compositions were linearly elastic to failure, although the ZrO_2 -Inconel 625 FGM flexure bars showed similar behavior to the ZrO_2 -304 S.S. bars with strengths approaching 400 MPa for the metal side. The FGM billets containing NiAl as the metal side all exhibited low strengths. Polycrystalline NiAl is known to be a brittle metal with typical tensile strengths of only 250 MPa for this stoichiometric composition.

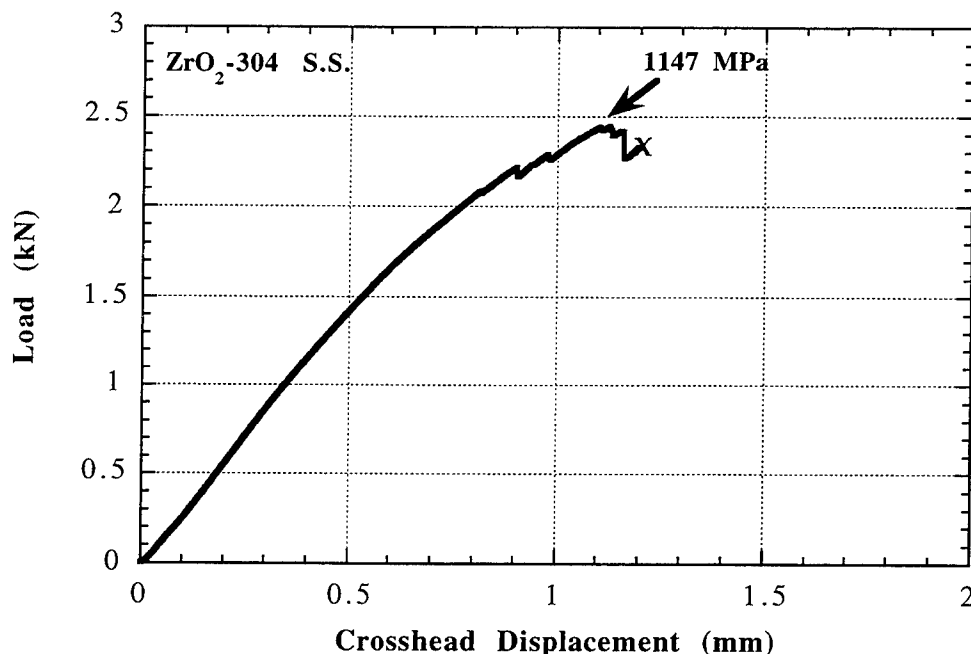


Figure 4. Load-deflection curve for a ZrO_2 -304 S.S. four-point bend test bar. The bar was tested with the 304 S.S. side of the bar in tension and the ZrO_2 side in compression.

CONCLUSIONS

This study demonstrated that extrusion freeform fabrication (EFF) is a versatile method for the fabrication of functionally graded materials (FGMs). While not all of the FGM billets turned out to be crack-free and 100% dense, there were some very promising FGM systems with intriguing mechanical properties. As an example, the ZrO_2 -304 S.S. system achieved ~95% of its theoretical density and yielded strengths greater than 1000 MPa. We firmly believe that careful control of the hot-pressing conditions (slower cooling from the sintering temperature) and some lower temperature sintering aids for the ceramic phases would ultimately result in crack-free and dense FGM structures for most of the rest of the systems. The nine different ceramic-metal FGMs produced in the program clearly shows the technology as a viable method for both screening and producing potential FGM systems and components.

ACKNOWLEDGMENTS

This research was supported by the Ballistic Missile Defense Organization under grant DAAH04-95-C-0049. A special thanks to Bruce King at the University of Michigan for performing the mechanical property evaluations.

REFERENCES

1. P. Jacobs, "Fundamentals of Stereolithography," Society of Manufacturing Engineers, Dearborn, MI. 1992.
2. Proceedings of the Third European Conference on Rapid Prototyping and Manufacturing, P.M. Dickens, Ed., University of Nottingham, England. 1994.
3. Solid Freeform Fabrication Symposium, H.L. Marcus, J.L. Beaman, J.W. Barlow, D.L. Bourell, and R.H. Crawford, Eds., University of Texas, Austin, TX. 1994.
4. Solid Freeform Fabrication Symposium, H.L. Marcus, J.L. Beaman, J.W. Barlow, D.L. Bourell, and R.H. Crawford, Eds., University of Texas, Austin, TX. 1993.
5. P. Calvert, R. Crockett, J. Lombardi, J. O'Kelley, and K. Stuffle, "Extrusion Methods for Solid Freeform Fabrication," pp. 50-55, in Solid Freeform Fabrication Symposium, H.L. Marcus, J.L. Beaman, J.W. Barlow, D.L. Bourell, and R.H. Crawford, Eds., University of Texas, Austin, TX. 1993.
6. K. Stuffle, A. Mulligan, P. Calvert, and J. Lombardi, "Solid Freebody Forming of Ceramics from Polymerizable Slurry," pp. 60-63, in Solid Freeform Fabrication Symposium, H.L. Marcus, J.L. Beaman, J.W. Barlow, D.L. Bourell, and R.H. Crawford, Eds., University of Texas, Austin, TX. 1993.
7. M. A. Janney, "Method for Molding Ceramic Powders," U.S. Patent No. 4 895 194, Jan. 16, 1990
8. A. C. Young, O. O. Omatete, M. A. Janney, and P. A. Menchofer, "Gel Casting - A New Ceramic Forming Process," *J. Am. Ceram. Soc.*, **74** [3], 612-618 (1991).
9. G. Odian, *Principles of Polymerization*, 3rd ed. - pp. 219-222, John Wiley & Sons, New York, NY, 1991.
10. A. R. Bobrowsky, "The Applicability of Ceramics and Ceramals as Turbine-Blade Materials for the Newer Aircraft Power Plants," *Trans. ASME*, **8**, 621-629, 1949.
11. N. M. Parikh and M. Humenik, Jr., "Cermets: II, Wettability and Microstructure Studies in Liquid-Phase Sintering," *J. Am. Ceram. Soc.*, **40** [9], 315-320, 1957.
12. C. F. Yen, C. S. Yust, and G. W. Clark, "Enhancement of Mechanical Strength in Hot-Pressed TiB₂ Composites by the Addition of Fe and Ni," *ORNL Technical Report*, CONF-81093-2, Oak Ridge, TN, 1979.
13. M. K. Ferber, P. J. Becher, and C. B. Finch, "Effect of Microstructure on the Properties of TiB₂ Ceramics," *J. Am. Ceram. Soc.*, **66** [1], C2-C3, 1983.
14. V. J. Tennery, C. B. Finch, C. S. Yust, and G. W. Clark, "Structure-Property Correlations for TiB₂-Based Ceramics Densified using Active Liquid Metals," pp. 891-909 in Science of Hard Materials. Edited by R. K. Viswanadham, D. J. Rowcliffe, and J. Gurland. Plenum Press, New York, NY, 1983.
15. R. F. Snowball and D. R. Milner, "Densification Processes in the Tungsten Carbide-Cobalt System," *Powder Metal.*, **11** [21], 23-40, 1968.
16. D.-Y. Kim and A. Accary, "Mechanisms of Grain Growth Inhibition During Sintering of WC-Co Based Hard Metals," pp. 235-244 in Materials Science Research, Vol. 13, Sintering Processes. Edited by G. C. Kuczynski. Plenum Press, New York, NY, 1980.
17. H. A. Barnes, pp. 116-119 in An Introduction to Rheology, Elsevier, Amsterdam, 1989.
18. P. J. Whitcomb and C. W. Macosko, *J. Rheology*, **22**, 493-505, (1978).

Filament Feed Materials for Fused Deposition Processing of Ceramics and Metals

M.K. Agarwala, R. van Weeren, A. Bandyopadhyay,
A. Safari, and S.C. Danforth
Center for Ceramic Research, Rutgers University

W.R. Priedeman
Stratasys Inc.

Fused Deposition of Ceramics (FDC) and Metals (FDMet) are SFF techniques, based on commercial FDM™ technology, for fabrication of ceramic and metal components. The FD processes use feed material in the form of filaments which require certain physical and mechanical properties. FDC and FDMet processes employ filaments formed from ceramic or metal powders mixed with thermoplastic polymers. The thermoplastic polymers act as binder during the FDC and FDMet processing in forming a green part. Development of green ceramic or metal filaments for FDC or FDMet processing involves three critical steps : selection of an appropriate binder chemistry, appropriate mixing procedures and filament fabrication techniques. This study describes the properties required for filaments for successful FD processing and the approach taken in the development of a series of binder which meets these requisite properties for a wide range of ceramics and metals. Appropriate mixing and filament forming techniques are also discussed.

I. Introduction

Most of the SFF techniques for fabrication of ceramic and metal parts employ polymeric binder systems to bond the ceramic or metal particles together in forming a green part [1]. The green part is then processed to remove the binder from the part and then sintered or infiltrated with a lower melting second phase [1]. However, fabrication of green ceramic or metal parts by various SFF techniques have been far from trivial. First, effort is required in developing the proper binder chemistry to allow SFF processing. In addition, effort may be needed in developing suitable dispersants for the specific particulate system and the binder chemistry. Once an appropriate binder chemistry and dispersant have been selected, the ceramic or metal powder systems are processed with the binder and dispersant to form the feedstock in a suitable physical form (powder, sheets, filaments) for specific SFF processing [1].

Each SFF technique requires feedstock materials with certain physical and mechanical properties. Poor selection of binder chemistry, dispersant, and poor processing of the feedstock can lead to unsuccessful SFF processing. This study describes the development of green ceramic and metal filament feedstocks for successful processing by Fused Deposition of Ceramics (FDC) and Metals (FDMet). FDC and FDMet are SFF techniques, based on commercial FDM™ technology, which are being developed for a wide range of ceramics and metals to produce complex shaped ceramic and metal parts with functional properties [2-5]. This study discusses the various physical and mechanical properties required in the filament feedstock for successful FD processing. The study also describes the development of a binder system and the filament fabrication procedures employed for various ceramic and metal systems.

II. Filament Feedstock Characteristics for FD Processing

The commercial FDM™ systems fabricate wax and polymer parts using continuous spooled filaments as the feed material. The filament is fed through a position-controlled heated liquefier head which deposits molten material in precise locations [6,7]. For the filament to be successfully fed into the liquefier and extruded in molten form out of a nozzle, the filament must have certain properties. The filament, which is fed into the liquefier head by a pair of counter-rotating rollers, not only acts as the feed material, but also serves as an efficient piston for extrusion. Therefore, for a certain material viscosity the filament must have sufficient stiffness and

strength for extrusion, or else the filament will buckle or break after passing through the rollers and not be successful in extruding material [5,7]. Hence, necessary, but not sufficient, conditions for successful FD processing are low viscosity and high stiffness. In addition, the material must have good adhesive behavior for bonding between adjacent roads and layers of deposited material [5,7].

Although filaments with low viscosity, high stiffness, and good adhesion characteristics are sufficient to establish FD processing feasibility, for complete process optimization and automation, the filament feedstock must also possess high flexural modulus and flexural strength [5,7]. High flexural modulus and strength are needed to enable continuous spooling of the filaments onto a spool to provide continuous feedstock supply for the FDM™ system. These properties are also necessary to allow continuous un-spooling of the filament from the spool for uninterrupted feeding (without breaking of the filaments) of the liquefier during fabrication.

FDC and FDMet processing, using commercial FDM™ systems, require development of powder/binder filament feedstocks with the above mentioned properties, namely, low viscosity, high stiffness, good adhesion behavior, high flexural modulus and strength. This is done through binder development and selection of dispersant. In addition to these constraints, development of binder(s) and dispersant for FDC or FDMet must also address issues commonly relevant to all green forming techniques. The binder and dispersant have as high a solids loading as possible (>50 volume%), have good dispersion behavior, and must leave no residue after binder removal.

III. Binders for FDC and FDMet

The binders for green forming techniques typically consist of many components; each added for a specific role in the final mix. In this study a four component binder system has been developed for FDC and FDMet processing. As shown in Table I, each of these components plays a specific role in the final formulation. Table I also shows the temperature range at which each of these components volatilize during binder removal. The amount of each component in the formulation used for FDC or FDMet is varied to tailor the properties needed to allow successful FD processing of specific ceramic or metal system. The weight percent of each of these components varied in this study for FDC/FDMet is also shown in Table I. This binder system is designated RUx (x is the identification number of a particular binder formulation under consideration) [5].

The particulate systems studied for FDC and FDMet processing to date include silicon nitride, silica, lead zirconium titanate (PZT), stainless steel, and tungsten carbide-cobalt. Initial feasibility studies for each of these particulate systems were done by using the RU1 binder formulation which contains 30% wax, 35% polymer, 15% tackifier, and 20% elastomer by weight. 50 to 65 volume % powders were mixed the RU1 binder and fabricated into filaments for FD feasibility studies. In addition, viscosity measurements were made on the mixed feedstock. Based on the viscosity behavior and FD feasibility studies, the binder formulation were further optimized. Also, dispersants were selected and used for certain particulate systems to facilitate FD processing. Depending on the study done with each particulate system, the binder formulation development and dispersant selection was either limited to developing filaments which are FD process worthy but not flexible or was developed to produce FD process worthy and continuous and flexible filaments. Table II shows the different RU binder formulations used successfully for FDC and FDMet processing of various materials. The Table also shows the amount of powder used for FD processing of each system and the nature of the filament feedstock thus produced.

Binder and Dispersant Development for FDC of Silicon Nitride

Most significant FD process development to date has been done with Si₃N₄ [3-5]. Although initial FDC trials of 60 volume % Si₃N₄ with RU1 binder formulation were successful, the filaments were rigid and not flexible enough to enable spooling for continuous and automated

FDC processing. To facilitate continuous and automated FDC processing of Si_3N_4 , the RU binder was tailored and optimized by a linear Design of Experiments (DoE) [5]. Nine different RU formulations with a wide range of wax, polymer, tackifier, and elastomer contents were used. Viscosity measurements were made on each of these compositions as a function of temperature and shear rate to get the viscosity response as a function of each of the components. Similarly, glass transition temperatures (T_g) were measured for each formulation using Differential Scanning Calorimetry. T_g is commonly used as an indicator of the flexibility of the material. The data from the DoE was analyzed to determine the effects of the various components on flexibility and viscosity. Using a linear representations of the response,

$$\text{Response} = C_0 + C_1 [\text{tackifier}] + C_2 [\text{elastomer}] + C_3 [\text{polymer}] + C_4 [\text{wax}]$$

the coefficients (C_0 - C_4) for the effect of each component on viscosity and flexibility were calculated [5]. From this linear DoE study, the following conclusions were drawn:

- The tackifier and elastomer improve flexibility and the wax adversely affects the flexibility.
- Elastomer increases the viscosity and the wax lowers the viscosity.

Based on the results of DoE, the binder system RU9 was developed. RU9 formulation contains 20% wax, 19% polymer, 35% tackifier, and 26% elastomer by weight. In addition to developing RU9 binder formulation, a suitable dispersant was also selected. Selection of oleyl alcohol as dispersant was done by a screening process from among several commonly used dispersants for ceramics, especially silicon nitride [5]. The screening of dispersants was done by measuring the viscosity of 30 volume % Si_3N_4 loaded RU binder suspensions. For the dispersant screening experiments, the powder was pre-treated with varying amounts of different dispersants, prior to mixing in RU binder. Based on these screening experiments by measuring viscosity, as shown in Figure 1, 3 weight % oleyl alcohol, which exhibits the greatest decrease in the viscosity, was determined to be a suitable dispersant [5,8]. Hence, the Si_3N_4 powders used in the study were pre-treated with 3 weight % oleyl alcohol, prior to mixing with the RU9 binder formulation. As shown in Figure 2, filaments fabricated from green feedstocks, containing 45% RU9 binder and 55% Si_3N_4 powder by volume, pre-treated with 3 weight % oleyl alcohol, were flexible, continuous and easily wound onto a spool for successful FDC processing. Although the viscosity of Si_3N_4 FDC formulations were considerably higher than that of an FDM™ material, investment casting wax, Figure 3, FDC processing of these materials was equally successful.

Binder Development for FDC and FDMet of Other Materials

As indicated in Table II, binders for other material systems (silica, PZT, stainless steel, and tungsten carbide-cobalt) have not been optimized to result in continuous and flexible filaments. The binders for these materials were developed with appropriate viscosity to allow successful FD processing using small pieces (6"-12" in length) of stiff and rigid filaments, Figure 4. FDC and FDMet processing of 65 volume % silica and 60 volume % stainless steel was feasible with the RU1 binder without the use of any dispersant. However, the RU1 binder was tailored and developed to allow FD processing of PZT and WC-Co. Initial FD analysis of 50 to 55 volume % PZT and WC-Co with RU1 binder indicated viscosity levels much higher than permissible for successful FD processing. Therefore, suitable dispersants have been selected for PZT and WC-Co to lower the viscosity of 50 volume % powder in RU1 binder composition. Figure 5 shows such a lowering of viscosity of 50 volume % WC-Co when pre-treated with 1 weight % dispersant. Use of appropriate dispersants for PZT and WC-Co have enabled successful FD processing with 50 volume% loading in RU1 binder, although the filaments remain rigid. As was done for silicon nitride, it is expected that appropriate dispersant selection and RU binder optimization would result in continuous and flexible FD process worthy filaments for these materials and for other ceramic or metal systems.

IV. Compounding of Ceramic or Metal Powders with Binders

Once the powder, binder and dispersants have been selected for the FDC/FDMet process, the next concern is homogeneous mixing of these ingredients. Mixing or compounding is crucial, since deficiencies in the quality of mixed feedstock can not be corrected by subsequent processing adjustments. Failure to deagglomerate and evenly distribute the powder at this stage will result in downline defects in both FDC fabrication and post-processing operations. Various techniques, such as, measurement of mixing torque or energy, shear modulus, viscosity, etc. are used to assess the quality of mix and to ensure consistent and repeatable compounding from batch to batch.

Both heat and shear are required for efficient compounding of RU-type thermoplastic binders and the ceramic or metal powders. Therefore, torque rheometer mixing was selected as the method for compounding FDC/FDMet feedstocks. Torque rheometer mixing also measures the torque of mixing which is used in assessing the quality of mix. When dry powder is first added to the molten binder, a high torque value is recorded due to entrapment of the binder between and in the powder agglomerates. As the agglomerates break down by the shearing action of the blades, the immobilized entrapped liquid binder is released and hence the torque goes down to a constant level and stabilizes. The stabilized torque is determined by the solids loading, temperature of mixing, speed of mixing, and the dispersing qualities of the binder. Any change in mixer speed (shear rate) and temperature will cause the torque to change since the system viscosity, and hence the torque, are shear rate and temperature dependent.

Experimental Procedure and Results for Compounding:

In this study, the compounding procedure for incorporating ceramic or metal powder into the binder system involves the use of Haake Rheocord torque rheometer [9]. The torque rheometer is fitted with batch mixing bowls of capacities 50 cm³ and 250 cm³, with Z-blades to provide shear mixing. The maximum blade speed of the mixers is 150 rpm and the maximum temperature capability is 200°C. The mixing bowls are double walled with three independently heated zones. The middle zone is both air cooled and heated to maintain precise temperature control and prevent overheating due to heat dissipation during shear mixing. The temperature of mixing was determined by the viscosity of the system being compounded. The viscosity of the system being compounded determines the shear stresses generated, which in turn determine how effectively the agglomerates are broken and the particle system is dispersed. However, while generating high shear stresses to effectively break up agglomerates, care was taken not to exceed the torque limits of the mixer. Therefore, the temperature of mixing used for a specific system was dependent on the viscosity of the system. Higher temperatures (100-120°C) were used for systems with high viscosities and lower temperatures (70-90°C) were used for systems with low viscosities [5].

The required amount of binder is weighed and added to the mixer and allowed to melt completely. Once molten, dry powder is added in measured increments of 5-40 grams, depending on the viscosity of the binder system. After each addition, the torque of the system increases instantaneously and then slowly decreases and stabilizes over a period of few minutes. The next incremental amount is added after the steady state torque is reached. The process is continued until a desirable powder loading is achieved, after which mixing is continued for a fixed period of time (1-2 hours). The incremental amount of powder additions is decreased at high volume fractions (>45%). The rotor speed is kept at 100 rpm throughout the process. Figure 6 shows the spikes in torque values for each incremental addition of silicon nitride powder in the RU1 binder and subsequent torque stabilization and the final stabilized torque for one hour of mixing. The quality of mix from batch-to-batch of a particular formulation was constant as indicated by reproducible viscosity measurements made on different batches after compounding [5]. The compounded powder/binder system is removed from the mixer, cooled to room temperature, granulated and sieved to >1mm size for feedstock for subsequent viscosity measurement and filament fabrication.

V. Filament Fabrication

After compounding, the next step in preparing the feed material for FDC or FDMet process is to fabricate filaments of nominal diameter 0.070". The control software for the FDM™ system sets the roller speed, and hence the flow rate, for a given set of build conditions (road width, slice thickness and liquefier head speed) based on the assumption that the feed filaments are 0.070" in diameter. If the filament diameter is less than 0.070" then the flow rate is less than desirable, creating roads with smaller widths and thickness. Such underflow results in poor bonding between adjacent roads and layers or creates voids between adjacent roads and layers. If the filament diameter is much greater than 0.070" then either the filament is not fed into the liquefier, which typically has an opening of 0.073", or it may cause overflow resulting in poor definition of fine features in the part. Therefore, it is important to fabricate filaments for FD processing with very controlled diameter ($0.070" \pm 0.001"$). It is also important that the filaments maintain a circular cross-sectional geometry to be appropriately gripped and fed by the rollers. In dealing with ceramic or metal loaded filaments, it is also important to ensure homogeneous distribution of the binder and particle phases in the filaments with no density gradients and porosity.

In this study, filaments for FDC/FDMet processing were fabricated by two different techniques - capillary extrusion and single screw extrusion. Small quantities of straight, rigid filaments for FD trials were fabricated using an Instron capillary rheometer as a piston extrusion device. The capillary rheometer barrel and plunger are mounted on an Instron mechanical test frame. The barrel was heated to 60°C to 120°C, depending on the material under consideration, and filled with compounded and granulated green ceramic or metal feedstock. Extrusion was done by moving the plunger through the barrel at a constant speed of 1mm/minute. A capillary die of 0.070" was used to produce 6"-12" length segments of the filaments with a diameter of $0.070" \pm 0.002"$. The filaments used in this study for FDC and FDMet processing of SiO₂, PZT, WC-Co, and stainless steel were fabricated using the capillary rheometer approach.

Optimized feedstock formulations, such as 55 volume% silicon nitride (pre-treated with 3% oleyl alcohol) in RU9 binder formulation, were used to fabricate continuous and flexible filaments using a continuous single screw extrusion process. A Haake single screw extruder with a 1" diameter screw and L/D ratio of 20:1 was used [8]. The Haake torque rheometer drive unit, used for compounding feedstock, was used for driving the extruder also [8]. Compounded green feedstock material of particles size in the range of 1.4 mm to 4.0 mm were used as the feed material for extrusion through a die of 0.075" diameter attached to the extruder. Extrusion was done at a screw speed of 10 RPM and the temperature was controlled in four different zones along the length of the screw and barrel. Typically, the temperatures in the feed zone and the die region were kept low at 50°C and 65°C, respectively. The temperatures in the mid-section of the screw length were kept at 75°-100°C. As the filament was extruded, it directly passed onto a moving conveyor. The conveyor speed was adjusted and set to produce controlled drawing of the filaments into final diameter of $0.070" \pm 0.002"$ as it is extruded through a die of 0.075". From the conveyor, the filament passes through an *on-line* diameter measuring device, LaserMike, which continuously records the diameter of the filament. The continuously extruding filament, after passing through the LaserMike, were wound onto spools using an automatic winder. The spools used for winding the filaments are similar to those used in commercial FDM™ systems, shown earlier in Figure 3.

The diameters of filaments fabricated by single screw extrusion as well as capillary extrusion were consistently in the range of $0.070" \pm 0.002"$. Effort is being made to further enhance the diameter uniformity to $0.070" \pm 0.0005"$ by employing pressure control devices, such as a metering pump, in the single screw extrusion process line. The density measurements made on randomly chosen segments of filaments using He pycnometry consistently indicated 100% theoretical density of the mixed feedstock, suggesting no porosity or density gradients along the

lengths of the filaments. As shown in Figure 7, the microstructure of the cross-section of the green filaments exhibited uniform and homogeneous mixing with no phase separation.

VI. Conclusions

This study describes the various physical, thermal, and mechanical properties required in the filament feedstock for successful FDC and FDMet processing of ceramics and metals using commercial FDM™ systems. A unique binder series, designated as RU binders, for FDC and FDMet processing has been developed and successfully applied to a wide range of ceramic and metal systems. It has been shown that through optimization of the RU binder system and appropriate selection of dispersant for a specific particulate system, automated FDC and FDMet processing of many particulate ceramic, metal, and composite system is feasible. Appropriate green feedstock compounding and filament fabrication procedures for FD processing have been established. Green feed filaments with controlled diameter and material homogeneity have been successfully fabricated and used for FDC/FDMet processing.

Acknowledgments

The work on various material systems have been done through support from DARPA, ONR (Contract No. N00014-94-0115), and the New Jersey Commission on Science and Technology. The authors would like to thank Drs. P.J. Whalen and C.P. Ballard of AlliedSignal Inc., Drs. E. Krug and G. Carrasquillo of Certech Inc.

References

1. Proceedings of the Solid Freeform Fabrication Symposium, Vols. 1-7, 1990 - 1996, Edited by H.L. Marcus, et. al., The University of Texas at Austin, Austin, Texas.
2. M.K. Agarwala, et. al., "Fused Deposition of Ceramics and Metals: An Overview," *ibid.*, Reference #1, Vol. 7, 1996.
3. M.K. Agarwala, et. al., "Structural Ceramics by Fused Deposition of Ceramics," *ibid.*, Reference #1, Vol. 6, 1995, pp.1-8.
4. M.K. Agarwala, et. al., "Fused Deposition of Ceramics for Structural Silicon Nitride Components," *ibid.*, Reference #1, Vol. 7, 1996.
5. "Solid Freeform Fabrication of Advanced Ceramics," First Year Annual Report, Oct. 1994-Sept. 1995, Office of Naval Research, Contract No. N00014-94-C-0115.
6. U.S. Patent # 5,121,329, June , 1992.
7. J.W. Comb and W.R. Priedeman, "Control Parameters and Material Selection Criteria for Rapid Prototyping Systems," *ibid.*, Reference #1, Vol. 1993, pp. 86-91.
8. D.J. Shanefield, "Organic Additives and Ceramic Processing," Kulwer Academic Publishers, 1st Edition, 1995, pp. 251-254.
9. Haake Fisons Instruments, Paramus, New Jersey.

TABLE I
Binder Components in the RU Series of Binders

Binder Component	Weight % Range	Component's Role	Thermal Degradation Temperature Range
Polymer	10 -45	Acts as a backbone	100 - 510 °C
Elastomer	30 - 65	Imparts flexibility	275 - 500 °C
Wax	15 - 50	Viscosity modulator	200 - 500 °C
Tackifier	10 - 40	Promotes adhesion	190 - 475 °C

Table II
Binder Systems for FDC and FDMet

Particulate System	Binder System	Vol. % Solids	Dispersant	Filament Fabrication & Quality
Si ₃ N ₄	RU1	60	None	Capillary extruded: Straight & stiff pieces
Si ₃ N ₄	RU9	55	3% Oleyl Alcohol	Single screw extruded: Continuous, flexible, & spooled
SiO ₂	RU1	65	None	Capillary extruded: Straight & stiff pieces
PZT	RU1	50	1% Oleyl Alcohol	Capillary extruded: Straight & stiff pieces
WC-Co	RU1	50	1% Oleyl Alcohol	Capillary extruded: Straight & stiff pieces
Stainless Steel	RU1	60	None	Capillary extruded: Straight & stiff pieces

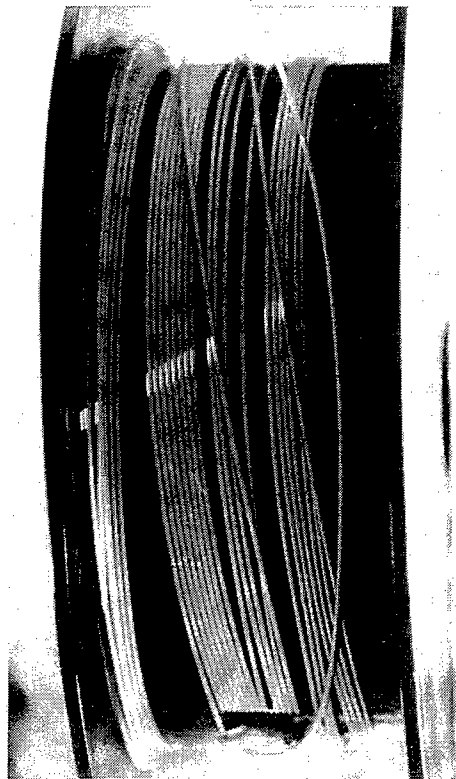


Figure 2: 55 vol.% Si₃N₄ green filaments fabricated using RU9 binder wound on a spool for commercial FDM™ systems.

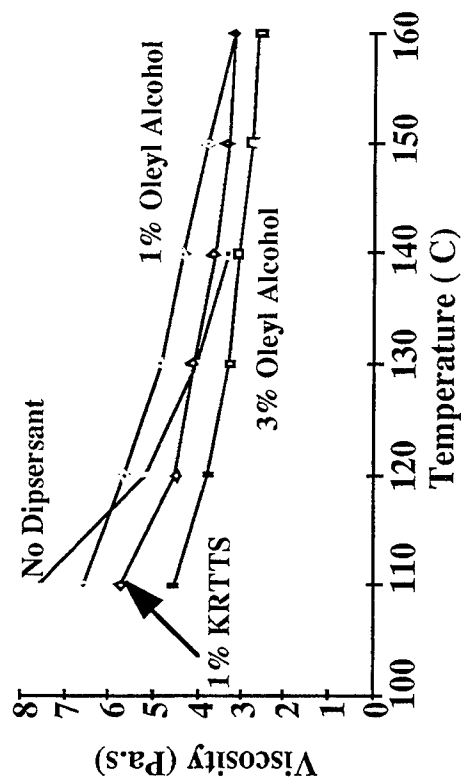


Figure 1: Viscosity as a function of temperature for 30 vol.% Si₃N₄ suspensions in RU1 binder with and without dispersants.

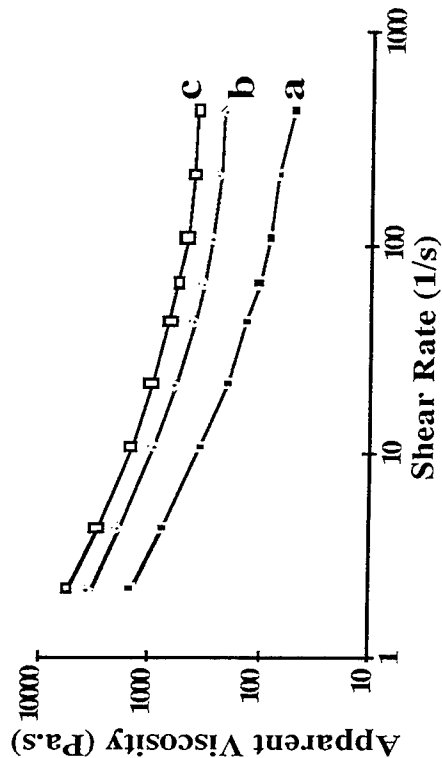


Figure 3: Viscosity vs. shear rate at FD processing temperatures; (a) investment casting wax at 70°C, (b) 55 vol.% Si₃N₄, with 3 wt.% oleyl alcohol, in RU9 binder at 130°C and (c) 60 vol.% Si₃N₄, without dispersant, in RU1 binder at 150°C.



Figure 4: Different ceramic and metal green filaments for FDC and FDMet processing (Top to bottom: Si_3N_4 , WC-Co, PZT, stainless steel, and SiO_2).

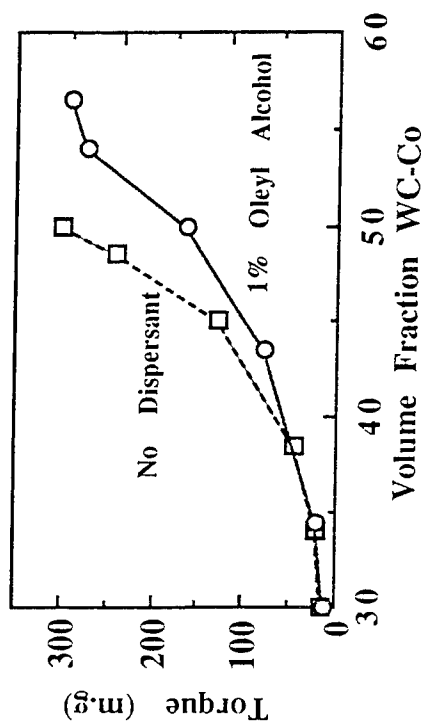


Figure 5: Final steady state compounding torque vs. volume fraction of WC-Co in RU1 binder with and without dispersant indicating a decrease in viscosity with use of dispersant.

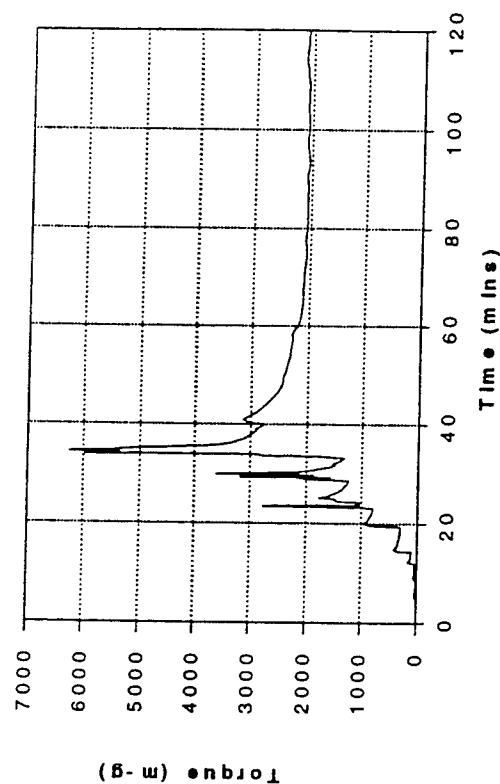


Figure 6: Compounding torque vs. time plot for 60 vol.% Si_3N_4 in RU1 binder using a torque rheometer. The peaks indicate the points of incremental powder additions.



Figure 7: SEM Micrograph of a cross section of green Si_3N_4 filament used for FDC processing.

Forced Convection in a Polymeric Powders

Jeffery L. Norrell Kristin L. Wood Richard H. Crawford
Graduate Research Asst. Associate Professor Associate Professor

Mechanical Engineering Department
The University of Texas at Austin

Theodore L. Bergman
Professor

Mechanical Engineering Department
The University of Connecticut

Abstract

In a Selective Laser Sintering (SLS) powder bed, thermal transfer occurs through multiple modes. Forced convection through the powder, or downdraft, has recently been implemented in SLS machines in an effort to enhance thermal transfer within the powder bed. In this paper, forced convection is analytically shown to be a significant thermal transfer mode for low porosities, such as seen in SLS powder beds. A polymeric powder bed subjected to downdraft is investigated with the goal of quantitatively determining thermal behavior. A numerical model describing heat transfer within a powder is presented. The design and construction of an experimental apparatus to measure the temperature profiles within a powder subjected to forced convection is described. Using the information gained in these experiments, it may be possible to better control the thermal environment of SLS powder beds, reducing growth and internal stress build-up.

Nomenclature

c_{pf}	= specific heat, fluid (J/kg K)
g	= gravitational acceleration (m/s ²)
K	= permeability (m ²)
k_{eff}	= effective thermal conductivity of powder (W/mK)
k_f	= thermal conductivity of fluid (W/mK)
p	= pressure (Pa)
T	= absolute temperature (K)
T_c	= cold temperature (K)
t	= time (seconds)
u, v	= x and y velocity components (m/s)
u_D, v_D	= Darcian x and y velocity components (m/s)
x, y	= horizontal and vertical coordinate (m)
β	= coefficient of thermal expansion (K ⁻¹)
ϕ	= volume-averaged porosity
μ_{eff}	= effective (in-powder) fluid viscosity (Ns/m ²)
μ	= fluid viscosity (Ns/m ²)
ρ	= density of fluid phase (kg/m ³)

Introduction

Selective Laser Sintering (SLS) is one of the many Rapid Prototyping methods currently available today. In SLS, a part is layer-wise formed by laser-melting a loose powder. Such a process is inherently dominated by thermal processes, both between the laser and powder and within the powder bed.

Typical gas-saturated, polymeric powder beds complicate control of the thermal environment by being excellent thermal insulators due to the low thermal conductivity of both the polymer and saturating gas. Thermal control of the powder bed is critical to prevent unwanted effects such as part growth and warping. Many methods, such as radiative surface heaters and resistive wall heaters, have been attempted to achieve fine, rapid control over the thermal state of a powder bed.

Another method, shown to have at least a qualitative effect on part quality, is forced convection through a powder. In current commercial SLS systems, a pressure drop is created below the powder bed to induce gas flow. Radiative heaters are used to heat the upper surface of the powder bed. In theory, gas then flows through this upper portion of the powder bed where the gas is heated. The gas then flows through the remaining portion of the powder bed, carrying thermal energy to the remainder of the powder.

The goal of this work is to create a numerical model describing forced convection within a powder. Once such a model is obtained, experiments will be performed for model validation.

Numerical Model

The two-dimensional arrangements depicted in Figure 1, display the computational domains considered. Figure 1(a) is the domain for a pure conduction simulation, whereas Figure 1(b) is the domain for a forced convection simulation, both with and without buoyant forces.

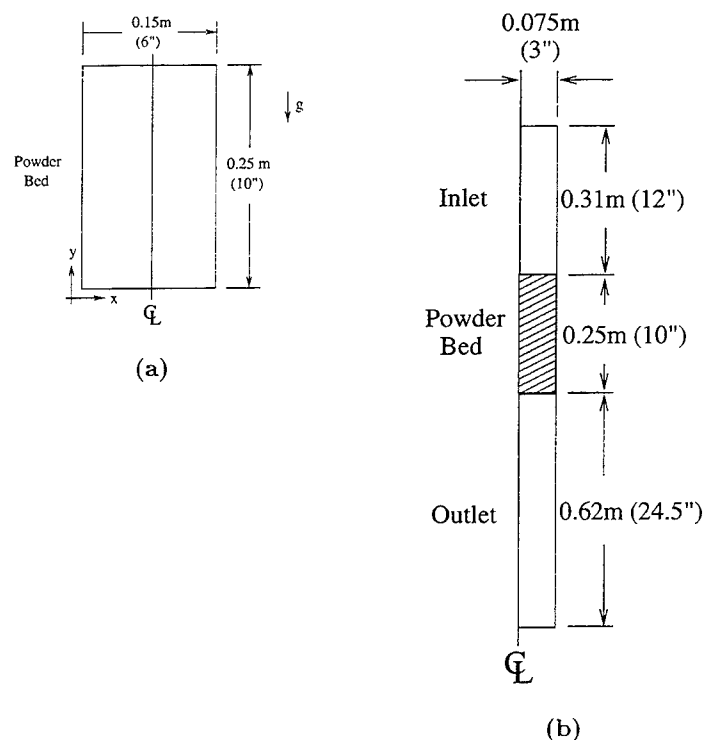


Figure 1: Computational domains.

In this simulation, heated air, assumed to be slug flow, enters the top of the inlet. The heated air then passes through the powder bed, leaving the system via the outlet. An analytical model is created to describe heat transfer in this system. The governing equations for the pure fluid and the

saturated porous medium are given separately. In writing the following equations, it is assumed that fluid flow is laminar, steady, incompressible, and two-dimensional.

For the pure fluid region, the two-dimensional, steady state Navier-Stokes equations are used [4]. Conservation of mass is given by,

$$\frac{\partial u}{\partial x} + \frac{\partial v}{\partial y} = 0. \quad (1)$$

Conservation of momentum within the pure fluid is described by,

$$\rho \left(u \frac{\partial u}{\partial x} + v \frac{\partial u}{\partial y} \right) = -\frac{\partial p}{\partial x} + \frac{\partial}{\partial x} \left(\mu_f \frac{\partial u}{\partial x} \right) + \frac{\partial}{\partial y} \left(\mu_f \frac{\partial u}{\partial y} \right), \quad (2)$$

and

$$\rho \left(u \frac{\partial u}{\partial x} + v \frac{\partial u}{\partial y} \right) = -\frac{\partial p}{\partial y} + \frac{\partial}{\partial x} \left(\mu_f \frac{\partial v}{\partial x} \right) + \frac{\partial}{\partial y} \left(\mu_f \frac{\partial v}{\partial y} \right) + \rho g \beta (T - T_c). \quad (3)$$

Conservation of energy is expressed as,

$$\rho c_{pf} \left(u \frac{\partial T}{\partial x} + v \frac{\partial T}{\partial y} \right) = \frac{\partial}{\partial x} \left(k_f \frac{\partial T}{\partial x} \right) + \frac{\partial}{\partial y} \left(k_f \frac{\partial T}{\partial y} \right). \quad (4)$$

It is important to note that the thermophysical properties of the pure fluid are assumed constant. The exception is during buoyant simulations, where a Boussinesq approximation of fluid density, in which density varies with temperature, is used.

For a fluid-saturated porous medium, the volumetrically-averaged laminar, inviscid, isothermal fluid flow is approximately described by the Darcy equation [1],

$$\frac{\Delta p}{\Delta y} = \frac{\mu_f}{K} v \quad (5)$$

To account for non-isothermal fluid flow, a Brinkman-Forchheimer extended version of the Darcy model is used [2,5]. Within the saturated powder Darcian, or volumetrically-averaged, velocities are used. Conservation of mass within the saturated powder is then given by,

$$\frac{\partial u_D}{\partial x} + \frac{\partial v_D}{\partial y} = 0. \quad (6)$$

Conservation of momentum is given by,

$$0 = -\frac{\partial p}{\partial x} + \frac{\partial}{\partial x} \left(\mu_{eff} \frac{\partial u_D}{\partial x} \right) + \frac{\partial}{\partial y} \left(\mu_{eff} \frac{\partial u_D}{\partial y} \right) - \left(\frac{\mu_f}{K} + \frac{\rho C}{\sqrt{K}} |\vec{u}_D| \right) u_D, \quad (7)$$

and,

$$0 = -\frac{\partial p}{\partial y} + \frac{\partial}{\partial x} \left(\mu_{eff} \frac{\partial v_D}{\partial x} \right) + \frac{\partial}{\partial y} \left(\mu_{eff} \frac{\partial v_D}{\partial y} \right) + \rho g \beta (T - T_c) - \left(\frac{\mu_f}{K} + \frac{\rho C}{\sqrt{K}} |\vec{u}_D| \right) v_D. \quad (8)$$

Equations (7) and (8) include the Brinkman extension (second and third terms) and the Forchheimer extension (the last term) to account for viscous and inertial effects, respectively.

Conservation of energy is described by,

$$\rho c_{pf} \left(u_D \frac{\partial T}{\partial x} + v_D \frac{\partial T}{\partial y} \right) = \frac{\partial}{\partial x} \left(k_{eff} \frac{\partial T}{\partial x} \right) + \frac{\partial}{\partial y} \left(k_{eff} \frac{\partial T}{\partial y} \right) \quad (9)$$

All thermophysical properties are again assumed constant, except for a Boussinesq density approximation in buoyant simulations. In Equations (7) and (8), $\mu_{eff} = \mu_f$, which has been

previously seen to agree well with experimental data [8]. It is important to note that Equations (6) through (8) neglect any radiation heat transfer between the fluid and powder or within the powder itself.

The term k_{eff} in Equation (9) is the effective thermal conductivity of the fluid-saturated powder bed. Though many expressions are available for k_{eff} [6,7,9,10], a simple weighted average,

$$k_{eff} = \phi k_f + (1 - \phi) k_s, \quad (10)$$

is used. The C term in equations (7) and (8) is the inertia coefficient given as [3],

$$C = \frac{1.75}{\sqrt{175}} \phi^{-3/2}. \quad (11)$$

The above analytical model is numerically solved for the two-dimensional, steady state temperature distribution within both the fluid and fluid-saturated powder using the commercial finite-element code FIDAP (version 7.5 from Fluid Dynamics International).

Experiments

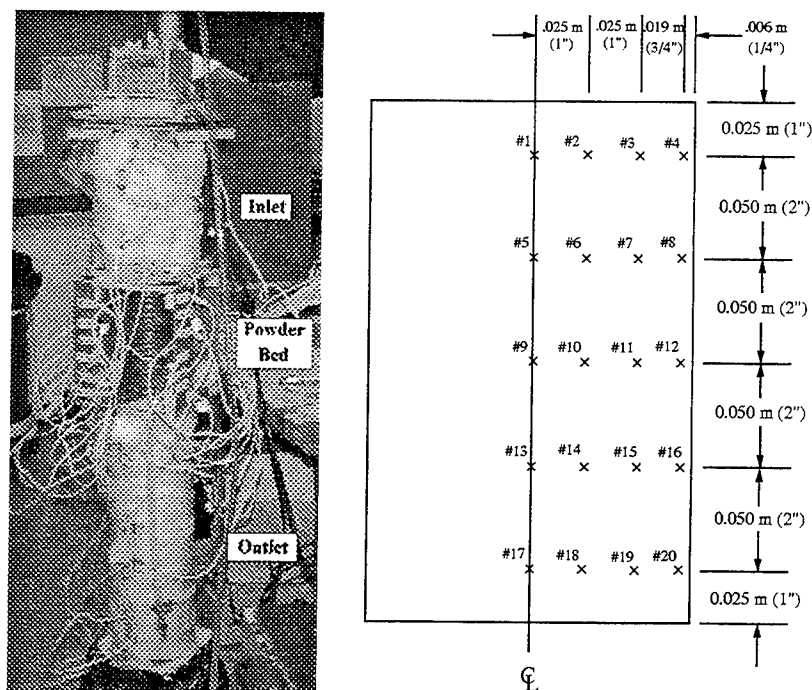
Test Materials

In order to experimentally verify the numerical model presented above, an experimental apparatus, shown in Figure 2(a), was constructed. The working fluid for these experiments is air, while the powder bed consists of polycarbonate with a nominal particle diameter of 150 μm and an average poured porosity of 0.5. Regarding permeability, there are no general equations relating permeability as a function of porosity [5]. A number of empirical models exist, but all have restrictions in their application. If we consider equation (5), we see that for an isothermal system with known geometry, we can control flow rate, measure the pressure drop across the powder, and calculate a permeability. For a 0.025 m (1") thick, 0.25 m (1") diameter powder sample, subjected to a flow of 0.31 m/s (20 SCFH) to 0.62 m/s (40 SCFH), a pressure drop of approximately 1 kPa is measured. From Equation (5), we then determine that the powder permeability is approximately $1.5 \times 10^{-10} \text{ m}^2$.

Experimental Instrumentation

Dimensions of the major sections of the experimental system are as shown in Figure 1(b). In the experiment, compressed air passes over PID-controlled baffle heaters and then enters a plenum. Once through the plenum, the heated air passes through the inlet, through the powder bed, and leaves the system via the outlet.

The baffle heaters are housed in a 0.10 m x 0.10 m (4" x 4") uninsulated plywood box. The baffles are separated vertically by 0.00635 m (1/4"). The baffle box opens into a 0.15 m x 0.15 m x 0.025 m (6" x 6" x 1") plywood plenum, which sits atop the inlet. The inlet section is constructed of 0.15 m (6") ID polyvinyl chloride (PVC) pipe. Mounted on the outside of the inlet section is a 100 W PID-controlled resistive heater covered with fiberglass insulation, used to maintain a quasi-isothermal boundary for the inlet. The inlet is mounted on top of the powder bed, which is housed in 0.15 m (6") ID steel pipe. The powder bed is surrounded by a fluid circulation jacket, also used to maintain an isothermal boundary. The powder bed sits atop a fine wire mesh, allowing airflow through the powder. Pressure drop across the mesh alone was measured to be less than 1 Pa. Below the powder bed sits the outlet, constructed of 0.15 m (6") ID PVC pipe. Given the relatively low temperatures in the outlet section and the high thermal mass of the PVC pipe, fiberglass insulation alone



(a) Apparatus.

(b) Thermocouple numbering.

Figure 2: Experimental system.

sufficiently maintains an isothermal boundary condition. An optional fan can be placed beneath the outlet to induce a pressure drop below the powder bed, further inciting airflow through the powder.

Throughout the experimental device, $125\ \mu\text{m}$ (5 mil), type K, PTFE-coated thermocouples are used to gather temperature data. A thermocouple is placed in the powder bed at each location marked with an "x" shown in Figure 2(b). Thermocouples also record air temperature in the inlet and outlet. All thermocouple data are collected and recorded with a Keithley 500A computer-controlled data acquisition unit.

The experimental system has several user-controlled inputs. Incoming compressed air can be heated from $25\ ^\circ\text{C}$ to $150\ ^\circ\text{C}$, over a flow range of $0.017\ \text{m/s}$ (40 SCFH) to $0.034\ \text{m/s}$ (80 SCFH) in the inlet. The inlet wall can be heated from $25\ ^\circ\text{C}$ to $100\ ^\circ\text{C}$. The fluid circulation jacket can be maintained over a range of temperatures from approximately $30\ ^\circ\text{C}$ to $100\ ^\circ\text{C}$.

Experimental Procedure

In preparing for the experiment, the powder bed, wire mesh, and outlet, all initially at room temperature, are assembled together. Next, $0.025\ \text{m}$ (1") of room temperature powder is poured inside. The steel powder bed wall is then repeatedly tapped, allowing the powder to settle. This procedure of pouring in powder then tapping is repeated, until the desired powder depth is achieved. The powder surface is then smoothed, and the remaining sections of the experimental device are assembled.

Once initial assembly is completed, data acquisition is started. Airflow into the system and fluid flow into the fluid circulation jacket are then begun. The heated baffles and inlet wall heater

are next ramped to temperature over a period of 30 minutes.

The system is left to run until thermal steady state is achieved. Typically, a run lasts from 8 to 15 hours. At this time, the recorded temperature data are downloaded and checked to verify that steady state has been achieved.

Results

Two separate tests were run for comparison with the numerical model. For these two tests, the temperature set point for the incoming air was kept constant at 100 ° C, while the flow rate was varied. For each test, three numerical simulations were performed.

The first test was run with an airflow of 0.017 m/s (40 SCFH). Measured temperatures as a function of time are shown in Figure 3. Data curve labels indicate the thermocouple number, with Figure 2(b) indicating the in-bed position of the given thermocouple.

For comparison, numerical simulations were also performed. Temperatures measured during the 40 SCFH experiment were used as boundary conditions in the simulations. Figure 4(a) shows the conduction heat transfer simulation for the powder bed. Figures 4(b) and 4(c), covering one-half of the experimental domain, show simulations that include both forced convection and conduction heat transfer. Figure 4(c), a buoyant simulation, also adds the Boussinesq air density approximation. The ΔT between isotherms in Figure 4 is 4° C.

The second experiment was run with an airflow of 0.025 m/s (60 SCFH). Figure 5 shows the measured temperatures as a function of time.

Figure 6 shows the numerical simulations run for the 60 SCFH experiment, where again Figure 6(a) is the conduction simulation, Figure 6(b) is the forced convection solution without buoyant forces, and Figure 6(c) is the convection solution with buoyant forces. As above, the ΔT between isotherms is 4 ° C.

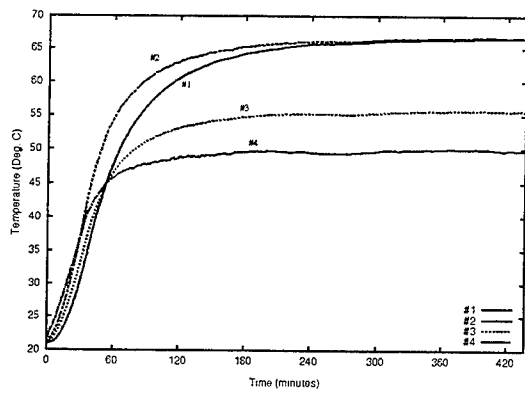
Discussion

In terms of numerical results, by comparing Figure 4(a) to 4(b) and Figure 6(a) to 6(b) we see that, *numerically*, forced convection can have a significant impact on heat transfer within a polymeric powder bed. Keep in mind that Figures 4(a) and 6(a) represent the entire powder bed and Figures 4(b) and 6(b) represent *half* of the physical domain. Comparison is then made by considering isotherms of the same value in Figures 4(a), 4(b), and 4(c), and their location within the powder bed region. From this comparison, we can see that, in effect, forced convection works to transport thermal energy further into the powder.

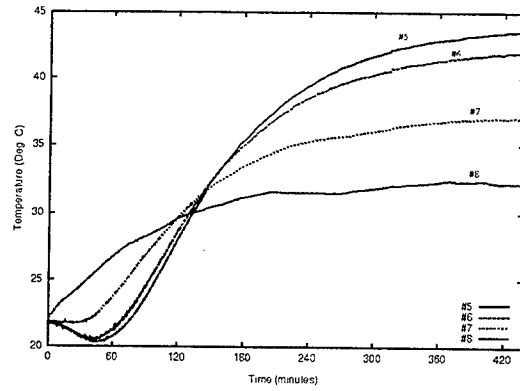
By considering Figure 4(b) versus 4(c) and Figure 6(b) versus 6(c), we can also see that natural convection, i.e. buoyancy-induced flow, can have a significant effect at these low flow rates. Also, from comparing Figure 4(b) to Figure 6(b), we see that increasing flow velocity through a powder increases thermal transfer into the deeper parts of the bed, as expected.

In terms of the experimental results, we can see from both Figures 3 and 5 that achieving steady state, the point where dT/dt approaches zero and the temperature versus time curves begin to flatten out, can take a significant amount of time, over 7 hours. Air and polycarbonate, both relatively good thermal insulators alone, make an even better thermal insulator in the form of an air-saturated powder bed.

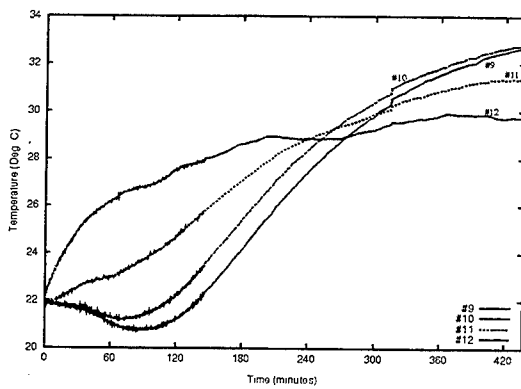
If we compare the experimental data to the forced convection simulations, both with and without buoyancy, we begin to see a discrepancy. The experimentally-measured temperatures are signifi-



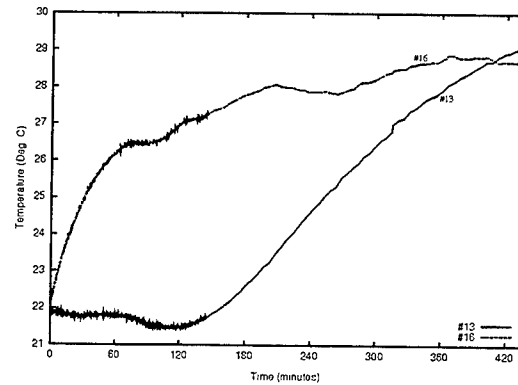
(a)



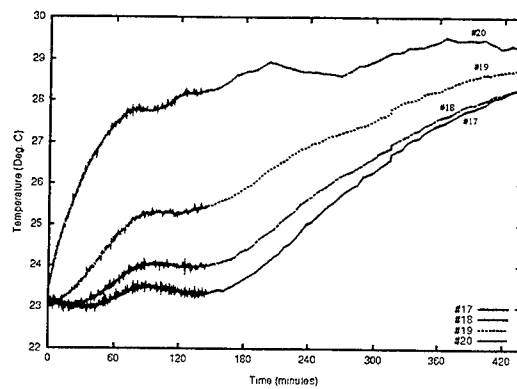
(b)



(c)

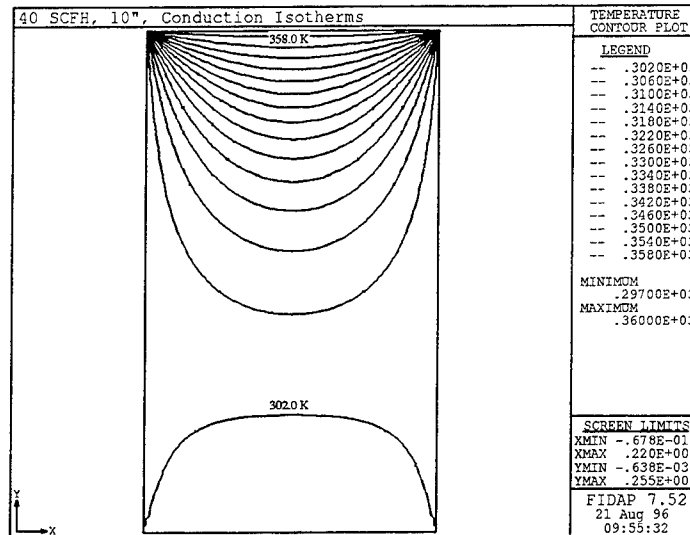


(d)

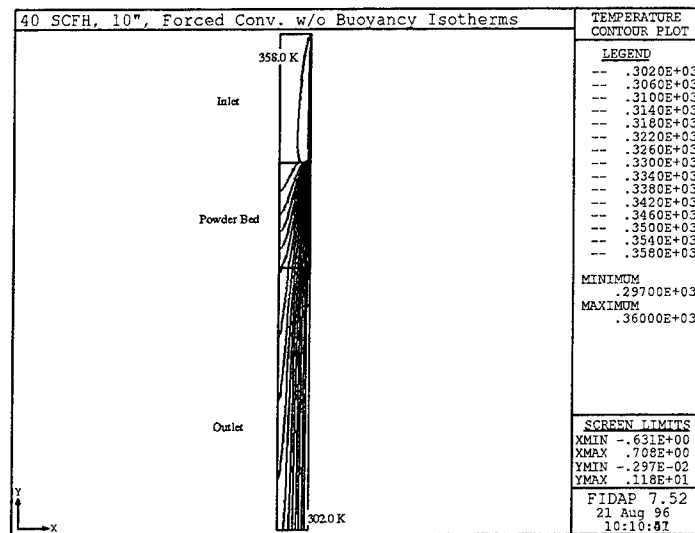


(e)

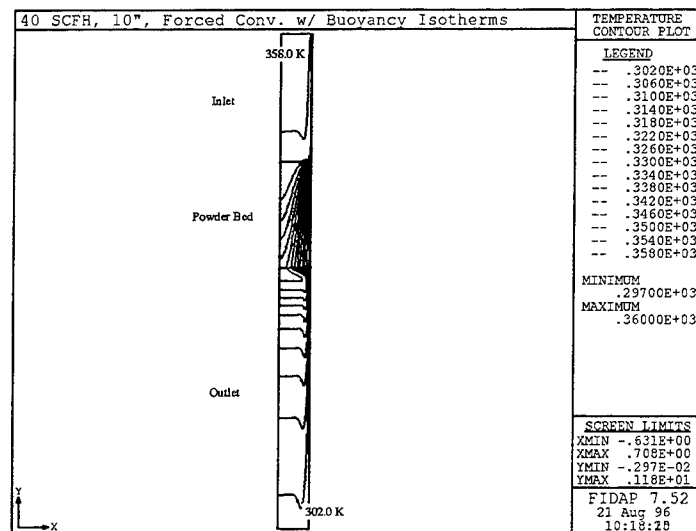
Figure 3: Experimental data for 40 SCFH simulation.



(a)

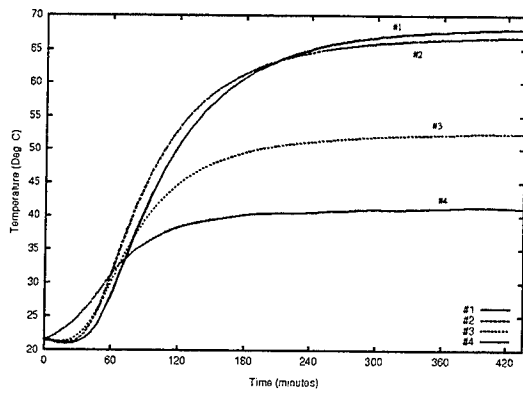


(b)

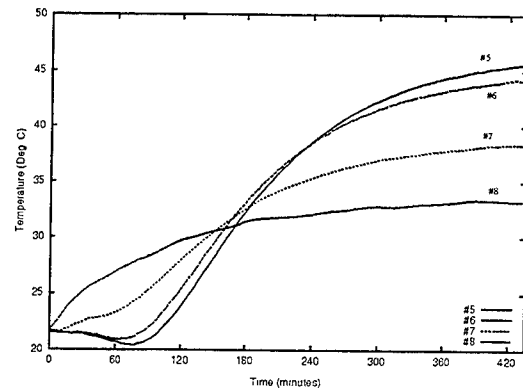


(c)

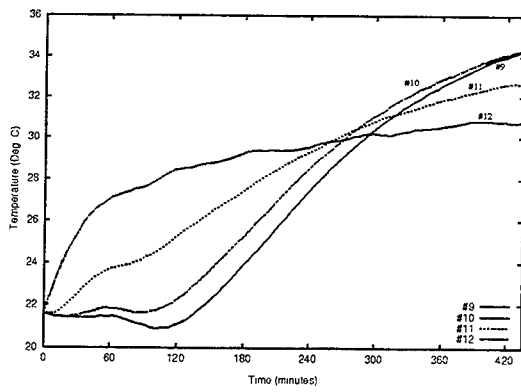
Figure 4: Isotherms for 40 SCFH simulation.



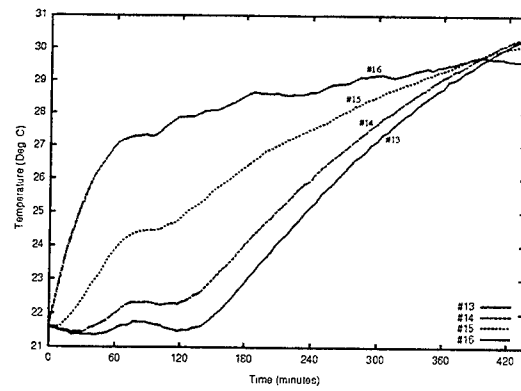
(a)



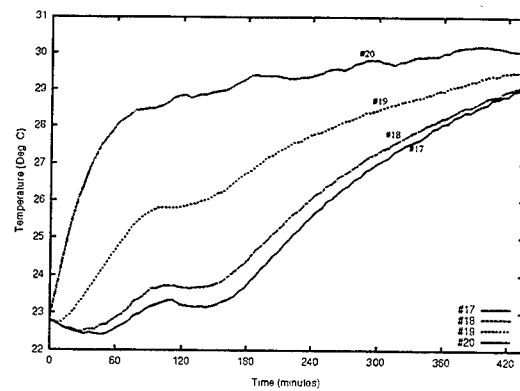
(b)



(c)

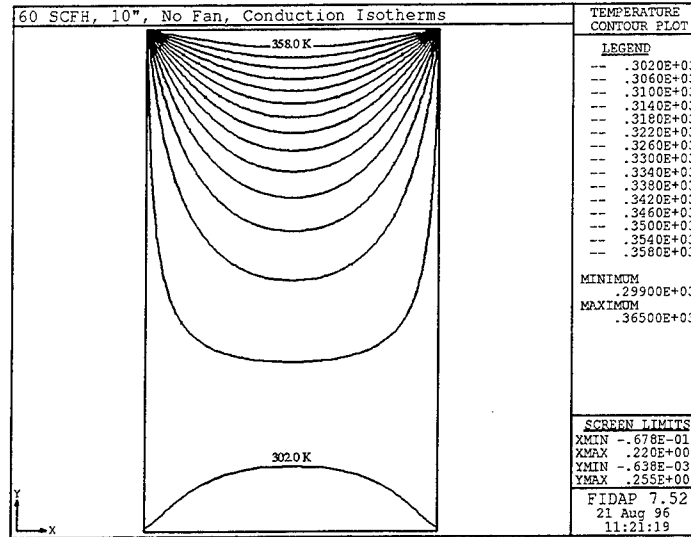


(d)

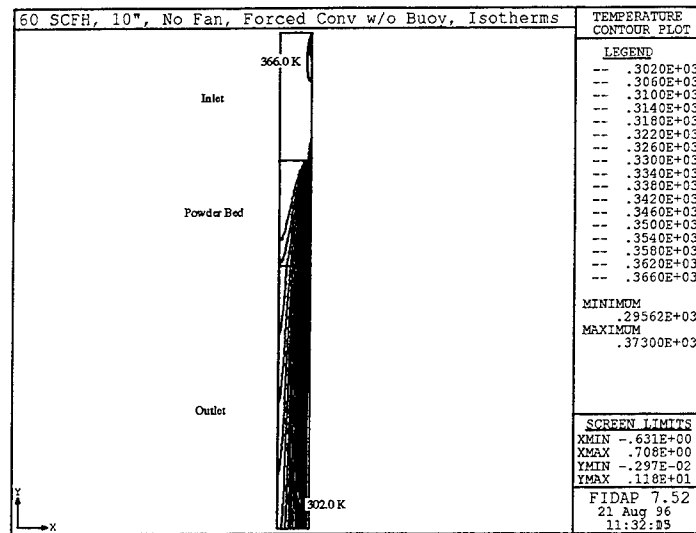


(e)

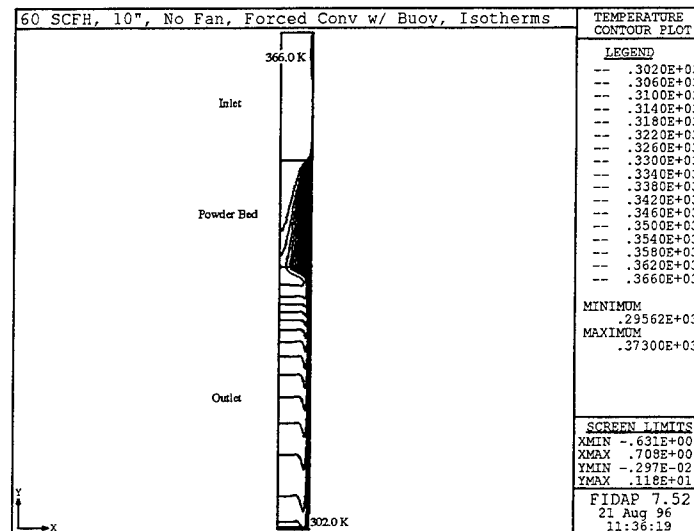
Figure 5: Experimental data for 60 SCFH simulation.



(a)



(b)



(c)

Figure 6: Isotherms for 60 SCFH simulation.

cantly lower than those predicted in the forced convection simulations. However, if the measured temperatures are compared to the *conduction* simulation, we see that there is excellent agreement.

As in any research, a discrepancy between model and experiment implies a flaw in the model. In this instance, it is believed that the numerical model does not adequately reflect the air leaks present in the experimental apparatus. In essence, the resistance to flow imposed by the low permeability powder forces the air out of mating surfaces in the experiment. At present, these leaks prevent any *experimentally* driven conclusions about forced convection heat transfer within a polymeric powder. However, we can easily see from Figures 3 and 5 that conduction heat transfer within a polycarbonate powder bed can take a significant amount of time to have any effect on the bed interior.

Conclusions and Future Work

Numerically, forced convection heat transfer is seen to have a significant effect on steady state temperatures within an air-saturated polymeric powder bed. It is also numerically shown that, at sufficiently low flow rates, natural convection, or buoyancy-induced flow, must be accounted for in simulations.

Experimentally, it is seen that the low permeability of fine powders, which are typically used in SLS, can have a drastic effect on attempts at generating flow through the powder. Much care must be taken to ensure that fluid is, in actuality, flowing through the powder.

Once true airflow through a powder is achieved and verified against the numerical model, fractional experiments will be performed. Control variables will be the initial air temperature, powder bed wall temperature, and airflow rate. In addition, a polymeric sintering model based on solid mechanics will be formulated and added to the numerical heat transfer. In conjunction with the model development, experiments will be undertaken wherein a heated object is embedded in the powder bed, reflecting the latent heat in a recently formed SLS part. In this way, sintering of the polymer under influence of forced convection can be studied. Information gained from these studies can then be used to better control the thermal state of a polymeric powder bed. More precise and rapid control may then help alleviate such nagging problems as growth and part warpage.

Bibliography

1. Bear, J., 1972, *Dynamics of Fluids in Porous Media*, American Elsevier, New York.
2. Beckermann, C., Ramadhyani, S., and Viskanta, R., 1987, "Natural Convection Flow and Heat Transfer Between a Fluid Layer and a Porous Layer Inside a Rectangular Enclosure," *J. Heat Trans.*, Vol. 109, pp. 363-370.
3. Ergun, S., 1952, "Fluid Flow Through Packed Columns," *Chem. Eng. Prog.*, Vol. 48, pp. 89-94.
4. Incropera, F.P., and De Witt, D.P., 1990, *Fundamentals of Heat and Mass Transfer*, Third ed., John Wiley and Sons, New York, NY.
5. Kaviany, M., 1991, *Principles of Heat Transfer in Porous Media*, Springer-Verlag, New York.
6. Krupiczka, R., 1967, "Analysis of Thermal Conductivity in Granular Materials," *J. Int. Chem. Eng.*, Vol. 7, No. 1, pp. 122-144.

7. Kubie, J., 1987, "Steady-State Conduction in Stagnant Beds of Solid Particles," *Int. J. Heat and Mass Trans.*, Vol. 30, No. 5, pp. 937-947.
8. Neale, G., and Nader, W., 1974, "Practical Significance of Brinkman's Extension of Darcy's Law: Coupled Parallel Flows Within a Channel and a Bounding Porous Medium," *Canadian J. Chem. Eng.*, Vol. 52, pp. 475-478.
9. Xue, S., and Barlow, J.W., 1991, "Models for the Prediction of the Thermal Conductivities of Powders," *Proceedings, Solid Freeform Fabrication Symposium*, H. Marcus, et al., ed., Austin, TX, pp. 62-69.
10. Yagi, S., and Kunii, D., 1957, "Studies on Effective Thermal Conductivities in Packed Beds," *J. AIChE*, Vol. 3, No. 3, pp. 373-381.

LOW SHRINKAGE, HIGH T_g LIQUID CRYSTAL RESINS FOR STEREOLITHOGRAPHY

J. S. Ullett, R. P. Chartoff, J. W. Schultz, J. C. Bhatt, M. Dotrong, and R. T. Pogue

The University of Dayton
Center for Basic and Applied Polymer Research
and
Rapid Prototype Development Laboratory
Dayton, OH 45469-0130, USA

INTRODUCTION

The applications for stereolithography parts have grown from simple visualization of engineering designs to fabrication of functional end-use prototypes. With the growth of applications has come a need for higher performance resins. In particular, the upper-use temperature of cured resins needs to approach or exceed 200 °C for applications such as directly formed molds for injection molding, and under-the-hood automotive applications. Improved mechanical properties such as modulus and impact strength are also important for these applications. Dimensional accuracy has been a key issue for rapid building of functional parts. Dimensional accuracy is a function of resin shrinkage, draw style patterns, beam diameter compensation, galvanometer calibration, etc. While part accuracy has improved dramatically since the inception of stereolithography, further improvements are possible.

The University of Dayton in partnership with researchers at Case Western Reserve University is currently developing liquid crystal (LC) monomers for stereolithography applications. LC materials contain stiff rod-like mesogenic segments which can be aligned and upon cure may have glass transitions approaching 200 degrees Celsius because of their rigid rod segmental structures, orientation, and high degree of crosslinking. Curing in an aligned state "locks" in the anisotropic structure resulting in materials with anisotropic physical and mechanical properties. Also, because the reactive end groups are more tightly packed, cure in an aligned state should result in lower shrinkage than is obtained with conventional resins.

The objective of this project is to produce LC diacrylate monomers that can be photopolymerized via stereolithography to produce parts having glass transition temperatures exceeding those possible with commercially available stereolithography resins, and having optimized mechanical properties. Parts with isotropic, anisotropic, or a combination (as a function of location in the part) of isotropic and anisotropic properties may be produced by varying the layer-to-layer alignment of the LC monomer or by varying the cure temperature (i.e., varying the mesogenic state). Realization of these goals will allow important new applications for stereolithography.

The research emphasis in the program has been on three areas: (1) synthesis of liquid crystal monomers suitable for use in stereolithography; (2) characterization of basic material properties and determination of processing parameters and

(3) stereolithography process optimization for LC monomers. The focus of this paper is on the last two areas.

LIQUID CRYSTAL CHARACTERIZATION

Like crystalline solids, LC materials have some kind of long range molecular order, however, they lack the three-dimensional translational order found in truly crystalline materials. The simplest type of mesogenic phase is called nematic. In nematic phases, the molecular axes are on average parallel but lack any kind of translational order as indicated in Figure 1a. Smectic phases have both uniaxial molecular orientation and some degree of translational order as indicated in Figure 1b. Many different types of smectic phases have been identified. Some are more fluid in nature (e.g., smectic A) while others are more solid in nature (e.g., smectic D). At the clearing temperature, order disappears and the phase structure becomes isotropic as indicated in Figure 1c. Because the viscosity of nematics can be considerably lower than that of smectic phases, working in the nematic phase may be more ideal for stereolithography. Smectics, on the other hand, have a higher degree of order which may lead to less shrinkage and higher crosslink densities. As a result, both mesophase types are of interest. In the present work, the identification of phase type, and phase transition temperatures was done by polarized optical microscopy and differential scanning calorimetry.

Identification of Phases

Liquid crystalline phases are birefringent, that is, the measured refractive index is directionally dependent. Particular phase structures can be identified by examining samples between crossed polarizers. A Nikon optical microscope fitted with polarizers and a Mettler FP-82 hot-stage was used to study the phase behavior of three LC reactive monomers. For example, Figure 2 is a photograph of a smectic A phase illuminated by polarized light.

Differential scanning calorimetry (DSC) is also used to measure phase transition temperatures and in addition measures the enthalpies of transitions. A TA Instruments model 2910 DSC was used to characterize the LC reactive monomers. The melting/crystallization behavior of the monomers was determined using multiple heating rates. The position of transitions depends on the heating rate and the (temperature) direction of the scan. Some mesogenic phases referred to as monotropic occur only upon cooling from the isotropic melt. The monomers were analyzed both with and without photo-initiators to establish the effect of photo-initiators on the breadth and position of the mesophases. Even small amounts of photoinitiator can have significant effects on the phase transitions. This information is needed to define the temperature range required for stereolithography operation.

Cure Analysis

The UV absorbance of purified monomer samples was measured using a Hewlett-Packard model 8452A diode array spectrophotometer. The UV absorbance spectra were used to determine the most appropriate laser wavelength for cure. Monomers with various photo-initiators were analyzed with a Perkin-Elmer photo-DSC-7. Photo-differential scanning calorimetry (PDSC) is a useful method for the rapid and comprehensive development of appropriate cure conditions for the monomers of interest.

With PDSC it is possible to determine cure information based on photo-initiator and sensitizer concentrations as well as cure temperature and irradiation wavelength. PDSC investigations of photoinitiator type and concentration have lead to optimal cure rates and have been useful in improving the glass transition temperatures of photo-polymerized samples. The cure rates observed are comparable to those of commercial acrylate stereolithography resins.

Glass Transition Temperature

The glass transition temperature of cured samples has been measured by a variety of techniques including DSC, dynamic mechanical analysis (DMA), and thermal mechanical analysis (TMA). Thus far, the results are encouraging in that the LC monomers under study form high T_g polymers upon cure. Figure 3 shows data from thermal mechanical analysis using a penetration probe for a sample photocured at 45 °C and thermally postcured by heating to 300 °C. The measured softening point for the sample was 210 °C. For materials cured with a scanning laser, the initial glass transition temperature is a function of the monomer temperature in the vat. Thermal postcures may be used to advance the glass transition temperature of photocured parts. We are currently studying the effects of UV postcure on T_g values

The birefringence technique developed to follow phase transitions in the monomers was also found to be useful in studying transitions in the polymers. Curves from the birefringence technique clearly showed where glass transitions occurred, even when DSC could not. They also indicated that additional polymerization continued after heating past the initial photocure temperatures. Comparisons of polymer films were made between randomly aligned and externally aligned polymers. These experiments showed evidence of additional relaxation effects at the glass transition presumably associated with the regions between liquid crystalline domains in the randomly aligned samples.

CREATING AND MEASURING ALIGNMENT

An important aspect of this project is an investigation of ways to align the liquid crystal monomers and ways to measure the alignment. Photopolymerization of the LC monomer in the aligned state may lead to stereolithography parts with superior mechanical properties and minimal cure shrinkage. In addition, it will be possible to build parts having anisotropic properties. This flexibility will allow a part's physical and mechanical properties to be optimized for particular applications. There are a number of ways to align a mesogen such as by application of: electric field, magnetic field, shear, rubbed films, and combinations of the aforementioned. Electric field alignment is used in most liquid crystal display (LCD) applications [1]. Alignment of an LC monomer in a stereolithography vat presents challenges not encountered in other LC applications because we are proposing to align the LC domains over large areas (e.g., 254 mm x 254 mm). A magnetic field is the method selected for alignment for this application.

Alignment Measurement and Alignment Kinetics

X-ray. The inter-molecular spatial relationships in a LC material are measured most accurately using X-ray diffraction. LC structures result in specific diffraction phenomena.

As described by Samulski in [2], the azimuthal intensity distribution, $I(\chi)$, comes from the superposition of scattering from many mesogens having a continuous orientation distribution of \mathbf{l} about the director \mathbf{n} symbolized as $W(\beta)$ where β is the angle between \mathbf{l} and \mathbf{n} . The measurable distribution $I(\chi)$ is related to $W(\beta)$ and $I(\omega)$, where $I(\omega)$ is the scattering intensity from a single prolate mesogen, by an integral equation as shown below [2].

$$I(\chi) \approx \int W(\beta) \cdot I(\omega) \sin \omega \, d\omega \quad (1)$$

The average orientation of \mathbf{l} relative to \mathbf{n} is the nematic order parameter S which is defined in terms of $W(\beta)$ as shown below.

$$S \equiv \int_0^{\pi/2} P_2(\cos \beta) \cdot W(\beta) \sin \beta \, d\beta \quad (2)$$

Typically, nematic LC materials, which have directional order but not positional order, create X-ray diffraction patterns having diffuse outer rings and sometimes diffuse inner rings [3]. Smectic LC materials consist of layers of directionally ordered molecules. In addition to having a diffuse outer ring, the large scale periodicity of the smectic layers causes small angle scattering, which appears as a sharp inner ring [3].

Although X-ray diffraction is probably the best method to determine the molecular orientation, other techniques can be used to calculate the order parameter or to measure changes in alignment. A sampling of these techniques include: NMR [4-6], SANS [7], FTIR [8], Raman spectroscopy [9-12], Mossbauer Effect spectroscopy [13], dielectric [14,15] and refractive index [16-18].

In this study dielectric and birefringence measurements have been used to detect changes in alignment of the LC materials with the application of a magnetic field. These techniques can also be used to follow relaxation of order after the aligning field has been removed.

Dielectric Analysis. Dielectric analysis techniques can be used as a means to calculate the molecular order parameter. Unfortunately, the relative convenience of measuring the dielectric permittivity of a liquid crystal under different orientations comes at the cost of a relatively complicated theory relating permittivity to the order parameter.

On the other hand, if the mesogens have little or no dipole moment, then the theory relating order parameter to permittivity anisotropy simplifies greatly. However, because the electric polarizabilities of the molecules cannot be measured in practice, an extrapolation method based on the nematic to isotropic transition temperature must be used to estimate them. In the case of a crosslinked polymer network, no transition to the isotropic state exists, so there is nothing on which to base the extrapolation. Hence only measurement of the monomers can provide quantitative estimates of the order parameter in this technique.

Preliminary experiments have been conducted with a Hewlett Packard 4192A impedance analyzer, with a frequency range of 10 Hz to 13 MHz. The samples were

placed between parallel plate electrodes with a spacing of approximately 300 microns. Alignment was created in the nematic state using a permanent magnet. For the monomers measured so far, there is little dipole moment, so the dielectric anisotropy is due solely to anisotropy in the polarizability. This results in dielectric permittivity differences of about 0.8 between parallel and perpendicular orientations of the magnet. Temperature studies are planned so that the extrapolation method can be extended to estimate order parameter as a function of temperature.

Birefringence. One of the simplest (and least expensive) ways to determine if a material is liquid crystalline, is to place it between crossed polarizers in a microscope and look for 'birefringence'. Unlike an isotropic fluid, the index of refraction in a liquid crystalline material is not constant. For the case of uniaxial nematics and smectics, the birefringence, Δn , is defined as the difference between the indices of refraction parallel to and perpendicular to the director,

$$\Delta n = n_{\parallel} - n_{\perp}. \quad (3)$$

This equation relates three quantities, so two separate measurements are needed to completely characterize the index of refraction of a liquid crystal: one to measure Δn and another to measure one of the components of n .

As in the dielectric method for estimating order parameter, an extrapolation based on the nematic to isotropic transition temperature must be used. This limits the usefulness of the method to the monomers. In the photopolymers, the multifunctional network locks in the liquid crystalline order, so no transition to the isotropic state occurs.

PROCESS MODIFICATIONS

Currently a modified version of the table-top SLA (TTSLA) device built at The University of Dayton and described in [19] is being used for experimentation with LC monomers. The principal modification to conventional stereolithography apparatus is the addition of a magnet outside the vat in order to align the monomer before cure. Figure 4 is a schematic of the TTSLA apparatus. The magnet is positioned on a rotatable platform so that alignment can be established at any angle relative to the galvanometer axes. A second requirement is to have temperature control of the vat over a wide range. This is desirable so that it is possible to work with all LC phases: smectic, nematic and isotropic. The third modification envisioned is a means to measure molecular alignment in-situ. An ellipsometry technique is being considered for this purpose, but is not yet fully operational. Ellipsometry is analogous to birefringence except that reflectance measurements are used instead of transmitted light.

Initial experiments in the TTSLA have focused on determining the effect of cure temperature, phase, and laser draw speed on cure depth and width (working curves). Strands and simple single-layer parts have been made with monomers in the nematic and isotropic states. In the nematic state, the curing laser beam is scattered much as it is in the two-phase resin SOMOS 2100 [20]. This effect results in cured strand widths being greater than the laser beam diameter. Future experiments will characterize scattering effects as a function of alignment direction relative to the draw direction. By the time of

presentation at the SFF Symposium we expect to have additional data based on the experiments cited above and from processing studies on multiple layer parts.

SUMMARY

Liquid crystalline reactive monomers are being studied for stereolithography applications. Various characterization techniques were used to determine the types of LC phases present and their temperature ranges. UV spectroscopy and photo-DSC were used to find applicable photoinitiators for the resins investigated. High glass transition temperatures, approaching 200 °C, have been measured for photo-polymerized resins that have been thermally post-cured.

Investigations of the alignment of LC materials have determined that alignment by a magnetic field is feasible. Initial experiments using newly synthesized LC monomers show that alignment over significant distances (3-10 cm) can be achieved. Experiments using a table-top SLA (TTSLA) device have shown that considerable scattering of the curing laser beam occurs when the monomer is in the unaligned nematic state. Work is underway to determine the effects of monomer temperature, alignment, laser power, and draw speed on working curve characteristics and final part properties.

ACKNOWLEDGMENTS

The authors thank Mary Galaska, John Murphy and Katy Weaver of The University of Dayton for their help in conducting the experiments discussed in this paper. This research was sponsored by the National Science Foundation under NSF Grant No. DMR-9420357.

REFERENCES

- 1) N. A. J. M. van Aerle and A. J. W. Tol, "Molecular Orientation in Rubbed Polyimide Alignment Layers Used for Liquid-Crystal Displays," *Macromolecules*, 27, 6520-6526 (1994).
- 2) E. T. Samulski, Ch. 5 in *Physical Properties of Polymers*, 2nd edition, American Chemical Society, Washington, DC, (1993).
- 3) A. A. Robinson, S. G. McNamee, Y. S. Freidzon, and C. K. Ober, "Novel Liquid Crystalline Thermosets: Microstructural Evolution of an LC Mesophase During the Curing Process," *Polym. Preprints* (Am. Chem. Soc., Div. Polym. Chem.), 34(2), pp. 743-4 (1993).
- 4) M. Brehmer, R. Zentel, "Liquid Crystalline Elastomers - Characterization as Networks," *Mol. Cryst. Liq. Cryst.*, 243, 353-376, (1994).
- 5) H.W. Spiess, "Structure and Dynamics of Liquid-Crystalline Polymers with Different Molecular Architectures from Multidimensional NMR," *Ber. Bunsenges. Phys. Chem.*, 97(10), 1294-1305, (1993).
- 6) B.C. Perry, J.L. Koenig, "Review: The Application of Solid-State NMR to Polymer Liquid Crystals," *J. Appl. Polym. Sci.: Appl. Polym. Symposium*, 43, 165-210, (1989).
- 7) M.D. Dadmun, "Shear-Induced Orientation of Liquid Crystalline Hydroxypropylcellulose in D2O as Measured by Neutron Scattering," ACS Symposium Series 597, *Flow-Induced Structure in Polymers*, A.I. Nakatani, M.D. Dadmun, ACS, Washington DC, chap 22, 320-334, (1995).
- 8) P. I. Ktorides, and D. L. Uhrich, *Mol. Cryst. Liq. Cryst.*, vol. 87 (1-2), pp.69-76 (1982).
- 9) J.A.J. Jansen, F.N. Paridaans, I.E.J. Heynderickx, "Molecular orientation in flat plates of liquid-crystalline polymer using low-cost reflectance Fourier-transform infra-red microscopy," *Polymer*, 35(14), 2970-2976, (1994).

- 10) E.B. Priestley, P.S. Pershan, "Investigation of Nematic Ordering Using Raman Scattering," *Mol. Cryst. Liq. Cryst.*, 23, 369-373, (1973).
- 11) G. Yuan, Y. Zhao, "Thermally Induced Relaxation and Recovery of the Macroscopic Orientation in a Side-chain Liquid Crystalline Polyacrylate," *Macromol. Chem. Phys.*, 195, 3281-3288, (1994).
- 12) D.J. Broer, G. N. Mol, G. Challa, "Temperature effects on the kinetics of photoinitiated polymerization of dimethacrylates," *Polymer*, 32, 690-695, (1991).
- 13) L.G.P. Dalmolen, W.H. de Jeu, "Order parameters of some nematic p, p' substituted tolans as determined by polarized Raman Scattering," *J. Chem. Phys.*, 78(12), 7353-7361, (1983).
- 14) T. Bruckert, A. Wurfliinger, and S. Urban, "Dielectric Studies on Liquid Crystals under High Pressure," *Ber. Bunsenges. Phys. Chem.*, 97, no 10, 1209-1213, (1993)
- 15) G. Vertogen, and W. H. de Jeu, *Thermotropic Liquid Crystals, Fundamentals*, Springer-Verlag, New York (1988).
- 16) N.H. Hartshorne, *The Microscopy of Liquid Crystals*, Microscope Publications Ltd, Chicago, (1974).
- 17) W.M. Gibbons, P.J. Shannon, S.-T. Sun, "Surface-Mediated Alignment of Liquid Crystals with Polarized Light," *SPIE Vol. 1665, Liquid Crystal Materials, Devices, and Applications*, 184-193, (1992).
- 18) E.E. Hall, A.A. Robinson, S.G. McNamee, C.K. Ober, Y.S. Freidzon, "Nematic-Smectic Biphase of a Main-Chain Liquid Crystalline Polyether," *J. Materials Sci.*, 30, 2023-2028, (1995).
- 19) M. Pellechia and A. Lightman, "Development of a Table-Top Stereolithography and Its Application to Solid Modelling of Human Tissue," *Proceedings of The Fifth Int. Conf. on Rapid Prototyping*, Dayton, OH., June 12 - 15, 1994, pp 99 - 108.
- 20) J. P. Heddleson, P. S. Fussell and E. P. Gargiulo, "Methods to Produce Desired Cure Depth Using SOMOS 2100 on the SLA-250," *Proceedings of The Fourth Int. Conf. on Rapid Prototyping*, Dayton, OH., June 14 - 17, 1993, pp 207 - 223.

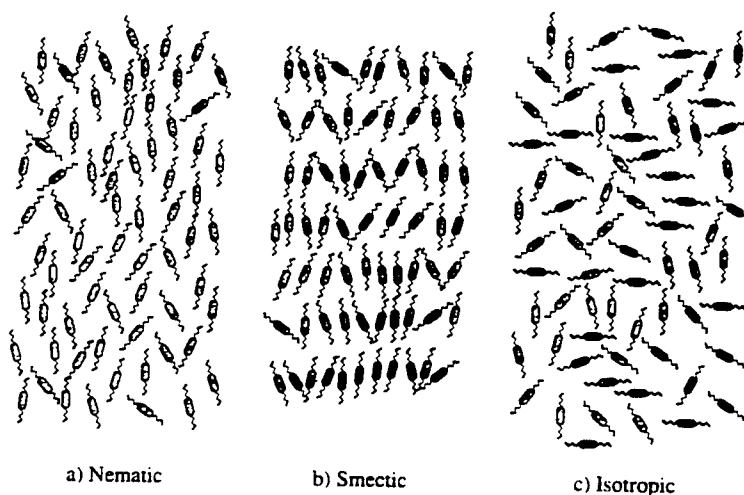


Figure 1. Schematic illustration of monomer molecules in a) nematic phase, b) smectic phase and c) isotropic phase

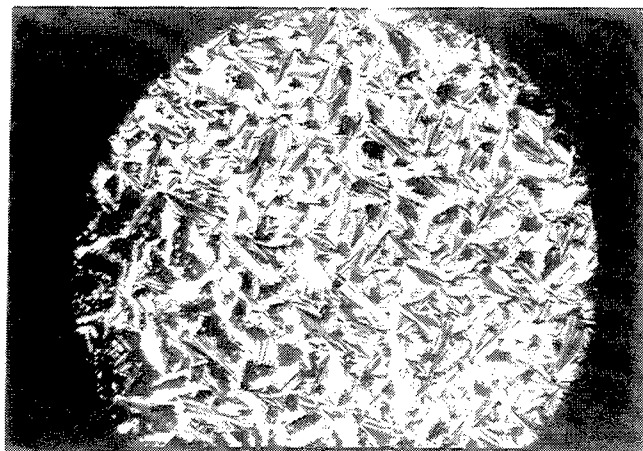


Figure 2. Photomicrograph taken using polarized light of a LC monomer in the smectic A phase.

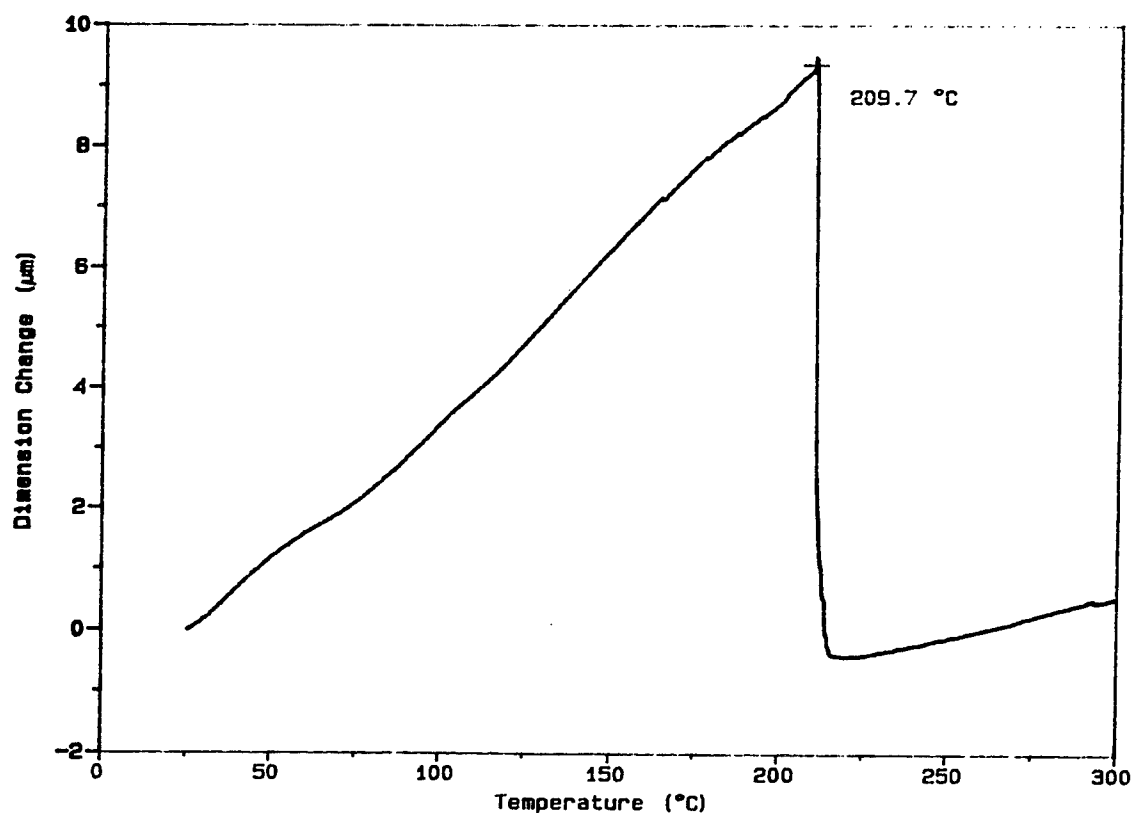


Figure 3. Example TMA data using penetration probe of LC material photocured using a wide-band UV source and thermally postcured by heating to 300 °C. Indicated glass transition temperature is 210 °C.

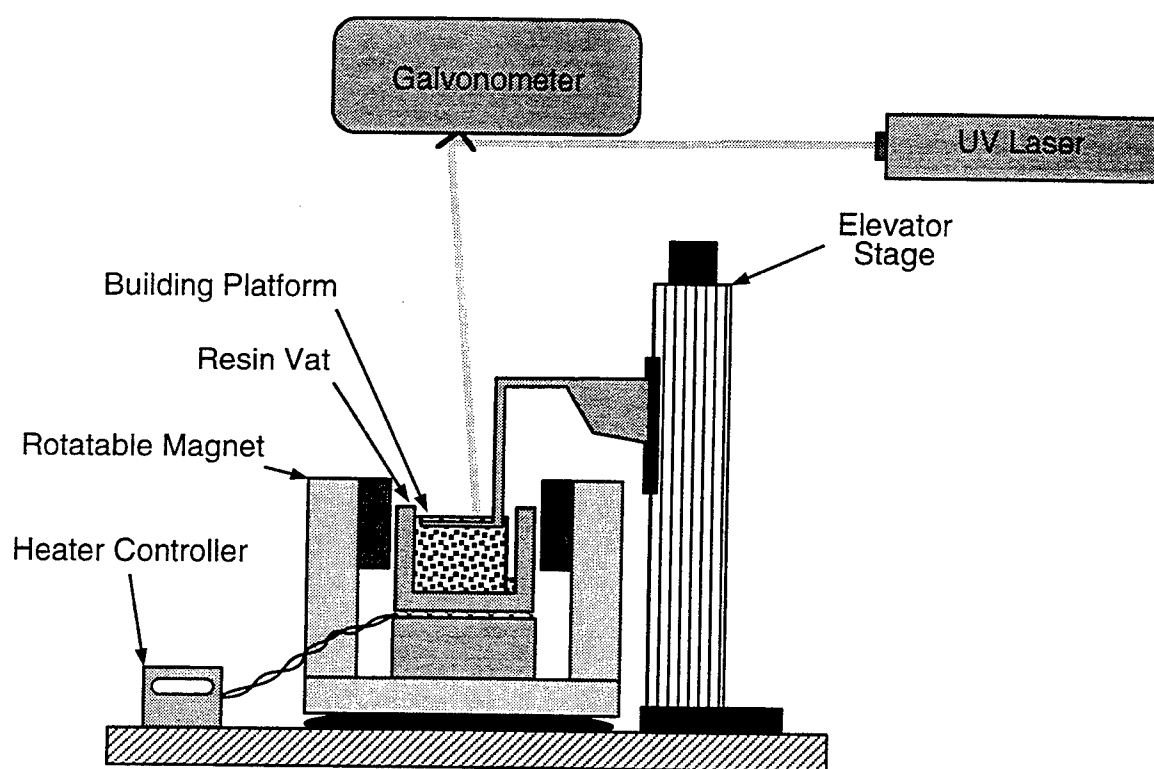


Figure 4. Schematic of modified stereolithography apparatus for use with liquid crystal monomers.

Interfacing Reverse Engineering Data to Rapid Prototyping

N.K. Vail, W. Wilke, H. Bieder, and G. Jünemann

Daimler-Benz Research Center
Optische Meßtechnik / Modelltechnik
Ulm, Germany D-89013

Abstract

Rapid prototyping has become an increasing part of product development process chains resulting in reduced time to market and reduced development costs. As manufacturers strive to further reduce development cycles to maintain market competitiveness, the use of reverse engineering technologies have started to play key roles in the product development cycles. Integration of these technologies into existing development cycles provides tools to maintain design integrity during development stages as well as between successive product lines. One aspect of reverse engineering is the interfacing of data obtained from these technologies to manufacturing processes such as rapid prototyping. This paper discusses work at Daimler-Benz to develop a set of interfacing tools as part of a larger reverse engineering process loop. These tools include facilities to generate contiguous surface meshes from a collection of measured views as well as automatic feature detection and hole closure.

(Keywords: Reverse Engineering, Rapid Prototyping, Mesh Generation, Point Clouds)

Introduction

As a developer and manufacturer of products targeted for the global marketplace, Daimler-Benz is committed to the development of methods that reduce both the cost and time of developing these products. Reverse engineering (REEN) technologies are beginning to playing a large role in helping to achieve this goal. This stems from the capabilities of REEN technologies to provide support to a broad range of applications such as continual maintenance of CAD data, on-line inspection techniques,¹ and virtual reality.

Within this framework we are developing the process loop shown in Figure 1. This reverse engineering process loop is seen to encompass all elements of the product development cycle. This process loop describes the flow of information from virtual world of the product description through manufacturing to the physical product and back to the virtual world through REEN technologies. At the peripheries of the central loop are the capabilities to support the input and output of conceptual and physical information. To realize this process loop we are actively involved in the research and development of the necessary technological aspects including optical measurement techniques, sensor navigation, data manipulation, and CAD support. At the heart of this system is a software package that is capable of performing tasks of the reverse engineering process loop such as sensor navigation and control, data acquisition and processing, CAD reconstruction, and interfacing to manufacturing processes. The complete system is modular in design and intended to be independent of target platforms whether they be the sensor device, navigation mechanism, or computing platform.

As indicated in Figure 1, interfacing reverse engineering data to manufacturing processes such as rapid prototyping (RP) technologies, is an important link in the realization of an effective reverse engineering process loop. Current implementations of RP technologies offer capabilities to fabricate functional objects using geometric data from a variety of sources. Traditionally the geometry data used by RP technologies have been derived from CAD information, either volume or surface element based. However, as a result of reverse engineering technologies, non-CAD based surface and volume coordinate data are being increasingly encountered in commercial development and manufacturing applications. In some areas, such as medical applications, only non-CAD based data exist. In this paper we will describe our efforts to link reverse engineering data to RP technologies.

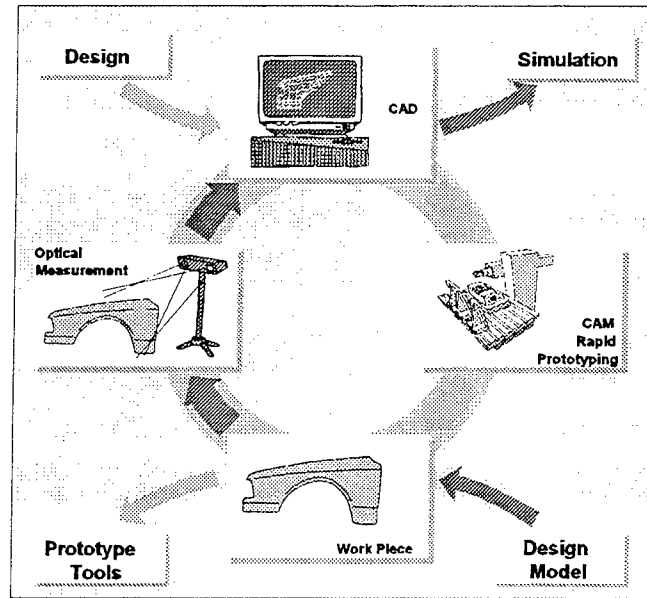


Figure 1. Reverse engineering process loop.

Reverse Engineering Data

Reverse engineering data can come from a variety of sources. Common examples include optical sensor data from devices such as structured light projectors,² laser range finders,³ and photogrammetry methods. Other sources include tactile devices, computed tomography (CT),⁴ non-destructive test methods, and finite element analysis. A complete discussion of the various data sources is beyond the scope of this paper. We will focus on data obtained from optical sensors and will note when data comes from other sources.

The initial step in any REEN operation is to obtain information about the geometry of an object. This is accomplished using optical sensors that project a series of structured light patterns onto the object and then, using a digital sensor, capturing each of the reflected patterns from the object, Figures 2 and 3. Using the coded information of the projected patterns and the geometry of the sensor system it is possible to determine the spatial position of a point on the object. The result is a matrix image of spatial points in the coordinate space of the sensor. This image is termed a view and can contain several thousand coordinate points. Generally, between five and fifty views may be required to obtain a complete description of an object. Each of the views in turn must be transformed into a common coordinate space. In current practice this transformation is accomplished by either mounting the sensor on a positioning system or by semi-automatic software registration. The final result is a cloud of points that describe the visible surface of the object, Figure 4. Representative point clouds can contain on the order of a few hundred thousand data points. The uncertainty of a data point is approximately $\pm 0.1\text{mm}$ in all directions.

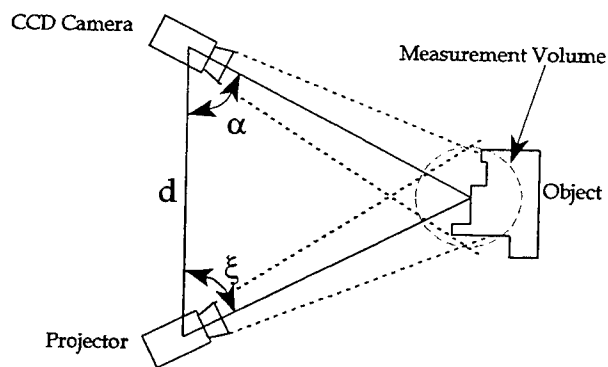


Figure 2. Optical measurement geometry.

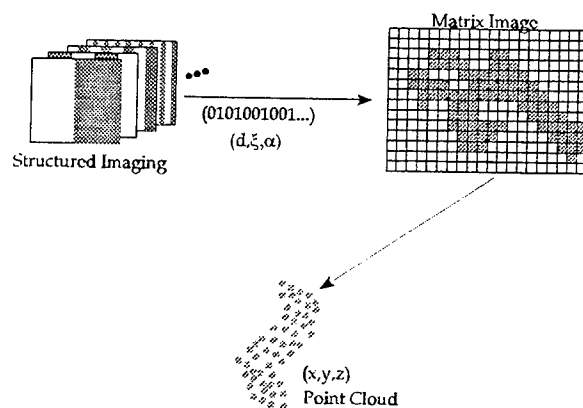


Figure 3. Construction of 3D point cloud data.

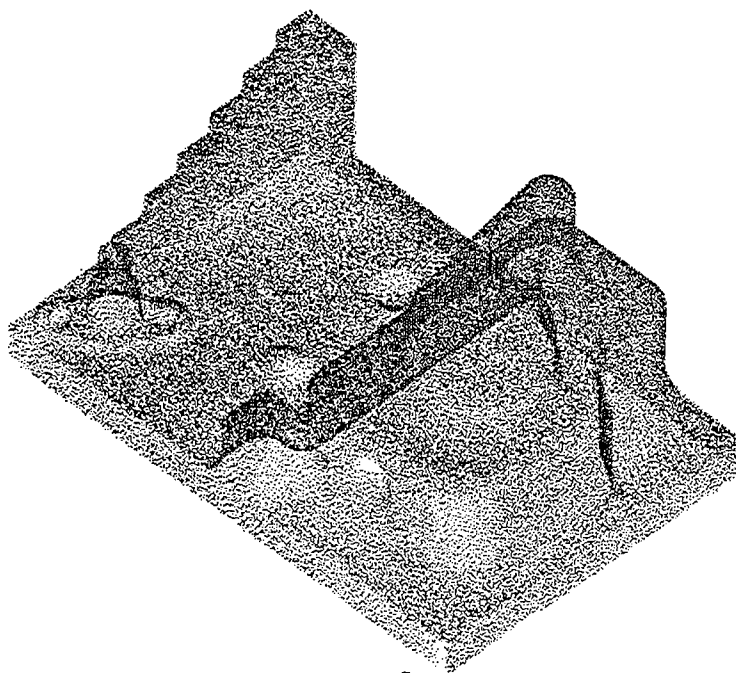


Figure 4. Point cloud obtained from optical measurement of the IMS-T1 standard test part. Approximately 250,000 points and ten views.

Requirements for Reverse Engineering Data Reduction

The intent is to create a data set suitable for input to rapid prototyping systems. Accomplishing this task requires transforming the point cloud with minimal computational time and effort while remaining faithful to the original data.

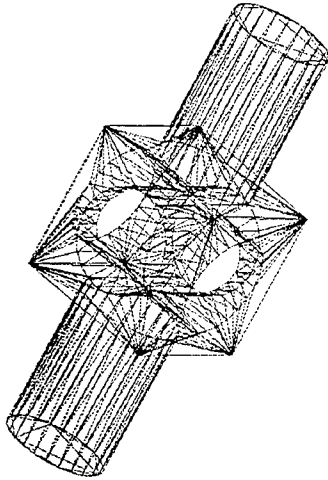


Figure 5. STL triangular mesh.

the logical form of the reduced REEN data. Before proceeding, however, let us discuss the other input formats.

Rapid prototyping methods may vary in their implementation but nearly all use the same geometry input format, the STL triangular mesh format introduced by 3D-Systems,⁵ Figure 5. Some RP platforms support more standard 3D-CAD object formats such as IGES. Still other platforms support input of geometric information corresponding to object contours which then translate directly into material slices. Contour interfaces are generally supported through public domain formats such as SLC supported by 3D-Systems,⁶ the CLI format developed through an initiative of the European Community,⁷ and the familiar HPGL format used by many laser printers. Because the STL format is the *de facto* standard, it is

To use 3D-CAD information as a source for RP processes requires a complete reconstruction of this information from the REEN data. While the reconstruction of 3D-CAD information is one of the primary goals of the reverse engineering process loop, complete reconstruction of 3D-CAD information is still labor intensive and the effectiveness of the reconstruction is dependent on model complexity. Certain aspects of 3D-CAD reconstruction such as recognition of regular geometries or global fitting of data by spline surfaces can be automated. However, considerable post-processing may be required to achieve a valid geometric representation. These operations are time intensive. In addition, the reconstructed model must be further processed to produce a triangular mesh model or sliced to yield contour data. Reconstruction of 3D-CAD data appears an unnecessary step as it would be more efficient to directly reconstruct the triangular mesh from the cloud data.

To use contour information as input to RP processes requires the extraction of this information from REEN data. This step is straightforward. Additionally, some data sets, such as those obtained by computed tomography (CT), are produced as contour information. However, contour data sets can have certain drawbacks in actual practice. A major drawback is the need for interpolation when processing contour data sets. If the contour data is extracted from a point cloud the possibility exists that the point density of the cloud is insufficient to produce a correct contour using the slice resolutions of RP processes. This is illustrated in Figure 6 which shows contour data obtained at a slice resolution of 1.0mm. The points are a result of all points in the cloud occurring in the slice volume element. In this case, the left part of the contour is quite good as this section of the object contains walls perpendicular to the slice plane. However, the right side of the contour is questionable since the object contains a sloped face in this region. Considerable smoothing as well as adjacent contour interpolation would be required to obtain an adequate contour description. It is clear from this example that a finer slice resolution would result in a poorly defined contour. Irrespective of slice resolution, the resulting contours would be a minimal approximation at best. It appears that a better approach would be to consider cloud data in a global manner thereby creating a better overall approximation of the object.

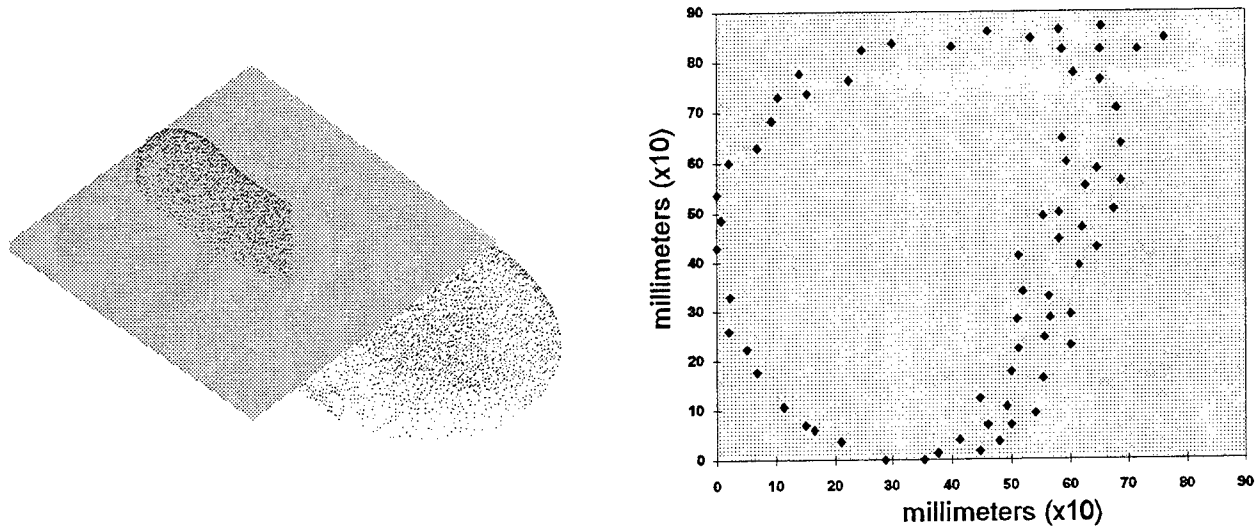


Figure 6. Contour data extracted from the point cloud on the left using a volume slice element thickness of 1.0mm.

Given the apparent drawbacks of using reconstructed 3D-CAD information or extracted contour information it is reasonable to consider the generation of triangular meshes directly from REEN data. Creating a valid triangular mesh is the first requirement of our approach to interfacing REEN data to RP processes. In practice, a triangular mesh is simply a piece-wise linear surface approximation composed of triangular facets, Figure 5. The creation of simplicial surfaces of this type from arbitrary point data has become a topic of considerable interest in recent years.^{8,9,10,11,12} Simplicial surfaces are not only important as input for RP processes, but they also have application in the fields of graphical rendering, virtual reality, and finite element modelling.

The criteria for triangular mesh generation is the ability to create the mesh with a minimal set of input parameters and reasonable execution times for all data sets. Additional requirements are: efficient, minimal user-interaction methods for mesh verification such as residual repairs of the generated mesh; normal orientation; and surface projection of incomplete meshes to create closed model volumes. There is currently no algorithm available in the literature that meets all of these criteria. The closest is perhaps the Rapid Prototyping Module available in recent versions of Surfacar. However, we have found this mesh generation algorithm and its accompanying utility algorithms for mesh verification to be poorly documented in operation and insufficient in practice.

Methods

The method we have chosen for mesh generation is a modified Delauney triangulation algorithm with elements of the marching cubes algorithm. Each of these algorithms are discussed extensively in the literature.^{8,13} In our approach the point cloud is treated as a contiguous data set. The underlying image matrix information for each view in the point cloud is presently not stored as part of the point cloud.

With a contiguous point cloud it is convenient to store the point data as a set of ordered voxels to optimize processing during visualization and other operations. Descriptions of voxel structures can be found in the literature.^{8,14,15} Currently we use two criteria for storing the point cloud as a voxel representation. In both cases voxels void of point cloud data are not stored. The simplest method is to create voxels of fixed size containing a maximum number of data points. The other method is to create voxels by recursive subdivision using the criteria that each voxel will contain a set of points with a minimal error to a best fit plane. This effectively segregates the point cloud into voxels of different sizes that contain nearly planar elements. One advantage of this last method is it tends to decrease the number of voxels, thus reducing processing overhead.

Our algorithm then uses a Delauney method to triangulate the data in each voxel. Delauney triangulation is defined for points in 2D space. Therefore, the algorithm creates a best fit plane of the voxel data onto which the voxel data points are projected. The plane is clipped by the voxel boundaries. The projected points on the best fit plane are sorted according to their distance from the center of the plane, thus optimizing execution. The criteria for Delauney triangulation is based on the idea that given a set of three points describing a triangle, a circumscribed circle of the triangle should not contain any additional points. If the circle contains points then the triangle must be split. However, to split a triangle properly one must check for adjoining triangles in order to avoid introducing topological errors. In our implementation, the method tends to grow a patch of triangles from the center of the best fit plane. When all triangles of the patch meet the Delauney criteria then triangles connecting the patch to the boundary points of the clipping plane are removed and a final post-processing check is done to remove boundary triangles with large angles. As long as all points in a voxel can be projected onto the best fit plane and the topology is not complex, the Delauney method will yield a valid triangulation devoid of redundant triangles and will not be self-intersecting.

After each voxel is triangulated it is merely a matter of stitching neighboring voxel patches together to obtain a contiguous mesh. Presently this step can introduce topologically incorrect triangles in areas of rapidly changing topology. These spurious triangles can be easily removed by a post-processing step to yield small gaps in the mesh. Gaps in the mesh can also occur due to sparse or missing data, excessive noise, or misalignment of the individual views. Because of the mesh generation method it will be necessary to harmonize surface normals. We have incorporated additional algorithms to handle these problems in both automatic and semi-automatic manners. For example, proper orientation of normals is an automatic feature. One merely determines the largest z-coordinate and propagates normals by traversing the minimal spanning tree that is inherent in the mesh structure. Other algorithms such as redundant triangle and mesh self-intersecting detection can also be automated. Gap closure can also be automated but we provide the opportunity for the user to inspect the gap before proceeding with the closure. We also provide the capability to create an offset surface of a triangular mesh as a means of creating a solid suitable for RP fabrication. This is necessary as we often encounter thin freeform surfaces.

Experiments

In this section we show some results of producing triangular meshes from reverse engineering data. First, as a comparison let us consider the point cloud data of the familiar IMS-T1 part¹⁶ shown

previously in Figure 4. This data set was converted to a surface model using algorithms developed at Daimler-Benz, Figure 7. This process required approximately eight hours and resulted in a surface model that could be used to generate a triangular mesh, Figure 8. However, mesh generation was not without problems. This is because the correctness of the reconstructed surface model depended heavily on the order in which fitted surfaces were extracted from the point cloud. Surface extraction order effects both how clipping planes are generated and how much data remains available to describe the original topology. Therefore, the generated mesh contained many errors including overlapping sections, non-joined sections, and secluded volumes. To repair these errors required about eight hours of intensive interaction. In contrast, Figure 9 shows a mesh generated directly from the same point cloud data. Time to complete the initial triangulation was only a few minutes on an SGI Indo Workstation. An additional one hour was required to complete and validate the mesh structure. Correctness of the resulting topologies can be seen in Figure 10. Here we show contours extracted from the given generated meshes compared to a contour extracted from the original CAD model. The contours shown are from the topologically complex stair region of the IMS-T1 part. The contour from the mesh generated from the surface reconstruction is inaccurate while the contour from the mesh generated from the point cloud data is more true to the original data.

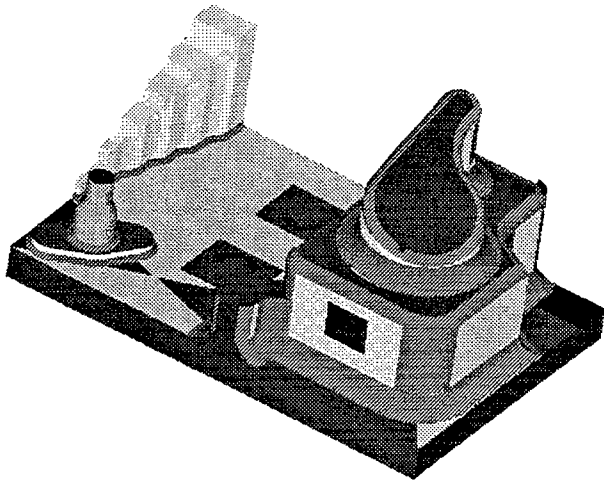


Figure 7. Surface model obtained from the point cloud data in Figure 4.

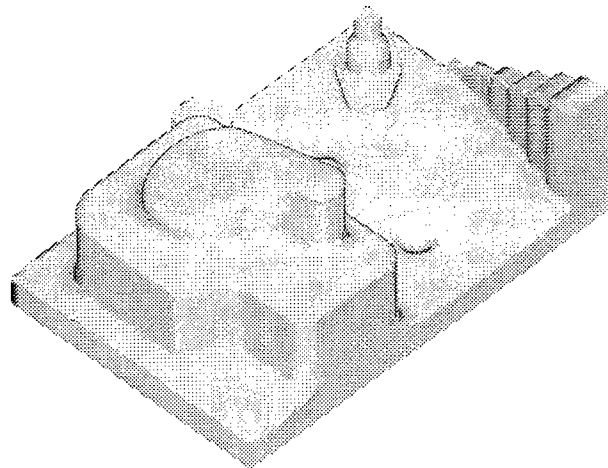


Figure 8. Triangular mesh obtained from the surface model in Figure 7.

Lastly, we show the familiar Mercedes-Benz star, Figure 11. This object is relatively small (~10cm diameter and 0.5cm in thickness) and, at first glance, seemingly simple in geometry. However, the star has many small faceted features of widely varying angles. To get an adequate description of this object required twelve views resulting in ~100,000 data points. Generating a mesh from these data was slightly more difficult resulting from the many fine features because many of the surfaces of the object meet to form small acute angles. The point cloud data in these fine regions become indistinguishable as the planes converge because of the small distances and inaccuracies in the measurement. As a result, the meshing algorithm generates erroneous triangles in these regions, thus leading to an invalid mesh. Repairing and closing this mesh required about one hour. The closed mesh is seen in Figure 12.

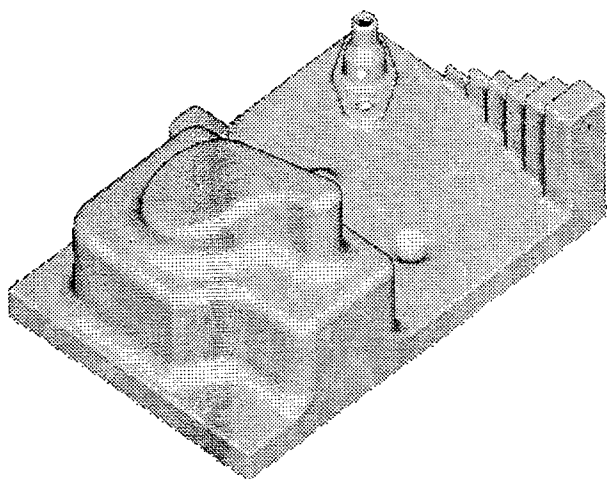


Figure 9. Triangular mesh generated directly from the point cloud data shown in Figure 4.

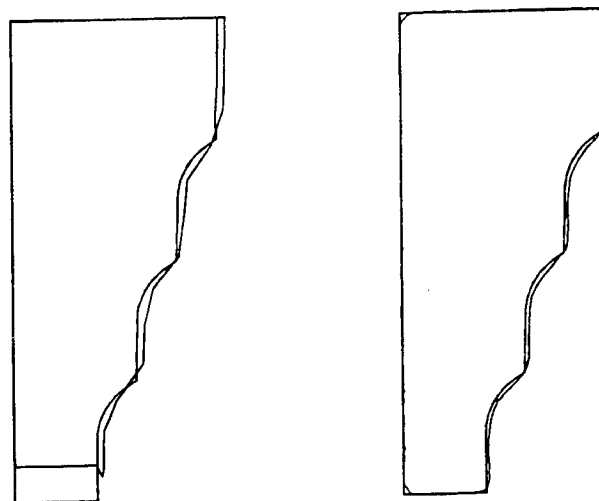


Figure 10. Comparison of contours extracted from the original CAD model and the meshes generated from the reconstructed surface model (left) and generated directly from the point cloud data (right).

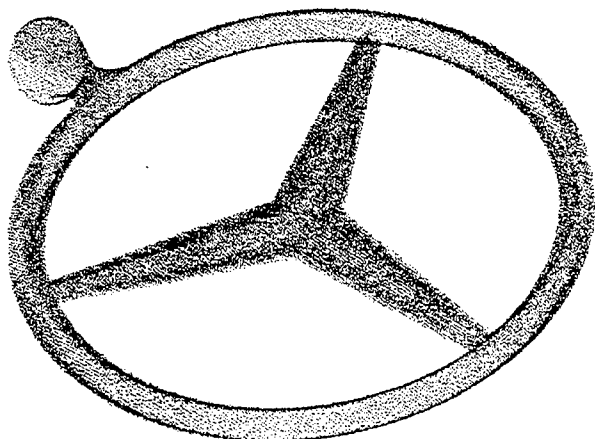


Figure 11. Point cloud data for the Mercedes-Benz star. Data is the result of twelve views yielding ~100,000 data points.

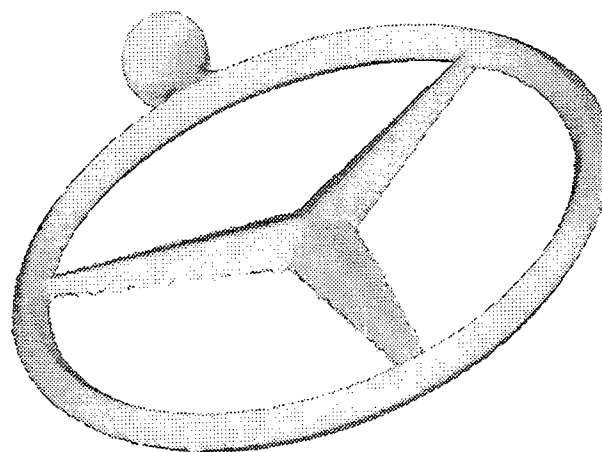


Figure 12. Triangular mesh of the Mercedes-Benz star obtained from the point cloud data in Figure 11.

Conclusions and Future Work

In this paper we have presented our approach to creating a triangular mesh suitable as input to solid freeform manufacturing process. This algorithm, along with a series of verification utilities, has been incorporated into the central software module of the reverse engineering process loop being developed by Daimler-Benz for use in product development and manufacturing applications. The mesh generation software in its present form adequately produces a representation that is faithful to the original point cloud data. The associated verification software has been used successfully to verify and repair meshes generated by our software as well as meshes generated by other software packages.

Currently our meshing algorithm does not handle certain types of data very well. Particularly troublesome is data with rapidly changing topology or data with excessive noise. Complex gaps in the mesh as well as the stitching of voxels still produce invalid triangles in areas of rapidly changing topology.

In the future we would like to perform as much data reduction as possible prior to mesh generation. One approach is to perform automatic geometric feature recognition to reduce the point cloud to a minimal representation of geometric objects and freeform surfaces described by the remaining point cloud. These elements are easily meshed using the algorithm described in this paper. In addition to data reduction, we are also investigating methods of mesh reduction.

Acknowledgements

The principle author would like to thank the Alexander von Humboldt Foundation for financial support to do this work.

References

1. Fürderer, K., "Projekt BDW: Beulen, Dellen, Welligkeiten. Der Kundenmaßstab", Internal Technical Report #TEP-94-016, pp. 18, (1994).
2. Post, D., Han, B., and Ifju, P., *High Sensitivity Moiré*, Springer-Verlag, New York, 1994.
3. Godin, G., Boulanger, P., and Rioux, M., "Direct Replication of Objects using 3-D Geometric Imaging and Rapid Prototyping", *The Fourth International Conference on Rapid Prototyping*, 159-168 (1993).
4. *Product Brochure*, Scientific Measurement Systems, Inc., 1995.
5. *Stereolithography Interface Specification*, 3D Systems, Inc., June, 1988.
6. *SLC File Specification*, Version 2.0, 3D Systems, Inc., November, 1994.
7. *Common Layer Interface (CLI)*, Version 2.0, Brite/EuRam Project #BE-5278 and #BE-5930, 1994.
8. Lorenen, W.E. and Cline, H.E., "Marching Cubes: A High Resolution 3D Surface Reconstruction Algorithm", *Computer Graphics: Siggraph '87 Conference Proceedings*, 21 [7], 163-169, 1987.

9. Hoppe, H., DeRose, T., Duchamp, T., Halstead, M., Jin, H., McDonald, J., Schweitzer, J., and Stuetzle, W., "Surface Reconstruction from Unorganized Data Points", *Computer Graphics: Siggraph '94 Conference Proceedings*, **26** [7], 71-78, 1992.
10. Chen, Y. and Medioni, G., "Surface Description of Complex Objects from Multiple Range Images", *Computer Society Conference on Computer Vision and Pattern Recognition*, June 1994.
11. Roth G. and Wibowo, E., "A Fast Algorithm for Making Mesh Models from Multi-View Range Data", In *Proceedings of the DND/CSA Robotics and Knowledge Based Systems Workshop*, St. Hubert, Quebec, October 1995.
12. *Surfacer V5.0 Manual*, ImageWare, Inc.,
13. Bern, M. and Eppstein, D., "Mesh Generation and Optimal Triangulation", in *Computing in Euclidean Geometry*, D.-Z. Du and F. Hwang, Eds., Lecture Note Series on Computing, **1**, 23-90 (1992).
14. Mäkelä, I. and Dolenc, A., "Some Efficient Procedures for Correcting Triangulated Models", *Solid Freeform Fabrication Symposium Proceedings*, **4**, 126-134 (1993).
15. Ashdown, I., "Octree Color Quantization", *C/C++ Users Journal*, **13** [3], 31-44 (1995).
16. IMS - Intelligent Manufacturing Systems, International Conference on Rapid Product Development, Stuttgart, Germany, 1994.

IVECS, Interactively Correcting .STL Files in a Virtual Environment

Stéphane M. Morvan
smorvan@eng.clemson.edu

Georges M. Fadel
gfadel@eng.clemson.edu

**Design Methodology Group
College of Engineering and Science
Clemson University,
Clemson, SC 29634-0921**

ABSTRACT

Free Form Fabrication (FFF) machines transform objects merely existing as 0s or 1s in a computer into a tangible object. FFF machines shift the paradigm of standard 2 Dimensional printers/paper printouts to 3 Dimensional printers/volumetric printouts (or 3D hardcopies). Currently, this technology is weakened by the link between computers and FFF machines: the .STL file, which contains a series of triangles representing the skin of the object to be prototyped. A prototype, reflecting precisely the evolution of a concept within a design cycle and allowing a systematic inspection/verification, is essential. A system responding to this need was designed at Clemson University for the inspection and the correction of such a file. IVECS, the Interactive Virtual Environment for the Correction of .STL files, is a tool that allows minute surgery to be performed on faulty tessellated models. IVECS allows STL files to be imported, tessellation errors to be detected and automatically or manually fixed. This paper expands on the use of IVECS for the inspection and the correction of .STL files. It extends the usefulness of the STL format by allowing designers to virtually prototype before actually building a physical model, thus contributing to a shorter design cycle.

INTRODUCTION

Bad .STL files have caused RP users to develop tools to correct errors within .STL files. These errors result from a poor tessellation algorithm that generates bad models not respecting the .STL format. The .STL file format [1] defines an .STL model as a set of triangles forming the material boundary. It specifies that an edge shall be shared by two and only two triangles and that each triangle obeys the right-handed rule (the vertices are ordered such that the cross product of the two edges should give an outward normal). Clearly, the triangles should intersect only at their edges and have exactly three adjacent triangles, one along each edge. Furthermore, an .STL model should be "water-tight": if water is poured inside the model, it should not leak. This is a necessary condition to generate a physically valid part.

Within an .STL file, several types of errors can be uncovered: those due to a weak tessellation algorithm in the CAD system which result in misoriented facets (e.g. outward normal not consistent throughout the model) and non-closed shells (presence of gaps or holes) and others due to the CAD user's ignorance of .STL files requirements (internal walls, self intersecting geometry). The internal walls problem does not really hinder the building of the part, but it may cause problems to the finished prototype. In the case of the stereolithography process in which a laser beam hardens the resin, the areas having internal wall problems are polymerized twice, resulting in overcure and possible warpage of surfaces.

PREVIOUS WORK

Most tessellation algorithms find their origins in the algorithms used by the CAD system to compute solid views (e.g. smooth shaded views). CAD systems rely at some point on an unevaluated, surface-based representation of solids: roughly all solids are assembled in surfaces (The B-Rep, or Boundary Representation). Each surface is mathematically defined by a function of two variables. These two variables are contained within a finite interval named the parameter space. When a surface is partially used within a CAD model (e.g. it is trimmed), the number of constraints on the parameters increases, leading to a more complicated parameter space [2]. A subdivision algorithm transforms surfaces into triangles by recursively dividing surfaces. When the surfaces obtained are flat enough, they are replaced by triangles. The process of dividing surfaces is a trivial problem [3]. In practice, surfaces are replaced by sculpted models, and the ordinary parameter space becomes increasingly complicated as surfaces get trimmed across most of their edges to form the desired geometry. Furthermore, the difficulty of correctly tessellating a model stems from boundary curves, which result from the intersection of two surfaces. A boundary curve belongs to two adjacent surfaces, and as such, is evaluated/sampled twice (once for each surface) during the tessellation. If the parameter space used to sample the curve differs slightly from one surface to the other, non-coincident vertices may emerge at the junction of the two surfaces.

Rock and Wozny[4] introduced the preliminary steps in correcting .STL files. The principle is that of inferring topology information from a "Bucket of Facets" (e.g. the unordered list of triangles) which is achieved using efficient detection techniques and intuitive data structures. The paper presents its "Topology Reconstruction Concepts" as based on the merger of vertices, the creation of faces and edges, and by determining face & edge relations. The merger of vertices consists of unambiguously identifying vertices listed throughout the .STL file, and assigning them a unique entry pointing to a list of vertices. The unambiguous identification of all equivalent vertices is difficult to achieve because of the round off error mentioned earlier; hence the requirement for a robust search/add algorithm to be used with a convenient data structure. The face and edge creation is straightforward from this point: a triangle and an edge are identified as a combination of respectively three and two integers that point to the list of vertices. Then, the face and edge relationships are created. Determining the face relationships is done by searching faces that share an edge, and cross referencing them; similarly the edge relationship is created (edge relationships are useful while slicing the part.)

The information gathered here (the indexed representation and the face relationships) clearly identifies errors in the file, and these serve as a basis for many related papers.

Böhn and Wozny[5] presented a simplistic, efficient approach to the correction of errors within a faulty .STL file. An intuitive algorithm to correct triangle orientation is presented, which is based on an indexed representation of the facets. The indexed representation is the first step for correcting .STL files, it consists of extracting and listing all the vertices forming the corners of the facets in a separate table. Triangles are now specified using pointers to the appropriate vertices. Using this, checking the orientation of triangles is straightforward: the neighbors of a triangle made from vertices #u, #v and #w must contain an indirect permutation of either #u and #v, #v and #w or #w and #u in the list of vertices. The iterative patching of triangles over holes (or punctures) with a “lid-surface” is outlined. Once a puncture has been detected, a closed curve made from the free edges is identified and is filled with facets of harmonious proportions: if a small triangle is near a big triangle, their common diagonal is flipped to create two equally sized triangles.

Mäkelä and Dolenc[6] described a set of procedures for correcting errors in .STL files, based on an adaptive space subdivision data structure. Several methods to automatically correct errors are presented: triangles are oriented using graph theory and small gaps are filled. Filling gaps attempts to preserve the local smoothness by considering the relative orientation of triangles rather than their size (as did the previous algorithm). Finally, the authors conclude by raising a philosophical issue while correcting faulty files: the protection of the original intents of the designer. More importantly, the authors mention the difficulty of algorithmic based approaches. They suggest what benefits could be drawn from an interaction between the user and the system.

More recently, Martin [7] proposed a public domain implementation of a correction suite for .STL files, ADMESH. The system performs surprisingly well on simple problems (misoriented normals and disjointed edges), but the patching of a hole is a more problematic task that works only in some cases. Also, ADMESH allows parts to be scaled, translated, mirrored and grouped, helping RP users to manipulate .STL models.

IVECS, THE INTERACTIVE VIRTUAL ENVIRONMENT FOR CORRECTION OF .STL FILES

The primary goal for IVECS was to allow users to virtually have their “hands on” .STL models by proposing the visualization and the correction of .STL files. IVECS detects errors and points them out to the user, who may choose to correct them. IVECS’ ability to automatically solve errors is limited to normal orientation problems and round-off errors. These two are performed automatically to reduce the number of errors present throughout the file, so that the user is solicited solely for the patching of holes or the removal of extraneous facets (e.g. the internal walls problems). Mainly, IVECS supports the addition, the removal, and the reversal of facets. Additionally, the offset of facet is also proposed. IVECS supports

both GUI (Graphical User Interface) and a VR based user interface, although the latter does not offer a comparable level of versatility.

IVECS uses OpenInventor [8] as a rendering engine. OpenInventor is available from Silicon Graphics as a toolkit designed to ease the manipulation of 3D objects. The rendering can be done in a variety of ways: with hidden lines, to show the tessellation, flat shaded, to show the product as it will built on an SLA apparatus, and finally smoothed, which shows the model with rounded edges, comparable to a sanded prototype. The initial goals for this system were to support the reversal of a facet, its removal or the patching of a crack in both the virtual environment and the conventional desktop based user interface. From this, and from geometries complicated to visualize, several functions emerged. These functions can be separated in two groups:

- Mode functions: these set the system in a particular type of mode such as “transparent mode” or “chrome plated mode.” Mode functions are not exclusive: a part can be chrome plated and transparent at the same time.
- Facet functions: these are the functions acting on facets. Some of these are: reversal of the normals, removal of a facet or creation of a set of contours.

On the left side of the rendered view is the toolbar. The upper half of the toolbar is dedicated to mode functions while the lower half is dedicated to facet functions. Most functions offer a “power user” mode activated by holding the shift key on the keyboard while selecting the button. This “power user” alternative offers additional control over each function. The upper and the lower half of the toolbar are separated by the “selection of facets” tool, that does not really belong to any of the previous groups. The selection of the facet tool allows facets to be selected. When this function is activated, the cursor changes from an arrow to a cross hair; and a facet is highlighted (e.g. selected) whenever it is clicked. Also, the multiple selection of facets is allowed when the shift key is held at the time the selection occurs, which results in several facets highlighted in red. A facet gets deselected if it is selected twice, and all facets are deselected if the mouse is positioned and activated on the empty space surrounding the artifact. The action of selecting the facets prepares the input for the facet functions. A set of facets can be selected and the mode functions can be accessed without interfering with the current selection.

MODE FUNCTIONS

The mode functions consist of: transparent, backface culling, errors, chrome, virtual reality, vertex and slicing plane. Toggling one mode on/off usually results in visible changes in the display area (the artifact gets rendered differently) and in the update of the icon placed on the button which reflects the state (on/off) of the current mode.

Transparent Mode



The part is rendered as if it is translucent to light, revealing internal details. The rendering of transparent parts uses an additive blending process, resulting in a greater opacity where many facets are aligned with the direction of sight.

Backface Culling Mode



Rendering can be quickened if one side of a facet is drawn on the screen. To achieve this, an assumption must be made on the side to render: the system computes the outward normal of each facet and determines if the facet is visible from the current point of view. When backface culling is on, the misoriented facets are not rendered correctly (visually behaving like holes in the skin of the artifact). By contrast, all facets are rendered when backface culling is off. Thus, by successively turning backface culling on and off, misoriented facets clearly appear in the rendered area.

Errors Mode



The Errors mode displays the errors found in the .STL file. The errors are displayed by coloring problematic facets with a shade differentiable from the overall color of the part. For instance, facets missing one neighbor are colored in pink, and those having an extraneous facet are colored in yellow.

Chrome Plated Mode



This mode makes the part look chrome plated. A texture is placed inside a sphere, and the reflection of that texture on the part is computed. Thus whenever the part is moved, the reflection is recomputed. Though this dynamic texturing scheme is computationally intensive, it results in an increased understanding of the geometry presented to the user. The principles which make this technique so efficient at grasping most of the geometric features in a single glance are based on surfaces interrogation techniques. Surfaces interrogation techniques [9] were used by car makers to match a stylist's freehand sketch with the machined prototype that emanated from it. Briefly, the technique consisted of observing the reflection of neon lights on the polished surface. The increased amount of information received from the reflection of a known pattern on a polished surface resulted in an intuitive, natural way of assessing the curvature of a surface. The chrome effect promotes the same type of natural experience with the user, and unexpected waviness resulting from a poor surface management at the CAD level is easily flagged. Several type of textures can be used: a scenic view consisting of flowers, sand and a blue sky and red stripes on a white background have been used to date.

Virtual Reality Mode



This mode allows the user to use Virtual Reality (VR) based techniques to interact with the system. After toggling it on, the user puts on the Head Mounted Display (HMD) and step in the Virtual Environment (VE.) Initially, the artifact is floating in the VE. Several interaction/navigation means have been established: the user can either “grab” the part, enlarge it to view details or navigate around it. [10] details the VE interaction techniques used in IVECS.

Clipping plane



The slicing plane is a recent addition to the system. It features a moving plane that prevents facets and vertices lying in its negative semi space to be drawn. The positive semi space is defined by the normal of this plane, the negative semi space being the other half. This plane can be conveniently oriented, allowing artifacts to exhibit their interiors. Also, it intuitively simulates the building process: its visual reconstruction from bottom to top helps to assess the best built direction and eventually confirm the result obtained later from a preprocessor of .STL files. Additionally, an auxiliary editor can be displayed to rotate the clipping plane or to key in the normal of the clipping plane.

Facet functions



The facet functions are the heart of this system: they allow the modification of the artifact in several ways. Facets can be added, deleted, offset, reversed, and color-coded contours scheme can be produced. Any of these functions affects only the selection, resulting in changes in the internal data structures. No undo function is provided, since an error can be easily recovered by either recreating a facet (case of an accidental deletion), removing it (case of the erroneous creation of a facet) or “re-reversing” it (case of the accidental reversion of a correctly oriented facet). They often result in minute changes in the geometry, as opposed to the immediately observable changes produced by the mode functions.

Creation of colored contours



To help visualize problems, sets of contiguous triangles are displayed in different colors: the neighbors (sharing one vertex) of a specific triangle are colored in red, the neighbors (“sub-neighbors”) of these neighbors are colored in green, the next one in blue, and so on, repeating red, green and blue patterns concentrically around the selected triangle. Whenever a triangle is flagged as problematic, its insertion in the current set of sub-neighbors is delayed to the next set of sub-neighbors. Thus, problematic facets break the color sequence:

instead of say, being colored in green they are colored in blue and the skipped color immediately flags the error and its effect on the arrangement of vertices. Also, non-intersecting solids can be flagged easily: since these isolated artifacts do not share common vertices, the contours do not spread from one artifact to the other, resulting in the coloring of one of the artifact while the other one is left untouched. Additionally, the colored contours can be transformed in an active selection, equivalent to individually selecting all the colored facets.



Patching of a hole

When filling holes, two approaches were considered: one trivial approach was vertex based while the other was triangle based. In both cases, the creation of the patch was subject to a test ensuring that the triangle was actually filling a hole. In the first case, once three appropriate vertices were selected (that is, vertices near an error), a triangle was computed, regardless of the arrangement of the vertices in space and allowing erroneous triangles (triangles not matching the geometry) to be created. It appeared that the adjacencies of the selected vertices had to be considered when the user attempted to map a patch.

An alternate approach was proposed: instead of selecting vertices, the user selects a pair of problematic triangles sharing one vertex and the system builds a triangular patch over the hole between the two triangles. If one (or both) of the triangles selected has more than one missing neighbors, several patches could be computed. In that case, the user browses through the set of possible solutions by repeatedly clicking on the mouse. The process is repeated until the hole is filled. If the Errors mode is on, the set of errors will be updated each time a new facet is created: pink facets are “moving” around the remaining holes, and when the surface finally gets closed, they (the pink triangles) totally disappear. This dynamic update guides the user towards achieving shell closure by drawing attention on remaining problems or newly created ones.

CONCLUSION

An environment to deal with .STL files and interactively correct them has been presented. It consists of both algorithmic tools to deal with easily correctable errors, and interactive tools that allow minute surgery. A short overview of some of the functions available in IVECS expands upon some of the techniques used. IVECS offers the opportunity to correct erroneous facets in a relatively short amount of time, but more importantly, provides the user with a tool to virtually prototype before building a physical artifact. After using such a tool, Rapid Prototyping facilities will increase their throughput since build problems will be eliminated.. Additionally the ability or visualizing a part in a VE complements ideally RP machines by offering a “print preview” function comparable to those found on popular word processors. It even helps the designer identify errors in the design before investing in a physical prototype.

REFERENCES

- [1]. 3D Systems Inc., StereoLithography Interface Specifications. Valencia, CA: 3D Systems Publications, 1989.
- [2]. H. Toriya and H. Chiyokura, "Chapter 8: Boolean Operations," in 3D CAD: Principle and Applications: Springer Verlag, 1991, pp. 182–195.
- [3]. X. Sheng and U. Tucholke, "On Triangulating Surface Model for SLA," presented at The Second International Conference On Rapid Prototyping, Dayton, OH, 1991.
- [4]. S. J. Rock and M. J. Wozny, "Generating Topological Information from a "Bucket of Facets"," presented at Solid Freeform Fabrication Symposium, Austin, TX, 1992.
- [5]. J. H. Böhn and M. J. Wozny, "Automatic CAD–model Repair: Shell–Closure," presented at Solid Freeform Fabrication Symposium, Austin, TX, 1992.
- [6]. I. Mäkelä and A. Dolenc, "Some Efficient Procedures for Correcting Triangulated Models," presented at Solid Freeform Fabrication Symposium, Austin, TX, 1993.
- [7]. A. D. Martin, "ADMESH 0.93," .
- [8]. J. Wernecke, The Inventor Mentor: Addison–Wesley, 1994.
- [9]. A. F. Lennings, J. C. Peters, and J. S. M. Vergeest, "An Efficient Integration of Algorithm to Evaluate the Quality of Freeform Surfaces," Computer & Graphics, vol. 19, pp. 861–872, 1995.
- [10]. S. Morvan and G. Fadel, "IVECS: An Interactive Virtual Environment for the Correction of .STL Files," presented at the ASME Design Technical Conferences, U. of California at Irvine, Irvine, CA, 1996.

An Adaptive Control Architecture for Freeform Fabrication

J.C. Boudreaux
Advanced Technology Program
National Institute of Standards and Technology

Introduction

Global competition is driving manufacturers to significantly reduce the length of the product development cycle while maintaining product quality. But this approach has the potential of exposing firms to huge design and engineering revision costs, since even a modest revision may give rise to a cascade of new change requests. It has been demonstrated conclusively, and repeatedly, that a work-faster strategy has the insidious negative effect of forcing workers to search for local optima, which are usually ones in which the burden is shifted either upstream or downstream. A more plausible strategy is to work smarter: by increasing the amount of information available at each stage, and by identifying and correcting problems as promptly as possible. The work-smarter strategy has been the root cause of the phenomenal growth of rapid prototyping technologies and especially solid freeform fabrication (SFF), which includes such technologies as stereolithography (SLA), selective laser sintering (SLS), laminated object manufacturing (LOM), and ballistic particle manufacturing (BPM).

Though differing in details, SFF technologies share a common operational methodology /9/. First, a computer-aided manufacturing (CAD) solid model of the part is constructed. This model defines the part boundary, which separates the interior (material) region from the exterior region. Second, the CAD solid is converted into a model in the STL file format, which is a *de facto* standard originated by 3D Systems. The STL model approximates the part boundary by a set of polygonal (in fact, triangular) facets. This representation permits efficient algorithms for the computation of planar intersections, but the number of polygons needed to approximate curved surfaces grows very rapidly with the geometric complexity of the surface. STL models are also subject to errors caused in part by finite-precision floating-point arithmetic /2/. Third, the STL model is mapped into the machine's coordinate frame and then sliced into vertical cross-sections. The size of the step between successive slices is a scalable parameter which typically varies from 100 to 500 micrometers. If the STL model has been correctly built, each slice will contain one or more polygonal regions. The fabrication process then produces thin polyhedra with the required polygonal profiles either by solidifying liquids or powders or by gluing together solid laminations and cutting along the polygonal edges.

In this working paper, an architecture for the adaptive control of solid freeform fabrication devices will be sketched. Close-loop controllers, such as proportional-integral-derivative (PID) controllers, are already in wide industrial use. Adaptive controllers are based on a feedforward scheme in which the behavior of an inner close-loop controllers is modified, or tuned, in response to predictions based on measured changes in the fabrication environment /1/, /8/. Adaptive control, if successful, would address many thorny issues of freeform

fabrication, permitting the identification and use of such process parameters as the traverse speed of the laser, optimal layer thickness, and tolerance bounds on STL models. Generally, the main advantage of adaptive control for SFF is to deepen and extend the predictive validity of fabricated artifacts for downstream manufacturing processes.

The Quality-in-Automation (QIA) Project: An Example

There is a connection between freeform fabrication and more traditional manufacturing technologies. This connection was stated very clearly by Chua Chee Kai in /9/, "Rapid prototyping systems are like a new type of numerically controlled (NC) tool. Unlike traditional NC, however, the algorithms needed to generate rapid prototype programs are simple. There are no tool changes to make, no multiple setups, no complex surfaces to follow and no pockets to mill." An interesting observation, but my experience with the NIST Quality-in-Automation (QIA) project suggests that the connection between NC machine tools and freeform fabrication may be closer than Kai suggests. As formulated by Yee and Donmez /6/, the QIA system was designed to be a "quality control/assurance system that exploits deterministic manufacturing principles ... based on the premise that most errors in the manufacturing process are repeatable and predictable..." The compensation strategy was achieved by implementing tool-path modification of the machine using a combination of kinematic, geometric, and thermal models of machine-tool errors. These models were obtained by pre-process machine characterization measurements of the machine tools involved in this project, including a Monarch VNC-75 Vertical Machining Center with a GE-2000M CNC controller and a Monarch Metalist Turning Center with a GE-2000T CNC controller. The QIA system supported two operational modes: a real-time mode and a process-intermittent mode.

In real-time mode, the compensation system monitored the machine tool and the metal cutting process, using sensory data obtained from thermal, vibration, force, and ultrasonic sensors, and then using model-based adaptive machining algorithms to do error correction by modifying the machine tool path as well as the speed and feed rates. After the appropriate error correction was calculated, as discussed by Boudreaux in /6/ and /4/, the required compensations was achieved by sending correction signals to a specialized electronic device, called the Real-Time Error Corrector (RTEC), "which is inserted between the position feedback device for each axis and the machine tool controller. It alters the feedback signal to cause the machine to go to a slightly different position to compensate for the predicted errors" /6/, /10/.

In process-intermittent mode, the compensation system would identify and measure part errors which were caused by the machining process, but which could not be accounted for by means of the deterministic model. For example, tool deflection or tool wear often cause errors of this kind. These form errors were detected experimentally by on-machine gauging between the semifinishing and finishing cuts. Once detected, the errors were corrected by either by using the RTEC feedback system with on-the-fly (and temporary) modifications of the error model for the finishing cut, or by generating a modified NC part program (understood to be coded in conformity with EIA RS-274-D) for the finishing cut, as discussed by Bandy in /6/.

To use part programs in an error compensation scheme some consideration must be given

to the methods of verifying and nominalizing them. Verification is the simpler of the two, since it can be accomplished by combining an elementary syntactic and semantic analysis of the part program with the creation of solid geometric model of the finished part and all of its intermediates. This solid model may be generated by joining the volumes created by sweeping the cutting tool profile through the tool path and then subtracting the resulting solid from a solid model of the initial blank. The part program is verified if this solid is indistinguishable from the solid CAD model of the part. Nominalization is more difficult. In fact, there is no general agreement about the conditions which a part program has to satisfy in order to be accepted as nominal. The idea is that a part program is nominal if it would generate an exactly accurate part, satisfying all of the design constraints, if it were executed on a perfectly conformant machine, that is, a machine with no systematic errors. Since interpolation methods are important sources of non-repeatability, it has been claimed that a nominal part program should only contain linear tool paths, and that all non-linear (circular or parabolic) tool paths should be replaced by a suitable linear approximations. It has also been claimed that the segmentation problem requires the off-line programming system to allow access not only to part programs, but also to process plans and CAD data. Such a data-rich framework would allow the programming system to maintain an internal representation of the nominal program so as to correctly propagate changes throughout the segments.

The QIA project suggests the following provisional sketch of an adaptive control architecture for solid freeform fabrication:

Adaptive Control Architecture. (1) *The inner, or core, controller accepts as command input any of an infinite set of syntactically well-formed control programs. Under the action of an algorithmic translator, the controller outputs to the plant a series of actuation signals, thereby causing the plant to perform a corresponding series of motions. In close-loop control systems, the controller has access to feedback signals which record measured deviations between the commanded and actual plant output.* (2) *The adaptive controller has access to the command input and feedback signals of the inner controller, and also to environmental parameters whose measured values have been correlated with future plant performance. Under the action of an algorithmic translator, the adaptive controller may respond in any combination of three fundamental modes:*

- I. feedback adaptation mode, in which the adaptive correction is accomplished by modifying one or more feedback signals (corresponding to the QIA real-time mode);*
- II. command adaptation mode, in which the adaptive correction is accomplished by modifying the inner controller's command input while preserving syntactic well-formity (corresponding to the QIA process-intermittent mode);*
- III. translator adaptation mode, in which the adaptive correction is accomplished by modifying the inner controller's translation algorithm.*

The third mode poses possibilities which are often discussed in the context of control systems based on neural net, fuzzy logic or genetic algorithm technology /1/, /8/. To make further progress, the notion of programmable devices will need to be considered more carefully.

A Theory of Programmable Devices

Devices are pieces of capital equipment that are used to modify the position, shape, size or material condition of manufactured parts. Examples of devices include numerically controlled machines, programmable fixtures, tool-changing devices, robots, and also the freeform fabrication devices mentioned above. More precisely, a device is an piece of capital equipment which (1) may be resolved into finitely many coupled components, each of which is itself a device, (2) has the capacity to perform a finite, but extensible, collection of industrially significant operations, and (3) may occupy any of a finite number of operational states. The first point says that devices may be nested within other devices, forming structures which resemble connected graphs. Since all devices have characteristic operations, industrial devices must support a concurrent, distributed processing model. That is, every device operation reduces to a series of concurrent operations by its component devices, the relative motions of which are precisely orchestrated. The controller converts these commands into a precisely structured sequence of signals to the actuation system. Thus, any realistic theory of devices must include an identification of the set of elementary or stereotypic motions that the device is able to produce, and also the definition of a method for combining elementary motions into more complicated motions.

A device is programmable if every motion in its behavioral repertory, however complicated, may be produced as a response to a well-formed combination of input commands to the inner controller. There is a close connection between a industrial programmable device and I/O devices such as floppy disk drives or printers. The behavior of disk drives or printers is defined in terms of the programmed commands that then can be given. For example, a disk drive can be commanded to **open** a file or to access a location in a file and return a piece of data, but neither command can be given to a printer, which can only be commanded to perform text or graphics output operations. A programmable device may require non-programmed machine-tending actions on the part of an operator. For example, the part to be machined may need to be properly fixtured or the cutting tools mounted in the turret, but these operations are no different in principle loading paper into the printer or putting a floppy disk in the disk drive.

Command expressions can be represented as a single phrase, consisting of a main verb, the symbolic representation of the operation, and an optional list of one or more modifiers /5/. For example, if a suitable coordinate frame has been defined, then one might imagine that a command of the form:

```
(MOVE (TO #(1.0 2.5 -1.0)) )
```

would cause a motion from an initial position to the position specified in the **TO** clause, provided the specified position is in the work volume of the machine tool. Without further qualification, the point-to-point specification of the motion permits an enormous range of acceptable path geometries. This range may be reduced by additional parametrization of the command. If one associates commands with actions by using a template mechanism, then the template mapping algorithm would take all of the parameters into account when generating the native language of the device controller /3/. The semantic interpretation of a parametrized verb phrase is the range of behavior which that phrase would cause if it were carried out by any appropriately configured device.

A Computational Framework

The task of any programming language for automated manufacturing is to provide a uniform programming language environment for the construction of control interfaces to industrial manufacturing processes, and an integrated system of software tools for translating product design and process planning specifications into equipment-level control programs. To provide support for the information requirement of programmable devices, an experimental Lisp-based programming language, called AMPLE /5/. This system was built in the mid 1980s for use in the NIST Automated Manufacturing Research Facility (AMRF) and was also used to design the QIA Quality Controller described above /4/, /10/.

AMPLE is an interpreted language. The behavior of the interpreter may be described as an infinite loop: (1) **read** an expression from an input stream, (2) **evaluate** the expression in the context of the symbolic environment (an ordered list of symbol/value pairs), and then (3) **write** the expression resulting from the evaluation to an output stream. The domain of AMPLE expressions is very simple. There are atomic expressions, including characters, strings, integers, floating point numbers, complex numbers, and arrays. When the interpreter is given any of these expressions to evaluate, it returns the expression itself. Symbols are atomic expressions which has a more complicated role. When the interpreter is given a symbol, the evaluation procedure tries to match the symbol with the all of the entries in the *symbolic environment*. If a match is found, then value corresponding to the symbol is returned. If there is no match found, then the interpreter returns a message to that effect. In addition to atoms, the only other class of expressions are lists. When the interpreter is given a list to evaluate, it assumes that the expression is the application of a function, which must be the first component of the list, to the interpreted values of the arguments, which must be the remaining components of the list. The value obtained is then returned as the value of the original list.

The value of an expression depends upon the operation of the interpreter and the current content of the symbolic environment. When initiated, AMPLE comes supplied with a set of primitive functions and variable symbols. This primitive environment may be dynamically altered by subsequent operations of the interpreter. As explained in /5/, some functions, when evaluated, cause new symbol/value pairs to added to the environment. For example, the evaluation of an assignment expression can cause the symbol **pi** to be added with the associated value 3.14159, or the evaluation of a function definition expression can cause a new function to be added. All symbolic environments are persistent objects which can be stored in external files and then loaded back when needed. The normal effect of reloading an environment is to restore the prior configuration, which means that AMPLE programming is focused on the construction of snap-on workspaces. Many workspaces have been developed, three of which are directly relevant to the topic of this paper: concurrency, code generation, and real-time processing.

Concurrency. There are two different issues that an industrial programming system must resolve: what operation, or operation sequence, needs to be performed, and when must the operations be initiated and terminated. The program needs to specify both the operations and the order in which the operations need to be done. Since a single device may actually contain

several controllers, and thus different operations can be executed concurrently, an efficient representation of these programs is by means of directed graphs (digraphs).

A set of basic functions for concurrency has been defined by Hoare /7/: **spawn** causes a new process to be created and added to the list of active processes, **block** causes a process to be unavailable for further processing by removing it from the active list, **activate** restores a blocked process to the active list, and **alt**, when given a set of alternatives, causes one of them to be selected. In addition, the function **par** causes agents to bring about explicit parallelism. When **par** is applied to a sequence of processes, called *children*, the process containing the occurrence of **par** being executed, called the *parent*, is immediately blocked. The children are concurrently spawned, and are then processed in the manner just defined. When all of the children have successfully terminated, and only then, the parent is reactivated. In many situations it is necessary for processing agents to coordinate their behavior. This is accomplished by means of *communication channels*. These are special processes which are used as structural members in order to establish a communication link between two or more processing agents, some of which want to participate in an input event, and others in an output event. For example, suppose that there is a Boolean-valued symbol, say **idle**, in the symbolic environment which is to be used to hold the current operating condition of a NC machine. This can be implemented by communication channels. The NC machine, actually a processing agent going proxy for the machine, is allowed to participate in output events with respect to **idle**, and any of a number of agents may participate in input events. The channel enforces a hand-shake discipline, that is, when the machine agent needs to output to **idle**, it acquires the output port, blocks all other input-requesting agents from acquiring the input port. The agent then updates **idle** and releases both the input port and the output port. If input-requesting agents are blocked, either by an update in process or by other inputting agents, they may, at their own option, either queue up to **peek** at **idle** or simply go about their business. This example shows that communication channels provide an elegant way to implement device states.

Code Generation. A code generator is a program which translates high-level device actions into low-level application programs in the device controller's native language. Code generation, which encourages effective re-use of existing control programs, is typically carried out in three stages. The first stage consist in the elaboration of precise definitions for the target family of devices. These definitions should group devices into classes based on their components, the operations that they can be commanded to perform, and their operating states. The second stage consists of the development of a library of program templates, each of which has been constructed by inserting parameters within carefully chosen fragments of control programs. The third, and last, stage is the definition of combinatorial rules for stringing templates together and uniformly replacing the embedded parameters with appropriate values.

There are many possible template processors techniques. One requires a distinction between a **context**, which is a linear sequence of characters, and algorithms or chunks of executable code, which are embedded within the context and whose interaction with it can be very complicated. The embedded code is prefixed by a selected special character, such as the at-sign **@**. The template processor scans each character in the source file in the normal left-to-right order and writes the character to the target file. When a special symbol is encountered, the template processor assumes that it is immediately followed by a legal

expression, which is to be passed to the interpreter for evaluation. The output to the target file is determined in the course of the evaluation of the embedded expression. In general, all template processors must include a completely unambiguous algorithmic presentation of the *mapping function* which, given any legal template and (possibly) any legal responses from external information sources, will generate the target text in a deterministic manner.

Real-Time Processing. Since all interpretive systems, need to reclaim memory, a process called garbage collection, which is a time consuming procedure, the interpreter has to have an internal *real-time processor (rtp)*. This processor is a programmable module, acting as a (virtual) coprocessor of the AMPLE interpreter. The **rtp** has a limited operation set but a sophisticated set of data structuring capabilities. This processor needs to address two conflicting design goals: it must be able to execute at very nearly compiled language speeds, and it must have direct access to objects dynamically created by the interpreter. This conflict can be resolved by using special off-line programming services to build the objects, which are then accessed and updated using the special access functions within **rtp**. Moreover, to prevent garbage collection, the access and update functions must never cause the allocation of any free memory cells.

Every **rtp** is linked to external consumer systems through **ports**. A port is a finite sequence of bytes which represent the remote communication between these systems together with a protocol which defines input and output behaviors of both systems. A clear example is a communication system in which one system, call it the target, writes instantaneous position information and reads correction signals, and the second system reads the position signal and writes the correction signal.

Any answer returned by **rtp** can be assessed in terms of its mathematical correctness, but real-time computing places an additional burden: the assessment of correctness also depends on a payoff function. For example, *hard real-time* systems are those whose payoff is a non-zero constant value if the correct value is returned within the allowed interval, and 0 everywhere else. In this case, there is a constant payoff for an answer delivered within the interval, but once the time interval has past, the answer has no value at all. A different payoff function might support different strategies. For example, given a payoff function with a non-zero initial value which slowly approaches 0, then there would always be at least a small advantage to returning an answer.

Discussion

The control problem for solid freeform fabrication devices has two classical aspects: the identification of basic operations, and the definition of a methodology for modifying, or adapting, these processes to specific situations. It has been proposed in this paper that the computationally difficult part of this problem can be handled by an very-high-level interpretive adaptive control architecture. This adaptive control family behaves as a system with a modal switch so that adaptation may be accomplished by modifications of the feedback system or the command system, both of which have been extensively investigated, or by structural modifications of the translation system of the inner controller, which is the most difficult case.

Until now, systems with this capacity have been based upon either neural nets, fuzzy logic, or the genetic algorithm. For example, a neural net consists of a network of active elements, called neurons. Each neuron may have several input connections, but all have only one output. Each input connection has an assigned weight. The value returned by each neuron is determined by multiplying each input value by its associated weight, summing these products together, and then by applying a sigmoid function to the computed sum. In this case, adaptation is a matter of updating (that is, incrementally revising) the associated weights. The adaptive control architecture sketched in this working draft suggests an approach to this problem through the design and implementation of what might be called an adaptation-instrumented command translator.

References

1. Astrom, K.J. and Wittenmark, B. *Adaptive Control*, Addison-Wesley, 1989.
2. Bohn, J.H. "Removing Zero-Volume Parts from CAD Models for Layered Manufacturing," *IEEE Computer Graphics and Applications*, November 1995, 27-34.
3. Boudreaux, J.C. "Code generation techniques to support device abstraction," *International Conference on Manufacturing Systems and Standardization, ICMSS '91*, Budapest, Hungary, 1991, 1-8.
4. Boudreaux, J.C. "A Programming Language Environment for Quality Control," *20'th International Programmable Controllers Conference, IPC'91*, 1991, 579-590.
5. Boudreaux, J.C. "Concurrency, device abstraction, and real-time processing in AMPLE," in W.A. Gruver and J.C. Boudreaux (eds.), *Intelligent Manufacturing: Programming Environments for CIM*, Springer-Verlag, 1993; 31-91.
6. Donmez, M.A. (ed.) *Progress Report of the Quality in Automation Project for FY 90, NISTIR 4536*, March 1991.
7. Hoare, C.A.R. *Communicating Sequential Processes*, Prentice-Hall, Englewood Cliffs, NJ, 1985.
8. Ioannou, P.A. and Sun, J. *Robust Adaptive Control*, Prentice-Hall, 1996.
9. Kai, Chua Chee "Three-dimensional rapid prototyping technologies and key development areas," *Computing and Control Engineering Journal*, August 1994; 200-206.
10. Yee, K.W., Bandy, H.T., Boudreaux, J.C., and Wilkin, N.D. "Automated Compensation of Part Errors Determined by In-Process Gauging," *NISTIR 4854*, 1992.

Thermomechanical Modeling of Successive Material Deposition in Layered Manufacturing

R.K. Chin, J.L. Beuth and C.H. Amon
Department of Mechanical Engineering
Carnegie Mellon University
Pittsburgh, PA 15213-3890

Abstract

Residual stress build-up due to successive deposition of superheated molten metal onto metal substrates is modeled for application to layered manufacturing methods. This work is specifically applied to microcasting, which is a deposition process used within shape deposition manufacturing. One-dimensional thermal and mechanical models are used to predict temperature and stress evolution related to two physical phenomena. First, the effect of thermal cycling by newly deposited material on stress states in previously deposited and cooled layers is investigated. Here, deposited molten metal solidifies and cools to room temperature before new molten metal is deposited. For this case, predicted stress distributions as a function of depth are relatively uncomplicated and can be related to residual stress-induced part tolerance loss. In the second case, the effect of localized preheating by previously deposited material is investigated. In this model, molten metal is successively deposited at a rate comparable to that used to deposit individual droplets in the microcasting process. Results indicate that although preheating by previously deposited material strongly affects transient stresses, final stress states are not substantially altered.

Introduction

A common characteristic of many layered manufacturing methods is the successive deposition of molten material. In such processes, the subsequent solidification and cooling of deposited material leads to differential thermal strains and the build-up of residual stress. Undesirable effects of residual stresses can include part warping, loss of edge tolerance and delamination between deposited layers. In parts subjected to applied loads, residual stress can also reduce apparent strength and service life. Ultimately, in order to control the undesirable effects of residual stresses through process changes and part design changes, it is necessary to understand how such stresses build up during manufacture.

Although the problem of residual stress build-up is inherent in any process involving successive deposition of molten material, attention is focused in this paper on modeling stress evolution in shape deposition manufacturing (SDM). SDM is distinct from other layered manufacturing processes in that it aims to directly build fully dense, functional metal parts to machined tolerances (Merz et al., 1994). After each layer is deposited, it is machined to specified dimensions prior to deposition of the next layer. Other processing operations, such as shot peening, can also be incorporated into the manufacture of a part. Within SDM, a process for depositing layers is required. The principal deposition process currently in use is termed microcasting, in which large (1-5 mm in diameter) droplets of molten material are deposited onto existing material which is at or near room temperature.

The goal of this work is to model successive deposition of superheated molten metal onto a metal substrate. In the next section, one-dimensional thermal and mechanical models are described which are used to study material deposition at two rates. Results are then presented for the case of material deposition occurring at a slow rate, such that existing material has reached a uniform room temperature before new material is deposited. These results are used to investigate how mechanical stress states in existing layers of material are altered by the deposition of newly applied layers. A second set of results is then presented for the case of material deposition occurring at a rate comparable to that at which droplets are deposited during microcasting. These results are used to

examine the thermal issue of localized preheating by previously applied droplets and the effect of this preheating on residual stresses.

Model Description

Figure 1 shows a schematic of the one-dimensional thermal and mechanical models used in this study. The models consist of a substrate which is 12.7 mm thick and five deposited layers, each having a thickness of 0.8125 mm. These dimensions match substrate and droplet thicknesses typical for microcasting. The thermal model used is explicitly one-dimensional and the mechanical model used is axisymmetric, with appropriate boundary conditions used to render the stresses at any time a function of the axial (z) coordinate only.

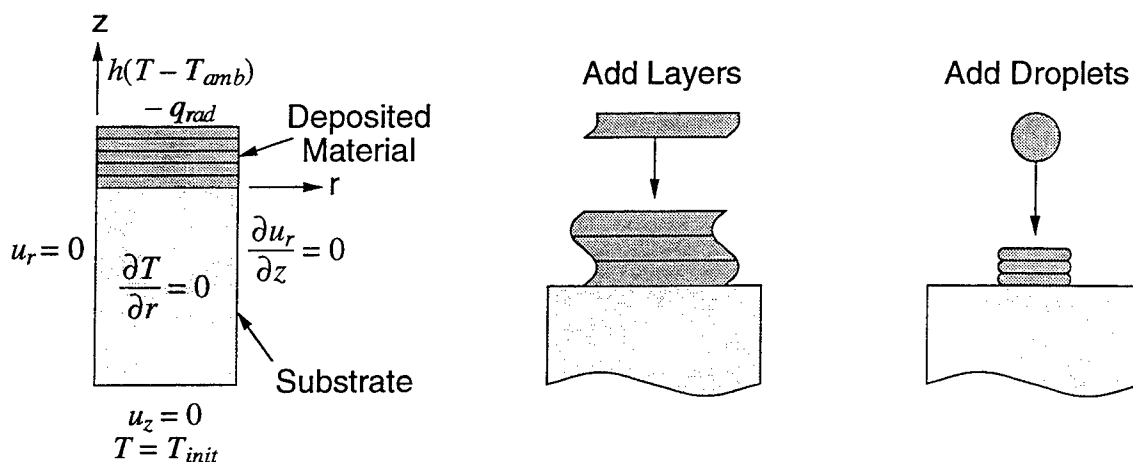


Figure 1. Thermal and Mechanical Models and Physical Problems Studied

The approach used in this study is to first obtain a thermal solution and to then use the temperature solution as an input to the mechanical model. In the mechanical model, loading is caused by differential thermal strains. Mechanically induced temperature changes are assumed to be negligible. The ABAQUS finite element package is used with thermal elements and stress elements having a quadratic interpolation of temperatures and displacements. The mesh resolution in the z direction is the same for each of the models. The thickness of each deposited layer is discretized by 10 elements of equal size and the substrate contains 18 elements through its thickness. The substrate mesh is strongly biased toward the top of the substrate. In this study, the deposition of medium carbon steel onto a medium carbon steel substrate is examined.

In the thermal model, boundary conditions modeling convection to the surroundings and radiation from a heat source (the welding torch for melting feedstock wire to create droplets) are imposed on the top surface of the newly deposited layer (Fig. 1). The convection heat transfer coefficient, h , is specified as $5.3 \text{ W/m}^2\text{-K}$, the ambient temperature, T_{amb} , is 323 K and the radiation heat flux, q_{rad} , is specified as 2092 W/m^2 . The ambient temperature is higher than room temperature because of the nearby heat source. These temperatures and thermal properties follow those used by Amon et al. (1996). Initial temperatures used in the model are 2573 K for the molten material (which is typical for microcasting of carbon steel) and 303 K (room temperature) for the substrate. At the bottom of the substrate, a fixed temperature equal to the initial temperature is imposed. The temperature-dependent thermal conductivity, specific heat and diffusivity used are based on data from Allard (1969) and Touloukian (1967) and are applicable to a low to medium carbon steel. The carbon steel is modeled as having a liquidus temperature of 1770 K , a solidus temperature of 1716 K and a latent heat of fusion of 272 kJ/kg .

In the mechanical model the top of the droplet is traction-free, with no imposed displacement constraints (Fig. 1). The centerline is constrained to have zero radial displacement,

while the outer wall is constrained to expand (or contract) uniformly in the radial direction. A condition of zero axial (z) displacement is applied at the bottom of the model. Because this model maintains straight vertical edges and a flat substrate bottom, deposition under the constraint of no bending deformation is modeled. In the microcasting process, parts are built on a large pallet which is very stiff in bending. Because the right edge of the model is free to expand or contract uniformly, the net radial force equals zero. These boundary conditions and the absence of radial temperature variation lead to a biaxial stress state $\sigma_{rr}(z) = \sigma_{\theta\theta}(z)$ with all other stresses equal to zero. The stress distribution at any time is therefore fully described by a plot of σ_{rr} vs. z .

The temperature-dependent Young's modulus used in the mechanical model is from data of Thomas et al. (1987), while the temperature-dependent linear thermal expansion coefficient is taken from the *ASM Metals Reference Book* (1981). To account for time-dependent creep deformation, a secondary (steady-state) creep law for a medium carbon steel in the austenitic phase is used. It is given by Thomas et al. (1987) as

$$\dot{\epsilon} = A(\sinh(B\sigma))^n \exp\left(-\frac{C}{T}\right), \quad (1)$$

where $\dot{\epsilon}$ = equivalent creep strain rate in seconds ⁻¹	$B = 0.0356$
σ = Mises equivalent stress in MPa	$C = 41938$
T = temperature in K	$n = 6.9$
$A = 907 \times 10^{10}$	

In this study, time-independent plasticity is not modeled. Through its stress dependence, however, the creep law in (1) approximately models temperature-dependent yielding without strain hardening. For example, at room temperature (303 K), a stress of 400 MPa results in a strain rate of 2.8×10^{-7} /s. As the stress is increased, the strain rate increases significantly. For example, at a stress of 430 MPa the strain rate equals 5.1×10^{-3} /s. Because a strain rate of 2.8×10^{-7} /s will result in insignificant stress relaxation under displacement controlled conditions, 400 MPa is a reasonable definition for an effective yield stress at room temperature based on the creep law in (1).

The thermal and mechanical models described above can be used to examine two types of physical problems, which are illustrated in Fig. 1. First, these models can be used to simulate temperature and stress evolution for the deposition of entire layers onto existing layers of a part and the substrate it is built upon. The results would be exact for the case of a part with insulated sides and with free edges constrained to displace uniformly in the radial direction, but they are also reasonable away from the free edges in a part built to be constrained from bending deformation. In relating this type of model to microcasting, effects associated with the drop-by-drop deposition of individual layers are neglected; however, such a model can give insight into how stresses develop on a layer level. Second, as noted in Chin, Beuth and Amon (1996), the thermal and mechanical models schematically illustrated in Fig. 1 can also be used to approximate conditions near the centerline of deposited droplets, where each droplet has a height that is small compared to its radius. For such droplet geometries, the radial displacement becomes increasingly uniform in the z direction and the heat transfer into the substrate becomes increasingly axial as the centerline is approached.

Recognizing the two physical interpretations outlined above, thermal and mechanical models are used in this paper to study two cases which differ in deposition rate. In the first case (related to the first physical interpretation), existing material is allowed to cool to room temperature before new material is deposited. Results from this modeling are used to investigate how deposition of new material layers alters residual stress states in existing layers. In the second case, new material is deposited onto material that has not had time to cool to room temperature, at a rate comparable to that used to deposit droplets in the microcasting process. Results from this

modeling are used to investigate how local preheating due to a previously deposited droplet affects stress evolution in droplets deposited on top of it. Although microcast droplets are typically deposited adjacent to each other, these results provide insight into multiple droplet deposition without having to resort to three-dimensional modeling. In both cases, deposition is onto a substrate that is initially stress-free and at room temperature.

Transient Results

In this section, transient temperature and stress results are presented for successive deposition of two layers or droplets of carbon steel onto a carbon steel substrate. Results for deposition of succeeding layers or droplets show similar trends. In the next section of this paper, final stress results are presented for the deposition of a total of five layers or droplets.

Slow Deposition

For the case of a slow rate of material deposition, Figs. 2 and 3 illustrate transient temperature and radial stress distributions due to deposition of a first layer of superheated carbon steel onto a stress-free room temperature carbon steel substrate. In the figures, temperatures and stresses are plotted as a function of the axial (z) coordinate at discrete times. An axial coordinate of zero represents the location of the interface between the substrate and the deposited material. The substrate has a negative coordinate and the deposited material has a positive coordinate.

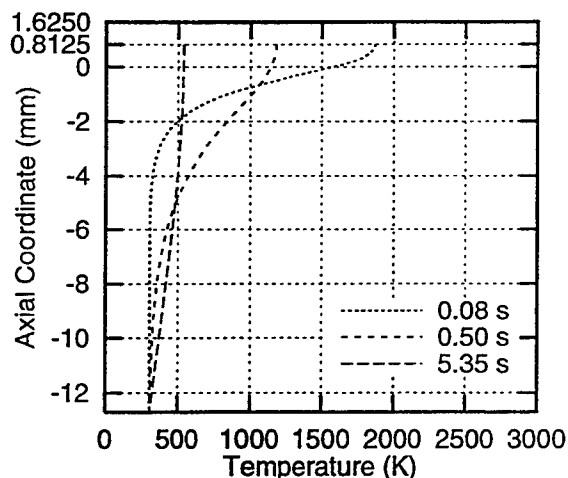


Figure 2. Transient Temperatures for Deposition of a Single Layer

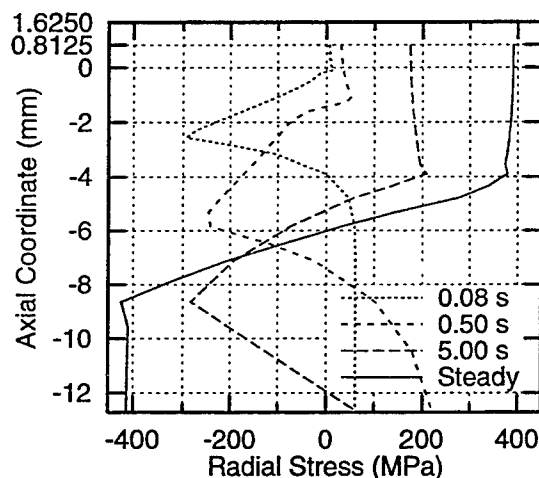


Figure 3. Transient Radial Stresses for Deposition of a Single Layer

As shown in Fig. 2, heat conducted from the molten material into the substrate initially raises the temperature of the top portion of the substrate hundreds of degrees K (see $t = 0.08$ s). Because this high temperature region is constrained against free expansion by the remainder of the substrate, this leads to compressive stresses (Fig. 3). As shown by the plot for $t = 0.08$ s in Fig. 3, inelastic straining occurs while the substrate is under compression at elevated temperatures, limiting the magnitude of the compressive stresses at the very top of the substrate. After the substrate material reaches its maximum temperature, which differs for each location, it begins to cool but is constrained from freely contracting. As this happens, the stress state in the top of the substrate turns from compression to tension (see Fig. 3 at $t = 0.50$ s and $t = 5.00$ s). To maintain zero net radial force, the stresses in the bottom of the substrate become compressive. Tensile stresses build up in the deposited layer due to constrained thermal contraction, but their magnitude at early times is limited by stress relaxation due to high temperature creep. As the temperature decreases further, the combination of further constrained thermal contraction and a diminished role of creep deformation increases the magnitude of tensile stresses in the layer. The final stress state consists of tensile stresses of large magnitude (near yield) in the deposited layer, which also extend to a depth of approximately 5 layer thicknesses into the substrate. The time to reach a steady-state

thermal condition, defined in this study as the time it takes for all portions of the model to be at or below 307 K, is approximately 30 seconds.

In the slow deposition rate simulations, layer 2 is deposited after both layer 1 and the substrate cool to steady state. Except for the effect of the addition of the thickness of the first deposited layer to the thickness of the substrate, thermal results for deposition of the second layer are identical to those for deposition of the first layer (Fig. 2). Therefore the transient temperature distributions for additional layers are not shown.

Figure 4 provides plots of radial stress as a function of the axial coordinate, z , at discrete times during deposition of a second layer. The initial stress distribution in the substrate and first layer is simply the final stress distribution shown in Fig. 3. In Fig. 4 it is evident that at early times (see data for $t = 0.08$ s), heat from the newly deposited second layer conducts into the first layer and the top of the substrate, relieving the large residual tensile stresses there and placing this region into compression. The compressive stresses do not extend as deeply into the existing material as they do at a similar time in Fig. 3. At later times, however, stress distributions in Fig. 4 become increasingly similar to those in Fig. 3. At steady state, the stress distribution is almost identical to the steady-state stress distribution shown in Fig. 3, with a similar tensile zone present in the deposited material and the top of the substrate. The tensile zone has moved upward slightly, however, compared to that in the initial stress distribution. Thus, although the initial stress state present in depositing a second layer alters stress distributions at early times, the final stress distributions are only slightly different.

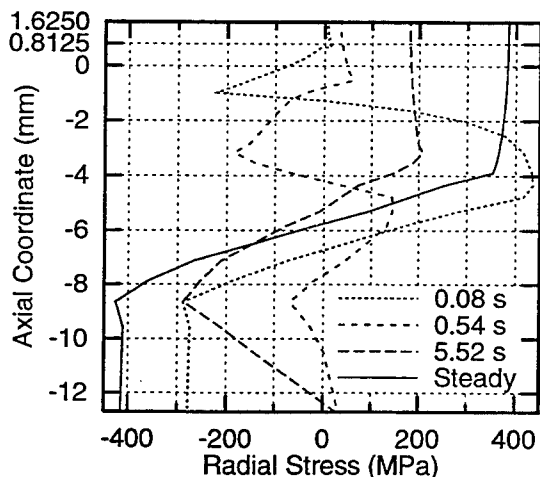


Figure 4. Transient Radial Stresses for Slow Deposition of a Second Layer

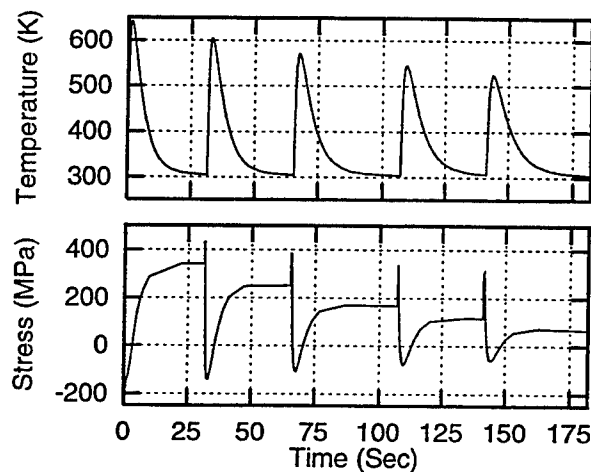


Figure 5. Temperature and Radial Stress at $z = -4.34$ mm (Slow Rate)

Another way to consider the transient behavior for the case of a slow rate of material deposition is to examine the history of temperature and radial stress at a particular point. This type of result is illustrated in Fig. 5 for a history point located approximately five layer thicknesses into the substrate, at a depth of 4.34 mm. The sharp peak in radial stress near $t = 30$ s in Fig. 5 corresponds to the maximum stress in Fig. 4 near $z = -4$ mm at a time of 0.08 seconds after the second layer is deposited. This peak in radial stress is brought about as a reaction to the compressive stress initially induced in the top of the substrate, due to the model requirement of no net force in the radial direction. This maximum in tensile radial stress, (and the compressive stresses in the top of the existing material that cause it) occurs over a very short period of time. The other sharp peaks in radial stresses in Fig. 5 correspond to similar maxima which occur after each succeeding layer is deposited. The periodic behavior observed in radial stresses is also seen in the temperature results plotted in Fig. 5. Temperatures rise rapidly after each layer is deposited,

due to conduction of heat from newly deposited material to the history point. The coinciding constrained thermal expansion results in compressive radial stress.

Rapid Deposition

For the case of a rapid rate of material deposition, material is deposited every 0.50 seconds, which is comparable to the rate at which droplets are deposited in the microcasting process. These simulations begin in the same manner as for slow deposition; however, 0.5 seconds after deposition of the first droplet, the existing distribution of temperature and stress is taken as the initial condition for deposition of the second droplet. After another 0.5 seconds, a third droplet is deposited and this procedure is repeated until the modeling of all droplet deposition is complete.

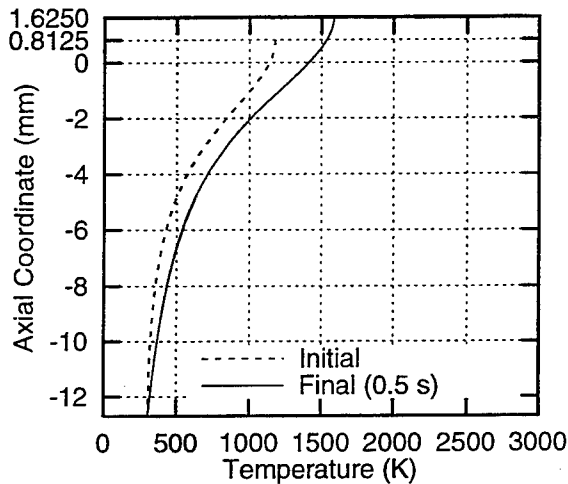


Figure 6. Transient Temperatures for Rapid Deposition of a Second Droplet

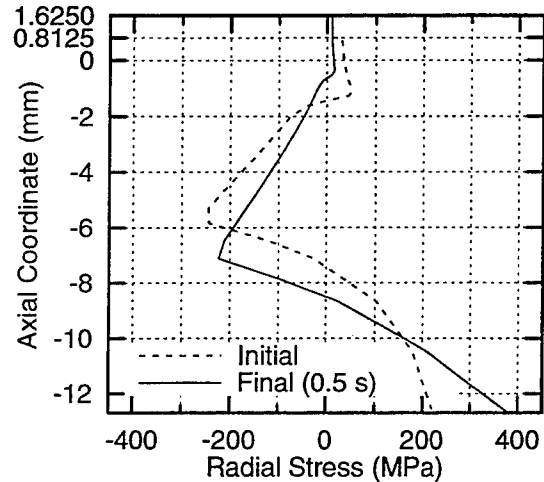


Figure 7. Transient Radial Stresses for Rapid Deposition of a Second Droplet

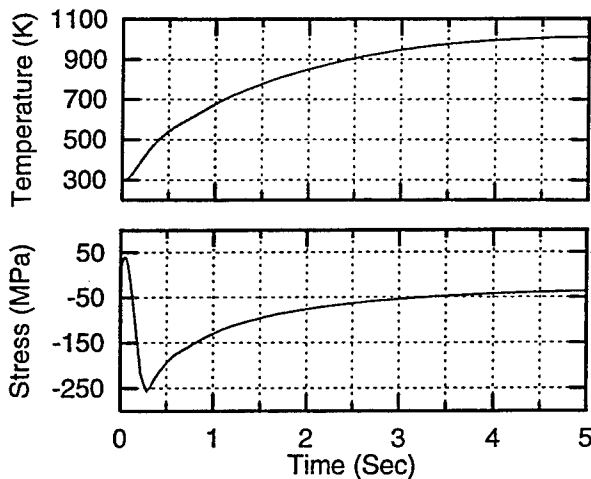


Figure 8. Temperature and Radial Stress at $z = -4.34$ mm (Rapid Rate)

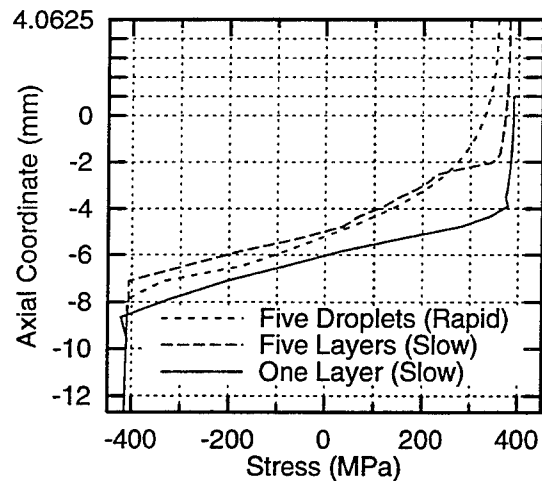


Figure 9. Final Radial Stress Distributions for Slow and Rapid Deposition

Figures 6 and 7 show the initial and final (after 0.50 s) distributions of temperature and stress due to deposition of a second droplet of material. Initial and final temperature and stress distributions are not substantially different and results are not plotted for other times because the distributions do not change substantially over the 0.50 seconds of the simulation. The first droplet and top portion of the substrate do experience an overall increase in temperature, however, due to heat conducted from the newly applied material.

In Fig. 8, results are plotted that are analogous to those plotted in Fig. 5, at the same location of $z = -4.34$ mm. The behavior is substantially different than that shown in Fig. 5, however. For the case of rapid material deposition, oscillations in temperature and radial stress are not apparent after the first droplet is deposited. Instead, as was noted in the results of Fig. 6, the addition of heat from newly applied material causes the temperature at this location to steadily rise. The compressive stress seen in Fig. 8 is a reaction to the tensile stresses in the top of the substrate and the deposited droplets. These stresses decrease primarily because increasing temperatures in the top portion of the model cause the tensile stresses there to be relieved due to creep. However, temperatures at the location $z = -4.34$ mm also become high enough to allow direct relaxation of the compressive stress.

Final Stress States

In this section, final states of stress are presented for the cases of slow and rapid deposition of superheated carbon steel onto an initially stress-free carbon steel substrate at room temperature. Deposition of a total of five layers or droplets is modeled and results are presented at a time after the last deposited material cools to room temperature. Figure 9 compares these results with the steady-state stress distributions due to the deposition of a single layer of material (the final stress state given in Fig. 3). The most striking characteristic of the plots provided in Fig. 9 is that they are not substantially different, despite the range of material deposition rates modeled and the different transient behavior observed. Also, all three plots show relatively simple residual stress distributions despite the complicated transient thermal and stress cycling that the material undergoes during the deposition process. It should be restated, however, that current material modeling does not include strain hardening. If hardening were included, the uniformity of stress states seen in Fig. 9 would be diminished.

During slow deposition, the small upward translation of the tensile zone observed in Fig. 4 after the second layer reaches steady state also occurs upon deposition of succeeding layers. The final stress distribution thus has the appearance of the stress distribution after deposition of a single layer, but with the tensile zone shifted upward. Also, the depth of the tensile zone is greater than that due to deposition of a single layer.

Separation of a part from the substrate upon which it is built will, in general, relieve a net residual force and bending moment in the deposited material, resulting in tolerance losses through part warping and contraction. In the building of parts by layered manufacturing, part warping is a significant concern because it can lead to substantial loss of dimensional tolerance. In the simulations presented here, however, a part separated from the substrate will contract, but not warp because there is essentially no net moment in the deposited material. For other configurations (e.g., different layer thicknesses), the same conclusion applies if the deposited material remains in the region of essentially uniform tension in the upper half of the deposited part and substrate.

The plot of final stresses for the case of rapid material deposition is similar to that for the case of slow material deposition; however, the tensile stress magnitudes are slightly lower. This is due to nonuniform preheating of the top portion of the existing material by prior droplets. The magnitude of the stress reduction is not large. A much larger reduction in residual stress magnitudes is indicated in simulations of uniform substrate preheating (Chin, Beuth and Amon, 1995, 1996).

Conclusions

In this paper results are presented for one-dimensional modeling of successive material deposition at two deposition rates. Results for a slow rate of deposition are related to the physical problem of successive deposition of material layers to build a part, providing insight into how residual stresses in existing material are affected by deposition of succeeding layers. Results for a rapid rate of deposition are related to the problem of successive deposition of molten droplets,

giving insight into how localized preheating by previously deposited droplets affects residual stress distributions.

Results for a slow rate of deposition suggest that existing stress states in previously deposited material do not significantly change final stresses compared to deposition on a stress-free substrate. Residual stress magnitudes in a deposited part can be large during deposition; however, these stresses are relaxed upon release of the part from the substrate it is built upon. The final stress state in the deposited material is essentially uniform biaxial tension. For such stress states, the deposited material will become essentially stress-free upon separation from the substrate, with a net contraction but no warping deformation. Results for a rapid rate of deposition indicate that preheating by previously deposited droplets alters transient temperature and stress distributions and increases the average temperature in the existing material. This preheating does not significantly reduce final stresses, however. This issue will be further explored through three-dimensional modeling of successive deposition of adjacent droplets. Overall, only minor differences in final stress states are observed over the range of deposition rates studied.

Acknowledgments

The authors gratefully acknowledge financial support from the Carnegie Mellon University Department of Mechanical Engineering and the National Science Foundation under Grants CMS-9411005, CTS-9311072 and DMI-9415001. The authors would also like to thank Lee Weiss and Fritz Prinz for their insights related to the application of this work to shape deposition manufacturing.

References

- Allard, S. (ed.) (1969). Metals thermal and mechanical data, *Metaux donnees thermiques et mecaniques. Tables internationales de constantes selectionnees 16*, Oxford, New York, Pergamon Press.
- Amon, C.H., Schmaltz, K.S., Merz, R. and Prinz, F.B. (1996). Numerical and experimental investigation of interface bonding via substrate remelting of an impinging molten metal droplet. *Journal of Heat Transfer 118*, in press.
- ASM Metals Reference Book: A handbook of data about metals and metalworking (1981). Compiled by The Editorial Staff, Reference Publications, American Society for Metals, 167.
- Chin, R.K., Beuth, J.L. and Amon, C.H. (1995). Control of residual thermal stresses in shape deposition manufacturing. *Proc. 1995 Solid Free-form Fabrication Symposium*, H.L. Marcus, J.J. Beaman, D.L. Bourell, J.W. Barlow and R.H. Crawford eds., Austin, August 1995, 221-228.
- Chin, R.K., Beuth, J.L. and Amon, C.H. (1996). Thermomechanical modeling of molten metal droplet solidification applied to layered manufacturing. Submitted to *Mechanics of Materials*.
- Merz, R., Prinz, F.B., Ramaswami, K., Terk, M. and Weiss, L.E. (1994). Shape deposition manufacturing. *Proc. 1994 Solid Free-form Fabrication Symposium*, H.L. Marcus, J.J. Beaman, D.L. Bourell, J.W. Barlow and R.H. Crawford eds., Austin, August 1994, 1-8.
- Thomas, B.G., Samarasekera, I.V. and Brimacombe, J.K. (1987). Mathematical modeling of the thermal processing of steel ingots: part II. stress model. *Metallurgical Transactions B 18B*, 131-147.
- Touloukian, Y.S. (ed.) (1967). *Thermophysical Properties of High Temperature Solid Materials*, Macmillan, New York.

PROCESS INSIGHT ABOUT LOM SYSTEMS

Chen Chi
Helisys, Inc.

ABSTRACT

A Laminated Object Manufacturing (LOM) machine offers much freedom in terms of system parameters: laser cutting speed, laser power setting, roller speed, roller temperature, and so on. Because of this freedom, users can choose any number, within certain limitations, to create well-constructed objects. Obviously, each user has a different definition for the quality of an object. Therefore this freedom has induced some confusion. Most commonly, each customer has his own preferred parameter data sets. These sets may not be the same but they are good sets. We need to devise a method as a guideline for system parameters to ensure a consistency in the construction of objects.

We have been studying actual laser power at different cutting speeds, actual cutting curves and bonding curves for different materials, actual temperature distribution, etc. These results have helped us find a proper way to set system parameters so that any user can run LOM machines without difficulty and confusion. The research methodology and results are elaborated in this paper.

INTRODUCTION

LOM is a patented rapid prototyping technique that allows the fabrication of 3-dimensional objects by sequentially laminating sheet materials and cutting the corresponding cross sections with a CO₂ laser beam. Because it is a high tech machine, it gives users the flexibility to manipulate the machine in such a way that good objects of any kind can be built. The flexibility comes from parameters in the LOMSlice program that can be changed. It is also assumed that users are knowledgeable about LOM machines. Without proper knowledge, it is hard to manipulate a LOM machine.

Helisys realizes that the flexibility sometimes derives complexity, hardship, confusion, and frustration. In order to eliminate those negative points, we have conducted research in various fields and seek improvements to continue offering customers a competitive edge. This paper only reports results related to the paper bonding process and laser cutting, two critical factors in the construction of quality objects. It is assumed that a LOM-2030E machine is used in this study.

LASER CUTTING

The system parameter menu in the LOMSlice software provides all the parameters for the motors, heater, laser, etc. In the menu, there are two parameters controlling the laser cutting: cutting speed and laser power setting [%]. Material type is another factor that affects object building process as well. For example, LPH042 and LPH080 are two commercially available paper types. For different paper types, different cutting behaviors should be observed.

Because of the complexity of the laser cutting process, it is difficult to derive a theoretical curve to represent the relationship between laser cutting speed and laser power. Therefore, an empirical result is presented.

Before beginning data collection, a machine is always checked to make sure it is in an optimal condition: the laser beam delivery system is aligned and the laser output power is at its maximum. Because the laser power setting represents the percentage of maximum laser power, it has a meaning only if we know actual laser power. In general, using the same laser power setting on different LOM machines does not guarantee that the same laser cut quality can be achieved. One laser used on various machines may put out different maximum power.

A Molectron laser power meter was used to measure actual laser power. It was placed right after the first mirror of a laser beam delivery system. The LOM machine has been designed in such a way that its actual laser power is a function of laser cutting speed and laser power setting. Different power readings should be displayed on a power meter at different cutting speeds. By changing the laser power setting and cutting speed in a LOMSlice program, maximum laser power readings on the meter were recorded. In order to make sure that a laser beam moves at the speed specified, a longer linear traveling distance of 30 inches was used. With recorded data, a series of curves have been drawn as shown on Fig. 1 which is called **laser power curve**. It is apparent that a laser can put out more power at faster speeds than slower speeds. But at higher cutting speeds, the maximum power a laser can put out is less than that at slower speeds. The same experiments have been conducted on other LOM-2030E machines. Curves similar to Fig. 1 are observed. Fig. 1 tells us laser power characteristics, but we need another curve to determine if a paper can be cut.

To determine proper cutting speed and laser power, we must define what a good cut is. One definition is that a laser beam should cut through all the required layers and a quarter inch deep into an additional layer. I found that it is difficult to visually determine the depth of the cut on the additional layer. Therefore we decided not to worry about the cut quality on additional layer. Instead, we tried to find out minimum laser power at which a laser beam can cut through all the required layers. The worst situation is that there are some strings on one side attaching paper to the other side. Many types of commercially available paper were used to find out the minimum power required to cut those papers. Data has been collected for a single layer cut, a double layer cut, and a triple layer cut (only for LPH042 paper). Only the data for LPH042 and LPH080 are reported here. Data for LPH042 is drawn on Figure 2 which is called **paper cutting curve**. It shows in the figure that any data point falling between curve A and B will cut a single layer; any

data point falling between curve B and C will cut double layers. The region defined by two adjacent curves apparently has a large area where many choices can be made. Because of this, each user may have a different pair of laser power setting and cutting speed. However, most parameter pairs will produce an overcut. In order to verify its validity, we have collected data for cutting parameters from people actually running LOM machines. This data has been plotted on Fig. 3. It is self-explanatory. Fig. 4 is for LPH080 paper.

Now we have two different figures: laser power curve and paper cutting curve. Each time a LOM machine operator wants to figure out values for laser power setting and cutting speed, he can follow the procedures as described below:

1. Select a paper type. Ex. LPH042.
2. Select a laser cutting speed. Ex. 15 (in/s).
3. From the paper cutting curve, select an actual laser power such that the corresponding point is between curve A and Curve B. Ex. 35 (w).
4. On the laser power curve, he can look for a curve corresponding to the cutting speed just selected, 15 (in/s). The right curve should be curve (C). From this curve, he can find a laser power setting associated with actual laser power, 35 (W). Therefore the laser power setting should be around 28 %.
5. Enter the pair data (15, 28) into the system parameter menu.

Here we have shown a logical procedure to find proper parameter sets for cutting objects. This procedure should not create controversy even though many different parameter pairs can be chosen.

The work shown so far assumes that a laser can put out maximum power and a beam delivery system has been cleaned and aligned properly. In the case that a LOM machine is not in optimal condition, one should do the following:

1. Use a laser power meter to measure maximum laser power at the HOME position.
2. User should know the power reading in an optimized LOM machine. Ex. 60 (w).
3. If a reading is 50 w, compute difference, i.e., 10w.
4. Follow the normal procedures described above. In step 3, the actual power becomes 45(= 35 + 10) (w).
5. Complete steps 4 and 5 of normal procedures. The laser power setting should be 34%.

Of course, a power reading can not be too low. If it is too low, a LOM machine can not cut objects. The lowest acceptable power depends on the cutting speed.

PAPER BONDING

The paper bonding process implemented in a LOM machine is a function of heated roller speed, roller temperature, roller pressure to paper, and paper itself. It is also affected by a platform's temperature and surrounding temperature and humidity. Because these factors are not directly controlled by a LOM machine, they are not considered in this study. This process starts by rolling a heated roller across a sheet of paper coated with a thin layer of thermoplastic adhesive on its bottom side. Due to the pressure of the roller to the paper and its rolling speed, a certain amount of heat will be transferred to the paper and adhesive beneath it. This amount of heat and roller pressure determines how well sheets of paper bond together.

It is assumed that a LOM machine is properly aligned and also the temperature distribution on a heated roller is uniform. To avoid temperature fluctuations, a temperature controller is used to indirectly control roller temperature. Because of this indirect temperature control, the actual temperature on a roller is not the same temperature as displayed on the controller. In order to study the actual bonding process, actual temperature distribution on a roller should be measured. An Omega temperature indicator and a J type thermocouple were used to measure temperature. The roller was about equally divided and marked so that there were 10 points of interest at which a J type probe touches. At each point the maximum reading was recorded. By changing the controller's temperature setting, a series of actual temperature distribution curves was recorded. The results are shown on fig. 5 which is called **roller temperature curve**. We notice on this figure that actual temperature is about two times higher than that of the controller's temperature. The actual temperature is evenly distributed.

Now we need to find out how much heat is transferred to the other side of paper. This transferred heat is a function of roller speed, roller pressure, and paper material. A LOMSlice program can be used to change roller speed and pressure. A pressure sensor was used to study how the actual pressure affects paper bonding process. We found out that this sensor is not reliable enough to provide some good data, but we noticed that the effect from pressure is not very pronounced. After we find a good sensor, we will report more quantitative information. A base of 10" x 10" was made first. A piece of paper of the same size was laid on top of the base. A J type probe was placed underneath the paper. By entering different values into the LOMSlice program, the maximum temperature reading was recorded. Temperature increase was computed and used to represent the amount of heat transferred to the adhesive. The roller speed range used was from 1 to 15 (in/s). The actual temperature range on the roller was from 423 to 731 (F), which are average temperatures computed from Fig. 5. The results are shown in Fig. 6 which is called **paper bonding curve**. Each curve represents temperature increase of the adhesive at different roller temperature. This curve can tell us actual temperature of the adhesive which should be equal to base temperature plus temperature increase at a specified speed. Once we know the temperature of the adhesive, we know if the adhesive should work. In this study we found the service temperature range of adhesive on the paper is about from 150 to 250 F. If it is outside of this range, paper will not be bonded well. The paper bonding curve for LPH080 is shown on Fig. 7.

For the bonding, two different figures, paper bonding curve and roller temperature curve, should be consulted to find proper roller speed and controller temperature. Additionally a pressure curve should be considered. Because of the explanation given in the previous paragraph, the results reported in this paper should still apply if the data for retract entered into a LOMSlice program is less than 0.015 in. The paper bonding curve is paper type specific. The roller temperature curve is machine specific. Each time a LOM machine operator can use the following procedures to find out proper roller speed and controller temperature:

1. In the beginning, measure platform temperature. Ex. 78 F.
2. Select a roller speed. Ex. 5 in/s.
3. Select a proper temperature increase from Fig. 6 so that the actual temperature at the adhesive is greater than 150 F but less than 250 F. Ex. 118 F.
Then actual temperature should be 196 F which is in the service temperature range. The point of (5 in/s, 118 F) is on curve A. The actual temperature of roller is about 731 F.
4. With Fig. 5, controller's temperature should be about 350 F.
5. Enter roller speed, 5 in/s, and controller temperature, 350 F, into the system parameter menu. Then a LOM machine should build an object with good bonding.

SUMMARY

This paper has shown a logical way to figure proper values for paper bonding parameters and laser cutting parameters. This eliminates any trial-and-error in determining system parameters. The methods reported in this paper save time in preprocessing and serve as a guideline to eliminate confusion and frustration. However, one may need many data curves; different materials will have different bonding curves and cutting curves. Therefore, a program is forming to implement suggested procedures. This program is about 40% complete. The completed portion has been tested in Helisys. The test result is good. After this program is completed and fully tested, it will be a part of LOMSlice program. Eventually the LOMSlice program will have some intelligence and the option to be a turn key system.

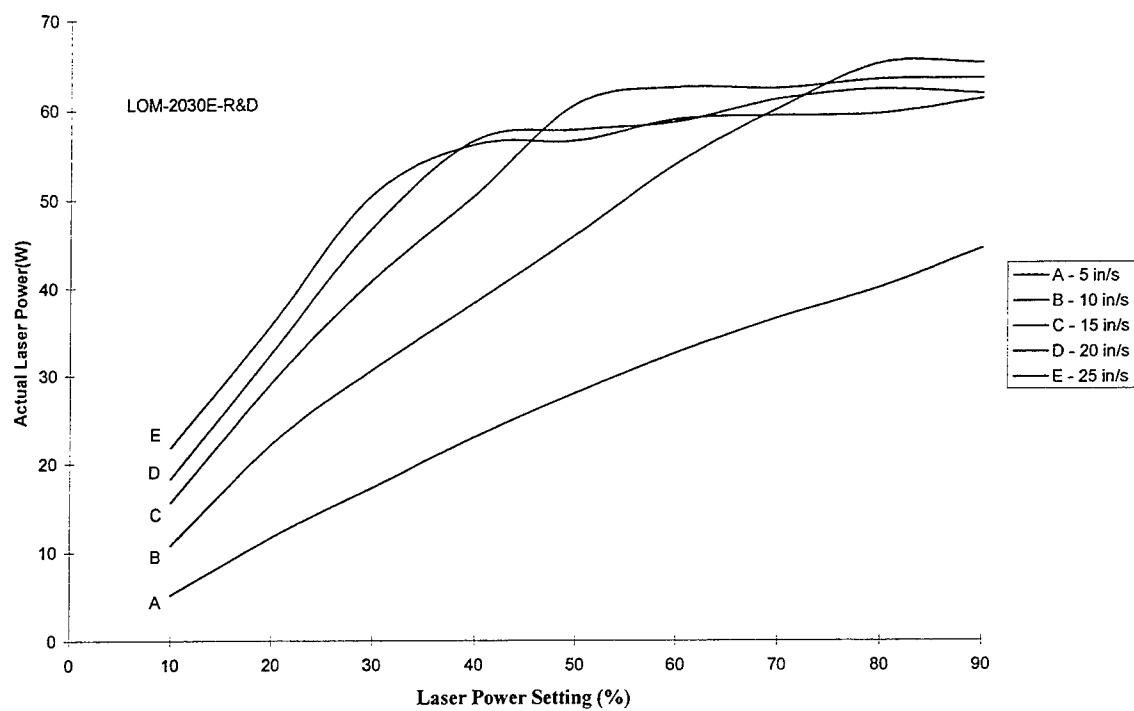


Figure 1. Laser Power Curve

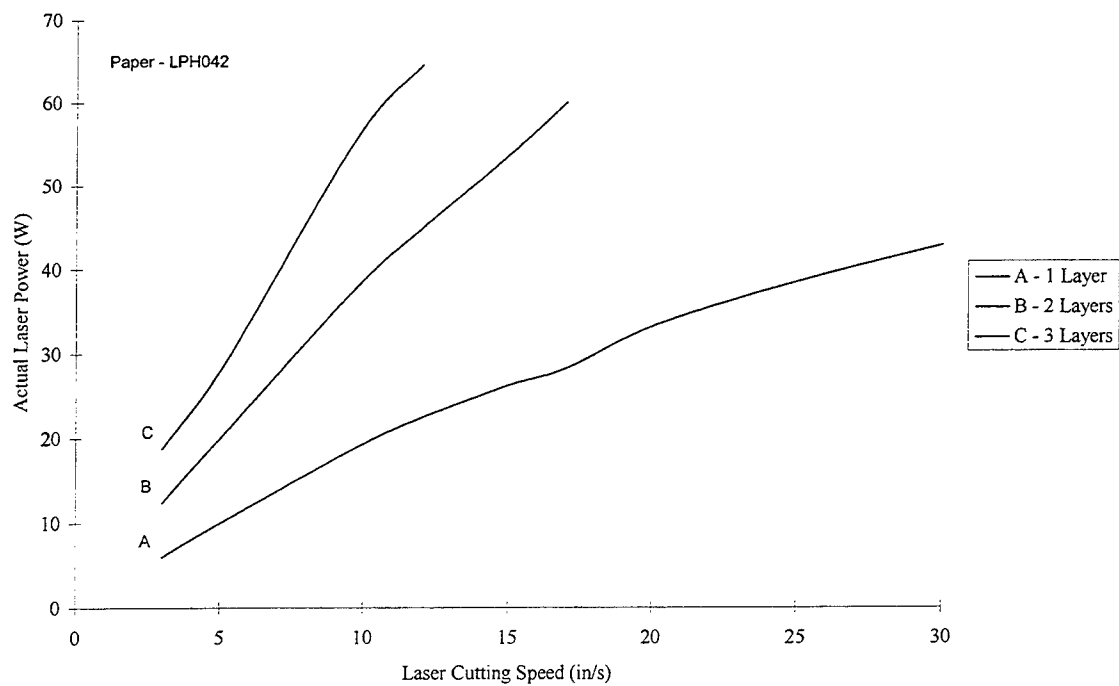


Figure 2. Paper Cutting Curve

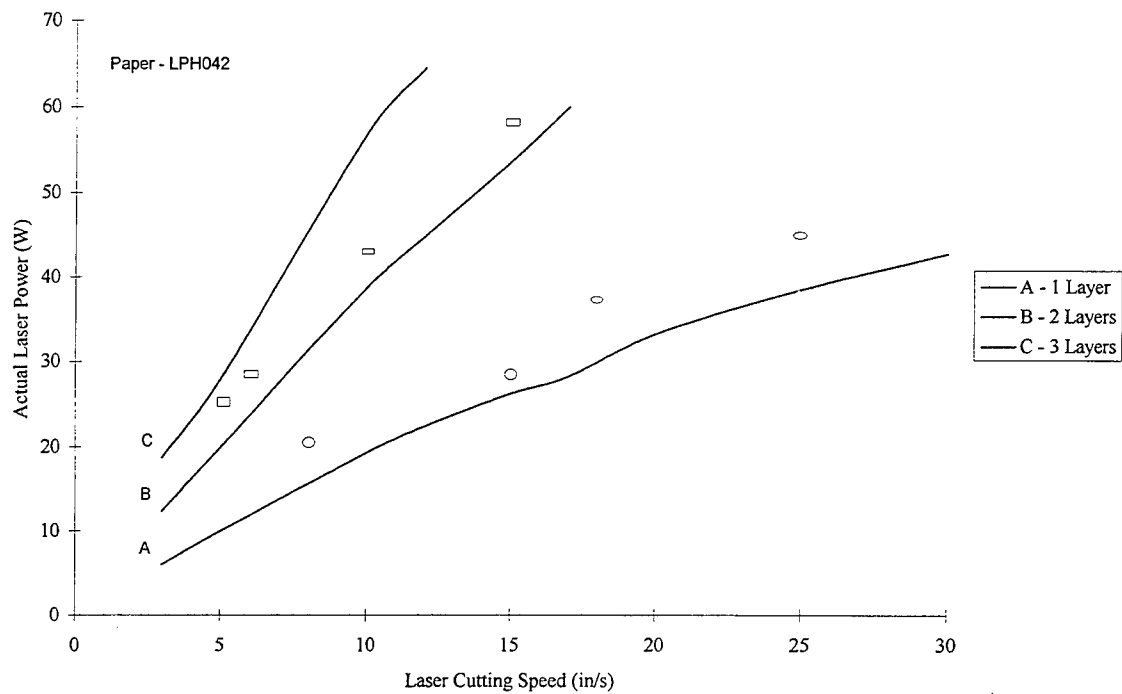


Figure 3. Collected Data Verifying Curve

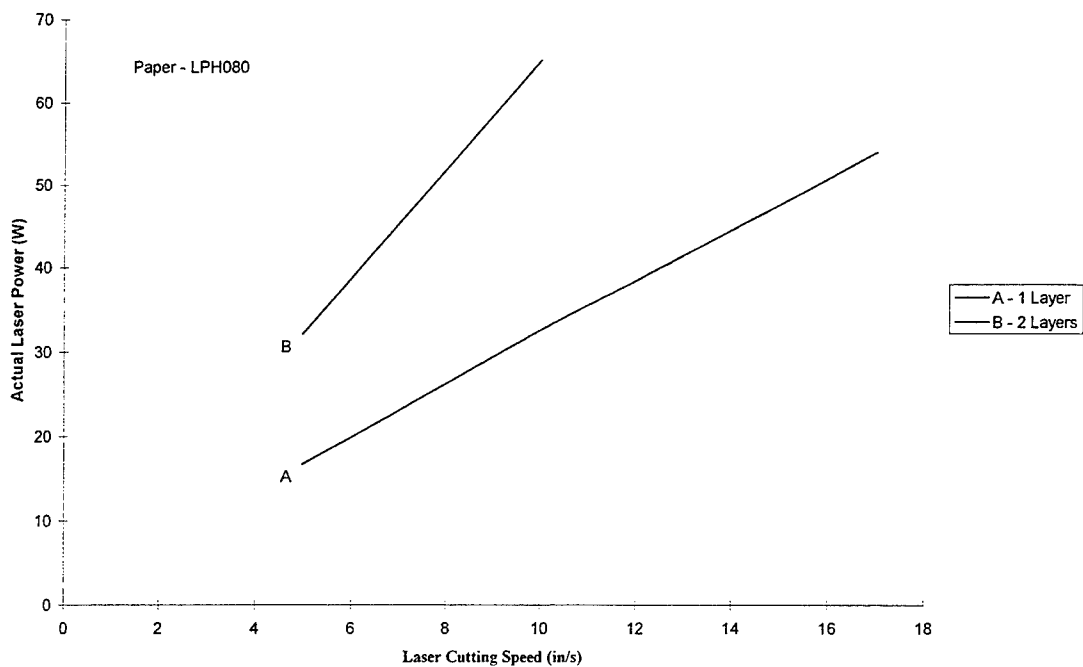


Figure 4. Paper Cutting Curve

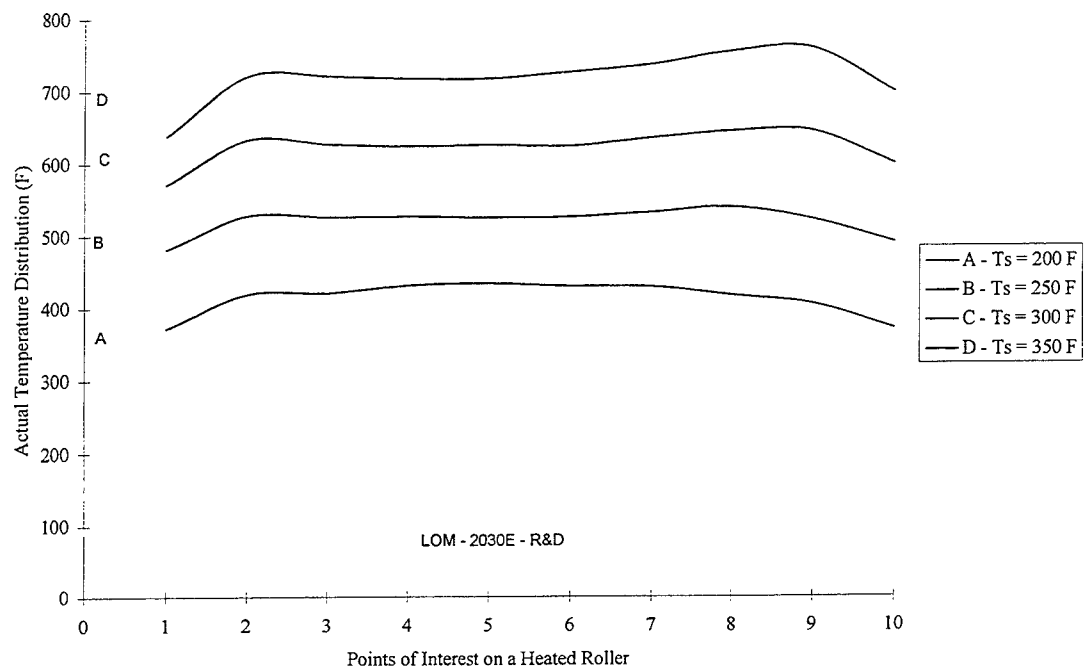


Figure 5. Roller Temperature Curve

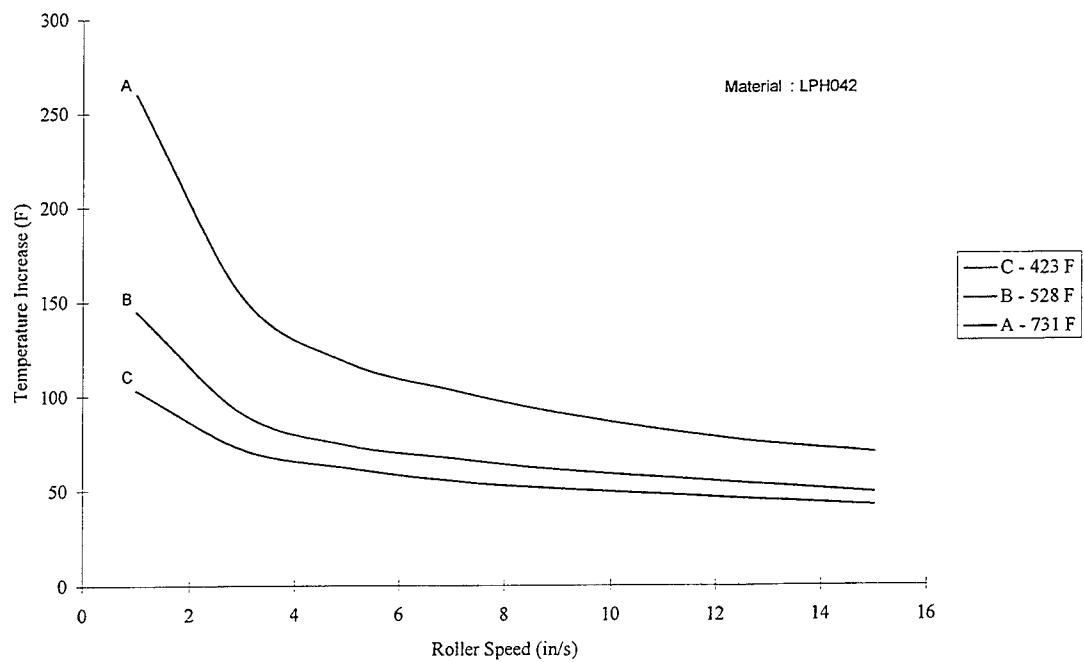


Figure 6. Paper Bonding Curve

FINITE ELEMENT ANALYSIS & STRAIN GAUGING OF THE STEREO LITHOGRAPHY / INVESTMENT CASTING SYSTEM

Richard Hague and Phill Dickens

Department of Manufacturing Engineering and Operations Management
University of Nottingham
Nottingham, UK

ABSTRACT

Many metal parts have been produced from stereolithography (SL) models via the investment casting route. However, it is still not possible for every foundry to directly use SL models as thermally expendable patterns and gain the same success as achieved with wax patterns. Significant drawbacks still exist with the QuickCastTM structure that restricts its use to specialist investment casting foundries who are willing to alter their standard techniques.

As part of a continuing work programme at the University of Nottingham, the stresses that are created in the SL/ceramic construction have been determined using simple stress analysis and finite element analysis techniques. Further work has involved connecting strain gauges and thermocouples to SL parts in order to confirm the results obtained with the theoretical stress analysis. Inspection of the results obtained is aiding the generation of new build structures to enable the successful autoclaving of SL models.

Details of the work to date are outlined in this paper, along with the results obtained.

INTRODUCTION

Since 1993, with the introduction of the original QuickCastTM build structure¹, it has been possible to gain functional metal parts from stereolithography (SL) models using the investment casting process. The accuracy of the SL models lends itself well to investment casting because of the high tolerances that can be achieved when using this casting method. Thousands of metal parts have now been produced² using the QuickCastTM process in a variety of different metals.

However, there are significant drawbacks associated with using SL models as thermally expendable patterns. The main problem area concerns the gross mismatch between the thermal expansions of the cured SL resin and the ceramic shell³. Because the epoxy resins used for the models are thermoset plastic materials, they do not melt under the influence of heat but continue to expand. It is this expansion that causes the catastrophic failure of the shells. The QuickCastTM build styles - effectively thin walled hollow parts with an internal open lattice structure of closed triangles (QuickCast1.0) or squares (QuickCast1.1) - were developed to allow the expanding SL parts some room to expand into and collapse during autoclaving. Yet, experience has shown that when using conventional autoclaving techniques for dewaxing (still necessary because of the wax tree that the SL models are usually connected to), the QuickCastTM models still generally cause the shells to crack.

Due to these difficulties associated with achieving a casting from an SL model, it has generally been the more progressive foundries⁴, more willing to adapt their existing techniques, who have been able to make the most of the stereolithography process for making one off or short-run metal components. However, it is desirable that all investment casting foundries should be able to take a stereolithography model and, by using their standard techniques (including the autoclave), be able to achieve a finished casting.

Work at the University of Nottingham is continuing into the investigation of the stresses caused by the expansion of the SL models in the green ceramic shells as the construction is passed through the autoclave cycle. This work is giving a much clearer understanding of what is happening to the SL / ceramic construction and is giving a clear indication of the necessary requirements for the design of 'successful' internal build structures.

This paper is a continuation and update of the work presented previously⁵. It gives details of the stress analysis performed to date and indicates the future direction of the research programme.

BACKGROUND WORK

Failure of SL Models

Due to the relatively large expansion of the cured epoxy resin, autoclaving *solid* SL models will cause the investment casting shells to crack. To overcome this, QuickCastTM models were developed to enable investment casting shells to survive the autoclave phase by allowing the models to soften and then collapse in on their own voids¹. Yet despite this, experience has shown that QuickCastTM models still generally cause the shells to fail in the autoclave phase⁶.

Thus, to enable QuickCastTM parts to be used as thermally expendable patterns, it has been recommended⁷ that foundries skip the steam autoclave phase and dewax shells containing these models directly in the flash-furnace. Even though this method (coupled with other significant modifications to the standard investment casting process) works, it should not be viewed as a viable solution to the problems of 'dewaxing' QuickCastTM models. What ideally required is a build structure that allows the direct substitution of the SL part for the wax, with out any variation to the standard investment casting process.

On a brighter note, trials have shown⁵ that it is entirely possible, without modification, to autoclave thin walled hollow parts. This indicates that it is very likely that a structure(s) exists in between a hollow and solid that will also allow the autoclaving of parts (built in that structure) to be successful. If a stereolithography / investment casting construction can make it through the autoclaving stage there will normally be no problem in achieving the resultant casting.

Sectioning of the autoclaved shells that contain these thin walled hollow parts shows that the SL models shatter within the confines of the shell. On investigation, this appears to contradict the QuickCastTM 'theory' of the part softening and then collapsing in on itself.

If the parts were to soften *and then* collapse (as the 'theory' states), then upon sectioning of the autoclaved shells you would expect to see merely a buckling away from the walls of the SL model. The shattering of the hollow parts indicates that the stereolithography parts have indeed failed before they have time to soften. This transforms the reasoning behind the design of new structures, in that models must therefore be designed to fail (under the influence of their own expansion) before their expansion causes the ceramic shell to crack.

Material Properties as a Function of Temperature

Determining the changes in material properties as temperature increases, especially of the cured SL resin, is fundamental to understanding why investment casting shells containing SL models are failing. The key to the failure of the shells lies in the high coefficient of thermal expansion (CTE) of the resin when compared to that of the green ceramic shell.

The determination of the material properties is crucial to enable stress calculations to be performed. The relevant properties obtained are used in simple stress analysis tools (such as Lames theories⁸) and more complex finite element analysis (FEA) packages.

A summary of the graphs for thermal expansion and Youngs modulus (*Figures 1 & 2*, respectively) are repeated in this paper for reference. Key points to note are the doubling in thermal expansion (from approximately 88×10^{-6} to 181×10^{-6}) that occurs around the glass transition temperature of the material. Correspondingly, there is a significant drop in the Youngs modulus at temperatures above the glass transition.

The graphs clearly show the sharp decrease in strength of the resin as the samples are ramped through an increase in temperature. This indicates that most of the problems *should* be occurring at the lower temperatures, where the QuickCastTM models still have enough material strength not to collapse but enough expansion to crack the shells.

STRESS CALCULATIONS

Finite Element Analysis: Thick Walled Cylinder

To complement the work previously performed using Lames theories to determine the stresses created in a simple stereolithography / investment casting construction, the Thick Walled Cylinder (TWC) problem was also modelled using an FEA package. (In summary, a TWC in this instance is taken to mean an open ended 'cylinder' of ceramic shell encasing a solid epoxy resin core. See ref. 5)

Figures 3 & 4 show the results obtained using Lames theories and the FEA package, respectively for resin cores of 1mm and 50mm diameters. There is a clear correlation between the results obtained using these different theoretical methods. The profile of the curves obtained from the FEA work match closely those obtained with Lames, except that there is a slight increase of temperature at which the maximum stress occurs with the FEA results. The magnitude of the stresses obtained with the two methods are also very similar to each other.

The similarities of the results from these two theoretical methods gives some degree of confidence as to suitability of using the FEA technique to model more complex examples.

Finite Element Analysis: 50mm CUBE

Basic theoretical stress analysis techniques, such as Lames theories, limit the complexity of the parts that can be analysed. Having confirmed the validity of the FEA package, the FE analysis was next extended to simulating the stresses induced in a SL 50mm cube encased in a shell 5mm thick; this represents a more complex geometry containing edges and corners. Though it is envisaged that eventually cubes containing QuickCast™ structures will be modelled, the FEA was (for the purpose of this paper) restricted to cubes of varying hollows. Initially, three variation of the 50mm cube have been analysed; these include:

- 50mm Cube; Solid
- 50mm Cube; Hollow with a wall thickness of 5.0mm
- 50mm Cube; Hollow with a wall thickness of 2.5mm

A schematic of the FEA model is detailed in *Figure 5*. It is hoped that in future, thinner walls as well as 'structured' parts will be modelled.

Figure 6 shows the stress profile over a range of temperatures for a solid 50mm block, a hollow 50mm block with a wall thickness of 5mm and a hollow 50mm block with a wall thickness of 2.5mm. All of the resin blocks are covered with a shell 5mm thick.

The introduction of corners have, predictably, had a great effect on the concentration and value of the stresses induced in the ceramic. For the solid 50mm block, there is a maximum stress of about 130MPa. Comparing this to the value obtained from the 50mm diameter core in the thick walled cylinder example of about 16MPa, it is clear that the corner has had a dramatic effect.

Though these hollow parts have been modelled with relatively thick walls, the effect on the induced stresses by introducing a hollow into a solid part is striking. There is a dramatic drop in stress as the wall thickness decreases. The block with a 2.5mm thick wall produces stresses in the ceramic approaching a value that is thought to be autoclavable. Interestingly, reducing the wall thickness has the same effect as reducing the resin thickness in the TWC problem, in that it decreases the temperature at which the maximum stress occurs (see *Figure 4*). It should be noted that the maximum induced stress (in the ceramic) occurs at the mid-point of each edge of the cube.

STRAIN GAUGING

Initial Strain Gauging

One of the principal reasons for performing the FEA was to identify not only the magnitude of the maximum stress, but also its location.

Initially a *Solid 50mm* stereolithography cube was built. This cube was then strain gauged and thermocoupled at the positions identified by the FEA work. An example of the strain gauging of the solid resin block can be seen in *Figure 7*. Having applied the gauges to the surface of the model, the initial face coat of the ceramic shell was applied and allowed to dry. With care, strain gauges were also applied to this initial face coat and the part was then coated with its subsequent ceramic layers, up to the normal thickness.

This strain gauged block was then placed into an oven and the results were recorded. A sample of the results can be seen in *Figure 8*. This figure shows the values gained for one of the strain gauges attached to the resin block and the equivalent gauge attached to the ceramic shell. It seems that there is a clear break in the ceramic around 60°C. This initial result was very encouraging because it seems to confirm the observation that the majority of the problems are happening at or below the glass transition temperature of the resin. *Figure 9* shows the shelled cube after it has gone through the heating process. It can just be seen that cracks have propagated from the centre of each edge which corresponds exactly with the predictions of the FEA. However, it is surprising that even though the ceramic shell has cracked under the influence of the heat, it has still remained mainly intact.

One initial drawback that became apparent during this test is that to gain a result from the strain gauged ceramic, it seems that a crack has to propagate directly over the strain gauge.

These results appear to go some way to confirming the work performed with Lames theory and the FEA work.

Further Strain Gauging

Having achieved a reasonable result in the initial laboratory based 'dewaxing', the strain gauging was then expanded to encompass the full range of examples that were simulated using the FEA. For comparative analysis, three (3) of each type were fabricated. The types built were:

- Solid blocks (Referred to as *Solid _1/2/ or 3*)
- Hollow blocks, wall thickness 5.0mm (Referred to as *Hollow 5.0mm _1/2/ or 3*)
- Hollow blocks, wall thickness 2.5mm (Referred to as *Hollow 2.5mm _1/2/ or 3*)

and also, to repeat previous work involving the autoclaving of thin-walled hollow parts

- Hollow blocks, wall thickness 1.0mm (Referred to as *Hollow 1.0mm _1/2/ or 3*)

As before, strain gauges and thermocouples were fixed onto the surface of the SL blocks and also attached to the initial 'face-coat' of the ceramic. For the Solid models, an additional thermocouple was also placed at the centre of the block. These blocks were then subjected to a real 'dewaxing' in a commercial steam autoclave.

A representative sample of the results obtained for the Solid block can be seen in *Figure 10* and, similarly, an example of the results for a Hollow block (in this instance, *Hollow5.0mm_1*)

is shown in *Figure 11*. As expected, all the shells failed except for the ones containing the *Hollow_1.0mm* samples.

DISCUSSION

The clear result from the initial strain gauge work has not been duplicated in the autoclaving trials. There seems to be a stark difference in the results achieved when the autoclave is used to 'dewax' the samples. The graphs are far more difficult to interpret, but one of the most obvious thing to note is the conspicuous increase of temperature at which the shells appear to fail.

This *apparent* increase can be explained if the temperatures recorded in the Solid block are referred to. *Figure 12* shows the temperatures recorded at the interface between the shell and the resin and also at the centre of *Solid_2*. The interface temperature has a very steep temperature gradient, but it can be clearly seen that the temperature at the centre of the block lags way behind this interface value. This demonstrates the insulative properties of the epoxy resin. Though the shells appear to be failing at about 120 to 130°C, it should be noted that this temperature is the *surface* temperature of the cube so, crudely speaking, the actual average temperature of the resin block at which the shells fail correlates to about 60 to 70°C. This is much more in line with the value predicted with the FEA package and demonstrated with the initial strain gauge trials.

The heat input rate is clearly much more of an issue than was previously thought. The autoclave that was used to 'dewax' these samples offered a very steep heating input, and consequently destroyed the shells (see *Figure 13*). The oven that was used to heat the solid block in the initial strain gauge work (described previously) provided a more gentle heating rate that allowed the resin cube to heat up more uniformly. The heating rate for the initial strain gauge work (again measured at the interface of the ceramic and model) is more in line with the rise in temperature recorded at the centre of the equivalent autoclaved block. (See *Figure 14*)

In order to initially simplify the problem, the theoretical work performed (Lames theory and FEA) assumed that the SL / investment casting construction reached an instant and *uniform* temperature throughout. For the initial strain gauge work, because the heat input rate was relatively slow, the temperature distribution through the resin cube was more uniform. It is for this reason that the initial strain gauge work reflects more closely the theoretical results. It should be noted that although the solid cube heated in the oven also failed, it did so far less catastrophically than the autoclaved version.

For samples that were heated in the autoclave, the resin cube can be separated into two areas: an outside 'skin' that is getting progressively hotter and an inner core that, due to the temperature lag, initially remains mainly at ambient temperature. (The outer layer, of course, eventually consumes the inner as the effects of the lag are diminished). However, whilst the inner core remains solid, it restricts the softening and expanding outer layer from deforming. So, as the outer 'skin' gets progressively hotter, its expansion increases to such a rate that it causes the shell to fail.

Summary

The relatively novel approach to using strain gauges appears to present some difficulties. There are clear problems associated with using strain gauges that are imbedded and adhered to the ceramic with an adhesive that has a thermal expansion far greater than that of the ceramic itself. The problem of the expanding adhesive simply reflects the original problem of the cured SL models causing the shells to crack due to the gross mismatch of thermal expansion.

SL parts that do not crack the shells during the autoclave phase (not published) show that the strain gauges are appearing to register a negative strain. This *apparent* compression of the ceramic runs entirely contrary to what actually happens. However, a logical explanation of this phenomena is that as the adhesive coating the strain gauge tries to expand under the influence of heat, it is unable to because it is itself encapsulated by the ceramic shell. As the ceramic is (relatively) not expanding, the strain gauge is forced into *compression*, and thus registers a negative strain.

CONCLUSIONS

There are clear similarities between stress values obtained for the thick walled cylinder using Lames equations and the results obtained with the FEA package.

Though these results are preliminary and simplified, they clearly show a general trend, and support the idea that the majority of the problems are occurring before or about the beginning of the glass transition temperature of the cured resin.

The initial strain gauge results that were performed in the low heat input oven offer good substantiation of the theoretical work performed. The results obtained from the more aggressive autoclave trials are more confusing and seem to highlight the difficulties of using strain gauges in such an environment.

ACKNOWLEDGEMENTS

The authors would like to thank 3D Systems Inc. and the UK Economic & Social Research Council (ESRC) for their help and financial support in this research programme.

REFERENCES

- 1 JACOBS, P.F. Stereolithography 1993: Epoxy Resins, Improved Accuracy & Investment Casting. *2nd European Conference on Rapid Prototyping & Manufacturing, Nottingham, England*, 15th-16th July, 1993. pp 95-113. Ed: P.M. DICKENS. ISBN 0 9519759 1 9
- 2 JACOBS, P.F. QuickCast™ 1.1 & Rapid Tooling. *4th European Conference on Rapid Prototyping & Manufacturing. 13th-15th June, Belgirate, Italy. 1995*. pp 1-27. Ed: P.M. DICKENS. ISBN 0 9519759 4 3

- 3 WIMPENNY, D. Rapid Prototyping: An Overview of the Technology Applied to Investment Casting. *8th World Conference on Investment Casting*. June 1993, p23-30.
- 4 DICKENS, P.M. *European Action on Rapid Prototyping (EARP) Newsletter*, No.6, July 1995. Pub: Danish Technology Institute.
- 5 HAGUE, R. & DICKENS, P.M. Stresses Created in Ceramic Shells Using QuickCastTM Models. *Solid Freeform Fabrication Symposium*, Aug 7-9, 1995, Austin, Texas. pp242-252
Ed: H. MARCUS
- 6 KOCH, M. Rapid Prototyping & Casting. *3rd European Conference on Rapid Prototyping & Manufacturing*., Nottingham, England, 6th-7th June 1994. pp 73-76.
Ed: P.M. DICKENS. ISBN 0 9519759 2 7
- 7 CORDES, J. 3D Systems QuickCastTM: How to assure success. *3D Systems Document*
- 8 BENHAM, P.P. & WARNOCK, F.V. *Mechanics of Solids and Structures*. pp 331-338
Published by Pitman International, ISBN 0 273 36186 4 .

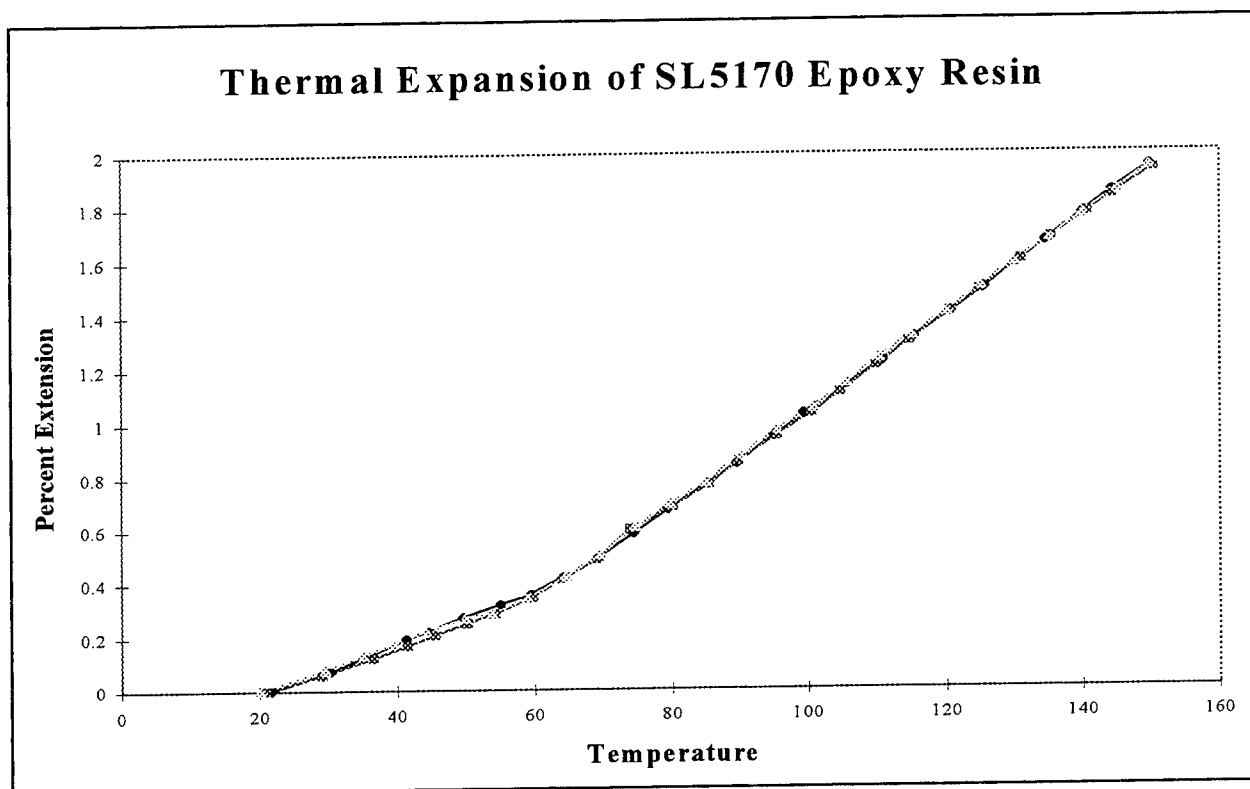


Figure 1

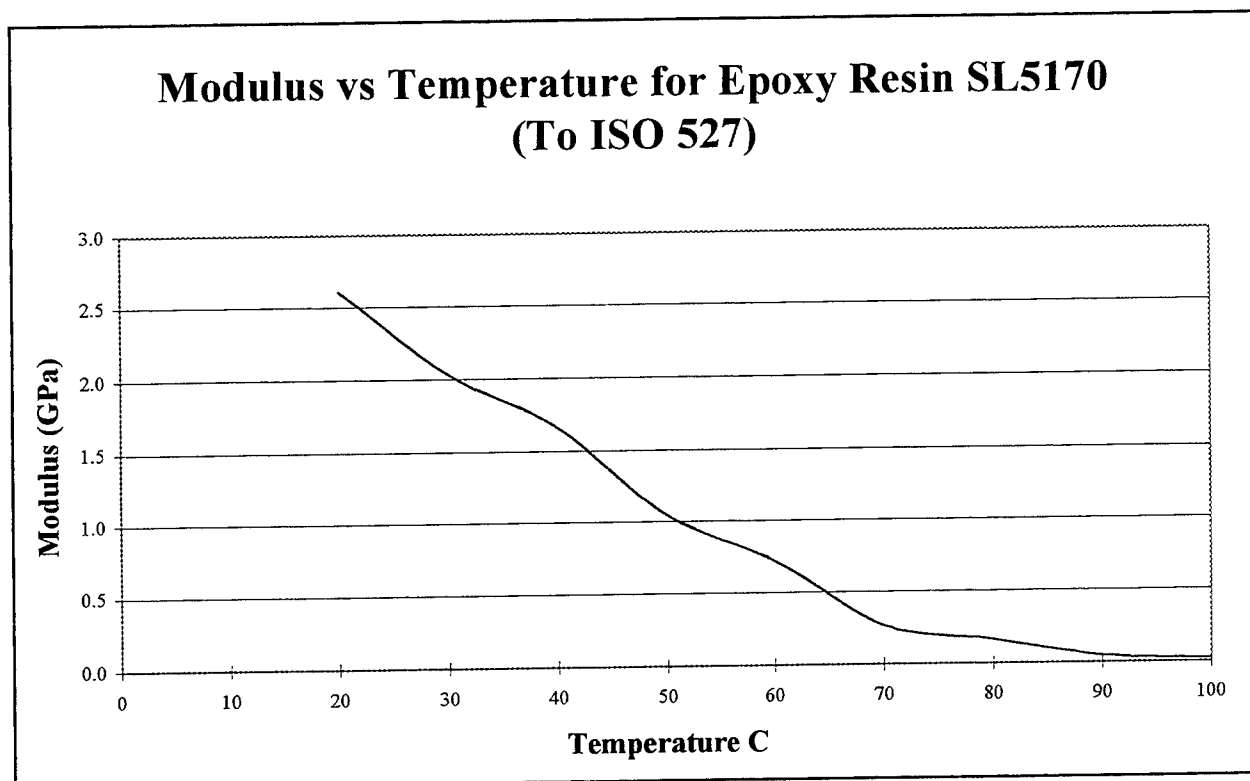


Figure 2

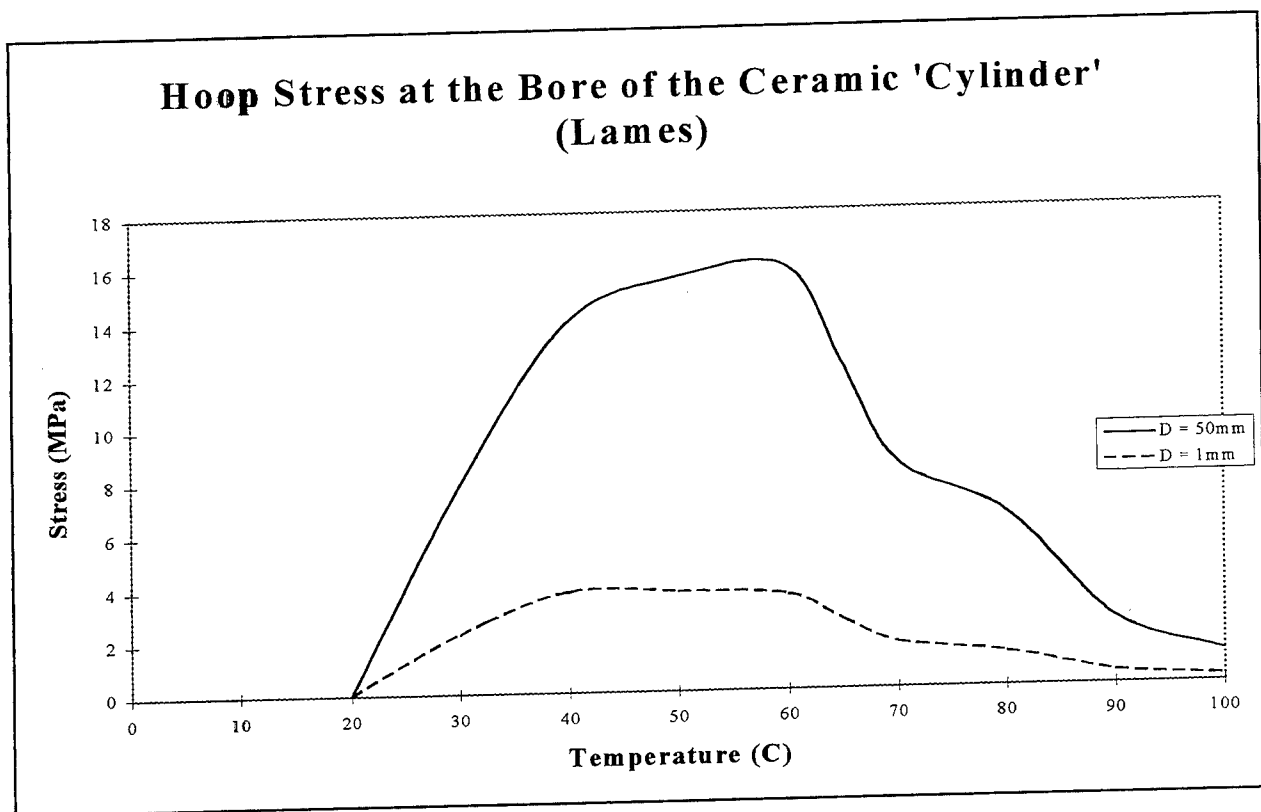


Figure 3

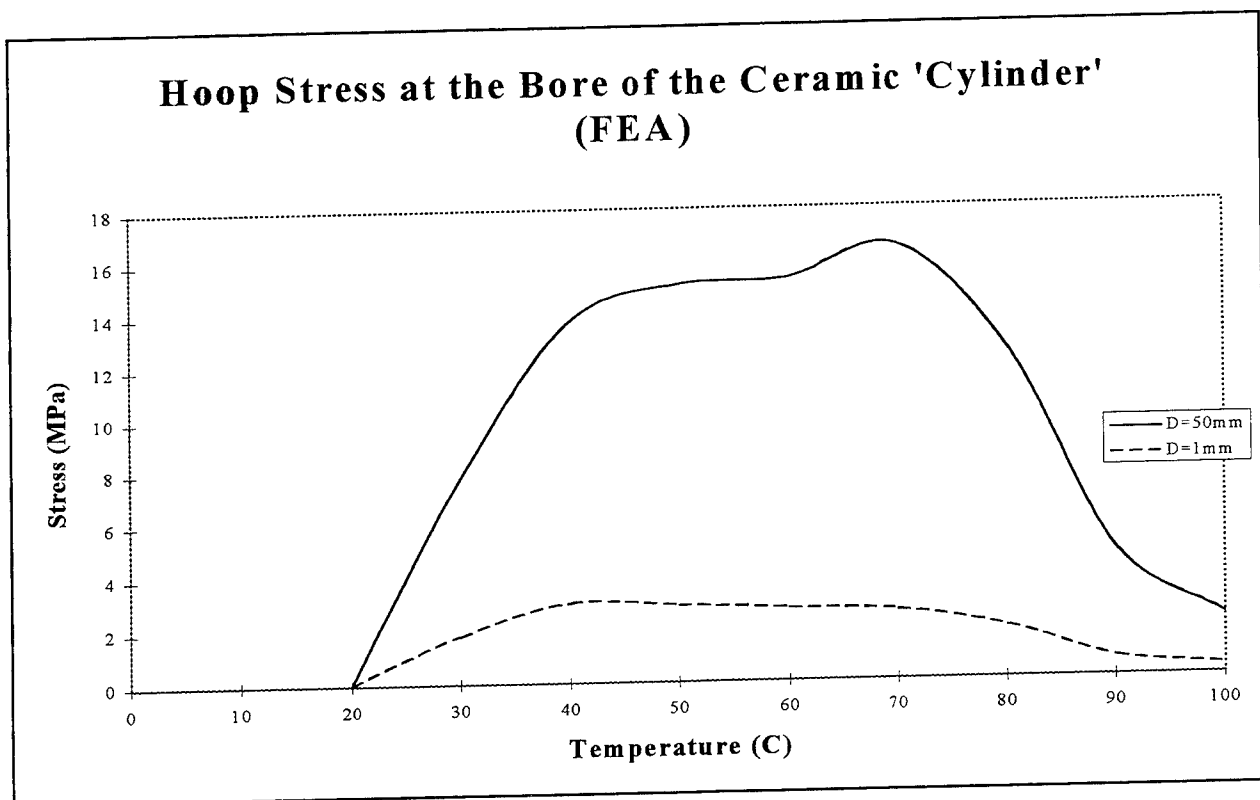


Figure 4

Schematic of FEA Model

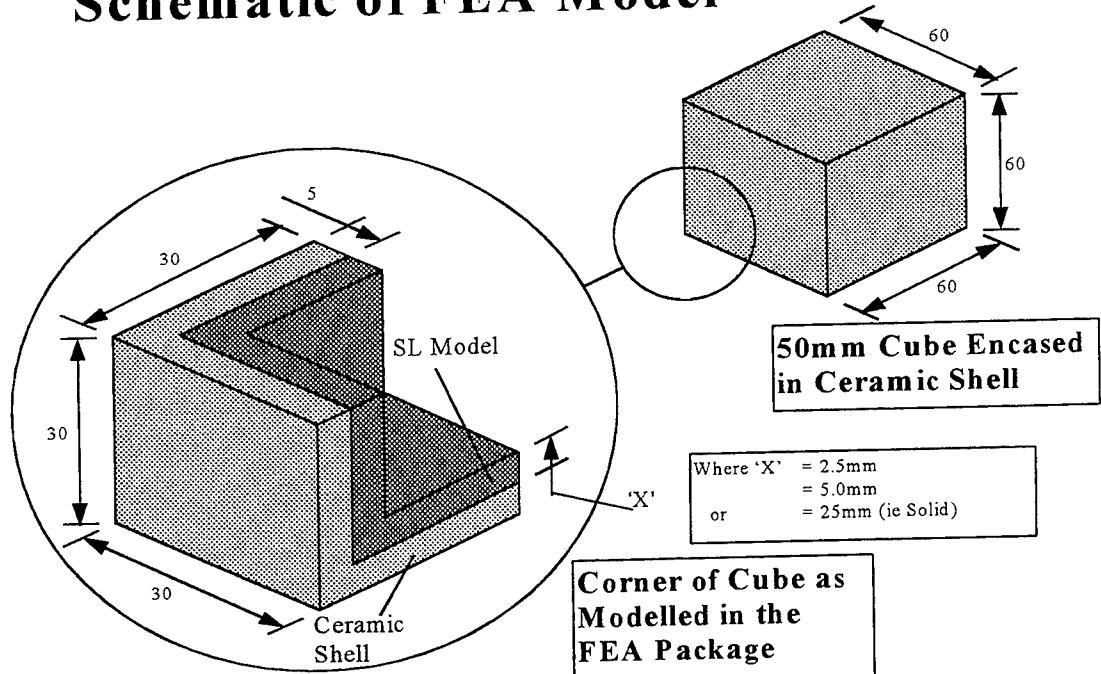


Figure 5

FEA Calculated Stresses in the Ceramic Shell Due to the Heating of the 50mm Block

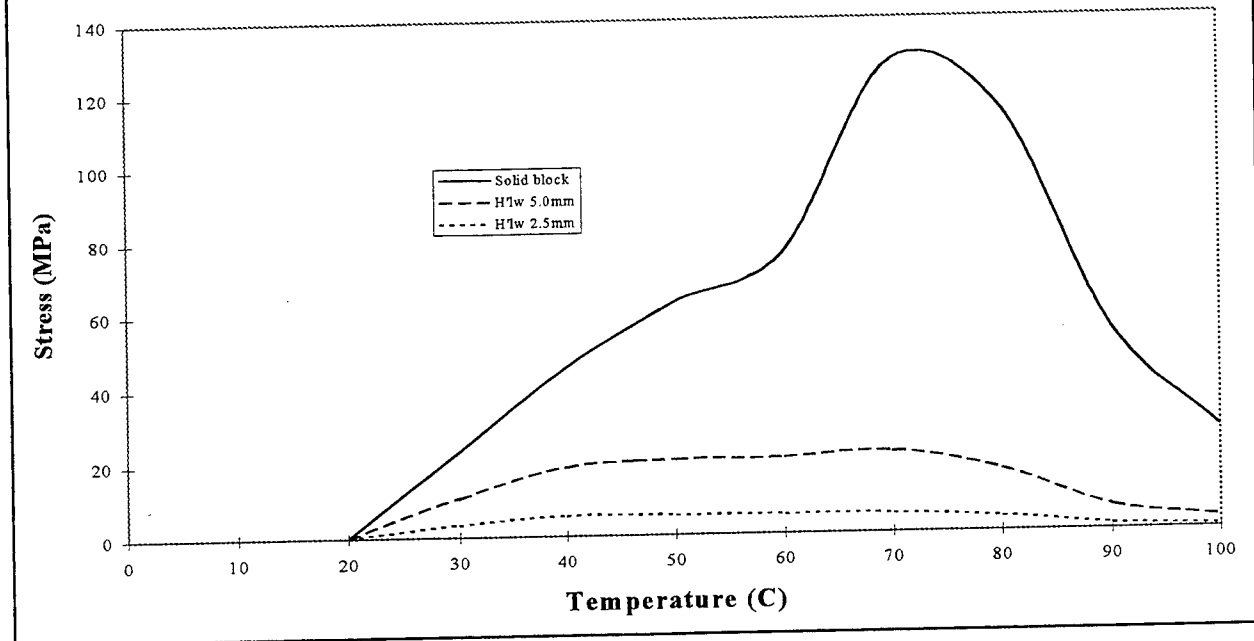


Figure 6

Example of Strain Gauging

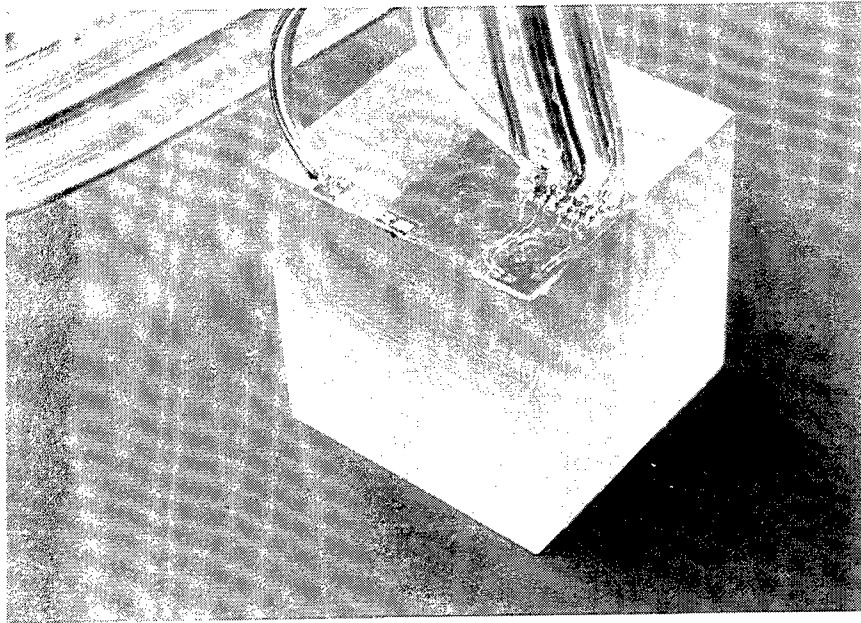


Figure 7

Strains Developed in Heated Solid Block

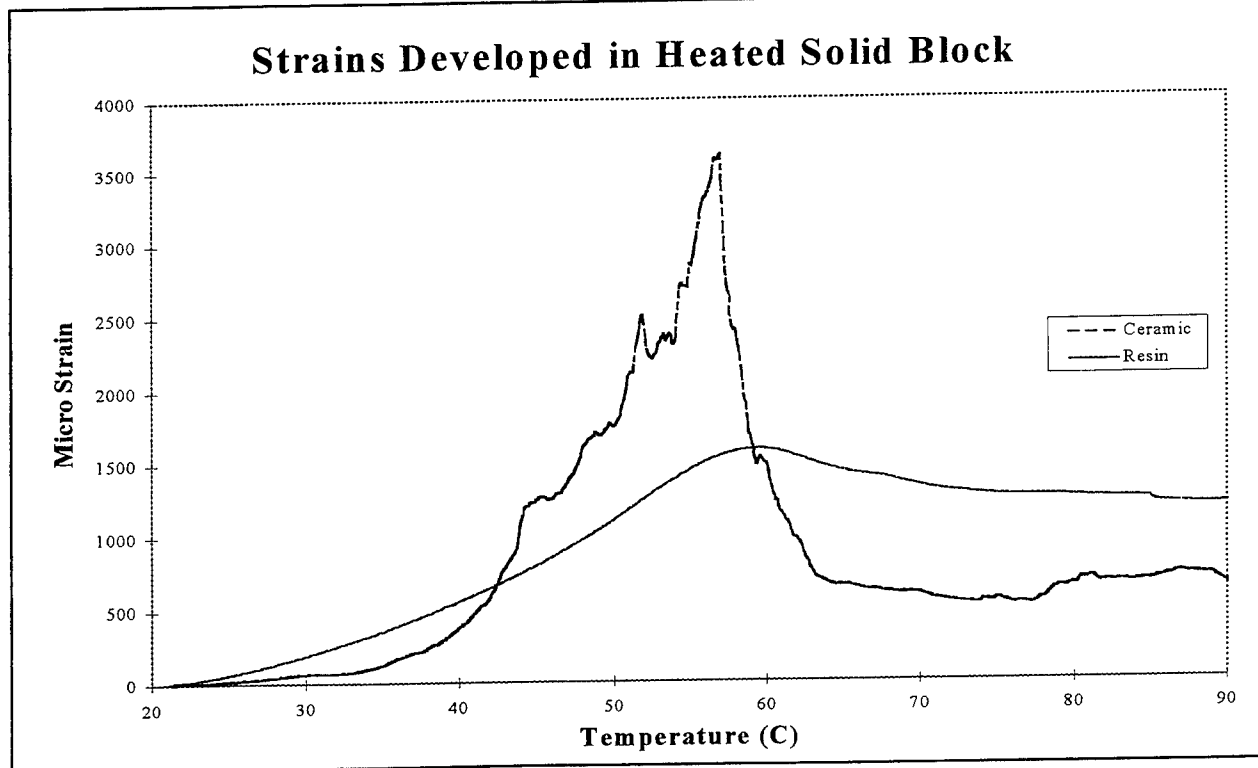
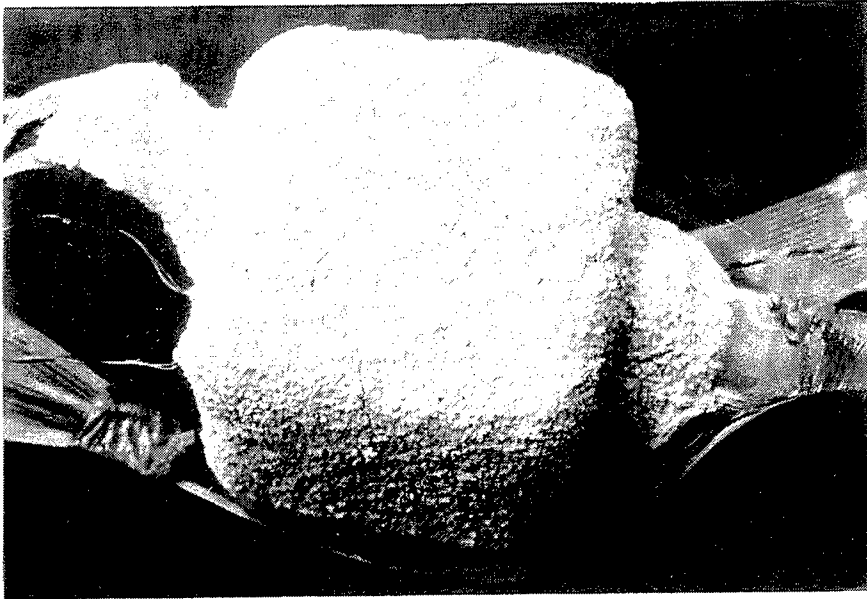


Figure 8

Shelled Solid Block After Oven Heating (Initial Strain Gauge Work)



Note that the cracks propagate from the centre of each edge. This is consistent with the FEA work previously done.

Figure 9

Strains Developed in Solid Cube During AutoClaving

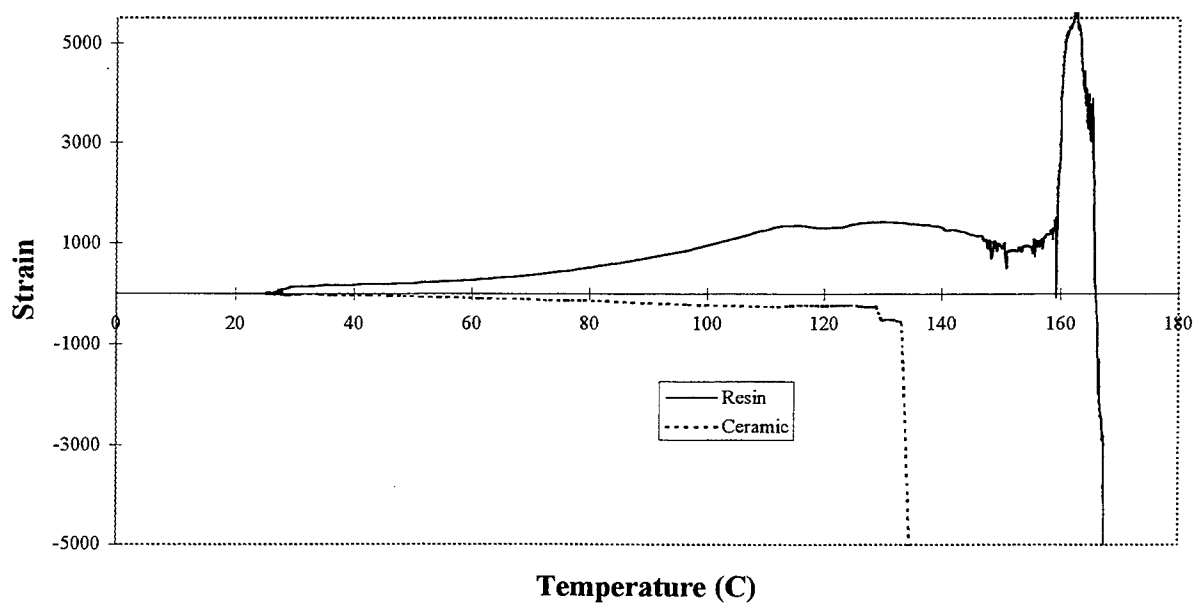


Figure 10

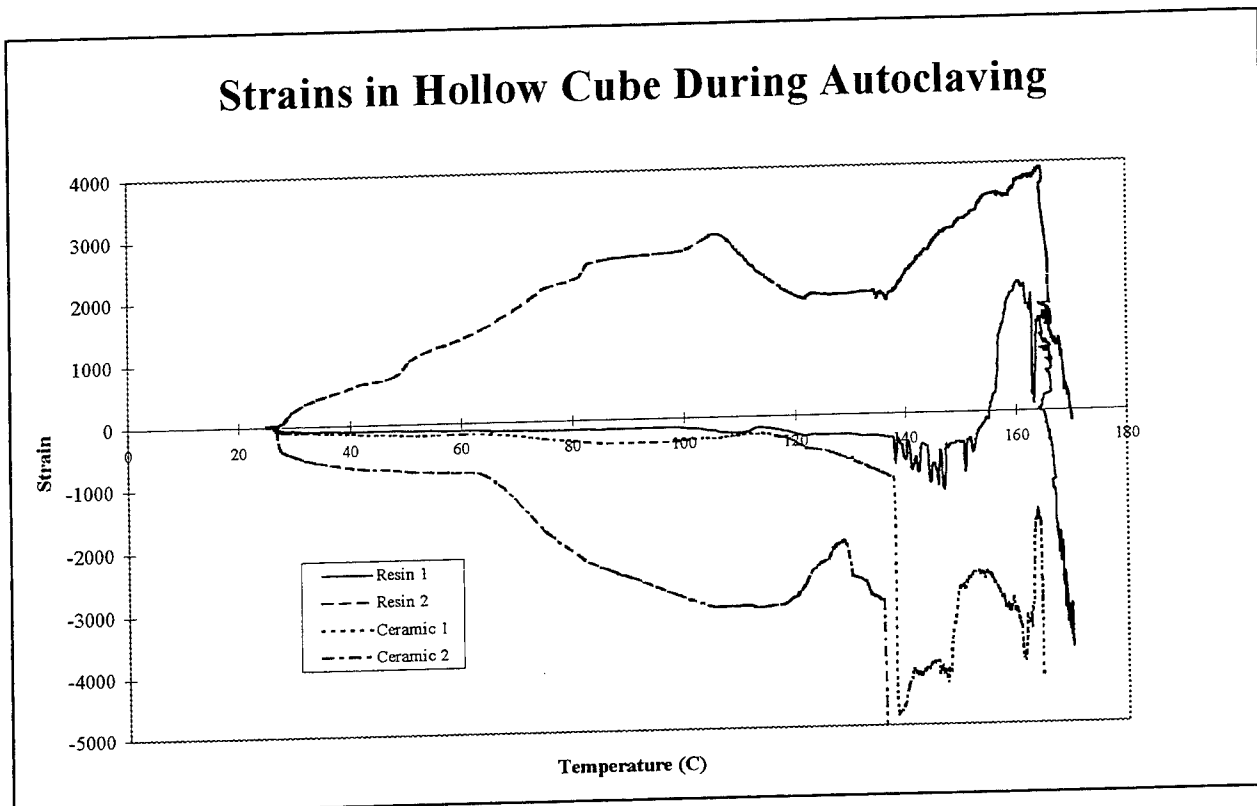


Figure 11

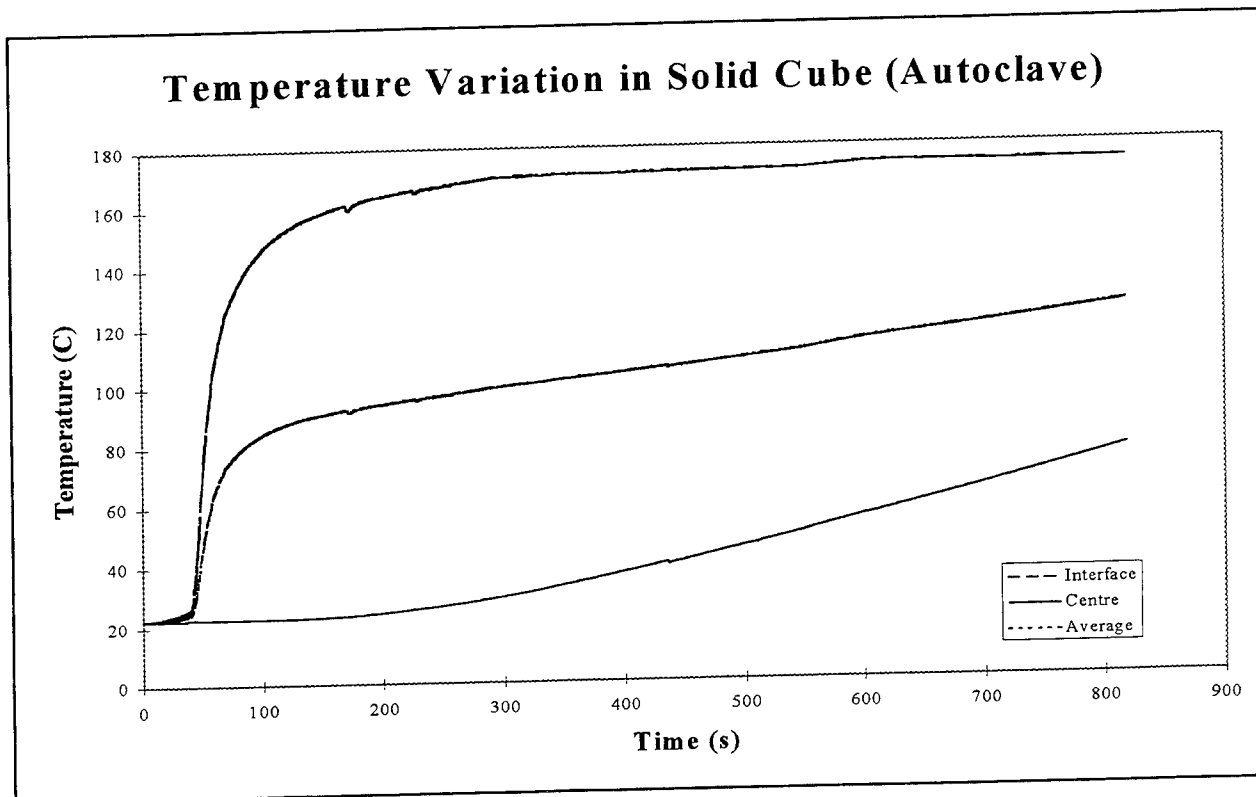


Figure 12

Shelled Cube after Autoclaving

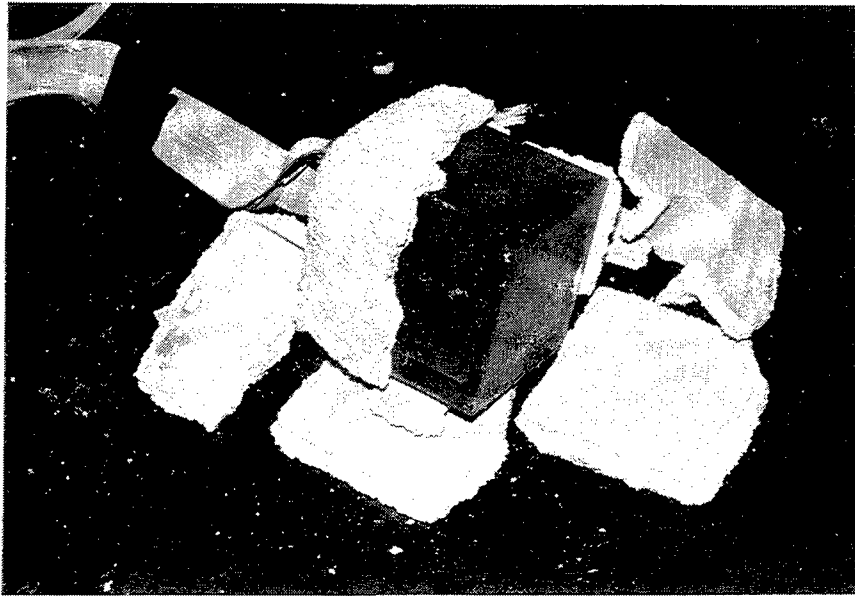


Figure 13

Temperature at Interface of Ceramic & Part (Initial Strain Gauge: Oven Heated)

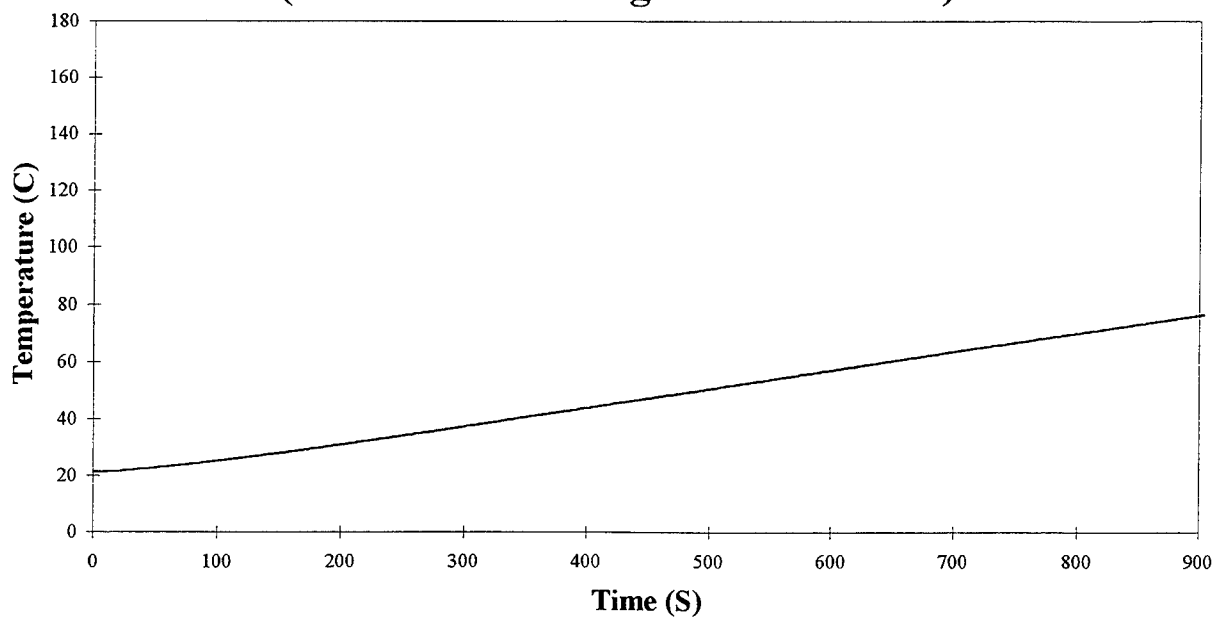


Figure 14

Part Quality Prediction Tools for Fused Deposition Processing

M. Atif Yardimci, Selcuk I. Guceri
Mechanical Engineering Department
University of Illinois at Chicago

Mukesh Agarwala , Stephen C. Danforth
Center for Ceramics Research
Rutgers University

Abstract

Fused Deposition process fabricates requested part geometries by sequentially depositing discrete curvilinear beads of material next to and on top of each other. The part integrity depends strongly on the bonding quality at the bead interfaces. Since diffusion bonding of thermoplastic components in the material system is thermally driven, temperature history of interfaces determine the bonding quality. Detailed thermal analysis of deposition region and layer building simulation for a model geometry have been performed to investigate local and global material behavior during processing. A simple transport property prediction model has also been developed for the determination of thermal transport properties of the particle loaded systems used in Fused Deposition. Based on the information obtained from thermal models, a computationally efficient part building model has been developed to predict bonding quality in the whole part. The model is driven by the same command file, *sml* file, that drives the Fused Deposition hardware; and hence is capable of replicating the building process. The model has been tested for a model geometry, spur gear, and three dimensional bonding quality distribution has been predicted for the part.

1. Introduction

Fused Deposition process has been available for a number of thermoplastic materials [1]. Recent research efforts have been directed towards production of ceramic and metallic green bodies with Fused Deposition technologies [2]. These green bodies then undergo binder burnout and sintering operations, which result in fully dense functional parts. Employment of particle filled material systems required hardware and software modifications for Fused Deposition, besides the ongoing development effort for fused deposition of neat thermoplastic materials [3].

As part of the ongoing development effort for fused deposition of particle filled systems, process analysis tools are being developed [4,5,6]. These tools will be instrumental in achieving relative materials selection and processing freedom in significantly large subsets of engineering materials space. The tools will also be utilized for manufacturability assessment, and part quality prediction purposes.

Present paper outlines the progress that has been made in the process analysis of road cooling and diffusion bonding phase of Fused Deposition. Next section describes a simple computational model, which is capable of predicting effective transport properties of particle loaded heterogeneous systems. Section three presents a detailed local model for thermal analysis of deposition region. Section four presents the semi-global heat transfer model for layer building, where the production of a whole layer is simulated. Section five outlines the heuristic part building model developed, which is capable of extracting geometrical information and process scenario out of the FD command file. Finally, conclusions are given in section six.

2. Thermal Conductivity Prediction

A simple numerical experiment has been devised to predict the thermal conductivity of particle loaded thermoplastic binder systems. A finite element model, which is capable of solving two-dimensional steady-state heat conduction equation on heterogeneous material systems, has been developed. A rectangular geometry has been chosen as the experiment geometry, Figure 1. Top and bottom sides of the rectangle are insulated, left boundary is kept at a constant temperature and constant heat flux boundary conditions are prescribed at the right boundary. A skin layer is generated along constant temperature and heat flux boundaries. Random pattern generators are utilized to generate random compositions for the specified particle volume percent.

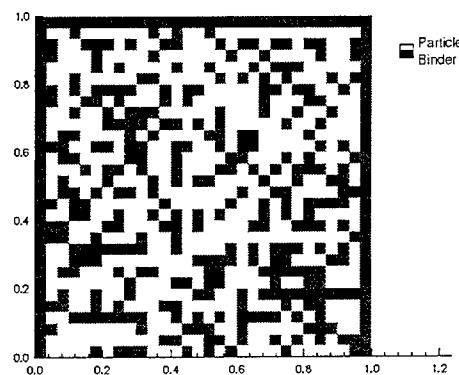


Figure 1. Sample Microstructure and Geometry

The heat transfer problem is solved, and average temperature is obtained for the constant heat flux boundary. Analytical solution for one-dimensional conduction problem is utilized to calculate the effective thermal conductivity of the part. The solution for a sample materials system is presented in Figure 2. Thermal conductivity prediction for

%56 has been validated with Modulated Differential Scanning Calorimetry for RU960, and the results are given in Table I.

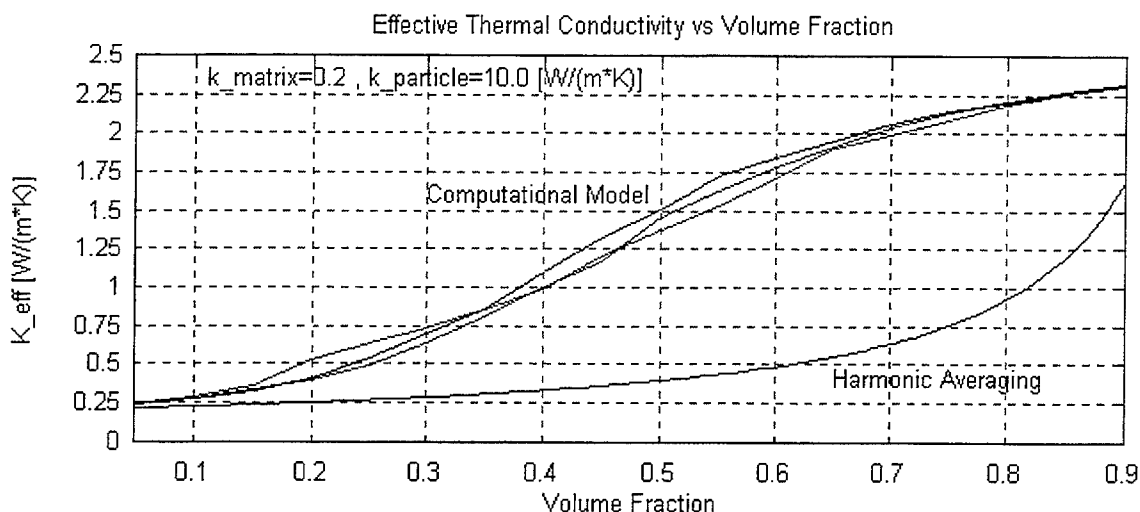


Figure 2. Dependence of Effective Thermal Conductivity on Particle Volume Fraction

Thermal Conductivities [W/(m*K)]	
Binder	Particle
0.1	20
Predicted Ke	Measured Ke
1.2 (+- 0.2)	1.17

Table I. Validation of Thermal Conductivity Model for RU960

It has been observed from simulations, that the effective material thermal conductivity is sensitive binder thermal conductivity. The dependence of k_{eff} on k_p , is weak especially for higher k_p to k_b ratios. Hence, a stainless steel particle loaded material system has more or less the same thermal conductivity of silicon nitride loaded material if particle volume fractions.

3. Detailed Thermal Analysis of Deposition Region

Current Fused Deposition hardware has been designed for thermoplastic material production. The liquefier temperature is set just above the viscosity drop temperature. Deposited material cools fast, forming a seam with previously deposited material. If the frame of observation is fixed with the deposition, it can be observed that the seam length and depth changes dynamically. For material systems loaded with particles to high volume fractions, and have the same thermoplastic materials binder; liquefier temperatures need to be elevated significantly (50 - 80 C) to enable FD of these materials. The modified rheology of the particle loaded materials necessitates this overheating. Magnitude of seam length and depth are changed significantly too due to the availability of the extra thermal energy.

A two-dimensional quasi steady-state thermal model has been developed to investigate the effect of process parameters as well as size effects on temperature distribution. It has been assumed that the deposition process takes place on an adiabatic table, previously deposited roads have been quenched to ambient temperature, and deposition head thermal dynamics may be replaced by a constant effective liquefier temperature and the worktable translating at a constant speed. Lateral cooling in z-direction may be represented by a sink term in the governing equation.

The governing equation becomes steady state two dimensional advection-convection equation with a convective cooling sink term. Constant ambient temperatures are specified at upstream boundary and no conduction boundary condition at the downstream boundary. Imperfect thermal contact is allowed between fresh road and substrate by defining a finite interface heat transfer coefficient, which makes the temperature field discontinuous across the interface. Constant effective liquefier temperature is assigned at deposition boundary, and convective cooling boundary conditions for the rest of the boundaries.

Finite volume method was used for discretization of governing equation as well as the boundary conditions. Upwinding methods have been utilized for the discretization of advective terms. Iterative solution schemes display relatively stable solution behavior due to the presence of sink terms in the governing equation.

Effects of process parameters on temperature distribution are described elsewhere [7]. Size dependence effects are depicted in this paper. Figure 3 shows the temperature distributions for three different number of roads in the substrate. RU960 material, with .508 mm road width and approximately 100 mm road length was simulated. Deposition speed was .5 "/s, ambient temperature was selected as 30 C, and effective liquefier temperature as 150 C. Empirical thermal properties have been used for RU960.

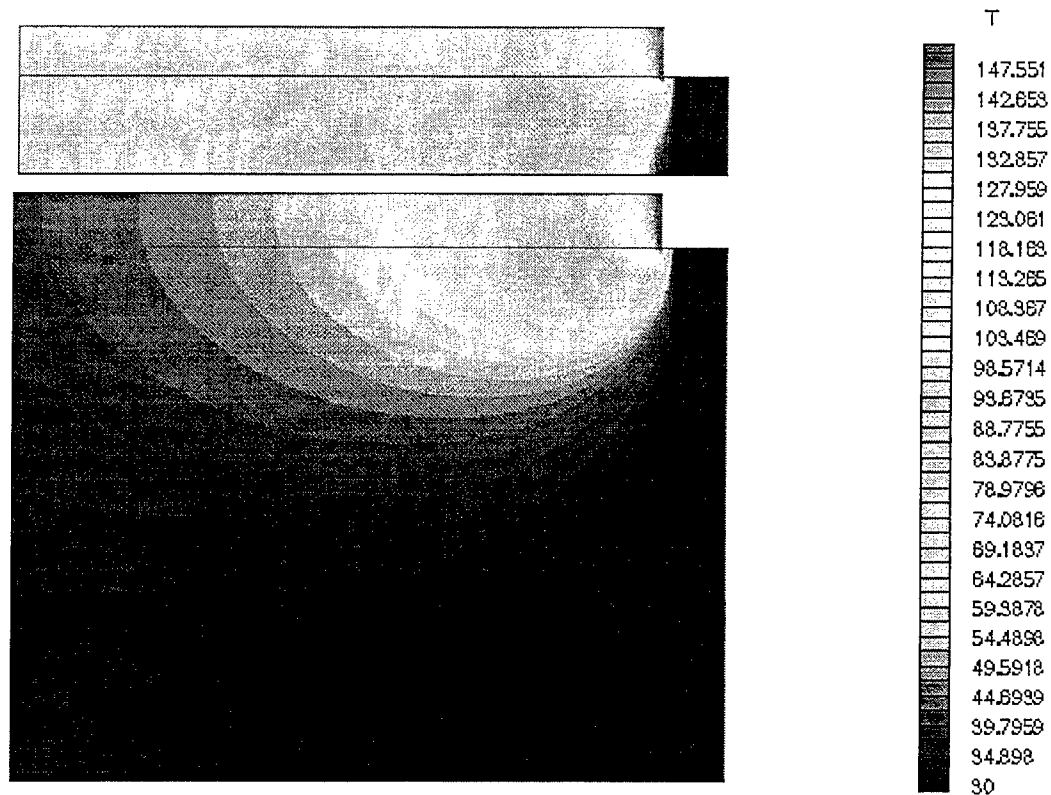


Figure 3. Temperature Distribution for Two and Ten Road Substrates

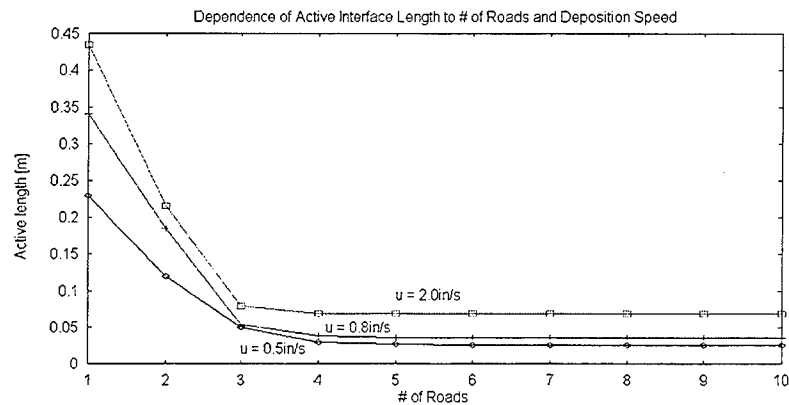


Figure 4. Size and Deposition Speed Dependence of Seam Length

Figure 4 shows the effect of deposition speed and substrate size on the seam length. The first two data points for each deposition speed curve have been interpolated from the available temperature data. The same figure also shows that the seam length becomes size independent for substrates which contain more than four roads. Hence the bonding enhancement per pass is greater for less populated road areas.

4. Layer Building Model

Although detailed information is produced through detailed local models, dynamic collective behavior of a roads that make up the part is also important. Previously developed [6] multi-road models have been extended to layer building model, incorporating perimeters/raster/grid style roads. For reasons of computational efficiency, the roads are idealized as one dimensional thermal entities, which are also capable of lateral thermal interactions with each other when brought together. Mathematical form of equations are the same as [6], bookkeeping algorithms needed to be developed for inclusion of perimeter and raster style roads. The temperature evolution of a sample rectangular layer, with long raster scans is shown in Figure 5.

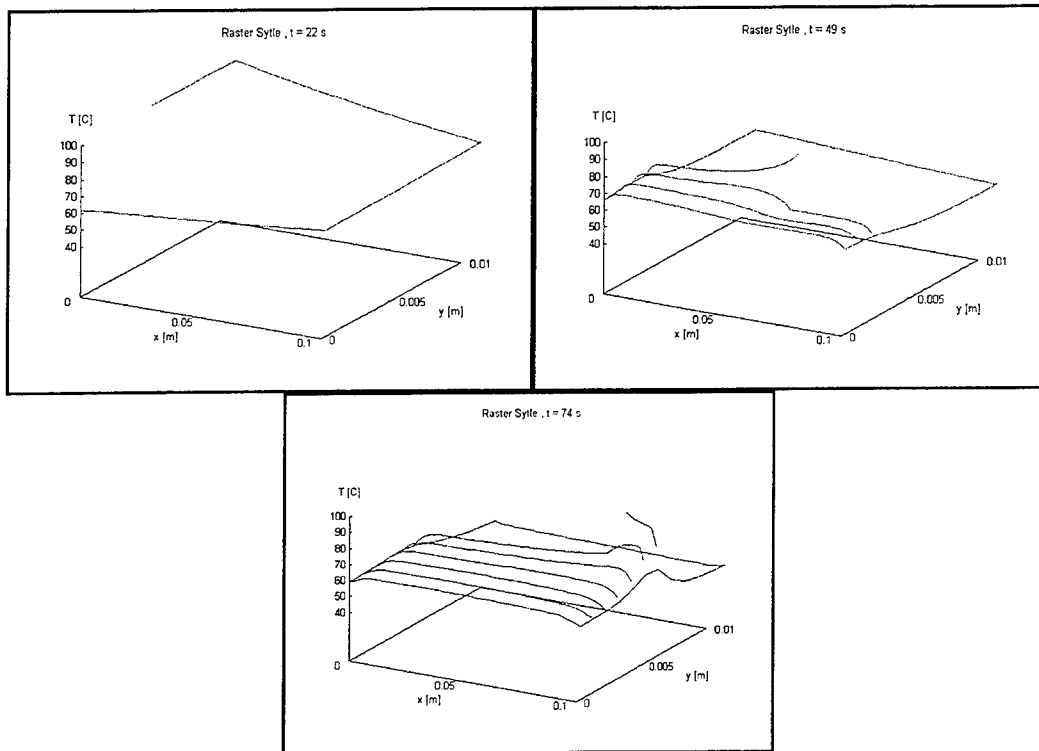


Figure 5. Temperature Evolution for Rectangular Layer Geometry

Temperature signatures shown in Figure 6, for long and short raster scans show different thermal paths the material points are experiencing. For long raster scans the material points that are at the center of the raster are visited twice as many times as the material points at raster ends; and the frequency of visits changes continuously along a raster line. For short raster lines on the other hand this effect becomes less pronounced, and the decoupling of material points occurs. Temperature measurements made with thermocouples, verified this behavior differences. Considering the geometrical complexity and arbitrariness of raster fills for real life parts, it is safe to hypothesize that different

material points in the layer may experience very different thermal histories during production.

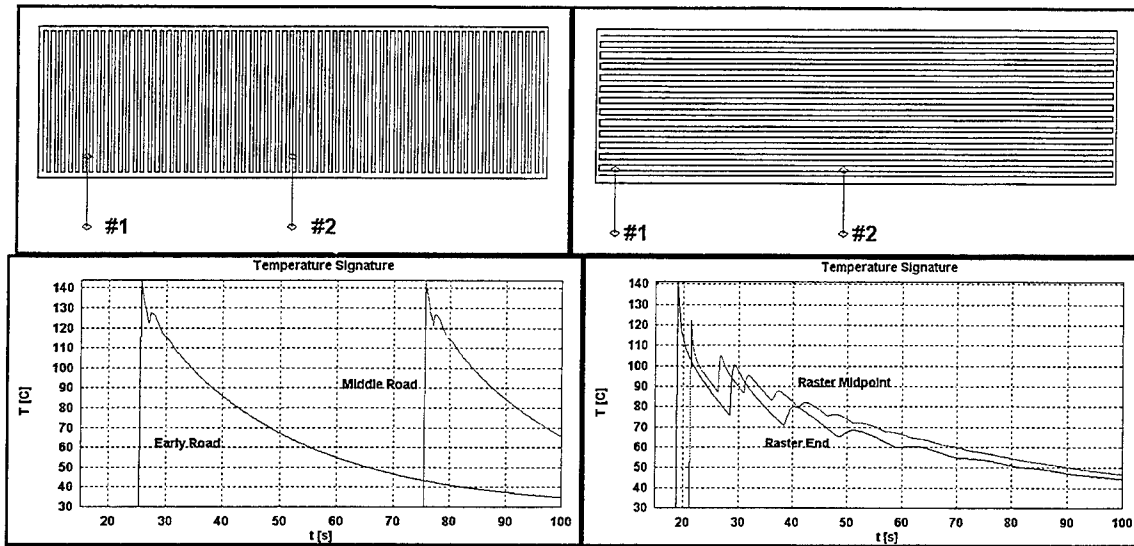


Figure 6. Temperature Signatures for Long and Short Rasters

5. Part Building Model

Thermal layer building model would be computationally expensive, if it would have been used for the simulation of production of whole part. All the geometrical information, and most of the process parameter information for the production of a given part is contained in an ASCII command file, *sml* file, which is sent to FD hardware controller for part production. Interpreter codes have been developed to extract geometrical and process parameter information out of this file, enabling the digital replication of building process. This replication capability introduced the possibility of detecting **internal** build errors.

It is assumed that bonding quality of interfaces in the part, is a monotonically increasing function of time spent above the critical bonding temperature and temperature differential. hence a heuristic geometrical model has been devised for part building simulation. The model may be summarized as :

1. An effect zone, bonding cloud, is attached to the deposition head during the production.
2. The shape of the cloud is allowed to change during the production, depending on the instantaneous process parameters and production scenario. For the simulation presented in this paper an ellipsoidal shape was utilized.

3. Bonding potential is null outside the bonding cloud. The bonding potential is maximum at the deposition tip, and decays exponentially with increasing distance from the deposition dip.
4. At each time step during the simulation, the material points which have already been produced and fall into the bonding cloud are detected.
5. The bonding metric at these material points is incremented by an amount determined by the local bonding potential distribution, and time step.
6. Time stepping is continued till the end of part building.

23 Layer Spur Gear

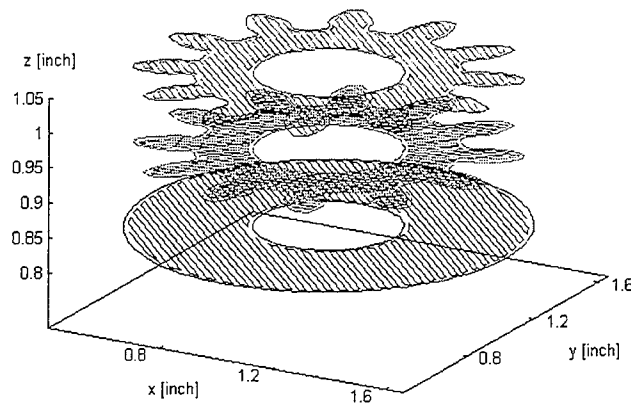


Figure 7. Geometry of Spur Gear, Layers 23, 12 and 1 (top to bottom)

A 23 layer spur gear geometry has been chosen as the test case. Selective layers of the part are shown in Figure 7. Figure 8 shows the corresponding bonding metric distribution in the depicted layers. The most important finding was the existence of bonding metric gradients across the part. Generally speaking topmost layers tend to have lower magnitudes bonding metric distributions. The absence or low levels of reheating due to subsequent layer deposition for top layers produces lower values for bonding metric. If on the other hand the spatial extent of bonding cloud was restricted to one interface, this gradient effect diminishes producing nearly uniform bonding metric distribution in z-direction. The bonding metric distribution in a given layer depends on the building style and how much time the deposition head spends at material points of interest.

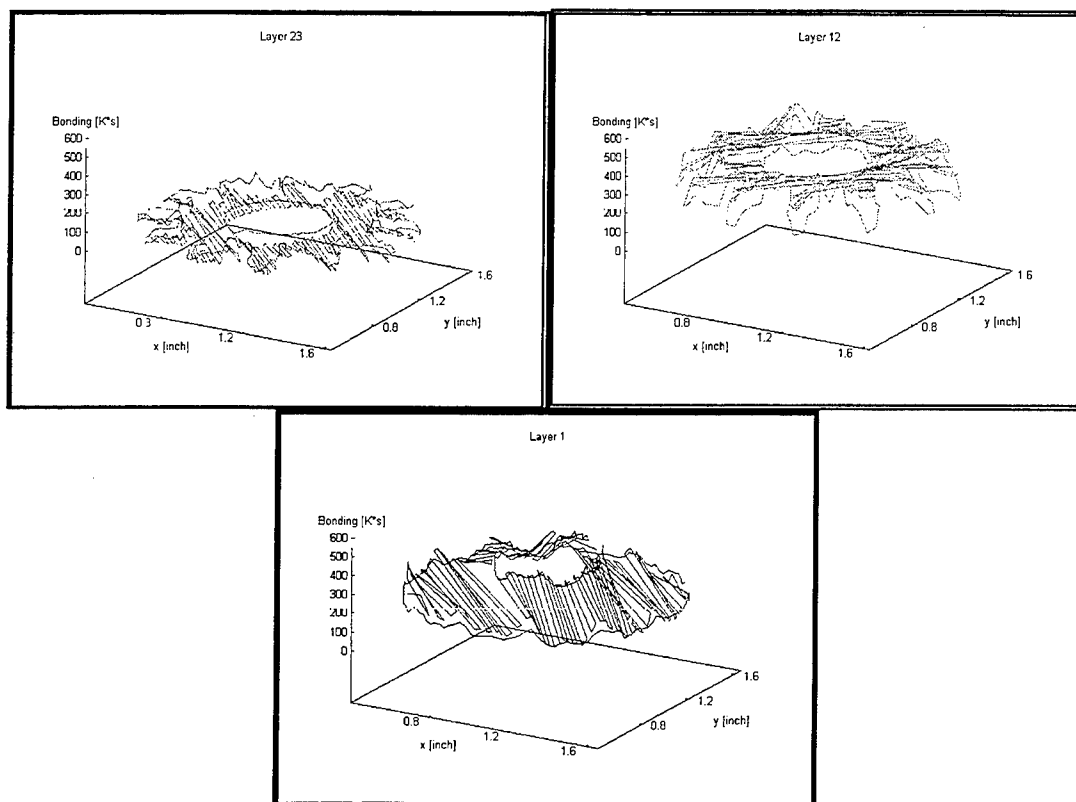


Figure 8. Bonding Metric Distributions for Layers 23, 12 and 1

6. Conclusions and Ongoing Work

Road cooling and bonding phase of Fused Deposition process has great influence on final part quality. Since green part quality effects the downstream operations of binder burnout and sintering, process analysis tools have been developed to understand and control this phase. A microstructure dependent transport property prediction tool has been developed for particle loaded systems. This prediction tool may be used to assess the thermal suitability of future binder and particle systems. Detailed thermal analysis of deposition region has been performed, and the effects of process parameters as well as substrate size have been quantified. It has been observed that the extent of remelt zone can extend as well as two road widths for materials systems of interest. An unsteady layer building model has been developed and employed for dynamic thermal behavior of a model layer geometry. Predicted temperature signatures show a variety of different cooling behavior categories even in a single layer. Also, temperature measurements have been performed with thermocouples to investigate the temperature signature of material points in multi-layer parts. Significant behavior differences have been found for different build styles. Since thermal simulation of whole part building is computationally expensive, a command file (*sml*) driven heuristic part building model has been developed. The model is tested using a realistic part, namely 23 layer spur gear. Model predicted bonding quality gradient between layers (poor bonding for top layers), and also within a given layer.

Nonisothermal bonding behavior of particle loaded material systems employed in FD is being assessed, to calibrate and validate bonding quality distributions predicted by part building model. Local deposition model is being extended into three-dimensions. Layer building model is also being extended to include up to four layers.

7. Acknowledgments

Current work is supported by ARPA/ONR Contract No. N00014-94-C-0115. Authors also would like to thank other members of SFF/Fused Deposition of Ceramics team, for their ideas, help and interest.

8. References

- [1] Comb J.W., Priedeman W.R., Turley P.W., "Control Parameters and Material Selection Criteria for Fused Deposition Modeling", Proceedings of The Fifth International Conference on Rapid Prototyping, pp. 163 -170, June 12-15 1994
- [2] Agarwala M., van Weeren R., Vaidyanathan R., Bandyopadhyay A., Carrasquillo G., Jamalabad V., Langrana N., Safari A., Garofalini S.H., Danforth S.C., Burlew J., Donaldson R., Whalen P., Ballard C., "Structural Ceramics by Fused Deposition of Ceramics", Proceedings of Solid Freeform Fabrication Symposium 1995, pp. 1-9, August 7-9 1995, University of Texas at Austin
- [3] Comb J.W., "Stratasys FDM Speed and Accuracy", May 1996,
<http://www.stratasys.com/sme96jc.html>
- [4] Yardimci M.A., Guceri S.I., Danforth S.C., "A Phenomenological Numerical Model for Fused Deposition of Particle Filled Parts", Proceedings of SFF Symposium 1995, pp. 189-190, U. Texas at Austin, August 7-9 1995.
- [5] Yardimci M.A., Guceri S.I., Danforth S.C., "Process Modeling for Fused Deposition of Ceramics", Ceramics Science and Proceedings, ACerS 1996 Cocoa Beach Meeting (in press).
- [6] Yardimci M.A., Guceri S.I., "Conceptual Framework for the Thermal Process Modeling of Fused Deposition", RP Internet Conference, December 15 - March 31 1996 via <http://www.mcb.co.uk/>
- [7] Yardimci M.A., "Two Dimensional Steady-State Road Cooling Model for Fused Deposition Process", December 1995,
<http://www2.uic.edu/~ayardi1/papers/ss2d/ss2d.html>

Selective Laser Sintering Part Strength as a Function of Andrew Number, Scan Rate and Spot Size

John Williams, David Miller and Carl Deckard
Clemson University
Clemson, SC 29634

Selective Laser Sintering has been modeled analytically and numerically, and studied experimentally. Further investigation is necessary to couple the results of modeling with experimental data. At Clemson University, numerical modeling of heat transfer phenomena is used to predict temperatures within the powder layer as a function of process parameters. Efforts are focused on delivering process speed up through improved process understanding. Initial modeling results and current understanding of the effects of process parameters on the strength properties of freeform parts produced by the SLS process are presented.

Objective

The objective of this work is to improve the understanding of the Selective Laser Sintering process in order to further improve the process by predicting "good" combinations of process parameters. Current work is focused on process understanding of heat transfer within the powder layer with process speedup as the most significant performance improvement priority.

Issues

One logical approach to process speed up is to increase the laser power and laser beam velocity proportionally. A practical limit to this approach has been found by SLS workstation operators. In fact, the maximum default laser power setting for processing of polycarbonate powder is 16-20 watts even though the commercial SLS workstations are capable of delivering about 2-3 times that power to the image plane. The energy delivery is limited due to an increase in the thermal gradient within the layer as the laser power is increased. The result is a greater peak temperature at the surface with a less significant average temperature rise within the layer. As the peak temperature increases, the heat lost by radiation increases. As velocity and power are increased the degradation temperature of the powder will be exceeded leading to a reduction in mechanical properties and a loss of energy.

Minimizing thermal gradients within the powder layer is a major process issue in SLS. Deckard [1] has proposed SLS process speed up through improved modeling and control of thermal gradients. Many research efforts, such as investigation into active energy delivery control [2], will benefit from development of a closed form model predicting physical properties of freeform parts as a function of the process parameters.

Previous Modeling

Selective Laser Sintering has been modeled analytically and numerically, and studied experimentally. Analytical modeling does not lead to a closed form solution if radiation or degradation is included. Numerical modeling and experimental studies lead to an understanding of the effects of input parameters on temperature within a layer and part strength among other physical properties. However, it is necessary to relate the results of such modeling to process understanding to produce an equation, or set of equations, for predicting part strength as a function of all the key input parameters taking into account all of the significant phenomena.

Nelson [3] has developed a relative measure of the energy density delivered to the image plane. The Andrew number, A_N , is the relative energy density defined as a function of three independent process parameters,

$$A_N \equiv \frac{P}{V \cdot HS} \quad (1)$$

where P is the laser power in [W], V is the laser beam velocity in [m/s], HS is the hatch spacing in [m] and A_N is measured in [J/m^2]. It has been shown that the energy density is useful for relating physical properties of parts built by SLS to the three independent process parameters [4]. In its simplest form, the energy density can be used to predict physical properties such as flexural strength, σ , by including an empirical constant, k_1 ,

$$\sigma = k_1 A_N \quad (2)$$

It is apparent that this model has some limitations. First, equation (2) predicts an extremely high flexural strength for parts produced at a very high laser power or a very low laser beam velocity. Clearly, this is not accurate. From this argument, one can see that this equation is only valid over a small range of energy density and that this equation is most useful for looking at the tradeoffs between the three independent process parameters that make up the Andrew number. Second, equation (2) does not directly account for re-radiation of the laser beam energy from the powder surface and energy lost during the time between successive scans. Third, equation (2) does not directly account for the effects of thermal degradation of the powder.

Designed experiments were conducted at Clemson University using polymer coated steel powder. Miller [5] developed a measure of build speed for the SLS process. The scan rate, SR , is defined as the area scanned by the laser beam per unit time,

$$SR \equiv V \cdot HS \quad (3)$$

where V is the laser beam velocity in [m/s], HS is the hatch spacing in [m] and SR is measured in [m^2/s]. By combining scan rate and an empirical constant, k_2 , with equation (2),

Miller determined the flexural strength of composite parts could be accurately predicted using equation (4),

$$\sigma = k_1 A_N - k_2 SR \quad (4)$$

Equation (4) demonstrates that a larger proportional increase in power is necessary to maintain a desired strength as scan rate is increased. This model is also only valid over a small range of energy density.

To improve understanding of the strength and physical properties of freeform parts produced by the SLS process, a model which accounts for losses due to radiation and thermal degradation in addition to the energy density is necessary.

Approach

General Overview: A finite difference heat transfer model is used to generate data relating maximum temperature at the surface and interior of the powder layer to input parameters. Data from the finite difference model and experimental data generated in the previous phase of the project are fit with equations of a form suggested by process understanding and research. Finally, experimental studies to verify the equation are conducted.

Finite Difference Modeling: A four element, one-dimensional finite difference heat transfer model with material properties which are assumed invariant with changes in temperature is used. Heat generated by previously scanned layers is ignored. The assumptions of one dimensional heat transfer and constant material properties has been shown to yield reasonable results [3,6]. The finite difference model is used to predict temperature profiles at the surface and three depths within the powder layer for a given set of material properties and process parameters. The general validity of the finite difference model was confirmed by comparing results from the one dimensional conduction model presented by Mendez [6]. For this study, laser power, laser beam velocity, scan spacing, scan line length and laser beam spot size are the five independent process parameters of interest.

Determining the Equation: The maximum temperature reached at each node for a combination of process parameters is recorded. A candidate equation with unknown coefficients is proposed based on process understanding. An unconstrained nonlinear optimization routine is implemented to fit the proposed equation to the simulation data determining the unknown coefficients.

Modeling Results

For the purpose of demonstration a base case is chosen using polycarbonate powder and typical process parameters listed in Table 1.

Case	Radius, R [m]	Power, P [W]	Velocity, V [m/s]	Hatch Spacing, HS [m]	Length, L [m]	Energy Density, A_N [J/m ²]
1	1.53E-4	18	1.64	5.10E-5	2.54E-2	2.15E+5
2	5.08E-4	36	1.64	1.02E-4	2.54E-2	2.15E+5

Table 1. Base case process parameters

Figure 1 shows the temperature profile for the four nodes in the finite difference model using the small laser beam spot size and the process parameters listed as case 1. In this figure the temperature at the surface is represented by the temperature at node 1, T1, and the temperature within the layer is represented by the interior node temperatures in order of increasing depth, T2, T3 and T4. Figure 2 shows the temperature profile for the same four nodes using the large laser beam spot size and the process parameters listed as case 2. It should be noted that case 2 using the large spot size has twice the scan rate, twice the number of exposures to laser beam irradiation, the same energy density and a small reduction in the peak temperature as compared to case 1 using the small spot size.

Figures 3 and 4 show the maximum temperature attained at each node while varying laser power for case 1 and 2 respectively. The figures show a linear increase in both the maximum temperature at each node and the thermal gradient with an increase in power. An overall reduction in the thermal gradient is shown for the case using the large spot size.

Figures 5 and 6 show the maximum temperature attained at each node while varying laser beam velocity for case 1 and 2 respectively. The figures show a nonlinear decrease in maximum temperature at each node as well as a decrease in the thermal gradient within the layer as laser beam velocity is increased. An overall reduction in the thermal gradient is shown for the case using the large spot size.

For the purpose of modeling, interior node 3 is used to represent temperature within the layer. Figures 7 and 8 show the maximum temperature attained at node 3 as a function of velocity for four different energy density values. In order to maintain a constant energy level, power and velocity are varied proportionally and hatch spacing is constant. The plots show that the maximum temperature attained at node 3 is constant over the range of velocity at each energy density. Therefore, equation (2) is adequate for predicting temperatures in this region. The dashed lines are the results from fitting equation (2) to the data represented in figures 7 and 8. This result is contrary to expectations. Studies have shown a great dependence of physical properties in SLS parts on the velocity, scan line length and time delay between scans [5,7]. Figures 7 and 8 seem to indicate little dependence of temperature on radiation. This leads one to believe that thermal gradients and thermal degradation have a greater influence on the physical properties of freeform parts than energy loss due to radiation.

Conclusions

Current modeling of strength properties of freeform parts built by the SLS process was presented. Further investigation into coupling experimental results with numerical modeling have been initiated. A numerical model for predicting temperature profiles within a powder layer was implemented successfully. Initial results show process parameter effects on maximum temperature. It can be concluded from the results presented that thermal gradients within the layer can be reduced and scan rate increased using the large laser beam spot size.

Contradictions between model results and process experience indicate a need for expanding the numerical model to include temperature dependence of the material properties and losses due to thermal degradation. More work is necessary to define an explicit equation which yields insight into the effects of process parameters on the development of thermal gradients and mechanical properties of SLS freeform parts.

References

1. Deckard, C., Miller, D., *Energy Delivery for Selective Laser Sintering: Issues and Directions*, Solid Freeform Fabrication Symposium, Austin, Texas, 1995
2. Benda, J., *Temperature Controlled Selective Laser Sintering*, Solid Freeform Fabrication Symposium, Austin, Texas, 1994
3. Nelson, J. C., *Selective Laser Sintering: A Definition of the Process and an Empirical Sintering Model*, Ph.D. Dissertation, University of Texas at Austin, Austin, Texas, 1993
4. Vail, N. K., *Silicon Carbide Preforms for Metal Infiltration by Selective Laser Sintering of Polymer Encapsulated Powder*, Solid Freeform Fabrication Symposium, Austin, Texas, 1993
5. Miller, D., *Design and Evaluation of a Selective Laser Sintering Process for Enhanced Speed through Variable Beam Spot Size*, Clemson University, Clemson, SC, 1995
6. Mendez, P., *Modeling of selected SFF Process Limits*, Solid Freeform Fabrication Symposium, Austin, Texas, 1994
7. Terala, K., *Feed Forward Geometric Compensation for Selective Laser Sintering*, M.S. Thesis, Clemson University, Clemson, SC, 1996

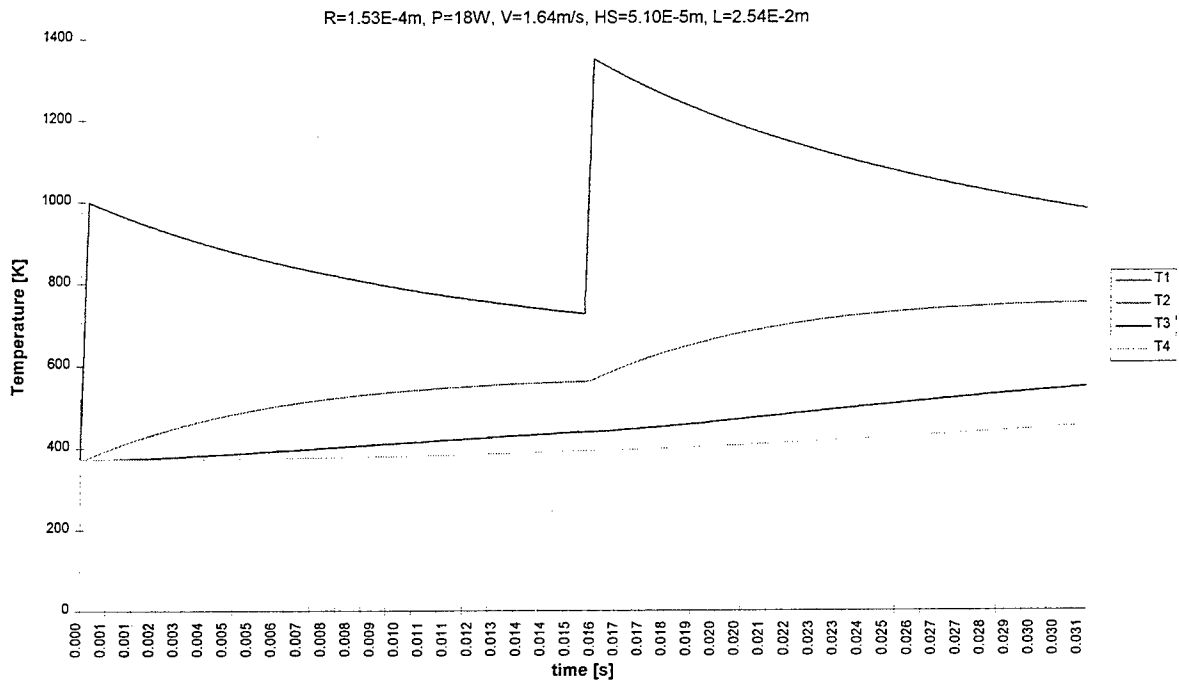


Figure 1. Temperature profile within a single layer for case 1 using the small spot size

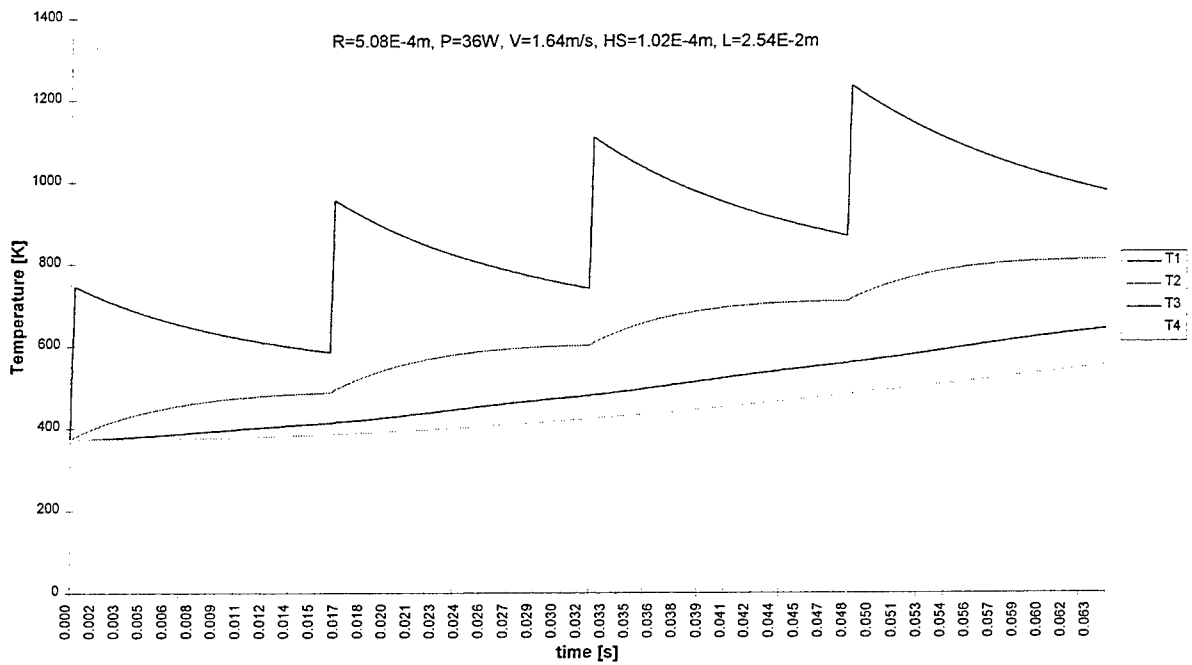


Figure 2. Temperature profile within a single layer for case 2 using the large spot size

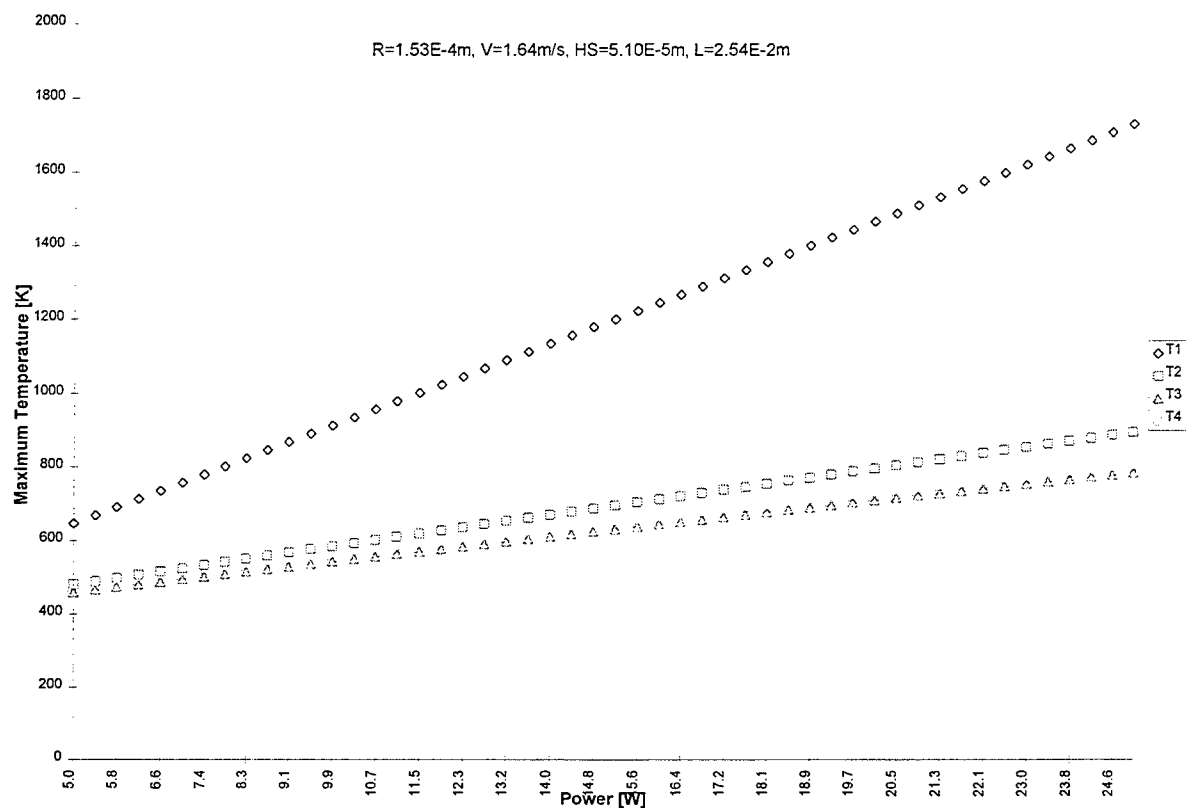


Figure 3. Plot of maximum temperature attained within a layer varying power using the small spot size

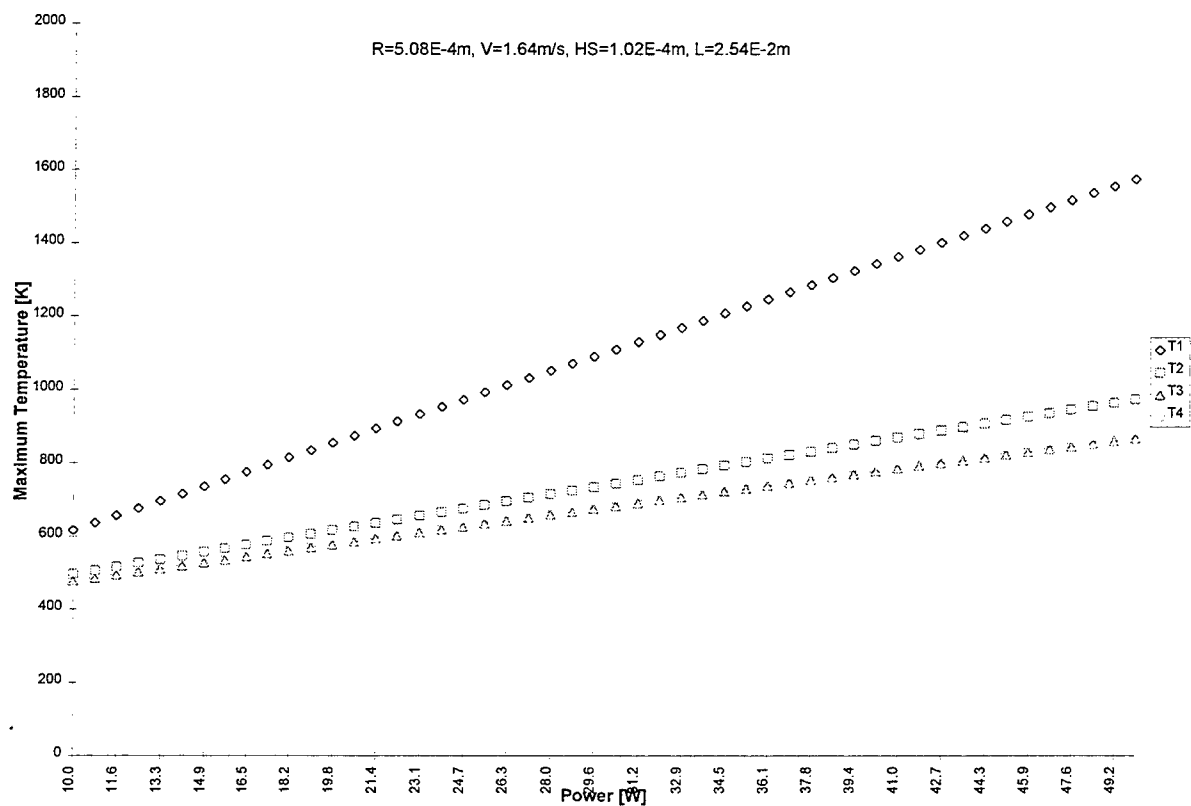


Figure 4. Plot of maximum temperature attained within a layer varying power using the large spot size

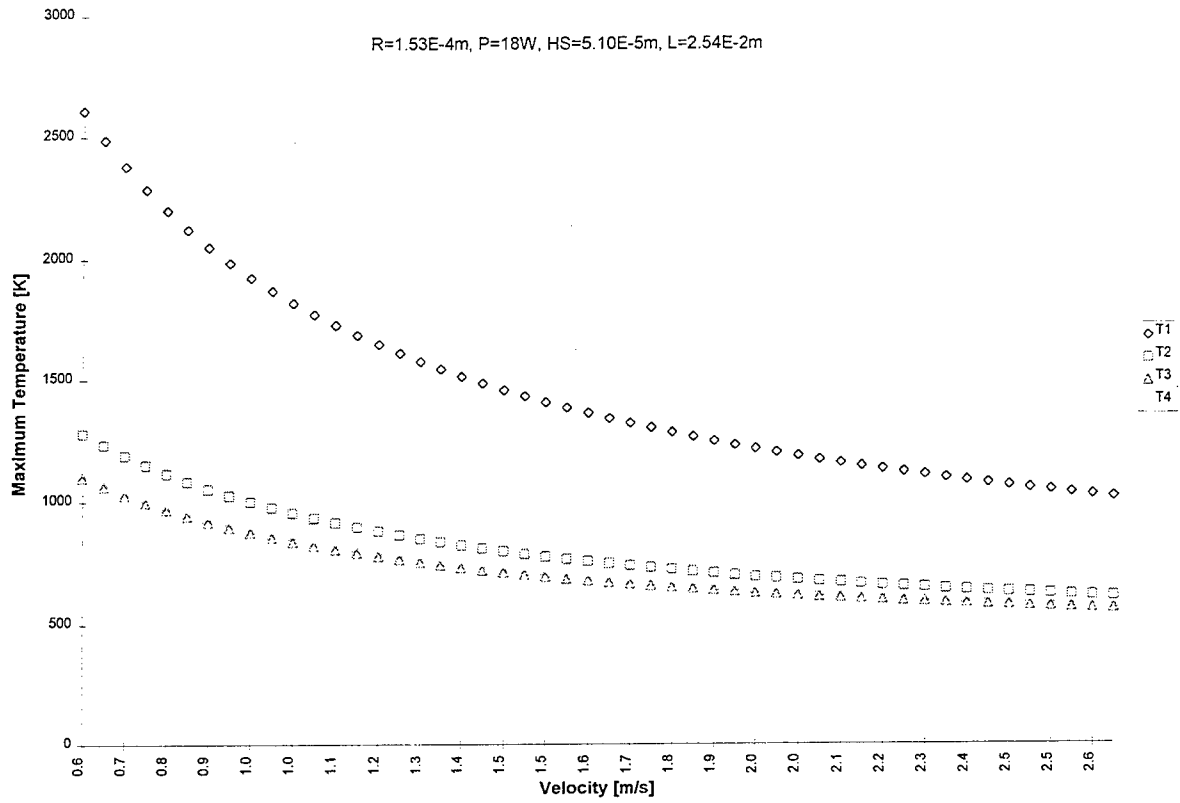


Figure 5. Plot of maximum temperature attained within a layer varying velocity using the large spot size

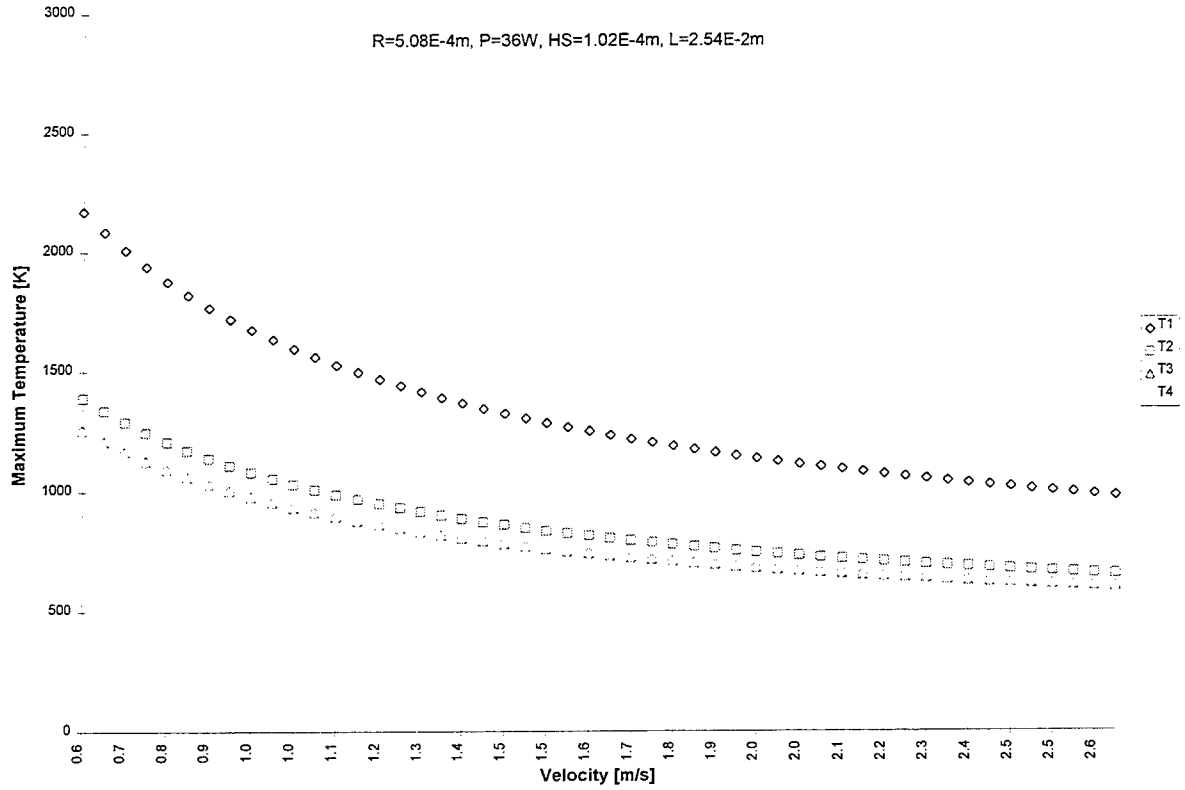


Figure 6. Plot of maximum temperature attained within a layer varying velocity using the large spot size

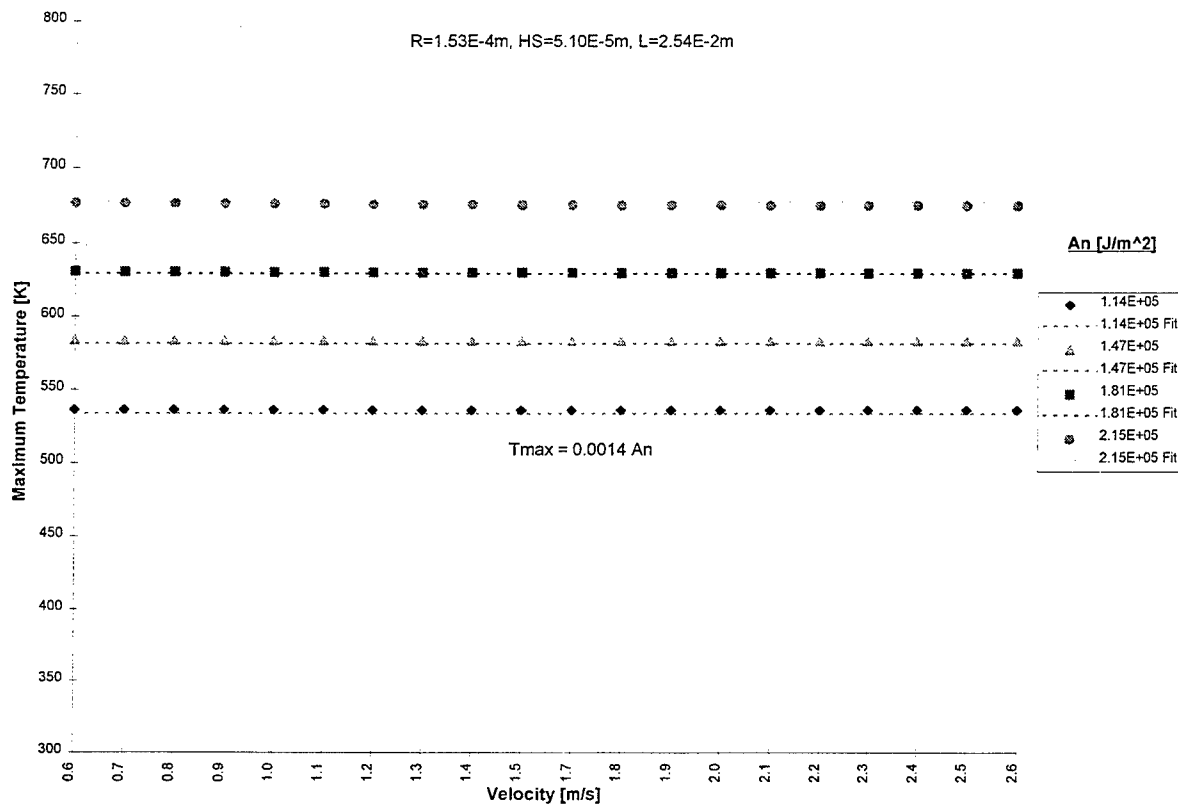


Figure 7. Plot of maximum temperature varying velocity and power for constant energy density using the small spot size

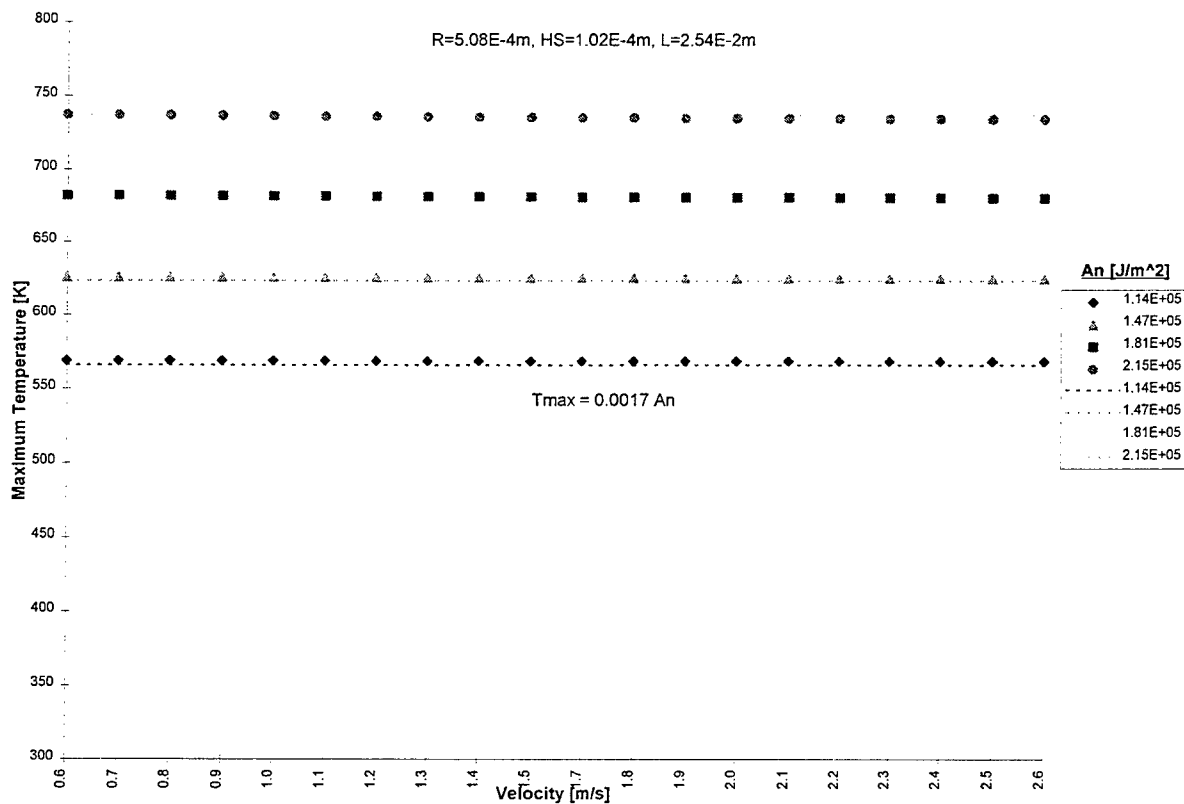


Figure 8. Plot of maximum temperature varying velocity and power for constant energy density using the large spot size

Finite Element Analysis of Curl Development in the Selective Laser Sintering Process

K.W. Dalgarno, T.H.C. Childs, I. Rowntree & L. Rothwell

Department of Mechanical Engineering, University of Leeds, Leeds, LS2 9JT, UK.

Abstract

The work reported within this paper is concerned with the development of analytical procedures which will allow the accuracy of parts generated by selective laser sintering to be predicted. One source of inaccuracy is curl, which results in curved part edges of flat plates manufactured lying horizontally in the part bed. This paper reports on the use of finite element techniques to model the development of curl. The models have been validated through comparison of f.e. results with the results of experimental builds, and extended to allow the influence of "bases" on the development of curl to be examined.

1. Introduction

Curl in selectively laser sintered parts arises mainly from thermal distortion of parts within the build volume during processing. This results in nominally flat surfaces which lie horizontally in the part bed becoming warped. Figure 1 shows schematically how a nominally rectangular 90 x 26 mm, 50 layers thick polycarbonate plate made by SLS will exhibit curl.

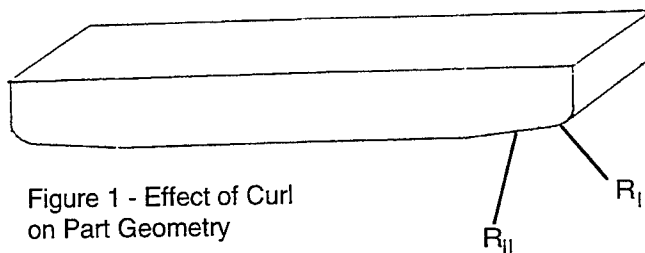


Figure 1 - Effect of Curl on Part Geometry

Previous work [1] has identified different regions of curl within a part. A microscopic amount of curl exists as a result of the definition which can be expected from the process. Thereafter the curl can be divided into two effects. The first of these appears over approximately the 2.5 mm of part closest to the edge of the part and on parts of with the geometry shown in Figure 1 has a radius (R_I in Figure 1) of around 20 mm. The second extends from the end of R_I approximately 10 mm further towards the centre of the part and has a radius (R_{II} in Figure 1) of around 60 mm. R_I curl has been seen to exist from the sintering of the first layer in part build, while R_{II} curl seems to develop as layers are added to the part. This paper reports on the use of the finite element method to analyse the development of R_{II} curl in rectangular polycarbonate plates made by the SLS process on a DTM Sinterstation 2000. One particular area of interest was the localised nature of the curl: previous work had failed to identify any reason why the curl should be confined to the part edges.

Previous work also investigated the effect of bases on R_{II} curl. Figure 2 shows results from an experimental investigation into the effect of the power input to the base, $[P/(Us)]_{base}$, on the resulting R_{II} curl. The graph in Figure 2 suggests that bases have no effect on R_{II} curl until the base is sufficiently dense to offer some restraint, but that thereafter no additional benefit is derived by further increasing the density of the base. The reasons for this were not fully understood and a further aim of the finite element work was an investigation of this effect.

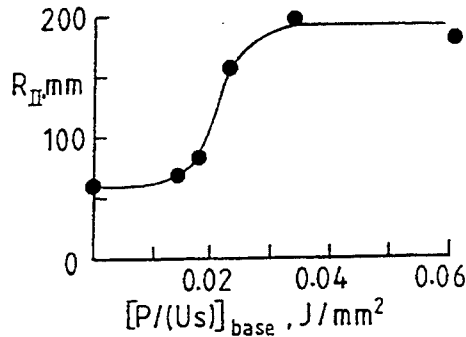


Figure 2 - Effect of Energy Input to Base on R_{II} Curl. From [1].

The finite element method has previously been used by Bugeda et al [2] to study curl development in the stereolithography process. They concluded that curl in stereolithography arose from volumetric shrinkage of the resin when cured. There are seen to be two mechanisms for curl development within selectively laser sintered parts. The first of these is shrinkage as a result of the sintering process, and the second is a thermal strain which results from powder to form the next layer being deposited on the most recently scanned layer. The fresh powder layer is at a lower temperature than the scanned layer, and so will produce some thermal contraction within the scanned layer. Both of these mechanisms result in compressive strains in the layers as they are built. The approach taken within the work reported here has been to use the finite element method to model part build by adding layers of elements to represent the addition of material to a part, and introducing compressive strains into the layers as they are added.

2. Finite Element Model of Part Build

The finite element solver used within the work described here was ABAQUS/Standard [3].

2.1 Geometry

Figure 3 shows the finite element mesh used within the analysis. The mesh represents the first 10 layers of the 90 x 26 mm rectangular polycarbonate plate part described above. All layers excepting the first two have a thickness of 0.125 mm, which was the default layer thickness within the manufacture of the parts. The first layer has a thickness of 0.66 mm, and the second a thickness of 0.25 mm. These thicknesses are based on measurement of layer thickness on one and two layer parts with the same cross sectional area. Further measurements indicated that subsequent layers were the expected 0.125 mm deep. The additional thickness in these first two layers is as a result of "bonus z", whereby additional material is sintered early in the build as a result of large thermal penetration into the part bed. The model was symmetric about the centre of the plate, and so only half the plate has been modelled. 2D analysis was used as it was the distortion along the 90 mm length of the plate that was of interest.

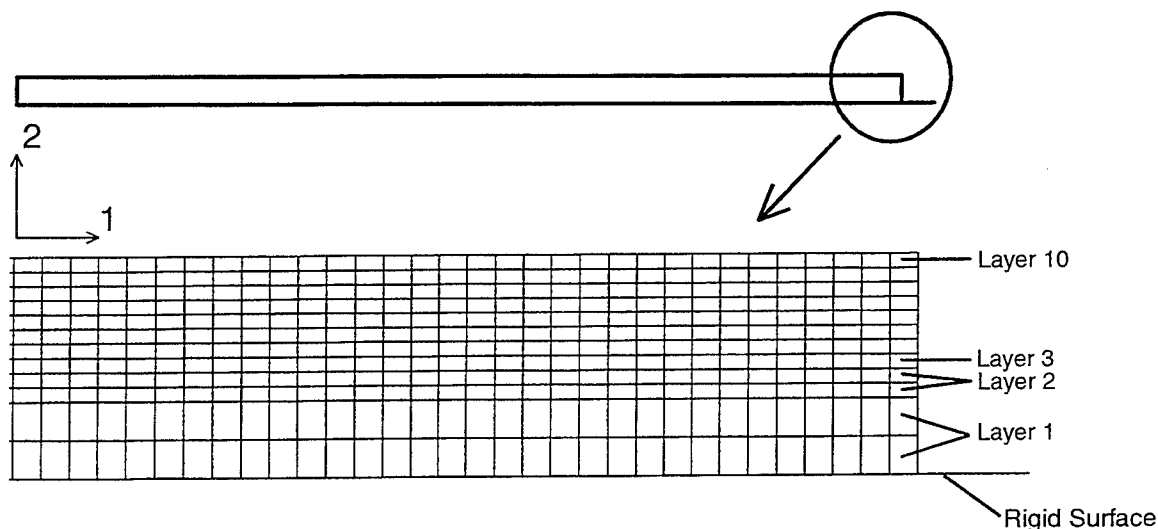


Figure 3 - Finite Element Mesh

The elements used within the analysis were four noded coupled temperature-displacement plane stress elements. Coupled elements allowed for the compressive strain to be introduced to the layers as they were built by artificially lowering the temperature locally within the mesh. The procedure used was to initially define the elements for all ten layers that would be built. The elements for layers two to ten were then removed from the analysis (using the *MODEL CHANGE card within ABAQUS) and re-introduced layer by layer as the analysis progressed.

The part bed has been modelled as a rigid surface. In practice the surface is unlikely to be rigid, but if the part bed is assumed to remain at the same temperature throughout the sintering process it is likely that the bed will be stiff relative to the part.

2.2 Material Properties

The parameters used in building the parts produced parts with a density of 700 kg/m^3 . The modulus of the polycarbonate within the analysis was assumed to be 50 MPa, with a Poisson's ratio of 0.4. There is no real scientific basis for the use of an elastic material model, or for its value. In the absence of better material property data a "smeared" elastic response has been assumed in order to evaluate the usefulness of the finite element method in modelling the selective laser sintering process. Further work is planned to gain more information on material property values through the sintering process.

The interaction between the part and the part bed was modelled with a coefficient of friction of 1. This high coefficient of friction value was chosen to reflect the fact that the real surfaces would be quite rough, giving high resistance to relative movement.

2.3 Boundary Conditions and Loading

The first step within the analysis was to analyse the first layer. The only boundary condition applied was to enforce symmetry; the nodes at the centre of the part were therefore constrained not to move in the 1 direction (shown in Figure 3). A gravity load was applied as a body force to

all elements active in the model. The compressive strain was then imposed on the layer by artificially reducing temperature within the model. The strain imposed using this method was 2.6×10^{-4} . Initially larger values for the developed strain were used, on the basis of calculations by Childs *et al* reported in [1], but these values were found to overestimate the amount of curl. It may be that initially large strains in the layers may be somewhat relaxed by temperatures developed in a layer while subsequent layers are being scanned. After the first layer has been loaded in this way the elements making up the second layer were introduced, and the gravity load and compressive strain applied to them, with this procedure repeated until all ten layers of the part had been introduced and loaded. Figure 4 shows a detail of the resulting displaced mesh.

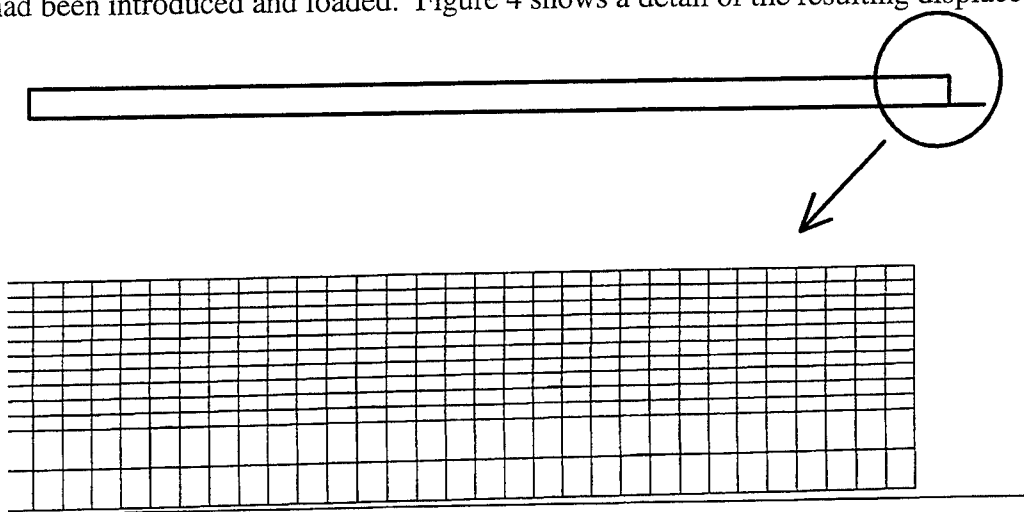


Figure 4 - Displaced Mesh

2.4 Results

In order to validate the analysis the results have been compared with the measurements of experimental builds. Table 1 shows how the results from the finite element model compare with measurements of distortion on two and ten layer parts of the same geometry. The data points used are away from the outer edge of the part to avoid confusion with R_I curl. The results shown in Table 1 were taken as indicating that the distortions predicted by the finite element model were of a similar order to those exhibited by the parts.

The results overall suggested that the combination of gravity loads, the strain induced within layers as they are manufactured, and part/bed interaction leads to R_{II} curl being seen only close to part edges.

Measured displacement in 2 direction 3.25 mm from part edge on two layer part	0.025 mm
FE predicted displacement in 2 direction 3.25 mm from part edge after two layers built	0.011 mm
Measured displacement in 2 direction 5.5 mm from part edge on ten layer part	0.05 mm
FE predicted displacement in 2 direction 5.5 mm from part edge after ten layers built	0.052 mm

Table 1 - Comparison Between FE Predictions and Measurement of Distortion

3. Analysis of the Effect of Bases

Figure 2 shows that the effect of bases on R_{II} curl is dependent on the power input per unit area to the base. The power input effectively defines the density developed within volume being scanned by the laser. It is assumed that the region in Figure 2 where the base has no effect is due to the lightly sintered powder being unable to sustain any load (and therefore acting in the same manner as the powder bed). In order to investigate the results shown in Figure 2 analyses with bases appropriate to $[P/(Us)]_{\text{base}}$ values of 0.035 and 0.06 J/mm² have been carried out, to try to identify why no further improvement occurs beyond that shown for a $[P/(Us)]_{\text{base}}$ value of 0.35 J/mm². These two values of $[P/(Us)]_{\text{base}}$ would be expected to generate base densities of 580 and 700 kg/m³ respectively (the higher value being a base with the same density as the part being built).

3.1 Model Development

The mesh used for analysing the effect of a base density of 580 kg/m³ is shown in Figure 5. The model operated in essentially the same way as that described for part build. The base used in the analysis is four layers thick, corresponding to those used to carry out the measurements shown in Figure 2. The depth of the first two layers in the build (in this case the first two layers of the base) has been changed as the "bonus z" effect increases with sintering power. Measurements on 50 layer parts gave "bonus z" values for a part made with a laser power of 0.035 J/mm² as around half of that for a part made with a laser power of 0.06 J/mm². The depth of the first two layers was therefore halved. The layer thickness in the model for a base with a density 700 kg/m³ was the same as for the analysis described in section 2.

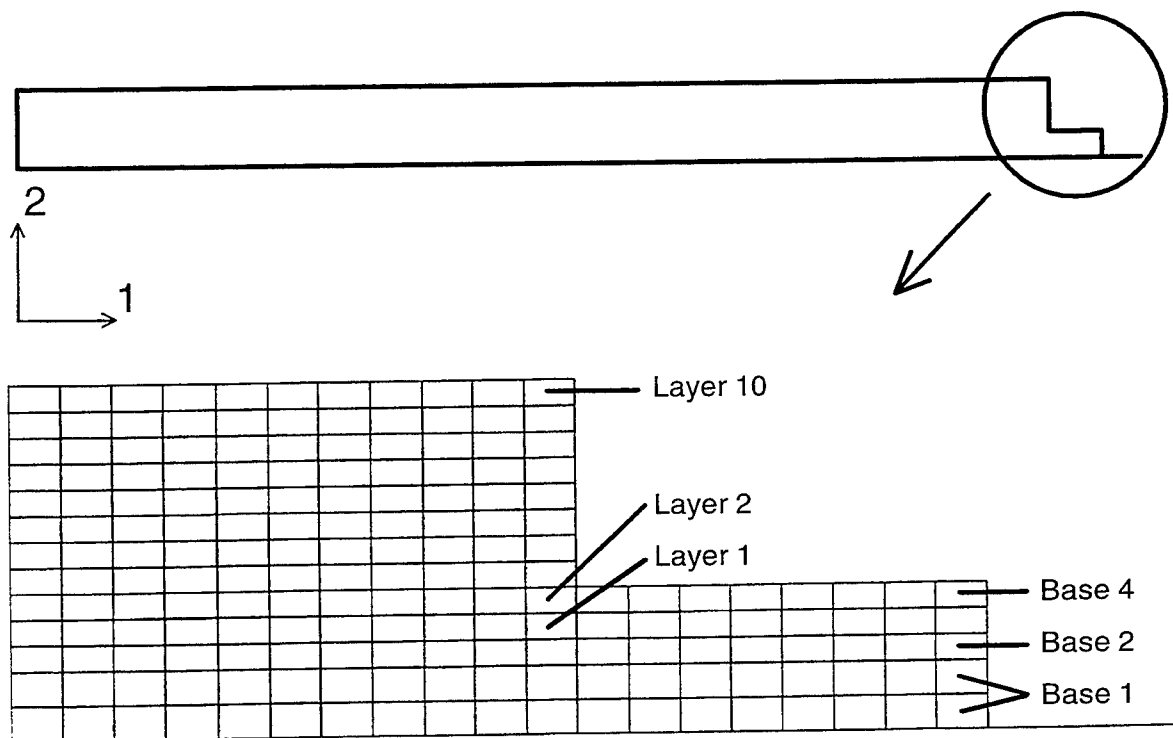


Figure 5 - Finite Element Mesh of Part Build with Base. Base Density 580 kg/m³.

In both cases the base was extended 2 mm beyond the part in the 1 direction. This is approximately what the radius of the base (which is cylindrical) would have been. The cylindrical shape of the base means that a 3D analysis would have been necessary to reflect the part geometry completely. A 2D analysis was retained for computational efficiency, although this means that the effect of a large area of base material is lost. The effect that the area of the base has on part curl was investigated by carrying out one further analysis with a base which extended 7 mm beyond the part. This analysis was carried out with a geometry and material properties appropriate to a base with a density of 700 kg/m^3 .

After the base and two layers of part contained within the base have been completed the addition of subsequent layers deposits powder on top of the protruding part of the base. The effect this has was modelled by applying a pressure load to the top of the elements of the fourth base layer.

When bases are used the layers which occupy space within the base cylinder and the part volume are scanned twice by the laser. The laser first rasters the base layer, with the laser power per unit area appropriate for the base, before rastering the part layer, again with the appropriate laser power per unit area. It has been assumed within the analyses that the second raster causes the strain developed during the first raster to be relieved (initial analyses suggested that if this were not the case the part made with a 700 kg/m^3 density base would curl more than the part made with no base at all). For the 700 kg/m^3 density base it has been assumed that all of the developed strain is relieved by the second raster. For the 580 kg/m^3 base it has been assumed that amount of strain developed during the first raster is proportional to the amount of densification which takes place. When the second raster occurs this strain is assumed to be relieved, but a further strain imposed, as the density of the layer goes from 580 kg/m^3 to 700 kg/m^3 . By this reasoning a strain of 1.46×10^{-4} is assumed to be developed within layers 1 & 2 in the model of the 580 kg/m^3 base build. The modulus of the 580 kg/m^3 base within the model was 16.7 MPa, experimental measurement of the room temperature elastic modulus of polycarbonate parts made by laser sintering suggested that a 580 kg/m^3 part would have one third of the modulus of a 700 kg/m^3 part. The modulus value for the 580 kg/m^3 dense material was therefore taken as one third of that used for the 700 kg/m^3 dense material. The Poisson's ratio was assumed to be 0.4. To further investigate the effect of the second raster releasing the strain in the layer as sintered one further analysis was carried out. This analysis used the same mesh as for the part built without a base, but assumed that the first two layers were rastered twice. The first two layers were therefore assumed to have no developed strain.

Other than the points mentioned above the analysis procedure, material properties and loading were the same as that for the part without a base described in section 2.

3.2 Results and Discussion

The results from the four analyses can be seen in Figure 6, where the position of the lower surface of the part after two and ten layers have been built within each of the analyses is plotted together with the results obtained for the analysis of a part without a base.

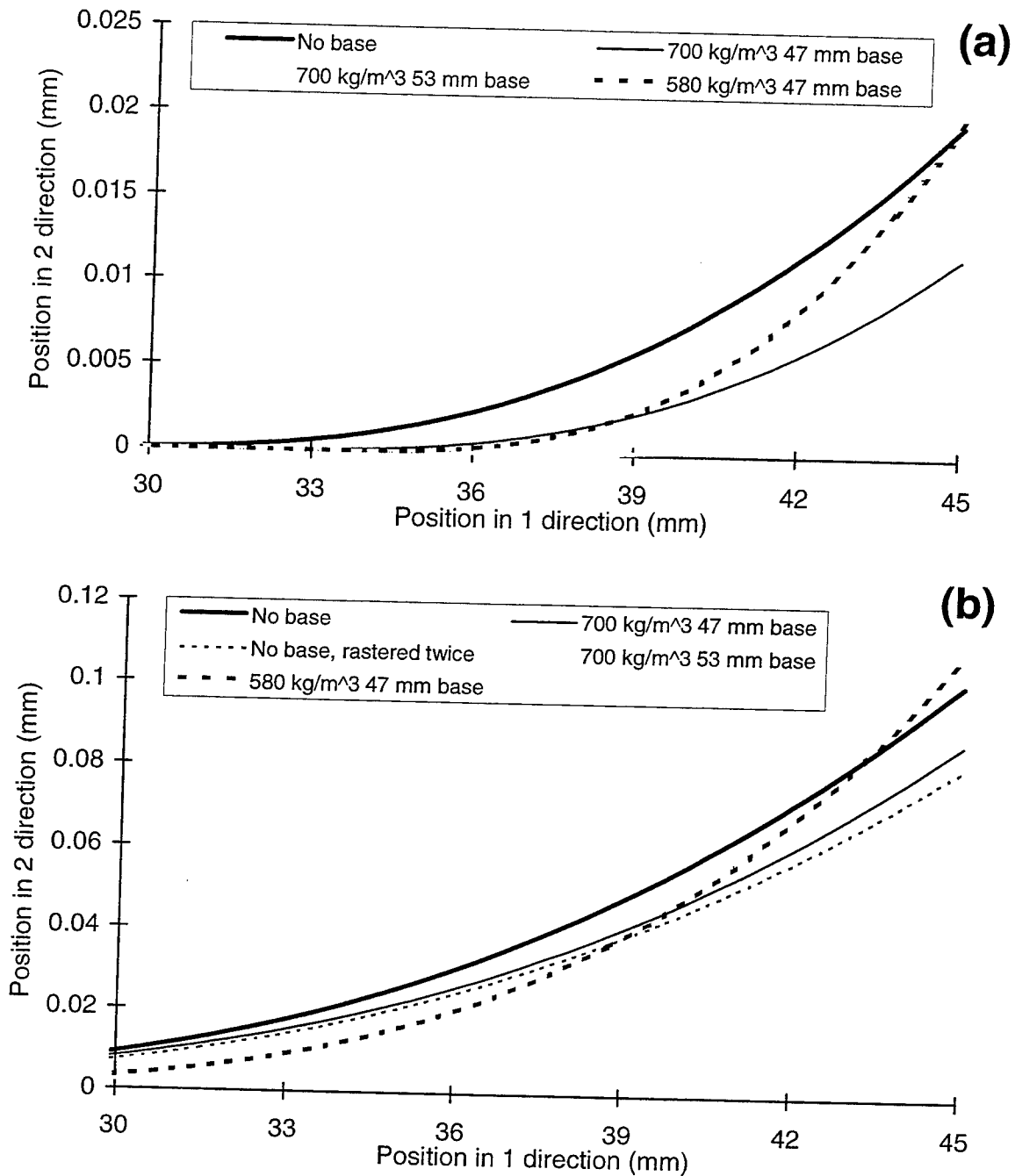


Figure 6 - Predicted Movement of Lower Part Surface Under Various Processing Conditions After (a) 2 Layers Modelled, and (b) 10 Layers Modelled.

Origin (0,0) at the Centre of the Lower Surface of the Plate.
(No Base, Rastered Twice - 2 Layers Showed No Movement).

Consideration of the results shown in Figure 6 leads to several observations:-

- (i) The use of a 2D analysis underestimates the effect the base has on reducing R_{II} curl. The results shown for the analysis of a 700 kg/m³ density base and a 580 kg/m³ density base do not

differ significantly from those of the part built without a base. The results for the analysis carried out where an additional 5 mm of base material were added show a significant reduction in the amount of curl generated. This would suggest that the additional area of cylindrical base not taken into account by a 2D model would have an effect on the amount of curl generated.

(ii) The analyses with the 580 kg/m^3 and 700 kg/m^3 density bases show very little difference in terms of the developed R_{II} curl. The residual strain in the first two layers of the part in the case of the 580 kg/m^3 density base is greater than that for the 700 kg/m^3 base, however this seems to be offset by this strain being applied to material with a lower density, modulus and (because of the effect of "bonus z") depth. This provides some insight into the effect shown in Figure 2.

(iii) The results suggest that sintering the first two layers twice to relieve the strain developed in these layers would reduce the amount of curl developed. As the results of the analyses of parts with bases is thought to underestimate the effect that the base has, further work will be required to assess whether or not the benefit derived is as great as that from using a base.

4. Conclusion

The finite element method has been shown to be of value in understanding curl in selectively laser sintered components. The characteristic shape of components exhibiting curl is considered to arise from the interaction of strain developed in the layers of the part during the build process and gravity forces. The effect of bases on R_{II} curl has also been analysed, and qualitative agreement between analysis and experiment shown. The work has made major assumptions with regard to material properties and viscosity, and further work will address these issues.

References

1. Berzins, M. *et al*, "Densification and distortion in selective laser sintering of polycarbonate parts", in Solid Freeform Fabrication Symposium 1995, pp 196-203, ISSN 1053-2153, Proc. of the Symp. held in Austin, Texas on Aug. 7-9, 1995, Pub. The Univ. of Texas at Austin.
2. Bugada, G. *et al*, "Numerical analysis of stereolithography processes using the finite element method", Rapid Prototyping Journal, pp 13 - 23, Vol. 1, No. 2, 1995.
3. ABAQUS/Standard Users Manual, Version 5.4, Hibbitt, Karlsson & Sorenson Inc.

Modelling Simple Feature Creation in Selective Laser Sintering

Ryder G. J., Berzins M., Childs T. H. C.

University of Leeds

A two dimensional finite difference thermal sintering model has been created to describe the Selective Laser Sintering process(SLS). It includes thermal property variation with position and temperature, and especially adaptive meshing to refine information in regions of high temperature gradients. It has been used to predict density and temperature in both single and multi layer sintering operations, corresponding to experimental results. This paper will present comparisons of theory and experiment for the SLS of simple geometries such as blocks, steps, and cylinders.

INTRODUCTION

Earlier work [1-3] has reported the advances in the modelling of the sintering process at Leeds. Initial thermal modelling with classical moving heat source theory has been superseded by finite difference numerical methods using adaptive meshing which is the key feature of the software VLUGR2 [4]. The work is currently restricted to two dimensional modelling. The work presented here takes this work a step further. Bonus Z (Z+), curl and growth are well reported [2,3] as the limiting accuracy associated with the sintering process. Z+, and growth are also known to be related to a build up of excess heat within the system. At least two types of curl have been distinguished. The first is as a result of the thermal stresses built up within a material as it shrinks, resulting in the curling of the whole layer or part, and will be referred to as 'major curl'. The second, that is confined to the very edges of a part, seems to be as a result of the original sintering of the powder, and will be known as minor curl. It is minor curl that can be illustrated in this work.

The present generation of SLS machines does not have the facility to vary energy input to the powder bed point to point. Some of the problems described above are orientation and part geometry dependent. Better understanding could lead to a reduction of the problems through the more flexible control of the laser operating parameters. The aim of this work is to develop strategies that will be applicable to future generations of sintering machines.

THEORY

Figure 1, [1], shows the simplified model of the rastering laser that has been introduced to describe SLS in two dimensions. As described in [1] when scan spacing, $s < \text{beam diameter}$, d and if the cycle time $2w/U$ is less than the time d^2/κ for heat to diffuse d (where κ is the thermal diffusivity), the laser spot, with power P , may be replaced by a rectangular blade source of side $d \times w$, of power Q per unit area, sweeping across the block with speed V in the x direction where

$$Q = \frac{P}{Usd} \quad (1)$$

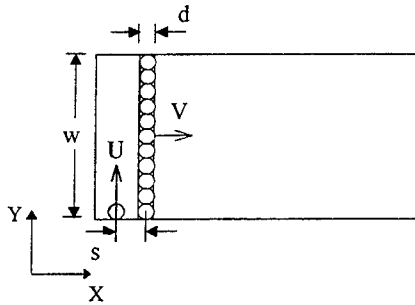


Figure 1: Scanning model.

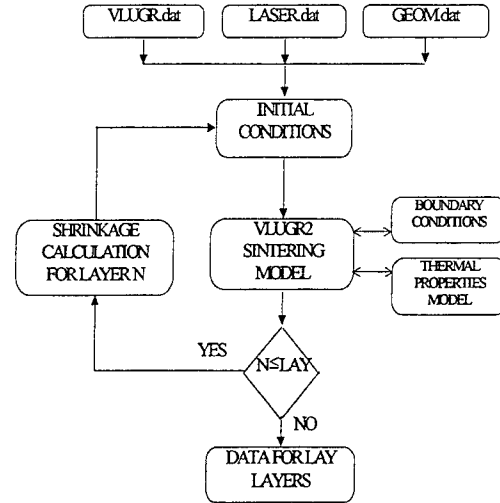


Figure 2: Flow chart of AMP2 model.

Figure 1 describes the laser tracking over a simple rectangular patch, to sinter one layer of a rectangular part. It may be thought of as one slice of a three dimensional part, in which shape can be created by displacing one layer in the X direction relative to the last and/or by changing the length of the layer in the X direction. This is the focus of this paper. A flow chart of the multi-layer computer model is shown in figure 2. The model has been called AMP2, or Accurate Multi-Layer Prediction model in 2D, and has been used in this report to generate simple geometries such as blocks, steps and cylinders that can be compared with experimental data. In this paper numerical results from AMP2 will mainly be discussed, and initial comparisons will be made with experimental work.

At the start of the run three external files are opened and their contents read into the program. VLUGR.dat contains information relevant to the running of the VLUGR2 software: domain data, tolerance data, and Partial Differential Equation(PDE) data. GEOM.dat contains the geometry data including the scan spacing, scan vector length, and the start and end coordinates of each layer. Finally LASER.dat contains the LASER data: laser power, laser spot size, and the scan speed. This data is used to create the specific sintering model within VLUGR2 which then calculates the temperature/time history and the sintering behavior of the model.

The model is based around two major PDEs, the heat conduction equation (2) and the viscous sintering equation (3) in which ϵ is the void fraction

$$\rho C_p \frac{\partial T}{\partial t} = K \left(\frac{\partial^2 T}{\partial x^2} + \frac{\partial^2 T}{\partial y^2} \right) + \frac{\partial K}{\partial T} \left(\left(\frac{\partial T}{\partial x} \right)^2 + \left(\frac{\partial T}{\partial y} \right)^2 \right) + \left(\frac{\partial K}{\partial x} \frac{\partial T}{\partial x} \right) + \left(\frac{\partial K}{\partial y} \frac{\partial T}{\partial y} \right) \quad (2)$$

$$-\frac{\partial \epsilon}{\partial t} = k'(\epsilon - \epsilon_\infty) \quad (3)$$

$$\text{where } k' = A \exp\left(-\frac{B}{RT}\right) \quad (4)$$

An important feature of equation (2) is that it retains terms in conductivity varying with position and temperature, as described briefly in ref(3). A difference from earlier papers [1] is that it does not contain a convection (moving heat source) term. In the present treatment, the moving heat source is treated as a moving flux boundary condition. The temperature/time history of the powder is calculated as the laser passes by. The void fraction variation described by equation (3) is calculated simultaneously, and this feeds back into the heat conduction equation via the variation of thermal conductivity with position. While the void fraction is calculated simultaneously, the overall shrinkage (depression of the powder surface) that takes place as a result of the solidification of the powder is calculated as a post processing operation, [1,2]. Because this is the case care is needed in the interpretation of the conductivity terms in eqn (2).

Equation 2 does not contain the latent heat terms that are required to model crystalline polymers. At this stage the model is still restricted to the modelling of amorphous polymers such as polycarbonate. For polycarbonate from Nelson [5],

$$C_p = 935 + 2.28T \quad (\text{J/Kg}) \quad (5)$$

while the thermal conductivity model is stated as

$$K_{solid} = 0.0251 + 0.0005T \quad (\text{W/mm-K}) \quad (6)$$

In previous work [2,3], a simplified expression was used for the conductivity of the powder or partially sintered material

$$K_{powder} = K_{solid}(1 - \varepsilon) \quad (7a)$$

As a result of measurements still in progress the following is now preferred

$$K_{powder} = K_{solid}(1 - \sigma\varepsilon) \quad (7b)$$

with a value of $\sigma = 0.5$. This empirical expression, valid for the range of void fraction seen in SLS, is still substantially simpler than the expression used by Nelson [5,6]. From equation 7b the temperature and spatial variation of K in equation 2 becomes

$$\frac{\partial K}{\partial T} = (1 - \sigma\varepsilon) \frac{\partial K_{solid}}{\partial T}, \quad \frac{\partial K}{\partial n} = -\sigma K_{solid} \frac{\partial \varepsilon}{\partial n} \quad (8)$$

where here n represents either the x, or y axes. Notice here that the K is the conductivity of the solid, while the K prefixing the first term on the right hand side of equation 2 and ρ on the left hand side is that of the initial bed density.

The sintering prediction is performed in two distinct operations. The first is to calculate the sintering behavior of the first single layer, in which the phenomenon of Z^+ is observed. It is this operation that has been reported previously [3]. The second is the sintering of the subsequent layers whose sintering behavior is affected by the presence of the immediately previous layer. The effect of this previous layer is to conduct the heat away from the sintering region more quickly resulting in a reduced sintering depth. AMP2 eliminates the computational expense of a large number of layers by only modelling two layers at a time, the layer being sintered and the immediately previous layer.

By sintering behaviour is meant the calculation of void fraction with position, from equations 2 and 3. The shrinkage of the layer is then calculated. Information of the density and shrinkage of the first layer are re-entered as initial conditions to the sintering calculation of the next layer. Once all layers have been modelled the complete layer data is entered into VLUGR2 and this data is the dump to an external file. Currently a single average run with $P=11W$, $s=0.15mm$, $U=1190\text{ mm/s}$, creating a part length of 5mm and 10 layers thick can take 30 hours using an average number of 35,000 grid points.

Two major geometries have been modelled using the AMP2 model: blocks and steps. A brief examination of cylinders has also been undertaken, but only a preliminary report of this is included here. The blocks are the simplest geometry. A simple diagram of the three dimensional geometry is shown in figure 3. This is in fact the geometry that was built within the SLS machine, the numerical model looked at the cross section of this part along the length, L . The step and cylinder geometries are likewise shown in figure 3.

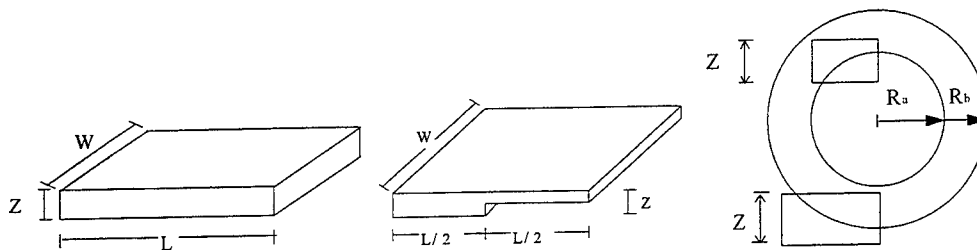


Figure 3: Block, step and cylinder geometries.

Only part of the cylinder geometry is modelled. The difference of scale between the overall size of the object and the area being sintered coupled with the memory requirements of the VLUGR2 software make it difficult to model the entire geometry. Therefore only those regions that are of interest are modelled. Region 1, the bottom of the cylinder, is prone to Z^+ on the bottom layer causing the geometry to become oval. Region 2, the top inside diameter, is known also to suffer this type of problem resulting in a flattening of this inside diameter.

The AMP2 model as presented here allows the user to control the sintering variables of laser power, scan spacing, scan vector length, dwell time, laser spot diameter, and laser scan speed. By manipulating these variables it is possible to model simple two dimensional sintering strategies.

EXPERIMENTATION

The numerical calculations from AMP2 have been compared with two types of tests: calibration experiments and ones in which blocks, and steps were created.

The calibration experiments have been reported before. Simple rectangular blocks were built with powers from 4 to 19Watts, scan speeds from 51 to 1206mm/s and scan spacings from 0.08 to 0.41mm. The densities of these parts were measured and the average layer density calculated. The AMP2 predictions are compared with this.

Experimental pieces ten layers thick corresponding to powers of 6, 11, and 22 Watts, $s=0.15\text{mm}$, $w=25\text{mm}$, and $U=1190\text{mm/s}$ were built in the SLS machine. Once built these were mounted for microscopic examination in EPOFIX cold setting resin using the vacuum impregnation technique. These were then ground, polished and photographed in order that they could be compared with the numerical results obtained from AMP2.

NUMERICAL AND EXPERIMENTAL RESULTS

Figure 4 shows the calibration tests. Figure 4a shows calculated layer thickness for the first, second and third layer of a part. The Z+ phenomenon is clearly visible as a greater thickness of the first few layers; the results are in accord with experiments [3]. Figure 4b shows the variation of the average layer density, once the steady state thickness of the layer has been obtained. The error bars mark experimental results, the line is the prediction from AMP2.

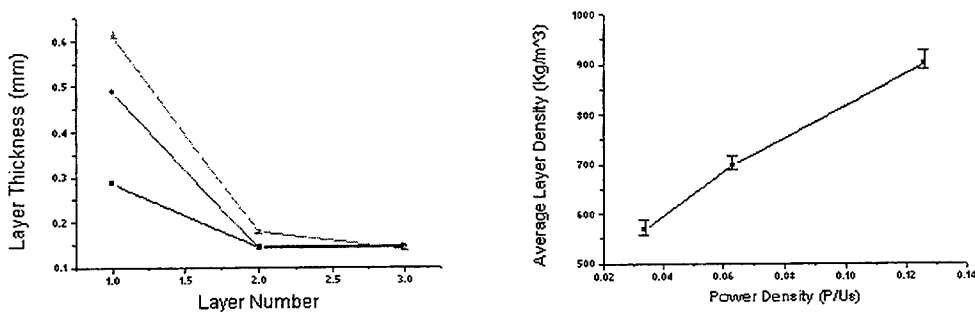


Figure 4: Multi layer model calibration data (a) layer thickness vs. layer number \blacktriangle 22W \blacksquare 11W \bullet 6W (b) layer density vs. power density for experiment and current AMP2 model.



Figure 5: Single layer after shrinkage calculation.

Contour plots of the densification data obtained from VLUGR2 are created using the UNIMAP software, a component of the UNIRAS suite. At this stage of the research they are a geometrical representation only: they show only the distinction between solid and powder. Figure 5 shows a single layer output from AMP2 after the shrinkage post processor has been applied. In this case it was built at $P=11W$, $U=860\text{mm/s}$, $s=0.203\text{mm}$. The cause of minor curl can clearly be seen on the downward facing surface, the rounding of the edge caused by the initial sintering of the layer.

Figure 6 shows AMP2 results for 10 layer thick block (a, close up d) and step (b, close up e) models built at 6W power (c defines the grey scales). The models, nominally 1.25 mm thick, are actually 1.3 mm as a result of only a small amount of Z+ creation. The model predicts some unsintered powder between each layer. In the step model, each of the top five layers shows a small step or change of level as it crosses over the edge of the step.

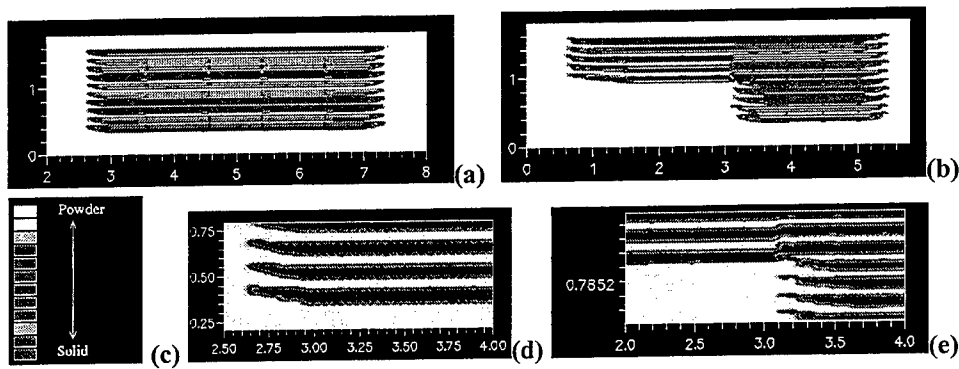


Figure 6: Geometry data for 6W, all dimensions mm.

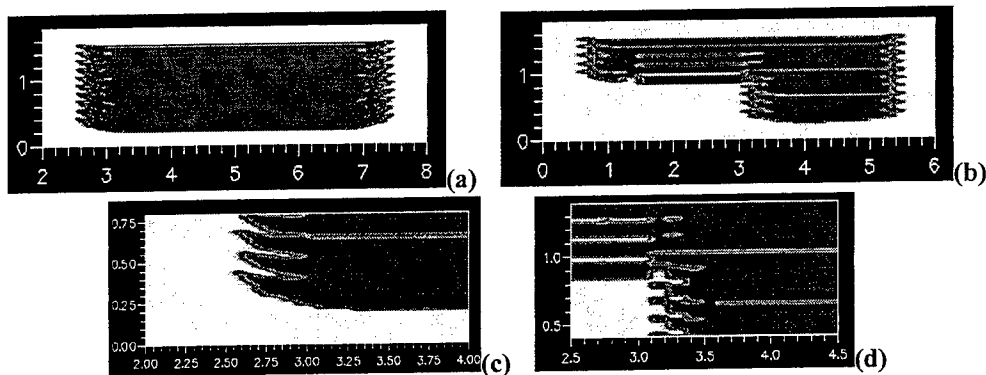


Figure 7: Geometry data for 11W, all dimensions mm.

Figure 7 shows the 11W power block and step AMP2 output. total thickness of the block has increased to 1.4 mm due to greater Z+. Little unsintered powder remains inside the model. In figure 7d, the change of the upper part of the model's layer level at the step edge cross-over can still be seen.

At 22W (figure 8), the block appears fully dense. It has become 1.7 mm thick, due to large Z^+ which also gives a marked rounding (curl) to the bottom surface.

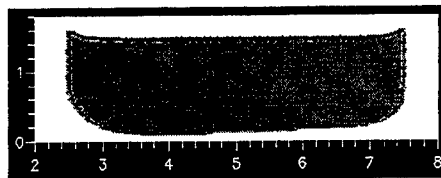


Figure 8 : Block geometry at 22Watts, all dimensions mm.

Figure 9 shows region 1 of the 11W AMP2 cylinder model as described in the theory section. The thickness of the 10 layers is 1.45 mm, corresponding to 0.2 mm Z^+ . The leading (left-hand) edge is rippled. This is the same effect as seen in the step models (figures 6d and 7d) in which layer level changes as it passes over the edge of a previously sintered layer.

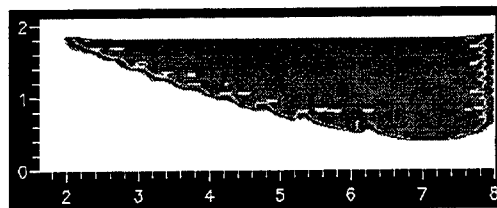


Figure 9: Cylinder multi layer model, region 1, all dimensions mm.

Initial experimental results are shown in figure 10. Part a shows the structure of a single layer block built at 11W: it shows the same curl as in figure 5. Part b is a 10 layer block to be compared with figure 7a: it is more clearly layered than is figure 7a; also the left-hand edge is clearly not as square as in figure 7a. Part c is a detail of a step to be compared with figure 7d: the change of level of a layer as it crosses the step edge can be seen. Part d is a 10 layer block built at 22W for comparison with figure 8. The large circular black regions are closed pores not predicted by the model and different in structure from parts made at 11W.

DISCUSSION AND CONCLUSION

The 2D AMP2 program, including variation of thermal conductivity with position and temperature and with an improved expression for thermal conductivity (equation 7b) accurately predicts part density and bonus Z (Z^+). It is starting to be used to model simple features in comparison with experiments and shows promise of being able to guide, after further post-processing development, strategies for more accurate sintering to shape. involving variable power according to part geometry. However some features on even simple shapes, such as the non-square edge in figure 10c, show the equal importance of being able to model post-sintering distortion due to viscous relaxation of internal stresses. Experimental studies also show that the sintering process itself, in extreme conditions such as the high laser power in figure 10d, is more complicated than suggested by the simple rate model of equation 3.

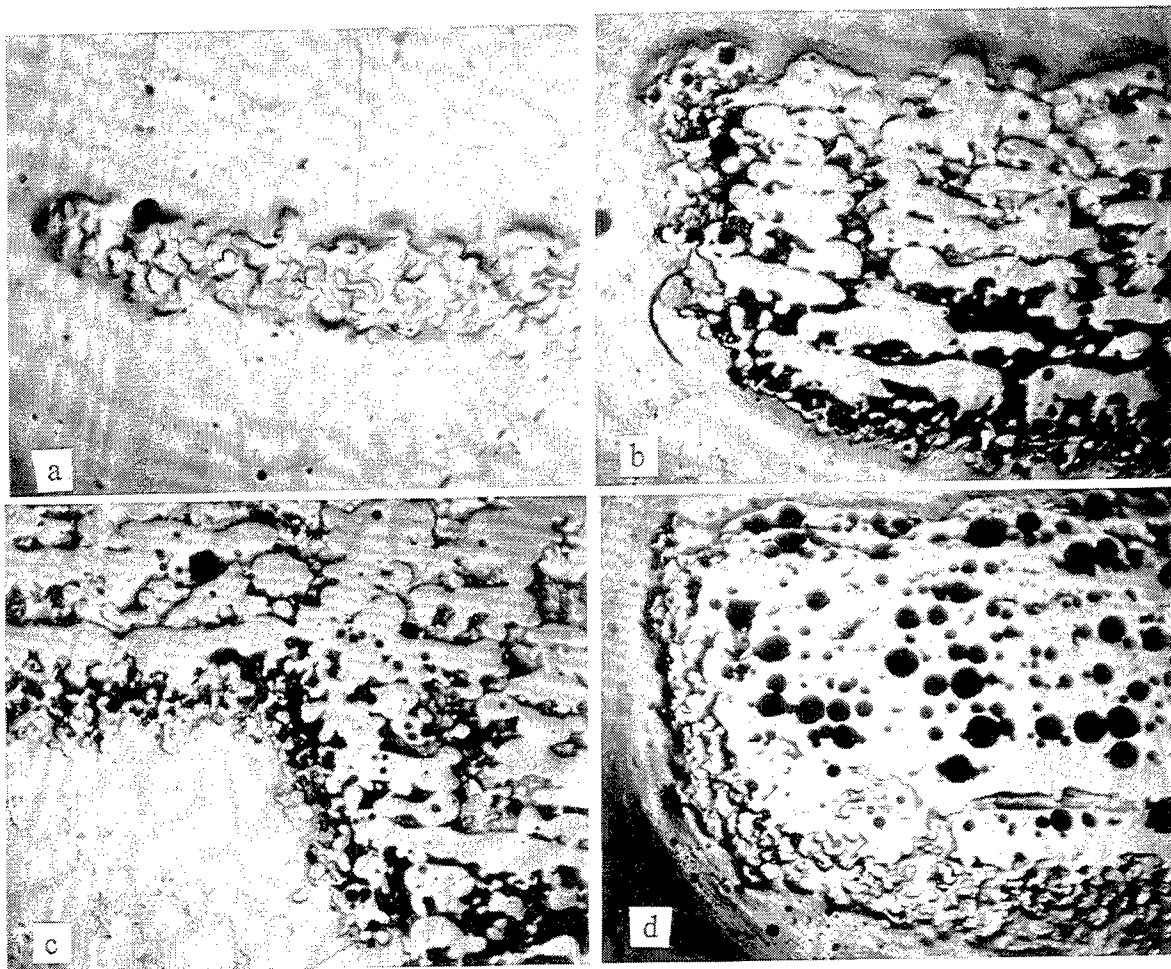


Figure 10. Microsections of parts built at 11W (a to c) and 22W (d), as described in text.

ACKNOWLEDGEMENTS

Gerard Ryder would like to thank the Keyworth Institute of Manufacturing and Information Systems Engineering for providing a research studentship.

REFERENCES

1. Childs, T. H. C. et al., 1994, Selective Laser Sintering of Polycarbonate at Varying Powers, Scan Speeds and Scan Spacings, Proc. 5th SFFF Symposium, 356-363, University Austin Texas.
2. Berzins, M., Childs, T. H. C., et al., 1995, Densification and distortion in Selective Laser Sintering of Polycarbonate, , Proc. 6th SFFF Symposium, 196-203, University Austin Texas.
3. Berzins, M., Childs, T. H. C., Ryder, G. J., The Selective Laser Sintering of Polycarbonate, Annals CIRP 44/1 (1996), to be published.
4. Blom, J. G. and Verwer, J. G., 1993, VLUGR2: A Vectorisable Local Uniform Grid Refinement Code for PDEs in 2D, to appear in ACM T.O.M.S. September 1996.
5. Nelson, J. C. et al., 1993, Model of the Selective Laser Sintering of Bisphenol-A Polycarbonate, Ind. Eng. Chem. Res., 32: 2305-2317.
6. Yagi, S., Kuni, D., Studies on Effective Thermal Conductivities in Packed Beds, AIChE J., 1957, 3, 373-381.

Extraction of Fault Patterns on SLS Part Surfaces Using the Karhunen-Loève Transform

Irem Y. Tumer Kristin L. Wood Ilene J. Busch-Vishniac
Graduate Research Asst. Associate Professor Professor

Mechanical Engineering Department
The University of Texas at Austin

Abstract

To gain a thorough understanding of the fault mechanisms in SLS machines, we decompose SLS profile signals into independent features using a novel tool called Karhunen-Loève (KL) transform. These individual features can then be studied separately to monitor the occurrence of fault patterns on manufactured parts and determine their nature. Analytical signals with known fault patterns, simulating profile measurement signals from SLS parts, are used to determine the suitability of the proposed method. Multi-component patterns are assumed to manifest on SLS part surfaces, resulting from faults in the machine, for example, the roller mechanism. The results of this work determine the suitability of the KL transform for condition monitoring and extraction of fault-indicating patterns.

Fault Patterns on Manufactured Parts

Detecting and quantifying faults that occur during manufacturing is necessary to ensure the efficient production of accurate parts. The field of fault detection and diagnosis in manufacturing aims at eliminating the occurrence of faults by continuously monitoring the process, detecting faults, and taking corrective action. In this paper, the focus is on monitoring the condition of surface quality. The surface is measured at regular intervals for the purpose of detecting any degradation on part surface quality. Faults or deviations in the dynamics of the manufacturing machine or its submechanisms are assumed to leave a "fingerprint" on the surface of the part being manufactured, which manifest as fault patterns. These are the fault patterns that we seek to detect, quantify, and diagnose, in order to take remedial action if necessary.

A fault is defined as the inability of a system to perform in an acceptable manner [9]. Faults typically manifest themselves as deviations in observed behavior from a set of acceptable behaviors. Fault detection is the recognition of an unacceptable behavior; and fault diagnosis is the identification of a component or set of components in the system that causes the fault [9]. As part of fault detection, analysts collect data, extract relevant features, and compare these extracted features to a specification of correct or incorrect data [5, 9].

The method of feature extraction and selection is a critical factor in detecting the correct fault-indicating features from manufacturing signals. Complex signals are best analyzed and processed using signal processing tools. In this research, we aim to develop a unified method to detect and diagnose the correct features in an accurate fashion.

The most reliable methods of fault diagnosis utilize signal processing algorithms to extract fault features. Poorly performing fault monitoring and diagnosis systems are common in industry, and they result in frequent false alarms or insensitivity to a legitimate failure condition [10]. It is often difficult to detect the proper features in the presence of random effects and nonstationarities. The

task of diagnosis is often too complex and unreliable because of errors introduced due to the careless selection of signal processing algorithms [10]. As a result, in this research, signal processing methods will be investigated to evaluate their suitability as feature extraction methods. Specifically, fault patterns on manufactured part surfaces will be analyzed to determine the character, severity, and origin of faults that result in poor surface quality.

Similarly, ongoing research aims at finding the best approach to classify the extracted features, in order to determine the existence and cause of a fault. This step typically relies on previously known limits and specifications, or previously known fault patterns. The most traditional approach to detect faulty features or patterns is to compare the observed features to previously known features. In this research, we want to develop a diagnosis method that does not rely on previous knowledge. A good example of such a case is a completely new system where there is not enough prior experience and system models for fault classification are not available. This constitutes a very difficult problem, as it requires any type of fault pattern to be recognized, quantified, and diagnosed, without prior knowledge of the expected faults.

We propose to develop a fault detection and diagnosis approach composed of signal processing tools that will detect and quantify a fault-indicating pattern (feature), regardless of the type and characteristics of the patterns and the observed signals, and that will diagnose the originating source of the fault, without relying on previous knowledge or known patterns of faults. We aim to do this in the context of monitoring and controlling part surface quality in manufacturing, specifically, in Selective Laser Sintering [12].

To satisfy our research goals, we propose a five-step approach, shown schematically in Figure 1. The main two general portions of this approach consist of feature extraction and quantification and

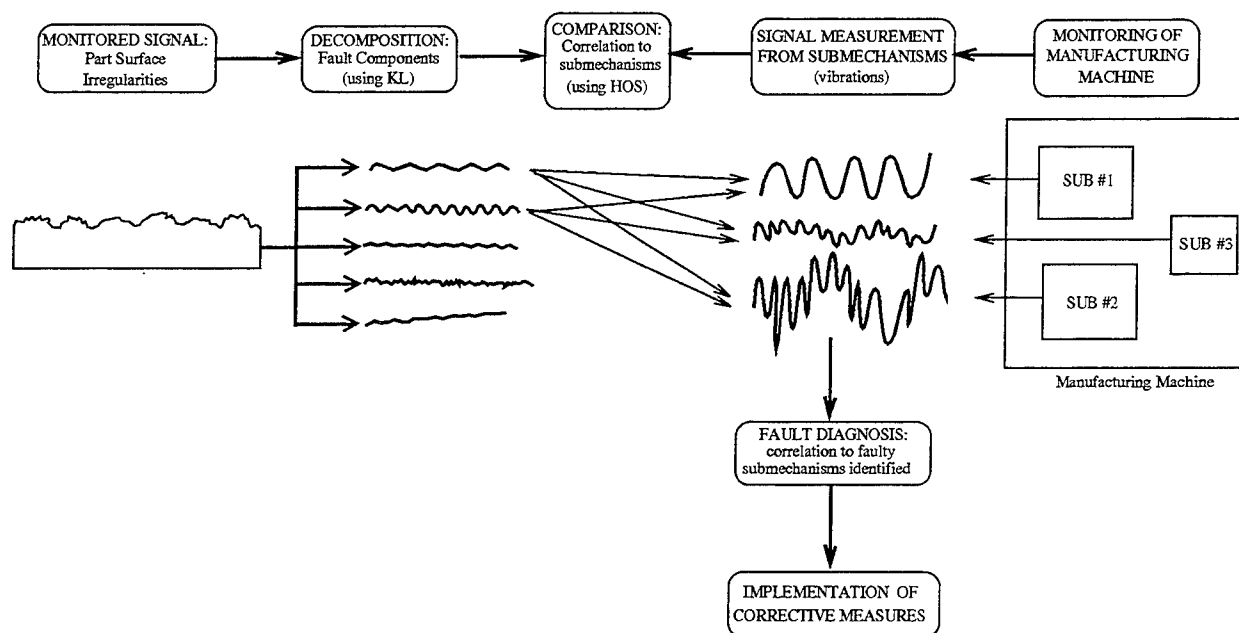


Figure 1: Feature Extraction and Fault Diagnosis Approach.

feature comparison for diagnosis. To obtain a decorrelated decomposition of the measured signal, we need to apply a mathematical transformation to the signal [1, 14]. The Fourier transform is such a tool, resulting in a decomposition into different frequency components based on sines and cosines as basis vectors. However, the decomposition is not accurate in the presence of nonstationary features.

An alternative is the Karhunen-Loève (KL) transform, an orthogonal transform which decomposes the signals into decorrelated components in the form of a few empirical basis functions that contain the majority of the variance in the original data. The most common application of this transform is to detect dominant features in order to reconstruct original signals with lower dimensionality. Recent applications include recognition of faces in vision and turbulent structures in fluids [3, 6, 8]. We want to use this tool in detecting features in manufacturing signals, specifically, surface profiles [11]. Our main purpose is to extract individual patterns and study their characteristics to determine whether they correspond to significant faults, and use these patterns to determine their origin.

This paper focuses on the first two steps. In particular, we investigate the suitability of the Karhunen-Loève transform to provide a proper decomposition leading to accurate fault detection, quantification, and monitoring. The following sections describe the theory and motivation of the KL transform and investigate its suitability based on analytical signals which model multi-component signals and the occurrence of faults.

Karhunen-Loève Transform

Orthogonal transforms, and, in particular, the optimal Karhunen-Loève transform (KL), otherwise known as the Principal Components Analysis in the statistical literature, are used in a variety of signal processing applications [1, 2, 3, 6, 8, 15]. However, they have never been used for the purposes of fault detection and diagnosis, or for the purposes of detecting and quantifying faults on manufactured part surfaces. In this work, we extend the KL transform to the extraction of physical patterns from surface signals; the purpose is to decompose multi-component signals into individual patterns and study their characteristics in order to determine the occurrence, severity, and shape of each fault. We want to assure that any pattern, including stationary and nonstationary, can be detected and extracted using the KL transform. This information will later be used to diagnose the origin of each individual fault.

The KL transform presents a great advantage when investigating the occurrence of faults, especially when the shape of the fault patterns are not known in advance. Orthogonal transforms provide a decomposition of the signal into its high-energy content basis functions, leading to an accurate decomposition picture in the time-domain [1, 7]. Because the KL method decomposes signals into empirically determined basis functions, rather than pre-defined sines and cosines, any fault pattern, including stationary and nonstationary patterns, can be detected in theory using this transform.

Theory and Mathematics

In the context of surface profile characterization, the signal being monitored is the surface profile of an SLS part. A total of M "snapshots" are assumed to be collected at regular intervals, with N points each, to allow for a continual monitoring of the state of operation.

We first compute the mean vector $\bar{X}_{ave} = \frac{1}{M} \sum_{m=1}^M \bar{X}_m$ over the total of M samples collected from the profile; then the deviation or departure $\bar{y}_m = \bar{X}_m - \bar{X}_{ave}$ of each sample signal from the mean is computed. The mean is removed to simplify the mathematical derivation of the covariances [4]. Next, the covariance matrix is computed as follows:

$$\bar{C} = \frac{1}{M} \sum_{m=1}^M \bar{y}_m [\bar{y}_m]^T \quad (1)$$

The eigenvectors of \vec{C} are the basis functions \vec{u}_i , computed from:

$$\vec{C}\vec{u}_i = \lambda_i\vec{u}_i \quad (2)$$

The eigenvalues λ_i are ordered and the relevant features are selected by choosing the first $n < N$ dominant eigenvalues from the set of solutions, following the feature selection criterion used in the literature (about 90% of the total energy is sufficient for reconstruction [3]). The coefficients a_i are computed by projecting each sample vector deviation \vec{y}_m onto the basis vectors \vec{u}_i from:

$$a_i = [\vec{y}_m]^T \vec{u}_i \quad (3)$$

For each deviation \vec{y}_m , there are $i = 1 \dots n$ coefficients, where n is the number of principal eigenvectors; there are a total of $m = 1 \dots M$ deviations (snapshots). From another point of view, for each principal eigenvector \vec{u}_i , $i = 1 \dots n$, there are $m = 1 \dots M$ coefficients. The collection of these M coefficients for each eigenvector is called the coefficient vector; hence, there are as many coefficient vectors as there are eigenvectors. Each original sample vector \vec{X}_m is then reconstructed with lower dimensionality by adding this linear combination to the sample mean:

$$\vec{X}_m = \vec{X}_{ave} + \sum_{i=1}^n a_i \vec{u}_i \quad (4)$$

Simulations using Analytical Signals

In this paper, faults are simulated in the context of parts from a Selective Laser Sintering machine. The roller in the SLS machine is responsible for depositing an even layer of powder on the powder bed [12, 13]. The quality (“evenness”) of the surface of the top layer of powder will determine, in part, the surface quality of the final manufactured part. In a previous paper, the authors have shown that, with certain types of powder, the roller leaves “chatter marks” on the surfaces of SLS parts [12, 13]. Any undesirable changes in the dynamics of the roller will result in a change in the surface quality of the part being manufactured. It is changes such as these that we want to be able to detect using the KL transform.

In order to test the suitability and limitations of the KL transform, we use analytical signals in which the fault patterns are known. This assures the accuracy of our results, since we know exactly what fault patterns the decomposition should provide, and when each type of fault pattern occurs. We first simulate cases where different faults occur during a manufacturing process, and compare these cases to the normal state of operation. With these simulations, we also want to assure that multicomponent signals are decomposed accurately, whether the components are deterministic, stochastic, stationary, or nonstationary. Deterministic and stationary changes are introduced, as well as nonstationary changes over the entire monitored profile.

The “normal” state of operation is assumed to produce a multicomponent signal with 2 sinusoids, in the form of $A_1 \sin(F_1 j) + A_2 \sin(F_2 j)$, one high frequency ($F_1 = 0.9 \text{ rad/sec}$), small amplitude ($A_1 = 1 \text{ mm}$), and the other low frequency ($F_2 = 0.2 \text{ rad/sec}$) and large amplitude ($A_2 = 2 \text{ mm}$), plus random (Gaussian) noise (zero mean and low variance of 0.09). This situation illustrates a typical operation state, in which rotating components, such as the SLS roller, introduce a fundamental sinusoidal pattern, plus a harmonic, accompanied with random noise from the machine operation or other conditions, such as the surface texture of the roller. Faults, such as bearing wear or misalignment, introduce either additional harmonics, or a change in the magnitude

Ind.	Normal	Abnormal 1a	Abnormal 1b	Abnormal 2a	Abnormal 2b	Abnormal 3	Abnormal 4
1	255.45	633.47	6938.42	1006.66	6232.03	1037.00	829.55
2	240.15	530.83	5738.31	956.76	5938.75	954.40	685.45
3	74.01	240.76	245.89	72.23	70.81	618.54	89.81
4	55.62	235.70	235.65	57.30	57.61	485.89	84.81
5	2.68	2.81	2.86	2.59	2.75	2.66	52.88
6	2.58	2.39	2.62	2.27	2.21	2.24	26.23
7	2.25	2.25	2.39	2.25	2.08	2.12	2.81
8	2.14	2.00	2.06	2.00	1.95	1.98	2.29
9	2.00	1.73	1.79	1.97	1.64	1.74	1.97
10	0.00	0.00	0.00	0.00	0.00	0.00	0.00

Table 1: Eigenvalues: Normal State vs. Abnormal States

of the fundamental frequency component. In addition, offsets or linear trends may be introduced as a result of misalignment in the non-rotating elements. In the following, These abnormal cases, as well as other nonstationary faults, are simulated and compared to the normal state of operation.

In the following, the “eigenprofiles” represent the principal basis patterns on the entire surface being monitored. Snapshots are collected at regular intervals to monitor the condition of the surface being manufactured. Significant “eigenprofiles” are derived from a covariance matrix to provide the shape of the dominant patterns on surface profiles; the eigenvalue corresponding to each eigenprofile indicates the effectiveness of each feature to represent the original profile. The features are the coefficient vectors corresponding to each eigenvalue; these indicate any change in amplitude of a dominant eigenprofile along the snapshots collected in time or in space, corresponding to the weight of each basis eigenprofile in each snapshot. The variance of the coefficient vectors follows the magnitude of the eigenvalue. There are as many coefficient vectors as there are dominant eigenprofiles. The coefficient vector contains M points, indicating the change over M profile snapshots.

Stationary Changes in Deterministic Components

In the first set of simulations, the normal state of operation is assumed to produce a multi-component signal with 2 sinusoids and random (Gaussian) noise. Ten snapshots are assumed to be collected over the entire profile; each snapshot has 256 sample points. The following set of simulations test the effect of stationary changes in the deterministic components.

Abnormal States 1a and 1b

In the first case, the high frequency component of the signal increases in magnitude, while the second component remains unchanged. Abnormal states 1a and 1b represent two different magnitudes. We are investigating whether changes in the amplitude of one of the sinusoidal components of the multi-component signal can be detected with the KL transform. This might, for example, simulate the case when a sinusoidal pattern on the SLS surfaces, caused by roller chatter [12], exceeds its normal limits in magnitude, thus reducing the surface precision and accuracy; remedial action will have to be taken to diagnose the cause of this increase.

The eigenvalues from abnormal states 1a and 1b, compared to the normal state, are shown in Table 1. The first observation is that, for the normal state of operation, the multi-component signal is decomposed into 4 significant eigenvalues, summing to 98% of the total energy in the signal. The first two eigenvalues (#1,#2) correspond to low-frequency sinusoidal eigenprofiles, while the next two eigenvalues (#3,#4) correspond to high-frequency sinusoidal eigenprofiles.

For abnormal states 1a and 1b, we also obtain 4 principal eigenvalues and eigenprofiles. As shown in Table 1, when we increase the magnitude of the high-frequency component of our original signal, we notice that the eigenvalues corresponding to the high-frequency component increase in magnitude. The eigenvalues corresponding to the low-frequency component remain approximately the same as in the normal state of operation.

These trends are more easily noticeable when we study the shape of the eigenprofiles and the corresponding coefficient vectors. The first four eigenvectors from abnormal states 1a and 1b, compared to the normal state, are shown in Figure 2. The corresponding coefficient vectors are

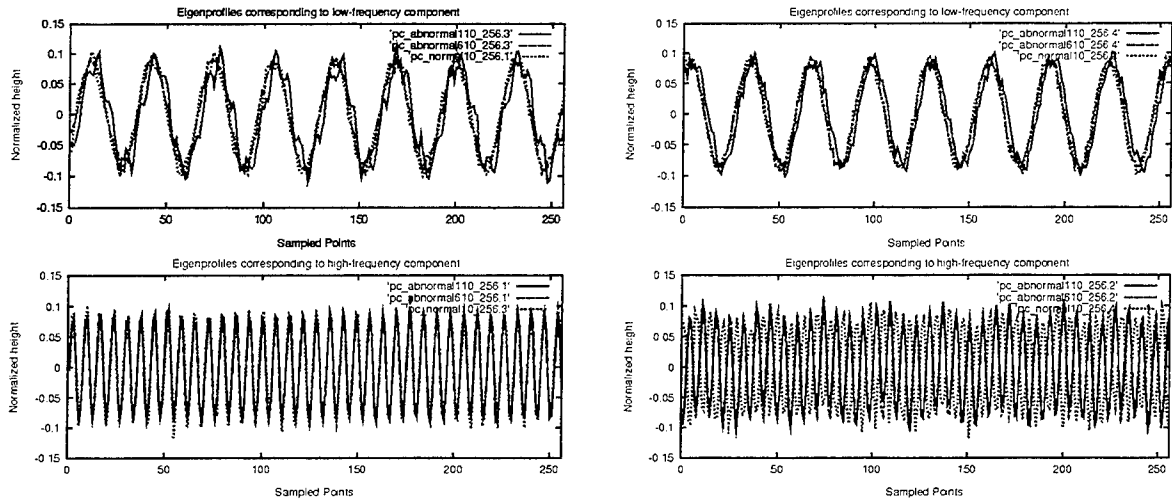


Figure 2: Principal Eigenprofiles from Normal vs. Abnormal States 1a & 1b

shown in Figure 3. Notice that the shape of the eigenprofiles are approximately the same for the

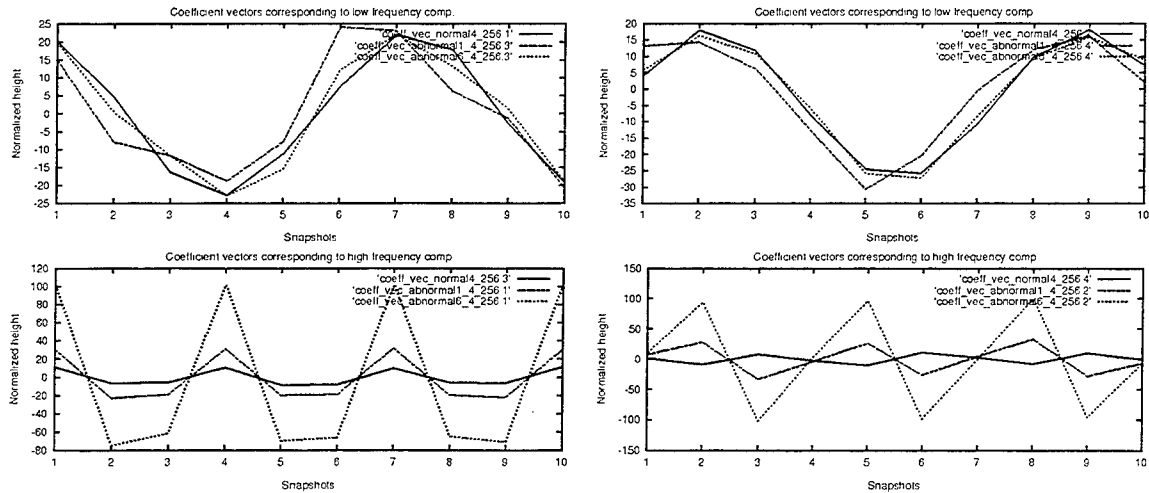


Figure 3: Coefficient Vectors: Normal vs. Abnormal States 1a & 1b.

normal state, and abnormal states 1a and 1b. This result is expected since we are only changing the magnitude of the high-frequency sinusoidal component, and not the frequency. The change in magnitude is detected using the coefficient vectors. Also notice that, the coefficient vectors corresponding to the high-frequency component show a steady increase in magnitude. On the other

hand, the coefficient vectors corresponding to the low-frequency component show no detectable change. The change in magnitude is successfully detected by monitoring the coefficient vectors.

Abnormal States 2a and 2b

In this case, we simulate an increase in the magnitude of the low-frequency component. The simulation results show that the eigenvalues corresponding to the low-frequency component increase in magnitude, as the magnitude of the low-frequency sinusoidal component increases. The eigenvalues corresponding to the high-frequency components remain approximately the same in magnitude as in the normal state (see Table 1).

In addition, the first four eigenprofiles from abnormal states 2a and 2b, are the approximately the same as in the normal state and in abnormal states 1a and 1b. This result is not surprising since we are not changing the shape of the pattern, but only the magnitude. The change in magnitude is properly detected with the corresponding coefficient vectors. In this case, the coefficient vectors corresponding to the high-frequency component remain unchanged, while the coefficient vectors corresponding to the low-frequency component show a steady increase in magnitude. Once again, the coefficient vectors can be monitored to detect the change in magnitude of any frequency component in the measured signal. In addition to these results, further simulation shows that, when both the high-frequency and the low-frequency components of the multi-component signal are increased in magnitude, the changes in magnitude are again successfully detected by monitoring the coefficient vectors (abnormal state 3, Table 1).

Abnormal State 4

Finally, we investigate whether the KL transform detects the occurrence of an unexpected fault. The fault, in this case, is introduced in the form of an additional frequency component. This simulates the case where the bearing of the roller in the SLS machine undergoes wear, hence introducing a harmonic, in addition to the fundamental frequency component. The first two sinusoidal components are the same as the normal state of operation; a third frequency component is added (abnormal state 4). In this case, the addition of a third frequency component introduces an additional set of eigenvalues (see Table 1). Therefore, the occurrence of an additional frequency component can be detected by monitoring the number of significant eigenvalues. The accuracy of this case needs to be investigated further.

Nonstationary Changes

The second set of simulations tests the effect of introducing sudden and/or gradual nonstationary changes to the monitored signal. These cases simulate the occurrence of faults after a certain point in time, introducing a nonstationary pattern over the monitored signal. Four cases are simulated, presented next. The eigenvalues for each of these cases, compared to the normal state of operation, are presented in Table 2.

Case 1

In the first case, signals from the normal state of operation are assumed to have a change in the mean offset after a certain period of time, hence introducing a nonstationary change in the signal that must be detected during monitoring; the first ten snapshots indicate normal status, while the next ten snapshots indicate an offset. This situation, for example, simulates a sudden change

Index	Normal	Case 1	Case 2	Case 3	Case 4
1	255.45	1602.78	3243.81	2253.35	346191.37
2	240.15	254.08	3191.27	2239.68	254.37
3	74.01	239.45	71.59	1397.22	240.01
4	55.62	69.86	56.26	69.79	69.38
5	2.68	55.23	1.52	56.32	56.66
6	2.58	1.66	1.49	1.20	2.36
7	2.25	1.41	1.36	1.08	2.21
8	2.14	1.32	1.33	1.05	2.11
9	2.00	1.24	1.26	1.01	1.92
10	0.00	1.22	1.22	0.92	0.03

Table 2: Results: Eigenvalues for Normal State vs. Cases 1 through 4

in the vertical position of the SLS part while it is being formed, caused by the residue deposited on the roller mechanism. As shown in Table 2, this fault manifests itself as an added principal eigenprofile, with a relatively large eigenvalue; the remaining eigenvalues are approximately the same as the normal state of operation. The simulation results show that the first eigenprofile resembles a straight line when plotted with the remaining sinusoidal eigenprofiles. In addition, the coefficient vector corresponding to the first eigenvalue shows the change in the mean offset very clearly, after the tenth snapshot, as shown in Figure 4. As a result, this additional pattern, defined by a straight line, can be detected by monitoring the occurrence of a fifth eigenprofile, while its significance can be evaluated by monitoring the shape of the coefficient vector. Note that no change is observed in the remaining eigenprofiles or coefficient vectors, when compared with the normal state of operation.

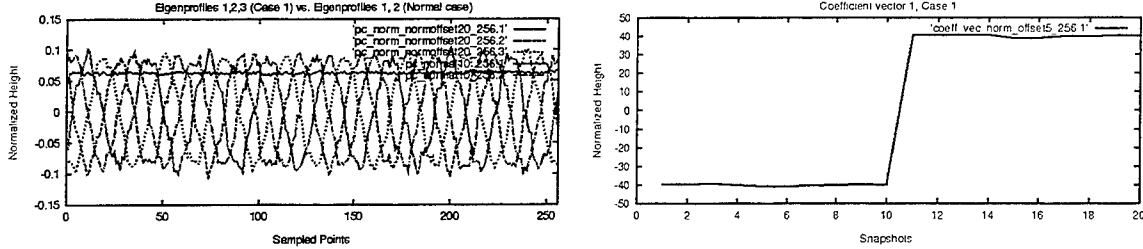


Figure 4: Principal Eigenprofiles and Coefficient Vector for Case 1.

Case 2

In this case, a situation similar to abnormal states #2 and #5 occurs, where the low-frequency component changes in magnitude, while the high-frequency component remains the same. We collect a total of twenty snapshots; a change occurs during the course of monitoring the signal, hence introducing a nonstationary change in the signal, after the tenth snapshot. The results show that, while the eigenprofiles remain the same as in the normal state of operation, the coefficient vectors corresponding to the low-frequency eigenprofiles increase in magnitude after the tenth snapshot, where the nonstationary change occurs (Figure 5). As expected, no change is observed in the high-frequency coefficient vectors (Figure 5). Also notice the increase in the eigenvalues for the first two eigenprofiles, while the eigenvalues for the next two eigenprofiles are approximately the same as the normal state of operation, as shown in Table 2.

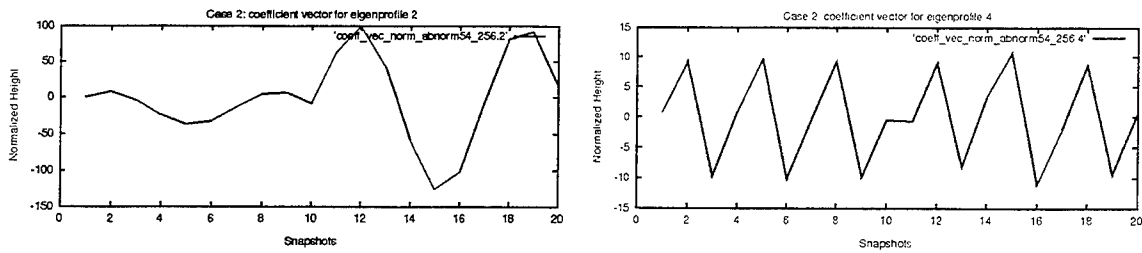


Figure 5: Principal Eigenprofiles from Normal State vs. Case 2.

Case 3

When both Case 1 and Case 2 take place, i.e., first the magnitude of the low-frequency sinusoidal component increases (after the tenth snapshot), then, a change in the mean offset is observed (after the twentieth snapshot), result show similar trends; in this case, we collect a total of thirty snapshots to observe both types of changes occurring at different points in time. A fifth eigenvalue/eigenprofile is observed, reflecting the change in the offset value, plus an increase in the first two eigenvalues, corresponding to the low-frequency eigenprofiles; the last two eigenvalues remain approximately the same as in the normal state of operation (Table 2, Case 3). In addition, as expected, the coefficient vectors corresponding to the low-frequency eigenprofiles show a change in magnitude after the tenth snapshot, and return to their original normal state after the twentieth snapshot. The coefficient vector corresponding to the third eigenprofile indicates the change in the offset value after the twentieth snapshot, while the coefficient vectors corresponding to the last two eigenprofiles show no change.

Case 4

In the final case, the normal state of operation is interrupted by the addition of a linear trend with a positive slope. This simulates, for example, a change in the table or powder bed slope while the SLS part is being manufactured. The results show the addition of a fifth eigenvalue (Table 2, Case 4) of large magnitude, while the remaining four eigenvalues are approximately the same as the normal state of operation. The first three eigenprofiles and the coefficient vector corresponding to the first eigenprofile are shown in Figure 6. As expected, the first eigenprofile represents a

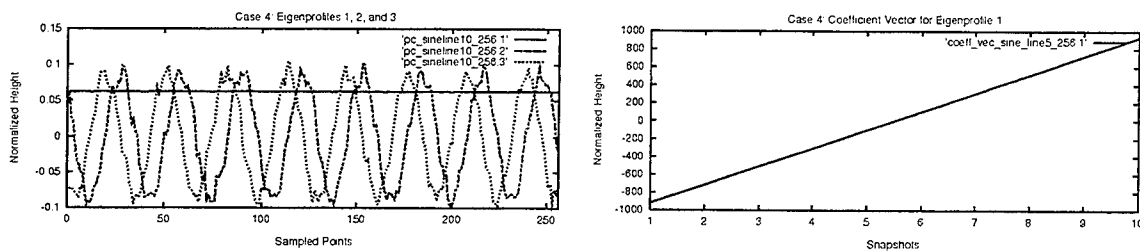


Figure 6: Principal Eigenprofiles and Coefficient Vectors for Case 4.

straight line as the basis vector, while the corresponding coefficient vector indicates the change in the magnitude of that principal eigenprofile, reflecting the slope in the linear trend.

Conclusions from the Simulation Results

The simulation results show that the KL transform presents a good potential for detecting, extracting, and monitoring fault patterns on surface profiles. First, the KL transform successfully decomposes the signal into its basis patterns (eigenprofiles). Changes in the magnitudes of these basis patterns are successfully reflected in the corresponding coefficient vectors. The introduction of additional patterns are also detected as additional basis patterns. For example, in case 1, the KL transform successfully decomposes the signal into its individual patterns, i.e., 2 sinusoids and a straight line. Monitoring is done by detecting a fifth eigenprofile and studying the change in the corresponding coefficient vector. In addition, the nonstationary change in the offset level is reflected in the relevant coefficient vector, hence allowing the effective monitoring of this nonstationary change in the normal state of operation. In case 2, the sudden change in the magnitude of the sinusoidal patterns is successfully reflected in the relevant coefficient vectors, while no additional patterns are extracted. In case 4, the KL transform extracts the additional basis pattern, represented as a straight line, and detects the introduction of a linear trend, which is reflected in the corresponding coefficient vectors as a linear increase in magnitude over the set of snapshots. Further simulations are necessary to assure that nonstationary patterns over snapshots (as opposed to patterns over the entire signal) are also detectable with this method. An example is a set of linear trends with differing slopes over each snapshot.

Conclusions and Future Work

This paper presents a study of the suitability of an orthogonal transform, namely the Karhunen-Loève transform, in decomposing signals measured from SLS part surfaces. We show that the KL transform can be used to detect stationary as well as nonstationary patterns, providing an accurate decomposition of multi-component signals. In addition, we show that the eigenprofiles and coefficient vectors derived using the KL transform can be used to effectively monitor and detect the occurrence of faults on measured SLS surface signals.

Stationary changes, including changes in the magnitudes of one or more sinusoidal components, are reflected as changes in the corresponding coefficient vectors. The introduction of an additional frequency component is reflected by an increase in the number of principal eigenvalues and eigenprofiles. Nonstationary changes in the normal state of operation, including a change in the mean offset level, and a change in the slope of the part surface, are reflected by the introduction of additional eigenprofiles and corresponding changes in the coefficient vectors. A sudden change in the magnitude of a sinusoidal pattern is reflected by an accurate change in the corresponding coefficient vector. As a result, the KL transform is shown to be a proper tool in extracting the relevant features and monitoring stationary and nonstationary changes in the normal state of operation, for those cases simulated in this paper. Further mathematical proof of these results will follow.

In addition to the work presented in this paper, the authors are currently simulating other fault components, such as transients, and other nonstationary fault components, such as a saw-tooth shaped pattern. Other transforms such as the wavelet transforms and higher-order spectral transforms are also being investigated as potential candidates to provide an effective and accurate decomposition of multi-component signals. The results of this work will be used to develop an accurate fault detection and diagnosis method to assure the quality of surfaces from manufacturing machines.

Acknowledgements

This material is based on work supported, in part, by The National Science Foundation, Grant No. DDM-9111372; an NSF Presidential Young Investigator Award; by a research grant from TARP; plus research grants from Ford Motor Company, Texas Instruments, and Desktop Manufacturing Inc., and the June and Gene Gillis Endowed Faculty Fellowship in Manufacturing.

References

- [1] A.N. Akansu and R.A. Haddad. *Multiresolution Signal Decomposition: Transforms, Subbands, Wavelets*. Academic Press, Inc., San Diego, Ca, 1992.
- [2] V. R. Algazi, K. L. Brown, and M. J. Ready. Transform representation of the spectra of acoustic speech segments with applications, part I: General approach and application to speech recognition. *IEEE Transactions on Speech and Audio Processing*, 1(2):180-195, April 1993.
- [3] K.S. Ball, L. Sirovich, and L.R. Keefe. Dynamical eigenfunction decomposition of turbulent channel flow. *International Journal for Numerical Methods in Fluids*, 12:585-604, 1991.
- [4] J. S. Bendat and A. G. Piersol. *Random Data: Analysis and Measurement Procedures*. John Wiley & Sons, New York, NY, 1986.
- [5] S. D. Eppinger, C. D. Huber, and V. H. Pham. A methodology for manufacturing process signature analysis. *Journal of Manufacturing Systems*, 14(1):20-34, 1995.
- [6] K. Fukunaga. *Introduction to Statistical Pattern Recognition*. Academic Press, New York, NY, 1972.
- [7] W. Kozek. Matched generalized gabor expansion of nonstationary processes. In *The Twenty Seventh Asilomar Conference on Signals, Systems, & Computers*, volume 1, pages 499-503, 1993.
- [8] L. Sirovich and L.R. Keefe. Low-dimensional procedure for the characterization of human faces. *Journal of the Optical Society of America*, 4(3):519-524, March 1987.
- [9] J. Sottile and L. E. Holloway. An overview of fault monitoring and diagnosis in mining equipment. *IEEE Transactions on Industry Applications*, 30(5):1326-1332, September/October 1994.
- [10] S. Spiewak. A predictive monitoring and diagnosis system for manufacturing. *Annals of the CIRP: manufacturing technology*, 40(1):401-404, 1991.
- [11] I.Y. Tumer, R.S. Srinivasan, and K.L. Wood. Investigation of characteristic measures for the analysis and synthesis of precision-machined surfaces. *Journal of Manufacturing Systems*, 14(5):378-392, September/October 1995.
- [12] I.Y. Tumer, D.C. Thompson, R.H. Crawford, and K.L. Wood. Surface characterization of polycarbonate parts from selective laser sintering. In *SFF Symposium Proceedings*, pages 181-188. The University of Texas at Austin, August 1995.
- [13] I.Y. Tumer, D.C. Thompson, K.L. Wood, and R.H. Crawford. Characterization of surface fault patterns with applicaiton to a layered manufacturing process. *Submitted for review to the Journal of Manufacturing Systems, Special Issue in Layered Manufacturing Systems*, February 1996.
- [14] D.J. Whitehouse. *Handbook of Surface Metrology*. Institute of Physics Publishing, Bristol, UK, 1994.
- [15] S. A. Zahorian and M. Rothenberg. Principal-components analysis for low-redundancy encoding of speech spectra. *Journal of the Acoustical Society of America*, 69(3):519-524, March 1981.

FEATURE EXTRACTION FROM TESSELLATED AND SLICED DATA IN LAYERED MANUFACTURING

Kamesh Tata
Prototype Express

Georges Fadel
Clemson University

Abstract

When parts are built in layers, the cross sectional area of each layer has to be defined and filled with a pattern of vectors. This filling process is called hatching and the vectors define the hatch pattern. To accurately reproduce a three dimensional object, key features need to be identified. In particular, top and bottom surfaces, edges, holes and protrusions must be recognized to ensure the slice plane does carry the critical information required for the build. This paper describes a technique to extract relevant features from a tessellated model to generate a correct sliced representation.

Introduction

Layered based manufacturing is based on a mathematical slicing operation that generates slices from an original boundary representation model (tessellated or triangulated model). Different processes use different devices to draw the hatch vectors which represent the areas to be filled or solidified in a slice. For instance, Stereolithography and Selective Laser Sintering use a laser to draw the vectors, while other processes may use a pattern mask or a binding agent.

Many slicing engines exist, in particular, the slicing program of 3D systems has a proven algorithm. Grogan [1990] described an algorithm based on sorting, Chalasani [1992] proposed two algorithms for slicing 3D objects that also rely on a sorting process to identify areas, Vouzelaud and Bagchi [1992] proposed an adaptive technique, Kirschman and Jara-Almonte [1992] investigated parallel slicing, and Dolenc and Mäkelä (1993) suggested slicing procedures which considered the identification of some features, notably peaks and flat areas.

This paper considers the issue of features and their extraction from the tessellated data. It highlights the capabilities of such an algorithm to identify manufacturing features and lists the pitfalls and their possible remedies.

The STL File

The *de facto* industry STL model representation defines CAD solid models as a set of triangular facets (3D Systems, 1989). Facet models represent solid objects by spatial boundaries which are defined by a set of planar faces. This is a special case of the more general boundary representation which does not require object boundaries to be planar (Mortenson, 1985). In general, the term facet is used to denote any constrained polygonal planar region used to define a model boundary; however, in the SFF community, the term facet is typically understood to mean triangular facet (Rock, 1991). Unfortunately, these facets are stored independently, as if each facet was created and tossed into a bucket with no particular ordering and without information relating a given facet to any other facet in the bucket (Rock, 1991).

Hole or Projection

One of the time consuming tasks of any hatching routine is identifying holes and projections. Holes should not be hatched, while projections should. At the time of hatch-

ing, the information about the solid is no more available in a single piece. Most of it is divided and stored in a number of 2-D slices and some of it is lost. This implies that identifying a single hole or a projection might require studying several slices together. This is computationally expensive. Thus there is a need for an efficient hatching algorithm which identifies, in the quickest possible way, areas that need to be filled and areas that need not be filled.

Strategy for Hatching

In order to identify the areas that need to be hatched, we examined various contours and derived the following rule : If a contour is surrounded by n contours and n is an even number, the contour represents a protrusion and should be filled. On the other hand, if n is odd, it the contour represents a hole and should not be filled. This rule, which is central to the hatching algorithm developed as part of this research, can also be explained in another way. Considering 3-D solid objects,

1. a solid is always bounded,
2. there cannot be a solid without thickness,
3. and there cannot be a hole without a solid.

These three simple and definitive statements ensure that when a solid is sliced the resulting contours are invariably closed and non-intersecting. Also, there will never be two holes adjacent to each other or one contained in the other without being separated by a definite distance. Furthermore, any unbounded contour (contours not surrounded by any other contour) can never be a hole.

Key Characteristics Identifier

A simple knowledge base, supported by a few rules, is created with an aim to recognize the following from a tessellated model:

1. base faces of features,
2. type of features (protrusion or depression), and
3. geometric shape and orientation of features.

The rules are mostly based on simple geometric and engineering principles, and derived by observation and logical reasoning. Some of the ideas discussed can be utilized for any solid model regardless of the representation scheme.

The Three Types of Base Faces

The top and bottom faces of any feature, including the object, may be termed as base faces. Recognition of base faces is essential to improve the tolerances of layered models. Since a polygon is comprised of only two basic entities, point and line, only their combinations will result in any topologically significant characteristic. Consequently, any solid represented by planar polygons can have only three types of base faces:

1. Horizontal surface: A horizontal surface is represented by a single or multiple polygons parallel to the slice plane. Figure 1 shows horizontal faces composed of triangular facets.
2. Pointed edge: When at least two non-co planar polygons share an edge, the edge may be termed as a pointed edge. This is illustrated in Figure 2, where a block with v-grooves is shown.

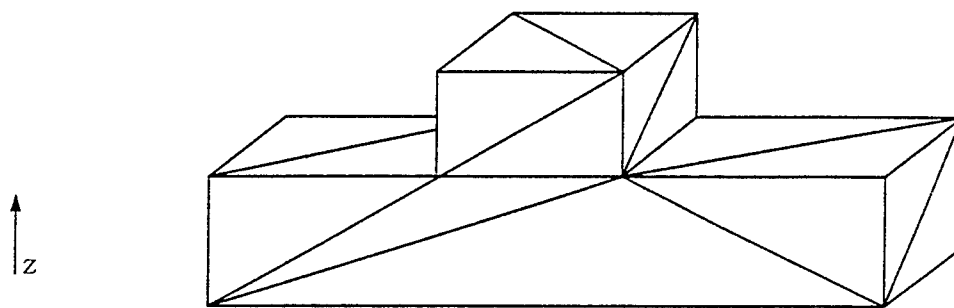


Figure 1. Multiple Facets Forming Horizontal and Vertical Surfaces

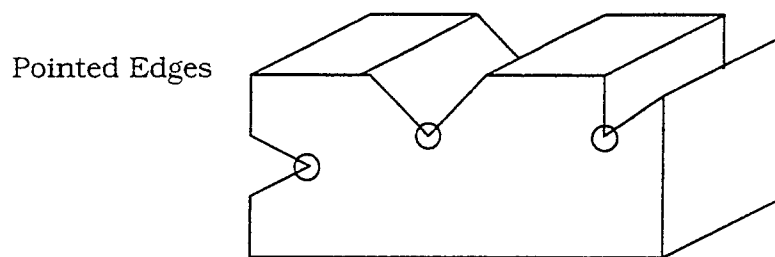


Figure 2. Block with Pointed Edges

3. Pointed End: When at least two non-co planar polygons share a vertex, the vertex may be termed as a pointed end. Tip of a cone and corner of a block, shown in Figure 3, are examples of pointed ends.

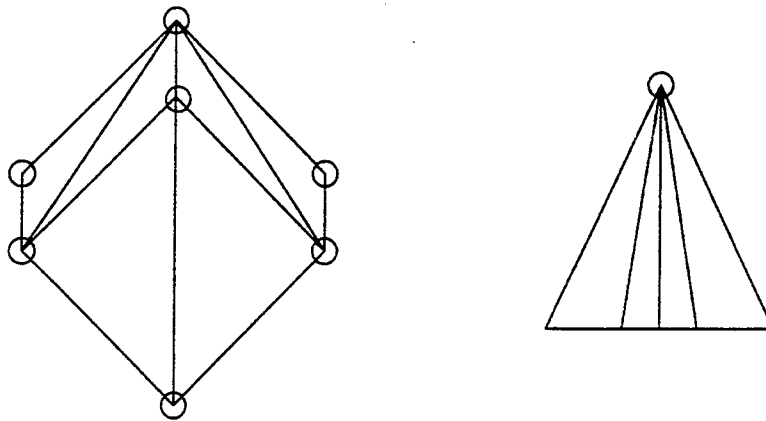


Figure 3. Examples of Pointed Ends

For the purpose of layered manufacturing, the effort must be to identify the existence and then to determine the height (along the slice axis and from a reference point) of each one of the above so that the slice plane can be forced to assume that height. Identification of these three types from an STL model format is basically a searching operation.

Identifying Horizontal Surfaces

Horizontal surfaces can be identified by checking unit normals or ordinate values of facets. If the unit normal of a facet describes 90^0 (or 270^0) with the slice plane, there lies a horizontal surface with that facet contained in that surface. Alternatively, if the z coordinate values of all the three vertices of a facet are equal, then that facet is part of a horizontal surface.

Vertical walls can be identified essentially using the same approach used to identify horizontal surfaces. If the unit normal of a facet makes 0^0 (or 180^0) with the slice plane, there exists a vertical wall with that facet contained in that wall.

Identifying Pointed Edges

According to the definition of a pointed edge, any edge shared by two non-co planar facets is a pointed edge. With this definition, there are twelve pointed edges, four vertical and eight horizontal, in a cube shown in Figure 4. It does not serve any purpose in the context of layered manufacturing to identify these edges separately, since the vertical and horizontal surfaces of which these edges are part of, can be easily identified using methods suggested earlier. Likewise, it is worthless to identify the edges of a tetrahedron shown in Figure 4 because none of the edges of the inclined surfaces are parallel to the slice plane. As we discussed previously, our primary goal is to identify key characteristics which are parallel to the slice plane so that we can retain them in the sliced model.



Figure 4. Unwanted Pointed Edges

It is, therefore, necessary to narrow the definition of a pointed edge, in the context of layered manufacturing. First, none of the polygons sharing an edge should be horizontal or vertical. This is due to that horizontal and vertical faces are already identified and with that all their edges. Further, the common edge must be parallel to the slice plane. (Only then a separate effort is required for its retention in the sliced model.)

A pointed edge can now be defined as: Any non-horizontal and non-vertical facet with two vertices having the same z coordinate value will form a pointed edge provided the second facet that shares these vertices (there will be only one such facet) is not in the same plane as the first facet and is non-horizontal and non-vertical. Also, the angle between those two facets need to be defined by the user. This is to avoid mistakenly identifying the edges of facets approximating curved surfaces as pointed edges. If we consider the faceted model of a sphere, according to the above definition, potentially every edge becomes a pointed edge. This can be avoided by defining the angle between the two facets sharing an edge to be less than a certain value, say, 120^0 , before the edge can be considered as a pointed edge.

This new and narrow definition of a pointed edge helps reduce the time required to search for such edges in a faceted model. However, identifying two vertices of a facet with the same z coordinate value, the very first step in identifying a pointed edge, demands virtually every vertex of all non-horizontal and non-vertical facets in the model to be searched. This again leads to high execution times.

Identifying Pointed Ends

Finally, pointed ends can be identified from an STL file by looking for a single vertex shared by several non-co planar facets. For example, the apex of a cone is shared by a number of non-co planar facets which form the conical surface. This calls for checking every vertex in the model for the number of facets that share the vertex and their unit normals.

Base Faces – Change in the Number of Contours

Clearly, identifying pointed ends and edges is a time intensive search operation. Isolation of a vertex that forms a pointed end or a facet side that forms a pointed edge demands a large scale search often covering every facet of the model. This problem can be largely overcome by adopting a new strategy. This strategy is based on the fact that whenever there is a change in the number of contours in successive slices, there lies a base face of a feature. The exact location of the base face can be anywhere between the two slice planes or contained in the slice plane which has the greater number of contours. Once a change in the number of contours is observed, the exact location of the base face can be found by considering facet groups in that region and applying the methods suggested above. However, this strategy requires slicing the model and counting the number of closed contours in each slice.

Slice Based Feature Recognition – Protrusions or Depressions

Protrusions are any projections on the object, such as pads, bosses, and mounds, while depressions are holes of any shape. The easiest way of finding the type of a feature is by studying the slices and the contours within each slice. The following rules will provide methods to distinguish between protrusions and depressions. These rules are simple, definite, unambiguous, and true for any solid.

Rule 1: When a solid is sliced by an imaginary plane, the resulting slice may contain a single or multiple, non-intersecting, closed contours. This is true regardless of the angle and the position of the slice.

Before going further, it is necessary to define certain key words used in the preceding part of this section.

1. Empty contour: An empty contour is one which does not contain any other contour within its bounds. In other words, an empty contour does not surround any other contour. See Figure 5.
2. Unbounded contour: An unbounded contour is one which is not surrounded or bounded by any other contour.

Rule 2: If a single or multiple empty contours are surrounded by a single larger contour, all inner contours represent depression features. This can be seen in Figure 6, where a rectangular block with several holes is shown. The slice at AA has several empty contours surrounded by a single large contour. Obviously, all inner contours represent holes and hence the rule 2 is satisfied.

Rule 3: If two or more contours are nested within each other, all even-numbered contours represent depressions while all odd-numbered contours represent protrusions, the outermost contour being number 1. Figure 7, where a cylindrical block with multiple holes one inside the other is shown, illustrates rule 3.

Rule 4: Any unbounded contour represents a protrusion feature. Figure 8, where a number of protrusions are shown on the top of a rectangular block,

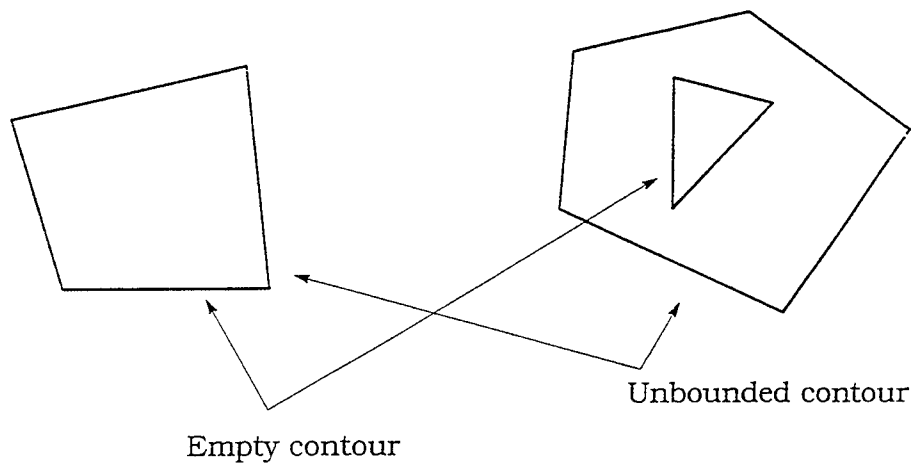


Figure 5. Empty and Unbounded Contours

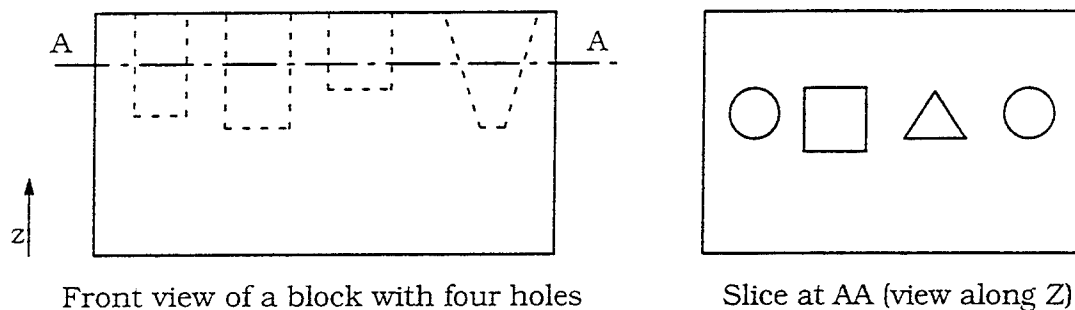


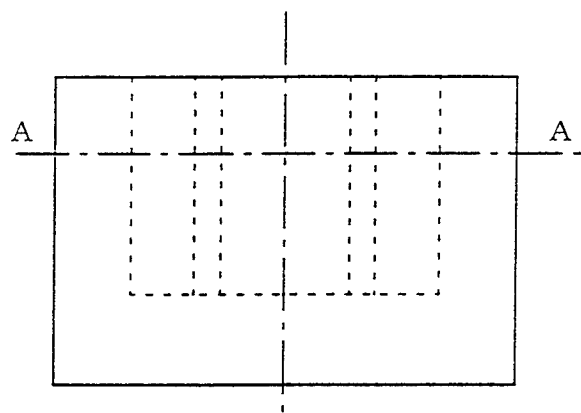
Figure 6. Multiple Empty Contours within a Larger Contour

clearly illustrates this point. The slice at AA contains several unbounded contours and all are, obviously, protrusions. This satisfies rule 4.

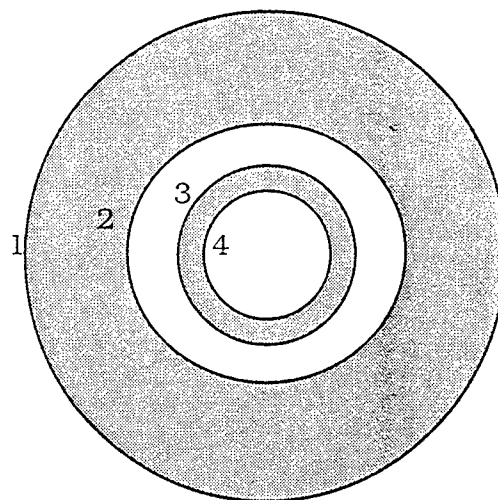
Shape and Orientation of Features

Once, location and type of a feature are determined, further details can be obtained by studying the unit normals of the facets the feature is comprised of. The following assumes that holes and projections, and base faces are already identified using the methods suggested above.

A feature is rectangularly shaped, if it is bounded by four faces, and each face is perpendicular to its adjacent face. Again, all four must be perpendicular to a common plane. If a fifth face that connects all four faces exists, the feature is closed at one end. It is closed at both ends if a sixth face also exists connecting the first four faces. Furthermore, the feature can be a rectangular pad or a rectangular hole depending upon its nature (protrusion or depression). Triangular pads or holes are bounded by three faces, where the sum of the included angles between the faces is exactly 180° and all three are perpendicular to a common plane. The type of triangle can also be easily established by studying the included angle between faces. This logic can be extended to identify pentag-



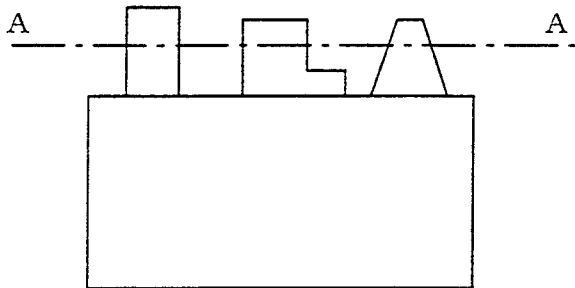
Front view of a cylinder with two holes



Slice at AA (view along Z)

Grey indicates solid
White indicates hole

Figure 7. Multiple Contours Surrounding Each Other



Front view of a block with three protrusions



Slice at AA (view along Z)

Figure 8. Unbounded Contours

onal, hexagonal or any polygonal feature. Orientation of the feature can be established by determining the angle between the slice plane and one of the bounding faces. Different types of features that can be easily identified are shown in Figure 9.

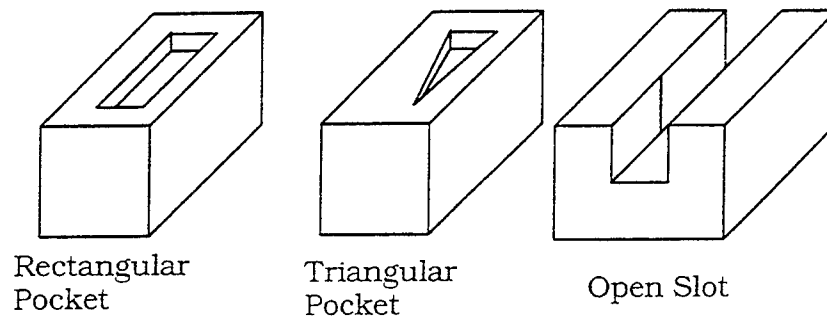


Figure 9. Typical Features Which Can Be Identified from Tessellated Models

One limitation with slice based feature recognition is that features parallel or at certain angles to the slice plane will be difficult to identify. In order for a comprehensive feature recognition, slicing may have to be done at different angles and the resulting slices studied independently and together. For example, in Figure 10, holes A and B, which are parallel to the slice plane, cannot be identified. Hole C, which is perpendicular to the slice plane, can be easily identified as a depression feature. In order to identify A and B, slicing has to be done along x or y. Feature recognition is a vast area and the work done here is only a small effort toward that goal.

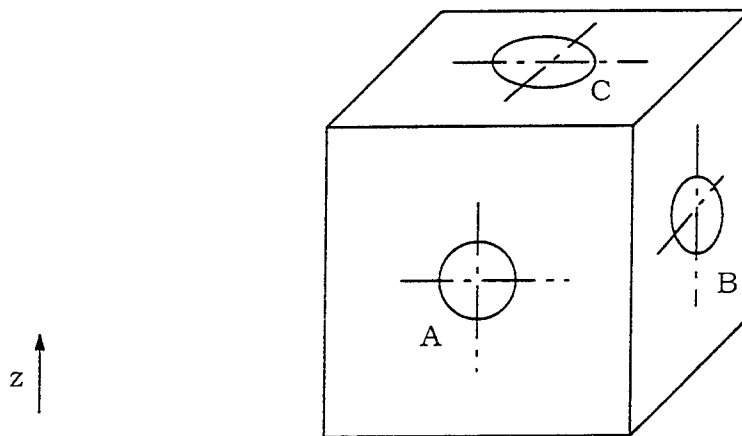


Figure 10. Block with Three Holes Along the Three Axes

Conclusions

This work describes a possible methodology for the identification of features from layered or tessellated data. A simple rule base is used to identify such features. The method does have significant limitations since features are only recognized when along the build axis. However, if one considers what features are used for, especially to identify hatching areas, then this feature recognition is sufficient. If the features are needed for

design purposes, then the approach has to be performed three times, one for each coordinate axis as the build direction.

References

1. 3D Systems Inc., (Valencia, CA), 1989, "Stereolithography Interface Specification."
2. Chalasani, K. L., Grogan, B., Bagchi, A., Jara-Almonte, C. C., Ogale, A. A., and Dooley, R. L., "An Algorithm to Slice 3-D Shapes for Reconstruction in Prototyping Systems", Computers in Engineering - Volume One, ASME 1991.
3. Chalasani, K. L., "Design and Implementation of Slicing and Hatching Algorithms for Freeform Fabrication", M. S. Thesis, Clemson University, Clemson, S. C., 1992.
4. Dolenc, A., and Makela, I., "Slicing Procedures for Layered Manufacturing Techniques", Otaniemi 1992/TKO-B83, Helsinki University of Technology, Finland.
5. Frank, D., Geuer, A., and Fadel, G. S., "Definition of Rules for a Preferred Orientation of Rapid Prototyping Parts with the Help of an Expert System", Technical University of Munich and Clemson University, 1993.
6. Grogan, B., "Development of a Slicing Algorithm for Laminated Part Manufacturing", Undergraduate Research, Clemson University, Clemson, S. C., 1990.
7. Kirschman, C., and Jara-Almonte, C. C., "A Parallel Slicing Algorithm For Solid Freeform Fabrication Processes", Proceedings of the 1992 Solid Freeform Fabrication Symposium, Austin, TX, August 3-5.
8. Mortenson, M. E., "Geometric Modeling", John Wiley and Sons, New York, N. Y., 1985.
9. Rock, S. J., and Wozny, "A Flexible File Format for Solid Freeform Fabrication", M. J., Rensselaer Design Research Center, Rensselaer Polytechnic Institute, Troy, N.Y., 1991.
10. Tata, K. M., "A Marching Algorithm for Adaptive Slicing of 3-D Parts for Reconstruction in Prototyping Systems", Course Project for CE 690, taught by Dr. N. M. Aziz, Clemson University, Clemson, S.C., 1993.
11. Vouzelaud, A. F., and Bagchi, A., "Adaptive Laminated Machining for Prototyping Dies and Molds", Solid Freeform Fabrication Symposium, Proceedings, August 3-5, 1992, University of Texas at Austin.

Parametric Representation of Part Contours in SLS Process

Kenwei Chen, Richard H. Crawford, and Joseph J. Beaman
Department of Mechanical Engineering
The University of Texas at Austin

ABSTRACT

Current layer-based SFF technologies process faceted geometric input data to produce polygonal contours of the part's boundary in each layer. However, for improved part quality, other more accurate representations of part contours are desirable. Likewise, implementation of Wu's minimum time optimal laser tracking control method for selective laser sintering (SLS) requires contour curves that exhibit higher order continuity. In this paper, we first analyze the requirements of optimal laser tracking to develop evaluation criteria for choosing a contour representation. Several possible representation methods are reviewed. We show that the Non-Uniform Rational B-Spline (NURBS) curve meets the criteria. A demonstration program illustrates the advantages of NURBS curves for representing contours with uniform point distributions. The results can be used in other control areas where uniform point distribution or constant velocity is required.

Keywords: computational geometry, NURBS, Bézier curve, tracking control, laser beam control.

1 INTRODUCTION

In layer-based solid freeform fabrication (SFF) processes, a three dimensional geometric description of a solid object is sliced into a stack of two dimensional cross sections whose normals are parallel to the build axis. Current layer data formats, such as CLI from Europe and SLC from 3D Systems, represent the part's boundary in each layer as a set of polygonal contours. SFF technologies then process the layer data differently, depending on the underlying physical process and the sophistication of the control software. For instance, in selective laser sintering (SLS), the laser is raster scanned to fill these cross sections and to build the parts layer by layer. The laser beam is directed by a pair of scanner galvanometers. With this type of process, there is a trade-off between productivity, in terms of build time, and part quality, in terms of surface accuracy, for a given laser power. To increase accuracy, a smaller laser spot is preferred, while productivity demands a larger laser spot to scan more area per unit time. To resolve this dilemma, a strategy based on boundary scanning of the layer contours, followed by a raster fill of the contour interiors, is proposed. Wu and Beaman (Wu and Beaman, 1990; Wu and Beaman, 1991; Wu 1992; Wu and Beaman, 1992) developed an optimal tracking control method for boundary scanning in SLS. The purpose of this paper is to evaluate different parametric representations for layer contours based on their applicability to Wu and Beaman's control method, and for SFF technologies in general.

1.1 Problem Description

Wu's tracking control algorithm is based on the assumption that the tracking path (*i.e.*, contour) is represented parametrically. Wu did not explicitly specify the requirements of the parametric form, but these can be obtained from the derivation of his control algorithm. In general, the parametric form must satisfy the following three requirements: (1) $n-1$ differentiability, except at corners; (2) parametrization by arc length, so that the first and second derivatives represent tangential velocity and acceleration; and (3) uniform distribution of points. Wu derived the dynamics of scanner galvanometer as a second order system. Therefore, the tracking path must exhibit C^1 continuity. Note that corners have specific meanings. Wu defined a corner as "a point in the prescribed path where tracking velocity must be zero due to the available bounded control torque". To handle corners accurately, the tracking path is divided into several segments such that

corners only exist at the start and end points of the segments. The third requirement allows “near constant tracking speed to gain uniform exposure of laser power”.

Three dimensional solid objects are transmitted to SFF processes according to some CAD geometric data format. The current standard for exchanging geometric data form is the so-called STL data file format, which is supported by most commercial CAD system. The STL format represents a 3D part as a triangulated approximation of the part's surfaces. Each facet is defined by its three vertices and its normal vector, which indicates the interior of the part. After slicing the STL data, layer contours are generated and represented by polygonal outlines of the cross-section. However, Wu's method is based on a parametric form meets the criteria described above. Thus, for applying Wu's method to STL data, the polygonal contours must be represented by higher degree parametric curves. On the other hand, other geometric data formats are possible (Darrah, 1990). This paper targets the generation of a parametric representation based on point data. However, we briefly discuss the applicability of parametric representations for contours generated from other 3D geometric data, such as IGES.

2 PARAMETRIC CURVE REPRESENTATIONS

Both parametric and nonparametric curve forms have useful applications. Parametric forms are more dominant in current geometric modeling practice because they are axis-independent, they facilitate redistribution of points along the curve length, they are convenient for generating coordinates of points on the curve, and they represent infinite slopes easily. The well-known and commonly-used parametric curves include the spline, Bézier, B-spline, and Non-Uniform Rational B-Spline (NURBS).

The spline is a set of piecewise polynomials of degree K with continuity of derivatives up to $K-1$ at the common joints between segments. The cubic spline has been found most useful for engineering applications, since it is the lowest order polynomial that allows an inflection point. The cubic spline exhibits second-order or C^2 continuity at the joints. There are three common parametrizations for spline curves (Lee, 1989; Rogers and Adams, 1990): equally spaced, cumulative chord length (which approximates a uniform parametrization), and the centripetal method. However, the spline curve has several disadvantages. In particular, the spline curve can be unstable, especially with higher degree curves (Rogers and Adams, 1990); it does not lend itself well to geometric interpretation, making interactive interfaces difficult; and it does not exactly represent all standard curves, such as conic sections.

To overcome these shortcomings, Bézier curves are used as the basis of many modeling systems. Bézier curves are determined by a defining polygon, which is composed of a set of control vertices. Bézier curves have a many attractive advantages, including recursive computational algorithms, the convex hull property, the variation-diminishing property, positivity of the basis functions, and simple degree elevation and reduction algorithms. One disadvantage of Bézier curves is that, except for the start and end points, they do not interpolate the control points. This characteristic makes the Bézier curve inappropriate for direct use for contour descriptions. However, as a special case of the B-spline curve (discussed below), a Bézier curve can be designed to pass through the given data by adding control points between the interpolated control points.

The B-spline curve has many of the advantages of the Bézier curve, while it overcomes some of the disadvantages. In particular, the order of the B-spline curve is not determined by the number of control points, as is the case for Bézier curves. The most general form, the non-uniform rational B-spline (NURBS) curve, is defined as:

$$C(t) = \frac{\sum_{i=0}^n w_i \mathbf{P}_i N_{i,k}(t)}{\sum_{i=0}^n w_i N_{i,k}(t)}, \quad (1)$$

where \mathbf{P}_i are the control points, w_i are the weights associated with the control points, and $N_{i,k}(t)$ are the B-spline basis functions of order k . Note that when all weights are 1, the NURBS curve degenerates to the B-spline, and when a special knot vector is chosen, its basis functions are exactly the same as those of the Bézier curve.

NURBS curves have many desirable properties for both representation and computation (Piegl 1991). Besides the properties mentioned for Bézier curves, NURBS curves: (1) provide a unified approach for modeling curves, including the conic sections; (2) provide greater flexibility; (3) exhibit computational stability and fast evaluation; (4) lend themselves readily to geometric interpretations; (5) are affine invariant; (6) is generally nonglobal with respect to changes to control points; and (7) provide generalizations of B-spline and Bézier curves. Powerful tool kits are available from the literature to provide knot insertion/refinement/removal, degree elevation, splitting, and other desirable operations. The only relative drawbacks to the NURBS representation are its extra storage requirements and computational overhead. However, with current computer technology, these are not the significant problems.

3 EVALUATION CRITERIA FOR PARAMETRIC REPRESENTATION TECHNIQUES

We base our criteria for choosing an appropriate parametric representation for contours on the three requirements for Wu's control method. First, arc length parametrization has been studied by several researchers (*e.g.*, Guenter, 1990). Other considerations arise when we consider particular SFF technologies, such as SLS. The accuracy of the parts is always a main objective. In SLS, the laser beam follows the tracking paths during boundary scanning. The laser beam is adjusted by scanners that are controlled by galvanometers in x and y directions. Thus, continuity of motion is another important issue. The dynamics of these motion components restrains the maximum acceleration of the scanners. As Wu pointed out, a straight-line vector scanning mode can be slow when curves exist in the contour path, due to repetitive starts and stops required to accurately approximate the curves. Other considerations include computational constraints. Based on these factors, we propose the following criteria for choosing a parametric representation for part contours:

1. **Accuracy, continuity, and uniform point distribution.** In tracking control, position accuracy and tracking speed smoothness are desired. As stated above, Wu's method requires the parametric form to be $n-1$ continuously differentiable. Thus, the parametric representation methods should have good approximation and continuity. Uniform point distribution requires the parametric form to produce equally spaced points along the contours.
2. **Interpolation of given point data.** In SLS, the point data given or calculated are normally exactly on the actual contours. Therefore, the parametric curves should pass through all data points.

3. **Robustness.** There are many subtleties in parametric representations, such as non-existent loops that often occur in spline representation. Many traditional parametric curve techniques are not developed for representing general paths. Also, there is usually not a unique curve for interpolating given input data. For example, there are infinitely many NURBS curves that interpolate a given set of data. Robustness here means that we will always get physically reasonable contours from sufficient input data, and no abnormalities will exist in the contours. The input data can be points or other description data, such as radii and center data for circles.
4. **Adaptability.** This property indicates the ability to handle special cases in contours, such as corners, straight line segments, and other local geometric features.
5. **Computational constraints.** Computational considerations include ease of implementation of algorithms, storage, and computation overhead. The floating value round-off problems should be avoided if possible.

Based on these considerations, we propose the NURBS curve for representing contours. In the remainder of the paper, we evaluate the performance of NURBS curves based on these criteria.

4 NURBS PARAMETRIC REPRESENTATION TECHNIQUES

Input to a representation problem generally consists of geometric data, such as points and derivatives. The output is a NURBS curve represented by control points, knots, and weights. Furthermore, the degree p must be specified. If C^r continuity is desired for a curve, then the chosen degree p must satisfy $p \geq r + 1$ (assuming no interior knots of multiplicity > 1).

4.1 Quadratic NURBS Representation

NURBS interpolation of a set of given data is introduced by Piegl and Tiller (1995). For uniform parametrization, we have improved his algorithm both in knot vector construction and derivation of continuity at the start and end points of a contour. Additionally, we select rules that are appropriate for physical mechanical parts. We assume $\{Q_k\}$, $k = 0, 1, \dots, n$, to be a set of contour data from slicing a part described by the STL format (see Figure 1). We also assume no tangent vectors T_k are provided. The method constructs n rational curve segments, $C_i(t)$, $i = 0, \dots, n-1$, such that Q_k and Q_{k+1} are the endpoints of $C_i(t)$. Neighboring segments are joined with some prescribed level of continuity, and the construction proceeds segment-wise, generally from left to right in the knot vector. Any basis equations are local to only a few neighboring control points.

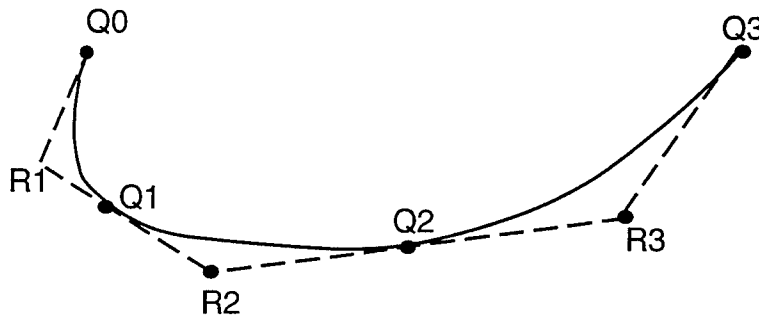


Figure 1. Quadratic B-spline representation.

Now let \bar{t}_i denote the start parameter of $C_i(t)$ and the end parameter of $C_{i-1}(t)$, where $C_i(t)$ and $C_{i-1}(t)$ meet at \bar{t}_i with G^1 continuity¹. Note that NURBS curves are continuously differentiable up to $n-1$ except at the knots. G^1 continuity is useful if we regard these knots as corners. C^1 continuity will be obtained later by using cubic Bézier based NURBS representation.

Obtaining the Bézier segments, $C_i(t)$, requires computation of the inner Bézier control points (one point for quadratics). These control points lie on lines that are tangent to the curve at the Q_k ; thus, we require tangent vectors T_k at each Q_k . In some cases, they can be input along with the Q_k . For instance, they can be obtained when computing intersection points between two surfaces. However, we can compute them approximately from the given data Q_k (Boehm *et al.*, 1984). The following steps are used to construct the NURBS representation from these data:

Step 1. Derive tangents at given data points. We choose the five point scheme to calculate the tangent vectors:

$$T_k = \frac{V_k}{|V_k|}, \quad (2)$$

where

$$V_k = (1 - \alpha_k)q_k + \alpha_k q_{k+1}, \quad (3)$$

$$q_k = Q_k - Q_{k-1}, \text{ and} \quad (4)$$

$$\alpha_k = \frac{|q_{k-1} \times q_k|}{|q_{k-1} \times q_k| + |q_{k+1} \times q_{k+2}|}, (k = 2, \dots, n-2). \quad (5)$$

The five-point method has the advantage that three collinear points, Q_{k-1} , Q_k , Q_{k+1} , yield a tangent T_k that is parallel to the line segment. The denominator of the five-point form vanishes if Q_{k-2} , Q_{k-1} , and Q_k are collinear and Q_k , Q_{k+1} , and Q_{k+2} are collinear. This implies either a corner at Q_k , or a straight line segment from Q_{k-2} to Q_{k+2} . In these cases α_k can be defined in a number of ways; we choose $\alpha_k = 1$, which implies $v_k = q_{k+1}$, producing a corner at Q_k . Whether or not to preserve corners depends on the application. The ends of the contour need special treatment:

$$\begin{aligned} q_0 &= 2q_1 - q_2, \\ q_{-1} &= 2q_0 - q_1, \\ q_{n+1} &= 2q_n - q_{n-1}, \text{ and} \\ q_{n+2} &= q_0. \end{aligned} \quad (6)$$

Note that the last form is used to force a closed contour by setting the end point equal to the start vector. From these forms, we obtain T_0 , T_1 , T_{n-1} , and T_n .

¹For a discussion of geometric continuity, see Barsky and DeRose, 1989.

Step 2. Determine the control polygon. We can reconstruct the control points and knot vector to create a NURBS curve. Let \mathbf{L}_k denote the directed line defined by $(\mathbf{Q}_k, \mathbf{T}_k)$, and \mathbf{R}_k the intersection point of \mathbf{L}_{k-1} and \mathbf{L}_k . Then the control points can be constructed by choosing both $\{\mathbf{Q}_k\}$ and $\{\mathbf{R}_k\}$, or only a subset of these points. Also, let $\bar{t}_0 = 0$, $\bar{t}_n = 1$, and $\bar{t}_{i-1} < \bar{t}_i < \bar{t}_{i+1}$. Then we choose a chord length parametrization to approximate a uniform distribution,

$\bar{t}_i = \bar{t}_{i-1} + |\mathbf{Q}_i - \mathbf{Q}_{i-1}|$. The control points, together with the knot vector

$\mathbf{t} = \left\{ 0, 0, 0, \frac{\bar{t}_1}{\bar{t}_n}, \frac{\bar{t}_1}{\bar{t}_n}, \frac{\bar{t}_2}{\bar{t}_n}, \frac{\bar{t}_2}{\bar{t}_n}, \dots, \frac{\bar{t}_{n-1}}{\bar{t}_n}, \frac{\bar{t}_{n-1}}{\bar{t}_n}, 1, 1, 1 \right\}$, defines a rational G^1 continuous, quadratic B-spline

curve interpolating the $\{\mathbf{Q}_k\}$. All weights at the \mathbf{Q}_k are set to 1; weights at the \mathbf{R}_k can be freely chosen. In order to maintain circular arc segments, the weights w_k at the \mathbf{R}_k can be set as follows (Piegl and Tiller, 1995):

1. If \mathbf{Q}_{k-1} , \mathbf{R}_k , and \mathbf{Q}_k are collinear, set $w_k = 1$.
2. If the triangle formed by \mathbf{Q}_{k-1} , \mathbf{R}_k , and \mathbf{Q}_k is isosceles, set $w_k = \frac{|\mathbf{Q}_{k-1} \cdot \mathbf{Q}_k|}{2|\mathbf{Q}_{k-1} \cdot \mathbf{R}_k|} = \cos \theta$, (a precise circle arc).
3. If the triangle is not isosceles, set w_k as follows (see Figure 2):

$$\mathbf{S} = (1 - s)\mathbf{M} + s\mathbf{R}_k, \text{ and}$$

$$w_k = \frac{s}{1 - s},$$

where $\mathbf{M} = \frac{1}{2}(\mathbf{Q}_{k-1} + \mathbf{Q}_k)$ and $\mathbf{S} = \frac{1}{2}(\mathbf{S}_1 + \mathbf{S}_2)$. Note \mathbf{S}_1 and \mathbf{S}_2 are respectively on the bisectors of $\angle \mathbf{Q}_k \mathbf{Q}_{k-1} \mathbf{R}_k$ and $\angle \mathbf{Q}_{k-1} \mathbf{Q}_k \mathbf{R}_k$. The parameter s determines the particular type of conic section that is generated. For $s = 0$, a line segment is generated, while $0 < s < 0.5$ gives an ellipse, $s = 0.5$ gives a parabola, and $0.5 < s < 1$ gives a hyperbola. For our implementation, described below, we chose $s = 0.5$.

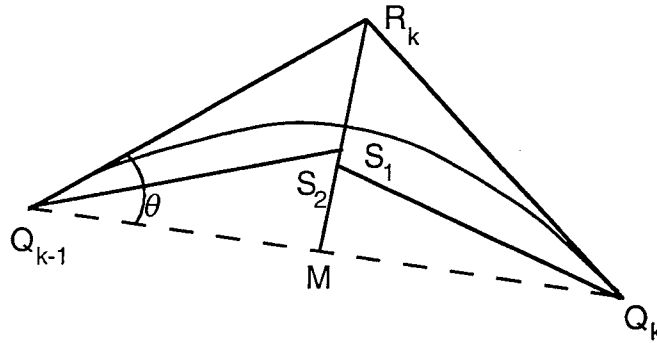


Figure 2. Determining the weight for a curve segment.

Step 3. Exception handling. The discussion above assumes that the intersections \mathbf{R}_k exist and that $\mathbf{R}_k = \mathbf{Q}_k + \gamma_{k-1} \mathbf{T}_{k-1}$ and $\mathbf{R}_k = \mathbf{Q}_k + \gamma_k \mathbf{T}_k$, where $\gamma_{k-1} > 0$ and $\gamma_k < 0$. The following special cases occur when \mathbf{R}_k cannot be computed by intersection:

1. \mathbf{T}_{k-1} and \mathbf{T}_k are parallel. This indicates collinear segments, an inflection point, or a 180° turn in the curve; or
2. If \mathbf{R}_k can be computed, but γ_{k-1} and γ_k do not satisfy the above relations. This indicates either an inflection point or a turn of more than 180° .

To handle case 1, set $\mathbf{R}_k = (\mathbf{Q}_{k-1} + \mathbf{Q}_k)$. All other special cases can be handled, for example, by creating two parabolic segments between $\mathbf{Q}_k + \mathbf{Q}_{k-1}$, instead of one. Figure 3(a) shows point data generated from slicing the STL file for a real part. The outline indicates the developed control polygon. Figure 3(b) is the quadratic Bézier based NURBS representation of these data. Note that NURBS curve maintains corners and straight lines.

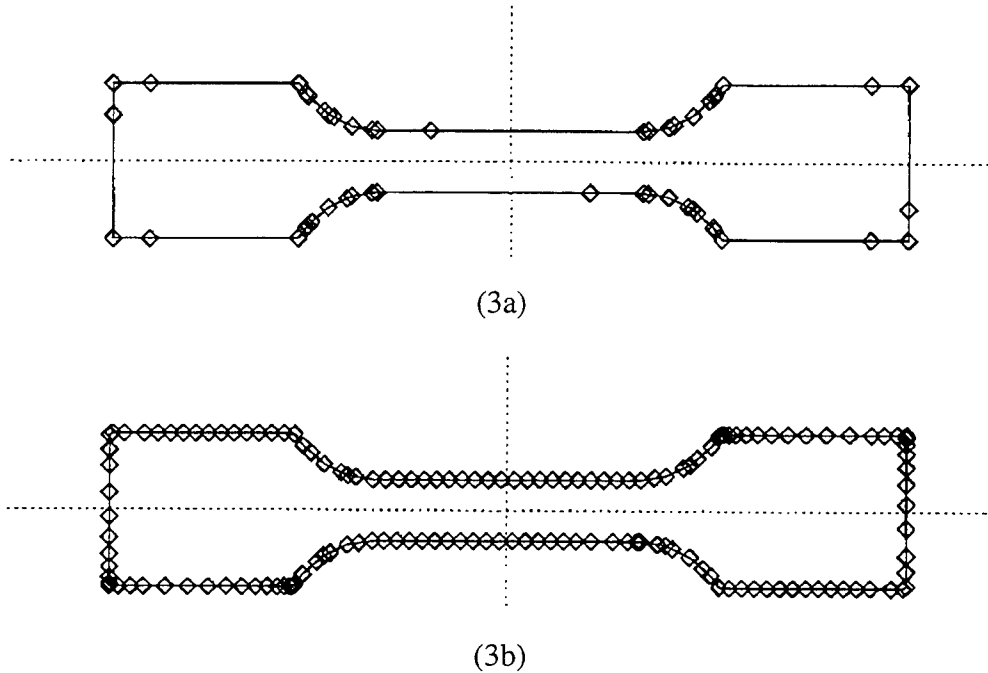


Figure 3. Original CAD data and developed control polygon (a), and NURBS representation by quadratic algorithm (b). (\diamond indicates points given or calculated.)

4.2 Bézier Based NURBS Representation

Cubics easily handle three-dimensional data and inflection points without special treatment. We begin by recalling a cubic Bézier curve's properties (see Figure 4). Let \mathbf{P}_0 and \mathbf{P}_3 be two endpoints, and \mathbf{T}_0 and \mathbf{T}_3 be the corresponding tangent directions with unit length. We want to find two additional control points \mathbf{P}_1 and \mathbf{P}_2 to construct a cubic Bézier curve, $\mathbf{C}(t)$, $t \in (0,1)$, constrained by $a = |\mathbf{C}'(0)| = |\mathbf{C}'(\frac{1}{2})| = |\mathbf{C}'(1)|$. From Bézier curve properties and the deCasteljau algorithm² (Farin, 1990) at $t = \frac{1}{2}$, the following relations hold:

²The deCasteljau algorithm is a subdivision algorithm for computing the coordinates of a point on a Bézier curve for a given parameter value.

$$\begin{aligned}
\mathbf{P}_1 &= \mathbf{P}_0 + \frac{1}{3}\alpha\mathbf{T}_0, \\
\mathbf{P}_2 &= \mathbf{P}_3 - \frac{1}{3}\alpha\mathbf{T}_3, \\
\mathbf{P}_0^3 &= \mathbf{C}\left(\frac{1}{2}\right), \\
\mathbf{P}_1^2 - \mathbf{P}_0^3 &= \frac{1}{8}(\mathbf{P}_3 + \mathbf{P}_2 - \mathbf{P}_1 - \mathbf{T}_0), \text{ and} \\
\mathbf{C}'\left(\frac{1}{2}\right) &= 6(\mathbf{P}_1^2 - \mathbf{P}_0^3),
\end{aligned} \tag{7}$$

where \mathbf{P}_1^2 and \mathbf{P}_0^3 are “intermediate deCasteljau points”. From these equations, we have

$$a\alpha^2 + b\alpha + c = 0, \tag{8}$$

$$a = 16 - |\mathbf{T}_0 + \mathbf{T}_3|^2,$$

where

$$b = 12(\mathbf{P}_3 - \mathbf{P}_0) \cdot (\mathbf{T}_3 + \mathbf{T}_0), \text{ and}$$

$$c = -36|\mathbf{P}_0 + \mathbf{P}_3|^2.$$

Equation 8 has two real solutions for α , only one of which is positive. Substituting this value into equations 7, we can obtain \mathbf{P}_1 and \mathbf{P}_2 .

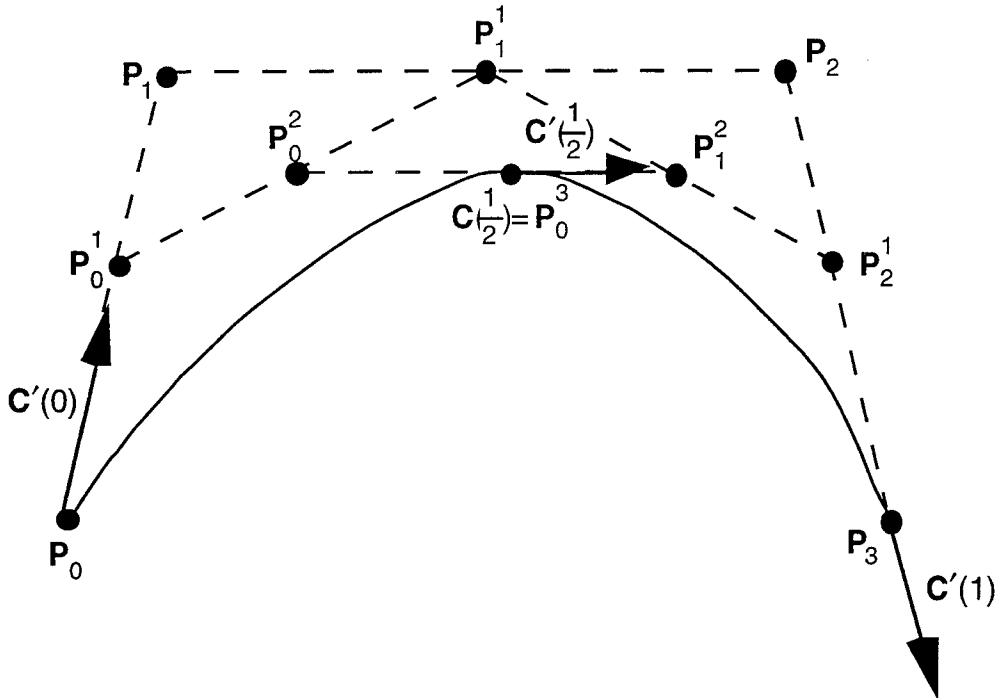


Figure 4. Cubic Bézier control polygon construction.

In general, a cubic curve segment $\mathbf{C}_k(t)$ can be constructed between each pair of data points, \mathbf{Q}_{k-1} and \mathbf{Q}_k . The corresponding control polygon consists of the points

$\mathbf{P}_k^0 = \mathbf{Q}_k, \mathbf{P}_k^1, \mathbf{P}_k^2, \mathbf{P}_k^3 = \mathbf{Q}_{k+1}$. The control points \mathbf{P}_k^1 and \mathbf{P}_k^2 can be calculated just as \mathbf{P}_1 and \mathbf{P}_2 above. The parametrization is set as $\bar{t}_0 = 0$ and, for a uniform point distribution,

$\bar{t}_{k+1} = \bar{t}_k + 3|\mathbf{P}_k^1 - \mathbf{P}_k^0|$. This yields the knot vector

$\mathbf{t} = \left\{ 0, 0, 0, 0, \frac{\bar{t}_1}{\bar{t}_n}, \frac{\bar{t}_1}{\bar{t}_n}, \frac{\bar{t}_2}{\bar{t}_n}, \frac{\bar{t}_2}{\bar{t}_n}, \dots, \frac{\bar{t}_{n-1}}{\bar{t}_n}, \frac{\bar{t}_{n-1}}{\bar{t}_n}, 1, 1, 1, 1 \right\}$. The algorithm produces n Bézier segments,

each with speed equal to 1 at the endpoint and midpoints with respect to their parameter ranges. Thus, a C^1 continuous cubic B-spline curve interpolating \mathbf{Q}_k is defined by the control points

$\mathbf{Q}_0, \mathbf{P}_0^1, \mathbf{P}_0^2, \mathbf{P}_1^1, \mathbf{P}_1^2, \dots, \mathbf{P}_{n-2}^2, \mathbf{P}_{n-1}^1, \mathbf{P}_{n-1}^2, \mathbf{Q}_{k+1}$. This scheme is more appropriate for our contour representation because it maintains constant speed and uniform point distribution on part contours. Figure 5(a) shows Wu's example for his optimal control algorithm (Wu, 1992). The outline indicates the developed control polygon. Figures 5(b) and 5(c) are the NURBS representations plotted with 100 and 150 points, respectively, on the contour. Note that NURBS curve maintains straight lines, and the corners maintained by putting close neighboring points at the corner. Figure 6 shows the same contour as Figure 3, but with a cubic NURBS representation. Compared with the results in Figure 3, this algorithm gives a more uniform point distribution.

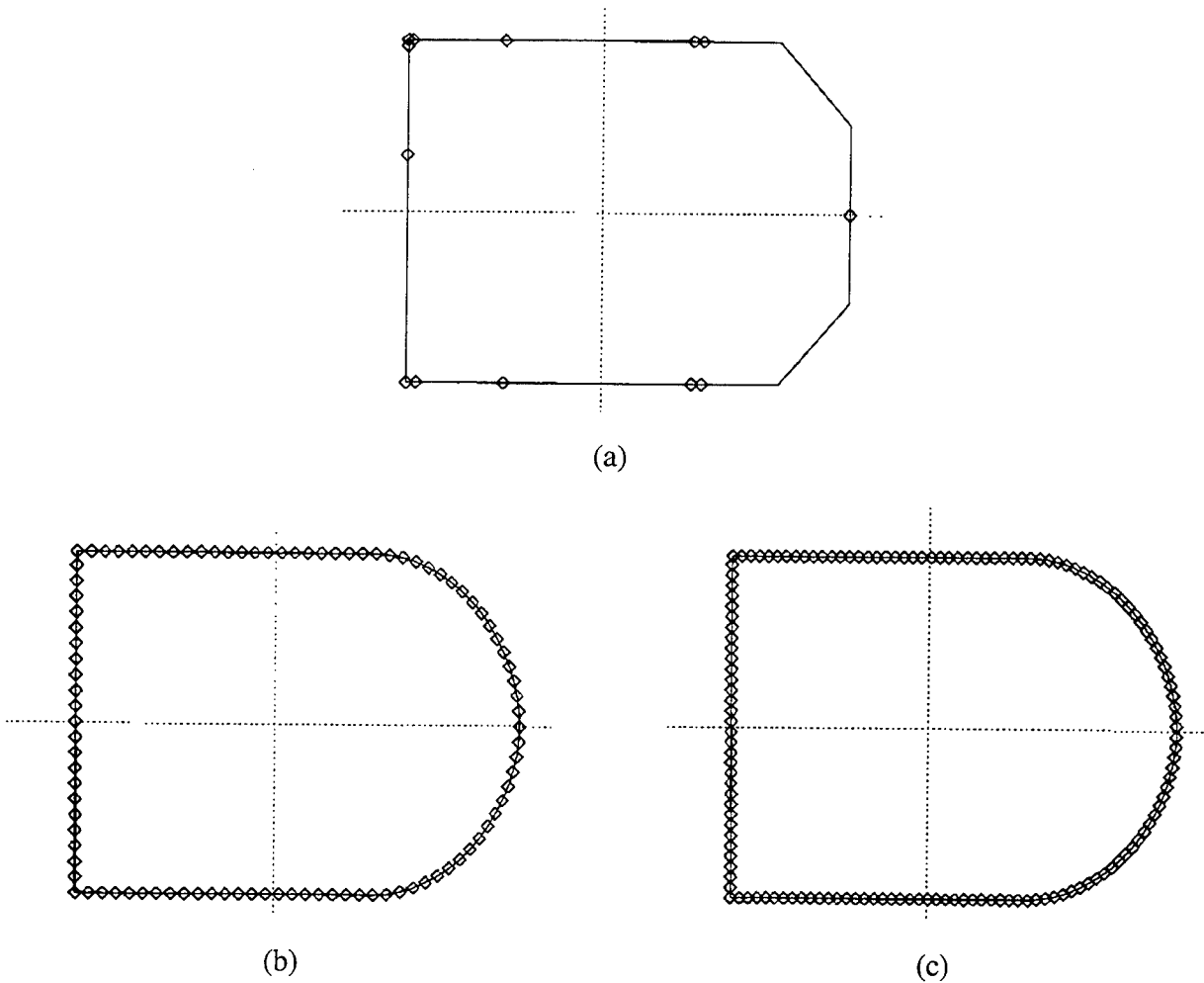


Figure 5. Given data and developed control polygon (a), and NURBS representation by Bézier algorithm with 100 points (b) and 150 points (c).

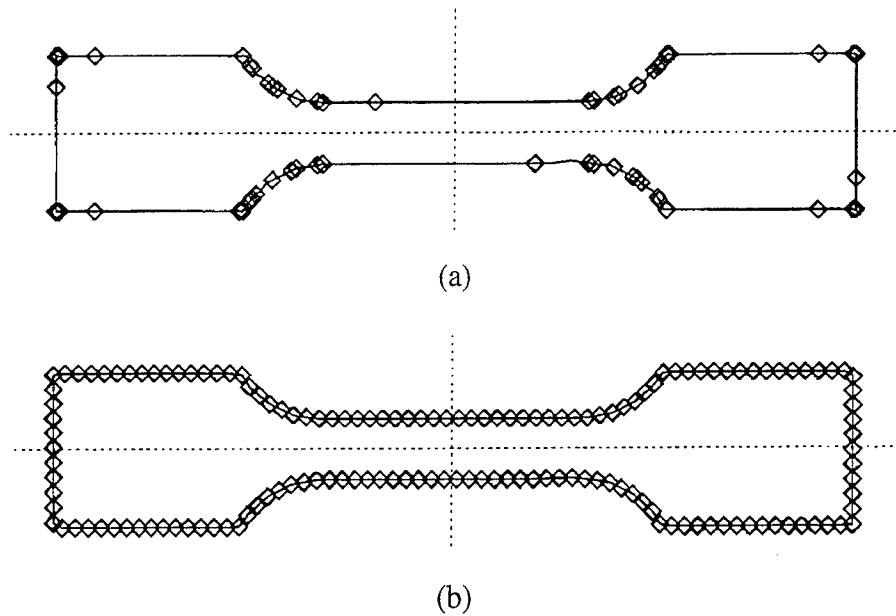


Figure 6. Cubic NURBS representation of the contour from Figure 3.

5 PARAMETRIC REPRESENTATIONS FROM OTHER GEOMETRIC DATA

Guduri *et al.* (Guduri *et al.*, 1992; Guduri, 1993; Guduri *et al.*, 1993) developed an approach to obtain an exact implicit form of part contours as piecewise curve segments with degree less than 4, such as conics, or an approximate implicit form for higher degree curves, such as the intersection curves generated by slicing a torus. The algorithm is based on constructive solid geometry input models. Using the CSG representation, an object is represented as a binary tree with geometric primitives (*e.g.*, spheres, cones, cylinders, parallelepipeds, torii, etc.) at the leaf nodes and regularized Boolean operators at the interior nodes. These primitives are first sliced to get the boundaries curves. These curves can be exactly or approximately represented by implicit second degree curves. Based on this result, the parametric form can be obtained by Abhyankar's method (Abhyankar and Bajaj, 1987). The Boolean operations are then applied to the primitive slices to obtain the part contour.

NURBS provide a single curve form that can exactly represent all Guduri's contours parametrically. NURBS can exactly represent all common curves, including circles, ellipses, parabolas, and straight lines. Additionally, NURBS are not limited in degree. Generally, intersection curves between higher order surfaces can not be analytically obtained. Parametric curve representation techniques can be used to represent higher order intersections and contours to any desired degree of accuracy. Many researchers have focused on the development of accurate and efficient surface-to-surface (or plane) intersection algorithms (Patrikalakis, 1993; Hanna, 1983; Lee, 1984). Generally, such intersection curves cannot be represented by a single analytical equation. Current approaches are based on numerical solutions. The NURBS representation can directly use numerical data to provide one form for modeling contours that consist of several connected intersection curves. Note that the NURBS basis functions are effective for only a few neighboring spans between control points. Also, the amount of data and shape of contours has little effect on the computing performance of NURBS curves.

6 DISCUSSION AND CONCLUSION

As we have been seen, NURBS are generally differentiable up to degree $n-1$ between adjacent knots, and are $n-p$ times continuously differentiable for knots of multiplicity p . Uniform

point distributions are generated by appropriately setting the knot vector. Since arc length parametrization has been developed by Guenter (1990), the NURBS representation satisfies Wu's requirements. Additionally, the NURBS curve has many advantages for curve and surface manipulation, and it provides a flexible and adaptable representation scheme. The NURBS curve form satisfies all the evaluation criteria outlined in the section 3. NURBS can approximate given data points to any degree of accuracy and with various continuity requirements. The NURBS form not only represents the conic sections exactly, but it also handles the special curve features, such as corners, and straight lines. NURBS algorithms are generally stable and robust. In geometric modeling, the NURBS form provides a common representation for a large variety of curves, with the resulting unified database for its implementation. The only drawbacks of the NURBS form are its extra storage and overhead compared to other parametric forms.

In this paper, we have shown that the NURBS parametric form is appropriate for Wu's control method. NURBS curves also provide a consistent representation for SFF that can handle both point data or higher order CAD data. Successful utilization of different geometric representations by SFF technologies requires the development of algorithms to extract and convert the geometric information correctly. NURBS can be used to represent these geometric features unless they are known or can be detected. Additionally, NURBS provide an approach that can represent higher degree contours to support, for example, the control models based on higher order dynamics.

REFERENCES

1. Abhyankar, S. S., and Bajaj, C., 1987, "Automatic Parametrization of Rational Curves and Surfaces 1: Conics and Conicoids", *Computer Aided Design*, Vol. 19, No. 1, pp. 11-14.
2. Barsky, B. A., and DeRose, T. D., 1989, "Geometric Continuity of Parametric Curves: Three Equivalent Characterizations", *IEEE Computer Graphics & Applications*, Vol. 9, No. 6, pp. 60-68.
3. Darrah, J., and Wielgus, M., "A New CAD Model Format for SFF Machines?", *Solid Freeform Fabrication Proceedings 1990*, Austin, TX, August 6-8, 1990, pp. 121-125.
4. Farin, G., 1990, *Curves and Surfaces for Computer Aided Geometric Design*, 2nd edition, Academic Press.
5. Guduri S., 1993, *A Method to Generate Contour Files Directly from Higher Level Geometry Representations For SFF*, M.S. thesis, The University of Texas at Austin, Austin, TX.
6. Guduri, S., Crawford, R. H., and Beaman, J. J., 1992, "A Method to Generate Exact Contour Files for Solid Freeform Fabrication," *Proceedings of the 1992 Solid Freeform Fabrication Symposium*, Austin, TX, pp. 95-101, August 3-5, 1992.
7. Guduri, S., Crawford, R. H., and Beaman, J. J., 1993, "Boundary Evaluation for Solid Freeform Fabrication," *Towards World Class Manufacturing 1993*, proceedings of the IFIP TC5 WG5.2/WG5.3 Conference, M. J. Wozny and G. Olling, eds., Litchfield Park, AZ, pp. 301-312, September 12-16, 1993.
8. Guenter B., 1990, "Computing the Arc Length of Parametric Curves", *IEEE Computer Graphics & Applications*, Vol. 10, No. 3, pp. 72-78.
9. Hanna, S. L., et al., 1983, "Intersection of Parametric Surfaces by Means of Look-Up Tables", *IEEE Computer Graphics and Applications*, October 1983, pp. 39-48.

10. Lee, E. T. Y., 1989, "Choosing Nodes in Parametric Curve Interpolation", *Computer-Aided Design*, Vol. 21, pp. 363-370.
11. Lee, R. B., 1984, "Intersection of Parametric Surfaces and a Plane", *IEEE Computer Graphics and Applications*, August 1984, pp. 48-51.
12. Patrikalakis, N. M., 1993, "Surface-to-Surface Intersections", *IEEE Computer Graphics and Applications*, January 1993, pp. 89-94.
13. Piegl, L., 1991 "On NURBS: A Survey", *IEEE Computer Graphics and Applications*, Vol. 10, No. 1, pp. 55-71.
14. Piegl, L., and Tiller, W., 1995, *A NURBS Book*, Springer-Verlag, Heidelberg, Germany.
15. Rogers, D. F., and Adams, J. A., 1990, *Mathematical Elements for Computer Graphics*, 2nd ed., McGraw-Hill, New York.
16. Wu, Y-J. E., and Beaman, J. J., "Solid Freeform Fabrication Laser Tracking Control", *Solid Freeform Fabrication Proceedings 1991*, Austin, TX, August 12-14, 1991, pp. 37-45.
17. Wu, Y-J. E., and Beaman, J. J., 1990, "Contour Following for Scanning Control in SFF Application: Control Trajectory Planning", *Solid Freeform Fabrication Proceedings 1990*, Austin, TX, August 6-8, 1990, pp. 126-134.
18. Wu, Y-J. E., and Beaman, J. J., 1992, "Laser Tracking Control Implementation for SFF Applications", *Solid Freeform Fabrication Proceedings 1992*, Austin, TX, August 3-5, 1992, pp. 161-173.
19. Wu, Y.-J., 1992, *A Minimum Time Laser Tracking Control Technique For Selective Laser Sintering*, Ph.D. Thesis, The University of Texas at Austin, Austin, TX.

Techniques for Improved Speed and Accuracy in Layered Manufacturing

Andrei Novac, Srinivas Kaza, Zetian Wang, Cheol Lee, Charles Thomas
Department of Mechanical Engineering
University of Utah

Abstract

The ability to improve the construction accuracy and/or the build speed for layered manufacturing techniques is demonstrated using a series of new techniques: (1) Parts can be decomposed into sections which are constructed in parallel and then assembled. This reduced the build time and material waste for a sheet foam process. (2) A more accurate interface based on direct slicing of the CAD model can be used to eliminate the need for the intermediary tessellation file. (3) The layer thickness can be adapted based on the part's geometric complexity to increase the surface quality, build speed, and z-axis accuracy.

Introduction

During the past three years, the focus of the research in the area of Solid Freeform Fabrication (SFF) conducted at the Manufacturing Processes Laboratory at the University of Utah has been on developing new Layered Manufacturing techniques. The results of this work are two technologies that address unique aspects of the Layered Manufacturing market.

Shapemaker I (SM I) (now commercialized as JP System 5 Desktop Rapid Prototyping by Schroff Development Corporation of Mission, Kansas) is a desktop prototyping technology dramatically less expensive than all other existing SFF technologies. SM I uses a plotter equipped with a cutting tool instead of a pen to create layer cross sections from adhesive backed materials. A software package allows the user to import, manipulate, and slice stereolithography format (.stl) files. The layers are registered and stacked manually using a construction table provided with registration pins. Materials used currently are: paper, foam, and vinyl sheet attached to a backing layer. The sheets are readily available in various sizes. The plotter cuts each slice, penetrating only as deep as the construction material layer. The layers are stacked on the construction table by matching the registration holes cut by the plotter on each sheet with the registration pins. After each individual layer is stacked, the backing layer is peeled off, thus exposing the adhesive and providing a bonding surface for the next layer. Once construction is completed, the parts are coated to improve their rigidity and aesthetic appearance and to cover any exposed adhesive.[1]

Shapemaker II (SM II) addresses another seldom approached aspect of Layered Manufacturing: the fabrication of large scale objects. While existing SFF devices are reportedly limited to a 39" x 31" x 20" volume [2], SM II allows the construction of large scale prototypes (up to 4' by 8' by any reasonable height). It consists of an electrically heated wire driven by a four-axis motion control device, a custom software package that allows the user to import,

manipulate, and slice .stl files, a pre-processing stand alone device that ensures the flatness and thickness accuracy of the foam material used, and a construction table provided with registration pins. The build material is foam, which is readily available in sheets of various thickness and sizes since it is commonly used for insulating buildings. The heated wire cuts the contour of each slice as well as the internal registration holes. The layers are stacked on the construction table using the registration pins and are bonded together by applying a thin and uniform layer of adhesive on one face of each slice.[3]

This paper discusses several techniques that have been implemented or are in the process of being implemented and are aimed at improving the build speed and the overall accuracy of components manufactured using the processes described above. While all of the techniques described in this paper have been used exclusively in conjunction with the Layered Manufacturing processes developed at the University of Utah, their realm of applicability can be extended to other processes.

Hierarchical Model Decomposition

Inherent to the nature of the SM I process is the ability to decompose an object into sections that can be built simultaneously. This allows the operator to save paper and dramatically increases the build speed. In fact, when building objects that are significantly smaller than the machine's build volume and consist of mostly solid geometry, SM I can be significantly faster than many existing SFF technologies.

In order to complete this decomposition, the software first evaluates the maximum number of part cross sections that can be built on a single sheet of construction material. Next, the part is sliced into a number of equal thickness sections and these sections are spread out to fill the construction sheet. Then, these sections are sliced to the thickness of the construction material. The result is a series of plot files, each containing several cross sections. The number of stacking operations that need to be performed when building an object is a function of the total number of layers, and the number of parallel sections. A theoretical minimum number of operations is achieved when these parameters fit the "square root" model. For example, on a stereolithography machine a 64 layer part would require 64 sequential operations to construct. If this part can be decomposed into 8 sections, the part can be built in a total of 16 operations. (8 operations simultaneously building 8 sections and 8 operations to put the sections together).

In addition to savings in time and materials, parallel decomposition of parts results in less need for support structures. If a part has a cantilever overhang, the operator can define a section break at the level of the overhang. This puts the overhanging material flush with the construction platform during the first stage build. During second stage build the sections are thick enough to be self supporting and do not require supports. The ability to custom define and manipulate sections has helped improve the accuracy of parts built.

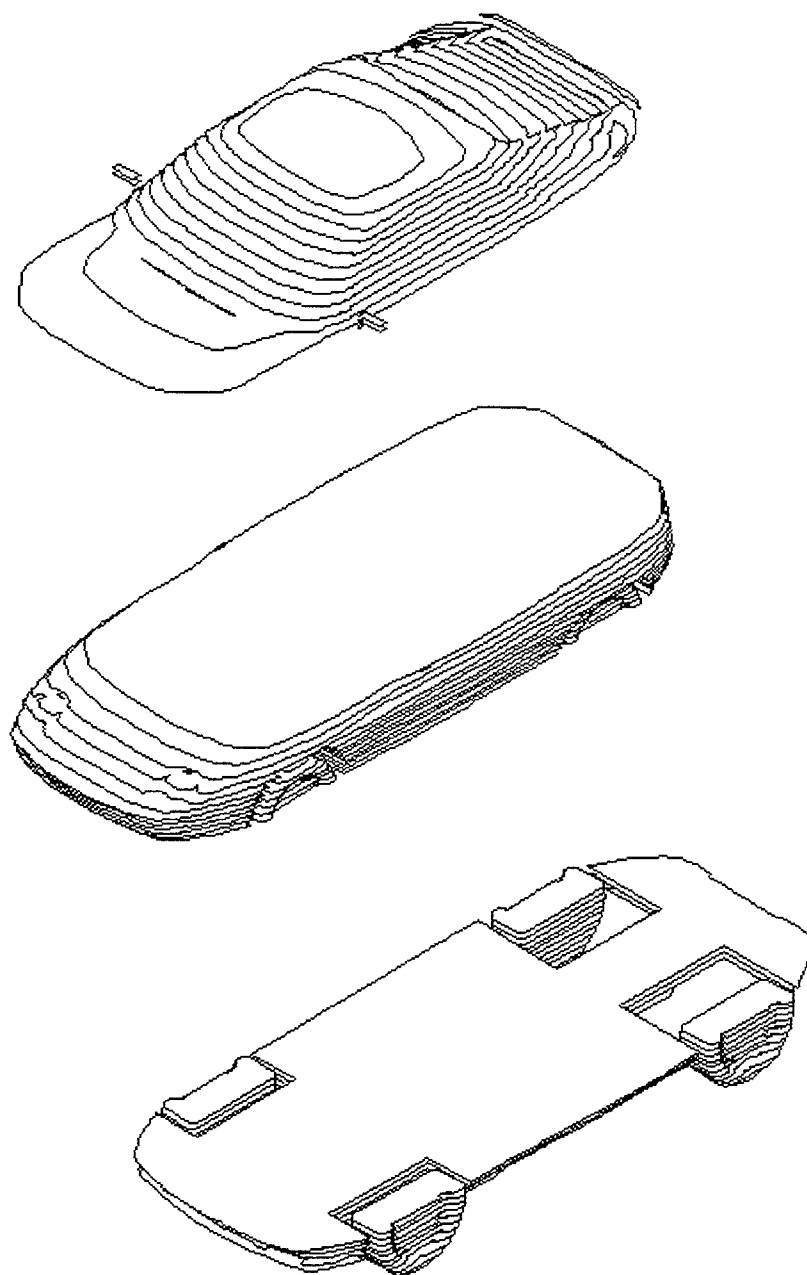


Figure 1. Hierarchical model decomposition with user-defined sections. The overhangs (mirrors) are built from largest cross-section up as part of the top section.

Section Orientation Mirroring

The cantilever effect associated with overhang features is an issue common to all Layered Manufacturing technologies. While most processes address this issue by constructing supports for the overhang features, SM I and II eliminate the need for support structures by decomposing the model in sections and mirroring the sections as necessary. As described above, all objects being built are first decomposed into sections with the user having full control of this process.

The software also allows the user to mirror the orientation of any section such that all sections are built from their largest cross-section up.(see Figure 2) This unique solution which allows the elimination of all support structures is a critical time saving feature.

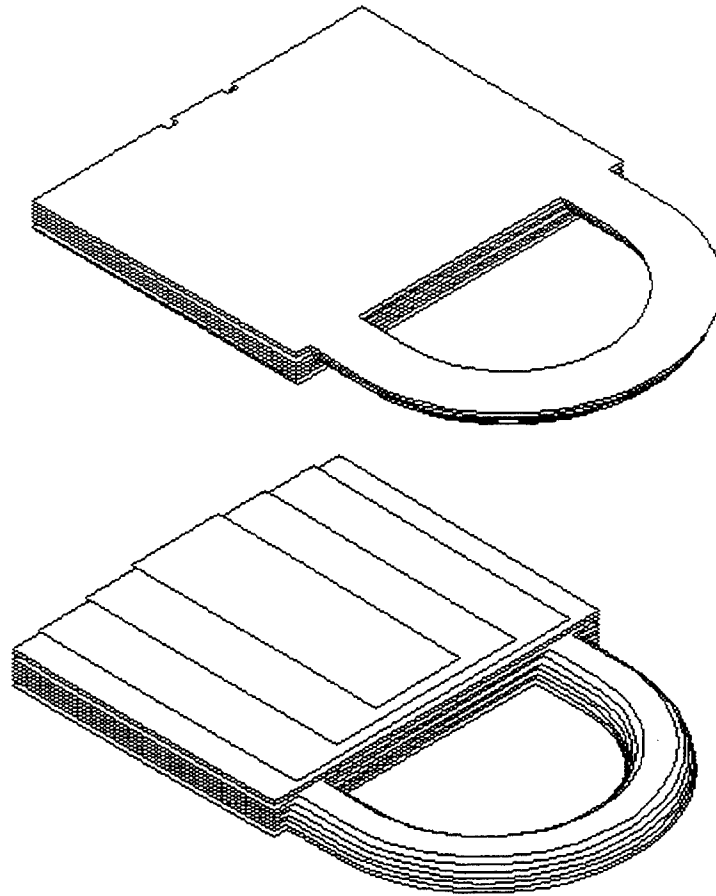


Figure 2. The need for support structures for this section of a lock pad (top) can be eliminated by mirroring the section and building from the largest cross section up (bottom)

Most SFF processes are accompanied by software packages which, among other functions, automatically generate the necessary supports. These automatically generated supports are often too few - causing inaccuracies or too many - slowing down the build time. The SM I and II solution eliminates at least three steps that are required by most other SFF processes: the generation of support structures in the slicing software, their physical creation, and their removal in the post-processing phase.

Direct Slicing

All SFF processes use as input an electronic file generated using a 3D Computer Aided Design (CAD) system. Since the CAD industry thrives on non-compatibility, a common interface had to be developed so that SFF and CAD could become fully integrated technologies. This interface is based on the principle of tessellation or mapping a triangular mesh over the

surface of the solid model. The current standard interface (the stl file format) was developed by 3D Systems, the inventors of the first SFF technology, Stereolithography. [4] SM I and II accept stl files as input for generating the slices.

This intermediary step between the CAD model and obtaining the cross sections that are used to manufacture the object layer by layer yields a loss of accuracy since the tessellation of any complex shape is an approximation. Therefore, there is much to be gained by eliminating this step and creating the slices directly from the CAD model. Such an interface was developed at the University of Utah to work with Layered Manufacturing processes such as SM I and II. This new C++ based interface called SLICE uses an HPGL (Hewlett Packard Graphics Language) compatible format to represent each cross-section. The HPGL format is used because it is already supported by all CAD systems. The output file created by SLICE contains information on all the slices of the object as well as any other information required to build and define the object completely. The following example illustrates how a slice of the object is represented by SLICE :

```

object OBJECT_NAME
  SOLIDS solid1,AL;solid2,Polystyrene;solid3,steel
  scale 1
  slice #x of x
    Z position 1.0500
    solid1
      80,-60;80,90;-70,90;80,90;80,-60;
    solid2
      100,0;120,0;120,-20;100,-20;100,0;
    .....
    solid3
    .....
    hole1
    .....
  endslice
  .....
endobject

```

Each cross section represented in the SLICE format is divided into a number of closed loops sorted clockwise. Each loop is represented individually and it could be made up of any specified material. If a loop is empty, the designated word “hole” will indicate that there is no material inside the loop. [5] A detailed description of SLICE will be published in [6].

Along with accuracy improvements, direct slicing also speeds up the process of converting the 3D CAD model into a physical object. Time compression is achieved through the reduction of pre-processing time and the elimination of the all too common process of “repairing”

the stl file, which becomes necessary because of the inconsistent implementation of the stl translators within the CAD systems available on the market. Direct slicing also produces files that are generally dramatically smaller than those produced through tessellation because the latter format incorporates much redundancy since information about each triangle is recorded and shared ordinates are repeated over up to five times. The reduction in file size is another incentive for pursuing direct slicing as an alternative to the stl file format.

Adaptive Slicing

Currently, the focus of our research is on integrating adaptive slicing capabilities into SLICE, the direct slicing interface discussed above. It is envisioned that by adding this feature to the interface the user will be able to optimize the layer thickness for accuracy as well as build speed. The interface will make use of the cusp height concept, which is similar to the chord height concept used by the tessellation based approach. The cusp height is a measure for the deviation of the surface of a part built in layers from the true surface of the 3D CAD model. The cusp height is defined by the maximum gap measured in the normal direction of the true surface.[7] Using this new interface, for a given input value for the maximum allowable cusp height, the object will be sliced using a small layer thickness to preserve the accuracy of sections that contain complex surfaces and a large layer thickness to improve the build speed of sections where there are no cross sectional changes in the direction of build. (see Figure 3)

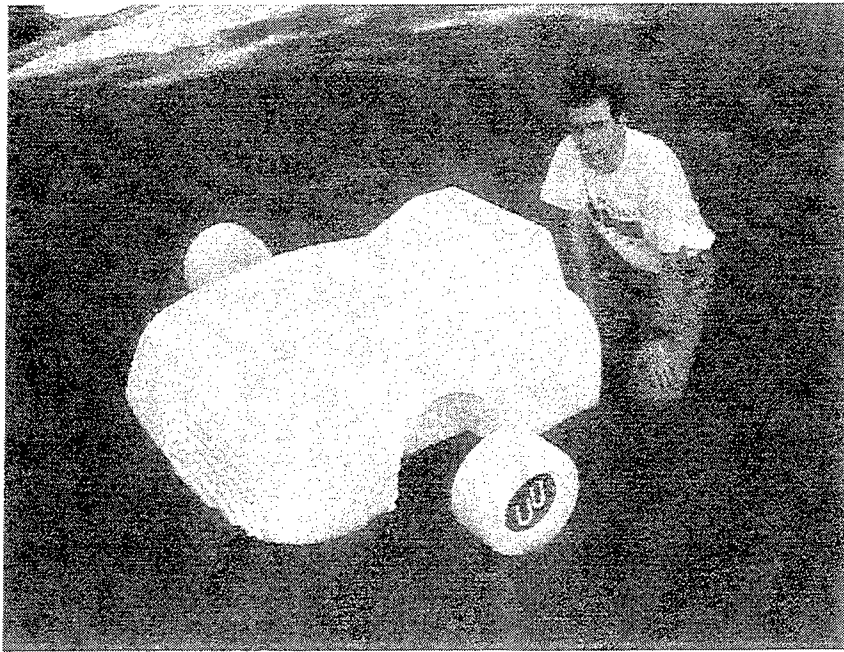


Figure 3. An object built with SM II using variable thickness layers.

The fabrication of large scale objects using a Layered Manufacturing process presents a unique set of challenges as far accuracy is concerned. The limiting factor for accuracy in the build direction for most Layered Manufacturing processes is the thickness of the slices used. This

problem is due to the use of constant layer thickness. If the distance between the end of the last layer and the end of the CAD model is smaller than the layer thickness, the physical object will be incomplete. This problem can be addressed through the use of variable thickness slices.

Another problem common to all Layered Manufacturing processes is due to the finite thickness of the layers. This problem occurs when trying to reproduce a curved surface and is referred to as the stair stepping effect or 3D aliasing. Slices as thin as 0.002", or about the diameter of a human hair, have been reportedly used in order to improve the accuracy in the build direction. [8] Clearly such thin layers would be impractical for manufacturing large scale objects. Extensive use of SM II has demonstrated the need for using slices thinner than the current 1" standard thickness in order to improve the accuracy with which objects containing curved surfaces are reproduced. SM II is capable of producing ruled cuts - not just stepped cuts, an implementation which has diminished the stair stepping effect (see Figure 4). Custom angled edges are cut on each layer, forcing the top of the layer to match the specified upper cross section and the bottom to match its corresponding cross section.[9] While this has improved the accuracy of the object being constructed, it hasn't eliminated the need for variable thickness slices.

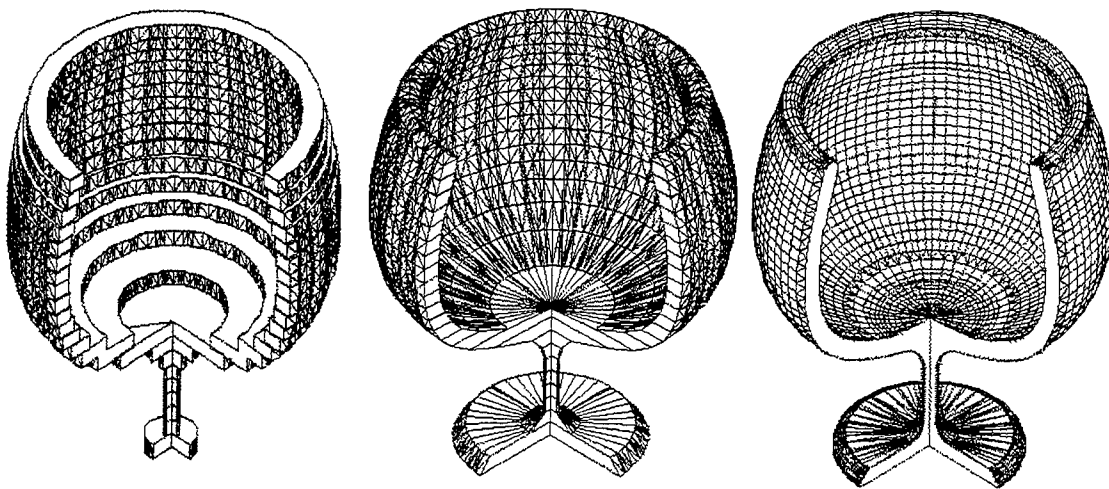


Figure 4. Current commercial systems produce layers with vertical edges (left). Shapemaker II produces layers with ruled surface edges (middle). Shapemaker III will produce layers with curved edges (right).

Future Work

Our future plans for enhancing the Layered Manufacturing processes discussed in this paper include the implementation of software as well as hardware changes that would support the use of non flat and non parallel layers. Objects will be sliced not only along a flat but also along a curved direction. The object will then be built around a non flat platform. The use of non parallel layers will improve the accuracy and build speed of curved objects. For example, a torus-

shaped object would be reproduced more accurately using wedge-shaped non parallel layers rather than the conventional flat layers.

Conclusion

The efforts aimed at improving the accuracy and the speed of construction of objects manufactured using the Shapemaker technologies have yielded promising results. These improvements have been achieved through software that allows hierarchical model decomposition and section orientation mirroring for SM I and optimization of direct slicing for SM II (the optimization process is still under development). Future improvements are to be achieved through implementation and use of non flat and non parallel layers.

Cost, versatility, accuracy, and speed of construction are the top four concerns with all SFF technologies. The order of importance of these factors depends upon the intended end use of the technology. SM I was designed with cost as the most important parameter. The price of the commercial system based on SM I is \$7500. This price is by far the lowest in a market where most systems sell for six digit figures. SM I and II cover a dimensional range unprecedented with any other Layer Manufacturing techniques, proving to be highly versatile. Parts less than 1 in³ have been built using SM I, while parts exceeding 90 ft³ have been built using SM II. When building objects with mostly solid geometry SM I has proven to be faster than most existing SFF processes, while building large scale objects using SM II is faster than using conventional fabrication techniques.

Acknowledgment

This work is supported by a Technical Innovation Grant from the University of Utah Research Foundation. Patents for the technologies presented in the paper are pending.

References

- [1] Thomas, Charles L., Wang, Zetian, Kaza, Srinivas, Bailey, Andrew - "Shapemaker I: An Inexpensive Introduction to Rapid Prototyping", Proceedings of the Sixth International Conference on Rapid Prototyping - 1995.
- [2] Burns, Marshall - "Automated Fabrication: Improving Productivity in Manufacturing", Prentice Hall, New Jersey, 1993, pg. 57.
- [3] Lee, Cheol H., Gaffney, Thomas M., Thomas, Charles L. - "Paradigms for Rapid Prototyping", Proceedings of the Sixth International Conference on Rapid Prototyping - 1995.
- [4] Jamieson Ron, Hacker Herbert - "Direct Slicing of CAD Models for Rapid Prototyping", Rapid Product Development Internet Conference, MCB University Press, West Yorkshire, England, 1996.

- [5] Kaza, Srinivas - "SLICE: A Proposed Alternative to the Stereolithography File Format for Rapid Prototyping", University of Utah, Master's thesis, February 1996.
- [6] Kaza, Srinivas, Thomas, Charles - "SLICE: An Alternative File Format for Rapid Prototyping", to be published.
- [7] Suh, Yong Seok, Wozny, Michael J. - "Adaptive Slicing of Solid Freeform Fabrication Processes", Proceeding of the Sixth Annual Solid Freeform Fabrication Symposium - 1995, pg. 404.
- [8] Jacobs, Paul F. - "The Role of Rapid Prototyping and Manufacturing", The CAD/CAM Handbook, McGraw-Hill, New York, 1996, pg. 98.
- [9] Thomas, Charles L., Gaffney, Thomas M., Kaza, Srinivas, Lee, Cheol L. - "Rapid Prototyping of Large Scale Aerospace Structures", Proceedings of the 1996 IEEE Aerospace Applications Conference.

THE INFLUENCE OF NATURAL CONVECTION AND RADIATION HEAT TRANSFER ON SINTERING OF POLYCARBONATE POWDERS

J. L. Norrell*, M. Kandis** and T. L. Bergman**

*The University of Texas at Austin
Department of Mechanical Engineering
Austin, Texas 78712

**The University of Connecticut
Department of Mechanical Engineering
Storrs, Connecticut 06269

ABSTRACT

The influence of surface radiation and natural convection on sintering of polycarbonate powders processed under non-isothermal conditions is investigated. These modes of heat transfer affect local powder temperatures and thus local sintering rates which in turn influence part growth (uncontrolled sintering). This paper presents a 2-dimensional sintering simulation of powder whose free surface exchanges energy with the surrounding enclosure surfaces. Modeling is accomplished using a commercial finite element code (FIDAP) in conjunction with a model for viscous sintering.

NOMENCLATURE

A	= sintering rate coefficient
C	= Ergun (inertial) coefficient
c_{pf}	= specific heat, fluid (J/kg K)
E_a	= activation energy for viscous sintering
g	= gravitational acceleration (m/s^2)
K	= permeability (m^2)
k_{eff}	= effective thermal conductivity (of powder) (W/mK)
k_f	= thermal conductivity (W/mK)
p	= pressure (Pa)
T	= absolute temperature (Kelvin)
T_c	= cold temperature (Kelvin)
u, v	= x and y velocity components (m/s)

u_D, v_D = Darcian x and y velocity components (m/s)
 x, y = horizontal and vertical coordinate (m)
 β = coefficient of thermal expansion (K^{-1})
 ϕ = volume-averaged porosity
 μ_{eff} = effective (in-powder) viscosity (Ns/m^2)
 μ_f = fluid viscosity (Ns/m^2)
 ρ = density of fluid phase (kg/m^3)

INTRODUCTION

Selective Laser Sintering (SLS) is among the many Solid Freeform Fabrication techniques presently available. Freeform parts produced by SLS typically remain buried in a bed of loose powder until they have cooled enough to be handled. Non-isothermal conditions result in heat transfer from the part to the surrounding powder which can cause secondary, uncontrolled sintering, or part growth. Part growth (densification) is accompanied by the formation of gas-filled voids as required by conservation of mass principles. The extent of growth is dependent upon local sintering rates which increase exponentially with temperature (Nelson, 1993). Hence, the ability to predict the temperature distribution induced by various modes of heat transfer might aid in the development of thermal control techniques to produce accurate (minimal part growth) final freeform part shapes.

In this paper, a first attempt is made to quantify the influence of surface radiation and natural convection heat transfer on the temperature distribution within a polycarbonate powder under non-isothermal conditions. At steady-state, local temperatures and sintering rates are obtained for cases involving pure conduction within the powder along with radiative and convective cooling of the powder surface. These results are compared to the base case involving pure conduction heat transfer through the powder and surrounding air.

MODEL

The 2-dimensional, non-isothermal arrangement of Figure 1 depicts the idealized scenario under consideration. Two concentric, square, isothermal tubes serve as heat source and sink. The outer tube is maintained at 180 °C while the inner tube is held at 50 °C. The powder has an initial porosity of 0.5. The region above the powder surface is occupied by air. The 2-dimensional, steady-state temperature distribution within both the air and powder is determined using the commercial code FIDAP with the following descriptive equations.

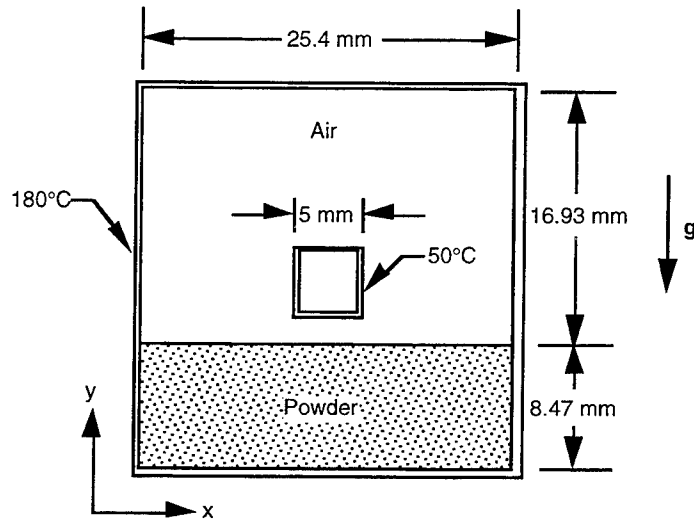


Figure 1. System configuration.

The governing equations for the pure fluid and the saturated porous medium are given separately. In writing the following equations it is assumed that fluid flow is laminar, steady, incompressible, and two-dimensional. For the pure fluid region, the two-dimensional, steady-state Navier-Stokes equations are used. Conservation of mass is given by

$$\frac{\partial u}{\partial x} + \frac{\partial v}{\partial y} = 0 \quad (1)$$

Conservation of momentum is described by

$$\rho \left(u \frac{\partial u}{\partial x} + v \frac{\partial u}{\partial y} \right) = -\frac{\partial p}{\partial x} + \frac{\partial}{\partial x} \left(\mu_r \frac{\partial u}{\partial x} \right) + \frac{\partial}{\partial y} \left(\mu_r \frac{\partial u}{\partial y} \right) \quad (2)$$

and

$$\rho \left(u \frac{\partial v}{\partial x} + v \frac{\partial v}{\partial y} \right) = -\frac{\partial p}{\partial y} + \frac{\partial}{\partial x} \left(\mu_r \frac{\partial v}{\partial x} \right) + \frac{\partial}{\partial y} \left(\mu_r \frac{\partial v}{\partial y} \right) + \rho g \beta (T - T_c) \quad (3)$$

Conservation of energy is expressed as

$$\rho c_{pf} \left(u \frac{\partial T}{\partial x} + v \frac{\partial T}{\partial y} \right) = \frac{\partial}{\partial x} \left(k_f \frac{\partial T}{\partial x} \right) + \frac{\partial}{\partial y} \left(k_f \frac{\partial T}{\partial y} \right) \quad (4)$$

All thermophysical properties of the pure fluid are assumed constant with the sole exception being density, where a Boussinesq approximation is used.

For the saturated porous medium, a Brinkman-Forchheimer extended version of the Darcy model is used, as discussed in Beckermann et al. (1987) and Kaviani (1991). It is important to note that the velocities within the saturated powder are Darcian, or volumetrically-averaged, velocities. Conservation of mass within the powder is given by

$$\frac{\partial u_D}{\partial x} + \frac{\partial v_D}{\partial y} = 0 \quad (5)$$

Conservation of momentum within the powder bed, given by

$$0 = -\frac{\partial p}{\partial x} + \frac{\partial}{\partial x} \left(\mu_{\text{eff}} \frac{\partial u_D}{\partial x} \right) + \frac{\partial}{\partial y} \left(\mu_{\text{eff}} \frac{\partial u_D}{\partial y} \right) - \left(\frac{\mu_f}{K} + \frac{\rho C}{\sqrt{K}} |\bar{u}_D| \right) u_D \quad (6)$$

and

$$0 = -\frac{\partial p}{\partial y} + \frac{\partial}{\partial x} \left(\mu_{\text{eff}} \frac{\partial v_D}{\partial x} \right) + \frac{\partial}{\partial y} \left(\mu_{\text{eff}} \frac{\partial v_D}{\partial y} \right) + \rho g \beta (T - T_c) - \left(\frac{\mu_f}{K} + \frac{\rho C}{\sqrt{K}} |\bar{u}_D| \right) v_D \quad (7)$$

incorporates the Brinkman extension (the second and third terms in the above equations) and the Forchheimer extension (the last term) to account for viscous and inertial effects. Conservation of energy is described by

$$\rho C_{\text{pf}} \left(u_D \frac{\partial T}{\partial x} + v_D \frac{\partial T}{\partial y} \right) = \frac{\partial}{\partial x} \left(k_{\text{eff}} \frac{\partial T}{\partial x} \right) + \frac{\partial}{\partial y} \left(k_{\text{eff}} \frac{\partial T}{\partial y} \right) \quad (8)$$

All thermophysical properties of the saturated powder are assumed to be constant, with the exception being a Boussinesq approximation for the air density. Permeability of the powder was measured to be $1.5 \times 10^{-10} \text{ m}^2$, as described in Norrell (1996). For the saturated powder μ_{eff} and k_{eff} are effective air viscosity and thermal conductivity, respectively. It has been found previously by Neale and Nader (1974) that using $\mu_{\text{eff}} = \mu_f$ within the Brinkman extension provides good agreement with experimental data. A simple weighted average given by

$$k_{\text{eff}} = \phi k_f + (1 - \phi) k_s \quad (9)$$

is used for the effective thermal conductivity. The C term in the Forchheimer extension is the inertia coefficient given in Ergun (1952) as

$$C = \frac{1.75}{\sqrt{175}} \phi^{-3/2} \quad (10)$$

Radiation view factors between the (radiatively black) powder and surrounding (black) surfaces are determined using the Hottel crossed-string method to obtain view factors at each powder surface node (Seigel and Howell, 1981). The radiative fluxes on the exposed powder surface are calculated and mapped into FIDAP as heat flux terms. Interparticle (within powder bed) radiation exchange is neglected here.

The model for viscous sintering is obtained from Nelson et al. (1993)

$$-d\phi/dt = K' \cdot (\phi - \phi_{\infty}) \quad (11a)$$

where the coefficient is

$$K' = A \cdot (-E_a / RT) \quad (11b)$$

The activation energy (E_a) and other powder properties are also obtained from Nelson et al. (1993). The sintering rate coefficient (A) used in this study is obtained from Kandis and Bergman (1996).

Solid shapes are estimated based upon the predicted steady state temperature distribution in the powder using an original consolidation model which is described in detail in Kandis and Bergman (1996). In short, the powder domain shape evolves in a stress-free manner, with local sintering rates inducing 2-dimensional solid phase velocities which are then integrated in time to yield the final powder region shape.

RESULTS

The pure conduction temperature distribution is presented in Figure 2a. Isotherms are separated by 10°C in all figures. The isotherms in the powder and surrounding air are roughly circular in shape with a discontinuity in slope at the powder surface. The highest sintering rates occur in the hottest regions (near the outer tube). Less sintering takes place near the central region of the powder surface where temperatures are lowest. The final predicted part shape as a result of part growth is shown in Figure 2b. This figure is

obtained by integrating local sintering rates in time for a period of 6 hours. The part contains a vertical crack in the center, surrounded by a shallow trough or semi-circular ditch. Crack formation is due to the migration of the solid phase toward rapidly-sintering, warm powder regions.

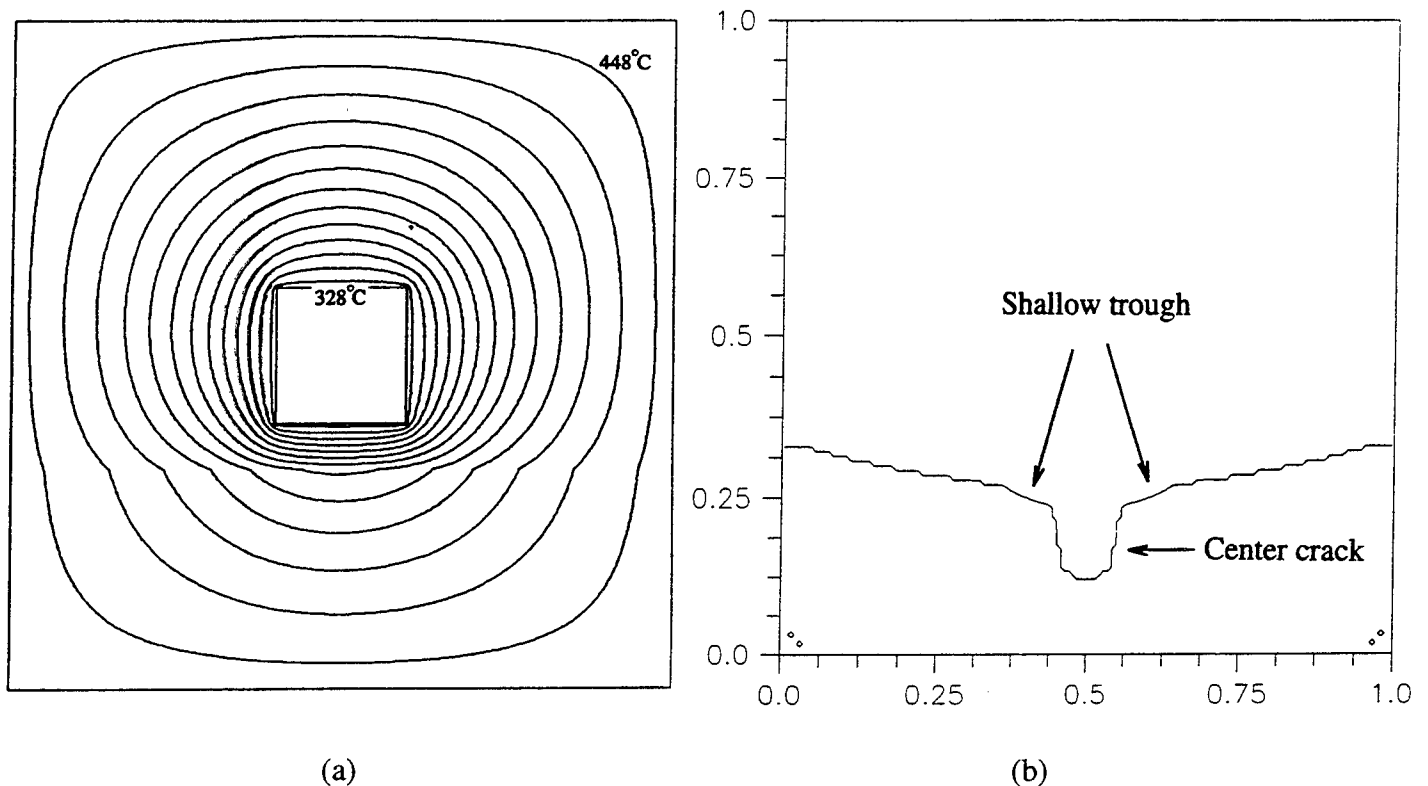


Figure 2. Temperature distribution and final part shape for conduction only case.

The temperature distribution and final part shapes for the case involving conduction and radiation are presented in Figures 3a and 3b. The shape and general features of the isotherms are similar to the pure conduction case, especially in the air gap region. Within the powder, temperatures decrease in the central region but increase slightly to the left and right of the center tube relative to the pure conduction case. Higher sintering rates near the outer tube provide for larger solid phase velocities toward the sides. Decreased sintering rates in the central region result in low porosity powder extending further into the bed (toward the bottom wall). The net result is a small decrease in the overall part growth or part size relative to the previous case.

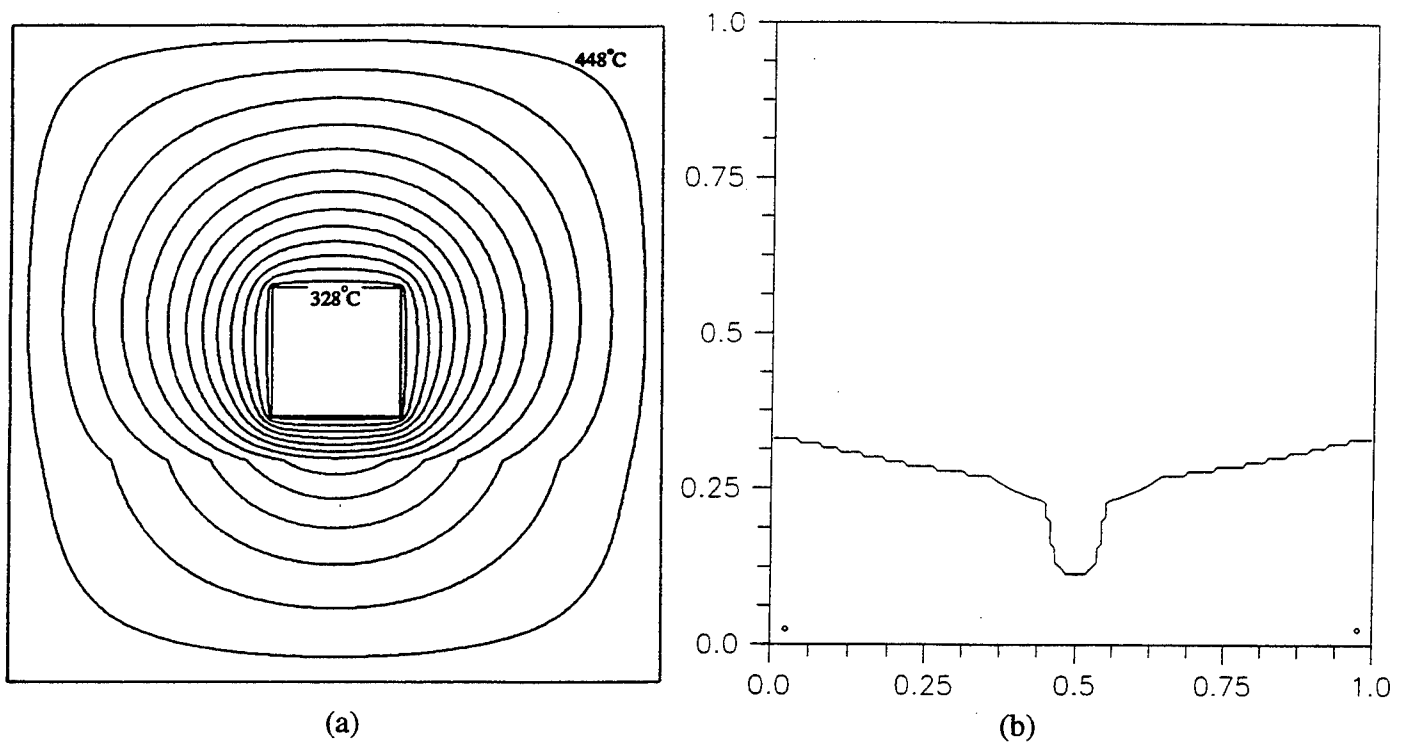


Figure 3. Temperature distribution and final part shape for conduction and radiation case.

Finally, adding convection to the previous case results in an increase in temperatures (Figure 4a) and sintering rates in regions to the left and right of the center tube. As a result of high sintering near the edges of the domain, the width and depth of the trough decrease as shown in Figure 4b. The crack dimensions change only slightly.

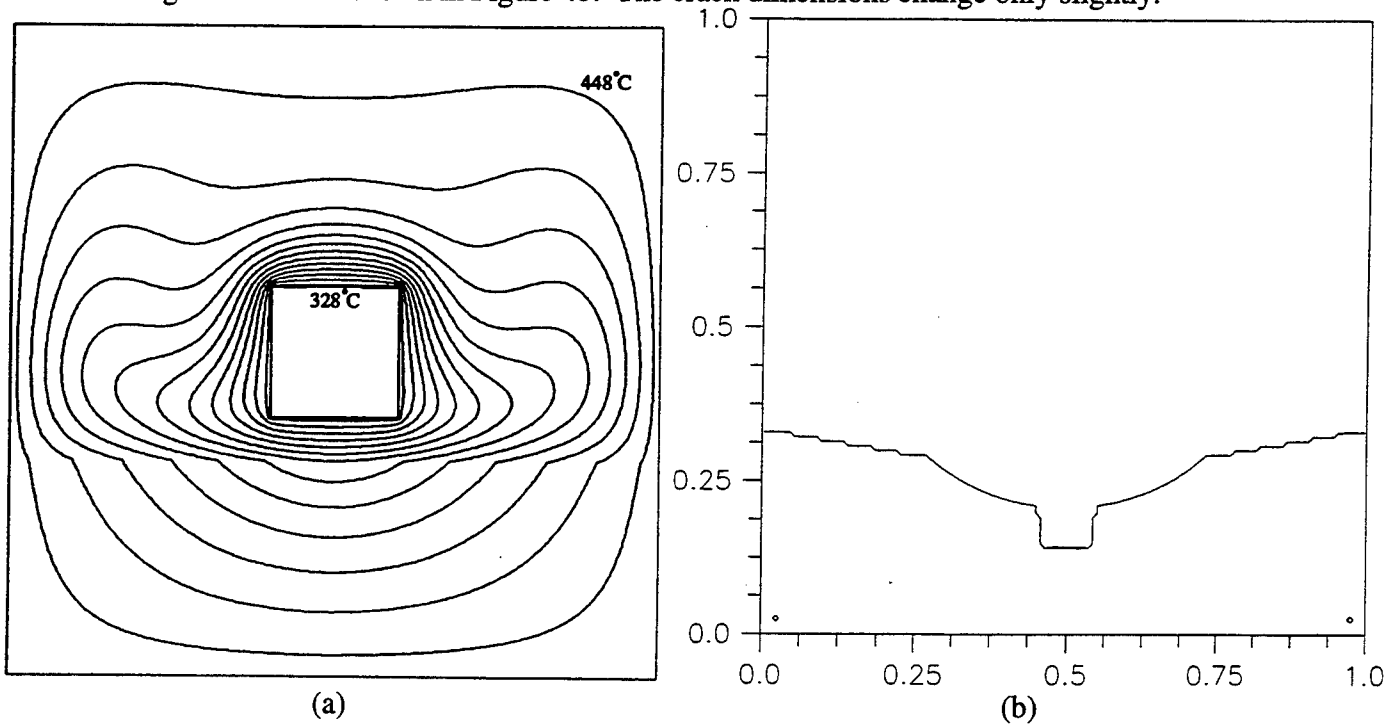


Figure 4. Temperature distribution and final part shape for conduction, radiation, and natural convection case.

Results from a sintering experiment (6 hours) of polycarbonate powder under identical conditions are presented in Figure 5. The sintered part has a solid and smooth texture along the bottom and sides (regions exposed to the hot outer tube) while the inner surface displays a soft, flaky appearance. Although not discernible from the photograph, a fine crack in the center of the trough runs axially along the length of the test specimen. Qualitatively, the part shape compares well with the shape in Figure 4b.

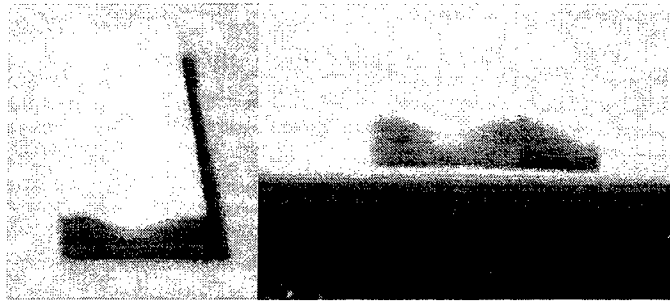


Figure 5. Experimentally-grown part shape.

CONCLUSIONS

The results presented in this study indicate that, for the material, geometry and thermal conditions considered here, surface radiation heat transfer has little effect on the temperature distribution and powder sintering. Only a marginal decrease in part growth is obtained with the inclusion of radiation. In contrast, natural convection (which may occur in large, buried voids which form in response to bed consolidation associated with part growth) can modify temperatures and sintering rates, in turn, affect part growth. Comparison with experimentally grown parts shows the influence of natural convection to be the more significant factor in determining part shape and growth.

REFERENCES

- Beckermann, C., Ramadhyani, S., and Viskanta, R., 1987, "Natural Convection Flow and Heat Transfer Between a Fluid Layer and a Porous Layer Inside a Rectangular Enclosure," *J. Heat Trans.*, Vol. 109, pp. 363-370.
- Ergun, S., 1952, "Fluid Flow Through Packed Columns," *Chem. Eng. Prog.*, Vol. 48, pp. 89-94.
- Kandis, M. and Bergman, T. L., 1996, "Void Formation and Crack Propagation in Polymer Parts Grown by Non-Isothermal Sintering," in *Proc. of the National Heat Trans. Conf.*, edited by V. Prasad et al., HTD-Vol. 323, ASME, New York, pp. 199-206.

Kaviany, M., 1991, *Principles of Heat Transfer in Porous Media*, Springer-Verlag, New York.

Neale, G. and Nader, W., 1974, "Practical Significance of Brinkman's Extension of Darcy's Law: Coupled Parallel Flows Within a Channel and a Bounding Porous Medium," *Canadian J. Chem. Eng.*, Vol. 52, pp. 475-478.

Nelson, J. C., Xue, S., Barlow, J. W., Beaman, J. J., Marcus, H. L. and Bourell, D. L., 1993, "Model of Selective Laser Sintering of Bisphenol-A Polycarbonate," *Ind. Eng. Chem. Res.*, Vol. 32, pp. 2305-2317.

Norrell, J., Wood, K., Crawford, R., and Bergman, T., "Forced Convection in a Polymeric Powder," 1996, to be published in *Proc. 1996 SFF Symposium*, Austin, TX.

Seigel, R. and Howell, J. R., 1981, *Thermal Radiation Heat Transfer*, Hemisphere Publishing Company, U. S. A.

Keyword Index

- accuracy - 559
- ACES - 313
- adaptive control - 499
- adaptive meshing - 567
- adaptive slicing - 609
- aircraft modification - 57
- bases - 559
- Bézier curves - 597
- binders - 335, 385, 451
- CAD model - 299
- CAM-LEM - 355, 377
- cast-in place process - 281
- casting - 159
- casting rate - 167
- ceramic processing - 71
- ceramic prototypes - 141
- ceramic tape - 291, 377
- ceramics - 159, 327, 377, 385, 403, 411, 443
- ceramics, piezoelectric - 335
- ceramics, structural and functional - 71
- chemical vapor deposition - 227
- complex components - 384
- composites - 105, 307
- computational geometry - 597
- computer packaging - 31
- control architectures - 499
- controlled metal buildup - 141
- conveyed-adherent fabrication - 281
- copper - 191
- data extraction - 587
- defects - 384
- design engineering - 57
- direct photo shaping - 327
- direct slicing - 609
- discharge lamp - 321
- dispersants - 451
- electro-discharge - 175, 191, 199
- electrodeposition - 191, 199
- electrodes - 175, 191, 199
- embedded electronics - 31
- Ennex Fabrication Technologies - 281
- Extrusion Freeform Fabrication - 443
- fabrication - 57
- fault mechanisms - 575
- feature extraction - 57
- feedstock - 451
- fiber reinforced ceramics - 291
- filaments - 451
- finite difference method - 567
- finite element analysis - 523, 559, 619
- form-then-bond fabrication - 281
- foundry - 313, 419, 523
- Free Form Fabrication (FFF) - 167, 327
- functionally graded materials - 443
- fused deposition modeling - 419, 539
- Fused Deposition of Ceramics (FDC) - 265, 335, 385, 451
- fused deposition of metals (FDMet) - 335, 451
- fused silica - 335, 451
- gas metal arc welding - 249
- gas phase deposition - 227
- gas precursor decomposition - 345
- gas-phase SFF - 345
- gel casting - 71, 443
- genie fabricator - 281
- geometrical discretion - 299
- glass transition - 393
- graphite - 227, 307
- heat deflection temperature - 393
- hierarchical model decomposition - 609
- hot isostatic pressing (HIP) - 349
- injection molding - 97, 133, 167, 419
- investment casting - 1, 313, 523
- iron - 227

IVECS - 491
 jet - 191
 JP System 5 Desktop Rapid Prototyping - 609
 Karhunen-Loève Transform - 575
 laminated object manufacturing (LOM) - 105, 273, 291, 355, 515
 large structures - 207, 299
 laser ablation - 291
 laser beam control - 597
 laser cutting process - 515
 laser deposition - 117, 125
 Laser Engineered Net Shaping (LENS) - 125
 laser generating - 141
 laser power curve - 515
 laser wavelength - 345
 laser, copper-vapor - 291
 laser, diode - 363
 laser, frequency-multiplied Nd - 291
 laser, solid state - 369
 LaserCast - 239
 layered manufacturing - 355, 609
 layout optimization - 299
 machining - 191
 make-up fabrication - 299
 manufacturing - 239
 manufacturing information systems - 499
 Mars, fabricators on - 23
 mechanical properties - 385, 419, 559
 mechanisms - 117, 175
 mesh generation - 481
 metal prototypes - 117, 141, 523
 metal, direct deposition - 249
 metallic powders - 79, 89, 117, 149, 349
 metals - 125, 227, 249, 377, 411, 443, 507
 microcasting - 507
 mixing - 451
 modeling - 491, 539, 549, 567, 587
 molds - 71, 207
 molybdenum - 349
 Moon, fabricators on - 23
 multimaterial - 117
 NASA, use of fabricators by - 23
 near shape - 239
 nickel and nickel alloys - 125, 227
 nickel-iron alloys - 227
 NURBS - 597
 optical fiber - 321
 orientation optimization - 299
 paper bonding curve - 515
 paper cutting curve - 515
 paper bonding curve - 515
 parallel exposure - 321
 pattern removal - 313
 photo-gel casting - 327
 photolithography - 307
 photopolymerization - 403
 photopolymers - 307, 321, 393, 411, 471
 PID process control - 227
 point clouds - 481
 polycarbonate - 619
 process modelling - 459, 575
 profiled-edge lamination - 215
 PZT - 335, 451
 QuickCast - 1, 313
 R/P system - 321
 rapid manufacturing - 133
 rapid prototyping (RP) - 1, 57, 79, 97, 159, 167, 199, 239, 249, 355, 403, 481
 rapid tooling - 1, 57, 117, 133, 141, 149, 167
 RapidTool - 97
 real-time systems - 499
 residual stress - 507, 523

resin tooling - 1
 reverse engineering - 481
 robotic manipulator, fabrication - 281
 robotics - 249
 roller temperature curve - 515
 rubber mold - 159
 SALDVI - 345
 sand casting - 133
 section orientation mirroring - 609
 selective - 191
 selective area laser deposition (SALD) - 227, 345
 selective laser sintering (SLS) - 15, 79, 89, 97, 141, 349, 459, 549, 559, 567, 575
 series properties - 133
 shape deposition manufacturing - 117, 507
 shape error - 199
 shape metal deposition - 249
 shapemaker II - 609
 sheet-based fabrication - 215, 273, 281, 377
 shell cracking - 313
 shrinkage - 385, 471
 silicon nitride - 327, 385, 411, 451
 silicon rubber tooling - 1
 sintering, metal - 133
 sintering, polymer - 619
 slip - 159, 167
 slurry - 159
 soft tooling - 1
 solar-powered fabricators - 23
 Solid Freeform Fabrication (SFF) - 31, 71, 191, 199, 265, 345, 355, 363, 443, 491
 solid modeling - 313
 space, fabricators in outer - 23
 stainless steel - 125, 167, 335, 349, 411, 451
 stereodeposition - 257
 stereolithography (SLA) - 1, 9, 57, 63, 175, 299, 313, 321, 369, 393, 403, 471, 523
 STL files - 491, 587
 strength - 385, 411, 549
 superalloy - 349
 surface reconstruction - 355
 surface roughness - 199
 tangential cutting - 355
 technical prototypes - 133
 temperature control loop - 345
 thermal modeling - 459, 539, 549, 567, 619
 thermal post curing - 393
 thermal stability - 393
 thermal stresses - 117
 thermomechanical modeling - 507
 titanium (alloys) - 239, 349
 tolerance - 199, 507
 tools and dies - 125, 191, 207, 215
 tracking control - 597
 trajectory generation - 355
 UV lasing - 291
 video monitoring - 345
 void filling - 419
 WC-Co - 335, 451
 wear - 175
 welding - 249

SFF Symposium - 1996

Attendee List

M.K. Agarwala
(71, 335, 385, 451, 539)
University of Dayton Res. Institute
300 College Park
Dayton OH 45469-0150
magarwal@caip.rutgers.edu

Daniel Anderson
DePuy
700 Orthopaedic Drive
Warsaw IN 46581-0988
Phone: 219-372-7360
Fax: 219-267-6003
dla@depuy.com

Ralph E. Anderson, Jr.
United Technologies/Pratt & Whitney
MS 706/06, P. O. Box 109600
West Palm Beach FL 33410-9600
Phone: 561-796-6530
Fax: 561-796-6063
anderral@pwfl.com

Tom Armer
Aeroquip Corporation
2323 Green Road
Ann Arbor MI 48105-1530
Phone: 313-741-5311
Fax: 313-741-5333
tarmer@trinova.com

Alan Arthur (175)
Department of Manufacturing and Operations Management
University of Nottingham
University Park
Nottingham NG7 2RD
UK
Phone: +115 9514068
Fax: +115 9514150
epzrpl@epnl.maneng.nottingham.ac.uk

Mansour Ashtiani (9)
General Motors Corp/Delphi
Interior & Lighting
1401 Crooks Rd.
Troy MI 48084
Phone: 810-696-5212
Fax: 810-696-5100

Clint L. Atwood (125)
Sandia National Labs
P.O. Box 5800
MS 0958
Albuquerque NM 87185
Phone: 505-844-0816
Fax: 505-844-5589
clatwood@sandia.gov

Richard Aubin
United Technologies Res. Center
411 Silver Lane
M/S 129-48
East Hartford CT 06108
Phone: 860-727-1697
Fax: 860-727-7880
aubinrf@utrc.utrc.com

Badrinarayan Balasubramanian
Plynetics Corporation
627 McCormick Street
San Leandro CA 94577
Phone: 510-613-0529
Fax: 510-613-6213
bbala@plynetics.com

Amit Bandyopadhyay
(265, 335, 385, 451)
Rutgers University
Center for Ceramics Research
Piscataway NJ 08855-0909
Phone: 908-445-5617
Fax: 908-445-3258
amitband@rci.rutgers.edu

Jan Barber-Doyle
Cal State University Los Angeles
1241 Foothill Blvd.
Santa Ana CA 92705
Phone: 714-731-4221
Fax: 714-660-0444

Joel Barlow (15, 39, 47)
University of Texas
Chemical Engineering
Austin TX 78712
Phone: 512-471-1271
Fax: 512-471-7060
barlow@che.utexas.edu

Brian Bauman
Prototype Express, Inc
1425 Payne Rd.
Schaumburg IL 60173
Phone: 847-925-9900
Fax: 847-925-9901
bbauman@proex.com

James Beals
United Technologies Res. Center
Silver Lane, MS 129-22
East Hartford CT 06108
Phone: 860-727-7011
Fax: 860-727-7879
bealsjt@utrc.utrc.com

Joe Beaman
(39, 47, 89, 349, 597)
University of Texas
Mechanical Engineering
MC C2200
Austin TX 78712
Phone: 512-471-3058

John Benda
United Technologies Res. Center
411 Silver Lane
MS 129-39
East Hartford CT 06108
Phone: 860-727-7215
Fax: 860-727-7852
bendaja@utrc.utrc.com

Theodore L. Bergman (459, 619)
University of Connecticut
Department of Mechanical Engineering
191 Auditorium Rd. U-139
Storrs CT 06269-3139
Phone: 860-486-4198
Fax: 860-486-5088

Jack Beuth (507)
Carnegie Mellon University
Department of Mechanical Engineering
5000 Forbes Ave.
Pittsburgh PA 15213-3890
Phone: 412-268-3873
Fax: 412-268-3348
beuth@andrew.cmu.edu

Attendee List

Britton Birmingham
University of Texas
Mechanical Engineering
MC C2200
Austin TX 78712
Fax: 512-471-7681

Laura Bishop
3D Systems, Inc
26081 Avenue Hall
Valencia CA 91355
Phone: 805-295-5600
Fax: 805-295-6951

Rick Booth
DTM
1611 Headway Circle, Bldg 2
Austin TX 78754
Phone: 512-339-2922
Fax: 512-339-0634
@dtm-corp.com

J. C. Boudreaux (499)
National Institute of Stand. Tech.
Admin Room A621
Advanced Technology Program
Gaithersburg MD 20899
Phone: 301-975-3560
Fax: 301-548-1087
jackb@enh.nist.gov

David Bourell (39, 47, 79, 89)
University of Texas Mech. Engg.
MC C2200
Austin TX 78712
Phone: 512-471-3170
Fax: 512-471-7681
dbourell@mail.utexas.edu

Allen Brady (403)
University of Michigan
2219 HH Dow Bldg
2300 Hayward
Ann Arbor MI 48109
Phone: 313-936-0177
Fax: 313-747-4802
galbrady@umich.edu

Robert L. Brown
The Gillette Company
Prudential Tower Bldg
49th Floor
Boston MA 01299
Phone: 617-421-7604
Fax: 617-421-8484
robert_brown@gillette.com

Lawrence Brown (39, 47)
Allison Engine Co.
PO Box 420
Speed Code W-08
Indianapolis IN 46206-0420
Phone: 317-230-6124
Fax: 317-230-4470
ieleb@agt.gmeds.com

Suzanne Buchele
Argonne Nat'l Laboratory/UT
Austin
Dept. of Computer Sciences
Taylor Hall 2.124
Austin TX 78712-1188
Phone: 512-471-9585
Fax: 512-471-7866
buchele@cs.utexas.edu

Marshall Burns (23)
Ennex Fabrication Tech.
10911 Weyburn Ave., Ste. 332
Los Angeles CA 90024
Phone: 310-824-8700
Fax: 310-824-5185
marshall@ennex.com

Ivan Byford
Solid Geometrics, Inc.
18 Rawhide Road
Dayton TX 77535
Phone: 713-466-8647
Fax: 713-466-8813

Brian Carr
DTM
1611 Headway Circle
Bldg. 2
Austin TX 78754
Phone: 512-339-2922
Fax: 512-339-0634
carrb@dtm-corp.com

James D. Cawley (377)
Case Western Reserve University
Dept. Materials Science & Eng.
10900 Euclid Avenue
Cleveland OH 44106-7204
Phone: 216-368-6482
Fax: 216-368-3209
jxc41@po.cwru.edu

Isaac Chang
Univ of Birmingham
School of Metallurgy & Materials
Edgbaston Birmingham B15 2
TT
UK
Phone: +44 121 414 5167
Fax: +44 121 414 5232
I.T.Chang@Bham.ac.uk

Richard Chartoff (105, 471)
Univ. of Dayton
Rapid Prototype Development
Laboratory
300 College Park Ave.
Dayton OH 45469-0130
Phone: 513-229-2517
Fax: 513-229-2503
chartorp@udri.udayton.edu

Ken Wei Chen (597)
University of Texas @ Austin
Dept. Mechanical Engineering
ETC 5.160, MC C2200
Austin TX 78712-1063
Phone: 512-471-5838
Fax: 512-471-8727
kenwei@mail.utexas.edu

Chen Chi (515)
Helisys, Inc.
24015 Garnier St.
Helisys, Inc.
Torrance CA 90505
Phone: 310-891-0600 Ext. 281
Fax: 310-891-0626

Mark Chung
DTM
1611 Headway Circle, Bldg 2
Austin TX 78754
Phone: 512-339-2922
Fax: 512-339-0634
markc@dtm-corp.com

Michael Cima
Massachusetts Institute of
Technology
77 Massachusetts Ave.
MIT Room 12-011
Cambridge MA 01239
Phone: 617-253-6877
Fax: 617-258-6936
mjcima@mit.edu

Attendee List

Brad Cleveland
Market Manager, Material
Processing Systems
MTS Systems Corporation
14000 Technology Dr.
Eden Prairie MN 55344
Phone: 612-937-4077
Fax: 612-937-4515
brad.cleveland@mts.com

Arjan Coremans
Bavarian Laser Center
Egerlandstr. 11
Bavarian Laser Center
Erlangen 91058
Germany
Phone: +49 9131 85-7960
Fax: +49 9131 36 403
co@terra.lft.uni-erlangen.de

Rich Crawford (459, 597)
University of Texas
Mechanical Engineering
MC C2200
Austin TX 78712
Phone: 512-471-3030
Fax: 512-471-7682
rhc@mail.utexas.edu

Scott Crawford
Stanford University
P. O. Box 9768
Stanford CA 94309
Phone: 415-725-2069
Fax: 415-723-5034
wsc@leland.stanford.edu

Jim Crocker (345)
University of Connecticut
197 N. Eagleville Rd, U-136
Storrs CT 06269-3136
Phone: 860-486-4410
Fax: 860-486-4745
jec96001@uconnvm.uconn.edu

R. S. Crockett (257)
University of Arizona
4715 E. Ft. Lowell Rd.
Tucson AZ 85712
Phone: 520-322-2968
Fax: 520-322-2993
crockett@u.arizona.edu

Cheng Dai
Rutgers University
Center for Ceramic Research
P. O. Box 909
Piscataway NJ 08855-0909
Phone: 908-445-5574
Fax: 908-445-3258
cdai@caip.rutgers.edu

Kenneth Dalgarno (559)
University of Leeds
Dept. of Mechanical Engineering
Woodhouse Lane
Leeds LS2 9JT
U.K.
Phone: +44 113 233 2234
Fax: +44 113 233 2150
k.w.dalgarno@leeds.ac.uk

Jim Darrah
DTM Corporation
1611 Headway Circle, Bldg 2
Austin TX 78754
Phone: 512-339-2922
Fax: 512-339-0634
@dtm-corp.com

Suman Das (39, 47, 89)
University of Texas @ Austin
Dept. Mechanical Engineering
ETC 5.160, MC C2200
Austin TX 78712-1063
Phone: 512-471-5838
Fax: 512-471-8727
das@sffoffice.me.utexas.edu

Carl Deckard (549)
Clemson University
Mechanical Engineering
P. O. Box 340921
Clemson SC 29634-0921
Phone: 864-656-5642
Fax: 864-656-4435
carl.deckard@ces.clemson.edu

Mike Diamond
Helisys
24015 Garnier
Torrance CA 90505
Phone: 310-891-0600
Fax: 310-891-0626
miked@deltanet.com

Phill Dickens (175, 523)
University of Nottingham
University Park
Dept. of Man. Eng. & Ops.
Mangmt.
Nottingham NG7 2RD
England
Phone: +44 115 9514063
Fax: +44 115 9514000
philip.dickens@nottingham.ac.uk

Nick Dringenberg
Automation and Robotics Research
Institute
7300 Jack Newell Blvd. S
Ft. Worth TX 76118-7115
Phone: 817-272-5908
Fax: 817-272-5952
ndringen@arri.uta.edu

Patrick DuBois
University of Texas @ Arlington
7300 Jack Newell Blvd. South
Fort Worth TX 76118-7115
Phone: 817-272-5908
Fax: 817-272-5952
pdubois@arri.uta.edu

Ingo Ederer
FGB-TU-Munich
Arcisstr. 21
Munich 80290
Germany
Phone: +49 89 289 15 168
Fax: +49 89 289 15 192
ingo@fgb4.fgb.tu-muenchen.de

Harald Eifert
Fraunhofer USA
1 Innovation Way
Suite 301
Newark DE 19711
Phone: 302-369-6762
Fax: 302-369-6763
ei@ifam.fhg.de

Mike Ervin
DTM Corporation
1611 Headway Circle
Bldg. 2
Austin TX 78754
Phone: 512-339-2922
Fax: 512-339-0634
mikee@dtm-corp.com

Attendee List

Georges M. Fadel (491, 587)
Clemson University
Mechanical Engineering, EIB 202
Clemson SC 29634-0921
Phone: 864-656-5620
Fax: 864-656-4435
gfadel@eng.clemson.edu

John Fessler (117)
Stanford University
Department of Mechanical
Engineering
Stanford CA 94305-3030
Phone: 415-725-2031
Fax: 415-725-4862
fess@leland.stanford.edu

Tony Finizio
Sanders Prototype Inc.
P.O. Box 540
Pine Valley Mill
Wilton NH 03086
Phone: 603-654-5100
Fax: 603-654-2616

Eric Fodran (419)
ME Dept.
Cal Poly
San Luis Obispo CA 93407
Phone: 805-756-2153
efodran@tuba.aix.calpoly.edu

Paul Forderhase
DTM Corporation
1611 Headway Circle
Bldg. 2
Austin TX 78754
Phone: 512-339-2922
Fax: 512-339-0634
paulf@dtm-corp.com

Doug Freitag (349)
Bayside Materials Technology
17 Rocky Glen Ct.
Brookeville MD 20833
Phone: 301-570-3821
Fax: 301-570-3836
dfreitag@ix.netcom.com

Tim Fuesting (39, 47)
Allison Engine Co.
P. O. Box 420
Indianapolis IN 46206-0420
Phone: 317-230-5374
Fax: 317-230-4470

Paul Fussell
Alcoa Technical Center
100 Technical Dr
Alcoa Center PA 15069
Phone: 412-337-2721
Fax: 412-337-5944
fussell@atc.alcoa.com

Vito Gervasi
Milwaukee School of Engineering
1025 N. Broadway
Milwaukee WI 53202
Phone: 414-277-7189
Fax: 414-277-7470
gervasi@warp.mscoe.edu

Remy Glardon
Swiss Federal Institute of
Technology
Dept. of Mechanical Engineering
ME-ECUBLENS
1015 Lausanne
Switzerland
Phone: +21 693 5164
Fax: +21 693 3509
glardon@dgm.epfl.ch

Pam Goldston
Alcoa Fujikura Limited
12746 Cimarron Path, Ste. 116
San Antonio TX 78249
Phone: 210-208-8870
Fax: 210-558-6348
satcc01.goldst01@ssw.alcoa.com

Sundararaman Gopalan
University of Texas
Matl. Sci. and Engg.
MC C2200
Austin TX 78712
Phone: 512-471-3146
sgopalan@mail.utexas.edu

Damien Gray
DTM Corporation
1611 Headway Circle
Bldg. 2
Austin TX 78754
Phone: 512-339-2922
Fax: 512-339-0634
dfgray@dtm-corp.com

Alair Griffin
Lone Peak Engineering
12660 S. Fort St.
Draper UT 84020
Phone: 801-553-1732
Fax: 801-553-1734
alair@lonepeak.com

Curt Griffin
Lone Peak Engineering, Inc.
12660 South Fort St.
Draper UT 84020
Phone: 801-553-1732
Fax: 801-553-1734
lpe@lonepeak.com

Michelle Griffith (125)
Sandia National Laboratories
P. O. Box 5800, ms 0958
Albuquerque NM 87185
Phone: 505-284-2096
Fax: 505-844-5589
mlgriff@sandia.gov

Lance Groseclose (327)
Allison Engine Co
PO Box 420, Speed Code W-05
Indianapolis IN 46206-0420
Phone: 317-230-3806
Fax: 317-230-2866
ieleg@agt.gmeds.com

Richard Hague (523)
University of Nottingham
Manufacturing Engineering Dept.
University Park
Nottingham NG7 2RD
ENGLAND
Phone: +44 115 951 4033
Fax: +44 115 951 4150
epxrmh@epnl.nott.ac.uk

John W. Halloran (403)
The University of Michigan
2010 H. H.
Dow Bldg.
Ann Arbor MI 48109
Phone: 313-763-1051
Fax: 313-763-4788
John_Halloran@mse.engin.umich.edu

Attendee List

Gyoowan Han (291)
University of Dayton
300 College Park
Dayton OH 45469-0150
Phone: 513-299-3597
hang@udri.udayton.edu

Anne Hardy (327)
St. Gopain/Norton
Goddard Rd.
Northboro MA 01532
Phone: 508-351-7890
Fax: 508-351-7723
anne.b.hardy@sgc.infonet.com

Nicole Harlan (39, 47, 89)
The University of Texas at Austin
Dept. of Mechanical Engineering
MC C2200
Austin TX 78712
Phone: 512-471-3578
Fax: 512-471-7681

Shay Harrison (345)
University of Connecticut
97 North Eagleville Rd.
Storrs CT 06269
Phone: 860-486-4410
Fax: 860-486-4745
slh95001@uconnvm.uconn.edu

Marge Hartfel
3M
3M Center
Building 235-BC-09
St. Paul MN 55144
Phone: 612-737-2342
Fax: 612-736-1379
mahartfel@mmm.com

Ken Hayworth (281)
Ennex Fabrication Technologies
10911 Weyburn Ave., Ste. 332
Los Angeles CA 90024
Phone: 310-824-8700
ken@ennex.com

Uday Hejmadi (97)
DTM Corporation
1611 Headway Circle
Bldg. 2
Austin TX 78754
Phone: 512-339-2922
Fax: 512-339-0634
udayh@dtm-corp.com

Greg Hilmas (443)
Advanced Ceramics Research
841 E. 47th St.
Tucson AZ 85713
Phone: 520-792-2616
Fax: 520-792-2635
ghilmas@theriver.com

Robert Hoffman (443)
Advanced Ceramics Research
851 E. 47th St.
Tucson AR 85713
Phone: 520-792-2616
Fax: 520-792-2635
robert@theriver.com

Steven Hofhiens
Southwest Texas State University
1932 Squire Circle
New Braunfels TX 78130
Phone: 210-522-5389
Fax: 210-522-5720
shofhiens@swri.edu

Bernard Hon (167)
Rapid Prototyping Centre
Department of Industrial Studies
University of Liverpool
Liverpool L69 3BX
UK
Phone: +(44) 151-794-4680
Fax: +(44) 151-794-4693
hon@liverpool.ac.uk

Michael House (239)
The John Hopkins University
Applied Physics Laboratory
Johns Hopkins Rd.
MS 6/358
Laurel MD 20723-6099
Phone: 301-953-6000, Ext. 4662
Fax: 301-953-5937
michael.house@jhuapl.edu

Luca Iuliano (199)
Politecnico di Torino
Department of Production System
& Economics
Corso Duca degli Abruzzi 24
Torino 10129
ITALY
Phone: ++39 11 5647277
Fax: ++39 11 5647299
lppolito@polito.it

Ian Jackson (9)
Craniofacial Institute,
Providence Hospital
16001 W. Nine Mile Rd.
3rd Floor, Fisher Center
Southfield MI 48075
Phone: 810-424-5800
Fax: 810-424-5881

Todd Jackson
MIT
77 Massachusetts Ave.
Rm. 5-424
Cambridge MA 02139
Phone: 617-253-8295
trjackso@mit.edu

Kevin Jakubenas
The University of Texas at Austin
Center for MS&E
MC C2201
Austin TX 78712
kjjakubenas@mail.utexas.edu

Vikram R. Jamalabad (71, 335)
Allied Signal Res. & Technology
101 Columbia Rd.
Morristown NJ 07962-1021
Phone: 201-455-3668
Fax: 201-455-5991
jamalabad@research.allied.com

Suresh Jayanthi (393)
DuPont SOMOSTM
Solid Imaging Materials Group
Two Penn's Way, Ste. 401
New Castle Delaware 19720
Phone: 302-328-5635
Fax: 302-328-5693

Larry Jepson
University of Texas Mech. Engg
MC C2200
Austin TX 78712
Phone: 512-471-5838
Fax: 512-471-8727
larry@sffoffice.me.utexas.edu

Elizabeth Judson
Georgia Tech
2840 Windrush Ln
Roswell GA 30076
Phone: 770-442-5236
Fax: 770-475-5371
gt4684d@prism.gatech.edu

Attendee List

Gary Kalmanovich (273)
Helisys
24015 Garnier St.
Torrance CA 90503
Phone: 310-891-0600 Ext. 271
Fax: 310-891-0626
gkalman@cinenet.net

Bernd Keller
IKP, Institute of Polymer Testing
and Polymer Science
University of Stuttgart
Boeblingerstraße 78E
Stuttgart 70199
Germany
Phone: +49 711 641 2269
Fax: +49 711 641 2264
keller@ikpindy2.verfahrenstechnik.
uni-stuttgart.de

Andrew Kelley III
MIT
Ashdown House
305 Memorial Dr. 607-C
Cambridge MA 02139
Phone: 513-634-7379
Fax: 513-634-1509
kelley/a.@pg.com

John Kietzman
Stanford University
Bldg. 530 Rm. 128
Stanford CA 94305-3030
Phone: 415-723-0565
Fax: 415-723-5034
kietzman@leland.stanford.edu

Lena Apelskog Killander
The Swedish Institute of
Production Eng Research (IVF)
Research IVF
Brinellvagen 81
S-100 44 Stockholm
SWEDEN
Phone: +468 219864
Fax: +468 202227
lenaak@cadcam.kth.se

Hiroyuki Kishi
Nissan Res. and Development Inc.
39001 Sunrise Dr.
Farmington Hills MI 48331
Phone: 810-488-4016
Fax: 810-488-3914

Donald Klosterman (105)
University of Dayton
Rapid Prototype Development Lab.
300 College Park
Dayton OH 45469-0131
Phone: 513-229-2794
Fax: 513-229-2503
klosterman@udri.udayton.edu

Ronald Knight (349)
Lockheed Martin
M/S PT-91
P. O. Box 650003
Dallas TX 75265-0003
Phone: 214-603-7868
Fax: 214-603-9052
ronald.c.knight@lmco.com

Martin Koch (419)
IME Department Cal Poly
Cal Poly University
San Luis Obispo CA 93407
Phone: 805-756-1114
mkoch@calpoly.edu

Venkateswarlu Kondury
Protocepts (INDIA) PVT.LTD
8-3-960110, Sprinagar Colony
Hyderabad AP 500873
INDIA
Phone: (011)91 40 374 5118
Fax: (011)91 40 841 697

Ken Kornele
3M
6801 River Place Blvd.
Austin TX 78726
Phone: 512-984-6567
Fax: 512-984-5960
klkornele@mmm.com

Jack Lane
Metals Technology Corp.
P.O. Box 320
Shirley IN 47384
Phone: 317-737-6551
Fax: 317-737-6553

Cheol Lee (207, 609)
University of Utah
814 University Village
Salt Lake City UT 84108
Phone: 801-581-4133
cheol.lee@m.cc.utah.edu

Goon Hee Lee (15, 39, 47)
University of Texas
Chemical Engineering Department
Austin TX 78712
Phone: 512-471-6910
goonhee@che.utexas.edu

Derek Leighton
DTM Corporation
1611 Headway Circle
Bldg. 2
Austin TX 78754
Phone: 512-339-2922
Fax: 512-339-0634
derekl@dtm-corp.com

Allan Lightman (105, 291)
University of Dayton Research
Institute
300 College Park
Dayton OH 45469-0150
Phone: 513-229-3966
Fax: 513-229-3433
lightman@udri.udayton.edu

David Lucey
Pratt & Whitney
P.O. Box 109600
West Palm Beach FL 33410
Phone: 561-796-5690
Fax: 561-796-4500

John Male (1)
Ctr. for Rapid Design and
Manufacture
Dept. of Engineering Technology
Buckingham College, Queen
Alexandra Rd.
High Wycombe Buckinghamshire
HP11 2JZ
England
Phone: 01494 605085
Fax: 01494 538593
jmale01@buckscol.ac.uk

Gerald Manning
DTM Corporation
1611 Headway Circle
Bldg. 2
Austin TX 78754
Phone: 512-339-2922
Fax: 512-339-0634

Attendee List

Tariq Manzur (345, 363)
University of Connecticut
Photonics Research Center
260 Glenbrook Road, U-192
Storrs CT 06269-2192
Phone: 860-486-1961
Fax: 860-486-1033
tariq@eng2.uconn.edu

Harris Marcus (345, 363)
University of Connecticut
Institute of Materials Science
Storrs CT 06269-3136
Phone: 860-486-4623
Fax: 860-486-4745
hmarcus@mail.ims.uconn.edu

Yoji Marutani (321)
Faculty of Engineering
Osaka Sangyo University
3-1-1 Nakagaito
Daito-City Osaka 550
Japan
Phone: +81-0720-75-3001
Fax: +81-0720-70-1401
marutani@ise.osaka-sandai.ac.jp

James Maxwell (227)
Rensselaer Polytechnic Institute
45A Suncrest Dr.
Waterford NY 12188
Phone: 518-276-6999
Fax: 518-276-6025
maxwell@unix.cie.rpi.edu

Kevin McAlea (97)
DTM
1611 Headway Circle
Bldg. 2
Austin TX 78754
Phone: 512-339-2922
Fax: 512-339-0634
kevinmc@dtm-corp.com

Christopher McDowell (313)
Johnson & Johnson Professional, Inc.
325 Paramount Dr.
Raynham MA 02767-0350
Phone: 508-880-8102
Fax: 508-880-8122
cmcdowel@jjpraycl.jnj.com

David McKay (23)
Earth Science and Solar System
Exploration Div.
MC SN, L. B. Johnson Space Cntr
Houston TX 77058
Phone: 713-483-5048
Fax: 713-483-5347
dmckay@snmail.jsc.nasa.gov

Robert Merz (31, 117)
Stanford Univ
Mechanical Eng
Stanford CA 94305-3030
Phone: 415-725-0107
Fax: 415-723-5034
rmerz@leland.stanford.edu

Dan Mikel
Kodak Model Shop
210 Lake Shore Dr.
Hilton NY 14468
Phone: 716-726-3425
Fax: 716-726-5563
dmikel@kodak.com

Jon Miller
DTM Corporation
1611 Headway Circle
Bldg. 2
Austin TX 78754
Phone: 512-339-2922
Fax: 512-339-0634

Reza Mirshams
Southern University
Dept. of Mechanical Engineering
Baton Rouge LA 70813
Phone: 504-771-4701
Fax: 504-771-4877
mirshams@engr.subr.edu

Mike Mitchell
Astro Met
9974 Springfield Pike
Cincinnati OH 45215
Phone: 513-772-1242 x118
Fax: 513-772-9080

Takeo Nakagawa (159)
Institute of Industrial Science
University of Tokyo
22-1, ROPPONGI, 7-CHOME,
MINATOKU
Tokyo
Japan
Phone: +81-3-3402-6231 Ext.
2245
Fax: +81-3-3479-1523
noguchi@kappa.iis.u-tokyo.ac.jp

Rajiv Nambiar
University of Texas-Pan American
1201 W. University Dr.
Engineering Dept.
Edinburg TX 78539
Phone: 210-316-7056
nambiar@panam.edu

Kesh Narayanan
Nat'l Science Foundation
4201 Wilson Blvd., Rm 590
Arlington VA 22230
Phone: 703-306-1390
Fax: 703-306-0337
knarayan@nsf.gov

Christian Nelson
DTM Corporation
1611 Headway Circle
Bldg. 2
Austin TX 78754
Phone: 512-339-2922
Fax: 512-339-7981
nelson@dtm-corp.com

Wyatt Newman (355)
Case Western Reserve University
Cleveland OH 44106
wsnewma@isrc.sandia.gov

Hiroyuki Noguchi (159)
Institute of Industrial Science
University of Tokyo
22-1 Roppongi, 7-Chome, Minato-Ku
Tokyo 106
Japan
Phone: +81 3 3402 6231 ext. 2246
Fax: +81 3 3479 1523
noguchi@cc.iis.u-tokyo.ac.jp

Attendee List

Jeff Norrell (459, 619)
The University of Texas at Austin
ETC 4.118, C2200
Austin TX 78712
Phone: 512-471-7347
norrell@utnems.me.utexas.edu

Greg Norwood
The University of Texas at Austin
Mechanical Engineering
MC C2200
Austin TX 78712
USA

Andrei Novac (609)
University of Utah
3209 MEB
Salt Lake City UT 84112
Phone: 801-581-4133
asn8200@u.cc.utah.edu

Olli Nyrhila
Electrolux Rapid Development
Atiolantie 17
FIN 21290 RUSKO
Finland
Phone: +358 2 4365611
Fax: +358 2 4365620

Chris O'Neill
United Technologies-Pratt &
Whitney
400 Main St.
M/S 118-40
East Hartford CT 06108
Phone: 203-565-2729
Fax: 203-565-9614
oneillcf@pweh.com

Amod Ogale (307)
Clemson University
Dept. of Chemical Engineering
16 Earle Hall
Clemson SC 29634-0909
Phone: 864-656-5483
Fax: 864-656-0784
amod.ogale@ces.clemson.edu

Thomas Pang
Ciba-Geigy Corporation
5121 San Fernando Rd.
Los Angeles CA 90039
Phone: 818-265-7151
Fax: 818-507-0167
thomas.pang@usla.mhs.ciba.com

Jouni Partanen (63, 369)
3D Systems
26081 Avenue Hall
Los Angeles CA 91355
Phone: 805-295-5600 Ext. 2443
Fax: 805-295-0249

Jerri L. Paul (57)
University of Texas
1411 Mesa Park Dr.
Round Rock TX 78664
Phone: 512-310-9344
Fax: 817-867-2188
jerrip@mail.utexas.edu

Joseph Pegna (227)
RPI
Dept. of MEAE&M
JEC5022
Troy NY 12180
Phone: 518-276-6999
Fax: 518-276-2623
pegnej@rpi.edu

Elaine Persall
Clemson Univ
PO Box 340921
Clemson SC 29634-0921
Phone: 864-656-0321
Fax: 864-656-4435
persall@clemson.edu

Theo Pintat
Fraunhofer Institute fuer
angewandte Materialforschung IfaM
Lesumer Heerstr. 36
Bremen 28717
Germany
Phone: +49 421 6383153
Fax: +49 421 6383230
pi@ifam.fhg.de

Reginald D. Ponder
Georgia Tech
Manufacturing Research Center
813 Ferst Dr.
Atlanta GA 30332-0406
Phone: 404-894-7688
Fax: 404-894-0957
Reginald.ponder@marc.gatech.edu

Matthew Pope (411)
Ceramic Composites, Inc.
133 Defense Hwy
Suite 212
Annapolis MD 21401
Phone: 410-224-3710
Fax: 410-224-4678

William Priedeman (451)
Stratasys, Inc.
14950 Martin Dr.
Eden Prairie MN 55344-2020
Phone: 612-906-2226
Fax: 612-937-0070
bpriede@stratasys.com

Fritz Prinz (31, 117)
Stanford Univ
Dept of Mechanical Engineering,
Bldg 530
Stanford CA 94305-3030
Phone: 415-723-0084
Fax: 415-723-5034
fbp@cdr.stanford.edu

Brian Priore (105)
University of Dayton
Research Institute
300 College Park
Dayton OH 45469
Phone: 513-229-4363
bpriore@engr.udayton.edu

Sadegh Rahmati
University of Nottingham
The Department of Manufacturing
Engineering and Operations Mgmt.
University Park
Nottingham UK NG7 2RD
UK
Phone: (0115)951-4033
Fax: (0115)951-4150
epxsr@enpl.nott.ac.uk

Fred Ranieri
Rockwell Science Center
1049 Camino Dos Rios
Thousand Oaks CA 91360
Fax: 805-373-4775

Attendee List

Anshuman Razdan
PRISM
Arizona State University
MC 5106
Tempe AZ 85287-5106
Phone: 602-965-5368
Fax: 602-965-2910
razdan@asu.edu

Allan Rennie (191)
CRDM, Department of Engineering
Technology
Buckinghamshire College
High Wycombe
Buckinghamshire HP11 2JZ
UK
Phone: +(44) 1494 605085
Fax: +(44) 1494 538593
arenni01@buckscol.ac.uk

Fernando Ribeiro (249)
Universidade do Minho
Departamento de Electronica
Industrial
Campus de Azurem
4800 Guimaraes
PORTUGAL
Phone: +351 53 510190
Fax: +351 53 510189
Fernando@dei.uminho.pt

Andreas Rigel
IWB
Krautgartenweg 24
Leitershofen 86391
Germany
Phone: +49 821 433489

Stefan Rigel
IWB
Otto-Lindenmeyer-Straße 30G
Angsburg 86153
Germany
Phone: +49 821 56883 37
Fax: +49 821 56883 50
be@iwb.mw.tu-muenchen.de

Stephen J. Rock (149)
Rensselaer Polytechnic Institute
Center for Advanced Technology
CII 8015
Troy NY 12180
Phone: 518-276-8652
rocks@cat.rpi.edu

Albert Rodriguez
ALCOA
121 Johnson Blvd
Del Rio TX 78840
Phone: 210-703-7252

Joe Rosales
3M
6801 River Place Blvd.
A141-1N-10
Austin TX 78726-9000
Phone: 512-984-2728
Fax: 512-984-5960
jjrosales2@mmm.com

Carl Russo
Allison Engine Co.
P.O. Box 420
Speed Code W13
Indianapolis IN 46206-0420
Phone: 317-230-5961
Fax: 317-230-2990

G. R. Ryder (567)
Leeds University
Flat 433 Sentinel Towers
Burley Street
Leeds Yorkshire LS3 1LD
England
Phone: +44 113 233 5472
gerard@scs.leeds.uk.ac

Emanuel Sachs
Massachusetts Institute of
Technology
77 Massachusetts Ave, Rm 35-136
Cambridge MA 02139
Phone: 617-253-5381
Fax: 617-253-0209
sachs@mit.edu

Roy Sanders
Pine Valley Mall
Box 540
Wilton NH 03086
Phone: 603-654-5100-203
Fax: 603-654-2616

Marc Sauerhoefer
Pratt & Whitney Aircraft
400 Main St.
Mail Stop 11438
East Hartford CT 06018
Phone: 860-565-3264

Wayde R. Schmidt
United Technologies Res. Center
411 Silver Lane
MS 129-26
East Hartford CT 06108
Phone: 860-727-1660
Fax: 860-727-7879
schmidwr@utrc.utc.com

John Schultz (471)
University of Dayton
300 College Park, KLA-11
Dayton OH 45469-0131
Phone: 513-229-4363
Fax: 513-229-2503
schultjw@main.udri.udayton.edu

Sandra Seitz
DTM GmbH
Otto-Hahn-Str. 6
Hilden 40725
Germany
Phone: +49 2103 9577 16
Fax: +49 2103 52265
seitzs@dtm-corp.com

Mohammed Shaarawi
University of Texas
Mechanical Engineering
MC C2200
Austin TX 78712
USA

Kabot Simon
DTM
1611 Headway Circle
Bldg. 2
Austin TX 78754
Phone: 512-339-2922
Fax: 512-339-0634

Jean Smith
DTM
1611 Headway Circle
Bldg. 2
Austin TX 78754
Phone: 512-339-2922
Fax: 512-339-0634
jeans@dtm-corp.com

Attendee List

Norman T. Smith
Ford Motor Co.
36200 Plymouth Rd., Drop13
Livonia MI 48150
Phone: 313-523-5005
Fax: 313-523-0180
nsmith5@tc1448.ford.com

Steven Smith (57)
Chrysler Technologies Airborne
Systems
P.O. Box 154580
MS 2022
Waco TX 76715-4580
Phone: 817-867-4149
Fax: 817-867-2188
as08066@7601po.ctas.ctas.com

Geoff Smith-Moritz
Rapid Prototyping Report
1010 Turquoise St., #320
San Diego CA 92109
Phone: 619-488-0533
Fax: 619-488-6052
rpreport@aol.com

Kenneth R. Stanley Jr.
Clemson University
124 Fluor
Daniel Engg Innovation Bldg
Clemson SC 29634
Phone: 864-226-8709
kstanle@clemson.edu

Jim Stewart
Delco Electronic
2212E CO R.d 300 S
Danville IN 46122
Phone: 317-745-5133
Fax: 317-745-5133

Rocky Stewart
DTM
1611 Headway Circle
Bldg. 2
Austin TX 78754
Phone: 512-339-2922
Fax: 512-339-0634
rocky@dtm-corp.com

Brent Stucker
Texas A&M University
Mechanical Engineering Dept.
College Station TX 77843-3123
Phone: 409-847-9234
Fax: 409-845-3081
stucker@tamu.edu

Kevin Stuffle (443)
Materials and Machines, Co.
5775 S. Old Spanish Tr
Tucson AZ 85747
Phone: 520-647-3437
Fax: 520-647-3448
stuffle@theriver.com

Richard Sudduth
Mississippi Polymer Institute
Box 10003
Hattiesburg MS 39406
Phone: 601-266-4607
Fax: 601-266-5504
rsudduth@whale.st.usm.edu

Atul Sudhalkar
Aeroquip Corporatin
2323 Green Rd
Ann Arbor MI 48105-1530
Phone: 313-741-5318
Fax: 313-741-5333
atuls@umich.edu

Bill Swanson
Stratasy
14950 Martin Dr.
Eden Prairie MN 55344
Phone: 612-906-2282
Fax: 612-937-0070
bswanson@stratasy.com

Shoichi Terashima
Nissain DTM Co., Ltd.
Kyoto Research Park, Sci. Ctr.
Bldg. 3
1, Awata-Cho, Chudoji
Shimogyo-Ku Kyoto 600
Japan
Phone: +81 -75 315 9800
Fax: +81- 75 315 9811
KYA02310@niftyserve.or.jp

Charles L. Thomas (207, 281,
609)
University of Utah
Department of Mechanical
Engineering
Salt Lake City UT 84112
Phone: 801-585-6939
Fax: 801-581-8692
cthomas@me.mech.utah.edu

Jim Tobin
Procter & Gamble
6110 Center Hill Ave.
Cincinnati OH 45224
Phone: 513-634-2392
Fax: 513-634-4588
tobin.jr@pg.com

Irem Tumer (575)
The University of Texas at Austin
Dept. of Mechanical Engineering
Graduate Research Assistant
Austin TX 78712
Phone: 512-471-7347
Fax: 512-471-8727
irem@bertoni.me.utexas.edu

Jill S. Ullett (471)
University of Dayton Res. Institute
Dayton OH
Phone: 513-229-3609
ullettjs@udri.udayton.edu

Neal Vail (481)
Daimler Benz Research Center
P. O. Box 2360
Wilhelm-Runge-Strasse 11
Ulm D-89013
Germany
Phone: +49 731-505-2885
Fax: +49 731-505-4212
vail@dbag.ulm.DaimlerBenz.COM

Douglas VanPutte
Eastman Kodak Company
1669 Lake Ave., Bldg. 604
Rochester NY 14652-4102
Phone: 716-477-1492
Fax: 716-722-0810
vanputte@kodak.com

Attendee List

Susanna Ventura (327)
SRI International
333 Ravenswood Ave.
Menlo Park CA 94025
Phone: 415-859-4467
Fax: 415-859-2316
Susanna_Ventura@qm.sri.com

Craig Wadham
DTM
1611 Headway Circle
Bldg. 2
Austin TX 78754
Phone: 512-339-2922
Fax: 512-339-0634
craigw@dtm-corp.com

Daniel Walczyk (149, 215)
Rensselaer Polytechnic Institute
Department of Mechanical
Engineering
Jonsson Engineering Center
Troy NY 12180-3590
Phone: 518-276-2397
Fax: 518-276-2623
walczd@rpi.edu

Jian Xin Wang
University of Texas
Mechanical Engineering
MC C2200
Austin TX 78712
Phone: 512-471-5838
wangjx@mail.utexas.edu

Wanlong Wang (299)
National University of Singapore
Department of Mechanical &
Production Engineering
10 Kent Ridge Crescent
Singapore 119260
Singapore
Phone: +65 7726483
Fax: +65 7791459
mpewwl@leonis.nus.sg

Paul Wehner
Fraunhofer USA
15 St. Mary's St.
Boston MA 02215
Phone: 617-353-1836
Fax: 617-353-1896
pwehner@fraunhofer.bu.edu

Lee Weiss (31, 117)
Carnegie Mellon University
207 Smith Hall
Pittsburgh PA 15213
Phone: 412-268-7657
lew@cs.cmu.edu

Christian Wilkening (133)
EOS GmbH
Pasingenstr. 2
Munich 82152
Germany
Phone: +49 89-89913132
Fax: (+49) 89-8599962

John Williams (549)
Clemson University
109 Pleasant View Dr.
Clemson SC 29631
Phone: 864-654-6661
Fax: 864-656-4435
willia4@ces.clemson.edu

Holger Wirtz (141)
Fraunhofer Institute of Production
Technology
Steinbachstr. 17
Aachen 52074
Federal Republic of Germany
Phone: +49 241 8904 120
Fax: +49 241 8904 198
wiz@ipt.twth-aachen.de

Martin Wohler (79)
University of Texas at Austin
Material Science and Engineering
Austin TX 78712-1063
Phone: 512-471-3578
Fax: 512-471-7681
mwohler@mail.utexas.edu

Joseph Wright (349)
Lockheed Martin Vought Systems
P.O. Box 650003
Mail Stop SK-03
Dallas TX 75265-0003
Phone: 214-603-2507
Fax: 214-603-0419
wrightjm@vs.lmco.com

M. Atif Yardimci (539)
University of Illinois at Chicago
842 W. Taylor
2039 ERF (m/c 251)
Chicago IL 60607-7022
Phone: 312-413-7408
Fax: 312-413-0447
ayardil@uic.edu

Stephen A. Yencho
Stanford University
Bldg. 530 Rm 214
Stanford CA 94301-3030
Phone: 415-723-0234
Fax: 415-723-5034
yencho@leland.stanford.edu

Walter Zimbeck (411)
Ceramic Composites, Inc.
133 Defense Hwy., Ste. 212
Annapolis MD 21401
Phone: 410-224-3710
Fax: 410-224-4678
tatinc@aol.com